European
Seismological Commission

IUGG

31st General Assembly

Short Papers

Creta Maris Conference Center

Hersonissos, Crete island, Greece

7-12 September, 2008

The Concepts of Complex Network Advance Understanding of Earthquake Science

Abe S (1,2), Suzuki N (3)

(1) Department of Physical Engineering, Mie University, Tsu, Mie 514-8507, Japan, suabe@sf6.so-net.ne.jp
(2) Institut Supérieur des Matériaux et Mécaniques Avancés, 44 F. A. Bartholdi, 72000 Le Mans, France
(3) College of Science and Technology, Nihon University, suzu@phys.ge.cst.nihon-u.ac.jp

Keywords: earthquake, complex network, scale-freeness, small-worldness, hierarchical organization

Introduction

There is growing interest in the earthquake phenomenon from the view point of the science of complex systems. Though seismicity is characterized by remarkably rich phenomenology, some of known empirical laws are rather simple. The scale-free natures of the cerebrated Omori law (Omori, 1894), and the Gutenberg-Richter law (Gutenberg & Richter, 1944), indicate existence of long-time correlation and difficulty of distinguishing earthquakes by the values of magnitude.

In the recent works (Abe & Suzuki, 2003, 2005a), we have found that both spatial distance and time interval between two successive events well obey the *q*-exponential distributions in nonextensive statistics (Tsallis, 1988; Abe & Okamoto, 2001), which offers a statistical-mechanical framework for describing complex systems. The fact that two successive events obey such definite laws means that successive events are strongly correlated no matter how large spatial distance is. There is, in fact, an observation (Steeples & Steeples, 1996) that an earthquake can be triggered by a foregoing one, which is more than 1000 km away. This implies that the seismic correlation length can enormously be large and long-wave-length modes of seismic waves play an important role. This has a strong similarity to phase transitions and critical phenomena. Thus, it may not be appropriate to put spatial windows in analysis of seismicity, in general, and whole data in a relevant area (ideally the whole globe, though still not satisfactorily available) should be treated based on the nonreductionistic standpoint.

In contemporary science, much attention is paid to statistical mechanics of complex networks (Albert & Barabási, 2002; Dorogovtsev & Mendes, 2003), which provides a novel procedure for analysis of man-made as well as natural complex systems. In the network picture, vertices and edges represent elements and interrelation (i.e., interaction or correlation) between them, respectively. A primary purpose there is to understand the topological, statistical, and dynamical features of the networks.

Such a concept was introduced to seismology by the present authors in 2004 (Abe & Suzuki, 2004a) in order to represent complexity of seismicity. The seismic time series data are mapped to a growing stochastic network in a simple and an unambiguous way (see *II-2*). Vertices and edges of such a network correspond to coarse-grained events and event-event correlations, respectively. Yet unknown microscopic dynamics governing event-event correlations and fault-fault interactions is replaced by these edges. Global physical properties of seismicity can then be explored by examining its geometric (e.g., topological etc.) and dynamical features. It turns out that earthquake network has a number of interesting properties, some of which are shared by many other natural as well as artificial systems including metabolic networks, food webs, the Internet, and the world-wide web and so on. This, in turn, enables seismologists to study seismicity in analogy with such relatively better understood complex systems. Thus, the network approach offers a novel way of analyzing seismic time series and casts fresh light on the physics of earthquakes (Abe & Suzuki, 2008).

Materials and Methods

The Data

In this article, we have analyzed the seismic data taken from California [the Southern California Earthquake Data Center (http://www.data.scec.org/)] in the following two spacio-temporal regime:

data (A) The time interval analyzed is between 00:25:8.58 on January 1, 1984 and 22:21:52.09 on December 31, 2003. The region covered is 29°06.00'N–38°59.76'N latitude and 113°06.00'W–122°55.59'W longitude with the maximal depth 175.99km. The total number of events is 367613,

data (B) The analyzed period is between 00:25:8.58 on January 1, 1984 and 22:50:49.29 on December 31, 2004. The region covered is 28°36.00'N–38°59.76'N latitude and 112°42.00'W–123°37.41'W longitude with the maximal depth 175.99km. The total number of the events is 379728.

Both data contain no threshold for magnitude (but “quarry blasts” are excluded from the analysis).

The Method

The method of the construction of the complex network for earthquakes is as follows (Abe & Suzuki, 2004a). A geographical region under consideration is divided into a lot of small cubic cells. A cell is regarded as a vertex if earthquakes with any values of magnitude occurred therein. Two successive events define an edge between two vertices. In this way, the complex fault-fault interaction is replaced by this edge. If two successive events occur in the same cell, a tadpole loop is attached to that vertex. This procedure enables one to map the seismic time series to an evolving network (see Figure 1(a)).
This construction contains a unique parameter which is the cell size. Once the cell size is fixed, an earthquake network is unambiguously defined. However, since there exist no *a priori* operational rules to determine the cell size, it is of importance to examine how the properties of an earthquake network depend on this parameter.
An earthquake network is a directed network in its nature. Directedness does not bring any difficulties to statistical analysis of connectivity (degree, i.e., the number of edges attached to the vertex under consideration) since, by construction, in-degree and out-degree are identical for each vertex except the initial and final ones in analysis. Thus, we shall not distinguish in-degree and out-degree from each other in the analysis of the connectivity distribution (see *III-1* and *III-4*). However, directedness becomes essential when the path length (the number of edges) between a pair of connected vertices, i.e., the degree of separation between the pair, is considered. This point is explicitly discussed in the analysis of the period distribution in *III-5*.
A full directed earthquake network has to be reduced to a simple undirected network, when its small-worldness and hierarchical structure are examined (see *III-2* and *III-3*). There, tadpole loops are removed and each multiple edge is replaced by a single edge (see Figure 1(b)). The path length in this case is the smallest value among the possible numbers of edges connecting a pair of vertices.

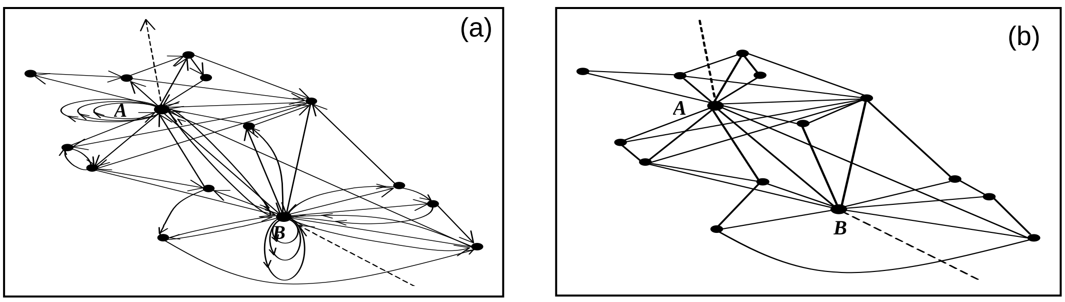

Figure 1. (a) A schematic description of an earthquake network. The dashed lines correspond to the initial and final events. The vertices, A and B, contain main shocks and play roles of hubs of the network. (b) The undirected simple network reduced from the network in (a).

Results and Discussion

Scale-Free Nature of Earthquake Network

We study the scale-free nature of an earthquake network by evaluating the connectivity distribution (or, the degree distribution), $P(k)$, which is defined as the probability of finding vertices with k edges in a network. Connectivity of a classical random network obeys the Poissonian distribution in the limit of the large number of vertices, $P(k) = e^{-\lambda}\lambda^k / k!$ (λ: a positive parameter, $k = 0,1,2,\ldots$), whereas a scale-free network (Albert & Barabási, 2002; Dorogovtsev & Mendes, 2003) has a power-law shape for large k,

$$P(k) \sim k^{-\gamma}, \qquad (1)$$

where γ is a positive exponent.

We present the connectivity distribution of the full earthquake network with tadpole loops and multiple edges in Figure 2 (Abe & Suzuki, 2004a, 2006a). From it, we see that the earthquake network in fact obeys the connectivity distribution of the form in Eq. (1) and therefore is scale free. The smaller the cell size is, the larger the exponent, γ, is. This is natural since the number of vertices with large values of connectivity decreases as the cell size decreases. However, trend remains unchanged for the different values of the cell size.

The scale-free nature of the earthquake network can be interpreted as follows. The earthquake network has a few special vertices which have large values of connectivity (see the vertices A, B in Figure 1). Such vertices are termed “hubs”. A striking feature we discovered from the data analysis is that aftershocks associated with a main shock tend to return to the locus of the main shock, geographically, making the vertex of the main shock a hub. The situation is analogous to the preferential attachment rule for a growing network. According to it, a newly created vertex tends to be connected to the (already existing) i th vertex with connectivity k_i with probability, $\Pi(k_i) = k_i / \sum_j k_j$. This rule can generate a scale-free network characterized by the power-law connectivity distribution of the form in Eq. (1) (Barabási & Albert, 1999). As mentioned above, aftershocks associated with a main shock tend to be connected to the vertex of the main shock, satisfying the preferential attachment rule. On the other hand, the Gutenberg-Richter law states that frequency of earthquakes decays slowly as a power law with respect to released energy. This implies that there appear quite a few giant components, and accordingly the network becomes highly inhomogeneous.

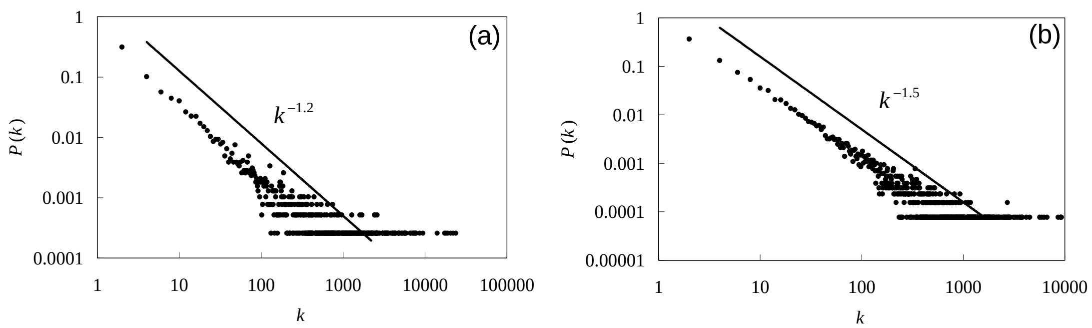

Figure 2. The log-log plots of the connectivity distributions of the earthquake network constructed from the data (A). Two different values of the cell size are examined: (a) 10Km× 10Km×10Km and (b) 5Km×5Km×5Km . All quantities are dimensionless.

Small-World Nature of Earthquake Network

The small-world nature shows how a complex network is different from both regular and classical random networks (Watts & Strogatz, 1998). A small-world network resides in-between regularity and randomness, analogously to the edge of chaos in nonlinear dynamics.
Because one is concerned only with a simple linking pattern of vertices in the small-world picture, a full network has to be reduced to a simple undirected network: that is, tadpole loops are removed and each multiple edge is replaced by a single edge (see Figure 1b).
A small-world network is characterized by a large value of the clustering coefficient in Eq. (3) (see below) and a small value of the average path length. The clustering coefficient quantifies the adjacency of two neighboring vertices of a given vertex, i.e., tendency of two neighboring vertices of a given vertex being connected to each other. Mathematically, it is defined as follows. Assume the i th vertex to have k_i neighboring vertices. There can exist at most $k_i(k_i-1)/2$ edges between the neighbors. Define c_i as the ratio

$$c_i = \frac{\text{actual number of edges between the neighbors of the } i\text{th vertex}}{k_i(k_i-1)/2} . \qquad (2)$$

Then, the clustering coefficient is given by the average of this quantity over the network:

$$C = \frac{1}{N}\sum_{i=1}^{N} c_i , \qquad (3)$$

where N is the total number of vertices contained in the network. A small-world network has a large value of it, whereas its value for the classical random network is very small (Watts & Strogatz, 1998; Albert & Barabási, 2002; Dorogovtsev & Mendes, 2003): $C_{\text{random}} = \langle k \rangle / N << 1$, where N and $\langle k \rangle$ are the total number of vertices and the average value of connectivity, respectively.
In Table 1, the results are presented for the clustering coefficient and the average path length (Abe & Suzuki, 2004b, 2006a). One finds that the values of the clustering coefficient are in fact much larger than those of the classical random networks and the average path length is short. Thus, the earthquake networks reduced to simple networks exhibit important features of small-worldness.

Table 1. The small-world properties of the undirected simple earthquake network. The values of the number of vertices, N , the clustering coefficient, C , (compared with those of the classical random networks, C_{random}) and the average path length, L are presented.

cell size	$10\,\text{km}\times 10\,\text{km}\times 10\,\text{km}$	$5\,\text{km}\times 5\,\text{km}\times 5\,\text{km}$
number of vertices	$N = 3869$	$N = 12913$
clustering coefficient	$C = 0.630 \quad (C_{\text{random}} = 0.014)$	$C = 0.317 \quad (C_{\text{random}} = 0.003)$
average path length	$L = 2.526$	$L = 2.905$

Hierarchical Structure

In order to investigate complexity of earthquake network further, one may examine if it is hierarchically organized (Abe & Suzuki, 2006b). The hierarchical structure can be revealed by analyzing the clustering coefficient as a function of connectivity. The connectivity-dependent clustering coefficient, $c(k)$, which is defined by

$$c(k) = \frac{1}{NP_{SN}(k)}\sum_{i=1}^{N} c_i \delta_{k_i,k} , \qquad (4)$$

where c_i is given in Eq. (2), N the total number of vertices, and $P_{SN}(k)$ the connectivity distribution of an undirected simple network. Its average is the clustering coefficient in Eq. (3): $C = \sum_k c(k) P_{SN}(k)$. Then, a network is said to be hierarchically organized if $c(k)$ decays with respect to k , typically due to a power law,

$$c(k) \sim k^{-\beta} \qquad (5)$$

with a positive exponent β. This quantifies adjacency of two vertices connected to a vertex with connectivity, k.

In Figure 3, the plots of $c(k)$ are presented (Abe & Suzuki, 2006b). As clearly seen, the clustering coefficient of the undirected simple earthquake network asymptotically decays as a power law in Eq. (5). This highlights hierarchical organization of the earthquake network. In view of seismicity, the decay of $c(k)$ with respect to k is due to the fact that the vertices of aftershocks tend not to be connected to each other directly: they are connected through the vertices of the associated main shock as mentioned earlier.

Existence of the hierarchical structure is of physical importance. The earthquake network has growth with preferential attachment (Barabási & Albert, 1999; Albert & Barabási, 2002; Dorogovtsev & Mendes, 2003). It is known, however, that the standard preferential-attachment model does not generate hierarchical organization (Ravasz & Barabási, 2003). To mediate between growth with preferential attachment and presence of hierarchical organization, the concept of vertex deactivation has been introduced in the literature (Vázquez et al., 2003). According to this concept, in the process of network growth, some vertices deactivate and cannot acquire new edges any more. This has a natural physical implication in the case of the earthquake network. Active faults may be deactivated through the process of stress release, in general. In addition, also the fitness model (Vázquez et al., 2002) is known to generate hierarchical organization. This model generalizes the preferential attachment rule in such a way that not only connectivity but also "charm" of vertices are taken into account. Seismologically, fitness is considered to describe intrinsic properties of faults (e.g., geometric configuration, stiffness, and so on). Both of these two mechanisms lead to the complex hierarchical structure, which means that a relatively new vertex has a chance to become a hub of the network, in contrast to the standard preferential-attachment model. In the case of an earthquake network, it seems plausible to suppose that the hierarchical structure may be due to both deactivation and fitness.

A point of particular interest is that the hierarchical structure disappears if weak earthquakes are removed. For example, setting the threshold for magnitude, say $M_{\mathrm{th}} = 3$, makes it hard any more to observe the power-law decay of the clustering coefficient. This implies that the hierarchical organization is mainly supported by weak shocks.

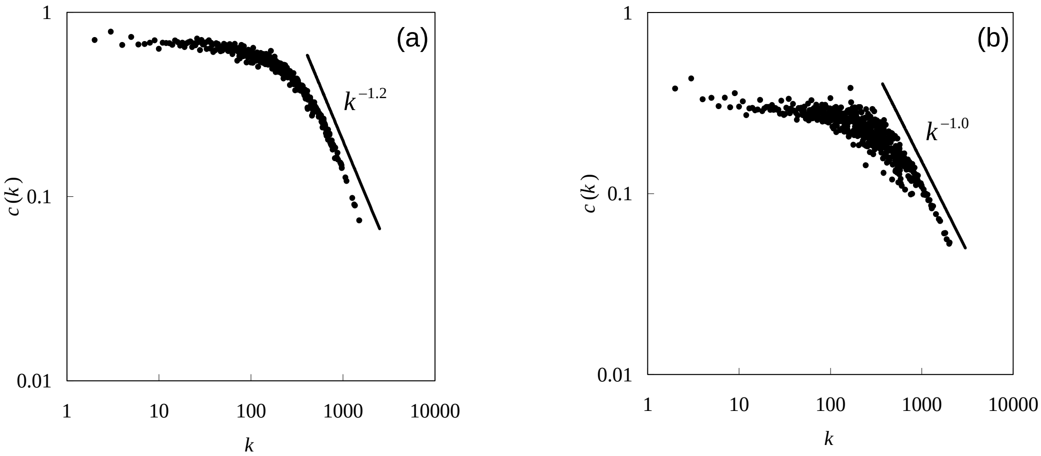

Figure 3. The log-log plots of the connectivity-dependent clustering coefficient of the earthquake network constructed from the data (B). Two different values of the cell size are examined: (a) $10\ \mathrm{km} \times 10\ \mathrm{km} \times 10\ \mathrm{km}$ and (b) $5\ \mathrm{km} \times 5\ \mathrm{km} \times 5\ \mathrm{km}$. All quantities are dimensionless.

Mixing Property

The scale-freeness, small-worldness, growth with preferential attachment and hierarchical organization all indicate that an earthquake network is very similar to, for example, the Internet as a complex network. However, there exists an essential difference between the two. It is concerned with the mixing property, which is relevant to the concept of the nearest-neighbor average connectivity, $\bar{k}_{nn}(k)$ of a full network with tadpole loops and multiple edges. This quantity is given as follows. Let us consider the conditional probability, $P(k'|k)$, of finding a vertex with connectivity k' linked to a given vertex with connectivity k. Then, the nearest-neighbor average connectivity of vertices with connectivity k is defined by (Pastor-Satorras et al., 2001; Vázquez et al., 2002)

$$\bar{k}_{nn}(k) = \sum_{k'} k' P(k'|k) . \quad (6)$$

If $\bar{k}_{nn}(k)$ increases (decreases) with respect to k, mixing is termed assortative (disassortative). A simple model of growth with preferential attachment is known to possess no mixing, that is, $\bar{k}_{nn}(k)$ does not depend on k.

The plots of this quantity are presented in Figure 4. There, the feature of assortative mixing (Abe & Suzuki, 2006b) is observed, since $\bar{k}_{nn}(k)$ increases with respect to connectivity k. Therefore, vertices with large values of connectivity tend to be linked to each other. In other words, vertices containing stronger shocks tend to be connected among themselves with higher probabilities. On the other hand, the Internet is of disassortative mixing (Pastor-Satorras et al., 2001; Vázquez et al., 2002). That is, the mixing properties of the earthquake network and the Internet are opposite to each other. We should note however that the presence of tadpole loops and multiple edges is essential for assortative mixing: an undirected simple network obtained by reducing a full earthquake network turns out to have disassortative mixing.

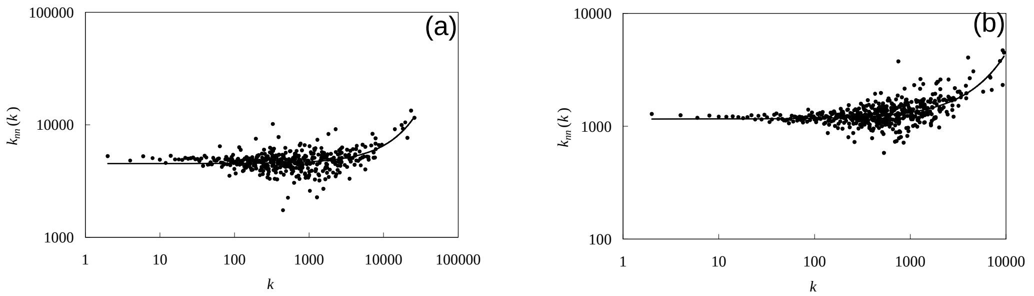

Figure 4. The log-log plots of the nearest-neighbor average connectivity of the earthquake network constructed from the data (B). Two different values of cell size are examined: (a) 10Km× 10Km×10Km and (b) 5Km×5Km×5Km. All quantities are dimensionless.

Period Distribution

So far, directedness of an earthquake network has been ignored. The full directed network picture is radically different from the small-world picture for a simple undirected network. It enables one to consider interesting dynamical features of an earthquake network. As an example, we here consider period in the network (Abe & Suzuki, 2005b). This concept is relevant to the question that after how many earthquakes an event returns to the initial cell, statistically, and therefore it is of obvious interest in view of earthquake prediction.

We define period in a directed network as follows. Taken a vertex of a network, there are various loops starting from and ending at this chosen vertex. Period, L_p, of a chosen loop is simply the number of edges forming the loop (see Figure 5). The period distribution, $P(L_p)$, is defined as the number of loops. The results are presented in Figure 6 (Abe & Suzuki, 2005b). As can be seen there, $P(L_p)$ decays as a power law

$$P(L_p) \sim (L_p)^{-\alpha}, \quad (7)$$

where α is a positive exponent. This implies that there exist a number of loops with significantly long periods in the network. This fact makes it highly nontrivial to statistically estimate the value of period.

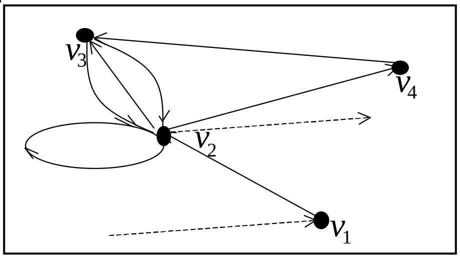

Figure 5. A full directed network: $\cdots \to v_1 \to v_2 \to v_3 \to v_2 \to v_2 \to v_4 \to v_3 \to v_2 \to \cdots$. The period associated with v_3 is 4, whereas v_2 has 1, 2 and 3.

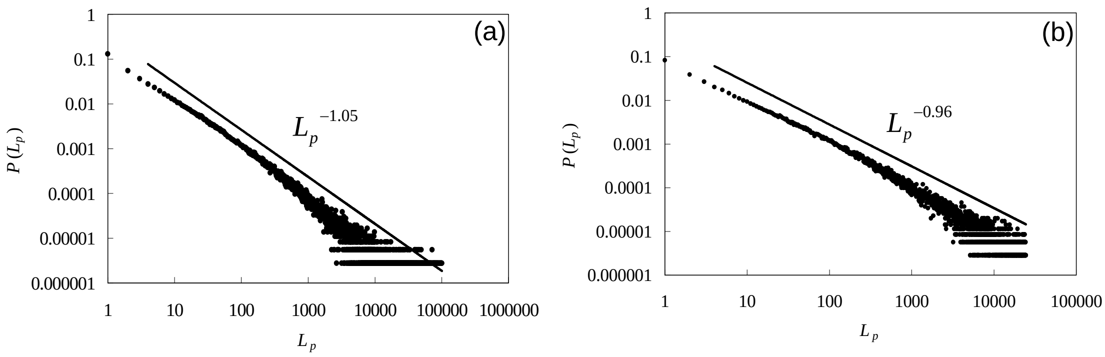

Figure 6. The log-log plots of the period distribution of the earthquake network constructed from the data (A). Two different values of cell size are examined: (a) 10Km× 10Km×10Km and (b) 5Km×5Km×5Km. All quantities are dimensionless.

Conclusion

We have discussed the complex-network approach to seismicity and have shown how such an approach sheds new light on complexity of the phenomenon. We have analyzed various properties of the earthquake network constructed from the seismic data taken from California. However, it has been ascertained that the laws and trends discussed here are universal and hold also in other geographical regions including Japan.

The main results we have shown in this article are as follows. Firstly, we have shown that the earthquake network is scale free being characterized by the power-law connectivity distribution. We have given a physical interpretation to this result based on network growth with the preferential attachment rule together with the Gutenberg-Richter law. Secondly, we have studied the small-world structure of the earthquake network reduced to an undirected simple network. The value of clustering coefficient is found to be much larger than that of the classical random network. In addition, average path length is very small. Thirdly, we have found that the earthquake network possesses hierarchical organization. We have interpreted this fact in terms of vertex fitness and vertex deactivation by the process of stress release at the faults. Fourthly, We have shown that the earthquake network has the property of assortative mixing. This point is an essential difference of the earthquake network from the Internet that has disassortative mixing. Finally, we have reported the discovery of a scale-invariant law of the period distribution in the directed earthquake network, which indicates that after how many earthquakes an earthquake returns to the initial location. This result manifests the fundamental difficulty in statistically estimating the value of period.

In the present work, the long-time properties of an earthquake network have mainly been considered. On the other hand, given a value of the cell size, an earthquake network represents all dynamical information contained in a seismic time series. Therefore, study of its time evolution may give a further insight into seismicity and may offer a novel way of monitoring seismicity.

For example, recently we have investigated how the clustering coefficient changes in time as an earthquake network dynamically evolves. According to our result (Abe & Suzuki, 2007), the clustering coefficient remains stationary before a main shock, suddenly jumps up at the main shock, and then slowly decays to become stationary again following the power-law relaxation. In this way, the clustering coefficient characterizes aftershocks in association with main shocks in a peculiar manner.

A question of extreme importance is if precursors of a main shock can be detected by monitoring dynamical evolution of earthquake network. Clearly, further developments are needed in science of complex networks.

References

Abe S. & Okamoto Y Eds. (2001). Nonextensive Statistical Mechanics and Its Applications. *Springer-Verlag, Heidelberg, 272p.*

Abe S. & Suzuki N (2003). Law for the distance between successive earthquakes. *J Geophys Res, 108 No. B2, 2113 ESE 19–1-4.*

Abe S. & Suzuki N (2004a). Scale-free network of earthquakes, *Europhys Lett 65, 581-586.*

Abe S. & Suzuki N (2004b). Small-world structure of earthquake network, *Physica A., 337, 357-362.*

Abe S. & Suzuki N (2005a). Scale-free statistics of time interval between successive earthquakes, *Physica A., 350, 588-596.*

Abe S. & Suzuki N (2005b). Scale-invariant statistics of period in directed earthquake network, *Eur Phys J B, 44, 115-117*.

Abe S. & Suzuki N (2006a). Complex-network description of seismicity, *Nonlin Processes Geophys,13, 145-150.*

Abe S. & Suzuki N (2006b). Complex earthquake networks: Hierarchical organization and assortative mixing. *Phys. Rev. E., 74, 026113–1-5.*

Abe S. & Suzuki N (2007). Dynamical evolution of clustering in complex network of earthquakes, *Eur. Phys. J. B., 59, 93-97*.

Abe S. & Suzuki N (2008). Complex earthquake network. in *Encyclopedia of Complexity and System Science, edited by B.Meyers et.al., Springer*, in press.

Albert R. & Barabási A-L (2002). Statistical mechanics of complex networks. *Rev. Mod. Phys., 74, 47-97.*

Barabási A-L. & Albert R (1999). Emergence of scaling in random networks, *Science, 286, 509-512.*

Dorogovtsev S.N. & Mendes J.F.F (2003). Evolution of Networks: From Biological Nets to the Internet and WWW, *Oxford University Press, Oxford. 264p.*

Gutenberg B. & Richter C.F. (1944). Frequency of earthquakes in California, *Bull. Seismol. Soc. Am., 34, 185-188.*

Omori F. (1894). On the after-shocks of earthquakes. *J Coll Sci Imper Univ Tokyo 7, 111-200.*

Pastor-Satorras R., Vázquez A. & Vespignani A. (2001). Dynamical and correlation properties of the Internet, *Phys. Rev. Lett., 87, 258701–1-4.*

Ravasz E. & Barabási A-L .(2003). Hierarchical organization in complex networks, *Phys. Rev. E., 67, 026112–1-7.*

Steeples D.W. & Steeples D.D (1996). Far-field aftershocks of the 1906 earthquake, *Bull. Seismol. Soc. Am., 86, 921-924.*

Tsallis C. (1988). Possible generalization of Boltzmann-Gibbs statistics, *J. Stat. Phys., 52, 479-487.*

Vázquez A., Pastor-Satorras R. & Vespignani A. (2002). Large-scale topological and dynamical properties of the Internet, *Phys. Rev. E., 65, 066130–1-12.*

Vázquez A., Boguña M., Moreno Y., Pastor-Satorras R. & Vespignani A. (2003). Topology and correlations in structured scale-free networks, *Phys. Rev. E., 67, 046111–1-10.*

Watts D.J. & Strogatz S.H (1998). Collective dynamics of 'small-world' networks. *Nature, 393, 440-442.*

Rupture Histories of Strong Earthquakes

Agalos A (1), Papadimitriou P (2), Makropoulos K (3)

(1) University of Athens, Department of Geophysics and Geothermics, Panepistimiopolis, Zographou, Athens, Greece, email aagalos@geol.uoa.gr
(2) University of Athens, Department of Geophysics and Geothermics, Panepistimiopolis, Zographou, Athens, Greece, email ppapadim@geol.uoa.gr
(3) University of Athens, Department of Geophysics and Geothermics, Panepistimiopolis, Zographou, Athens, Greece, email kmacrop@geol.uoa.gr

Keywords: rupture histories, slip models

Introduction

Digital broadband teleseismic records of P and *SH* waves are used to invert for rupture histories of recent strong earthquakes worldwide. In addition the strongest earthquakes that occurred in Greece from 1995 are also studied. The waveform data usually filtered between 0.01 to 1 Hz are used in a finite-fault inversion technique to determine the source complexities. The rupture history describes the slip distribution as a function of position and time on the fault. The advantage of using broadband records at teleseismic distances is that strong motion data are not always available or are frequently absent.

The followed finite-fault inversion approach does not permit the rupture velocity to change but the use of multiple time windows permits the same subfault to rupture multiple times. A linear least squares approach like the one followed gives a similar solution to a global search algorithm where the velocity can change relative to the position on the fault. The followed inversion approach permits the rake of the earthquake to vary upon the fault.

In cases where it is difficult to distinguish the rupture plane between the two nodal planes, the inversion procedure was applied twice. For the same set of parameters, the nodal plane which corresponds to the rupture plane, in most cases permits better fit between data and synthetics. The calculated rupture histories show the source complexity and directivity of the studied earthquakes. Slip models are calculated for several earthquakes in order to compute detailed static stress changes and synthetic peak ground velocity maps. In this study the results for two recent events are presented. These are the 2006 Kythira (Greece) earthquake and the 2007 Chile earthquake.

Data Used and Inversion Method followed

The last few years many studies have revealed the importance of the finite fault inversion procedure to our understanding of the earthquake rupture process which is able to provide an accurate spatial and temporal evolution of the coseismic slip on the ruptured fault. The finite fault inversion technique (Hartzell and Heaton 1983, Hartzell and Langer 1993, Hartzell et al., 1996, Mendoza and Hartzell 1999, Segikuchi and Iwata, 2002, Ji et al., 2002, Yagi et al., 2004) has been applied using teleseismically recorded waveforms or strong motion data. Several source inversion procedures that used teleseismic waveforms provided similar slip models using also other types of data such as geodetic (Wald and Heaton, 1994).

An inversion approach is applied for P and SH broadband waveforms at teleseismic distances between 30° and 90° from the earthquake epicenter. The stations belong to the Global Digital

Seismograph Network and are downloaded through the IRIS Data Management Center. The selection of the stations permitted the best possible azimuthal coverage which is always needed in this kind of inversion procedures. The teleseismic waveforms are instrument response corrected, integrated to displacement, band – pass filtered from 0.01 to 1 Hz using a Butterworth filter and re-sampled to 0.2 samples per second.

The finite fault inversion method followed developed by Hartzell and Heaton, (1983), is capable of estimating the spatial distribution of slip and risetime distribution on the ruptured fault. The application of this method starts by constructing a rectangular fault plane which is discretized to a number of uniform cells which are called subfaults. The source parameters (strike, dip, rake and source depth) are used as input to produce the elementary synthetics for each subfault. A total of 10 point sources were distributed over each subfault. The point sources are necessary to simulate a continuous rupture.

For every earthquake several different values of source velocity, varying from 2.6 to 3.5 km/sec, risetime, fault dimensions and time lag were used. The source of the elementary synthetics is of trapezoidal shape. The width of the source is chosen to be short compared to the total risetime on the fault. In most of the studied earthquakes the crust models used to produce the synthetics interpolated from the code CRUST2 (Bassin et al., 2000). The amount of slip in successive time intervals for each subfault is lagged in time by the width of the source. In this way, as described by Hartzell and Langer (1993), risetime functions are constructed and are free to vary as a function of position on the fault plane. The subfault may fail within the maximum allowed time window. The final rise time is obtained by the summation of the individual rise time functions for each time window. In most of the finite fault inversion studies the source velocity is taken as the 80 or 90% of the median S wave velocity.

The point source responses were computed with a code based on the generalized ray theory (Langston and Helmberger, 1975). The exact way these synthetics were constructed was discussed in the study of Heaton (1982), assuming that circular rupture fronts propagate at a given rupture velocity everywhere on the assumed fault plane. The absolute size of dislocation is specified to be related to the position on the fault. The elementary synthetics are always filtered with the same filter as the data and are convolved with an attenuation operation assuming t*=1 sec for P and t*=4 sec for SH waves.

In the finite fault inversion some trials are also made with the rake to vary across the dimensions of the fault, as it is used by Hartzell et al. (1996). In this case each subfault has n*2 model parameters to change during the inversion, where n is the number of time windows and 2 is for two mechanisms. The multiple time window approach of Hartzell and Heaton (1983) allows each subfault to rupture in any of the time windows used, based on the detail of the waveforms.

The observed waveforms and the synthetics produce an overdetermined system of linear equations of the form, **Ax**=**B**, where **A** and **b** are matrices concerning the joined elementary synthetics and teleseismic waveforms respectively, **x** is the solution vector including dislocation weights to be given at each subfault so that the final synthetics fit well the original data. The solution revealed from these matrices is not always stable and several constraints are needed. The constraints usually used at this kind of studies are well analyzed and explained in the studies of Hartzell and Heaton (1983) and Hartzell et al. (1991). Usually two constraints are used the moment minimization and smoothing.

In cases where there is no information about the rupture plane, the calculations are made twice using the two nodal planes of the focal mechanism. The nodal plane which is also the rupture plane, for the same parameters with the other plane used, would permit better fit between data and synthetics, as it is discussed by Mori and Hartzell (1990).

In conclusion the inversion method followed permits the identification of the fault plane, the calculation of the moment magnitude, the source time function, the fault dimensions and the detailed temporal and spatial position of slip on the fault.

Slip model of January 2006 Kythira, Greece earthquake and static stress transfer

On 8 January 2006 at 11:34 UTC a strong, thrust type faulting, earthquake (M_w=6.6) occurred in Southern Greece. The mainshock was located at 36.232°N, 23.395°E at the depth of 64 km. The data include 25 teleseismic P waveforms and 5 SH, of 60 sec duration, which were selected based upon data quality and azimuthal distribution. The waveforms were first converted to displacement by removing the instrument response and then used to constrain the slip history based on the linear finite fault inverse algorithm of Hartzell and Heaton (1983).

A surface of 70 km length and 24 km width was discretized by 108 subfaults, 18 along strike and 6 along dip. The surface edge of the fault starts at 48 km depth from the Earth surface and the down deep edge is at 72 km depth, the hypocenter is situated at 64 km depth and at a distance of 35 km from the left edge of the fault. Several rupture front velocities were tested. The fixed velocity value for rupture propagation of 3 km/sec produced the best fit between data and synthetics. The rake was left to change during the inversion between 70º and 160º, 6 time windows with 0.7 sec time lag duration for each one were used.

The fit between data and the calculated synthetics is presented in figure 1. The results show that the mainshock's moment magnitude is Mo=1*10^{26} dyne*cm, Mw=6.6 and the event ruptured a fault of nearly 30 km length. The nodal plane dipping southeast fits better the synthetics. The total duration of the mainshock is nearly 14 sec, with the majority of slip occurring between 3 and 8 sec of the far-field source time function. The inversion revealed one main region with significant slip. This region with significant slip is situated near the event's hypocenter with a maximum of 0.8 m slip, as presented in figure 2. The rake upon the fault mainly changes between 90º and 140º.

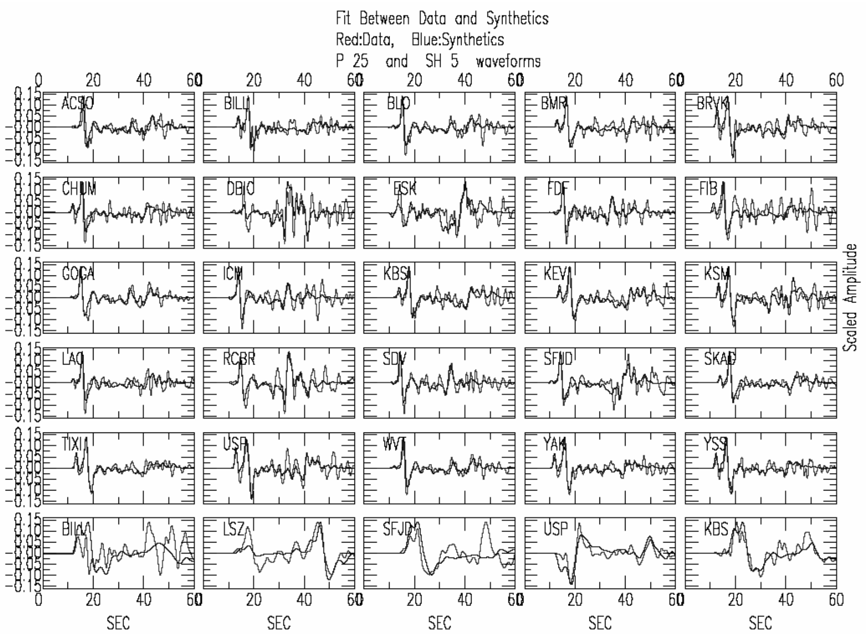

Figure 1. Comparison of observed and synthetic teleseismic waveforms. Synthetic to observed amplitude waveforms are indicated.

The slip model distribution revealed from the finite fault inversion procedure was used to compute the coseismic Static Coulomb Stress Changes in elastic half space. As it is presented from King et al. (1994); Harris and Simpson (2002), positive stress changes of 0.5

bars are able to trigger nearby events and negative values of the same amount are able to suppress them. Recent studies have revealed also stress transfer related with strong events occurred in Greece (Papadimitriou E., 2002, Ganas et al., 2006, Papadimitriou P. et al., 2006).

Earthquake induced stress changes, which are applied to a fault plane, are estimated using rectangular dislocation calculations that simulate static earthquake slip in an elastic halfspace (Okada, 1992). This technique is performed using the change of the Coulomb Failure Stress ΔCFS, (Harris and Simpson, 2002):

$$\Delta CFS = \Delta\tau + \mu(\Delta\sigma + \Delta p)$$

where $\Delta\tau$ is the change in shear stress on the failure plane in the expected rake direction on the target fault, μ is the coefficient of friction, $\Delta\sigma$ is the change of normal stress (positive for tension) and Δp is the change in pore fluid pressure. The value for the internal coefficient of friction used was μ=0.6 which is an intermediate value for Coulomb studies. For this calculation μ is considered constant and it is assumed not to change as a function of slip and time on the rupture plane. Robert's Simpson DLC software is used which is based on subroutines of Okada (1992) to calculate the displacements and their derivatives using Poisson's ratio 0.25 and a shear modulus of 0.33 Mbars.

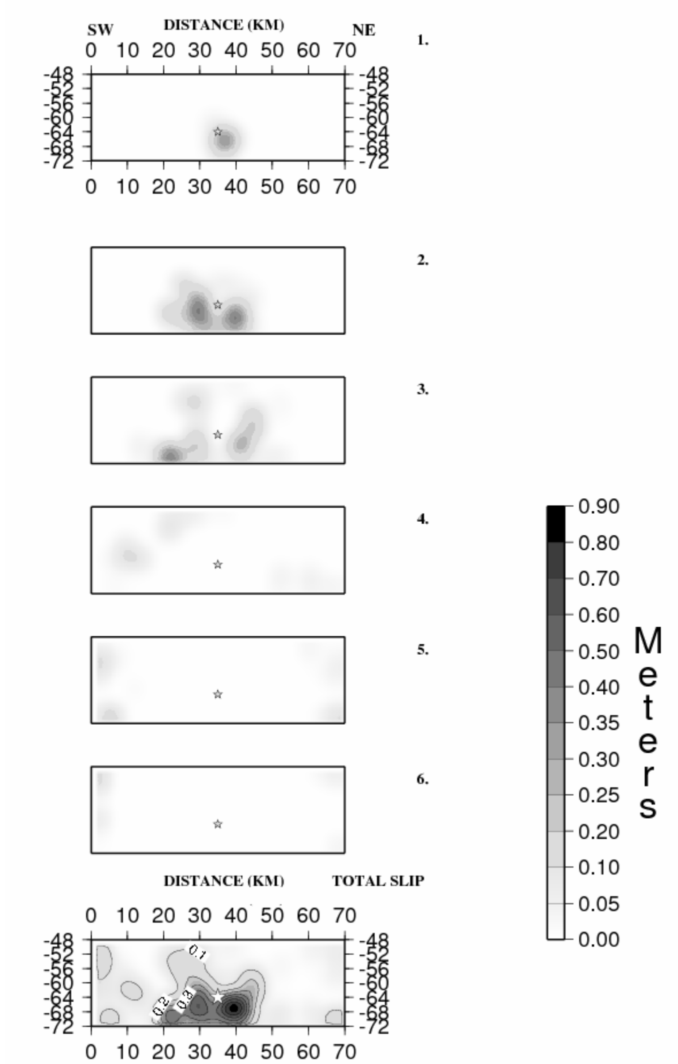

Figure 2. Temporal and Spatial Slip distribution on the ruptured fault plane. The first 6 sub-figures are snapshots with 3 seconds time difference between them. The seventh sub-figure presents the total slip on the ruptured fault.

In most of the papers studying the static stress changes uniform slip is usually adopted across the ruptured fault and most often the epicenter is selected to be in the center of the theoretical fault rupture. This assumption does not always provide any detail on calculations. In figure 3 it is showed the distribution of stress changes based on the suggested slip model of this study. The strongest static changes are concentrated in regions in the east of Kythira Island, mostly southern the fault rupture. The obtained Coulomb stress pattern indicates positive values of stress in the direction where the Leonidio earthquake occurred in January of 2008, but it is not clear that it was triggered by the Kythira event because of the very low values of transferred stress.

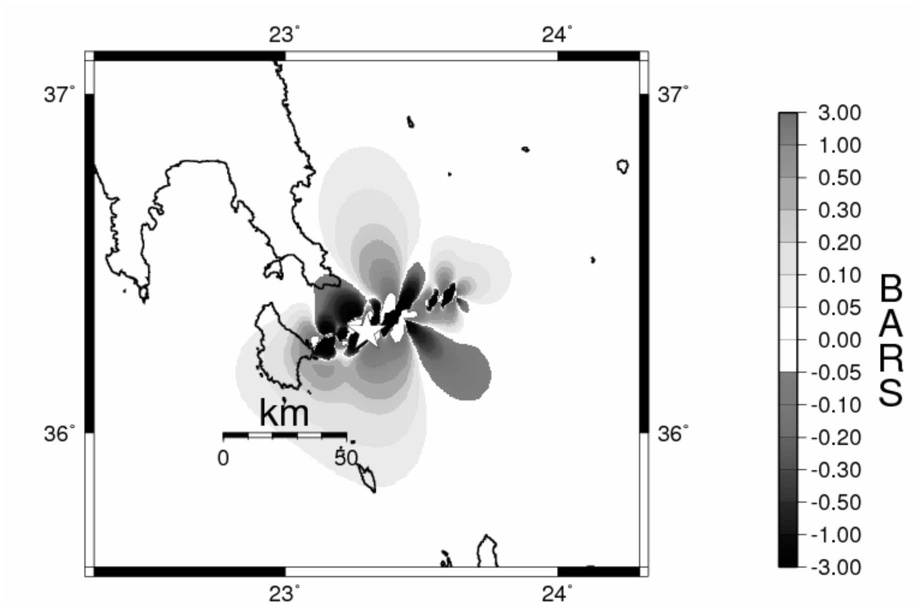

Figure 3. Calculated coseismic static stress changes for Kythira earthquake using the slip model revealed from the finite fault inversion procedure. White star represents the epicenter of the mainshock.

Slip model of November 2007 Chile earthquake and Synthetic PGV map

On 14 November at 15:40:50 UTC a very strong, thrust type faulting, earthquake (M_w=7.7) occurred in Chile. The rupture process and history are studied using broadband teleseismic data. The mainshock was located by USGS at 22.204°S, 69.869°W and EMSC at 22.17°S, 69.97°W about 165 km NNE of Antofagasta, Chile. The data include 12 teleseismic P waveforms and 12 SH waveforms which were selected based upon data quality and azimuthal distribution. These waveforms were first converted to displacement by removing the instrument response and then used to constrain the slip history based on the linear finite fault inverse algorithm of Hartzell and Heaton (1983). The broadband teleseismic data, downloaded through Iris Wilber II application, were inverted by allowing a variable dislocation rise time at each point on the fault. A surface of 180 km length and 30 km width was discretized by 108 subfaults, 18 along strike and 6 along dip. The surface edge of the fault is at 20 km depth and the down deep edge at 50 km depth, the hypocenter is situated at 37 km depth and at a distance of 120 km from the left edge of the fault. Several rupture front velocities were tested. The fixed velocity value for rupture propagation of 2.6 km/sec produced the best fit between data and synthetics. The velocity model used to produce the elementary synthetics is provided by Mendoza et al. (1994) who studied another strong event in Chile.

The results show that the moment magnitude of the mainshock is, $Mo=5*10^{27}$dyne*cm, Mw=7.7 and the event ruptured a fault of nearly 120 km length. The nodal plane dipping-west fits the data better. The total duration of the mainshock is 56 sec, with the majority of slip occurring the first 40 sec of the far-field source time function. The inversion revealed two main regions with significant slip (figure 4). The first region, at the northern part of the fault, extends around the earthquake's hypocenter and the second which has two maximum peaks is found at the southern part of the fault nearly 40 km from the first region. In the finite fault inversion 6 time windows with 2 sec time lag duration for each one were used. The rake which was left to vary during the inversion approach between 90° and 180° mainly varied between 90° – 100°. Figure 5 shows the Peak Ground Velocity distribution using the calculated slip model and the code of Bouchon (1981).

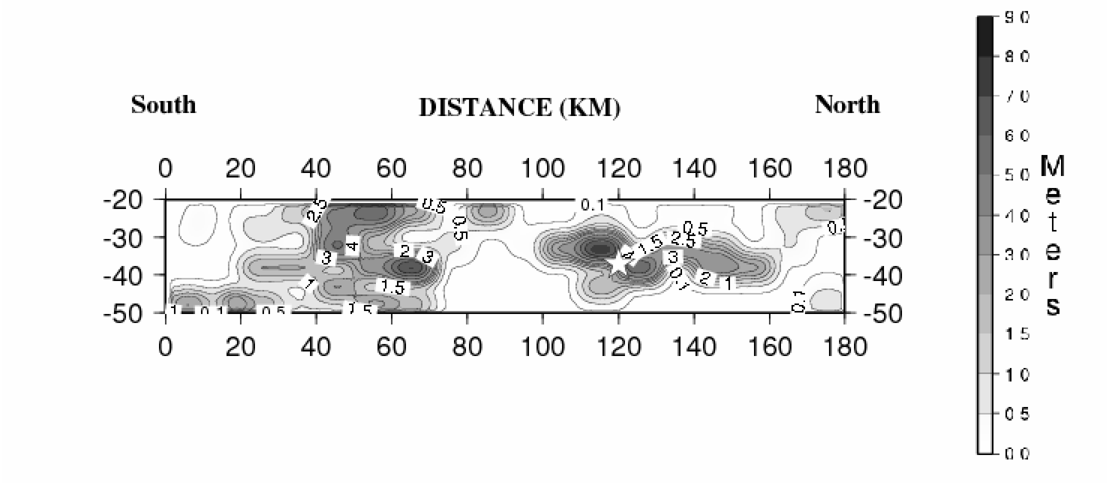

Figure 4. Slip distribution on the ruptured fault plane for 2007 Chile earthquake.

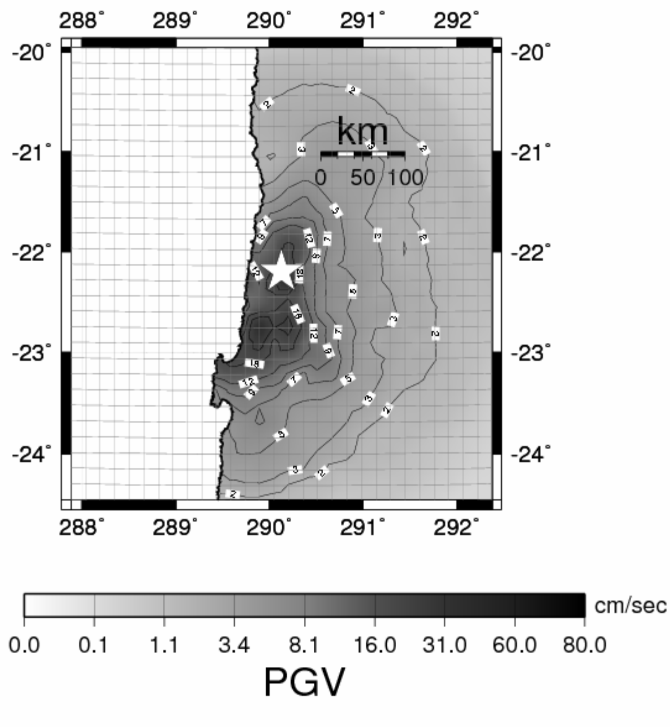

Figure 5. Synthetic Peak Ground Velocity map estimated using the slip model retrieved by the waveform inversion. The white star indicates the earthquake's epicenter.

Conclusions

In this study two detailed coseismic slip models are presented for the January of 2006 Kythira, Greece earthquake and the 2007 Chile earthquake. Both earthquakes are related with thrust type faulting. The inversion approach applied revealed the spatial and temporal distribution of slip. The slip model of Kythira earthquake is quit simple. The dimension of the ruptured fault is about 30x10 km with a maximum slip of 0.8 m close to 68 km depth. Static Coulomb stress analysis, using the calculated slip model, did not reveal clearly stress transfer to the Leonidio earthquake occurred two years after.

The slip distribution of Chile earthquake is complex with at least two sources. The dimension of the ruptured fault is about 120x15 km with a maximum slip of 7 m close to 35 km depth. The determined slip model is used to calculate the spatial distribution of the peak ground velocity (PGV). The strongest values of PGV are concentrated in two regions which can be related with the two revealed main sources.

Acknowledgments

We would like to thank Dr. Stephen Hartzell for explaining and providing the finite fault inversion codes used in this study, Robert Simpson for providing the code that used to compute the static stress changes. Most of figures were made using the GMT software (Wessel and Smith, 1981).

References

Bassin C, Laske G & Masters G (2000). The Current Limits of Resolution for Surface Wave Tomography in North America, *EOS Trans AGU, 81, F897.*

Bouchon M (1981). A simple method to calculate Green's functions for elastic layered media, *BSSA, 71, 4, 959-971.*

Ganas A., Sokos E., Agalos A., Leontakianakos G., Pavlides S (2006). Coulomb stress triggering of earthquakes along the Atalanti Fault, central Greece: Two April 1894 M6+ events and stress change patterns, *Tectonophysics, 420, 357-369.*

Harris R. A. & Simpson R. W (2002). The 1999 MW 7.1 Hector Mine, California Earthquake - A test of the stress shadow hypothesis?, *BSSA, 92, 4, 1497-1512.*

Hartzell S. H. & Heaton T. H (1983). Inversion of strong ground motion and teleseismic waveform data for the fault rupture history of the 1979 Imperial Valley, California, earthquake, *BSSA, 73, 1553-1583.*

Hartzell H., Stephen, Stewart S. Gordon & Mendoza C (1991). Comparison of L1 and L2 norms in a teleseismic waveform inversion for the slip history of the Loma Prieta, California, earthquake, *BSSA, 81, 1518-1539.*

Hartzell H., Stephen & Langer C (1993). Importance of Model Parameterization in Finite Fault Inversions: Application to the 1974 Mw 8.0 Peru Earthquake, *JGR, 98, B12, 22123-22134.*

Hartzell H., Stephen, Pengcheng, Liu & Mendoza C (1996). The 1994 Northridge, California earthquake: investigation of rupture velocity, risetime and high-frequency radiation, *J.G.R, 101, 20091-20108.*

Heaton T. H. (1982). The 1971 San Fernando earthquake: a double event?, *BSSA, 72, 2037-2062.*

Ji C., Wald D. J., & Helmberger D. V (2002). Source description of the 1999 Hector Mine, California earthquake; Part I: Wavelet domain inversion theory and resolution analysis, *Bull. Seism. Soc. Am., Vol 92, 4, 1192-1207.*

King G. C. P., Stein R. S., & Lin. J (1994). Static Stress changes and the triggering of earthquakes, *BSSA, 84, 935-953.*

Langston C. A. & Helmberger D. V (1975). A procedure for modeling shallow dislocation sources, *Geophys. J. Roy. Astr. Soc., 42, 117-130.*

Mendoza C. & Hartzell S (1999). Fault-slip distribution of the 1995 Colima-Jalisco, Mexico,Earthquake, *BSSA, 89, 5, 1338-1344.*

Mori, Jim & Hartzell S (1990). Source inversion of the 1988 Upland, California, earthquake: determination of a fault plane for a small event, *BSSA, 80, 507-517.*

Okada, Y (1992). Internal deformation due to shear and tensile faults in a half-space, *BSSA, 82, 1018-1040.*

Sekiguchi H. & Iwata T (2002). Rupture process of the 1999 Koaceli, Turkey, earthquake estimated form strong-motion waveforms, *BSSA, 92, 300-311.*

Papadimitriou E (2002). Mode of Strong Earthquake Recurrence in the Central Ionian Islands (Greece): Possible Triggering due to Coulomb Stress Changes Generated by the Occurrence of Previous Strong Shocks, *Bulletin of the Seismological Society of America, 92, 8, 3293-3308.*

Papadimitriou P., Kaviris G., Makropoulos K (2006). The Mw=6.3 2003 Lefkada earthquake (Greece) and induces stress transfer changes, *Tectonophysics, 423, 73-82.*

Wald D. J. & Heaton T. H (1994). Spatial and temporal distribution of slip for the 1992 Landers, California, earthquake*, BSSA, 84, 3, 668-691.*

Wessel P. & Smith W. H. F (1991). Free software helps map and display data, *EOS Trans. AGU, 72, 441.*

Yagi, Yugi, Mikumo, Takeshi, Pacheco, Chavier, & Reyes G (2004). Source Rupture Process of the Tecoma´n, Colima, Mexico Earthquake of 22 January 2003, Determined by Joint Inversion of Teleseismic Body-Wave and Near-Source Data, *BSSA, 94, 5, 1795-1807.*

Instrumental and Macroseismic Database for Regional Seismic Hazard and Risk Studies

Alcaz V (1), Zaicenco A, Isiciko E

(1) Institute of Geology and Seismology, 2028, Academiei 3 str., Cishinau, Republic of Moldova, alcazv@yahoo.com

Keywords: Vrancea seismic zone, seismic records, geotechnical data, damage data

Introduction

The territory of the Republic of Moldova is exposed to influence of earthquakes generated by Vrancea intermediate-depth seismic zone. Earthquake related studies are guided by the quality of the available data. The paper presents the database designed for the purpose of seismic hazard and seismic risk studies of the territories affected by the Vrancea earthquakes.

Data

Instrumental Data

There are five recording stations in Moldova for which strong and moderate earthquake data ($4.0 \le M_{GR} \le 7.2$) were obtained during the 1977-2008 period. Currently, the database stores over 450 recorded ground motion recorded horizontal components from 52 events.

Macroseismic Data

Macroseismic part of the database includes information on building damages and geotechnical conditions at sites where these buildings are located. Moldova suffered heavy damage and losses as a consequence of the 1977 and 1986 Vrancea zone earthquakes. These earthquakes have provided ample damage data of the existing building stock. After the March 4, 1977 earthquake (M=7.2), 2765 (i.e. 23% of total investigated 11849) buildings were completely destroyed and 8914 (75%) were seriously damaged. Similar statistics for the August 30,1986 earthquake (M=7.0) showed 1169 (i.e. 2%) of total investigated 58538 buildings were completely destroyed and 7015 (12%) of them were seriously damaged.

Geotechnical data

Geotechnical data contain information concerning stratification of soils on 1210 sites.

Database structure

The adopted model of database includes four tables for instrumental and nine tables for macroseismic data respectively. The instrumental data consists of: Catalog, Stations, Station Soil Profile Characteristics and Records. Two main tables containing macroseismic data there are: Macro (buildings location, damage degree of buildings, type of buildings, number of floors) and Geophysical Profile (soils velocity values, attenuation parameters). Additionally, the information about the geomorphology of territory, soil lithology, bedrock depth, underground water level, thickness of water saturated soil, densification capacity of soil and seismic category of soil according to current aseismic code MD SNiP II-7-81can be found.
In this way, the database provides the necessary information for investigation associated to soil-related earthquake response and structural damages.

Schematic representation of the database is shown in the Figure 1.

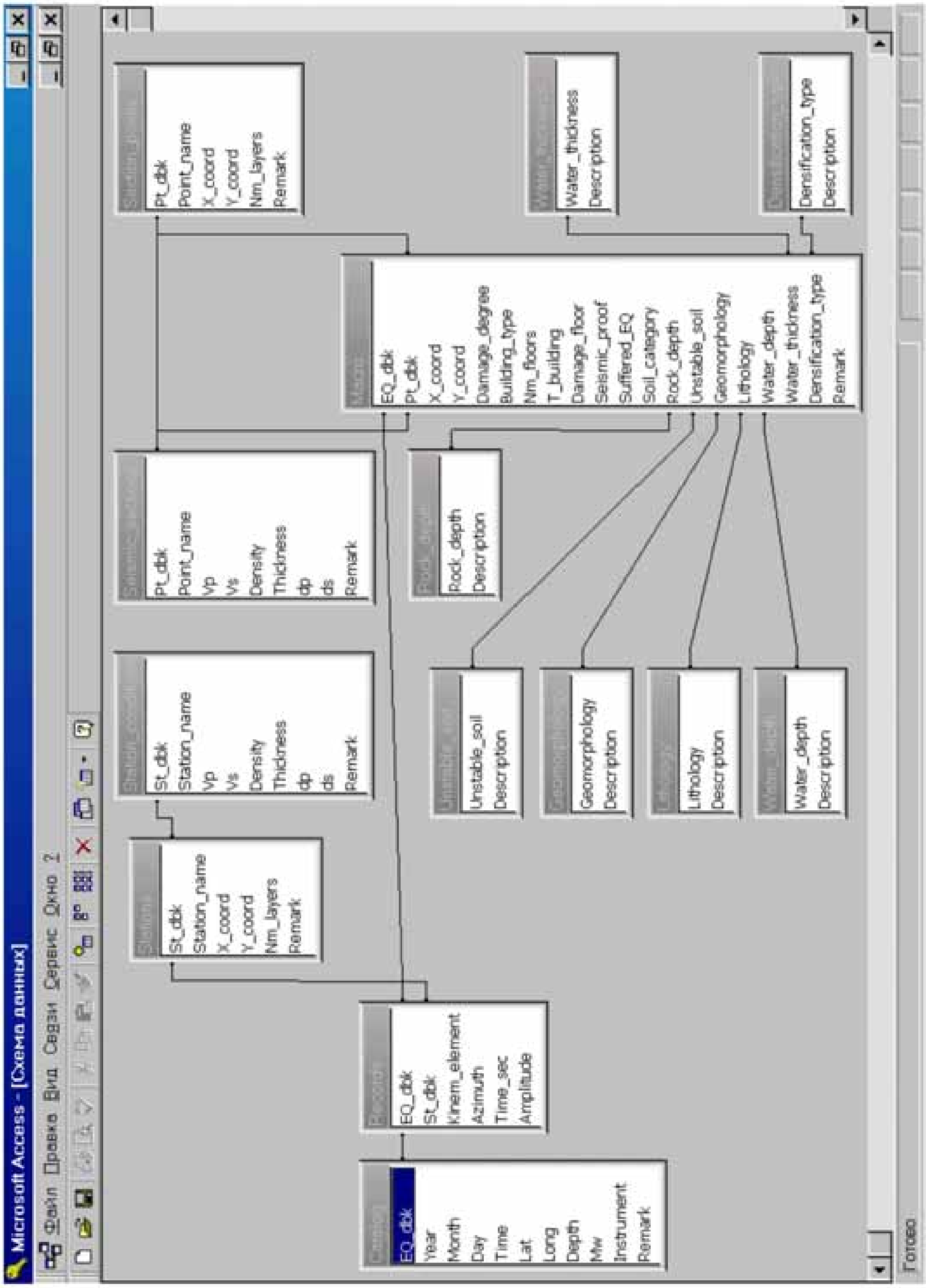

Fig.1. Schematic representation of the database

Output Example of the Elaborated Database

With the help of the compiled database different procedures could be performed, such as calculation of natural periods of soil vibration, amplification functions as well as construction of various associated maps in function of specific task. Namely the last feature of the created database – ability to produce seismic hazard and risk related maps is considered as the main advantage. Furthermore, the whole research is aimed on creating the tool that could generate ground-shaking response for a scenario seismic event, or explain properly the spectral content of seismic records on the given site, and to correlate them with the observed structural damage. The presence of the strong and moderate intensity seismic records on the given site contributes positively to the accuracy of the data and the applied methods. Besides, the variation of the depth and elastic properties of soft soil deposits resulted in significant differences of the amplification capacity that is recognized by the existing maps of seismic microzonation for the studied site, outlining zones with VII and VIII degrees of intensity (MSK scale). Utilization of database allowed constructing the maps containing information on spatial distribution of soil amplification factor. Evidently combination of different unfavorable soil conditions usually results in a strong response of the structures and higher damages during strong Carpathian (Vrancea) earthquakes. In this way, the August 30, 1986 Vrancea earthquake with magnitude M_{GR}= 7.0 and epicentral distance of ~220 km to the south-west of Chisinau resulted in a devastating damage of numerous buildings, including seismic-resistant structures in some areas of the city (Alcaz, 1999). The correlation of buildings' damage degree d_{av} with soil amplification factor A was studied. The result of analysis is presented in Fig.2 showing coefficient of correlation 0.6. It is necessary to note that the damage data are characterized by high dispersion, but it is dear that damage degree is proportional to the amplification factor of sites.

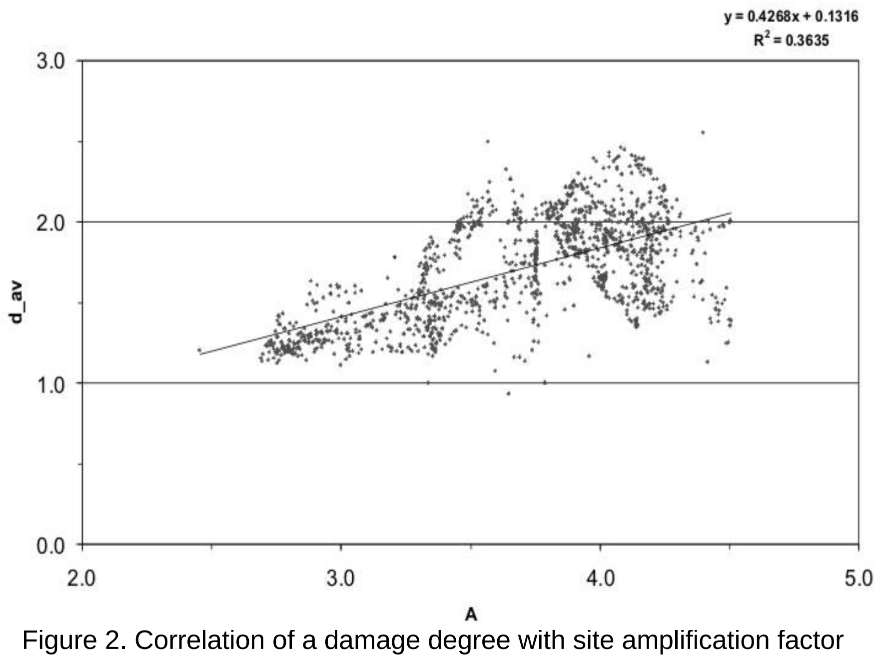

Figure 2. Correlation of a damage degree with site amplification factor

The city is a densely constructed zone, especially in central part were 1870 of buildings with high share of low- to moderate-code masonry buildings already have experienced 2-4 strong seismic events (1940, 1977, 1986 and 1990). The assessment of seismic risk for these buildings, some of which are the historical monuments, accounting for the observed degrees of damage, with the use of compiled database could obviously represent the main goal in the future investigations.

Utilization of the database could also lead to the improvement of macroseismic scale MSK, which could define the alternative criteria for assessment of seismic intensity on the basis of instrumental data**.**

Conclusions

The Vrancea earthquake records, damage data and dynamical properties of the soft soils were collected, structured and digitized in a uniform format that will stimulate development of the innovative methodologies for seismic hazard and risk forecasts.

Acknowledgements

This research is sponsored by NATO's Scientific Affairs Division in the framework of the Science for Peace Programme, project SfP-980468. Support provided by INTAS project 05-104-7584 is gratefully acknowledged.

References

Alcaz V (1999). Influence of Local Soil Conditions on Earthquake Motion in the Territory of Moldova Republic. In: Earthquake Hazard and Risk, (Ed. F. Wenzel, D. Lungu), *Ser.: Advances in Natural and Technological. Hazards Research, Kluwer Academic Publishers, 1999, p. 187-195.*

Atlas of Armenian Strong Earthquakes as an Example of the Accessible for Seismic Hazardous Countries Complex, Unified Knowledge Methodology on Compiling Earthquake Data Base and Maps

Babayan T Ho (1)

(1) Institute of Geophysics and Engineering Seismology of the National Academy of Sciences of the Republic of Armenia 5, V. Sargisyan, Gyumri, 3115, Republic of Armenia, iges@shirak.am

Keywords: Strong earthquakes, database, isoseismal maps, catalogue

Introduction

Earthquakes are terrible catastrophic natural phenomena, which within several seconds destroy people, the whole cities and villages, cultural and material assets created by the people for centuries and years, change ecological balance of environment and reject back all spheres of the sustainable development of a human society of the region, subjected to the earthquake. In the developing countries, seismic hazard, vulnerability to earthquake disaster and, therefore, economic damage have increased during the beginning of the 21st century, as rapid urbanization, uncontrolled growth of large cities and building development, lead to the occupation of areas along active faults that are prone to seismic activity.

The damage and fatalities caused by the regional earthquakes seem to be associated with high population density in the epicentral area, the vulnerability of poor erected structures, and faults of their design, the ground-hydrogeologic conditions of the building territory, seismo-geological appearances (rock falls, landslides, subsidence, etc.) related to earthquakes, underestimating the earthquake-fault hazard, as well as lack of knowledge in seismic hazard and risk definition methodology.

In order to minimize the loss of lives, property damage and social-economic disruption caused by destructive earthquakes it was necessary to have a reliable and homogenous seismotectonic and earthquake data source. Any advancement in our knowledge of assessing and mitigating earthquake risk must be based on the rigorous collection and analysis of reliable seismological and geological observational data. An earthquake catalogue and isoseismal maps of strong earthquakes are the first and more fundamental step towards knowledge assessing earthquake hazard, seismic risk and short-, mid- and long-term earthquake prediction. They will allow to solve the problem of a long-term forecasting of the place and the force of earthquakes, that is to allocate those territories, where the earthquakes of the defined maximum intensity are possible, and also those territories, where each earthquake was expressed by the greatest force (pleistoseistal areas), thus dividing territory of countries on zones of different seismic hazard and allowing to compile or to reexamine seismic zoning maps of their territories, and also seismic microzoning maps for populated points of different scale, which will be submitted to the governments for practical application as the normative documents.

At the maiden stage of works, that is in 1970-1975 we went through the possible sources containing items of information on earthquakes, including far past events. In this connection a rich manuscript, fund, literary and other materials of Armenian historians, fundamental description catalogues of E.I. Byus and V.A. Stepanyan and others were looked over. By uniform, complex methodology collection and analysis of all available data about earthquakes having place on territory of the Republic of Armenia from most ancient times up to 1975 are held. The catalogue of these earthquakes is composed. The outcomes of works are included in the book “New Catalog of Strong Earthquakes in the USSR From Ancient Times Through 1975” published in 1977, Moscow [NC1 (1977)]. In 1982 the book is reprinted in USA, California with some corrections and additional information, including earthquakes having place up to half of 1977 [NC2 (1982)].

Other part of the problem, that is publication of isoseismal maps of strong earthquakes, due to some circumstances, was not realized.

In different time various authors (E.I. Byus, N.N. Ambraseys, M. Berberyan, G.P. Gorshkov, T.Ho. Babayan, A.A. Nikonov, E.A. Egorova, H.V. Sargsyan, N.M. Sargsyan, S. Gengoglu, A. Gurpinar, E.G. Geodakyan, P.A. Aghamirzoev, V.A. Kasparova, Z.Z. Soultanova, L.V. Shahsouvaryan et al) have made isoseismal schemes or maps of some strong earthquakes of Armenia and adjacent territories with various approaches and with various detail and, very often, without taking into account geologic-tectonic conditions of environment, macroseismic field legitimacies and ground-geomorphologic conditions etc.

In this connection and with such approach we compile the Atlas (T.Ho.Babayan, 2006), which includes the catalogue and isoseismal maps, also the maps of pleistoseistal areas and seismotectonics of strong earthquakes of the Republic of Armenia, Mountainous Karabagh (Artsakh) and adjacent territories on more complete primary data on earthquakes, covering the longest possible time period.

Materials and Methods

The great volume of source information is used. All known manuscript, archival, historical, archeological and literature sources, describing strong earthquakes were gathered. To collection and processing of description macroseismic data especially rich ancient Armenian bibliography assisted.

Having accounted for probable sources of exaggeration and error, it was necessary reevaluate the historical seismic data from the point at which they correlate satisfactorily with historical evidence. Sources, surveyed at the maiden stage of works are looked over, additional references that became available for me after publication of [NC1, 1975 and NC2, 1982], and domestic and foreign sources including macroseismic and instrumental information about earthquakes having place in RA after that publication, as well as sources of data on strong earthquakes occurred out of the borders of the RA, are used and interpreted. More complete list of available sources is composed.

During the collection, processing and retrieval phase of the preliminary data on earthquakes, it became clear that most of earthquake catalogues and reports have many shortcomings, differences, mis-interpretations and erroneous estimation of the earthquake parameters, which are needed in overestimation. In the present work we treated all available and also additional accessible data, and have compiled new, corrected variants of isoseismal maps.

In the Atlas earthquakes, which were not involved in the last edition of the New catalogue [NC2, 1982], and also events for subsequent more than 25 years after its last date are included. A number of strongest earthquakes, isoseismals of which of intensity 5 and more partially covered territory of RA or MK, though their epicenters were outside of this territory, in boundary with other states zones, are included in the Atlas as well, due to close link between the geologic-tectonic conditions, newest movements and seismicity of these territories. It was also necessary to include these earthquakes in the work, as the earthquakes occurring outside are essential for estimating the seismic hazard and seismic risk within our territory.

All data of more complete primary sources are considered critically and if necessary corrected or reestimated. For every earthquake joint processing of all known macroseismic, instrumental, seismo-geological, engineering-geological and built-construction data, and the critical analysis and reinterpretation are carried out, in particular when there were differences and possible errors in their evaluation, as well as in the case of divergence of data found in different sources. At the same time the quality and reliability of scientific level of information was taken into account. Macroseismic data were reexamined and generalized and then compared with instrumental data if there were any.

The data of the earthquakes were checked, provided a uniform level of estimation on the uniform system of classification for all earthquakes and for some earthquakes overestimated chiefly on the basis of the earliest original sources. For a homogenization of intensity estimations of all earthquakes and affected populated points if possible they were estimated for unified conditions, which were not taken into account in compiling of the publishing versions of the catalogues. All information was processed including also negative information. Data on source parameters which we determined by source data and isoseismal maps of the given earthquake in catalogue are marked. Dates of earthquakes are marked on new chronology, and time is transferred in GSM.

For compilation of isoseismal maps and catalog the exact definition of the degree of seismic intensity by the uniform, homogeneous level of an estimation and system of classification for all earthquakes and settlements probably plays the main role. For this purpose the transition from descriptive estimations to estimations for average ground conditions (sandy clays-clayed sands, with a ground-water level lower than 5 meters from a daylight level and a plain relief) and buildings of an average rigidity (T = 0.2-0.5s) is whenever possible realized. Both epicentral intensity and intensity at settlements for each earthquake were revised and estimated by critical approach according to the scale MSK.

An important step toward standardizing earthquake data was the choice of the macroseismic intensity estimation scale. In this connection there were compared and analyzed the macroseismic intensity estimation scales working nowadays in the world practice (MM, EMS-98, MSK). The variant of the scale, i.e. MSK scale was chosen, which mostly corresponds to buildings and constructions widely spread in our region, and also to our building types, classification of the description and degree of damages, quantities and formulation, as well as effects on environment, described in our sources. That allowed transmitting from verbose description of earthquake effects to estimating an intensity degree for the epicenter and every populated point of every earthquake. Besides there are not essential distinctions between intervals of different intensities of MM, EMS-98 and MSK scales.

It is important to take into account, that in ancient Armenian historiographical traditions in information on earthquakes only an injured large city, a monastery or a church are usually marked, or it is mentioned that the earthquake took place in the country or in any region, and there are no data on its consequences in small cities and villages. For such ancient destructive earthquakes there weren't enough macroseismic data in sources to compile an isoseismal map. But, as without these data, in particular, without earthquakes with intensity 8 and more, the estimation of the seismic hazard of the considered territories would not be high-grade. Therefore we included 21 such earthquakes in the given atlas, having compiled theoretical isoseismal of maximal intensity limiting the most injured area (i.e. pleistoseistal area) for each of these earthquakes.

The scientific interpretation of available seismological, macroseismic, historical, built-construction, built environment conditions etc. were given. In the Atlas (T.Ho. Babayan, 2006) the new compiled catalogue, isoseismal maps and descriptions of strong earthquakes are composed and included.

Data on focal basic parameters which we determined on sources and isoseismal maps, together with all available international source data in new catalogue are presented.

On isoseismal map of every earthquake main parameters of the earthquake source and the list of settlements exposed to that earthquake with corresponding intensities were presented.
Every earthquake has a description of its consequences, quoted from the primary sources, and comments on the event if necessary. Descriptional data are presented so that the values of parameters of the earthquakes should be based on facts. Texts are accompanied by

complete references on the event, which include the complete macroseismic information for descriptive text.

Data about fault tectonics and seismotectonics of the Republics of Armenia, Mountainous Karabagh and adjacent territories with various types and details are involved in works of large experts in this area: L.A. Vardanyants, K.N. Paffenholc, A.A. Gabrielyan, A.T. Aslanyan, M. Berberian, I.V. Ketin, V.G. Papalashvili and M.S. Ioseliani, M.G. Aghabekov, E.Sh. Shikhalibeili, etc

Generalizing all materials the map of seismotectonics of RA, MK and adjacent territories including tectonic conditions and pleistoseistal areas of strong earthquakes compiled.

The received data and the maps were finally made out on the computer. It is noteworthy, that mainly the use of computer-based methods in the evaluation of works finally contributed to a better definition of the scale, coordinates, design and base-map, as well as correction of typing errors, elimination of duplications, etc.

Results and Discussion

Critical reexamination and homogenization of the combined instrumental and macroseismic data resulted in the compiling isoseismal maps and the new catalogue of strong earthquakes. They include representative, and homogenous data on nature, parameters and affected areas of earthquakes, defined by the improved methods of analyzing descriptive macroseismic and instrumental data, as well as methods of scientific interpretation of materials, compiling of isoseismal maps and defining main parameters of earthquakes. To make values of intensity homogenous, for each populated point all data have been revised, assessed damage grades and if necessary, overestimated by unified methodology, taking into consideration shaking effects, construction and soil types, topographical conditions etc. Improved methods of analyzing and interpretation of materials, compiling maps and definition source parameters allowed to exceed homogenous data for all earthquakes.

Atlas includes isoseismal maps of earthquakes with intensity of 5-6 and more, occurring in the Republic of Armenia, Artsakh and adjacent territories from most ancient times through 2003, scale 1:1000000.

The identical scale - 1:1000000 of compiling of all isoseismal maps is one of terms for providing their identical condition. For 6 strongest earthquakes the more detailed isoseismal maps, scale 1:500.000, for their more affected areas are also composed, to take in all affected populated points more clearly.

Atlas includes: principles, procedures and methodology of compiling corrected, unified and homogenized isoseismal maps, catalogue and descriptions; 86 isoseismal maps, and a unified homogenous data catalogue on earthquakes having place in RA, Arthakh and adjacent territories from ancient times through 2003; a description of the effect of every earthquake and 6 other events, which in sources are marked among destructive earthquakes, settling their origin, location and character; the seismotectonic maps i.e. the maps of seismicity of the Republic of Armenia, Artsakh and neighboring territories showing tectonic faults and confined them strong earthquakes pleistoseistal areas (including theoretical pleistoseistal areas of 21 earthquakes) and the location of strong earthquakes sources with corresponding parameters; and a list of the used bibliography.

Conclusions

Total 107 strong earthquakes occurred from 600 B.C. till 2003 in territory of Republic of Armenia, Artsakh and adjacent parts of Transcaucasus are included in the Atlas.
Atlas contains isoseismal maps of strong earthquakes compiled for the first time. It includes a reexamined, corrected and unified homogenous data catalogue, isoseismal maps and descriptions of 86 strong earthquakes, compiled by the improved on newest scientific level uniform, complex methodology presented in work. Each of isoseismal maps of 86

earthquakes with the same scale compiling 1:1000000, and for more affected area of 6 of them scale 1:500000 includes isolines, shocked localities with seismic intensity degree in this points and source parameters determined according to given isoseismal map and source data. In the same way information on 21 ancient disastrous earthquakes, for which are constructed theoretical isoseismals limiting pleistoseistal areas (areas limiting by isoseismal of maximal intensity) are included. In the new catalog of all earthquakes the errors in determination of their basic parameters and full source data for every earthquake are also included.

Description of each event quoted from the primary sources accompanied by necessary comments and followed by the list of references. Actually, the work is a full database about the strong earthquakes taken place on the considered territory.

All data generalized in the map of the main tectonic faults and peistoseistal areas and also in the map of sources of strong earthquakes (including theoretical peistoseistal areas and sources of 21 strong events), scale 1:1500000.Actually, work is a database about the strong earthquakes taken place on the considered territory.

The Atlas is compiled for the use by specialists in different spheres of Earth sciences, seismology, geology, geophysics, geography, seismic resistant construction, projectors, earthquake prediction, seismic risk and earthquake hazard estimation, history, as well as by the general public.

The methodology of the fulfilling of strong earthquakes complete knowledge database and isoseismal and seismotectonic maps, and also analyzing and estimation of strong earthquakes consequences may be successfully used in international requirements and activities.

I want to mention memory of Prof. N.N. Shebalin (IPhE of the Ac.Sc. USSR) for directing me at initial stage of works, when I was composing Armenian part of the “New Catalog of Strong Earthquakes in the USSR” [NC1, 1977 and NC2, 1982].

References

Babayan T.Ho (2006). Atlas of the Strong Earthquakes of the Republic of Armenia, Artsakh and Adjacent Territories From Ancient Times Trough 2003, Tigran Mets Publishing House. Armenia*, ISBN: 99941-0-168-4, 140p*

NC1 (1977). New Catalog of Strong Earthquakes in USSR From Ancient Times Trough 1975. Ed. N.V.Kondorskaya and N.V. Shebalin*, Ac.Sc.USSR, Nauka, Moscow, 536p.*

NC2 (1982). New Catalog of Strong Earthquakes in U.S.S.R. From Ancient Times Trough 1977. Ed. N.V.Kondorskaya. N.V. Shebalin, World Data Center A For Solid Earth Geophysics, July*, Boulder, Colorado, USA, 600p.*

Seismic Site Effect Modelling based on in Situ Borehole Measurements in Bucharest, Romania

Bala A (1), Balan S F (1), Ritter J R R (2), Hannich D (2), Rohn J (3)

(1) National Institute for Earth Physics, Bucharest-Magurele, Romania, bala@infp.ro
(2) Universität Karlsruhe (TH), Germany, joachim.ritter@gpi.uni-karlsruhe.de
(3) University of Erlangen-Nürnberg, Germany

Keywords: site effects, seismic measurements, spectral acceleration, microzonation.

Introduction

Within the NATO Science for Peace Project 981882 *"Site-effect analyses for the earthquake-endangered metropolis Bucharest, Romania"* we determined a unique, homogeneous dataset of seismic, soil-mechanic and elasto-dynamic parameters. Ten 50 m deep boreholes were drilled in the metropolitan area of Bucharest in order to recover cores for dynamic tests and to measure vertical seismic profiles. These are used for an updated microzonation map related to earthquake wave amplification. The boreholes are placed near former or existing seismic station sites to allow a direct comparison and calibration of the borehole data with actual seismological measurements. A database is assembled which contains P- and S-wave velocity, density, geotechnical parameters measured at rock samples and geological characteristics for each sedimentary layer. Using SHAKE2000 we compute spectral acceleration response and transfer functions obtained from the in situ measurements. The acceleration response spectra correspond to the shear-wave amplifications excited in the sedimentary layers from 50 m depth (maximum depth) up to the surface. We present the acceleration response results from four sites.

Bucharest, the capital of Romania, with more than 2 million inhabitants, is considered, after Istanbul, the second-most earthquake-endangered metropolis in Europe. It is identified as a natural disaster hotspot by a recent global study of the World Bank and the Columbia University (Dilley *et al*., 2005). Four major earthquakes with moment magnitudes between 6.9 and 7.7 hit Bucharest in the last 68 years. The most recent destructive earthquake of 4 March 1977, with a moment magnitude of 7.4, caused about 1.500 casualties in the capital alone. All disastrous earthquakes are generated within a small epicentral area –the Vrancea region- about 150 km northeast of Bucharest (Figure 1). Thick unconsolidated sedimentary layers below Bucharest amplify the arriving seismic waves causing severe destruction. Thus, disaster prevention and mitigation of earthquake effects is an issue of highest priority.

There are only a few sites which were investigated coincidently with geophysical and geotechnical techniques to relate the local geology with seismic wave propagation properties in Bucharest City (especially amplitude-amplification properties). Therefore, the main purpose of the NATO SfP Project 981882 is to obtain a unique, homogeneous dataset of soil-mechanic and elasto-dynamic parameters of the subsurface of Bucharest from ten new boreholes to model the so-called seismic site responses. Here we present the seismic measurements and modelling results from 4 selected sites.

NATO Science for Peace Project 981882

The zoning of the metropolitan area of Bucharest for seismic amplification pattern (microzonation) has been pursued with great effort since the 1977 disastrous event. Geophysical groups at the National Institute for Earth Physics (NIEP) and civil engineers at the National Institute for Building Research worked on this problem, as well as foreign institutions like the Universität Karlsruhe (TH), the University of Trieste and the Japanese International Cooperation Agency. Their work resulted in an improved seismic database obtained from modern seismic observation networks as well as several borehole analyses. Based on these observations recent microzonation studies were done by e.g. Aldea *et al.* (2004), Cioflan *et al.* (2004), Kienzle *et al. (*2004), Moldoveanu *et al.* (2004), Mandrescu *et al.* (2007) and Wirth *et al.* (2003). However, all of these studies could cover only fraction of the microzonation problem, because either seismic data alone (Wirth *et al*., 2003) or numerical modelling based on the assumed geological layering (Cioflan *et al.,* 2004) was done. Sokolov *et al*. (2004) used spectral amplification factors and a probabilistic method to determine ground motion site effects in Bucharest. A major drawback of all studies is missing geophysical and geotechnical information from well-distributed boreholes in the Bucharest City area.

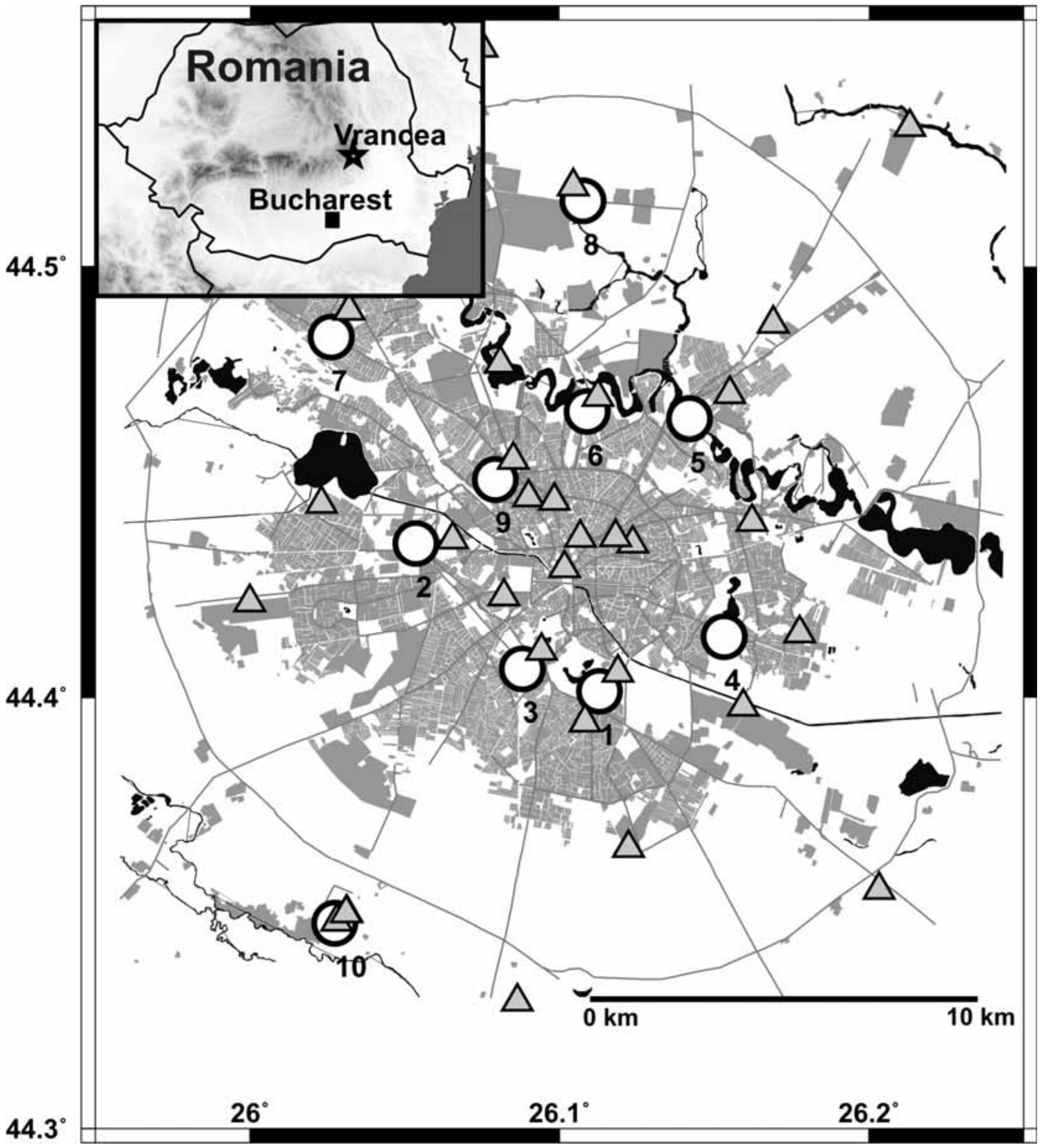

Figure 1. Map with area under investigation. The metropolitan region of Bucharest, Romania, is mainly inside the characteristic ring road with a diameter of about 20 km. Residential and industrial areas are indicated in grey; lakes, channels and rivers in black. The ten borehole sites are shown as circles and numbers. Sites with

broadband instruments during the URS experiment (Ritter *et al*., 2005) are indicated with triangles.

New high-quality seismic waveforms were measured during the URS (URban Seismology) Project from October 2003 until August 2004 (Fig. 1). Within this project 32 state-of-the-art broadband stations were continuously recording in the metropolitan area of Bucharest (Ritter *et al.,* 2005). This unique dataset provides important information on the seismic amplitude variation across the area. Additionally, there is a modern ground acceleration observation network (K2-network) which has been upgraded in the last years by the Universität Karlsruhe (KA) and NIEP and which is run by NIEP. From this network a database with valuable strong motion recordings emerged.

To complement the seismic data with a coherent set of borehole measurements and dynamic core analysis, we received funding from NATO to drill ten boreholes in the city, to recover cores for dynamic geotechnical testing and to conduct seismic borehole measurements. The main objective of the project is earthquake risk mitigation and better seismic safety of Bucharest. The boreholes are placed near URS stations (Urban Seismology project 2003/2004 - (Ritter *et al.,* 2005) or K2 stations (a strong-motion recording network) of the National Institute for Earth Physics, Bucharest (NIEP) to allow a direct comparison and calibration of borehole data with actual seismic measurements. The determined dynamic material parameters and the structural information will be used as input for linear and non-linear waveform modelling to estimate the seismic amplitude amplification at specific sites in Bucharest. These modelled waveforms will be compared and calibrated with observations from seismic stations in the city. The results from the site-effect analysis will be gathered in an updated seismic microzonation map of Bucharest which will be disseminated to the public and especially to the end-users who will introduce our results in the future city planning.

Results of the down-hole seismic measurements

Most P-wave seismic velocities (*Vp*) values recorded in Bucharest City are in a narrow range (Table 1) . The velocities recorded at the Ecologic University site are a bit larger. The seismic shear wave velocities (*Vs)* are in a very close range: between 120-160 m/s at the surface and 400-440 m/s at 50 m depth. Results obtained by the down-hole method in 4 boreholes drilled in Bucharest City are presented in Table 1. They were used as input data in the program SHAKE2000 as described below.

Table 1. Mean weighted seismic velocities for the first 5 (of 7 types) of Quaternary layers in 4 boreholes in Bucharest City (Figure 1). For a description of the layers see Ciugudean-Toma and Stefanescu (2006), Bala *et al.* (2007b), Mandrescu *et al*. (2007) or Ritter *et al*. (this vol ume).

Geological layer	1		2		3		4		5		Mean *Vs* for the first	
											30m	50 m
Mean weighted velocities	*Vp* m/s	*Vs* m/s	*Vp* m/s	*Vs* m/s	*Vp* m/s	*Vs* m/s	*Vp* m/s	*Vs* m/s	*Vp* m/s	*Vs* m/s	Vs_{30} m/s	Vs_{50} m/s
Tineretului Park (site 1)	180	140	570	220	943	316	---	--	1790	400	289	332
Ecologic Univ (site 2)	300	120	118 0	220	1250	241	1770	378	2170	410	316	356
Astronomic Inst. (site 3)	200	120	914	281	1200	330	1713	380	2160	440	296	337
Titan2 Park (site 4)	290	160	800	250	800	250	980	350	1675	406	326	366
Mean weighted *V*	233	138	870	270	995	297	1555	374	1812	407		

The mean weighted seismic velocities for the first 5 (of 7 types) of Quaternary layers are computed and given also in the Table 1 for the four sites, in order to be compared with seismic velocity values obtained from previous seismic measurements. Weighted mean values for V_S are computed according to the following equation (1):

$$\overline{V}_S = \frac{\sum_{i=1}^{n} h_i}{\sum_{i=1}^{n} \frac{h_i}{V_{Si}}} \qquad (1)$$

where h_i and V_{Si} denote the thickness (in meters) and the shear-wave velocity (in m/s) of the *i*-th layer, in a total of *n* layers for the same type of layer (Romanian Code for the seismic design for buildings - P100-1/2006). According to the same code, the weighted mean values $\overline{V}_S$, computed for at least 30 m depth, determine 4 classes of the soil conditions:

1. Class A , rock type : $\overline{V}_S \geq 760$ m/s;
2. Class B, hard soil : $360 < \overline{V}_S < 760$ m/s;
3. Class C, intermediate soil: $180 < \overline{V}_S < 360$ m/s;
4. Class D, soft soil: $\overline{V}_S \leq 180$ m/s;

All the $V_{S\text{-}30}$ values in Table 1 belong to type C (intermediate soil) after this classification (Romanian Code for the seismic design for buildings - P100-1/2006). Even the $V_{S\text{-}50}$ values in Table 1 fall in the type C of the classification. According to this code, the elastic response spectra characterising the 4 classes of the soil conditions will be determined using the methodologies in the international practice.

One-dimensional ground response analysis at 4 sites in the Bucharest City area

A ground response analysis consists of studying the behaviour of a soil/rock deposit subjected to an acceleration time history applied to a layer of the profile. When dealing with earthquake ground motions, the acceleration time history is usually specified at the bedrock. Examples of response quantities that can be obtained are the acceleration, velocity, displacement, stress, and strain time histories for any layer. Some of the applications of these analyses are the liquefaction potential or the seismic risk assessment in earthquake-prone regions.

Different methods of ground response analysis have been developed including one dimensional, two dimensional, and three dimensional approaches. Various modelling techniques like the finite element method were implemented for linear and non-linear analysis. Extended information on these analyses is given by Kramer (1996). Here we apply an equivalent linear one-dimensional analysis, as implemented in the computer program SHAKE2000 (Ordónez, 2003). The term one-dimensional refers to the assumption that the soil profile extends to infinity in all the horizontal directions and the bottom layer is considered a half space. Only the vertical propagation of seismic waves is considered, usually shear waves. The equivalent linear one-dimensional analysis is often an approximate linear approach. The non-linear behavior of the soil is accounted for by means of an iterative process in which the soil damping ratio and shear modulus are changed such that they are consistent with a certain level of strain calculated with linear assumptions. The non-linearities of the soil are not implicitly considered as in fully non-linear methods; rather at each iteration cycle the equations of motion solved are those of an equivalent linear model.

The equivalent linear method was proved to obtain good approximations of the response of a soil deposit subjected to an earthquake. and it had been successfully compared with finite element methods and fully non-linear analysis. A recent comparison made with finite element non-linear codes was performed in a seismic amplification study in Lotung, Taiwan (Borja, *et al.*, 2002).

Input Data

The *static soil properties* required in the 1D ground response analysis with SHAKE2000 are: maximum shear wave velocity or maximum shear strength and unit weight. Since the analysis accounts for the non-linear behaviour of the soils using an iterative procedure, *dynamic soil properties* play an important role. The shear modulus reduction curves and damping curves are usually obtained from laboratory test data (cyclical triaxial soil tests). The variation in geotechnical properties of the individual soil layers are mostly impossible to model because of the lack of appropriate data. Therefore, these poorly constraint properties should be assumed constant for each defined soil layer. In built shear modulus reduction curves and damping curves for specific types of layers are used in SHAKE2000 based on published geotechnical tests (Ordonez, 2003).

As input data the interval seismic velocities *Vs* (in m/s), as well as the natural unit weight (in kN/m^3) and thickness of each layer (in m) are used. All these data are stored in a database for four new borehole sites in Bucharest area (Table 1, after Bala *et al*., 2007a). The velocity values from Table 1 are close to other measured values by Hannich *et al*. (2006) and Bala *et al.* (2007b). The recorded motion of the 27.10.2004 earthquake (Mw=5.8) at K2 accelerometer station BBI in Bucharest is used as seismic input motion. All 3 components (one vertical and two horizontal components) were available. This station is placed in the borehole at INCERC site at 100 m depth. The strong motions BBI_E (east-west component) and BBI_N (north-south component) were chosen as being a representative acceleration recorded in a borehole in Bucharest from a moderate Vrancea earthquake.

Acceleration response spectra obtained at 4 sites in the Bucharest City central area

Acceleration response spectra computed at different depth levels with the programme SHAKE2000 show the amplification due to the package of sedimentary layers from 50 m depth to the surface (Figures 2-6). These response spectra are thought to represent the case of a moderate to strong earthquake motion (see above).

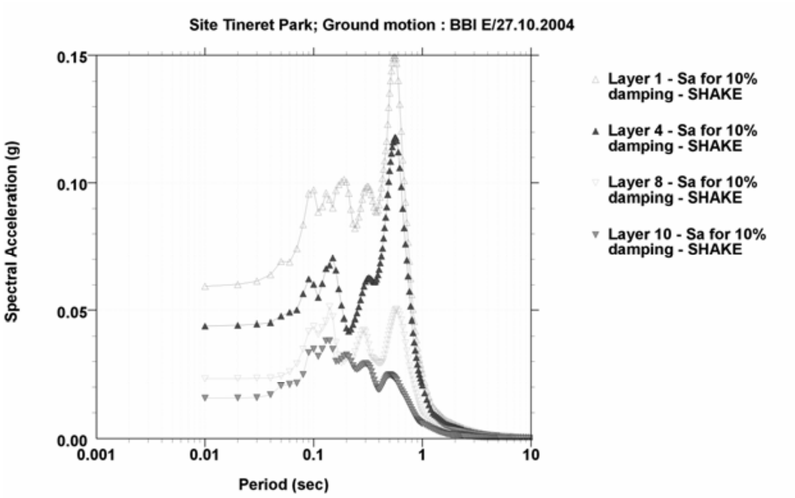

Figure 2. Calculated spectral acceleration response computed for the site Tineretului Park (site 1 in Figure 1). As input wavelet the strong motion from BBI_E is taken (see text). Results for four layers are shown.

The response diagramme for Astronomic Institute (Figure 3) is very similar to the diagramme for Tineretului Park (Figure 2), with a peak of 0.16 g acceleration at 0.55 s period. For the site Ecologic University (Figure 4), near Dambovita river, we find 2 acceleration peaks, one at 0.2 s (0.14 g), especially in the first layer, and another again at 0.55 s (0.15 g). For the site Titan

2 Park (Figure 5), the amplification occurs between 0.09-0.2 s (0.12 g) and also at 0.5 s (0.15 g).

The EUROCODE 8 currently proposes two standard shapes for the design response spectra. Type 1 spectra are enriched in long periods and are suggested for high seismicity regions and magnitude $M_S > 5.5$. Type 2 spectra are proposed for moderate seismicity areas and exhibit both a larger amplification at short periods, and a much smaller amplification at long period contents, with respect to Type 1 spectra ($M_S < 5.5$). In Figure 6 the type 1 spectral acceleration was found (EUROCODE8) as determined from the comparison with the spectral acceleration at the site Astronomic Institute.

Finally, SHAKE2000 needs specific geotechnical inputs such as: input signal (scenario earthquakes), shear wave velocity and soil thickness. Some real borehole profiles are available now with shear wave velocity and soil thickness, including some measurements on the core samples. The proper input signal, either a real earthquake or an artificial strong motion created with SHAKE2000, remain to be chosen and tested in future work. The level in the geologic profile considered "bedrock", where this input signal should be applied, should be properly documented from field measurement.

Conclusions

1. A new international research project was initiated in 2006 - NATO SfP Project 981882: *Site-effect analyses for the earthquake-endangered metropolis Bucharest, Romania*. This project, conducted by the *National Institute for Earth Physics*, Bucharest, Romania and *Universität Karlsruhe (TH)*, Germany, has the target to fill the gap in the knowledge concerning seismic and geotechnical parameters in the shallow (H < 50 m) layers in Bucharest, especially in the Quaternary layers 1 - 5, as they are described by Ciugudean and Stefanescu, 2006.
2. The computed values for seismic velocities are in the same range as others obtained by *in situ* seismic measurements of different types. They are added to the database at NIEP, which is a valuable collection of elastic and dynamic parameters of the sedimentary rocks obtained by direct measurements. The values will be used for further studies on the seismic microzonation of Bucharest City using linear and non-linear approaches.
3. The velocity values obtained in the first 3 layers (Table 1) are very important and among the first results measured in these sedimentary layers and reported for Bucharest City. They are well correlated with the values obtained in Bucharest by Hannich *et al*. (2006) using the SCPT method.

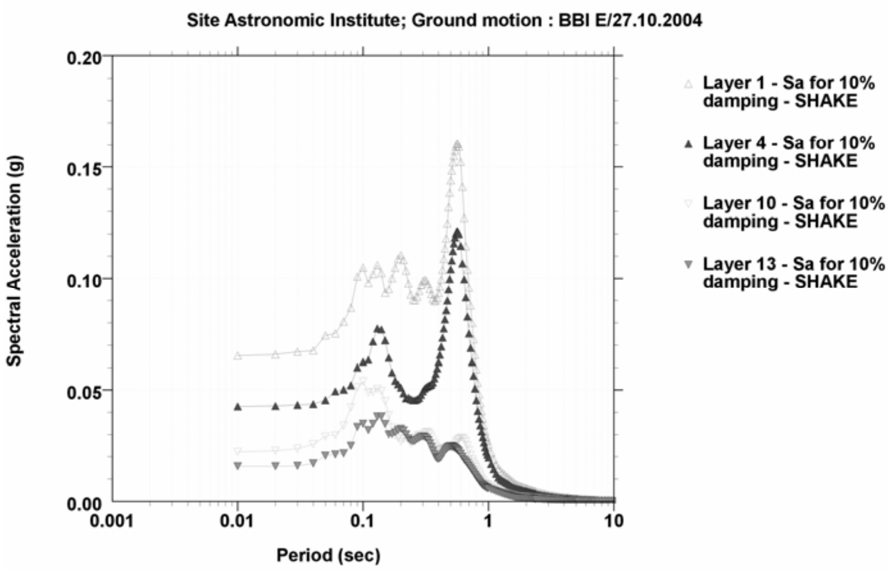

Figure 3. Calculated spectral acceleration response computed for the site Astronomic Institute.

Acknowledgments

This paper is a result of the NATO SfP Project 981882 “Site-effect analyses for the earthquake-endangered metropolis Bucharest, Romania”. This research is sponsored by NATO's Scientific Affairs Division in the framework of the Science for Peace Programme.

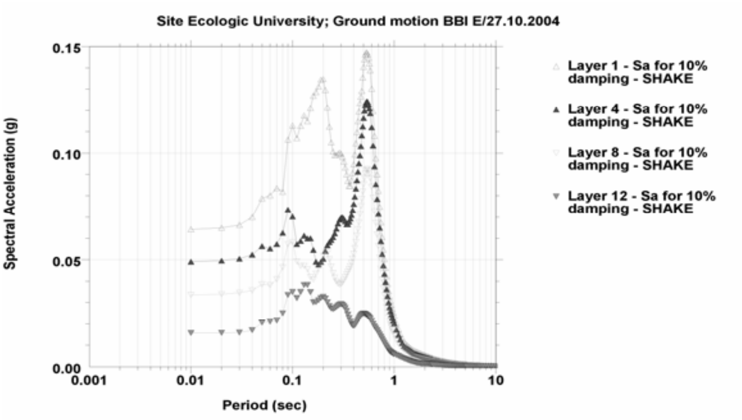

Figure 4. Calculated spectral acceleration response computed for the site Ecologic University.

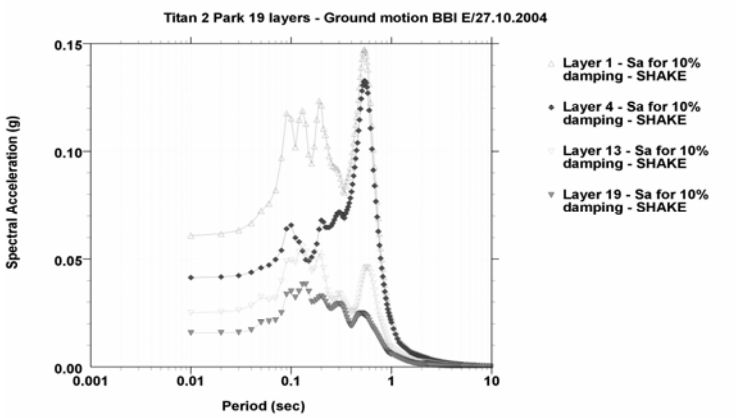

Figure 5. Calculated spectral acceleration response computed for the site Titan2 Park.

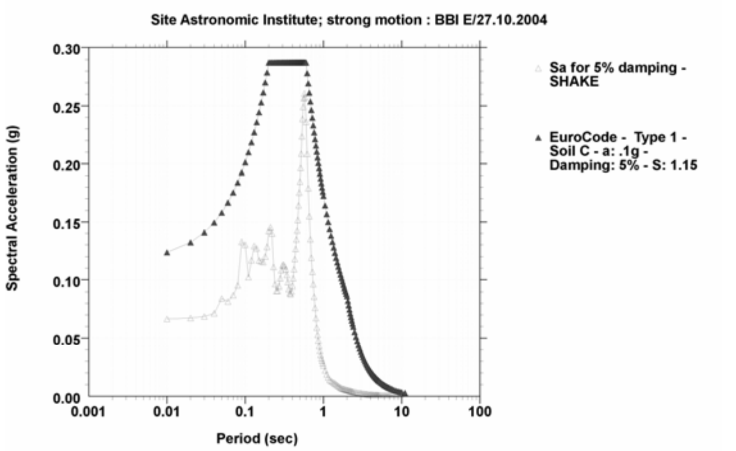

Figure 6. Calculated spectral acceleration response (5% damping) computed for the site Astronomic Institute and the corresponding design spectra from EUROCODE 8 (Type 1 - soil C).

References

Aldea A., Lungu D. & Arion C (2004). GIS mapping of seismic microzonation and site effects in Bucharest based on existing seismic and geophysical evidence. In*: Lungu D., Wenzel F., Mouroux P. & Tojo I. (eds.), Earthquake loss estimation and risk reduction 1, 237-249p.*

Bala A., Raileanu V., Zihan I., Ciugudean V., Grecu B (2006). Physical and dynamic properties of the shallow sedimentary rocks in the Bucharest Metropolitan Area, *Romanian Reports in Physics, Vol. 58, no. 2, 221-250.*

Bala A., Ritter J.R.R., Hannich D., Balan S.F., Arion C (2007a). Local site effects based on in situ measurements in Bucharest City, Romania *, Proceedings of the International symposium on Seismic Risk Reduction, ISSRR-2007, paper 6, 367-374, Bucharest.*

Bala A., Zihan I., Ciugudean V., Raileanu V., Grecu B. (2007b). Physical and dynamic properties of the Quaternary sedimentary layers in and around Bucharest City*, Proceedings of the International symposium on Seismic Risk Reduction,ISSRR-2007, paper 7, 359-366, Bucharest.*

Borja R. I., Chao H. Y., Montáns F.J. & Lin C.H (1999). Nonlinear Ground Response At Lotung LSST Site, *Journal of Goetechnical and Geoenvironmental Engineering, ASCE, Vol. 125, No. 3, 187-197p.*

Cioflan C.O., Apostol B.F., Moldoveanu C.L., Panza G.F. & Marmureanu G (2004). Derministic approach for the microzonation of Bucharest, *Pure appl. geophys., 161, 1-16.*

Ciugudean-Toma V., Stefanescu I (2006). Engineering geology of the Bucharest city area, Romania, paper no. 235*, IAEG -2006 Proceedings, Engineering Geology for Tomorrow's Cities.*

Dilley M., Chen R.S., Deichmann U., Lerner-Lam A.L. & Arnold M. with Agwe J., Buys P., Kjekstad O., Bradfield Lyon B. & Gregory Yerman G (2005). Natural disaster hotspots: A global risk analysis, synthesis report.

Hannich D., Huber G., Ehret D., Hoetzl H., Balan S., Bala A., Bretotean M., Ciugudean V (2006). SCPTU Tecniques Used for shallow geologic/hydrogeologic Site Characterization in Bucharest, Romania*, 3-rd International Symposium on the Effects of Surface Geology on Seismic Motion, Grenoble, France, 30 Aug.-1 Sept. 2006, paper 71.*

Kienzle A., Hannich D., Wirth W., Ciugudean V., Rohn J. & Czurda K (2004). Seismic zonation of Bucharest. In: Lungu, D., Wenzel. F., Mouroux, P. & Tojo, I. (eds*.), Earthquake loss estimation and risk reduction 1, 251-259p.*

Moldoveanu C.L., Radulian M., Marmureanu Gh. & Panza G.F (2004). Microzonation of Bucharest: State of the art, *Pure appl. geophys., 161, 1125-1147*.

Mandrescu N., Radulian M. & Marmureanu Gh (2007). Geological, geophysical and seismological criteria for local response evaluation in Bucharest urban area*, Soil Dyn. Earthq. Engin., 27, 367-393.*

Ordónez G.A. (2003). SHAKE2000: A computer Program for the 1-D Analysis of Geotechnical Earthquake Engineering Problem.

Ritter J.R.R., Balan, S., Bonjer K.-P., Diehl T., Forbriger T., Marmureanu G., Wenzel F. & Wirth W (2005). Broadband urban seismology in the Bucharest metropolitan area, *Seism. Res. Lett., 76, 573-579.*

Ritter J.R.R., Balan S., Bala A., Rohn J (2006). Annual Technical Report for the NATO SfP Project 981882 (Oct. 2006 and 2007), Bucharest and Karlsruhe.

Sokolov V.Y., Bonjer K.P. & Wenzel F (2004). Accounting for site effect in probabilistic assessment of seismic hazard for Romania and Bucharest: a case study of deep seismicity in Vrancea zone*, Soil Dynamics and Earthquake Engineering, 24, 927-947.*

Wirth W., Wenzel F., Sokolov V.Y. & Bonjer K (2003). A uniform approach to seismic site effect analysis in Bucharest, Romania*, Soil Dynamics and Earthquake Engineer, 23, 737-758.*

Romanian Code for the seismic design for buildings - P100-1/2006.

EUROCODE-8 - prEN1998-1-3 (2001) - Design provisions for earthquake resistance of structures, European Committee for Standardisation.

Methods to Assess the Site Effects Based on in situ Measurements in Bucharest City, Romania

Bala A (1), Aldea A (2), Hannich D (3), Ehret D (4), Raileanu V (1)

(1) National Institute for Earth Physics, Bucharest - Magurele, Romania, bala@infp.ro
(2) Technical University for Civil Engineering, Bucharest, Romania, aldea@utcb.ro
(3) University of Karlsruhe, Dept. of Applied Geology, Karlsruhe, Germany
(4) University of Erlangen-Nürnberg, Germany

Keywords: Peak ground acceleration, characteristic site period, shear wave seismic velocity, amplification factor.

Introduction

In seismic microzonation we want to display the variation in seismic response of the subsurface and subsequently determine where the soil is being amplified to a level that may damage existing buildings or other structures. Frequently *peak ground acceleration (PGA)* is used to determine the maximum horizontal forces that can be expected. The method is not always adequate, because PGA often correspond to high frequencies, which are out of range of the natural frequencies of most structures.

The largest amplification of the soil will occur at the lowest natural frequency or its *fundamental frequency*, which corresponds to the *characteristic site period.* In situ measurements of shear wave velocity in the soil and the soil thickness, provide a direct measure of the characteristic site period. Extensively seismic noise measurements is a much accessible method and computed H/V spectral ratio can also provide a good indication on the fundamental frequency of the site.

Average shear wave velocity in the first 30 m depth (V_S-30) as defined in EUROCODE 8 and Romanian Code P100-1 is a useful indicator in seismic microzonation, showing zones with low values of average seismic velocities in Bucharest.

Peak Ground Acceleration determination in Bucharest

Bucharest is one of the most affected cities by earthquakes in Europe. Situated at 140 – 170 km distance from Vrancea epicentral zone, Bucharest had suffered many damages due to high energy Vrancea intermediate-depth earthquakes. For example, the 4 March 1977 event produced the collapse of 32 buildings with 8-12 levels, while more than 150 old buildings with 6-9 levels were seriously damaged. Since then the occurrence of 3 other earthquakes (1986 /M=7.1; 1990 /M=6.9; 2004 /M= 6.0) demonstrated that the Vrancea seismic activity is continuing, permanently threatening the Bucharest City area.

The studies done after 1977 earthquake had shown the importance of the surface geological structure upon ground motion parameters and emphasized the need for new methods of quantifying the site effects.

The earthquake from 27.10.2004 was one of the most studied as there were many good recordings in the Bucharest City area. The accelerometer network of National Institute for Earth Physics has recorded this earthquake and the PGA map for Bucharest was computed for the 3 components. Considering only the EW horizontal component, they show variation in the PGA with amplitudes with ratio from 1 to 4 (16 to 60 cm/s2) in the city area (Fig. 1).

Most of this variation is due first to the package of the Quaternary sedimentary layers which amplify the original strong motion arrived from the earthquake to the bedrock.

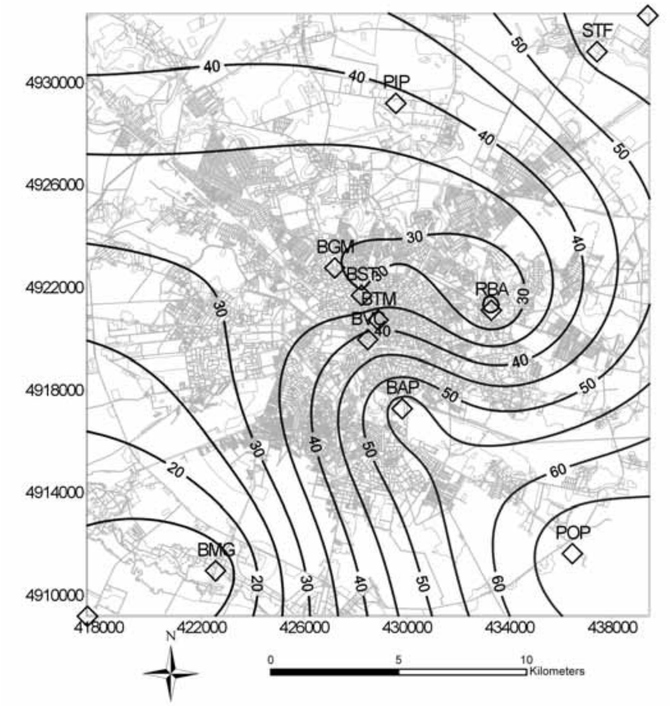

Figure 1. Map of the interpolated values of PGA_EW [cm/s^2] in Bucharest for the earthquake of 27.10.2004. Coordinates are in UTM.

Geology of the Bucharest area

Bucharest City is situated in the central part of the Moesian Platform, an important structural unit of Romania which corresponds to the Romanian Plain.
The Moesian Platform has a basement with 2 structural units: a lower one with chloritic and sericitic schists of Precambrian age and an upper one made up of old Paleozoic folded marine formations going back to the Middle Carboniferous age. The sedimentary cover of the Moesian Platform is relatively thick, exceeding 6000 m. The Cretacic basement was identified at about 1000 – 1500 m depth and it is covered by Sarmatian and Pliocene deposits. The sea disappeared gradually and heterogeneous Tertiary and Quaternary deposits are composing the surface geology in Bucharest City area. The Tertiary formations in Bucharest area are estimated to be about 700 – 800 m thick and they are covered by Quaternary sediments.

The cohesionless Quaternary deposits are largely developed in the Bucharest area, with thickness of about 200 m in the south to 300 m in the north (Figure 2). The existing amount of geologic, hydrogeological and geotechnical data make possible to know the general lithological succession from the bottom upwards for the Lower and Upper Quaternary deposits. They are represented in Figure 2 by seven main lithologic complexes consisted mainly of gravel, sands and shales or clays. For a description of the layers see Ciugudean-Toma and Stefanescu (2006), Bala *et al.* (2007b), or Ritter *et al*. (this volume).

The local geology above the 7-th layer, the Fratesti layer A, which is 100 m depth in the south to 200 m depth in the north, is very rapidly changing from one point to another in only a few hundreds of meters (Bala et al., 2006). The real succession of the 7 principal layers as well as their physical properties can be ascribed only by in situ measurements in boreholes.

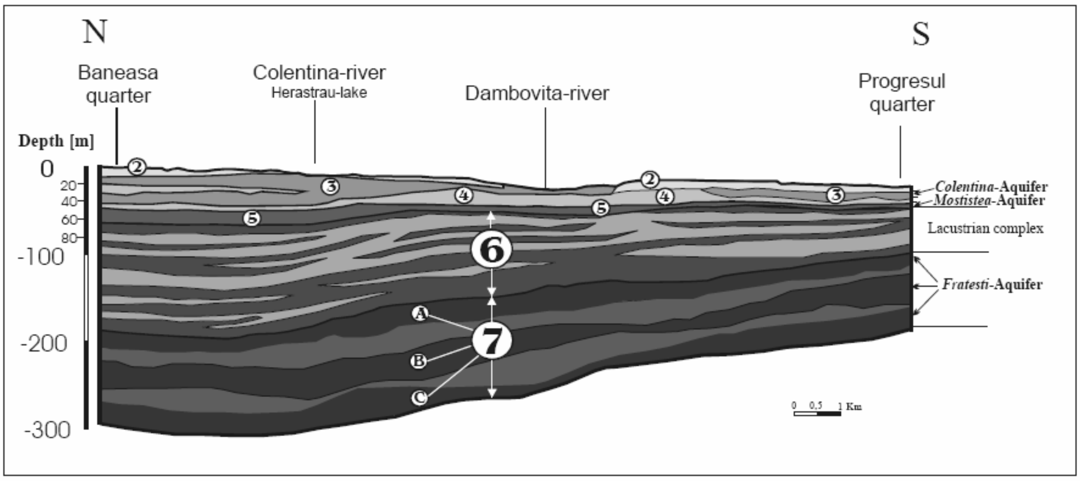

Figure 2. Geological cross-section in a N-S direction in Bucharest City.

Physical Parameters of Quaternary Sedimentary Layers in Bucharest

Down-hole seismic measurements were performed by a combined effort of National Institute for Earth Physics (NIEP), SC “Prospectiuni” S.A. and SC METROUL SA in 12 sites (boreholes) from Bucharest City in the frame of the CERES Project 34/2002 and CERES Project 3-1/2003. Detailed information about the measurements and seismic velocity values obtained was presented by Bala et al., 2006 and 2007b.
Mean weighted values for Vp and Vs are computed for each of the 12 boreholes according to the following formula:

$$\overline{V_S} = \frac{\sum_{i=1}^{n} h_i}{\sum_{i=1}^{n} \frac{h_i}{V_{Si}}} \qquad (1)$$

Where h_i and V_{Si} denote the thickness (in meters) and the shear-wave velocity (in m/s) of the i-*th* layer, in a total of *n* layers, existing in the same type of stratum (Romanian Code for the seismic design for buildings - P100-1/2006 and EUROCODE 8).

The site Bazilescu was excluded from presentation due to low velocities recorded in all the layers, for which a satisfactory explanation was not yet found. However in a recent paper (Hannich et al, 2006) seismic measurements using SCPTU techniques are presented for the same site (BAZI) and low Vs values are presented of about 250 m/s at 26 m depth, with a large drop (150 m/s) between 7 - 11 m depth. This confirmation of low velocity of the shear waves in the same site put into evidence by another method will lead us to reconsider our measurements in Bazilescu site.

The National Center for Seismic Risk Reduction (NCSRR, Bucharest) instrumented in 2003 seven sites in the northern half of Bucharest City (Aldea et al., 2006) in cooperation with the Japan International Cooperation Agency (JICA). NCSRR performed downhole measurements at all sites that were instrumented, the deepest investigation was down to 140 m depth. All the results of the mean weighted seismic velocities (Aldea et al., 2006) are gathered in the Table 1.

Other shear wave velocity values for the shallow layers (down to 50 m depth) were obtained in the frame of the NATO SfP Project 981882 in the years 2006 - 2007 and they were reported by Bala et al., 2007a and Ritter et al., 2007.

Characteristic Site Period

The largest amplification of the soil will occur at the lowest natural frequency or its fundamental frequency. The period of vibration corresponding to the fundamental frequency is called the characteristic site period (see Eq. 2). The characteristic site period, which only depends on the soil thickness and average shear wave velocity of the soil, provides already a very useful indication of the period of vibration at which the most significant amplification can be expected.
Using the velocity data from 8 of the boreholes of the 12 presented by Bala et al., 2007b, the map from Figure 2 was computed according to the formula:

$$T = 4h/VS \quad (2)$$

In which T = characteristic site period in seconds and VS is the average velocity until the Fratesti layer, considered to be the basement layer and h is the total thickness of the sedimentary layers.

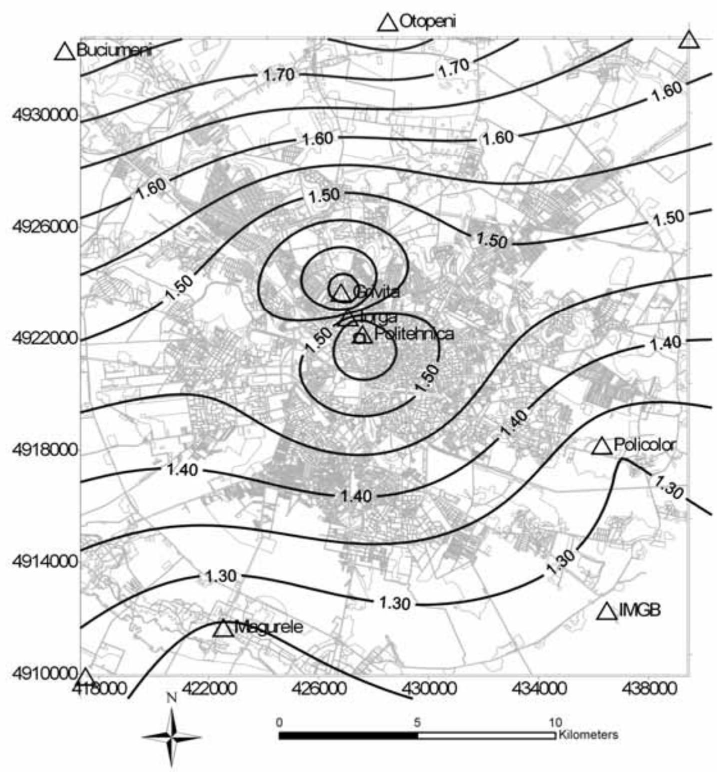

Figure 3**.** Map of the characteristic site period (in seconds) for the Bucharest City. Coordinates are given in UTM system [meters].

The characteristic site period was computed with h being the total thickness of the main geologic layers until the 7-th layer (Fratesti Layer, described by Ciugudean and Stefanescu, 2005). VS is computed as mean weighted velocity value down to the same geologic layer for each of the 8 sites.

The map from Figure 3 shows an increase in the characteristic site period, from 1.25 s in the south (NIEP-Magurele) to 1.75 s in the north (Otopeni site), due to the general increase of the depth to Fratesti Layer from south to north. In the meantime due to the different values of mean weighted velocity for each site, some variations in the characteristic site period appear right in the central part of Bucharest, which is the most sensible zone vulnerable to strong seismic events. In the near future some new data must be recorded in this central part of the city in order to obtain better geophysical characteristics of the sedimentary layers.

Mean Weighted Seismic Velocity V_{S-30} and V_{S-50}

Seismic velocities in the Table 1 are obtained by several authors by seismic measurements in boreholes. They were gathered in order to compute the mean weighted seismic velocity for the first 30 m depth (VS-30), for each case according to formula (1). A first map of VS-30 is presented in the Figure 4.

Table 1. Mean weighted seismic velocity for the first 30 m depth (V_{S-30}) and 50 m (V_{S-50}) obtained in different sites in Bucharest City

No.	Borehole	V_{S-30}	V_{S-50}	References
1.	Grivita_110	330.9	341	Bala et al., 2006, 2007b.
2.	Politehnica_200	297.2	310	
3.	Policolor_100	286.0	292.5	
4.	Otopeni_200	243.1	274	
5.	Magurele_112	289.8	313	
6.	Iorga_170	245.1	254.6	
7.	Foradex_81	295.7	315.4	
8.	Buciumeni_150	255.8	281	
9.	Bazilescu_172	247.3	248.2	
10.	Centura 1	288	318.4	
11.	Centura2	260.5	292	
12.	Tineretului Park	263	304	Bala et al., 2007a.
13.	Univ_Ecologica	281	326	
14.	Inst_Astronomic	283	320	
15.	Titan2 Park	308	341	
16.	Motodrom Park	288	327	Ritter et al., 2007
17.	Student Park	295	319	
18.	Romanian Shooting Fed.	297	347	
19.	Geologic Museum	320	328	
20.	AGRO	311	--	Hannich et al., 2006
21.	BAZI	267	--	
22.	INCERC	311	--	
23.	INMH	264	--	
24.	METRO	303	--	
25.	MOGO	281	--	
26.	VICT	290	--	
27.	City Hall	219	258	Aldea et al., 2006
28.	Municipal Hospital	245	281	
29.	NCSRR/ INCERC	270	302	
30.	Piata Victoriei	284	310	
31.	UTCB -Pache	288	318	
32.	Civil Protection	293	309	
33.	UTCB - Tei	309	326	

According to the map in Figure 4 the Vs-30 have a range from 220 – 320 m/s. The north part of Bucharest is characterized by rather low velocity values, under 280 m/s, while in the south medium values are encountered. The central part is characterized by a low value zone around City Hall and Municipal Hospital, followed to the north by high values (Grivita) and to the east by medium values (UTCB Tei).

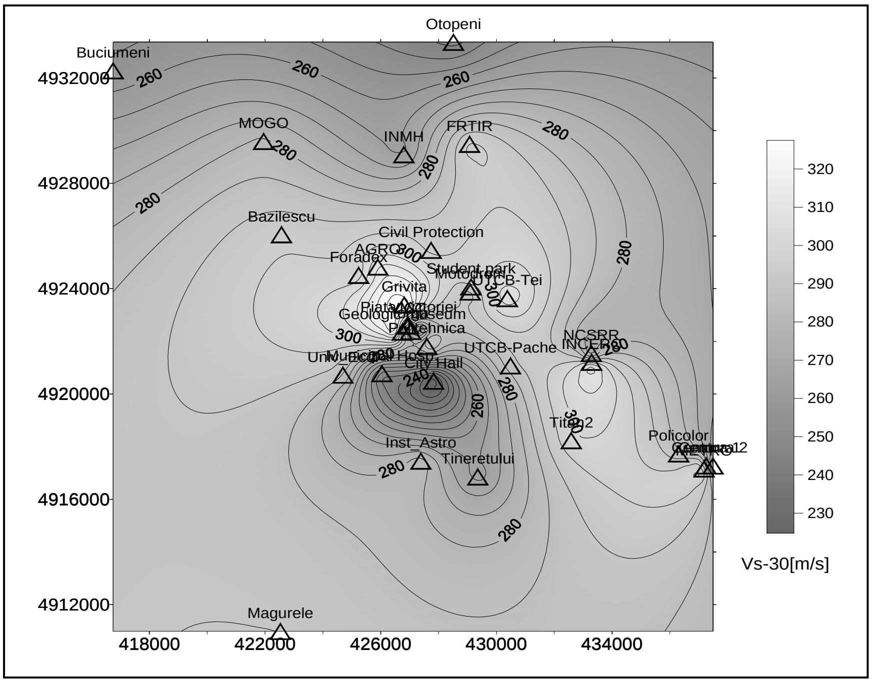

Figure 4. Map of the mean weighted seismic velocity (V_{S-30}) in Bucharest City from downhole seismic measurements. Coordinates are given in UTM system (meters).

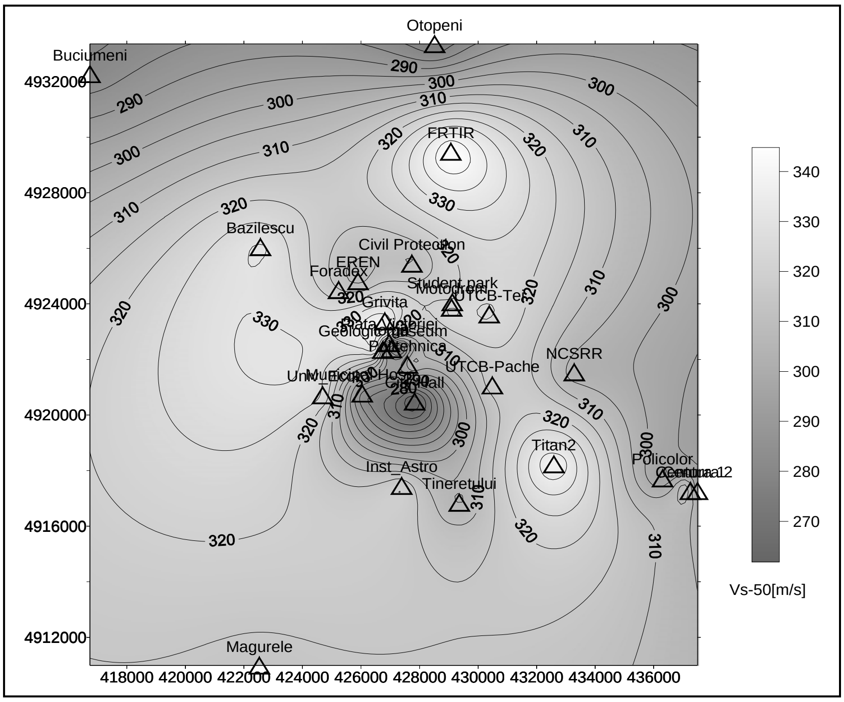

Figure 5. Map of the mean weighted seismic velocity (V_{S-50}) in Bucharest City from downhole seismic measurements. Coordinates are given in UTM system (meters).

The VS-50 map shows the a range of higher velocity values, from 270 – 340 m/s, with low values in the north, and medium to high values in the central part of the city (Figure 5). A pronounced low is present in the center around the sites of City Hall and Municipal Hospital, both located near Dambovita river, with velocity values under 300 m/s. Some 2 sites show high values of up to 340 m/s (Romanian Shooting Federation and Titan 2 Park).

Conclusions

The earthquake from 27.10.2004 was one of the most studied as there were many good recordings in the Bucharest City area. The free field accelerometer network of National Institute for Earth Physics has recorded this earthquake and the PGA map for Bucharest was computed for the 3 components. Considering only the horizontal EW component, it shows variation in the PGA with amplitudes ratio of 1/4 (16 to 60 cm/s2) in the city area (see Figure 1). Most of this variation is due to the package of the Quaternary sedimentary layers which amplify the original strong motion arrived from the earthquake at the bedrock.

The Quaternary local geology in Bucharest City is very rapidly changing from one point to another in only a few hundreds of meters (Bala et al., 2006 and 2007a). The geological layer which is considered the bedrock is the Fratesti layer A, which depth is at 100 m in the south and 200 m depth in the north. The real succession of the 7 principal layers as well as their physical properties can be ascribed only by in situ measurements in boreholes.

The largest amplification of the soil will occur at the lowest natural frequency or its fundamental frequency. The period of vibration corresponding to the fundamental frequency is called the characteristic site period. The characteristic site period, which only depends on the soil thickness and average shear wave velocity of the soil, provides already a very useful indication of the period of vibration at which the most significant amplification can be expected. The map (Figure 3) shows an increase in the characteristic site period, from 1.25 s in the south to 1.75 s in the north, due to the general increase of the depth to Fratesti Layer A from south to north. In the meantime due to the different values of mean weighted velocity for each site, some variations appear right in the central part of Bucharest, which is the most sensible zone vulnerable to strong seismic events. The values of the characteristic site period have the same values as those computed in the same sites using an entirely different method: the spectral ratio H/V method (Bala et al., 2007 a, b).

Seismic velocities in the Table 1 are obtained by several authors by direct seismic measurements in boreholes. They were gathered in order to compute the mean weighted seismic velocity for the first 30 m depth (VS-30) and 50 m depth (VS-50), for each case, according to formula cited in the Romanian Code for the seismic design for buildings - P100 - 1/2006 and in EUROCODE 8. All the VS-30 values in Table 1 belong to type C of soil after this classification (Romanian Code for the seismic design for buildings - P100-1/2006). Even the VS-50 values in the Table 1 fall in the type C of the classification (180 m/s < $\overline{V}_S$ < 360 m/s).
According to this code, the elastic response spectra characterizing the 4 classes of the soil conditions will be determined using the methodologies in the international practice.

A first map of VS-30 is presented in the Figure 4 for the Bucharest City area. According to this map, the north part of Bucharest is characterized by rather low velocity values, while in the south-west medium values are encountered. The central part is characterized by a complex mixture of low values (Iorga_170) with medium (Politehnica_200) and high values (Grivita_110).
The VS-50 map shows the range of the velocity values from 270 – 340 m/s, with low values in the north, and medium to high values in the central part of the city (see Figure 5).
This image shows that in the central part of the Bucharest, where low value areas are mixed with high values, new seismic measurements are needed in order to have an improved image of this important parameter which has a great impact on the microzonation map of the Bucharest City, Romania.

Acknowledgements

The research work presented in this paper is realized in the frame of the research project PNCDI 31-038/2007, funded by the Romanian Ministry for Education, Research and Youth, Bucharest, Romania.

References

Aldea A., Yamanaka H., Negulescu C., Kashima T., Radoi R., Kazama H., Calarasu E (2006). Extensive seismic instrumentation and geophyiscal investigation for site-response studies in Bucarest, Romania, *Proceedings of the Third International Symposium on the Effects of Surface geology on Seismic Motion*, Grenoble France, 30 Aug. – 1 Sept. 2006, paper 69.

Bala A., Raileanu V., Zihan I., Ciugudean V., Grecu B. (2006), Physical and dynamic properties of the shallow sedimentary rocks in the Bucharest Metropolitan Area, *Romanian Reports in Physics, Vol. 58, no. 2, 221-250.*

Bala A., Ritter J.R.R., Hannich D., Balan S.F., Arion C (2007a). Local site effects based on in situ measurements in Bucharest City, Romania*, Proceedings of the International symposium on Seismic Risk Reduction, ISSRR-2007, paper 6, 367 - 374, Bucharest.*

Bala A., Zihan I., Ciugudean V., Raileanu V., Grecu B (2007b). Physical and dynamic properties of the Quaternary sedimentary layers in and around Bucharest City*, Proceedings of the International symposium on Seismic Risk Reduction, ISSRR-2007, paper 7, 359-366, Bucharest.*

Ciugudean V., Stefanescu I (2006). Engineering geology of the Bucharest city area, Romania*, paper no. 235 submitted to IAEG -2006, Engineering Geology for tomorrow's cities.*

Hannich D., Huber G., Ehret D., Hoetzl H., Balan S., Bala A., Bretotean M., Ciugudean V. (2006). SCPTU Techniques Used for shallow geologic/hydrogeologic Site Characterization in Bucharest, Romania, *3-rd International Symposium on the Effects of Surface Geology on Seismic Motion, Grenoble, France, 30 Aug. - 1 Sept. 2006, paper 71.*

Ritter J.R.R (2006). Tiefe Einblicke - NATO finanziert Bohrprojekt im erdbebengefährdeten Bukarest, In *UNIKATH, Karlsruhe, Germany, 3, 31p.*

Ritter J.R.R., Balan S., Bala A., Rohn J (2007). *Annual Technical Report for the NATO SfP Project 981882 (Oct. 2007)*, Bucharest and Karlsruhe.

Romanian Code for the seismic design for buildings - P100 -1/2006.

EUROCODE-8 - prEN1998-1-3 (2001) - Design provisions for earthquake resistance of structures, European Committee for Standardisation.

Geotechnical Investigations at Core Samples from the Bucharest Metropolitan Area

Balan S F (1), Ritter J R R (2), Bala A (3), Huber G (4)

(1) National Institute of R-D for Earth Physics, sbalan@infp.ro
(2) Universität Karlsruhe (TH), Joachim.Ritter@gpi.uni-karlsruhe.de
(3) National Institute of R-D for Earth Physics, bala@infp
(4) Universität Karlsruhe (TH), Gerhard.Huber@ibf.uni-karlsruhe.de

Keywords: geotechnical investigations, dynamic tests, microzonation, borehole.

Introduction

Bucharest, the capital of Romania, with more than 2 million inhabitants, is considered after Istanbul the second-most earthquake-endangered metropolis in Europe. It is identified as a natural disaster hotspot by a recent global study of the World Bank and the Columbia University (Dilley *et al*., 2005). Four major earthquakes with moment-magnitudes between 6.9 and 7.7 hit Bucharest in the last 68 years. The most recent destructive earthquake of 4th March 1977, with a moment magnitude of 7.4, caused about 1.500 casualties in the capital alone. All disastrous earthquakes are generated within a small epicentral area – the Vrancea region - about 150 km north of Bucharest. Thick unconsolidated sedimentary layers in the area of Bucharest amplify the arriving seismic shear-waves causing severe destruction. Thus, disaster prevention and mitigation of earthquake effects is an issue of highest priority for Bucharest and its population.

As a major scientific aim we develop calibrated seismic response laws which can be used to describe the seismic wave amplification in Bucharest. Several seismic recording stations from different institutions are running in the Bucharest area. There are also numerous shallow boreholes from different institutions which were used to map the subsurface lithology. However, there are only 16 boreholes which were partly geotechnically investigated to relate the local geology with seismic wave propagation properties (especially amplitude-amplification properties). Therefore, a NATO Science for Peace project (SfP 981882) was initiated to obtain a unique, homogeneous dataset of soil-mechanic and elasto-dynamic parameters of the subsurface of Bucharest. Within this project 10 new, 50 m deep, boreholes were drilled to recover cores for geotechnical laboratory measurements and to measure *in situ* seismic velocities. These parameters are the input information to model the so-called seismic site responses (see Bala et al., this volume). In a second step these modelled site responses will be compared to already available observed site responses (measured seismograms) to derive the relationship between the measured subsurface soil / rock properties and the observed seismic amplitudes. Then this calibrated relationship can be applied to other available borehole lithologies in the metropolitan area of Bucharest. Thus in the end this research programme will help to develop an optimised seismic microzonation of the metropolitan area of Bucharest which will be implemented for the future urban planning. In this contribution we report about the geotechnical measurements that are later used for linear and non-linear wave propagation simulations.

Drilling Programme

According to the proposed plan of the project ten new boreholes with a depth of 50 m were drilled in the metropolitan area of Bucharest in order to obtain the necessary data for a new and modern map with site effects related to earthquake wave amplification. The boreholes (Figure 1) are placed near URS stations (URban Seismology project 2003/2004, Ritter *et al*.,

2005) or K2 stations (a strong-motion recording network) of the National Institute for Earth Physics, Bucharest (NIEP) to allow a direct comparison and calibration of borehole data with actual seismic measurements. The positions of the ten proposed boreholes were also chosen in order to fill geophysical and geotechnical information gaps in the metropolitan part of Bucharest.

Four boreholes were drilled in spring 2006. These boreholes are in the following locations: Titan 2 Park, Tineretului Park, Ecologic University (near Dambovita River) and the Astronomic Institute of Romania (near the Carol Park). In 2007 another six boreholes were drilled at the following sites: Motodrom Park, Tei Park, Bazilescu Park, Romanian Sport Shooting Federation, Geological Museum (Victory Place – central Bucharest) and the last one in southern part of the city, at the National Institute of Earth Physics (NIEP), in Magurele. The sites can be seen in Figure 1, for further information see Ritter *et al*. (this volume).

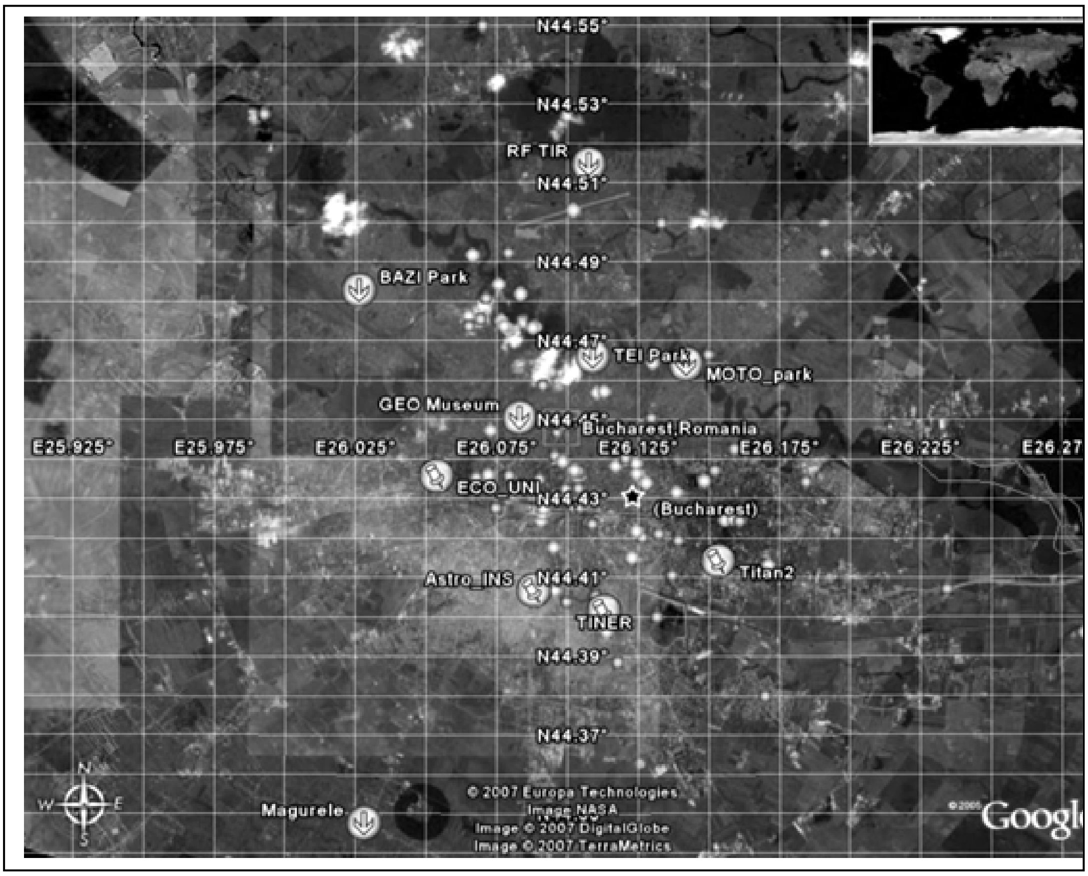

Figure 1. Arial view of Bucharest and its surroundings. The positions of the boreholes are indicated with pins for 2006 sites and with arrows for 2007 sites, together with abbreviated site names.

Geotechnical Investigations

A total number of 250 soil and rock samples were gathered from the 10 drill sites at different depths by the Department of Engineering Seismology (NIEP). These samples were carefully selected mainly without disturbances for cohesive material (sampling as it was recovered from the tube of the drilling machine) and partly disturbed for cohesionless material (soil samples which had no proper consistency). With the data from these samples we created a data base, which contains the following parameters:

- drill location,
- GPS coordinates of drill,
- date of recover,

- depth of sample,
- short geological and mechanical characterisation of each sample.

In Table 1 all geotechnical experiments performed with the samples from the ten sites are summarized.

Table 1. Overview on the geotechnical experiments conducted with the recovered core samples; ss: soft soil; sh: hard soil

Operation	No.	Objective
Drilling of 50 m deep boreholes	10	Drilling and Probing Operations
Resonant column tests	58	Dynamicac parameters for linear and non-linear modelling of wave propagation
Triaxial tests (dynamical, undrained);	15	Dynamical and mechanic parameters
CU Triaxial test	6 (ss) 6 (sh)	Standard geotechnical experiment
Edometric tests	19	
Angle of repose	7	Standard geotechnical experiment
Granulometry	54	Standard geotechnical experiment
Maximum and minimum compactness	6	Standard geotechnical experiment
Determination of e_min and e_max	12	Standard geotechnical experiment
Determination of liquid and plastic limit	4	Standard geotechnical experiment

Results and discussions of some tests

After a first close examination of the database with the core samples, 58 samples were chosen from representative geological layers for tests in the resonant column. One sample was chosen from a soil layer. The Drnevich resonant column is used for the experimental determination of the dynamic soil response at harmonic oscillations, through soliciting a cylindrical sample with harmonic stationary vibrations, torsional and/or longitudinal in resonance mode. In our case the torsional mode is applied. Inside the resonant column cell the geological pressure of the sample is simulated.

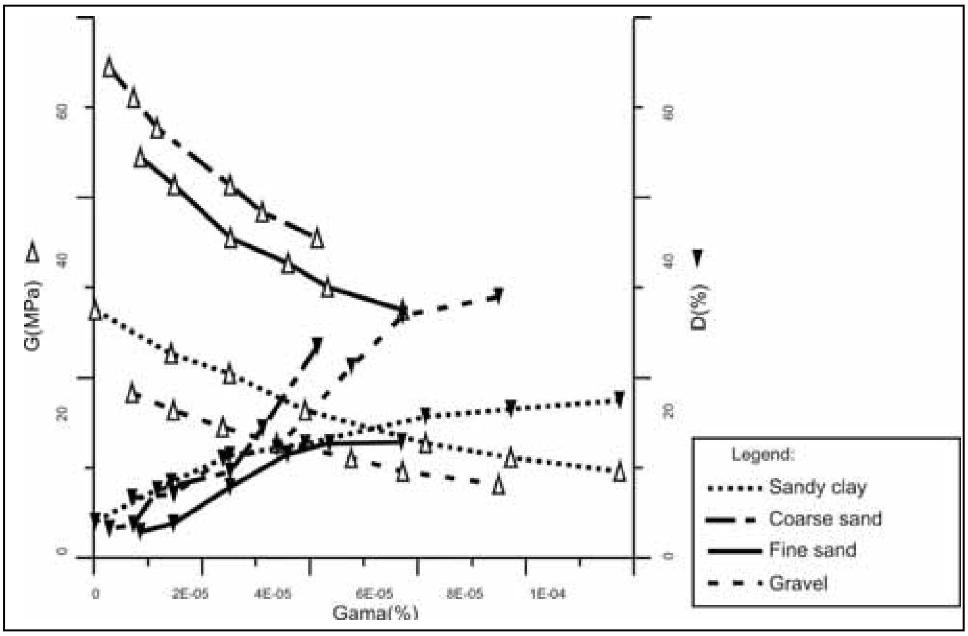

Figure 2. Resonant column tests with different core samples from the Tineretului Park. G is the shear modulus, Gama is the shear strain, D is the damping ratio.

In Figure 2 the result of a resonant column test is presented which was conducted in a Drnewich apparatus with different soils from the site Tineretului Park. The dynamic triaxial tests for the determination of the deformability properties of the core samples were done in accordance to international specifications, e.g. with the Romanian standard P125 – 84 "The Determination of Shear Resistance of Soils under Cyclic Dynamic Load through Cyclic Compression Tests", but also the restrictive Japanese norm: "Standards of Japanese Geotechnical Society for Laboratory Shear Tests – JGS 0542-2000 – Method for Cyclic Triaxial Test to Determine Deformation Properties of Geomaterials". The triaxial apparatus used is the model: DTC – 367 (Seiken Inc. Japan). In Figures 3 and 4 CU triaxial test results are presented for the Magurele borehole site with samples from 3.5 – 5.0 m depth (Figure 3) and 21 – 25 m depth (Figure 4).

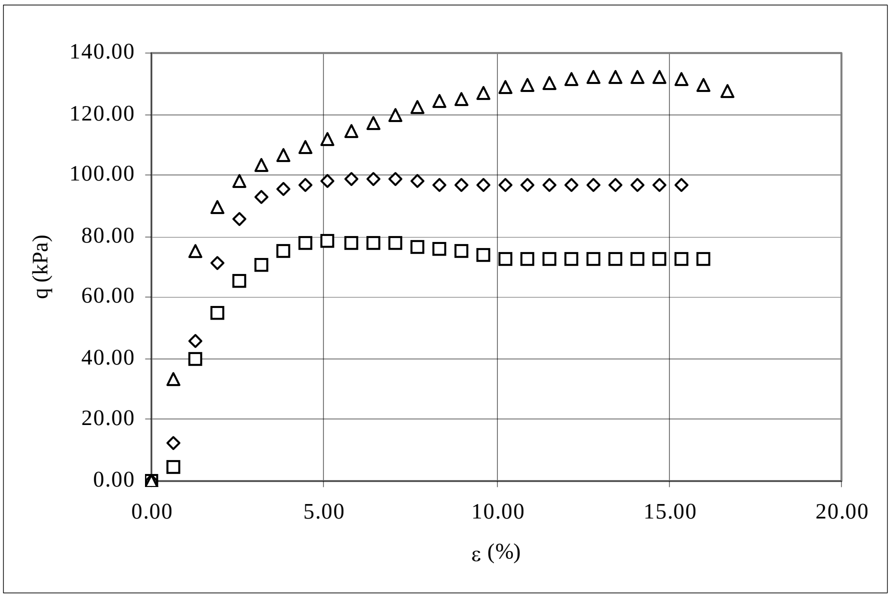

Figure 3. CU triaxial test. q is the load in kPa, ε is the deformation in %.

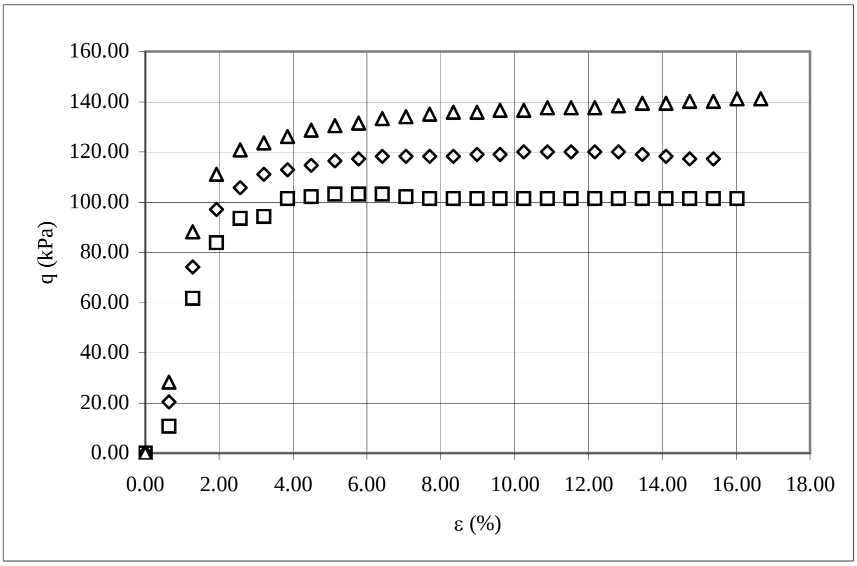

Figure 4. CU triaxial test. q is the load in kPa, ε is the deformation in %.

The tests were made with three samples from the same depth interval. Thus one can observed the influence of the geological pressure for obtaining the same deformation. The strengths of the soil samples is similar as for other data of the Bucharest area.

In Table 2 we present the results for the identification of the sample in the laboratory (1), identification of the sample after the Ternary Diagram (2), granulometry, mass and humidity. The sample chosen is from Tineretului Park.

Table 2 Core sample analysis results from Tineretului Park. m is mass of sample, m_d is dry mass of sample, w is humidity of the sample, w_{medium} is medium humidity of sample. The samples description contains percent of: clay / dust / fine sand / medium sand / coarse sand / gravel and the density of the mineral skeleton (g/cm^3) with the particle percentage with diameter d < 2 µm.

Sample (ID)	Depth (m)	m (g)	m_d (g)	w (%)	w_{medium} (%)	Sample description
P1	3.0-3.5	**Without humidity**				(1) Sandy clay, red brown
						(2) sandy clay
						16/26/48/6/2/2
						2.7, 10
P2	3.5-4.0	30.87	23.64	30.58	31	(1) Grey clay, with grey dots, with red insertion
		35.91	27.70	29.64		(2) clay
		31.59	24.21	30.48		34/36/20/6/2/2
		33.34	25.60	30.23		2.72, 28
		147.27	112.65	30.73		Edometric test
P3	4.0-4.5	30.45	23.28	30.80	31	(1) Brown clay, with brown dots, and red insertion, plastic soft
		31.78	24.36	30.46		(2) clay
		33.03	25.34	30.35		34/44/22/0/0/0
		37.14	28.42	30.68		2.72, 22
		147.26	113.52	29.72		Edometric test
P6	7.0-8.5	**Without humidity**				(1) Coarse sand yellow grey, a little dusty
						(2) dusty sand
						0/14/4/22/58/2
						2.65, -
P18	35.0-37.0	**Without humidity**				(1) Gravel in clay mixture, medium size
						(2) dusty sand
						0/12/4/4/4/76
						2.65, -

In Table 3 the results from the test of compression-settling are presented for core samples from the boreholes in Tineretului Park and Astronomic Institute. The results show the general characteristics of samples of the Bucharest area.

Table 3. Tests of compression–settling. Core sample identification: 1.1: Tineretului Park 3.5-4.0 m depth; 1.2 Tineretului Park 4.0-4.5 m depth; 3.1 Astronomic Institute 3.0-3.5 m depth; 3.2 Astronomic Institute 5.0-5.5 m depth; 3.3 Astronomic Institute 47.0-48.0 depth;
Parameters: $M_{0.5\text{-}1}$: edometric modulus (in kPa) in the pressure range 50-100 kPa; $M_{1\text{-}2}$: edometric modulus (in kPa) in the pressure range 100-200 kPa; $M_{2\text{-}3}$: edometric modulus (in kPa) in the pressure range 200-300 kPa; ε_2 : specific deformation (in %) at a pressure stage of 200 kPa; a_v: volumic compressibility coefficient (in kPa^{-1}); n: porosity (in %); e: pore index (dimensionless); S_r: saturation range (in %).

Sample	1.1	1.2	3.1	3.2	3.3
$M_{0.5\text{-}1}$=	4545	3333	25000	10000	16667
$M_{1\text{-}2}$=	5263	3774	25000	12500	18182
$M_{2\text{-}3}$ =	5556	5882	15385	15385	16667
ε_2 =	4.10	5.40	0.75	2.10	1.15
a_v=	$3.347\ 10^{-04}$	$3.136\ 10^{-04}$	$1.046\ 10^{-04}$	$1.036\ 10^{-04}$	$1.013\ 10^{-04}$
γ =	19.1	19.1	19.9	20.3	19.6
n=	46	46	38	37	41
e=	0.86	0.84	0.61	0.59	0.69
S_r=	0.98	0.97	0.80	0.87	0.87

In Table 4 the plastic limit determination is given for core samples from the boreholes Tineretului Park and Astronomic Park. The results have the general characteristics of the Bucharest area.

Table 4. Plastic limit determination. Core sample identification: 1.1: Tineretului Park 3.5-4.0 m depth; 1.2 Tineretului Park 4.0-4.5 m depth; 3.1 Astronomic Institute 3.0-3.5 m depth; 3.2 Astronomic Institute 5.0-5.5 m depth;
Parameters: w: humidity; wp kneading limit [%]; wL: flow limit [%]; Ip: plasticity index [%], IC consistency index; IA activity index.

Sample	1.1	1.2	3.1	3.2
$\% < 2\mu m$	28	22	31	29
w	31	31	19	19
wp	22	20	17	17
wL	62	51	45	47
Ip	40	31	28	30
IC	0.78	0.65	0.93	0.93
IA	1.43	1.41	0.90	1.03

Conclusions

A drilling and core recovery project was conducted in Bucharest, Romania. By obtaining the geotechnical parameters of the core samples for these ten sites situated at different locations in the Bucharest area, we cover zones where these parameters were not known before. This makes our effort unique and of great importance for the new comprehensive data bank acquired during the project. The geotechnical data vary at the different location sites in the city, but have the general characteristics of Bucharest geotechnical parameters. This data acquisition is part of a comprehensive project where also geophysical and geological data were gathered. Their combined interpretation makes this project of great significance for seismic risk mitigation for the Bucharest city area, for a safer seismic design and for the improvement of microzonation efforts.

Acknowledgments

The authors are grateful to NATO - Science for Peace Project grant SfP 981882 which permitted the funding of this research. The URS project was financed by the Deutsche

Forschungsgemeinschaft, the National Institute for Earth Physics (Bucharest-Magurele), the Universität Karlsruhe (TH) and the State of Baden-Württemberg.

References

Balan S.F.; Cioflan C.O.; Apostol B.; Tataru D. & Ritter J.R.R (2007). Urban Seismology Research in the Metropolitan Area of Bucharest*, EGU2007-A-02272 ,EGU General Assembly 2007, 15-20 April 2007, Wien, Austria.*

Balan S.F, Apostol B., Bala A., Ritter J.R.R. & Huber G (2008). New Geotechnical Tests in the Bucharest Metropolitan Area, *EGU General Assembly 2008, 12-18 April 2008, Wien, Austria.*

Dilley M., Chen R.S., Deichmann U., Lerner-Lam A.L. & Arnold M. with Agwe J., Buys P., Kjekstad O., Bradfield Lyon B. & Gregory Yerman G (2005). Natural disaster hotspots: A global risk analysis, *synthesis report*.

Ritter J.R.R., Balan S.F., Bonjer K.-P., Diehl T., Forbiger T., Marmureanu Gh., Wenzel F. & Wirth W (2005). Broadband Urban Seismology in the Bucharest Metropolitan Area, *Seismological Research Letters, Volume 76, No. 5, 574-580.*

Influence of Soil Property Uncertainty on Ground Motion Amplification

Barani S (1), De Ferrari R (1), Ferretti G (1), Eva C (1)

(1) Dipartimento per lo studio del Territorio e delle sue Risorse – University of Genoa, Viale Benedetto XV 5, 16132 Genoa, Italy, barani@dipteris.unige.it

Keywords: Monte Carlo simulation, non-linear dynamic analysis, amplification factor

Introduction

Modern building codes for seismic design define the seismic action in terms of damped elastic response spectra. Spectral ordinates account for site effects through the use of specific soil amplification factors, F_a, that are a function of site category and, in some cases, of the shaking level for the reference site condition (e.g., National Earthquake Hazard Reduction Program – NEHRP (Building Seismic Safety Council – BSSC, 2003), Norme Tecniche per le Costruzioni – NTC (Ministero delle Infrastrutture e dei Trasporti, 2008)). The reference shaking level can be obtained from probabilistic or deterministic seismic hazard analyses while soil classes are defined on the basis of the average shear wave velocity in the upper 30 m of a soil profile, V_{S30}

For a given site class, F_a defines how much the ground motion that would be expected for the reference site condition (e.g., rock condition) is amplified by that particular soil type. Different definitions of F_a can be found in literature. In the NEHRP provisions, F_a represents the ratio of the spectral acceleration, $S_a(T)$, for a given site condition to the value of the spectral acceleration corresponding to the reference condition. In Eurocode 8 – EC8 (Comitè Europèen de Normalisation – CEN, 2003), it is defined as the ratio of the average acceleration response intensity (Von Thun, 1988), *ASI*, for a specific soil category to the acceleration spectrum intensity for the reference site condition. A similar definition is given by Pergalani et al. (1999), Pergalani et al. (2003), and Barani et al. (2008) but the pseudo-velocity response spectrum intensity (Housner, 1952), *SI*, is used to quantify the ground motion level at the site of interest instead of *ASI*. The use of an amplification factor based on integral measures of the ground motion intensity, such as *SI* and *ASI*, has the advantage that these quantities relate better to the building damage than other ground motion parameters such as PGA, PGV, and $S_a(T)$ (e.g., Miyakoshi & Hayashi, 2000). Indeed, both *ASI* and *SI* account for the amplitude and frequency content of earthquakes in a single parameter (Kramer, 1996; Miyakoshi & Hayashi, 2000).

The amplification factors defined in building codes can be evaluated by using empirical data recorded during earthquakes or, alternatively, are the results of analytical studies consisting of one-dimensional (1-D) equivalent linear or nonlinear ground response analyses (e.g., Dobry et al., 1994; Seed et al., 1994). In this latter case, the degree of knowledge of geophysical and geotechnical parameters used in defining the 1-D model of the soil column may have an important role on the final F_a values. Hence, the uncertainty in the soil properties should be considered for the characterization of the ground response of a soil column and, consequently, for the quantification of F_a. To this purpose, Bazzurro and Cornell (2004) propose to include the uncertainty in the soil properties through a Monte Carlo approach that consist of randomly varying the soil parameter values.

The main objective of this work is to quantify the influence of the uncertainty in the soil parameters on the ground motion amplification. Two sites in Tuscany (Northern Italy), representative of different case studies, are considered here. These sites presents similar characteristics except for bedrock (i.e., infinite half-space at the bottom of a soil profile) depth that, in one case, is known from boreholes and geophysical data while, in the other, is highly uncertain. The ground response of the profiles considered is evaluated by driving a suite of real accelerograms recorded at rock sites through different samples of each soil model. Each sample is obtained by randomization of the soil properties (Bazzurro & Cornell, 2004). A computer program that accounts for the nonlinear behavior of soils is applied to evaluate the site response.

Methodology

In order to evaluate the ground response of each profile the following procedure is applied:

- a conventional probabilistic seismic hazard analysis – PSHA (Cornell, 1968) is performed to choose earthquake time histories (seismic input) for dynamic analyses and to scale records to ground motion levels with a certain probability of exceedance in a given period of time. Specifically, the 5%-damped uniform hazard spectrum (UHS) for a mean return period of 475 years is calculated for a dense range of frequencies. The UHS refers to rock conditions. Then, the peak ground acceleration, PGA, and 1.0s spectral acceleration, S_a(1.0s), hazard are disaggregated in order to define the magnitude-distance (*M-D*) scenarios dominating the rate of exceeding the target ground motion values. In this application, we have deliberately ignored the epistemic uncertainty affecting input models (e.g., recurrence models, attenuation models) and parameters (e.g., earthquake recurrence parameters). An exhaustive PSHA including epistemic uncertainty in the calculations is not the purpose of the work;
- a large number of real accelerograms recorded at rock sites are collected according to the *M-D* pairs controlling the site hazard (4.5 < M < 6.0 and 0 < D < 20km) and the focal mechanism prevailing in the study area (normal and strike slip). Subsequently, an automatic procedure based on Monte Carlo sampling is applied to select the suite of acceleration time histories whose average 5%-damped response spectrum best matches the target UHS (for details see Barani et al., 2008). A group of 10 accelerograms is selected. The corresponding acceleration response spectra are shown in Figure 1 where they compared with the reference UHS.

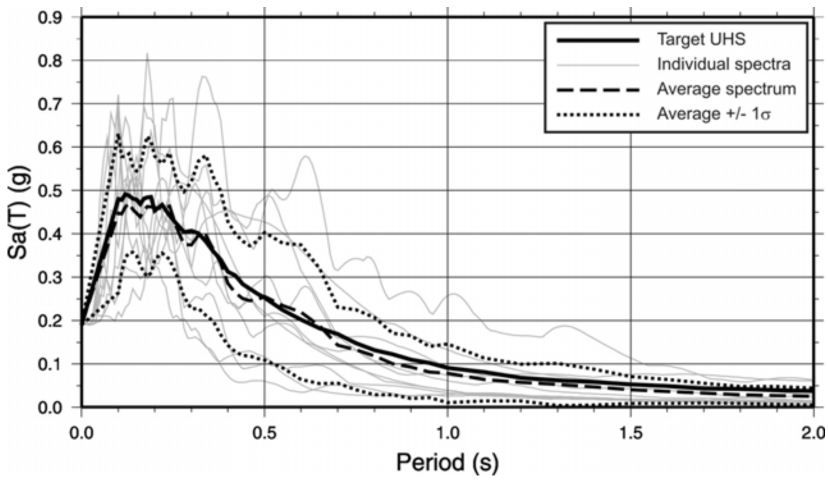

Figure 1. Matching between the target UHS and the average of 5%-damped response spectra of selected accelerograms.

- geotechnical and geophysical data (e.g., shear waves velocity profiles, horizontal to vertical (H/V) spectral ratio measurements), are acquired in order to define 1D models of the soil columns. H/V measurements are also used to assess the reliability of amplification functions, *AF*(*f*), obtained from dynamic analyses;
- numerical ground response analyses are performed using Shake91 (Schnabel et al., 1972; Idriss & Sun, 1993), a computer program that uses an iterative, equivalent linear approach to approximate the nonlinear, inelastic behaviour of soils. This program computes

the response of a soil deposit that is idealized as a system of homogeneous visco-elastic layers of infinite horizontal extent overlying a uniform half-space (bedrock) subjected to vertically propagating shear waves. Each layer is homogeneous and isotropic with known thickness, unit weight, maximum shear modulus, modulus reduction curve, and damping curve. Dynamic analyses are performed both for the *base case*, with soil properties whose values are equal to those obtained from field or laboratory tests, and the *randomized case*, with uncertain soil properties;

- the soil amplification (and its related uncertainty) is evaluated for each site by a frequency-independent amplification factor defined as:

$$F_a = \frac{ASI^s}{ASI^r} \tag{1}$$

where ASI^s and ASI^r indicate the acceleration spectrum intensity at the surface and at the rock outcrop, respectively.

The acceleration spectrum intensity is calculated as in EC8 (Rey et al., 2002):

$$ASI = \int_{0.05}^{2.5} \overline{S_a(T)} dT \tag{2}$$

where $\overline{S_a(T)}$ indicates the average acceleration response spectrum and T the spectral period.

Description of the sites and soil modelling

In this study the ground response of two sites located on an alluvial terrace of the Serchio River in Northern Tuscany (Italy) is analyzed. These sites present similar stratigraphic profiles with Quaternary alluvial deposits overlaying Pleistocene fluvio-lacustrine materials. The main difference concerns the depth of the bedrock, the infinite half-space at the top of which the input motion has to be assigned to. At one site (site S1), it is known from boreholes, down-hole measurements, and seismic refraction profiles. At the other (site S2), instead, it can be roughly estimated as a function of the fundamental frequency of vibration of the soil column (Ibs-von Seht & Wohlenberg, 1999):

$$H = \left[\frac{V_0(1-\alpha)}{4F_0} + 1 \right]^{1/(1-\alpha)} - 1 \qquad [1]$$

where H is the thickness of the soil deposit above the bedrock, F_0 the fundamental frequency of the soil column, V_0 the surface shear wave velocity, and α gives the depth dependence of the velocity.
The values of V_0 and α are obtained by analyzing several shear wave velocity (V_S) profiles relevant at some sites within the Serchio Valley (http://www.rete.toscana.it/). Specifically, the value of α is obtained from regression analysis of V_S versus depth (z). The (log) regression model fitted through V_S data is represented by the following equation:

$$\ln(V_S) = \ln(V_0) + \alpha \ln(1 + z/z_0) \qquad (\sigma_{\ln V_S} = 0.235) \qquad [2]$$

where z_0 = 1 m, V_0 = 195 m/s, and α = 0.320 (+/- 0.011).

As stated above, both the sites considered are characterized by a quite homogeneous stratigraphy with Quaternary alluvium overlaying Pleistocene fluvio-lacustrine soils. Alluvial deposits consist mainly of sands and gravels whose relative proportions vary slightly with depth (i.e., the percentage of sand varies from about 44% to 46% while that of gravel from 10% to 29%). The total unit weight (γ) is about 21.5 kN/m^3 while the maximum shear modulus (G_{max}), which was established on the basis of V_S, varies from 197 to 226 MPa. Fluvio-lacustrine materials, instead, consist of a stratigraphic alternation of gravels, sandy gravels, and silty clay. The total unit weight is about 21.8 kN/m^3. G_{max} is in the range of 623 to 1355 MPa. The bedrock at the base of these deposits consists mainly of sandstones belonging to the Oligocene-Miocene "Macigno" formation. Thin layers of siltstone and limestone can be observed. The mean values of γ and G_{max} for the bedrock are 25.4 kN/m^3 and 2971 MPa respectively. For all these materials, modulus reduction and damping curves were obtained from specific laboratory tests (http://www.rete.toscana.it/; Foti et al., 2002).

As stated in the previous section, two different numerical characterizations of the soil column are considered to estimate F_a, namely the *base case* and the *randomized case*. The former is based on the best engineering estimates of the soil properties. The latter, instead, includes the uncertainty in the soil parameters through a Monte Carlo approach that consists of randomly varying γ, V_S, modulus reduction and damping curves. The uncertainty in modulus reduction and damping curves is modelled by varying the shear strain value at 64% of G/G_{max}, $\varepsilon_{64\%}$ (Bazzurro & Cornell, 2004). The same random perturbation factor is applied along the entire modulus reduction and damping curves. These three random variables (RVs) are considered lognormally distributed. In particular, for site S1, we assume $\sigma_{\ln\gamma} = 0.06$ (e.g., Lancellotta, 1995), $\sigma_{\ln V_S} = 0.19$ (estimated from site-specific data), and $\sigma_{\ln\varepsilon_{64\%}} = 0.35$ (Bazzurro & Cornell, 2004). For site S2, we adopt the same values of standard deviation except for $\sigma_{\ln V_S}$ that is set to 0.350 according to what obtained from regression analysis (see Equation 1). Distributions are truncated at $\pm 2\sigma_{\ln RV}$ to prevent unrealistic parameter values. The uncertainty associated with the soil geometry is also considered by randomizing the thickness (h) of each layer of the soil profile. For all the layers of profile S1, we assume that h follows a normal distribution with σ_h equal to 0.5 m. This uncertainty level is adopted also for profile S2 with the exception of the layer just above the bedrock. For this layer, indeed, the uncertainty affecting h reflects the uncertainty in bedrock depth – that is, it depends on the uncertainty in F_0 ($\sigma_{\ln F_0} = 0.228$), V_0 ($\sigma_{\ln V_0} = 0.146$), and α ($\sigma_\alpha = 0.011$). The value of F_0 is obtained from H/V spectral ratios of microtremor recordings (Figure 2).

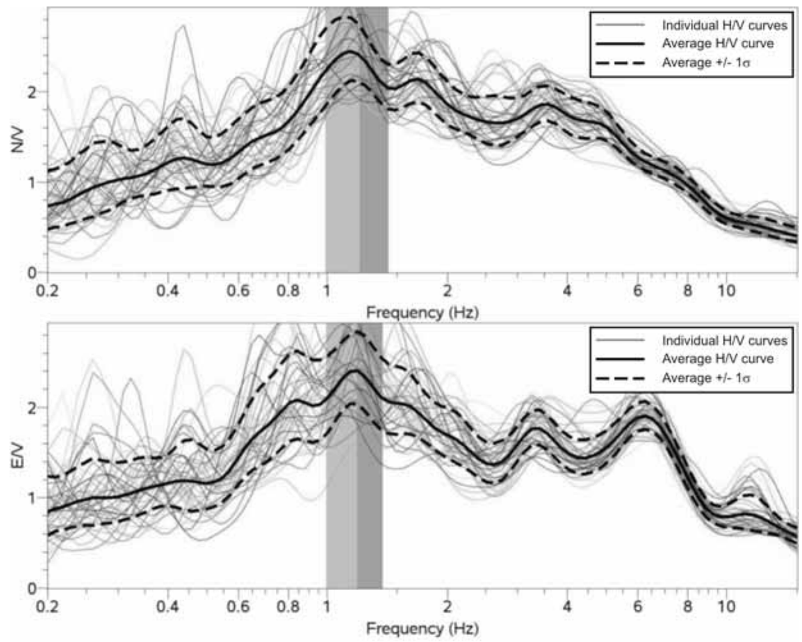

Figure 2. H/V curves for site S2.

However, in many situations microtremor measurements are unavailable and the value of F_0 is unknown. In these cases, the bedrock depth can be estimated with great uncertainty only by interpretation of local geology and geomorphology. Common practice is to perform different numerical analyses increasing progressively the depth of the boundary where the seismic excitation is applied. Thus, it is possible to evaluate the effect of bedrock depth on site response. To account for these situations we consider an alternative randomized case for site S2 (hereinafter case S2b) assuming that the bedrock depth, H, can take on any value between 30 m (bottom of soil profile from borehole) and 150 m (bottom of soil profile assumed from interpretation of geomorphology) independently of F_0. In other words, we assume that H follows a uniform distribution.

For site S1, Figure 3 compares the *base case* with 1000 characterizations of the soil column, each one generated via Monte Carlo simulation. An analogous figure (Figure 4) is shown for site S2 when the uncertainty in bedrock depth is modelled as a function of F_0 (hereinafter case S2a).

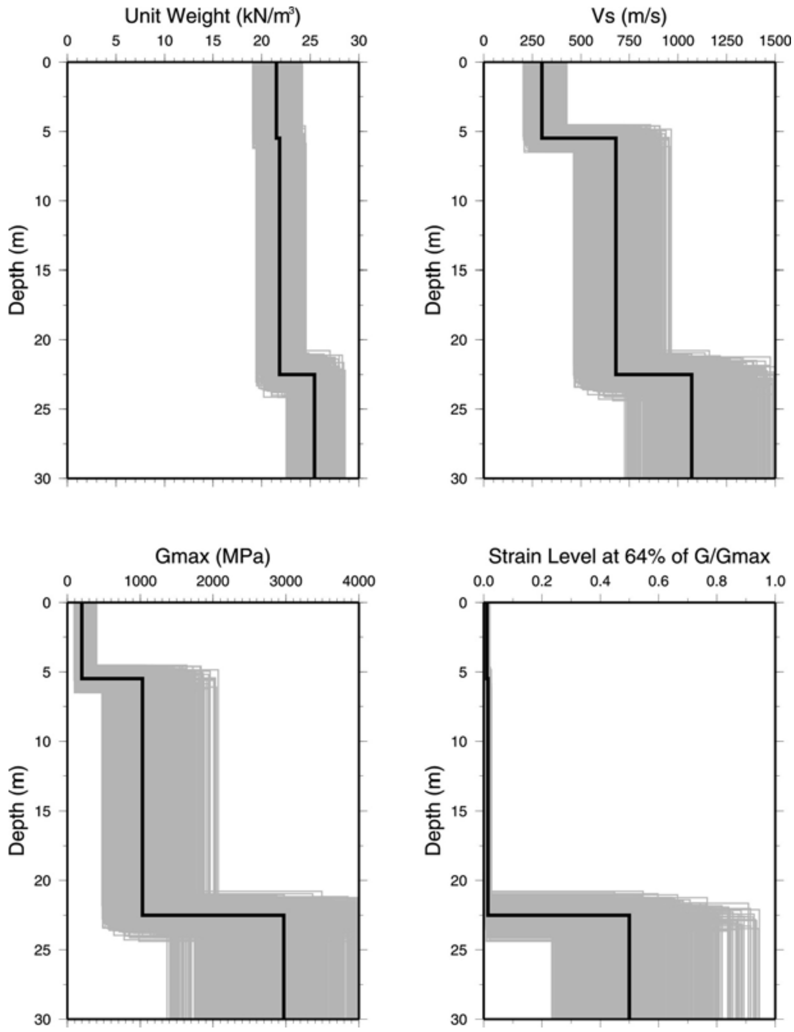

Figure 3. One thousand samples of randomized soil properties for site S1 (grey lines). The *base case* is superimposed (black line).

Results and Discussion

To study the influence of the uncertainty of the soil properties on the site response, ten accelerograms selected as described previously are driven through each sample of the soil columns.

For site S1, Figure 5 compares the average amplification function *AF*(*f*) (defined as the modulus of the corresponding transfer function; for details see Kramer (1996)) and the average surface response spectrum for the *randomized case* with those for the *base case*. The amplification functions for the two cases are very similar to each other up to a frequency of 10 Hz. In this frequency range, the reader can observe a slight difference in the values of the first resonant frequency that, for the *randomized case*, is shifted towards lower frequencies. For higher frequencies, the average *AF*(*f*) for the *randomized case* appear to be smoother than the *AF*(*f*) for the *base case* that clearly shows an amplification peak at approximately 14 Hz. Response spectra for the two cases are nearly identical with the spectral ordinates for the *randomized case* that are slightly greater between 0.15s and 0.25s. This implies a mean value of F_a that is 3% greater than that obtained for the *base case* (see Figure 7, to come).

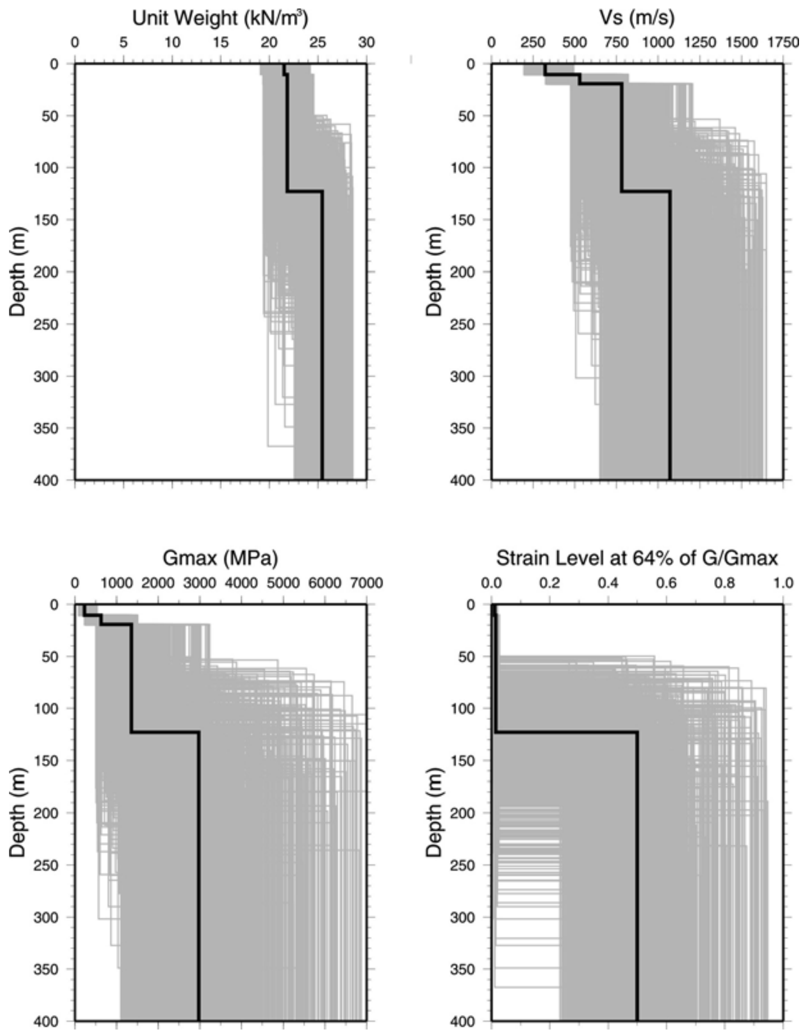

Figure 4. One thousand samples of randomized soil properties for site S2a (grey lines). The *base case* is superimposed (black line).

Figure 6 shows results for site S2. The left and right panels display the *AF*(*f*) curves and surface response spectra for case S2a and S2b respectively. In both cases, the average amplification function obtained from randomization is significantly smoother than that for the *base case* that, besides the fundamental frequency, allows the identification of two amplification peaks at about 4 Hz and 6 Hz. These peaks can be also observed by inspecting the H/V curves in Figure 2 (bottom panel). Note that, for case S2b, we assume as base model the same profile adopted for case S2a where the bedrock depth was calculated from Equation 1. The average *AF*(*f*) curves for the two *randomized cases* are similar in shape but differ in the amplification level that is slightly greater when the information on F_0 is neglected (case S2b). In this case, moreover, the average *AF*(*f*) does not allow a clear identification of the first resonant frequency of the soil column. Note, finally, that both the amplification functions for the *randomized* and the *base case* show a de-amplification for frequencies greater than 9-10Hz. Contrary to the *AF(f*) curves, which show substantial differences, response spectra for the *randomized* and the *base case* are very similar to each other.

For the two site considered, the values of F_a obtained for the *randomized* and the *base case* are displayed in Figure 7. For the *randomized case* we present the mean, median, and modal values of the amplification factor. Analyzing the figure shows that the uncertainty in the geometrical and geotechnical properties of the soil columns has a large role on the F_a variability that is quantified here in terms of standard deviation. The largest uncertainty is observed for case S2b where the standard deviation is equal to 0.26. As expected by comparing the surface response spectra, the mean value of F_a for the *randomized case* and that for the *base case* do not show significant differences (generally lower than 4%).

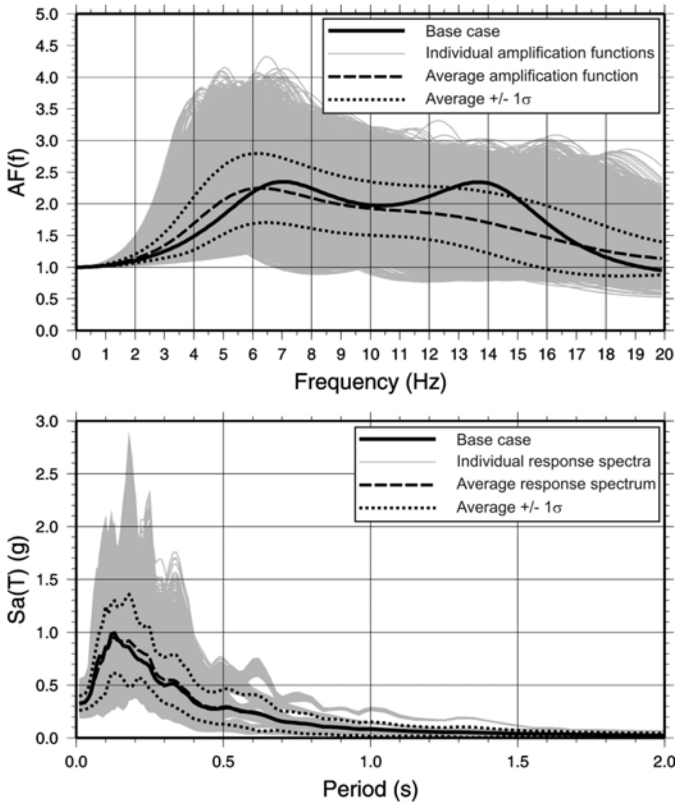

Figure 5. Amplification functions and surface response spectra for site S1.

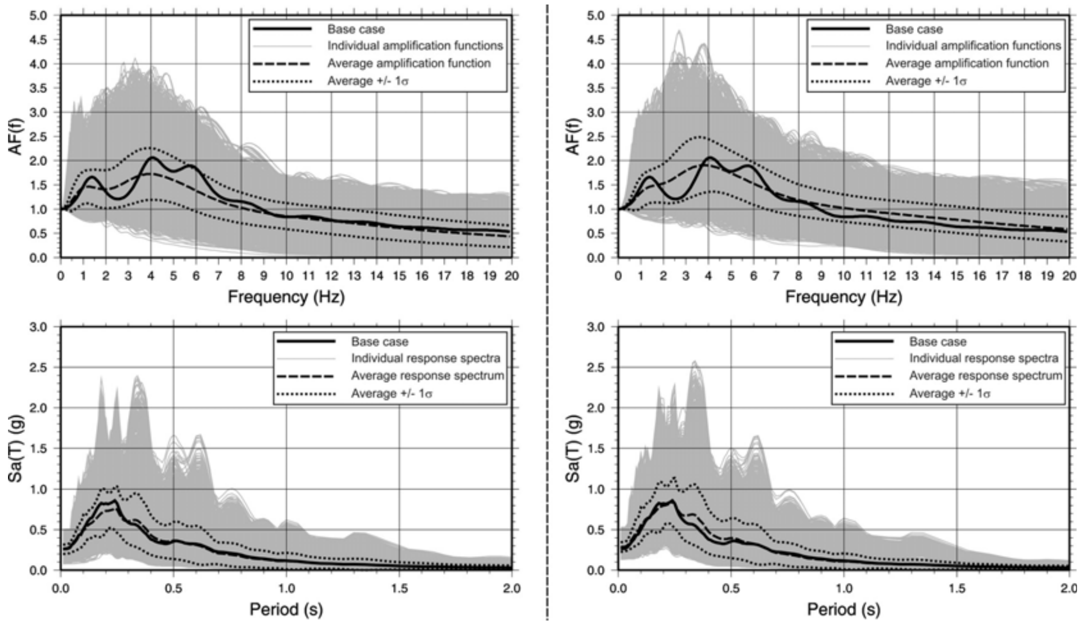

Figure 6. Amplification functions and surface response spectra for site S2. Both cases S2a (left panel) and S2b (right panel) are shown.

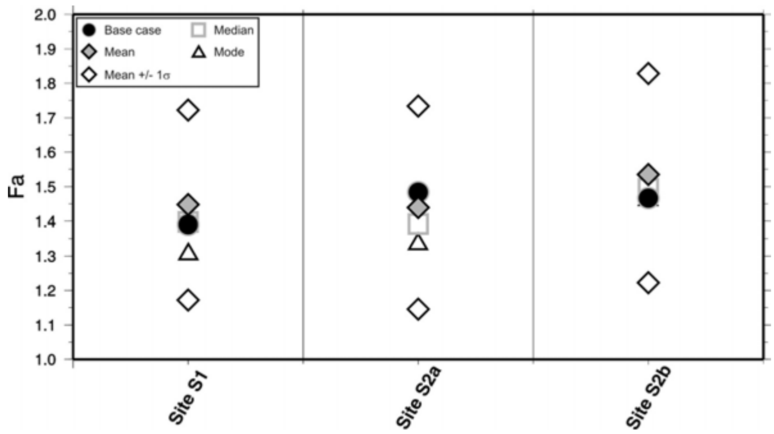

Figure 7. Values of the amplification factor for each site analyzed.

Conclusions

In this study we have investigated the influence of the uncertainty in the soil parameters on the ground response of two sites in Tuscany. In particular one site presents a rather thick soil deposit above the bedrock whose depth is highly uncertain. In order to account for the uncertainty in the soil characteristics a Monte Carlo approach consisting of randomly varying the soil parameter values is applied. The ground response of each sample of the soil model was evaluated by using a computer program that approximates the nonlinear, inelastic behaviour of soils using an iterative, equivalent linear approach. A suite of real accelerograms, which reflect the scenario events controlling the site hazard, was driven through each profile. As a result, the amplification function, $AF(f)$, the acceleration response spectra at the free surface, and the soil amplification, quantified here by a frequency-independent amplification factor, F_a, were obtained.

Comparing the average amplification functions obtained after randomization of the soil parameters (*randomized case*) with those obtained by using the best engineering estimate of the soil characteristics (*base case*) shows that former are generally smoother. This behaviour, which is not manifested by the surface response spectra, is more evident as the uncertainty in bedrock depth increases (compare site S1 with site S2b). Although the differences in the $AF(f)$ curves for the *randomized* and the *base case* can be significant, our results reveals that the amplification functions for the *base case* are generally within 1σ of the average curve obtained by randomizing the soil properties. Comparing response spectra, instead, does not indicate significant differences between the *randomized* and the *base case*. This is reflected in the values of F_a. The *randomized case*, indeed, gives F_a values similar to the *base case*.
Finally, our results provide an independent check of site factors published in EC8 and in the Italian building code (Ministero delle Infrastrutture e dei Trasporti, 2008). The values of F_a calculated in this study are similar to that proposed by EC8 for Type B sites ($360 \le V_S < 800$ m/s) whose seismic hazard is dominated by earthquakes with magnitude less than 5.5 (F_a = 1.35). For the same soil category, the value of the amplification factor proposed by the Italian building code appears unconservative, being equal to 1.20. This value corresponds to about the mean minus one standard deviation F_a shown in Figure 7. As a consequence, in some cases, the spectral ordinates proposed by the Italian code could be exceeded by those obtained from dynamic analyses (e.g., Barani et al. 2008).

References

Barani S., De Ferrari R., Ferretti G. & Eva C (2008). Assessing the effectiveness of soil parameters for ground response characterization and soil classification, *Accepted for publication on Earthquake Spectra, 24, August 2008, 34p*.

Bazzurro P. & Cornell C.A (2004). Ground-motion amplification inj nonlinear soil sites with uncertain properties, *Bull. Seism. Soc. Am., 94, 2090-2109*.

Building Seismic Safety Council (2003). NEHRP Recommended provisions for seismic regulations for new buildings and other structures, *Federal Emergency Management Agency – FEMA, Report No. 450, Washington DC, USA*.

Comitè Europèen de Normalisation (2003). prENV 1998-1 – Eurocode 8: Design of structures for earthquake resistance. Part 1: General rules, seismic actions and rules for buildings, *Draft No. 4, Brussels, Belgium*.

Cornell C.A (1968). Engineering seismic risk analysis, *Bull. Seism. Soc. Am.,* 58, 1583-1606.

Dobry R., Martin G.R., Parra E. & Bhattacharyya A. (1994). Development of site-dependent ratios of elastic response spectra (RRS) and site categories for building seismic codes, *Proceedings of 1992 NCEER/SEAOC/BSSC Workshop on Site Response During Earthquakes and Seismic Code Provisions, edited by G.R. Martin, University of Southern California, National Center for Earthquake Engineering Reasearch Special Publication NCEER-94-SP01, Buffalo,NY*.

Foti S., Lo Presti D., Pallata O., Rainone M. & Signanini P (2002). Indagini geotecniche e geofisiche per la caratterizzazione del sito di Castelnuovo Garfagnana, *Rivista Italiana di Geotecnica, 3, 42-60.*

Housner G.W (1952). Spectrum intensities of strong motion earthquakes, *Proceedings of Symposium on earthquake and blast effects on structures, EERI, Oakland, California, USA, 20-36*.

Ibs-von Seht M. & Wohlenberg J (1999). Microtremor measurements used to map thickness of soft sediments*, Bull. Seism. Soc. Am., 89, 250-259.*

Idriss I. M. & Sun J.I (1993). User's manual for Shake91: A computer program for conducting equivalent linear seismic response analyses of horizontally layered soil deposits, *Center for geotechnical modeling, Dept. of Civil and Environmental Engineering, University of California, Davis*.

Kramer S.L (1996). Geotechnical earthquake engineering, *Prentice-Hall, New Jersey, 653p*.

Lancellotta R (1995). Geotechnical engineering, *Rotterdam, Balkema, 352-357*.

Ministero delle Infrastrutture e dei Trasporti (2008). Norme tecniche per le costruzioni – NTC, D.M. 14 Gennaio 2008, Supplemento ordinario alla Gazzetta Ufficiale No 29, 4 Febbraio 2008.

Miyakoshi J. & Hayashi Y (2000). Correlation of building damage with indices of seismic ground motion intensity during the 1999 Chi-Chi, Taiwan earthquake, *Proceedings of International Workshop on Annual Commemoration of Chi-Chi Earthquake, Taipei, Taiwan, 18-20 September 2000, 12p*.

Pergalani F., Compagnoni M. & Petrini V (2003). Evaluation of site effects in some localities of 'Alta Val Tiberina Umbra' (Italy) by numerical analysis, *Soil Dynamics and Earthquake Engineering, 23, 85-105*.

Pergalani F., Romeo R., Luzi L., Petrini V., Pugliese A. & Sanò T (1999). Seismic microzoning of the area struck by Umbria-Marche (Central Italy) Ms 5.9 earthquake of 26 September 1997, *Soil Dynamics and Earthquake Engineering, 19, 279-296*.

Rey J., Faccioli E. & Bommer J.J (2002). Derivation of design soil coefficients (S) and response spectral shapes for Eurocode 8 using the European Strong-Motion database, *Journal of Seismology, 6, 547-555*.

Schnabel P.B., Lysmer J. & Seed H.B (1972). SHAKE: a computer program for earthquake response analysis of horizontally layered sites, *Report No. UCB/EERC-72/12, Earthquake Engineering Research Center, University of California, Berkeley, 92p*.

Seed R.B., Dickenson S.E., Rau G.A., White R.K. & Mok C.M (1994). Observations regarding seismic response analyse for soft and deep clay sites, *Proceedings of 1992 NCEER/SEAOC/BSSC Workshop on Site Response During Earthquakes and Seismic Code Provisions, edited by G.R. Martin, University of Southern California, National Center for Earthquake Engineering Reasearch Special Publication NCEER-94-SP01, Buffalo,NY*.

Von Thun J.L., Rochim L.H., Scott G.A. & Wilson J.A (1988). Earthquake ground motions for design and analysis of dams, in Earthquake Engineering and Soil Dynamics II – Recent

Advance in Ground-Motion Evaluation, *Geotechnical Special Publication, 20, ASCEE, New York, 463-481*.

ROSERIS: A Software Platform for the Assessment of Seismic Risk in Romania

Craifaleanu I G (1), Lungu D (2), Aldea Al (2), Vacareanu R (2), Arion C (2), Anicai O (3)

(1) National Institute for Building Research, INCERC, 266 Pantelimon St., RO-021652, Bucharest, Romania, e-mail: i.craifaleanu@gmail.com
(2) Technical University of Civil Engineering Bucharest, 124 Lacul Tei Blvd., RO-020396, Bucharest, Romania, e-mail: aldea@utcb.ro
(3) Institute for Computers, ITC, 167 Floreasca St., Sector 1, Bucharest, Romania, e-mail: oanicai@itc.ro

Keywords: seismic risk, GIS technologies, general building stock, software

Introduction

The development of methodologies and software applications for the seismic risk assessment of building stock is currently a major challenge both for professionals and for decision-makers in countries affected by earthquakes. Several applications have been created during recent years, each being designed according to the specific requirements of the concerned country. The HAZUS methodology and software [HAZUS, 1999] are one of the most complex and robust applications, designed to include multiple types of hazard, in a comprehensive approach.

During the last three years, a research project has been conducted in Romania, by an interdisciplinary team, aimed to develop a software platform for the seismic risk assessment of general building stock. The project has benefited of the experience and results from several studies performed during the last two decades by the participants, in the framework of national and international research programs.

Materials and Methods

The Data

The platform is structured around the ROSERISdb geodatabase, which contains data on the building stock, spatial references and seismic hazard data.

Data concerning building stock includes key attributes to be used as an input for the seismic risk assessment methodology, as well as auxiliary attributes, as building occupancy or area, which are used for a better definition of building stock properties. The key attributes are derived based on “primary” attributes, as structure type, number of stories and year of construction (Fig. 1).

Each building is assigned a unique identifier, which serves for creating relationships to spatial references and to other data.

Seismic hazard is defined in a simplified manner, according to the prescriptions of the new Romanian seismic design code, P100, enforced in 2006 [P100-1, 2006]. The new code is harmonized with Eurocode 8 [EN 1998-1, 2004]. Seismic hazard data is specified, for a mean recurrence interval of 100 years, by the values of peak ground acceleration, a_g, and of control periods, T_B, T_C, T_D. The functions which define the shape of the design spectrum are built in the software application. Alternatively, the variation can be specified by the user.

The Methodology

The seismic risk assessment methodology implemented in the ROSERIS platform is summarized in Fig. 1.

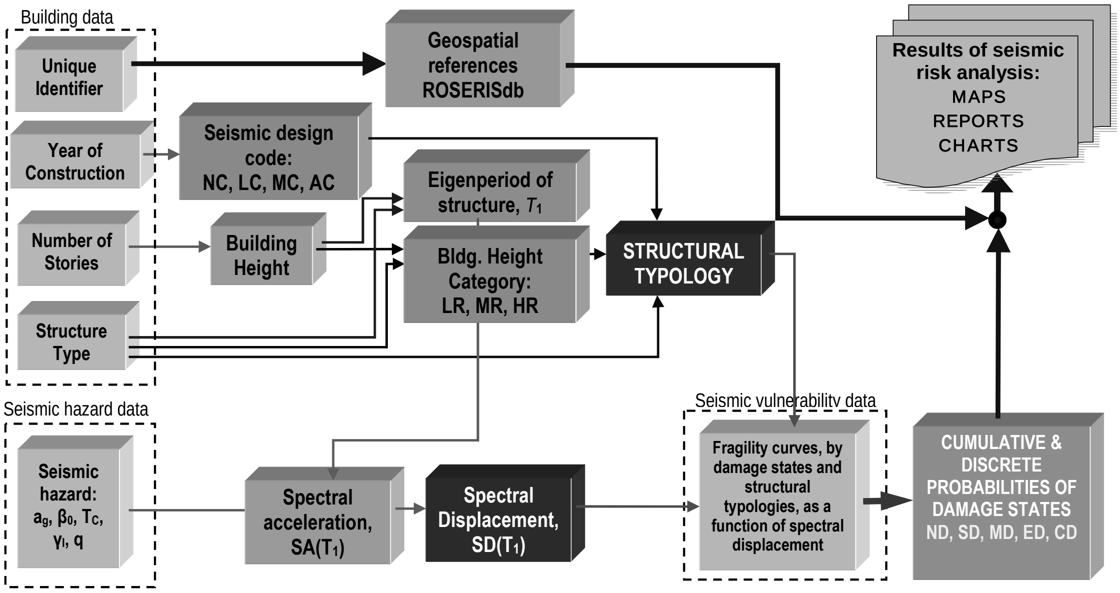

Figure 1. Flowchart of the seismic risk assessment methodology implemented in the ROSERIS platform

As it can be seen in Fig. 1, seismic design code is determined based on the year of construction, as shown in

Table 1. The years in the table are specified according to the timeline of seismic design code development in Romania.

Table 1. Classification according to year of construction

Year of construction	Seismic code category	Description
<= 1963	NC	No Code
1964…1977	LC	Low Code
1978…1991	MC	Moderate Code
>= 1991	AC	High Code

The building height category (low-rise, LR, medium-rise, MR, and high-rise, HR) is determined based on the number of stories, correlated with structure type.

The structural typology is then determined based on structure type, building height category and code level category.

The other key parameter is spectral displacement. In order to calculate it, the eigenperiod of the building, T_1, is first computed, by using the approximate formula provided by the P100-1 code:

$$T_1 = C_t \cdot H_C^{3/4}, \qquad (1)$$

where H_C is the building height and C_t is a coefficient depending on structure type.

Then, by using formula (2), the spectral displacement, in centimetres, is obtained.

$$SD(T_1) = c(T_1) \cdot q \cdot \left(\frac{T_1}{2\pi}\right)^2 \cdot SA(T_1) \cdot 100 . \tag{2}$$

In the above formula, q is the behaviour factor, $SA(T_1)$ is the design acceleration spectrum, and $c(T_1)$ is a coefficient, determined according to the prescriptions of the P100 code, as a function of T_1 and T_C.

$$1 \le c(T_1) = 3 - 2{,}5\frac{T_1}{T_C} \le 2 . \tag{3}$$

The structural typology and the spectral displacement are used as input parameters with the fragility curves, in order to determine the probabilities of the buildings of being in one of the following damage states: ND (no damage), SD (slight damage), MD (moderate damage), ED (extended damage) and CD (complete damage).

Fragility curves are provided, for different building typologies, based on previous studies of the university members of the team and on the indications of the HAZUS methodology. The values of the parameters of the fragility curves are built in the software module dedicated to seismic risk assessment.

Figure 2 shows an example of fragility curve used in the methodology, for reinforced concrete structures.

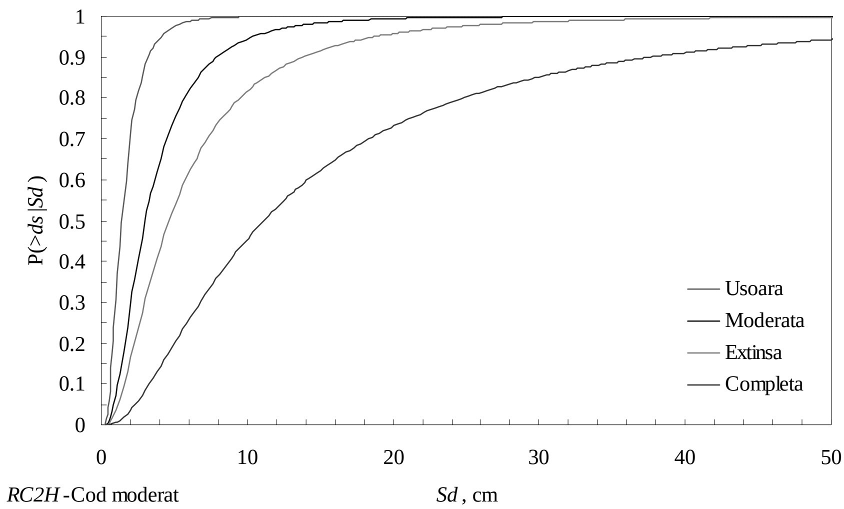

Figure 2. Example of a fragility curve determined for reinforced concrete structures

Additionally, a mean damage ratio is calculated, based on cumulative probabilities.

The Software

The structure of the platform consists of a core GIS application, which performs both the management of own built-in modules and the launching of two “satellite” applications, MAGDA and EVARISX. These applications can either be launched by the core GIS application or they can be run independently on any computer, without requiring the installation of other platform components. The feature is aimed to ensure maximum flexibility in performing various operations on different computers, in order to allow contributions from multiple operators.

The application for building stock data collection and management, MAGDA, was developed for creating and editing records in the ROSERISdb database. In the first phase of data collection, MAGDA can be used by different operators, which are not necessarily instructed in the use of the entire ROSERIS platform. Only basic computer knowledge is required for these operators, whose role is to collect and transmit data to the central dispatcher. Figure 3 shows one of the screens of the MAGDA application.

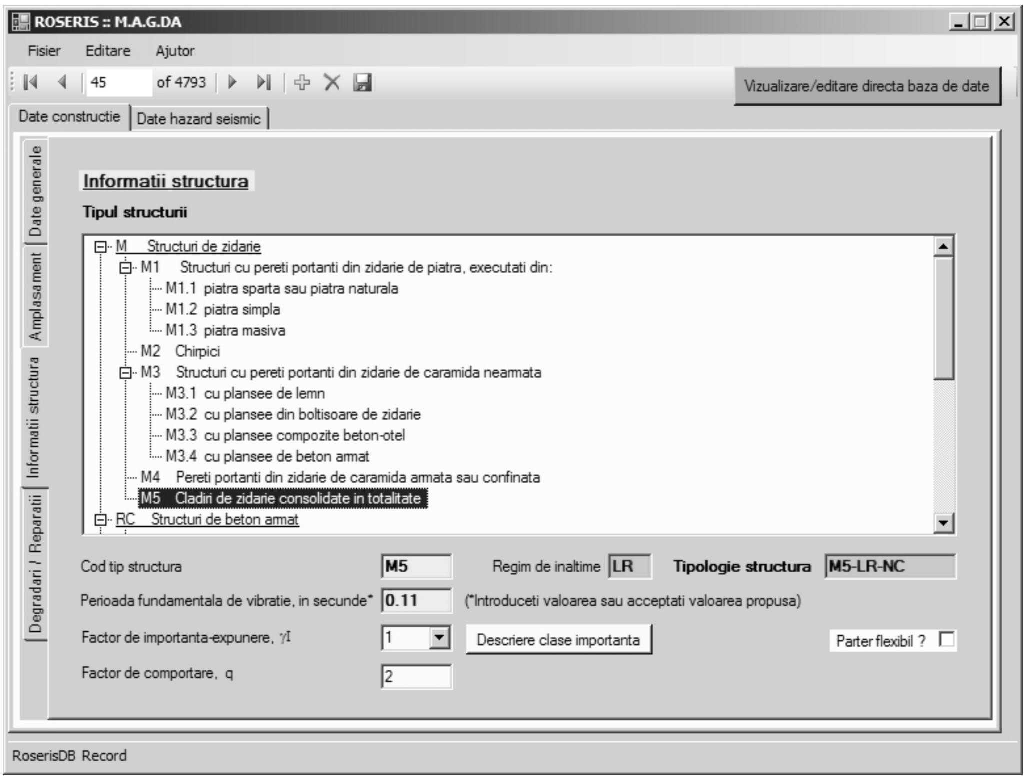

Figure 3. Screen of the MAGDA application

Besides data collection and editing, MAGDA also performs some preliminary data processing, in order to determine the building typology and the eigenperiod, T_1. Obtained values are stored in the ROSERISdb database.

The application for seismic risk analysis, EVARISX, performs the final calculations in the seismic risk analysis, obtaining the probabilities for damage states and the mean damage ratio. Resulted values are stored in the ROSERISdb database. EVARISX provides also the capability of viewing and editing the records in the database.

It shoud be mentioned that, in this stage of operation, geodatabase features are not included in ROSERISdb. This phase is accomplished by the GIS ROSERIS core application, which also creates relationships with spatial data, based on the unique identifiers of buildings.

The interface of the GIS ROSERIS application is shown in Fig. 4.

The GIS ROSERIS application provides the capability of displaying both input and output of the methodology on maps, and of presenting data in reports and graphs. A sample report is presented in Fig. 5.

The GIS ROSERIS application allows the generation of maps, reports and graphs for all significant input and output data of the analysis, allowing a thorough and accurate understanding of the results. This capability is probably one of the most important component of the interaction and communication between scientists and decision makers.

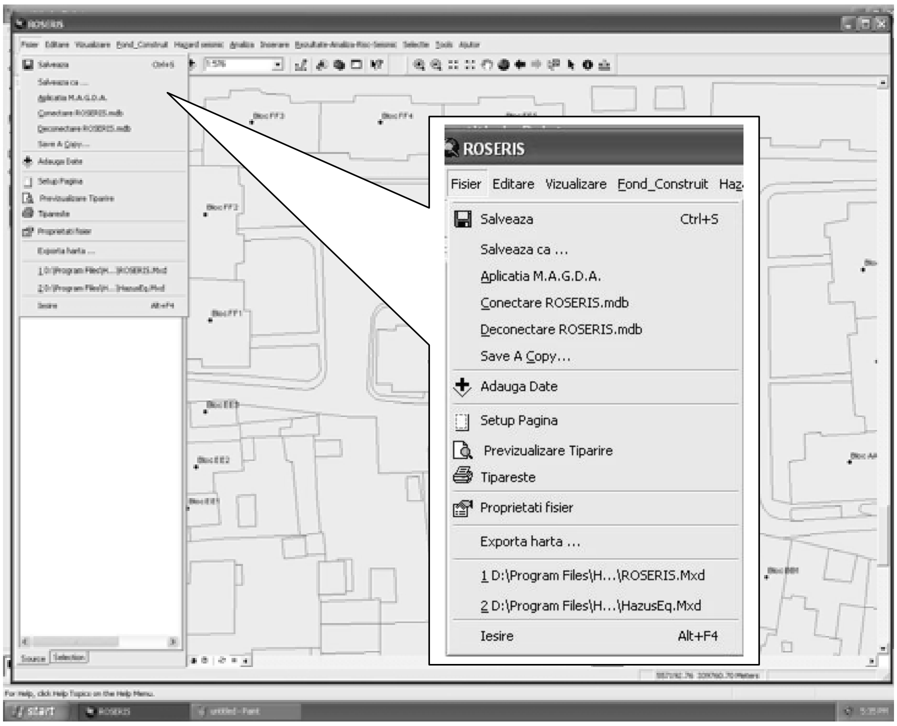

Figure 4. Screen of the GIS ROSERIS core application

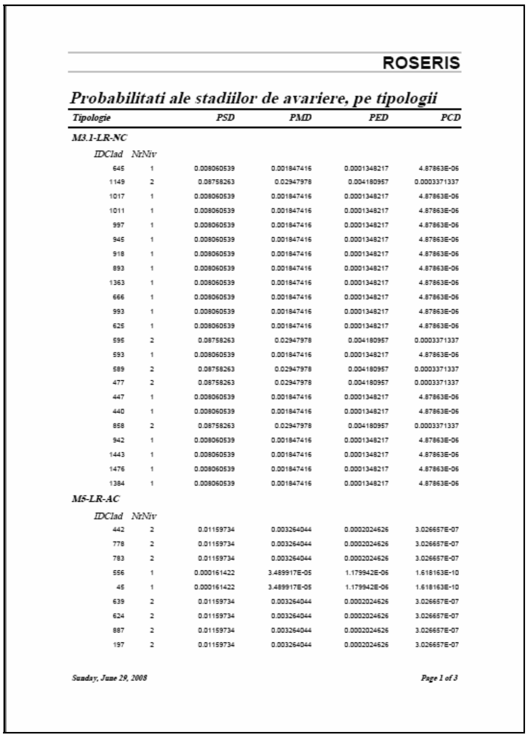

ROSERIS

Probabilitati ale stadiilor de avariere, pe tipologii

Tipologie		*PSD*	*PMD*	*PED*	*PCD*
M3.1-LR-NC					
IDClad	*NrNiv*				
645	1	0.008060539	0.001847416	0.0001348217	4.87863E-06
1149	2	0.08758263	0.02947978	0.004180957	0.0003371337
1017	1	0.008060539	0.001847416	0.0001348217	4.87863E-06
1011	1	0.008060539	0.001847416	0.0001348217	4.87863E-06
997	1	0.008060539	0.001847416	0.0001348217	4.87863E-06
945	1	0.008060539	0.001847416	0.0001348217	4.87863E-06
918	1	0.008060539	0.001847416	0.0001348217	4.87863E-06
893	1	0.008060539	0.001847416	0.0001348217	4.87863E-06
1363	1	0.008060539	0.001847416	0.0001348217	4.87863E-06
666	1	0.008060539	0.001847416	0.0001348217	4.87863E-06
993	1	0.008060539	0.001847416	0.0001348217	4.87863E-06
625	1	0.008060539	0.001847416	0.0001348217	4.87863E-06
595	2	0.08758263	0.02947978	0.004180957	0.0003371337
593	1	0.008060539	0.001847416	0.0001348217	4.87863E-06
589	2	0.08758263	0.02947978	0.004180957	0.0003371337
477	2	0.08758263	0.02947978	0.004180957	0.0003371337
447	1	0.008060539	0.001847416	0.0001348217	4.87863E-06
440	1	0.008060539	0.001847416	0.0001348217	4.87863E-06
858	2	0.08758263	0.02947978	0.004180957	0.0003371337
942	1	0.008060539	0.001847416	0.0001348217	4.87863E-06
1443	1	0.008060539	0.001847416	0.0001348217	4.87863E-06
1476	1	0.008060539	0.001847416	0.0001348217	4.87863E-06
1384	1	0.008060539	0.001847416	0.0001348217	4.87863E-06
M5-LR-AC					
IDClad	*NrNiv*				
442	2	0.01159734	0.003264044	0.0002024626	3.026657E-07
778	2	0.01159734	0.003264044	0.0002024626	3.026657E-07
783	2	0.01159734	0.003264044	0.0002024626	3.026657E-07
556	1	0.000161422	3.489917E-05	1.179942E-06	1.618163E-10
45	1	0.000161422	3.489917E-05	1.179942E-06	1.618163E-10
639	2	0.01159734	0.003264044	0.0002024626	3.026657E-07
624	2	0.01159734	0.003264044	0.0002024626	3.026657E-07
887	2	0.01159734	0.003264044	0.0002024626	3.026657E-07
197	2	0.01159734	0.003264044	0.0002024626	3.026657E-07

Sunday, June 29, 2008 *Page 1 of 3*

Figure 5. Report generated with the GIS ROSERIS application

Results and Discussion

The ROSERIS software platform provides a basic tool for the assessment of seismic risk. Its structure is adapted to the seismicity of the country, characteristics of the building stock and regulatory context.

The functionality of the platform allows an efficient work procedure, by de-coupling the operations of data collection, analysis and presentation.

The main advantages of the ROSERIS platform reside in the simple and robust seismic risk assessment methodology, compatible with European standards, and in the capacity of providing intuitive representations of the spatial distribution of significant input and output characteristics.

Acknowledgements

The work presented in this paper was performed under Contract No. 119/CEEX II 03/2006, financed by the Romanian National Agency for Scientific Research, ANCS.

References

Craifaleanu I. G (2002). An Improved Evaluation of Maximum Displacements în the Romanian Seismic Design Code*, Proceedings of the International Conference ‚Earthquake Loss Estimation and Risk Reduction, Bucureşti, 24-26 Oct, Vol. 2, p. 81-90.*

Craifaleanu I. G., Lungu D., Borcia I. S (2006). Shake Maps of Nonlinear Spectral Ordinates for Romanian Earthquakes*, Proceedings of the First European Conference on Earthquake Engineering and Seismology (a joint event of the 13th ECEE & 30th General Assembly of the ESC), Geneva, Switzerland, 3-8 September 2006, Paper Number: 1257 (on CD ROM).*

Craifaleanu I. G (2007). Damage Spectra and Damage Maps for Romanian Vrancea Earthquakes, *Proceedings of the International Symposium on Seismic Risk Reduction, The JICA Technical Cooperation Project în Romania, ISSRR2007, Bucharest, 26-27 April, p. 413 420.*

Lungu D., Aldea A., Arion C., Cornea T., Văcăreanu R (2004b). RISK UE, WP1: European Distinctive features, inventory database and typology, *Proceedings of the International Conference "Earthquake Loss Estimation and Risk Reduction" 24-26, Oct. 2002, Bucharest, volume 2, Romania, p. 251-272.*

Văcăreanu R., Lungu D., Arion C., Lancovici M (2002a). Assessment of Seismic Behavior and Fragility of Buildings using HAZUS and ATC 40 Methodologies – Case Studies*, Proceedings of the International Conference "Earthquake Loss Estimation and Risk Reduction", Bucharest, 24-26 oct., vol. 2, p. 33-42.*

Văcăreanu R., Aldea A., Arion C (2002b). Probabilistic Risk Assessment of Current Buildings, *Proceedings of the International Conference ‚Earthquake Loss Estimation and Risk Reduction, Bucharest, 24-26 Oct., vol. 2, p. 305-317.*

FEMA-NIBS (1999a). Earthquake Loss Estimation Methodology HAZUS99. Technical Manual, Washington D.C.

FEMA-NIBS (1999b). Earthquake Loss Estimation Methodology HAZUS99. User's Manual. ArcView Version, Washington D.C.

FEMA-NIBS (2003). HAZUS MH MR1. Advanced Engineering Building Module. Technical and User's Manual, Multi hazard Loss Estimation Methodology, Earthquake Model, Department of Homeland Security, Emergency Preparedness and Response Directorate, FEMA Mitigation Division, Washington D.C.

P100-1 (2006). Romanian seismic design code.

RISK UE – An advanced approach to earthquake risk scenarios with applications to different European towns, FP5 Programme – 1999-2003.

Experimental Testing of New Type Vibration Generator in order to Estimate the Dynamic Characteristics of Building

Enomoto T (1), Wen Y (2), Navarro M (2), Vidal F (3)

(1) Dept. of Architectural and Building Engineering, Kanagawa University, Yokohama, Japan, enomot01@kanagawa-u.ac.jp
(2) Dept. of Architectural and Building Engineering, Kanagawa University, Yokohama, Japan, ywen01@kanagawa-u.ac.jp
(3) Depart. of Applied Physics, Almeria University, Almeria, Spain, mnavarro@ual.es
(4) Andalusian Institute of Geophysics, Granada University, Granada, Spain, fvidal@ugr.es

Keywords: Vibration generator, performance test, dynamic characteristic, electromagnetism actuation

Introduction

In 1995 at Kobe, Japan, the great eartquake named Hyogo-ken Nanbu Earthquake of magnitude Mj7.3 was occured just under the Kobe urbanized area and many building structures were destroyed along to the coast of Osaka Bay due to the strong motions. And also in 2007, Kashiwazaki, Japan, the big earthquake named Niigata-ken Chuetsu-oki Earthquake of magnitude Mj7.2 was occured at near the Kashiwazaki coast of Japan Sea and hevy damages of many buildings were appeared at soft soil condition's area in Kashiwazaki City. These damages of building structures are caused by site effect of soft soil conditions generating the amplification of strong motions and also building structural dynamic characteristics. In 1994 at Adora, Spain, it was appeared very clear phenomena on the damages of RC buildings due to the resonant effect with predominant period of soil and natural period of RC building (Navarro M, 2007). These building structural damages were appeared commonly in the earthquake damages at many places in the world.

Accurate prediction of the response of buildings subject to strong motions requires the information of in situ dynamic properties of the building, including natural frequencies and damping ratios. In particular, the damping ratios of in situ buildings are difficult to estimate, yet these parameters have significant effects on the response due to external excitations. Usually, ambient excited vibration data is recorded, and various methods, such as Fourier Spectrum analysis and wavelet analysis, have been developed to identify structural dynamic characteristics. However, these methods based on the ambient vibration data meet their difficulty to identify the characteristics of higher modes that contributed the vibration, especially for the damping ratios (Yang J.N., 2004). In addition, the structural damping ratio may change with the response amplitude, and there is a little different between the dynamic characteristics obtained from the ambient vibration data and that obtained from the strong motion record (Enomoto T., 2002; Wen Y.K., 2006).

To estimate the structural dynamic characteristics exactly, the free vibration of higher mode with large amplitude response using rotor machine is necessary. However, there are many limitations of the available rotor machine, which constraint their applications. For example, the quality of actuation force of the type with electric servo motor is low when it operates in small amplitude; there needs large space for the rotor machine with oil servo to provide the necessary oil sources. In addition, the vibration noise is to be easily produced because of their operation mechanism. In this study a new type vibration generator of which the shaking force is generated from sliding mass system actuated by linear motor using electromagnetism actuation is developed. The excitation force of the vibration generators manufactured approaches 900 kN, and the operating frequency ranges from 0.1 Hz to 20.0 Hz. The machines can be easily installed on the top of buildings because of little space needed. In this paper, the formulation, mechanism and characteristics of the developed vibration generator are introduced firstly. Then, to test its performance, basic performance test and excitation experiments of a three-floor building are carried out.

Outline and mechanisim of vibration generator

To reduce the installation space and to be transported conveniently, the vibration generator with electromagnetic motor has small size. As shown in Figure 1, it has a box shape with 178.0 cm of length, 61.0 cm of width and 30.0 cm of height excluding fixing jig. The total weight is 1140.0 kg, and the full actuation force is 9.0 kN. A summary of the specifications is given in Table 1 (Servo Technos Co., Ltd., 2006).

The manufactured machine of vibration generator is shown in Figure 2. The main body composes of base plate, side plate, cover, guide rail, mass, coils, permanent magnets and displacement sensors etc (Figures 3). The parts of the machine can be dismantled into pieces with a maximum approximate weight of 20. 0 kg, and they can be assembled freely. In addition, the whole system includes the control device, power system and output device, etc.

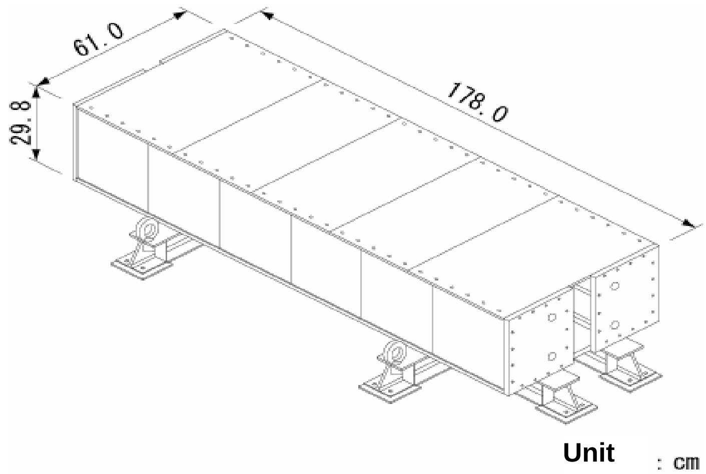

Figure 1. Outline of the vibration generator

(a) Machine of vibration generator

(b) Power control board

(c) Signal generator and sampling board

Figure 2. Photo of the vibration generator and control system

The vibration generator is actuated by electromagnetic force using the electromagnetic fields theory. The winding coil is fixed on the sides of the mass. When servo electronic current flows down the coil, air gap magnetic field occurs. It moves straight according to the phase sequence depending on the control of electronic current and is called walking wave magnetism field. The magnetism field interacts with the field produced by the permanent magnets that configured on both inner sides of main body. Electromagnetic force is then produced by the interaction and actuates the mass to move straight. Therefore, by the adjustment of frequency and amplitude of electronic current through signal generator and the adjustment of servo power amplifier, the movement of the mass is controlled. In addition, a feedback control system is designed, by which the real position of the mass is checked comparing with the target position and rectified in real time when the position error appears.

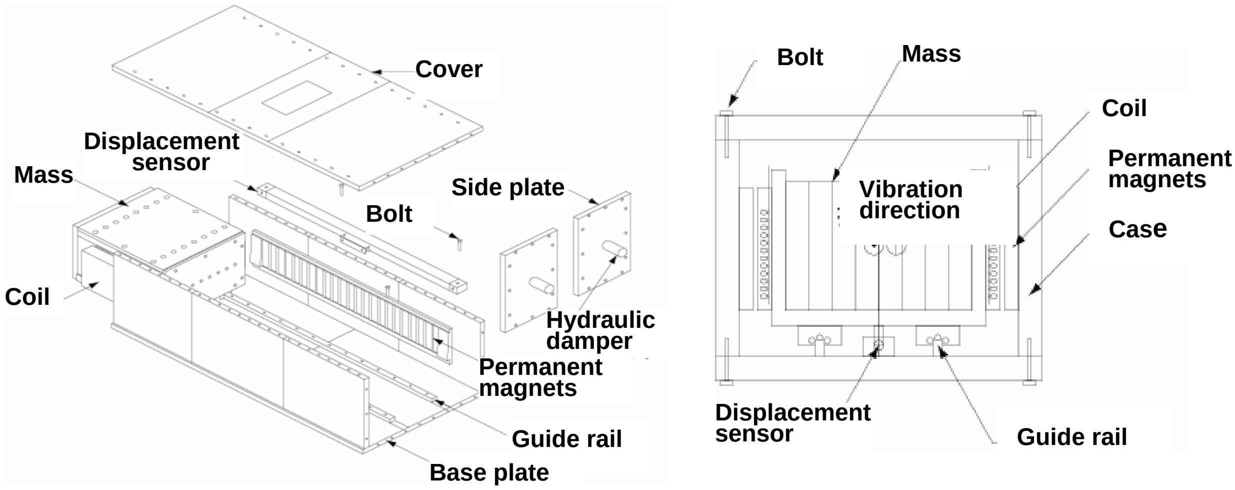

Figure 3. Configuration of the vibration generator

Table 1. Specification of vibration generator

Items	Specification
Excitation force	**3kN×3=9kN**
Maximum amplitude	**±250mm**
Maximum velocity	**±1500mm/sec**
Excitation frequency	**0.1Hz ~ 20Hz**
Excitation direction	**Horizontal Direction**
Control function	**Displacement control**

Outline and mechanisim of vibration generator

Basic Performance Test

Experiments are carried out to test the basic performance of the vibration generator. Harmonic wave is selected as input signals with a certain frequency of 3.7 Hz taken as an example. The tested vibration response is compared with the theory values. Figure 4 gives the comparison results, and the response amplitude is 1.74 cm, 0.83 cm and 0.37 cm respectively, to evaluate the performance of small amplitude actuation considering the limitation of the vibration generator with electronic motor. It has shown that the tested movements of the mass agree well with the theory wave. The displacement errors are given in Table 2. It shows that the absolute values of maximum error almost do not change with the reduction of the peak response of the mass, and the maximum amplitude error is lower than 1mm. Even the relative errors enlarge following with the decrement of peak response, for example the relative error approaches 16.0 % at time of amplitude of 0.37 cm. However, the average relative error also keeps small level and is lower than 5.0 %.

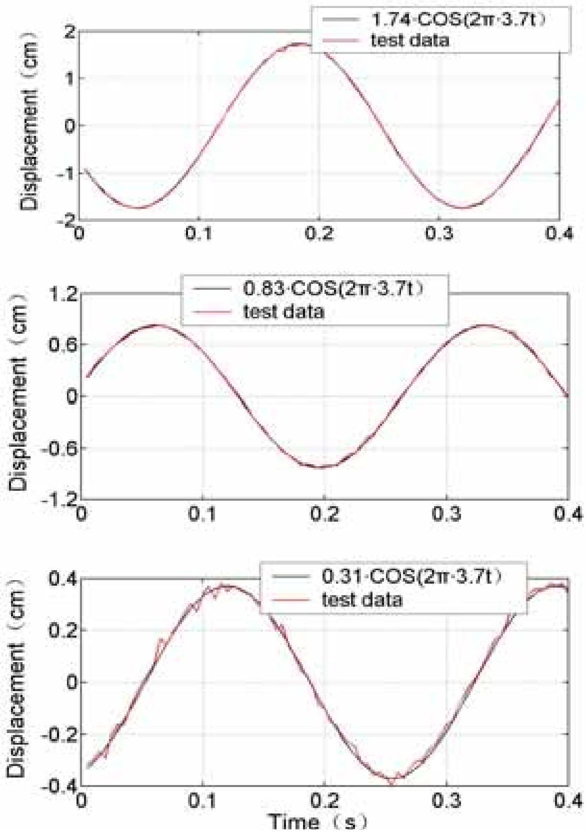

Figure 4 Comparison of measurements and theoretical values

Table 2. Errors between results of basic performence test and theoretical value

Amplitude A(cm)	Maximum error D(cm)	Error ratio D/A(%)	Average error Dav(cm)	Average error ratio Dav/A(%)
1.74	**0.08**	**5.0**	**0.013**	**1**
0.83	**0.04**	**5.0**	**0.013**	**2**
0.37	**0.06**	**16.0**	**0.016**	**4**

Application of Dynamic Characteristic test

To evaluate the efficiency for practical application of the vibration generator, a 3-story building with steel frame is taken as an example and the structural dynamic characteristics is tested. The building has a measurement of 15.0 m in longitudinal direction, 8.0 m in transversal direction and 10.0 m in height (Figure 5). The dynamical characteristic test of the building will focus on following aspects: by ambient vibration, sweep vibration and sinusoidal excitation of the building, the frequency and damping ratio of the building was tested; and by emergency operating stop experiments of mass the damping ratio of the building was measured. During the excitation tests of the building, the performance and operation stability of the vibration generator was evaluated at the same time.

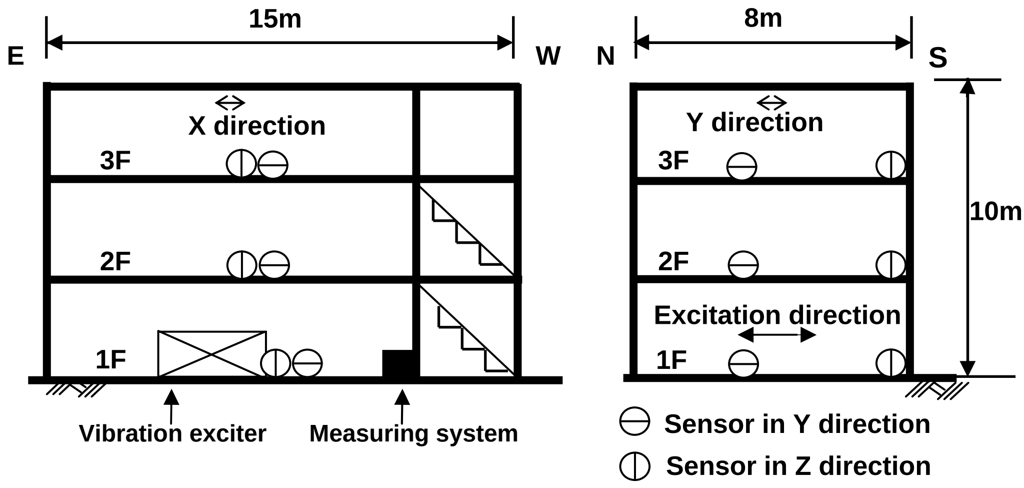

Figure 5. Building and disposition of vibration generator and sensors

The disposition of the vibration generator and sensors are shown in Figure 5. The vibration generator is disposed at the centre of 1st floor of the building, and the excitation is in Y direction. To measure the response of the building, velocity sensors are used, and are positioned in Y direction (Horizontal Direction) at the centre of each floor and in Z direction (Vertical Direction) at the edge of each floor.

Ambient Vibration

To compare with the result of excitation test by the vibration generator, time history response of the building under ambient vibration was measured by all sensors for 10.0 minutes prior to the excitation test, and the sampling frequency was 50.0 Hz. Then modal analysis was carried out. Fast Fourier Transform with number of samples being 1024 was used to analyze the power spectral of the test data. Velocity amplitude spectra of sensor points in Y direction and Z direction are given in Figure 6. From the figures, it shows that there are two predominant frequencies of 0.3 Hz and 3.7 Hz. And the peak values of power spectral at 3.7 Hz decrease with the floor number changing from 3F to 1F. It is determined that 3.7 Hz is the building's natural frequency. Meanwhile, the fact that the peak values at 0.3 Hz are almost the same between each floor shows quite a deep ground effect. It is inferred that 0.3 Hz is predominant frequency of soil ground.

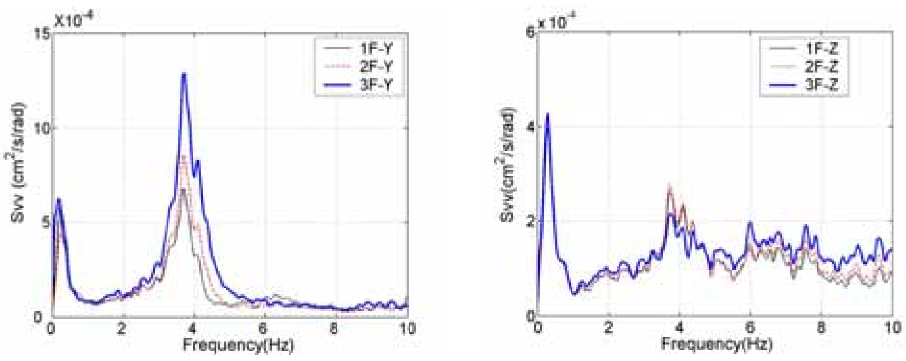

(a) Y direction **(b) Z direction**

Figure 6. Power spectral density of velocity

Sweep Vibration and Sinusoidal Excitation

Sweep vibration test of the building was carried out with frequency ranging from 0.1 Hz to 10.0 Hz by the vibration generator. A resonance-phase curve of the velocity data on 3rd floor measured in Y direction is shown in Figure 7(a). In the figure, there is a large peak in amplitude at 3.7 Hz and the phase delay shows 90º, from which that 3.7 Hz is the building's first natural frequency can also be determined. A peak is also shown at 7.0 Hz which is considered to be the building's second natural frequency.

To recognize the performance of the sweep excitation of the machine, sinusoidal excitations to the building with frequency changing from 2.5 Hz to 7.5 Hz and with same amplitude was carried out by the vibration generator. Time history of velocity was recorded. Figure 7(b) gives the resonance-phase curve results of the 3rd floor in Y direction, which also shows the same regulation of amplitude and phase following with frequency as that of sweep vibration. The phase changes at 7.0 Hz, however the amplitude is not large. It can be inferred that when the excitation amplitude was enlarged, the vibration amplitude contributed by second mode, at the frequency of 7.0 Hz, will be excited easily. In this view, the test shows that the vibration generator has good operation performance of sweep excitation. Comparing with the result of ambient vibration, the second mode can be easily identified by the excitation test.

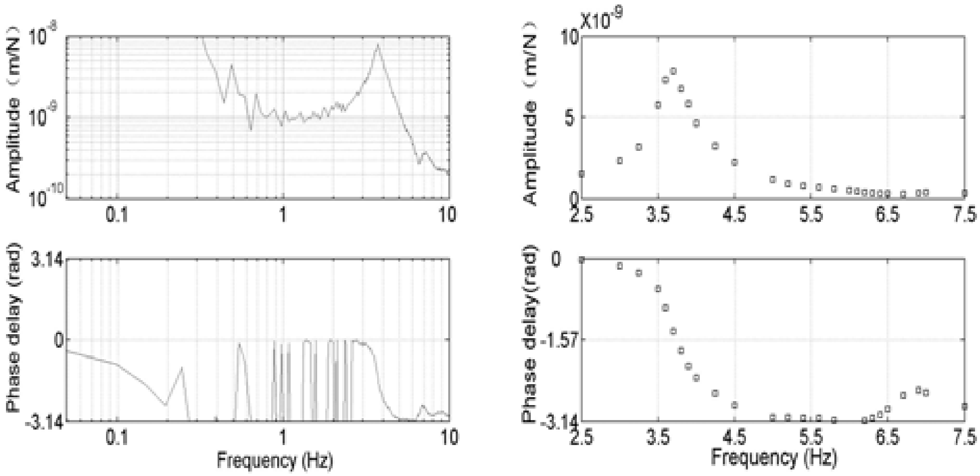

(a) sweep vibration **(b) sinusoidal excitation excitation)**

Figure 7. Resonance and phase curve of the velocity response of the 3rd floor

Free vibration test

When the vibration generator operates at the resonance frequency, the first natural frequency of 3.7 Hz, large response of the building will happen. Stop the machine's operation urgently, and then free vibration of the building is continued. Time history of displacement of the machine and that of velocity of the 1st floor in Y direction are shown in Figure 8. By power spectral analysis and logarithm decay rate method respectively the natural frequencies and decay constants are analyzed. The results are given in Table 3.

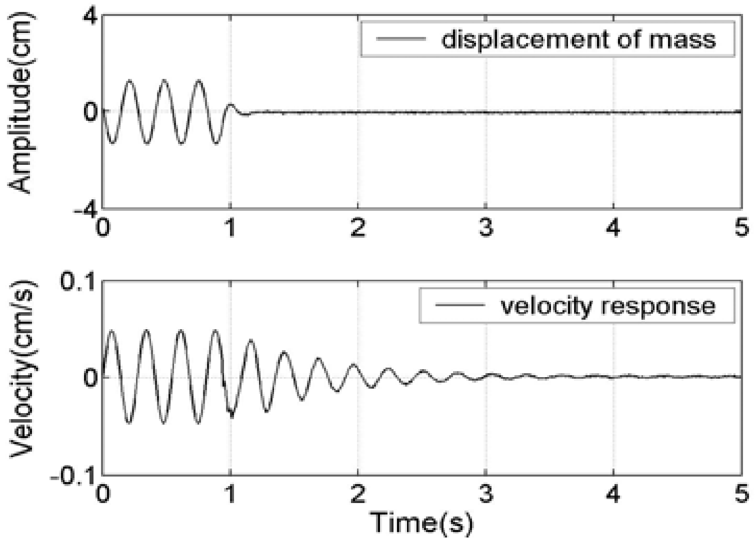

Figure 8. Operating stop of mass and free vibration response of building

Table 3.Test results of frequency and damping ratio of the building

Vibration test	Natural frequency (Hz)	Damping ratio
Ambient vibration	**3.7**	–
Sweep excitation	**3.7**	–
Sinusoidal excitation	**3.7**	**0.06**
Free vibration test	**3.7**	**0.06**

Results and Discussion

A new type vibration generator actuated by electromagnetism is developed in the paper. The parameters and magnetism of the vibration generator is introduced. The basic performance test and building excitation test show that the machine has good performance of low amplitude operation and is efficient for the dynamic characteristic test of buildings, especially for structural damping ratio and high modal frequency.

The vibration generator has perspective application. Its strong movement excitation can also be adopted to test dynamic characteristic of soil ground, such as the effect analysis of the neighbouring building to dynamic of the on site ground (Navarro M, 2007). The paper gives a simple example of performance test. Complicated tests, such as realization of random vibration and the time delay during input signal and its operation, will be carried out later.

Acknowledgements

This research is a part of the “Academic Frontier Research Project”, titled as “Risk Management with soft & Hard Measures on natural Disaster Risk Reduction” in Kanagawa University, through the grant in aid from “Ministry of education, culture, sports, science and technology”. This research could not be done without the effective cooperation of the members of Academic Frontier Research Project of Kanagawa University. The authors are greatly appreciated to their helpful contributions, especially Mr. Toshio Kikuchi and Mr. Toshio Yamamoto. And also, the authors are gratefully acknowledged to Mr. Yasuo Aoki, Servo Technos Co., and Mr. Hiroshi Ohtaki, Techno Link Co.

References

Enomoto T et al (2002). Dynamic Characteristics of Seismically Isolated RC Building Using Strong Motions Recorded by Vertical Array Observation System, *Fifth European Conference on Structural Dynamics, Munich, Germany.*

Navarro M. et al (2007). Analysis of the Weightiness of Site Effects on Reinforce Concrete (RC) Building Seismic Behaviour: the Adra Town Example (SE Spain), *Earthquake Engineering and Structural Dynamics.*

Servo Technos Co., Ltd (2006). Introduction Manual of Vibration Generator - Experimental Equipment for Horizontal Excitation.

Wen Y.K et al (2006). Vibration Control of Steel Tower of Large Span Cable-Stayed bridge under Construction. *Journal of Tongji University(Chinese) 34:9, 1152-1158.*

Yang J.N et al (2004). Identification of Natural Frequencies and Dampings of In Situ Tall Buildings Using Ambient Wind Vibration Data. *Journal of Engineering Mechanics 130:5, 570-577*.

National Seismic Network System of Turkey (USAG)

Eravcı B (1), Erkmen C (1), Zünbül S (1)

(1) Turkish Republic Ministry of Public Works and Settlement General Directorate of Disaster Affairs Earthquake Research Department, Eskişehir Yolu 10.km, 06530, Lodumlu Ankara Türkiye. eravci@deprem.gov.tr , erkmen@deprem.gov.tr , sami@deprem.gov.tr

Keywords: Turkey, seismic network

Introduction

In order to mitigate disaster losses, it is necessary to establish an effective disaster management and risk system. The first step of the management is constituted by preparedness studies before the earthquake (disaster). In order to determinate disaster and risk information it is necessary to have a seismological observation network.

Due to the monitoring of the earthquakes in the country-wide scale, recording, evaluation, achieving and to inform to the public authority, the project named “Development of the National Seismic Network Project-USAG” has been started. 7 Three Component Short Period, 65 Local Network- Broad-band, 57 Broad-band, 13 One Component Short Period stations and 209 accelerometers have been operated in the frame of this project. All of the stations transmit continuously their signal to the ERD (Earthquake Research Department) seismic data center in Ankara.

Earthquake activity in Turkey and surrounding region has been observed 7 days / 24 hours, in ERD data center in Ankara. Data exchange has been carried out EMSC-CSEM.

Weak Ground Motion

Investigate the causes of earthquake and determine reliable earthquake parameters by tracing active faults perform studies on earthquake hazard and risk analysis, determine the reoccurrence period of the earthquake prediction research are the purposes of the project. 142 seismic stations have been operated in the frame of this project (Figure.1).
Observation studies along North Anatolian Fault System have been carried out since 1990 by continuous and online data acquisition. Especially since 2000, earthquakes occurred in the country have been observed continuously on real-time basis. A high quality data has been provided by broad band stations of GDDA (General Directorate of Disaster Affairs)-ERD.

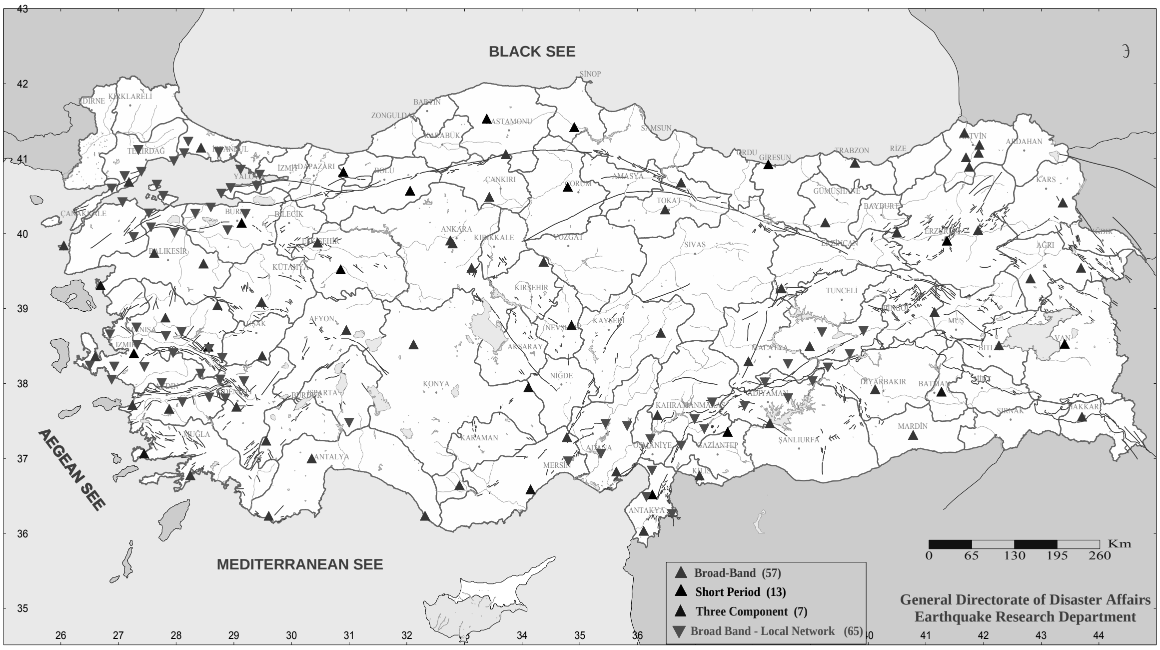

Figure 1. Seismic stations of USAG.

Data presentation and revision of data base studies were completed in December 2007.
The data is provided by Scream or Earthworm in real-time.
Data format (SUD, SAC, (mini) SEED)
Request methods (FTP)
Continuous data
Data acquisition format GCF
Archiving (Scream and Earthworm for waveform data)
MSSQL for bulletin and catalog
Quality control
Power spectral density

Strong Ground Motıon (TKYH)

The main purpose for the operating strong ground motion network is;
-to measure the acceleration and forces that cause damage to the buildings
-to develop the methods of constructing earthquake resistant structures,
-to collect the data intended for the preparation of the microzoning map and the constitution of the data base also for the studies of the earthquake hazard and risk, earthquake master plans and earthquake scenarios of the provinces.
At present, 209 accelerometers have been operated in National Strong Ground Motion Network (Figure.2). It is necessary to increase the number of accelorometeres at least 1000. This network has been operated only by our Ministry in the county-wide scale.

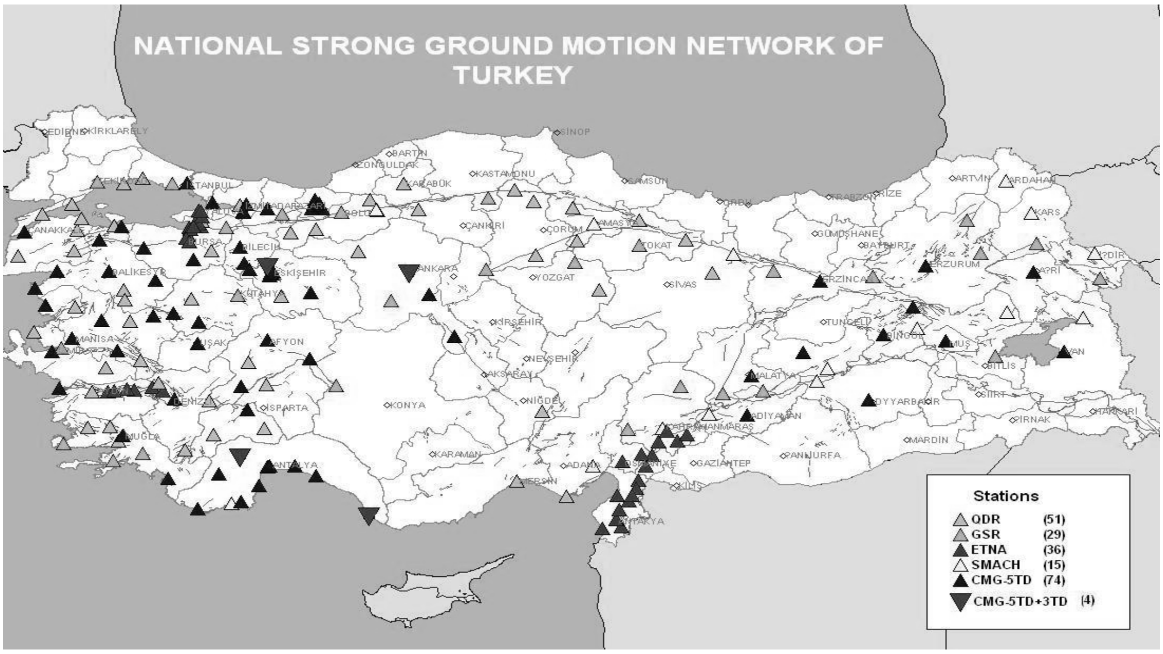

Figure 2. Stations of National Strong Ground Motion Network

Operatıon of the Local Networks In the Scope of the Tkyh

Under the frame of the "the Development of the National Strong Motion Recording System and the Establishment of the Dense Local Networks" project; BYTNet (Bursa-Yalova 14 instruments), DATNet (Aydın-Denizli 6 instruments), MATNet (K.Maraş-Antakya 18 instruments), ANTNet (Antalya 10 instruments), DNet (Düzce 5 instruments) and ANANet (Eskişehir 4 instruments) local networks have been established (Figure.3).

Figure 3. Local Networks of Strong Ground Motion

TURDEP (The Research Project On The Earthquake Behavıor Of The Regıons Wıth Hıgh Seısmıc Rısk (Geo-Strategıc) But Dıfferent Tectonıc Regımes By A Multıdıcıplınary Approach)

For earthquake hazard reduction, it is aimed to observe earthquake activity and earthquake precursors by multidisciplinary studies related to the three main fault zones in our country and to introduce the earthquake hazard seriously in the regions under risk (Figure.4). Thus, a data base information will be obtained for a disaster management system in the international standards. 14 universities participate in this project which is supported by Tubitak- Marmara Research Center.

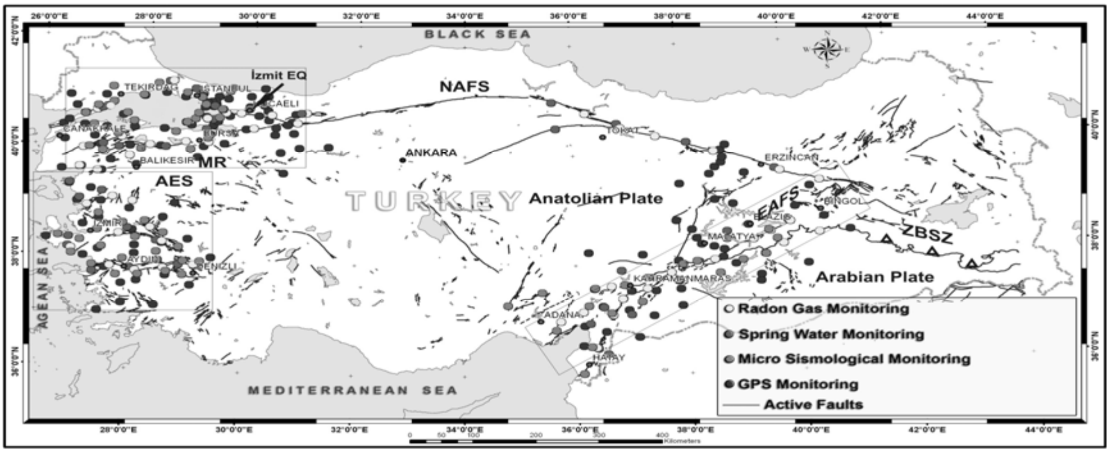

Figure 4. Investigation regions and distribution of stations

Benefits of the USAG Project

-Investigate the causes of earthquakes
-Determine the origin time, magnitude, location and depth of earthquakes
-Observe all active faults
-Study on earthquake hazard and risk analysis
-Determine the reoccurrence period of the earthquakes
-Study on the earthquake prediction research
-Prepare hazard maps and to direct Emergent Aid System
-Prepare bulletins, earthquake catalogs and archive data
-Constitute data base for the earthquake information system
-Inform immediately scientific institutions, press, public and national-local Crisis Center
-Improve earthquake resistant building techniques,
-Provide the utilization of the network as Early Warning System at the places which have strategical importance.

Revised Destructive Earthquake Catalogue for Turkey and Nearby Surrounding Area between 1900-1930

Erkmen C (1), Eravcı B (1)

(1) Turkish Republic Ministry of Public Works and Settlement General Directorate of Disaster Affairs Earthquake Research Department, Eskişehir Yolu 10.km, 06530, Lodumlu Ankara Türkiye. erkmen@deprem.gov.tr , eravci@deprem.gov.tr

Keywords: Turkey, destructive earthquakes, earthquake catalogue

Introduction

Information related to earthquakes and accuracy of earthquake data have been increased in the instrumental period of which the begining can be accepted as the year 1900. When the earlier period of time is considered, comprehensive macroseismic data, historical records of earlier period of time, indirect common records and the prehistorical paleoseismic data are restricted means which are useful for earthquake information.

From 1900 approach to today, the number of destructive earthquakes in Turkey increased. After all, in the first 30 years, the relative decrease is remarkable (Figure.1). The reason is, not to be aware of macroseismic effects of earthquakes and having no issue on this subject, rather than not to be occurence of destructive earthquakes. Depending on the increase of seismic records and quality after 1960 the number of recorded earthquakes was increased and smilar to this after 1930's an increase occurs in obtaining extensive macroseismic earthquake data.

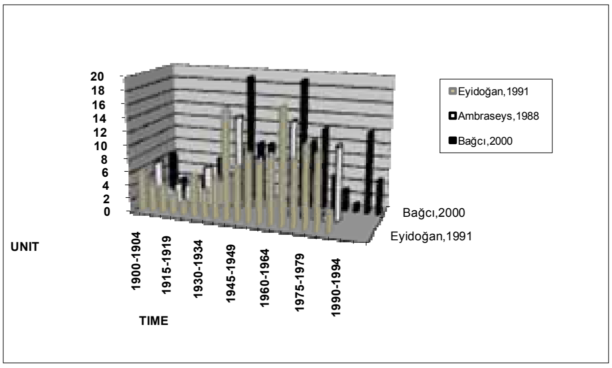

Figure 1.Year-earthquake number diagram of various catalogues (Ambraseys, 1988; Eyidoğan et al., 1991; Bağcı et al., 2000)

But, evaluation of all destructive earthquakes occurred in the last century in the same window causes misapprehension and incorrect acceptations. Because of that reason, we discuss destructive earthquakes occurred in Turkey in two sub-periods as the years between 1900-1930 and 1930-present. Although it is difficult to put a definite border between these periods, the methods to obtain this data , variation and reliability af data have an important role in this seperation. In this study, the first period which data is more restricted relatively has been discussed. First ten years of this term represents the period of time that Otoman Empire was in great difficulties in terms of administration and coordination and communication was at lowest level. In the second ten years, destructive wars including "First World War" occurred and these wars caused the diffucilties to obtain data and this period, turned in to a dark situation. In the third ten years of this period, although the difficulties during the constitution of republic, administrative treatment become regular in short period of time. For these terms, the most distinctive feature is that all records are in Otoman Turkish language till the year 1928. Transcription of these documents needs a spesific culture and because of that reason it become difficult for the researchers today to obtain these documents written in this language from the old archives.

In this study we tried to homogenize the window of the years between 1900 and today. Although it is impossible in terms of regional effects (the number of records for western Anatolia is more than that of Eastern Anatolia) we think inhomogenities were eliminated.
Criterions and reasons to compile this catalogue are given below.
Less number of catalogues which were not regional and include Turkey and nearby surrounding area.
Not to be aware of the period of time 1900-1930 comprehensively.
Not to consider the earthquakes occured beyond the political borders but caused damage in Turkey.
Available catalogues includes many errors. For the epicenter, differences more then hundereds of kilometers (Table.1); for origin time of some earthquakes, errors in mounth level and the error confusing the effects of earthquakes occured in approximate time and nearby places can be shown as examples.

Table 1. Earthquakes with great differences in location, origin time, magnitude and macroseismic effects compared to the previous studies.

May 31 1901 Balchık (Bulgaria) Earthquake MS=7.2 43.40N-28.70E		
Öcal (1968)	41.00 N-29.00E İstanbul (270 km)	MS=5.5
December 04 1905 Pötürge (Malatya) Earthquake MS=6.8 38.12N-38.63E		
Öcal (1968) Eyidoğan et al. (1991)	39.00 N-39.00E Harput (38.70 N-39.20E) (88km)	MS=6.7 MS=6.8
Ayhan et al. (1980)	39.00 N-39.00E Çemişkezek (103km)	MS=6.8
June 03 1907 Muş Earthquake MS=5.0 38.70N-41.50E		
Local sources confuse the effects of this earthquake with the effecets of earthquakes occurred on 1891 and 1903.		
May 28 1914 Gemerek Earthquake MS=5.6 39.25N-36.00E		
Öcal (1968); Karnik (1969) Eyidoğan et al. (1991)	39.70 N-36.00E Akdağmağdeni (50km)	MS=6.7 MS=5.6
Alsan et al. (1975); Ayhan et al. (1980)	39.84 N-35.80E Akdağmağdeni (70km)	MS=5.4
May 13 1924 Horasan Earthquake MS=5.3 40.00N-42.00E		
Alsan et al. (1975)	41.24 N-42.39E Şavşat (140km)	MS=5.0
Öcal (1968)	40.00 N-42.00E Pasinler-Horasan	MS=6.7
Karnik (1969)	39.70 N-42.80E Eleşkirt-Ağrı(80km)	MS=5.3
Pınar and Lahn (1952) declare that no earthquake occurred on May 13 1924 and it was confused with September 13 1924. But, decision of council ministers confirms the earthquake and the damage (BCA, 30.18.01.01..010.37.9).		
November 20 1924 Çobanlar (Afyon) Earthquake MS=5.9 38.55N-30.78E		
Öcal (1968)	39.00 N-31.00E Emirdağ (Afyon) (55km)	MS=4.0
Karnik (1969); Shebalin et al. (1974)	38.30 N-30.20E Kızılören (Afyon) (30km)	MS=5.9
Ambraseys (1988)	39.00 N-30.00E Altıntaş (Kütahya) (85km)	MS=6.0
January 09 1925 Ardahan Earthquake MS=6.0		
Although Pınar and Lahn (1952), Öcal (1968), Ergin et al. (1971) give the date of earthquake as February 08 1925; Karnik (1969), Alsan et al. (1975), Ayhan et al. (1980) and ISC (International Seismological Centre) give the date of earthquake as January 01 1924.		
August 07 1925 Dinar-Bozkurt Earthquake MS=5.9 38.10N-29.80E		
Öcal (1968) Eyidoğan et al. (1991)	37.40 N-30.50E Bucak (Burdur) (100km)	MS=5.7 MS=6.0
Alsan et al. (1975)	37.91 N-29.33E Çal (45km)	MS=5.9

Ergin et al. (1967); Okamoto et al. (1970)	38.00 N-30.50E Senirkent (Isparta) (65km)	MS=5.0
Karnik (1969)	38.00 N-30.50E Senirkent (Isparta) (65km)	MS=5.9
March 01 1926 Acıpayam-Denizli Earthquake MS=6.0 37.40N-29.30E		
Öcal (1968) Shebalin et al. (1974)	36.80 N-30.00E Elmalı (Antalya) (90km)	MS=4.0 MS=6.4
Karnik (1969)	36.80 N-30.00E Elmalı (Antalya) (90km)	MS=5.8
Comninakis and Papazachos (1986)	37.00 N-29.40E Altınyayla (Burdur) (45km)	MS=6.2
Alsan et al.(1975), Ayhan et al. (1980)	37.03 N-29.43E Altınyayla (Burdur) (45km)	MS=6.1
June 26 1926 Rhodos Earthquake MS=7.4 36.50N-26.86E		
Galanopoulos (1961) Duda (1965) Karnik (1969) Comninakis and Papazachos (1986); Papazachos and Papazachou (1989)	36.50 N-27.50E	MS=8.7 MS=8.3 MS=7.7 MS=8.0
Shebalin et al. (1974)	36.10 N-27.80E	MS=6.9
Alsan et al. (1975) Ayhan et al. (1980)	36.54N-27.33E	MS=7.3 MS=7.7
Makropoulos (1978)	36.75N-26.98E	MS=7.3
Ben-Manehem (1979)	36.50N-26.86E	MS=8.0
Eyidoğan et al. (1991)	36.00N-28.00E	MS=7.0
May 02 1928 Emet (Kütahya) Earthquake MS=6.2 39.50N-29.10E		
Pınar and Lahn (1952) Ergin et al. (1967) (03.05.1928)	40.65 N-26.80E Gelibolu (Saros K.) (235km)	- -
Öcal (1968) (Defined as Gelibolu) Karnik (1969)	39.70 N-29.30E Harmancık (30km)	MS=5.5 MS=6.1
Okamoto et al. (1970) (03.05.1928)	40.50 N-26.80E Gelibolu (Saros K.) (225km)	MS=5.8
Shebalin et al. (1974)	40.50 N-26.50E Gelibolu (Saros K.) (250km)	MS=6.1
Eyidoğan et al. (1991)	39.70 N-29.70E Domaniç (60km)	MS=6.2
Pınar ve Lahn (1952) and Öcal (1968) mention that earthquake caused damage in Gelibolu, Bolayır, Enez and Kavak and the earthquake ruptured for 25km long part of the fault ruptured for 50km long during the 1912 earthquake extending from Saros Bay to Şarköy. The effects this earthquake was confused with the effects of Chirpan and Plovdiv (Bulgaristan) earthquakes occurred on April 14-18 1928. Although these earthquakes were felt strongly in the North-west part of Turkey, probably they might cause also damage in Thrace.		

Materials and Methods

In the firsr stage of the study 17 different catalogues which include all of the region or some parts of region have been used (Table.2). The parameters of earthquakes with M≥4.5 have ben complied and tehese catalogues have been compared for each year.

Table 2. Catalogues used in this study

Calvi (1941)	2000 BC - 1900
Pınar and Lahn (1952)	11-1952
Ergin et al. (1967)	2-1965
Öcal (1968)	1850-1960
Karnik (1969)	1901-1955
Okamoto et al. (1970)	1600-1964
Shebalin et al. (1974)	1901-1970
Alsan et al. (1975)	1913-1970
Ben-Manehem (1979)	92 BC-1980
Ayhan et al. (1980)	1881-1980
Comninakis and Papazachos (1986)	1901-1985

Ambraseys and Finkel (1987a)	1899-1915
Ambraseys (1988)	1899-1988
Eyidoğan et al. (1991)	1900-1988
Ambraseys and Jackson (1998)	464 BC-1995
Ambraseys and Jackson (2000)	1509-1999
Bağcı et al. (2000)	1900-2000

In the second stage of the study effects of the earthquakes known as destructive earthquakes or earthquakes with magnitude which could be caused damage have been searched from different sources. These sources:

- Explanations in catalogues,
- Earthquake news of the papers puplished in Ottoman Turkish language such as Vakit, Tercuman-ı Hakikat, Milliyet and Cumhuriyet,
- Ottoman Archives of Prime Ministry for the years 1900-1920 (In Otoman Turkish language)
- Republic Archives of Prime Ministry for the years 1920-1930 (Otoman Turkish Language for the years 1920-1928)
- Earthquake Reports (General Directorate of Disaster Affairs (GDDA) Earthquake Research Department (ERD) archives)
- Local libraries and yearbook of provinces.
- Earthquake reports in Turkish or foreign languages and other puplications.

Iınformation data collected from all these sources have been complied as a result of careful research . All of the different options from these sources have been given without comment not to direct the last users.

Results and Discussion

In the “Revised Destructive Earthquake Catalogue for Turkey and Nearby Surrounding Area Between 1900-1930” 60 earthquakes have been studied. In this paper catalogue have been tried to be told generally without macroseismic details of all earthquakes.

Unlike the previous studies in this study, earthquakes occurred beyond the borders of Turkey but caused damage in Turkey such as 1900 Eastern Mediterranean, 1901 Balchik (Varna), 1904 Samos Island, 1905 Black Sea (East), 1901 Finike- Kaş (Mediterranean), 1922 Rhodos Island, 1926 Kos Island, 1926 Kaş (Mediterranean), 1926 Rhodos Island, 1926 Akyaka- Leninakan, 1930 Salmas earthquakes and also the earthquakes occurred in Turkey but their damages not known before have been studied (Table.3). In the avaliable catalogues, the uncertanities on location, date and effects of earthquakes except the mentioned ones have been tried to be eliminated by the official sources and new findings of historians and geologists.

Table 3. Destructive earthquakes that their damages not known before

19.02.1900	Doğubayazıt	Ms=4.8
27.04.1900	Yozgat	I0=Vıı
16.05.1900	Eskişehir	Ms=4.7
18.08.1910	Palu (Elazığ)	Ms=5.0
30.03.1912	Şemdinli (Hakkari)	Ms=5.1
10.08.1912	Şarköy- Mürefte	Ms=6.2
13.09.1912	Şarköy- Mürefte	Ms=6.8
09.08.1918	Çankırı	Ms=5.8
13.05.1924	Horasan	Ms=5.3
03.10.1924	Zara (Sivas)	I0=Vii
20.11.1924	Çobanlar (Afyon)	Ms=5.9

22.10.1926	Akyaka-Gümrü	Ms=6.0
29.12.1926	Kadişehri (Yozgat)	I0=Vii
18.05.1929	Suşehri (Sivas)	Ms=6.1
10.12.1930	Erzincan	Ms=5.6

After the establishment of Republic of Turkey alteration of the names of districts and sub-districts in the new administrative system, also connection of these regions to different provinces caused great difficulties to find the recent equivalent names of the locations mentioned in the sources of that period with old names. Because of that reason, for some earthquakes, the revised old names of the places given in parenthesis together with the names used recently (Figure.2). This study having a property of source list for that period is in the characteristics of an archive compilation. Only the list of earthquakes is given here without touching on the explanations (Table.4).

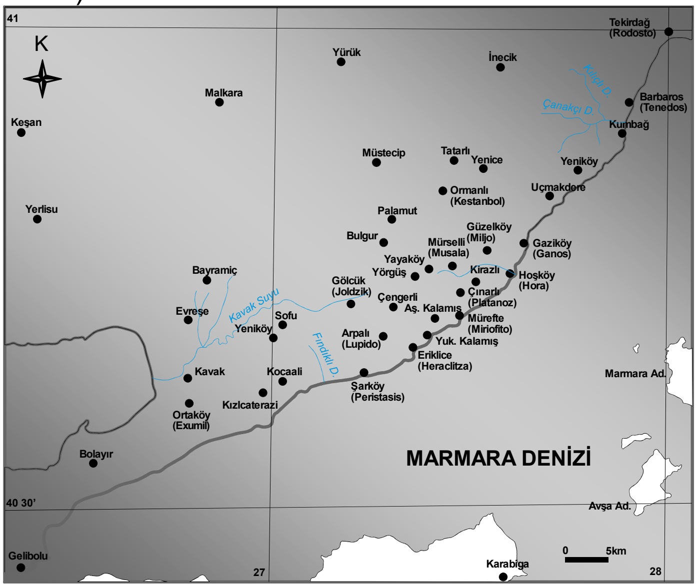

Figure 2. The region with maximum damage during 09.08.1912 Şarköy-Mürefte Earthquake.

References

Akın, F., 2000. Burdur'da Deprem (3/4 Ekim 1914). *Toplumsal Tarih Dergisi s.79, 38-41. Temmuz-2000*

Akyol, İ. H. & Pamir, H. N., 1929. 30-31 Mart 1928 tarihindeki Tepeköy-Torbalı İzmir zelzelesi hakkında rapor, İstanbul Darülfünun *Jeoloji Enstitüsü Neşriyatı, No :3*

Alsan, E., Tezuçan, L. & Bath, M., 1975. An Earthquake Catalogue for Turkey for the Interval 1913-1970. Kandilli Observatory Seismological Department and Seismological Institute Sweden. *Report No.7-75*

Altınok, Y., Alpar, B. & Yaltırak, C., 2003. Şarköy-Mürefte 1912 Earthquake's Tsunami, extension of the associated faulting in the Marmara Sea, Turkey. *Journal of Seismology 7:329-346,2003. Kluwer Academic Puplishers*

Ambraseys, N., 1988. "Engineering Seismology" , *Jour. Earthq.Eng. Struck.Dyn., vol.17, pp.1-105*

Ambraseys, N. & Finkel C., 1987a. "Seismicity of Turkey and Neigbouring Region 1899-1915".*Annales Geophys., vol .5B, pp. 701-26*

Ambraseys, N. & Finkel C., 1987b. The Saros-Marmara earthquake of 9 Agust 1912, *Jour. Earthq.Eng. Struck.Dyn., 15, 189-211*

Ambraseys, N.N., 1997.The Little-known earthquakes of 1866 and 1916 in Anatolia (Turkey). *Journal of Seismology 1:289-299.1997*

Ambraseys, N. N., & Adams, R. D., 1998. The Rhodes Earthquake of 26 June 1926. *Journal of Seismology 2: 267-292, 1998. Kluwer Academic Puplishers.*

Ambraseys, N.N. & Jackson, J.A., 1998. Faulting associated with historical and recent earthquakes in the Eastern Mediterranean region. *Geophys. J. Int., 133, 390-406*

Ambraseys, N.N. & Jackson, J.A., 2000. Seismicity of Sea of Marmara(Turkey) since 1500, *Geophys. J. Int. 141 F1-F6*

Angelier, J., Dumont, J. F., Karamanderesi, H., Poisson A., Şimşek, S. & Uysal, ş., 1981. Analyses of fault mechanisms and expansion of southwestern Anatolia since the late Miocene, *Tectonophysics, 75, 1-9*

Atalay, İ., 1982. Türkiye Jeomorfolojisine Giriş, s.28 İzmir-1982

Ateş, R. & Tabban, A., 1976. 9 Ağustos 1912 Şarköy-Mürefte Depremi çalışmaları ön raporu. T.C. İmar ve İskan Bakanlığı Deprem Araştırma Enstitüsü Başkanlığı.ss:20 Temmuz 1976-Ankara.

Aydan, Ö., 1997. The Seismic Characteristics and The Occurece Pattern of Turkish Earthquakes. *TDV Türkiye Deprem Vakfı. TDV/TR 97-007. January 1997*

Ayhan, E., Alsan, E., Sancaklı, N. & Üçer, S.B., 1980. Türkiye ve Dolayları Deprem Kataloğu 1881-1980.Boğaziçi Üniversitesi.

Bağcı, G., Yatman, A., Özdemir, S. & Altın, N., 2000. 1900-2000 yıllarında Türkiye'de hasar yapan depremler. Jeofizik Bülteni Eylül 2000 Yıl:12 Sayı 37 S:91-93

Barka, A. & Er, A., 2002. Depremini bekleyen şehir İstanbul. Om Yayınevi-İstanbul

Barut, Z., 1976a. 21 Şubat 1315- 3 Kasım 1316 Rumi (4 Mart 1900- 16 Kasım 1900 Efrenci-Alafranga-Miladi.)tarihli Tercuman-I Hakikat Gazetelerindeki deprem haberleri . (içerisinde) Türkiye Genelinde Oluşan Toplu Deprem Raporları. Afet İşleri Genel Müdürlüğü Deprem Araştırma Dairesi Kütüphanesi rapor no 891-1

Barut, Z., 1976b. 3 Şubat 1318- 6 Ağustos 1328 Rumi (16 Şubat 1903- 19 Ağustos 1912 Efrenci-Alafranga-Miladi.)tarihli Tercuman-I Hakikat Gazetelerindeki deprem haberleri . (içerisinde) 1900-1912 Deprem Raporları- Toplu Deprem Raporları. Afet İşleri Genel Müdürlüğü Deprem Araştırma Dairesi Kütüphanesi rapor no 914-1

Barut, Z., 1976c. 3 Mayıs R. 1330 (16 Mayıs M. 1914)-1 Nisan 1928 tarihli Vakit-Milliyet-Cumhuriyet Gazetelerindeki deprem haberleri . (içerisinde) 1914-1928 Deprem Raporları-Toplu Deprem Raporları. Afet İşleri Genel Müdürlüğü Deprem Araştırma Dairesi Kütüphanesi (rapor numarası yok).

BCA, 30.18.1.1..10.37.9, Tarih :03.08.1924. Sayı :752.Fon Kodu :30.18.1.1 Yer No :10.37.9

BCA, 30.18.1.1..12.69.2, Tarih :23.01.1925. Sayı :1392. Dosya :99-10. Fon Kodu :30.18.1.1 Yer No :12.69..2

BCA, 30.10..119.837.2, Tarih:18.12.1924. Sayı:3856. Dosya:99B2. Fon Kodu: 30.10. Yer No:119.837.2 Sayfa:2

BCA, 30.18.01.01.011.43.15, Tarih:17.09.1924. Sayı:879. Fon Kodu: 30.18.1.1. Yer No:11.43..15

BCA, 30.10..119.837..7, Tarih:28.10.1926. Dosya:99B7. Fon Kodu: 30.10.0.0. Yer No:119.837..7

BCA, 30..18.1.1..18.17..20, Tarih:10.03.1926. Sayı:3302. Fon Kodu: 30..18.1.1. Yer No : 18.17..20.

BCA, 30..18.1.1..19.37..1, Tarih:30.05.1926. Sayı:3680. Dosya: 99-18. Fon Kodu: 30..18.1.1. Yer No : 19.37..1

BCA, 30..18.1.1..18.21..5, Tarih:21.03.1926. Sayı:3367. Dosya: 99-17. Fon Kodu: 30..18.1.1. Yer No : 18.21..5

BCA, 30..10.0.0..119.837..7, Tarih:16.01.1927. Dosya: 99B8. Fon Kodu: 30..10.0.0. Yer No : 119.937..7

BCA, 30.10.0.0..117.818.26, Tarih: 25/5/1929 Sayı: Dosya: 99A6 Fon Kodu: 30..10.0.0 Yer No: 117.818..26. Şebinkarahisar, Sivas ve Adana vilayetlerinde meydana gelen depremler ve neticelerine dair rapor.

BCA, 30.10.0.0..12.818.26,Tarih: 22/6/1929 Sayı: Dosya: 11144 Fon Kodu: 30..10.0.0 Yer No: 12.73..7.

Suşehri'nde meydana gelen deprem, verdiği zararlar ve alınan tedbirlerhakkında İçişleri Bakanı Şükrü Kaya'nın Başbakan'a telgrafı.

BCA, 30.10.0.0..119.837.11,Tarih: 0/0/1929 Sayı: Dosya: 99B11 Fon Kodu: 30..10.0.0 Yer No: 119.837..11. Sivas ve köylerinde meydana gelen depremi gösterir harita.

BCA, 30.10.0.0..119.837.14,Tarih: 22/05/1930 Sayı: Dosya: 99B14 Fon Kodu: 30..10.0.0 Yer No: 119.837..14. Başkale depreminin can ve mal kaybına yol açtığı.

BCA, 30.10.0.0..119.837.16,Tarih: 16/12/1930 Sayı: Dosya: 99B16 Fon Kodu: 30..10.0.0 Yer No: 119.837..16. Erzincan, Gümüşhane, Tokat, Malatya ve Şebinkarahisar'da meydana gelen depremin verdiği hasar.

BCA, 30.10.0.0..119.837.19,Tarih: 17/01/1931 Sayı: Dosya: 99B19 Fon Kodu: 30..10.0.0 Yer No: 119.837..19. Refahiye'de meydana gelen depremin Ekecik ve Gölcük köylerinde hasara yol açtığı.

Ben-Manehem, A., 1979. Earthquake Catalogue for the Middle East (92 BC.-1980 A.D.). *Bolletinodi Geopisic Teoricaed Applicate.Vol XXIN.81. Decembre 1979.*

Calvi, S., 1941.Türkiye ve bazı Komşu ülkelerin deprem kataloğu. *Çeviren Erdoğan Kumcu. 1979 İstanbul.*

Cancani, A., 1902. Terremoto del 31 Marzo nel Mar Nero, *Notizie sui Terremoti Osservati in Italia, 1901, 75-87, Rome.*

Cavasino, A., 1927. Macrosismi avvertiti in Italia e Colonie nell'ano 1926*. Boll. Soc. Sism. Italia.27, 25-40*

Comninakis, P.E. & Papazachos, B.C., 1986. A Catalogue of Earthquakes in Greece and the Surrounding Area for the Period 1901-1985. Un. Of Thessaloniki Geophysical Lab. Pup.No.1,1986.

Çakıcı, B., 2000. 1914 Isparta ve Burdur depremi. İçerisinde Tarih Boyunca Anadolu'da Doğal Afetler ve Deprem Semineri.22-23 Mayıs 2000 Bildiriler 2. Baskı İstanbul 2002. s.219-248.

Çemen, İ., Gökten, E., Varol, B., Kılıç, R., Özaksoy, V., Erkmen, C. and Pınar, A., 2000. Turkish earthquakes reveal dynamics of fracturing along a major strike- slip fault zone. *EOS American Geophysical Union, Volume 81, Number 28, Washington, USA.*

Demirtaş, R. 2000. 17 Ağustos 1999 İzmit Körfezi Depremi Raporu. T. C. Bayındırlık ve İskan Bakanlığı Afet İşleri Genel Müdürlüğü Deprem Araştırma Dairesi Başkanlığı, Ankara.

Demirtaş, R. & Yılmaz, R., 1996. Türkiye'nin Sismotektoniği. Sismisitedeki uzun süreli değişim ve güncel sismisiteyi esas alarak deprem tahminine bir yaklaşım.T.C. Bayındırlık ve İskan Bakanlığı Ankara-Temmuz-1996 s:91

Duda, S. J., 1965. Secular seismic energy release in the circum-Pacific belt. *Tectonophysics 2, 409-452.*

Dumont, J. F., Uysal, Ş., Şimşek, S., Karamanderesi, H., & Letouzey, J. 1979. Formation of the grabens in southwestern Anatolia, *Bull. Min. Res. Explor. Ins. Turk., 92, 7-18 p.*

Eginitis, D., 1912. Catalogue des treblements de terre observes en Grece. 1909-1911. *Ann. Obs. Natl. Athenes, 6, 304-33*

Elmacı, M.E., 2000. Güneş Tutulmasının ardından gelen Burdur-Isparta Depremi (1914). *Toplumsal Tarih Dergisi s.73 pp:50-52. Ocak-2000*

Ergin K.,Güçlü U. & Aksay G., 1967. Türkiye ve Civarının Deprem Kataloğu (MS 2 yılından 1964 sonuna kadar olan). T.C*. İstanbul Teknik Üniversitesi Maden Fakültesi Arz Fiziği Enstitüsü Yayınları No:28.*

Erler, M. Y., 1996. 1912 Marmara Havzası Depremi.*Toplumsal Tarih Dergisi s.35 pp:30-35. Kasım-1996*

Eyidoğan, H., Güçlü, U., Utku, Z. & Değirmenci E., 1991. Türkiye büyük depremleri makrosismik rehberi (1900-1988). *İTÜ Maden Fak. Jeofizik Müh. Böl*.

Galanopoulos, A., 1961. On the magnitude determination using macroseismic data. *Annali Geofis. 14, 225-253.*

Gelescova, A., 1902. Le tremblement de terre du district de Baltchik-Varna, 31 mars 1901. *Bull. Soc. Astron. France, 6,42-44. Paris.*

International Herald Tribune. 1928 Earthquakes Hit Turkey.In our pages: 100, 75 and 50 years ago. *Published: WEDNESDAY, MAY 7, 2003.*

Karacakaya, R., 2000. Şarköy Mürefte Depremi (1912). İçerisinde Tarih Boyunca Anadolu'da Doğal Afetler ve Deprem Semineri.22-23 Mayıs 2000 Bildiriler 2. Baskı İstanbul 2002. s.203-218.

Karnik, V., 1969. Seismicity of the European Area Part1. D. *Reidel Puplishing Company Dordrecht-Holland.*

Karnik, V., 1971. Seismicity of the European Area Part2. D. *Reidel Puplishing Company Dordrecht-Holland.*

Kuran,U.,2002. Linear Elastic Fracture Mechanics Approach to fatigue life prediction [or earthquake prediction]along the NAF and EAF zones. *The Antakya-2002 Workshop*

Kuran, Uğur & A.C., Yalçıner, 1993. Crack Propagations, Earthquakes and Tsunamis in the Vicinity of Anatolia. Stefano Tinti (Editor), *Kluwer Academic Publishers.*

Macovei, R., 1912. Sur le Tremblement de Terre de la Mer de Marmara le 9 aout 1912, *Bull. Section Sc. Academic Roumaine 1, 1-9*

Makropoulos, K., 1978. The statistics of large earthquake magnitude and evaluation of Greek seismicity. *PHD Thesis, University of Edinburgh.*

Margottini, G., 1982. Osservazioni su alcuni grandi terremoti con epicentro in oriente. Campo macrosismico in Italia del terremoto greco del 1903, Rep. CNEN-RT/AMB(82)3, *Comit, Naz. Energ. Nucleare, Rome.*

Mehmet Sadi, 1912a. Marmara havzası'nın 26-27 Temmuz Hareket-i Arzı 15 Eylül 1328, *İstanbul Resimli Kitap Matbaası, 45s. (Osmanlıca)*

Mehmet Sadi, 1912b. . Marmara havzası'nın 26-27 Temmuz 1328 (1912) (Depremi) yer sarsıntısı nedenleri. İstanbul Resimli Kitap Matbaası, 8s (Osmanlıca)

Mihailovic, J., 1927. Memoir-Sur les Grands Tremlement de Terre de la Mer de Marmara-Belgrade-1927

Navaro-Neumann, E., 1919.Les principaux macroseismes des annees 1915 a 1918, Ciel & Terre p.20, Bruxelles.

Ohta, Y., Ohashi, H. & Tabban, A., 1983. Macro statistical analysis on earthquake damages in Turkey. A comprehensive study on earthquake disasters in Turkey in view of seismic risk reduction. Edited by Yukata OHTA. March 1983.Dep. of Arch. Eng. Faculty of Eng. Hokkaido University Sapporo, Japan.

Okamoto, S., Tabban, A. & Tanuma, T., 1970. Mühendislik Hizmetlerinde Kullanılmak Üzere Düzenlenen Grafiklerle Türkiye Deprem Şiddetleri Kataloğu. T.C. İmar ve İskan Bakanlığı Afet İşleri Genel Müdürlüğü Deprem Araştırma Enstitüsü Başkanlığı. Ankara 1970.

Öcal N., 1968. Türkiye'nin Sismisitesi ve Zelzele Coğrafyası, 1850-1960 Yılları için Türkiye Zelzele Kataloğu. Milli Eğitim Bakanlığı İstanbul Kandilli Rasathanesi Sismoloji Yayınları: 8, İstanbul 1968.

Papazachos, B. & Papazachou, K., 1989. Oi seismoi tis Hellados, Thessaloniki, 313-314.

Pınar N. & Lahn E., 1952. Türkiye Depremleri İzahlı Kataloğu. T.C. Bayındırlık Bakanlığı Yapı ve İmar İşleri Reisliği Yayınlarından Seri:6, Sayı:36, Ankara 1952.

Salomon-Calvi, W., 1940, 21-22 Eylul 1939 tarihinde vukua gelen Dikili-Bergama Zelzelesi, *Maden Tetnik Arama Enstitusu (MTA) yayini, Seri B, 5, 31-45.*

Shebalin, N. V., Karnik, V. & Hadzievski, D., 1974. Catalogue of Earthquakes PartI,1901-1970/ PartII, prior to 1901. *UNDP/UNESCO Survey of the Seismicity of the Balkan Region. UNESCO Skopje,1974.*

Siberg, A., 1928. Das Korinther Erdbeben vom 22 April 1928, Jenaische Zeitschr. F. Naturwiss. 64,7-12.

Sieberg, A., 1932. Erdbebengeographie, in ed. B. Gutenberg, *Handbuch der geophysik 4:775-812. Berlin.*

Şaroğlu,F.,Emre, Ö. & Boray, A., 1987. Türkiyenin diri fayları ve depremsellikleri (Active faults of Turkey and their seismicity*). MTA Report no.8174 (unpublished), Ankara, p. 394.*

Tchalenko, J.S., 1977. A reconnaıssance of the seismicity and tectonics at the northern border of the Arabian Plate (Lake Van region). *Revue de Geographie Physique et de Geologie Dynamique. Vol. XIX, Fasc. 2, pp 189-208, Paris, 1977.*

Tchalenko, J. S. & Berberian, M., 1974. The Salmas (Iran) Earthquake of May 6th, 1930. *Annali di Geofisica. Vol. XXVII-N.1-2-1974.*

Umar, B., 1993. Türkiye'deki Tarihsel Adlar. Türkiye'nin tarihsel coğrafyası vetarihsel adları üzerine alfabetikdüzende bir inceleme. *İnklap Kitapevi 2. Baskı, 1993.*

Westeway, R., 1990. Block rotation in Western Turkey: 1. Obsevational Evidence*. Journal of Geophysical Research 95. 19857-19885.*

Yaltırak, C., Alpar, B., Sakınç, M. & Yüce, H., 2000. Origin of the strait of Çanakkale (Dardanelles): regional tectonics and the Mediterranean-Marmara incursion*, Marine Geology 164, 139-156*

Yanatma, S., 2001. Fethiye Depremi (1957). *Toplumsal Tarih Dergisi sayı:86. ss:52-60 Şubat-2001*

A Straightforward Method Applicable to Earthquake Damage Scenarios and Early Loss Assessment in Urban Areas of Southern Spain

Feriche M (1), Vidal F (1), Jimenez C (2), Navarro M (3)

(1) Andalusian Institute of Geophysics, Granada University, 18080 Granada, Spain, feriche@ugr.es, fvidal@iag.ugr.es
(2) LIDYCCE, Campanillas, 29590 Malaga, Spain. cjimenez@lidycce.es
(3) Depart. of Applied Physics, Almeria University, 04120 Almeria, Spain mnavarro@ual.es,

Keywords: expected earthquake damage, earthquake damage scenarios, building vulnerability, losses, earthquake emergency planning.

Introduction

The estimation of expected damage during a future strong earthquake before or just after its occurrence is a difficult task because it depends on the characteristics of earthquake source, the site conditions, and the building vulnerability itself. However, at present it is possible to estimate seismic motion in solid bedrock and at surface soil in the potential shaken area and at each urban area point also if soil characteristics are known. Furthermore, it is also possible estimate damage to buildings and probable casualties (Vidal et al., 1996; 2008).

A reliable forecast of the distribution of future earthquake damage in urban areas is an adequate way for reducing the impact of future earthquakes. Thus, the development of straightforward methods to estimate Earthquake Damage Scenarios (EDS) and Early Earthquake Loss Assessment (EELA) may be considered as the first level evaluation of earthquake impact for Civil Defense in order to apply Earthquake Disaster Prevention measures in the first case (EDS) and for Emergency Planning in both cases (EDS & EELA).

In the western Mediterranean region there are zones with moderate to low seismic hazard level but unfortunately, due to their high building vulnerability conditions they have a moderate to high seismic risk level. In these zones it is necessary to perform upgraded data bases on elements at risk, a reliable vulnerability assessment of these elements, and an adequate study of soil conditions to achieve a detailed estimation of ground shaking distribution (Earthquake Scenarios, ES) and expected damage and losses (EDS). That estimates can be calibrated by mean historical earthquakes. Furthermore, the methods must be applicable not only to regional scales but urban areas to.

When the main factors involved in seismic risk such as attenuation characteristics, soil amplification, building vulnerability, and so on, are desegregated in a Geographical Information System (GIS) and jointly combined with a direct damage estimation method it is possible to obtain easily ES, EDS and also EELA for emergency purposes. This assessment of potential earthquake damage in urban areas provides a basis for seismic risk reduction and earthquake risk management.

The Southern Spain region is the most hazardous seismic zone of Spain, especially the Granada, Malaga and Almeria provinces (Vidal, 1986). In this zone more than ten moderate magnitude but destructive historical earthquakes have occurred in the last five centuries. In 2002 an Early Damage Estimation computer program (SES2002) was implemented by Civil Defense at national level. To regional scale and for Emergency Planning also, a seismic risk evaluation has been recently carried out for Andalusian region (SISMOSAN Project, 2007).

Nevertheless, only a few earthquake risk evaluation studies have been developed recently in in Spain corresponding to the urban areas of Malaga (Irizarry et al, 2006, 2007), Barcelona (Irizarry, 2004; Lantada et al., 2007), Motril (Perez et al., 2007) and Granada (Feriche et al., 2008; Vidal et al., 2008).

In this work a methodology to obtain EDS in urban areas it is presented. The amplification factors have been obtained by seismic-geotechnical classification of soils; the building vulnerability was evaluated from Building Typology Matrix and Vulnerability Index (Milutinovic & Trendafiloski, 2003) and finally, earthquake damage were estimated by using Probability Damage Matrix and with a Geographical Information System (GIS). This methodology has been applied to an Andalusian moderate-sized urban area (Velez Malaga town).

Materials and Methods

Soil classification, amplification factor and seismic hazard map

A preliminary 1:10.000 geotechnical map as a guide, borehole database, local site stratigraphy, SPT data, Vs of subsurface materials estimated from SPT values, and several geological cross-sections, previously obtained by Lidycce Group (Nogués, 2002), were used to characterize the geo-technical properties of geological surface units and estimate the soil structure of Velez Malaga urban area (Figure 1). The effects related with local ground conditions: Amplification of ground motion by soft soils, liquefaction of water-saturated thick soils (sand, silt, gravel) and landslides triggered by shaking have been analyzed from these data. For obtaining the ground shaking amplification by surface soil layers, a local geomorphological division of the surface materials has been carried out taking into account both the geological and geotechnical characteristics of them and the nature of the substrate.

Following the Building Seismic Safety Council (BSSC, 2004) and the Eurocode 8 (EC8), average shear-wave velocity in the upper 30 m of soil, V_S^{30}, has been used for site classification sites according soil type. To assign the V_S^{30} value at each material group, the values proposed empirically by Borcherdt (1994), NEHRP, 2003, Yamazaki et al. (2000), Dobry et al (2000), Stewart (2003) and those obtained in recent investigations developments in this field in southern Spain (Delgado et al., 2000; Navarro et al., 2001, 2007; Benito et al, 2006; Garcia-Jerez et al., 2007) have been taken into account. Then, the geological sites were grouped in six soil categories on the basis of averaged shear wave velocity V_S^{30} (Table 1). This classification has similarities with that adopted in the 2003 *NEHRP Provissions*, (BSSC, 2004). In relation with the four soil types proposed by the Spanish Building Code (NCSE-02), the current classification subdivide first soil class of NCSE-02 in two new ground categories (I_A and I_B), and the four in IV_A and IV_B new ones. Only soil types I_B, II and III are found inside Velez Malaga town and soil type IV_A at the Velez river zone (Table 1) close to the urban area.

Table 1. Soil types according BSCC 2004, EC8 (*Eurocode 8*) and PW (Present Work) and PGA Amplification Factors (AF) used in this work.

SOIL TYPE			Description		V_S^{30} m/s		AF
BSCC	**EC8**	**PW**	**General**	**Velez Malaga**	**BSCC**	**EC8**	
A	A	I_A	Hard rock	Not found	> 1500	>800	0.9
B		I_B	Rock	Schisst massif	760-1500		1.0
C	B	II	Soft rock & Very dense soil	Silty clay & silt	360-760	360- 800	1.2
D	C	III	Stiff soil	Fillings, sandy silt, red ravel,	180-360	180- 360	1.4
E	D	IV_A	Soft soil	Alluvial of the Vélez river	<180	<180	1.8
F	E	IV_B	Special soils	Not found		S_1<100 S_2 liq.	≥ 2.0

The shear-wave velocity was used here to characterize the liquefaction potential (Andrus and Stokoe, 1997; Seed et al, 2003) joint to likely depths to groundwater. Although recent, loose and granular soils are present in the Velez riverside, placed close but outside of the urban area (Figure 1), the groundwater levels indicate liquefaction could be possible for strong shakings along Velez riverbeds.

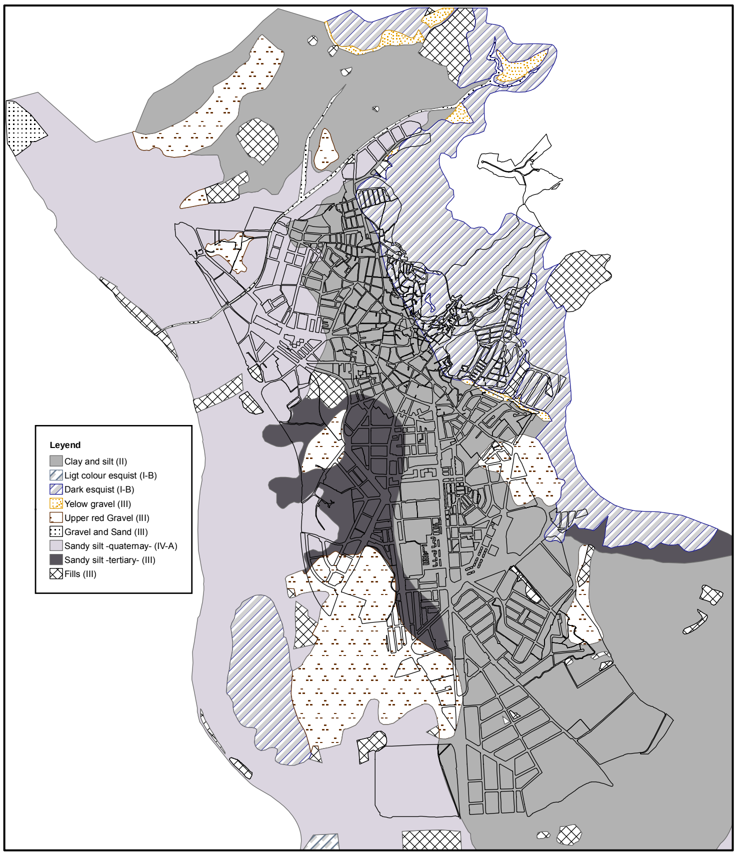

Figure 1. Simplified geotechnical map of the Velez Malaga town showing lithology distribution and soil classification based on the V_S^{30} values.

The earthquake-induced landsliding has been assessed with slope data derived from digital cartography, geologic maps and from air photo interpretation. No landslides are hoped for inside the urban area but could occur in slopes placed northward of town near rivers, gullies and roads. Tabla 5: clasificación de suelos de la NCSE-02 y factores.

The estimation of seismic ground motion was obtained firstly calculating shaking on the bedrock site (soil type I_B) and secondly by adding the influence of shallow ground conditions. Depending of final target, the seismic motion on rock could be obtained from probabilistic seismic hazard map, or from historical earthquakes intensity data, or by using deterministic methods. To calculate seismic ground motion expected in each point of the urban area we use PGA and SA(T) values in the bedrock multiplied by the amplification factors of the site.

Due to the fact that seismic hazard maps (incorporating soil conditions) can be the basis for a seismic emergency planning purposes, the expected ground motions have been expresed by means of Macroseismic Intensity (I) parameter.The intensity is obtained from PGA and SA(T) data applying Okada et al (1991) relationship. When starting from EMS intensity values reached on rock in historical earthquakes the final intensity on soil can be roughly estimated increasing 0.5 and 1 degree for soils III and IV_A , respectively, and ≥1.5 for soils type IV_B , according toTiedemann (1992) assumptions.

Building vulnerability assessment and Earthquake damage evaluation

Building vulnerability is the degree of damage to given building subjected to ground shaking of a given intensity. Vulnerability assessment based on past earthquake damages (empirical vulnerability) assumes that certain groups of buildings characterized by a similar seismic behaviour tend to experience similar earthquake damage also and constitute vulnerability classes. Thus, a series of empirical vulnerability functions can be obtained for these vulnerability classes from field damage observations (e.g. the ATC-13, 1985 functions).

To proceed to the vulnerability evaluation for each building of Velez Malaga town, we used the vulnerability index and damage functions methodology (Bernardini, 2000; Giovinazzi & Lagomarsino, 2004**)** defined as level I in the Risk-UE project (Vacareanu et al, 2004; Giovinazzi, 2005). Thus, structural typology, age and other characteristics (as regularity, position...) of the buildings have been considered. First step was to define a Building Typology Matrix (BTM) from specific features of buildings of the town, considering the BTM established by Risk-UE project and assigning average vulnerability indices to the vulnerability classes according to proposal of Milutinovic & Trendafiloski (2003). Risk-UE define 23 building classes for European countries: 10 classes for masonry (M), 7 for reinforced concrete (RC), 5 for steel (S) and 1 for wooden (W) buildings.

Vulnerability index VI values range between 0 and 1, being their higher values for the most vulnerable buildings and lower to higher resistant buildings. For each building type Risk-UE calculates four vulnerability indices: VI* most probable value of VI; [VI- ; VI+] bounds of the plausible range of VI (usually obtained as 0.5-cut of the membership function); [VImin; VImax] upper and lower bounds of the possible values of VI (Giovinazzi and Lagomarsino, 2004). The vulnerability index value VI for each building is calculated simply summing to the characteristic vulnerability index VI* (according to the building type) two modifier factors ΔVR (to take into account the particular quality of building construction) and ΔVm (that considers the effects due to state of preservation, seismic design level, number of floors, irregularity, soft-story, foundation an soil morphology):

$$\overline{V}_I = V_I^* + \Delta V_R + \Delta V_m \tag{1}$$

The main vulnerability modifier is seismic design level being 0.16 for pre or low code level and -0.16 for high level. The remainder modifiers have lower values, generally 0.04, except for buildings with 6 or more stories and low code level that reach 0.08. For these reasons a first simplified estimate of the vulnerability index is here used that considers: typologies, periods of construction according to seismic design level and also the following modifier factors: bad maintenance, serious irregularity, soft-story in the building and more than 6 stories.

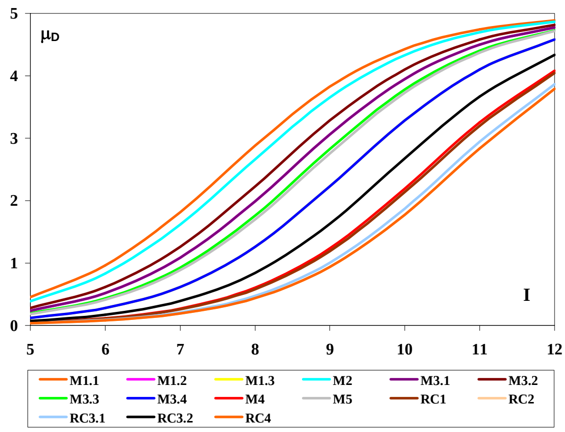

Figure 2. The mean semi-empirical vulnerability functions for the most common Risk-UE building typologies (Giovinazzi & Lagomarsino, 2002).

Once the vulnerability index is assigned, the evaluation of building earthquake damage was obtained by using the intensity function proposed by Sandi and Floricel (1995) and applied by Giovinazzi and Lagomarsino (2002) and (Giovanazzi, 2005). This semiempirical function (based in observed damage in past earthquakes) correlates the mean damage degree μ_D with the seismic action at each site (characterized by means macroseismic intensity I (EMS)) and the building vulnerability (with vulnerability index VI) (Figure 2):

$$\mu_D = 2.5\left[1 + \tanh\left(\frac{I + 6.25\,V_I - 13.1}{2.3}\right)\right] \qquad (2)$$

Six damage states are considered labelled as: None, Slight, Moderate, Substantial to Heavy, Very Heavy and Destruction. The probability of each state of damage, or the damage probability matrix (DPM), can be calculated from mean damage μD using the beta distribution. Thus potential physical damage scenarios have been obtained and plotted for the Velez Malaga town (and for any selected area) in mean damage values or in terms of each damage state of EMS scale.

Results and Discussion

A column soils classification based on V_S^{30} values (estimated mainly from geotechnical, borehole and SPT data) was performed and a detailed ground amplification map has been obtained (Figure 3). The resulting amplification factor values vary from nought, where engineering bedrock (Soil type I_B), is exposed, to medium (1.4 for PGA and 2.4 for SA(T)) where stiff soils are present. Outside of the urban area (at the western zone of the town) appear soils of type IVA, and soil liquefaction could be possible for strong shakings.

After a historical seismicity revision, the largest historical event affecting Velez Malaga has been used to estimate a scenario earthquake. This historical event corresponds to the 1884 Andalusia earthquake (M~6.8) located around 15 km far away from Velez Malaga. Thus, an intensity of VII-VIII on bedrock has been considered to estimate the EDS in terms of probability of damage.

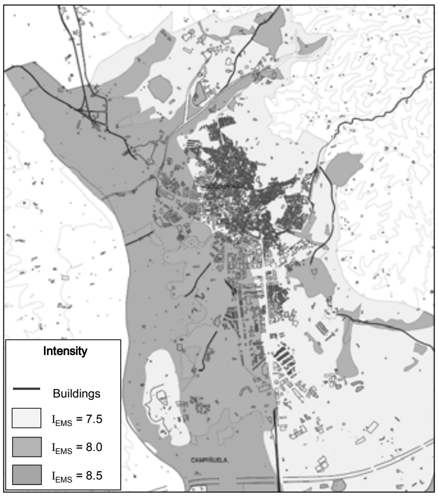

Figure 3. Macroseismic intensity distribution map for an event similar to 1884 earthquake

The population and building data of INE 2001 census for Velez Malaga town are: 35.322 inhabitants and 5.520 buildings. The typology, conditions and vulnerability of 4.957 buildings were evaluated; more than 65 % are RC buildings and masonry the remainders (mainly of brick walls). 72% of the buildings have one or two stories and 3% have 6 or more stories. 7 BTM classes were finally identified: 4 for Masonry (M1.2, M1.3, M3.1, M3.4) and 3 for Reinforced Concrete (RC1, RC3.1, RC3.2). The minimum typology vulnerability index V* obtained is 0.40 and the maximum 0.74. When modifier factors are considered minimum total vulnerability index VI is 0.40 and the maximum is 0.94. According to EMS-98 scale, the majority of the buildings belong to the A, B, and C classes, and less frequent to D class (Figure 4). The damage distribution for tested buildings is shown in Table 2.

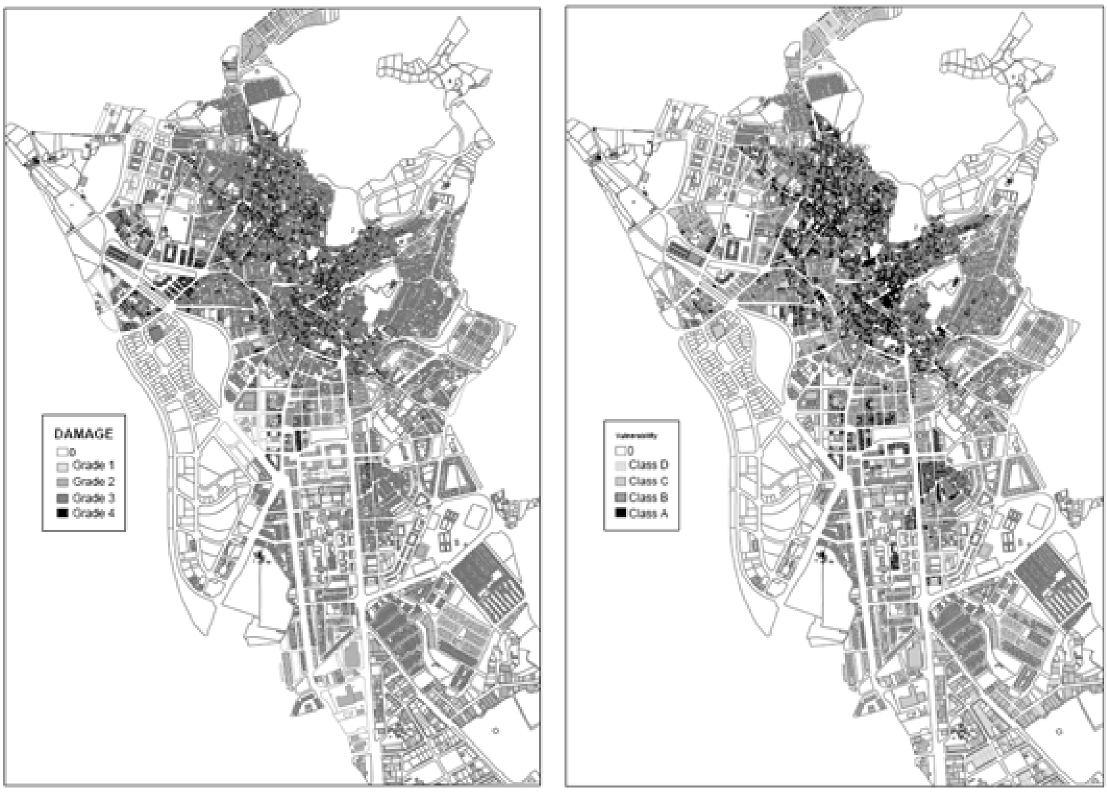

Figure 4. a) EMS-98 Vulnerability classes of the buildings (left). b) Earthquake damage of Velez Malaga down-town obtained with VI* (righ).

For damage estimation two typology vulnerability indices have been considered: VI* (the most probable value of VI), and VI+ (the maximum plausible value of the VI). The total VI has been calculated in both cases taken into account the modifiers. The more serious damage appears in the old buildings located in the northern part of the city. The number of uninhabitable tested buildings is 619 (12%) and as far as 1.184 (24%) when VI+ it is used.

Table 2. Number of buildings affected for each EMS damage degree

EMS Damage degree	**Damaged buildings** (*only tested buildings*) **(I_{rock} = VII-VIII)**	
	V*+modifiers	**V^+ + modifiers**
0	231	-
1	1.165	-
2	2.303	207
3	1.238	1.955
4	20	2454
5	-	341

Conclusions

Several aspects of the proposed methodology applied to a moderate-sized town of the southern Spain with a low-to-moderate seismic hazard must be emphasized: Firstly, the advantage to use V_S^{30} data instead of shallow lithological data for a more consistent soil classification and soil amplification factor estimates. For example, thin surface layers of dry loose soils (less than 5 m thick) overlying deposits (of sand, gravel or stiff clay) of high density (soils type III) or very high density (type II) are detected in Velez Malaga and the soil columns have V_S^{30} values corresponding to site class III. Consequently a more reliable ground motion and intensity values distribution is obtained and a better final prediction of damage distribution also.

Secondly, a more accurate vulnerability assessment of the building is achieved apliying the vulnerability index method. In this case, the vulnerability index VI* has been more realistic than VI+. The total vulnerability indices VI of the buildings of the historical quarter (central part of the town comprised by old masonry building structures) are high values, generally greater than 0.8.The highest damage is predicted in this quarter putting in evidence building vulnerability has a higher influence on damage distribution than ground amplification in this case.

Thirdly, the worst scenario calculated for Velez Malaga (Intensity on rock of VII-VIII) forecasts 12% and 24% of uninhabitable buildings depending of typological vulnerability index used. EDS obtained using only typological index VI* or building vulnerability classes of EMS scale provide lower prediction of earthquake damage, being crucially sensitive to use behaviour modifiers in vulnerability assessment as has been carry out in this work. Comparing final predictions of damage, fatalities, homeless, etc. apliying VI indices with that obtained using Chavez (1998), the last gives intermediate values between those calculated with VI* and VI+.
Finally, it is remarkable the methodology possibilities to estimate earthquake ground motion, vulnerability and finally potential building damage and direct human consequences by means of different approaches. This methodology gives reliable and very useful results for improving seismic-risk reduction and risk management policies at local level.

Acknowledgements

The authors are gratefully acknowledged to Drs. L.Pujades, N. Lantada, A. Posadas, and J.A. Pérez for their valuable comments and sugestions during this work. Our special thanks go to LIDYCCE and Andalusian Institute of Geophysics members for their help during the urban surveys. This research was supported by the MEC project CGL2007-66745-C02-01/BTE.

References

Andrus R.D. & Stokoe K.H (1997). Liquefaction resistance based on shear-wave velocity. in Youd, T.L., and Idriss, I.M., eds., *Proceedings of the NCEER Workshop on Evaluation of Liquefaction Resistance of Soils, National Center for Earthquake Engin. Research Technical Report NCEER-97-0022, 89-128.*

ATC-13 (1985). Earthquake damage evaluation data for California, ATC-13, *Applied Technology Council, Redwood City, CA.*

Benito M.B., Gaspar-Escribano J.M., García-Mayordomo J., Jiménez Peña M.E., García Rodríguez M.J (2006). Seismic Risk in the Region of Murcia, RISMUR Project, *vol 1. Seismic hazard evaluation, Politechnic University of Madrid. Madrid (in Spanish).*

Bernardini A (2000). The vulnerability of buildings - Evaluation on the national scale of the seismic vulnerability of ordinary buildings, *CNR-GNDT, Rome*.

Borcherdt R.D (1994). Estimates of Site-Dependent Response Spectra for Design (Methodology and Justification), *Earthquake Spectra, 10, pp 617-673.*

Building Seismic Safety Council. BSSC 2004. *NEHRP Recommended Provisions for Seismic Regulations for New Buildings and Other Structures* (2003 edition) [S]. Washington D C: Building Seismic Safety Council, FEMA 450/451.

Dobry R., Borcherdt R.D., Crouse C.B., Idriss I.M., Joyner W.B., Martin G.R., Power M.S., Rinne E.E. & Seed R. B (2000). New site coefficients and site classification system used in recent building seismic code provisions, *Earthquake Spectra 16, 41–68*.

Eurocode No.8 (1998, 2005). Design of structures for earthquake resistance, Commission of the European Communities, *Doc CEN/TC250/SC8/N335.*

Chavez J (1998). Evaluación de la vulnerabilidad y el riesgo sísmico a escala regional: Aplicación a Cataluña, *PhD, Politecnic University Catalonia, UPC, Barcelona, Spain, 343 p.*

Delgado J, López Casado C, Estévez A.C., Giner J, Cuenca A, Molina S (2000). Mapping soft soils in the Segura river valley (SE Spain): a case study of microtremors as an exploration tool, *Journal of Applied Geophysics 2000; 45:19-32.*

Feriche M., Vidal F., Azañón J.M., Navarro M., Ocaña, E., Garcia-Jerez A (2008). Un escenario de daños sísmicos preliminar en Granada (España), *6ª Asemblea Hispano Portuguesa de Geodesia y Geofisica. Tomar 2008.*

García-Jerez A., Navarro M., Alcalá F.J., Luzón F., Pérez-Ruíz J.A., Enomoto T., Vidal F., Ocaña E (2007). Shallow Velocity Structure Using Joint Inversion of Array and H/V

Spectral Ratio of Ambient Noise: The Case of Mula Town (SE Spain), *Soil Dynamics and Earthquake Engineering, Vol. 27, 907-919.*

Giovinazzi S.& Lagomarsino S (2002). WP04: Guidelines for the implementation of the I level methodology for the vulnerability assessment of current buildings, Genova.

Giovinazzi S & Lagomarsino S (2004). A macroseismic method for vulnerability assessment of buildings, *Proceedings of the 13th World Conference on Earthquake Engineering. Vancouver, B.C., Canada, August 1-6, 2004, Paper ID 896.*

Giovinazzi S (2005). The vulnerability assessment and damage scenario in seismic risk analysis, *Ph. D. Thesis, Technical University of Braunschweig. Alemania, 300 p.*

Grünthal G (editor) (1998). European Macroseismic Scale 1998. *Cahiers du Centre Européen de Géodynamique et de Séismologie, 7, Luxembourg, 99 p.*

Irizarry J (2004). An Advanced Approach to Seismic Risk Assessment. Application to the Cultural Heritage and Urban System of Barcelona, *Ph. D. Thesis, Universitat Politècnica de Catalunya, 406 p.*

Irizarry J., Macau A., Goded T., Clavero D., Pazos A., Figueras S., Garcia R. & ERSE Working Group (2006). Preliminary Seismic Risk Scenarios for Malaga, Spain, *8th U.S. National Conf. on Earthquake Engineering, San Francisco, USA, 10.*

Irizarry J., Macau A., Susagna T., García R., Figueras S., Goded T, Clavero D., y Pazos A (2007). Escenarios de riesgo sísmico para la ciudad de Málaga. *3er Congreso Nacional de Ingenieria Sísmica, 8-11 Mayo 2007, Girona, 11.*

Lantada N (2007). Escenarios de riesgo sísmico en la ciudad de Barcelona. *Tesis Doctoral. U.P.C. Barcelona.*

Lantada N., Pujades L. G. Y., Barbat A.H (2007). Métodos avanzados para la obtención de escenarios de riesgo sísmico. Aplicación a Barcelona (España), *3er Congreso, Nacional de Ingeniería Sísmica, Girona, Mayo de 2007.*

Milutinovic Z. V. & Trendafiloski G. S (2003). WP4: Vulnerability of current buildings, *Risk-UE project Handbook. September 2003. Risk-UE project report, 111 p.*

Mouroux P. & Lebrun B (2006). RISK-UE project: an advanced approach to earthquake risk scenarios with application to different European towns, In: C. S.Oliveira, A. Roca and X. Goula, (Editors), *Assessing and Managing Earthquake Risk, 479-508p, Springer.*

Navarro M., Enomoto T., Sánchez F.J., Matsuda I., Iwatate T., Posadas A., Luzón F., Vidal F., Seo K (2001). Surface Soil Effects Study Using Short-period Microtremor Observations in Almeria City, Southern Spain, *Pure Appl. Geophys, 158, 2481-2497.*

Navarro M., Vidal F., Enomoto T., Alcalá F.J., Sánchez F.J. & Abeki N (2007). Analysis of site effects weightiness on RC building seismic response. The Adra (SE Spain) example, *Earthquake Engineering and Structural Dynamics, Vol. 36: 1363-1383.*

Nogués R (2002). Riesgos geologicos en el termino municipal de Velez Malaga. *Indycce SL. Malaga. 99 p.*

NCSE-02 (2002). Normativa de Construcción Sismorresistente Española, Comisión Permanente de Normas Sismorresistentes, Real Decreto 997/2002, *Boletín Oficial Del Estado No. 244, 11 October, 2002, Spain.*

Okada S., Pomonis A., Coburn A.W., Spence R.J.S., Ohta Y (1991). Factors Influencing Casualty in Buildings Damaged by Earthquakes. *Collaborative Report. Hokkaido University, University of Cambridge, University of Tokio, 16 p.*

Pérez-Ruiz J. A., Posadas A., Lantada N. Y L. G. Pujades (2007). Un método avanzado de generación de escenarios de riesgo sísmico. Aplicación a la ciudad de Motril (España), *3er Congreso Nacional de Ingeniería Sísmica, Girona, 2007.*

Seed R. B., Cetin K. O., Moss R.E.S., Kammerer A.M., Wu J., Pestana J.M., Riemer M.F., Sancio R.B., Bray J.D., Kayen R.E., Paris A (2003). Recent advances in soil liquefaction engineering: an unified and consistent framework. *Keynote presentation, 26th Annual ASCE Los Angeles Geotechnical Spring Seminar, Long Beach.*

SES 2002. Simulador de Escenarios Sísmicos (SES 2002). Estimación rápida preliminar de daños potenciales en España por terremotos. Manual de usuario. D.G. de Prot. Civil. Available in: www.proteccioncivil.org/pefn/gt/manuales/m_usuario.pdf

Stewart J.P., Liu A.H & Choi Y (2003). Amplification Factors for Spectral Acceleration in Tectonically Active Regions, *Bull. Seism. Soc. Am., 93, 332-352.*

Tiedemann H (1992). Earthquakes and Volcanic Eruptions, *a Handbook on Risk Assessment, Swiss Re Publication, Zurich. 951 p.*

Vacareanu R., Lungu D., Aldea A., y Arion C(2004). WP07. Report Seismic Risk Scenarios Handbook, *Risk-UE Project, Bucarest. 50 p*.

Vidal F (1986). Sismotectónica de la región Béticas-Mar de Alborán, *Tesis Doctoral, Universidad Granada, 457 p.*

Vidal F., Feriche M., Navarro M (1996). Estimación de daños sísmicos en áreas urbanas para la planificación de emergencias sísmicas, in *Homenaje Prof. F. Miguel, 769-808p*.

Vida F., Feriche, Navarro M., Vidal L & Morales J (2008). A Simple Method to evaluate Potential Physical Damage in Urban Areas for Risk Management Purposes, *Fifth International Conference on Urban Earthquake Engineering, 529-534.*

Yamazak F., Wakamatsu K., Onishi J., Shabestari K.T (2000). Relationship between geomorphological land classification and site amplification ratio based on JMA strong motion records, *Soil Dynamics and Earthquake Engineering 2000: 19(1), 41-53*

Faulting of the Roman Aqueduct of Venafrum (Italy); Investigation Methodology and Preliminary Results

Galli P A C (1), Naso J A (1), Capini S (2), Giocoli A (3), Hailemikael S (4), Piscitelli S (3), Rizzo E (3), Scaroina L (5)

(1) Dip. Protezione civile, Via Vitorchiano 4 00189 Rome, Italy, paolo.galli@protezionecivile.it
(2) Direzione Regionale Beni Culturali e Paesaggistici del Molise, Campobasso, Italy
(3) CNR - Istituto di Metodologie per l'Analisi Ambientale, Tito Scalo (PZ), Italy
(4) Università La Sapienza, Dip. Scienze della Terra, Rome, Italy
(5) Istituto Nazionale di Archeologia e Storia dell'Arte, Rome, Italy

Keywords: archaeoseismology, surface faulting, Roman aqueducts, seismic hazard

Introduction

The effects recognition of ancient earthquakes on archaeological relics has always been a matter of debate in archaeoseismology (Karcz and Kafri, 1978; Stiros, 1996), being always difficult (and often impossible) to ascertain whether observed damage should be related to seismic shaking or to other causes (i.e., wars, floods, burns, time-decadence, etc.).
This issue becomes particularly critical when facing with single buildings and/or if observations can not be extended to wide areas (i.e., to different settlements). Moreover, once hypothetically assessed that the observed effects (i.e., structural damage) were seismically induced, it is very uncertain to infer the earthquake epicentral parameters.
On the other hand, the faulting of archaeological sites - even of a single relic - although representing an exceptional case, provides certain and reliable data on the causative earthquake (e.g. in Galli and Galadini, 2001). For instance, surface faulting always coincides with the earthquake mesoseismic area, and – in terms of energy release - it always yields the overtaking of a minimum threshold of magnitude (e.g., Mw>6). In favorable stratigraphical contexts, the analysis of faulted archaeological relics - more than a classic paleoseismological trench-study - gives reliable information concerning the dating of the earthquake(s), the kinematics, and the associated magnitude of the responsible seismogenic source (i.e., by measuring slip direction and offset amount, respectively).
In this paper, we present analyses carried out in the Molise region (central-southern Italy), along an almost unknown 1st-cent.-BC Roman aqueduct (Fig. 1). By means of detailed, and often blind field surveys, we were able to individuate the underground traces of the aqueduct, and in particular in the trait which we supposed to be affected by a primary active fault.
Our preliminary results yield the occurrence of repeated faulting of the water supply in the past two millennia, i.e. during large historical earthquakes, the last being one of the strongest event known in the Middle Age (September 1349, Mw=6.6).

Seismotectonic overview of the region

Briefly, this sector of the chain of the southern Apenninic Arc (i.e., a buried duplex system of Mesozoic–Tertiary carbonate thrust sheets, overlaid by a thick pile of rootless nappes; see Patacca and Scandone, 2007) is currently characterized by NE-SW extensional processes, evidenced by the studies on the active faults of the area (see Galadini and Galli, 2000; Galli and Galadini, 2003; see Fig. 1), by the (few) focal mechanisms of the local earthquakes, and by recent GPS analyses (Giuliani et al., 2007).
Actually, large earthquakes (Mw>6.5) devastated the entire region in the past (Fig. 1), both in the first millennium AD (346/355 and 847 events), and in the second one (1349, 1456, 1805 events). While the 1456 and 1805 events have been related to the activity of the N-Matese

fault system (together with an unknown event of the early 3rd cent. BC; see Fig. 1 and Galli and Galadini, 2003), the 346/355, 847 and 1349 earthquakes are still poorly defined. Nevertheless, in-progress paleoseismological researches allow to identify an unknown active fault (Aquae Iuliae fault, AIF in Fig. 1) to which the 1349 event is surely linked (Galli et al., 2008). Since this fault affects the aqueduct path near Venafro, we though that the study of the crossing zone was an exceptional choice for obtaining valuable information on the fault activity and for earthquakes recognition.

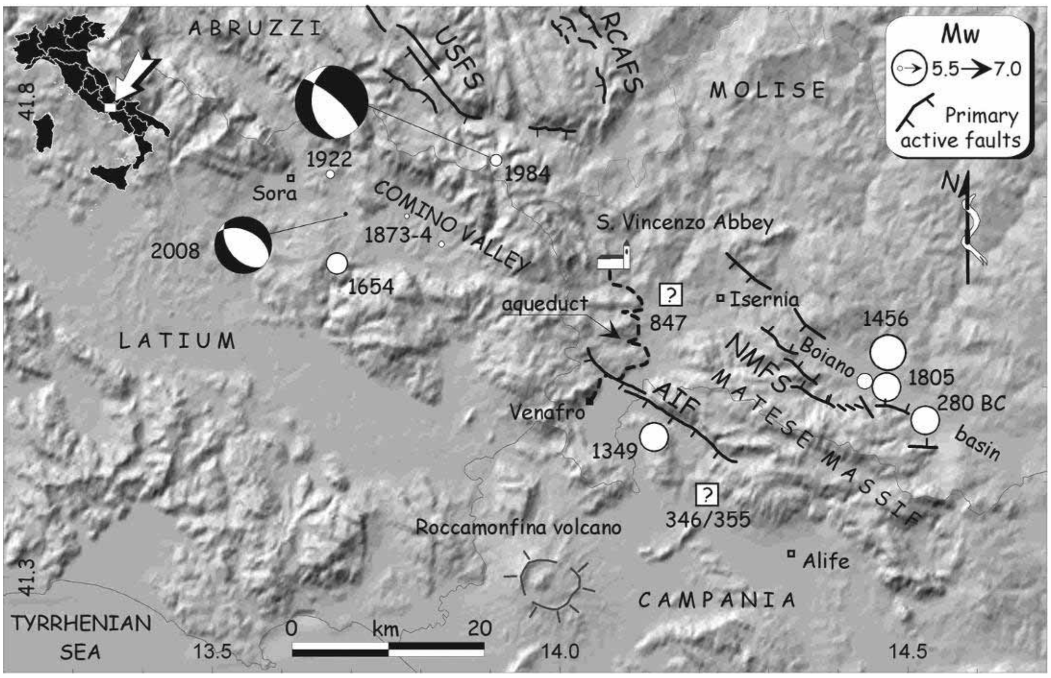

Figure 1. DEM of central-southern Apennine (see upper-left inset) showing the epicentre of the main earthquakes (Mw>5.5; from CPTI04, except: 280 BC: Galli and Galadini, 2003; 346/355: based on data in Galadini and Galli, 2004; 847: based on data in Figliuolo and Marturano, 2002; 1349: Galli et al., 2008), and the known normal primary active faults (USFS, Upper Sangro fault system; RCAFS, Mount Rotella–Cinquemiglia–Aremogna Plains fault system; NMFS, northern Matese faults; AIF, Aquae Iuliae fault). The two focal mechanisms are the Mw=5.8, May 5, 1984 event (Anderson and Jackson, 1987), and the Mw=4.2 event occurred on February 20, 2008 (MedNet, 2008). Both show NE-SW extension driven by NW-SE normal faults.

The Venafrum aqueduct

This aqueduct is archaeologically worldwide known because of the famous Edict of the emperor Caesar Augustus (*Tabula Aquaria*, dated from 17 to 11 BC: CIL 10, 4842; see Mommsen, 1883; Pantoni, 1961), which contains a unique collection of regulations concerning the use and maintenance of water supplies.

Nevertheless, although the existence and general path of this aqueduct has been known since Ciarlanti (1644) and Cotugno (1824), its structure and precise location has never been investigated, with the exception of a quick survey performed in the 1930s by Frediani (1938).

The aqueduct starts from the spring of the Volturno River (548 m a.s.l.) near the famous Benedictine San Vincenzo a Volturno Abbey (Fig. 1), and after a 200-m-abrupt step, it runs along a flat 31-km-long winding track, until it arrives at Venafro (225 m a.s.l.). It mainly runs through a tunnel (*specus*; see Fig. 2) inside the carbonate and marly hill slopes, overtaking the *talweg* of streams by arched bridges, most of which have now collapsed (Fig. 3).

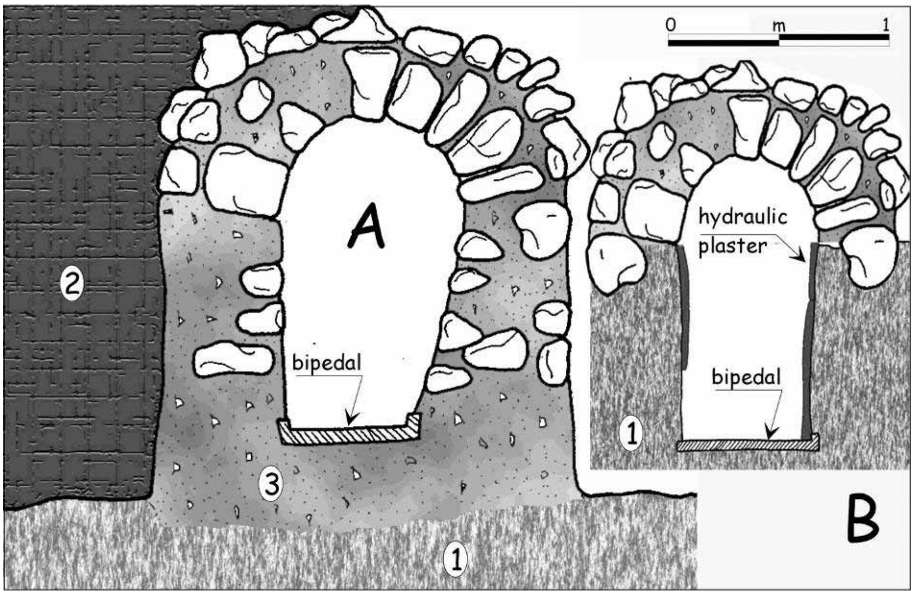

Figure 2. Sketch of different typologies of the buried *specus* of the Venafrum aqueduct; A, arched stone-masonry (3) in loose terrains (2); B, lined trench in clayey terrains (1). Note the bipedals at the bottom.

In the flat areas, where the subsoil is made up of alluvial/colluvial or clayey deposits, the Romans built it into a trench and then covered the excavation (Fig. 2B). The *specus* is 0.6 m wide and 1.6 m high, with a round stone arch and an external structure in *opus incertum* (irregular stone masonry).

Figure 3. View of the *specus* of the aqueduct that we discovered along the hillside of Venafro. On the right, the hanging relic of the *specus* at the crossing of a deep *talweg*.

The internal walls are coated with hydraulic plaster (i.e., *opus signinum*=cocciopesto mortar), whereas the bottom is lined with bipedals (i.e., typical Roman 61x58 cm bricks).
The aqueduct was built in the first half of the 1st century AD, as has been deduced from a letter of M. Tullius Cicero (living between 106 and 42 BC; see Cicero 1st century BC) to his

brother (*Ad Quintum fratrem*, 3, 1), and it was then finished or restored by Emperor Augustus at the end of the same century. Conversely, we do not known when it ceased to function, although it is reasonable to believe that it fell into disuse during the fall of the Roman Empire (4^{th}-5^{th} century) due to the lack of maintenance or due to a traumatic event. Near the village of Pozzilli, we attempted to date the first mud layer filling the bottom of the tunnel, but we obtained an absolute age (780 to 410 BC 2σ calibrated age), which is not consistent with the history of the aqueduct, and it probably belonged to the parent material of the deposit that penetrated inside the *specus*.

The survey of the Venafrum aqueduct

As aforementioned, neither the survey quoted by Frediani (1938) nor others studies contain analytical information concerning the location and elevation of the aqueduct. Therefore, we carried out a specific survey that was aimed at discovering and measuring aqueduct relics across the fault zone (Fig. 4). Due also to information obtained from the people of the area, we found aqueduct relics in a dozen different localities, nine of which have been directly inspected. The elevation of each point (generally the level of the *bipedali*, or the inner arch) was then measured by means of topographic levellings (associated error ±10 cm), and positioned on 1:5,000 maps. We finally traced the path of the aqueduct by following the altimetric gradient between each observed point, obtaining a detailed map from which we have derived an actual topographic section along the 8,500 m of the investigated track.

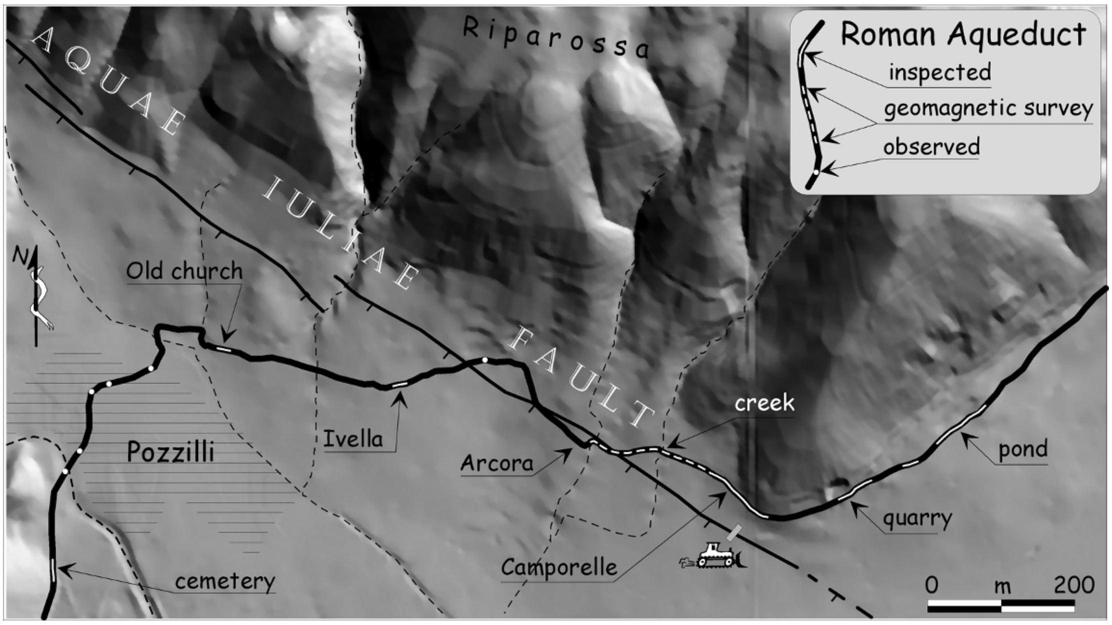

Figure 4. DEM of the aqueduct/fault crossing area (detail of Fig. 1; from Galli and Naso, submitted). The bulldozer symbol indicates one of the paleoseismological trench excavated across the fault.

We focused our efforts along the fault zone (Arcora site in Fig. 4), where we also carried out a geomagnetic survey using a portable caesium vapour magnetometer/gradiometer; Figure 5 shows the magnetic anomaly that was measured in the footwall, which perfectly depicts the aqueduct in depth.
These results are summarized in Figure 6, which shows the aqueduct profile from the villages of S. Maria Oliveto to Venafro. The first section, from S. Maria Oliveto to the quarry site, has a 3.5/1,000 gradient, which is lower, at 2/1,000, going on towards the creek, and it reaches 1/1,000 between the Arcora and Ivella sites. It then rises again, to 3.2/1,000, towards the Pozzilli cemetery, and to 2/1,000 towards Venafro.
For our specific aims, the most significant result relates to the net step between the last observed point at Camporelle site (bipedali level at 244.8 m a.s.l.) and the one in Arcora (240.4 m a.s.l.), which are only ~200 m away from each other. By adopting the gradient

measured between the quarry site and Camporelle (2/1,000), and taking the aqueduct trace towards the Arcora site, the step between the two strands is at least 3.6 m high, and it occurs exactly in the fault zone.

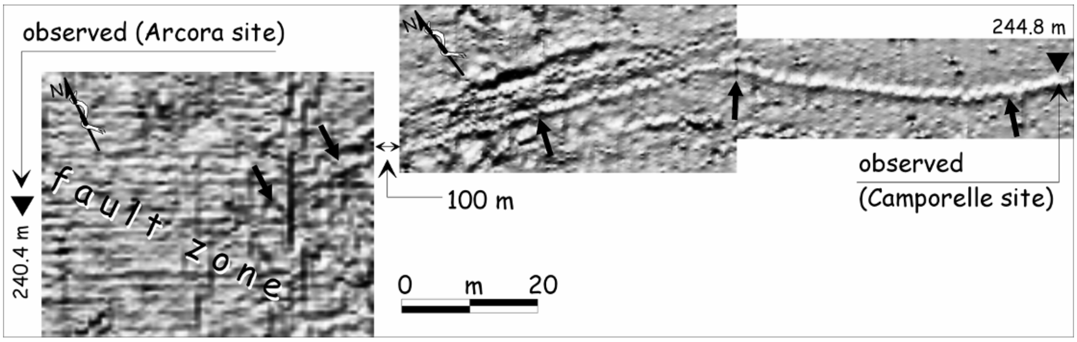

Figure 5. Shaded relief elaboration of part of the geomagnetic survey performed along the aqueduct trace (Camporelle–Arcora tract in Fig. 4). Arrows indicate the net magnetic anomaly fitting with the aqueduct path. In the right panel, the *specus* is sub-outcropping (~0.5 m, as checked in some pits excavated *ad hoc*), whereas farther east (left panel) it disappears nearing the fault zone (i.e., it is dismantled and eroded by the progressive process of fault scarp retreating). Triangles are observed and levelled points.

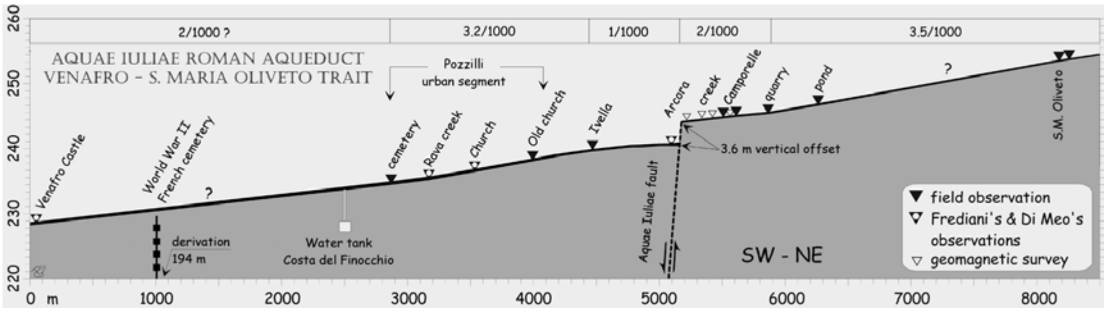

Figure 6. Section of the Roman aqueduct across the Aquae Iuliae fault. Note the step seen between the two strands (Venafro–Arcora vs Camporelle–S. Maria Oliveto), which occurs just at the fault crossing point. A continuous deformation, revealed by the lowering of the gradient, occurs as nearing both the fault on both sides. For simplicity, this section does not show other possible fault/aqueduct intersections between Arcora and Ivella (e.g., in Fig. 5).

Considering that it would have been absolutely senseless for the Romans to have intentionally lost more than 3 m in altitude before arriving at their final destination (Venafro; as verified all along the 8-km-long path surveyed), and, furthermore, to have done this in a flat and clayey zone, we believed that this 3.6-m-high step was actually due to surface faulting. Unfortunately, in this sector the aqueduct almost parallels the fault (Fig. 4), and due to the erosion of the raised block (i.e., due to fault scarp retreat processes), a dozen meters or so of its structure has been completely lost (Fig. 7).
This is confirmed by the geomagnetic analyses that progressively “lose” the aqueduct traces as it neared the fault (Fig. 6). At this stage, the excavation of the aqueduct was not possible because of the presence of large olive trees.
Anyway, the fault has been detected in several trenches that were dug along its surficial trace (Galli et al., 2008), one of these located just 200 m from the crossing site (see Fig. 4)

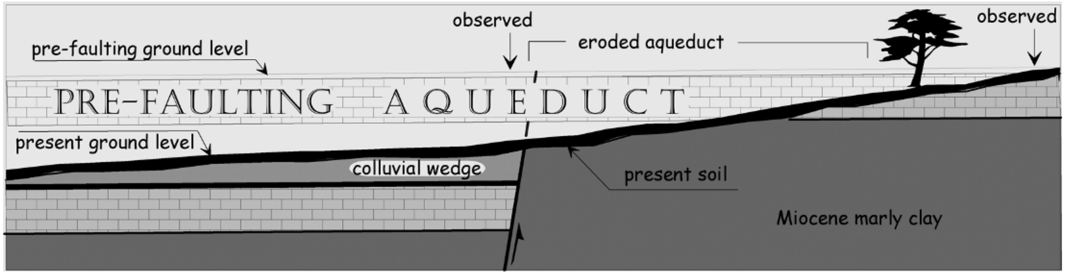

Figure 7. Sketch of the aqueduct (brick) in the fault zone (not to scale). Relics of the aqueduct were observed and their altitude were calculated, both in the hangingwall and in the footwall (arrows). Here, the absence of the tunnel nearing the fault has been confirmed by geomagnetic analyses. At present, all of the area is occupied by olive trees, which hampered the excavation of the trenches.

Conclusion

These preliminary results, coupled with those gathered through paleoseismological analyses carried out along the Aquae Iuliae fault (Galli et al., 2008), allow to locate definitely (and for the first time) the large 1349 earthquake (i.e., absolute ages in trenches postdate the faulting to 1150-1270 AD, and 1290-1420 AD; others predate it to 1450-1650 AD; Galli and Naso, submitted), providing reliable epicentral parameters for this Middle Age event.
In facts, the fault length (~22 km) and the offset per-event (~1 m) derived from both archaeoseismological and paleoseismological data yield a Mw~6.6.
Moreover, the amount of the total offset of the Venafrum aqueduct across the fauilt zone (~3.6 m) is obviously not consistent with a single coseismic rupture, accounting for at least other two 1349-like surface ruptures occurred after the 1st cent. BC (age of its construction). Actually, these ruptures have been observed in the paleoseismological trenches, and they have been constrained between 240-560 AD, and 1020-1210 AD, even if it was impossible to provide more detailed ages on each single events.
However, if we look at the known earthquakes of the area during the 1st millennium AD (Fig. 1), and if we consider the distribution of their effects (Galadini and Galli, 2004; Figliuolo and Marturano, 2002), both the 346/355 AD and the 847 events could be considered as possible candidates for these ruptures/offsets.
Ongoing researches are aimed at excavating the fault/aqueduct crossing zone, in order to obtain more reliable data on the number and age of coseismic faulting of this Roman work.

References

Anderson H. & Jakson J. (1987). Active tectonics of the Adriatic Region, *Geophysical Journal of the Royal Astronomic Society, 91, 937-983*.

Ciarlanti G.V. (1644). Memorie historiche del Sannio chiamato hoggi Principato Ultra, contado di Molisi e parte di terra di lavoro, *provincie del Regno di Napoli, Isernia, 530 p.*

Cicero, M.T. (1st cent. BC). Epistulae ad Quintum fratem, A. Salvatore, *ed., Mondadori Milano, 1989, 126 p*.

Cotugno G. (1824). Memorie istoriche di Venafro, Napoli, 348 pp.

Figliuolo B. & Marturano A. (2002). Terremoti in Italia meridionale dal IX all’XI secolo, *in Marturano, A. ed., Contributi per la storia dei terremoti nel bacino del Mediterraneo (secc. V-XVIII), Laveglia, Salerno, 33-67.*

Frediani F. (1938). L’acquedotto augusteo di Venafro. Riassunto e rilievi a cura dell’Ente Volturno. *Istituto di Studi Romani, Campania Romana, Studi e Materiali, Rispoli Anonima Ed., Napoli, 163-185*.

Galadini F., & Galli P. (2000). Active tectonics in the central Apennines (Italy) – Input data for seismic hazard assessment, *Natural Hazards, 22, 202-223*.

Galadini F. & Galli P. (2004). The 346 A.D. earthquake (central-southern Italy): an archaeoseismological approach, *Annals of Geophysics, 47, 885-905*.

Galli P. & Galadini F. (2001). Surface faulting of archaeological relics. A review of case histories from Dead Sea to the Alps, *Tectonophysics, 335, 291-312.*

Galli P. & Galadini F. (2003). Disruptive earthquakes revealed by faulted archaeological relics in Samnium (Molise, southern Italy), *Geophys. Res. Lett., 30(5), 1266, doi:10.1029/2002GL016456.*

Galli P., Naso G., Piscitelli S., Giocoli A., Hailemikael S. & Rizzo E. (2008). Unmasking the 1349 earthquake fault: paleoseismological indications from the Latium-Campania border (central Italy), EGU General Assembly 2008, Geophysical Research Abstracts, 10, EGU2008-A-01427, 2008.Karcz I. and Kafri U. (1978). Evaluation of supposed archaeoseismic damage in Israel, *J. Archaeological Science, 5, 237-253.*

Giuliani R., Bonci L., Calcaterra S., D'Agostino N., D'Anastasio E., Gambino P., Mattone M., Merli K. & Peperoni A. (2007). Campo di deformazione attiva da dati GPS in appennino centro-meridionale (Molise): un contributo alla definizione dei tassi di accumulo sulle strutture sismo genetiche, *Extended abstracts of the 26° GNGTS Congress, Rome 13-15 November 2007, 243-245.*

Karcz I. & Kafri U. (1978). Evaluation of supposed archaeoseismic damage in Israel, *Journal of Archaeological Science, 5, 237-253.*

MedNet (2008). Mediterranean Very Broadband Seismograghic Network, http://mednet.rm.ingv.it/., last access February 2008.

Mommsen T., (1883). ed.: Inscriptiones Bruttiorum, Lucaniae, Campaniae, Siciliae, Sardiniae Latinae, G. Reimerum, Berlin, 1229 p.

Pantoni A. (1960/61). L'editto augusteo sull'acquedotto di Venafro e una sua replica alle fonti del Volturno, *Rend. Pont. Accad., XXXIII, 155-171*.

Patacca E. & Scandone P. (2007). Geology of the Southern Apennines, *Bollettino della Società Geologica Italiana, Spec. Issue 7, 75-119.*

Stiros S.C. (1996). Identification of earthquakes from archaeological data, *In Stiros S., Jones R.E. (eds.), Archaeoseismology, British School at Athens, F.L. Occ. Paper 7, 119-152.*

Working Group (2004). CPTI Catalogo Parametrico dei Terremoti Italiani (versione 2004, CPTI04), Internet website INGV Sezione di Milano, http://emidius.mi.ingv.it/CPTI/ (last revision 27 May 2004).

On Geodynamic Model of the Source of the Spitak Earthquake Dec. 7, 1988

Geodakyan E G (1)

(1) Institute of Geophysics and Engineering Seismology of the National Academy of Sciences of the Republic of Armenia, 5, V. Sargisyan, Gyumri, 3115, Republic of Armenia, iges@shirak.am

Keywords: earthquakes, source mechanism, seismodislocatins, aftershock

Introduction

Colossal socio-economic damage of the Spitak earthquake complex character of its manifestation attracted attention and became a subject for observations for many specialists of the leading seismological centers of the world. One of the main approaches of the investigations was the study of the fracture formation process and seismic radiation during the main shock of earthquake, definition of its kinematical and dynamic properties. The analysis of the wave fields according to the instrumental records of the teleseismic and regional stations, utilization of the inversion methods at record processing of volumetric seismic waves gave a base to prove that the source process during the Spitak earthquake had a multiplet character and represented a multiact process of rupture formation of the source zone [1.2.3]. This conclusion was further confirmed by the results of the detailed geological observations at the period of the aftershock process development in an epicentral zone [6,7,8]. Moreover the structural analysis of the primary seismic dislocations in a pleistoseismal zone and location of the hypocenters of the first strong aftershocks put forward the complex geometry of the fracture formation. From the positions the Spitak earthquake's source represents a complex of the surface breaks along which mobilities occurred at a definite sequence explaining the complex radiation of seismic energy. The model reflecting geometry of these surfaces and defining the mobility sequence is proved to be called the geodynamical model of the focus. For the Spitak earthquake several variants of the model focuses were suggested consisting of 3, 5 and 16 subsources [1,2,3]. The first two variants are based on the investigation of the wave picture of the instrumental records of teleseismic stations in base of 16 subsources models the results of the complex geological and instrumental observations are accepted in epicentral zone. The strongest aftershocks are taken in the capacity of subsources. This model doesn't naturally reflect the fracture formation process of the main shock but it rather concerns the development of the whole aftershock process. The inversion method of volumetric waves according to records of the nearest stations is used in work [3] for source modeling. On the basis of the instrumental record "Ghoukasyan" station accelerogram the displacement of ground on the station was counted and further by means of exhaustion of subsources quantity in a source a satisfactory correspondence of theoretical and experimental data was achieved. As a result of observations a model was chosen consisting of 5 subsources. The rupture formation of the source occurred in a horizontal direction. It contradicts the results of many observations proving the bilateral simultaneous rupture formation of source with output break to south-east of the earth's surface and depression up to 12km deep to west and north-east.

Results and Discussion

Proceed from the above stated an attempt was made to ascertain the model of the Spitak earthquake on the basis of the complex results of geological and instrumental observations and data or sources mechanisms in different segments of aftershock field. The formation of geodynamic model which is considered to be the strongest earthquake's source in region was very important for real seismic hazard assessment and forecast observations organization. Adequately built geodynamic model essentially clears up conditions of seismogenesis, gives an opportunity to reveal which seismotectonic structures are embraced by the source field and which mode of seismic mobilities occurred in its various segments (subsources).

Seismotectonic conditions of the strained state of the source zone

The source region of the Spitak earthquake is located in a zone of the Pambak-Sevan fault which being northeastern branch of the Northern Anatolian deep fault in Asia Minor. To the meridional direction the Aragats-Spitak lineament stretches which is one of the tectonic lines bounding the Transcaucasus dihedral uplift [4]. Crossing of these 3 main directions of tectonic dislocations presents a huge disjunctive node where a pleistoseismal zone is settled (fig.1) [5,6,7,8]. According to geomorphological observations data in epicentral zone a system of shallow faults of the young late quanternary age is located on northern slopes of the Pambak ridge and Pambak basins oriented to north-west [8]. The strained state of the earth's crust of region is well studied in work [9] and is represented in the form of complex system of fracture dislocations of various mode. The dominated stress here is undoubtedly the submeridional compression which is approved by the convergence of the Arabian and Eurasian plates.

The analysis of the strained state of the region on the whole according to the earthquake's source mechanism shows the stress compression in a short horizontal plane to north-east 15^0-20^0 and the stress tension in a vertical plane from 30^0-60^0 [10]. The analysis of deformed state of the central part in Asia Minor by tensors of strongest earthquakes' seismic moments revealed that the uniaxial horizontal tension with the thrust mobilities elements is considered to be the characteristic deformation process. The tension is oriented in azimuth $66^0 \pm 180^0$ and the compression in azimuth is $24^0 \pm 18^0$ on the earth's surface. The deviator modulus of sum tensor of relative deformation for this region is $2.04 \cdot 10^7$ and the corresponding value of sum velocity of the relative deformation is $9.73 \cdot 10^{-9}$ [11]. The presence in source zone of these deformation processes forms a complex picture as from the point of region's geodynamic and the description of earthquake's source mechanism and mobilities in them as well.

The focus mechanism of the main shock is defined by many observations. The received solutions do not contradict each other. One of the planes has a short-meridianal stretching ($A_z=296^0$), with a dip to north-east at an angle about 55^0. The second nodal plane has a short –meridianal direction with microseismic data and also with geological observations data gave an opportunity to choose a short-longitudinal direction in the capacity of true plane strike [6, 7, 8, 13]. The source mechanism considers the thrust-strike-slip mode with predominance of mobility thrust component of fracture strike. By selected fracture plane abruptly falling to north the fracture of the northeastern wing happened accompanied by the right-lateral slip. The data on the main shock's mechanism are in a good agreement with the earth's crust disturbance complex which happened in a pleistoseismal zone of a focus and were studied in detail during geological field observations [6,7,8].

To seismodislocations of the Spitak earthquake refer:

The earth's surface uplift over an extent of 60km to the center in region of Spitak town according to repeated levelling on route Leninakan-Spitak-Kirovakan [14]; the primary seismogenous fractures, cracks, seismic gravitational phenomenon; landslides without displacement along the slope, landfalls, hillsides, subsidences of fill-up soils. According to data [6, 7, 8] the total longitude of zone of traced fractures was about 35km and allowing for seismic gravitational phenomenon the total longitude of disturbances reached up to 50km (fig.1).
All researchers distinguished 3 extended sections (8-9km) of intensive display of primary seismic dislocations. The first southeastern section located from Alavar village to the valley of the Spitak river is expressed by the right-lateral thrust-strike-slip and strike slip fractures system. Amplitude of the mobility in the central part of the fracture reached 1.5m and decreased up to zero values to the direction of the sections' edges. The same picture was observed with the horizontal amplitude of the right-shift displacement. The azimuth strike of

the southeastern seismic dislocations segment was 130^0-140^0. The second section of primary seismic dislocations adopted as central segment extended from the western margin of Spitak town through Geghasar village up to the right board of the Chichkhan river to the short-latitudinal direction. The residual disturbances of the surface on the segment were more defined. The quantities of the maximal, vertical and horizontal right-shift displacement reached 1.5÷1.8m. It is important to note that most of geologists while observing the epicentral zone stated the belonging of seismodislocations displayed on the seismogeneous fracture.

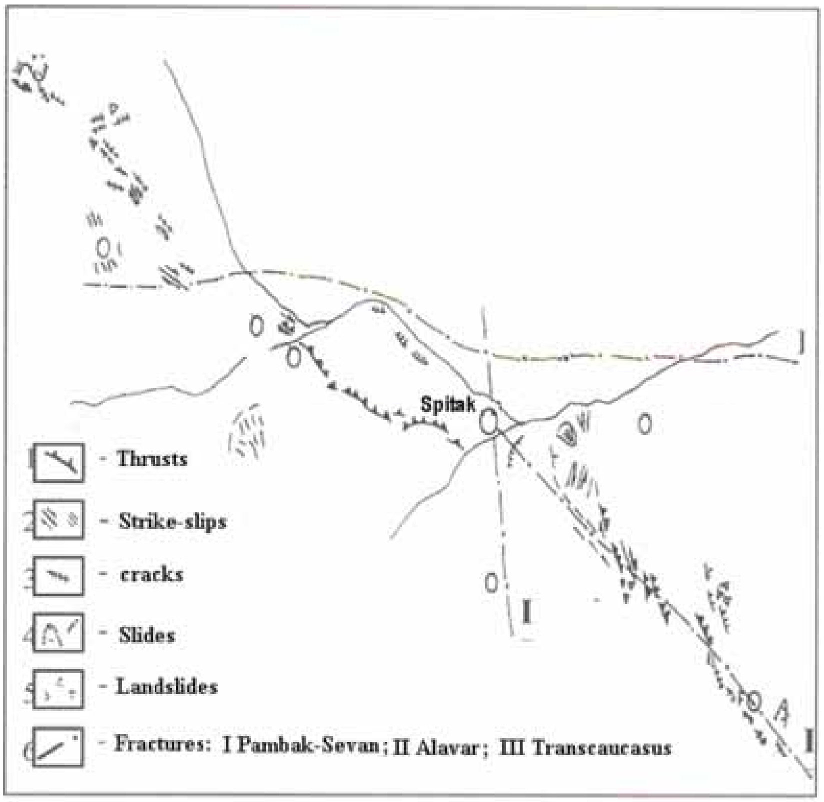

Figure 1.

The third section northwestern segment of seismic dislocations system was placed on the southern slope of the Bazum ridge. Especially short, thin rents without displacements were developed on the segment. Evidently this mode of dislocations is connected with the source which did not emerge the surface and is the result of a strong shaking.

Two fractures of the right-shift and thrust mode are distinguished which have an extent of about 200m. The orientation of these fractures is 310^0÷320^0.

Source parameters of the Spitak earthquake were studied according to large spectrum instrumental data of short-period, mid-period and long-period broad-line equipments. Bibliography of the research results in this field is extensive enough. We studied the research results given in the works [1, 15, 16]. The volumetric waves data recorded on 14 digital seismic stations in a diapason of epicentral distances 30^0-90^0 gave a base to reveal the movement peculiarities in a source zone [1]. The process mechanism was selected in a focus in the form of three subsources and the parameters are shown in a table 1.

table 1

$Mx10^{28}$ din.sm	φ^0	λ^0	H_{km}	A_z	Angele of bedding	A slip angele

1	0.64	40.90	44.27	2.5	290	44	131
2	0.58	40.80	44.37	6.0	314	83	151
3	0.51	40.93	43.90	7.3	269	71	142

The diagram analysis of frequency-temporal field of the Spitak earthquake according to digital station "Obninsk" carried out in work [15] points to 2 eruptions of energy emission P-wave. One of them is at an interval from 7 till 21sec and the second one from 31 till 31sec. Intensity and duration of the first eruption exceeds 2 times the second one and obviously include the group of intensive subsources. The utilization of the method of complex signal while data processing of digital seismic stations at epicentral distances $10^0 \div 20^0$ [16], gave an opportunity to display on the record of a direct P-wave separate source impulses on the record of a definite P-wave. For the impulses the time lage is defined relatively to the first arrival –+t, visible periods-T, duration-τ, magnitude-M_{pv}. The data are given in table 2.

table 2

N	1	2	3	4	5 (aftershock)
+t sec	0	3.5	5	19	260
T sec	2	1.0	5.5	5	
τ sec	2.5	1.5	9	6	

By Fourier transformation digital records and digital station code method the spectral composition of P wave is studied. The Pwave spectrum and also source spectrum by digital station code have 2 angular frequencies 0.03 and 0.15Hz (angular periods 30 and 6.7sec), and it shows the presence of several subsources with angular frequency spectrum of about 0.15Hz.

The following main source parameters of the Spitak earthquake are calculated from the source spectrum:

Seismic moment M_0=1.85*10^{19}N,M.
Energy logarithm in J lgE=15.35
Seeming strain η^{σ}=40bar
Source length L=45km
Mean shift along the fault D=1.3m

The aftershock field analysis of the Spitak earthquake has a significant meaning for the reveal of geometry surface of rupture formation in a source. The results of high-precise epicentral instrumental observations are served as a base with a system of telemetric and analogous temporal seismic stations [17, 18]. The hypocenter definition and aftershock process analysis during the first days after the main shock were carried out according to data of regional seismic stations of the Caucasus. The first primary data showed the complex character of the space-temporal aftershock distribution [19, 20]. The definite part of the aftershocks occurred in groups or by the so-called epicentral chains. The trajectory of the epicentral chains distinguished 3 separate epicentral field sites: central site with an epicenter of the main shock and aftershock, southeastern and western sites. Later on taking into account the instrumental data, the development of aftershock process in a structure of aftershock field 4 main sites differing by seismic fault dip plane and source mechanisms (fig.2) were distinguished by all researchers.

Aftershock field of the Spitak earthquake and source mechanisms on different sites of the field are in detail studied in [21]. According to the given data in this work it is possible to analyze the characteristic peculiarities of the aftershock field (fig.3, a, b). It includes: changing geometry along the definition zone, correspondence of the distinguished sites to the results of seismic dislocations geological data and also the study results of subsources impulses in a wave field of longitudinal P-wave.

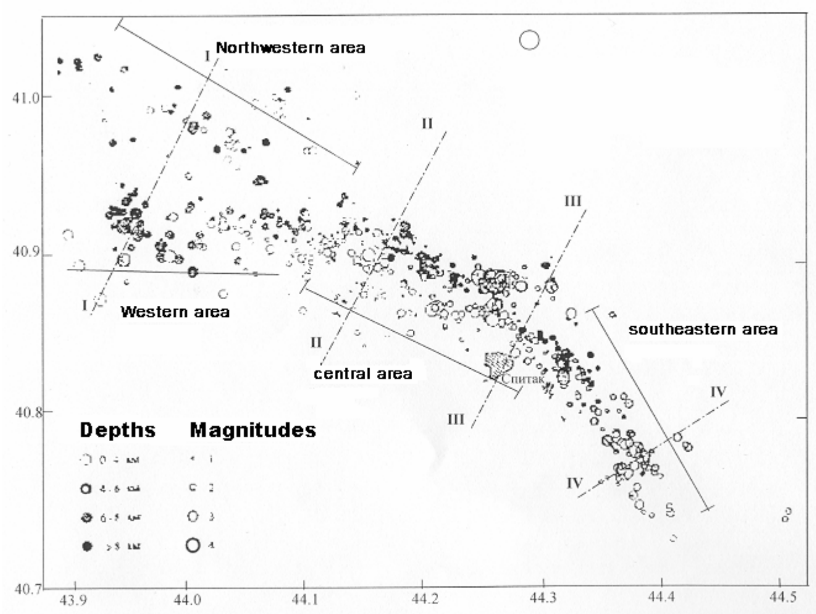

Figure 2.

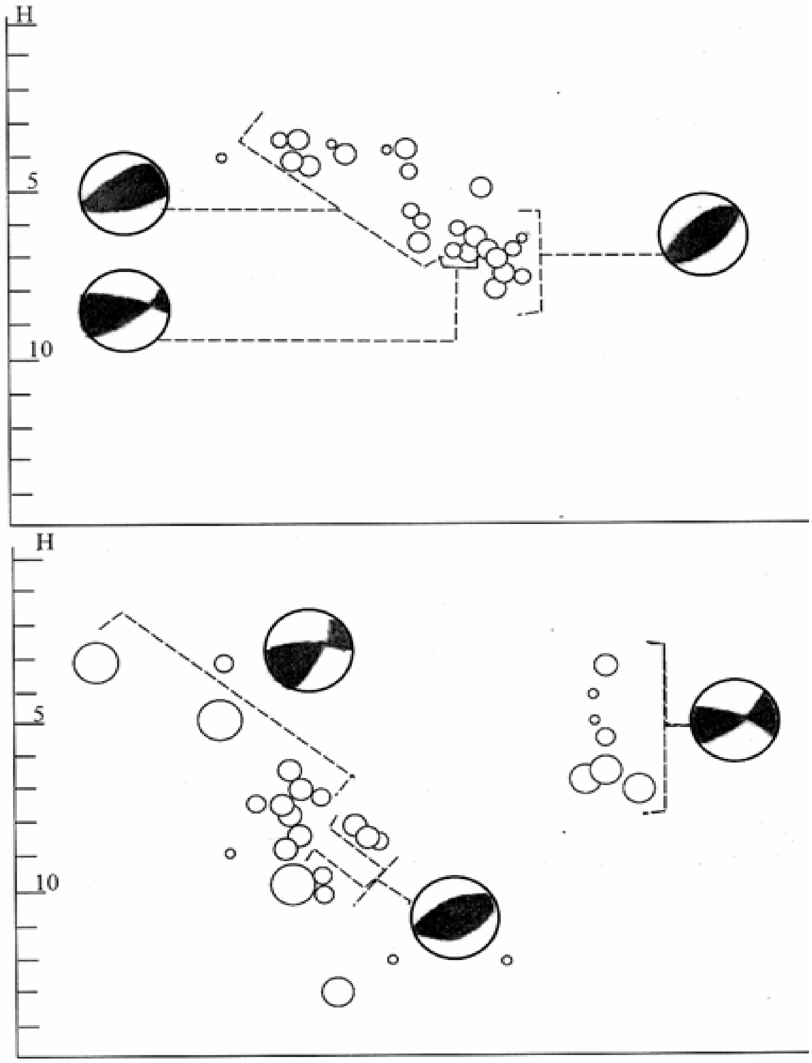

Figure 3a,b. Vertical transversal profiles of Spitak earthquake aftershock zone

Conclusion

Analyzing the whole complex of the above mentioned seismological and geological data one may conclude that the rupture formation of the Spitak earthquake had a complex character. It will be reasonable to adopt the geodynamic model of the Spitak earthquake's source consisting of 4 subsources (fig. 4).

The scheme of rupture formation represented the fault on a central site corresponding the Pambak-Sevan fault with the further simultaneous bilateral spreading of fracture to south-east and west-north-west.

The southeastern direction coincided the Alavar regional fault. To the western and northeastern directions the gradual depression of the focus happened which was located at 12-15km deep along the Pambak-Sevan fault and 12km deep along the diagonal continuation of the Alavar fault. The northwestern continuation had a tendency of spreading to the direction of the strongest earthquakes' focus zones of the Djavakhet plateau.

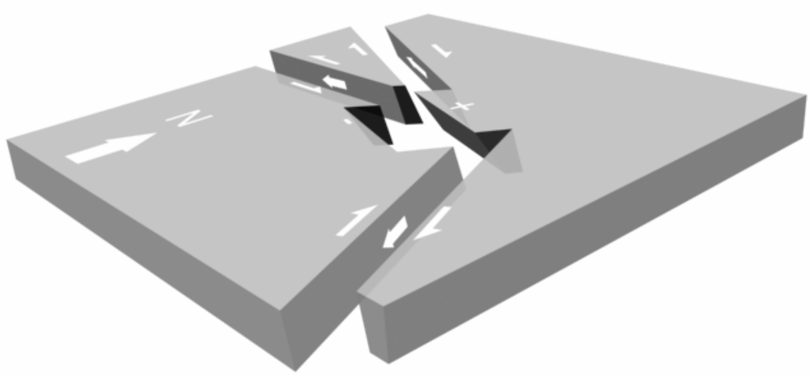

Figure 4. Geodynamic model of Spitak earthquake

References

Pacheco J.F., Estabrook C.H., Simpson D.W. & Nabelek J (1989). Teleseismic body wave analysis of the 1988 Armenian earthquake, *Geophys. Research Letters*, *16, N12, 1425-1428.*

Cisternas A., Philip H., Bousquet J.C. et al (1989). The Spitak (Armenia) earthquake of Dec.7, 1988, Field observations; Seismology and Tectonics, *Nature*, *339, N6227, 675-679.*

Grizer V.M., Cisternas A., Dorbat L. & Philip H (1988). The source modeling of the Spitak Earthquake Dec.7, Izv. Ac.Sc. of the USSR, *Physics of the Earth, 1991, 12, 46-55.*

Gabrielyan A.A., Sarkisyan O.A. & Simonyan G.P (1981). Seismotectonics of Arm.SSR, Yerevan, *Publ. YSU, 282 p.*

Milanovski E.E (1990). Geological structure of the region of the disastrous Spitak earthquake in northern Armenia and tectonic conditions of its origin, *Geotectonics*, *1, 3-13*.

Trifonov V.G., Karakhanyan A.S. & Kojhurin A.I (1990). The Spitak earthquake as a manifestation of modern tectonic activity, Izv. Ac.Sc. of the USSR, *Geotectonics, 6, 32-46.*

Rogojin E.A. & Ribakov L.N (1990). Tectonic position and geological manifestation of the Spitak earthquake Dec.7, 1988, Izv. Ac.Sc. of the USSR, *Geotectonics, 6, 32-46.*

Nikonov A.A (1990). The disastrous Spitak earthquake Dec.7, 1988 in northern Armenia, Problems of seismotectonics and source mechanism, Izv. Ac.Sc. of the USSR, *Geotectonics, 1, 14-32.*

Rastsvetaev L.M (1989). The shift and the Alpian geodynamics of the Caucasus, Geodynamics of the Caucasus, M., *Publ. Nauka, 106-113.*

Geodakyan N.E. & Geodakyan E.G (1996). The analysis of the strained state of the main seismotectonic zone of the Armenian plate, Abstracts of the jubilee scientific conference dedicated to the 35th year of the foundation IGES NAS RA, *Gyumri, 18-19.*

Geodakyan N.E., Voronina V.E. & Geodakyan E.G (1996). Modern state of the strained processes in the Earth's crust of the Caucasus region, Abstracts of the jubilee scientific conference dedicated to the 35th year of the foundation IGES NAS RA, *Gyumri, 17-18.*

Geodakyan E.G., Aharonyan V.J., Danilova N.A. & Yunga S.L (1989). Peculiarities of focal mechanisms of the Spitak earthquake aftershocks, Izv. Ac.Sc. of Arm.SSR, *Nauki o Ziemle, XII, 3, 71-77.*

Geodakyan E.G., Galinski G.L., Papalashvili V.G., et al (1991). Spitak earthquake Dec. 7, 1988, Isoseismal maps, Earthquakes in the USSR, 1988, M., *Publ. Nauka, 74-86.*

Balyan S.P., Lilienberg D.A. & Milanovski E.E. (1989). The latest and modern tectonics of seismoactive orogens of Armenia and the Spitak earthquake region, Geomorphology, *4, 3-16.*

Moskvina A.G., Gosbatova I.V., Zakharova A.I. et al (1991). Several peculiarities of source process of the Spitak Earthquake, Izv. Ac.Sc. of the USSR, Physics of the Earth, N11, M., *Publ. Nauka, 39-55.*

Novikova E.I. & Rautian T.G (1991). The parameters of the Spitak Earthquake source Dec.7, 1988, Izv. Ac.Sc. of the USSR, Physics of the Earth, N12, M., *Publ. Nauka, 32-46.*

Arefyev S.S., Tadevosyan R.E., Parani I.E., Geodakyan E.G., Cisternas A. et al (1990). The Spitak earthquake Dec.7, 1988, Seismic observations, Problems of Egineering Sismology, issue 31, Sources and influence of disastrous seismic motions, M., *Publ. Nauka, 4-29.*

Arefyev S.S., Aptekman J.Ya., Gosbatova I.V., Geodakyan E.G. et al (1991). Aftershock catalogue of the Spitak Earthquake Dec. 7, 1988, Izv. Ac.Sc. of the USSR, Physics of the Earth, N11, M., *Publ. Nauka, 60-73.*

Godzikovskaya A.A., Geodakyan E.G. & Tovmasyan A.K (1990). The Aftershock process in the Spitak source zone according to regional stations data at the interval of 7.12.1988-24.01.1989, Problems of Engineering Seismology, issue 31, M., *Publ. Nauka, 29-35.*

Teitelbaum Yu.M., Nikonov A.A., Godzikovskaya A.A. & Geodakyan E.G (1990). Aftershocks and fractures in the source of the Spitak earthquake Dec. 7, 1988, Izv. Ac.Sc. of the USSR, Physics of the Earth, N5, M*. Publ. Nauka, 16-27.*

Dorbat K., Dorbat L., Aptekman J, Ya. et al (1991). Source geometry of the Spitak Earthquake according to the detailed aftershock study data, Izv. Ac.Sc. of the USSR, Physics of the Earth, N11, M*. Publ. Nauka, 86-95.*

Bucovina Romanian Seismic Array (BURAR) - Contributions to the On-Line Seismic Monitoring in South-Eastern Europe

Ghica D V (1), Popa M (1), Radulian M (1), Raileanu V (1)

(1) National Institute for Earth Physics, P.O. Box MG-2 Magurele, Romania, daniela@infp.ro, mihaela@infp.ro, mircea@infp.ro, raivic@infp.ro

Keywords: seismic array, seismic monitoring, detection capability, detection threshold

Introduction

The Bucovina Romanian Seismic Array (BURAR) was deployed in 2002, in the northern Romania, into South-Eastern Europe, under a joint effort of the Air Force Technical Applications Center (AFTAC) of the United States of America and the National Institute for Earth Physics (NIEP), Romania. BURAR array is located in Suceava County, near the border to Ukraine (Figure 1). The geographical coordinates of the reference station (BUR01) are 47.6088°N, 25.2168°E and an elevation of 1151 m.

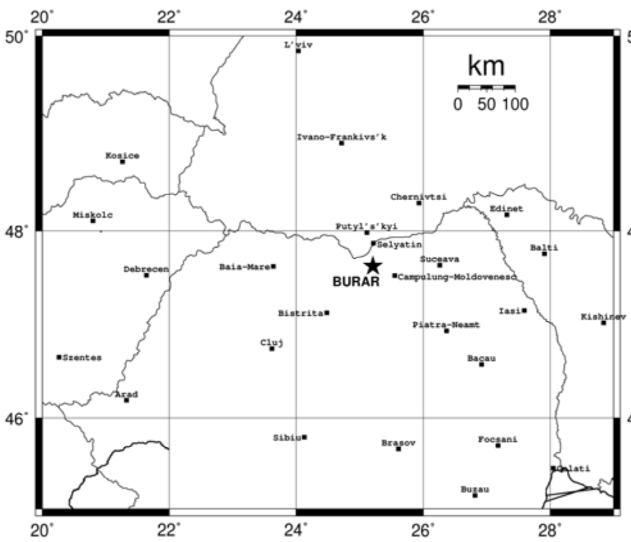

Figure 1. Geographical location of the BURAR array

BURAR consists of 10 seismometers located in boreholes and distributed over an area of km^2; inter-element distance varies between 500 m and 2000 m (Figure 2). A vertical-component short-period (1 Hz natural frequency) Geotech Instruments GS21 type instrument is placed in each of nine sites. The tenth site of array (BUR31) is equipped with a three-component broad-band Geotech Instruments KS54000 type instrument (flat to acceleration response), placed near short-period site BUR08. The sampling rate is 40 samples per second for both short-period and broad-band data. Data from each receiver are digitized, time-tagged and transmitted in real time, via radio data link (2.4 GHz frequency band), in the CD-1.1 format, to an unmanned central recording subsystem, in the field site facility (FSF), located near BUR04 site. From FSF, data are directly forwarded by satellite link in CD1.1 format, to the Romanian National Data Centre (RO_NDC), and re-transmitted from here, in real-time, to the National Data Center of USA (US NDC), in Florida.

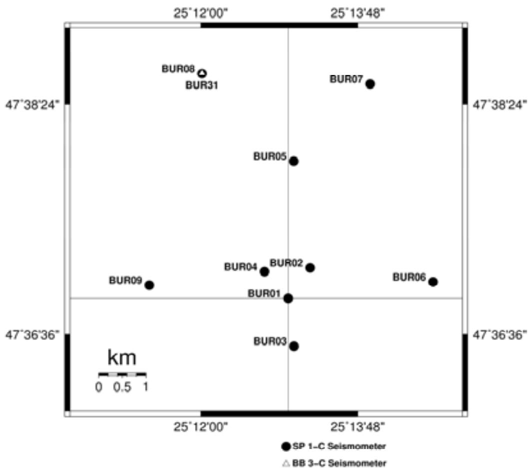

Figure 2. Configuration of the BURAR array

When arriving to RO_NDC, the data in diskloop are converted to continuous CSS3.0 database format. This database file system is the input to the automatic array data processing tasks, used for the on-line monitoring with BURAR system (*Ghica and Schweitzer, 2007*). At RO_NDC, an on-line data processing has been implemented, based on the RONAPP signal analysis software package (*Mykkeltveit and Bungum, 1984*), kindly supplied by NORSAR, and customized for BURAR. Seismic data are constantly scanned by automatic detection algorithms and analyzed with automatic routine processing (*Fyen 1989, 2001, Schweitzer et al., 2002*), consisting of three steps: detection, phase identification, and localization (see also *Schweitzer et al., 2002, Ghica and Schweitzer, 2007*). The automatic on-line processing provides daily listing with the results of all three steps.

The purpose of the paper is to investigate the BURAR detection capabilities, using the automatic processing results (i.e., identified phases), in order to verify the array contribution to the on-line seismic monitoring in the South-Eastern Europe.

Data and Methods

Data Sources

BURAR data recorded between January 2005 and December 2007 have been analyzed to test the array monitoring capabilities. For this time period automatically detected and identified phases were investigated to associate them to events listed in seismic bulletins. Automatic estimates of back-azimuth, phase velocity and origin time for each detection are given by the frequency-wavenumber (f-k) analysis step included in the on-line data processing.
To identify the events detected by BURAR, from the recording of automatic identified phases, two types of lists with reference events are used. Therefore, for teleseismic observations ($\Delta > 20^o$) the list was compiled from the PDE bulletins, while for the list of regional and local events ($\Delta \leq 20^o$), PDE bulletins and Romanian Earthquake Catalogue are merged together, the double entries being carefully eliminated. Additionally, for teleseismic distances, a magnitude detection threshold has been set to 4.5. Consequently, the final lists comprise 22,249 reference teleseismic events and 17,707 reference regional events. For all these events, the epicentral distances and the corresponding back-azimuth values were calculated.

Association of Automatically Observations to Reference Events

To identify the automatic observed phases with BURAR from the reference events, a program was used for automatically associating of the observed onsets with theoretically estimated onsets calculated for the bulletins (*Schweitzer, 2001*).

The procedure compares the possible phases calculated from *ak135* tables (*Kennett et al., 1995*) with the detected onsets. The absolute onset times of first and later arrivals were

estimated for BURAR array, using distance, depth and origin time of the event. To reduce the number of erroneous associations, some restrictions related to epicentral distance and event magnitude are introduced, and all theoretical phases to be considered for comparison with observed ones had to be separated in time by least three seconds (*Schweitzer, 2001*). Then the list of onsets was compared with the parameters automatically calculated for detected onsets with BURAR. Additional restrictions for the automatic procedure are described by *Schweitzer (2001)*.
For this study, only first arrival identified by above technique was used to define the events observed with BURAR array.

During the considered time interval, from a total of about 23,700 events detected by BURAR (Figure 3), 13,261 teleseimic events and 2,821 regional events were kept to be complied with initial terms (epicentral distance and magnitude threshold).

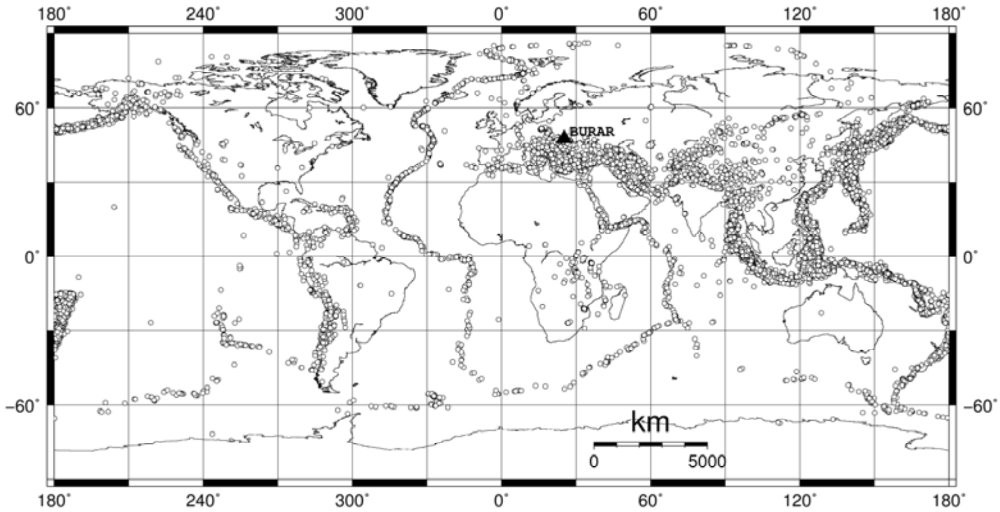

Figure 3. Events detected with BURAR array between the 2005 and 2007 years

Results and Discussion

To show the capabilities of BURAR, some results of evaluation of the array detection ability should be discussed:

a) Teleseismic Distances
As a result of the aperture, geometry and number of elements of the array, BURAR is very efficient to detect teleseismic events (Δ > 20^{o}). Considering a detection threshold for magnitude of 4.5, BURAR onsets could be associated to almost 60% of all events in the teleseismic distance range, for the time interval considered (Figure 4).

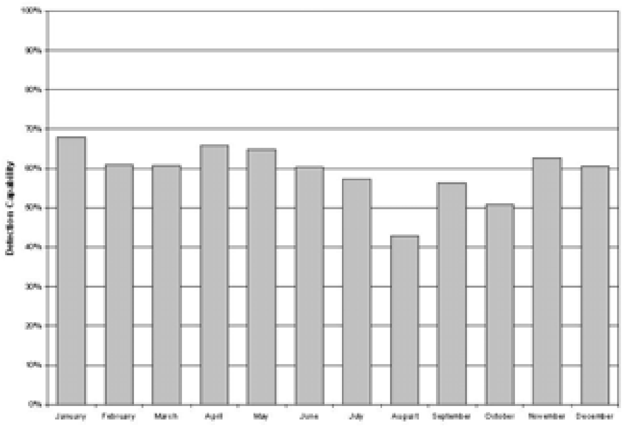

Figure 4. BURAR monthly detection capability for teleseismic events between 2005 and 2007

In terms of monthly statistics, the highest rate of events detected from the total reference events (detection capability) was observed mostly for the winter and spring month (November, December, January, February March, April and May); the rate decreases by 20% in the summer season (especially in August), when the thunderstorms associated with lightning activity damage the electrical equipment and introduce noise into the system (Figure 4), and the local roads traffic is increased.

Thus, the middle part of winter is the best time for operation of the BURAR array, due to the restraining of the local specific activity (especially agriculture and farming) and of the road traffic. Moreover, the large falls of snow in the BURAR area influence the increasing of the array detection capability, since the snow is acting as a noise attenuator.

Generally, the good detection capability of BURAR for teleseismic events is due mainly to the general low level of background noise at low frequencies (below 3 Hz) (*Ghica et al., 2005*), as well as to the application of the advanced array techniques to recognize P and PKP onsets.
Regarding rate of detected events per epicentral distance, BURAR detection capability clearly decreases beyond 90° (Figure 5), and starts to increase from about 120° for PKP phases. This decreasing part emphasizes the influence of the core shadow zone on BURAR recordings and consequently, the rapid decaying of signal amplitudes and the defocusing effects of the body-waves which reach array site.

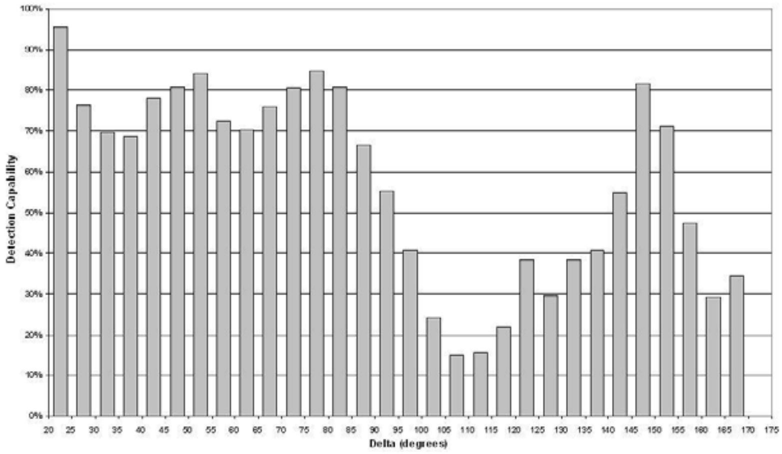

Figure 5. BURAR detection capability for teleseismic events versus epicentral distance

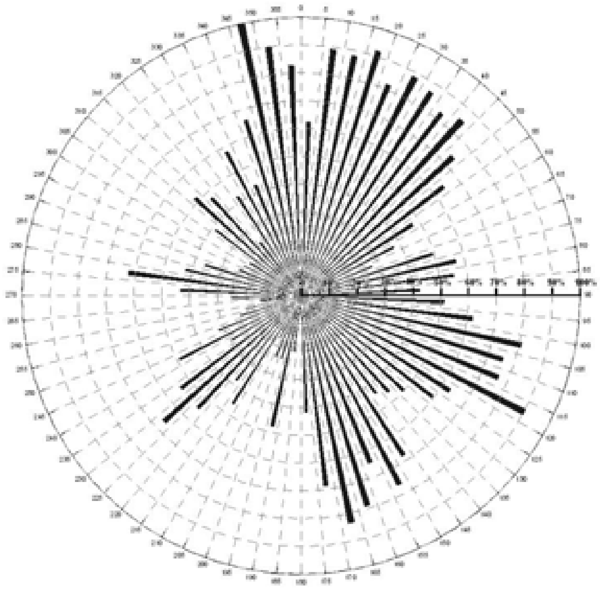

Figure 6. BURAR detection capability for teleseismic events versus back-azimuth

On the other hand, the detection capability is higher for the distances between 140^o to 155^o, around the PKP caustic, along with the detection peak for PKP near 145^o, caused by the focusing effect of the Earth's outer core on the recorded amplitudes.

In terms of back-azimuth, the detection capability of BURAR for teleseismic events is higher, especially for the 5^o to 45^o back-azimuth range (Figure 6), generally corresponding to the Japan, Kamchatka, and Kuril regions (an epicentral distance of around 75^o), and to the PKP caustic (Tonga region). Also, detection capability is once more increased in the 115^o – 120^o back-azimuth range, subsequent to a distance of 20^o – 30^o (Iran, Pakistan, Afghanistan regions).

b) Regional Distances

For regional distances ($\Delta \leq 20^o$), the BURAR efficiency in the events detection decreases to about 18% of all events within this area (Figure 7). The monthly detection capability for regional events generally follows the same trend as for teleseismic observations, with a diminishing of the number of events detected during the summer time (Figure 7), caused by the specific seasonal activity and atmospheric conditions.

Furthermore, the local site conditions (crustal structure and high frequencies cultural noise), and array dimension affect the signal coherency, and reduce the array detection capability.
Within local distances ($\Delta \leq 5^o$), BURAR capability is relatively high (Figure 8), with a decline in the 2 – 4^o range, for the earthquakes produced in the Romanian seismogenic zones as Banat, Danubian zone, Predobrogean Depression and Intramoesian Fault, where the rate of seismic activity is moderate to relatively high, but the magnitude has a low level (*Radulian et al., 2000*).

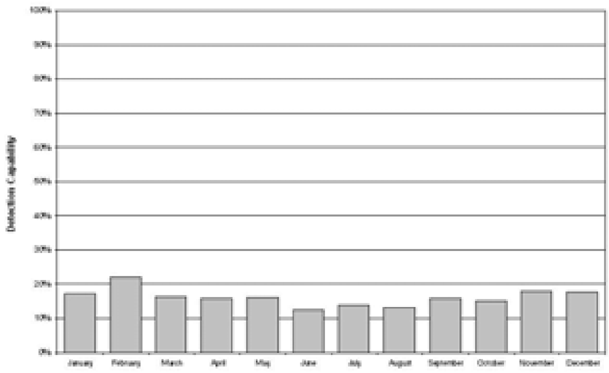

Figure 7. BURAR monthly detection capability for regional events between the 2005 and 2007 years

A detection peak is present near 5^{o} (Figure 8) that could be related to the induced seismicity in the Polish mining area. This area, present also the azimutal distribution for the BURAR capability (Figure 9), could be correlated with the weak attenuation in the lithosphere structure on that direction.

After a strong decreasing zone beyond 6^{o} (Figure 8), mainly corresponding to the Greece and Italy area seismicity, the regional detection capability of BURAR raises again, for distances between 13^{o} to 17^{o}, to reach a relative peak near 17^{o}, coincident with the distance range of caustic for regional P-waves (Pn), according to the global velocity models.

For the analyzed data, azimuthal variation of detection threshold was observed for BURAR array (Figure 9). Therefore, a very good effectiveness in detecting events from East-South-East direction, for an 80^{o} – 115^{o} back-azimuth range (Caucasus, Anatolian region), is pointed out. This is most likely due to the high seismicity of the region, with large magnitude of the events, and to the low attenuation along the travelling path.

A good detection capability of BURAR is also observed for the regional events in North-West direction, which can be associated with the induced events, occurred in the two large mining areas (see also *Wiejacz and Kowalski, 2007; Stec, 2007*): Upper Silesian Coal Basin (delta around 5^{o} and back-azimuth range of 300^{o} – 307^{o}) and Lubin Copper Basin (delta about 7^{o} and back-azimuth between 303^{o} and 310^{o}).

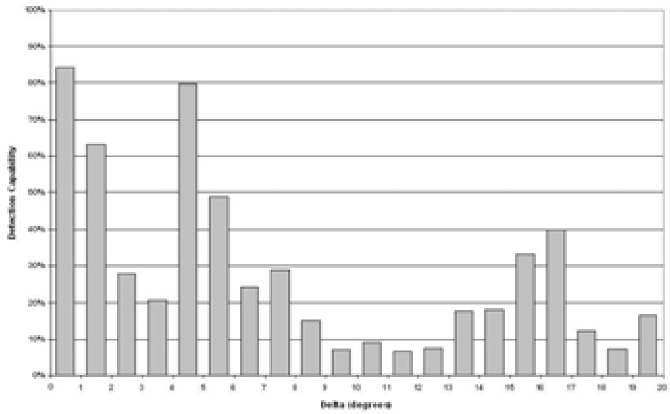

Figure 8. BURAR detection capability for regional events versus epicentral distance

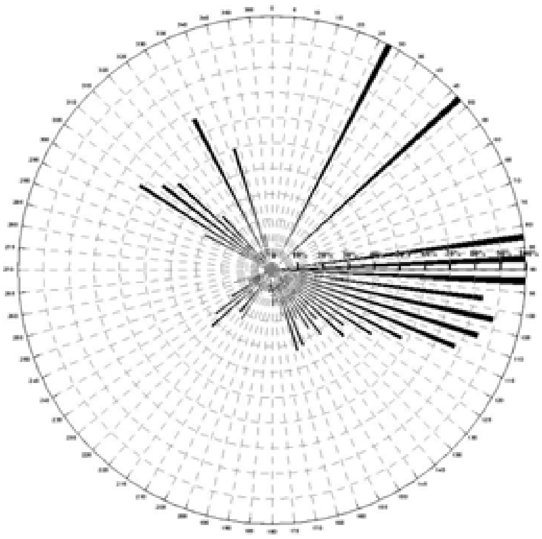

Figure 9. BURAR detection capability for regional events versus back-azimuth

On the other hand, the detection capability of BURAR is highly decreasing to the West-South-West direction, corresponding to a 245^o – 295^o back-azimuth range and epicentral distance larger than 8^o (Italy and Western Europe area). We assume that this situation is probably caused by the low magnitude of seismicity (magnitude below 5.0) and by the lithosphere complex structure, i.e., tectonics of the Dinarid – Pannonian Basin – Carpathians region. Travel path is crossing the thin Hungarian Plain lithosphere, which ovelies an astenospheric dome, with lower seismic velocities and higher attenuation (*Posgay et al., 1996*).

Additionally, BURAR efficiency is low for events originating from South-South-Western direction, corresponding to an azimuthal range of 165^o – 210^o and an epicentral distance between 9^o to 12^o. This decreasing of array capability is matching the region of Hellenic arc (Figure 10), along which the Africa plate subducts beneath the Aegean Sea plate. The area is characterized by shallow intermediate depth earthquakes produced on faults in the boundary-region of the two plates, for which the magnitude threshold of detected events by BURAR raises to 3.5.

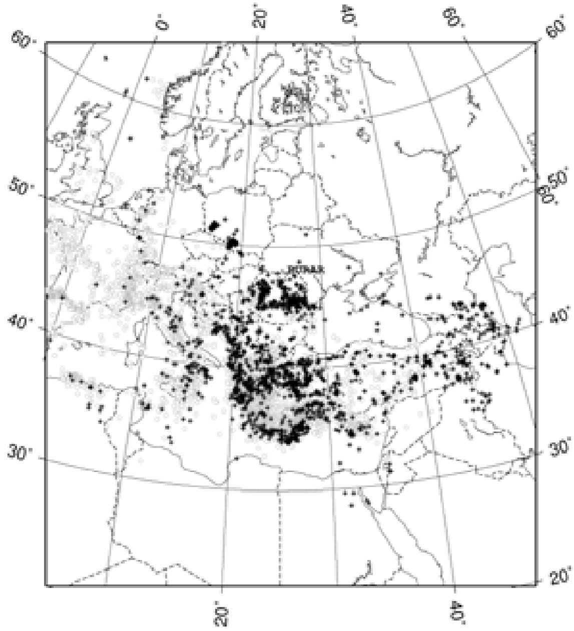

Figure 10. Detection capability of BURAR for regional distances. Cross symbols describe events detected by BURAR; grey circles depict reference events reported in bulletins

Within regional distances, the statistical analysis is not relevant for the North-Eastern azimuthal domain (back-azimuth range of 345^o – 80^o), which is characterized by a low seismicity, therefore very few BURAR detections are observed.

A variation curve of magnitude detection threshold with regional epicentral distance shows the BURAR efficiency (Figure 11).

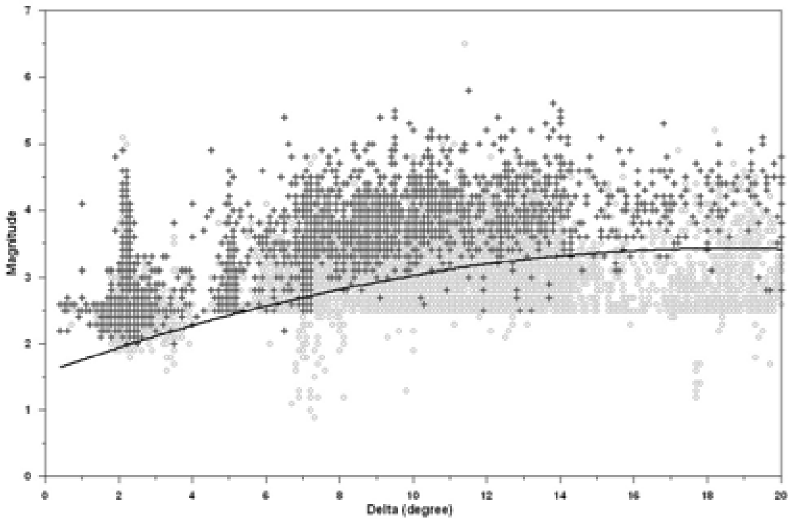

Figure 11. Local magnitude versus epicentral distances for regional events. Cross symbols describe events detected by BURAR; grey circles depict reference events reported in bulletins

The detected magnitudes increases with distance: for delta smaller than 3.5^o, the detection threshold decreases to 2.0, while for delta beyond 14^o, the detection capability of BURAR can be estimated to local magnitude threshold of 3.5. Moreover, for epicentral distances below 3.5^o, BURAR array observes about 86% from total events with local magnitude $\geq$ 3.5, whereas for delta beyond 3.5^o, over 65% of reference events with the same magnitude are missed by the array.

Conclusions

Analyzing data recorded between 2005 and 2007, it is obvious that BURAR is a sensitive station that provides a good seismic monitoring coverage of the South-Eastern Europe, by on-scale recording of weak-to-strong events in a large range of epicentral distances.
A good detection capability for teleseismic distances was demonstrated, since almost 60% of BURAR onsets could be associated to the reference events, with a detection threshold magnitude of 4.5.

BURAR effectiveness for the regional distances slightly exceeds 18%, being influenced by the low coherency of the signal at frequencies higher than 3 Hz, caused by the array dimension and the crustal structure beneath the station. Furthermore, BURAR shows a strong azimuthally variable detection capability within regional range, which seems to be related both to local site conditions and travelled structure effect on the array observations.
The magnitude of events observed with BURAR is variable with epicentral distance within regional range, generally increasing with delta.

Acknowledgements

The results have been partly achieved under a visit at the NORSAR institute, and was sponsored through the Romanian Ministry of Education, Research and Youth, in the framework of the CEEX project no. 726 / 2006. The first author would like to gratefully

acknowledge the kind and permanent support of Dr. Johannes Schweitzer, for his special efforts in providing help and knowledge.
Maps were created using GMT software (Wessel & Smith 1995).

References

Fyen J (1989). Event processor program package, *in NORSAR Semiannual Technical Summary, 1 October 1988 – 31 March 1989, Scientific Report 2-88/89, NORSAR, Kjeller, Norway.*

Fyen J (2001). NORSAR seismic data processing – user guide and command reference, *NORSAR (contribution 731) Kjeller, Norway.*

Ghica D., Radulian & M., Popa M (2005). Noise level analysis for BURAR seismic array, Romania, *EGU General Assembly 2005, Austria, poster presentation*

Ghica D. & Schweitzer J (2007). Automatic Data Processing at BURAR Seismic Station, *Proceedings of International Symposium on Strong Vrancea Earthquakes and Risk Mitigation, Oct. 4-6, 2007, Bucharest, 164-169p.*

Kennett B.L.N., Engdahl E.R., & Buland R (1995). Constraints on seismic velocities in the Earth from travel times, *Geophys. J. Int., 122, 108-124.*

Mykkeltveit S. & Bungum H (1984). Processing of regional seismic events using data from small-aperture arrays, *Bull. Seism. Soc. Am. 74, 2313-2333.*

Posgay K., Takacs E., Szalay I., Bodoky T., Hegedus E., Kantor J.I., Timar Z., Varga G., Berczi I., Szalay A., Nagy Z., Papa A., Hajnal Z., Reilkoff B., Mueller S., Ansorge J., De Iaco R., Asudeh I (1996). International deep reflection survey along the Hungarian Geotraverse, *Geophysical Transactions 1996, Vol. 40, No. 1-2, 1-44p.*

Radulian M., Mandrescu, M.N., Panza, G.F., Popescu, E., Utale, A (2000). Characterization of Seismogenic zones of Romania, *Pure Appl. Geophys., 157, 57–77.*

Stec K (2007). Characteristics of seismic activity of the Upper Silesian Coal Basin in Poland, *Geophys. J. Int. 168, 757–768.*

Schweitzer J (2001). Slowness Corrections – One Way to Improve IDC Products, *Pure and Appl. Geophys., vol. 158, 375-396.*

Schweitzer J., Fyen J., Mykkeltveit S.& Kværna T (2002). Seismic arrays. *In P. Bormann (edt), New Manual of Seismological Observatory Practice, Potsdam, 51 p.*

Wiejacz P. & Kowalski P (2007). Comparison of ISC seismic event locations, with data of Polish mining industry, *IUGG General Assembly, Italy, 2007, presentation.*

MMAI Array Analysis for Experimental Explosions in Israel and Jordan

Gitterman Y (1), Pinsky V (1), Hofstetter R (1), Polozov A (1)

(1) The Geophysical Institute of Israel, P.O. Box 182, 71100, Lod, yefim@seis.mni.gov.il

Keywords: MMAI array, GTI0 explosion, F-K estimations, error analysis

Introduction

A small-aperture seismic array MMAI at Mt. Meron, Galilee (in operation since January 2003) was established by CTBTO as station AS049 of the International Monitoring System (IMS). Since then a number of experimental and calibration explosions with Ground Truth Information GTI0 were conducted in Israel and Jordan. Good recordings of signals from most of the shots were obtained at MMAI. We collected raw data of 17 explosions and evaluated back-azimuth and apparent velocity using the common F-K analysis procedure incorporated in a software package jSTAR by GII. Based on accurate explosion parameters (coordinates and origin time) we computed deviations of estimated azimuth and velocity from Ground Truth values. A systematic eastward bias was determined for explosions located to the south of the array.

Materials and Methods

The used explosions

A number of large-scale calibration explosions of different design were conducted recently in Israel and Jordan, under close collaboration of national seismological institutions (Gitterman et al. 2006). The experiments were in the context of CTBT monitoring in the Middle East, and aimed to improve the velocity models for calculating travel times to regional and IMS stations and to extend the Ground Truth (GT0) database. Recently source phenomenology explosion experiments of special design were conducted for empirical modelling of nuclear test seismic source, investigation of explosion phenomena, dynamic parameters and spectral features of radiated seismic waves (Gitterman, in review). Locations of the explosions and the array are shown in Figure 1, Ground Truth parameters and design details for the selected explosions are presented in Table 1. Shots in several experimental series (Bet Alpha, Oron) were closely placed, providing almost the same distance and azimuth, therefore they were fixed for a central point of a series.

The Data

A small-aperture (2.53 km × 2.58 km) seismic array MMAI at Mt. Meron consists of 16 elements (Figure 2): 16 vertical SP sensors in boreholes about 50 m deep, the central station MMA0 includes also a BB seismometer in a 103 m deep borehole (coordinates MMA0: 33.01527N, 35.40305E). In some explosions a few (1-5) elements were excluded from processing due to malfunctioning or strong noise.

The Method

A standard broadband F-K analysis procedure was used for evaluation of back-azimuth to an explosion and apparent velocity (e.g. Kvaerna and Ringdahl, 1986). The procedure is incorporated in a software package jSTAR developed by GII (Pinsky et al., 2007). For pre-processing visualization of recorded signals we used filtering range 1-10 Hz; for preliminary processing a fixed time window 3 sec since first P-arrival (actually P and Pn phases) and F-K analysis frequency range 1-5 Hz were chosen.

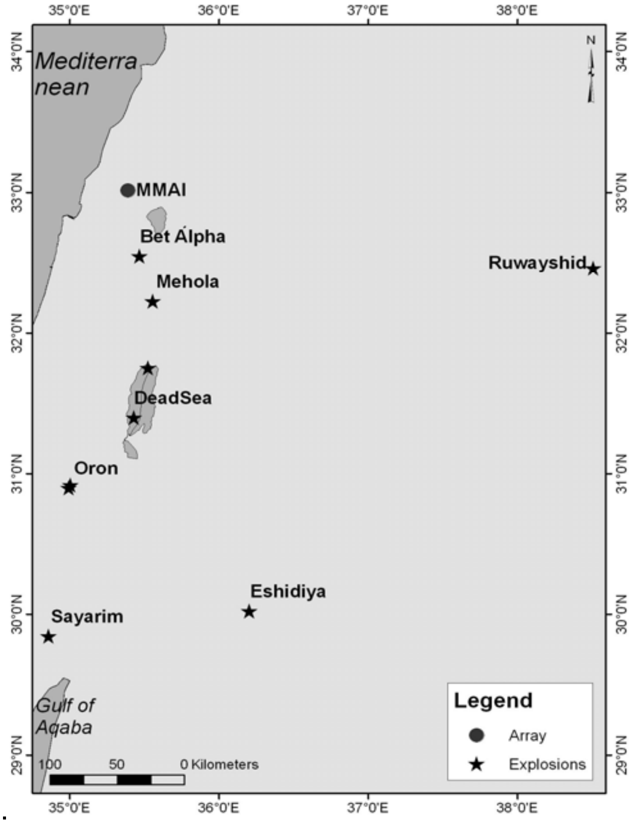

Figure 1. Locations of the selected GTI0 explosions and the array.

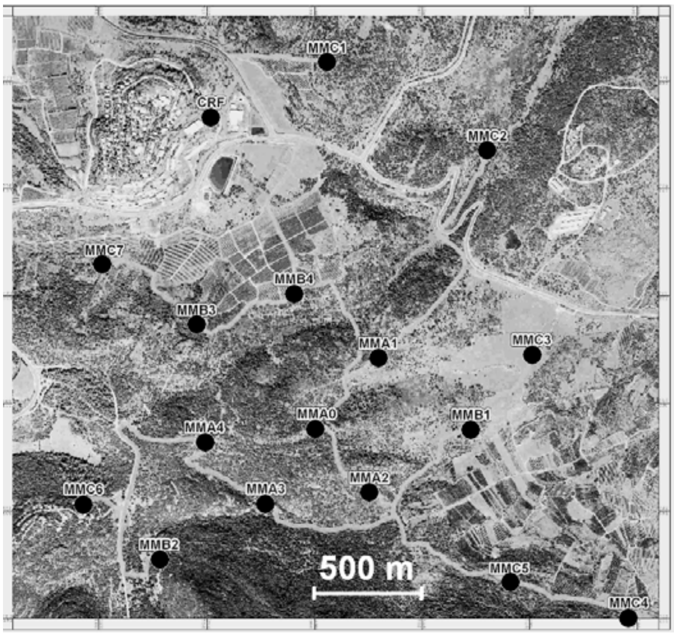

Figure 2. Configuration of small-aperture array MMAI (AS049) at Mt. Meron (aerial photo).

Results and Discussion

The results of the F-K analysis applied to the selected explosions are presented in Table 2 and some examples of recorded signals and processing results are shown in Figure 3.

Table 1. Parameters of GTI0 explosions in Israel and Jordan, observed at MMAI array.

#	Location	Date	LatitudeN LongitudeE	Origin Time, GMT	Local mag. M_D	Charge ton	Design
1	Sayarim (Israel)	15.06.04	29.84188 34.85851	13:00:01.49	3	32.5	in 11 holes diam. 0.7m,depth H~20m
2	Mehola (Israel)	20.10.04	32.22269 35.55644	12:15:00.0	2.4	3.0	in a hole diam. 0.6m, H~35m
3	DeadSea (South)	20.10.04	31.3949 35.43104	15:05:00.0	3.2	0.75	underwater, H~50m
4	DeadSea (North)	21.10.04	31.74982 35.5270	15:05:00.0	3.1	0.75	underwater, H~50m
5	Ruwayshid (Jordan)	4.12.04	32.457 38.509	15:00:02.18	2.7	40.0	in 20 holes diam.D =0.55m, H=20m
6	Eshidiya (Jordan)	17.01.05	30.019 36.204	13:00:02.64	2.6	20.0	in 14 holes D=0.46m, H=20m
7	Bet Alpha (Israel)	6.06.05	32.545 35.469	10:05:01.42	1.5	0.5	in a hole D=0.55m, H=15m
8				10:30:01.60	1.5	0.5	in a hole H=16m
9				11:00:01.33	1.4	2.0	in 2 holes H=15m
10				12:00:01.53	2.6	20.0	in 20 holes H~15m
11	Oron (Israel) Decoupling experiment	17.07.06	30.916 35.007	13:30:02.38	2.0	1.24	H=26.5m, decoupl.
12				13:56:40.99	1.5	1.24	H=63m, decoupled
13				14:15:02.14	2.4	1.24	H=30m, coupled
14				14:18:53.40	1.8	0.31	H=30m, coupled
15	Oron DOB experiment	2.01.07	30.896 34.993	09:31:12.32	2.7	4.2	H=26m, coupled
16				10:01:13.44	2.6	4.2	H=45m, coupled
17				10:30:31.28	2.5	4.2	H=59m, coupled

Table 2. Estimation by standard F-K analysis of back-azimuth (Az) and apparent velocity (V).

#	Distance, km	Real parameters		Estimates				
		Az,°	V, km/s	Az,°	error	V, km/s	error	Z
1	355.5	188.2	7.95	175.2	-13	6.92	-1.05	0.288
2	89.0	170.7	6.23	164.9	-5.8	6.19	-0.03	0.444
3	179.7	179.2	7.95	169.2	-10	7.80	-0.15	0.630
4	140.8	175.3	7.95	170.1	-5.2	7.14	-0.85	0.715
5	297.6	102.8	7.95	100.8	-2	7.80	-0.15	0.501
6	340.7	167.3	7.95	153.4	-13.9	7.45	-0.5	0.395
7	52.5	173.3	6.23	159.4	-13.9	6.50	0.27	0.299
8				162.3	-11	6.35	0.12	0.334
9				171.3	-2	6.34	0.11	0.357
10				163.7	-9.6	6.67	0.44	0.699
11	235.7	189.0	7.95	182.3	-6.7	6.66	-1.29	0.393
12				170.5	-18.5	9.13	1.18	0.172
13				175.2	-13.8	6.92	-1.03	0.519
14				172.2	-16.8	7.51	-0.44	0.493
15	238.1	189.3	7.95	175.0	-14.3	7.22	-0.73	0.641
16				177.4	-11.9	7.57	-0.38	0.586
17				174.8	-14.5	7.54	-0.41	0.359

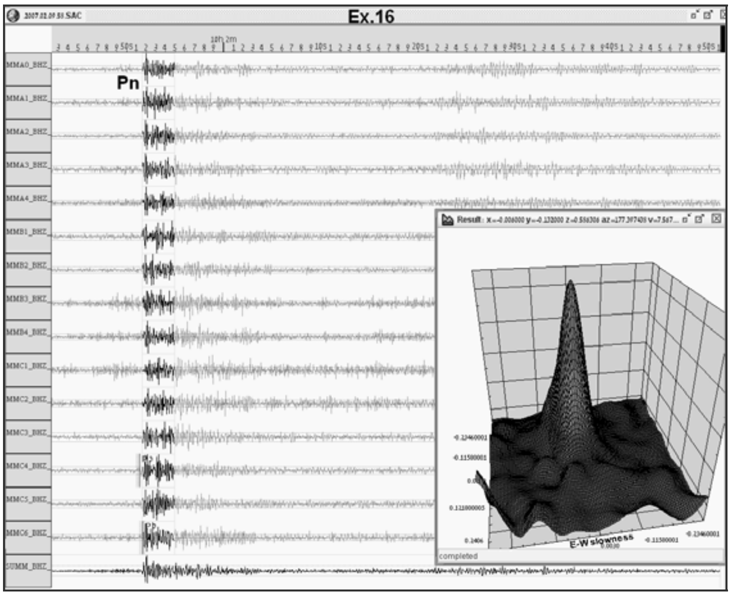
Ex.16
Pn
E-W slowness
completed

a)

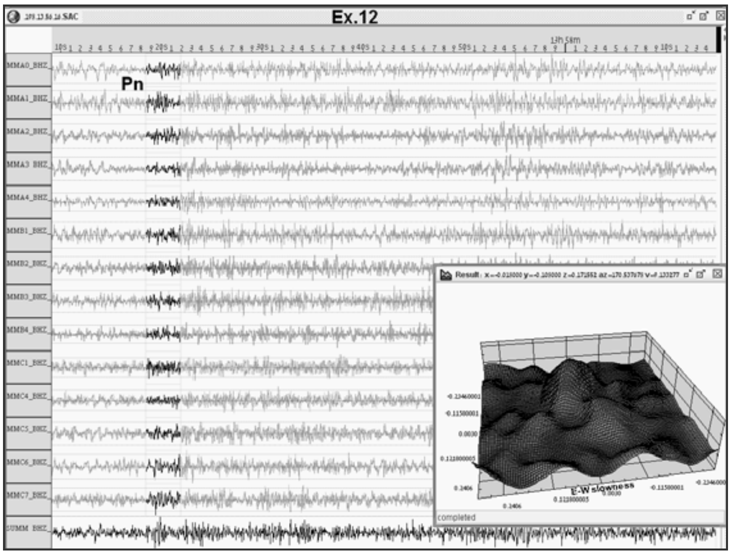
Ex.12
Pn
E-W slowness
completed

b)

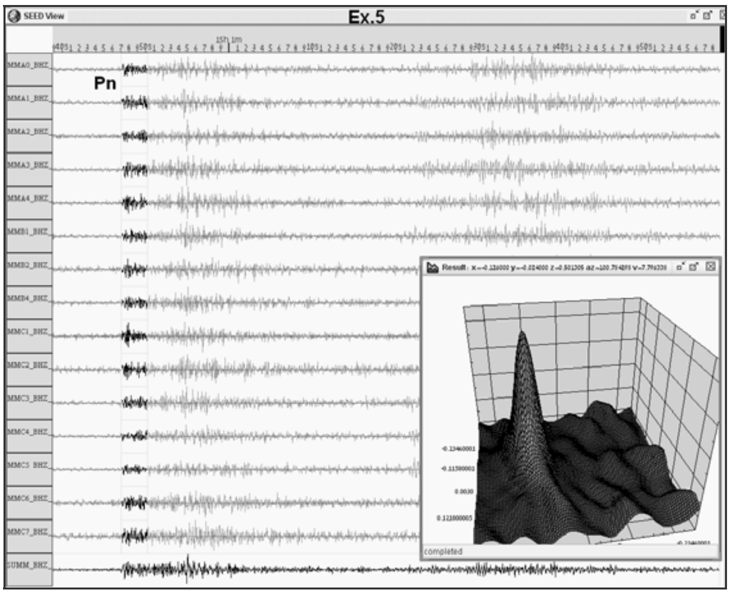
SEED View
Ex.5
Pn
completed

c)

Figure 3. Samples of records and F-K analysis results for Ex.16 with high SNR (a), Ex.12 with low SNR (b) and Ex.5, the only from the East (c). Filtering 1-10 Hz was applied.

Obtained F-K azimuths and apparent velocities are compared to real azimuths, due to accurate explosion coordinates, and to reference apparent velocities due to precise distance and local 1D velocity model used in GII routine earthquake location (Table 2). Estimation errors were also calculated as difference between estimated and real values. Target Z-function values are presented also in the table, illustrating Signal-to-Noise Ratio (SNR) and demonstrating reliability of F-K estimations. High Z-values are found for most explosions with high SNR (Figure 3,a,c), whereas Ex.12 with very low SNR (Figure 3,b) showed a low Z-value and large estimation errors (Table 2).

Conclusions

All azimuthal values are under-estimated, significant systematic errors about 10-14° are found for most explosions located southward of the MMAI array. For the only explosion from the East (Ex.5) the error is very small (2°). Most of apparent velocity values are also under-estimated but not significantly, except of Ex.7-10 at a close distance (~50 km), and a remote Ex.12 with very low SNR, providing therefore an unreliable estimation.

In order to improve azimuth and apparent velocity estimations and reduce errors, array analysis of the selected dataset will be continued, using different length time windows, processing frequency range, seismic phases (e.g. Pg, Sg); a new-developed robust array processing tool (Pinsky, 2004) will be also applied to the data.

References

Gitterman Y., Pinsky V., Amrat A-Q., Darwish J., Mayyas O., Nakanishi K. &Hofstetter R (2006). Source features, scaling, and location of calibration explosions in Israel and Jordan for Comprehensive Test Ban Treaty (CTBT) monitoring, *Isr. J. Earth Sci. 54: 197–215*.

Gitterman Y (in review). Source Phenomenology Experiments with borehole explosions of special design in Israel. To be submitted to *Bull. Seism. Soc. Am.*

Kvaerna T. & Ringdahl F (1986). Stability of various f-k estimation techniques, in Semi-annual Technical Summary, 1 October 1985 -31 March 1986, *NORSAR Scientific Report, 1-86/87, Kjeller, Norway, 29-40.*

Pinsky V., Polozov A., Kadosh D., Avirav A. & Hofstetter R (2007). New seismic system for acquisition and analysis in Israel, *Abstracts of XXIV General Assembly of IUGG, July 2-13, 2007, Perugia, Italy.*

Pinsky V (2004). Array location with automatic outlier suppression, *Proceedings of XXIX General Assembly of European Seismological Commission, Potsdam,* Germany, September 12-17, 2004.

Contribution of the 1976 Friuli Earthquake Experience to the Development of an Holistic Multidisciplinary Approach in the Regional Management of Seismic Risk

Grimaz S (1)

(1) Dipartimento di Georisorse e Territorio – Università degli Studi di Udine via Cotonoficio 114, 33100 Udine Italy, stefano.grimaz@uniud.it

Keywords: natural disaster, Friuli earthquake, civil protection, risk mitigation

Introduction

"*Learning the lesson .. or at least how it should be done*". From this perspective it is interesting to look back and analyze the changes to the local understanding of seismic risk and the awareness of the problem determined by the 1976 Friuli Earthquake (N-E of Italy). More than thirty years form that experience, it can be observed that a lot of things have changed with respect to risk management in the Friuli Venezia Giulia Region, either for the researchers from the local scientific institutions or for the politicians and the public administrators. In particular, from a point of view of civil protection, the reciprocal relationships and the synergy among those subjects have contributed to meaningful improvements and they are the main reasons for the progressive advancements in the definition of a modern, concrete and rational action of prevention for seismic risk mitigation. *"A posteriori"* analysis allows us to derive important lessons in the field of seismology, earthquake engineering, urban planning, sociology but also other useful information could still be derived. In this work, in particular, a rereading of the activities developed by the seismic research group of the University of Udine (I) on the basis of both the Friuli earthquake data and the relative lessons that can be learned will be delineated.

1976, Friuli Earthquake and the development of an awareness for risk management

On May 6, 1976, an earthquake of magnitude 6.4 on the Richter scale struck central Friuli, a region located in the North-Eastern part of Italy at the borders of Austria and Yugoslavia (now Slovenjia). On September 11, 1976 the earth shook again; two more shocks occurred followed four days later by one of magnitude 6.1.

The devastated area covered about 1800 km^2. Over one hundred villages were almost destroyed. More than 17,000 houses, a large number of schools, churches, town halls and factories were ruined. In many places there were important art treasures and historical landmarks. In Udine, the biggest urban centre of the affected part of region, with almost 100,000 inhabitants, more than 50% of dwelling units were damaged.

From a seismological point of view, although the Friuli region has a long seismic history, the magnitude of the two earthquakes were, as far as it was known, unprecedented and therefore unexpected. As result, no consciousness of the real seismic risk was present in the population and in the public administrators.

The sequence of the two earthquakes resulted in a demoralizing effect on Friuli inhabitants but also provided evidence of the deficiencies in the knowledge both in the technical and planning field. People responded to the first shock by endeavouring to rebuild their houses and to resume quickly their business activities.

In a very short time after the May 1976 earthquake, about 85000 buildings were inspected as required by a subsequent regional law (LR. 17/76 - Friuli Venezia Giulia Region), and the same number of data sheets were filled and collected. The aim of that collection was to define the number of dwellings not usable after the earthquake and to assess the cost of retrofitting. On the basis of that law a large number of damaged buildings were retrofitted using the techniques provided by the regional administration.

But in September the second earthquake showed, in a dramatic way, the complete inadequacy of the strategy adopted and the knowledge deficiencies in the management of the problem. This forced the administrators and the scientists to deepen their knowledge and to redefine the strategies. The following reconstruction management produced very good results. The disaster marked the infusion of a lot of investments, the modernisation of machinery and the re-launching of the industrial sector, which increased job opportunities (Geipel, 1980a and 1980b). As result, the whole Friuli region experienced new dynamic trends and accelerated the economic development (Cattarinussi et. al, 1981) of the area. So, the Friuli reconstruction became an example of success in the international panorama and an element of pride for the Friulian people.

From a socio-economic point of view, the two earthquakes were, together, an agent of social changes (Barbina G., 1979). For scientists, technicians and administrators, the combination of the two events and the failure of the first strategies of the retrofitting of buildings imposed a serious opportunity for reflection to enable a definition of a response based on the risk concept.

As part of the reconstruction plan of Friuli, in 1978, the University of Udine (also called University of Friuli) was founded. Together with the other scientific institutions of the Region (University of Trieste, Experimental Observatory of Geophysics of Trieste, Institute of International Sociology of Gorizia and International Centre For Mechanical Sciences of Udine) developed intensive studies and researches on the earthquake related problems from a plurality of points of view (seismological, engineering, sociological, economic, cultural).

At the same time, a group of UNESCO international experts met in Paris (Founier d'Albe, 1979) and had discussions on the risk conceptualization in the field of natural disasters. Risk was related to three main components: hazard, vulnerability and value of elements at risk. At that time it was a revolutionary way of conceptualizing the problem and allowed us to delineate a modern view for defining risk mitigation strategies.

In the middle of the eighties taking in account both the catastrophic experience of the 1976 earthquakes and the new approach introduced by UNESCO, the government of Friuli Venezia Giulia Region enacted a law (L.R. 64/86)[1] aimed to institute a regional system of Civil Protection. The final scope of the law was the protection of environment and citizens against natural and man-made risks. The strategy to reach the objectives was based on the following main activities:
- Prevision;
- Prevention;
- Rescue.

Prevention was not only conceived as a technical action but was considered as part of a risk culture and as a primary public concern and task. The regional Government holds the coordination of the whole civil protection activities on its territory.

The regional act was very innovative in the Italian scenario. In fact in Italy, at that time, the civil protection was intended as an organization only finalized to intervene in the post seismic

1 At that time Prof. Marcello Riuscetti of the University of Udine (I) – seismologist, head of the seismic risk group of research - was member of the Council of the Friuli Venezia Giulia Region. He was one of the promoters of the law and gave his determinant contribute for transferring the more advanced scientific knowledge in the vision and organization of the regional civil protection system.

event. At national level the concepts of prevention, prediction and protection were introduced only six years later by the law on the institution of the national civil protection (L. 225/92).

Since the official foundation in 1986, the regional civil protection has grown up and has always been considered as an advanced model of reference in the national panorama, becoming another element of pride for the friulian people and local administrators. With the L.R. 19/2000 and L.R. 1/2001 the competences of the regional civil protection were enlarged to the international and national solidarity respectively.

All these facts together defined the conditions allowing the start of a progressive definition of robust knowledge and methodology for the management of risk. Scientists, people and public administrators were not only involved but also motivated to provide their contribution to an unique design of civil protection structured on a modern vision of the management of risk. In accordance with this vision a sequence of finalized projects were financed and supported which permitted the definition of an important feedback from research and operative worlds.

Overview on the "*a posteriori*" studies

After earthquakes in 1976, Friuli and 1980, Irpinia (South of Italy) much progress was obtained in the seismological field and in the definition of the seismic hazard of the whole national territory. The "Geodinamica" project of the National Council of Research (CNR-PFG, 1980) led to the development of new criteria of seismic classification based on the best and more advanced knowledge at that time.

However, not so much effort was provide to improve the knowledge on vulnerability. Only at the end of eighties the National Group of Defence from Earthquakes began to study this issue. The data of damages of the Friulian village of Venzone were taken as reference for a first test of an index methodology of vulnerability assessment. At that time the vulnerability represented the less known parameter in the UNESCO's conceptualization of risk.

In that context a strategic partnership between the scientific institutions and Civil Protection of the Friuli Venezia Giulia Region commenced. During the years the feedback between the subjects produced a virtuous sequence of activities which led both to a progressive increasing of knowledge and a definition of support tools required for risk management.

Two main phases can be distinguished. The first one was addressed to collect the data of the 1976 Friuli earthquake which was considered useful for "*a posteriori*" analyses. The second one, currently still in progress, has the aim to develop specific finalized studies to support the management of risk.

First phase

At the end of the eighties the components of seismic group of research of the University of Udine posed the following question: what we can learn from an "*a posteriori*" analysis of the Friuli earthquake experience, in particular in term of the vulnerability of masonry buildings? As part of an answer, the research group started the difficult acquisition and reorganization of the data derived from the technical investigations carried out after the LR 17/76, in a specific database, called Fr.E.D. (acronym of Friuli Earthquake Damages). At the beginning of the nineties, a first release of the database was completed. Another research team of the Institute of Architecture of Venice (I) and of the Polytechnic of Milan (Doglioni et al., 1979) started with the systematic acquisition of the whole photographic material collectable on the Friulian churches damaged by the earthquake. These operations of reconstruction and reorganization of data were financed by Civil protection of Friuli Venezia Giulia Region and by National Group of Defence from Earthquakes of the National Council of Research. It is important to underline that these operations were considered as preventative activities.

On the basis of these data, many investigations have been carried out. Seismic vulnerability of residential buildings, also referring to the masonry buildings in historical centres, was studied (Grimaz, 1993). Relationships between ground motion and damageability power were investigated (Casolo et. al, 1994) and fragility curves of buildings of different levels of vulnerability were derived (Grimaz et al. 1997). Riuscetti et al. (1997) and Carniel et al. (2001) elaborated statistically the Fr.E.D.'s data and defined six classes of vulnerability (meaningfully different) corresponding to six typologies of buildings.

Grimaz et al. (1996) developed an expert system for damage assessment of buildings in the seismic area, based on functional criteria and on a scale of synthetic damage judgements (GSD scale). The GSD scale allowed us to relate the physical damage to the indirect consequences, as: reparability, usability and possibility to cause victims. This scale was also related to the levels of the EMS98 damage scale (Grünthal, 1998)

Other studies carried out in the fields of geology, seismology and seismic hazard by researchers of the University of Trieste and the Experimental Geophysics Observatory of Trieste (an overview can be found in Carulli and Slejko, 2005).

Second phase

Taking into account the new knowledge derived from the "*a posteriori*" studies developed in the first phase, the research group of the University of Udine, together with the researchers of the other two scientific institutions, began to support the Civil Protection of the Friuli Venezia Giulia Region in the definition and implementation of actions with a multidisciplinary risk approach.
Three main projects were designed and carried out (fig. 1).

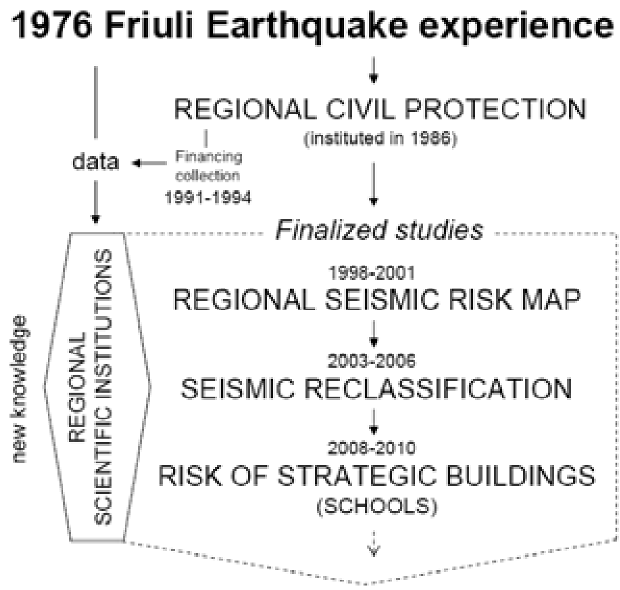

Figure 1. Interaction between civil protection and scientific institutions for the applied research in the seismic risk management field

The first two projects have been completed, while the last one has just started. It is interesting here to underline that each finalized study has been generated by the results of the previous one. The seismic risk map was proposed taking into account the knowledge derived from the studies carried out in the first phase, in particular in the field of vulnerability. We can say that the "*a posteriori*" studies on the 1976 Friuli earthquake data have permitted to set out the basis for the development of seismic risk studies and, together with the results of the finalized studies, have also produced useful lessons to learn from the point of view of seismic risk.

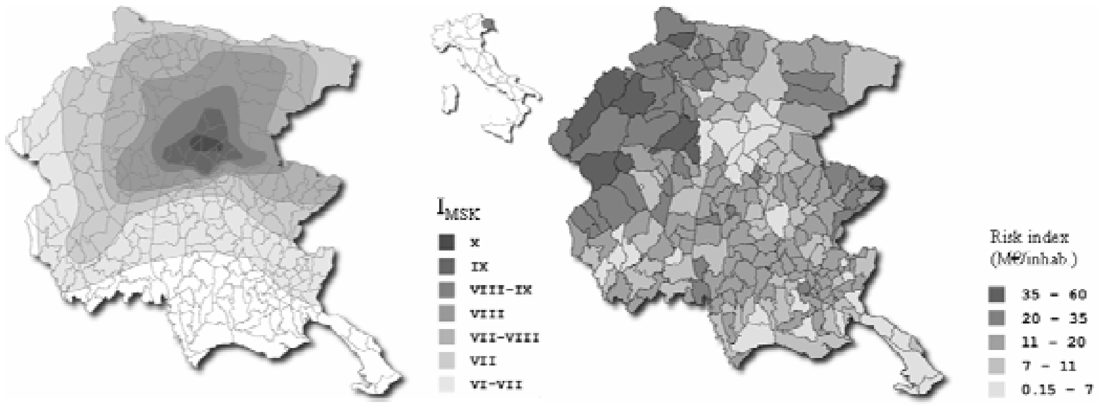

Figure 2. Comparison between I_{MSK} macroseismic map of 1976 May Friuli earthquake (at left) and seismic risk map of Friuli Venezia Giulia Region (at right). *In the risk map the darker is grey the higher is the risk of the municipality (M€/inhabitant for recovering predicted damages)*

Lessons to be learnt

The lessons to be learnt from the "*a posteriori*" studies on the 1976 Friuli earthquake experience and from the more recent applications of the politic on risk management in the Friuli Region can be summarized referring to the main components of the UNESCO's conceptualization of risk.

About the hazard:

In a region of moderate seismic activity a probabilistic approach is preferable. Two types of event must be taken into consideration: the more frequent with destructive power, in the short period, and the biggest foreseeable, in a long period.

Caution has to be exercised in order to define the maximum event predictable on the base of the historical earthquakes catalogue. For the 1976 Friuli case, never in the previous 2,000 years had another event of the same magnitude been observed. In order to resolve this problem, the same researchers working in the finalized project cited above, in a recent study on the Venetian-Friulian area (AA.VV., 2008), have proposed the consideration of different hazard scenarios. In particular they have taken into account not only the historical earthquakes but also those evaluated as possible on the basis of seismo-tectonic considerations, even though they are not included in the seismic catalogue.

The differences in terms of local effects in a Region with flat plains, hills, mountains, and valleys are relevant. A recent study based on Fr.E.D. database information (Grimaz, 2008, submitted) quantified the morphologic effects founding they are larger than lyto-stratigraphic effects. Secondary effects of hazard must be taken into account in the definition of seismic actions on the elements at risk.

About the element at risk:

Not only people and buildings constitute elements at risk. Loss can be also recorded in term of the compromisation of the functionality or performance of infrastructures, life-lines, social relationships, etc. Different types of losses can be strictly correlated. Cultural and sociological values have a great role in the post earthquake dynamics and in the human behaviour. Disaster contributes to the provision of evidence to the priority given to the values by the community affected.

About the vulnerability:

In an area of moderate seismic activity, the vulnerability is the principal element defining the damage and the main parameter from which it is possible to define preventive actions for risk reduction. This means that the vulnerability must be well known before the earthquake. Also, the strategies for its reduction must be applied, thus optimizing the resources available. Both the vulnerability of the physical system and the vulnerability of organizational and sociological systems must be taken into account. Tools for prediction of impact scenarios in terms of usability and potential deaths, should be developed (Grimaz, 2008, *submitted*).

About the risk in the post restoration:

The restoration interventions after a disaster could determine a disparity between the level of risk in the affected area and the level of risk in the surrounding area. Integrative interventions should be actuated to equalize the level of risk in the whole territory This fact is clearly shown in the previous figure 2 where the actual lower seismic risk levels in the Friuli Venezia Giulia region (right picture) correspond to the epicentral area of the isoseismic map (left picture).

About the risk management approach:

Civil protection has to manage a plurality of risks (of natural and man-made origin), therefore a global vision allowing us to manage at the same time the different risks of a region would be desirable. There is still a lot of differences in the language of the different subjects managing the risk, either among scientists of different disciplines and among technician of public institutions involved in different type of risk management. The introduction of a common language is extremely important.

Other lessons:

A global systematic and finalized registration of the data of the various aspects of the disaster immediately after the event and during all the successive period has an enormous value for improving knowledge. The lessons learned deriving from "*a posteriori*" analyses of the data constitute a fundamental basis for activity of prevention and contribute to the preparedness in terms of definition of the best ways and strategies of data collection for the future. But if on one hand the analysis of past experiences is a useful action of prevention, on the other hand it is necessary to keep memory of the data of the past, because it is not so easy to rebuild them even just a few years later.

Toward an holistic and multidisciplinary vision of seismic risk management

The original UNESCO's model R=R(H,V,E) has been developed by the researchers of the University of Udine who have given to the vulnerability a more extensive meaning within a cause-effect interpretation of the problem.

In particular an holistic conceptual model, compatible with the UNESCO original formulation , has been elaborated. In that model hazard, vulnerability and elements at risk, even though they are separate concepts, are considered together. A damage process, in a logic of cause and effect, is taken as reference (fig. 3). The elements at risk are individuated as target containing values recognized as such (human life, strategic values, economic values, etc) on which one or more adverse actions (the seismic action or other indirect actions caused by earthquake like landslides, differential failure, ect.) can act. In this conceptualization the vulnerability describes the response characteristic of the systems containing the values, in terms of concurrence in the damageability.

CAUSE → EFFECT

action → response → consequence

Figure 3. Exploitation of a cause-effect problem in an elementary process conceptualization

The elementary process defined in fig. 3 can be transformed in a more elaborate conceptual process which considers an adverse event producing adverse actions on a system containing a target with values (fig. 4). In this formulation the losses occur when the adverse action reaches and interacts with the target with an adverse power capable of producing a negative alteration of the value. The formulation could be compared directly to the UNESCO's components of risk.

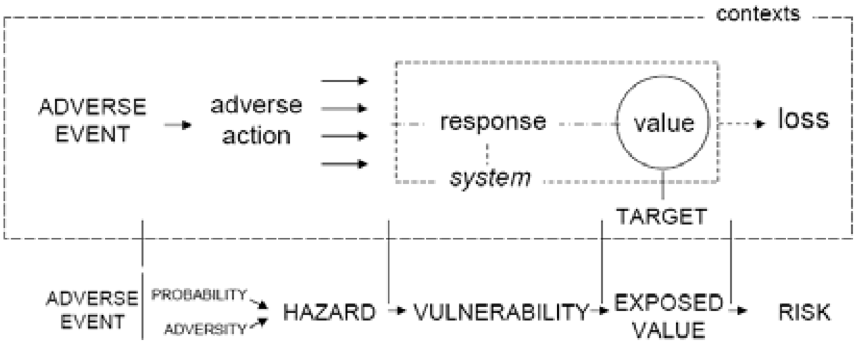

Figure 4. Correspondence between the holistic process formulation (above) and the UNESCO's combination of risk component (below)

For the case of seismic risk, the adverse event is the earthquake. If we consider the human life as exposed value and the people as the target, the response of the buildings to the ground motion defines one type of vulnerability. With this conceptualization, a plurality of sub-systems and their interrelations can be considered in the vulnerability definition (physical, engineering, sociological, economic, human behavioural, etc) and such an approach allows us to consider that the whole seismic scenario can be read within an unique global interpretative scheme.

On the basis of this vision, recently the research project on scholastic buildings in the Friuli Venezia Giulia Region has just commenced. More than 1200 buildings will be inspected and characterized in terms of seismic risk. Landslope and idrogeological risks will be also taken into account. The study will be a first test of interaction of different disciplines that so far have worked separately. The priority of intervention on the schools will be defined considering the different types of potential actions that could be interact with the values present or associated to the schools. As values, people and strategic function of the school in the ordinary and emergency situations will be considered.

Conclusions

The studies developed after the 1976 Friuli earthquake demonstrated that, if a disaster is regarded as an experience from which it is possible to learn, it could be an important occasion to improve the scientific knowledge and the capability to manage a complex problem. But this is possible only if the data of the experience has been, in some manner, recorded.

Sudden and massive disasters, such as earthquakes, are a "total" phenomena because they affect the physical and social aspects of human living. The holistic understanding of all the factors contributing to a successful disaster-risk management cannot be provided by any single discipline. Technical adequacy of the mitigation policies are not valuable without proper geological and engineering knowledge; and at the same time, we cannot understand post-earthquake dynamic without analysing the socio-cultural, political and economic configuration of the affected society. In a few words, what the Friulian community has learnt from the past disasters is that the management of risk reduction is a multidisciplinary task requiring an holistic and systemic approach. It is now known that it is opportune to generate a synergyic intraction between public administrators and researchers, so to take into account the lessons to be learnt, the operative needs, and to allow the transfer of knowledge.

The holistic vision illustrated above can help in the advancement of this proposal.

Acknowledgements

The largest part of the studies has been developed thanks to the funding of Civil Protection of Friuli Venezia Giulia Region and Italian National Council of Research and has been carried out in collaboration with the regional scientific institutions. My best sincere thanks to the leaders of the research units: prof. M. Riuscetti, dott. D. Slejko, prof. G.B. Carulli, prof. F. Cucchi, and to the Director of the Civil Protection, dott. G Berlasso.

References

AA.VV. (2008). Seimic damage scenaios in the Venetia-Friulian area, *Boll. Geof. Appl., 49, in press*

Barbina G (1979). The Friuli earthquake as an agent of social change in a rural area, *Mass Emergencies, 4, 145-149*

Carulli G.B. & Slejko D. (2005). The 1976 Friuli (NE Italy) earthquake, *Giornale di Geologia Applicata, 1, 147-156*

Carniel R., Casolo S. & Grimaz S (1994). Caratterizzazione sintetica degli accelerogrammi e stima del danno strutturale atteso tramite un modello di strutture in muratura geometricamente regolari, *Ingegneria Sismica n. 2/94 Patron, Bologna, 55-64*

Carniel. R., Cecotti C., Chiarandini A., Grimaz S., Picco E. & Riuscetti M (2001). A definition of seismic vulnerability on a regional scale: the structural typology as a significant parameter, *Boll. Geof. Teor. Appl.* , *42, 1-2 , 137-157*

Cattarinussi B., Pelanda C. & Moretti A (1981). Il disastro: effetti di lungo temine, *Grillo Editor Udine 21*

CNR-PFG (1980). Proposta di riclassificazione simica nazionale, *ESA Editor, Rome.*

Dolgioni F., Moretti A. & Petrini V (1994). Le chise e il terremoto, *Lint Editor Trieste.*

Fournier D'Albe E.M (1979) Earthquake prediction and risk management, UNESCO Paris

Geipel R (1980a). Friuli. Aspetti sociogeografici di una catastrofe sísmica, *Geografia, Roma, 161-162*

Geipel R (1980b) Il progetto Friuli, *Quaderni di Ricostruire*, *Strassoldo Editore, Udine.*

Grimaz S (1993). Valutazione della vulnerabilità sismica di edifici in muratura appartenenti ad aggregati strutturali sulla base di analisi a posteriori, *Ingegneria Sismica n. 3/93– Patron, Bologna, 12-22*

Grimaz S., Meroni F., Petrini V., Ranù G., Tomasoni R. & Zonno G (1996). Expert system for Damage assessment of buildings in seismic areas, *Cahiers du Centre Européen de Géodynamique et de Séismologie Volume 12. Luxembourg*

Grimaz S., Meroni F., Petrini V., Tomasoni R. & Zonno G (1997). Il ruolo dei dati di danneggiamento del terremoto del Friuli nello studio di modelli di vulnerabilità sismica degli edifici in muratura, *in La scienza e i terremoti Forum editor, Udine, 89-96*

Grünthal G. editor (1998). European Macroseismic Scale 1998, *Cahiers du Centre Européen de Géodynamique et de Séismologie Volume 15. Luxembourg*

Riuscetti M., Carniel R., & Cecotti C (1997). Seismic vulnerability assessment of masonry buildings in a region of moderate seismicity, *Annali di Geofisica*, *40, 1405-1413*

Contribution to Recent Seismicity Evaluation in Surroundings of High Dam, Aswan, Egypt

Haggag H M (1), Kaláb Z (2), Lednická M (3)

(1) Aswan Earthquake Research Center, P.O. Box 152, Aswan, Egypt, haggaghm@yahoo.com
(2) Institute of Geonics of the ASCR, Studentská 1768, CZ 708 00, Ostrava – Poruba, Czech Republic; also VSB-Technical University of Ostrava, kalab@ugn.cas.cz
(3) VSB-Technical University of Ostrava, 17. listopadu 11, CZ-708 33 Ostrava – Poruba, Czech Republic, also Institute of Geonics of the ASCR, Ostrava, lednicka @ugn.cas.cz

Keywords: recent seismicity, High Dam, explosion

Introduction

Aswan reservoir on the Nile River in the southern Egypt, called High Dam, is one of the largest reservoirs in the world that controls the electricity and irrigation in the prevailing part of country. Construction of the High Dam began on 1960 and completed on 1972. The reservoir extends over about 500 km in the Egyptian and Sudan territory; it has a capacity of approximately $162*10^9$ m^3, of which about $130*10^9$ m^3 is effectively considered for live storage. The maximum water depth in the dam site area is about 111 m. The reservoir was filled in 1964 and reached a water level of above 177.47 m above the mean sea level on November 1978, which correspond to an average depth of 50 m (according to Selim et al., 2002).

Many dam designers and operators have tended to close their eyes to the engineering problems posed by reservoir induced earthquakes. This is because of four factors (for details see www.seis.com.au/Basics/Dams.html):

- Dams are often built in active earthquake areas.
- Reservoirs can trigger earthquakes.
- Some water supply structures are susceptible to earthquake motion.
- The consequence of a dam or water supply failure is high.

Summary of 10 largest reservoir induced earthquakes is possible to find on asc-india.org/gq/ris10.htm (Tab.1). The earthquakes at Aswan (Egypt, 1981, M_L = 5.6) and Burragorang (Australia, 1973, M_L = 5.5) were also in the magnitude range than 5.5. However, due to a lack of information regarding a comparable magnitude they have not been included. Reservoir seismicity has been observed at many dams all over the world and the list presents only the ten largest events for which seismic information was available. The seismic activity at Lake Crowley, believed to have been reservoir related, is considered doubtful. A rough estimate of the moment magnitude of the Xingfengjiang earthquake has calculated using an empirical relation between surface-wave magnitude M_S and moment-magnitude M_w as determined by Chen.

Studies that described knowledge about reservoir induced seismicity were published, e.g. Allen (1982), Gupta (1992) and Talwani (1997).

This study summarizes results that document increasing of seismicity in Aswan area after filling of reservoir.

Table 1. Summary of 10 largest reservoir induced earthquake (asc-india.org/gq/ris10.htm)

No.	Date	Origin time UTC	Magnitude M_w	Location
1	11 December 1967	22:51:19	6.6	Koyna, India
2	5 February 1966	02:01:45	6.2	Lake Kremasta, Greece
3	19 March 1962		6.2	Xinfengjiang, China
4	20 July 1938	00:23:35	6.0	Oropos, Greece
5	22 April 1983		5.8	Srinagarind, Thailand
6	1 August 1975	20:20:12	5.8	Oroville, U.S.A.
7	23 September 1963		5.8	Kariba, Zimbabwe
8	13 April 1969	17:58:39	5.7	Kinnersani, India
9	14 September 1941	18:39:12	5.4	Lake Crowley, U.S.A.
10	4 October 1978	16:42:48	5.4	Lake Crowley, U.S.A.

Aswan area seismicity

The Aswan High Dam is located in a region of very infrequent earthquake occurrence, as revealed by 5000 years record of Egypt. Thus, the sudden occurrence of the November 14, 1981 earthquake (M_s 5.3) with its large number of aftershocks was a significant concern to scientists and engineers either inside Egypt or internationally. The occurrence of this sequence of earthquakes raised broad questions about the possibility of future local earthquake activity and the seismic safety of the Dam. In particular, the proximity of the earthquake activity to the lake High Dam and the lack of reported earthquake activity prior to the filling of the reservoir have suggested the possible influence of the reservoir as an earthquake triggering machine. The recorded earthquake history began about 5000 years ago with the hieroglyphic texts of Pharaonic Egypt, and is continuing in the present with the operation of microcomputer-based Telemetry seismic Network by the Helwan Institute of Astronomy and Geophysics, Department of Seismology staff.

For a long time, Aswan area was considered aseismic area where no earthquakes were reported, except some historical events that have been taken place inside the area. However, recording of many events with low or moderate magnitude after filling of the Aswan reservoir in 1964 and the installation of Aswan seismic network in 1982 has suggested the possible influence of the reservoir as an earthquake-triggering tool. After the occurrence of the 1981 earthquake, a local seismic network was installed around the northern part of Aswan reservoir to monitor the seismic activity in the area. A review of current seismicity and referring seismological studies were published, e.g. Mohamed (1997, 2003), Selim et al. (2002) and Haggag et al. (2008).

Geology and tectonics of the Nile Valley

Said (1962, 1981) and Issawi (1981) studied the area of the Nile Basin. These papers were aimed at obtaining information about the drainage system, the stratigraphy and structural geology on this part of Egypt. The stratigraphy of the Nile Valley, extending from Assiut to Aswan, is generally dominated by a sedimentary succession ranging from lower Cretaceous to Pleistocene-Holocene (Quaternary) (Fig. 1). It has an average thickness of about 1500 m. The thickness of the sedimentary succession decreases southward until it reaches 60 m in certain locations such as west Aswan City where the sediments are composed mainly of Nubia formation of Cambrian to Cretaceous (Issawi, 1981). These sediments overlie, unconformably, the Pre-Cambrian basement. The Nubia formation is mainly composed of sand and sandstone with some clay and shale intercalations.

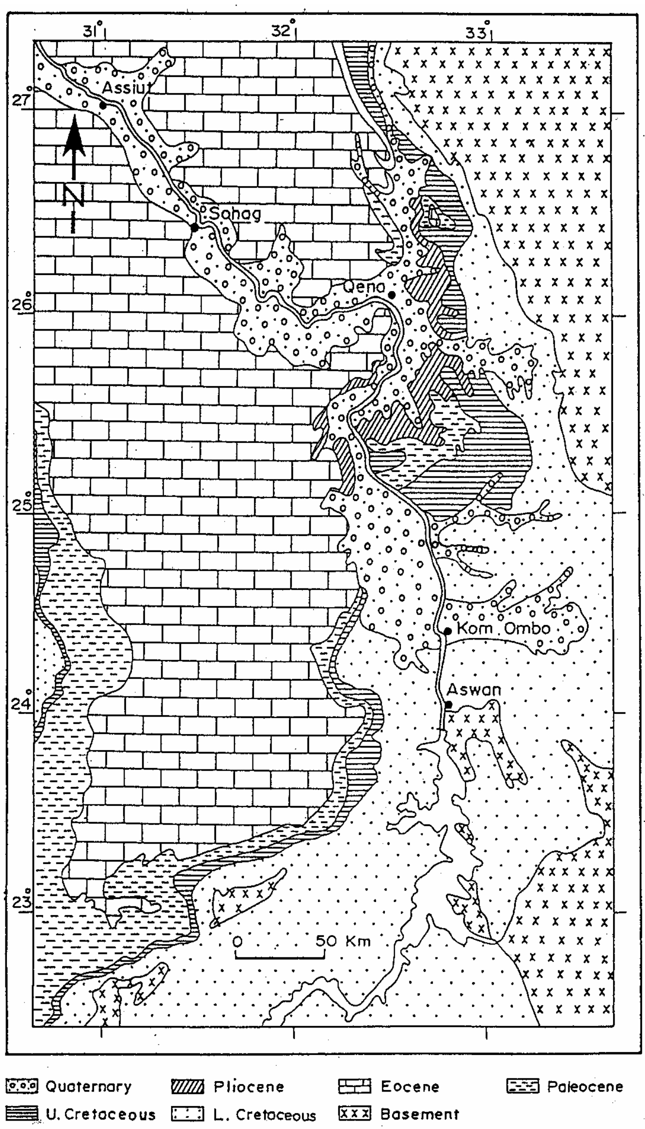

Figure 1. Geological map of the Nile Valley and surrounding parts (compiled after The Egyptian geological survey and mining authority, 1981).

WWCC, 1985, showed that the nature of the tectonic stress system presently acting on and within the Aswan region is indicated through two lines of evidence; a) earthquake focal mechanism and b) the pattern of late Cenozoic faulting. This evidence directly reveals the effect of the stress regime and from the causative stresses or sets of stresses may be inferred.

a) Earthquake focal mechanisms: As a result of the very low level of seismicity in Upper Egypt, few large earthquakes within and near the study area have been sufficiently well recorded to obtain focal mechanism solutions.

b) Late Cenozoic faulting: Within the Aswan study region the late Cenozoic faulting has been observed in two areas; predominantly normal faulting on the Red sea fault system east of the crest of the Red Sea Mountain; and strike slip faulting on the faults of the western desert fault system.

The western desert faults that cross the area are classified into several systems depending on their trends; the most important of these are the east-west system that exhibit right-slip displacement, and the north-south system that exhibit left-slip displacement. The east west faults dominate in the region, they are longer and have larger total displacements than the north south faults (Fig. 2). The E-W fault system includes a) Kalabsha fault that crosses along Gabel Marawa, it was identified as the most active fault in the area and the source of 1981 earthquake, it is also dominated by a right-lateral slip motion (Kebeasy et al., 1987) and b) The Seiyal fault, it is about 12 km to the north of Kalabsha fault. The N-S fault system includes Gabel El-Barqa fault, Kurkur fault, Khour El-Ramla fault, Gazelle fault and Abu Dirwa fault.

Aswan Telemetric Seismic Network

After the main shock of November 14, 1981, it was of great importance to monitor and to study the seismic activity in this area, particularly for the safety and stability of the Aswan High Dam.

In late June 1982, a telemetric seismic network of eight seismograph stations was installed around the northern part of Aswan reservoir. A ninth station was added in December 1982, after that in 1985 the Network was expanded to thirteen stations. It is now a part of the Egyptian National Seismic Network and operates by the satellite system. The main purpose of this network was to monitor the seismic activity along the Kalabsha fault which continuously occurs in the area (Kebeasy et al., 1987). Fig. 3 shows the geographical location of the seismic stations.

Seismic zones

The largest recorded earthquake that took place in Aswan area in the recent history occurred on November 14, 1981 with a magnitude 5.3, the event has been occurred at Gebel Marawa (Kebeasy et al., 1987). The main shock was distinctly felt as far as Assiut (450 km to the north of Aswan) and Khartoum, Sudan (650 km to South). Since that time, the Aswan area considered to be a low active seismic area.

Most of the seismic activity in the area concentrates in the intersection between the east-west and north-south fault systems. The most active zone is located on and around the east-west Kalabsha fault as shown in fig. 2.

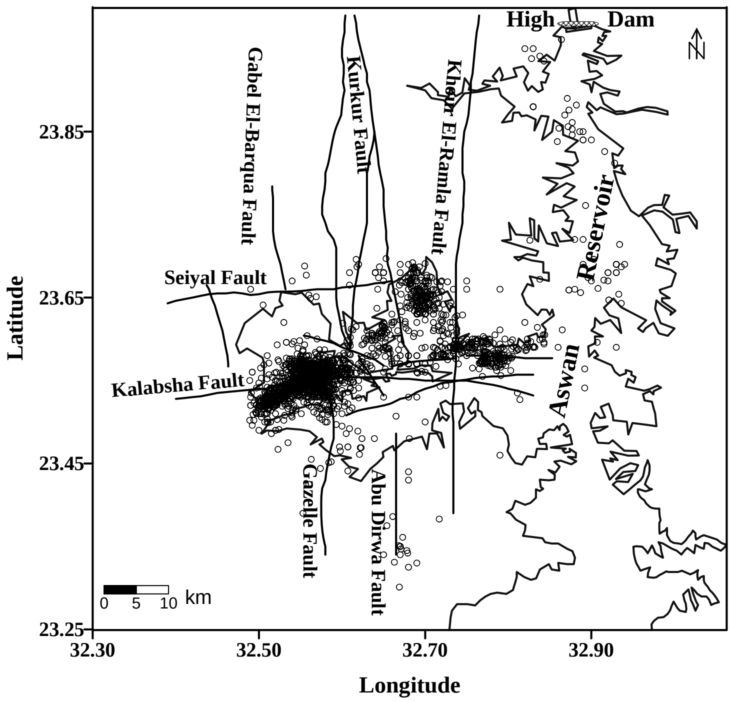

Figure 2. Location map of the earthquake epicenters recorded during the period from1982 to 2007 and the significant faults in the area

The fig. 3 indicates that the activity is concentrated in the Kalabsha area and can be divided into the following seismic zones according to the level of the seismic activity.

Seismic Zone (A)
A few number of events were located to the west of the High Dam, they are of low magnitude and focal depth.

Seismic Zones (B) and (C)
Scattered micro-earthquakes have occurred in the River Nile channel north of the Kalabsha faults .These events are not associated with Dabud fault which lies east of the cluster, but they may be associated with a major North-South fault trend (Youssef, 1968).

Seismic Zone (D)
It is a zone of the highest seismic activity, with focal depths almost between 15-25 km, which is concentrated in and around the Gebel Marawa seismic station along the most active Kalabsha fault and in which the main shock is occurred (Kebeasy et al., 1987).

Seismic Zone (E)
This zone lies 20 km east-north east of GMR seismic station. It represents the activity aligned along the Kalabsha fault trend. Magnitude range is between 1.7 - 3.4 with focal depth between 2-7 km.

Seismic Zone (F)
It is a very shallow zone relative to zone (A), with a focal depth between 1-3 km. It lies to the east of seismic zone (E) along the Kalabsha East - West fault.

Seismic Zone (G)
It lies to the West of Khore El-Ramla fault near KRL seismic station. It can be considered as the second active zone after Marawa zone and characterized by a focal depth extends down to 8 km.

Seismic Zone (H)
The Abu Dirwa seismic zone, it is located near the NAL seismic station along the Abu Dirwa N-S fault, the general character of the fault suggests that it has a low degree of activity (WWCC, 1985).

The activity in Kalabsha area as a general can be also divided according to the focal depth into two seismic zones with different focal depths as following: a zone with focal depth less than 12 km, and another one with focal depth greater than 12 km.

Discrimination between earthquakes and explosions

Earthquakes have foci usually deeper than explosions, with different media physical behavior and surface influence, and, therefore, their respective wave fields possess different kinematic characteristics. The enhanced development of regional surface waves from shallow events is well known and widely used to make easier discriminations mentioned in heading. In recent years, many investigators have demonstrated different solutions of this problem, e.g. using amplitude, spectra, spectral ratios, velograms (e.g. Baumgardt and Zigler, 1988, Kim et al., 1994, Pinski et al., 1996). To solve the problem of discrimination between earthquakes and explosions in the Aswan area, our initial studies were performed.

The first results of elaboration indicate that spectral analysis (Fast Fourier transform) of velocity records from seismic stations in Aswan area is possible to use for fast decision. Typical spectrum of earthquake is presented in fig. 4, typical spectrum of explosion in fig. 5. Both events were recorded at station KRL that is situated near reservoir (zone G). The main difference is narrow interval in small values of frequencies for explosions and broadband spectrum for earthquakes. However, it was also documented more complicated spectra for booth types of events.

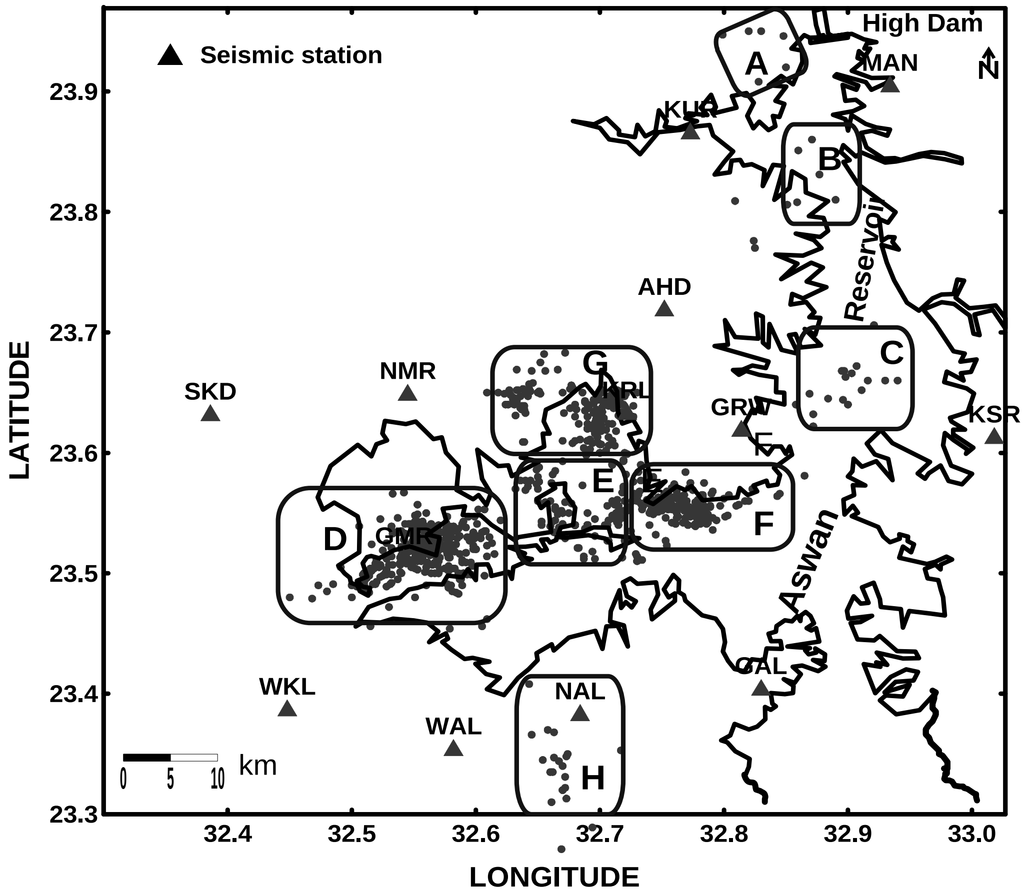

Figure 3. Sketch of position of seismic stations, epicenters location (monitored by Aswan Telemetric Seismic Network during 1981-2007) and seismic zones

Conclusion

Current pattern of seismicity in the Aswan area was presented in this paper. Today, set of recorded events is compound of three types of records: earthquakes, reservoir induced earthquakes and seismic events generated by explosions in quarries. To discriminate explosions from earthquakes of both natures, spectral analyses of records are possible to use for fast decision. The main difference is narrow interval in small values of frequencies for explosions and broadband spectrum for earthquakes. However, this is the simplest method and detailed study has to come after. Simultaneously, it is studied the discrimination using other techniques as amplitude ratio of P and S wave (e.g. Dahey, 1997).

Whole studied region with recorded epicenters is possible to divide into eight geographical zones (zone A – zone H, see fig. 3). These zones are possible to be described using not only geographical viewpoint but also basic parameters of earthquakes. Evaluation of seismicity in the area under study is concentrated in the Kalabsha part (e.g. Haggag et al., 2001). At the same time, studies that evaluated the effect of the fluctuation of the water level in reservoir are performed (e.g. Haggag and Sayed, 2001, Selim et al., 2002, Mekkawi et al., 2004).

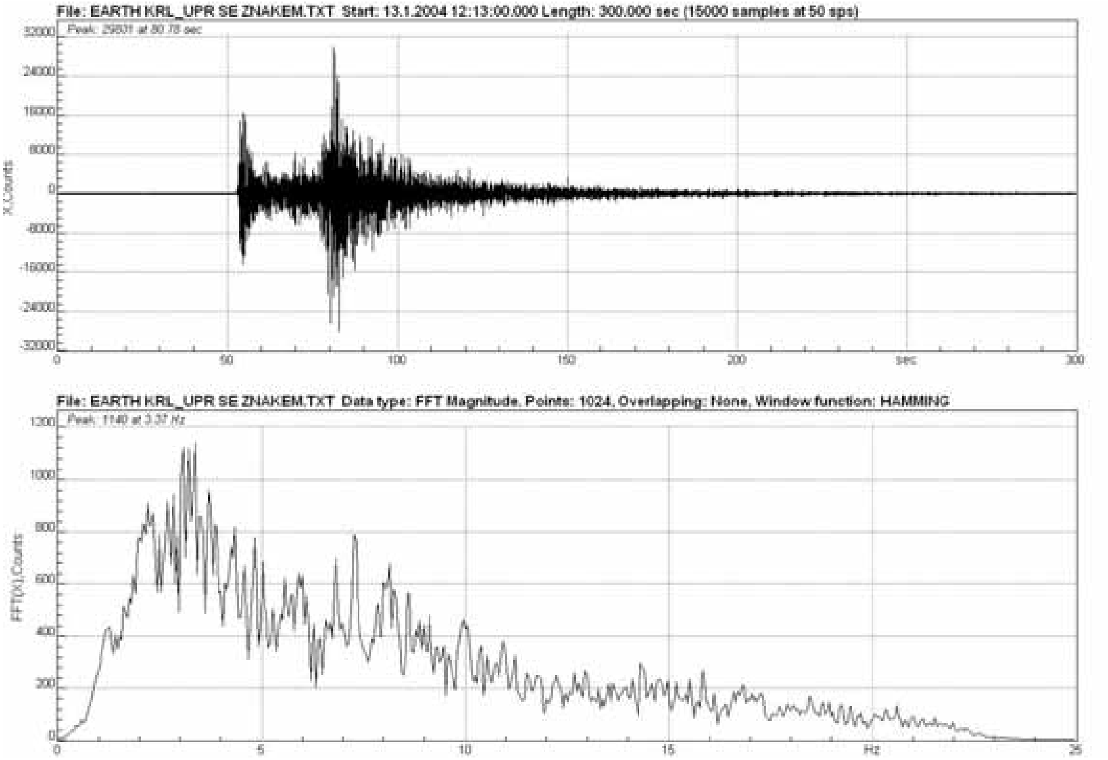

Figure 4. Wave pattern (Z component) and relevant FFT spectrum of earthquake (January 13, 2004) recorded at station KRL

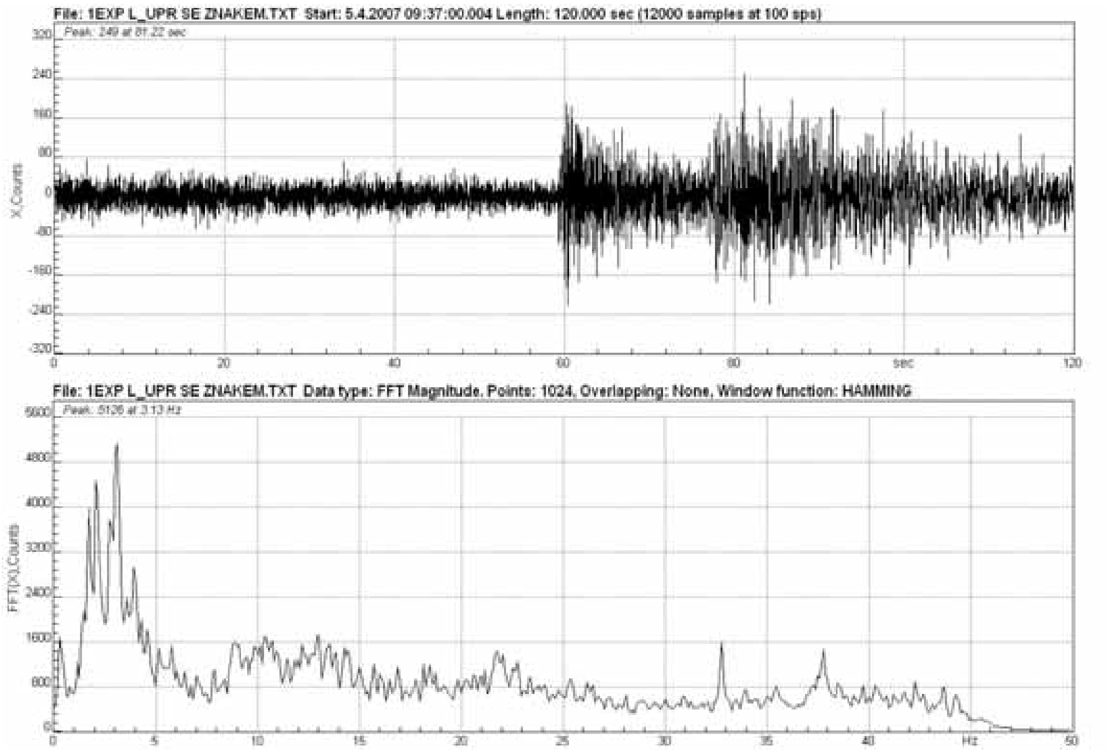

Figure 5 Wave pattern (Z component) and relevant FFT spectrum of explosion (April 5, 2007) recorded at station KRL

Acknowledgement

This research is partly sponsored by Research Programme of Academy of Sciences of the Czech Republic, OZ30860518

References

Allen C. R (1982). Reservoir-induced earthquakes and engineering policy, *California Geology, Vol. 35, No. 11, www.johnmartin.com/earthquakes/eqpapers/00000054.htm*

Baumgardt D. R. & Zigler K. A (1988). Spectral evidence of source multiplicity in explosions: application to regional discrimination of earthquakes and explosions, *Bull. Seism. Soc. Am., 78, 1773-1795.*

Dahey (1997). Seismic methods for monitoring and identification of underground explosions. *Ph.D. thesis, Aswan Faculty of Science, South Vallay University.*

Gupta H.K (1992). Reservoir-induced seismicity, Developments in Geotechnical Engineering. Elsevier.

Haggag H. M. & Sayed A. D (2001). Relation between daily fluctuation of the water level and earthquake size at Aswan reservoir, Egypt, *The second international conference on the geology of Africa, Proceedings, Vol. I B, 725-733.*

Haggag H. M., Tae-Seob K. & Chang-Eob B (2001): Focal mechanism determination based on the polarity and SV-P amplitude ratio in the Kalabsha area, Aswan, Egypt, *Geosciences Journal, Vol. 5, No. 2, 165-171.*

Haggag H. M., Gaber H. H., Sayed A. D. & Ezzat M. El-A (2008). A review of the recent seismic activity in the southern part of Egypt (Upper Egypt), *Acta Geodyn. Geomater., Vol. 5, No. 1(149), Prague, 19-29.*

Kebeasy R. M., Maamoun M., Ibrahim E., Megahed A., Simpson D. W. & Leith W (1987). Earthquake studies at Aswan reservoir, *J. Geodynamics, 7, 173-193.*

Kim W. Y., Simpson D.W. & Richards P. G (1994). High frequency spectra of regional phases from earthquakes and chemical explosions, *BSSA, 84, 1365-1386.*

Mekkawi M, Grasso j.-R. & Schnegg P.-A. (2004). A long-lasting relaxation of seismicity at Aswan reservoir, Egypt, 1982-2001, *BSSA, Vol. 94, No. 2. 479-492.*

Mohamed H. H (1997). A study about the characteristics of the seismic activity at Kalabsha area and Aswan reservoir, *Ph.D. Thesis, Qena Faculty of Science, South Valley University.*

Mohamed H. H (2003). Seismic energy released and its relation to the water level, water capacity and seismic activity in Aswan reservoir and its vicinity, *J. Appl. Gopphs., Vol. 2, 261-266.*

Pinski V., Shapira A. & Gitterman Y (1996). Multi-channel velogram analysis for discriminating between earthquakes and quarry blasts, *In: Seismology in Europe, Proceedings of ESC, Reykjavík, Iceland, 581-586.*

Said R (1962). Geology of Egypt, *Elsevier Publishing Company, Amsterdam, New York, 377 pages.*

Said R. (1981). The geological evaluation of the river Nile, *Springer, 152 pages.*

Selim M.M., Imoto M. & Hurukawa N. (2002). Statistical investigation of reservoir-induced seismicity in Aswan area, Egypt, *Earth Planets Space, No. 54, 349-356.*

Talwani P (1997). On the nature of reservoir-induced seismicity, *Pure Appl. Geophys., No. 150, 473-492.*

Youssef M.I (1968). Structural pattern of Egypt and its interpretation, *The American Association of Petroleum Geologists Bulletin. 52(4), 601-614.*

WWCC (Woodward-Clyde Consultant) (1985). Identification of earthquake source and estimation of magnitudes and recurrence intervals, *Internal report, High Dam Authority, Egypt. 135 pages.*

Ground Motion Analysis of the 2003 Zemmouri, Algeria, Earthquake

Hamdache M (1), Peláez J A (2), López Casado C (3)

(1) CRAAG, B.P. 63-Bouzaréah, 16340-Algiers, Algeria, mhamdache@hotmail.com
(2) Dpt. of Physics, University of Jaén, Jaén, Spain, japelaez@ujaen.es
(3) Dpt. of Theoretical Physics, University of Granada, clcasado@ugr.es

Keywords: strong ground motion, 2003 Zemmouri earthquake

Introduction

On 21 May 2003, an earthquake with magnitude Mw 6.8 (Ms 6.9) struck the environs of Algiers, the capital of Algeria, causing extensive damages in different provinces in the north-center of the country. This earthquake took place where we have no evidence of previous significant earthquakes, either instrumental or historical. It was been felt with macroseismic intensity IX-X in two small cities near the epicenter, Boumerdes and Zemmouri, and an intensity of VII-VIII in several districts of Algiers, where many modern building collapsed and many others were seriously damaged. It has been one of the most destructive events in northern Algeria since the 10 October 1980, El Asnam earthquake (Ms 7.3) (Hamdache *et al*., 2004).

The northern Algeria area, as a part of the Ibero-Maghrebian region, have experienced different moderate to low seismic events as a result of the compressional movement between the African and Eurasian plates. The tectonics of this region has been the subject of numerous studies, including Meghraoui (1988), Yielding *et al*. (1989), and Aoudia and Meghraoui (1995). The main structures are briefly and clearly summarized in Peláez *et al*. (2003, 2005). The studied earthquake occurred at the eastern part of Algiers city, in the region of Boumerdes, which is located on the coast, in the central part of Algeria. Much of the coastal area is characterized as broad alluvial plains punctuated by metamorphic rocks from the Atlas thrust belt to the south. The gently sloping alluvial plains have been uplifted by past earthquakes. The marine terraces along the coastline have been uplifted at an estimated rate of about 0.25 mm/yr (Wang *et al*., 2004). This region is the eastern edge of the Quaternary Mitidja basin (figure 1), which has been formed during north-south Miocene extension (Philip, 1983).

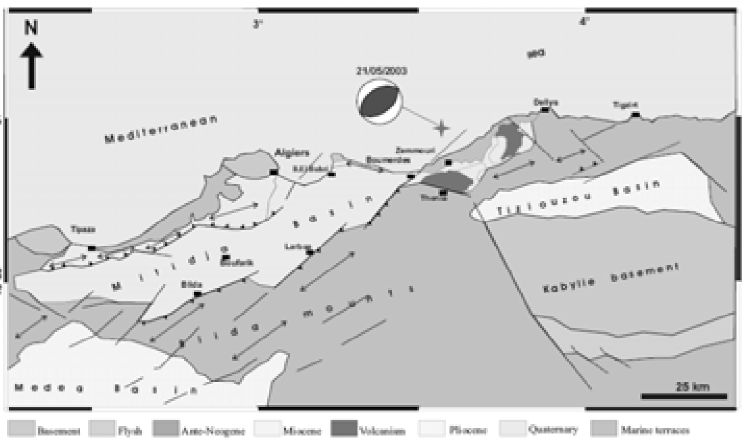

Figure 1. Tectonic map of the Mitidja basin (Ayadi *et al*., 2003)

This extension has been followed by a north-south to NW-SE compression. The compressional movement continued during the Quaternary (Meghraoui, 1988; Boudiaf *et al*., 1998) and is still active, as shown by recent recorded seismicity (Mokrane *et al*., 1994) and re-cent deformation. This deformation is represented by active folding oriented northeast-southwest (Meghraoui, 1988). The east-west to ENE-WSW trending Mitidja basin is bordered, as shown in figure 1, by the Mediterranean sea and Blida mountains to the north and south, respectively. Long term regional seismicity reveals several large earthquake in the Algiers region, including the 1365 earthquake (Io = IX), and the 28 January 1716 event, which was felt with intensity X, destroying Algiers and causing more than 20000 deaths (Mokrane *et al*., 1994). The region of Zemmouri and Boumerdes has been affected by recent small earthquakes with magnitude up to ML 5.3. The most important seismic event near Algiers during the twentieth century was on 16 September 1987 (mb 5.2). This earthquake did not cause significant damage. Others minor events occurred in the region including some felt events.

In this study, we present the results obtained in the processing of the accelograms recorded on 21 May 2003 earthquake, which occurred on the north-east edge of the Mitidja basin, on the Zemmouri coast.

Ground motion records

The 21 May 2003 earthquake was characterized by an offshore reverse faulting resulting from the compressional movement described above. The focal mechanism corresponded to an in-verse fault with ENE-WSW direction dipping towards the S (figure 2). The modelled rupture (Yagi, 2003) corresponded with a plane of 75 km in length and 20 km in width. The duration of the rupture modelisation was about 18 s, producing a maximum displacement throughout the surface of the fault of about 2.3 m (figure 2).

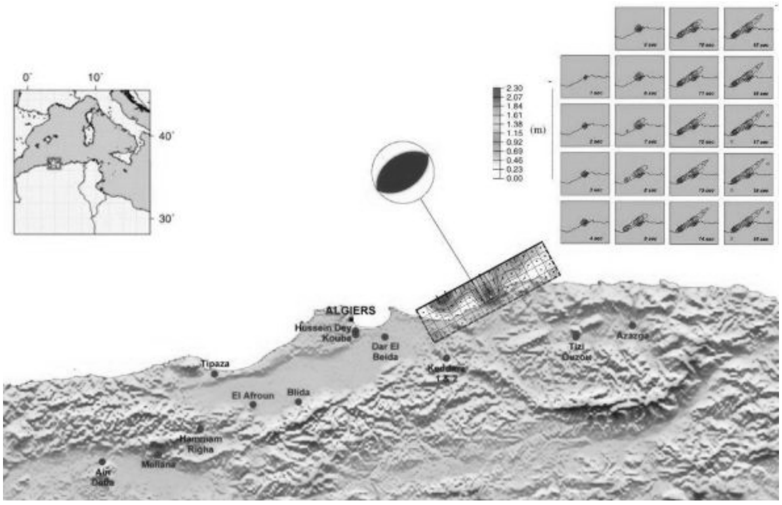

Figure 2. Map showing the modelled rupture (Yagi, 2003), the focal mechanism and the accelerograph stations that properly recorded this event

The rupture pattern is characterized by an asymmetric bilateral propagation of the rupture, propagating from the epicenter about 30 km towards the WSW. Two asperities are clearly distinguished. It is shown that the rupture propagation condition influences the obtained records at accelograph stations. At this point, the Algerian network of accelerographs, monitored by the CGS (Centre National de Recherche Appliquée en Génie Parasismique), consisted of a total of 87 stations; 29 digital stations (Etna and SSA-1), and the rest analogical ones (SMA-1, with photographic records). From all of them, only 13 records have been usable, corresponding to the stations shown in the figure 2. Unfortunately, the quality of these 13 records is not optimal, presenting and/or displaying some of them problems that determine their use and the results, like wrong operation of the instrument at diverse moments, spikes, and records without coda or pre-event.

As shown in the figure 2, most of the accelerograph stations are located to the SW of the fault area, with a very poor azimuthal coverage. Stations are located in different soil type as defined by CEN (2003): 3 stations are on soil type A (BLI, HAM and MEL), 8 on soil type B (TIZ, KED1, KED2, AZA, HUS, KOU, TIP and AIN), and the two others on soil type C (DAR and AFR). The distance of the stations to the rupture plane varies between 9.8 km (KED1 and KED2) and 136.0 km (AIN). The geological site conditions are related to the Quaternary Mitidja basin; almost of them can be characterized by a stuffed sedimentary river basin of alluvial quaternary deposits. Especially the two stations located at Dar El Beida (station DAR) and El Afroun (AFR) are exactly within the own river basin. It is important to point out that stations KED1 and KED2 are located at the same site and distant only 150 m. The first station is in the embankment of a dam, down, just on the basement, whereas the second one is something remote of the dam. Other two stations, HUS and KOU, are only 1.5 km distant.

Processed records

The previously quoted 13 accelerogram records have been considered as optimal. The records obtained at the different stations, shown in the figure 3, have been processed with great attention to derive reliable results for seismic engineering purposes. The records are used to derive in a first step the corrected acceleration, velocity and displacement time histories. The obtained results show some particularities.

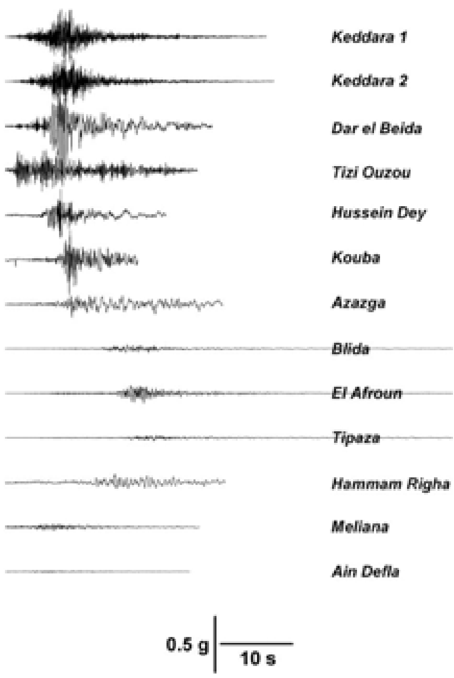

Figure 3. Corrected acceleration records. NS component

The predominance, in average, of the obtained results in the EW components, is opposed to the NS ones. In the opposite, the computed displacement shows a great predominance of the NS component. Considering the a_{rms} and maximum pseudo-acceleration spectra values derived for each component, in average, any predominance of any component on other is observed. The maximum obtained PGA value is equal to 0.59g, occurring at the KED2 station, on the EW component, which is associated to a frequency of 12.5 Hz. At the DAR station, a PGA value equal to 0.51g is obtained on the EW component, associated in this case with a frequency equal to 3.6 Hz. The same component at the DAR station provides a maximum computed PGV value equal to 40.3 cm/s, and a maximum computed PGD value equal to 17.3 cm. For each NS and EW component, the Arias and Housner intensities have been derived. For example, the obtained results at DAR station are the following. For the Arias intensity, 3.8 m/s for the horizontal intensity, and 4.2 m/s for the total intensity have been obtained. For the Housner intensity, 101 and 124 cm for components NS and EW, respectively, have been obtained. For the maximum pseudo-acceleration spectra, with a 5% damping, 2.06g and 1.94g, for NS and EW components, respectively, have been computed. The maximum displacement in the horizontal hodogram is equal to 18.6 cm. The particularity of the DAR station is the fact that it is located in the Mitidja basin (figure 2), at only 16.2 km of the rupture, on a soil type C and, just in the direction of the rupture propagation, showing a clear directivity effect. All these parameters have been clearly influenced the record in this station.

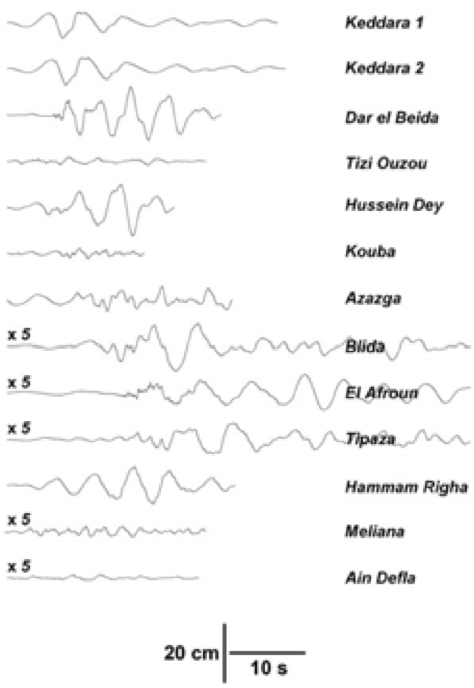

Figure 4. Computed displacements. NS component

The results displayed in figures 3 and 4 show a clear amplification at the HAM station, which is not explain by the site soil type (figure 2). At the stations BLI, AFR and TIP a clear ground wave pattern appear on the acceleration plots (figure 3), which is more clearly observed on the plot displaying velocity and displacement (figure 4). This result could be explained by the fact that stations are located on the border of the Quaternary Mitidja basin (figure 2) and some edge effect is observed.

The records at the two stations located around the Keddara dam (KED1 and KED2) show some similarities. The distance between these two stations is about 150 m, and computed displacements are practically the same. Nevertheless, in other two stations 1.5 km distant (HUS and KOU), any similarities appear neither on the acceleration records nor on displacement or velocity.

The 21 May 2003 earthquake is the most destructive event since the 1980 El Asnam earthquake. This event caused extensive damage on building. It is one of the most and best documented event from the macroseismic point of view (figure 5). Preliminary macroseismic investigations and macroseismic map have been published by Ayadi *et al*. (2003).

This map is considered at this moment the most appropriate, and it agrees very well with our computed data. It is possible to relate obtained instrumental results to the macroseismic intensity assigned to the site. Thus, station DAR is located within the isoseismal of degree VIII, stations HUS and KOU within the one of degree VII, and stations KED1, KED2 and BLI within the one of degree VI. The Dar El Beida site (DAR) is, comparatively to the other sites, where the higher macroseismic intensity and the biggest computed values for all parameters, except for the PGA value, are obtained.

The Housner intensity is probably the most appropriate value related to the damage level that we have computed at each station site. The obtained results are the following: 113 cm at the DAR site, 62 cm at HUS, 46 cm at KOU, and 33.4 and 31.9 cm at KED1 and KED2, respectively. The extensive damage on recent buildings, suggest us to compare the pseudo acceleration spectra derived from the recorded accelerograms at each station with the design spectra proposed by the CEN (2003) code and the uniform hazard spectra (UHS) obtained in previous works (Peláez *et al*., 2006) using a probabilistic approach.

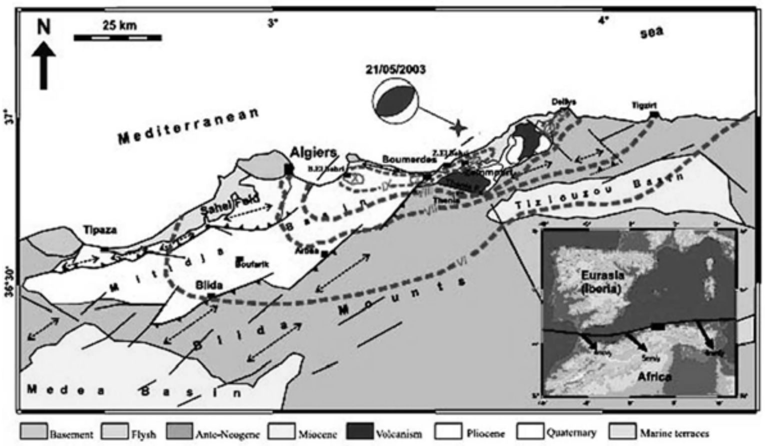

Figure 5. Isoseismal map for the 21 May 2003 earthquake (Ms 6.8) (Ayadi *et al*., 2003)

The pseudo acceleration spectra derived from records agree with the two others graphs in most stations, nevertheless, in other ones the computed pseudo acceleration spectra is clearly greater than the design spectra proposed by the CEN (2003) code and the UHS proposed in the paper by Peláez *et al*. (2006). The obtained results at the DAR station are shown in figure 6.

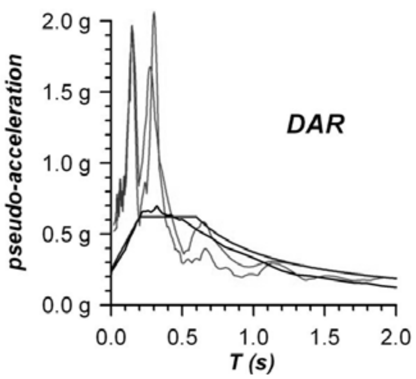

Figure 6. Pseudo acceleration spectra (in red) for the NS and EW components, UHS (in black) specifically computed for the site, and EC-8 horizontal elastic response spectra (in blue), all damped at 5%, for the DAR station

This case has been pointed out by other authors (v.g. Bommer et al., 2002) in other earthquakes. It proposes the fact to promote or not a change in the building code in the site or region, by considering or not this computed pseudo-acceleration spectra. In our case (figure 6), they appear values of about 2.0g in the range 0.0-0.4 s, a period range very interesting in any building code.

Finally, the duration of the records obtained from the horizontal components in the stations less than 25 km away of the rupture plane is of about 10.2 s.

Site effects, attenuation and directivity

Here we examine some aspects related to the site effects, ground motion attenuation and directivity in the occurrence of the main event.

The site effect has been examinated in detail at each station using the well known approach of spectral H/V ratio (horizontal-to-vertical ratio) from pseudo acceleration spectra and from Fourier spectra. Clear site effects can be observed at DAR (figure 7) and AFR stations, for frequencies of the order of 3.5 and 2.0-3.5 Hz, respectively. In the other stations, typical consolidated site ratios are obtained.

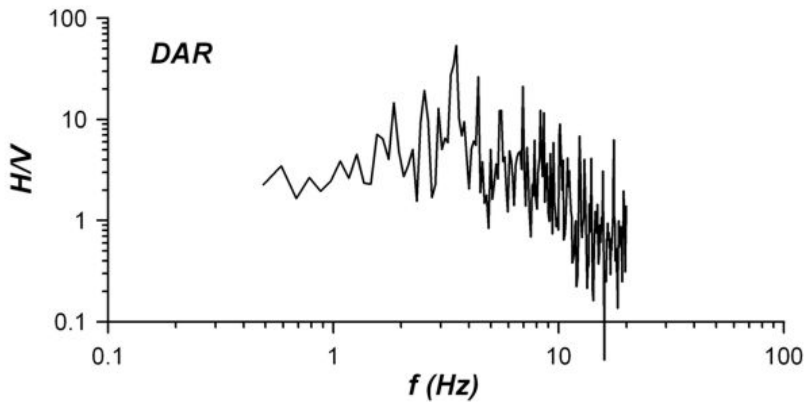

Figure 7. Computed H/V spectral ratio at the DAR station

The ground attenuation for different parameters has been carried out using the Joyner-Boore distance, that is, the distance to the rupture. Taking into account the insufficient records, the clear amplification in some stations, the observed directivity, especially in the nearest stations, and the poor azimuthal coverage, data don't allow us to model in a suitable way the ground motion attenuation. For example, figure 8 shows the PGA values, computed for the two horizontal components, versus the Joyner-Boore distance.

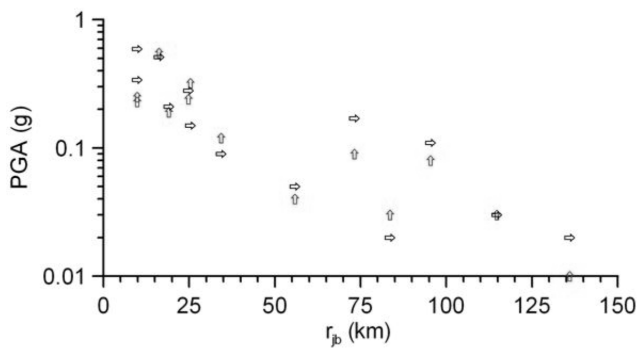

Figure 8. PGA vs. r_{jb}. EW component: ⇨. NS component: ⇧

The behavior showed in figure 8 is observed independently of the used parameter. A clear amplification in the AFR and HAM stations, located 73 and 95 km distant to the fault plane, respectively. This is explained by the soil type conditions and topographic effects. In the nearest stations, below 30 km, there is not a clear behavior, very influenced by the directivity.
The last step in the record processing has been devoted to derive the hodogram. To do so, we have composed the first 15 s of computed NS and EW displacements from the arrival of the more energetic phase. Obtained results are shown in figure 9, where we have added surface fault projection.

On the one hand, the obtained results in DAR, KOU, HUS and TIP approximately show a polarization of the displacement in the direction of the rupture propagation, that is, NE-SW. Coseismic deformations measured in this zone (Yelles Chauche *et al*., 2004) show net displacements in this same direction. The results obtained in KED1, KED2, TIZ and AZA show a polarization of the displacement in direction practically perpendicular to the previous one. They agree with the focal mechanism and the propagation of a less energetic NW-SE rupture (focal mechanism). Also they agree with the coseismic deformations measured in this area (Yelles Chauche *et al*., 2004). Finally, in stations BLI, AFR and HAM, although it is not so clear, it can be seen a displacement also in the NW-SE direction due to surface waves (Semmane *et al*., 2005).

A similar pattern was observed in the 1994 Northridge, California, earthquake (Wald *et al*., 1996). The earthquake keeps a great parallelism with the one from Algiers in magnitude, focal mechanism and focal parameters. In this case, a strong directivity due to the directivity in the propagation of the rupture was also observed.

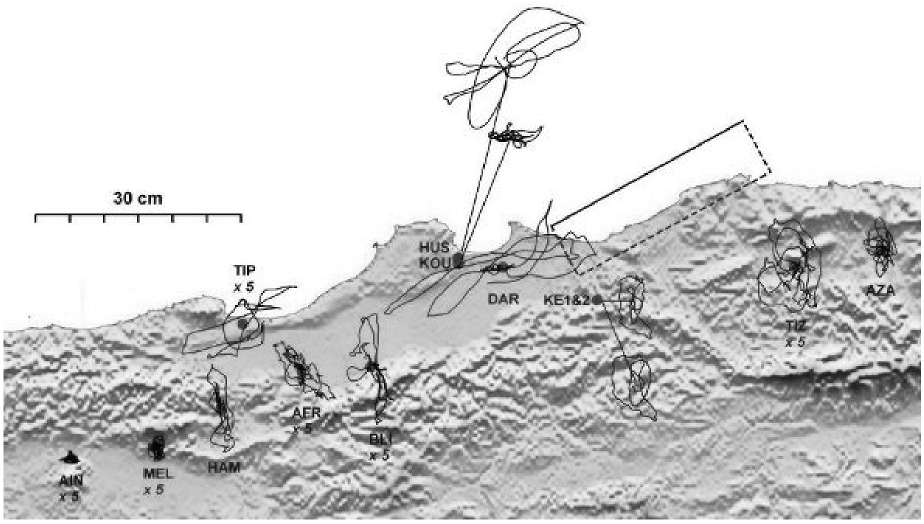

Figure 9. Computed hodograms and surface fault projection

Conclusions

The aim of this study has been the process of the recorded accelograms during the 21 May, 2003 earthquake. The process takes into account the specificity of the different records and the insufficient data to derive suitable attenuation of the ground motion. Nevertheless, with these data, some important results have been obtained related to the station soil type and to the directivity. The results obtained at some stations like KED1 and KED2, or at HUS and KOU, have been examined in detail to derive possible similarities. The horizontal hodograms obtained at each station agree with the fault rupture model derived by using coseismic deformation data. This result has been also obtained for the Northridge earthquake. Great attention has been made to the relation between estimated ground motion parameters and macroseismic intensity, finding a clear similarity between Housner intensity and damage. The extensive damage generated by this earthquake suggest us to compare the pseudo spectral acceleration derived from the records, the design spectra suggested by EC-8 and the uniform hazard spectra estimated through probabilistic methods. The obtained result is similar to the one obtained for the 2001 El Salvador earthquake.

References

Aoudia K. & Meghraoui M (1995). Seismotectonics in the Tell Atlas of Algeria: The Cavaignac (Abou El Hassan) earthquake of 25.08.1922, *Tectonophysics*, *248*, *263-276*.

Ayadi A. & 24 authors (2003). Strong Algerian earthquake strikes to near capital City, *EOS*, *84*, *561-563*.

Bommer J.J., Benito M.B., Ciudad Real M., Lemoine A., López Menjívar M.A., Madariaga R., Mankelow J., Méndez de Hasbung P., Murphy W., Nieto Lovo M., Rodríguez Pineda C.E. & Rosa H. (2002). The El Salvador earthquakes of January and February 2001: context, characteristics and implications for seismic risk, *Soil Dynamics and Earthquake Engineering*, *22*, *389-418*.

Boudiaf A., Ritz J.F. & Philip H. (1998). Drainage diversions as evidence of convergence of propagating active faults: Example of the El Asnam and Thenia faults, Algeria, *Terra Nova*, *10*, *236-244*.

CEN (Committee Européen de Normalization) (2003). Design provisions for earthquake resistance of structures - Part 1-1: General rules Seismic actions and general requirements for structures, European Prestandard ENV 1998-1-1. Comité Européen de Normalisation, Brussels.

Mokrane A., Ait Messaoud A., Sebai A., Menia N., Ayadi A. & Bezzeghoud M. (1994). Les séismes en Algérie de 1365 à 1992, (Bezzeghoud M. & Benhallou H., eds.), Alger.

Hamdache M., Peláez J.A. & Yelles Chauche A.K (2004). The Algiers, Algeria earthquake (Mw 6.8) of 21 May 2003: Preliminary report, *Seismological Research Letters*, *75*, *360-367*.

Meghraoui M (1988). Géologie des zones sismiques du nord de l'Algérie (paléosismologie, tectonique active et synthése sismotectonique), *PhD dissertation*, *Universite de Paris Sud*.

Philip H (1983). La tectonique actuelle et récente dans le domaine Meditérranen et ses bordures, ses relations avec la sismicité, *PhD dissertation*, *University of Languedoc*.

Peláez J.A., Hamdache M. & López Casado C (2003). Seismic hazard in northern Algeria using spatially smoothed seismicity: Results for peak ground seismicity, *Tectonophysics*, *372*, *105-119*.

Peláez J.A., Hamdache M. & López Casado C (2005). Updating the probabilistic seismic hazard values of northern Algeria with the 21 May 2003 M 6.8 Algiers earthquake included, *Pure and Applied Geophysics*, *162*, *2163-2177*.

Peláez J.A., Hamdache M. & López Casado C (2006). Spectral Seismic hazard in terms of accelerations and uniform hazard spectra in Northern Algeria, *Pure and Applied Geophysics*, *163*, *119-135*.

Semmane F., Campillo M. & Cotton F (2005). Fault location and source process of the Boumerdes, Algeria, earthquake inferred from geodetic and strong motion, *Geophysical Research Letters*, *32*, *Art. N0 L01305.*

Wald D.J., Heaton T.H. & Hudnut K.W (1996). The slip history of the 1994 Northridge, California, earthquake determined from strong ground motion, teleseismic, GPS and levelling data, *Bulletin of the Seismological Society of America*, *86*, *S49-S70*.

Wang Y., Edward C., Yashinsky M., Kartoum A. & Hamdache M. (2004). May 21, 20003 Zemmouri Algeria earthquake: Geoscience and lifeline damage, *11th International Conference on Soil Dynamic and Earthquake Engineering*, *Berkeley*.

Yagi Y (2003). http://iisee.kenken.go.jp/staff/yagi/eq/algeria20030521/algeria2003521.html

Yelles Chauche A.K., Lammali K., Mahsas A., Calais E. & Briole P (2004). Coseismic deformation of the May 21st, 2003, Mw=6.8 Boumerdes earthquake, Algeria, from GPS measurements, *Geophysical Research Letters*, *31*, *Art. No. L13610*.

Yielding G., Ouyed M., King G.C.P. & Hatzfeld D (1989).Active tectonics of the Algerian Atlas Mountains: Evidence from aftershocks of the 1980 El Asnam earthquake, *Geophysical International Journal*, *99*, *761-788*.

Mean PGA, SA, UHS and Design Spectra in Northern Algeria

Hamdache M (1), Peláez J A (2), López Casado C (3)

(1) CRAAG, B.P. 63-Bouzaréah, 16340-Algiers, Algeria, mhamdache@hotmail.com
(2) Dpt. of Physics, University of Jaén, Jaén, Spain, japelaez@ujaen.es
(3) Dpt. of Theoretical Physics, University of Granada, clcasado@ugr.es

Keywords: probabilistic seismic hazard, PGA, SA, UHS, design spectra

Introduction

In the last years, a new probabilistic seismic hazard assessment for Northern Algeria has been carried out. To do it, the used catalog for this study mainly consists of those published by the Spanish IGN, supplemented for the Algeria zone with data published by the CRAAG, and initially updated to 2002. The data published for the region by the EMSC and by the USGS have also been incorporated into the data file. Afterwards, the catalog was updated to June 2003, including the 21 May 2003, M 6.8, Algiers earthquake. The non poissonian events identified via EPRI methodology have been removed. Four complete and Poissonian seismic models were established and used, considering the seismic characteristics of the catalog: those with a seismicity of a) M ≥ Ms 2.5 after 1960; b) M ≥ Ms 3.5 after 1920; c) M ≥ Ms 5.5 after 1850; and d) M ≥ Ms 6.5 after 1700. The spatially smoothed seismicity approach was used for the computation of the seismic hazard. The reason is that this methodology combines both parametric and non-parametric probabilistic methods. Besides, it is well adapted to model disperse or background seismicity, *i.e.*, the seismicity that cannot be assigned to specific geologic structures. Initially, this approach was proposed and developed by Frankel (1995). Seismic hazard map in term of PGA with 10% probability of exceedance in 50 years is obtained for rock, which correspond to a seismic hazard map for a return period of 475 years. Afterward, we have derived SA values for rock (Vs > 750 m/s), corresponding to soil types A in the Eurocode 8 and S1 in the Algerian building code, damped at 5%, for different periods. The obtained results were plotted as contour maps as well. In addition to the seismic hazard assessment at different periods, we have computed the UHS at different locations. The used attenuation model allows us a high definition in the computation of the spectra.

Finally, from the computed uniform hazard spectra for different type of soils, and estimated specifically for the most important cities, those obtained for a return period of 475 years and a 5% of damping are used to propose design spectra. We have used the Newmark-Hall (1982) approach with certain modifications. The spectral acceleration for 0.2-sec is used to establish the spectral region for lower periods (region controlled by the acceleration), while spectral acceleration value for 1.0-sec is used to establish the spectral region for intermediate periods (region controlled by the velocity), as such it is proposed in the most recent International Building Code.

Obtained results have been published in terms of PGA (Peláez *et al*., 2003 & 2005), SA and UHS (Peláez *et al*., 2006) and response elastic spectra (Peláez *et al*., 2007).

Data and methodology outline

As has been pointed out before, the used catalog for this study mainly consists of those published by the Spanish IGN, supplemented for the Algeria zone with data published by the CRAAG, and initially updated to 2002. Data from the EMSC and the USGS have also been incorporated in the catalog. Afterwards, it was updated to June 2003, including the 21 May

2003, M 6.8, Algiers earthquake (Hamdache *et al.*, 2004) and the reappraisal of significant earthquakes which occurred in the 19th century, mainly in northeastern Algeria (Harbi *et al*., 2003). All the magnitudes and intensities were converted to Ms magnitudes, and all the non-Poissonian earthquakes identified via the methodology proposed by EPRI (1986) were removed. The attenuation relationship developed by Ambraseys *et al*. (1996) was employed in our study. Finally, four complete and Poissonian seismic models were established and used, considering the seismic characteristics of the catalog: those with a seismicity of *a)* M ≥ Ms 2.5 after 1960; *b)* M ≥ Ms 3.5 after 1920; *c)* M ≥ Ms 5.5 after 1850; and *d)* M ≥ Ms 6.5 after 1700. The final result was obtained by weighting the partial results derived from each of the models.

Results

Among obtained results, initially we detail mean PGA values with 10% probability of exceedance in 50 years, *i.e.*, for a return period of 475 years, for rock (Vs > 750 m/s) (figure 1). The greatest values of the seismic hazard appear in the central area of the Tell Atlas. In particular, in the province of Chlef, including the city of El Asnam, and the western part of the provinces of Tipaza and Ain Defla, the mean PGA values are above 0.24g, and reaches 0.48g in the epicentral areas of the 1954 and 1980 El Asnam earthquakes. We can observe in the seismic hazard map another lobe, with a lower value, around 125 km to the east of the previous one. It includes the provinces of Blida and mostly Algiers, including the city of Algiers. Values above 0.24g are also reached in this area.

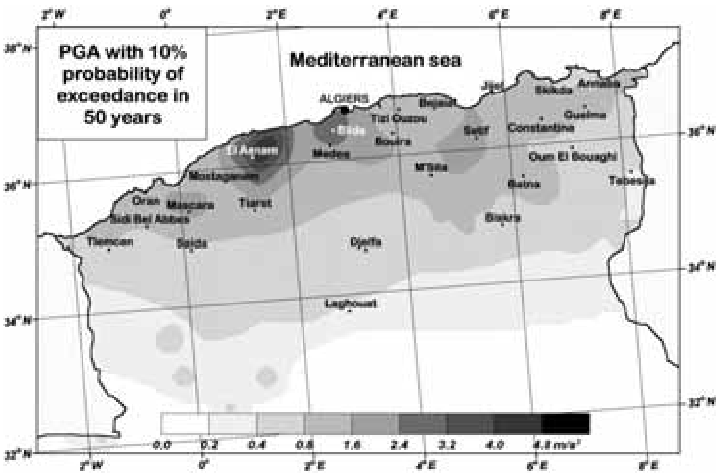

Figure1. Seismic hazard map in terms of PGA for a return period of 475 years

Afterwards, we have derived SA values for rock, corresponding to soil types A in the Eurocode 8 and S1 in the Algerian building code, damped at 5%, for different periods. The obtained results were plotted as contour maps as well. These plots commonly show that maximum values occur again in the central part of the Tell Atlas, close to the location of the historical earthquake of January 15, 1891 (macroseismic magnitude Ms 7.0), and to the more important recent instrumental earthquakes of September 9, 1954 (Ms 6.8), and October 10, 1980 (Ms 7.3). The maximum SA value in this region, for a return period of 475 years, is 0.95g at 0.2-sec and 0.4-sec, and 1.07g at 0.3-sec. This region appears clearly as the seismic source generating the higher seismic hazard level, independently of the return period being considered. As example, obtained results for periods of 0.2 and 1.0-sec are shown in figures 2 and 3. All the calculations are done for rock, 5% damping and a return period of 475 years.

In both cases, although with different level of hazard, the maximum spectral acceleration values are observed in the central region of the Tell, in particular, in the region of the Chleff (El Asnam). As has been pointed before, this is the epicentral area of the 1954 (Ms 6.8) and 1980 (Ms 7.3) earthquakes. In the city of El Asnam, for return periods of 100 and 475 years, values of spectral acceleration of the order of 0.4g and 1.0g are obtained, respectively, in the range of periods 0.2-0.3-sec.

The uniform hazard spectra (UHS) have been also derived at different locations. To use the Ambraseys *et al*. (1996) attenuation relationship allows us to compute spectra with a high resolution. An example, the UHS for Algiers, is showed in the figure 4.

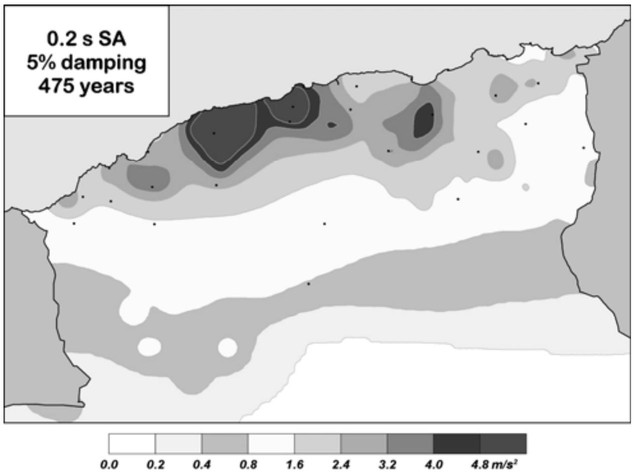

Figure 2. Seismic hazard map in terms of SA for a period of 0.2-sec. It has been computed for rock, 5% damping, and a return period of 475 years

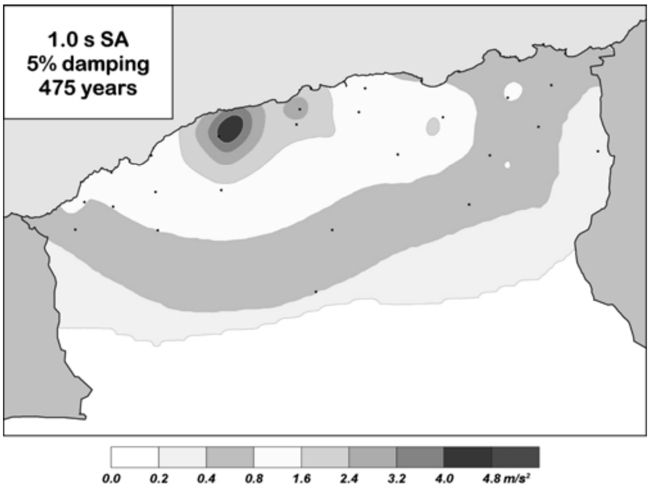

Figure 3. Seismic hazard map in terms of SA for a period of 1.0-sec. It has been computed for rock, 5% damping, and a return period of 475 years.

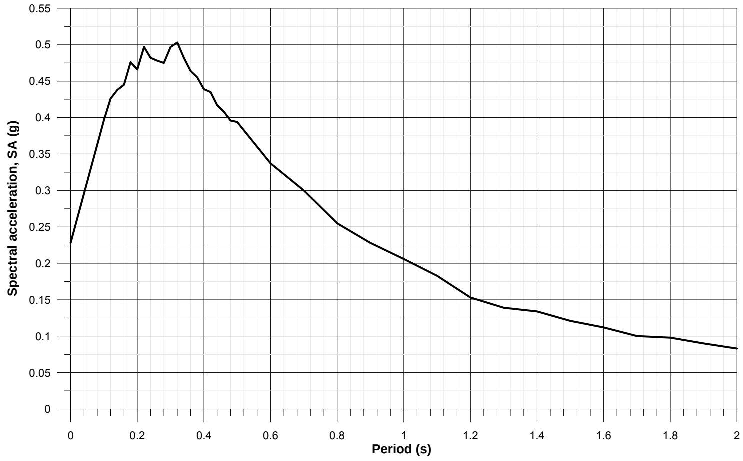

Figure 4. Uniform hazard spectrum for Algiers. It has been computed for rock, 5% damping and a return period of 475 years (Peláez *et al*., 2006).

Design spectra. Preliminary results

The method used here in order to know the design spectra for a certain return period and damping coefficient, need as input only values of the spectral acceleration for two periods, 0.2 and 1.0-sec (Malhotra, 2005). Initially it must be computed the value

$$T_s = 1s \, \frac{SA(1s)}{SA(0.2s)}$$

Next, the design spectrum is defined as

$$SA(T) = \begin{cases} 0.4SA(0.2s) + 3SA(0.2s)\dfrac{T}{T_s} & T < 0.2T_s \\ SA(0.2s) & 0.2T_s < T < T_s \\ SA(1s)\dfrac{1s}{T} & T > T_s \end{cases}$$

The final result is a simplified design spectrum in where, strictly speaking, only the spectral accelerations for 0.2 and 1.0-sec correspond to the return period for which this spectrum has been computed.
In the following table (table 1), the values that define the design spectrum for some of the most important cities in the north of Algeria, for different soil types, and for a return period of 475 years, are shown.

Cities	***rock***		***soft***		***stiff***	
	SA (0.2 s)	***SA (1.0 s)***	***SA (0.2 s)***	***SA (1.0 s)***	***SA (0.2 s)***	***SA (1.0 s)***
Oran	0.289	0.111	0.394	0.149	0.400	0.161
Mostaganem	0.270	0.126	0.368	0.169	0.374	0.208
Medea	0.493	0.218	0.683	0.360	0.672	0.293
Mascara	0.369	0.150	0.504	0.201	0.512	0.248
El Asnam	0.865	0.441	1.180	0.593	1.200	0.731
Tiaret	0.262	0.145	0.358	0.194	0.364	0.239
Argel	0.466	0.206	0.636	0.760	0.646	0.340
M'Sila	0.309	0.113	0.421	0.151	0.428	0.186

Tizi-Ouzou	0.211	0.103	0.287	0.138	0.291	0.170
Blida	0.638	0.264	0.871	0.355	0.885	0.437

Table 1. SA (g) for a return period of 475 years, periods of 0.2 and 1.0-sec, and 5% damping. Soil types are according to the classification by Ambraseys *et al*. (1996).

In the figure 5 some results are shown. We can see for the cities of the El Asnam, Algiers and Oran the design spectra for rock (Vs > 750 m/s, corresponding with the soil type A of EC 8) and soft soils (180 < Vs < 360 m/s, corresponding with the soil type C of EC 8).
Finally, in figure 6 we show the clear relationship among SA(0.2 s) values and the PGA value obtained at the same location, the same return period, and the same soil type. We can observe that, independently of the return period, the spectral acceleration value for a period of 0.2-sec is the double of the PGA value for rock, and of the order of 2.6 for other types of soils. This dependency implies that we can use as parameters to define the proposed design spectra the pair (SA(0.2 s), SA(1.0 s)) or the pair (PGA, SA(1.0 s)) with the same reliability.

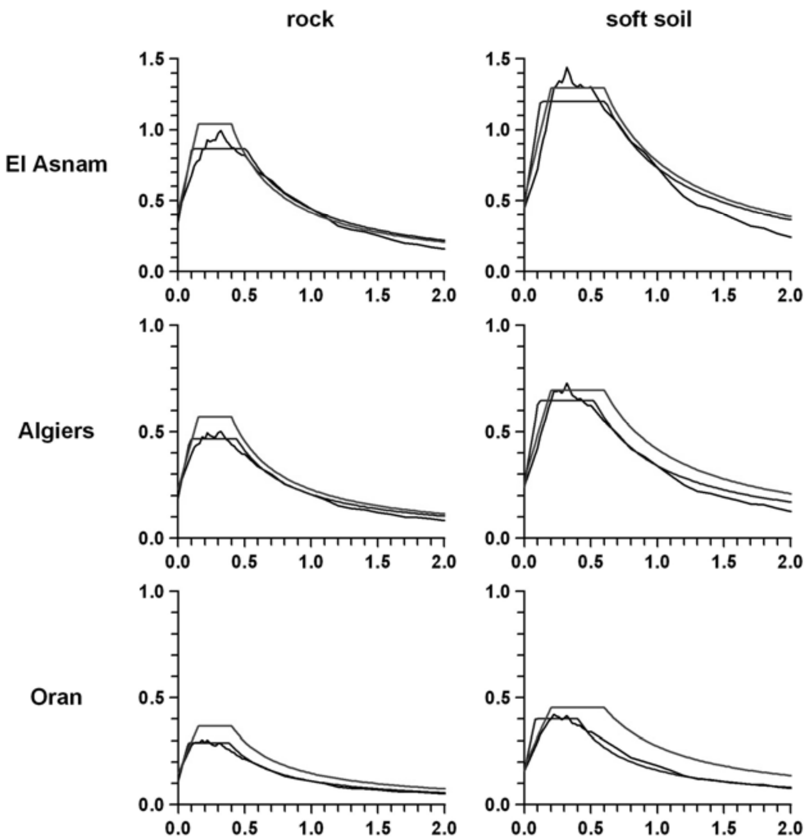

Figure 5. Uniform hazard spectra (pseudo-acceleration (g) *vs.* period (s)) for a return period of 475 years and 5% damping, computed for the cities of the El Asnam, Algiers and Oran. Uniform hazard spectra (in black), elastic design spectra proposed in this work (in blue) and elastic design spectra proposed in the EC-8 (in red).

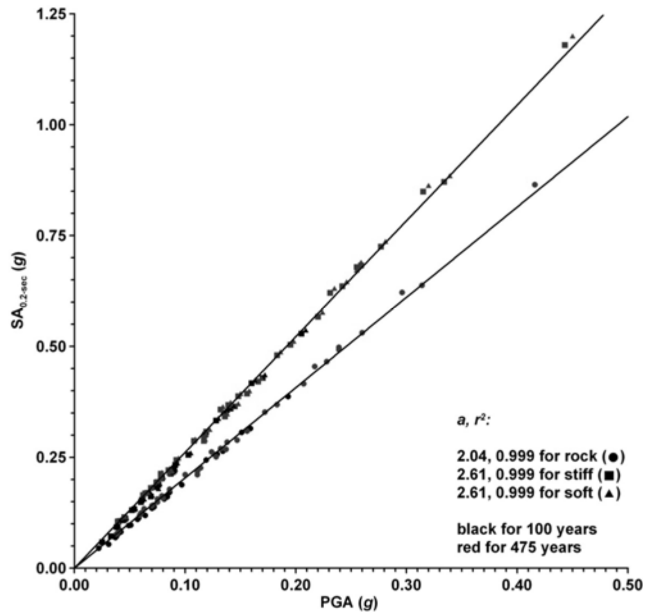

Figure 6. Relationship between SA(0.2 s) and PGA. For each type of soil, slope (a) and coefficient of determination (r^2) values are showed

Conclusions

This study gives a large overview on seismic hazard estimation obtained in northern Algeria. The obtained results are used to propose design spectra in this region. The advantage of the proposed approach is the use of only two parameters obtained for a specific return period, soil type and damping.

In our case, we have used the parameters obtained from the estimation of uniform hazard spectra (UHS) obtained previously at different locations in northern Algeria.

After comparing design spectra, uniform hazard spectra and elastic response spectra according with EC 8, we observed that design spectra obtained using the procedure explained in this study, are easier to define, presenting a high reliability in mostly cases, especially for intermediate and long periods.

References

Ambraseys N.N., Simpson K.A. & Bommer J.J. (1996). Prediction of horizontal response spectra in Europe, *Earthquake Eng. Struct. Dyn.*, *25*, *371-400*.

EC 8 - Eurocode 8 (1998). Design provisions for earthquake resistance of structures - Part 1-1: General rules. Seismic actions and general requirements for structures, European Prestandard ENV 1998-1-1, Comité Européen de Normalisation, Brussels.

Electric Power Research Institute (1986). Seismic Hazard Methodology for the Central and Eastern United States, *EPRI Report NP-4726*, *Palo Alto*, *California*.

Frankel A (1995). Mapping Seismic Hazard in the Central and Eastern United States, *Seismol. Res. Lett.*, *66*, *8-21*.

Hamdache M., Peláez J.A. & Yelles Chauche A.K (2004). The Algiers, Algeria, earthquake (Mw 6.8) of 21 May 2003: Preliminary report, *Seismological Research Letters*, *75*, *360-367*.

Harbi A., Benouar D. & Benhallou H. (2003). Re-appraisal of seismicity and seismotectonics in northeastern Algeria. Part I: Review of historical seismicity, *J. Seismol.*, *7*, *115-136*.

Malhotra P.K. (2005). Return period of design ground motions, *Seismol. Res. Lett.*, *76*, *693-699*.

Newmark N.M. & Hall W.J (1982). Earthquake spectra and design, *Earthquake Engineering Research Institute Monograph Series no. 3*, Berkeley, California, USA.

Peláez J.A., Hamdache M. & López Casado C (2003). Seismic hazard in northern Algeria using spatially smoothed seismicity, *Tectonophysics*, *372*, *105-119*.

Peláez J.A., Hamdache M. & López Casado C (2005). Updating the probabilistic seismic hazard values of northern Algeria with the 21 May 2003 M 6.8 Algiers earthquake included, *Pure Appl. Geophys.*, *162*, *2163-2177*.

Peláez J.A., Hamdache M. & López Casado C (2006). Seismic hazard in terms of spectral accelerations and uniform hazard spectra in northern Algeria, *Pure Appl. Geophys.*, *163*, *119-135*.

Peláez J.A., Hamdache M. & López Casado C (2007). Una propuesta de espectros de respuesta de diseño para el Norte de Argelia, *3er Congreso Nacional de Ingeniería Sísmica*, *Girona*, *Spain*.

Exploring Phenomena and Mechanisms of Abnormal Mass Magnetic Susceptibility in Archaeological Strata at Lajia Site, Qinghai Province, China

Jie O (1), Cheng Z (2), Maolin Y (3), Xiaoyan R, Jian Z, Linhai C, Kezhou H, Qing Z

(1) School of Geographic and Oceanographic Sciences of Nanjing University, Nanjing, 210093, oyang692000@yahoo.com.cn
(2) School of Geographic and Oceanographic Sciences of Nanjing University, Nanjing, 210093, zhuchengnj@yahoo.com.cn
(3) The Institute of Archaeology, Chinese Academy of Social Sciences, Beijing, 100710, kgsyeml@sina.com

Keywords: Lajia Site, mass magnetic susceptibility (MMS), paleo-earthquake, magnetic memory, mutation strata

Introduction

Lajia Site of Minhe County, Qinghai province, in China, which occupies the front of the second terrace along the northern bank of Yellow River, is above 25 m high the river and I km distance (Fig. 1). It is located in the southern Guanting Basin where the Yellow River flows from west to east and forms three terraces there(Yang X Y, Xia Z K, Ye M L, et al. 2003, 2004).
A paleo-earthquake measuring above 7 on the Richter scale with intensity of □ hit Lajia Site which probably was epicenter, it maybe occurred at 3900B.P. or so based on data of aging of the Institute of Archaeology of Chinese Academy of Social Sciences and Archaeology Department of Peking University. The main types of paleo-earthquake relics in the Guanting Basin where Lajia Site is located were dikes, craters, sandblasts and local depressions without sills (Yang X Y, 2003).
The paper contrasts and analyzes 46 samples obtained from three sections at Lajia Site, explores phenomena as well as mechanisms. The kernel of the paper is to explore mechanisms of abnormal MMS occurred in mutation strata shaped by sandblasts of paleo-earthquake, speculate general modes of MMS influenced by earthquake and explore mechanisms of abnormal MMS through the whole processes of earthquake (earthquake in pregnancy, eruption and ending) firstly.

Figure 1. Position of the Lajia Site (from Google Earth, been revised).

Figure 2. Human remains in the fourth house unearthed in 2000.

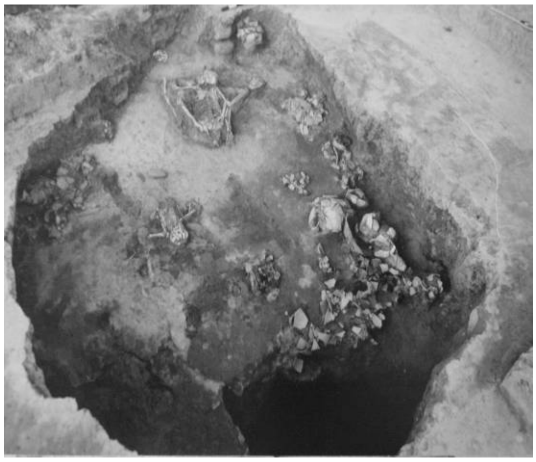

Figure 3. Interior of the seventh house unearthed in 2000.

Figure 4. Phenomenon of rolling ground of the Square V unearthed in 2001.

Figure 5. The northern wall of Lajia Site □T1106-1102.

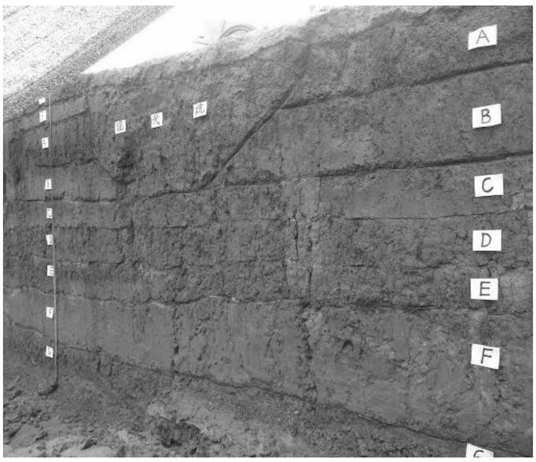

Figure 6. The western wall of Lajia Site □T1106-1105.

Figure 7. The natural section of Wangshigou.

Materials and Methods

Not only may the magnetic minerals which sediments carry reflect the climate condition in specific depositional environment but they also have sensitive responses to paroxysmic geological disaster events such as volcano, paleo-earthquake (Nils-Axel Mörner, 2008) and mudslide.

Abundant studies have been done from home and abroad (Li J S, et al, 1999; Tsafrir Levi, et al.2006), but It is rare to explore mechanisms of MMS from internal force, especially from the whole processes of earthquake as a systemic study. The mechanisms of abnormal MMS have not been explained synthetically and deeply yet, and that is what just will be discussed in this paper.

Invited, helped and participated directly by Ye M L, Researcher of Chinese Academy of Social Sciences institute of archaeology, also the leader of archaeology group of the Lajia Site, 46 samples were collected respectively: 17 and 14 samples were gained at the northern wall of T1106-1102 and the western wall of T1106-1105 of the northern Lajia Site(GPS geographical position: 35°51.843′N, 102°48.615′E, altitude: 1804m); 15 samples were gathered from the natural section of Wangshigou of the eastern Site (GPS geographical position: 35°51.788′N, 102°48.847′E, altitude: 1801m).

MMS data were obtained as follows: the gathering samples were dried in laboratory naturally first, and then tested the entire MMS using the tool of KLY-3 produced by AGICO Corporation of Czech Republic in the Nanjing University Region Environment Evolution Research Institute Environment Magnetism Laboratory.

Results and Discussion

Abnormal MMS of Wangshigou natural section

Abnormal MMS of Wangshigou natural strata occur at the 5th and 11th samples, the two peak values whose strata correspond to pale black and brown clay are 540 and 587(×10-8SI)or so. They also are located at two obvious high value areas of I and II of Rb/Sr whose data were obtained from the Chemistry Analysis Center of Nanjing University.

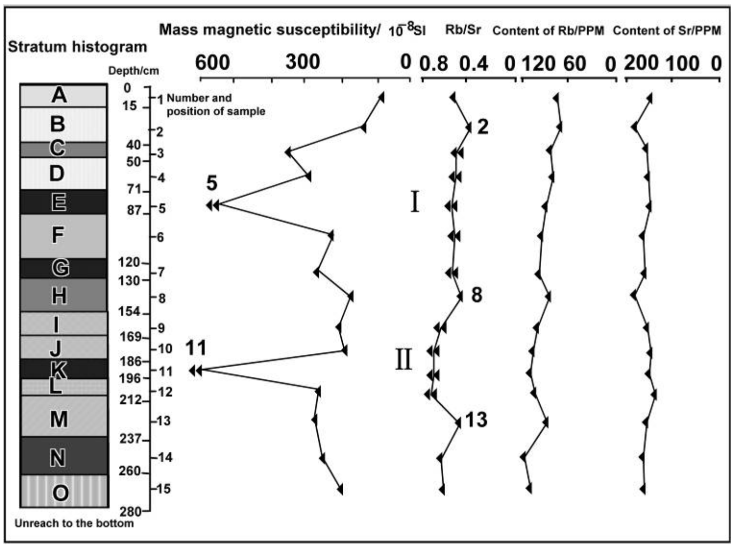

Figure 8. Curves of soil MMS and Rb/Sr of Wangshigou natural section

Brief description to strata: A: red moderate silver sand B: brown red grained sand C: scarlet red silt D: Brown red grained sand E: ash black clay F: pale red grained sand G: pale brown clay H: brown yellow clay I: red clay J: red clay K: pale brown clay L: pale yellow clay M: Brown yellow rd clay N: scarlet red clay O: loess

Through analysis on experimental granularity data gained from Nanjing Normal University: Probability cumulative curves of the granularity of the four samples of the strata with peak values of MMS and the adjacent down strata are all “three segments” (Fig. 9) and “single peak” of frequency curves of granularity(Fig. 10).

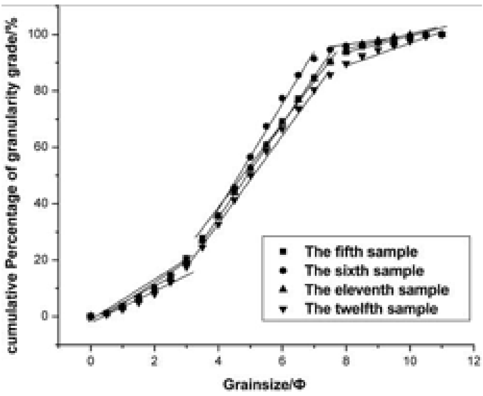

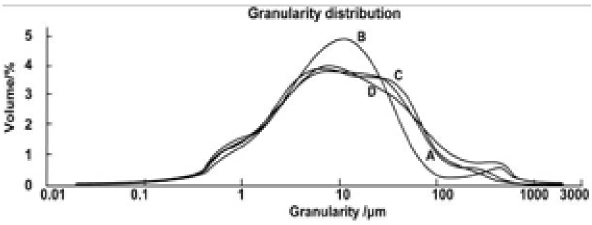

Figure 9. Figure 10.

Figure 9. Probability cumulative curves of granularity of four points of Wangshigou.

Figure 10. Frequency curves of granularity of four samples of Wangshigou (single peak). (A: the fifth sample point B: the sixth sample point C: the eleventh sample point D: the twelfth sample point)

Why the phenomenon of abnormal MMS of Wangshigou natural section appeared at dark brown clays perhaps has a connection to paleo-flood. Red clays were probably brought onto the terrace from the bottom of the riverbed and ambient mountains and converged there first when deluging during the Tertiary Period, then marshes and prosperous plants lived in the floodplain after flood withdrawal. Abundant organic materials magnetite were made in the body of iron bacterium of soil organic materials while absorbing iron from the outside(Sun J M et al. 1995)，so dark soils such as pale black or brown clays onto the red clay were formed.

They are basic features of sediment in a river environment and high rainfall with probability cumulative curves of “three sections” , frequency curves of granularity with “single peak”, and high values of Rb/Sr(Chen J, et al.1997).

Abnormal MMS of the western wall of T1106-1105

Two peak values of MMS of western wall of T1106-1105 (Fig.11)appear at points of A2 and F1 whose strata are pale brown clays also. This is the same phenomenon as Wangshigou natural section, that is to say: MMS of pale black and brown clay are higher than the yellow and red of the main soils in the local area obviously.

Probability cumulative curves of granularity are same as natural section of Wangshigou with “three segments” (Fig.12); but frequency curves of granularity of the western wall are complicated: the B1 and F2 are “single peak” (Fig.13), but points of A2 and F1 where mutuation of MMS appeare with intricate “double peaks” (Fig. 14) which maybe were interrupted by human activities. Farther researches will be done in the future but without deep discussion here.

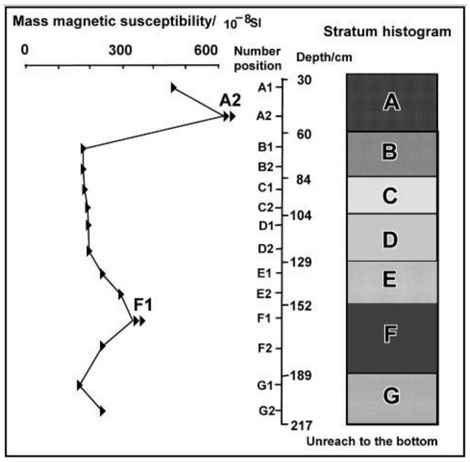

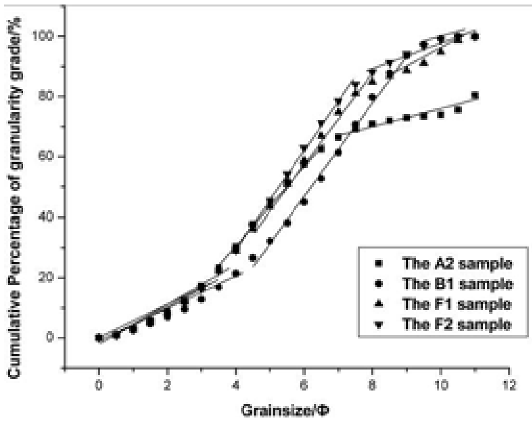

Figure 11. Figure 12.

Figure 11. Stratum diagram and curve of soil MMS of western wall of T1106-1105. (A pale brown clay B brown yellow clay C pale red clay D pale red clay E pale red clay F pale brown clay G yellow red clay)

Figure 12. Probability cumulative curves of granularity of four samples.

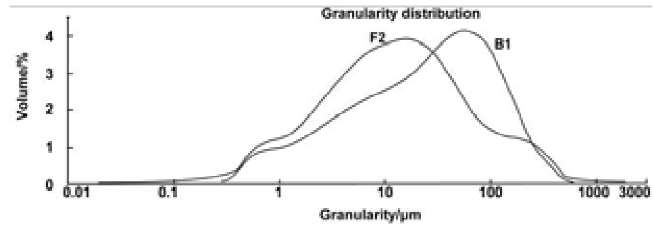

Figure 13. Frequency curves of granularity of B1 and F2 samples (single peak).

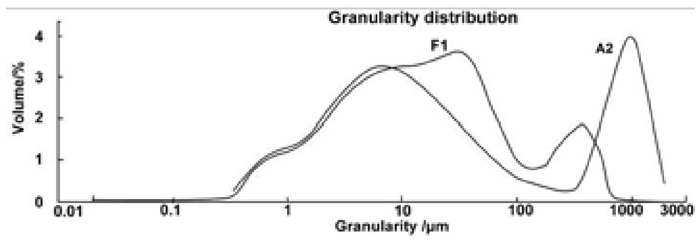

Figure 14. Frequency curves of granularity of A2 and F1 samples (double peaks).

In brief, contrast and analyze strata to extract authentic information of paleo- environment change not only through up and down of MMS to restore paleo-environment for the reasons of many interacted factors but also through synthetic analysis on experimental data of granularity, Rb/Sr, etc.

Abnormal MMS of northern wall of T1106-1102

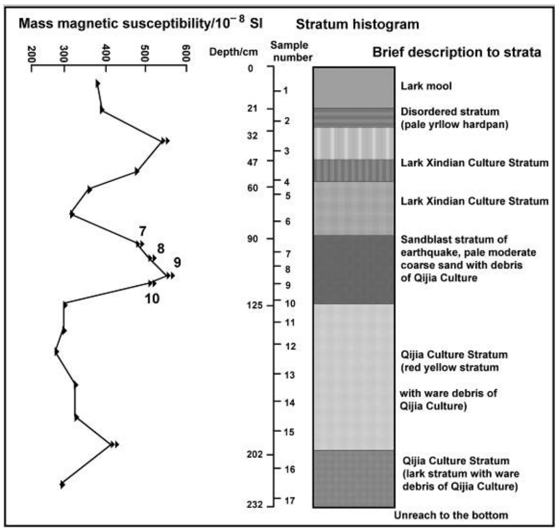

Figure 15. Strata histogram of the northern wall and curve of MMS of T1106-1102.

The northern wall contains only 8 strata but with high fluctuated MMS which maybe was influenced by human activities (Shi Wei et al. 2007). But the most important discovery is that a huge increment of MMS appears obviously from the 7th to the 10th samples (Fig. 15) which are sites of earthquake sandblast through macroscopicaldiscernment.

Abundant minerals such as magnetite, red limonite, epidote, garnet, tourmaline, hornblende, chlorite, picrite, zircon, rutile, leucoxene etc. (Table 5) are found in the 8 samples of the northern wall of T1106-1102 by Geological Survey of Jiangsu Province. The highest peak values of magnetite content appear at strata of sand blow of the 7th and 10th samples are 683.6 g·t-1 and 976.9 g·t-1respectively; values of other six samples are between 195.8 g·t-1 to 39.3g·t-1, so the abnormal MMS mutation of stratum of sandblast is caused by very high magnetite content with maximum of several tens of times compared to other strata, and MMS experience intricate processes as magnetic grains change with outside environment such as temperature, stress when earthquake eruption.

Table 5 Parts of experimental data of heavy mineral of northern wall of T1106-1102

Strata	Mineral Content	magnetite	Limonite	Epidote	Garnet	Tourmalin	Hornblende
N3-3	Weight/g	0.0160	0.1164	0.1041	0.0521	Small	0.0214
	Content/$g \cdot t^{-1}$	74.1	539.6	482.6	241.5	Small	99.2
N5-5	Weight/g	0.0046	0.1183	0.1097	0.0317	Small	0.0144
	Content/$g \cdot t^{-1}$	195.8	497.1	461.0	133.2	Small	60.5
N6-7	Weight/g	0.1968	0.3088	0.2794	0.0882	Small	0.0368
	Content/$g \cdot t^{-1}$	683.6	1072.7	970.5	306.3	Small	127.8
	Mineral feature	Black,semi-pien grain, magnetism	Black,brown, semi-pien grain	Pale yellow-green semi-pien grain	Pale pink,orange, semi-pien grain	Pale brown, trigonal prism	Dim green, prismatical
N6-10	Weight/g	0.1781	0.3339	0.2922	0.1252	Small	0.0417
	Content/$g \cdot t^{-1}$	976.9	1831.5	1602.8	686.7	Small	228.7
	Mineral feature	Black,semi-pien grain, magnetism	Black,brown, semi-pien grain	Pale yellow-green semi-pien grain	Pale pink,orange, semi-pien grain	Pale brown, trigonal prism	Dim green, prismatical

N7-11	Weight/g	0.0131	0.0847	0.0577	0.0252	Small	0.0090
	Content/$g \cdot t^{-1}$	39.3	254.4	173.3	75.7	Small	27.0
N7-13	Weight/g	0.0221	0.0688	0.0635	0.0247	0.0018	0.0071
	Content/$g \cdot t^{-1}$	79.4	247.4	228.4	88.8	6.4	25.5
N7-15	Weight/g	0.0078	0.0393	0.0483	0.0090	Small	0.0067
	Content/$g \cdot t^{-1}$	43.5	219.6	269.9	50.2	Small	37.4
N8-17	Weight/g	0.0106	0.0315	0.0462	0.0049	Small	0.0157
	Content/$g \cdot t^{-1}$	69.5	206.8	303.3	32.1	Small	103.0

Note: Small：<10 granules; Single：1~2 granules

General models of MMS influenced by the whole processes of earthquake

Three procedures of earthquake in pregnancy, eruption and ending are speculated to generalize general models of MMS influenced by the whole processes of earthquake respectively.

Earthquake in pregnancy (Abnormal period of MMS)

Earthquake in pregnancy has tight relation with rock strain and rupture in the adagio time with high temperature and stress(Wang J T, et al, 2000), although the primary factor influencing rock magnetic susceptibility is the ferromagnetism mineral content. There is a close relation with pellet size of magnetism mineral and structure, as well as factors of temperature, stress and so on (Cheng Y X, 2005).

The magnetostriction phenomenon is produced when the shape and the volume of rocks are changing as the ferromagnetic crystal of rocks magnetized in the outside magnetic field. The relationships between magnetic susceptibility and stress is based on the magnetocrystalline free energy minimum principle at the situation of low pressure (0~30MPa)of random orientation to the magnetocrystalline(Ding J H, 1994):

$$\chi_{\parallel}=\chi_0(1-S_\chi\sigma)$$

$$\chi_{\perp}=\chi_0(1+\frac{1}{2}S_\chi\sigma)$$

In the equation above: χ_0 is isotropy magnetic susceptibility without stress, S_χ is stress sensitivity of magnetic susceptibility, $\chi_{\parallel}$ is magnetic susceptibility of parallel direction of pressure axis, $\chi_{\perp}$ is magnetic susceptibility of vertical direction of pressure axis.

Considering the complexity of actual procedure of the earthquake, Hao Jinqi et al.(1999) simulated the physical condition of epicenter. The experimentation suggested magnetic rock samples underwent a rheological process at conditions of high-temperature, high-pressure and low-strain-rate values, during rehological process. The degree of anisotropy of magnetic susceptibility (AMS) reached highest value of 1.025 in 700-800℃ at the phase of tight plastic deformation and stable creep deformation, the maximum principal axis direction of ellipsoid of magnetic susceptibility departed from the direction of press axis from 2.6°to 15.2°, the “Effect of rock rheology on rock susceptibility” that rheology make rocks change magnetic susceptibility was confirmed (Hao J Q, et al. 1999).

Earthquake eruption (Huge change period of MMS)

Physical changes

Extremely complex affects were influenced by temperature increment with the released internal energy suddenly to magnetic susceptibility of different magnetic substance, the magnetic susceptibility of ferromagnetic material (magnetic-order) is specially positive big number, the spontaneous magnetization produces below the ferromagnetic Curie temperature T_C and becomes paramagnetic materials above high temperature and obeys the Law of “Curie--Weiss”. The magnetic susceptibility χ has the relation to the thermodynamic temperature (T) as shown below:

$$\chi = \frac{C}{T - T_C}$$ (C□Curie constant);

Chemical changes

The MMS increase also may be caused by complex chemical changes of certain minerals as temperature is elevated. The change process of MMS becomes more complex. Generally speaking, the most important materials of carrying magnetite are ferrimagnetism melnikovite of iron sulphides and pyrrhotite, Li H Y (Li H Y et al.2005) carried on detailed experiments on characteristics of magnetic susceptibility of pyrite samples changing with temperature. Two probable ways that pyrite is transformed into pyrrhotite were speculated: one is that pyrite pellets first transform into magnetite through the oxidation of surface adsorption oxygen. More pyrrhotite was formed through deep response between new production of magnetite and sulfur volatilized from pyrite crystal lattice with temperature increment, two chemical equations are as shown below□

$3FeS_2 + 8O_2 = Fe_3O_4 + 6SO_2$; $Fe_3O_4 + 5S = 3FeS + 2SO_2$

Another way which is main source of the pyrrhotite is probably that the pyrite transforms into the pyrrhotite by direct desulphurization. All these changes may make accretion and complexity to the soil magnetic susceptibility.

Electrokinetic magnetic effect

Besides temperature and pressure influences on magnetic susceptibility to soil or rock, analyzed above, bunkers (the sites of earthquake sandblast) were found in the □T1106-1102 of the Lajia Site. The sand with water suspending liquid possibly broke through the weak spot of soil layer or spurted to the surface along cracks under the high temperature and high pressure during earthquake. Streaming potential and induction magnetic field may be produced as sand blowing, dross remnant magnetization (DRM)(R.Thompson, et al. 1995)was made when sands with the magnetic pellets subsided in the water and made themselves along the magnetic field orientation outside at the same time.

Earthquake ending (Record period of MMS)

According to the theory of magnetic memory at present, the phenomenon of magnetic memory depended on synthetic actions of geomagnetic field and stress. After the earthquake energy was released suddenly, the deposit compacted again and MMS recorded the earthquake information while experiencing the complex change of the earthquake process. Because of the function of magnetic memory of the magnetic mineral grains, the coercive force of magnetic mineral grains swelled after earthquake and got very stable remanence while recording the information of environment mutation even in weak geomagnetism at that time.

Conclusions

Abnormal mass magnetic susceptibility(MMS) usually appears in strata influenced obviously by external force (flood, human activities etc.) or internal force (earthquake).

The mutation of MMS of natural sections at Lajia Site usually appear at strata of black clay or pale grown clay which perhaps have relations with paleo-flooding; MMS of cultural strata influenced by human activities is relatively intricate; the most obvious abnormal MMS at Lajia Site come forth in mutation strata shaped by sandblasts of paleo-earthquake.

It is beneficial to gain a comprehensive and embedded understanding of abnormal MMS at Lajia Site since it is the first time that through the whole processes of earthquake (earthquake in pregnancy, eruption and ending) to explain the mechanisms. We can generalize probable mechanisms influenced by earthquake through theories of piezomagnetic, rheologic magnetic effect, and magnetic memory etc., in each period of earthquake respectively. It is also beneficial as a methodology to detect environmental mutation in local area within a relative short time span based on data of granularity, Rb/Sr, heavy mineral and dating etc.

Acknowledgements

This work was supported by the Key Project of the National Natural Science Foundation of China (Grant No. 90411015), the University Doctoral Foundation (Grant No. 20050284011), Open Foundation of the State Key Laboratory of Loess and Quaternary Geology from the Institute of Earth Environment, CAS (Grant No. SKLLQG0503), the Physical Geography of "985" Items, "211" Subject Construction and the Test Foundation of Modern Analyses Center of Nanjing University (Grant No. 0209001309). And helped by the Chinese Academy of Social Sciences institute of archaeology and the Qinghai Province cultural relic institute of archaeology the joint archaeology team of the Lajia Site vigorously and assisted by my classmate Zhu Qing to cooperate the experiment, all of them are greatly appreciated!

References

Chen J, Qiu G, Lu H Y et al (1997). An Variation of summer monsoon intensity on the loess plateau of central China during the last 130 ka- Evidence from Rb and Sr distribution [J], *Chinese Science Bulletin, 42 (6), 473-475*

Cheng Y X, Yang J (2005). Conspectus of environmental geo-physics, *the Geological Publishing House, Beijing, 70-85*

Ding J H, Lu Z Y, Huang X X (1994). Seism Geomagnetism. Seismological Press, Beijing, 104-163

Hao J Q, Gu Z J, Zhou J G et al (1999). The relationship of rheology of magnetite rock with anisotropy of magnetic susceptibility, *Chinese Journal of Geophysics, 42 (1), 112-119*

Li J S, Song X L, Sun Y L et al (1999). The magnetic susceptibility measurements of turbidity current sediments from Fuxian Lake of Yunnan Province and their correlations with earthquakes, *Acta Seismologica Sinica, 21(1), 83-88*

Li H Y, Zhang S H (2005). Detection of mineralogical changes in pyrite using measurements of temperature-dependence susceptibilities, *Chinese Journal Geophysics, 48 (6), 1384-1391*

Nils-Axel Mörner, Guangyu Sun (2008). Paleoearthquake deformations recorded by magnetic variables, *Earth and Planetary Science Letters 267, 495-502*

R.Thompson, F. Oldfield, translated by Yan Y J et al (1995). Environmental Magnetism, *The Geological Publishing House, Beijing, 1995, 20-22*

Sun J M, Ding Z L (1995). Preliminary studying on the physical mechanism of magnetic susceptibility of Chinese loess, *Progress in Geophysics, 10 (4), 88-93*

Shi W, Zhu C, Xu W F et al (2007). Relationship between abnormal phenomena of magnetic susceptibility curves of profiles and Human Activities at Zhongba Site in Chongqing, *Acta Geographic Sinica, 62 (3), 257-267*

Tsafrir Levi, Ram Weinberger, Tahar Aïfa et al (2006). Earthquake-induced clastic dikes detected by anisotropy of magnetic susceptibility, *Geology, 34(2): 69-72*

Wang J T, Gu X Z, Gong Y (2000). Probe into earthquake prediction from variation of electricity of rock associated with its strain and fracture, *Journal of Seismology, 20(3): 1-8*

Xia Z K, Yang X Y, Ye M L (2003). Prehistoric disasters at Lajia Site in Qinghai, *Chinese Science Bulletin, 48 (11), 1200-1204*

Yang X Y, Study environmental archeology based on different spatial scales (2003), *academic dissertation for Doctor's Degree of Peking University, 15-49*

Yang X Y, Xia Z K, Cui Z J, Ye M L (2004). Environmentalsettings of archaeology sites depositional processes and distribution at Guanting Basin, *Acta Geographic Sinica, 59 (3), 455-461*

Yang X Y, Xia Z K, Ye M L (2003). Prehistoric disasters at Lajia Site, Qinghai, China, *Chinese Science Bulletin, 48 (17), 1877-1881*

Analysis of Seismic Clusters near the Itoiz Reservoir Dam

Jiménez A (1), Luzón F (1), Santoyo M A (1), Al-Yuncha Z (1), García-Jerez (1), Romacho M D (1), García-García J M (1)

(1) University of Almería, ajlloret@ual.es

Keywords: declustering, reservoir induced seismicity, ETAS model, complex networks

Introduction

Triggering of earthquakes by filling of artificial water reservoirs is known for over six decades. Even if this happens at only a small percentage of reservoirs in the world, up to 90 sites have been globally identified where earthquakes have been triggered by filling of water reservoirs (Gupta, 1992; Talwani, 1997; Gupta, 2002). The reservoir-triggered seismicity usually appears under special conditions and is controlled by factors as the geology of the region, fracture location and directions, appropriate ambient stress field conditions, hydromechanical properties of the rocks, as well as the size of the reservoir, and specially the water depth, or the periodicity and extent of the water level fluctuations (Ruiz et al., 2006).

On September 18, 2004, a 4.6 mbLg (magnitude derived from surface amplitude) earthquake occurred in the western Pyrenees, at around 20 km ESE from Pamplona city. The epicenter is located at around 4 km distance from the Itoiz dam, which started impounding in January 2004. We decided to study the aftershock sequence and to compare it with others occurred at the same area in order to evaluate weather this could be a case of reservoir induced seismicity. In order to do so, we first decluster the catalogue by means of a link algorithm whose distance is based on the ETAS model. We then analyze the different clusters obtained by analyzing their fractal dimension and the properties of the complex network they form.

Materials and Methods

The study area is located in a region with a complex thin-skinned structure belonging to the South Pyrenean Zone (Ruiz et al., 2006), and represents a square of 2ºx2º centred in the 111-m high Itoiz dam (42.8N, 1.35W). The data used have been recorder by the Instituto Geográfico Nacional (IGN), and contains earthquakes from 1999 to 2008. In total, 2350 earthquakes with magnitude greater than 1 have been used. The *a* and *b*-values of the Gutenberg-Richter law (Gutenberg and Richter, 1956) for all earthquakes are: a = 0.95±0.16 and b = 1.11±0.09, with correlation coefficient of 0.9566. It was obtained by fitting the probability density function (pdf).

In order to study the September 18, 2004, 4.6 mbLg, aftershock sequence, we first proceed to decluster the catalogue. In the literature of seismology, people traditionally use some window-based methods or link-based methods to decluster the catalogue or to identify earthquake clusters (Zhuang et al., 2004). The main problem is to identify which earthquakes are correlated, because there is no unique operational way to distinguish between aftershocks and main shocks (Baiesi and Paczuski, 2005). In this work, we use a correlation function based on the ETAS model. The likelihood of two earthquakes to be correlated is given by (Helmstetter and Sornette, 2002):

$$\Theta_{m_i}(t-t_i, \vec{r}-\vec{r}_i) = \rho(m_i)\Psi(t-t_i)\Phi(\vec{r}-\vec{r}_i) \qquad (1)$$

where $\Theta_{m_i}(t-t_i, \vec{r}-\vec{r}_i)$ is the seismic rate induced by a single "mother", or the "bare propagator". $\rho(m_i)$ gives the number of "daughters" born from a mother of magnitude m_i :

$$\rho(m_i) = K10^{\alpha(m_i - m_0)} \qquad (2)$$

which is justified by the power law dependence of the volume of stress perturbation as a function of earthquake size. *α* quantifies how fast the average number of aftershocks per main shock increases with the magnitude of the main shock (mother). We will set it to the *b*-value $b = \alpha = 1$. m_0 is a lower bound magnitude bellow which no aftershock is triggered. *K* is a constant that will be embedded in the correlation threshold.

$$\Psi(t-t_i) = \frac{1}{(c+t-t_i)^p} \qquad (3)$$

$\Psi(t-t_i)$ accounts for the Omori's law (Omori, 1894). We assume *p*=1 and *c*=0.001 (Helmstetter and Sornette, 2002). Finally,

$$\Phi(\vec{r}-\vec{r}_i) = \frac{\mu}{d\left(\frac{|\vec{r}|}{d}+1\right)^{1+\mu}} \qquad (4)$$

$\Phi(\vec{r}-\vec{r}_i)$ is the spatial "jump" distribution from the mother to each of the daughters, quantifying the probability for a mother to be triggered at a distance $|\vec{r}-\vec{r}_i|$. We set *μ*=1 and *d*=1 (Helmstetter and Sornette, 2002).

We first calculate the distance between events as *Θ*. We then create a hierarchical cluster tree where two events are linked if their correlation is higher than certain threshold, where we have more than only one giant component. Then, we already have a complex network we can analyze.

The basic characteristics of a complex network are its degree distribution, its average length and its clustering coefficient, that are described below.

The degree (or connectivity) d_i of a node *i* is the number of edges incident with the node. The characteristic path length *Lp* is the mean of the shortest path (expressed in number of edges) connecting any two vertices on the graph. We used Dijkstra's algorithm to implement this calculation (Dijkstra, 1959).

The cluster coefficient *Cp* is the likelihood (between 0 and 1) that the *kv* neighbors of vertex *v* are also connected to each other, averaged over all vertices. Regular networks or graphs have a high *Cp* (*Cp* ≈ 3/4) but a long characteristic path length (*Lp ≈ N/2k*); random graphs have a low *Cp*(*k/N*) but the shortest possible path length (*Lp ≈ ln(N)/ln(k)*). A network is said to present the "small world" behaviour when it has a clustering coefficient close to that os a regular network but a low path length, similar to that of a random network (Watts and Strogatz, 1998).

In order to better describe the aftershock sequences, we also calculate their correlation dimension (Grassberger and Procaccia, 1983).

Results and Discussion

Once we applied the described declustering algorithm to the data, we obtained a declustered catalog with 994 mainshocks, which follows a Gutenberg-Richter power law with *a*=

1.17±0.22 and *b*=0.68±0.08. The threshold that gives more than 1 giant component is *Θ*>1. Since the locations in depths were not very accurate, and in most of the cases the location algorithm does not give the depth of the earthquakes, we decided to do the study in two dimensions.

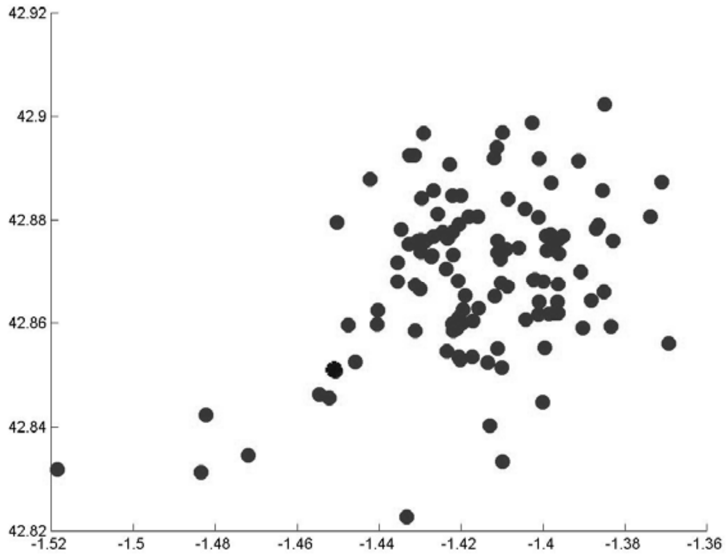

Figure 1. Main cluster corresponding to the m=4.6, September 18, 2004 earthquake. In blue we show the main shock.

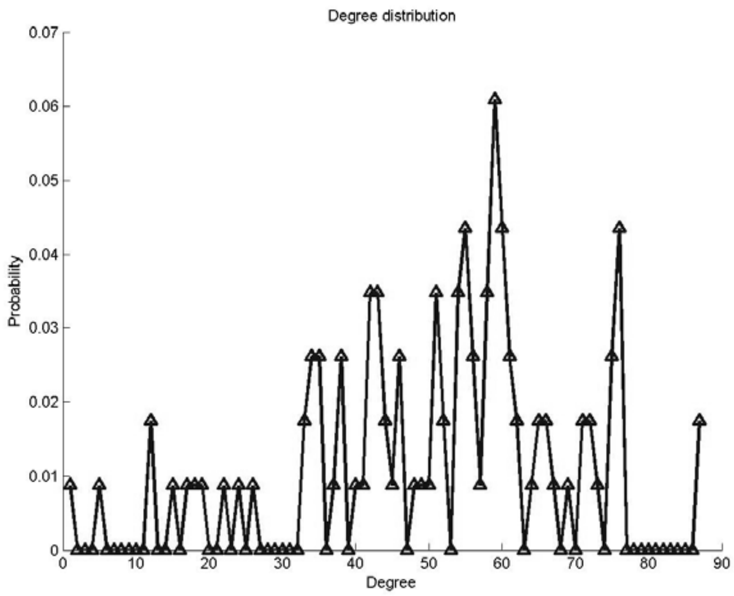

Figure 2. Degree distribution corresponding to the m=4.6, September 18, 2004 earthquake.

In Fig. 1 we show the main cluster, corresponding to the m=4.6, September 18, 2004 earthquake, and with 115 earthquakes with magnitude greater than 1. The correlation dimension is 1.44±0.03. In Fig. 2 we show the degree distribution corresponding to the complex network obtained for this aftershock sequence. The corresponding clustering coefficient and average path length are C=0.42 and L=1.48. As we can see, the clustering coefficient is low. The clustering coefficient corresponding to a random network would be Crand=0.49 in this case, higher than the one obtained, and the path length would be Lrand=1.18, lower than the one obtained. So, no small world behaviour is found.

We now proceed to study other aftershock sequences obtained in the same region. The first one corresponds to the m=3.8, February 21, 2002 earthquake, with 83 aftershocks with magnitude greater than 1. The correlation dimension found is 1.08±0.04, which approaches a line. Note the difference with the one obtained for the m=4.6, September 18, 2004 earthquake, where the aftershock sequence seems to be more diffused. Note also that the m=3.8, February 21, 2002 earthquake occurred before the Itoiz reservoir impoundment.

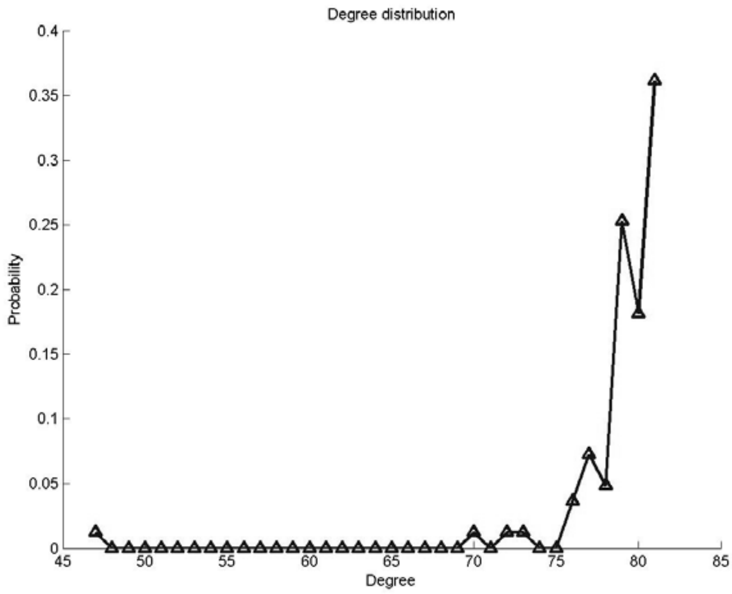

Figure 3. Degree distribution corresponding to the m m=3.8, February 21, 2002 earthquake.

In Fig. 3 we show the degree distribution corresponding to the m=3.8, February 21, 2002 earthquake. As we can see, the nodes are highly correlated between them. This is reflected in the clustering coefficient, C=0.97, higher than the corresponding to a random network, Crand=0.95. Its average path length is L=1.00, lower than the corresponding to a random network, Lrand=1.01. We observe that there is a small world behaviour, and that the network is very close to a random network.

Other important cluster is the m=3.4, May 4, 2006, with 41 earthquakes. The degree distribution is very similar in shape to the m=3.8, February 21, 2002 earthquake, except that the maximum degree is around 41. The correlation dimension is 0.52±0.03, in between a point source and a line. The clustering coefficient is C=0.93, and the corresponding to a random network would be Crand=0.88. The average path length is L=1.02, and for the random network would be Lrand=1.04. As we can see, there is also small world behaviour.

Finally, the cluster corresponding to the m=3.1, June 22, 2007 has 30 earthquakes with magnitude greater than 1. The degree distribution is very similar to the two preceding earthquakes. The correlation dimension is 0.74±0.02, and the clustering coefficient and average path length are C=0.93 and L=0.97, respectively. The corresponding to a random network are C=0.90 and Lrand=1.03, so it is also a small world network, close to a random one.

As we can see, the only cluster with no small world behaviour is the one corresponding to the m=4.6 September 18, 2004 earthquake. It also has other differences, as the shape of the degree distribution and the correlation dimension. It can be caused by the higher magnitude, so that the aftershock sequence is more diffused in space. It also can be due to the 2D analysis, imposed by the data, so that the other earthquakes are more vertical that this one. Other cause can be a difference in the source, and could be a reservoir-triggered earthquake, because of the first impoundment at the Itoiz 111 high dam. Other authors (Ruiz et al, 2006) found that this earthquake is a case of rapid response of reservoir-triggered earthquake. Our analysis shows that other seismic series at the same area have different behaviour than this one, either before or after impoundment of the reservoir. So, in case of being a reservoir-triggered earthquake, it would correspond to the initial seismicity, that is the most widely observed category of reservoir-triggered seismicity.

Acknowledgments

This work was partially supported by Ministerio de Medio Ambiente, Spain, under Grant 115/SGTB/2007/8.1, by the EU with FEDER, and by the research team RNM-194 of Junta de Andalucía, Spain.

References

Baiesi M. & Paczuski M (2005). Complex networks of earthquakes and aftershocks, *Nonlin. Processes Geophys., 12,1-11.*

Dijkstra E. W (1959). A note on two problems in connection with graphs, *Numerische Math., 1, 269-271.*

Grassberger P. & Procaccia I (1983). Characterization of Strange Attractors, *Phys. Rev. Lett.*,50, 346–349.

Gupta H. K (1992). Reservoir-induced earthquakes, *Elsevier, Amsterdam, 364 pp*.

Gupta H. K (2002). A review of recent studies of triggered earthquakes by artificial water reservoirs with special emphasis in Koyna, India, *Earth-Sci. Rev., 58, 279-310.*

Gutenberg B. & Richter C. (1956). Earthquake magnitude, intensity, energy, and acceleration, *Bull. Seism. Soc. Am., 46, 105-145.*

Hemlstetter A. and Sornette D. (2002). Diffusion epicenters of earthquake aftershocks, Omori's law, and generalized continuous-time random walk models, *Phys. Rev. E, 66, 061,104.*

Instituto Geográfico Nacional (IGN). http://www.ign.es/ign/es/IGN/home.jsp

Omori F. (1894). On the aftershocks of earthquakes, *J. Coll. Sci. Imp. Univ. Tokyo, 7, 111.*

Ruiz M., Gaspà O., Gallart J., Díaz J., Pulgar J. A., García-Sansegundo J., López-Fernández C., and González-Cortina J. M (2006). Aftershocks series monitoring of the September 18, 2004 M=4.6 earthquake at the western Pyrenees: A case of reservoir-triggered seismicity?, *Tectonophysics, 424, 223-243*.

Talwani P. (1997). On the nature of the reservoir-induced seismicity, *Pure Appl. Geophys., 150, 473-492*.

Watts D. J. & S. H. Strogatz (1998), Collective dynamics of 'small-world' networks, *Nature, 393, 440-442*.

Zhuang J., Ogata Y. & Vere-Jones D (2004). Analyzing earthquake clustering features by using stochastic reconstruction, *J. Geophys. Res., 109, B05,301.*

Seismic Station with Geomechanical Network in Medieval Mine

Kaláb Z. (1), Knejzlík J. (2), Lednická M. (3)

1) Institute of Geonics of the ASCR, Studentská 1768, CZ 708 00, Ostrava – Poruba, Czech Republic; also VSB-Technical University of Ostrava, kalab@ugn.cas.cz
(2) Institute of Geonics of the ASCR, Studentská 1768, CZ 708 00, Ostrava – Poruba, Czech Republic, knejzlik@ugn.cas.cz
(3) VSB-Technical University of Ostrava, 17. listopadu 11, CZ-708 33 Ostrava – Poruba, Czech Republic, also Institute of Geonics of the ASCR, Ostrava, lednicka @ugn.cas.cz

Keywords: seismic load, medieval mine, geomechanical network

Introduction

The beginnings of underground mining of tin-tungsten deposits in the area of Slavkovský les Mts. date back to the first half of the 16th century. The mining at Čistá – Jeroným Mine (Sokolov district, West Bohemia) - began much later than in the surroundings. Although the development of mining in this mine was rapid, it did not last long. However, the mining and sporadic exploitation continued with many interruptions until the beginning of the 20th century. Detailed description of mining history in the locality of Čistá was realized by Žůrek and Kořínek (2001/2) and Kaláb et al. (2008). The Jeroným Mine is "textbook" of mining methods (rock breakings), e.g. hammers of various dimensions and so-called bits (wedges, Fig. 1), work done with fire (fire setting, Fig. 2), blasting (from 1774, Fig. 3).

Figure 1. Jeroným Mine – rock breaking using traditional hand tool – hammer and bit

Figure 2. Jeroným Mine – rock breaking using "fire setting" (soot on wall)

Figure 3. – Jeroným Mine – gallery exploited using blasting

The Jeroným Mine was "forget and re-appeared" (historical documentation was destroyed during fire in 1772). This mine is undoubtedly such an engineering monument with European significance. In 1990, the Jeroným Mine was declared as cultural monument of the Czech Republic. This mining locality is not open for public in the present time but in connection with the assumed utilization of the mine for the purpose of tourism, in 2001, works started to obtain more objective and specific idea about the stress-strain and stability state of this shallow mine (Kaláb et al., 2006). Integral part of this study is also evaluation of seismic load of the Jeroným Mine. Seismological monitoring and first data are described in this contribution.

Instrumentation

Seismological monitoring has started together with the reconstruction of old drainage adit in 2004 because significant load by vibrations occurred (drilling and blasting especially). Seismic recording apparatus PCM3-EPC (e.g. Knejzlík and Kaláb, 2002) with special modification for environment with high air humidity and drip water (inner and outer housing IP55) was realized. Therefore, signal cables (connection with the DCF 77.5 kHz time receiver, seismometer junction box and GSM modem) are pulled-on to additional silicon tube. The seismic apparatus with three seismometers of SM-3 type and with telemetric transmission of data through the GSM net is used for triggered registration of events. The apparatus consists of data acquisition system PCM3 and a single board PC (Advantech Biscuit PC PCM-3864). During the period when recording of seismic data is not triggered, the PC decodes only the time information of DCF. It means that free machine time is available in this mode. This can be advantageously utilized for Master Unit functioning in the built distributed control and measurement network. The apparatus is telemetrically connected to the Institute of Geonics, which will enable the remote control of station operation, a change in the setting of operating parameters and data transmission to the interpretation centre.

Observing of stability of underground spaces began in 2001 when quarterly inspection of selected parameters started (changes in mine water level fluctuation – 4 points, measurement of openings of joints - 10 points, measurement of horizontal and vertical directions of cross-section convergence – 21 points). Using results from mathematical modeling of stress distribution (Hrubešová et al., 2007), new set of points for continuous monitoring was selected.

To have more detailed information about rock massif behavior, distributed control and measurement network for evaluation of hydrologic, geomechanical and other parameters has been built up in the Jeroným Mine from the first half of 2006. Instrumentation is generally based on commercial control kit and sensors (Knejzlík, 2006, Knejzlík and Rambouský, 2008). Current monitoring points include (Fig. 4):

- KV2 and KV3 for measurement of changes in mine water level fluctuation
- KD1 – KD4 for measurement of openings of joints (aperture of joints)
- KK1 for measurement of vertical direction of cross-section convergence
- KT1 and KT2 for measurement of temperature of mine atmosphere
- CCBM1 and CCBM2 for measurement of change of tensor stress state of rock mass (e.g. Staš et al., 2005)
- LD1 laser distance meter

Distributed control and measurement network system is integrated to the existing seismic recording station (equipped by data transmission via GSM network to registration centre in Ostrava). Completely monitoring system is performed as modular to have possibility to change configuration of this system.

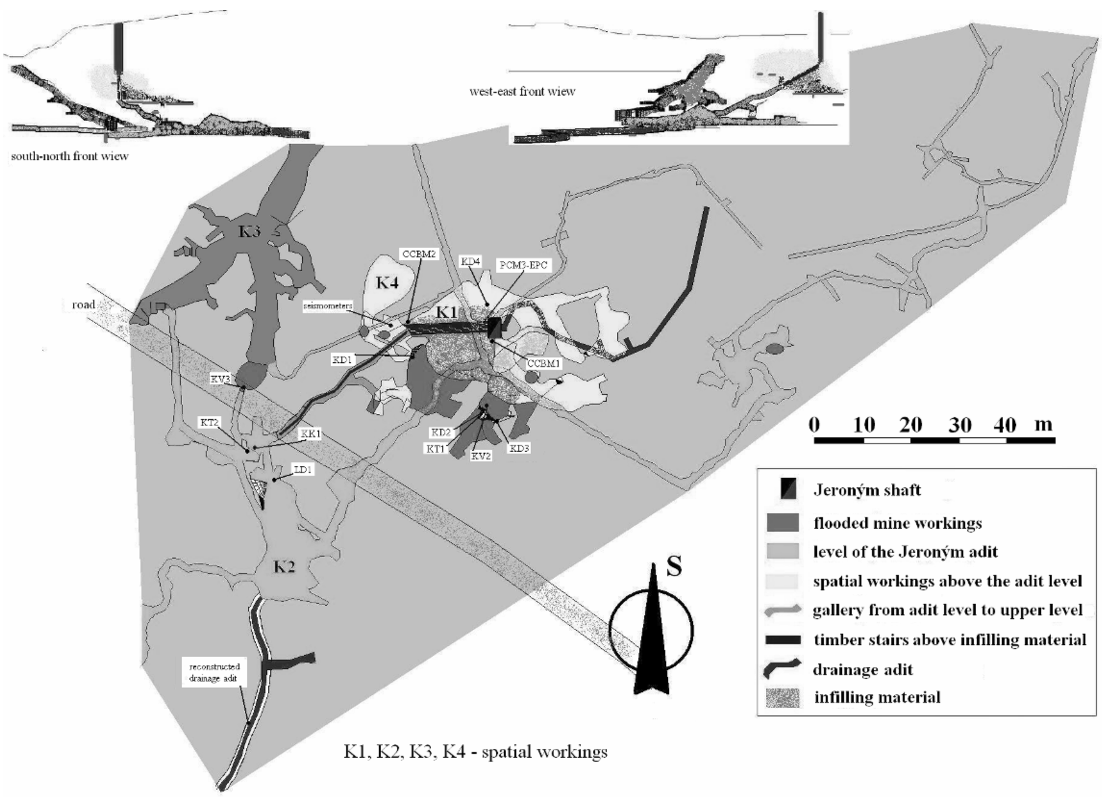

Figure 4. Sketch of Jeroným Mine (part called Abandoned Mine Workings) including two cross-sections and positions of measurement points (see text)

Seismological Monitoring

The North-West Bohemia/Vogtland is the nearest region with natural seismicity (Kracke et al., 2000) that is located about 25 km to the west from the mine. The 1985/86 swarm (December – February) ranks among the largest in the whole region under discussion. More than 8000 events were recorded in its course, the two largest (M_L =4.6 and M_L = 4.1) of them caused partial damages of buildings (Fischer and Horálek, 2003). A characteristic feature of this region is the repeated occurrence of intraplate earthquake swarms with M_L< 5.0. In the past decade, swarms that occurred in January 1997and August-December 2000 were dominant seismic activity within this region (e.g. Horálek et al., 2003, Nehybka and Tilšarová, 2007). The strongest, macroseismically felt shock of swarm of 1997 had a local magnitude of 3.0. However, seismological monitoring in the Jeroným Mine does not exist during that time.

First evaluation of seismic loading of the Jeroným Mine was published by Kaláb (2003). Experimental measurement contributed evaluation of ambient seismic noise during common activities in the underground spaces; maximum velocity values does not exceed $2*10^{-5}$ $m.s^{-1}$ on vertical component and $5*10^{-6}$ $m.s^{-1}$ on horizontal ones. Seismic effect of heavy traffic on road above the mine represented the most significant manifestations. Nevertheless, the building operations during reconstruction of old drainage adit increased the seismic load.

In June 2004, together with initialization the old adit reconstruction, seismological monitoring was started by means of a station installed directly in the mine working. Seismometers SM3 type with upper limit frequency 80 Hz were used because main aim was detecting vibrations generated by blasts using as a part of technology during renovation of passage for drainage and ventilation. Three sensors in geographical organization are anchored on concrete pillar in underground space to have possibility to detect the highest frequencies of recorded vibrations. Velocity amplitude of the seismic channel was 0.5 $mm.s^{-1}$.

More than 250 events of blasting operations were recorded during reconstruction of the adit. The wave patterns consisted of several wave groups that represent individual stages of blasting (Fig. 5).

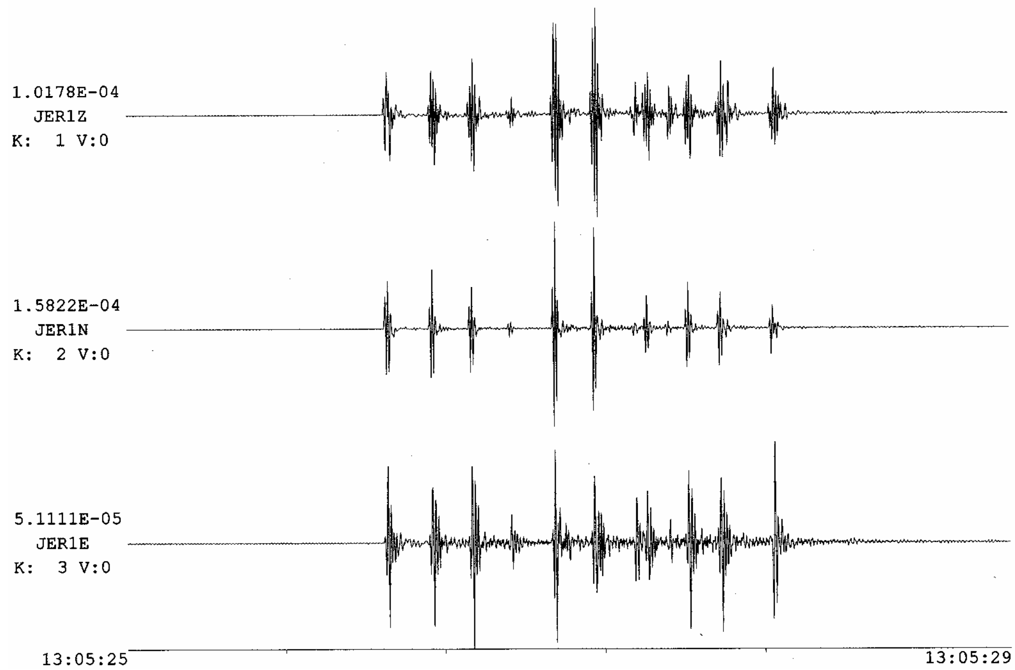

Figure 5. Example of wave pattern (January 10, 2006, loc. time 13:05) of blast generated in the Jeroným adit (horizontal axis is local time, vertical, N-S and E-W components [in $m.s^{-1}$] are displayed top down)

Particular aims of seismic monitoring were:

- To maximize breakup without failure of rock in the surroundings,
- To minimize seismic effect in underground spaces,
- To use the most value of boreholes with explosives and specific timing.

Main aim of the monitoring was to avoid damages to the monuments in the mine. Using the Czech technical standard 73 0040 and an expert opinion, the limit value of maximum oscillation velocity in the working was fixed to 0.1 mm.s^{-1}. It was necessary to regulate parameters of blasting operations when this value was exceeded (see it in Fig. 6 – October, 27, Dec. 11 and Dec. 16). Maximum measured velocity value, i.e. 0.16 mm.s^{-1}, was detected at the vertical component (component Z). Relation between maximum values of vertical component of velocity and distances was good (Fig. 7); correlation coefficient R^2 = 0.51 using 230 input data from years 2005 and 2006, changes in blast scheme were not take into account. Relations for horizontal component were not so good.

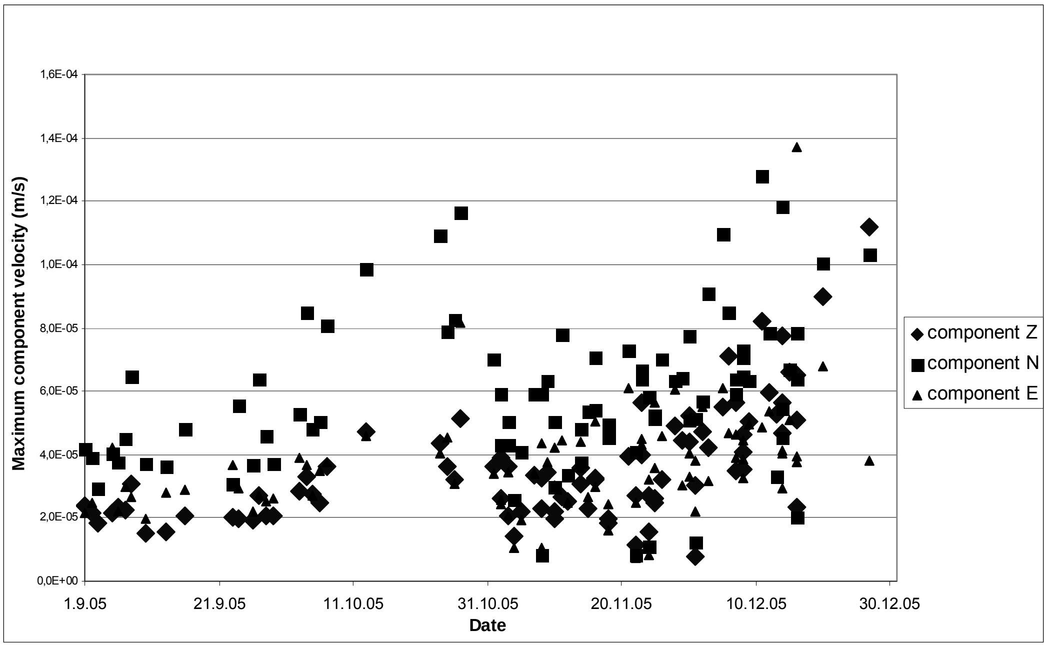

Figure 6. Trends of maximum values of component velocity generated by blasting operations in Jeroným adit through time period 01.09.2005 – 31.12.2005 (date in format day.month.year)

After finishing of reconstruction works, seismic load of mining spaces very decreased. It was possible to set lower trigger level. Current recorded seismic events (triggered regime) are possible to divide into following groups:

- Earthquakes from West Bohemia/Vogtland region (Fig. 8)
- Seismic events from “surroundings” (firstly earthquakes from Alps and mining induced seismicity from Lubin area in Poland, Fig. 9)
- Far distant earthquakes (only small parts - garbled signal due frequency range of apparatus)
- Technical seismicity (especially heavy lorries)
- Seismic effects of quarry blasts (mainly feldspathic quarry Krásno and stone-pit Vítkov)
- Ambient noises and indefinable signals

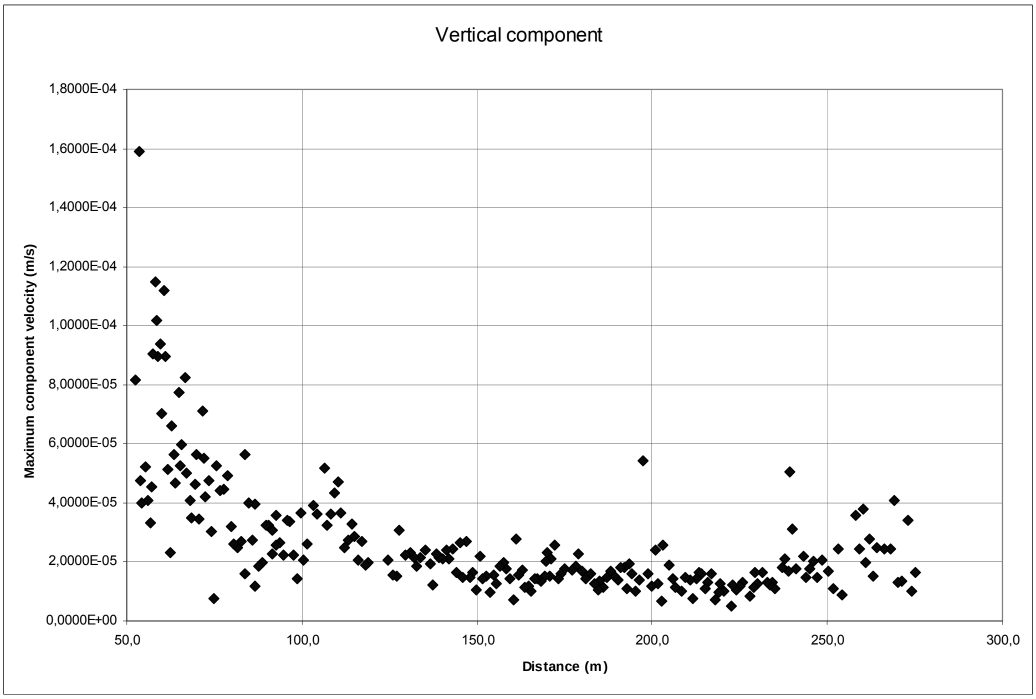

Figure 7. Relation between maximum values of component velocity generated by blasting operations in Jeroným adit in the period 01.01.2005 – 28.2.2006 (date in format day.month.year) and distances

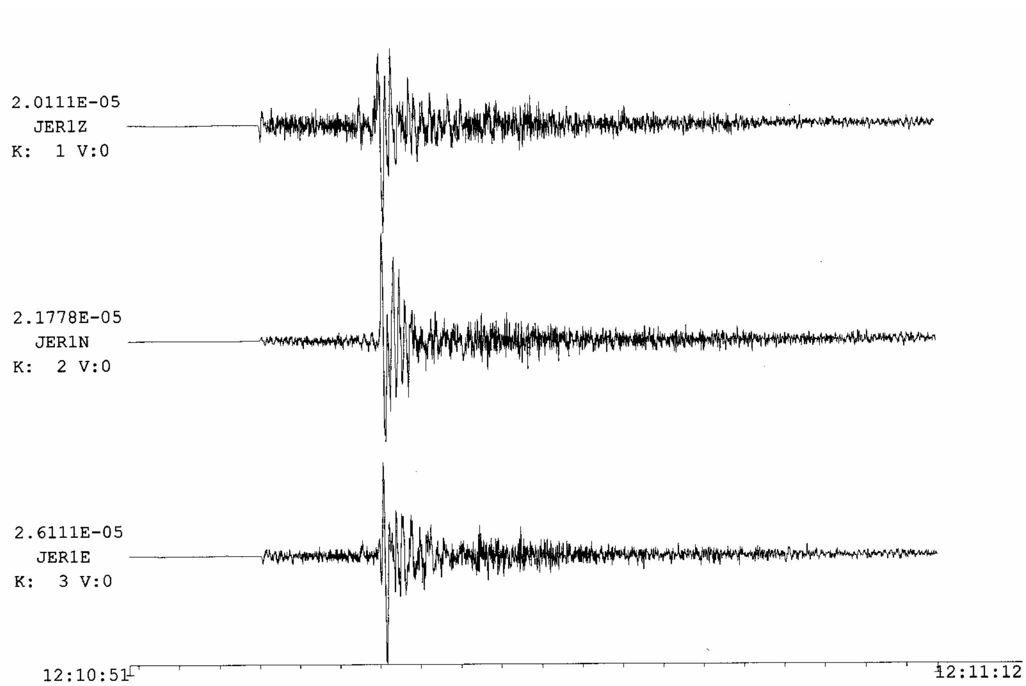

Figure 8. Example of wave pattern (January 27, 2008, loc. time 12:10) of earthquake from West Bohemia/Vogtland region, ML=2.5 according IG ASCR Prague (horizontal axis is local time, vertical, N-S and E-W components [in m.s^{-1}] are displayed top down)

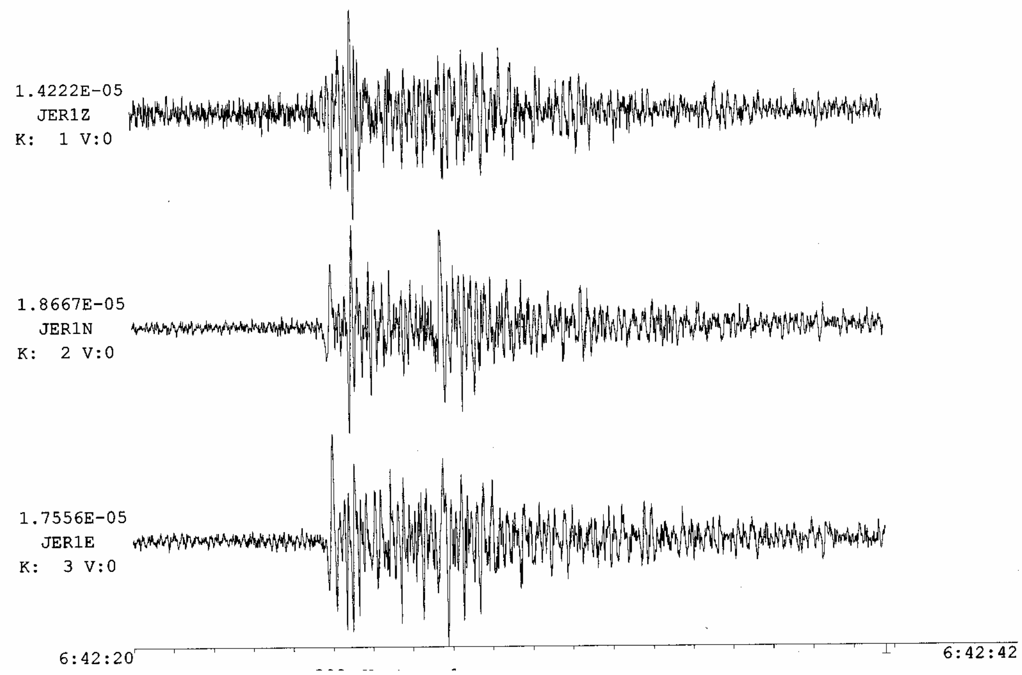

Figure 9. Example of wave pattern (October 19, 2007, loc. time 06:42) of tectonic event from Germany, ML=3.6 according NEIC-HDF (horizontal axis is local time, vertical, N-S and E-W components [in m.s^{-1}] are displayed top down)

Number of events in individual groups in 2007 was 15 – 21 – 17 – 80 – 124 – 150 records (the same sequence of groups as above). Maximum values of velocity interpreted from wave patterns of events mentioned above are usually up to 10^{-2} mm.s^{-1}. Therefore, it is necessary to say that current seismic load of Jeroným Mine is low and, probably, it do not have influences on stability of underground spaces.

Conclusion

Methodology of evaluation of seismic load of historical mining monuments has to respect strict protection of conserved parts, careful installation of instrumentation and individual evaluation of measured data. From the seismological point of view, common technique was accepted:

1. Evaluation of natural seismicity in near surroundings
2. Expected manifestations of technical seismicity (generated by traffic, quarries, …)
3. Short term experimental measurements of ambient noise
4. Design of seismological monitoring
5. Installation of sensors and seismic apparatus
6. Monitoring and/or experimental measurements, interpretation of data
7. Evaluation of influence of vibrations on stability of underground spaces

Current evaluation of seismic load of the Jeroným Mine documents slight manifestations of vibrations in underground spaces. However, the seismological measurements described above are very important for detailed assessment of rock stability. From the other hand, it is necessary to evaluate influence of subsequent reconstructions in the mine (for example, a gallery connecting the Old Mine Workings and Abandoned Mine Workings parts is planned).

Acknowledgement

This research is performed with the financial support of the Czech Science Foundation, No. 105/06/0068 “Researches into Factors Affecting the Stability of the Medieval Jeroným Mine at Čistá”.

References

Fischer T. & Horálek J. (2003). Space-Time Distribution of Earthquake Swarms in the Principal Focal Zone of the NW Bohemia/Vogtland Seismoactive Region: Period 1985-2001, *J. Geodynam., 35, 125-144.*

Horálek J., Brož M., Nehybka V., Novotný O., Ulrych J. & Korková J. (2003). Recent Geodynamics of West Bohemia in Relation on the Crustal Structure (Unique Natural Laboratory). *Acta Montana IRSM ASCR, Ser. AB, No. 11 (128), 55-74.*

Hrubešová E., Kaláb Z., Kořínek R. & Žůrek P. (2007). Geotechnical Monitoring and Mathematical Modelling in Medieval Mine Jeroným (Czech Republic), *Górnictwo i Geoinżynieria, Vol. 31, Zeszyt 3, 183-190.*

Kaláb Z. (2003). Evaluation of Seismic Loading of Medieval Mine Jeroným in the Czech Republic. *Acta Montanistica Slovaca, Vol. 8(2003), No.1, Košice, Slovakia, 36-41, in Czech.*

Kaláb Z., Knejzlík J., Kořínek R. & Žůrek P. (2006). Cultural Monument Jeroným Mine, Czech Republic – Contribution to the Geomechanical Stability Assessment, *Publs. Inst. Geophys. Pol. Acad. Sc., M-29(395), Warszawa, 137-146.*

Kaláb Z., Hrubešová E. & Lednická M. (2008). Mining History and Present State of Medieval Mine Jeroným, *Zeszyty Naukowe Politechniki Śląskiej, Ser. Górnictwo z. 283, Nr. 1781, Gliwice, 61-70.*

Knejzlík J. (2006). Distributed Control and Measurement System for Monitoring in the Jeroným Mine in Čistá (Czech Republic), *Transactions, Civil Engineering Series, VI, No.2/2006, VŠB –Technical University of Ostrava, Czech Rep., 181-187, in Czech.*

Knejzlík, J. and Kaláb, Z. (2002): Seismic Recording Apparatus PCM3-EPC. *Publs. Inst. Geophys. Pol. Acad. Sc., M-24(340), 187-194.*

Knejzlík J. & Rambouský Z. (2008). Current Solution for Distributed Control and Measurement System in the Jeroným Mine – Modular System, *Acta Geodynamica et Geomaterialia, Vol. 5, No. 2(150), Prague.*

Kracke D. et al.: Seismic Hazard Assessment of the East Thuringian Region/Germany – Case Study, *Studia geoph. et geod., Vol. 44/4, AS CR, Prague, 2000, 537-548.*

Nehybka V. & Tilšarová R. (2007). Seismic Activity in West Bohemia from 2001-2006, *Acta Geodyn. Geomater., Vol. 4, No. 4(148), 51-57.*

Staš L., Knejzlík J. & Rambouský Z. (2005). Conical Strain Gauge Probes for Stress Measurement, *Int. Symp. ISRM Eurock 2005 - Impact of Human Activity on the Geological Enviroment, Brno, Czech Rep., Balkema, Rotterdam, 587-592.*

Žůrek P. & Kořínek R. (2001/2). Opening of the Medieval Jeroným Mine in the Czech Republic to the Public, *Journal of Mining & Geological Science, Vol. 40-41, 51-72.*

Spectral Ratio Evaluation of Mining Induced Seismic Events from Karviná Region (Czech Republic)

Kaláb Z. (1), Knejzlík J. (2)

1) Institute of Geonics of the ASCR, Studentská 1768, CZ 708 00, Ostrava – Poruba, Czech Republic; also VSB-Technical University of Ostrava, kalab@ugn.cas.cz
(2) Institute of Geonics of the ASCR, Studentská 1768, CZ 708 00, Ostrava – Poruba, Czech Republic, knejzlik@ugn.cas.cz

Keywords: mining induced seismic events, Karviná region, spectral ratio

Introduction

Karviná region, part of the Upper Silesian Basin (Czech Republic and Poland, Fig. 1), where intensive mining induced seismic events have been documented for a long time (e.g. Holub, 1995, 1996, Kaláb and Knejzlík, 2002), is the area with underground exploitation of hard coal. Underground exploitation in this region is implicating changes in configuration of stress-strain conditions in rock massif. Subsequently, overrun of limiting state of elastic parameters can evoke brittle fractures and radiation of seismic energy (mining induced seismic event). These events have similar character as weak natural earthquakes and they are closely connected in space and time with current mining activities. There are frequent origins of mining induced seismic events here because significant part of production has been doing in seams with high seismic risk.

Figure 1. Geographic location of a part of the Upper Silesian Coal Basin situated on the territory of the Czech Republic (Takla et al., 2005)

Very intensive seismic events are documented in area under discussion (e.g. Rudajev, 1993) - the most intensive events originated in April 1983; radiated seismic energy about 10^{10} J (local magnitude about 3.7). Today, seismic network operated in this area by mines authority records as much as 30 thousand seismic events per year and quantity from 100 until 500 of them with seismic energy greater than 10^4 J (local magnitude about 1). With the exception of two rockbursts in 1983, no rockburst with energy more than 10^8 J was recorded. Monitoring seismic activity in the Karviná part of Upper Silesian Coal Basin contributes to the formulation of mining operation strategy and the situating of workings. At present, it is an inseparable part of the prevention strategies in rockburst condition.

Mining induced seismicity does not only implicate number of problems in underground workings, but the most intensive seismic events have also significant macroseismic effect on the surface (e.g., Kwiatek, 1998, Kaláb, 2004). This seismic effect on surface structures in Karviná region is monitored using solitaire seismic stations operated by the Institute of Geonics. Experimental investigation shows that seismic velocity component of the most intensive shocks exceeds the value of 10 $mm.s^{-1}$; value of acceleration component reaches 500 $mm.s^{-2}$ (e.g. Kaláb and Knejzlík, 2002). There exist real possibilities of damaging buildings due to overcrossing of the limit values according the Czech Technical Standard CSN 73 0040 “Loads of technical structures by technical seismicity”. Vibrations will also evoke unpleasant feeling of inhabitants.

The most popular seismological method for evaluation of seismic site response is based on Fourier transform of records and on horizontal to vertical spectral ratio method, so called horizontal to vertical spectral ratio (HVSR) method or Nakamura´s method. Principles and theoretical reasons of this method were described in details in many papers, e.g. Borcherdt (1970), Nakamura (1989) or Abott et al. (2001). Nakamura´s method is usually used with earthquakes. However, this method has number of modifications that were presented, for example, during 30th General Assembly of ESC in Geneva in 2006. Paper presented by Olszewska and Lasocki (2004) documents that the HVSR method can be successfully used to evaluate the local influence of the surface layer also for induced seismicity, in spite of the fact that in this case the conditions for application of the method essentially differ from the conditions met in natural seismicity. Interesting results from Poland were published also by Frej (2006, 2007).

Seismic effect on the surface

The main parameters influencing values of seismic effect on the surface were as follows (e.g. Doyle, 1995, Shearer, 1999, and others):

- Seismological parameters - “size” of seismic event (magnitude, seismic energy), prevailing frequencies of vibrations, duration of maximum phase, size and depth of focus, distance between evaluated point and epicenter,
- Geological parameters - local geological setting (response of surface and sub-surface layers), location of faults, elastic properties of medium in which seismic waves propagate,
- Constructional (structural) parameters - type of subsoil, connection between base and subsoil, dimensions and types of structures, distribution of masses in building, resonance characteristics of structures.

Specificity of seismic loading in areas with underground mining activities (e.g. Kaláb, 2004):

- „Quick“ migration of focus areas in time and space (depending on current position of mining operations),
- Foci in shallow depths (compared with depths of earthquakes) with significant event frequency,
- Wide amplitude range (up to tens of $mm.s^{-1}$ in epicentral areas) and frequency range (from 0.1 up 30 Hz at least),
- Complicated source mechanisms (explosive, implosive, composite) => complicated wave field on surface (deformed by local inhomogeneities).

Single Station Spectral Ratio

Methodology for our calculation of spectral ratios:

- Mining induced seismic events are recorded (velocity records) using PCM3-EPC apparatuses (Knejzlík and Kaláb, 2002),
- Spectra for horizontal and booth vertical components are calculated using FFT algorithm,
- The resulting vertical and horizontal spectra are smoothed with spline function,
- The two horizontal spectra are averaged to form one horizontal spectrum,
- Single station spectral ratio is calculated.

The main principles were presented e.g. by Nakamura (1989), Abbott et al. (2001), Lermo and Chavez-Garcia (1994) and others. We developed software for our records that is called MISS (Mining Induced Seismic events).

Initial results from calculation of spectral ratios for data recorded in the Karviná region were presented by Kaláb and Knejzlík (2006a, 2006b, 2006c), Kaláb and Lyubushin (2008) or Kaláb et al. (2008).

Partial results from these experimental calculations with individual events can be compiled:

- Spectral ratios of records of mining induced seismic events from different stations in Karviná region show individual shapes (related to sensor location and local geology)
- Two or more maxima are detected, which indicate complexity of the subsurface layers in this place (due to natural conditions or situation after sinking due to mining)

Experiment with weak and strong events sets

Karviná region contains many technical sources of vibrations with different intensities, partly inside the area under study, partly in the nearest surroundings. First results using ambient noise records document rather different shapes of spectral ratios comparing with ratios of seismic events (Kaláb and Lyubushin, 2008). Therefore, two sets of mining induced seismic events from three seismic stations were prepared. The first sets contain events whose values of recorded component velocity on given station exceed 1 $mm.s^{-1}$; these sets are signed using name of station with index *strong*. The second sets contain events with recorded component velocity in range 0.5 – 1 $mm.s^{-1}$; these sets are signed using name of station with index *weak*.

Obtained results are presented in figures 2 – 7. All sensors are located in concrete cellars of large buildings; therefore, spectra are significantly influenced in higher frequencies (up to 15 Hz). Thickness of sedimentary rock (unconsolidated and consolidated, generally strongly faulted) above the Carboniferrous massif are 400 m (seismic station Darkov 1), 450 m (seismic station Karviná 1) and 550 m (seismic station Stonava 1). Quaternary sediments, i.e. soils, loess, fluvial and redeposited materials, have thickness very variable, usually not higher than 15 m. Levels of groundwater ranged from 2 m up 10 m below surface.

The shapes and maximum values of spectral ratios for data recorded at Stonava station are very similar to each other for both data sets (STO^{strong}, STO^{weak}). The maximum value of H/V ratios (thicker lines) is about 8 at 2.3 Hz. Less significant peaks are at about 11 Hz. The second set pair was prepared for data recorded at Karviná station. The H/V ratios for both data sets are again similar; the maximum value of ratios is about 6 at 1.4 Hz. The set KAR^{strong} has also second significant peak of the same value at 5.5 Hz. It is question if it is effect of local geology or effect of resonant vibrations of structural element in building. Spectral ratios for data sets from Darkov station show substantial differences. The set DAR^{strong} has only one significant wide maximum about 8 at 2 Hz. However, the set DAR^{weak} has one wider maximum about 10 at 1.7 Hz and second one about 6 at 3.7 Hz. The results of H/V ratios for data sets from last mentioned station are not comparable. Perhaps, this effect is consequence of interference of vibrations generated by mining induced seismic events and next source of technical seismicity from surroundings. From the methodical point of view, it is possible to add that character of spectral ratios is determined using about 15 – 20 events in elaborated set of events from given station (averaged spectral ratios do not changed).

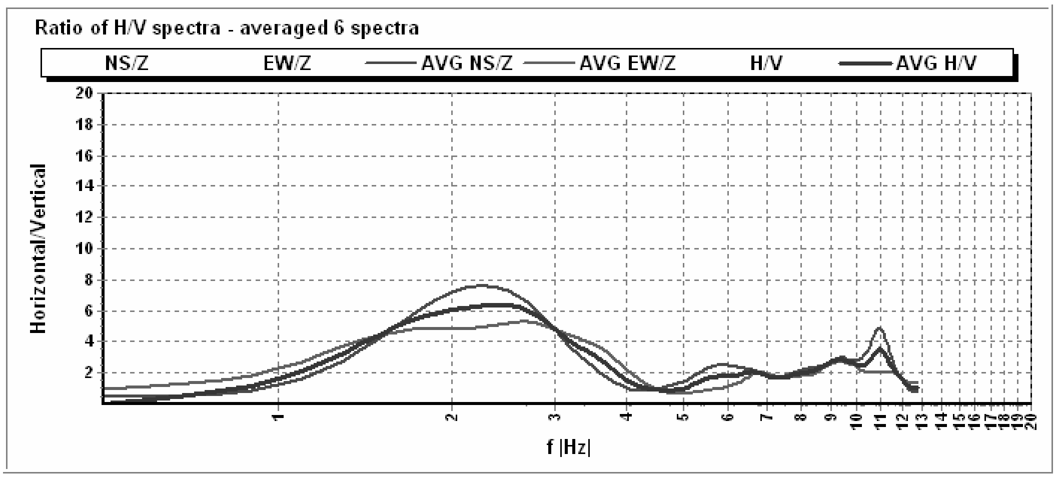

Figure 2. Averaged ratios of H/V spectra for Stonava 1 seismic station, set STO^{strong} (events whose value of recorded component velocity exceed 1 mm.s^{-1})

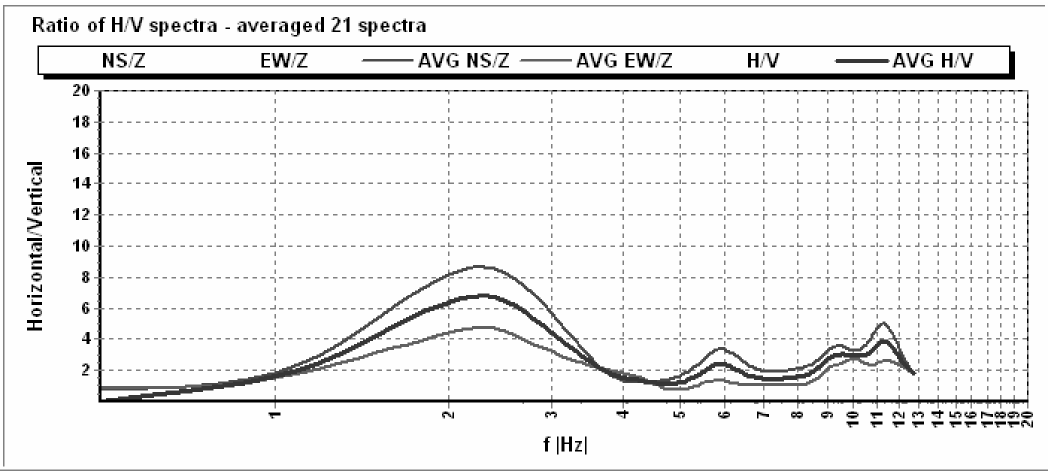

Figure 3. Averaged ratios of H/V spectra for Stonava 1 seismic station, set STO^{weak} (events with recorded component velocity in range 0.5 – 1 mm.s^{-1})

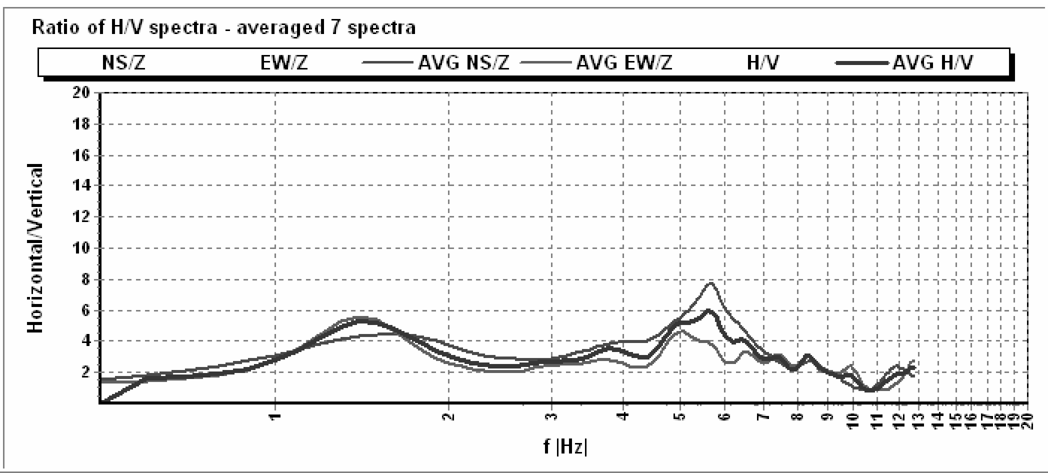

Figure 4. Averaged ratios of H/V spectra for Karviná 1 seismic station, set KAR^{strong} (events whose value of recorded component velocity exceed 1 mm.s^{-1})

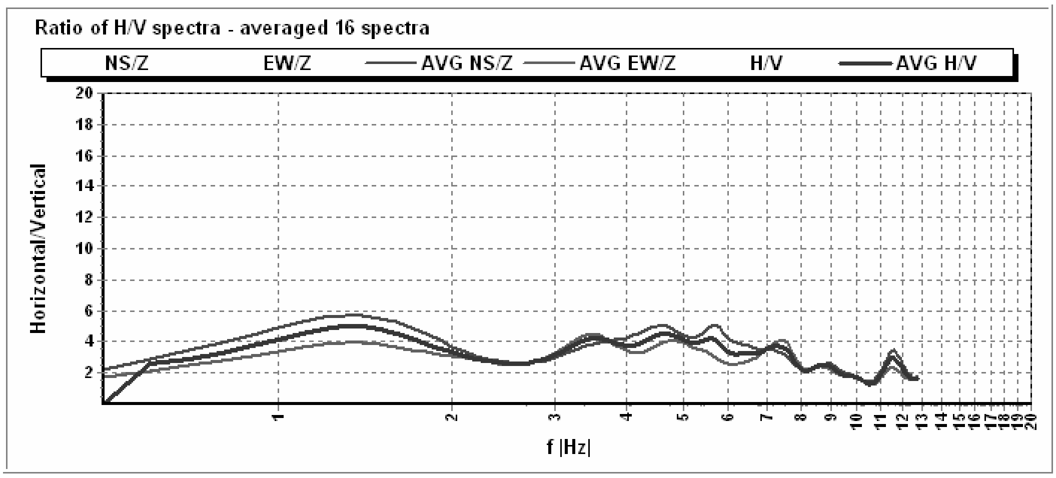

Figure 5. Averaged ratios of H/V spectra for Karviná 1 seismic station, set KAR^{weak} (events with recorded component velocity in range 0.5 – 1 mm.s^{-1})

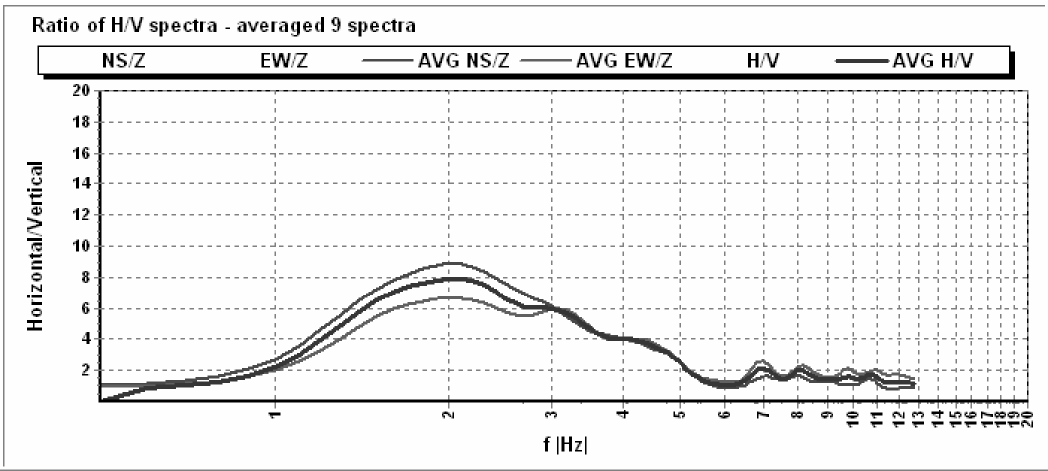

Figure 6. Averaged ratios of H/V spectra for Darkov 1 seismic station, set DAR^{strong} (events whose value of recorded component velocity exceed 1 mm.s^{-1})

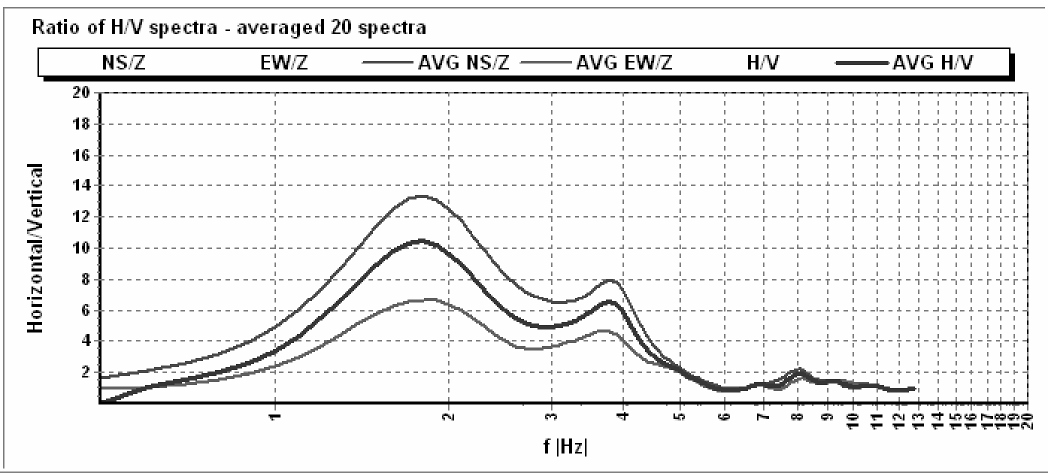

Figure 7. Averaged ratios of H/V spectra for Darkov 1 seismic station, set DAR^{weak} (events with recorded component velocity in range 0.5 – 1 mm.s^{-1})

Conclusion

Using of mining induced seismic events for determination of influence of local geology on seismic manifestation on the surface was documented by several authors, especially by Olszewska and Lasocki (2004). Comparison of H/V spectral ratios for two sets of mining induced seismic events from three seismic stations operated in Karviná region is presented in this paper. One group of data sets contains seismic events with significant manifestations in given point; second one was compounded from seismic events with manifestation of medium intensity. Obtained results document that it exists points with significant differences in the H/V spectral ratio curves and points with the same shapes of the H/V spectral ratio curves. Significant sources of vibrations in surroundings of seismic station are probable reason of this effect. Industrial seismicity (factory, forging shop, mining ventilation …) has significant sense in the Karviná region.

Acknowledgement

This paper has been achieved with the financial support of Czech Science Foundation, project No. 105/07/0878

References

Doyle H. (1995). Seismology, *John Wiley & Sons, Chichester, 218p*.

Frej A. (2006). Application of HVSR technique for estimation of site response, *Transactions of VSB – Technical University of Ostrava, Civil Eng. Series, Vol. VI, No.2/2006, 63-70 (in Polish).*

Frej A. (2007): The influence of geological structure on size of amplification in Bytom region, *Transactions of VSB – Technical University of Ostrava, Civil Eng. Series, Vol. VII, No.2/2007, 63-66 (in Polish).*

Holub K. (1995). Space and time patterns of induced seismicity, In: H. P. Rossmanith (ed.). Mechanics of Jointed and Faulted Rock., A. A. Balkema, Rotterdam, 657-662.

Holub K. (1996). Space-time variations of the frequency-energy relation for mining-induced seismicity in the Ostrava-Karviná mining district, *Pure appl. geophys., 146, No. 2, p. 265-280.*

Kaláb Z. (2004). Impact of seismicity on surface in mining affected areas: General description, *Acta Geodyn. Geomater., Vol. 1 (133), Prague, 35-39.*

Kaláb Z. & Knejzlík J. (2002). Systematic measurement and preliminary evaluation of seismic vibrations provoked by mining induced seismicity in Karviná area, *Publs. Inst. Geophys. Pol. Acad. Sc., M-24(340), 95-103.*

Kaláb Z. & Knejzlík J. (2006a). Field measurement of surface seismic vibrations provoked by mining in Karvina region, *Publs. Inst. Geophys. Pol. Acad. Sc., M-29(395), Warszawa, 185-194.*

Kaláb Z. & Knejzlík J. (2006b). Analysis of mining induced seismic events from the Karviná region in frequency domain, *Transactions of VSB – Technical University of Ostrava, Civil Eng. Series, Vol. VI, No.2/2006, 147-154 (in Czech).*

Kaláb Z. & Knejzlík J. (2006c). Response of selected sites in Karviná region during mining induced seismic events, *Abstract in: First European Conference on Earthquake Engineering and Seismology – Abstract book, Geneve, Switzerland, 320-321.*

Kaláb Z. & Lyubushin A. A. (2008). Study of site effect using mining induced seismic events and ambient noise from Karviná region, *Acta Geodyn. Geomater.,Vol. 5, No. 2(150), Prague,105-113.*

Kaláb Z., Knejzlík J. & Hrubešová E. (2008). Influence of local geology on ground velocity on the surface in Karviná area, *Journal Coal-Ores-Geological Survey, No. 1/2008, 26-31 (in Czech).*

Knejzlík J. & Kaláb Z. (2002). Seismic recording apparatus PCM3-EPC, *Publs. Inst. Geophys. Pol. Acad. Sc., M-24(340), 187-194.*

Kwiatek J. et al. (1998): Protection of building constructed on undermined areas, *Wydavnictwo Głównego Institutu Górnictwa, Katowice, Poland, 726p (in Polish).*

Olszewska D. and Lasocki S. (2004). Application of the Horizontal to Vertical Ratio Technique for Estimating the Site Characteristics of Ground Motion caused by Mining Induced Seismic Events, *Acta Geophysica Polonica. Vol. 52, No. 3, 302-318.*

Rudajev V. (1993). Recent Polish and Czechoslovakian rockburst research and the application of stochastic methods in mine seismology, *In: Young, R.P. (ed.): Rockbursts and Seismicity in Mines 93. Proceedings, A.A. Balkema, 157-161.*

Shearer P. M. (1999). Introduction to seismology, *Cambridge University Press, 260p.*

Takla G., Ptáček J., Holečko J. & Koníček, P. (2005). Stress state determination and prediction in rock mass with rockburst risk in Ostrava-Karviná Coal Basin, *In: Konečný, Pa. (ed): EUROCK 2005 – Impact of Human Activity on the Geological Environment, A.A.Balkema Publisher, Leiden, 625-628.*

Seismic Influence on Archaeological Objects in Syria

Karakhanian A S (1), Trifonov V G (2), Ivanova T P (3), Dodonov A E (2), Bachmanov D M (2), Minini H (4), Al-Kafri A-M (4)

(1) Institute of Geosciences of NAS, 24a Marshal Bagramyan Ave., Yerevan, Armenia, georisk@sci.am
(2) Geological Institute of RAS, 7 Pyzhevsky, Moscow 119017 Russia; trifonov@ginras.ru
(3) Institute of Dynamics of Geospheres of RAS, B. 6, 38 Leninsky Ave., Moscow 117334 Russia, trifonov@ginras.ru
(4) General Organization of Remote Sensing, P.O. Box 12586, Damascus, Syria, gors@mail.sy

Keywords: archaeoseismology, archaeological dating, seismic destruction

Introduction

Syria is the country of intensive active tectonics that are manifested by Late Pleistocene and Holocene faulting, folding, deformation of marine and river terraces and volcanism. Majority of them are concentrated in Western Syria, representing the northern part of the Dead Sea Transform zone (DSTZ) and adjacent southwestern termination of the East Anatolian fault zone (EAFZ) (Fig. 1). The DSTZ and EAFZ include their main active segments and associated active faults as well as some older strands that were active mainly in Miocene and Early Pliocene, but demonstrate fragmental younger activity up to now and can be qualified as possibly active faults. Some possibly active faults have been identified also in the Palmyride thrusted-folded belt; the Jhar fault seems to be the most active there. The Late Quaternary volcanism is concentrated in the Jebel Arab highland (Harrat Ash Shaam), Southern Syria and perhaps the adjacent part of Jordan.

Archaeological signs of the Homo inhabitancy document the Lower, Middle and Upper Paleolith (in the Euphrates valley, Palmyrides and DSTZ) and the Neolith (in the DSTZ, Upper Euphrates valley and its northern tributaries) as well as the continuous sequence of the Bronze and Iron Ages, Phoenician, Hellenistic, Roman, Byzantine and Islamic cultures. The oldest manifestations of seismic influence were found in walls of the Bronze Age Khirbet El-Umbashi (the Jebel Arab highland) and the Phoenician town of Ugarit (1365 or 1300 B.C.). Numerous data on seismic destructions were obtained in the Roman, Byzantine and Medieval Islamic buildings. The first historical data on the strongest earthquake are related to the ~760 B.C. event (Book of Prophet Zacharia 14: 4–5). There are a lot of reported data on the Hellenistic and younger strong seismic events. So, the archaeoseismological data can define more exactly parameters of known historical earthquakes rather than identify new ones.

The goal of this paper is to demonstrate results of studies of seismic influence on archaeological objects that were carried out for seismic hazard assessment in Syria. The studies included: (1) Archaeological dating of geological structures, characterizing the Late Quaternary tectonic activity and seismic rupturing; (2) registration of displacement and deformation of ancient constructions to define sense and rates of motion on active faults; (3) studies of seismic destruction and damage of ancient constructions to obtain characteristics of historical earthquakes.

Figure 1. Active faults and discussed archaeological sites: Ap, Aphamea; Ar, Arwad Island; Ha, Al Harif aqueduct; Kc, Krak des Chevaliers; Ku, Khirbet El Umbashi; Mh, Minet et-Halwa; Pa, Palmyra; Sm, St. Simeon Monastery; Ug, Ugarit. JH, Jhar fault; JA, Jebel Arab highland

Archaeological dating of active geological structures and seismic ruptures

The archaeological data have been obtained for dating both the prehistorical and historical geological structures which are important for seismic hazard assessment of the region. For example, the Tartus offshore active fault zone, associated to the DST is represented by the sinistral en echelon row of small anticlines in the shallow shelf of the Mediterranean. Two of them form small islands: Arwad and El Abbas. Structure of the anticlines is manifested by deformation of the Tyrrhenian marine terrace which is exposed in these islands and the adjacent parts of the Mediterranean coast. The lower limit of the age of deformation was defined by dating of the terrace with using two methods. At first, shells within the limestones and sandstones of the terrace cover gave the U-Th age from 83.4+4.6/-4.4 Ka to 128.5+10.4/-9.2 Ka (99.9+7.4/-6.8 Ka in the Arwad Island) (Dodonov et al., 2008). At second, the marine terrace was correlated with the river one whose cover contains the Middle Paleolithic artifacts. Both methods define the marine terrace age as beginning of the Late Pleistocene and

correspondingly the age of deformation as the Late Pleistocene and Holocene. It permits to qualify the Tartus zone as active one and to estimate preliminary its Mmax as 7.3.
The archaeological method was used also for dating of small seismic graben in the eastern side of El Ghab pull-apart basin of the DSTZ in the recent town of Afamia near ruins of the Roman–Byzantine city of Aphamea (Fig. 2). The graben is filled by debris with the Roman ceramics that proves the younger age of the earthquake.

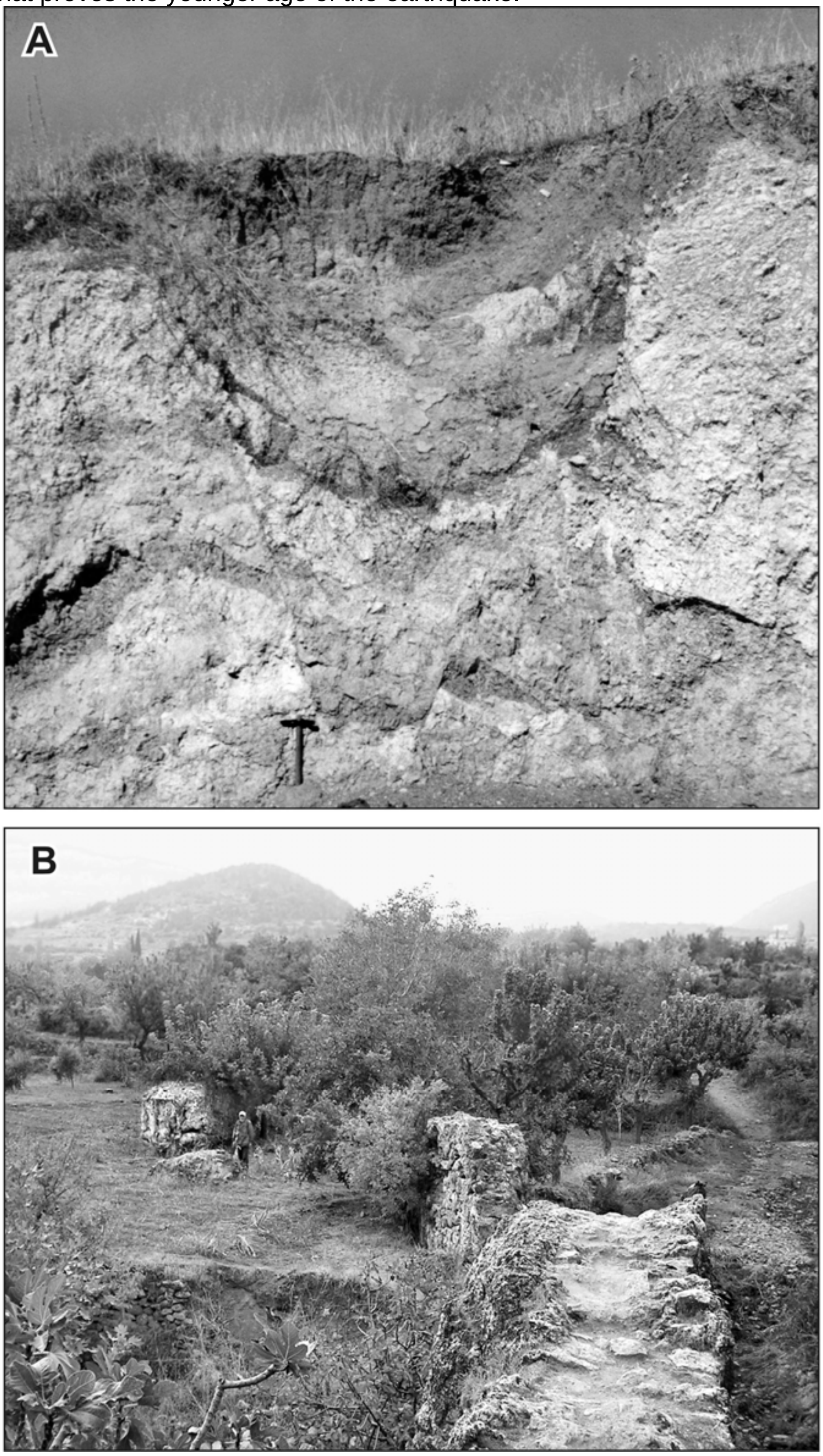

Figure 2. Archaeologically dated seismic ruptures. (A) Seismic micrograben in the eastern side of the El Ghab pull-apart basin near the city of Aphamea. (B) 12-meter sinistral offset of the Roman aqueduct on the El Ghab fault near the village of Al Harif

Displacement and deformation of ancient constructions on active faults

Offsets or deformation of ancient constructions in active fault zones are rare, but very important as exact data for definition of sense, average rate and sometimes regime (seismic or creep origin) of motion on the fault. One of the most spectacular examples is the 12-meter sinistral offset of Roman aqueduct on the El Ghab segment of the DST near the village of Al Harif, 5 km northward town of Myssiaf (Fig. 2). Trenching of the fault zone near the aqueduct dated it by the I century A.D. and showed that the offset was a cumulative effect of 3 seismic events; the youngest of them corresponded to the 1170 earthquake (Meghraoui et al., 2003).

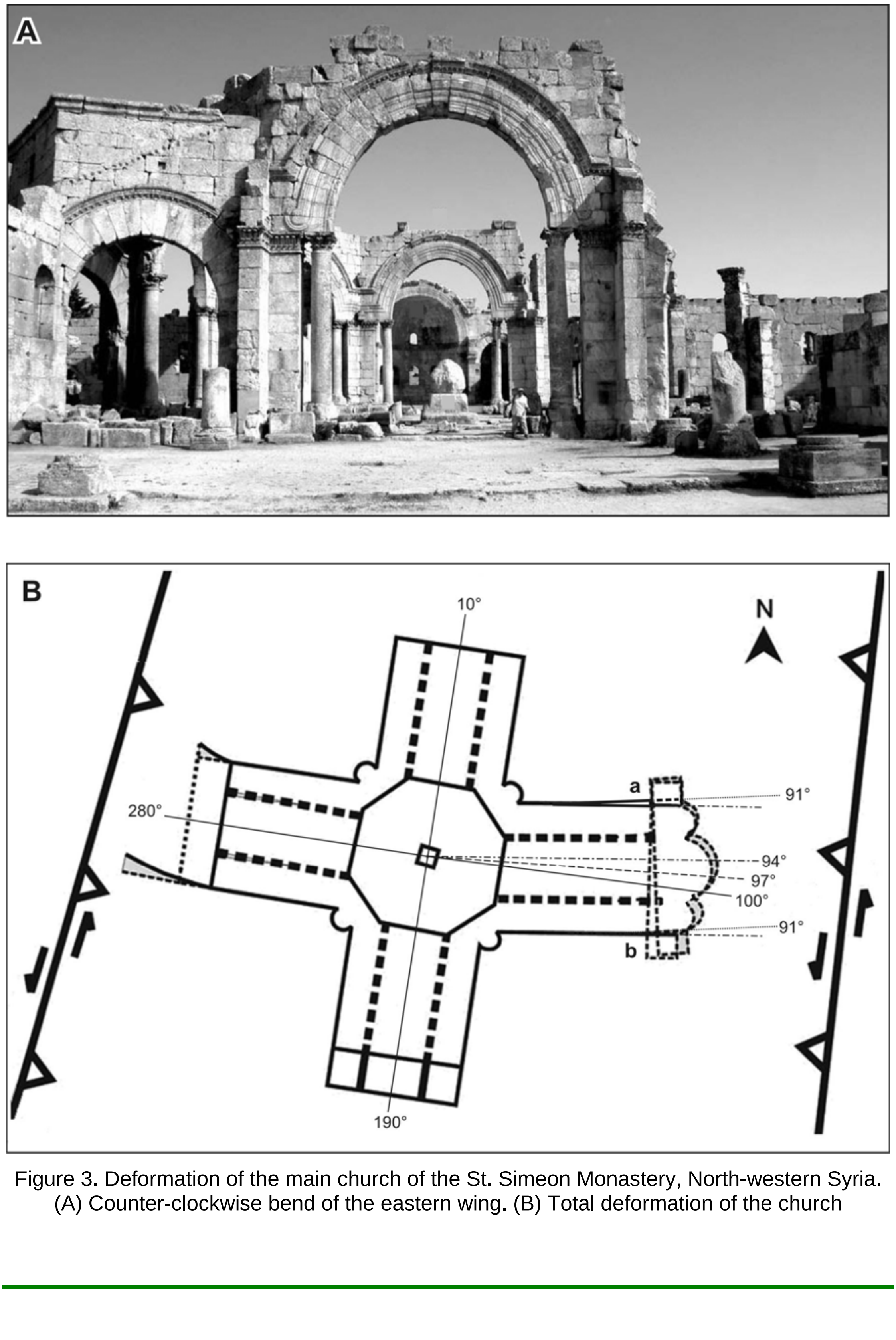

Figure 3. Deformation of the main church of the St. Simeon Monastery, North-western Syria. (A) Counter-clockwise bend of the eastern wing. (B) Total deformation of the church

Another example is deformation of the St. Simeon Monastery (490 A.D.) between two en echelon strands of the St. Simeon sinistral fault (Karakhanian et al, 2008). 4 wings of the cruciform main church were built as 3-nave basilicas, surrounding an atrium with ruins of the St. Simeon-Stylist pillar in the center; probably, the atrium was originally covered by dome. The church was destroyed in the first half of the VI century, when it lost the dome (Tchalenko, 1953) and an entrance was replaced from the western wing to the southern one. The restored church was destroyed and reconstructed in the X century, but later was ruined again. The eastern wing is curved now counter-clockwise relative to the axis of symmetry, characteristic for other constructions of the church, to 3º, if the curved continuation of the axis follows from the pillar to the central apse, and to 6º, if it is parallel to the northern and southern walls of the eastern wing (Fig. 3). Maximum total bend of the eastern wing can reach ~3 m. Near the recent walls, fragments of the older walls (a & b in Fig. 3, B) are curved to 3º more, up to ~1 m relative to the recent walls and up to ~4 m relative to the axis of symmetry. Fragments of walls of the primary entrance near the western wing are curved clockwise to 9º (up to 3 m).

The described curves of the church walls prove deformation between two strands of the St. Simeon fault with bending and pushing of the central block to the S. If we take into account also hypothetic counter-clockwise rotation of the wall of the former reservoir in front of the western wing, the pushing could be accompanied by S-type deformation. Numerous evidence of seismic destruction and damage both in the St. Simeon Monastery and the Byzantine town of Telanissos to the SW of it (on the western side of the St. Simeon fault) prove seismic origin of the deformation. If we consider the bend of the eastern wing by element of architectural design or construction error (that seems to be doubtful), the seismic deformation is limited by the bend to ~1 m of the older walls relative the recent ones in the eastern wing and bends near the western wing; the single strongest earthquake in the first half of the VI century would be enough to produce such bends and the later seismic influence was not accompanied by the deformation of constructions. If we consider the total bend of the eastern wing by seismotectonic deformation also, its curve reaches ~4 m and requires as minimum 2 or 3 earthquakes: in the first half of the VI century and before and after reconstruction of the X century. The seismotectonic deformation in the first half of the VI century is identified with the 528/529 seismic event (Ms=7.5). After it, the church was restored to the middle of the VI century, but could be destroyed or damaged again by strong earthquakes in 587/588, 854 and others. After the reconstruction in the end of X century, the monastery could be destroyed by the strong earthquakes in the XII century and 1822 (Karakhanian et al., 2008).

Seismic destruction and damage of ancient constructions

The most typical manifestations of seismic influence are: lateral and/or vertical bend of walls; rotation of wall blocks; one way fall of walls and columns. Lateral bend of the wall without ground rupturing (Fig. 4, A) as well as other signs of seismic influence were found in the Phoenician town of Ugarit. According to the historical documents, the town was destroyed approximately in the second half of the XIV century B.C. The obtained data argue into the seismic origin of the destruction. Lateral and/or vertical bends of the walls were found also in ruins of the Roman terms in Minet et-Halwa northward the city of Latakia, the Hellenistic construction of the Arwad Island and the St. Simeon Monastery. Rotation of stone blocks in the walls are the most characteristic for the ruined buildings of the St. Simeon Monastery (Fig. 4, B) and the adjacent town of Telanissos. The latter demonstrates one way rotation of the blocks in several buildings.

Figure 4. Seismic destruction of archaeological sites. (A) Deformation of the wall in the town of Ugarit. (B) Rotation of wall blocks in the St. Simeon Monastery. (C) One-way collapse of the south-eastern wall of Agora in the city of Palmyra. (D) New tower was built on the former one, destructed by the ~1170 earthquake in Krak des Chevaliers

One way collapse of the southeastern wall of Agora in the town of Palmyra to the SE looks as a result of seismic influence (Fig. 4, C). It impelled us to study directions of fall of columns in the town. Majority of them fell also to the S115–130ºE (Fig. 5). Palmyra was destroyed by the Romans in the III century A.D. and later was mainly in ruins, although a part of the town was inhabited. The ruins were covered by the 1–2 m thick layer of dust and debris and were excavated by archaeologists which reconstructed a part of constructions. So, the fallen columns could be partly replaced. It is necessary to take into account also the NW–SE and NE–SW directions of the main Palmyra streets. Nevertheless, the southeastern maximum of the fallen columns is the serious argument for strong seismic influence on the town. It is important that we documented a lot of fallen columns on the debris layer surface. The lower parts of some columns, situated within the debris layer did not fall. The same is characteristic for the lower part of the southeastern Agora wall. This means that the destroying earthquake took place, after the Romans had destroyed the town, probably in the Medieval times. Direction of the column fall shows that the earthquake epicenter was situated to the NW of the town in the Palmyride folded-thrusted belt, probably in the Ghar fault zone.

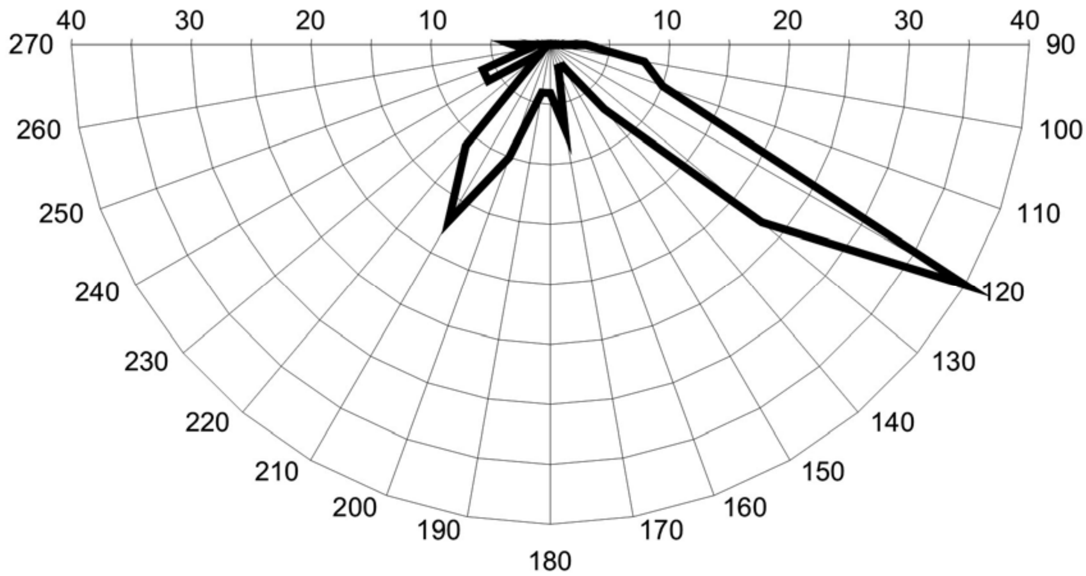

Figure 5. Rose-diagram of directions of fall of columns in the city of Palmyra

Discussion and conclusion

Two groups of the tasks, related to seismic hazard assessment in Syria are solved with using archaeological data. The first group is definition of sense, average rate and regime (portion of seismic displacement) of motion on active faults. The group includes offsets or deformation of archaeological constructions (the El Ghab and St. Simeon faults) as well as geological and geomorphologic features dated by archaeological means (the Tartus fault zone). The data are used to estimate parameters of active fault as potential seismic zones. The found sites, related to the first group are situated on active strands of the DSTZ.

The second group is estimation of seismic destruction and damage of archaeological constructions to define epicenters, age and intensity of the earthquakes. The most evident manifestations of seismic influence are: lateral and/or vertical bend of walls; rotation of wall blocks; one way fall of walls and columns. Because the strongest seismic events were fixed in the historical documents, the archaeseismological data are usually identified with some historical earthquakes and give a possibility to define more exactly their parameters. For example, in the fortresses of Krak des Chevaliers, we found indications of destruction of the original Crusaders' fortress in ~1170 (Fig. 4, D) and multiple damage after occupation of the rebuilt fortress by the Mamelukes in 1271. Correlation of the obtained data and historical documents helped to constrain the epicentral area of the 1170 earthquake (Ms=7.7) more accurately. The previous investigators attributed the earthquake to the Antioch area. But large destruction in the Krak des Chevaliers and the offset of the aqueduct near the village of Al Harif (Meghraoui et al., 2003) as well as the historical data on destruction in Tripoli, some other towns in the Tripoli–Krak des Chevaliers area and even in the town of Accon show that the 1170 seismic destruction spread far to the south. This can have two explanation. The first is that two earthquakes happened in ~1170 with the epicentres near Antioch and in the Tripoli–Krak des Chevaliers area. The second proposes the single catastrophic event with epicenter in the southern part of the El Ghab fault zone and seismic influence up to Accon and Antioch.

Majority of the archaeological manifestations of seismic influence are situated in and near active and possibly active strands of the DSTZ and EAFZ, but not only. Signs of seismic destruction in Palmyra demonstrate influence of the Medieval strong earthquake, whose epicenter was located in the Palmyride folded-thrusted belt, probably in the Jhar fault zone. These are necessary to take into account for seismic hazard assessment in Syria.

References

Dodonov A.E., Trifonov V.G., Ivanova T.P., Kuznetsov V.Yu., Bachmanov D.M., Minini H., Ali O. & Al-Kafri A.-M. (2008). The Late Quaternary marine terraces in the Mediterranean coastal area of Syria, *Quaternary Intern., in press*.

Karakhanian A.S., Trifonov V.G., Ivanova T.P., Avagyan A., Rukieh M., Minini H., Dodonov A.E., Bachmanov D.M. (2008). Seismic deformation in the St. Simeon Monastery (Cala'at Sim'an), Northwestern Syria, *Tectonophysics, in press*.

Meghraoui M., Gomez F., Sbeinati R., Van der Woerd J., Mouty M., Darkal A.N., Radwan Y., Layyous I., Al Najjar H., Darawcheh R., Hijazi F., Al-Ghazzi R. & Barazangi M. (2003). Evidence for 830 years of seismic quiescence from palaeoseismology, archaeoseismology and historical seismicity along the Dead Sea fault in Syria,, *Earth and Planet. Sci. Let., 210, 35-52*.

Tchalenko G. (1953). Villages antiques de la Syrie du Nord, parts I & II, *Institut Françats D'Archaeology de Beyrouth, Biblioteque Archaeologique et Historique, 50, Paris.*

Combined Seismic and Gravity surveys in fault detection and liquefaction risk assessment. Case study of Nafplion city, Greece.

Karastathis V.K.(1), Karmis P.(2), Novikova T.(1), Roumelioti Z.(3), Gerolymatou E.(1), Papanastassiou D.(1), Liakopoulos S.(1), Giannoulopoulos P.(2), Tsombos P.(2) , and G. A. Papadopoulos (1)

(1) National Observatory of Athens, Geodynamics Institute
(2) Institute of Geology and Mineral Exploration
(3) Aristotle University of Thessaloniki

Keywords: seismic techniques, faults detection, liquefaction

Introduction

The urban planning of many cities is usually based on economic and social factors, without taking always into account the local geology and the active geodynamic processes. The problems emerging due to this constraint are accentuated with the increase of the population, the industrialization and the seismic impact during the last decades. Nafplion is one of these cities (see Figure 1), originally founded on safe ground, but it is expanding in recent years along the coastline on ground of questionable safety factor with reference to seismic and liquefaction risk.

The need to set up and test a methodology, able to give reliable evaluation of the seismic and liquefaction risk for extensive areas, is considerable, especially for the countries with high seismicity, like Greece.

The methodology, we followed, combined the usual borehole testing measurements of the standard regulation for the seismic and liquefaction risk with geophysical measurements, in order to spread out high credibility information to wider areas.

The geophysical techniques also aided to the detection and study of the large active faults as possible earthquake sources.

The gravity survey, as a reconnaissance method, is suitable to locate possible deformations of the bedrock, which can be attributed to faults. As a follow-up survey, seismic depth imaging can delineate the structure if this is related to an active or inactive fault. In the case of active faults, the dip and the total throw are usually examined. These are related to seismological records and geological observations for further investigation of their characteristics. Their seismic activity can also be evaluated after few months earthquake monitoring from portable seismographic network.

With the knowledge of the characteristics of the seismic sources we can proceed with stochastic modelling to estimate the expected seismic movement (calculation of PGA) at a specific site, in case of a hypothetical activation.

The procedure for liquefaction assessment included the calculation of the Factor of Safety (FS) against liquefaction and the potential of liquefaction in terms of probability, (where FS = cyclic shear stress required to cause liquefaction / equivalent cyclic shear stress induced by earthquake), the evaluation of liquefaction time history for any earthquake scenario and the analysis of site response in region of Nafplion taking into account the liquefaction susceptibility of the stratum.

Figure 1: Location map of the survey area (small box) close to Nafplion city

Geological setting

The regional geology of the Argos plain is composed of: Coastal deposits, made of loose, fine silty sands and silty-clayey soils, alluvial fans and fluviotorrential deposits. The sediments' bedrock includes alpine and post-alpine sediments, such as flysch, limestone and Neogene marl conglomerates. The investigation area (see Figure 2) is formed by alluvial, mainly lagoonal deposits, overlying flysch and limestone formations.

With regards to groundwater regime, within the Quaternary deposits, successive groundwater aquifers are developed, being under intensive exploitation by well boring. This resulted to a considerable sea water intrusion in recent years. Within some parts of the investigation area, at an altitude lying of a few meters above sea level, a weak unconfined coastal aquifer is developed at a small depth near surface, which is underlain by deeper confined aquifers. This shallow unconfined aquifer belongs to a local marshland. The sand-silty, clayey-silty nature of soils and the presence of the ground water table near the surface, constitute a particularly unfavorable regime concerning the foundations. Within this regime an attentive control of the liquefaction potential is pertinent.

In the Argos plain, where Nafplion is situated, a liquefaction has been recorded in the past, happened on 2/6/1898 and caused from an earthquake of M=7 with epicenter (37.6o, 22.5o) only 27 km far (NWW) from Nafplion. Three important seismic zones in the wider region of Nafplion have given strong earthquakes in the historic era (Argos fault, Epidaurus fault and Xylokastro fault) (Papazachos and Papazachou, 2003).

Geophysical investigations

The geophysical techniques were carried out in the area aiming at: a) the detection of possible seismic faults (important for the seismic hazard analysis) and b) the determination of the velocity models in order to contribute to the estimation of the amplification of the possible peak ground acceleration (PGA) in the study area and the evaluation of the Factor of Safety against Liquefaction.

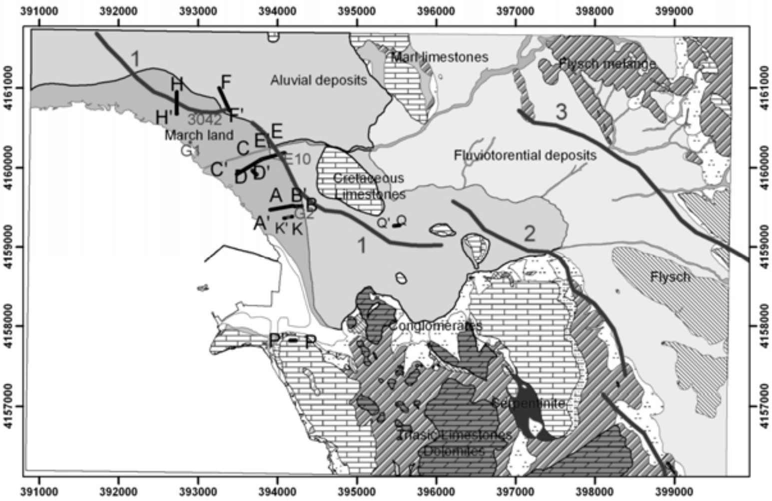

Figure 2: Geological map of the investigated area. The seismic lines are presented with black colour. The numbered curves indicate the possible faults as derived from the gravity survey.

Geophysical investigations for mapping the bedrock relief and detection of possible faults

Gravity survey

The gravity survey covered an area of 35 km^2 with 270 stations, conducted with a Scintrex CG-5 gravity meter.

From the Bouguer map (Figure 3) a residual map was extracted and the locations of the maximum gradient were plotted (shown with the numbered curved lines in Figure 2). These indicate possible geological contacts or fault positions. Two major lineaments can be seen possibly attributed to faults: The first one lies at the eastern side of the area with NW-SE direction. This is a known fault that has been mapped in the past from geologists as an inactive one. The second one, at the western part of the map, runs through the investigation area. Further investigation work with seismic methods was considered necessary.

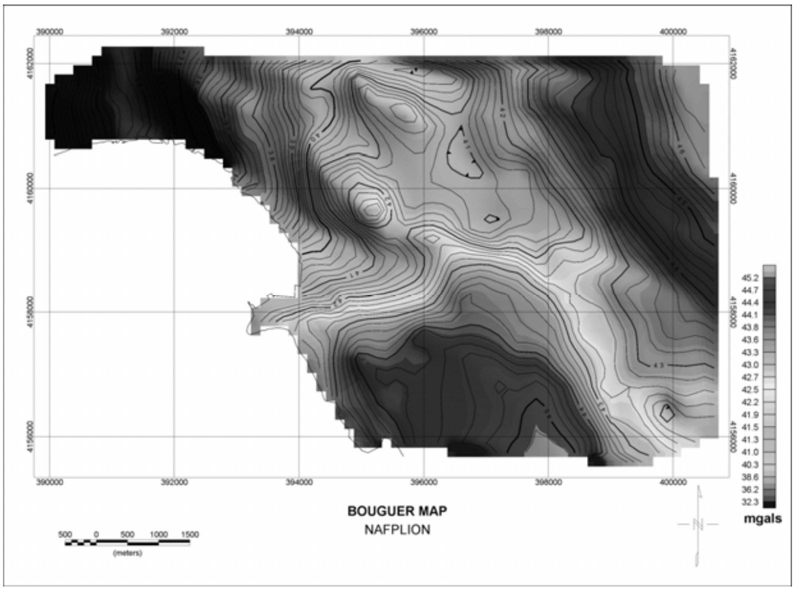

Figure 3: The Bouguer map indicates the existence of two possible faults at the investigation area.

Seismic Survey

We conducted seismic survey to delineate the suspected fault as pointed out from the gravity survey. Each of the seismic profiles (see Figure 2) AA´, CC´, EE´, FF´ was about 300 m long. The line HH´ was 180 m long. The main target of the seismic profiles was the determination of the dip of the bedrock surface and whether this could be associated to an active fault plane.

The survey layout for the shallow reflection seismics mostly used, was the “fixed spread” instead of the usual “roll-along”. The “fixed spread” layout was not only easier in acquisition, in the case of urban environment, but was also very valuable since permitted us to acquire data usable for refraction – wide angle reflection velocity modelling. A reliable velocity model is needed for depth migrating seismic data. We must bear in mind that if a fault is present in a seismic profile, then migration is a prerequisite.

The seismic source utilized, was an accelerated dropping weight and provided us with high quality records in all the seismic lines.

The joined lines EE´ and CC´ run perpendicular to the strike of the gravity lineament.

The first arrivals of the refracted waves in both profiles after tomographic processing, did not succeed to reach the bedrock. However the arrivals of reflected waves were processed by Zelt and Smith (1992) code, and produced velocity models with excellent fitting between calculated and observed arrival times (Figure 4a). The resulted velocity models (Figure 4b) indicate a fairly smooth layering to the bedrock. The bedrock is detected at 90 m depth at the beginning of the line EE´, reaching the 200 m at the end of CC´. The results are in agreement with an old water-wall at the starting edge of EE´, which intersected the limestone bedrock at 93 m depth.

Two layers can be distinguished above the bedrock at line CC´. The second layer, probably flysh, pinches out within the line EE´, but this cannot be resolved due to the limitation of vertical resolution.

Figure 5 shows the joined time migrated profile with simple depth conversion. Figure 6 shows the resulted profile after Kirchhoff depth migration with the use of the velocity model of the Figure 4b. The slope of the bedrock surface is steeper at the depth migrated profile.

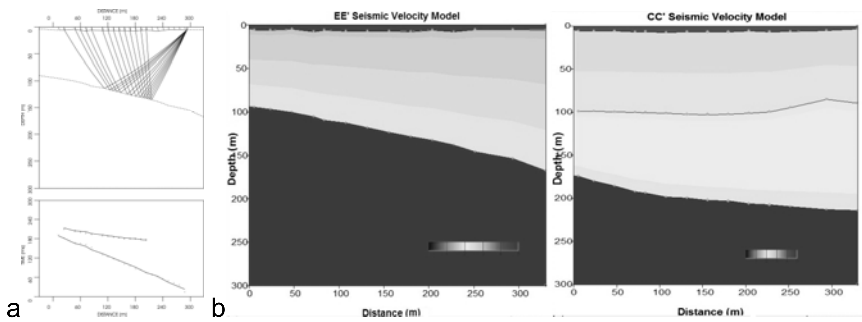

Figure 4: Velocity modeling of the profiles EE´ and CC´

The results of the depth migration (Figure 6) of the EE´ and CC´ lines suggest that the gravity lineament is caused by two smooth subsidence features of the bedrock at the starting parts of CC´ and EE´. Both dip values are at about 25^{o} and cannot suggest an active seismic fault. It is noted that apparent dips are measured and probably at a direction different of the bedrock gradient. Assuming that the strike the gravity lineament (305N) follows that of the sloping bedrock, the CC´ profile is at an angle of 28^{o} with this. Therefore after simple calculations we can estimate the real value of the dip at 28^{o}.

Dip values of 28^o were also obtained in the AA´ profile after similar processing and calculations. The profile FF´ confirmed also the pinch out of flysh layer. Figure 7 shows also the results of HH´ processing in different stages. The results of HH´ are also in full accordance with these of the other profiles.

In conclusion, the linear features of the Bouguer map cannot be attributed to active seismic faults but only to small and low dip inactive faults.

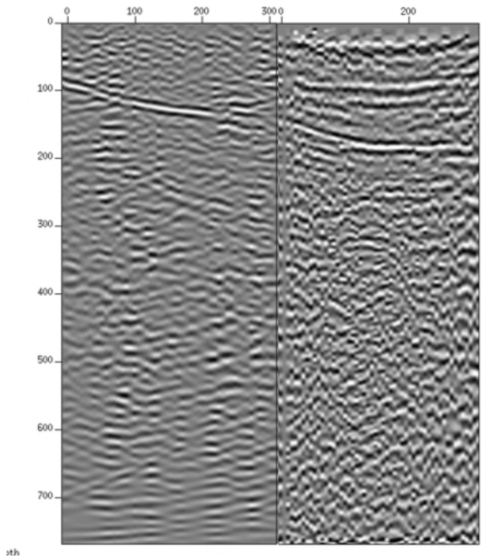

Figure 5: Time migrated and depth converted joined seismic section of the profiles EE´and CC´.

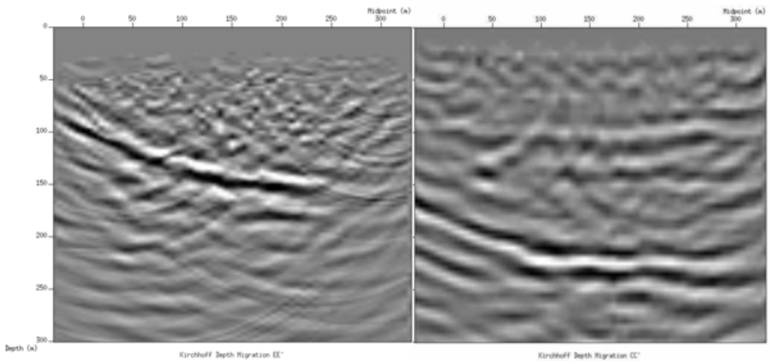

Figure 6: Kirchhoff depth migrated profiles EE´and CC´.

Geophysical investigations to the characterization of foundation ground

Aiming to the assessment of the foundation ground, crosshole seismic tests were conducted at two sites within the study area, along with SPT testing and laboratory tests on borehole core samples.

In addition seismic surveys were jointly carried out between the boreholes in such a way to fill in with the adequate information. Figure 2 shows all the sites where the seismic surveys were conducted. At BB´, DD´, KK´, PP´, QQ´, the methods of seismic refraction of P and S waves, MASW (Xia et al. 1999) as well as microtremors analysis were applied. Additionally at the sites AA´, CC´, EE´ and FF´ where seismic reflection and refraction data were acquired, we also applied MASW.

The seismic crosshole tests were conducted according to the ASTM D4428/D4428M-07 standard. At each site a pair of boreholes was drilled at 5 meters distance, at the depth of 40 meters. The results showed that the shear wave seismic velocity values in the loose sandy-silt and clayey silt intercalating formations did not exceed 0.4 km/s, but moreover there are parts with values lower than even 0.2 km/s. The P-wave velocity is high due to the saturation from the sea intrusion at the area. The results of the crosshole testing G2 and borehole log (Figure 2) are presented in Figure 8.

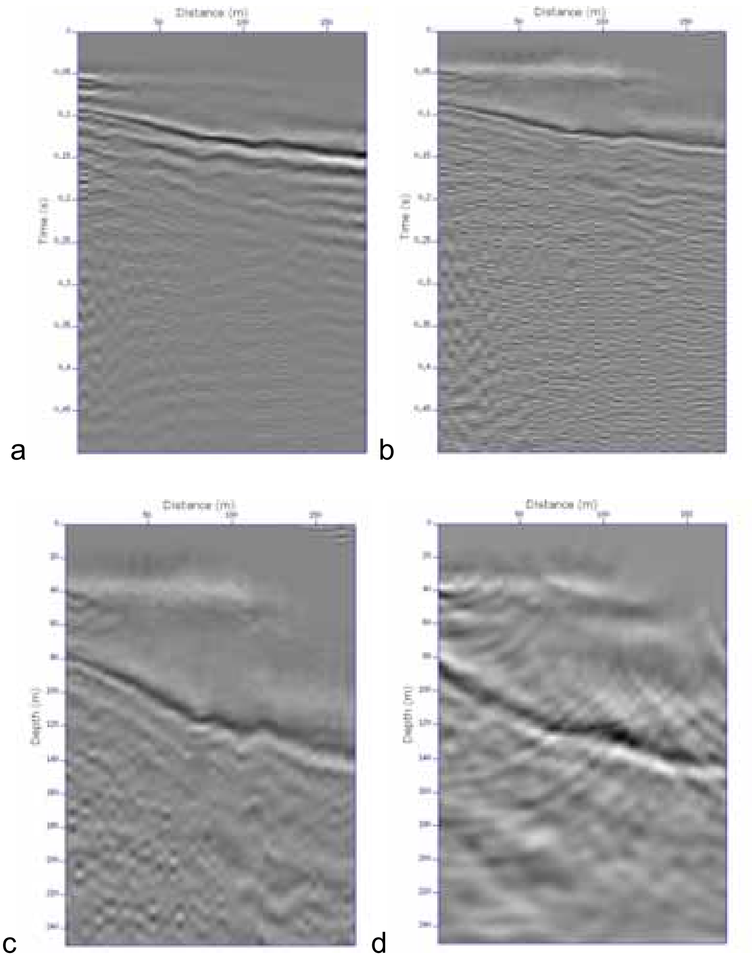

Figure 7. a. Unmagrated stack section of the profile HH΄ b. A section after deconvolution c. A deconvolved section after depth conversion d. Time migrated and depth converted section

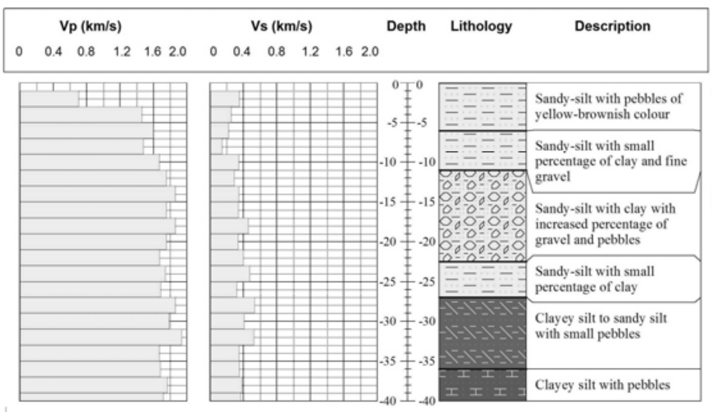

Figure 8: Crosshole test results with the geological log.

At the site of borehole G2 (Figure 2) we also conducted Reverse VSP (RVSP) modelling with the seismic source in the borehole and the receivers at the surface. The results of tomographic algorithm (Hayashi and Takahashi, 2001) were excellent and it was found that the drilling of second hole could be spared.

Figure 9 shows the result of the RVSP modeling and a comparison diagram with the crosshole test.The crosshole testing and RVSP were also used to calibrate and validate the results of MASW.

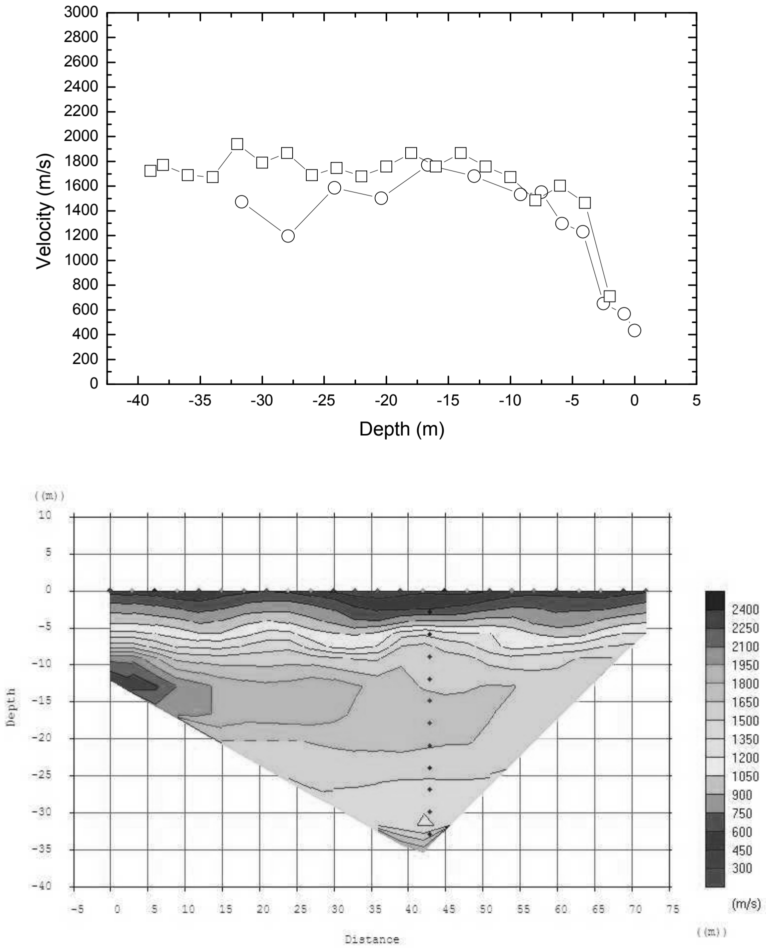

Figure 9: Above: Comparison of RVSP (circles) with crosshole testing (squares). Below: The velocity model of RVSP at the site K.

The application of MASW gave satisfactory results and detected low S-wave velocity zones. In a close distance to G2 borehole we applied MASW and the result were in full accordance to the crosshole test.

As shown in Figure 10 the S-wave velocity presents low velocities in the first 10 m in all investigated area. This is also found from S-wave seismic refraction profiles.

Microtremors analysis also gave good description of the deeper S-wave velocity variation.

From information derived from the local boreholes the layer corresponding to the low S-wave velocity values is sandy-silt to silty-sand, soft formation without plasticity. From the laboratory analysis we found sand concentration of 29% and 66% at 4.90- 5.55 m and 7.90 - 8.55 m depth respectively. This evidence supports the high liquefaction risk.

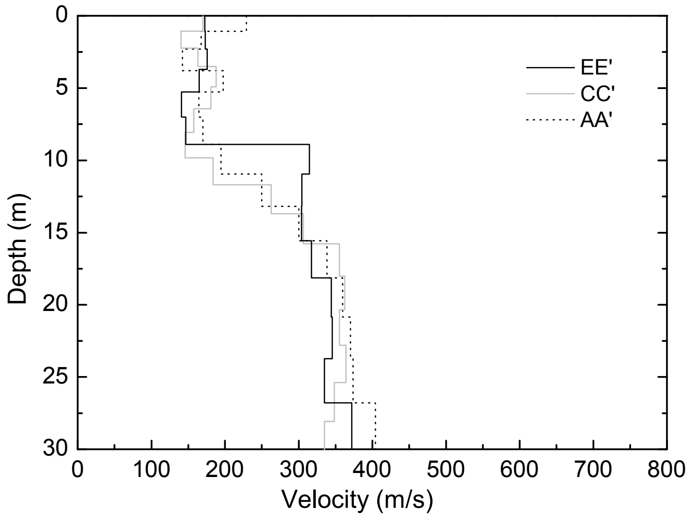

Figure 10. MASW results systematically showed low S-wave velocity values at the first 10 m depth.

Liquefaction analysis

We used the S-wave velocity logs as calculated from the crosshole and seismic techniques along with SPT data and synthetic accelerograms from earthquakes scenarios to estimate liquefaction susceptibility. We utilized the FINSIM code based on stochastic method to calculate the seismic motion to the bedrock level and D-MOD2000 code based on effective stress analysis to transfer the motion till to the surface

.

For the hypothetical earthquake scenarios of Argos (M=6.4) and Epidaurus (M=6.3) faults we found that liquefaction is highly possible at the depths between 5 and 10 m (up to 80%). In contrast to the above, the Xylokastro hypothetical earthquake resulted to negligible liquefaction probability.

Conclusions

The combined use of gravity and seismic methods is an efficient tool to examine large areas for active seismic faults.The modern seismic methods can act complementary to the standard borehole testing to cover wide areas for liquefaction and seismic risk.

Acknowledgments

This study was implemented in the frame of the project “Collection and Documentation of Geothematic Information for Urban Areas in Greece”. Funded by Competiveness Priority Axis 7: Measure 7.3 and ERDF.

References

Hayashi K. & Takahashi T. (2001). High resolution seismic refraction method using surface and borehole data for site characterization of rocks, *International Journal of Rock Mechanics and Mining Sciences, 38, 807-813*.

Papazachos, B.C. and Papazachou, C. B., (2003). Οι Σεισμοί της Ελλάδας, Θεσσαλονίκη, Εκδ. ΖΗΤΗ, 286p. (Oi seismoi tis Ellados, Thessaloniki, Ziti Edit., 286pp.) Spector and Grant (1970)

Zelt, C. A. &. Smith R. B, (1992). Seismic traveltime inversion for 2-D crustal velocity structure, *Geophysical Journal International, 108, 16-34.*

Determination of Site Response in Lefkada Town (W. Greece) by Ambient Vibration Measurements

Kassaras I (1), Voulgaris N (1), Makropoulos K (1)

(1) National and Kapodistrian University of Athens, Faculty of Geology and Geoenvironment, Department of Geophysics-Geothermics,, Panepistimioupolis, Zografou, Athens 15784, kassaras@geol.uoa.gr

Keywords: seismic microzonation, site effects, ambient noise, spectral ratio

Introduction

Lefkada together with the nearby Ithaki, Cephalonia, and Zakynthos islands are considered the most active areas of shallow seismicity in the Aegean Sea and the surrounding continental area. The region is dominated by the activity of the Cephalonia transform fault which comprises two distinctive fault segments (Louvari et al., 1999), the Lefkada segment to the north and the Cephalonia segment to the south. During instrumental times Lefkada Island has suffered from several earthquakes with magnitudes in the range 6.0-6.5. These events caused similar geotechnical damage consisting of rock fall, massive landslides, liquefaction, lateral spreading, and harbor quay wall failures (Benetatos et al., 2007). The hazard due to this fault system was updated to a peak ground acceleration of 0.36g in the current Greek Antiseismic Code. However, site-effects may increase the response beyond the provisions of local Codes or Standards. Especially in urban areas, like the Lefkada town, which is located on soft soil layer, waves of seismic events can be major amplified. That was the case during the 14 August 2003 Lefkada earthquake (Mw=6.2) which caused extremely high PGA=0.42g in Lefkada exceeding the PGA Standards. It is therefore strongly recommend determining possible site-effects and furthermore enforcing the proposed microzonation of Lefkada town to enhance the standard of seismic hazard analysis.

The analysis of ambient seismic vibration recordings for site effect estimation is considered a low-cost alternative to expensive investigation methods such as drilling or active seismic experiments. This study presents results of ambient noise measurements carried out in 78 locations in the town of Lefkada. The horizontal-to-vertical spectral ratios (Nakamura 1989) of ambient noise were used to approximate the fundamental resonance frequencies of the subsurface and their associated amplitudes. Summarizing the experiences of different authors with respect to ambient vibration processing, we selected transient free time windows for further analysis. Additionally, we calculated the site responses with respect to the reference site and compared the results with those obtained from the H/V technique. The fundamental frequency and the corresponding amplification factor were calculated for each site. Under the assumption that the H/V spectral ratios of ambient noise coincide with the amplification levels at the dominant frequency of the site response functions, the fundamental frequencies (f_0) and amplification factors (A_0) were compiled on ARC-INFO GIS software and corresponding maps were developed.

Materials and methods

Short geological description of the investigated area

Lefkada Island is separated from the Greek mainland by the Lefkada Sound, a shallow lagoonal environment. Lefkada town lies at the north-eastern corner of Lefkada Island at around 1-5 m above present mean sea level. It is situated on low resistance and rigidity

Holocene deposits of a few meters thick. They consist of alluvial and lagoon deposits, i.e. alternating soft clay, sometimes with organic content and sand-silt layers overlying a stiff marl formation (Gazetas et al., 2004). It should be noted that the quasi-uniform geological settlement of the neighboring area denotes that the whole town of Lefkada is predominantly characterized by similar formations of almost horizontal layering. The soil structure beneath the town is classified as category C according to the current Greek Antiseismic Code. On the basis of existing geological information (Gazetas et al., 2004), the top of the stiff marl formation is located at 9 m depth at northern Lefkada, at 16 m at the central town while it emerges southern in the area of Lygia harbor. This configuration implies for the presence of a geological trough. The stiff marl formation was found in all geotechnical depth profiles conducted by Gazetas et al., (2004), but its thickness is still unknown. Therefore the marl formation can be likely considered as typical "seismic bedrock" of Lefkada town. That means that seismic noise at all sites in the town encompass commonly the marl formation.

Ambient noise monitoring in Lefkada town

The investigated area was covered by seismic stations, each section comprising a discrete measurement site as shown in Figure 1. A total of 78 measurements were performed in October 2007 by two research groups, during daytime. The acquisition equipment included: 24-bit REFTEK 72A 3-channel digitizer, GPS (for timing and positioning), 3-component Guralp CMG40T sensor with a natural frequency of 1.0 Hz, portable PC. Digital recordings were made with a sampling rate of 100 samples per second. The duration of each 3-component recording was at least 20 minutes. The sensors were installed on soil conditions and sheltered in order to decrease weather and atmospheric disturbances. All the equipment – sensor, recorder, portable computer and connectors – were transported either by car or a trailer which served as the recording centres. Throughout the measurements the guidelines developed for ambient vibration measurements by the EU funded project SESAME (SESAME Guidelines 2004), were adhered to. At each location field measurements sheet was filled in which described the time, date, operator name, coordinates etc of the location the onset and the duration of the measurement. As reference site we selected Katouna village, situated ~5 km south of Lefkada town on stiff marl formations and performed a 36 hours continuous recording.

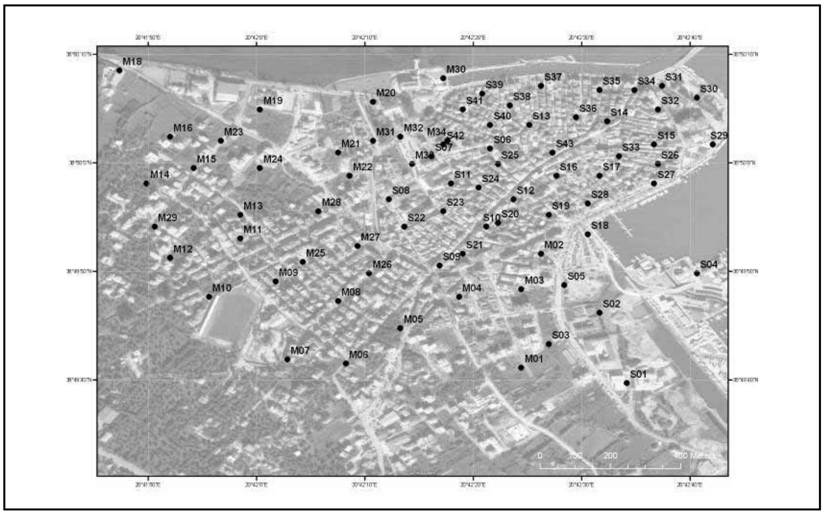

Figure 1. Satellite map of the study area and locations of the observation points.

Ambient noise H/V analysis

Data were processed applying the horizontal–to vertical (H/V) spectral ratio (Nakamura, 1989) method, using the GEOPSY software. The fundamental frequency (f_0) was calculated for each point. The H/V spectral ratios are those of selected time windows of recorded ambient noise using an anti-triggering algorithm. The selected time windows were Fourier transformed, using cosine-tapering before transformation and then smoothed following Konno & Ohmachi (1998) approach. The selected and analyzed time windows were 20 s long. We did, however, experiment with a range of values in order to find the window length that yielded satisfactory resolution of the peak being studied but was still stable in the frequency. After several tests, we concluded that a 20 s window provides stable results. The selected time window was free from recordings of passing vehicles, noticeable harmonic noise from nearby machinery, spiky data and other transient signals. All the selected time windows of each time series were corrected for the base line. The Fourier spectra were calculated for all segments using the Fast Fourier Transform (FFT). The Fourier amplitude ratio of the two horizontal Fourier spectra and one vertical Fourier spectrum were obtained using Equation:

$$r(f) = \frac{\sqrt{F_{NS}(T) \times F_{EW}(T)}}{F_z} \qquad (1)$$

Where r(f) is the horizontal to vertical (H/V) spectrum ratio, F_{NS}, F_{EW} and F_Z are the Fourier amplitude spectra in the NS, EW and Vertical directions, respectively. After obtaining the H/V spectra for the selected segments of the signal, the average of the spectra were obtained as the H/V spectrum for a particular site. The same procedure was repeated at all locations. The peak of the H/V spectrum plot shows the predominant frequency of the site (f_0) and the amplification factor (A_0). Additionally, calculation of standard deviation for each point was done.

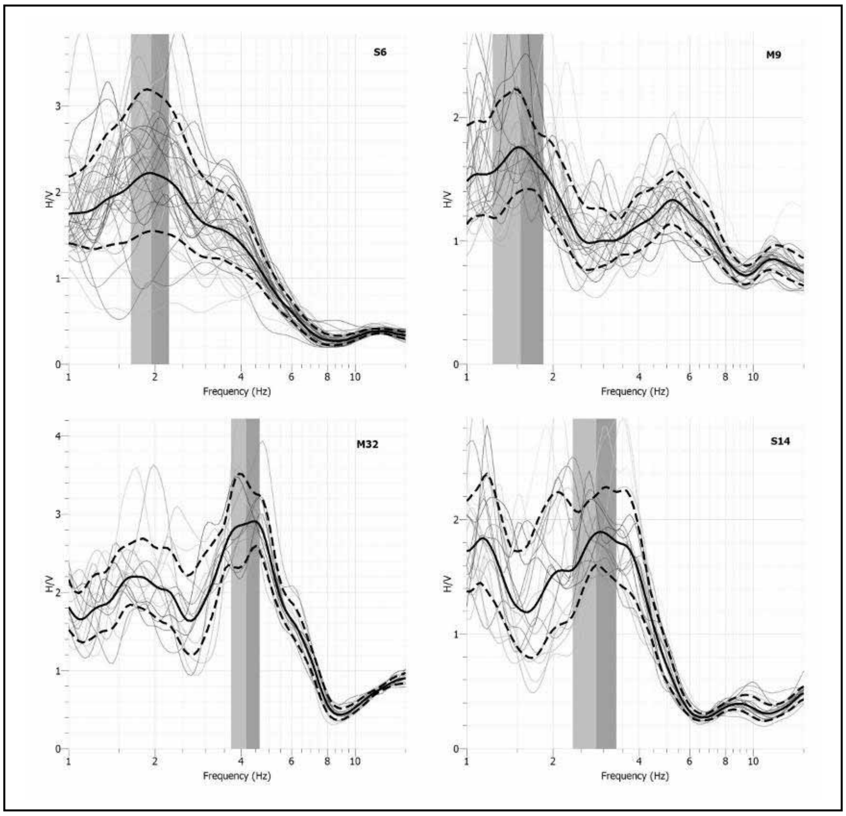

Figure 2. Fundamental Frequency & H/V ratio analyzed at 4 locations in Lefkada town. Thin lines are H/V curves for each selected window. Thick black line is the average H/V curve. Dashed black lines indicate standard deviation of the H/V curve. Grey vertical bars show the selected H/V peak. The width of the vertical bars denotes the range of the peak frequency.

Large standard deviation values often mean that ambient vibrations are strongly non-stationary and undergo some kind of perturbations, which may significantly affect the physical meaning of the H/V peak. In order to assess the reliability and stability of the H/V curves, we examined for each location the individual averaged 3 component spectra for the selected signal windows. In case that the H/V peak lied near or coincide with the spectra peaks (non stationary signal) we reduced the anti-triggering parameter STA/LTA until both sufficient number of windows were present in the calculations and the transient signal was efficiently removed. Following this procedure, we succeeded to define clear H/V peaks independent from transient noise and reduced standard deviation of the H/V curve. Furthermore, the spatial density of measurements allowed the direct comparison of H/V peaks between neighbouring points, as an additional criterion of the H/V clarity and reliability. Two measurements that failed to satisfy the set criteria were excluded from the subsequent developed maps for predominant frequency value and amplification. The increased success rate was mainly due to the knowledge and experience of the operators e.g. avoiding measuring near a tree, and setting of equipment etc likely contributed. In Figure 2 typical examples of calculated H/V curves at various locations are displayed.

Ambient noise SSR analysis

The SSR (Standard Spectral Ratio) technique was applied using the Katouna recordings as reference signal. We performed manual analysis using SAC2000 (1995). All the waveform data were corrected for the DC component and trend. The signals were Fourier transformed, using cosine-tapering before transformation. The amplitude spectra for each location and each component (NS, EW, Z) were smoothed by an appropriate moving average and then divided by the corresponding component of amplitude spectra of the reference site, yielding 3-component SSR curves. The average SSR curve at each site was estimated and the fundamental frequency was visually picked. Due to the reference site installation conditions (buried sensor, no human activity), the small amplitude of the denominator yielded very large, unrealistic amplification factors, which consequently were rejected.

Figure 3 displays the comparison between the H/V and SSR peaks, showing large discrepancies for the majority of locations. This led us to apply the same criteria as for the H/V calculations (examining individual spectra, manually selecting windows of stationary signal etc). However, it was not possible to manually isolate a sufficient number of stationary signal windows for SSR calculations, for numerous sites. The procedure was successful for only 33 locations, for which H/V and SSR peaks show a good correlation (Figure 4). Those 33 SSR amplification frequencies (f_0) were finally adopted. The limited success of the SSR method (less than 45%) compared to H/V shows that transient signal of the temporary stations (human activities, external conditions) is crucial. Therefore, the conditions of installations for both temporary and reference stations should be common, which is not easily applicable in urban areas.

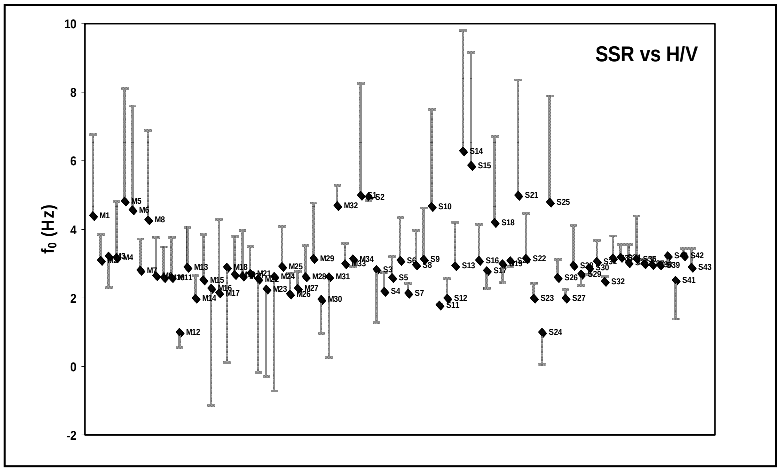

Figure 3. Tomographic slices of the shear velocity model at different depths. Tomograms start at 30 km depth. The velocity perturbations are indicated with a color scale in percent relative to a common reference model, derived from the average shear velocity at each depth.

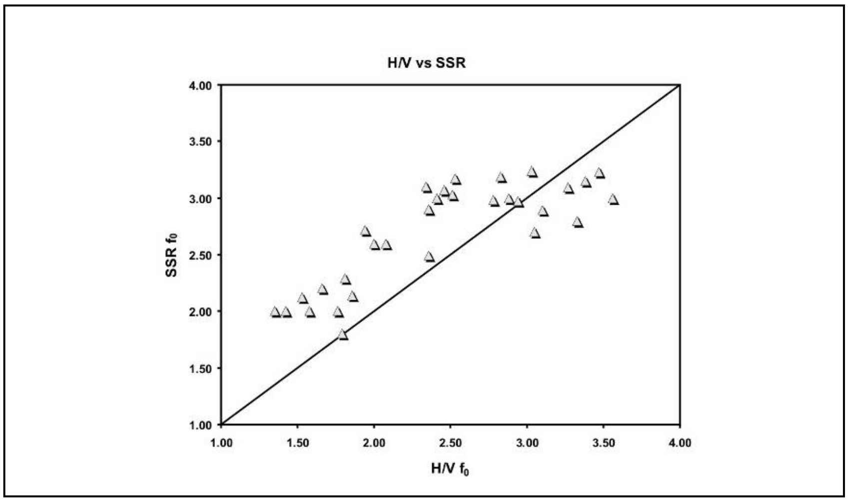

Figure 4. Comparison between H/V and SSR frequency peaks (f_0) for 33 selected locations.

Results and discussion

As previously mentioned, in urban areas, particularly during the day, local noise sources could affect spectral shapes. This effect, however, does not affect the H/V spectral ratios. Thus, the systematic and consistent spectral ratios extracted in this study, likely reflect the physical properties of the local site at the measuring point. On the other hand, the SSR technique was successful for less than 45% of our measurements, yielding however similar peak frequencies to the H/V peaks.

Predominant frequencies (f_0) range between 1-6 Hz. The majority of sites exhibit frequencies between 1.5-3.0 Hz. This distribution of f_0 is in agreement with results obtained by strong motion recordings (experimental and synthetics) at various locations in the town of Lefkada (Gazetas et al., 2004). It is also in agreement with Triantafyllidis et al., (2006) who found predominant frequencies in Lefkada in the range 2-4 Hz, using both seismic and microtremor data. In figure 5 the response spectrum of the 14-8-2003 earthquake recorded at the local Hospital of Lefkada (Benetatos et al., 2007) is shown together with the ambient noise H/V curve recorded at the same location. The predominant PSA frequency of the earthquake is around 2 Hz (0.5 s), similar to the H/V peak frequency, implying that the PGA=0.42g recorded at Lefkada Hospital during the 14-8-2003 strong earthquake was likely the result of resonance phenomena due to the local site response.

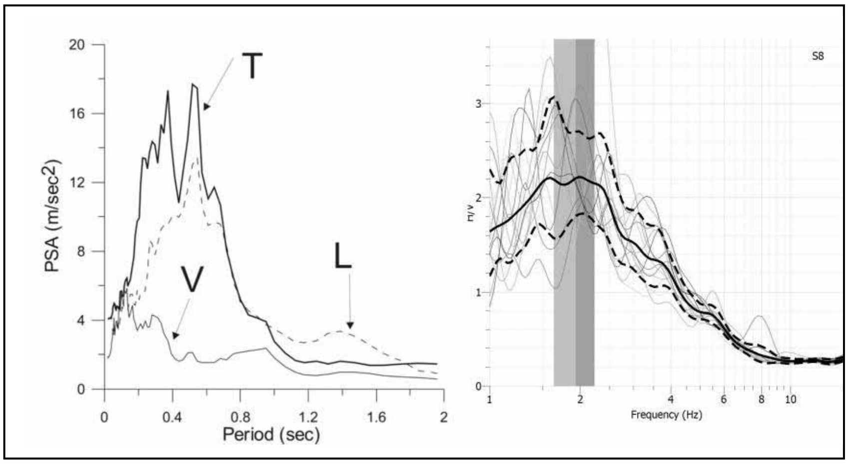

Figure 5. Left: 3-component (L,V,T) Response spectra of the 14-8-2003 Lefkada earthquake recorded at the local hospital (Benetatos et al., 2007). Right: ambient noise H/V curve at the same location.

Amplification factors (A_0) of the H/V curves range between 1.5-3.5. Research experience (SESAME Project) shows that ambient noise H/V peaks show a good correlation with earthquake data concerning the predominant frequencies, however the amplification factors of the H/V amplification factors are decreased by about the order of 2 when compared to earthquakes. Hence, the H/V amplification factors calculated in this study should be considered only as an indicative measure of the expected site amplification in case of earthquake disturbance, but in no case a realistic response parameter. Our results should be evaluated by earthquake recordings from a dense local seismological network installed in the future in the town of Lefkada.

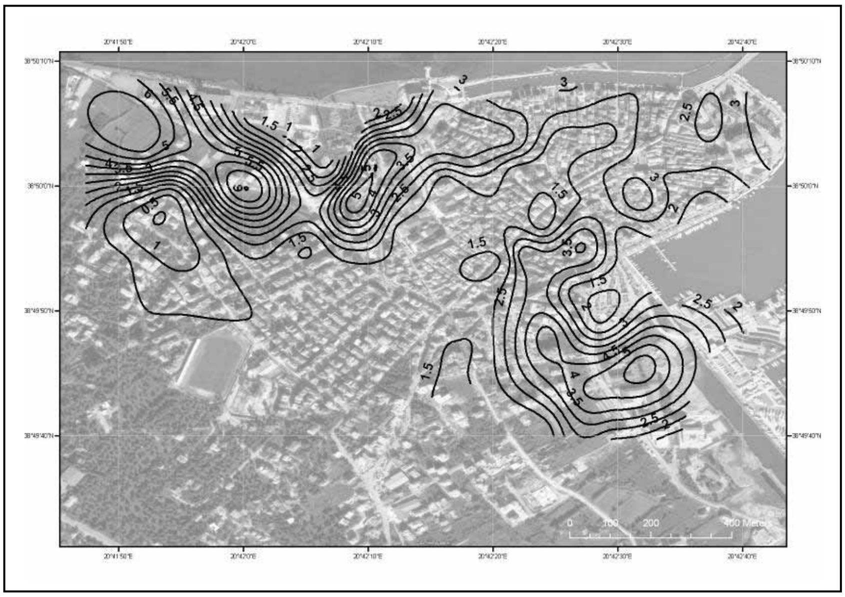

Figure 6. Lateral variations of H/V predominant frequencies (f_0) in the town of Lefkada.

The ambient noise H/V predominant frequencies (f_0) and amplification factors (A_0) were compiled on a ARC-GIS software and corresponding maps of their lateral variations were developed. As we can see in Figure 6, although the geological setting in Lefkada is quasi-uniform, predominant frequency exhibit significant lateral variations throughout the study area.

Higher amplification frequencies are observed along the seaside zone of the town, between $2.4 \leq f0 \leq 3.1$ Hz, in contradiction with the southern promenade where low frequencies are observed (1.7-1.8 Hz). These low frequencies are likely due to the significant thickness (~5 m) of shallow deposits, as data from available boreholes indicate (Papathanassiou et al., 2005). It is highly plausible that extensive ground and wall failures as well as liquefaction phenomena took place in this particular area of the town during the 2003 earthquake, because of interaction of the thick shallow deposits with the strong motion predominant frequency 1.6-3 Hz), which produced severe resonance phenomena.

The area of the north promenade exhibits higher predominant frequencies, ranging between 2.4-3.1 Hz. In that area, damages observed (mainly ground failures) during the 2003 earthquake were of lower magnitude. However, those failures could be possibly associated with resonance phenomena, while the site response frequency lies within the range of the strong motion predominant frequency.

Low frequencies are seen in the central sector of the old town (<2 Hz). The diversification with the area of the north promenade could be associated with the thickness alteration of shallow deposits, which appear thicker by 5 m in the central part of the town (Gazetas et al., 2004).

Low frequencies predominate in the area of the new Lefkada town (western sector), however, the lack of geotechnical information in this area does not allow the direct association with the predominant frequency distribution.

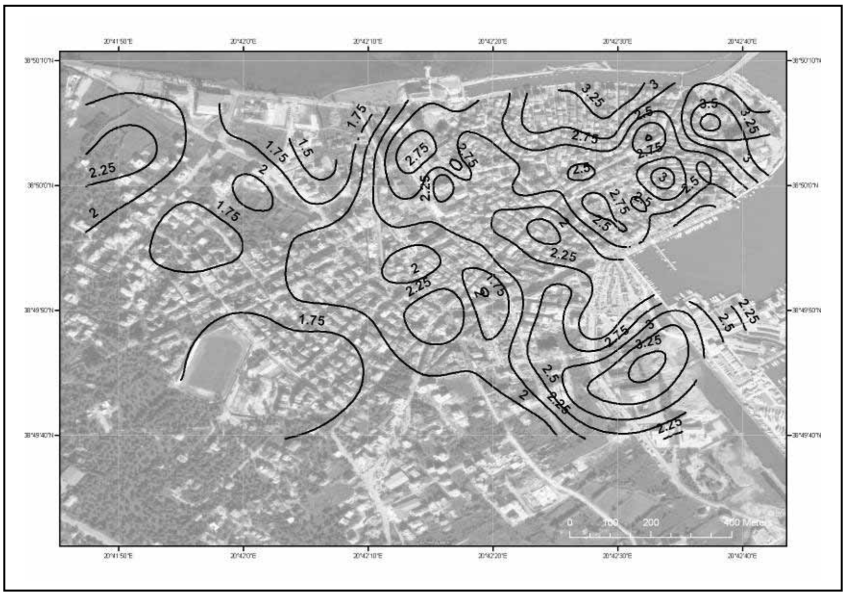

Figure 7. Lateral variations of H/V amplification factor (A_0) in the town of Lefkada.

In Figure 7, lateral variations of the amplification factor (A_0) are displayed. Although results concerning the amplification factor extracted by the H/V ratios are only indicative, it is worth to mention the following:

1. High amplification is observed in the area of the north and the southernmost promenade.
2. Lower amplification in the central sector of the old town.
3. Low amplification in the southern part of the port as well as in the area of the new town.
4.

In general, the region of the old Lefkada town presents higher amplifications with respect to the region towards the west, where the urban area is expanded. Concerning the area of the southern promenade, it is more likely that the observed failures during the 2003 earthquake are due to resonance phenomena rather than seismic energy local amplification due to site amplification.

Conclusions

The large number of ambient noise measurements conducted in Lefkada town allows to draw the following conclusions:

1. Microtremor monitoring is a valuable tool to determine dominant frequency of motion at sites were local site effects are suspected and where microzonation is necessary, particularly in the absence of a large number of strong motion recorders and large number of records over a long period.
2. The methodology adopted and described above proved to be easy, systematic and relatively cheap and the results attained proved to be reliable and repeatable. The H/V peaks appear systematically independent of transient signal peaks, thus can be reasonably associated with the amplification levels at the dominant frequency of the site response functions.
3. The SSR technique was of limited success due to transient noise presence in the temporary measurements. It was not possible to extract realistic amplification factors through

the SSR technique due to the different installation conditions between the temporary measurements in the urban environment and the reference station.
4. Lithology of surface layers must be, as expected, the most important factor controlling the predominant frequency. In general the predominant frequencies appear indicative of the thickness of the sacrificial sediments under the sites.
5. High predominant frequencies (2.4-3.1 Hz) are distributed along the seaside zone of the town, except the area of southern promenade where low frequencies are observed (1.7-1.8 Hz). Low frequencies are met in the central sector of the old town (<2 Hz) and in the area of the new town (<2 Hz).
6. High amplification is seen in the zone of the north promenade, the southernmost port, and at the new town. No amplification is observed at the marl bedrock.
7. The configuration of the sites response frequencies accounts for resonance phenomena during the strong earthquake of 2003 and is possibly the main reason for the extended ground failures and construction damages documented.

Those results are indicative of the site response functions and the 2-D models developed in the study should be considered as preliminary microzonation maps, providing resources to enhance seismic hazard assessment for the town of Lefkada. Our results should however be in the future cross-checked with additional geotechnical information as well as with strong motion responses regarding the local, intermediate and far wavefield.

Aknowlengments

This work was elaborated in the framework of the Project “Development of seismological networks and geodesy observations in the Ionian Islands Prefecture”, funded by the Greek GSRT.

References

Benetatos C., Dreger D. & Kiratzi A. (2007). Complex and Segmented Rupture Associated with the 14 August 2003 Mw 6.2 Lefkada, Ionian Islands, Earthquake, *B.S.S.A., Vol. 97, No. 1B, pp. 35–51, February 2007, doi: 10.1785/0120060123*.

Gazetas G. (2004). Geotechnical aspects of the Ms 6.4 Lefkada Island, Greece, 2003 earthquake: preliminary assessment, *Presented at the Proc. of the 5th Int. Conf. on Case Histories in Geotechnical Engineering, New York, New York, 13–17 April 2004, paper no. 13*.

Guidelines for the implementation of the H/V spectral ratio technique on ambient vibrations measurements, processing and Interpretation, *SESAME European research project, No. EVG1-CT-2000-00026, December 2004.*

Konno K. & Ohmachi T. (1998). Ground-Motion Characteristics Estimated from Spectral Ratio between Horizontal and Vertical Components of Microtremor, *Bull. Seism. Soc. Am., Vol. 88, No.1, 228-241.*

Louvari E., Kiratzi A.A., Papazachos B.C. (1999). The Cephalonia Transform Fault and its extension to western Lefkada Island (Greece), *Tectonophysics 308, 223–236.*

Nakamura Y. (1989). A Method for Dynamic Characteristics Estimation of Subsurface using Microtremor on the Ground Surface, *Quarterly Report of Railway Technical Research Institute (RTRI), Vol. 30, No.1.*

Papathanassiou G., Pavlides S., Ganas A. (2005). The 2003 Lefkada earthquake: Field observations and preliminary microzonation map based on liquefaction potential index for the town of Lef kada, *Engineering Geology 82 (2005) 12– 31*.

SAC2000, Seismic Analysis Code, 1995, *The Regents of the University of California, copyright 1987*.

Triantafyllidis P., Theodoulidis N., Savvaidis A., Papaioannou Ch., Dimitriou P. (2006). Site effects estimation using earthquake and ambient noise data: the case of Lefkas town (w. Greece), *13th ECEE & 30th General Assembly of the ESC, Geneva, Switzerland, 3-8 September 2006, Paper Number: 1249.*

Wathelet M., 2002-2007. GEOPSY, Geophysical Signal Database for Noise Array Processing, copyright 2002-2007.

Shear velocity and intrinsic attenuation variations within the Aegean lithosphere deduced from surface waves

Kassaras I (1), Louis F (1), Makropoulos K (1), Magganas A (2)

1) National and Kapodistrian University of Athens, Faculty of Geology and Geoenvironment, Department of Geophysics-Geothermics,, Panepistimioupolis, Zografou, Athens 15784, kassaras@geol.uoa.gr
2) National and Kapodistrian University of Athens, Faculty of Geology and Geoenvironment, Department of Mineralogy & Petrology, Panepistimioupolis, Zografou, Athens 15784, amagganas@geol.uoa.gr

Keywords: Rayleigh wave, Phase velocity, Attenuation, Aegean Sea

Introduction

An overall description of the lithosphere and upper mantle in the Aegean area is given by several researchers. The majority of studies on deep lithosphere and upper mantle velocity structure are based on P wave propagation (e.g. Spakman et al., 1993; Papazachos and Nolet 1997; Tiberi et al., 2000). Seismic surface waves have been used to study the shear-wave velocity variation in the Aegean (most recently Marone et al., 2004; Bourova et al., 2005; Kassaras et al., 2005; Karagianni et al., 2005). Several Q studies have been carried out in Greece. Shear and Coda waves for high frequencies have been used to study Q_b and Q_c in Greece (e.g. Kovachev et al., 1991; Hatzidimitriou, 1993). However, evident is the lack of surface wave attenuation studies, which, in contradiction to body or coda waves can provide information on the depth dependence of Q, inferring resources to understand the material and physical conditions in the lithosphere.

This paper presents a new shear velocity and attenuation model for the lower crust and lithosphere of the Aegean region, obtained by inversion of broadband surface-wave phase velocities and attenuation coefficients. We have two main motivations for conducting this study. First, knowledge of the regional structure of the Aegean lithosphere is fundamental for understanding the tectonic framework and mantle dynamics, posing constraints on possible models of deformation and evolution. Second, the exponential dependence of Q with temperature implies that attenuation tomography could explain better hot regions (high attenuation) than elastic tomography. Furthermore, elastic velocity is highly influenced by the constitution of the medium. In case of strong lateral Q variations, elastic parameters also vary. Hence, it is important to combine results of elastic and anelastic tomography. Apparently, the high rates of deformation in the Aegean constitute this region particularly interesting in this perspective.

Materials and methods

In the present study, phase velocities and attenuation coefficients of the fundamental mode of Rayleigh wave propagated across the Aegean were used. Approximately 430 teleseismic earthquakes with M>5.0, recorded during a 6 month experiment by 12 broadband stations installed in the Aegean were considered. Data from 3 GEOFON stations in south Aegean were also used. Figure 1 presents the locations of the 15 stations used.

Out of all the recorded earthquakes of epicentral distance larger than 300, waveforms generated by 386 events showing a good-quality signal at most of the stations were analyzed. Given the different sensors and recorders, the data were first corrected for the instrument response. Phase velocities and attenuation coefficients for Rayleigh wave were determined between selected pairs of stations located on the same great circle as the epicenter, within 2-3º.

Phase velocities of the fundamental mode Rayleigh wave have been determined for periods 10-100 sec by the two-station method along 36 interstation pathways covering the Aegean region (figure 2A). The period range our measurements is not the same for all paths. This firstly arises by the fact that the instruments used were not of the same response, hence, several paths were not sampled beyond 60 sec. The second reason was that not all paths were sampled below ~20 sec, due to multiple arrivals and multipathing effects, which could not be excluded through the multiple filtering procedure. In order to encompass homogeneous sampling of the under study area, we only consider waves with periods 20-60 sec.

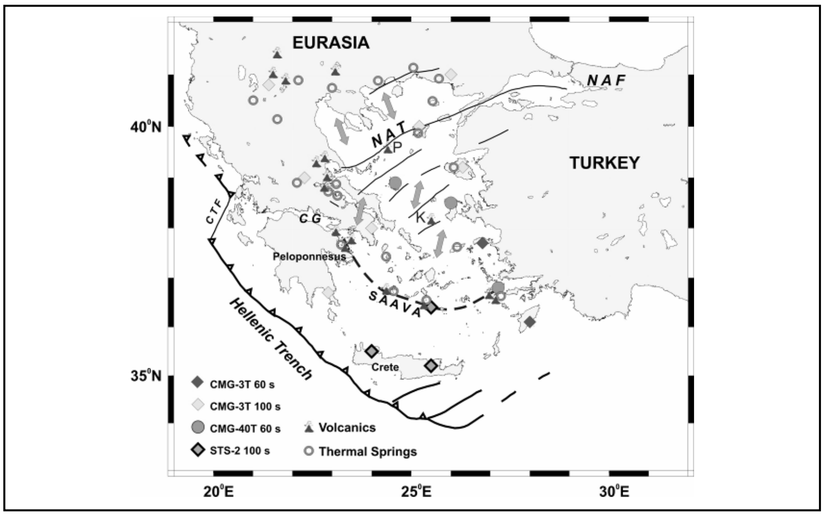

Figure 1. Map showing the location of the stations used in the present study, main active tectonic features of the Aegean, Pliocene to Recent volcanic centers and main thermal springs. Abbreviations for geographical names: CG = Corinth Gulf; NAT = North Aegean Trough; NAF = North Anatolian Fault; SAAVA = South Aegean Active Volcanic Arc; CTF = Cephalonia Transform Fault; P = Psathoura; K = Kalogeri.

For each profile the average experimental dispersion curve has been inverted to obtain 1-D horizontal average shear wave velocity models. The method of damped least-squares solution (stochastic inverse solution) was applied. To constrain our dispersion curve inversions, the depth of the Moho discontinuity was set for every path following a 2-D Moho depth model proposed by Karagianni et al., (2005). The 36 horizontal average shear velocity models determined by the inversion process were restricted between 30-120 km depth, sampling the lower crust and the upper mantle of the region.

Attenuation coefficients have been determined for periods 10-100 sec by the two-station method along 17 interstation pathways across the Aegean. The Multiple Filtering Technique (Herrmann 1973) was utilized for the identification of the fundamental Rayleigh waves and to extract group velocities and spectral amplitudes. Attenuation data were carefully verified for effects of focusing, defocusing, departures from the great-circle path and multipathing, which impact the quality of the empirical attenuation coefficient.

As expected, given the strong impact of the above effects, the largest part of the analyzed dataset exceeded the tolerance range and was consequently rejected. In conclusion, we adopted 75 interstation attenuation curves as representative of 17 paths across the Aegean (figure 2B) and calculated the average value and the corresponding standard deviation of attenuation coefficient (γ) for each period and each path. For the single period measurements, a value of 0.5×10-3 km^{-1} was chosen as a conservative error estimate.

Anelastic structures in terms of Q_b^{-1} distribution with depth were derived by stochastic inversion of attenuation coefficients (Herrmann 1994). The inversion process yielded 17 path-average Q_b^{-1} models with depth. As attenuation coefficient measurements for periods <20 and >60 sec were possible for only a few paths, we restrict those models between 30-120 km depth.

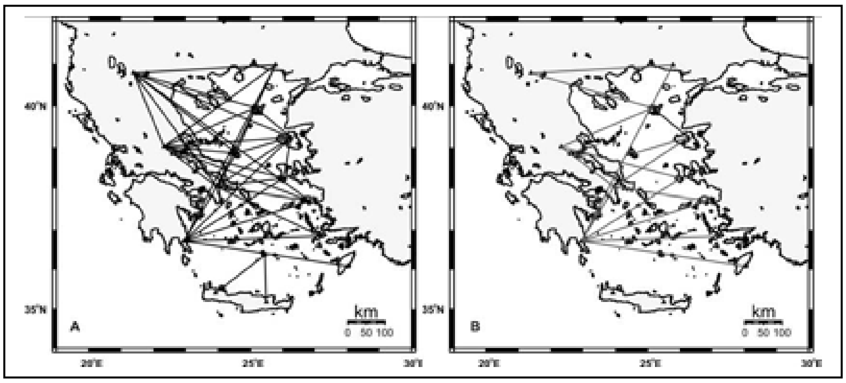

Figure 2. Paths for which phase velocities (A) and attenuation coefficient measurements (B) were obtained.

Tomography of elastic and anelastic parameters

A classical approach in surface wave tomography is to create a 3-D model in two stages. The first step is the calculation of 1-D path average models and the second step is the regionalization of these models to obtain local models. The tomographic scheme used consists of a continuous formulation of the inverse problem and the least-square criterion. The algorithm used in this study was developed by Debayle and Sambridge (2004) and it is an optimized version of the Montagner (1986) approach for continuous regionalization of surface wave path-average measurements. In the continuous regionalization algorithm, the lateral smoothness of the inverted model is obtained by assuming a priori a Gaussian correlation between neighboring points with a specified scale length L_{corr} and a scale factor σ(r). The a priori standard deviation σ(r) controls the amplitude of the perturbation allowed in the process and the horizontal correlation length is a spatial filter that constrains the lateral smoothness of the model.

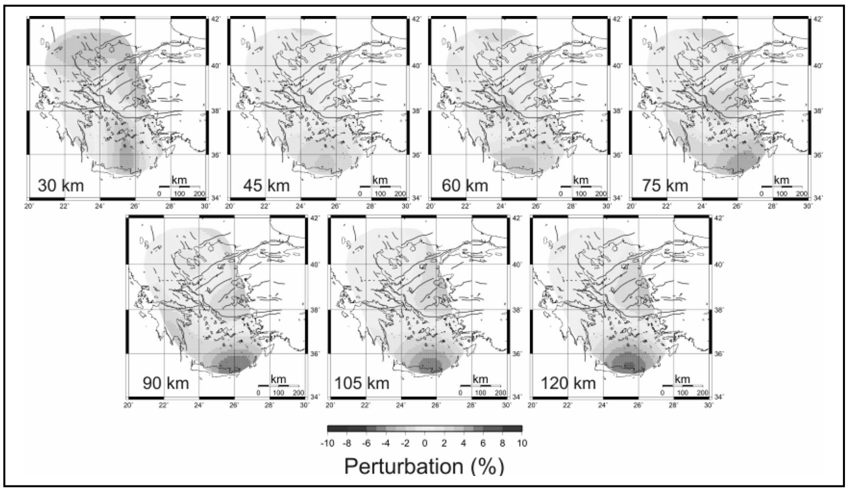

Figure 3. Tomographic slices of the shear velocity model at different depths. Tomograms start at 30 km depth. The velocity perturbations are indicated with a color scale in percent relative to a common reference model, derived from the average shear velocity at each depth.

The 36 1-D velocity models obtained were combined over a 1×1 degree grid into a single 3-D model for the lateral variations in shear velocity. The a priori standard deviation σ(r) was taken equal to 0.05 km/s, according to average phase velocity error estimate at periods 20-60 sec. The choice of an appropriate correlation length depends on the path coverage and on the period range of the inversion. After several trials L_{corr} was chosen equal to 150 km, thus favoring a smooth model considering our ray density and shortest wavelengths used (figure 3).

The 17 path-average 1-D Q_b^{-1} models with depth obtained by the inversion of attenuation coefficient curves were employed to the continuous regionalization scheme in order to obtain local Q_b^{-1}. The path-average Q_b^{-1} models with depth were combined over a 1×1 degree grid into a 3-D model for the lateral variations of Q_b^{-1}. L_{corr} was chosen equal to 150 km. Conclusions about the distribution of Q should therefore be based only on the gross features of models and fine-scale features should be ignored. σ(r) was taken equal to 5×10^{-3}. The depth range of the computed tomograms was restricted between 30 and 120 km (figure 4).

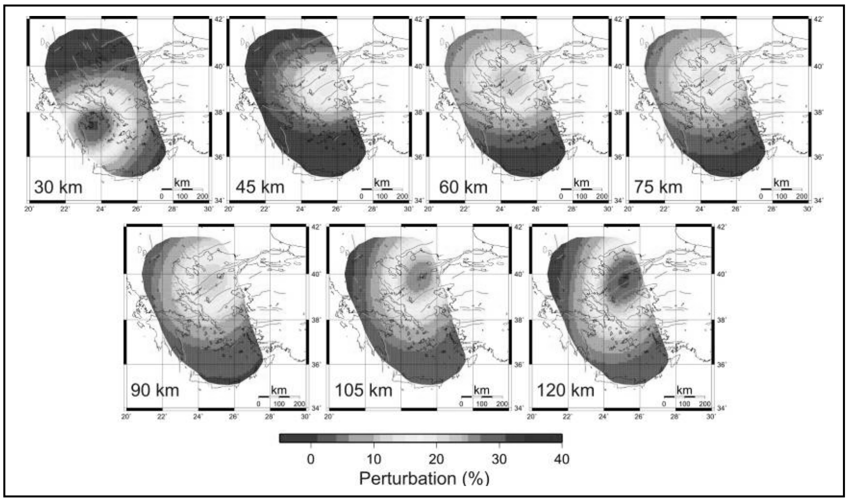

Figure 4. Tomographic slices of the Q_b^{-1} model at different depths. Tomograms start at 30 km depth. The Q_b^{-1} perturbations are indicated with a colour scale in percent relative to a common reference model, derived from the average Q_b^{-1} at each depth.

Resolution assessment of the tomographic models

The estimation of resolution is one of the main problems in seismic tomography. As the solution is not unique, the input data do not contain the information of seismic waves in every point of the medium. Although the under study area is of small dimensions, the algorithm used is inverting for local velocity over a 1×1 degree global grid and consequently the posteriori covariance matrix cannot be computed. This fact limits our ability to apply formal statistical theory to analyze the reliability and precision of the resulting tomograms. Two different approaches were applied, in order to produce a qualitative estimation of models constraint as a function of geographical position.

The Null Space Energy indicator (NSE) was used to assess the lateral resolution of the shear velocity tomograms. NSE provides an estimate of the local reliability in model space displaying areas where the data cannot reconstruct features with the desired resolution (Vesnaver 1994). This statistical tool is a function of the ray distribution and the grid size. Each component n_j of the NSE is associated with the j_{th} pixel:

$$n_j = \sum_i V_{ij}^2$$

where V_{ij} are the elements of the matrix V. The summation is performed for the indexes i of the singular values that are below the chosen threshold. We consider that two decimal points for the elements of matrix G reflect the desired actual accuracy and for this reason two orders of magnitude are the limit for the singular values that contribute positive to the solution. High values of NSE indicate solution vagueness at the corresponding pixels and vice versa. Figure 5 presents the NSE distributions along with the corresponding ray hits per cell.

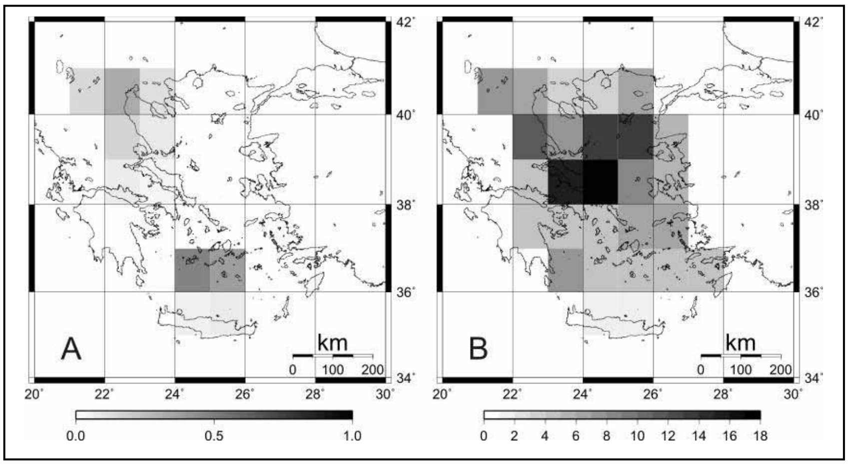

Figure 5. Null space energy (NSE) distributions (A) & the corresponding ray density map (B).

From the above figure, it is obvious that the largest uncertainties occur at the lower boundary of the model as a direct effect of limited ray coverage. In general the NSE is quite low, while in some areas it is almost zero (North East part of Figure 5A).

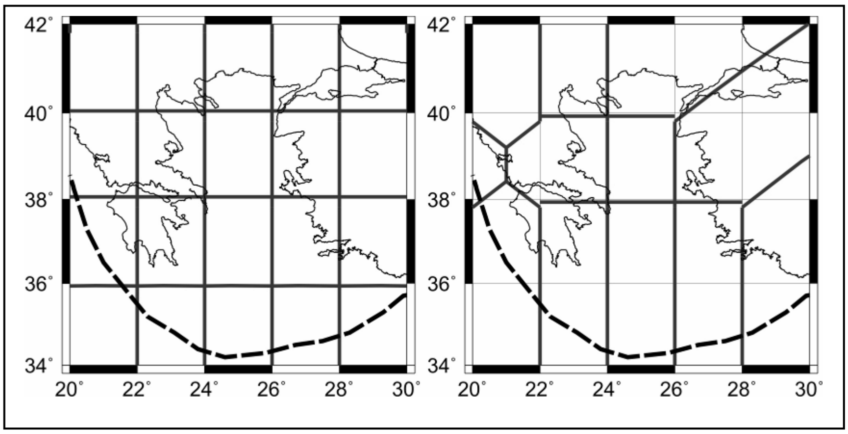

Figure 6. Voronoi diagrams to assess the anelastic model constraint as a function of geographical position. Left: Initial Voronoi diagram over a 2° × 2° grid. Right: Optimized Voronoi diagram.

In order to estimate the variation of the Q_b^{-1} model constraint provided by the ray path coverage we used Voronoi polyhedra, by applying a technique proposed by Debayle and Sambridge (2004). In two dimensions a Voronoi diagram divides the plane into a set of polygons, one about each node, such that all points in a particular cell are closer to its defining node than any other node. To produce a qualitative measure of model constraint we aim to build an optimized parameterization of the model in which each geographical point belongs to the smallest cell for which an appropriate quality criterion is satisfied. The overall pattern of the optimized parameterization will reflect variations in model constraint.

As a starting point we built an initial Voronoi diagram falling on a 2° × 2° grid. From this starting Voronoi diagram we proceeded iteratively by building new diagrams in such a way that a particular quality criterion depending on the ray distribution is satisfied for each cell. The process of generating the new optimized Voronoi diagram is a matter of deleting nodes which do not match the criterion and then recalculating the Voronoi cells about the remaining nodes. When nodes are deleted, the neighbouring Voronoi cells inherit the area and ray paths previously contained in the deleted Voronoi cell. This makes the new cells larger on average and more likely to satisfy the quality criterion. In the final optimized diagram (figure 6) each cell denotes the size of the structures our inversion can model. As it can be seen in figure 6b, best resolution is achieved in the central region. In northern and southern region, resolution is not efficient, but it is better in the E-W direction.

Results and Discussion

The amplitude of S-wave velocity variations (approximately -3% to +8%) is compatible with phase velocity variations derived in the study of Kassaras et al., (2005). This fact implies a good compromise between experimental measurements and the inverted model. The amplitude of the velocity variations is in agreement with previous studies in the Aegean based on local and teleseismic tomography (Papazachos and Nolet, 1997; Tiberi et al., 2000) and surface wave tomography (Bourova et al., 2005).

Perhaps the most dominant feature of the model is the velocity contrast in Central and North Aegean. This tendency is evident in almost the whole depth range of the model. Papazachos and Nolet (1997), observed a low velocity zone beneath North Aegean at about 100 km depth. However, our model can not be directly compared with velocities derived from body waves tomography because of anelastic effects. Low shear velocities were observed by Bourova et al. (2005 in this area) at depths 50-120 km. The amplitude of the observed velocity contrast is between -1% and -3%. Interpretations of seismic velocity heterogeneities are generally based on thermal variations. Vs variations of 1% to 3% over distances of a few hundred kilometers, as observed in our model, can be obtained with temperature variations of 70 to 200 °C (Goes et al., 2000), which may result to melts and/or fluids circulation. Moreover, Pleistocene to Recent trachyandesitic volcanism and high heat flow, as expressed by hot springs in Central Greece (SE Thessaly and N. Evoicos Gulf), can be the result of mantle-originated magmas differentiated during their ascent through the relatively thin crust of the area (Makris et al., 2001). The southwestwards NAF propagation during the last 5 Ma, which has reached the eastern continental coast of Central Greece, may also be of significant importance to both volcanism and low velocity zone in this particular location.

High velocities are observed in continental Greece at depths 45-120 km. This is compatible with Papazachos and Nolet (1997), Marone et al., (2004), Bourova et al., (2005). The observed high velocity zone extends from north-western Greece to the Turkish coast, going through western Greece and southern Aegean and subparallel to the Hellenic trench. Marone et al., (2004) interpret this structure as the subducted lithospheric African plate, which is bounded to the east of the study area, in the region of southwestern coast of Turkey.

One of the main features of our model is a high-velocity anomaly in south Aegean, associated with the slab. However, a limited resolution and better path coverage is required to obtain constraints on the slab geometry. North of NAT, a high velocity anomaly is observed (Figure 3), possibly associated with the southern margin of the Eurasian continental lithosphere. Although null space energy is high at this part of our model (poor resolution) the pattern is compatible with a high velocity anomaly found at the same area by Papazachos and Nolet (1997).

As expected, the attenuation pattern follows that of shear velocities. Within the examined depth range (30-120 km) the amplification of perturbations in the anelastic tomograms is between 0-20 % with respect to the background model, about 2 times higher than shear velocity perturbations, magnitude compatible with attenuation observations elsewhere (Mitchell, 1995).

Except in the case of 30 km depth, where elastic tomography is highly connected with crustal thickness, high attenuation is associated with low shear velocities, apparently in the North Aegean region. As in elastic tomography this region is about 200 km wide and extends in depth possibly deeper than our model. The resolution assessment shows that in this particular area the structures which can be retrieved are of similar dimensions, thus the possibility of an artefact intrusion is quite low.

The presence of this zone could be attributed to several reasons, including melting in the lithospheric mantle or asthenosphere and distributed deformation. Indeed, the NAF in the area and the associated intense north-south extension caused rapid tectonic instability in the area expressed in both mantle and crustal levels. NAT and Orfanos Gulf basins are their crustal surface results. NE-SW mantle olivine anisotropy (Hatzfeld et al., 2001) and extension in about the same direction suggest upper mantle deformation or flow. Recent magmatic mantle processes are manifested in the small volcanic islets of Psathura and Kalogeri of Northern and Central Aegean, respectively (Figure 1). They consist of sodic basalts derived from oceanic island basalt (OIB) asthenospheric mantle source similar in geochemical character to Pliocene basalts of Western and Central Anatolia (Pe-Piper and Piper, 2002; Fytikas et al., 1984; Innocenti et al., 2005). High heat flow in the area of N. Aegean, signified by many hot springs in its islands, as well as the above mentioned petrogenetic and tectonic processes, indicate a relatively thin crust (<28 km) or a lithospheric delamination (Al-Lazki et al., 2004; Karagianni et al., 2005). Moreover, the high attenuation mantle zone depicted clearly in the northern part of the area presumably suggests magma either underplates the crust or most possibly remains further below at lithospheric-asthenospheric mantle levels, and the lithosphere-asthenosphere boundary is within our model depths, that is at depths less than 120 km beneath northern Aegean.

At about 30 km depth, the high attenuation anomaly observed in the southern part of the study area could be associated with thermal activity from hot fluids and/or magma residing in deep crustal to lithospheric mantle levels below the South Aegean active volcanic centers, and originated in the asthenospheric mantle wedge above the dehydrating African subducted slab. Reactions of the released fluids with peridotitic lithospheric mantle can also cause serpentinization, which further may decrease the seismic velocity and increase attenuation. Low attenuation is now observed throughout the Hellenic mainland likely attributed to subducted features.

Conclusions

From the study of tomographic schemes of path-average phase velocities and attenuation coefficients of fundamental Rayleigh wave crossing the Aegean a 3-D model of shear velocity variation and a 3-D model of Q_b^{-1} variation down to 120 km were obtained.

The most prominent features in the tomograms are:

1) A low shear velocity zone in central and north Aegean, which correlates well with the derived anelastic tomograms which present high attenuation in this area. This low velocities/high attenuation zone, which indicates the lithosphere-asthenosphere boundary occurs at depths less than 120 km beneath the area, could be attributed to:
   i) High extensional strain rates related with the NAF system within the Aegean, slab roll back and distributed deformation of the upper mantle, and/or
   ii) A hot or most probably partially molten lithosheric and uppermost asthenospheric mantle, which generates subordinate Pleistocene to Recent volcanism and high heat flow in the area.
2) A high velocity/low attenuation zone in the southern part of the study area and deeper than 30 km indicating the cool subducted African lithosphere beneath the South Aegean.
3) A high attenuation zone observed in the South Aegean at about 30 km depth that probably corresponds to serpentinization, hot fluids and/or magma batches residing in deep crustal to lithospheric mantle wedge levels.

4) A low attenuation region throughout the Hellenic mainland at crustal depths, which is likely ascribed to the subducted slab.

References

Al-Lazki A.I., Sandvol E., Seber D., Barazangi M., Turkelli N. and Mohamad. R. (2004). Pn tomographic imaging of mantle lid velocity and anisotropy at the junction of the Arabian, Eurasian and African plates, *Geophys. J. Int. 158, 1024–1040.*

Bourova E., Kassaras I., Pedersen H.A. Yanovskaya T., Hatzfeld D. & Kiratzi A. (2005). Constraints on absolute S velocities beneath the Aegean Sea from surface wave analysis, *Geophys. J. Int, 160, 1006-1019*.

Debayle E. & Sambridge M. (2004). Inversion of massive surface wave data sets: model construction and resolution assessments, *J. Geophys. Res., 109, B02316, doi:10.1029/2003JB002652.*

Fytikas M., Innocenti F., Manetti P., Mazzuoli P., Reccerillo A. & Villari, L. (1984). Tertiary to Quaternary evolution of volcanism in the Aegean region, In: Dixon, J.E. & Robertson A.H.F. (eds): *The geological evolution of the eastern Mediterranean., Geol. Soc., London, Spec. Publ., 17, 687-699.*

Goes S., R. Gover & P. Vacher (2000). Shallow mantle temperatures under Europe from P and S wave tomography, *J. Geophys. Res., 105, 11,153– 11,169.*

Hatzfeld D., Karagianni E., Kassaras I., Kiratzi A., Louvari E., Lyon-Caen H., Makropoulos K., Papadimitriou P., Bock G. & Priestley, K. (2001). Shear wave anisotropy in the upper mantle beneath the Aegean related to internal deformation, *J. Geophys. Res., 106, No. 12, 30737-30753.*

Hatzidimitriou P. (1993). Attenuation of coda waves in Northern Greece, *Pure Appl. Geophys., 140, 63–78.*

Herrmann R.B. (1973). Some aspects of band-pass filtering of surface waves, *Bull. Seism. Soc. Am., 62, 129-139.*

Herrmann R.B. (1994). Computer programs in Seismology, User's manual, *St. Louis University, Missouri.*

Innocenti F., Agostini S., Di Vincenzo G., Doglioni C., Manetti P., Savascin M.Y. & Tonarini S. (2005). Neogene and Quaternary volcanism in Western Anatolia: Magma sources and geodynamic evolution, *Marine Geology, 221, 397– 421.*

Karagianni E.E., Papazachos C.B, Panagiotopoulos D.G., Suhadolc P., Vuan A. & Panza, G.F. (2005). Shear velocity structure in the Aegean area obtained by inversion of Rayleigh waves, *Geophys. J. Int., 160, 127-143.*

Kassaras I., Makropoulos K., Bourova E., Pedersen H. & Hatzfeld, D. (2005). Upper mantle structure of the Aegean derived from two-station phase velocities of fundamental mode Rayleigh waves, *The South Aegean Active Volcanic Arc, Developments in Volcanology, Volume 7, Hardbound, ISBN 0-444-52046-5, Imprint ELSEVIER: 19-45.*

Kovachev S.A., Kuzin I.P., Shoda O.Yu. (1991). Attenuation of S waves in the lithosphere of the Sea of Crete according to OBS observation, *Phys. Earth Planet. Inter., 69, 101– 111.*

Makris J., Papoulia J., Papanikolaou D. & Stavrakakis G. (2001). Thinned continental crust below northern Evoikos Gulf, central Greece, detected from deep seismic soundings, *Tectonophysics, 341, 225–236.*

Marone F., van der Lee S. & Giardini D. (2004). Three-dimensional upper mantle S-velocity model for the Eurasia–Africa plate boundary region, *Geophys. J. Int., 158, 109–130.*

Mitchell B.J. (1995). Anelastic Structure and Evolution of the Continental Crust and Upper Mantle From Seismic Surface Wave Attenuation, *Rev. Geoph., vol. 33, no. 4, 441–462.*

Montagner J. (1986). Regional three-dimensional structures using long period surface waves, *Ann. Geophys., B, 4, 283-294.*

Papazachos C. &Nolet, G. (1997). P and S-wave velocity structure of the Hellenic area obtained by robust nonlinear inversion of travel times, *J. Geoph. Res., 102, B4, 8349-8367.*

Pe-Piper G. & Piper D.J.W. (2002). The igneous rocks of Greece, *Gebruder Borntraegen, Berlin-Stuttgard, 573p.*

Spakman W., Van der Lee S. & Van der Hilst R.D. (1993). Travel-time tomography of the European-Mediterranean mantle down to 1400 Km, *Phys. Earth Planet. Inter., 79, 3-74.*

Tiberi C., Lyon-Caen H., Hatzfeld D., Achaeur U., Karagianni E., Kiratzi A., Louvari E., Panagiotopoulos D., Kassaras I., Kaviris G., Makropoulos K. & Papadimitriou P. (2000). Crustal and upper mantle structure beneath the Corinth rift from a teleseismic tomography study, *J. Geophys. Res., 105, 28159-28171.*

Vesnaver A. (1994). Towards the uniqueness of tomographic inversion solutions, *J. of Seismic Explor., 3, 323-334.*

An Overview of Anisotropy Studies in Central Greece using recordings around the Gulf of Corinth (Greece) and aftershocks of the 1999 Athens Earthquake

Kaviris G (1), Papadimitriou P (1), Makropoulos K (1)

(1) Department of Geophysics, University of Athens, 157 84 Athens, Greece, gkaviris@geol.uoa.gr
(2) Department of Geophysics, University of Athens, 157 84 Athens, Greece, ppapadim@geol.uoa.gr
(3) Department of Geophysics, University of Athens, 157 84 Athens, Greece, kmacrop@geol.uoa.gr

Keywords: Anisotropy, shear wave splitting, Gulf of Corinth, stress field, EDA model

Introduction

The Gulf of Corinth is considered as one of the most active tectonic rifts around the world. The high level of seismicity (Makropoulos and Burton, 1984; Ambraseys and Jackson, 1990), the quaternary local faulting and the 10 to 15 mm/year approximately N-S extension rate (Figure 1), imply that the Gulf of Corinth is a key place in Europe for the study of various physical processes related to the origin of earthquakes. Seismological and tectonic studies indicate that the morphology of the Gulf of Corinth is mainly due to repeated earthquakes that have occurred on 40° to 60° north-dipping normal faults. The Gulf is characterized by the long term subsidence of the northern coast and upward displacement of the main footwalls. Several large historical earthquakes have destroyed cities in the Gulf, the most well-known of which is the Heliki earthquake of 373 BC, but only few of them have provided information about the faults that produced them. Recent large events are characterized by normal faulting with an approximately E-W direction, while their focal depths are about 10 km.

In the framework of the present study, analysis of data recorded by the Cornet network and by a temporary seismological network installed in the western part of the Gulf of Corinth revealed the existence of an anisotropic upper crust around both parts of the Gulf. Furthermore, shear wave splitting analysis was performed in the region of Attica using aftershocks of the 1999 Athens earthquake (Mw=6.0) that caused 143 fatalities. The methods used in all the above mentioned regions for the determination of the splitting parameters are the polarigram and the hodogram. For each selected event the direction of polarization of the fast shear wave, the time delay between the two split shear waves and the polarization direction of the source were measured.

Cornet Network – Method used

The Cornet (Figure 2) seismological permanent network (Kaviris et al., 2007) has been installed since 1995 around the eastern Gulf of Corinth (Greece). The shear-wave splitting phenomenon has been observed during the analysis of the Cornet data set. The selected events have clear and impulsive S wave arrival phases on the horizontal components. In addition, the amplitude of the S wave phase on the vertical component is smaller than on the horizontal ones. A visual inspection and a plot of the particle motion in the three planes of projection were used to select the events that match the criteria mentioned above.

The representations used in the present study in order to determine the polarization direction of the S_{fast} wave and the time delay between the two split shear waves are the polarigram (Bernard and Zollo, 1989) and the hodogram.

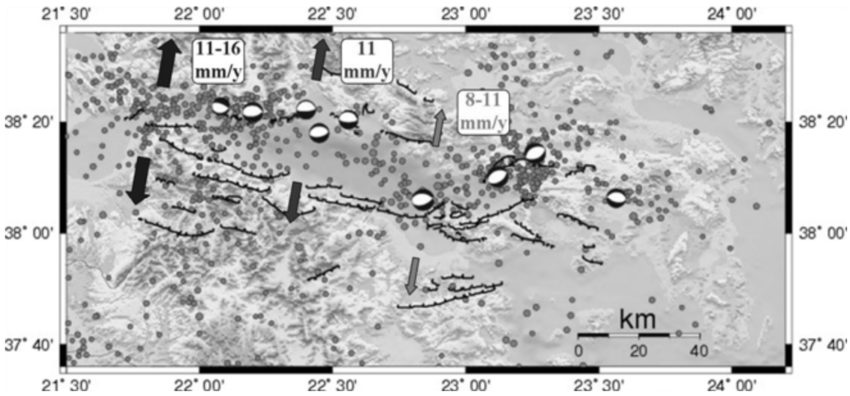

Figure 1. Active normal faults of the area and epicenters located by the Cornet network. The arrows present the extension of the Gulf of Corinth. Focal mechanisms of large events are also presented.

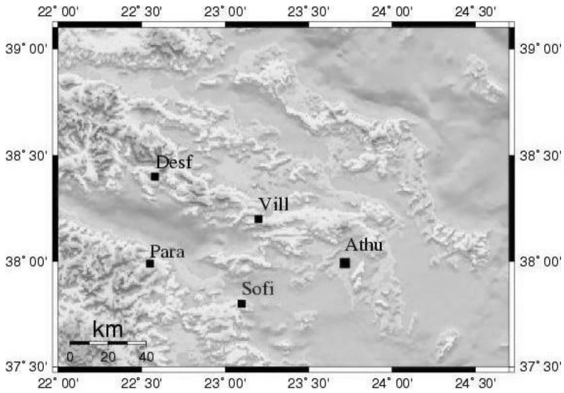

Figure 2. The permanent Cornet Telemetric Network.

An example of an event located close to the Sofiko station is presented (Figure 3a), where the polarigrams in the E-Z and N-Z planes are plotted. The polarization vector is oriented almost parallel to the horizontal component, showing that the vertical component has smaller amplitudes than the horizontal ones. This fact indicates that the shear waves are propagating approximately vertically through the anisotropic media. In the same figure, the polarigram of the N-E plane is also presented, where shear-wave splitting is evident. The angle between the north and the fast axis is the polarization direction, which is equal to N120°. Then the seismograms are rotated in the fast and slow directions and the obtained polarigram is presented in Figure 3 (b). In this figure the obtained polarization vector is oriented almost parallel to the fast component. The measured time delay is equal to 0.040 sec, represents the magnitude of anisotropy and is removed in order to obtain the polarization direction of the source.

To measure the polarization of the source, the fast component is temporally moved towards the slow one for an interval of time equal to the time delay (0.040 sec) and the obtained waveforms are presented in Figure 4 (a). The obtained polarization angle is F5°. The polarization direction of the source is the sum of this angle and of the polarization direction (N120°) and is equal to N125°. Following (Figure 4(b)), the horizontal components are rerotated to their initial directions (E-W, N-S, angle of rotation -120°). The obtained waveforms are theoretically those that would be recorded in the case that the medium between the hypocenter and the station (Sofi) was not anisotropic. The polarization direction of the source is directly measured and is found equal to N125°.

Results of the Anisotropy Study - Cornet Network

The S_{fast} polarization directions for each Cornet station are presented on equal-area projections of the upper hemisphere in Figure 5. The outer circle defines the S-wave window and represents an angle of incidence of 45°. The length of the bars is proportional to the time delay between the fast and slow shear waves. The values of the time delays for the 75 events analyzed at Sofiko station vary between 0.024sec and 0.160sec, while the polarization directions of the fast shear wave vary between N78° and N126°. The coherence of the fast shear wave polarizations at Sofiko station, irrespective of the azimuth of each event, is consistent with shear-wave splitting due to the seismic wave propagation through an anisotropic medium. The same observation is evident for the Paradeisi and Villia stations. The values of the time delays at Paradeisi station, where 47 events were analyzed, vary between 0.024sec and 0.128sec, while at Villia station (57 analyzed events) between 0.040sec and 0.184sec. The polarization directions of the fast shear wave at Paradeisi station vary between N125° and N165°, while at Villia station between N125° and N163°. For Desfina station the 101 events that were analyzed present more complicated results as the shear wave polarizations present two different and quasi-perpendicular main directions. The values of the time delays at Desfina station vary between 0.016sec and 0.096sec, while the polarization directions of the fast shear wave vary between N16° and N160°. Comparing the calculated time delays, we observe that they have higher values in the stations situated in the eastern part of the Gulf (Sofiko and Villia).

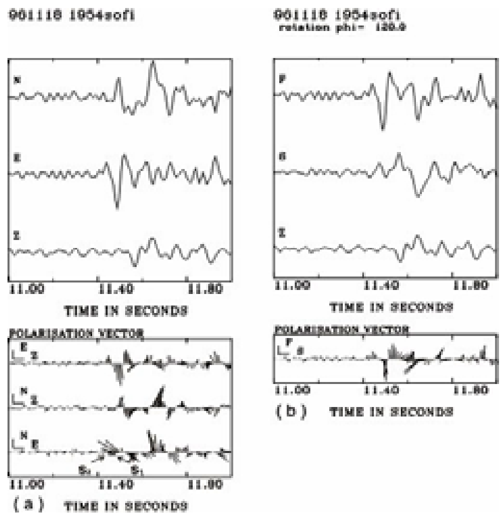

Figure 3. (a) Earthquake recorded at Sofiko station. Original traces are presented at the top. At the bottom the polarization vector is presented in the E–Z, N-Z and N–E planes. In the north-east plane the polarization directions of the fast (S_1) and the slow (S_2) shear waves are indicated. (b) Seismograms are rotated parallel and orthogonal to the polarization direction of the fast shear waves and the waveforms are presented at the top. At the bottom the polarization vector is presented in the fast-slow plane where the time delay is measured.

The S_{fast} polarization directions at each Cornet station are presented in Figure 6 using equal-area rose diagrams. The mean direction at Sofiko station is N106º ± 13º. At Paradeisi station we observe two directions of anisotropy with a mean value equal to N142 º ± 13°, while at Villia station there are three directions with a mean value equal to N142° ± 10°. Finally, at Desfina station various directions of anisotropy are observed (Papadimitriou et al., 1999). However, two main directions are distinguished, approximately N55° and N143°.

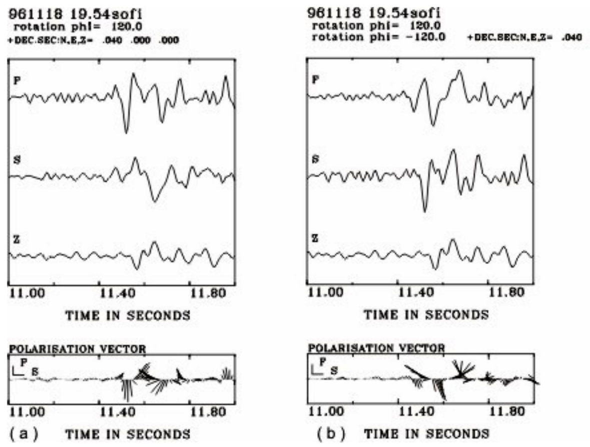

Figure 4. (a) Measurement of the time delay for the event presented in Figure 3. (b) Measurement of the polarization direction of the source on waveforms rerotated in the initial direction after time correction.

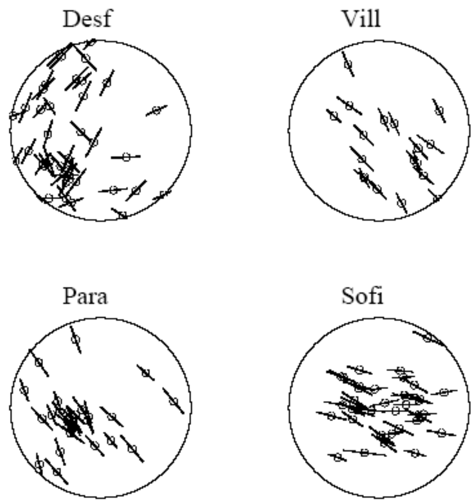

Figure 5. Polar equal-area projections on the upper hemisphere of the fast shear wave polarizations measured at each Cornet station.

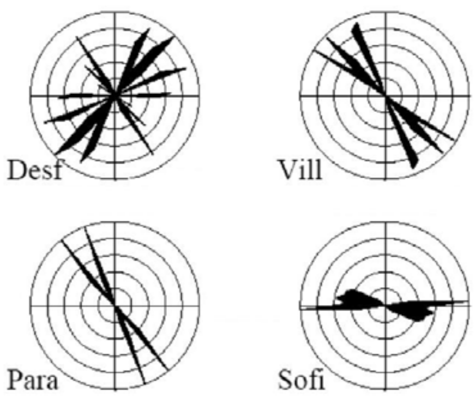

Figure 6. Rose diagrams of the fast shear wave polarization directions at all Cornet stations.

Results of the Anisotropy Study - CORSEIS Network

The CORSEIS seismological network (Figure 7) that consists of nine seismological stations has been installed at the western part of the Corinth Gulf, around the city of Aigion, and at the northern coast of the Gulf, around the Trizonia islands, on April 2000.

The seismological station Psar is located on the south edge of the Psaromita peninsula (northern part of the Gulf of Corinth). The azimuthal distribution of the events that were selected for the anisotropy study is very satisfactory.

An event is analyzed (Figure 8) using the polarigram, as well as the hodogram representation. The linearity of the particle motion is clear, as well as its deviation caused by the arrival of the slow shear wave. The measured S_{fast} polarization direction of this event is equal to N105° (Fig. 8a). The time delay, measured after rotating the waveforms to the S_{fast} polarization direction, is equal to 0.056s (Fig. 8b). The polarization of the source is measured after the correction of the time delay (Fig. 8c) and is equal to N130° (Fig. 8d).

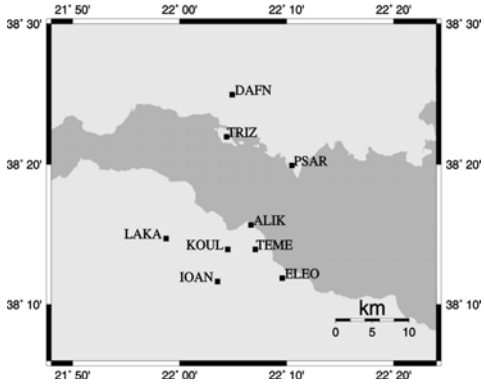

Figure 7. The CORSEIS Seismological network.

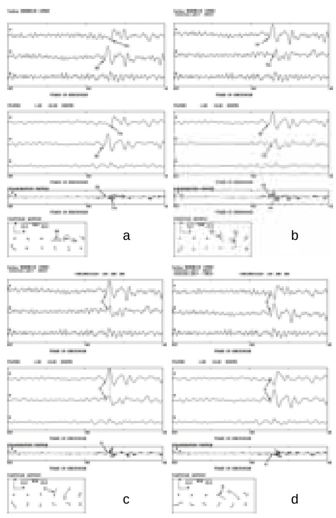

Figure 8. (a) Original traces of an earthquake recorded at Psar station, filtered traces, polarigram and hodogram in the N-E plane. (b) Traces rotated parallel and orthogonal to the polarization direction of the fast shear waves, filtered waveforms of the rotated traces, polarization vector and hodogram in the fast-slow plane. (c) Traces rotated parallel and orthogonal to the polarization direction of the fast shear waves after the correction of the time delay, filtered waveforms, polarigram and hodogram. (d) Traces rerotated to the North and East directions, filtered waveforms of the rerotated traces, polarization vector and hodogram.

Anisotropy study was performed on 5 stations of the CORSEIS Network, 3 of which are located on the northern part of the Gulf (Dafn, Psar and Triz), while 2 on the southern part (Alik and Laka).

Figure 9 presents the S_{fast} polarization directions on equal-area projections of the upper hemisphere for the CORSEIS stations. The values of the time delays at Dafnochori station vary between 0.016sec and 0.120sec, while the polarization directions of the fast shear wave vary between N57° and N113°. The polarization directions of the fast shear wave at Trizonia station vary between N88° and N138° whereas, the time delays range between 0.016sec and 0.128sec. The values of the time delays at Psaromita station vary between 0.016sec and 0.128sec, while the polarization directions of the fast shear wave vary between N78° and N140°. Concerning Laka station, the values of the time delays vary between 0.024sec and 0.104sec, while the S_{fast} polarization directions vary between N72° and N150°. Finally, the values of the time delays at Aliki station vary between 0.032sec and 0.128sec, with their majority between 0.064sec and 0.096sec. This station presents the highest time delay values. A possible explanation is that Aliki is the only CORSEIS station that is situated on sediments, while the others are situated on rock. Anisotropy directions for Aliki station vary between N75° and N130°.

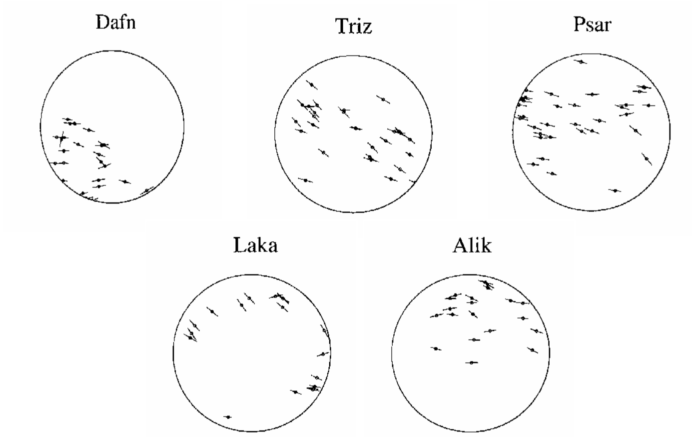

Figure 9. Polar equal-area projections on the upper hemisphere of the fast shear wave polarizations measured at CORSEIS stations.

Rose diagrams for the CORSEIS stations are presented in Figure 10. Concerning the Dafnochori station, the main S_{fast} polarization direction is N93°, while a secondary one equal to N110° is also observed. The rose diagram for Trizonia station reveals that the main S_{fast} polarization direction is about N130°, while a secondary one equal to N110° is also observed. The main S_{fast} polarization direction for Psaromita station is N105°, which is the best defined for all the stations used in the anisotropy study for CORSEIS network, since no secondary direction is observed. For Laka station the main S_{fast} polarization direction is N123°, while a secondary one equal to N100° is also observed. Finally, the main S_{fast} polarization direction for Aliki station is N90°, with a secondary one equal to N110°.

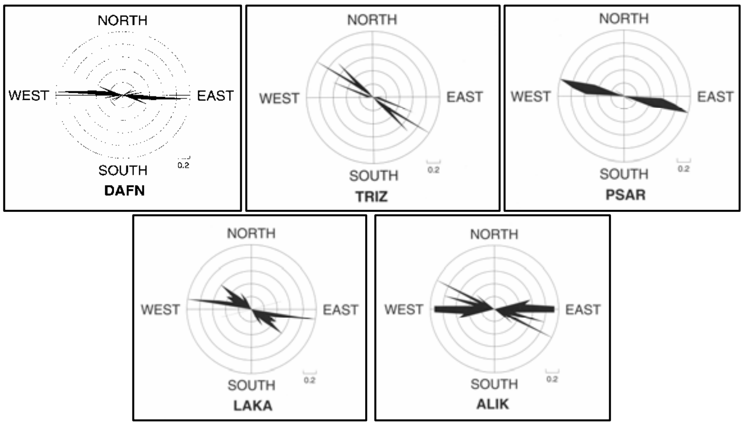

Figure 10. Rose diagrams of the fast shear wave polarization directions at CORSEIS stations.

Results of the Anisotropy Study using aftershocks of the 1999 Athens Earthquake

On 7 September 1999, an earthquake (Mw=6.0) occurred northwestern of Athens, the capital of Greece (Papadimitriou et al., 2002). A temporary seismological network (Figure 11) was installed in Western Attica, very close to the main fault one day after the main shock and a large number of aftershocks were recorded. During the analysis of these aftershocks the existence of shear-wave splitting was revealed.

An example of an earthquake recorded by the Zofr station is presented using the polarigram representation in the three planes of projection (Fig. 12a). Inspecting the projection on the E-Z and the N-Z planes, it is evident that the direction of polarization is almost parallel to the horizontal component. The polarigram on the N-E plane reveals that the motion of the fast shear-wave is linear with a polarization direction equal to N113°. The original waveforms are rotated to the fast and slow direction to measure the time delay (Fig. 12b). The polarization vector of the fast shear wave is oriented almost parallel to the fast direction, which means that the measurement of this direction is correctly performed. The time interval between the two shear wave arrivals is the time delay, which is equal to 0.030 sec. The measured time delay is then corrected and the seismograms are rerotated to their original directions. The obtained polarisation vector, which is equal to N317°, is the polarization of the source.

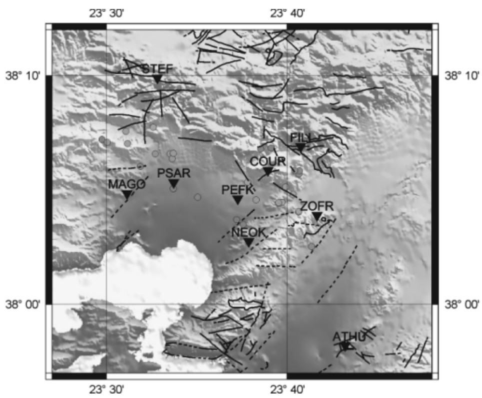

Figure 11. Seismological Network in Western Attica.

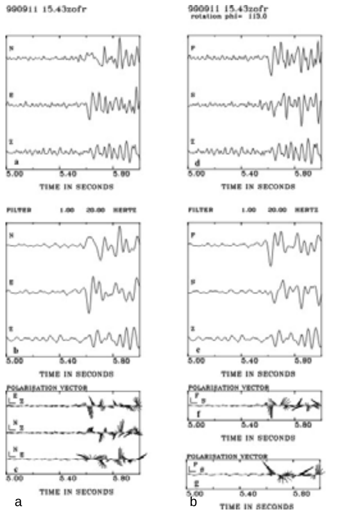

Figure 12. (a) Original traces of an event recorded at Zofr station, filtered traces, polarigrams in the three planes of projection. (b) Traces rotated parallel and orthogonal to the polarization direction of the fast shear waves, filtered waveforms of the rotated traces, polarization vector in the fast-slow plane and polarigram from which the polarization of the source is estimated.

The polarization directions of the analyzed events are presented using equal-area rose diagrams (Figure 13). The S_{fast} polarization directions for the Neok station vary between N78° and N114°, while the time delays vary between 0.025 sec and 0.060 sec. The polarization directions of the fast shear wave for the Mago station vary between N77° and N113°, while the time delays between 0.055 sec and 0.060 sec. The time delays of the Fili station vary between 0.025 sec and 0.075 sec and the polarization directions of the fast shear wave between N85° and N113°. The values of the S_{fast} polarization directions for the Psar station vary between N80° and N114°, while the time delays between 0.025 sec and 0.100 sec. Finally, the polarization directions of the fast shear wave for the Zofr station vary between N74° and N113°, while the time delays between 0.030 sec and 0.085 sec.

Discussion

Analysis of the data revealed the existence of an anisotropic upper crust around the Gulf of Corinth. The large number of events that were processed ensures the detailed study of anisotropy, as well as the validity of the conclusions. Using the appropriate selection criteria, a dataset of events was winnowed. For instance, scattered and converted phases that could lead to false identification of the split shear waves were identified and rejected.

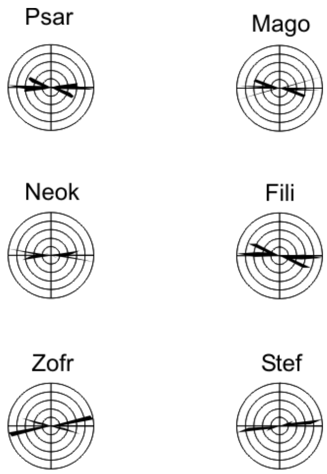

Figure 13. Rose diagrams of the fast shear wave polarization directions.

All Cornet stations presented almost linear polarization with mean values of anisotropy (Fig. 14a) N106° (Sofi), N142° (Para), N142° (Desf, main direction) and N142° (Vill). Mean polarization directions at Para, Desf and Vill stations coincide, while the mean polarization direction at Sofi station is closer to E-W. Mean values of the anisotropy direction of the CORSEIS stations vary between N90° and N120° and are presented in Figure 14b.

The uniformity of the fast shear wave polarizations at each station around the Gulf of Corinth (Cornet and CORSEIS networks), irrespective of the azimuth of each event, is consistent with what is expected for shear-wave splitting due to propagation through an anisotropic medium. These observations are consistent with the general NNE-SSW direction of extension in the Gulf and, therefore, in agreement with the extensive dilatancy anisotropy (EDA) model.

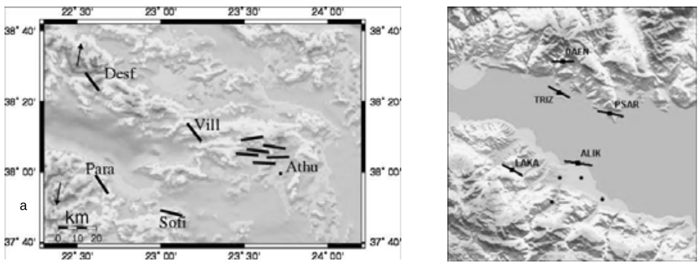

Figure 14. Mean S_{fast} polarization directions for (a) Cornet Network and temporary network installed in Western Attica and (b) CORSEIS Network.

An anisotropy study was also performed at Western Attica using aftershocks of the 7th September 1999 Athens earthquake. Mean anisotropy directions (Fig. 14a) at all stations are almost parallel, varying between N87° and N99°. The only exception was the mean direction calculated at Stef station (N81°). Mean directions are almost parallel to the azimuth of the main fault. The observed anisotropy is in agreement with the stress field of Western Attica and can be explained by the extensive dilatancy anisotropy (EDA) model.

References

Ambraseys N.N. & Jackson J.A. (1990). Seismicity and associated strain in central Greece be-tween 1890 and 1988, *Geophys. Jour. Inter., 101, 663-708.*

Bernard P. & Zollo A. (1989). Inversion of near-source S polarization for parameters of double-couple point like sources, *Bull. Seism. Soc. Am., 79, 1779-1809.*

Kaviris G., Papadimitriou P. & Makropoulos K. (2007). Magnitude Scales in Central Greece, *Bull. Geol. Soc. Greece, vol. XXXX, part 3, p. 1114-1124.*

Makropoulos K.C. & Burton P.W. (1984). Greek tectonics and seismicity, *Tectonophysics, 106, 275-304.*

Papadimitriou, P. Kaviris G. & Makropoulos K. (1999). Evidence of shear wave splitting in the eastern Corinthian Gulf (Greece), *Physics of the Earth and Planetary Interiors*, 114, 3-13.

Papadimitriou P., Voulgaris N., Kassaras I., Kaviris G., Delibasis N. & Makropoulos K. (2002). The Mw=6.0, September 7, 1999 Athens earthquake, *Natural Hazards, 27, 15-33.*

A simple method for tsunami wave form re-calculation through the shelf

Kaystrenko V (1)

(1) Institute of Marine Geology and Geophysics, 1 B, Nauki St., Yuzhno-Sakhalinsk, 693022 Russia, Vict-K@mail.ru, victor@imgg.ru

Keywords: Tsunami on a slope, numerical modeling, transformation

Introduction

It is rather difficult to calculate the tsunami propagation from source to the coastal zone within the scope of single numerical model. It is known that the tsunami field varies highly near the coastal zone because of relatively small wave length. Therefore the tsunami calculation in this zone needs a small grid step size about 10 - 100 meter, and consequently the calculation of tsunami propagation in domain 1000 km x 1000 km needs a grid dimension up to 10^5x10^5. Really a such small grid step size is needed for tsunami description in shallow water only. Therefore usually the full domain is divided into several parts in which a different grids or different methods are used.

Anyway, tsunami wave form have been calculated by the grid model up to minimal depth *H* (10-20 meter). After them the tsunami record on the artificial "wall" can be re-calculated to the coast using N.Shuto's (1981) factor for quasi monochrome waves over the slopping bottom:

$$R/a = 2\cdot\{J_o^2(\frac{4\pi L}{\tau\sqrt{gH}}) + J_1^2(\frac{4\pi L}{\tau\sqrt{gH}})\}^{\frac{1}{2}}$$

where *L* is a distance of the artificial boundary in numerical model from the coast line, τ is wave period and J_0 and J_1 are Bessel's functions. Unfortunately, the inverse Fourier transform for this factor is unknown. Using physical consideration we will obtain a special integral transformation for tsunami wave form re-calculation from the depth *H* to the shore line.

Coming and reflected waves on a slope

Let *x* axis is horizontal and directed from the coast to the sea and the depth variation is described with a formula $h(x) = k\,x$.

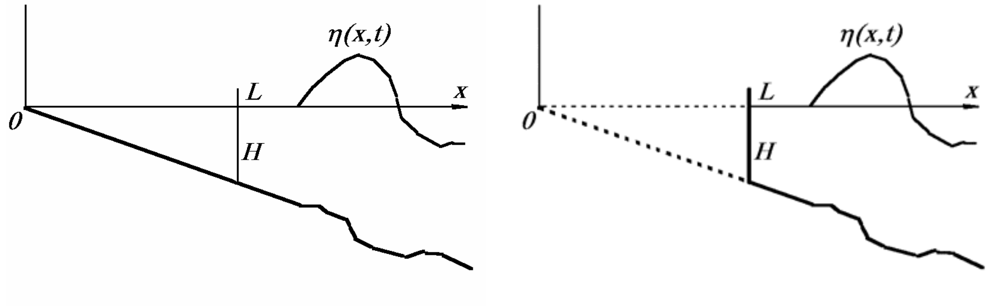

Figure 1. Two models for tsunami propagation near the shore:
real one and another one accompanied by an artificial "wall".

We consider tsunami propagation in two models with same bottom profile and same initial data (tsunami source is locating in the deep water area far from the coast). The first model is continuing up to the shore line and another one is “cut” by the artificial wall near the shore. We will obtain the formula for re-calculating the wave form on the “wall” in the second model into the wave form on the shore (x=0) in the first model. In this case the shallow water equation for both models is following

$$(gkx \cdot \eta_x)_x = \eta_{tt}\,, \tag{1}$$

where g is the weight acceleration and $\eta(x,t)$ describes the water level oscillations.

The general solution of this equation can be represented using Fourier transformation:

$$\eta(x,t) = \frac{1}{2\pi}\int_{-\infty}^{\infty} \tilde{\eta}(x,\omega)\cdot e^{-i\omega t}\,d\omega\,, \tag{2}$$

where Fourier transform $\tilde{\eta}(x,\omega)$ is the solution of the equation

$$(gkx \cdot \tilde{\eta}_x)_x + \omega^2\tilde{\eta} = 0\,, \tag{3}$$

which can be transform to Bessel equation with substitution x of variable $z = 2\omega\sqrt{\frac{x}{kg}}$.

$$\tilde{\eta}'' + \frac{1}{z}\tilde{\eta}' + \tilde{\eta} = 0\,. \tag{4}$$

The solution of last equation can be represented via Hankel functions

$$\tilde{\eta}(x,\omega) = a(\omega)\cdot H_0^{(1)}(z) + b(\omega)\cdot H_0^{(2)}(z)\,. \tag{5}$$

The phases of the asymptotics of Hankel functions

$$H_\nu^{(1,2)}(z) \approx \sqrt{\frac{2}{\pi z}}\cdot e^{\pm(z-\nu\frac{\pi}{2}-\frac{\pi}{4})}\,, \quad |\arg(z)| \le \pi \tag{6}$$

show that first term in (5) gives a reflected wave and the second term gives a wave coming to shore from the source. All the given formulae are valid for two models.

Numerical model for tsunami propagation over the slope uses often an artificial "reflected wall" condition on this boundary with h=h_0. That means for the second model

$$\left.\frac{d\tilde{\eta}_2}{dx}\right|_{x=L} = 0 \quad \Rightarrow \quad a(\omega)\cdot H_1^{(1)}(z_0) + b(\omega)\cdot H_1^{(2)}(z_0) = 0\,, \tag{7}$$

Where

$$z_0 = 2\omega\sqrt{\frac{L}{kg}} = \frac{2\omega L}{\sqrt{gH}}\,. \tag{8}$$

The equations (5) and (7) for $x = L$, $z = z_o$ can be considered as a system of equations to find an amplitudes of the coming and reflected waves $b(\omega)$ and $a(\omega)$ from Fourier transform of tsunami record at the point $x = L$ ($h=h_o$) for the second model:

$$a(\omega) = -\frac{i\pi z_0 H_1^{(2)}(z_0)}{4}\tilde{\eta}_2\big|_{x=L} \qquad b(\omega) = \frac{i\pi z_0 H_1^{(1)}(z_0)}{4}\tilde{\eta}_2\big|_{x=L}. \qquad (9)$$

The boundary with "reflected wall" at the point $x = L$ ($h=h_o$) is artificial one and we can continue a having coming wave up to the shore.

The wave field near the coast without the model wall can be described via same formula (5) generally with another amplitudes $a_1(\omega)$ and $b_1(\omega)$. The amplitudes of the coming waves should be equal $b_1\omega) = b(\omega)$ because the coming wave is known, and $a_1(\omega) = b_1(\omega)$ because the solution in the first model should be limited at x=0. Therefore the solution for the zone near the coast should be represented via Bessel function

$$\eta(x,\omega)\big|_{0\le x\le L} = 2\cdot a_1(\omega)\cdot J_0(z)\,. \qquad (10)$$

Taking into account formula (9) we receive a Fourier transform of the record on the shore:

$$\eta_1\big|_{x=0} = \pi\sqrt{\frac{L}{kg}}\cdot H_1^{(1)}(2\omega\sqrt{\frac{L}{kg}})[-i\omega\tilde{\eta}_2\big|_{x=L}]. \qquad (11)$$

The absolute value of the transform kernel, related to formula (11) is

$$R/a = \pi\omega\sqrt{\frac{L}{kg}}\cdot\{J_1^{\,2}(2\omega\sqrt{\frac{L}{kg}}) + Y_1^{\,2}(2\omega\sqrt{\frac{L}{kg}})\}^{\frac{1}{2}},$$

and its values are close to the ones given by Shuto's formula.

The inverse Fourier transformation of product of the functions gives a convolution. Therefore the needed transformation is following

$$\eta_1(t)\big|_{x=0} = \int_0^{T-t}\frac{t-\tau}{\sqrt{(t-\tau)^2 - T^2}}\eta_2'(\tau)\big|_{x=L}\cdot d\tau\,, \qquad (12)$$

where $t > T$ and $T = 2\ L/kg = 2L\ /\ gH$ is the travel time from point $x = L$ to the coast. Integrating formula (12) by parts we receive another form of needed transformation more convenient for calculation.

$$\eta_1(t)\big|_{x=0} = \int_0^{t-T}\sqrt{(t-\tau)^2 - T^2}\cdot\tilde{\eta}_2''\ (\tau)\big|_{x=L}\cdot d\tau\,. \qquad (13)$$

We assumed that the initial wave field near the point x=L equal to zero: $\eta_2(0) = \eta_2'(0) = 0$ near the coast (tsunami source is locating in the deep water area far from the coast).

Results and Discussion

Formulae (12) and (13) for tsunami wave form re-calculation through the shelf were found using the linear shallow water model up to the shore. Non-linear effects in the near shore zone can be taken into account using the linear solution (Kaistrenko at al., 1991).

These formulae are simply to analyze and calculate.

These formulae are containing only one parameter *T* being the travel time from point $x = L$ at an "artificial wall" to the coast. Some examples show that increasing of travel time *T* means delay together with tsunami height amplification. The last effect can be essential.
Let we consider the model record on the "artificial wall" as $\eta_2(t) = x(t) = \sin(2\pi t/50)\exp(-t/100)$ with travel times T = 10 and 50.

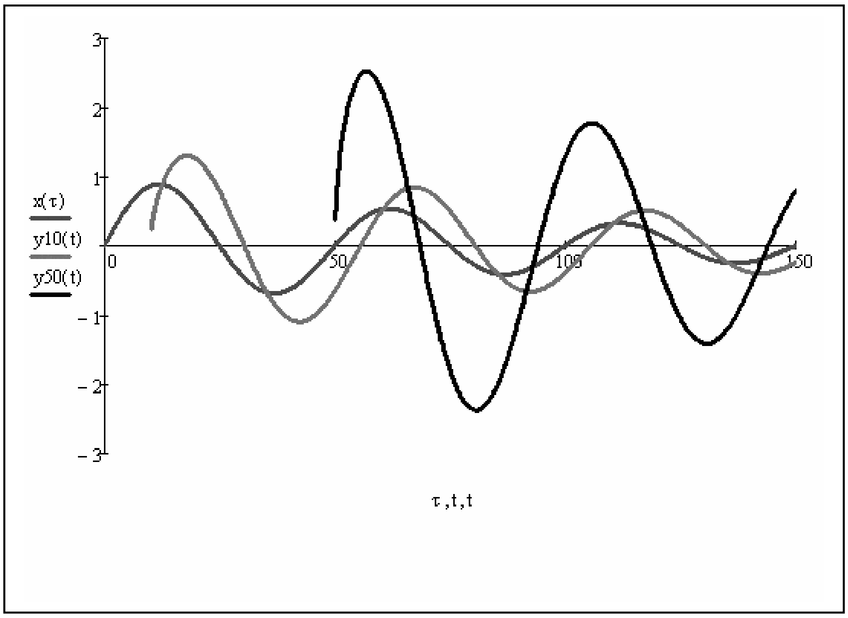

Figure 2. Two examples of the wave form re-calculation with travel times T = 10 and 50.

The last figure shows that the travel time equal to wave period gives a wave height amplification about three times.

Really, this re-calculation method yields for open parts of the coast with a smooth coastal line.

The work was supported by the Russian foundation for basic research, grant 08-05-01096.

Dr. G. Shevchenko and Dr. I. Fine are acknowledged for the useful discussions.

References

Kaistrenko, V.M., Mazova, R.Kh., Pelinovsky, E.N., and Simonov, K.V. (1991). Analytical Theory for Tsunami Run Up on a Smooth Slope, *Sci. Tsunami Hazards, v. 9, No 2.*
Shuto, N.(1981). Standing waves in front of a sloping dike, *Coastal Engineering in Japan, 15, 13-23*.

Real-time Seismology and Shake Maps in Greece

Kiratzi A A (1), Roumelioti Z (2), Benetatos C A (3)

(1) Prof of Seismology, Dept of Geophysics, Aristotle University of Thessaloniki, 54124 Greece, kiratzi@geo.auth.gr
(2) Dr. Dept of Geophysics, Aristotle University of Thessaloniki, 54124 Greece, zroum@geo.auth.gr
(3) Dr. Dept of Geophysics, Aristotle University of Thessaloniki, 54124 Greece, chmpenet@geo.auth.gr

Keywords: seismology, Aegean, earthquake, ground motion, shake maps

Introduction

The effective reduction of the impact of future earthquakes is, or at least should be, one of the primary targets in Greece, a region of intense seismic activity. A national seismic hazard mitigation program, in order to be realistic, should have the following steps, fulfilled over different time scales:

Long term stage: This time scale is usually of the order of decades and the main target is to improve the Building Code, and at a second stage the land-use regulations. In Greece, the currently applied building code is the “Hellenic Building Code” e.g. EAK (2003).

Medium term stage –The stage of preparedness: Over time scales of few years, national measures should be taken aiming at preparing for possible earthquakes. In this stage, for example, all the methods that concern the simulation of expected ground motion in urban regions should be taken into account. These scenario earthquakes provide the means to evaluate in advance the level of shaking in a specific urban region (for the region of Greece e.g. Benetatos and Kiratzi, 2004; Roumelioti et al., 2004; Theodulidis et al., 2006). Moreover, at this specific stage of preparedness, the evaluations of the time – dependent earthquake predictability models should also be considered, taking into account the uncertainties of the methods.

Short term stage: At this stage, with time scales from months to days, accurate predictions would be required, but as we must all admit, for the time being, the seismological community is still very far from this target. Thus, we must focus our attention to best dealing with the aftermath of an earthquake, and this is the main subject of the present paper.

After the earthquake: Following the occurrence of a strong event it is required to have the source parameters of the event and to identify the areas of strongest shaking. At this stage, we are not talking about a scenario event as in the previous cases, but we have an event, where seismologists will be asked to provide shake maps as soon as possible.

Here, we present an information system tool – called hereafter “SEIS-MOTION”- which was installed in order to compute, in near-real time, the moment tensor, the finite fault slip models and provide shake maps after the occurrence of strong and moderate size earthquakes in Greece. The system operates through the Seismological Network of the Aristotle University of Thessaloniki (AUTH), as this is maintained by the faculty and staff of the Dept of Geophysics. “SEIS-MOTION” offers important information beyond magnitude and location of an earthquake by depicting the geographic distribution of the strongest ground shaking within a time interval which is much shorter than the one required for *in-situ* reconnaissance. From an emergency management perspective, although this information can contain significant uncertainty (as it is based on synthetic values in the near-field of the earthquake), it is preferable to make decisions based on some scientific results than on guesswork or even rumours in some cases.

Flow – chart of SEIS-MOTION

The codes of "SEIS-MOTION" have been mainly written in FORTRAN and C, while PERL and a variety of shell-scripts are also used. The codes have been compiled to be executed in Linux or UNIX environment (Roumelioti et al., 2008b). The analysis procedure as schematically shown in Figure 1 and includes the following steps:

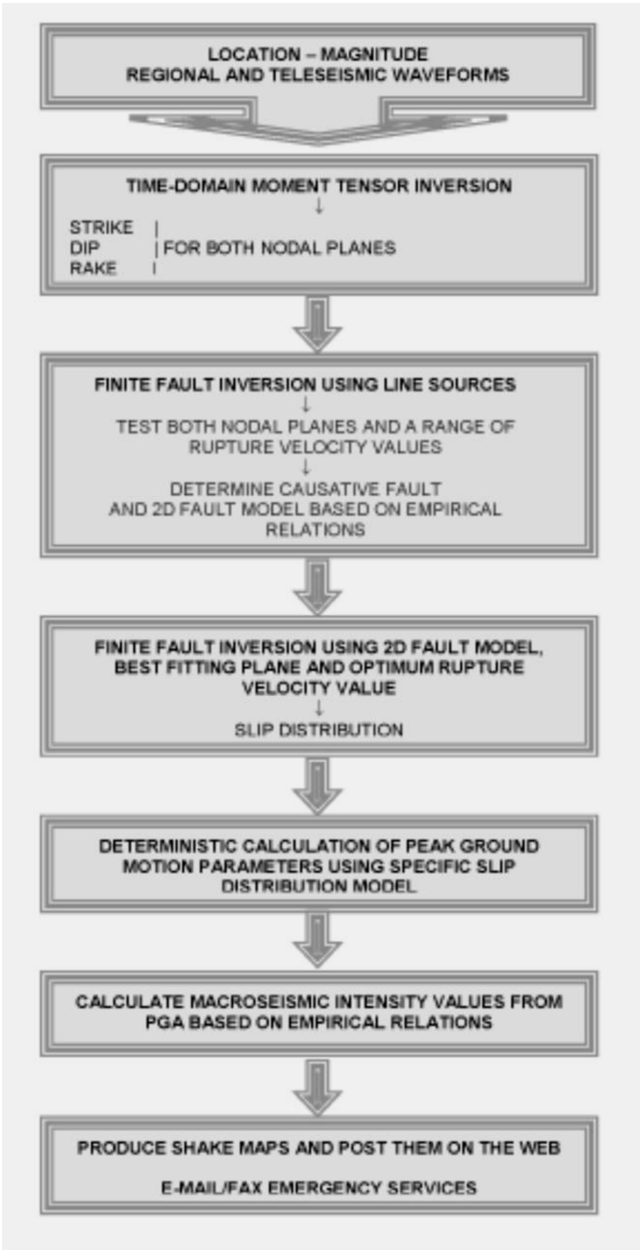

Figure 1: Flow chart of the procedures of the "SEIS-MOTION" system tool

1. Broadband waveforms are corrected for the instrument response and filtered in appropriate frequency windows, depending on the magnitude of the earthquake, which at a first stage is obtained from the automatic alerts.

2. The focal mechanism is determined using time-domain moment tensor inversion. The finite fault model is determined based on empirical relations between the earthquake magnitude and the dimensions of the ruptured area.
3. Broadband waveforms are inverted using a line or planar source representation to compute a slip distribution model (Kaverina et al., 2002).
4. The computed slip distribution model is used for the deterministic computation of peak ground acceleration (PGA), peak ground velocity (PGV) and peak spectral acceleration (PSA) distribution in the near field of the earthquake.
5. Site effect corrections are incorporated using categorization of the surface geology and empirical amplification factors (NEHRP, 1994, 2000; Margaris and Boore, 1998; Klimis et al., 1999).
6. Synthetic peak ground motion values are used to construct PGA, PGV and PSA shake maps. These model predictions can then be used to interpolate actual strong motion observations (when available).
7. Scaling relations between intensities and accelerations, applicable to Greece are used to calculate intensity maps, which are more understandable by people.

In the following we briefly discuss the methods used in the different steps of “SEIS-MOTION”.

Step 1: Time-domain moment tensor inversion

The computation procedure followed in AUTH (Roumelioti et al., 2008a) is based on the Time-Domain Moment Tensor inversion method (TDMT_INV) developed at the Berkeley Seismological Laboratory (Dreger, 2002, 2003). Full waveforms of the three recorded components of motion are low-pass filtered and inverted to derive the moment tensor. The tensor is then decomposed into a scalar seismic moment, double couple (*DC*) orientation components and a percentage of compensated linear vector dipole (*CLVD*). Synthetics for the three fundamental faults are combined with 1-D velocity models proposed for the Aegean area (e.g. Novotny et al., 2001; Karagianni et al., 2005) to form a library of Green’s Functions, computed with the code of Saikia (1994), which are used to match the observed waveforms. The filtering of the observed data and of the Green’s functions used depends on the magnitude of the event. Usually, data for earthquakes of Mw>5.0 are band-pass filtered in the range 0.02 to 0.05 Hz and data for smaller earthquakes are filtered in the range 0.05 to 0.08 or 0.05 to 0.10 Hz. We usually invert a time window of 120 seconds, although this may vary (from 60 to 180 sec) depending on the magnitude of the event and/or the signal/noise ratio, i.e. in cases when a second event follows closely in time we are forced to shorten the inverted time window of the studied event. The quality of a solution is determined by the goodness of the fit between synthetic (*s*) and observed (*d*) waveforms, which is quantified through the Variance Reduction, *VR*, a measure defined as:

$$VR = \left(1.0 - \frac{\int [d-s]^2 dt}{\int d^2 dt}\right) \times 100 \qquad (1)$$

For each solution, the inversion is run with the point source depth at various levels (incremental step of 2 km within the range 2 to 40 km for shallow (h≤40 km) events and step of 5 km for intermediate-depth events). The optimum solution is identified as the one for which both the variance reduction and percent of double couple are maximized.

Step 2: Slip Distribution Model

We use the methodology of Dreger and Kaverina (2000) and Kaverina et al. (2002) in which regional distance ground motions recorded on very broadband instruments are inverted for slip following the representation theorem for an elastic dislocation. We use a variety of simplifying assumptions including constant rupture velocity and dislocation rise time. We further apply slip positivity, seismic moment minimization and smoothing constraints to provide stability to the inversion. Validation of the methods in previous events (e.g. Benetatos et al., 2007) indicate that the methodology is capable of uniquely determining the causative fault plane of the earthquake, the dimensions of the slip patches (both along strike and down dip), the earthquake rupture velocity, and a reasonable characterization of the gross slip distribution, suggesting that the derived source parameters may be used to simulate near-source strong ground motions.

The simulation of near-source strong ground motions, described in the next step, solves the forward problem (above) using Green's functions appropriate for the near-source region and the regionally derived fault slip distribution.

Step 3: Deterministic Computation of PGA, PGV maps – Correction for site effects

The regionally derived fault slip maps are used to simulate the distribution of near-source strong ground motion, and to compare the model predictions with observations to calibrate the methodology. The basic method of ground motion simulation is one in which the fault slip is deterministically integrated using appropriate local Green's functions. The PGA, PGV and PSA maps satisfactorily outline the area of observed large ground motions (Roumelioti et al., 2008a, b). Then the predicted strong motion parameters are improved by applying site corrections to the synthetic ground motions. We utilize the methodology implemented by Wald and Allen (2007) who classified the site geology based on the topography gradient. Based on this approach Wald and Allen (2007) have produced global estimates of Vs_{30} – an indicator of the site effect. We use these values (and the NEHRP, 1994; Klimis et al., 1999) categorization to correct for the site effect. For reasons of comparison we also compute PGV maps using empirical relations applicable to Greece, and in this work we chose the relations proposed by Skarlatoudis et al. (2003, 2007).

Application Example – The earthquake of June 29, 2007 M5.4 near Paxoi Island

A. Time domain moment tensor inversion to obtain the focal mechanism

The June 29, 2007 M5.4 (18:09:11.8 GMT, 39.24^{o}N, 20.31^{o}E) event occurred in a region where focal mechanisms (Fig. 2 top) indicate low-angle thrust and reverse faulting along coastal Albania, western Greece, which also continues along the convex side of the Hellenic arc (SW of Zante up to NE of Rodos island). The faults are parallel to the coastline and dip with low angles towards the land. This type of faulting, in NW Greece and Albania, is attributed to the continental collision, between the Eurasian and the Adriatic plates. Thrusting and reverse faulting along the Hellenic arc is attributed to the northward motion of Africa and the subduction along the Hellenic trench.

Thus, for the event near Paxoi Island the focal mechanism MT solution we obtained is in accordance with the regional tectonics as previously described in brief. We used in the inversion the waveforms from eight stations (Fig. 2) and the returned best solution has high variance reduction and acceptable deviation from double – couple (CLVD=23%).

The event was strongly felt along the western coasts of Greece and Albania, causing no damage due to its very moderate magnitude. The strongest shock of June 29 was followed by many aftershocks until the end of July 2007, with magnitudes in the range 2.9 to 4.8.

Using the two nodal planes of Fig. 2 (lower panel) and following the previously discussed methods we inverted for different rupture velocities. The nodal plane which dips towards west resulted in the highest Variance Reduction compared to the other plane and was assumed to be the fault plane for the inversions that follow.

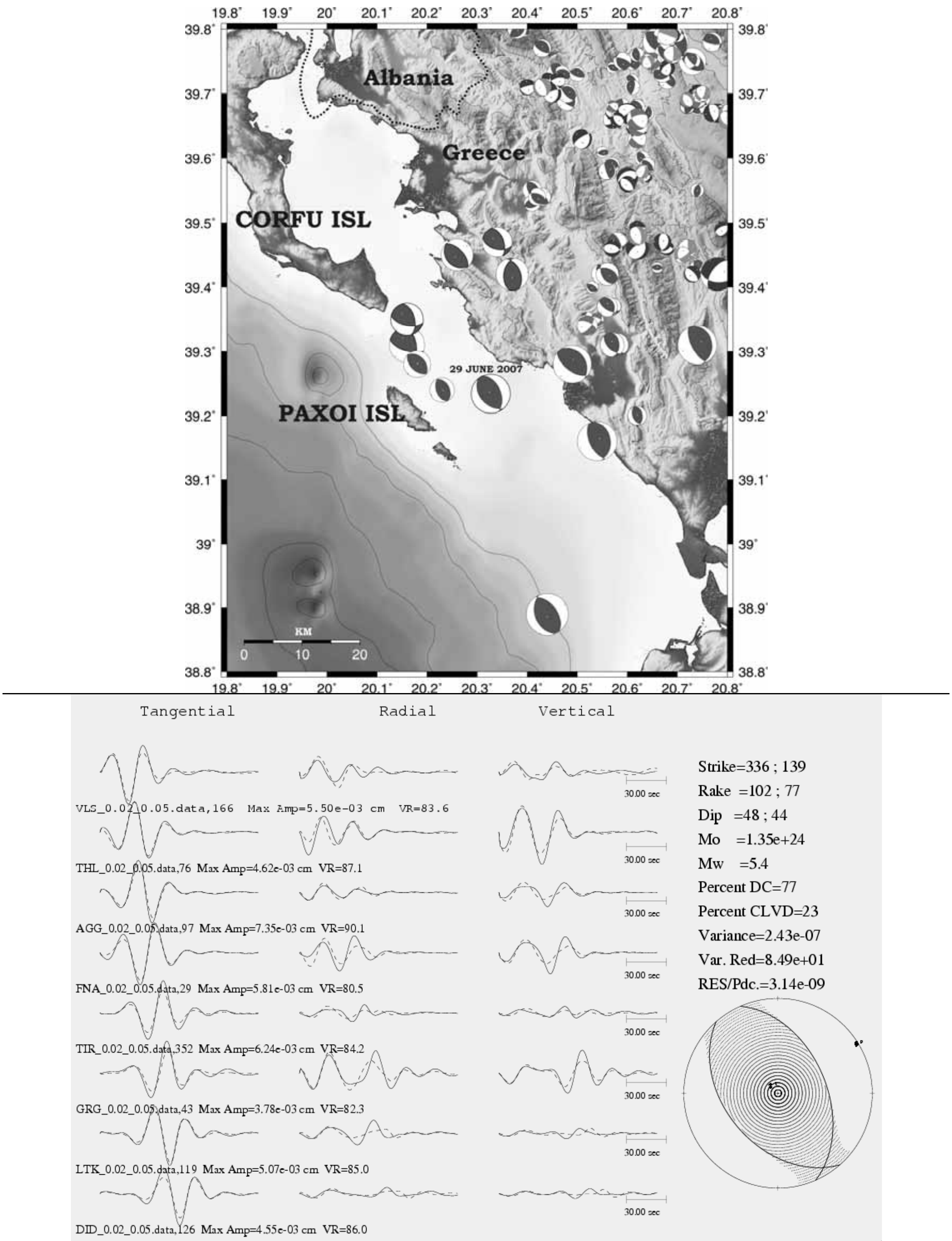

Figure 2.Top panel: The region of Corfu and Paxoi Island indicating reverse and low angle thrust faulting, parallel to the coastlines; Lower panel: the focal mechanism of the June 29, 2007 event whose mechanism we determined with the SEIS-MOTION codes (straight lines=observed waveforms; dashed lines=synthetic waveforms)

B. The slip model for the 29 June 2007 Paxoi Island event

The slip distribution model mapped onto the identified fault plane (Fig. 3) was determined using broad band waveforms and the inversion method of Kaverina et al. (2002). The obtained slip model reveals two slip patches, in which the strongest moment release occurred. One observation is the fact that the hypocentre (asterisk in Fig.3) and the regions of maximum strongest release are not collocated, as observed elsewhere in the world and in most of our slip models for recent events in Greece (e.g. Benetatos et al., 2007). The slip increases towards SSE and the maximum slip is of the order of 11 cm, acceptable for a M5.4 event from scaling relations. Actually, the region of the strongest slip is ~2.5x2.5 km^2 in the slip patch 2.

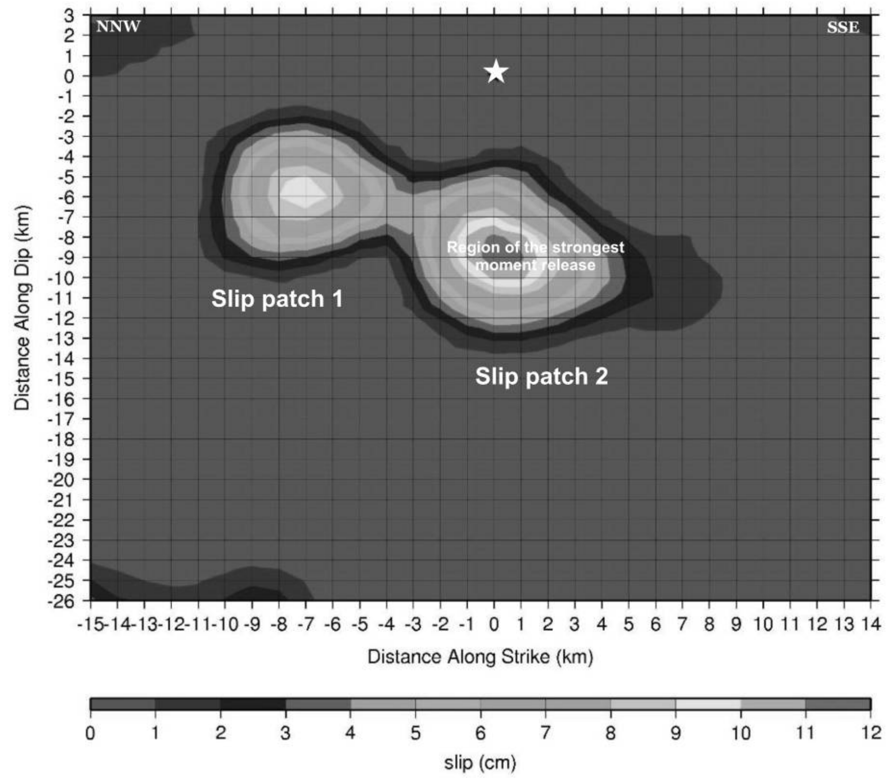

Figure 3. Slip distribution (slip in cm) for the June 29, 2007 event projected onto the fault plane that dips to the west. The slip has a characteristic two-lobe shape, observed elsewhere in Greece (Benetatos et al., 2007) with the SSE slip patch 2 to show the strongest moment release.

C. Shake Maps for the 29 June 2007 Paxoi Island event

The slip model (Fig.3) was used in order to obtain the maps showing the distribution of the maximum peak ground velocity (PGV, Fig. 4-left) and of the macroseismic intensity (Fig. 4-right). The figures – originally produced in colour scale where the gradually scaled colouring shows the results much better – indicate that the maximum strong ground motion values (~10 cm/sec for PGV) are observed to the NW of the epicentre.

Due to the moderate size of the event, the intensity values are of the order of VI to VII in the mezoseismal region, while close to the coastline the earthquake was felt with an intensity of the order of V.

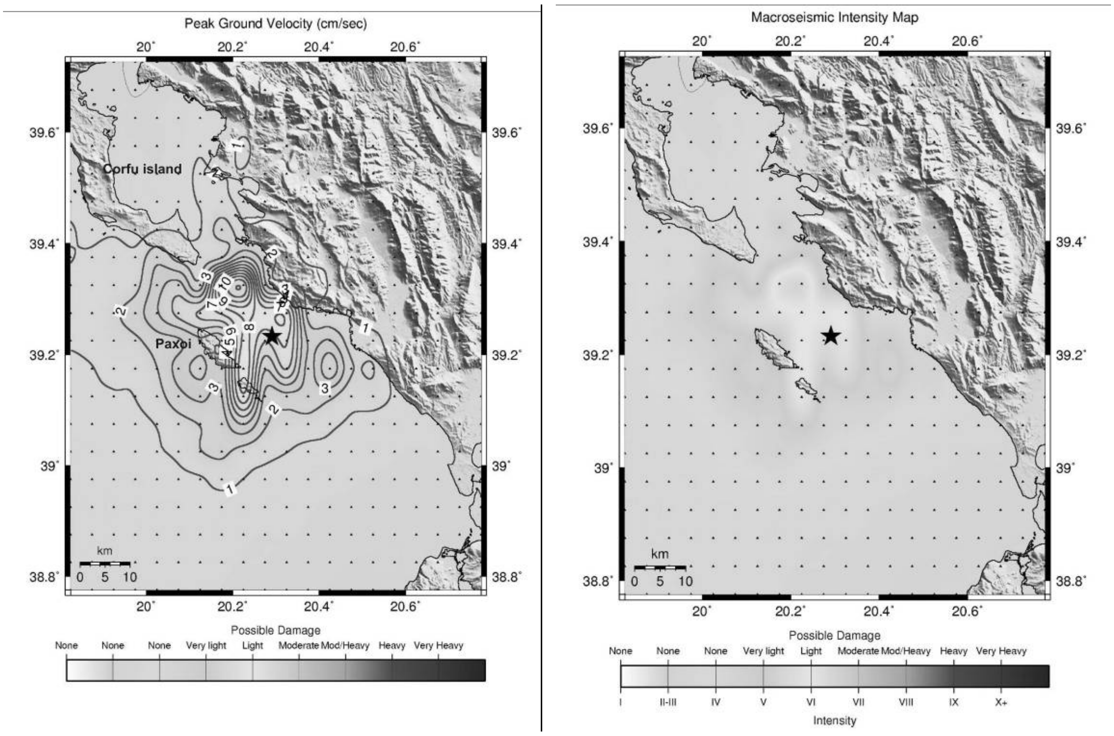

Figure 4. *Left:* Distribution of synthetic PGV's for the 29 June 2007 event, based on the slip model of Fig. 3. *Right:* Distribution of macroseismic intensities – which were calculated from the PGV values. The intensities are moderate due to the moderate size of the event.

The synthetic ground motions shown in Fig.4 were in accordance with the levels of shaking expected from the empirical relations of Skarlatoudis et al. (2003, 2007).

Results and Discussion

We have installed at the central Seismological Station of Thessaloniki a multi-staged algorithm to generate a shake map, following the current trend developed in many other parts of the world (e.g. USA (California), Japan). At first, line source or course planar inversions are performed to determine the rupture velocity, causative fault plane and slip dimension of an earthquake. The computed slip distribution model is used for the deterministic computation of near-source synthetic time series from which values of PGA, PGV and spectral acceleration (PSA) may be inferred. We normally compute PSA's at 0.2, 0.6 and 1.0 sec period, chosen to be representative of the built environment for the significant and densely populated urban regions in Greece. Site adjustments are applied to the rock ground motions using categorization of the surface geology and empirical amplification factors (NEHRP, 1994, 2000; Margaris and Boore, 1998; Klimis et al., 1999). Synthetic peak ground motion values are used to construct PGA, PGV and PSA shake maps. Then the predicted strong motion parameters are improved by applying site corrections to the synthetic ground motions. We utilize the methodology implemented by Wald and Allen (2007) who classified the site geology based on the topography gradient.

We plan to use these model predictions of synthetic peak ground motions in order to interpolate actual strong motion observations, from the strong motion networks in Greece. These networks, operated now by different institutes, are planned to be combined to form a Unified Hellenic Strong Motion Network, following the best practices from the Unified Hellenic Seismograph Network, which was recently implemented from national and European funding. With a relatively dense coverage, the map would be data driven with model predictions contributing only to the regions where there are gaps in instrumental coverage. At the final stage, scaling relations between intensities and accelerations, applicable to Greece, are used to calculate intensity maps, which are more understandable by people.

In Greece, a region of intense earthquake activity, the social demand for earthquake information soon after a damaging earthquake begins with estimates of the event origin time, the location of the epicentre and hypocentre, an estimate of the magnitude, and fairly recently of a seismic moment tensor solution, which provides a more robust estimate of earthquake size and of the radiation pattern. This information in Greece is now provided to the European Mediterranean Seismological Centre (EMSC) soon after an earthquake by the Geodynamic Institute of Athens, the Seismological Lab of the University of Patras and by the Seismological Lab of the University of Thessaloniki. While such basic information is essential in the rapid characterization of the likely damage due to strong ground motions from the earthquake it is a rather limited characterization. It is more essential to provide information regarding the regions where the strongest shaking occurred. Our recent research has taught us that in a large extended earthquake, it is very likely the area of strongest shaking to be away from the epicentre's location

In conclusion, we showed here the algorithms used to calculate model dependent shake maps in Greece. These results are posted on the WEB, and for the time being, even though the entire procedure can run automatically, we still manually revise our results. In the immediate future, we plan to refine our models and validate our results with strong recent events.

Acknowledgements

Thanks are due to Douglas Dreger from the Seismological Laboratory of the University of Berkeley, California for his support and cooperation. This research was financed by the General Secretariat of Research and Technology (GSRT), Ministry of Development of Greece. Most of the maps were produced using the GMT software (Wessel and Smith, 1998).

References

Benetatos Ch. & Kiratzi A.A (2004). Stochastic simulation of intermediate depths earthquakes: The cases of May 30, 1990 Vrancea region (Romania) and January 22, 2002 Karpathos (Greece) deep focus earthquakes, *Soil Dynamics and Earthquake Engineering, 24, 1, 1-9.*

Benetatos C., Dreger D. & Kiratzi A (2007). Complex and segmented rupture associated with the 14 August 2003 (Mw 6.2) Lefkada (Ionian Islands) earthquake, *Bulletin of the Seismological Society of America, Vol. 97, No. 1B, 35–51, doi: 10.1785/ 0120060123.*

Dreger D. S (2002). Time-Domain Moment Tensor INVerse Code (TDMT_INVC) *Version 1.1, Berkeley Seismological Laboratory, 18p.*

Dreger D. S (2003). TDMT_INV: Time Domain Seismic Moment Tensor INVersion, International Handbook of Earthquake and Engineering Seismology, *W. H. K. Lee, H. Kanamori, P. C. Jennings and C. Kisslinger (eds.), Vol. B, 1627p.*

Dreger D. S. & Kaverina A (2000), Seismic remote sensing for the earthquake source process and near-source strong shaking: a case study of the October 16, 1999 Hector Mine earthquake, *Geophys. Res. Lett. 27, 1941–1944.*

EAK (2003). Greek Seismic Code, Earthquake Planning & Protection Organization, Athens-Greece, ed., 72 pp and 7 appendices (in Greek).

Karagianni E.E., Papazachos C.B., Panagiotopoulos D.G., Suhadolc P., Vuan A. & Panza G.F (2005). Shear velocity structure in the Aegean area obtained by inversion of Rayleigh waves, *Geophys. J. Int., 160, 127-143.*

Kaverina A., Dreger D. & Price E (2002). The Combined Inversion of Seismic and Geodetic Data for the Source Process of the 16 October 1999 Mw 7.1 Hector Mine, California, Earthquake, *Bull. Seism. Soc. Am. 92, 1266-1280.*

Klimis N. S., Margaris B. N. & Koliopoulos P. K (1999). Site dependent amplification functions and response spectra in Greece, *Journal of Earthquake Engineering 3(2), 237–247.*

Margaris B. & Boore D (1998): Determination of $\Delta\sigma$ and κo from response spectra of large earthquakes in Greece, *Bulletin of the Seismological Society of America, 88, 170-182.*

NEHRP Recommended Provisions for the Development of Seismic Regulations for New Buildings (1994). Part 1: Provisions, Federal Emergency Management Agency (FEMA) 222A, Washington, D.C.

NEHRP Recommended Provisions for New Buildings and Other Structures (2000). (FEMA 368), Washington, D.C.

Novotný O., Zahradník J. & Tselentis G. A (2001). North-Western Turkey earthquakes and the crustal structure inferred from surface waves observed in Western Greece, *Bull. Seismol. Soc. Am., 91, 875-879.*

Roumelioti Z., Kiratzi A. & Theodoulidis N (2004). Stochastic Strong Ground Motion Simulation of the 7 September 1999 Athens (Greece) Earthquake, *"Bulletin of the Seismological Society of America", 94(3), 1036 – 1052.*

Roumelioti Z., Benetatos C., Kiratzi A. & Dreger D (2008a). Near-real time moment tensors for earthquakes in Greece based on seismological data of the Hellenic Unified Seismological Network, *3rd National Conference of Earthquake Engineering and Engineering Seismology, Athens, 5-7 November, 2008, paper ID:1789.*

Roumelioti Z., Kiratzi A. & D. Dreger (2008b). Near-Real Time Shake Maps for Earthquakes in Greece: pilot application, *3rd National Conference of Earthquake Engineering and Engineering Seismology, Athens, 5-7 November, 2008, paper ID: 2105.*

Saikia C. K (1994). Modified frequency-wavenumber algorithm for regional seismograms using Filon's quadrature; modeling of Lg waves in eastern North America, *Geophys. Journ. Int., 118, 142-158.*

Skarlatoudis A. A., Papazachos C. B., Margaris B. N., Theodulidis N., Papaioannou Ch., Kalogeras I., Scordilis E. M., & Karakostas V (2003). Empirical peak ground-motion predictive relations for shallow earthquakes in Greece, *Bull. Seism. Soc. Am. 93, pp. 2591-2603.*

Skarlatoudis A. A., Papazachos C. B., Margaris B. N., Theodulidis N., Papaioannou Ch., Kalogeras I., Scordilis E. M. & Karakostas V (2007). Erratum to "Empirical peak ground-motion predictive relations for shallow earthquakes in Greece, *Bull. Seism. Soc. Am. 97(6), 2219-2221, doi: 10.1785/0120070176.*

Theodulidis N., Roumelioti Z., Panou, A., Savvaidis A., Kiratzi A., Grigoriadis V., Dimitriou P. & Chatzigogos T (2006). Retrospective Prediction of Macroseismic Intensities Using Strong Ground Motion Simulation: The Case of the 1978 Thessaloniki (Greece) Earthquake (M6.5), *Bulletin of Earthquake Engineering 4 (2), 101-130p.*

Wald D. J., & Allen T. I (2007). Topographic slope as a proxy for seismic site conditions and amplification, *Bull. Seism. Soc. Am. 97(5), 1379-1395, doi: 10.1785/ 0120060267.*

Wessel P. & Smith W.H.F (1998). New improved version of the Generic Mapping Tools released", *EOS Trans. AGU 79, 579.*

Recent activity of the Concud fault (Jiloca graben, NE Spain) from structural, morphotectonic and paleoseismological analysis.

Lafuente P (1), Simón J L (2), Arlegui L E (3), Liesa C L (4)

Dpt. Ciencias de la Tierra, Universidad de Zaragoza. C/Pedro Cerbuna, 12 50009 Zaragoza (Spain). (1) palomalt@unizar.es; (2) jsimon@unizar.es; (3) arlegui@unizar.es; (4) carluis@unizar.es

Keywords: Concud fault, Intraplate tectonics, Paleoseismology, Geomorphic indices, Trench survey

Introduction

The Concud fault constitutes the northeastern boundary of the southern sector of the Jiloca semigraben (Iberian Chain, Spain; Fig. 1a). It is an almost pure normal fault trending WNW-ESE in average. The Concud fault has been active during most of the Late Pliocene and Quaternary times, under a still acting multidirectional extension stress field (σ_1 vertical, $\sigma_2 \approx \sigma_3$; Simón, 1989; Cortés, 1997; Arlegui *et al*., 2004) with σ_3 trending ENE. The aim of this research is to characterize recent to present-day activity of the Concud fault using structural, morphotectonic and paleoseismological methods, as well as its potentiality as seismic source.

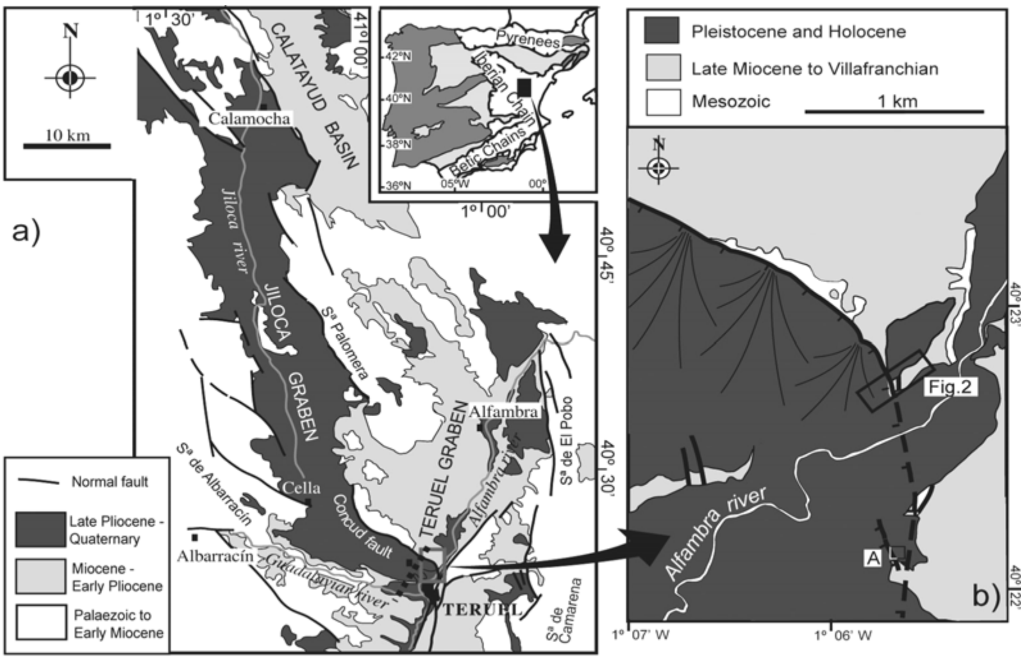

Figure 1. a) General location of the Concud fault. b) Southeastern sector of the fault. Rectangle corresponds to Fig. 2.

Materials and methods

Mesozoic units and the Neogene fill of the Teruel Graben (alluvial and lacustrine materials) appear in the footwall of the Concud fault. This Neogene fill is constituted by the Peral (Vallesian), Alfambra (Upper Vallesian-Turolian), Tortajada (Upper Turolian) and Escorihuela (Ruscinian, Lower Pliocene) formations. The top of the pretectonic series is dated by paleontological methods in 3.6 My, at the end of the Ruscinian (MN 15b biozone; Godoy *et al*., 1983; Opdyke *et al*., 1997; Alcalá *et al*., 2000). A syntectonic series constituted by the top of the Escorihuela Fm. (Lower Villafranchian), the “Rojo 3” unit (Villafranchian), the Gea glacis deposits (Upper Villafranchian) and Quaternary materials overlies unconformably the pretectonic units.

The Quaternary is represented by three terrace levels of the Alfambra and Guadalaviar rivers, and some alluvial fans developed from the fault escarpment. The Upper Terrace has an unknown age, but absolute dating of the other terrace levels is available. The Middle Terrace has yielded absolute ages in three different outcrops: (i) U/Th age in calcareous tuffa overlying the fluvial clastic sequence (169±10 and 116±4 ka; Arlegui *et al*., 2004); (ii) TL age in fine-grained clastic deposits on the opposite bank of the Alfambra river (138±10 ka; Santonja *et al*., 1994); (iii) OSL age in a sand bed of a slightly lower fluvial terrace that could represent a sub-level within the Middle Terrace (90.5±5.3 ka; Lafuente, 2007). The Lower Terrace has also OSL absolute dating, with ages of 15±9 ka (Gutiérrez *et al*., 2005), 14.9±1 ka and 15.6±1.3 ka (Lafuente, 2007). There are also some absolute ages in the alluvial fan deposits: 64±4 to 62±7 ka, in the middle part (Gutiérrez *et al*., 2005), and 32.1±2.4 ka on the top (Lafuente, 2007).

Structural, paleoseismological and morphotectonic methods have been used to analyze the activity and paleoseismic behaviour of the Concud fault. Applying different methods allows us to compare their results in order to assess how valid they are.

Using displacements measured in dated stratigraphical levels, it is possible to calculate the average slip rates in different periods. It is also important to discriminate if the fault is segmented or not, in order to measure appropriately its longitude and hence to estimate the paleoseismic parameters of the fault (moment magnitude, associated coseismic displacement, average recurrence period) using empirical correlations. We have applied correlations proposed by Wells & Coppersmith (1994) and its modifications by Stirling *et al*. (2002) and Pavlides & Caputo (2004).

Morphotectonic analysis in the mountain front permits us to check the level of fault activity. The Mountain-front sinuosity index (S_{mf}) and the Valley width/height ratio (V_f) (Bull & McFadden, 1977) have been used for this purpose. To calculate S_{mf}, the fault has been divided into two parts according with the different lithologies of the mountain front (Mesozoic limestones in the NW, and Miocene deposits in the SE). The V_f ratio has been calculated on 17 gullies that cross the fault scarp, 250 and 500 m upstream from the fault trace. These geomorphic indexes, together with other geomorphological evidences such as triangular facets, allow us to classify the fault activity according to the classifications proposed by McCalpin (1996) and Silva *et al.* (2003).

The occurrence of soft-sediment deformation structures interpreted as seismites is an evidence of large earthquakes in the past, and allows us to constrain the time when they were formed. Furthermore, the detailed paleoseismological study of a trench makes possible to compare the results obtained from empirical correlation with a real case, since it permits to distinguish individual earthquakes and to calculate real average recurrence periods and coseismic displacements.

Results and discussion

Structural study: fault length and slip rates

Detailed mapping of the fault trace characterizes the Concud fault as a continuous, 13.5 m-long structure (Fig. 1a). It shows an overall WNW-ESE strike, which veers towards N-S at its southern sector, where it articulates with the N-S striking Teruel fault (Fig. 1b). We have carefully analysed the possibility of seismic segmentation, paying attention to two hypothetic geometric barriers: (a) the change in direction at the southern sector: this change does not exceed 60º, so it should not represent a geometric barrier in the case of a normal fault (Wheeler, 1987); (b) a small transverse fault appearing at the middle part of the Concud fault: it does not seem to represent seismic segmentation because it does not interrupt the main fault trace (Wheeler, 1989). We therefore interpret that the Concud fault does not present seismic segmentation, and has a total length of about 13.5 km.

Slip rates have been calculated for the whole fault activity period, as well as for different time lapses. Knowing the age of the last pretectonic level (limestones of Escorihuela Fm., 3.6 Ma), and its total displacement (255 m), a slip rate of 0.07 mm/y for the whole activity period is calculated. The slip rate since Middle-Pleistocene times can be inferred in a specially interesting outcrop (*Los Baños*) where the Middle Terrace appears displaced 39 m. Considering the age of the tuffa at the top of the terrace (between 169±10 and 116±4 ka), we obtain a slip rate of 0.23 to 0.33 mm/y. In the same outcrop we can also estimate the intra-Late Pleistocene movement thanks to dating of the lower part (64±4 ka) and the upper part of the alluvial fan deposits (32±2 ka). Sedimentary thickness between these sampling points is 7 m, which corresponds to a temporal lapse of 32±6 ka. Assuming the sedimentation of this deposit kept pace with fault movement, the sedimentation rate must approach the slip rate, 0.23 mm/y.

Morphotectonic analysis

The Concud fault is expressed in the landscape by a fault-generated mountain front 60 to120 m high. The front scarp is dissected by transverse gullies that model some triangular facets. Those facets are better conserved on the central part of the fault, especially where they are modelled on Mesozoic limestones. From the fault scarp, a number of short alluvial fans are developed; some of them are downcut by the large streams that go across the fault, whereas other minor gullies incised on the footwall suddenly vanish as they enter the Quaternary deposits of the hanging-wall. That indicates that the rate of subsidence of the hanging-wall is lower than the downcutting rate of the large streams, but higher than that of minor gullies. The apexes of most alluvial fans are displaced by the fault, indicating a recent movement (Bull, 1977).

The Mountain front sinuosity index (S_{mf}) has been calculated separately for the NW and SE sectors of the fault, obtaining low and very similar values: S_{mf} = 1.16 and S_{mf} = 1.14, respectively. This suggets that the whole Concud fault has undergone homogeneous activity during recent times, and gives support to our interpretation of a non-segmented fault.

The gullies crossing the fault trace have a soft V-shaped cross section. Values of the Valley width/height ratio (V_f), measured 250 m upstream from the fault trace, range from 0.11 to 0.87; those measured 500 m upstream range from 0.098 to 0.40. As a general rule, in our study area, this index mainly depends on lithology. Higher values are obtained in the hard Jurassic rocks of the northwestern sector, whereas lower values correspond to recessive Neogene rocks of the southeastern one.

These geomorphic indexes, together with another available geomorphological information, can be entered into the classifications proposed by McCalpin (1996, adapted from Bull & McFadden, 1977) and Silva *et al*. (2002) in order to characterize the fault activity. According to McCalpin's classification, the Concud fault corresponds to classes 2 to 3 ('rapid' to 'slow'). According to Silva *et al*. (2002), the fault belongs to classes 1 ('active tectonics') to 2 ('moderate tectonics'). Both classifications assign characteristic slip rates to each class. In this way, our fault should have a slip rate ranging from 0.03 to 0.5 mm/y (McCalpin, 1996; Silva *et al*., 2002).) It can be observed how these values are in total consonance with slip rates obtained from structural methods.

Paleoseismological characterization of the Concud fault: *estimating magnitude, coseismic displacement and recurrence period*

Considering the fault length (at least 13.5 km), its non-segmented character, and using empirical correlations proposed by different authors (Wells & Coppersmith, 1994; Stirling *et al*., 2002; Pavlides & Caputo, 2004), an evaluation of the paleoseismic behaviour of the fault can be achieved. In this way, the moment magnitude of the maximum expected earthquake and the associated coseismic displacement have been estimated (Table 1).

	Wells & Coppersmith (1994)	Stirling *et al*. (2002)	Pavlides & Caputo (2004)
Moment magnitude (M_w)	6.37	6.78	6.47
Average coseismic displacement (m)	0.35	2.02	0.39

Table 1. Moment magnitude and average coseismic displacement from empirical correlations.

Considering these coseismic displacements together with the calculated slip rates, the average recurrence period for each temporary lapse is directly obtained (Table 2).

Period	Slip rate (mm/y)	Average recurrence period (ka)		
		Wells & Coppersmith (1994)	Stirling et al. (2002)	Pavlides & Caputo (2004)
Post-Ruscinian	0.07	5.0	28.9	5.6
Post-Middle Pleistocene	0.23-0.33	1.1-1.5	6.1-8.8	1.2-1.7
Intra-Late Pleistocene	0.23	1.5	8.8	1.7

Table 2. Average recurrence periods (ka) from slip rates and previously calculated coseismic displacements.

Seismites

Soft-sediment deformation structures have been observed in sand levels of the Middle Terrace in the neighbourhood of both the Concud and the Teruel faults. Some of them are sand dikes produced by sand fluidization, which intrude either conglomerates or silt overlying beds. They are interpreted as seismites because only the upper part of the sand is affected, whereas the lower, laminated part do not show any sign of deformation. On the other hand, the dykes have a planar shape and an attitude consistent with the coeval extensional stress field (either parallel or orthogonal to the Concud fault). We have also observed mushroom-like structures in sand, limited above and below by laminated sands. This arrangement, together with the fact that mushroom structures and a sand dyke coexist in the same sand bed, support the hypothesis of seismic liquefaction. The occurrence of these deformations implies seismic magnitude over 5-6,5, depending on the type of structure, but under 7,5 in any case, as the lack of liquefaction of gravels suggests. This magnitude range is consistent with the maximum potential earthquakes obtained from empirical correlations.

Paleoseisms in the geologic record: trench study

To better understand the paleoseismic behaviour of the Concud fault, a detailed study of the already quoted *Los Baños* outcrop has been made (see location in Fig. 1b). At this site, a 13 m deep trench of an ancient railway provides an excellent, nearly perpendicular exposure of the fault surface. Upper Miocene lacustrine carbonates on the footwall, folded in a gentle, hectometric-scale drag fold, are in contact with Pleistocene fluvial and alluvial materials on the hanging wall (Fig. 2). We have interpreted a minimum of six large single events (probably seven). The first one is represented by the rupture and displacement that affect fluvial deposits (A in Fig. 2) outcropping at the lower part of the trench. Although more than one paleoearthquake would be probably related to the deformation of those deposits, those could not clearly distinguished. This/those event/s took place soon before the deposit of a sedimentary bed (B; dated on 71.6±5 ka BP) that overlies the terrace. The second event is represented by a colluvial wedge of grain supported pebbles with sandy matrix (C). This colluvial wedge is cut and displaced almost 1 m as a consequence of the third event. From that moment on, the fault behaved on a different manner, and the next three (or four) paleoearthquakes involved both downthrow displacement and fissure opening. The fissures (D, E, F) are filled by falling debris from the footwall, and subsequently slope deposits overly the deformed materials. The last fissure fill (F) yielded an OSL age of 32.1±2 ka. Computing a minimum of five events between 71.6±5 and 32.1±2 ka BP, an average recurrence interval of about 8 ka is obtained. The sedimentary thickness accumulated during this time lapse (9-10 m) probably approaches the total coeval fault throw, which provides an estimate of around 2 m for the average coseismic displacement. However, the occurrence of either a number of events not recorded in the trench or creep episodes between seismic periods is not discarded.

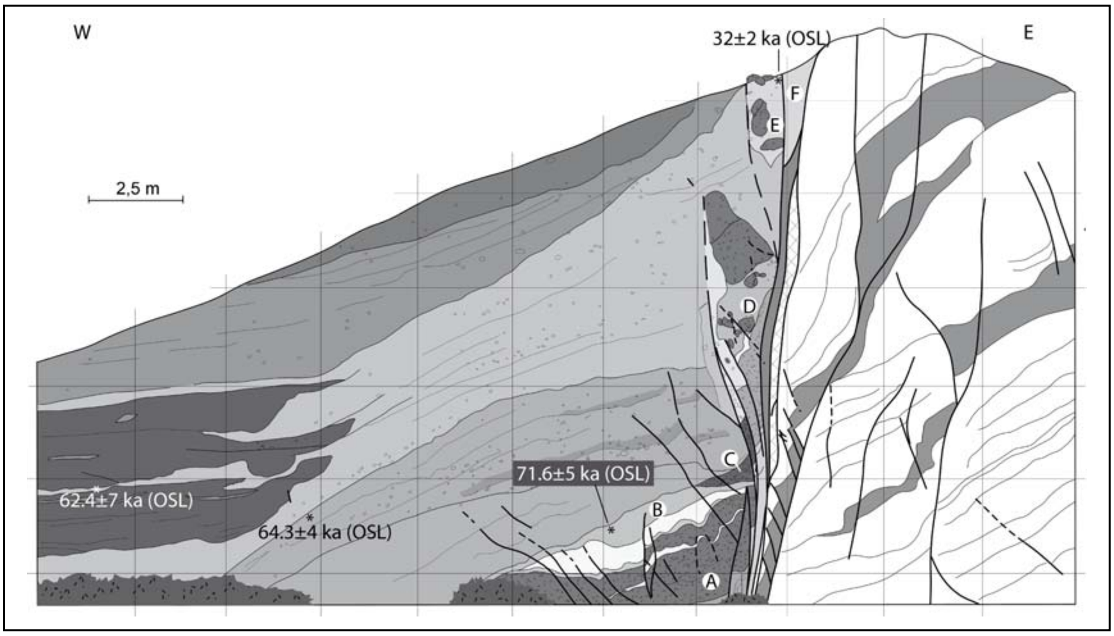

Figure 2. Log of *Los Baños* trench (absolute dating from Gutiérrez *et al*., 2005 and Lafuente, 2007). Letters A-F: sedimentary units as described above in the text.

The detailed study of a second exposure allows us to approach the time of the last movement recorded in the Concud fault. In this outcrop, located 2 km northeast of Teruel city (see Fig. 1b), the Lower Terrace is offset 2 m by a normal fault that probably is a secondary branch of the Concud fault. Two absolute OSL ages are available: one in the youngest pre- or sintectonic sediments (15.6±1.3 ka), and another one in the oldest deposits overlying the fault (14.9±1.0 ka). That permits to constrain the time of this (hypothetically) last coseismic displacement around 15 ka BP.

Discussion

The results obtained from each part of our study are consistent as a whole. The quantitative geomorphic analysis at the mountain front indicates a degree of fault activity that could be estimated, in terms of slip rate, in the range of 0.03 to 0.5 mm/y. These values are similar to those calculated from geologic data (0.07 to 0.33 mm/y).

With respect to paleoseismic parameters estimated from different correlation models (Wells & Coppersmith, 1994; Stirling *et al*., 2002; Pavlides & Caputo, 2004), the moment magnitudes are similar, whereas the coseismic displacements strongly differ from each other. Furthermore, since the average recurrence period is calculated using the estimated coseismic displacement, a wide range of values is also obtained for the former one.

Our field results agree with values inferred using the correlation of Stirling *et al*. (2002), which could be therefore considered as the most appropriate for our study area. On the contrary, they are not compatible with those estimated using the other correlation models. The average recurrence period (8 ka) and the average coseismic displacement (about 2 m) interpreted for the upper part of the syn-tectonic sequence at *Los Baños* trench closely approach the estimate from Stirling *et al*.'s correlation. On the other hand, we are not sure that the offset of 2 m observed in the Lower Terrace really represents the latest, single event in the Concud fault. But, if this were indeed the case, the coseismic displacement would also coincide with the estimate from that model, and the hypothetic quiescence period of about 15 ka would be within the 'predicted' range of 6.1 to 28.9 ka. This scenario should be confirmed or rejected by means of a specific paleoseismological analysis that we are carrying out in Late Pleistocene and Holocene deposits on the fault trace.

Conclusions

The Concud extensional fault has been active during Late Pliocene and Quaternary times, moving at slip rates between 0.07 and 0.33 mm/y and constituting an important seismic source. Geomorphic indexes calculated at the mountain front characterize a degree of fault activity in agreement with this slip rate.

The fault shows a non-segmented, 13.5 km long trace. Using the correlation model proposed by Stirling *et al*. (2002), which appears to be the most appropriate for our study area, this length provides an estimate of:
(1) the moment magnitude of its largest potential seisms, within the range of 6.4-6.8; this is corroborated by the occurrence of soft-sediment deformation structures (sand dykes and mushroom-like structures) in syntectonic (Middle and Upper Pleistocene) fluvial deposits near the fault;
(2) the average coseismic displacement, about 2.0 m; it coincides with the average offset attributed to a series of five seismic events identified in *Los Baños* trench, as well as with the latest, single offset observed in the Lower Terrace NE of Teruel (about 15 ka BP).

As a corollary, the most probable recurrence periods of paleoearthquakes associated to the Concud fault range from 6.1 to 28.9 ka. Again, our empirical results fit this estimate: the series of five seismic events at *Los Baños* trench occurred between 71.6 and 32.1 ka BP, showing an average recurrence period of about 8 ka. No movement younger than 15 ka BP is recorded at the studied trenches and natural outcrops. If this actually were the present-day quiescence period, it would be also compatible with that range of recurrence periods.

Acknowledgements

The research is financed by projects CGL2006-09670/BTE (Spanish Ministerio de Ciencia e Innovación and FEDER) and Consolider CGL2006-041 («Topo-Iberia»).

References

Alcalá, L., Alonso-Zarza, A.M., Álvarez Sierra, M.A., Azanza, B., Calvo, J.P., Cañaveras, J.C., van Dam, J.A., Garcés, M., Krijgsman, W., van der Meulen, A.J., Morales, J., Peláez-Campomanes, P., Pérez González, A., Sánchez Moral, S., Sancho, R. & Sanz Rubio, E. (2000). El registro sedimentario y faunístico de las cuencas de Calatayud-Daroca y Teruel. Evolución paleoambiental y paleoclimática durante el neógeno, *Revista de la Sociedad Geológica de España*, 13 (2), 323-343.

Arlegui, L.E., Simón, J.L., Lisle, R.J. & Orife, T. (2004). El campo de esfuerzos extensional plioceno-cuaternario en el entorno de la falla de Concud (fosa del Jiloca, Teruel), *Geotemas*, 6(3), 131-134.

Bull, W.B. (1977). The alluvial-fan environment, *Progress in Physical Geography*, 1, 222-270.

Bull, W.B. & McFadden, L.D. (1977). Tectonic geomorphology north and south of the Garlock fault, California. In: *Geomorphology in Arid Regions (D.O. Doehring, ed.), The Binghamton´ Symposia in Geomorphology: International Series*, nº 8, 115-138.

Cortés, A.L. & Simón J.L. (1997). Campo de esfuerzos recientes en la fosa de Alfambra-Teruel-Mira. In: *Avances en el conocimiento del Terciario Ibérico (J.P. Calvo and J. Morales, eds.), Actas III Congreso del Grupo Español del Terciario*, Cuenca. UCM-CSIC, 65-68.

Godoy, A., Ramírez, J.I., Olivé, A., Moissenet, E., Aznar, J.M., Aragonés, E., Aguilar, J.J., Alberdi, J.T., Giner, J., Gutiérrez Elorza, M., Portero, J.M. & Gabaldón, V. (1993). *Mapa Geológico de España 1:50.000, hoja nº567 (Teruel)*, IGME.

Gutiérrez, F., Gutiérrez, M. & Gracia, F.J. (2005). Karst, neotectonics and periglacial features in the Iberian Range, *Field Trip Guide-C5, Sixth International Conference on Geomorphology*, Zaragoza, 64 p.

Lafuente, P. (2007). *Actividad reciente de la falla de Concud (Teruel, Cordillera Ibérica): criterios estructurales, geomorfológicos y paleosismológicos*. Memoria Postgrado de Investigación, Facultad de Ciencias, Universidad de Zaragoza, 127 p.

McCalpin, J.P. (1996). *Paleoseismology*. Academic Press, 588p.

Opdyke, N., Mein, P., Lindsay, E., Pérez-González, A., Moissenet, E. & Norton, V.L. (1997). Continental deposits, magnetostratigraphy and vertebrate paleontology, late Neogene of Eastern Spain, *Palaeogeography, Palaeoclimatology, Palaeoecology*, 133, 129-148.

Pavlides, S. & Caputo, R. (2004). Magnitude versus faults´ surface parameters: quantitative relationships from the Aegean Region, *Tectonophysics*, 380, 159-188.

Santonja, M., Moissenet, E., Pérez-González, A., Villa, P., Sesé, C., Soto, E., Eisenmann, V., Mora, R. & Dupré, M. (1994). Cuesta de la Bajada: un yacimiento del Pleistoceno Medio en Aragón, *Arqueología Aragonesa (DGA)*, 21, 61-68.

Silva, P.G., Goy, J.L., Zazo, C. & Bardají, T. (2003). Fault-generated mountain fronts in southeast Spain: geomorphologic assessment of tectonic and seismic activity, *Geomorphology*, 50, 203-225.

Simón, J.L. (1989). Late Cenozoic stress field and fracturing in the Iberian Chain and Ebro Basin (Spain), *Journal of Structural Geology*, 11 (3), 285-294.

Stirling, M., Rhoades, D. & Berryman, K. (2002). Comparision of Earthquake Scaling Relations Derived from Data of the Instrumental and Preinstrumental Era, *Bulletin of the Seismological Society of America*, 92 (2), 812-830.

Wells, D.L. & Coppersmith, K.J. (1994). New Empirical Relationships among Magnitude, Rupture Length, Rupture Width, Rupture Area, and Surface Displacement, *Bulletin of the Seismological Society of America*, 84, 4, 974-1002.

Wheeler, R.L. (1987). Boundaries between segments of normal faults: Criteria for recognition and interpretation. In: *Proceedings of Conference XXXIX; Directions in Paleoseismology, U.S. Geol. Surv. Open File Rep*, 385-398.

Wheeler, R.L. (1989). Persistent segment boundaries on basin-range normal faults. In: *Fault Segmentation and Controls of Rupture Initiation and Termination (D.P. Schwartz and R.H. Sibson, eds.), U.S. Geol. Surv. Open File Rep*, 89-315, 432-444.

Evaluation of Seismic Loading of Structures in Undermined Area

Lednická M (1), Kaláb Z (2)

(1) VSB-Technical University of Ostrava, 17. listopadu 11, CZ-708 33 Ostrava – Poruba, Czech Republic, also Institute of Geonics of the ASCR, Ostrava, lednicka @ugn.cas.cz
(2) Institute of Geonics of the ASCR, Studentská 1768, CZ 708 00, Ostrava – Poruba, Czech Republic; also VSB-Technical University of Ostrava, kalab@ugn.cas.cz

Keywords: maps of clash of opinions, mining induced seismicity, seismic load

Introduction

"Maps of clash of opinions" for evaluation of seismic loading are so created that they provide basic information about character of seismic loading of structures for given places. Methodology of maps elaboration enables using GIS technology for creation of result maps of clash of opinions. The main principle is confrontation of three basic input themes – area of interest, seismic loading and constructional objects and structures. Selected thematic layers with their characteristic parameters will be related to each of these three input themes. These thematic layers will be prepared in the form of map layers. The regions of Ostrava and Karviná were selected for determination of methodology and for creation of the first maps of clash of opinions. The main reasons of our choice is the occurrence of mining induced seismicity in this area and existence of complicated geological conditions.

Basic Methodology

Maps elaboration methodology was published in Lednická et al., 2006. As it was mentioned above, the main principle is confrontation of three basic input themes – area of interest, seismic load and constructional objects and structures.

After basic methodology elaboration, it was necessary to solve the problem of great number of thematic layers entering the result map of clash of opinions. Consequently, detailed evaluation of three input themes for the Karviná region was elaborated.

Ways of clash determination

There are two different ways of clash determination. Each of thematic layers can enter the map of clash of opinion as an individual unit. Than the confrontation between for example only two parameters of thematic layers (regardless of other layers parameters) will be the resulting clash of opinion.

For example, if we are interested only in mining induced seismic load of masonry structures (one of the parameters of seismic load and one of the parameters of used structure material), thematic layer of mining induced seismic load (value of oscillation velocity) will be confronted with thematic layer of used material, regardless of economic and social significance of analysed objects.

But for the general seismic load assessment of interested area, it is necessary to take into account all of the thematic layers parameters. However, the basic problem of thematic layer parameters confrontation arises here. These parameters cannot be compared with each other directly.

Therefore, new terms for each input theme were established. These new terms include information about parameters of appropriate input theme and they are established for better orientation in the maps of clash of opinions and for the purpose of clash of opinions interpretation only.

New terms of input themes

New term “seismic characteristic of foundation conditions” is established for evaluation of selected parameters of area of interest and includes all useful information about area of interest (Lednická & Kaláb, 2008). New thematic layer “seismic characteristic of foundation conditions” displays this new parameter and will be created based on thematic layers of area of interest. Some of parameters of input thematic layers are varying in time (for example active landslides, depth to water-table, etc.) so the thematic layer “seismic characteristic of foundation conditions” will be elaborated for given time period.

Term “structure vulnerability level” is established for evaluation of parameters of input theme constructional objects and structures and includes all information about structural object (Lednická, 2006). This new parameter will be displayed in thematic layer “structure vulnerability”.

Only mining induced seismicity load was elaborated in detail for the present for input theme seismic load. New term “total value of velocity in given point for analyzed period” is established for evaluation of mining induced seismicity load in maps of clash of opinions (Kaláb, 2007; Lednická, 2007). The main aim is to take into account an amount of the mining induced seismic events, especially number of the intensive ones. This thematic layer will be also elaborated for given time period (as the thematic layer seismic characteristic of foundation conditions).

Seismic characteristic of foundation conditions

Thematic layer named “seismic characteristic of foundation conditions” will be created based on parameters of selected thematic layers of interested area. Following classes of foundation conditions were selected for the purpose of clash of opinions interpretation:

- optimal foundation conditions
- favourable foundation conditions
- unfavourable foundation conditions
- critical foundation conditions

Class of foundation conditions will be selected according to summary of values of specified significance. Different values of specified significance will be assigned to selected parameters of interested area thematic layers. Rate of this value describes how the parameter influences effect of seismic loading at the surface. The higher is weighted value of parameter, the worse influence has this parameter for seismic effects to constructions. Summary of values of specified significance for individual classes of foundation conditions for Karviná region are in tab. 1. For other area of interest, it is necessary to change weighted values according to the character of the area and according to set of thematic layers.

Table 1. Summary of values of specified significance for individual classes of foundation conditions (for Karviná region)

class of foundation conditions	summary of values of specified significance
optimal	0-2
favourable	3-4
unfavourable	5-6
critical	over 6

Values of specific significance are applied only to those thematic layers, whose parameters can be confronted mutually. These thematic layers of interested area are chosen for Karviná region:

- subsurface geology
- depth to water-table
- deformation of surface due mining
- landslides

Weighted values of parameters of these four thematic layers are in tab. 2 – 5, example of determination of thematic layer „seismic characteristic of foundation conditions“ is in fig. 1.

Table 2. Values of specified significance of thematic layer “subsurface geology” according to soil and rock classes (for the signs of soils and rocks see Czech technical standard CSN 73 1001)

<table>
<tr><th rowspan="6">ground-bearing capacity

(for specific boundary conditions)</th><th>$R_{dt} \leq$ 0.15 MPa</th><th>0.15 MPa < $R_{dt} \leq$ 0.6 Mpa</th><th>R_{dt} > 0.6 MPa</th></tr>
<tr><td>*fine-grained soils of soft consistency:*
CH CV CE CL CI CS CG
MH MV ME MI ML MS MG</td><td rowspan="2">rest of *fine-grained soils of stiff, solid and/or firm consistence*</td><td rowspan="2"></td></tr>
<tr><td>*fine-grained soils of stiff consistency:*
CH CV CE CL CI CS
MH MV ME MI ML</td></tr>
<tr><td>*sand soils:*
S-F *of medium compactness*
SC *of stiff and/or solid consistence*
(width of foundation b=0,5 m)</td><td>rest of *sand soils*</td><td></td></tr>
<tr><td>*gravel soils:*
GC *of stiff and/or solid consistence*
(width of foundation b=0,5 m)</td><td>rest of *gravel soils*</td><td></td></tr>
<tr><td>*rocks :*
class of rock R6 – *with very high and/or extremely high density of discontinuities*</td><td>*rocks:*
class R3 R4 R5 - *with very high and/or extremely high density of discontinuities*
class R4 R5 R6 - *with medium and/or high density of discontinuities*
class R5 R6 - *with very low and/or low density of discontinuities*</td><td>rest of *rocks*</td></tr>
<tr><td>value of specified significance</td><td>**2**</td><td>**1**</td><td>**0**</td></tr>
</table>

Table 3. Values of specified significance of thematic layer “depth to water-table”

depth to water-table under the surface	**< 2.5 m**	**from 2.5 to 4.5 m**	**> 4.5 m**
value of specified significance	**5**	**3**	**0**

Table 4. Values of specified significance of thematic layer “deformation of surface due mining” according the activity of deformations

deformation of surface due mining	active deformation for given time period	inactive deformation for given time period	area without deformation
		deformation expected in the future	no deformation expected in the future
value of specified significance	5	2	0

Table 5. Values of specified significance of thematic layer “landslides” according the activity of landslides in given time period

landslides	active landslides	potential landslides	stabilized landslides
		potential landslides due mining	buried landslides
weighted valuation	5	2	0

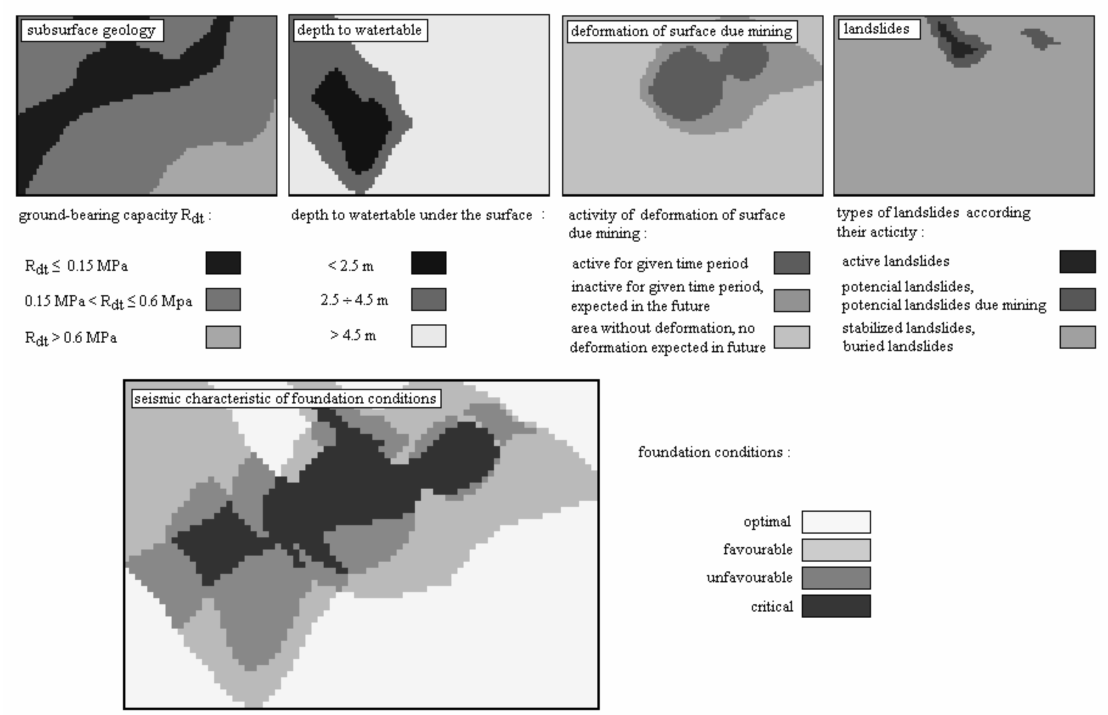

Figure 1. Example of determination of „seismic characteristic of foundation conditions“ based on four individual thematic layers of input area.

Structure vulnerability level

“Structure vulnerability level” (α, β, γ, δ, ε) is established according to class of resistance and economic and social significance (Czech technical standards CSN 730040 and CSN 730031). As we can see in the tab. 6, “structure vulnerability level” do not includes all combinations of resistance class and economic and social significance. For the purpose of maps of clashes of

opinions, only the structures with the most rigorous criteria of seismic load evaluation are important.
"Structure vulnerability level" is characterized directly by the parameters of resistance class and economic and social significance. Specific interpretation (according to the CSN 73 0040) is required for the parameters of other constructional thematic layers (age of buildings, cultural monuments, technology construction, used materials). This specific interpretation enables classification of objects to the resistance class. "Structure vulnerability level" determination results from the input data assessment and interpreter's discretion.
Possible interpretation procedure for individual thematic layers is described below.

Age of buildings and structures
For the "structure vulnerability level" determination, the age of building (thematic layer parameter) is important in case of very old structures only. Objects with resistance class A according to the CSN 73 0040 are mean in this case. If the object cannot be classed, surely as the resistance class A, next classification results from another thematic layers parameters assessment.

Cultural monuments
This thematic layer represents special group of objects with specific parameter. It is generally A resistance class subset.

Technology construction
Resistance class can be determined based on (together with used material knowledge):
monolithic structure – resistance class E
framed structure – resistance class D
half-timbered structure - resistance class D
building up to three-storeys– resistance class B
panel prefabricated structures – resistance class C

Used materials
Resistance class can be determined based on used material (together with technology construction knowledge):
stone - resistance class A
masonry - resistance class A, B, C
concrete - resistance class C, D
steel - resistance class D, E
steel concrete - E

If we have a choice of several resistance classes, determination depends mainly on interpreter's discretion. Than, all input data is necessary to take into account. Example of "structure vulnerability level" determination based on individual thematic layers is in fig. 2.

Table 6. Structure vulnerability level depending on class of resistance (CSN 73 0040) and class of significance (CSN 73 0031)

Structure vulnerability level				
class of resistance	class of significance U	I	II	III
A	α	β	γ	δ
B	β	γ	δ	–
C	γ	δ	–	–
D	δ	ε	–	–
E	δ	–	–	–
F	ε	–	–	–

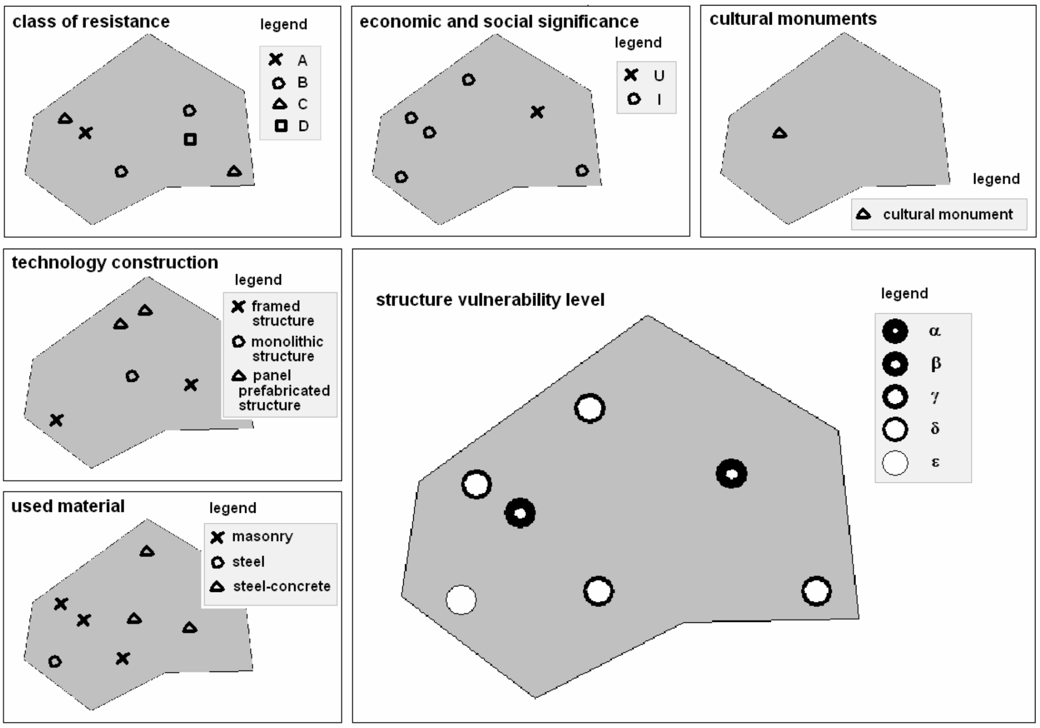

Figure 2. Example of "structure vulnerability level" determination based on individual thematic layers

Total value of velocity in given point for analyzed period

The main aim is to take into account an amount of the mining induced seismic events, especially number of the intensive ones. High number of seismic events is typical also for mining induced seismicity in the Karviná region; about 40 thousand or more seismic events are recorded annually – according to the sensitiveness of seismic apparatus (Kaláb & Knejzlík, 2002). Resultant value of the calculation is so called "total value of velocity in given point for analyzed period" x_T (and/or components u_T, v_T, w_T) where x_T is result for input data set containing absolute values of space component; u_T , v_T , w_T are results for input data set containing individual components.

Input data set includes only those seismic events that exceed the value of 0.5 mm.s^{-1} at least on one measured component. Analysed period T is 12 months.

Basic equations are as follows:

$$x_T = x_{max} * C_N * C_M$$
$$u_T = u_{max} * C_N * C_M$$
$$v_T = v_{max} * C_N * C_M$$
$$w_T = w_{max} * C_N * C_M$$

x_{max} … maximum calculated absolute value of space component in given period T
u_{max} , v_{max} , w_{max} … maximum component value in given period T
C_N … coefficient that takes into account the number of recorded seismic events in given period T
C_M … coefficient that takes into account the number of recorded intensive seismic events in given period T

The coefficients are calculated using equations:

$$C_N = \frac{1}{11} \operatorname{arctg} \left(\frac{N - 200}{100} \right) + 1.1005$$

$C_M = C_{M0} * C_{M1} * C_{M2}$

N … total number of recorded seismic events with value of minimally one component higher than 0.5 mm.s^{-1} in given period T
C_{M0} … partial coefficient that takes into account number of recorded seismic events in given period T with maximum value in range 3 – 6 mm.s^{-1}
C_{M1} … partial coefficient that takes into account number of recorded seismic events in given period T with maximum value in range 6 – 10 mm.s^{-1}
C_{M2} … partial coefficient that takes into account number of recorded seismic events in given period T with maximum value above 10 mm.s^{-1}

The partial coefficients are defined using equations:

$C_{M0} = 0.0204 * \ln(N_0) + 1.0126$
$C_{M1} = 0.0254 * \ln(N_1) + 1.0361$
$C_{M2} = 0.039 * \ln(N_2) + 1.071$

Numbers in individual data sub-sets are defined:

N_0 … number of recorded seismic events in given period T with maximum value in range 3 – 6 mm.s^{-1}
N_1 … number of recorded seismic events in given period T with maximum value in range 6 – 10 mm.s^{-1}
N_2 … number of recorded seismic events in given period T with maximum value above 10 mm.s^{-1}

Table 7. Summary of input data sets (station STO 1), symbols in text

STO 1						
year		2002	2003	2004	2005	2006
N		***17***	***21***	***52***	***88***	***129***
x_{max}	**mm.s^{-1}**	**7.60**	**4.97**	**4.47**	**9.37**	**8.47**
u_{max}		**6.12**	**1.81**	**4.09**	**7.50**	**7.61**
v_{max}		**4.29**	**4.68**	**3.12**	**3.52**	**4.39**
w_{max}		**1.39**	**0.825**	**1.37**	**4.37**	**3.02**

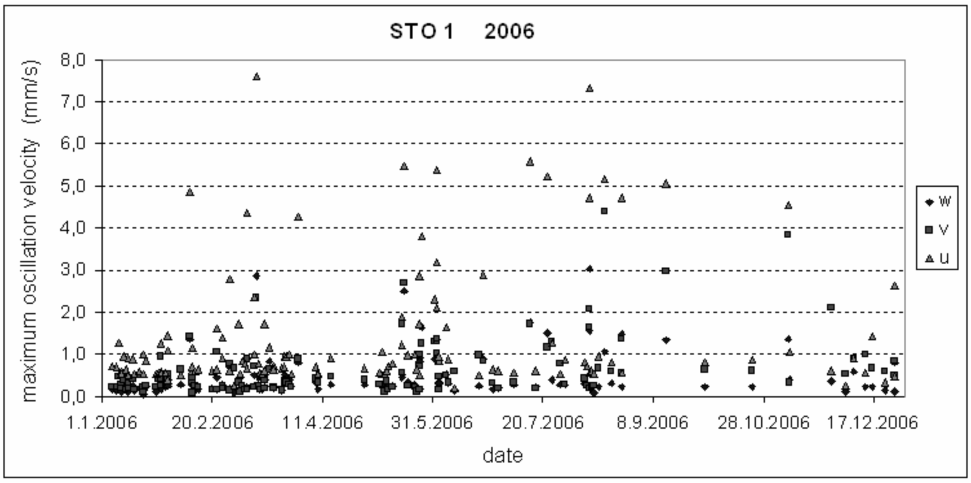

Figure 3. Maximum oscillation velocity values measured at station STO 1 in 2006

Table 8. Total values of velocity in given point for analyzed period

		2002	2003	2004	2005	2006
w_{max}	$mm.s^{-1}$	***1.39***	***0.83***	***1.37***	***4.37***	***3.02***
w_T		1.39	0.83	1.39	4.53	3.20
C_N*C_M		**1.003**	**1.004**	**1.012**	**1.037**	**1.058**
v_{max}	$mm.s^{-1}$	***4.29***	***4.68***	***3.12***	***3.52***	***4.39***
v_T		4.36	4.82	3.20	3.65	4.71
C_N*C_M		**1.016**	**1.031**	**1.024**	**1.037**	**1.072**
u_{max}	$mm.s^{-1}$	***6.12***	***1.81***	***4.09***	***7.5***	***7.61***
u_T		6.36	1.82	4.31	8.31	8.93
C_N*C_M		**1.039**	**1.004**	**1.053**	**1.108**	**1.174**
x_{max}	$mm.s^{-1}$	***7.60***	***4.97***	***4.47***	***9.37***	***8.47***
x_T		7.90	5.13	4.73	10.52	10.19
C_N*C_M		**1.039**	**1.031**	**1.058**	**1.123**	**1.203**

Tab. 7 contains summary of input data for using presented methodology – numbers of recorded seismic events from station STO1 for selected periods (2002–2006) and values of maximum velocity amplitudes. Example of input data set from the year 2006 is presented at fig. 3. Total values of velocity in given point (STO1) for analyzed periods (2002–2006) are presented in tab. 8. Values of C_N*C_M present how often the total values of velocity are higher than the maximum measured values.

Results and Discussion

Presented methodology enables evaluation of mining seismicity loading of structures in undermined area by using of “maps of clash of opinions”. For general seismic load assessment of interested area, three new thematic layers were established – seismic characteristic of foundation, structure vulnerability level and total value of velocity. Maps of clash of opinions enable evaluation of seismic loading of existing structures, or provide information about seismic loading and geological conditions for designed constructions.

Acknowledgement
This paper has been achieved with the financial support of the Ministry of Education, Youth and Sport of the Czech Republic, Project no. 1M6840770001.

References

Kaláb Z. (2007). Evaluation of Load on Structures Caused by Mining Seismicity for Maps of Clash of Opinions – Methodology. *Zeszyty Naukowe Politechniki Śląskiej, Ser. Górnictwo z.276, Nr. 1751, Gliwice, 33-42.*

Kaláb Z. & Knejzlík J. (2002). Systematic Measurement and Preliminary Evaluation of Seismic Vibrations Provoked by Mining Induced Seismicity in Karviná Area. *Publs. Inst. Geophys. Pol. Acad. Sc., Vol. M-24(340), s. 95-103, 2002.*

Lednická M. (2006). Classification of buildings and structures for elaboration of maps of clash of opinions. *Ph.D. Workshop 2006 - Proceedings, Ostrava, 31-34.*

Lednická M. (2007). Evaluation of Load on Structures Caused by Mining Seismicity for Maps of Clash of Opinions – First Results. *Zeszyty Naukowe Politechniki Śląskiej, Ser. Górnictwo z.276, Nr. 1751, Gliwice, 101-110.*

Lednická M. & Kaláb Z. (2008). Maps of Clash of Opinions - Classification of Geological Conditions in Karviná Region. *Zeszyty Naukowe Politechniki Śląskiej, Ser. Górnictwo z. 283, Nr. 1781, Gliwice, 139-147.*

Lednická M., Luňáčková B., Kaláb Z., Hrubešová E. & Kořínek R. (2006). Contribution to Evaluation of Technical Seismicity Effect on Buildings - Case Study. *Earth Sciences Research Journal (formerly Geofisica Colombiana), Vol. 10, No. 1, 7-14.*

The Relative Importance of Site Effects in Seismic Hazard Analysis

Leonard G (1), Steinberg D M (2), Hashavia E (3)

(1) Licensing Division, Israel Atomic Energy Commission, Israel
(2) Department of Statistics and Operations Research, Tel-Aviv University, Israel
(3) Safety Division, Soreq NRC, Israel

Keywords: Building codes; Ground acceleration; Preparedness; Seismic hazard; Shear-wave velocity.

Introduction

Large earthquakes have drawn attention to the expected large casualties from the earthquake threat. Losses in life and extensive damage are a function of strong vibratory ground motion at specific sites, inadequate building codes at the time when buildings were constructed, and inappropriate construction of buildings.

There are two main areas in which decision makers can act to reduce the damage and injuries from major earthquakes. The first area is in the establishment and enforcement of appropriate building codes. Improving construction and reinforcing sensitive structures should be an important effort, however such an endeavor could take many years. Thus, from a short-term standpoint, a major focus should be placed on the second area, the preparedness of rescue and relief operations.

Much of the preparedness effort is based around scenarios for seismic damage. One of the difficult problems that face decision makers in constructing realistic scenarios is the inability to accurately predict the extent of ground shaking and resultant damage from a major earthquake. Important sources of uncertainty include the source-to-site distance, the magnitude and the site response. The objective in this work is to provide some simple methods that can be used to evaluate the tradeoffs among these input factors and thus to help guide research efforts that can eliminate some of the uncertainty. In particular, the article examines the importance of site effects relative to other factors in damage scenarios. The methods that are developed will be useful in cost-benefit analyses of research efforts.

Materials and Methods

Site effects are represented using shear velocity in the upper 30 meters beneath the site, as in Boore et al. (1997). Other researchers have also found that the shear wave velocity is an effective way to represent site effects (Abrahamson and Silva 1997, Wills et al., 2000, Fujimoto and Midorikawa 2002, and Gomberg et al. 2003). Boore et al. (1997) estimated ground motion prediction equations of the form:

$$ln(Acc)=b_0+b_1 ln(d)+b_2(M-6)+b_3(M-6)^2+b_4 ln(V_S/V_{ref})+\varepsilon \qquad (1)$$

Here Acc is acceleration, d is the hypocentral distance to the site, M is the magnitude, V_S is the shear wave velocity, V_{ref} is a reference velocity and ε is a random error term. Boore et al.

(1997) presented a table of frequency-specific coefficients for this equation. The dependence of acceleration on shear velocity is independent of distance and magnitude in the equation.

The effects of the input parameters on both the median acceleration and on the distribution of acceleration are considered, incorporating also the random error term. For the effects on median acceleration, magnitudes ranging from 5.5 to 7.5 were studied, a range that most hazard analysts would certainly regard as generating quite distinct hazard scenarios. Analyses are presented primarily for 3 Hz, which has the highest predicted accelerations in the Boore et al. (1997) equations. Similar results were obtained for other frequencies.

Median acceleration is analyzed using the coefficients in the Boore et al. equation to convert changes in magnitude and distance to equivalent changes in shear velocity. A change of ΔM magnitude units, from *M* to $M + \Delta M$, corresponds to a change of $b_2\Delta M + b_3\Delta M^2 + 2b_3\Delta M(M-6)$ in the logarithm of the acceleration. If the shear velocity is multiplied by a factor of F_V, the resulting change in the logarithm of the acceleration is $b_4\, ln(F_V)$. Thus the change in magnitude from *M* to $M + \Delta M$ is equivalent to a change in shear velocity by a factor of

$$F_V = exp\left(\left[b_2\Delta M + b_3\Delta M^2 + 2b_3\Delta M(M-6)\right]/\, b_4\right). \qquad (2)$$

Similarly, this change in shear velocity is equivalent to multiplying the source-to-site distance by the factor

$$F_d = F_V\, exp(b_4 / b_1)\,. \qquad (3)$$

In analyzing the complete distribution of acceleration, the magnitude range was limited to 6.0 to 7.5 and the source-to-site distance to 25 km. The results of these analyses are described by graphs that depict both the median acceleration and the scatter about the median corresponding to the error term in equation (1).

Results

The median acceleration predicted by the Boore et al. ground motion equation shows a clear dependence on shear wave velocity. For example, a five-fold difference in shear velocity (say 200 m/s vs. 1000 m/s) corresponds to a two-fold difference in acceleration. For velocities above 1000 m/sec, there is little effect of shear wave velocity on the median acceleration.

Figure 1 shows the median acceleration from equation (1) at 25 km and 3Hz, as a function of magnitude and shear wave velocity. The dependence of median acceleration on Vs is strongest at lower frequencies and is less pronounced at higher frequencies. The equation predicts higher accelerations for higher magnitudes. However, there is a “saturation” effect for high magnitudes at high frequencies; at 10 Hz, for example, there is only a small difference in the predicted accelerations between a magnitude 7.0 and a magnitude 7.5 earthquake.

Table 1 expresses changes in shear wave velocity and in distance that generate the same changes in predicted acceleration at 3 Hz as changes of ½ (Table 1a) or 1 (Table 1b) magnitude unit, based on the Boore et al. ground motion prediction equation. As the equation is quadratic in magnitude, the base magnitude is also needed to compute these equivalent changes in shear wave velocity and distance. The tables show, for several different base magnitudes, the difference in log acceleration from a change of ½ or 1 magnitude unit, the amount by which the predicted acceleration is multiplied, and corresponding change factors for shear velocity and distance. Acceleration is an increasing function of magnitude, but a decreasing function of shear velocity and distance. Thus the equivalence factors F_V and F_d are both less than 1 here. The tables show the inverse of these factors, i.e. the factor by which one would need to *decrease* the shear velocity or distance, respectively, to have the same effect on predicted acceleration achieved by the increase in magnitude.

Table 1. Changes in shear wave velocity and in distance that generate the same changes in predicted acceleration at 3 Hz as changes of ½ (Table 1a) or 1 (Table 1b) magnitude unit, based on the Boore et al. ground motion prediction equation.

(a)

Magnitude change	∆ln(Acc)	Acc Multiplication Factor	$1/F_V$	$1/F_d$
5.5 – 6	0.43	1.54	2.69	1.63
6 – 6.5	0.36	1.43	2.28	1.51
6.5 - 7	0.29	1.34	1.94	1.39
7 – 7.5	0.22	1.24	1.64	1.28

(b)

Magnitude change	∆ln(Acc)	Acc Multiplication Factor	$1/F_V$	$1/F_d$
5.5 – 6.5	0.79	2.21	6.13	2.46
6 – 7	0.65	1.92	4.42	2.09
6.5 – 7.5	0.51	1.66	3.19	1.78

Table 1b shows that, for a fixed distance and shear velocity, a change in magnitude from 6 to 7 increases the acceleration by a factor of ~ 2. The same effect is achieved by decreasing the shear wave velocity by a factor of 4.4. Thus, with the Boore et al. equation, a magnitude 7 event with V_S = 900 m/s has almost the same predicted acceleration as a magnitude 6 event with V_S = 900/4.4 ≈ 200 m/s. The same effect on predicted acceleration is also achieved by decreasing the distance by a factor of 2.1. Thus a magnitude 7 event has almost the same predicted acceleration 40 km from the hypocenter as a magnitude 6 event at a distance of 40/2.1 ≈ 20 km from the hypocenter.

The error term in the ground motion prediction equation describes the uncertainty in predicting ground acceleration even when the magnitude, distance and shear wave velocity are known. Figure 2 summarizes this uncertainty for ground motion at 3 Hz, 25 km from the epicenter. Figure 2 displays the probability density functions of ground acceleration at 3 Hz for four magnitudes (6.0, 6.5, 7.0 and 7.5) and three shear wave velocities (200, 400 and 1000 m/s). The acceleration distributions are represented by line segments that extend from the 5th to the 95th percentile of the distribution, a point at the median acceleration and hatch lines at the 16th and 84th percentiles. The 84th percentile is one standard deviation above the median when the accelerations are converted to a log scale and is sometimes used in deterministic seismic hazard analysis as a “conservative” alternative to the median acceleration.

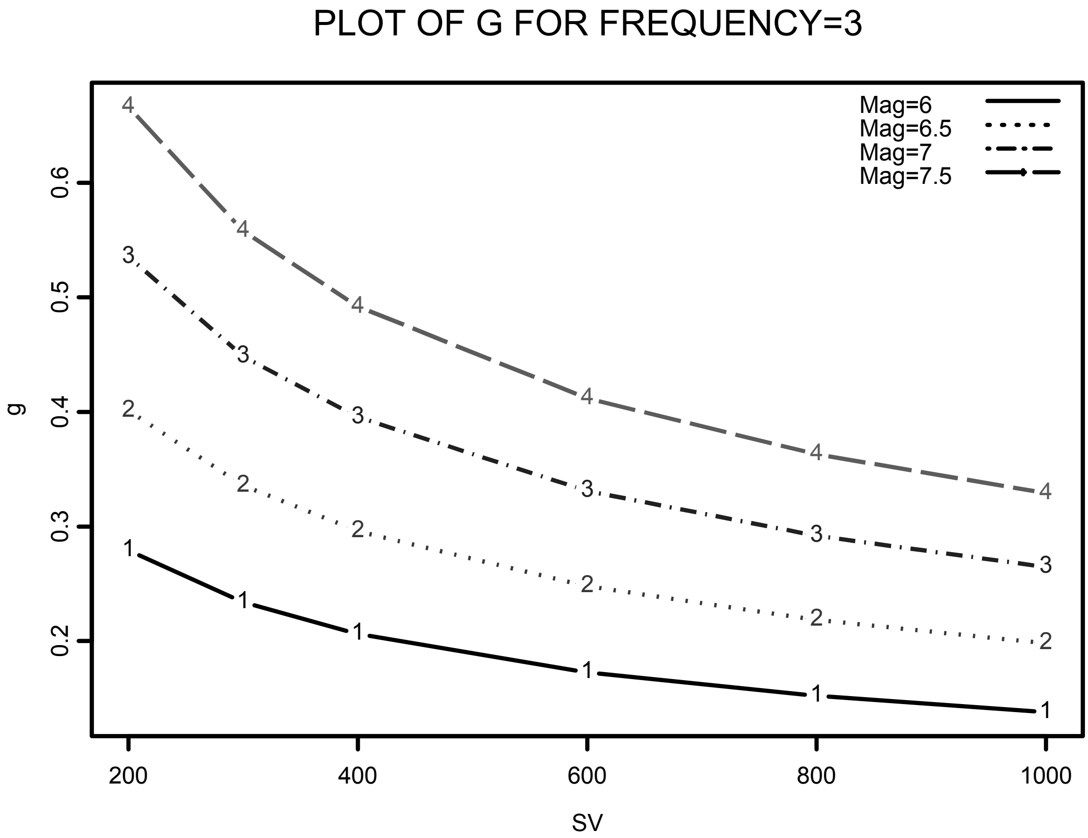

Figure 1. Plot of predicted median acceleration at 25 km and 3 Hz (from the Boore et al equation) as a function of shear wave velocity. The four curves correspond to earthquakes of magnitudes 6.0, 6.5, 7.0 and 7.5.

Figure 2 indicates that the effect of Vs on acceleration may have important practical implications. As an example, consider a scenario for ground motion at a site located 25 km from the epicenter of a magnitude 6.5 earthquake. Figure 2 shows that the probability of exceeding 0.4 g at 3 Hz is about ½ if Vs is 200 m/s, but is only about 1/10 if Vs is 1000 m/s. The change in median acceleration (on the log scale) when comparing these two shear velocities is about 1.4 standard deviations. Thus the effect of shear velocity on predicted acceleration is also large in comparison to the remaining uncertainty in the ground motion prediction.

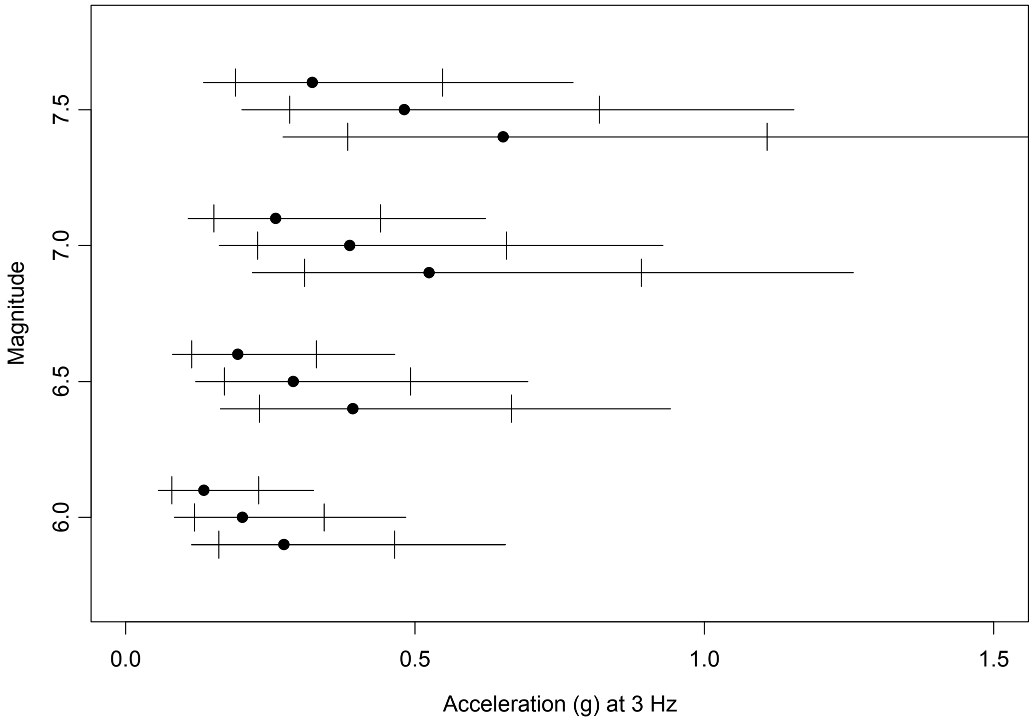

Figure 2. Plot of the uncertainty in predicting acceleration at 3 Hz 25 km from the epicenter (from the Boore et al equation). The 12 lines are grouped in 4 sets, corresponding to earthquakes of magnitudes 6.0, 6.5, 7.0 and 7.5. The top line in each set corresponds to a shear wave velocity of 1000 m/sec, the middle line to a shear wave velocity of 400 m/sec and the bottom line to a shear wave velocity of 200 m/sec. The lines extend from the 5th to the 95th percentile of the acceleration distribution, the point is located at the median acceleration and the hatch lines at the 16th and 84th percentiles.

Discussion

The ground motion prediction equations of Boore et al. (1997) were used to assess the importance of site effects in earthquake damage scenarios.

It was found that the impact of a change in magnitude on acceleration can be related to an equivalent change in shear velocity and/or in distance. Thus one can calibrate the value of knowledge of Vs in terms of a comparable knowledge of magnitude. Lack of knowledge about site effects may correspond to a difference of as much as one magnitude unit in a damage scenario. The impact of site effects on predicted acceleration was also found to be comparable to the uncertainty reflected by the standard deviation in the acceleration distribution.

Earthquake preparedness planning may require substantial investment of time, labor and money. Decisions must be made whether to carry out detailed building surveys or to invest in expensive efforts to strengthen construction. The ability to assess likely ground shaking from a major earthquake will be an important element in these decisions. The methods developed here can be useful for quantifying the penalty for lack of knowledge about site effects and thereby for evaluating the impact of research on site effects in a cost-benefit analysis of construction.
To limit uncertainty in acceleration to differences of at most 30% requires knowledge of shear velocities to an accuracy of at least 80%. Knowledge of the shear velocity to within a factor of 1.8 is equivalent to specifying the magnitude to within about ½ magnitude unit. For example, with Vs = 900, predicted accelerations are 30% lower than with Vs = 500. A similar comparison holds for Vs = 720 vs. Vs = 400 or Vs = 360 vs. Vs = 200.

It is important to point out that the choice of the ground motion prediction equations is an important element of the results that we derived here. The results here are based on the work of Boore et al. (1997), in which site effects are modeled using the shear wave velocity in the upper 30 m. In a study of the Los Angeles basin, Wald and Mori (2000) found that the shear wave velocity, in particular at 1-3 Hz, had higher correlation with strong ground motion than did other suggested site response factors (see also Fujimoto and Midorikawa 2002). Nonetheless, substantial uncertainty remained. As Boore et al. (1997) observed, lower soil layers can also affect amplification and these influences are ignored in our analysis. Although the upper shear wave velocity is not a perfect predictor of site response, it is currently a reasonable choice and has been used in developing hazard maps (see, for example, Wills et al. 2000 and Gomberg et al. 2003).

Other equations have also been developed to predict strong ground motion. Lee et al. (2000) review 5 different equations (Abrahamson and Silva 1997, Boore et al. 1997, Campbell 1997, Sadigh et al. 1997 and Lee and Trifunac 1995). Although the general form of all the equations is similar, there are some important differences. First, each equation uses a different method for modeling local site effects. Some of the equations include particular effects like magnitude saturation at short distances. The Boore et al. equation assumes that the effect of shear velocity on acceleration is identical at all magnitudes, whereas other equations include the possibility that this effect differs with magnitude. None of the competing ground motion equations were examined here. Thus some of the results and conclusions may be specific to the Boore et al. equation.

References

Abrahamson, N.A. & Silva W. (1997). Empirical response spectral attenuations relations for shallow crustal earthquakes, *Seismological Research Letters, 68, 94-127.*

Boore D.M., Joyner W.B. & Fumal T.E (1997). Equations for estimating horizontal response spectra and peak acceleration from Western North American earthquakes: A summary of recent work, *Seismological Research Letters, 68, 128-153.*

Campbell K.W (1997). Empirical near-source attenuation relationships for horizontal and vertical components of peak ground acceleration, peak ground velocity, and pseudo-absolute acceleration response spectra, *Seismological Research Letters, 68, 154-179.*

Fujimoto K. & Midorikawa S. (2002). Ground-shaking mapping for a scenario earthquake considering effects of geological conditions: a case study for the 1995 Hyogo-ken Nanbu, Japan earthquake, *Earthquake Engineering & Structural Dynamics, 31, 2103-2120.*

Gomberg J., Waldron B., Schweig E., Hwang H., Webbers A., VanArsdale R., Tucker K., Williams R., Street R., Mayne P., Stephenson W., Odum J., Cramer C., Updike R., Hutson S. & Bradley M. (2003). Lithology and shear-wave velocity in Memphis, Tennessee *Bulletin of the Seismological Society of America, 93, 986-997.*

Lee Y., Anderson J.G. & Zeng Y. (2000). Evaluation of empirical ground-motion relations in Southern California, *Bulletin of the Seismological Society of America, 90, 136-148.*

Lee V.W. & Trifunac M.D (1995). Frequency dependent attenuation functions and Fourier amplitude spectra of horizontal strong earthquake ground motion in California, *Final task report on characteristics of earthquake ground motions for seismic design, submitted to State of California Department of Transportation, Los Angeles County Department of Public Works, City of Los Angeles Department of Public Works, December 1995.*

Sadigh K., Chang C.Y., Egan J.A., Makdisi F. & Youngs R.R (1997). Attenuation relationships for shallow crustal earthquakes based on California strong motion data, *Seismological Research Letters, 68, 180-189.*

Wald L.A. & Mori J. (2000). Evaluation of methods for estimating linear site-response amplifications, *Bulletin of the Seismological Society of America, 90, 32-42.*

Wills C.J., Petersen M., Bryant W.A., Reichle M., Saucedo G.J., Tan S., Taylor G. & Treiman J. (2000). A site-conditions map for California based on geology and shear-wave velocity, *Bulletin of the Seismological Society of America, 90, 187-208.*

Seismic Hazard Analysis for Critical Infrastructures in Stable Continental Regions of Russia

Levshenko V T (1), Yunga S L (2)

(1) Institute of physics of the Earth, Russian academy of sciences, B.Gruzinskaya, 10, Moscow, 123995, Russia, syunga@ifz.ru
(2) Institute of physics of the Earth, Russian academy of sciences, B.Gruzinskaya, 10, Moscow, 123995, Russia, levshenko@ifz.ru

Keywords: seismic hazard analysis, earthquake engineering

Introduction

Assessment of the seismic potential and related risk level of stable continental regions (SCR) is a highly complex problem, as the applicability of techniques developed for seismically active areas to the areas that have no or limited seismic records is still under discussion. On the other hand, the geological knowledge on low seismicity areas is rather high. While most of the critical infrastructures situated at stable continental regions (SCR) of Russian Federation, nevertheless for its seismicity evaluation we need use many parts of geophysics: seismotectonic, seismology, seismic hazard analysis and engineering seismology studies. The goal of this paper is to present a comprehensive summary of our recent experience in the deterministic and probabilistic approaches for seismic hazard analysis (SHA).

The Russian Federation consists mainly of old geologic and tectonic terraines that are located far from plate boundaries. Rather little work has been done to study intraplate shocks in SCR outside of the most active regions. Seismicity of Russia is controlled by more then 150 seismic stations and 9 centers for data collecting and processing. Besides twelve IRIS digital instrumental seismic stations are situated in Russia since 1988 (Rogozhin & Yunga, 2000). For investigated SCR coveraged by the present Russian national network catalog for the last two decades is complete now only at the M >4 level (Starovoit, 1994). Knowledge of intraplate earthquakes and the state of stress in the earth's lithosphere are fundamental to the accurate estimation of earthquakes hazards and risk, assessing methods to identify various types of seismic events under the critical facilities

The Institute of physics of the Earth Rus. Ac. Sci. has coordinated the seismic hazard mapping for the whole territory of Russia and border regions (Ulomov & Shumilina,1999). A several years program was conducted to assemble for the whole area the unified seismic catalogue, the strong motion databank and the seismic zones model (lineament-domain-source), which form the basis of computation of seismic hazard assessment (OSR-97). From time of the introducing of a new map in 1997 the considerable progressing was received in the methodical base of seismic hazard assessment of objects of atomic engineering. However, it has to be pointed out that seismic zoning map OSR-97 is not a substitution for the detailed seismic zoning of critical infrastructures.

Materials and Methods

Materials

The seismotectonic data of the SCR are very poor because of low seismic activity and an insufficient seismological monitoring system. On the other hand, the geological knowledge is rather good owing to extensive geological and geophysical surveys held during the past decades. Accordingly, the deterministic approach is preferred in the seismic hazard assessment.

Following IAEA safety guides (IAEA, 2003) and national guidelines (Bugaev et al, 2001; NP-031-01, 2002) for seismic hazard evaluation the following geological and geophysical data were used:

Geologic maps,
Map of active faults,
Remote sensing data - maps of interpreted satellite imagery of different scales,
Neotectonic map of vertical movements,
Geodesy data,
Stratigraphic columns and descriptions of the major lithologic units,
Deep seismic sounding or other seismic profiles,
Detailed map of the gravity and magnetic fields,
Moho and Basement maps,
Detailed digital topography,
Catalogs and maps of earthquake epicenters,
Paleoseismic evidences,
Recurrence (magnitude-frequency) plot for local seismicity,

Seismic moments-magnitude plots for SCR regions,

Soil data.

In addition for specifying geodynamic zones (capable faults) within the investigated territory are carried out detailed geophysical and geological field observations. For this aim we used high sensitive mobile digital equipment for registration of geophysical field parameters. Detailed field works include microearthquake registration, thermal and geochemical (radon) measurements, paleoseismic observations.

Methods

In accordance with modern practice, seismic load specification is most suitably expressed in the form of ground response spectra from which the synthetic time-histories of ground motions are derived. The assessment of the seismic load is performed in two main steps: (1) estimation of the seismogenic potential of the area, and (2) derivation of the site-specific ground response spectra and the synthetic time-histories.

Digital data base is compiled from all collected data. Procedure of its interpretation use current internationally recognized methods and criteria and include several stages:

1) Microearthquake detection on the base of seismograms which used polarization analysis, artificial intellect method, wavelet analysis;

2) Microearthquakes, prehistorical, historical and instrumentally recorded earthquakes, paleoearthquakes are investigated;

3) The faults capability are analysed and appropriate seismotectonic model is created;

4) Amplitudes of neotectonic vertical movements, basement and Moho boundaries are interpreted quantitevely in terms of deformation of earth crust in the investigated region through curvatures calculations;

5) Seismotectonic deformation rate (seismic strain release) are estimated analytically and thus it dependence from maximum earthquake magnitude (Mmax) and the seismic activity parameters are derived;

6) Maximum earthquake potential Mmax of capable faults is evaluated on the base of comparison of geological and seismic deformation. Magnitude of design basis earthquake is estimated using recurrence plot.

7) Engineering Seismology Studies included estimation of peak ground acceleration (PGA) and duration of strong shaking. The PGA is derived from the regional attenuation lows for ground motion versus distance. Strong shaking spectral representation in the form of target response spectrum is based on European and national strong motion data bases. At least, synthetic accelerograms were simulated corresponding with target response spectrum.

Results and Discussion

We apply the above approach to the several critical facilities which have been investigated during last years. The critical infrastructures of Novovoronezh, Kursk, Kalinin and Leningrad regions are located on the East European platform. Bilibino critical infrastructure is located within the North American plate in the northeastern part of the Mesozoic Verkhoyansk-Chukotka fold belt.

The ground motion of an earthquake having a local magnitude M and occurring at a distance R (km) from the site has been empirically estimated through attenuation equation. Authoritative review of recent attenuation is given by Abrahamson and Shedlock (1997). A number of published ground motion attenuation models are available. However, the choice of a single, most suitable attenuation model for such SCR like East Europen platform (EUP) is hindered by the lack of strong motion recordings. In this regard, we find after special analysis of mutual consistency equations with each other and with macroseismic data that attenuation relationship suggested in the work (Bugaev, Topchiyan, 1995) is the most appropriate for East Europen platform.

Duration of strong motion computed using the regression of Hernandez and Cotton (2000).

log (Duration) = a + b Magnitude + c log (Distance)+ d Soil's +/-sigma,

where log is the natural logarithm; Duration is the significant duration in seconds; Magnitude is the local magnitude for magnitude less than 6 and the surface wave magnitude for the greater events; Distance is the closest distance between the fault and the site; and Soil is equal to 1 if the S-wave velocity of the site is less than 750 m/s and 0 if it is a rock site. The regression parameters are as follows: a=-1.04, b=0.44, c=0.19, d=0.04, and standart deviation sigma=0.48.

For specifying geodynamic zones (capable faults) within the investigated territory are carried out microearthquake registration. Automatic phase pickers are designed for seismogram processing. Automatic detection of micro earthquake on the base of STA/LTA ratios jointly with polarization analysis was performed. STA/LTA stands for Short Term Averaging / Long Term Averaging. The ratio of the STA to the preceding LTA is a measure of the local signal-to-noise. An envelope function is generated from the each signal. Two moving averages are taken along the envelope function, an LTA followed directly by an STA. The ratio of the STA to the LTA is taken at every digitization point; these STA/LTA values define the ratio function. Wavelet analysis was used as additional tool for seismogram processing. P- and S-waves usually are clearly recognized. Magnitudes of this events are roughly estimated on the base of duration as mainly negative. The envelope function was used also to distiguish technogenal events and micro earthquakes. Then so called index K of geodynamic activity was evaluated. The K is defined by ratio of N_{eq} to the time of registration T.

Tectonic moment release rates for the seismogenic part of the lithosphere are calculated numerically from a flexural-plate model on the base of neotectonic data. Seismic moment release rates for the same part of the lithosphere are calculated analytically from Gutenberg-Richter (G-R) frequency-magnitude law and relation between seismic moment and magnitude. The result of integration include maximum magnitude. Thus the neotectonic bending strain rate and the seismotectonic strain rate, which depend on the Mmax and seismicity parameters are determined. As a result, an expression for evaluating Mmax , which is a function of one normalizing constant, is obtained (Grachev, Mukhamediev, Yunga, 1996).

Maximum magnitudes are found to be in the range 4-4.5 for the investigated regions. This results indicate that in the considered SCR the absence of large events with M > 6.5 in earthquake catalogs cannot be attributed to an incomplete record.

Three different approaches were applied in estimating target response spectrum. A comprehensive collection of seismic records from near-field earthquakes is provided from West Europe. Taking into consideration similar parameters of the earth's crust of some regions of West Europe and considered sites 30 strong motions data were investigated. At the first approach generalized response spectrum was calculated based on this data. The parametrisation of Eurocode 8 (1998) can be used with classification of the soil at the second approach. Third approach used parametrisation of standart spectrum spectra from Guideline NP-031 (2002).

With the help of TARSCTHS Software (Deodatis, 1996) single component artificial ground time history acceleration was synthesized on a basis of standard generalized ground spectra. Example is given in the fig.1.

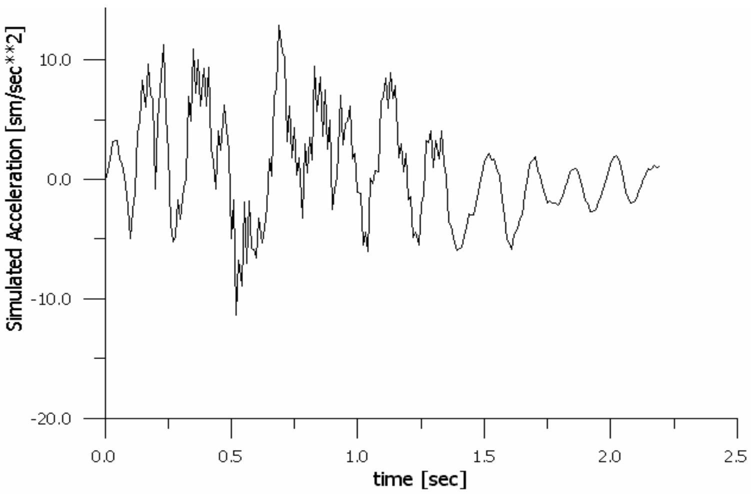

Figure 1. Synthetic accelerogram (time–history of the horizontal component) derived from target ground response spectrum

Designed response spectrum from developed time history acceleration and standard one are represented in Fig 2.

Thus, known seismic activity in intraplate regions of Russia is generally lower than that in the SCR of North America and Australia. The absence of large events with M > 6.5 is demonstrated. We apply SHA approach to the several critical facilities which have been investigated during last years. The critical infrastructures of Novovoronezh, Kursk, Kalinin and Leningrad regions are located on the East European craton. Bilibino critical infrastructure is located in the Mesozoic Verkhoyansk-Chukotka fold belt. Maximum magnitudes for all the above mentioned sites are found to be in the range 4-4.5 The intensity I of strong shaking is less than 5 balls.

It has to be pointed out that seismic zoning map OSR-97 is not a substitution for the detailed seismic zoning of critical infrastructures.

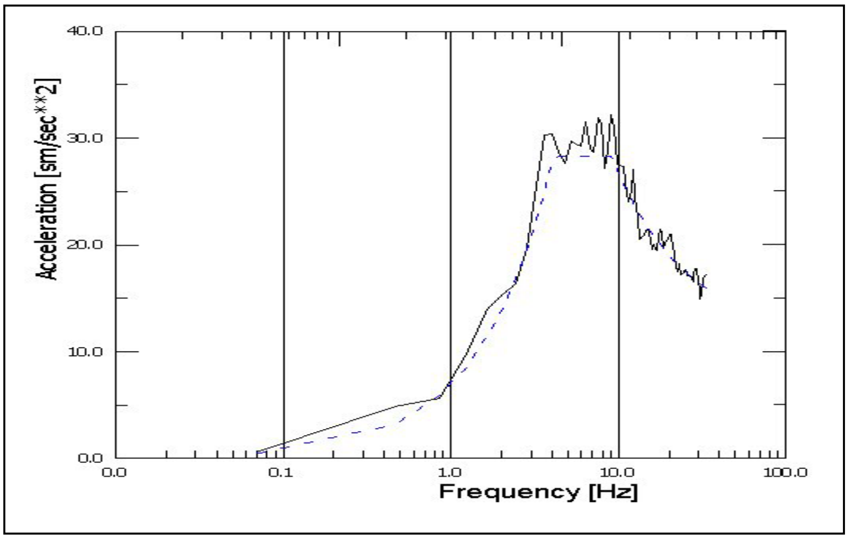

Figure 2. Designed (solid line) and target (dashed line) response spectra (damping 5%)

Acknowledgments

This work was partly supported by RFBR № 07-05-00436.

References

Abrahamson N.A., & Shedlock K.M. (1997). Some comparison between recent ground motion relations, *Seismological Research Letters, 68,1,24-40.*

Bugaev E., Kaliberda I., Lavrov I, Fiheeva L., Benedik A, Stepanov V., Shvarev S.& Yunga S. (2001). Seismic hazard estimation of places of allocation nuclear and radiation dangerous objects on the basis of geodynamic data, *GOSATOMNADZOR, Russia, Moscow, RB-019-01. 29p.*

Deodatis G. (1996). Non-Stationary Stochastic Vector Processes: Seismic Ground Motion Applications, *Prob. Eng. Mech., 11, 149-167*.

Eurocode 8 (1998). Design of structures for earthquake resistance, Part 1, *General rules, seismic actions and rules for buildings, 12 p.*

Grachev A., Mukhamediev Sh.& Yunga S. (1996). Maximum Earthquakes Magnitude Estimation in East European Platform Based on Neotectonic and Seismic Strain Analysis. In: Seismology in Europe, *ESC the XXY General Assembly, Reykjavik, Icelandic Meteorological Office, 1996, 623-628.*

Hernandez B. & Cotton F (2000). Empirical determination of the ground shaking duration due to an earthquake using strong motion accelerograms for engineering applications, *12 WSEE, Paper-ID: 2254/4/A*

IAEA (2003). INTERNATIONAL ATOMIC ENERGY AGENCY, Seismic Design and Qualification for Nuclear Power Plants: *Safety Guide No. NS-G-1.6, Vienna.*

NP-031-01 (2002). Norms for Seismic-Resistant Design of Nuclear Plants *GOSATOMNADZOR OF RUSSIA, 38 p.*

Rogozhin E. A. & Yunga S. L. (2000). The Geological and Geophysical Environment at Russian IRIS GSN stations. *Publ. of UIPE RAS, Moscow, 128 p.*

Starovoit, O. Ye. (1994).Seismological network of the Russian Academy of Sciences, Federal System for Seismological Observations and Prediction of Earthquakes, *Information-Analytical Bulletin, 1, 1, 22-29.*

Ulomov V.I. & Shumilina L.S. (1999). Komplekt kart obshchego seismicheskogo raionirovaniya territorii Rossiiskoi Federatsii – OSR-97. Masshtab 1:8000000. *Ob"yasnitel'naya zapiska i spisok gorodov i naselennykh punktov, raspolozhennykh v seismoopasnykh raionakh. M.: OIFZ. 57 s.*

Mean Multifractal Properties of Low-Frequency Microseismic Noise

Lyubushin A A (1)

(1) Institute of the Physics of the Earth, B.Gruzinskaya, 10, Moscow, 123995, Russia, lyubushin@yandex.ru

Keywords: singularity spectra, microseismic noise, seismicity

Introduction

Low-frequency microseismic field is an important source of geophysical information [Kobayashi & Nishida, 1998; Tanimoto et al. 1998; Tanimoto, Um, 1999; Tanimoto, 2001, 2005; Kurrle, Widmer-Schnidrig, 2006]. Atmospheric and oceanic processes are the main generators of low-frequency microseisms. But the energy from these sources is transferred through the Earth’s crust. Thus, the changes within Earth’s crust must influence the structure of noise and parameters of microseismic noise structure could reflect thin peculiarities of tectonic processes. Usual spectral analysis turns to be rather rough instrument which does not allow deep insight in the noise studies because low-frequency microsesimic noise does not include narrow-banded or monochromatic components. Investigation of fractal and multifractal properties of geophysical processes [Currenti et al., 2005; Ramirez-Rojas et al., 2005; Ida et al., 2005; Telesca et al., 2005] seems to be much more perspective in noise studies just because this approach allow explore signals which are not interesting from spectral point of view. This idea was the main in investigations [Lyubushin & Sobolev, 2006; Sobelev & Lyubushin, 2007; Lyubushin, 2007] of the noise multifractal structure and seeking precursors of strong earthquakes as coherent effects between variations of multifractal singularity spectra parameters calculated within adjacent “small” time intervals for different broadband seismic stations. In this article these investigation are continued in the direction of estimating a mean parameters of singularity spectra by averaging their values over a large number of broadband seismic stations, covering some seismically active region.

Materials and Methods

For the analysis a vertical broadband seismic components with 1-second sampling (LHZ-records) from 54 F-net seismic stations from Japan were downloaded from internet address http://www.fnet.bosai.go.jp for time interval 1997 – April 2008. The whole list of F-net seismic stations includes 83 positions but a lot of them form a very dense spatial cluster especially in Central Japan. That is why only 54 stations were taken for analysis in order to avoid dominating information from some regions. The positions of these stations are presented on the Fig.1 with epicentre of Hokkaido earthquake 25.09.2003, M=8.3 which turns to be an important change point for behaviour of noise multifractal singularity spectra parameters.

Multifractal singularity spectrum $F(\alpha)$ of the signal $X(t)$ is defined as a fractal dimensionality of time moments τ_α which have the same value of local Lipschitz-Holder exponent $h(t) = \lim_{\delta \to 0} \frac{\ln(\mu(t,\delta))}{\ln(2\delta)}$, i.e. $h(\tau_\alpha) = \alpha$, where $\mu(t,\delta) = \max_{t-\delta \le s \le t+\delta} X(s) - \min_{t-\delta \le s \le t+\delta} X(s)$ is a measure of signal variability in the vicinity of time moment t [Feder, 1989]. If the signal $X(t)$ is a usual self-similar monofractal signal with

Hurst exponent value $0 < H < 1$ [Taqqu, 1988], then $F(H) = 1, \quad F(\alpha) = 0 \; \forall \alpha \neq H$ but finite sample estimate of singularity spectrum does not obey these rigorous theoretical conditions of course. Practically the most convenient method for estimating singularity spectrum is a DFA-method – detrended fluctuation analysis [Kantelhardt et al., 2002] which is used here. Technical details of computing could be found in [Lyubushin & Sobolev, 2006; Lyubushin, 2007].

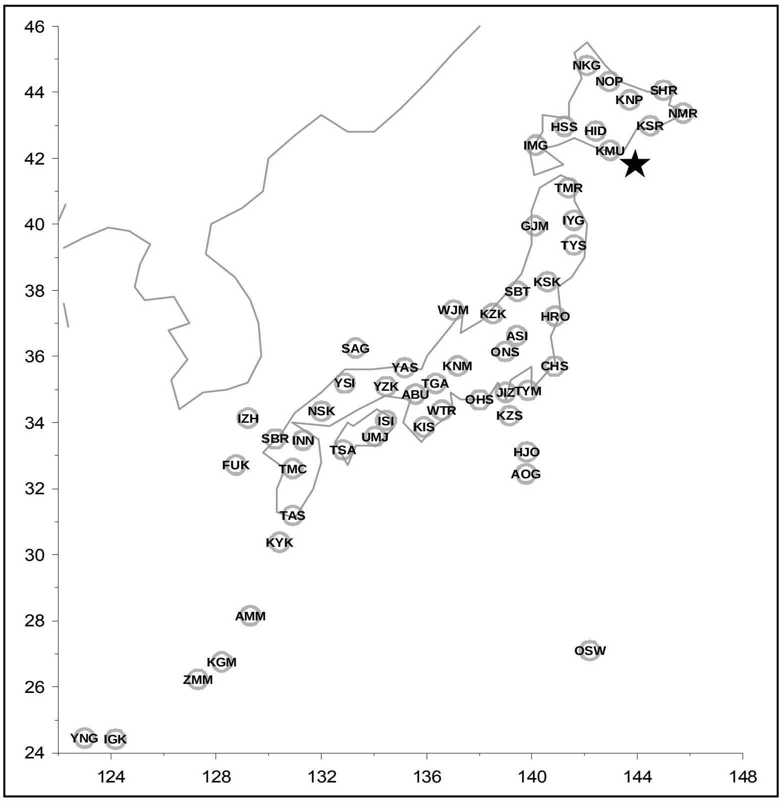

Figure 1. Circles – positions of 54 F-net broadband seismic stations in Japan with their 3-letters codes. Star – epicenter of Hokkaido earthquake, M = 8.3, 25.09.2003, Latitude = 41.81°, Longitude = 143.91°

Singularity spectra were estimated within adjacent time intervals of 0.5 hour length (1800 1-seconds samples) for 54 stations presented at the Fig.1. A typical graphics of singularity spectra estimate for one of the 0.5 hour time interval and for one of the stations is presented at the Fig.2. The function $F(\alpha)$ could be characterized by following parameters: $\alpha_{\min}, \alpha_{\max}, \Delta\alpha = \alpha_{\max} - \alpha_{\min}$ and α^* - an argument providing maximum to singularity spectra: $F(\alpha^*) = \max_{\alpha} F(\alpha)$. Parameter α^* could be called a generalized Hurst exponent and it gives the most typical value of Lipschitz-Holder exponent.

Parameter $\Delta\alpha$ could be regarded as a measure of variety of stochastic behavior. It should be noticed that usually $F(\alpha^*) = 1$ – maximum of singularity spectra equals to the dimensionality of embedding set, i.e. to dimensionality of time interval. But time intervals could occur for which $F(\alpha^*) < 1$. It means that the behavior of the noise within these time intervals strongly differ from behavior of multifractal signal.

Computing median values of $\Delta\alpha$ and α^* over all seismic stations which have registration within current "small" 0.5 hours time interval produces an averaged time series of $(\Delta\alpha, \alpha^*)$ -

variations which gather information from all station of the seismic net. The behavior of these time series is a main object for data analysis. Besides that another statistics were constructed similarly by calculating median values of $(\Delta\alpha, \alpha^*)$-variations for seismic records after coming to 1-minutes sampling time interval within "big" adjacent time intervals of the 1 day length (1440 1-minutes samples). These time series (more long periodic) were investigated as well. For estimating singularity spectra within 0.5 hour intervals local scale-depended trends were removed by polynomials of 4th order, whereas for the case of 1-day time interval – by polynomials of 8th order.

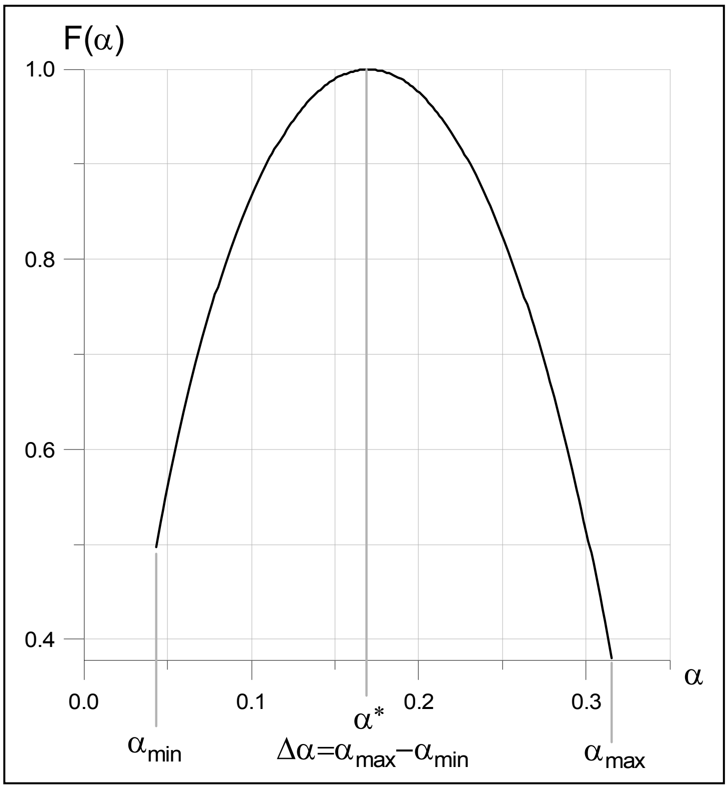

Figure 2. Example of multifractal singularity spectra estimate for 30-minutes time interval.

Results and Discussion

Figures 3 and 4 present the main results. Figures 3(a) and 4(a) are identical and illustrate the sequence of strong earthquakes (M ≥ 6.0) inside a rather wide neighbourhood of Japan islands – in the rectangular 20° ≤ Latitude ≤ 60°, 120° ≤ Longitude ≤ 160°. The arrow indicates a time moment of Hokkaido earthquake 25.09.2003, M=8.3.

Figure 3(b) presents variations of median value of singularity spectra parameter $\Delta\alpha$, estimated within 0.5 hours time intervals (grey line) and result of its averaging using Gaussian kernel smoothing with averaging radius 200 days (bold black line). This Gaussian kernel trend $\overline{z}(t\,|\,r)$ with averaging radius $r > 0$ for the signal $z(t)$ is defined by the formula [Hardle, 1989]:

$$\overline{z}(t\,|\,r) = \int_{-\infty}^{+\infty} z(t + r\cdot\xi)\cdot\psi(\xi)\,d\xi \bigg/ \int_{-\infty}^{+\infty} \psi(\xi)\,d\xi\,, \quad \psi(\xi) = \exp(-\xi^2)$$

The main peculiarity of the Fig.3(b) is a statistically significant change of $\Delta\alpha$ mean value from 0.322 for 1997-2003 till 0.307 for 2004-2008 which began 0.5 years before Hokkaido earthquake M=8.3, 25.09.2003. Taking into account interpretation of the parameter $\Delta\alpha$ as a measure of noise behavior variability, this effect could be regarded as a decreasing of hidden "number of freedom" of the Earth's crust before the strong earthquake which dramatically changes the state of lithosphere as a transfer element from atmosphere-ocean processes to low-frequency microsesimic oscillations.

It should be noticed that using median values of singularity spectra parameters (like any other way of averaging) is some kind of extracting common signal which exists in variations of noise multifractal parameters at different stations but could be hidden within individual statistical fluctuations of finite sample singularity spectra estimates. Besides that, using median is a robust way of struggle with existence of gaps in registration at different seismic stations.

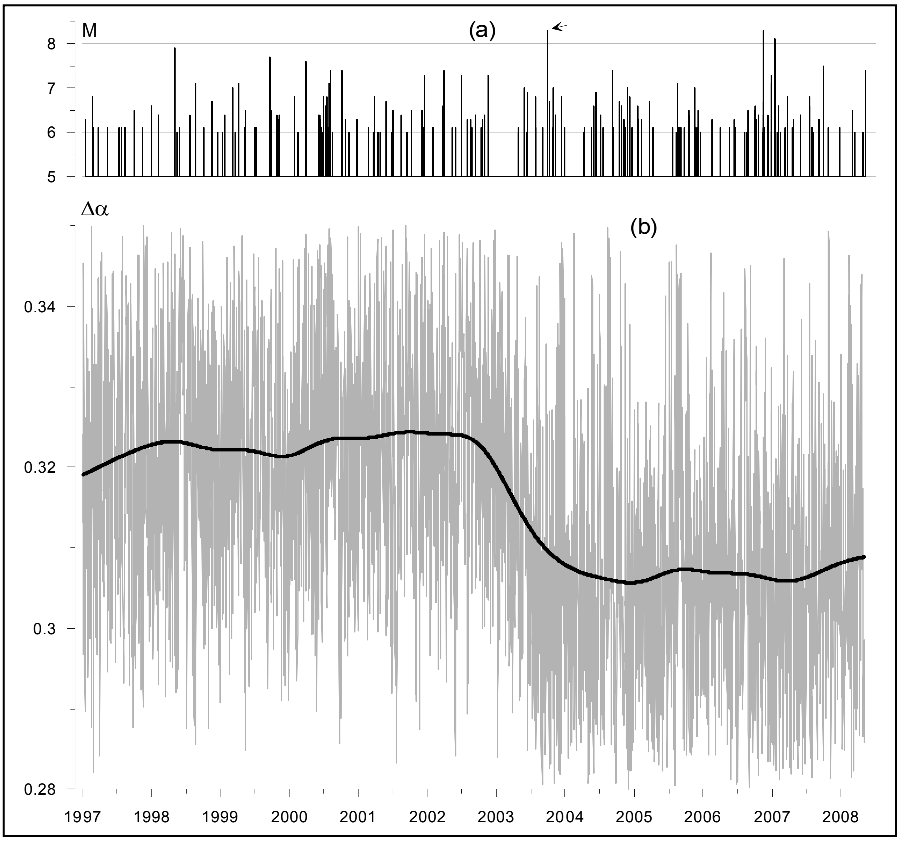

Figure 3. (a) - Sequence of strong earthquakes, arrow indicates Hokkaido earthquake; (b) - Low-frequency component (after coming to 1 day sampling) of median values of singularity spectra support width $\Delta\alpha$ (grey lines) and its mean values computed by Gaussian kernel smoothing with radius 200 days (bold black line).

Figure 4(b) presents Gaussian kernel trend with averaging radius 13 days for variations of median value of generalized Hurst exponent α^*, estimated within 1 day time intervals after transition from 1-sec sampled signals to 1-minute sampling by averaging initial LHZ seismic records into 60 times. Thus, singularity spectra were estimated within adjacent time intervals of 1440 1-minutes samples length.

This transition from 1-sec sampling to 1 minute gives an opportunity to investigate temporal variations of multifractal properties in more low-frequency range. Such transition is not correct from a rigorous mathematical point of view because multifractal and self-similar behavior means scale invariance. But in geophysics we need investigate temporal variations of these properties within time windows of finite length. This finite length gives a limit for large scales which could be studied. Thus, in order to cover more wide range of scale it is necessary to use different sampling.

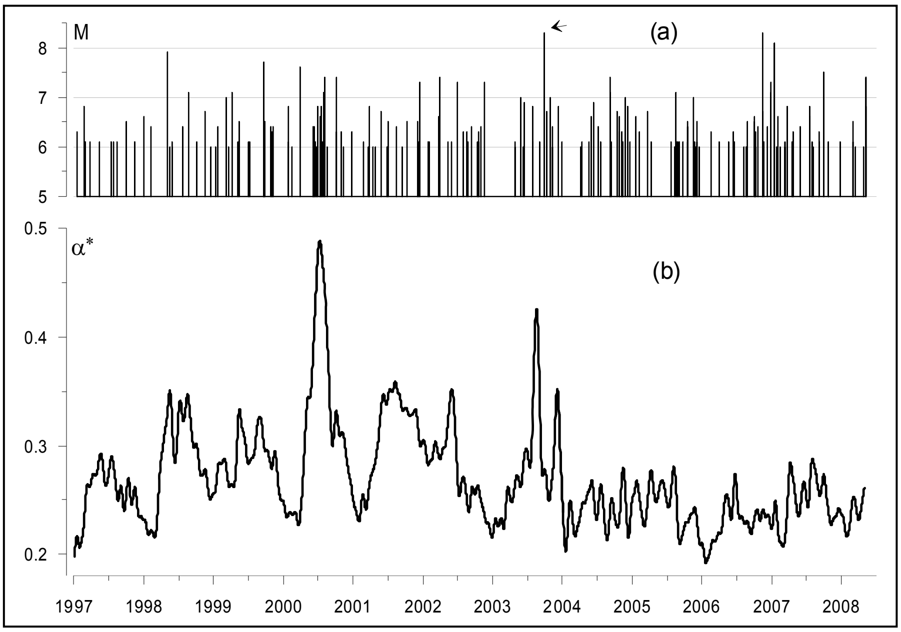

Figure 4. (a) - Sequence of strong earthquakes, arrow indicates Hokkaido earthquake; (b) - mean values (computed by Gaussian kernel smoothing with radius 13 days) of medians of singularity spectra parameter α^* estimated for seismic records after coming to 1-minutes sampling within adjacent time intervals of 1 day length.

The Fig.4(b) confirms a previous conclusion that Hokkaido earthquake is a change point for behavior of microseismic oscillations field at the Japan islands – it is obvious that explicit seasonal (1 year period) trend component during 1997-2003 disappear after this earthquake.

Thus, using mean (in our case – median average) of singularity spectra parameters of low-frequency microseismic noise at different stations of the net covering large seismically active region allows extracting rather thin and hidden properties of microseismic field and connect changes of these properties with seismic process.

The author thanks Dr. Furumura Takashi from Earthquake Research Institute, University of Tokyo for attracting the author's attention to internet F-net data base.

References

Currenti G., del Negro C., Lapenna, & Telesca L. (2005). Multifractality in local geomagnetic field at Etna volcano, Sicily (south V.ern Italy), *Natural Hazards and Earth System Sciences, 5, 555-559.*

Feder J. (1989). Fractals. *Plenum Press, New York, London, 247 p*.

Hardle W. (1989). Applied nonparametric regression, *Cambridge University Press, Cambridge, New York, New Rochell, Melbourne, Sydney, 333 p*

Ida Y., Hayakawa M., Adalev A. & Gotoh K. (2005). Multifractal analysis for the ULF geomagnetic data during the 1993 Guam earthquake, *Nonlinear Processes in Geophysics, 2005, 12, 157-162*

Kantelhardt J. W., Zschiegner S. A., Konscienly-Bunde E., Havlin S., Bunde A. & Stanley H. E. (2002). Multifractal detrended fluctuation analysis of nonstationary time series, *Physica A, 316, 87-114.*

Kobayashi N., & Nishida K. (1998). Continuous excitation of planetary free oscillations by atmospheric disturbances, *Nature, 395, 357-360.*

Kurrle, D. & Widmer-Schnidrig R. (2006). Spatiotemporal features of the Earth's background oscillations observed in central Europe, *Geophys. Res. Lett., 33, L24304.*

Lyubushin A.A. & Sobolev G.A. (2006). Multifractal Measures of Synchronization of Microseismic Oscillations in a Minute Range of Periods, *Izvestiya, Physics of the Solid Earth, 42, No.9, 734-744*.

Lyubushin A.A. (2008). Microseismic Noise in the Low Frequency Range (Periods of 1-300 min): Properties and Possible Prognostic Features, *Izvestiya, Physics of the Solid Earth, 44, No. 4, 275-290*.

Ramirez-Rojas A., Munoz-Diosdado A., Pavia-Miller C. G. & F. Angulo-Brown (2004). Spectral and multifractal study of electroseismic time series associated to the Mw=6.5 earthquake of 24 October 1993 in Mexico, *Natural Hazards and Earth System Sciences (2004) 4, 703-709.*

Sobolev G.A. & Lyubushin A. A. (2007). Using modern seismological data to reveal earthquake precursors, *Russian Journal of Earth sciences, 9, ES2005,* http://dx.doi.org/10.2205/2007ES000220, http://www.agu.org/WPS/rjes/

Telesca L., Colangelo G. & V. Lapenna (2005). Multifractal variability in geoelectrical signals and correlations with seismicity: a study case in southern Italy, *Natural Hazards and Earth System Sciences, 5, 673-677.*

Tanimoto T., Um J., Nishida K. & Kobayashi N. (1998). Earth's continuous oscillations observed on seismically quiet days, *Geophys.Res.Lett. 1998, 25,1553-1556.*

Tanimoto T. & Um J. (1999). Cause of continuous oscillations of the Earth, *J. Geophys. Res. 104,No28,723-39.*

Tanimoto T. (2001). Continuous Free Oscillations: Atmosphere-Solid Earth Coupling, *Annu. Rev. Earth Planet. Sci., 29, 563-84.*

Tanimoto, T. (2005). The oceanic excitation hypothesis for the continuous oscillations of the Earth, *Geophys. J. Int., 160, 276-288*.

Taqqu M.S. (1988). Self-similar processes. *Encyclopedia of Statistical Sciences, 8, 352-357, Wiley, New York.*

Numerical Modeling of Basin Effects for the Taipei Basin

Miksat J (1), Wen K-L (2), Chen Ch-T (2), Sokolov V (1), Wenzel F (1)

(1) Geophysical Institute, Karlsruhe University, Hertzstr. 16, 76187 Karlsruhe, Germany, joachim.miksat@gpi.uni-karlsruhe.de
(2) Institute of Geophysics, National Central University, No. 300, Jhongda Rd. Jhongli City, Taoyuan County 32001, Taiwan (R.O.C),

Keywords: basin effects, spectral amplification, wave propagation, numerical modeling, finite-difference method

Introduction

The city of Taipei in northern Taiwan is located on a sedimentary basin and was affected by several destructive earthquakes in the past. As the seismicity of Taiwan is very high and the Taipei basin area is covered with a dense strong motion network, which is operated in the frame of the TSMIP (Taiwan Strong Motion Instrumentation Program) conducted by the CWB (Central Weather Bureau), a detailed analysis of observed ground motion can be performed. Recent analysis of this data showed significant difference between records for deep and shallow events. Chen *et al.* (pers. comm., 2008) showed that the H/V ratios for stations in the central part of the basin are larger for shallow than for deep earthquakes in the low frequency range (f < 2 Hz - 3 Hz). For stations located directly along the basin edges, no clear difference is observable. When comparing shallow earthquakes of different azimuths, the resulting H/V ratios in the low frequency range differ clearly at some stations. Sokolov *et al.* (2008a, 2008b) calculated the spectral ratios between a VHR (very hard rock) model and the actual observed records. The results also show that the spectral ratios for stations in the central part of the basin are larger for shallow than for deep earthquakes for frequencies up to 3 Hz. Furthermore, they found that spectral ratios of the deep earthquakes can be modelled by applying a 1D model based on the structural and geotechnical information for the corresponding stations.

We apply 3D finite-difference (FD) modelling of wave propagation in order to understand the observed peculiarities. Wave propagation through the Taipei basin is simulated for an incident S-wave front with varying incidence angles and azimuths in order to explore the influence of deep and shallow earthquakes and of earthquake azimuth. We evaluate PGV (peak ground velocity), significant duration and spectral amplification for frequencies up to 1 Hz. As bridges and high-rise buildings are very sensitive to this low frequency part a detailed knowledge of these effects and an extension of the observations by numerical modeling is very important.

The Method

Subsurface Structure

The knowledge of the underground structure is essential for FD simulations of wave propagation. The structure of the Taipei basin is known from shallow reflection seismic experiments along many profiles through the city and on borehole drilling data (Wang *et al.*, 2004). The Taipei basin can be divided into a deep western and a shallow eastern part (Fig. 1). Based on the given depths of the Tertiary basement and the SRTM 90 m (CIAT, 2004) data, we constructed the sediment-bedrock boundary layer. From the data given in Wang *et al.* (2004), we calculated a velocity-depth function in order to assign proper P- and S-wave velocities for the basin. The minimum shear wave velocities of the uppermost layer, the so called Sungshan formation, is 170 m/s. Fig. 2 shows a slice through the created model. For the FD simulations the model is discretized with 50 m and 25 m in horizontal and vertical direction, respectively. The horizontal (EW and NS) extensions of the model are 27.8 km to 27.8 km. Depending on the simulated scenarios, model depths vary between 2.6 km and 12 km.

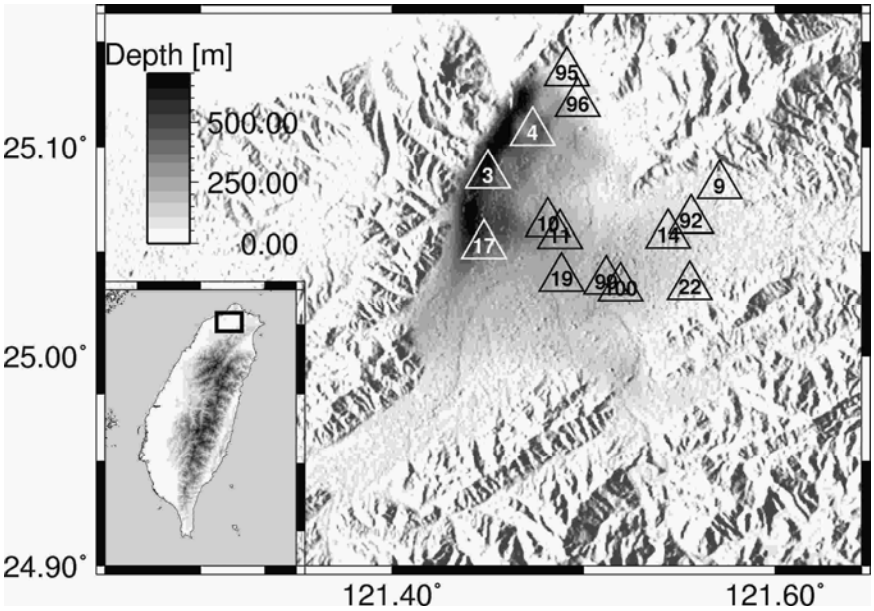

Figure 1: Map of the triangle shaped Taipei basin in northern Taiwan. The depth to the Tertiary basement is indicated by the grayscale. Triangles mark strong motion stations of the TAP network that are evaluated in this paper.

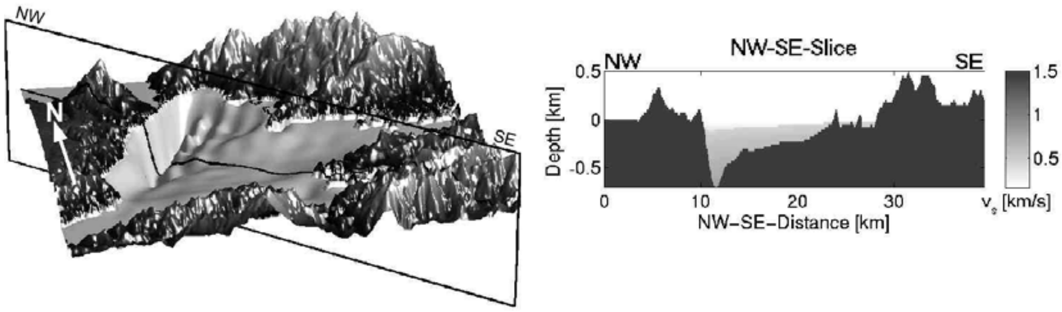

Figure 2: Left: Created topography-basement surface based on SRTM (CIAT, 2004) and Wang *et al*. (2004). Right: NW-SE slice through the model.

Simulation of Wave Propagation with Finite-Differences (FD)

We use a 3D FD method in order to simulate wave propagation for the Taipei basin (Furumura and Chen, 2005; Furumura *et al.*, 2003). The code is 4th (vertical direction) to 16th (horizontal direction) order in space and second order in time. 3 grid points per minimum wavelength in horizontal and 6 grid points per minimum wavelength in vertical direction are needed in order to obtain accurate results. Consequently, based on the minimum shear wave velocity and grid spacing, maximum frequency of our simulations is 1 Hz. At the sides and the bottom of the model damping and one-way absorbing boundary conditions are applied. The free surface is implemented by using the vacuum formulation, which allows to include topography.
In order to explore the Taipei basin response, we simulate planar S-wave front incidence on the basin for different incidence angles, which correspond to different earthquake depths. We also explore the azimuth dependence of the basin response by simulating wave front

incidence for different azimuths. For each source grid point of the planar wave front, a double couple source is applied so that a pure S-wave front results in propagation direction. The resulting S-wave polarisation of the source depends on the actual choice of the applied moment tensor components. In this paper we simulate wave propagation for SH-polarized wave fronts. The source time function of the added stress glut (see Miksat *et al.*, 2008) at each grid point is described by a Herrman window with a width of 0.5 s. Deep earthquakes are described by a wave front incident from the bottom (incidence angle i = 0°) and shallow earthquakes are simulated by incidence angles of 90° for different azimuths (90° and 180°). S-polarizations of the source is in EW-direction for the deep earthquake and the shallow earthquake south of the basin. S-polarization is NS for the scenario east of the basin.

We perform the simulations for two different subsurface structures, the developed Taipei basin model (see section "Subsurface Structure") and a homogeneous model with v_p = 3 km/s, v_s = 1.5 km/s. These values correspond to the bedrock velocities in the Taipei basin model. Topography is included in both models. Frequency dependent spectral ratios are calculated by dividing the Fourier amplitude spectra (FAS) of the simulation with the basin structure by the FAS resulting from the simulation for the homogeneous model. Consequently, the spectral amplification show the effects of basin geometry and the properties of the layers within the basin.

Results and Discussion

Deep and Shallow Earthquakes

We compare the basin response of an incident planar S-wave front from the bottom (deep earthquake) with a vertically incident wave front from the East (shallow earthquake). The PGV distribution is relatively homogeneous for deep earthquakes compared to the simulated shallow earthquake (Fig. 3). The visible pattern of the PGV distribution for the deep scenario reflects mainly the basin depth. This suggests that the response for deep earthquakes can be calculated by considering the 1D soil structure beneath the stations, which was also found by Sokolov *et al*. (2008a, 2008b). Only in the north-western part, we obtain large values, where the basin slope is highest. This indicates that basin-edge effects due to the Tertiary basin geometry occur in this area.

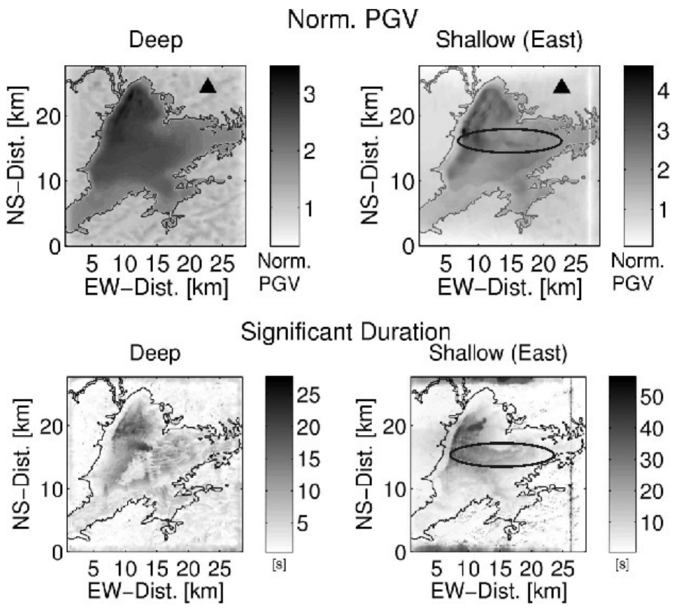

Figure 3: PGV and significant ground motion duration (time needed to increase from 5% to 95% of the Arias intensity) distributions for a planar wave front incidence from the bottom (=deep earthquake) and East (=shallow earthquake). PGV is scaled to the PGV value at a reference station outside the basin (black triangle). The shallow earthquake generate surface waves at the eastern basin edge, which travel to the West along the marked path.

We calculate maximum significant ground motion duration (time needed to increase from 5% to 95% of the Arias intensity, see e.g. Erdik and Durukal, 2003) . Maximum significant ground motion duration is about two times longer for the shallow earthquake (Fig. 3). For the shallow scenario surface waves are generated at the eastern basin edge and channeled to the western deep part. This produces an east-west orientated band of relatively long ground motion duration between the eastern basin edge and the deepest part of the basin. Because of trapped waves and consequent long reverberation, significant ground motion is largest for the deepest part of the basin for both the deep and shallow scenario.

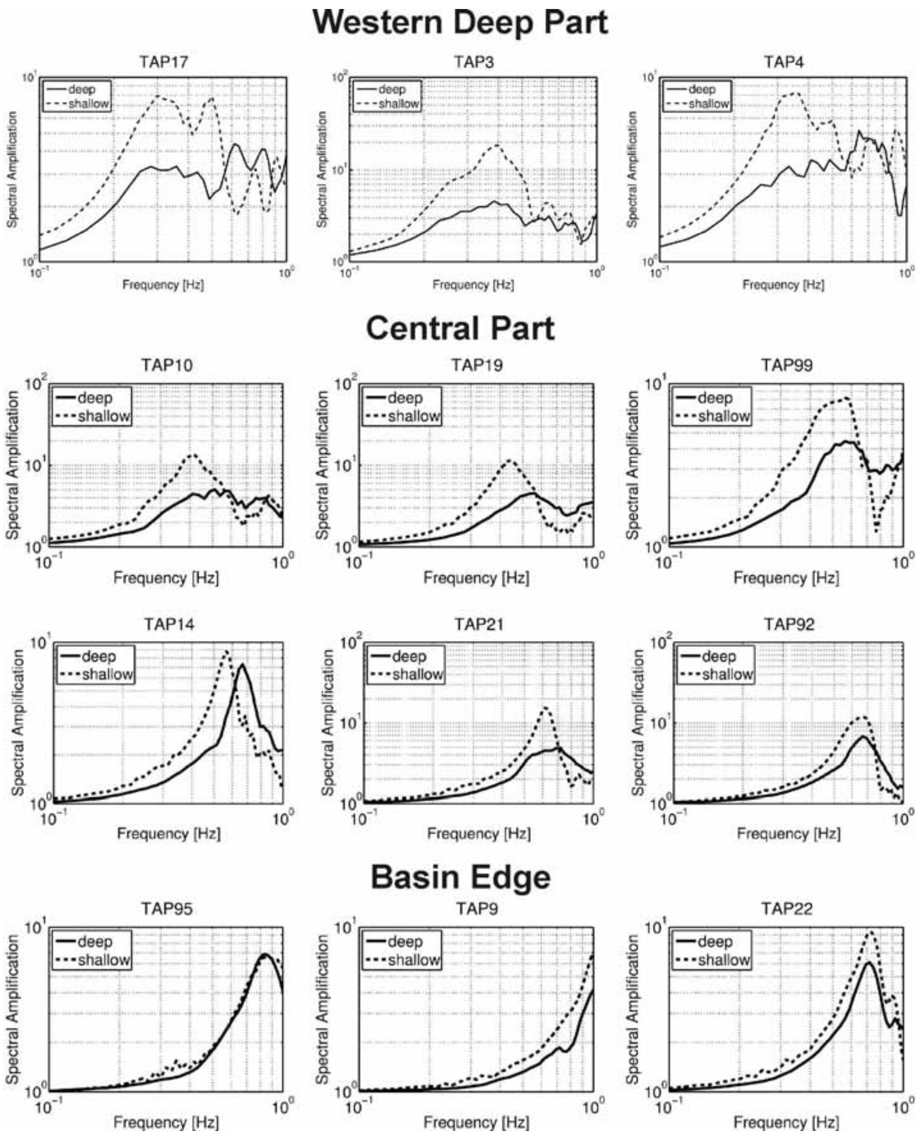

Figure 4. Modeled spectral amplification for the shallow and deep scenario. For stations in the western and central part, the amplifications of the shallow scenario are clearly larger than for the deep event. Maximum amplification occurs for stations at the deepest part at 0.3 Hz to 0.4 Hz. and for stations in the central part for 0.4 Hz to 0.6 Hz. For stations at the basin edge, spectral amplifications are similar for the deep and shallow scenario.

In Fig. 4 spectral amplifications are given for stations in the western deepest part of the basin, the central part and for stations at the basin edge. Because of the polarization of the source, we calculate spectral amplifications for the deep scenario from the EW-component and for the shallow scenario from the NS-component (see "Simulation of Wave Propagation with Finite-Differences (FD)"). For all stations within the western and central basin spectral amplification are larger for shallow earthquakes. However, along the basin edges the difference of spectral amplifications is very small. This behavior was also found by Sokolov *et al.* (2008a, 2008b) and Chen *et al*. (pers. comm., 2008). Amplification vary between 1 and 15, which is the same range as derived by Sokolov *et al.* (2008a, 2008b). Maximum amplifications for shallow earthquakes occur for stations at the deepest part of the basin at about 0.3 – 0.4 Hz and in the central part at 0.4 – 0.7 Hz. The same frequency dependence of the maximum amplification can also be seen in the VHR studies performed by Sokolov *et al*. (2008a, 2008b).

Azimuth Dependence

Next, we compare the azimuth dependence of the Taipei basin response for shallow earthquakes. Fig. 5 shows snapshots of the wave propagation for an incident wave front of 90° from the South and East. The snapshots show clearly the generation of surface waves at the southern and eastern basin edge for both scenarios. For the earthquakes in the South, strongest surface waves amplitudes are generated in the south-western edge of the basin and guided along the deep part of the basin to the North. When the earthquake occurs east of the basin, strong surface waves are excited at the eastern edge and at the eastern rim of the northern embayment of the basin and travel to the western deepest part of the basin. The waves generated at the eastern edge of the basin are guided mainly along a relatively deep channel to the West.

Looking at the PGV distribution (Fig. 6), the largest values occur for both cases for the deeper parts of the basin. However for the wave front from the South, these values are extended from South to North. For the wave front from the East the larger values are confined to the central part of the deep western basin, where the strong surface waves that have been generated at the eastern basin edge penetrate into the deepest part of the basin.

Significant ground motion durations (Fig. 6) with maximum values of about 50 s are similar for both azimuths. However, for earthquakes in the South, large values also occur in the northern tip of the basin, which is not the case for shallow earthquakes in the East.

Fig. 7 compares spectral amplifications of both azimuths. For stations in the central part of the basin (TAP4, TAP11, TAP100) there is almost no difference between the two azimuths. Because of the generated surface waves, stations at the eastern edges of the basin (TAP96, TAP92) show larger spectral amplifications for earthquakes in the East and TAP17, located at the south-western edge, shows larger amplification for earthquakes in the South. Sokolov (pers. comm., 2008) calculated the influence of the basin for large and small events for TAP17. Additionally, he did this analysis separately for the aftershocks of the Chi-Chi earthquake, which occurred approximately south of the basin (Fig. 8). Like the modeling results (see Tap17 in Fig. 7), he found that the earthquakes of the Chi-Chi aftershock sequence produce larger amplifications than average. Our modeling suggests that this can be explained by the generation of strong surface waves at the south-western basin edge of the Taipei basin.

Discussion

In applying numerical modeling of an incident S-wave front, we were able to reproduce the observed differences of the spectral amplifications between stations in the deepest and central part of the basin and along the basin edges as well as the differences between deep and shallow earthquakes.

However, the accurate simulation of the observed amplification pattern for a certain station is a task. More simulations of different azimuths are needed in order to compare the observed spectral amplifications with the observed ones for certain stations. Furthermore, the applied simulation approach of an incident S-wave front is limited because source effects and path effects outside the basin, that may strongly depend on earthquake depth and earthquake azimuth, are neglected. These uncertainties could be avoided by simulating full wave propagation for a certain earthquake from the hypocenter to the Taipei basin. However, this approach is more computer memory and time intensive.

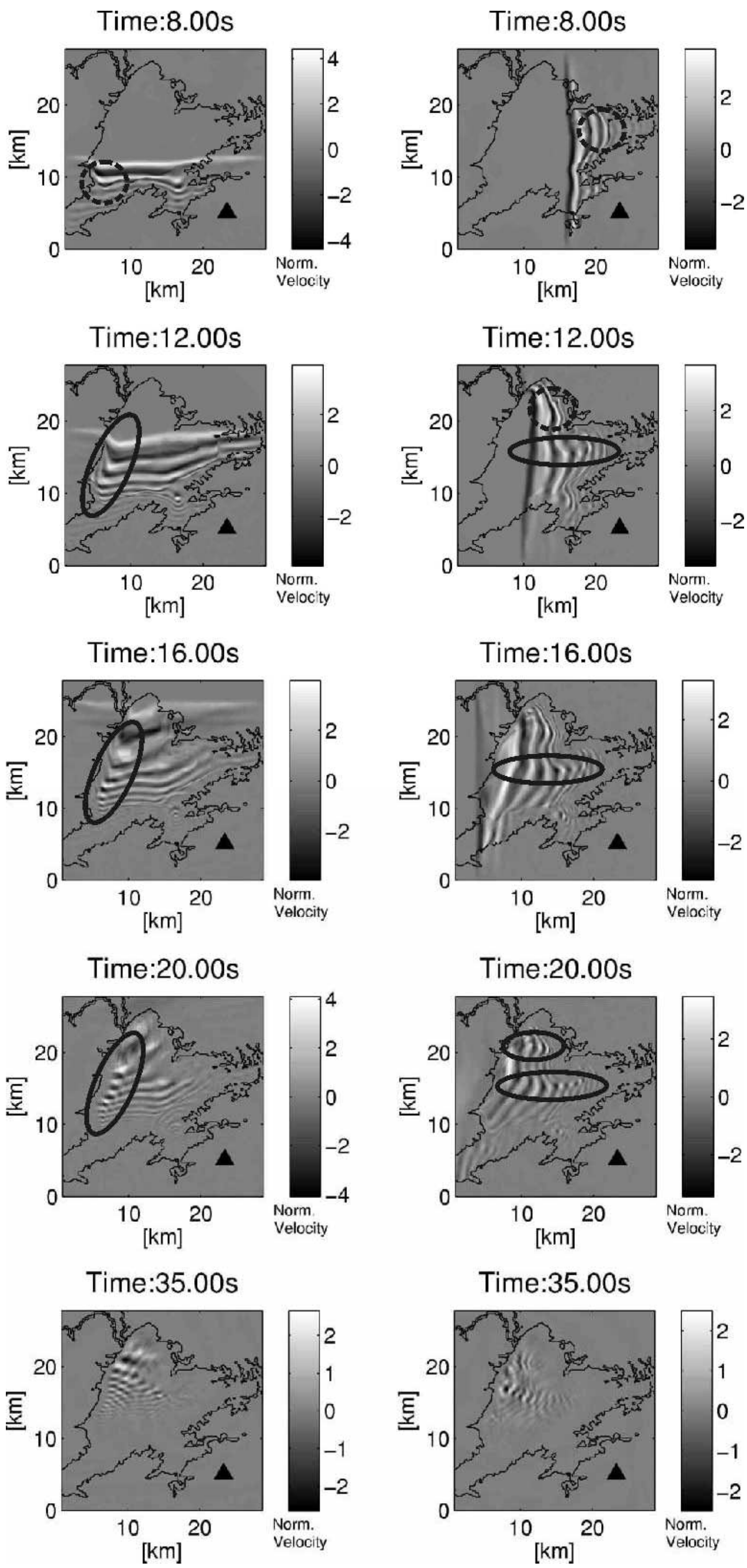

Figure 5: Snapshots of the wave field for wave incident of a shallow earthquake in the South (left column) and East (right column). Surface waves are generated in the marked areas

(dashed circles) and travel along the solid marked paths. Velocity is scaled to the PGV at the marked station outside the basin (black triangle).

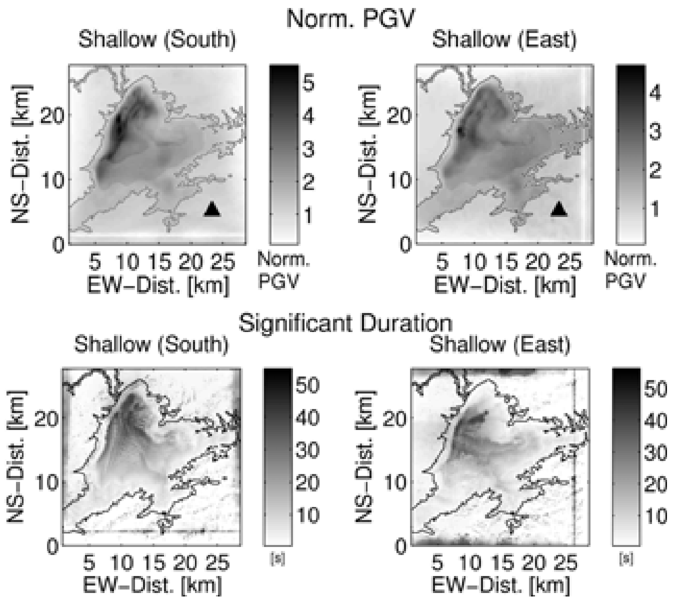

Figure 6: PGV and significant ground motion duration (time needed to increase from 5% to 95% of the Arias intensity) distributions for a planar wave front incidence from the South and East. PGV is scaled to the PGV value at a reference station outside the basin (black triangle).

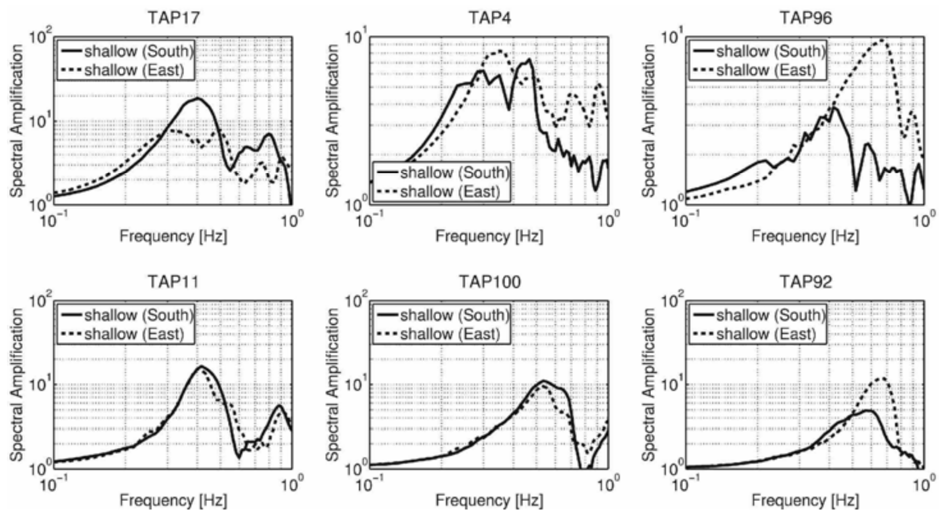

Figure 7: Modeled spectral amplification for shallow earthquakes south and east of the basin.

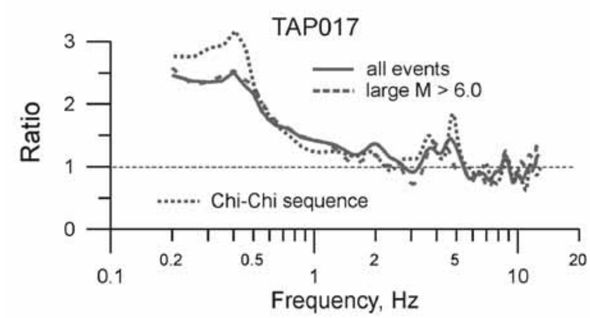

Figure 8: Basin effect for all events, large events and the Chi-Chi aftershock sequence, which occurred approximately south of the basin (Sokolov, pers. comm., 2008). As our modeling for earthquake scenarios in the South, the basin influence shows large amplifications for the Chi-Chi sequence up to 0.5 Hz.

Conclusions

By applying FD simualtions of wave propagation for an incident planar S-wave front on the Taipei basin, we reproduced spectral amplification characteristics derived from analysis of observed data (Sokolov et al, 2008, 2008b, Chen *et al.*, pers. comm., 2008). We showed, that the strong amplifications for shallow earthquakes in the low frequency range can be attributed to the generation of surface waves at the basin edges. Furthermore, the modeling underlines the strong aziumth dependence of the resulting ground motion for shallow earthquakes, which can also be seen in the analysis of the recorded data. We discussed that more modeling scenarios, especially of different azimuths, are needed in order to explore the accuracy of numerical modeling of spectral amplifications for certain stations. Our studies suggest that modeling can be useful to extend the observed data base for areas where the station network is not dense enough (e.g. in the western deep part of the basin). As high-rise buildings and high-way bridges are sensitive to the considered low frequency range, such simulations are very important.

Acknowledgements

We thank Takashi Furumura for providing is 3D Finite-Difference code. The simulations were performed on the HP XC6000 of the Scientific Super Computing Centre Karlsruhe. This research is funded by the Deutsche Forschungsgemeinschaft (DFG), Germany (project WE-1394/13-1) and the NSC (National Science Council), R.O.C (grant NSC 96-2119-M-008-007).

References

CIAT (2004). Void-filled seamless SRTM data V1, 2004, International Centre for Tropical Agriculture (CIAT), available from the *CGIAR-CSI SRTM 90m Database*: http://srtm.csi.cgiar.org.

Erdik, M. & Durukal, E. (2003). Simulation Modeling of Strong Ground Motion in Chen, W.-F. and Scawthorn (editors), *Earthquake Engineering Handbook*, CRC Press, Boca Raton, London, New York, Washington D.C.

Furumura, T., & L. Chen (2005). Parallel simulation of strong ground motions during recent and historical damaging earthquakes in Tokyo, Japan, *Parallel Comput., 31, 149–165.*

Furumura, T., B.L.N. Kennett & K. Koketsu (2003). Visualization of 3D wave propagation from the 2000 Tottori-ken Seibu, Japan, earthquake: observation and numerical simulation, *Bull. Seism. Soc. Am., 93, 870–881.*

Miksat, J., Müller, T. M. & Wenzel, F. (2008). Simulating three-dimensional seismograms in 2.5-dimensional structures by combining two-dimensional finite difference modelling and ray tracing, *Geophysical Journal International, 174(1), 309-315.*

Sokolov, V., Wen, K.-L., Miksat, J., Wenzel, F.& Chen C.-T. (2008a). Analysis of Taipei basin response on earthquakes of various depth and location using empirical data, *31st General*

Assembly of the European Seismological Commission ESC 2008, Hersonissos, Crete, Greece (submitted).

Sokolov, V., Wen, K.-L., Miksat, J., Wenzel, F.& Chen C.-T. (2008b). Analysis of Taipei basinresponse on earthquakes of various depth and location using empirical data*, Terr. Atmos. Ocean. Sci. (submitted).*

Wang C-Y, Lee Y-H, Ger M-L, & Chen Y.-L. (2004). Investigating subsurface structures and P- and S-wave velocities in the Taipei Basin*, Terr. Atmos. Ocean. Sci., 15 (4), 609–627.*

Seismic Hazard Assessment in the Western Part of the Moesian Platform - Romania

Moldovan I A (1), Popescu E (2), Constantin A (3), Cioflan C O (4)

(1) National Institute for Earth Physics,P.O.Box MG-2, 0077125, Magurele, Ilfov, Romania, iren@infp.ro
(2) National Institute for Earth Physics,P.O.Box MG-2, 0077125, Magurele, Ilfov, Romania, epopescu@infp.ro
(3) National Institute for Earth Physics,P.O.Box MG-2, 0077125, Magurele, Ilfov, Romania, angela@infp.ro
(4) National Institute for Earth Physics,P.O.Box MG-2, 0077125, Magurele, Ilfov, Romania, cioflan@infp.ro

Keywords: seismic, hazard, probabilistic, deterministic, Romania

Introduction

The seismic hazard assessment in dense-populated geographical regions and subsequently the design of the strategic objectives (dams, nuclear power plants, etc.) are based on the knowledge of the seismicity parameters of the seismogenic sources which can generate ground motion amplitudes above the minimum level considered risky at the specific site and the way the seismic waves propagate between the focus and the site.
Extremely vulnerable objectives, like large cities, hidroenergetic dams or nuclear power plants, are present all arround Romania, and not only in the Vrancea intermediate earthquakes action zone. The best example is the western part of the Moesian Platform that is affected both by Vrancea intemediate earthquakes and by the crustal sources as well. In this part of the country are cities like Drobeta Turnu Severin and Ramnicu Valcea were we can also find nuclear facilities, Craiova and Slatina and the "Portile de fier I and II" and Orsova hidroenergetic dams.
The purpose of this paper is to provide a complete set of information required for a probabilistic assessment of the seismic hazard in the Western part of the Moesian Platform - Romania (MP-R) relative to the crustal and intermediate seismic sources. The analysis that we propose implies: (1) geometrical definition of all seismic sources affecting Romania, (2) estimation of the maximum possible magnitude, (3) estimation of the frequency magnitude relationship, (4) estimation of the attenuation law and, finally, (5) computing PSH with the classical Cornell-McGuire algorithm (1976) and (6) comparing the results with the data provided by deterministic hazard studies.

Seismic Sources Characteristics

The first step in the determination of probabilistic crustal hazard consists in defining the seisogenic sources. It is necessary to point out and to delimit the seismic areas from the Romanian territory and adjacent zones that contribute to the seismic hazard values in the Western part of the MP-R. The seismogenic sources (Figure 1) that affect the studied territory are: Fagaras-Campulung-Sinaia crustal sources (CMP=FG+CP+SI), Transilvanian Depression crustal source(TD), Banat crustal source (BAN), Danubian crustal earthquakes (DAN), IBAR (Serbia) zone and Vrancea intermediate seismogenic zone.

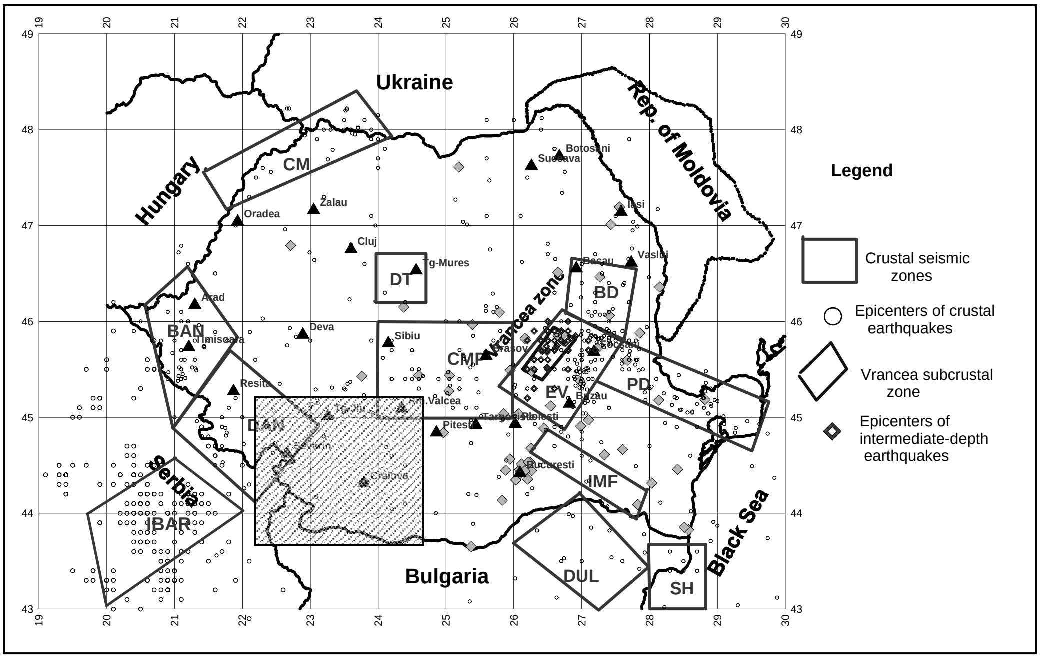

Figure 1. Seismic active zones in Romania and adjacent areas and their geometrical characteristics; the MP-R is marked with a textured square

Fagaras-Campulung-Sinaia and Transilvanian Deppression crustal sources (CMP and DT)

The sources are located in the Southern Carpathians, Romania, adjacently to the West of Vrancea seismic region and are part of the major dome uplift of the Getic Domain basement. They are bordered at Northern and Southern edges by first order crustal fractures and consist of three seismogenic zones: Fagaras zone containing Lovistea Depression and North Oltenia (FG), Campulung (CP) and Sinaia (SI) zones. The earthquake activity is related to intracrustal fractures extending from 5 to 30 km depth.

The earthquakes in this zone are generated at South, on deep fractures extending on inherited hercynian lines along NW and NE alpine origin directions and at North, throughout Transylvania, along a stepped fault system separating the Carpathian orogen from its intermountain depression. In the western part of Fagaras Mountains, the earthquakes have a typical polikinetic character, with many delayed aftershocks, especially for large events, as the one produced in 1916. Preferential centers and lines of seismicity were identified after the occurrence of the large earthquakes and the subsequent aftershock activity.

Most of the earthquakes are of low energy, but once per century a large destructive event with epicentral intensity larger than VIII is expected in Fagaras area. The last major shock occurred in January 26, 1916, Mw = 6.5, Io = VIII-IX. Fagaras seismogenic region is the second seismic source in Romania as concerns the largest observed magnitude (Mw = 6.5), after the Vrancea intermediate-depth source (with maximum magnitude Mw ~ 7.7-7.8).

The Transilvanian Depression (DT) seismogenic zone is defined only based on historical information, with the maximum reported earthquake Mw=6.5. The seismic activity at present is mostly absent.

The Crustal Sources from the Western Part of Romania

The western and southwestern territory of Romania is the most important region of the country as concerns the seismic hazard determined by crustal earthquakes sources. The seismic risk in the region is also very high due to the local risk factors and vulnerabilities: weak dwellings, old and unprotected buildings in the large cities, dams and chemical factories, high density of localities, great towns, and so on.

The seismogenic Danubian zone (DA) represents the western extremity, adjacent to the Danube river, of the orogenic unit of the Southern Carpathians. The rate of seismic activity is

relatively high, especially at the border and beyond the border with Serbia, across the Danube river. The magnitude does not exceed 5.6.
The fault plane solutions are available for three earthquakes (the largest earthquake M_w=5.6 occurred in July 18, 1991) and indicate normal faulting with the T axis striking roughly N-S, in agreement with the general extensional stress regime in the Southern Carpathians.
The contact between the Panonnian Depression and the Carpathian orogen lies entirely along the western part of the Romanian border. Even if no significant tectonic or geostructural differences are noticed, two enhancements in the seismicity distribution can be identified in two relatively distinct active areas: Banat zone (BA) to the south, and Crisana-Maramures zone (CM) to the north.
The seismicity of the Banat zone is characterized by many earthquakes with magnitude M_w>5, but not exceeding 5.6. The largest earthquake occurred after 1900 is the one from July 12, 1991 (Mw=5.6). Historical information suggests potential earthquakes greater than 6 in Crisana-Maramures, but only one event approaching magnitude 5 was reported in this century. The largest reported earthquake was Mw=6.5 on October 15, 1834.
The Serbian seismogenic source named IBAR (Musson, R. 2000) is characterised by the occurrence of numerous crustal earthquakes with Mw>5.0. The largest earthquake occurred in the zone on April 08, 1893, has the magnitude Ms=6.6 (Shebalin, N. V 1998).

Vrancea Intermediate Sources

The geometry of the Vrancea subcrustal source together with the epicentral distribution of the earthquakes with Mw> 5.0 occurred between January 1900 and June 2008 (225 events) are plotted in Figure 1. To define the source geometry, only earthquakes occurred after 1950 were considered, for which more complete instrumental information is available. The location coordinates and magnitudes are taken from the Romanian catalog (Oncescu et al., 1999). The average annual number of earthquakes with magnitude greater than 5 is 1.78 earthquakes/year. The maximum magnitude instrumentally determined for Vrancea earthquakes is Mw = 7.7 (MGR=7.5), associated to the major earthquake of 10 November 1940. The largest magnitude in the Romanian catalog Romplus (Oncescu et al., 1999) is Mw = 7.9 (MGR=7.7) for the earthquake of 1802. We consider this value as the maximum possible magnitude for the Vrancea region with errors of the order of 0.1

The Frequency-Magnitude Distribution For The Defined Sources

The frequency-magnitude distribution for Fagaras-Campulung-Sinaia crustal source regions for a magnitude interval [5.0, 6.5], leads to equation (1) and for a magnitude interval [4.0, 6.5] leads to equation (2) and the distributions are both plotted in Figure 2:

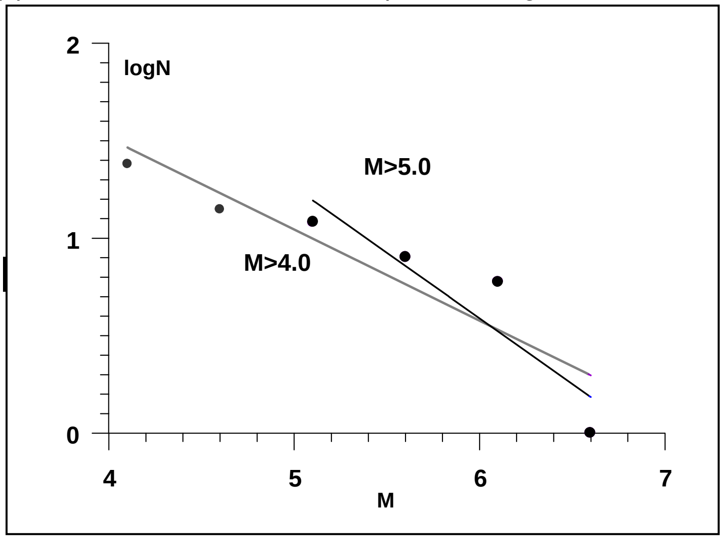

Figure 2. The frequency-magnitude distribution for Fagaras-Campulung-Sinaia crustal sources, for 2 sets of data

$$lg\ N_{cum} = -(0.67 \pm 0.21)M_w + (4.62 \pm 0.26) \quad (1)$$

with the correlation coefficient $R = 0.91$ and the standard deviation $\sigma = 0.24$ and

$$lg\ N_{cum} = -(0.47 \pm 0.1)M_w + (3.38 \pm 0.56) \quad (2)$$

with the correlation coefficient $R = 0.91$ and the standard deviation $\sigma = 0.21$.

Banat region on the magnitude interval [4.0, 5.6], for the entire time interval of the catalogue (equation 3) and after 1900 (equation 4):

$$lg\ N_{cum} =- (0.82 \pm 0.08)M_w + (4.73 \pm 0.38) \quad (3)$$

with the correlation coefficient $R = 0.98$ and the $\sigma = 0.12$.

$$lg\ N_{cum} =- (0.74 \pm 0.06)M_w + (4.31 \pm 0.27) \quad (4)$$

with the correlation coefficient $R = 0.99$ and the $\sigma = 0.09$.
Danubian crustal earthquakes was determined for magnitudes between [4.0, 5.6] for two time intervals. One for the whole catalogue of earthquakes (equation 5) and the other for the earthquakes occurred after 1900:

$$lg\ Ncum = -(0.82\pm 0.09)M_w + (4.94 \pm 0.46) \quad (5)$$

with $R = 0.97$ and $\sigma = 0.15$.

$$lg\ Ncum = -(0.62\pm 0.06)M_w + (3.74 \pm 0.31) \quad (6)$$

with $R = 0.98$ and $\sigma = 0.10$.
The noncumulative and cumulative distributions are plotted in Figure 3, for both time intervals and regions.

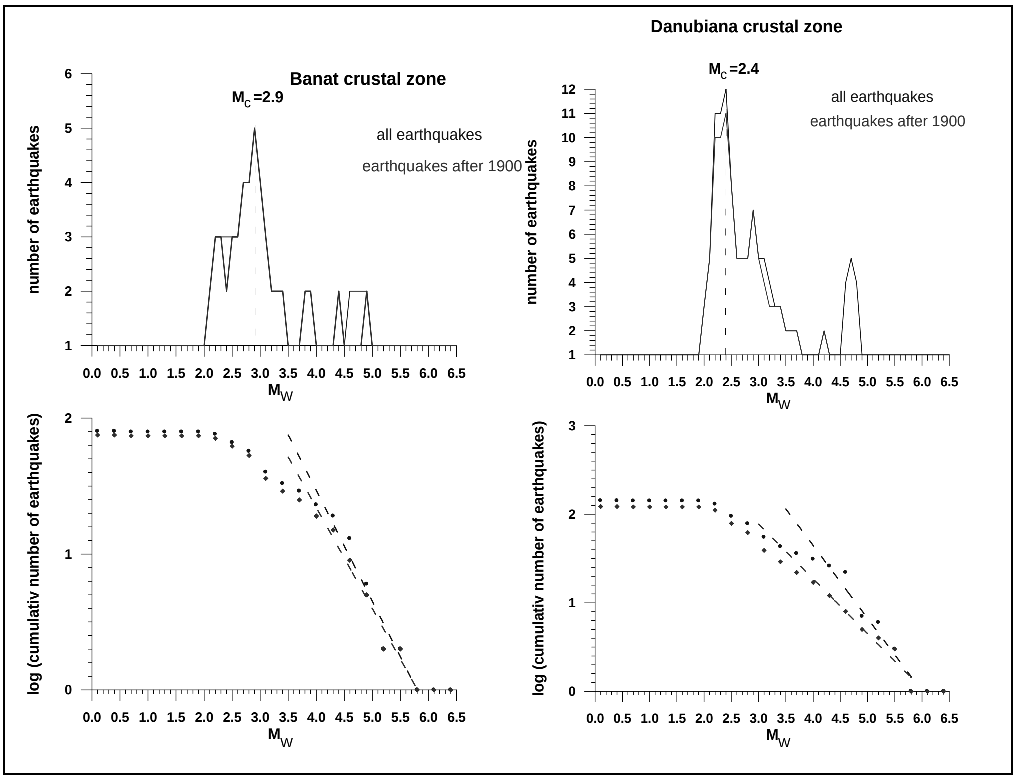

Figure 3. Noncumulative and cumulative relation for Banat and Danuabian crustal sources

The frequency-magnitude distribution for the Serbian seismogenic source named IBAR is estimated for the magnitude interval [3.7, 6.6] in equation 7 and for the intensity interval [4.5,9.0] in equation 8

$$lg\ N_{cum} = -(0.87 \pm 0.03)Ms + (5.68 \pm 0.18) \qquad (7)$$

with $R = 0.99$ and $\sigma = 0.11$,

$$lg\ N_{cum} = -(0.50 \pm 0.03)Io + (4.82 \pm 0.19) \qquad (8)$$

with $R = 0.98$ and $\sigma = 0.18$, and are both plotted in Figure 4.

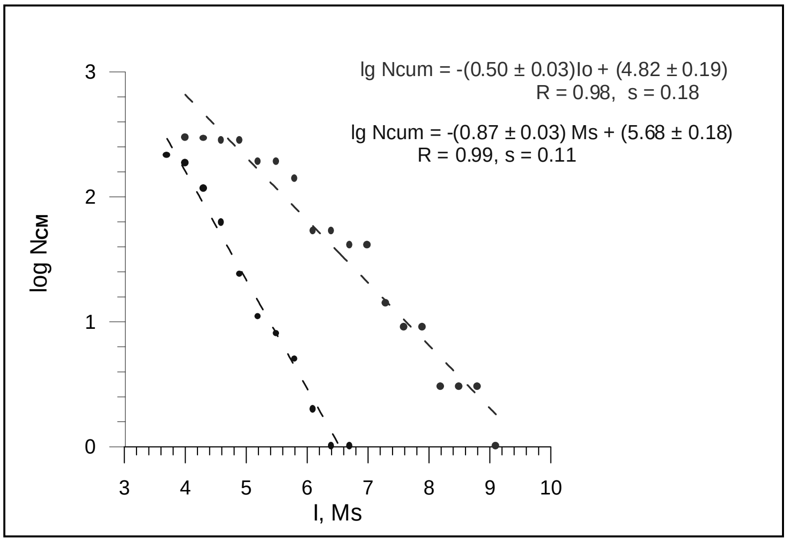

Figure 4. The frequency-magnitude distribution for IBAR zone.

The frequency-magnitude distribution for Vrancea subcrustal region is estimated on the magnitude interval [5.0, 7.7]. The distribution is plotted in Figure 5. The equation of the regression line is: log Ncum = (-0.83 ± 0.03) MW + (6.47 ± 0.18) with the correlation coefficient R = 0.99 and the standard deviation 0.07.

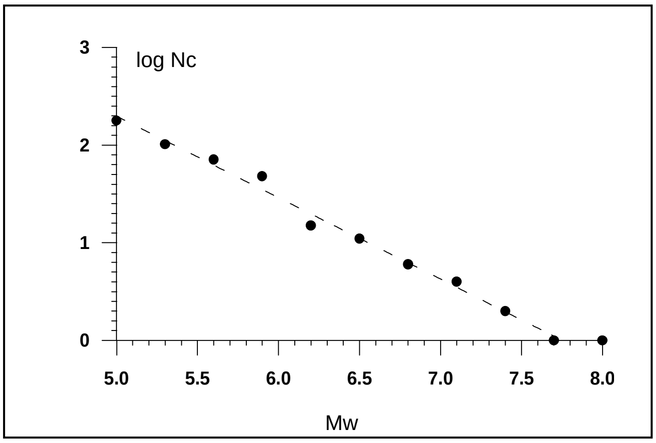

Figure 5. The frequency-magnitude distribution for Vrancea zone.

In Table 1 are presented the characteristics of each source that will be used in the seismic hazard assessment. In the table the Fagaras-Campulung-Sinaia zone have been divided in 3 subzones: FG, CP and SI. The βi value has been computed from the intensity - frequency distribution, using the formula from the following equation: $\beta_i = b \ln 10$.

Table 1. Input parameters for probabilistic hazard assessment using crustal and subcrustal sources

Seismic sources	Coordinates	**h**	Mmin	Mmax	b	Imin	Imax	bi	βi	Activity rate
VRI	26.00/45.50-26.45/45.25 26.43/46.10-27.10/45.87	200	4.0	7.4	0.75	4.0	10.5	0.49	1.10524	1.762380
FG	24.10/45.40-24.60/45.15 24.10/45.90-24.80/45.60	15	4.0	6.5	0.76	5.0	8.5	0.50	1.15325	0.247403
CP	24.95/45.00-25.30/45.10 24.95/45.50-25.30/45.50	15	4.0	5.0	0.66	5.0	6.0	0.44	1.01820	0.0865384
TD	23.50/46.00-24.50/46.10 23.50/46.90-24.50/46.90	10	4.0	6.5	0.89	5.0	7.0	0.59	1.36774	0.010254
SI	25.05/45.70-25.50/45.40 25.20/45.80-25.50/45.60	15	4.0	4.9	0.65	4.5	6.0	0.43	0.98781	0.076923
DAN	21.00/44.90- 22.30/44.15 21.80/45.70- 23.00/44.80	15	4.0	5.6	0.71	5.5	9.0	0.43	0.98091	0.276700
BAN	21.00/44.90- 21.90/45.80 20.70/4610- 21.30/46.40	10	4.0	5.6	0.82	5.5	9.0	0.50	1.16056	0.128800
IBAR	19.80/44.00- 20.80/44.60 21.00/43.10- 21.80/43.80	14	3.7	6.6	0.87	4.5	9.0	0.54	1.24340	0.556203

Attenuation Laws

It is essential, for a probabilistic estimation of the seismic hazard, to constrain as much as possible how the energy of the seismic waves attenuates when propagating from the source to the site. The attenuation law for the crustal sources is given in the equation 9:

$$I = Io - c_1 \,.\, \log(D_h/h) - c_2 \,.\, \alpha.\log(e).(D_h - h); \qquad (9)$$

where: c_1, c_2 and a are different for each region; $log\ (e)$=0.006514; D_h is the hypocentral distance, and h is the depth presented, for each seismic source, in Table 1.
For Fagaras-Campulung-Sinaia and Transilvanian Deppression zones we have used: c_1=3.46, c_2=3.12 and a = 0.0013 (1/m).
For the active zones from the southern and western part of Romania (BA and DA) and from Serbia (IBAR) we have used the attenuation law equation 10 obtained by Zsiros, 1996, with c_1=3.0, c_2=3.0 and α =0.0015 (1/m).

$$I = I_0 - 3.0 \log(D_h/h) - 3.0\, \alpha\ \log(e).(D_h - h) \qquad (10)$$

For the Vrancea subcrustal focus Southeastern Romania path, we adopt the attenuation relation for intensity and acceleration proposed by Moldovan I.A. 2000 and 2007.

Seismic Hazard Assessment

For the input data set obtained in the present work, we applied the algorithm of McGuire, 1976 to compute the seismic hazard map of Romania in the case of crustal and intermediate earthquakes. We present, in Figures 6, the hazard maps in terms of macroseismic intensities for different return periods of 50, 100, 150 and 500 years and in Figures 7 the hazard maps for 475 years period and two intensities (I=VIII and I=IX) for the zone represented in Figure 1 with a diagonal pattern marked square.

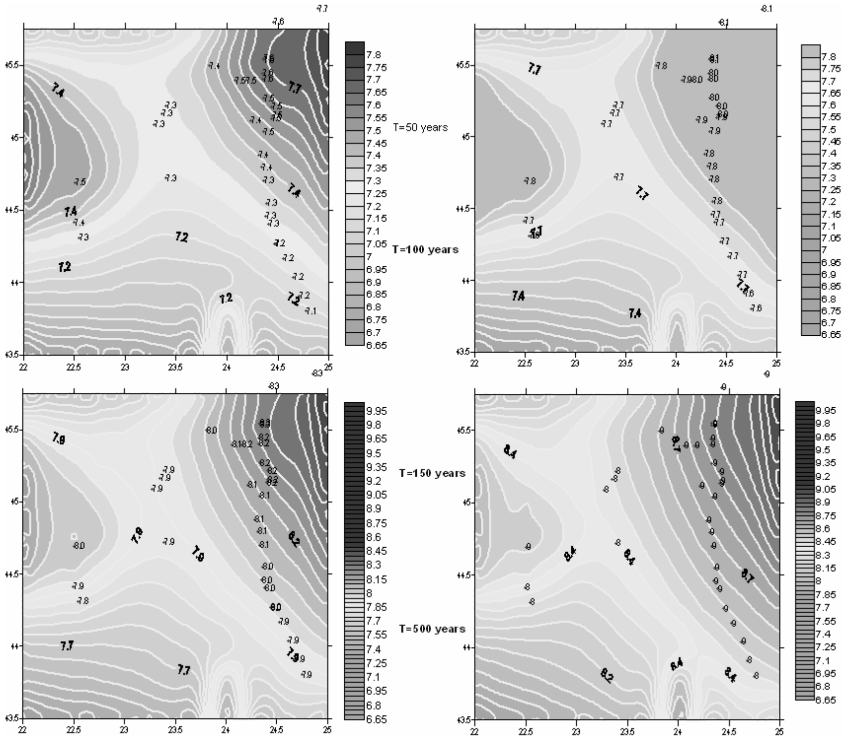

Figures 6

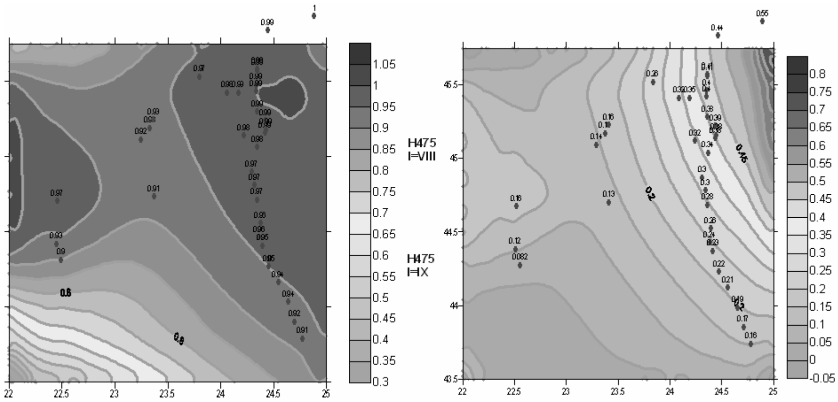

Figures 7

Results and Discussion

The hazard values are in good agreement with the deterministic approach. If we compare our results for the case for 50 years return period with the computed intensities (converted from the peak ground displacement, velocity or acceleration) obtained by Radulian et al. (2000 and 2002) using the deterministic approach, the differences are not exceeding 0.2 degrees in intensity (that is less than 0.5 - the minimum measuring unit for intensities).
We see that all the input parameters are directly related to the hazard pattern, as expected, and each of them is a crucial parameter in the seismic hazard probabilistic approach.
This work is a useful tool for the assessment of the seismic risk and implementation of antiseismic protection measures in the case of special constructions and strategic objectives, such as, nuclear power plants and other nuclear facilities, large cities and hydroenergetic large constructions.

References

McGuire R.K (1976). "EQRISK-Evaluation of Earthquake Risk to Sites," United States Department of the Interior, *USGS, Open File Report No. 76-67*.

Moldovan I.A., Enescu B.D., Ionescu C. (2000). Predicting peak ground horizontal acceleration for Vrancea large earthquakes using attenuation relations for moderate shoks, *Romanian Journal of Physics, 45, 9-10,785-800.*

Moldovan I.A.(2007). Statistical Methods and Models in Seismology with applications in the Complex Study of Earthquakes, *Morosan Publishing House, Romania, 236p.*

Musson R.M.W. (2000). Generalised seismic hazard maps for the Pannonian Basin using probabilistic methods, *Pure Appl. Geophys., 157, 147-169.*

Oncescu M. C., Marza V. I., Rizescu M., Popa M. (1999). The Romanian eartquake catalogue between 984-1997. Vrancea Earthquakes: Tectonics, Hazard and Risk Mitigation, F. Wenzel, D. Lungu (eds) & O. Novak (coed.), *Kluwer Academic Publishers, Dordrecht, Netherlands, 43-47.*

Radulian M., Vaccari F., Mandrescu N., Panza G. F.& Moldoveanu C. (2000). Seismic Hazard of the Circum-Pannonian Region, eds. G. F. Panza, M. Radulian, C.-I. Trifu, *Pure Appl. Geophys. 157, 221-247.*

Radulian M., Vaccari F., Mandrescu N., Moldoveanu C.L. & Panza G.F. (2002). Seismic hazard in Romania associated to Vrancea subcrustal source: deterministic evaluation, *Preprint ICTP IC/2002/131, Trieste, 24p.*

Shebalin N. V., Leydecker G., Mokrushina N. G., Tatevossian R. E., Erteleva O. O. & Vassiliev V. Yu.(1998). Earthquake Catalogue for Central and Southeastern Europe 342 BC - 1990 AD. *European Commission, Report No. ETNU CT 93 - 0087, Brussels.*

Zsiros T. (1996). Macroseismic focal depth and intensity attenuation in the Carpathian Region. *Acta Geod. Geophys. Hung., 31 (1-2),115-125.*

Vs^{30} Structure of Lorca town (SE Spain) from Ambient Noise Array Observations

Navarro M (1), García-Jerez JA (1), Alcalá FJ (2), Vidal F (3), Enomoto T(4), Luzón F (1), Creus C (5)

(1) Depart. of Applied Physics, University of Almeria, Almeria, Spain, mnavarro@ual.es, agj574@ual.es, fluzon@ual.es
(2) Estación Experimental de Zonas Áridas, CSIC, 04001 Almería, Spain, fjalcala@eeza.csic.es
(3) Andalusian Institute of Geophysics, University of Granada, Granada, Spain, fvidal@iag.ugr.es,
(4) Depart. of Building Engineering, University of Kanagawa, Yokohama, Japan, enomot01@kanagawa-u.ac.jp
(5) Open University of Catalunya, Barcelona, Spain, ccreus@uoc.edu

Keywords: soil classification, ambient noise, SPAC method, Rayleigh waves, Shear velocity profile.

Introduction

Lorca town is located in Murcia province (South-Eastern Spain), which is a zone with low to moderate seismicity in the Iberian Peninsula context (Vidal, 1986; Buforn et al., 2005). Three recent shocks occurred in the region (Mula, 1999, Bullas 2002 and La Paca, 2005), with magnitudes around 5 and macroseismic intensity VI-VII (EMS) in the epicentral area, have shown the special relevance of site effects in order to explain both the ground motion amplification caused by surface geology and the degree of building destruction and its spatial distribution (Navarro et al., 2000; Benito et al., 2006).

The evaluation of local site effect based on subsurface ground conditions is very important to accurately define seismic hazard for a city. The softness of the surface ground and the thickness of surface sediments have been observed as two important local geological factors that affect the level of earthquake shaking. Since the NEHRP classification in 1994, the mean shear wave velocity in the first 30 m (V_S^{30}) has been adopted as a representative site characteristic in several seismic codes (NCSE-02; Eurocode-8 (EC8)). This criterion is appropriated and widely used in building code applications (Dobry et al, 2000) and also for regional soil classification for seismic site effect evaluation (Alcalá et al., 2002; Ismet et al., 2006).

The relation between surface wave dispersion curves and elastic parameters of the ground has been extensively used in geophysical prospecting, using earthquakes or controlled sources for derivation of 1-D layered ground models (e.g. Nazarian, 1984; Navarro et al., 1997; Tokimatsu, 1997; Park et al., 1999). The capability of the spatial autocorrelation method for ambient noise analysis (SPAC method), based on the early work of Aki (1957) and reinterpreted by Henstridge (1979), for determining the elastic properties of shallow sedimentary deposits has been proved as an innovative and convenient technique for this kind of studies (e.g. Parolai et al., 2005; García-Jerez et al., 2007a; 2008).

The main goal of this study is to estimate the local site effect in Lorca town applicable to seismic risk management, performing a seismic-geotechnical classification of surface materials and obtaining a correlation between each type of shallow structure and its average shear-wave velocity.

Materials and Methods

Tectonic setting and Geological shallow structure estimate

Lorca town is located at the south-west of Murcia province (SE Spain), belonging to the eastern part of the Betic Cordillera (Figure 1). This is an alpine chain classically divided into two main domains: the Internal and the External Betic Zones. The first domain may be divided into three tectonic complexes: the Nevado–Filabride Complex, which does not outcrop in the vicinity of Lorca town; the Alpujarride Complex, which overlies the Nevado–Filabride Complex and consists of low to medium grade metamorphic rocks; and the Malaguide Complex, the upper and mainly unmetamorphosed complex (Egeler et al., 1969; Sanz de Galdeano et al., 1995). The external zone comprises highly deformed (thrusted and folded) Mesozoic and Paleogene marine sediments deposited along the former Iberian continental paleomargin. It can also be divided into two units: the Prebetic is composed by shallow marine platform deposits and the Subbetic by deep continental talus and pelagic sediments (García-Hernández et al., 1980).

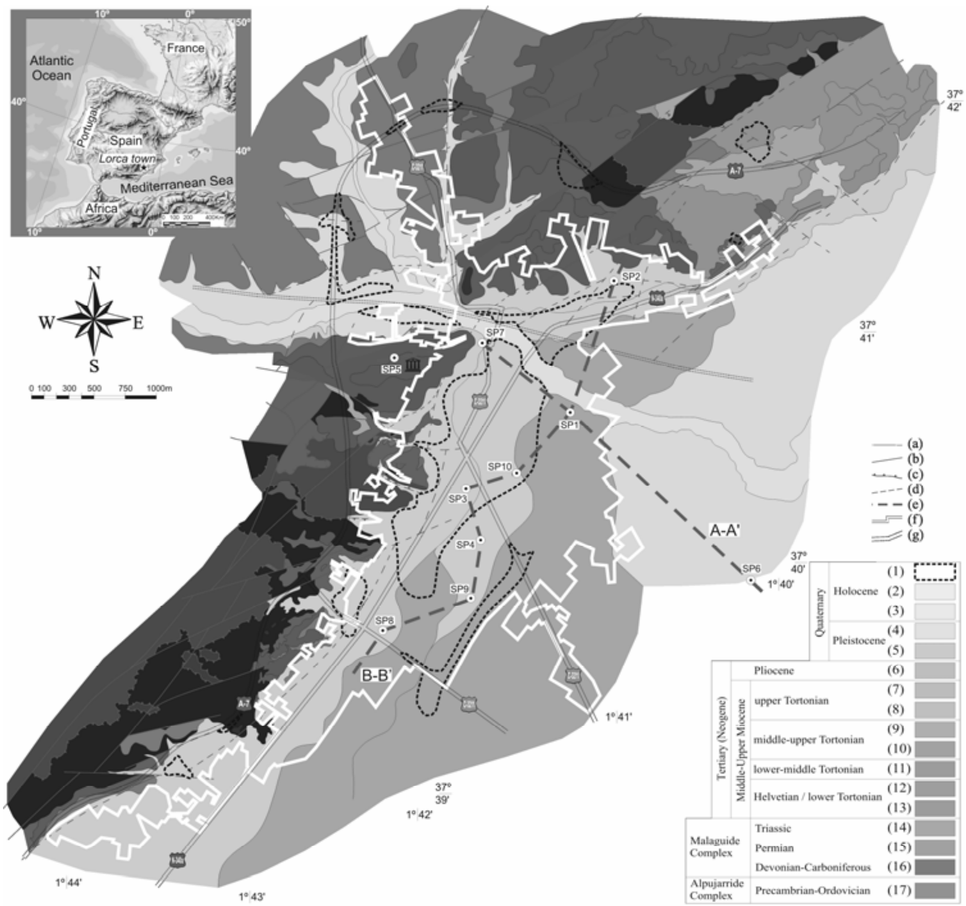

Figure 1. Geographical and geological sketches of Lorca town, scale 1:10.000. Urban boundary (white bold line) and anthropogenic filling (encircled by dashed black lines) are superimposed. A legend for the soil classification types is shown in the right lower corner as: 1 Anthropogenic fillings, 2 Alluvial terraces, 3 Colluvials, 4 Glacis III, 5 Glacis II, 6 Glacis I, 7 Sandy marls and breccias, 8 Gypsum and marls, 9 Marls, 10 Brecias and marls, 11 Conglomerates, sandstone and marls, 12 Marls, gypsum and sandstone, 13 Poligenic conglomerates, 14 Dolomitic limestone, 15 Red clays, slates and quartzites, 16 Phyllities, schists and quarzites, 17 Schists, phyllites and quartzites. (a) undifferentiated geological contact; (b) normal fault; (c) thrust fault; (d) inferred fault; (e) seismic cross-sections along

lines A-A' and B-B'; (f) superimposed urban boundary; (g) main roads. Array locations have been labelled from SP1 to SP10.

The Plio–Quaternary sedimentary record of Lorca town has been divided into 17 types of lithologies (Figure 1) grouped into 3 main geomorphological groups with different geotechnical and geophysical behaviour: i) Palaezoic to Triassic pre–orogenic hardest bedrock (including schists, phyllites, quartzites, dolomitic limestone); ii) lower to upper Tortonian post–orogenic hard bedrock (including conglomerates, marls, gypsum and sandstones); iii) Pliocene to Holocene sedimentary filling (including glacis, colluvial, alluvial and fillings).

The classification of shallow urban geology of Lorca town and their geometry was based on its geological cartography, geotechnical data and geophysical surveys on the different types of soils overlaying the two types of bedrock. The in situ geological recognition and the study of 37 N–SPT (Standard Penetration Test) values from 21 mechanical drillings performed in different locations let us draw up the urban geological map of Lorca at scale 1:10.000 (Figure 1). Data from other 19 mechanical drillings were also used to complement the subsurface geological information. Thickness of sedimentary materials has been obtained through the interpretation of 27 electrical geophysical tests performed by IGME (1992). The basement (including medium-hard and hard bedrock) was prospected around 30 m deep in the centre of Lorca town increasing depth to more than 100 m at southeast of the town. A set of faults linked to the Alhama de Murcia Fault System deepens the basin in this southeast direction.

Geotechnical and geological information has been complemented with very shallow refraction profiles (average 15 m deep) performed by the IGME (1992) in Lorca town. Four main groups of materials with different seismic behaviour were found: i) a shallowest layer of materials including alluvial, colluvial, anthropogenic fillings and cropland showing V_S between 150 and 350 m/sec; ii) a succession of three Pliocene and Pleistocene glacis generation with V_S between 300 and 500 m/sec; iii) a set of medium-hard bedrock Tortonian materials showing V_S between 500 and 800 m/sec; iv) a set of hard bedrock pre–Triassic materials with V_S from 700 to more than 1000 m/sec.

Rayleigh-wave phase velocities

The shallow structure of Lorca town has been studied using a Spatial Autocorrelation method (SPAC). The measurements were carried out at ten open spaces (Figure 1), obtaining Shear-wave velocity profiles by means of inversion from the Rg-wave dispersion curves.

Vertical components of soil motion, excited by ambient noise, were recorded using circular-shaped arrays. Five high sensitivity VSE-15D sensors surrounding a sixth central sensor with same characteristics and a SPC-35 digitizer have been used. The radii ranged from 3 m to 42 m at each point. We used different radii depending on the expected thickness of sediments and on the available space dimension. Recording time was 30 minutes, and the signal was sampled with a rate of 100 samples per second. These devices provide an acceptable response for frequencies ranging from 0.25 to 70 Hz. All records have been analysed by using an implementation of the SPAC method (Aki, 1957). In order to obtain the correlation coefficient ρ(f,R), the cross correlations between records on the circle and the central station were calculated in frequency domain. Then, the azimuthal average was divided by the autocorrelation at the central station. Finally, phase-velocity of the Rg-wave c(f) was computed for each frequency f (Figure 2) using equation (1), and applying a polynomical fit of the ρ vs. f relation.

$$\rho(f,R) = J_0\left(\frac{2\pi f}{c(f)}R\right) \tag{1}$$

where J_0 represents the zero-order Bessel function and R is the radius of the array.

The frequencies of the obtained curves ranged from 2.6 to 24.0 Hz and the phase velocity values varied between 184 and 750 m/sec. In general, a good agreement was obtained between the Rg dispersion curve shapes and the geological conditions of each site in spite of the sharp variations between adjacent geological formations.

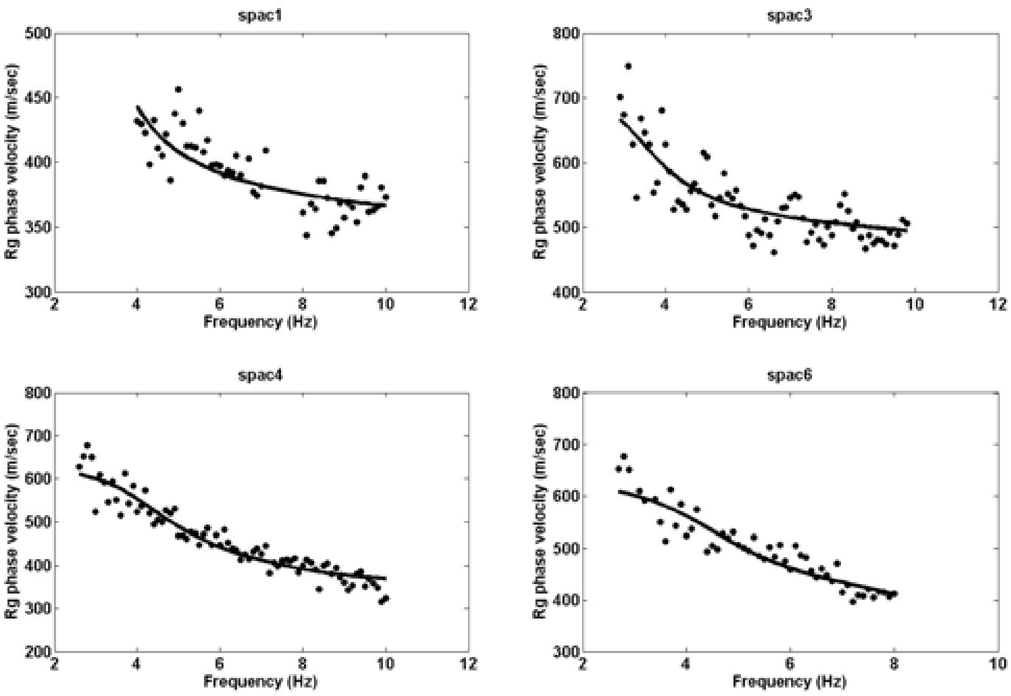

Figure 2. Some examples of Rg-wave phase velocities (black points) measured at different places (see Figure 1). Solid lines represent the fundamental-mode Rg dispersion curves corresponding to the 1D ground models obtained from the inversion process.

Shear-wave velocities

We have inverted Rg-wave phase velocities in order to obtain shear-wave velocities. As it is well known, most of iterative inversion methods require building up a proper initial ground model. Since we had serious uncertainties on the thickness or the stiffness of some sedimentary bodies in Lorca town, and in order to minimize the dependence on the initial model, a hybrid inversion scheme has been carried out in this work. It consists of a simple random search combined with a local optimization algorithm (Simplex-Downhill method), resulting in significant performance improvements. A parallelized implementation of this algorithm has been applied (García Jerez et al., 2007b) in order to deal with the computational cost. A master processor generates a random set of 100 initial models inside defined ranges of the ground parameters, obtained from the previous geological and geotechnical data, and distributes them to the cluster. Then, 100 iterations using the local optimization algorithm around such models were carried out by the other CPUs.

Because of the important differences among the dispersion curves, both in frequency and in phase velocities, the number of layers and the ranges for thicknesses and shear velocities were different for each site (Figure 3). Shear-wave velocity profiles obtained are shown in Figure 4 for depths from 0 to 70 m.

Finally, the average shear-wave velocity of the upper 30 m (V_S^{30}) can be computed in accordance with the following expression:

$$V_S = \frac{30}{\sum_{i=1}^{N} \frac{h_i}{v_i}} \qquad (2)$$

Where h_i and v_i denote the thickness (in meters) and shear-wave velocity of the i-th layer respectively, in a total of N, existing in the top 30 m.
The lowest values found for V_S^{30} were 327 and 334 m/sec, corresponding to the arrays SP9 and SP10 (Figure 1), located on Pliocene to Pleistocene consolidated sedimentary filling (Glacis III and Glacis II respectively). The highest value of V_S^{30} was 536 m/sec, corresponding to the array SP7, which is located into an area containing Pliocene Glacis I and lower to upper Tortonian post–orogenic medium hard bedrock, including conglomerates, marls, gypsum and sandstones.

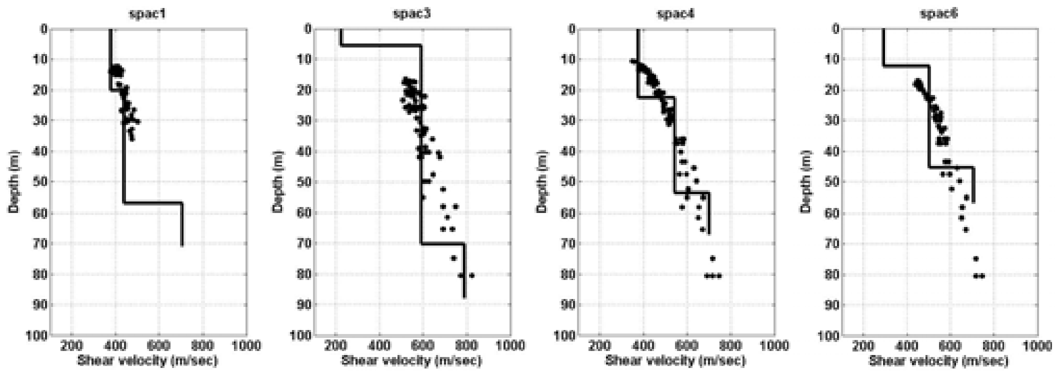

Figure 3. Some examples of Shear-wave velocity models derived from inversion of phase velocities in different places of Lorca town. Black points represent the S-wave velocity values obtained from the λ/3 criterion (Tokimatsu, 1997).

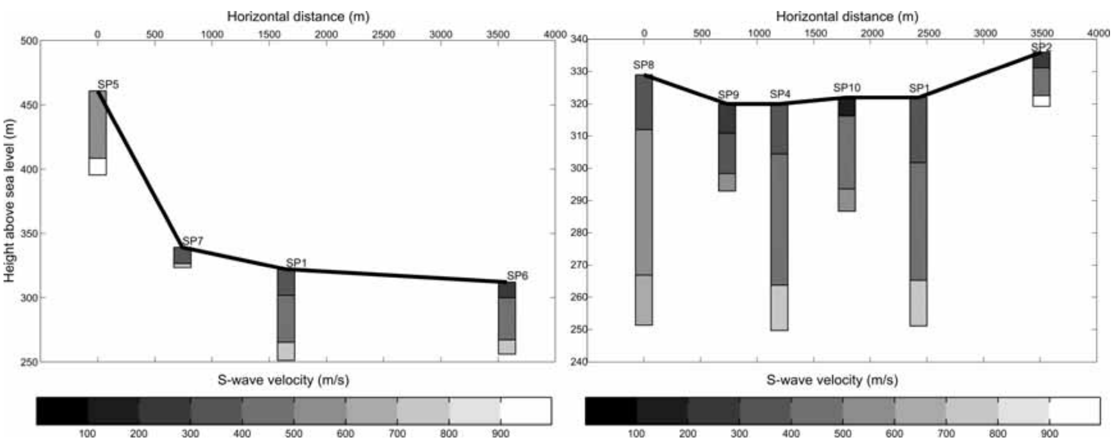

Figure 4. Shear-wave velocity models derived from inversion of Rg-wave phase velocity dispersion curves. (a) Seismic cross-section along line A-A'. (b) Seismic cross-section along line B-B'. Locations of the arrays are shown in Figure 1.

Results and Discussion

The geological record existing in Lorca town has been firstly classified into 17 lithological types (Figure 1) and after grouped into 4 main geomorphological formations (Figure 5), following geological criteria and geotechnical properties of materials. Seismic surveys and electrical and geotechnical prospecting provided valuable data for each geological formation, mainly those regarding their seismic behaviour. Direct measures of S-wave velocity at the first 30 m (V_S^{30}) obtained by means of SPAC surveys were used for characterization of the geological formations in terms of seismic response.

The first formation (geological materials 1 to 3 in Figure 1) consists of a shallow layer of Holocene unconsolidated sedimentary filling (including colluvials, alluvials and fillings) with V_S

values in the range of 180–380 m/sec and thickness between 1-5 m in the border of the town and up to 20 m at its southern part. These materials are classified as C by the EC8. Nevertheless, cropland and anthropogenic fillings with V_S around 180 m/sec and N-value lower than 15 could be classified as D ground class, according with the EC8.

The second formation (geological materials 4 to 6 in Figure 1) consists of Pliocene to Pleistocene consolidated sedimentary filling (including three generations of glacis and dispersed colluvials) with V_S ranging from 340 to 580 m/sec and thickness up to 50 m at the centre of the town. While the more extended Pleistocene glacis has a V_S around or slightly smaller than 500 m/sec, the more restricted and deep Pliocene glacis have V_S slightly greater than 500 m/sec. These materials are classified as B ground class by the EC8.

The third seismic formation (geological materials 7 to 13 in Figure 1) consists of a lower to upper Tortonian post–orogenic medium hard rock (including conglomerates, marls, gypsum and sandstones) with V_S values in the range of 660–800 m/sec and dispersed outcrops at north and northwest of the town. These materials are equally classified as B ground class by the EC8.

The fourth seismic formation (geological materials 14 to 17 in Figure 1) is a Palaezoic to Triassic pre–orogenic hardest metamorphosed bedrock (including schists, phyllites, quartzites and dolomitic limestone from the Alpujárride and Maláguide Complexes) with V_S values from 800 to more than 1000 m/sec. They are equally classified as A ground class materials by the EC8.

The depth of basement (including medium-hard and hard bedrock) was prospected from 50 m at the centre and southern part of Lorca town and to less than 10 m at northern and northwestern part of the town with different seismic response depending on the medium-hard and hard bedrock. The increment on sediment thickness towards the Guadalentín River Basin is favoured along the ENE–WSW direction active Alhama de Murcia Faults System.

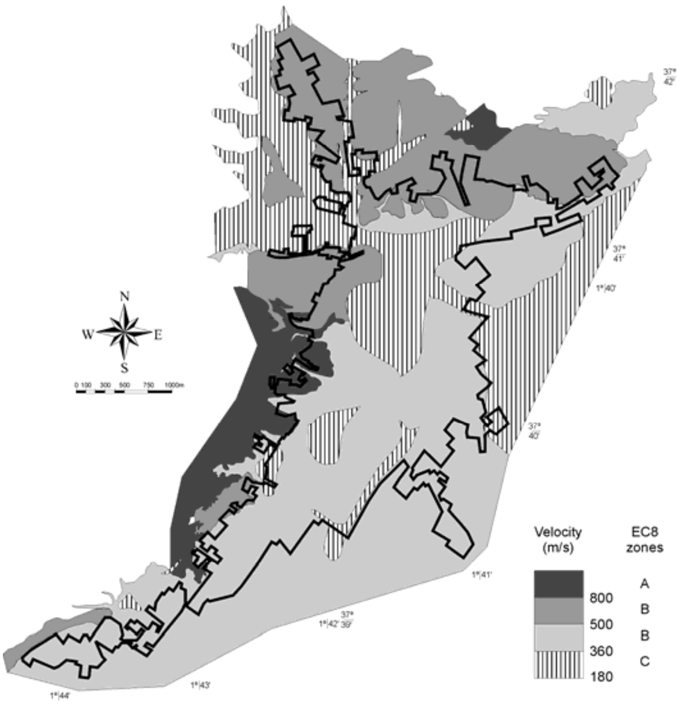

Figure 5. Soil classification map of Lorca town, according with EC8, based on the average shear-wave velocity distribution down to 30 m (V_S^{30}). Urban boundary is represented by a black bold line.

Conclusions

A ground classification of the shallow urban structures of Lorca town at scale 1:10.000 and their geometry has been performed on the basis of geological cartography, geotechnical data and geophysical surveys oriented to estimate ground motion amplification factors of different sites.

Detailed shear-wave velocity structure and depth of the basement at ten representative sites have been estimated by means of inversion of Rayleigh-wave dispersion data obtained from circular-shaped array records. The sites have been classified according to their seismic amplification capacity by means their average shear-wave velocity of the upper 30 m. The comparison of the inverted seismic velocities, which characterize each one of the urban zones of Lorca town, reveals a strong lateral variation in velocity. Finally, good agreement was found between shear-velocity models and subsurface soil conditions observed with other exploration methods.

A microzonation of ground conditions of Lorca town has been finally obtained according with EC8 soil classification. The more extended EC8 soil class is B. Urban zones with soil class B has been here subclassified in two new ones: very dense soil (500-800 m/sec) and stiff soil (360-500 m/sec), respectively, being more profuse the second one. An important area of the Lorca town is over soil class C (Soft soil). The city is growing towards areas of soil types B and C.

The results make possible to estimate the local site effect in Lorca town (Murcia, Spain), applicable to microzonation and seismic risk management purposes.

Acknowledgements

The authors gratefully acknowledge the help provided by the Civil Protection Staff of Lorca´s city and several members of Andalusian Institute of Geophysics during the geophysical surveys. This research was supported by the CICYT coordinate projects: REN2003-08159-C02-01-02, CGL2005-05500-C02-02/BTE and CGL2007-66745-C02-01-02/BTE. The third author is also grateful to the Ministry of Education and Science of Spain for a "Juan de la Cierva" Programme Contract (JCI–2007–334).

References

Alcalá-García F.J., Espinosa J., Navarro M. & Sánchez F.J (2002). Propuesta de división geológica regional de la localidad de Adra (provincia de Almería). Aplicación a la zonación sísmica, Rev. Soc. Geol. España, 15, 55-66.

Aki K. (1957). Space and time spectra of stationary stochastic waves, with special reference to microtremors, *Bulletin of the Earthquake Research Institute, 35, 415–456.*

Benito B., Capote R., Murphy P., Gaspar-Escribano J.M., Martínez-Díaz J.J., Tsige M., Stich, D., García-Mayordomo J., García Rpdriguez M.J., Jiménez M.E. Insua-Arévalo J.M., Alvarez-Gómez, J.A. & Canora C (2006). An Overview of the Damaging and Low Magnitude Mw 4.8 La Paca Earthquake on 29 January 2005: Context, Seismotectonics, and Seismic Risk Implications for Southeast Spain.

Dobry R., Borcherdt R.D., Crouse C.B., Idriss I.M., Joyner W.B., Martin G.R., Power M.S., Rinne E.E. & Seed R.B (2000). New site coefficients and site classification system used in recent building seismic code provisions, *Earthquake Spectra, 16, 41–68.*

Egeler C.G. & Simon, O.J (1969). Sur la tectonique de la Zone bétique, *25 (Cordillères bétiques, Espagne): Koninklijke Nederlandse Akademic Wetenschappen, 90p.*

Eurocode No.8 (1998). Design of structures for earthquake resistance. Commission of the European Communities. Doc CEN/TC250/SC8/N335,

García–Hernández M., López–Garrido A.C., Rivas P., Sanz de Galdeano C. & Vera J.A (1980). Mesozoic paleogeographic evolution of the External Zone of the Betic Cordillera. *Geol. Mijnbouw, 59, 155–68.*

García-Jerez A., Navarro M., Alcalá F.J., Luzón F., Pérez-Ruíz J.A., Enomoto T., Vidal F. & Ocaña E (2007a). Shallow Velocity Structure Using Joint Inversion of Array and H/V Spectral Ratio of Ambient Noise: The Case of Mula Town (SE Spain), *Soil Dynamics and Earthquake Engineering, 27, 907-919.*

García-Jerez A., Navarro M., Luzón F. & Pérez-Ruiz J. A (2007b) Obtención de modelos de velocidad de onda S a partir de las características de las ondas superficiales mediante combinación paralelizada de métodos iterativos de minimización local y métodos de búsqueda aleatoria. *Memorias del Tercer Congreso Nacional de Ingeniería Sísmica*, Girona (España), 8-11 mayo 2007. CD ROM, pp: 504-512. ISBN: 978-84-96736-17-7.

García-Jerez A., Luzón F. & Navarro M (2008). Determination of the elastic properties and the depth of shallow sedimentary deposits applying a spatial autocorrelation method. *Geomorphology* 93: 74-88.

Henstridge D.J (1979). A signal processing method for circular arrays. *Geophysics* 44, 179-184.

IGME (1992). Estudio de la peligrosidad y vulnerabilidad sísmica en Lorca y su término municipal. Ed.: IGME and Murcia Government. 197 pp.

Ismet A., Tildy P., Prónay Z., Pinar A. & Hermann L (2006). V_S^{30} mapping and soil classification for seismic site effect evaluation in Dinar region, SW Turkey. *Geophys. J. Int.* 165, 223-235.

Navarro M., Corchete V., Badal J.I., Pujades L., Canas J.A. & Vidal, F (1997). Inversion of Rg waveforms in southern Spain. *Bull. Seism. Soc. Am*. 87, 847-865.

Navarro M., Sánchez F.J., Enomoto T., Vidal F.& Rubio S (2000). Relation between the predominant period of soil ant the damage distribution afther Mula 1999 earthquake. *Sixth International Conference on Seismic Zonation* (6ICSC). November 12-15, 2000, Palm Spring, California, USA.

Nazarian S (1984). In *situ* determination of elastic moduli of soil deposits and pavement systems by spectral analysis of surface waves method. *Ph.D. dissertation*, Univ. of Texas, Austin.

NCSE-02 (2002). "Normativa de Construcción Sismorresistente Española. Comisión Permanente de Normas Sismorresistentes", Real Decreto 997/2002. *Boletín Oficial Del Estado No. 244,* 11 October, 2002, Spain.

NEHRP (2003). Recommendation prevision for seismic regulation for new buildings and other structures, Building Seismic Saftey Council, Washington, D. C Federal Emergency. FEMA.

Parolai S., Picozzi M., Richwalski S.M. & Milkereit C (2005). Joint inversion of phase dispersion and H/V ratio curves from seismic noise recordings using a genetic algorithm. *Geophysical Research Letters*, Vol. 32, L01303.

Park C.B., Miller R.D. & Xia J (1999). Multichannel analysis of surface waves. *Geophysics* 64(3), 800–808.

Sanz de Galdeano C., Lopez Casado C., Delgado J. & Peinado, M.A (1995). Shallow seismicity and active faults in the Betic Cordillera. A preliminary approach to seismic sources associated with specific faults. Tectonophysics. 248: 293–302.

Tokimatsu K (1997). Geotechnical site characterization using surface waves. In: Ishihara (Ed.), Earthquake Geotechnical Engineering. Balkema, Rótterdam, pp. 1333-1368.

Vidal F (1986). Sismotectónica de la región Béticas-Mar de Alborán. Tesis Doctoral. Universidad de Granada.

Relocating the Betics Seismic Catalogue from Andalusian Institute of Geophysics using Source-Specific Station Terms

Ocaña E (1), Shearer P M (2), Vidal F (1)

(1) Instituto Andaluz de Geofísica. Universidad de Granada. Cuesta del Observatorio s/n. 18071 Granada (Spain). elena@iag.ugr.es. fvidal@iag.ugr.es
(2) Institute of Geophysics and Planetary Physics. Scripps Institution of Oceanography. University of California San Diego (United States). pshearer@ucsd.edu

Keywords: earthquake location, station terms, Betics.

Introduction

The Betics-Rif orogenic belt, around the Gibraltar Arc, represents the westernmost part of the Mediterranean Alpine Belt.

Earthquakes located in the Betics Region have been studied using historical analyses (e.g., Vidal, 1986) and local seismicity data (e.g., Vidal et al., 1986; Buforn et al., 1991, Morales et al., 1997). Those earthquakes are mainly shallow and intermediate (h<150 km) tectonic events but also a few very deep and rare events (630 km depth) have been analysed since 1954 (Chung & Kanamori, 1976; Grimison & Cheng, 1986).

Traditional single-event location techniques are independently performed for each event through the P and S-waves arrival times recorded at each station, and picking errors and lateral velocity variations related to three-dimensional velocity structure introduce important errors in the resultant locations.

Many studies have demonstrated that modern location techniques which are applied simultaneously to a group of clustered earthquakes (p.e.: Pujol et al., 1989; Maurer & Deichmnann, 1995; Deichmann & García-Fernández, 2002) or even to a whole catalogue (p.e.: Richards-Dinger & Shearer, 2000; Shearer et al., 2005; Hauksson & Shearer, 2005) can significantly improve the accuracy of locations compared to those obtained by traditional single-event location techniques. Some of these new modern methods for the location include *joint hypocenter determination* (Pujol et al, 1989), *master-event relative location* (Stich et al., 2001; Saccorotti et al.; 2002, Ocaña et al., 2008), the *double-difference algorithm* (Hauksson & Shearer, 2005) and *source-specific station terms* (Richards-Dinger & Shearer, 2000; Lin & Shearer, 2005; Shearer et al., 2005).

Improvements in relative location accuracy among nearby events are obtained when these relocation methods are used, even when the arrival times are biased by the effects of three-dimensional structure,. Those improvements help to determine the spatial characteristics of seismicity and often produce a dramatic sharpening of seismicity patterns (Lin et al., 2007).

In the present work, the relevant seismicity (m_d > 3.0), occurring in the Betics region from 1998 to 2006, is relocated through the source-specific station terms technique (Richards-Dinger & Shearer, 2000; Lin & Shearer, 2005) with the purpose of improving the hypocentral parameters by considering the station corrections during the data processing. We have employed the programs included in the COMPLOC computer program package (Lin & Shearer, 2006), which apply the source-specific station terms method to solve for local earthquake locations using P- and S-wave phase data and a 1-D velocity model.

Materials and Methods

Source-specific station terms

Estimation of station corrections is necessary for correcting the differences between observed travel times and those predicted from the assumed model. When errors in the velocity model are confined to shallow depths and the earthquakes are all located in a small region compared to the event-station distance, the station correction can be made by assigning a single number for each phase at each station, which is called a *static station term*. When the seismicity spreads over a large region containing significant lateral velocity heterogeneity it is necessary for the station term to depend upon source position, which is called *source specific station term*.

Since the 1960s different attempts have been made to estimate station corrections or station terms dependent in some way on the position of the source (e.g. Cleary & Hales 1966; Herrin & Taggart 1968; Lilwall & Douglas 1970; Poupinet 1979; Dziewonski & Anderson, 1983; Pavlis & Hokanson, 1985; Zhou & Wang, 1994; Seeber & Armbruster, 1995; Cogbill & Steck, 1997; Robertson & Woodhouse, 1997; Schultz et al., 1998). The *source-specific station term* method has been recently performed by Richards-Dinger & Shearer (2000). For each source-receiver pair they calculate a correction which is the weighted median of the residuals al the given station from N nearby events. In order to determine such neighbouring events they use a natural neighbour tessellation. Here we have considered an iterative approach described in Lin & Shearer (2005) for estimating source-specific station terms. It considers the nearby events located within a sphere of radius r_{max} around the target event, and computes the station term for the target event as the median residual of those events. The cutoff distance is reduced at each iteration; therefore at the starting point all the events are included in the calculation of source-specific station terms and at the end just the closest events are taken into account.

Selection of data

We have selected the events included in the Andalusian Institute of Geophysics (IAG, University of Granada) catalogue from 1998 to 2006. We have confined our search to those earthquakes located between 36ºN-38.25ºN and 6ºW-1ºW. These data have been single-event located by an operator using Hypocenter (Lienert & Haskov, 1995) and they have been assigned a magnitude m_d based on the duration of the seismogram (De Miguel et al., 1988). As the distribution of seismic stations in the region is relatively sparse, mainly in the period prior to year 2000, when the broad band network started to be deployed, many of the microearthquakes that took place at the Western Betics were not detected by the operative stations. For that reason, and in order to estimate a threshold in the magnitude from which the catalogue can be considered complete, we have used the Gutenberg-Richter law. We have represented the cumulative number of earthquakes with magnitude greater than m_d versus m_d, and we have fitted the data to get **a** and **b** parameters taking into account only events with magnitudes greater than 3.0 (Figure 1). The result of the fit is: $\log N(m_d) = 1.78 – 1.40m_d$.

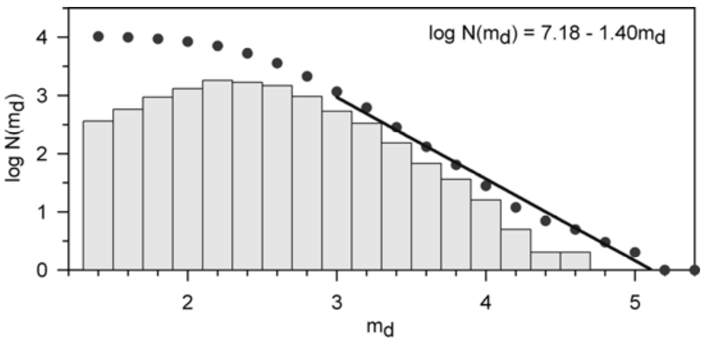

Figure 1. Gutenberg-Richter magnitude-frequency distribution for the period 1998-2006 taken from the IAG seismic catalogue. Through a least squares fit (R^2 = 0.9877) we have obtained values of 7.18 and 1.40 for **a** and **b** parameters. Dots represent the logarithm of the cumulative number of earthquakes with magnitude greater than m_d while bars represent logarithm of the number of earthquakes with magnitude equal to m_d.

Considering only earthquakes having magnitude $m_d \geq 3.0$, our data set consists of a total of 850 earthquakes (Figure 2) with m_d between 3.0 and 5.3 and depths in the range of 0-100 km. There are several clusters with greater densities of earthquakes which correspond to some of the seismic sequences and swarms previously mentioned (p.e.: 1998 Iznájar swarm; 1999, 2002 and 2005 seismic sequences in Murcia Region, or 2005 and 2006 series close to Cañete la Real). A total of 10,919 phases, which have been recorded at a total of 31 stations, are available for these events (6357 P-phases and 4562 S-phases). For some of the earthquakes, phases picked at stations belonging to Geographic National Institute (IGN) have been added to our IAG picks catalogue and the routine location has been performed with all of them.

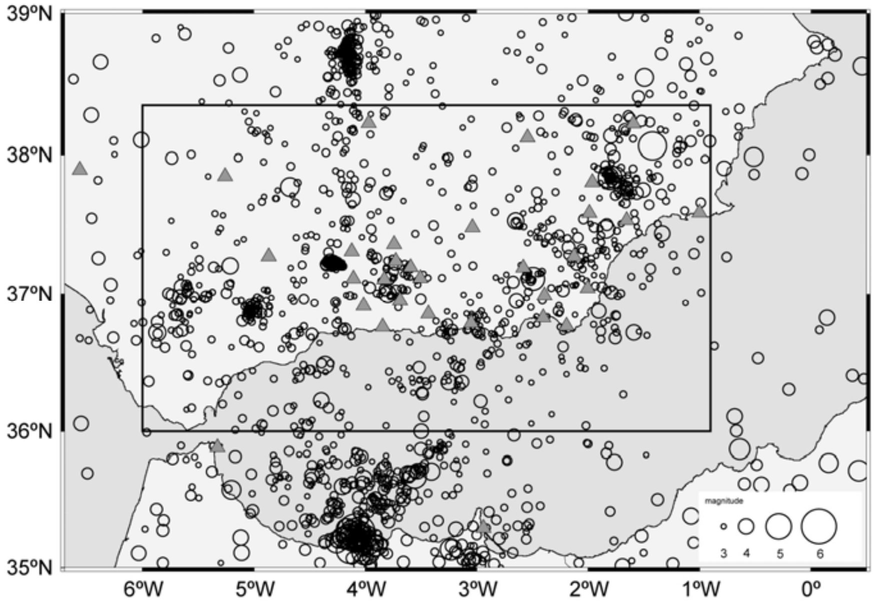

Figure 2. Seismicity ($m_d > 3$) in southern Spain, the Alboran Sea and northern Morocco from 1998 to 2006. The area of study has been delimitated with a rectangle. Seismic stations used in this study (from IAG and IGN) are plotted as triangles.

Data processing

The programs included in the COMPLOC Earthquake Location Package (Lin & Shearer, 2006) have been used for the relocation procedure. Before starting, a one-dimensional velocity model for the region is necessary. The IGN uses the same velocity model for the location of earthquakes all over Spain, while the model used by the IAG has been tested with earthquakes mostly located in the South of the Iberian Peninsula, especially those occurring in the Betics Cordilleras. For that reason we have selected a smoothed version of the velocity model used by the IAG, considering the S velocity model as a scaled version of the P velocity model, with a v_P/v_S ratio equal to 1.73 (Table 1). From these models we have computed P and S travel-time tables at 1-km intervals as a function of source depth and source-receiver distance. A 100-km distance cutoffs applied, so phase data from stations beyond this maximum distance are rejected. Only events having a minimum number of five phase picks are located (at least four picks are needed for the location, we require only five because a larger number would have restricted the locations to only the better recorded events). We have selected the L1-norm for the residual misfit function because it gives better results for real data, as it is more robust with respect to outliers and relatively insensitive to gross picking and timing errors (Lin & Shearer, 2006).

Three types of locations can be performed through COMPLOC: a *single event location*, a *static station term location* and a *source-specific station term location*. The single event location does not take into account any information from any other events and sets the number of iterations for both the static and the source-specific station terms to zero. The *static station term location* method solves iteratively for a custom set of station-timing corrections. It assigns a fixed number for each station and each P and S phase, regardless of the source position. These numbers are computed as the median (when the L1-norm has been chosen) of the residuals for each station. The source-specific station term location assigns a number for each event and each P/S phase. Therefore each station will have a station correction function dependent on source position. The method calculates a separate correction for each source-receiver pair at the given station using the residuals from the nearby events located within a sphere of radius r_{max} around the target event. We first start with a large value to include a large number of events in the calculation of station terms and progressively decrease it to calculate station terms just with the closest events.

Table 1. P-velocity model used in this study

Depth (km)	v_P (km/s)
0.0	4.0
10.0	6.1
40.0	6.3
40.0	7.8
100.0	8.1

In this work five iterations have been used to compute the static station terms and another ten have been used to compute the source-specific station terms. At each iteration the terms are computed by smoothing over the 1000 adjacent events located within a distance of 20 km from each target event. At the last one (10th iteration), only the 20 closest events located around 5 km are considered.

Results and Discussion

Our final catalogue obtained using the source-specific station term method includes the hypocentral locations, residuals and station terms for 385 events occurring in the South of Spain, nearly 50% of the initial dataset. The other half of the initial seismicity selected has not been located because one or more of the conditions imposed by the programmes were not satisfied (e.g., less than five P or S-phases from stations within 100 km). The epicentral locations of these 385 selected events are shown in Figure 3. We can again clearly distinguish groups of seismicity, which, after the station corrections, are even more compact than in the IAG catalogue. The seismic swarm in Iznájar (Córdoba) in 1998, the seismic series in La Paca (Murcia) in 2005 and sequences close to Cañete la Real (Málaga) in 2005-2006 are examples of clusters and have been plotted in Figure 3.

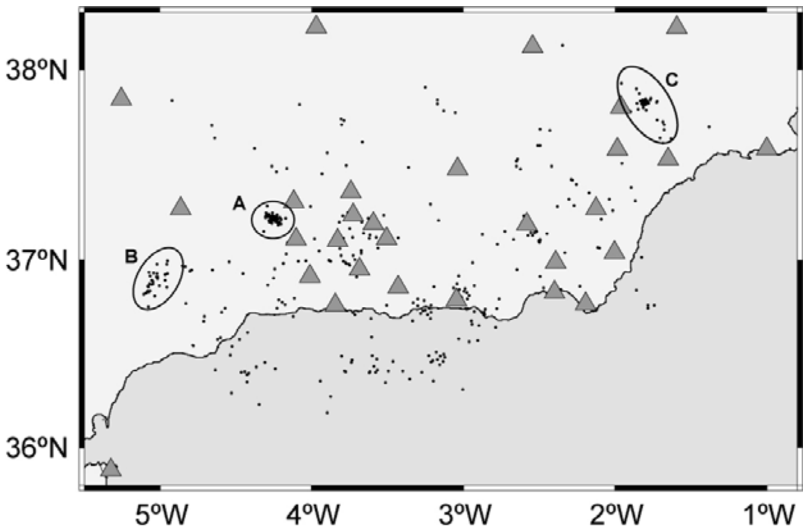

Figure 3. Map showing the position of all stations (IAG stations and IGN stations) included in the seismic catalogue plotted together with the final locations of the earthquakes involved in the study corrected using source-specific station terms. Three clusters of activity are labeled:

the 1998 Iznájar swarm, the 2005-2006 activity period in Cañete la Real and the 2005 La Paca series, noted as A, B and C, respectively.

Because of the lack of stations nearby or immediately above the earthquakes in some areas, depth is very difficult to determine reliably. Although it is not easy to determine the accuracy of the estimated depth for each individual event, some indication of the reliability of an earthquake location method can be obtained by studying the whole distribution of depths in a catalogue (Richards-Dinger & Shearer, 2000). With this purpose we have plotted the depth distributions from the IAG catalogue (our initial dataset), the IGN catalogue and our final located catalogue (Figure 4). Histograms from the IAG locations and the IGN locations show a large spike in the range 0-2km. The IAG catalogue contains 34.9% of the events in that range and in the case of the IGN catalogue this percentage is equal to 26.0%. This peak is due to the existence of many events whose depth has been fixed very close to the surface when manually locating. Besides this spike at 0.0 km, the IGN histogram also shows a peak at 10 km, which includes around 21% of the seismicity. The distribution of our source-specific station term relocated depths is smoother than the original distributions of both the IAG catalogue and the IGN catalogue and the large peak in the range 0-2 km does not exist. Almost the whole dataset is located not deeper than 25 km and an important part of the seismicity (around 35% of events) is located in the range 10-16 km, within the upper crust. A less significant portion of the events have depths from 25 to 75 km.

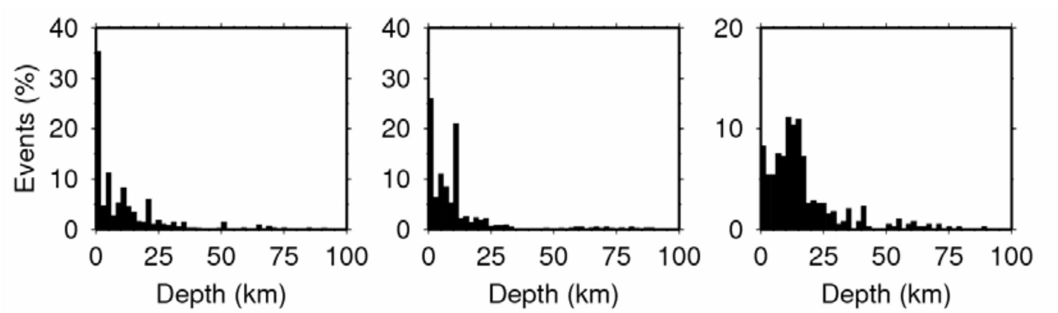

Figure 4. Depth histograms for IAG catalogue locations (left), IGN catalogue locations (middle) and our source-specific station term locations (right). Strong peaks at 0-2 km exist for the two first cases while the depth distribution for the relocated events is smoother.

Cross sections of areas close to Iznájar (A), Cañete la Real (B) and Murcia (C) where, as we have already pointed out, important clusters have occurred in different period of times, have been plotted in Figure 5.

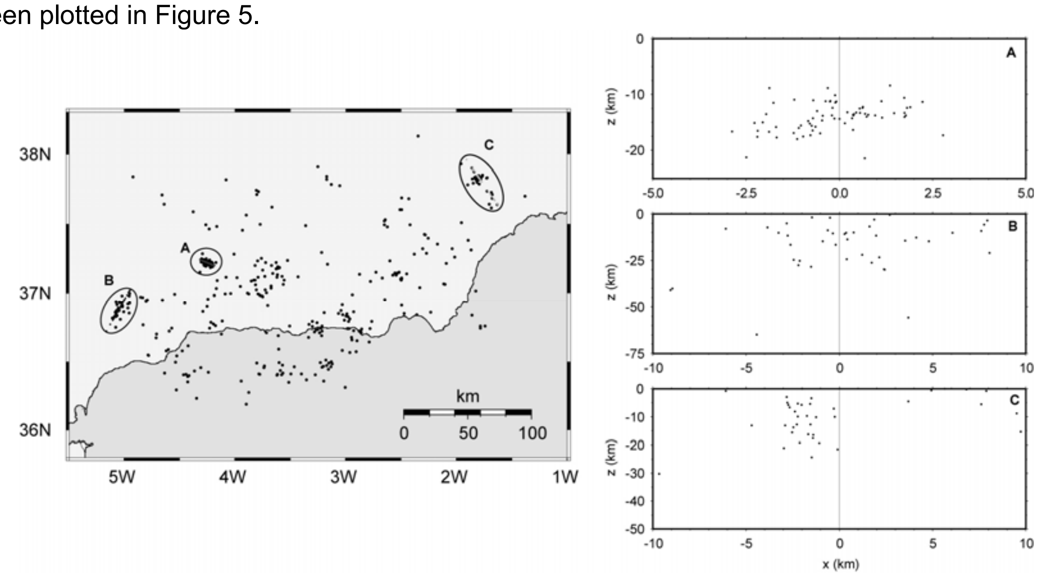

Figure 5. Map showing profiles of different regions in Betics Cordilleras: A (Iznájar, Central Betics), B (Cañete la Real, W Betics) and C (Murcia, E Betics). At the right the cross sections of the *source-specific station term* relocated seismicity along those profiles are shown.

Seismicity in case A is mainly concentrated from 10-20 km. A quite similar value (14-17 km) was found by Morales et al. (1997) for a dataset of earthquakes with m ≥ 2.5 occurring from 1983 to 1995 in the Granada Basin and they related it to a detachment that divides the crust into a brittle (upper crust) and a ductile (lower crust) zone. If we move to the Southwest (case B) depths are concentrated along the whole crust (25 km). However these values of depth tend to increase and we can find several earthquakes in the upper mantle, in the range 40-65 km. Morales et al. (1997) depths for earthquakes in this part of the Betics located in the Malaga zone are in agreement with our results. Finally, in the eastern part of the Betics (case C) events spread until 30 km depth, although their depths are mainly located from 0 to 20 km. A master event relative location was performed by Ocaña et al. (2008) for a seismic series occurring in 2005 in that region, which found that clusters of similar events had depths in the range 3-18 km, the same range as in the source-specific station term locations.

Figure 6 shows our computed P and S source-specific station terms for ATEJ station, located in the SW extreme of the Granada Basin. Values vary from -0.62 to 0.47s (for the case of P source-specific station terms) and from -0.71 to 0.23s (for the case of S source-specific station terms). The most obvious features in these maps are the positive (late) corrections located to the SW of the station and the NW of the Alboran Sea and the negative (early) values located to the NE and SE of the station, which indicate slow and fast velocities in these areas, respectively.

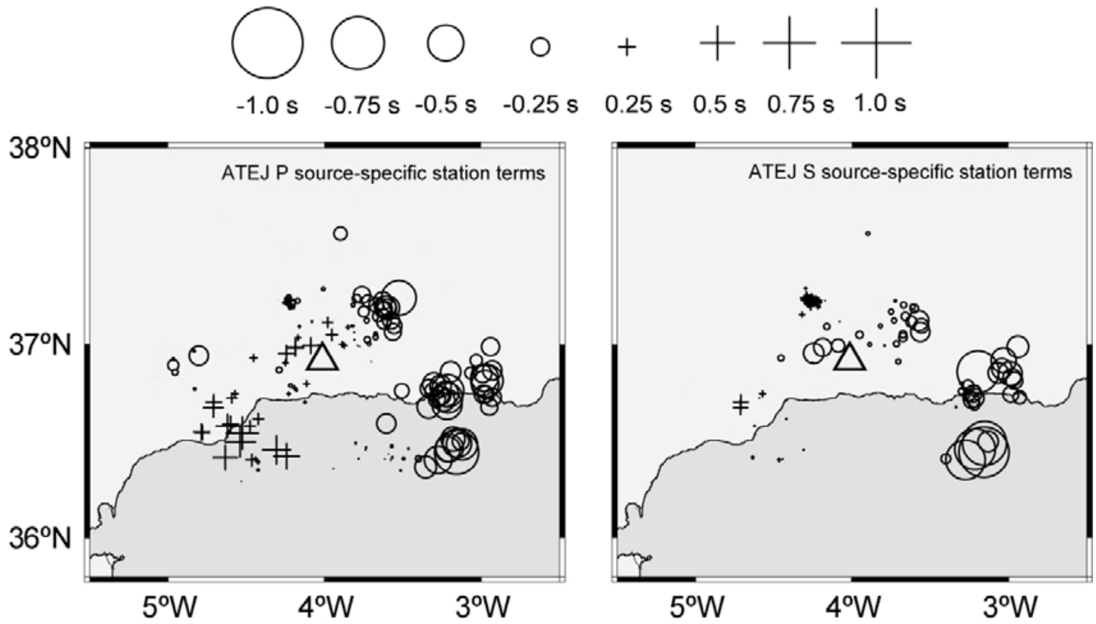

Figure 6. P (left) and S (right) source-specific station terms for all events recorded at station ATEJ (represented by a triangle), located in the SW extreme of the Granada Basin. Circles are negative values and crosses positive values.

Conclusions

From the entire 1998-2006 Betics Seismic Catalogue we first selected earthquakes with m_d ≥ 3.0. Only events having a minimum of five phase picks from nearby seismic stations (Δ ≤ 100 km) have been considered. Those selected events have been relocated using the L1-norm for the residual misfit function and source-specific station term corrections. The relative location accuracy for regional events has been improved, mainly among nearby events (clusters). The relocated events have smaller errors and are closer in space than in the initial catalogue. Scatter in the locations within three particular clusters has been reduced, mainly in depth, in comparison with the original catalogue and our results are in agreement with specific studies of seismicity in these areas. Source-specific station terms have values in the range -0.62 to 0.47s (P-phase) and -0.71 to 0.23s (S-phase).

Acknowledgements

We thank all the personal in the IAG who work in the maintenance of the Andalusian Seismic Network and make possible the existence of a complete seismic catalogue of events in the South of Spain. We are very grateful to Benito Martin, who helped us in the process of compiling P and S-wave phase data from both the IAG and the IGN catalogues, making this process much easier. This study has been supported by the Spanish Ministry of Science, Innovation and Technology (project CGL2007-66745-C02-01/BTE and FPI scholarship program).

References

Buforn E., Udías A. & Madariaga R. (1991). Intermediate and deep earthquakes in Spain. *Pageoph, 136, 375-393.*

Chung, W. & Kanamori, H. (1976). Source process and tectonics implications of the Spanish deep-focus earhtquake of 29 March 1954. *Phys. Earth Planet. Interiors 13, 85-96.*

Cleary J. & Hales A. (1966). An analysis of the travel times of P waves to north American stations in the distance range 30º to 100º, *Bull. Seismol. Soc. Am., 56, 467-489.*

Cogbill A. & Steck L. (1997). Use of propagation path corrections to improve regional event locations in western China. *Eos Trans. AGU, 78(46), Fall Meet. Suppl., F445*.

Deichmann N. & Garcia-Fernandez M. (1992). Rupture geometry from high-precision relative hipocentre locations of microearthquake clusters, *Geophys. J. Int., 110, 501-517.*

Douglas A., O'Mongain A.M., Porter D. & Young J.B. (2005). An analysis of P times reported in the Reviewed Event Bulletin for Chinese underground explosions, *Geophys. J. Int., 163, 559-566.*

Dziewonski A. & Anderson D. (1983). Travel times and station corrections for P waves at teleseismic distances, *J. Geophys. Res. 88, 3295-3314.*

Grimison, N. & Cheng, W. (1986). The Azores-Gibraltar Plate Boundary: Focal Mechanisms, Depths of earthquakes and their tectonics implications. *J. Geophys. Res. 91, 2029-2047.*

Herrin E., & Taggart J. (1968). Regional variations in P travel times, *Bull. Seismol. Soc. Am., 58, 1325-1337.*

Lilwall R. & Douglas A. (1970). Estimation of P-wave travel times using the joint epicentre method, *Geophys. J. R. Astron. Soc., 19, 165-181.*

Lin G. & Shearer P. (2005). Test of relative earthquake location techniques using synthetic data, *J. Geophys. Res., 110, B04304, doi: 10.1029/2004JB003380.*

Lin G. & Shearer P. (2006). The COMPLOC Earthquake Location Package, *Seism. Res. Letters, 77, 440-444.*

Lin G., Shearer P.M. & Hauksson E. (2007). Applying a three dimensional velocity model, waveform cross correlation and cluster analysis to locate southern California seismicity from 1981 to 2005, *J. Geophys. Res., 112, B12309, doi: 10.1029/2007JB004986.*

Maurer H. & Deichmann N. (1995). Microearthquake cluster detection based on waveform similarities with and application to the western Swiss Alps, *Geophys. J. Int., 123, 588-600*.

Morales J., Serrano I., Vidal F. & Torcal F. (1997). The depth of earthquake activity in the Central Betics (Southern Spain), *Geophys. Res. Lett. 24, 3289-3292.*

Ocaña E., Stich D., Carmona E., Vidal F., Bretón M., Navarro M. & García-Jerez A. (2008). Spatial analysis of the La Paca, SE Spain, 2005 seismic series through the relative location of multiplets and principal component analysis, *Phys. Earth Planet. Interiors, 166, 117-127.*

Pavlis G. & Hokanson N. (1985). Separated earthquake location. *J. Geophys, Res., 90, 12777-12789.*

Richards-Dinger K.B. & Shearer P.M. 2000. Earthquake locations in southern California, obtained using source-specific station terms, *J. Geophys. Res, 105, 10939-10960*.

Robertson G. & Woodhouse J. (1997). Comparison of P and S station corrections and their relationship to upper mantle structure, *J. Geophys. Res., 102, 27355-27366.*

Seeber L. & Armbruster J. (1995). The San Andreas fault system through the Tranvserse Ranges as illuminated by earthquakes, *J. Geophys. Res. 100, 8285-8310.*

Saccorotti G., Carmona E., Ibáñez J. M. & Del Pezzo E. (2002). Spatial characterization of Agron, southern Spain, 1988-1989 seismic series, *Phys. Earth Planet. Int. 129, 13-29.*

Schultz C., Myers S., Hipp J. & Young C. (1998). Nonstationary bayesian kriging: A predictive technique to generate spatial corrections for seismic detection, location and identification, *Bull. Seismol. Soc. Am. 88, 1275-1288.*

Stich D., Alguacil G. & Morales J. (2001). The relative locations of the multiplets in the vicinity of the Western Almeria (Southern Spain) earthquake series 1993-1994, *Geophys. J. Int. 146, 801-812.*

Vidal F. (1986). Sismotectónica de la Región Béticas-Mar de Alborán, *PhD Thesis. University of Granada. Spain.*

Zou H-W. & Wang H. (1994). A revisit for P wave travel time statics at teleseismic stations, *J. Geophys. Res., 99, 17489-17862.*

The Study of the 20th Century Strong Romanian Earthquakes using Historical Iinstrumental Data – a Success of EUROSEISMOS 2002-2006 Project

Oros E (1), Oros V (2)

(1) National Institute R&D for Earth Physics, Seismological Research Department – Timisoara Seismological Observatory, Martir P. Domasneanu str., bl. 45, ap. 8, 300351, Timisoara, Romania, eoros@mail.com
(2) "Politechnica" University of Timisoara, Martir P. Domasneanu str., bl. 45, ap. 8, 300351, Timisoara, Romania, valioros@yahoo.com

Keywords: EuroSeismos, historical seismograms, seismic bulletins, earthquakes, source parameters

Introduction

In this paper we present the main results obtained from the study of several Romanian earthquakes using the data gathered into the framework of EUROSEISMOS 2002-2006 Project. The sources parameters of the earthquakes occurred in the western part of Romania (often called Banat Seismic Region, BSR) have been reappraised using original historical seismograms and bulletins. Thus, new locations, depths and magnitudes of the strongest events occurred at the beginning of 20th Century were determined on instrumental data basis. Focal mechanisms solutions for two important earthquakes have been estimated, too. In addition, the new database recently elaborated for BSR (Oros et al., 2008) has a section that comprises all historical seismograms converted in digital format were obtained using Teseo software and a conversion routine. Many papers containing these results published and presented on last years.

Materials and Methods

The study of the strongest western Romanian earthquakes occurred in the first half of the 20th Century used only historical instrumental data collected and scanned into the framework of EUROSEISMOS 2002-2006 Project: i) 209 seismograms scanned and archived at INGV Rome (Sismos facility); ii) seismic bulletins: the ISS seismic bulletins and the single stations, observatories and/or seismological network bulletins (www.storing.ingv.it /es_web).
These materials and data were processed and analysed using IT technologies and modern methods following the next steps: i) collecting all the information about each event from the seismic bulletins: time arrivals of the seismic phases, amplitudes, waves periods, duration of the seismic signals, macroseismic data, etc.; ii) processing seismograms using the Teseo software (http://sismos.ingv.it/teseo/): vectorization and signal correction based of instrumental constants to obtain the digital seismograms; iii) developing computer programmes to correct and to convert the digital seismograms to Seisan waveform formats; iv) analysing the digital seismograms by Seisan software package to obtain the main focal parameters: origin time, geographical coordinates of the epicentres, focal depths, source characteristics (dimensions, stress drop), spectral parameters (corner frequency, omega zero), seismic moment and magnitudes (Mw) and focal mechanisms solutions (Fig. 1).
All digital historical seismograms obtained for the earthquakes occurred into BSR through EUROSEISMOS project and other archives feed a new elaborated database (Oros et al., 2008a, 2008b) (Fig. 2).

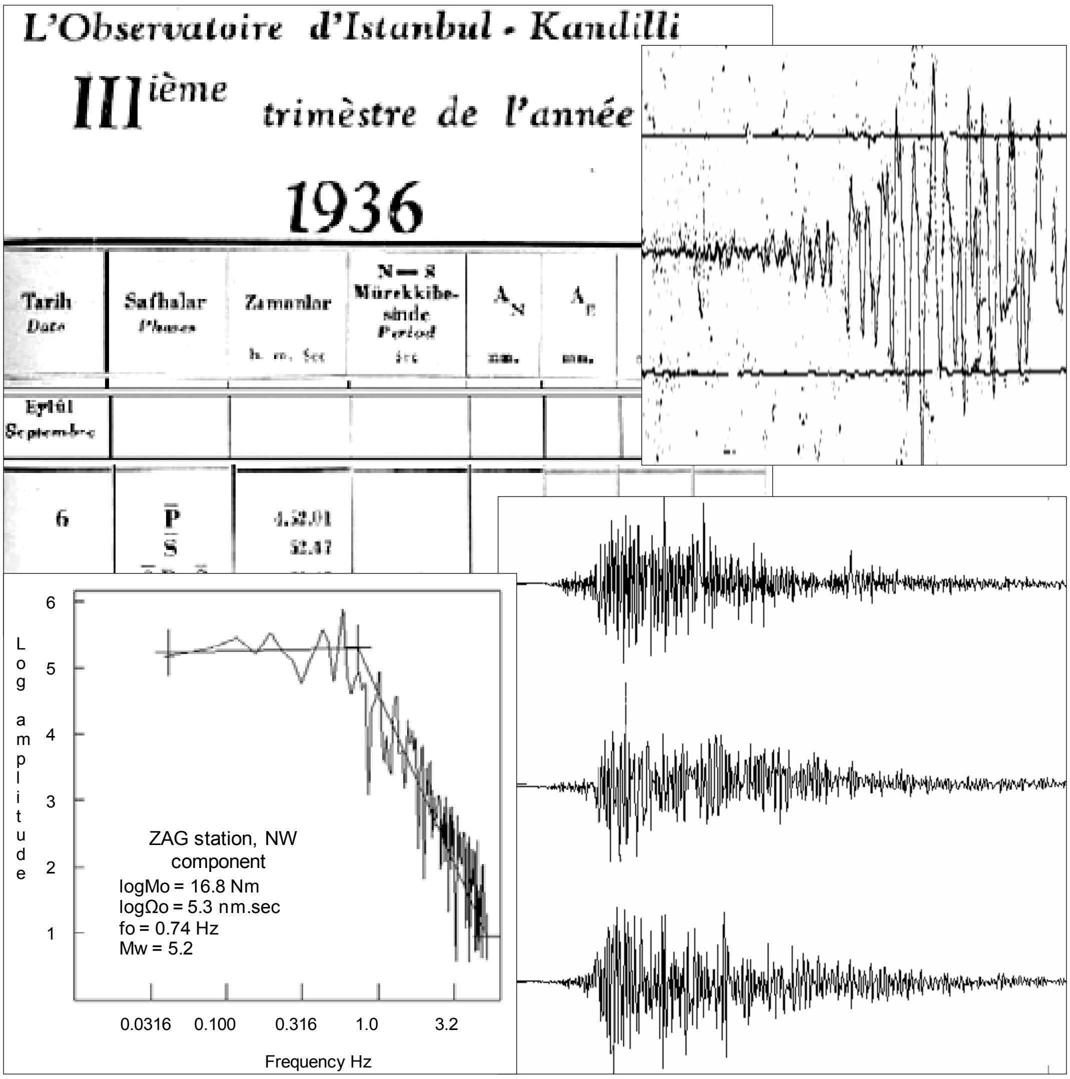

Figure 1. Examples of instrumental data used for reappraising the Mw5.2, 6th October, 1936: seismic bulletin from Kandili Observatory (left top), sample of a scanned seismogram recorded by ZAG station (right top corner), digital seismograms in Seisan format (right down corner) and the S wave/NW component spectrum computed for ZAG station (left down corner).

Results and Discussion

The main results obtained by using historical instrumental data since EUROSEISMOS Project started in 2002, are very significant for improving the existing seismological data-bases and have strong implications for a better understanding and modelling of the seismicity and seismotectonics in the western part of Romania (BSR).
Briefly, these most important results are the following:

i. New and high accuracy focal parameters were obtained for the strongest earthquakes occurred in BSR before 1970's years (Table 1). The differences in epicentral coordinates, depths and magnitudes are often significant when we compare the new values with those obtained by different authors, as it can be seen in Table 1, Figure 2 and Figure 3. Obviously, it can be noticed that the geological structures and tectonics correlate better with the new epicentres. The new data is useful for a critical analysis of previous catalogues and to assure a high level of their transparency. The smallest differences in locations/geographical coordinates of epicentres (diff.<10 km) appear generally between the new locations and the ones from Shebalin et al. (1998) and

Table 1. The instrumental parameters of the major historical earthquakes occurred into Banat Seismic Region of Romania between 1900 and 1970 (after Caciagli and Oros, 2006; Oros, 2008c).

Date	Origin time hhmmss.s	latN degree	longE degree	h km	Io	M	References
02.04.1901	1717	45.500	20.700	15	8.5	Mm=5.8	Karnik, 1968
	165430.0	45.510	20.750	17	6.5	Ms=5.0	Shebalin et al.1998
	1647	45.510	20.640	12	7	Ms=5.0	Zsiros, 2000
	165430.0	45.500	20.700	18.0	7	Mw=5.0	Oncescu et al.1999
	165416.0 ±5.0	45.433 ±30	20.673 ±36	18.4 ±21		MLH=5.6 Ms=5.2	Oros et al., 2008a
19.10.1915	0830	45.400	21.200	n	9	MLH=4.8	Karnik 1968
	084354.0	45.400	21.100	7.0	7.5	Ms=4.8	Shebalin et al.1998
	0830	45.420	21.100		7	Ms=4.8	Zsiros 2000
	0830	45.400	21.100	5.0	7.5	Mw=4.8	Oncescu et al. 1999
	084354.0 ±0.67	45.470 ±6.7	21.206 ±6.7	8.6 ±3.6		Mw=5.2 ±0.1	Caciagli and Oros 2006
06.09.1936	044902.0	45.400	20.900	N		MLH=4.8	Karnik 1968
	044902.0	45.700	21.100	8.0	7	Ms=4.8	Shebalin et al.1998
	044902.0	45.700	21.100	5.0	7	Ms=4.8	Zsiros 2000
	044902.0	45.700	21.100	5.0	7	Mw=4.8	Oncescu et al.1999
	044901.4 ±5.1	45.710 ±12	21.026 ±11	15.4 ±13		Mw=5.2 ±0.2	Caciagli and Oros 2006
	044901.6 ±2.6	45.766 ±9	21.035 ±6	16.1 ±6.9		Mw=5.2 ±0.2	Oros et al. 2008a
30.08.1941	044144.0	45.800	20.800	(25)	6	MLH=4.8	Karnik 1968
	044144.0	45.800	20.800	7.0	7	Ms=4.8	Shebalin et al.1998
	054144.0	45.660	20.790		6	Ms=4.8	Zsiros 2000
	044144.0	45.800	20.800	7.0	7	Mw=4.8	Oncescu et al.1999
	044109.7 ±4.5	45.734 ±10	20.661 ±15.1	19.9 ±26			Caciagli and Oros 2006
	044109.5 ±2.2	45.721 ±12	20.635 ±9	19.5 ±12		MLH=5.2	Oros et al. 2008a
27.05.1959	203825.0	45.640	21.180	6.0	7.5	Ms=5.0	Shebalin et al.1998
	203828.0	45.630	21.150		7.5	Ms=5.0	Zsiros 2000
	203826.0	45.700	21.100	5.0	7.5	Mw=5.0	Oncescu et al.1999
	203825.7 ±0.79	45.649 ±3	21.100 ±3	5.4 ±3.4		MLH=5.1	Caciagli and Oros 2006
	203825.7 ±0.79	45.636 ±3	21.087 ±3	8.8 ±3.4	8	Ms=5.3	Oros et al. 2008a
22.10.1960	191748.0	45.610	21.100	12	6	Mw=4.2	Oncescu et al.1999
	191747.10 ±2.59	45.609 ±6.4	21.158 ±8.1	19.1 ±5.4			Caciagli and Oros 2006

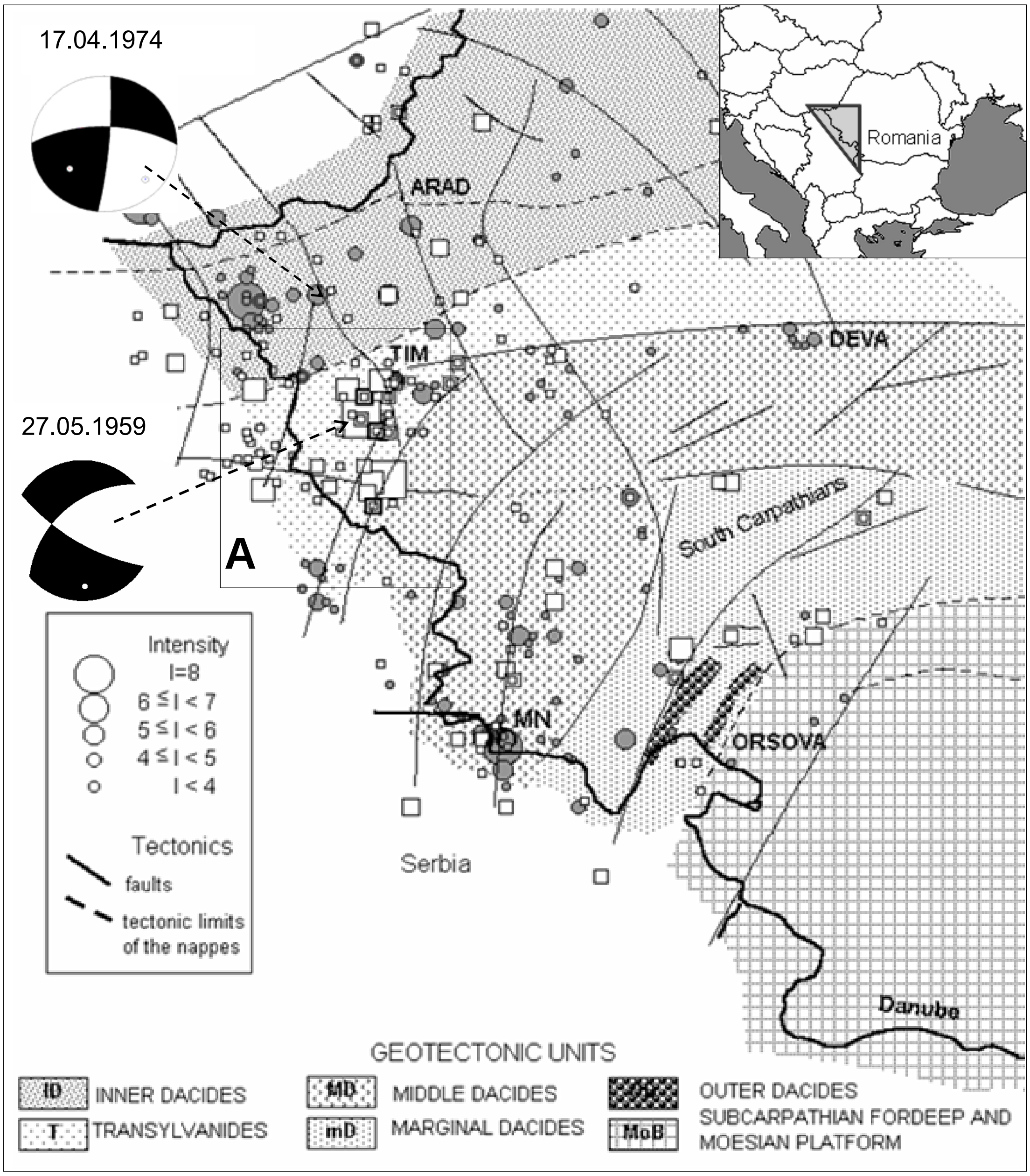

Figure 2. Banat Seismic region (BSR) of Romania (Oros et al., 2008): Map of epicenters and major geological structures (after Sandulescu, 1984). Insert: (right corner, top) geographical position of Banat Seismic Region; the detail A is presented in Figure 2. Epicenters symbols: gray circles-epicenters before 1900; white squares-epicenters between 1901 and1980. TIM-Timisoara, MN-Moldova Noua. Intensity is in EMS degree

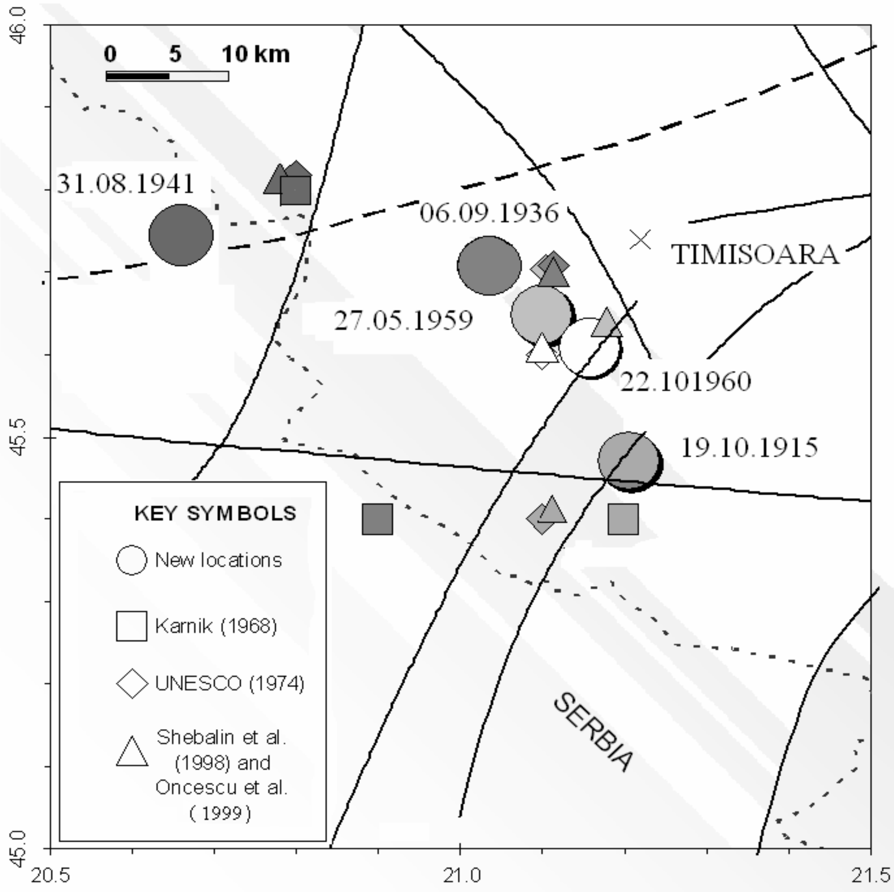

Figure 3. Detail A from Figure 1. New and old locations for the main earthquakes occurred in BSR between 1900-1970. Black lines-faults, dashed line-thrusts, dotted line-official border between Romania and Serbia.

Oncescu et al. (1999) in the cases of the 06.09.1936, 27.05.1959 and 22.10.1960 events. The greatest differences are identified for the 31.08.1941 event (in the case of all previous catalogues) and for the 06.09.1936 event (in the case of Karnik (1968) catalogue). The new parameters improved the data-base recently elaborated for BSR by Oros et al. (2008a). These data are very important for the new local and regional hazard and risk assessment, especially for the city of Timisoara.

ii. New focal mechanisms were determined by the first P waves polarities method using Seisan software (Havskov and Ottemoller, 2004). These solutions (Table 2 and Figure 2) made up the focal mechanisms solutions catalogue (Oros et al., 2008b) and bring useful data for seismotectonic and stress field modelling. Thus, the focal mechanism solution for the 27th May, 1958 event shows a normal faulting on a plane probably oriented NE-SW (Plane 1 in Table 2) towards Timisoara. This fault plane corresponds to the modified macroseismic field of the earthquakes (Shebalin, 1974).

iii. all historical seismograms available in digital format represent a valuable complementary data set that integrates as part of the Seismological Data-Base elaborated by Oros et al. (2008a, 2008b). The waveforms can be accessed by local stations with historical records (Timisoara-TIM, Susara-SSR, Gura Zlata-GZR, Buzias-BZS) and by earthquakes (the historical earthquakes are grouped according the major seismogenic zones of Romania). A special link to the EUROSEISMOS raster and preview historical data (seismograms and bulletins) was created for both, new materials (online) and the already downloaded materials (offline). The digital waveforms are storaged in different

Table 2. Focal mechanisms solutions obtained by first P wave polarities method (Seisan software package, Havskov and Ottemoller, 2004).

No	Date			Ho		lat	long	h	M_w	Plane 1			Plane 2			P		T		Po
	d	m	y	h	m					Az	Di	Sl	Az	Di	Sl	Az	Pl	Az	Pl	
1	27	5	1959	20	38	45.64	21.09	9	5.0	229	49	-153	121	70	-44	76	45	180	13	19
2	17	4	1974	1	31	46.03	21.04	16	4.9	271	61	172	5	83	29	135	15	232	25	18

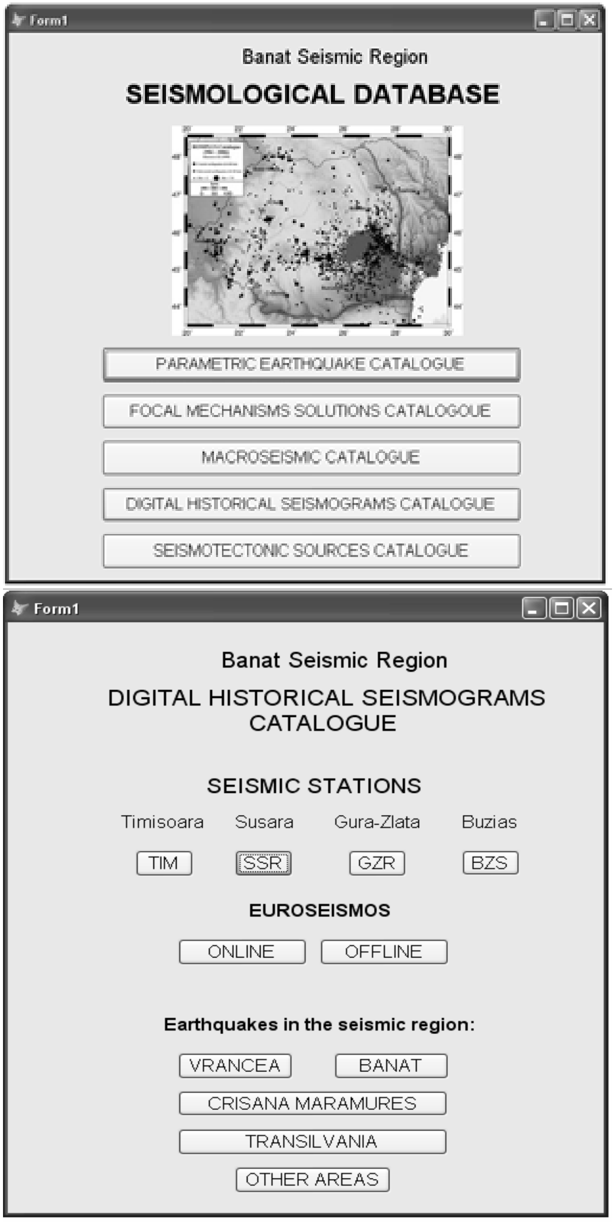

Figure 3. The main forms of the Seismological Data-Base for Banat Seismic Region: - the Digital Historical Seismograms Catalogue: the waveforms can be accessed by stations with historical records (TIM, SSR, GZR, BZS) and by earthquakes (the historical earthquakes are grouped according to the major seismogenic regions of Romania). A special link to the

EUROSEISMOS raster historical data (seismograms and bulletins) was created for both, new materials (online) and downloaded materials (offline)

common formats (e.g sac, Seisan). Future developments are planed for the access to all data and their processing.

Conclusions

The paper present several results obtained by the authors in the study of Romanian earthquakes using historical instrumental data (seismograms and bulletins) gathered into the framework of EUROSEISMOS 2002-2006 Project (www.storing.ingv.it/es_web). All these results emphasize the great importance of this kind of seismological data in the study of seismicity, seismotectonics, hazard and risk, source parameters, etc. This work and many others papers elaborated by many researchers last years proved again a known reality: using new technologies and modern methods for processing and analysing the historical data/materials, we are able to get and to exploit more and of high quality information. For example we can use more objective data (instrumental data) for studying major historical earthquakes and for knowing their relationship with actual tectonics and geological structures. We can also to know more correctly how we must use and calibrate other historical data (e.g. macroseismic data), and so on. We can be finally able to better understand one of the most complex fields of geosciences: Earthquake Seismology and Seismotectonics. Also of importance, we can provide the next generations of scientists with valuable data and information.

Acknowledgements

This paper could be accomplished only since the beginning of EUROSEISMOS Project and only with the contribution of all the partners and especially the work of Dr. Graziano Ferrari and his team from SGA Bologna (especially Dr. Marco Caciagli and Dr. Gabriele Tarabusi) and of the INGV Rome/Sismos team. The authors thanks to the all colleagues, who helped them to search, find, preserve and archive the bulletins and seismograms recorded by the seismic stations of Timisoara Seismological Observatory.

Referencies

Caciagli M., Oros E (2006). On the XXth Century strongest western Romanian earthquakes: preliminary results from EuroSeismos Project. "*First European Conference on Earthquake Engineering and Seismology", 3-8 Sept. 2006 Geneva, Switzerland (Joint ESC/EAEE Conference)*

Havskov J., Ottemoller L., (eds.) (2004). Seisan: Earthquake analysis software, *Inst. Of Solid Earth Physics,Univ. of Bergen, Norway (www.ifif.uib.no).*

Karnik V. (1968). Seismicity of the European Area Part 1 Catalogue of earthquakes (1901-1955), P*ublishing House of the Czechoslovak Academy of Sciences, Prague.*

Oncescu M.C., Marza V., Rizescu M., Popa M. (1999). The Romanian earthquakes catalogue between 984-1997. In Vrancea Earthquakes: Tectonics, Hazard and Risk Mitigation. F, Wenzel, D. Lungu (editors), Kluwer Academic Publishers, Oland, 43-47p.

Oros E., Nitoiu L (2002). Timisoara (Romania) Seismological Observatory – sixty years of existence. Abstracts, *XXVIII General Assembly of ESC, 1-6 Sept. 2002, Genoa, Italia, (www.dipteris.unige.it/geofisica/esc2002), Book of Abstracts, SCB-5_06-P, 187 p.*

Oros E (2004). Ioan Curea, the founder of the Timisoara Seismological Observatory (Romania) and pioneer of the modern Romanian seismology-A short biography, *XXIX General Assembly of ESC, 12-16 Sept. 2004, Potsdam, Germania, Book of Abstracts and CD Rom, SCB-3 P 107 23.*

Oros E., Popa M., Moldovan I. A (2008a) Seismological Data-Base for Banat Seismic Region (Romania) - Part 1: The Parametric Earthquake Catalogue. Romanian Journal of Physics, 53, 7-8 (in print)

Oros E., Popa M., Moldovan I. A., Popescu E (2008b). Seismological Data-Base for Banat Seismic Region (Romania) - Part 2: The Catalogue of the Focal Mechanism Solutions, *Romanian Journal of Physics, 53, 7-8, (in print).*

Oros E (2008c). Review of Historical Seismicity in the western and south-western territory of Romania (Banat Seismic Region). Acta Geodaetica et Geofisica Hungarica, 43, 2-3, pp.153-161, *Paper presented at the 3rd International conference "Science and Technology for Safe Development of Life Line Systems, Progress on seismic and geotectonic modelling across CEI territory and implications on preventing and mitigating seismic risk, October 24th – 26th, 2007, Bucharest, Romania*

Pintore S., Quintiliani M., Franceschi D (2005). Teseo: a vectoriser of historical seismograms, *Computers & Geosciences, http://dx.doi.org/10.1016/j.cageo.2005.04.001*

Sandulescu M (1984). Geotectonics of Romania. Technical Press, Bucharest, Romania.

Shebalin N.V (1974). Map of maximum observed intensity in the Balkan region, *Proc. Of the Seminar on the seismotectonic map of the Balkan region, Dubrovnik, 17-26 April 1973, UNESCO, Skopje, 290 pp.*

Shebalin, N.V., Leydecker, G., Mokrushina, N.G., Tatevossian, R.E., Erteleva, O.O., Yu. Vassiliev (1998). Earthquake Catalogue for Central and South-eastern Europe 342 BC - 1990 AD, *European Commission, Report No., ETNU CT 93 - 0087, Brussels.*

The M6.4, 26th January, 1916 Earthquake under Review: ew Data on the Seismicity of Fagaras Seismogenic Region (Romania)

Oros E (1), Paulescu D (2), Popa M (3)

(1) National Institute R&D for Earth Physics, Bucharest, Timisoara Seismological Observatory, Martir Petru Domasneanu str, bl. 45, ap. 8, Timisoara, Romania, eoros@mail.com
(2) National Institute R&D for Earth Physics, Bucharest, Calugareni str, no. 12,Bucharest, Romania, paulescudaniel@yahoo.com
(3) National Institute R&D for Earth Physics, Bucharest, Calugareni str, no. 12,Bucharest, Romania, mihaela@infp.ro

Keywords: historical seismograms, bulletins, seismicity

Introduction

This paper presents an instrumental review of the strongest crustal Romanian earthquake occurred last Century, namely the M6.4, 26th January, 1916 event. The earthquake occurred in Fagaras Seismogenic Zone that lies in the central part of South Carpathians. The maximum intensity reported by different authors for this event is Imax=9MM (Atanasiu, 1961) or Imax=8MSK (Oncescu et al., 1999; Shebalin et al., 1998). The data obtained from the historical seismograms and bulletins were used to re-determine its main focal parameters using modern methods. Thus, new geographical coordinates of the epicenter, focal depth, magnitudes and focal mechanism solution have been derived by processing the data using Seisan Software package (Havskov and Ottemoler, 2004). In comparison with previous parameters, our results bring some new information very useful for the local and regional seismicity analysis and modeling

Materials and Methods

The data used in the paper derived from: i) 42 digitized historical seismograms recorded by 15 European seismic stations (Figure 1 and Figure 2); ii) Bulletins (arrival times of P, S and R/L phases, coda, amplitudes and periods).
All these materials were obtained into the framework of EUROSEISMOS 2002-2006 Project (www.storing.ingv.it/ es_web).

The procedure and the method of the analysis consists of many steps like those applied by Caciagli and Oros (2004), Oros (2008) and Oros et al. (2008), who studied the major earthquakes occurred in the western part of Romania. Firstly, the historical materials were collected and prepared for processing and analysis. The historical seismograms gathered in a raster format obtained by high resolution scanning at Sismos Centre, INGV Rome, Italy (http://sismos.rm.ingv.it). Then, the scanned seismograms were digitized and vectorized using Teseo software (Pintore et al., 2005) and finally they have been converted in Seisan format using a specialized routine. The data picked from the digital seismograms and read from bulletins (14 P and S phases and S-P differences) were used to obtain new location, focal depth and magnitudes (MLH, Ms, Mc), as well as the focal mechanism solution, using the Seisan software package and 13 polarities (Havskov and Ottemoller, 2004).

The data on the earthquake and the local seismicity were compiled from Atanasiu (1961), Oncescu et al. (1999) and Romplus-updated version (www.infp.ro), Shebalin et al. (1998).

The magnitudes MLH, Ms and Mc were derived according Karnik (1968) and Kondurskaia and Kopnichev (1982), respectively. Sometimes, if there are available, relationships calibrated for specific stations were used.

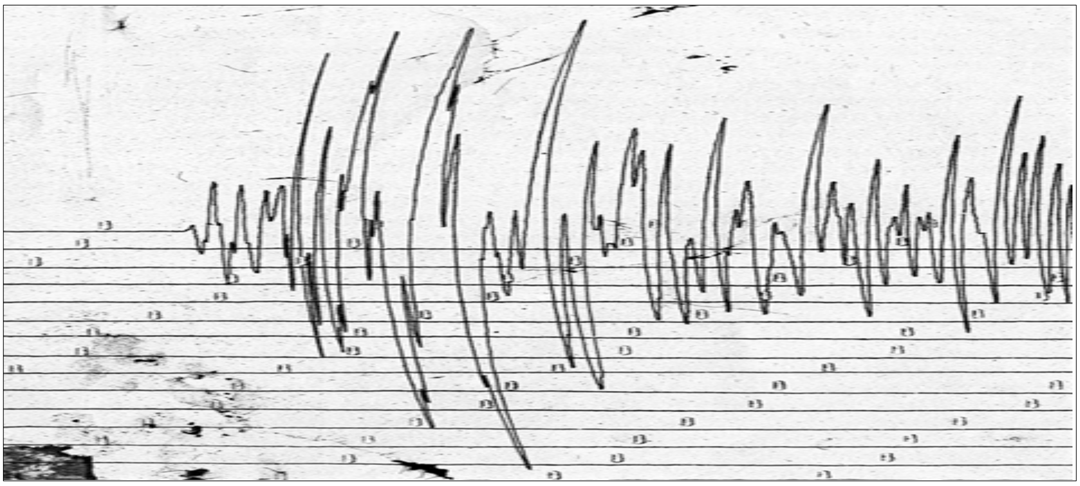

Figure 1. Sample of the smoked paper seismogram recorded by Bucharest seismic station for the M6.4, 26th January, 1916 earthquake (Bosch seismograph)

Results and Discussion

In Table 1 we present the main focal parameters obtained in this paper. The local seismicity of Fagaras Seismogenic Zone with the new location is displayed in Figure 1. It can be noticed the acceptable distribution of the stations around the epicentre to assure reliable values for the focal parameters (dist. min= 100 km, gap=162, rms=0.32).

The focal mechanism solutions obtained in this paper were determined with a good accuracy (Figure 2). The chosen solution has the following values: Plane 1: dip=68, strike=284, rake= -136; Plane 2: dip=50, strike=174, rake= -29; P: trend=305, plunge=42; T: trend=147, plunge=11, and it corresponds with normal faulting in good agreement with the extensional tectonic regime characteristic for South Carpathians (Enescu et al., 1996, Radulian et al., 2000).

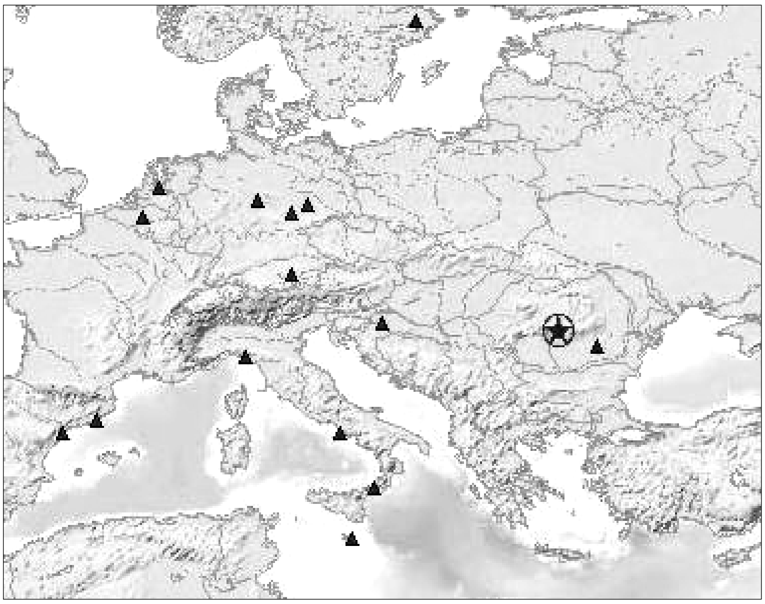

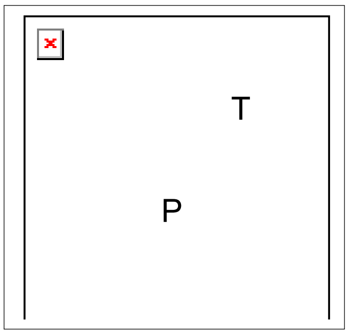

Figure 2. The map of the seismic stations that recorded the Mw6.4, 26th January, 1916 Romanian earthquake after www.storing.ingv.it/es_web (left) and the lower hemisphere range of the focal mechanism solutions obtained by first P waves polarity method (right).

Table 1. The new focal parameters for the 26th January, 1916 Romanian earthquake occurred in Fagaras Seismogenic Zone (South Carpathians).

Date	Origin Time	latN	longE	h (km)	MLH	Ms	Mc	mb	Mw	reference
26.01.1916	073810.4 ±0.79	45.212 ±3.5km	25.370 ±4.5km	15.7 ±3.3	6.5	6.4	6.0			This paper
26.01.1916	073754.0	45.400	24.600	21.0					6.4	Io=8MSK Oncescu et al. (1999), and Romplus
26.01.1916	073755.0 ±10.0	45.500 ±25km*	24.600 ±25km*	24.0*				6.4+		Io=8MSK±0.5 Shebalin et al. (1998)

Type of determination: *macroseismic, +instrumental

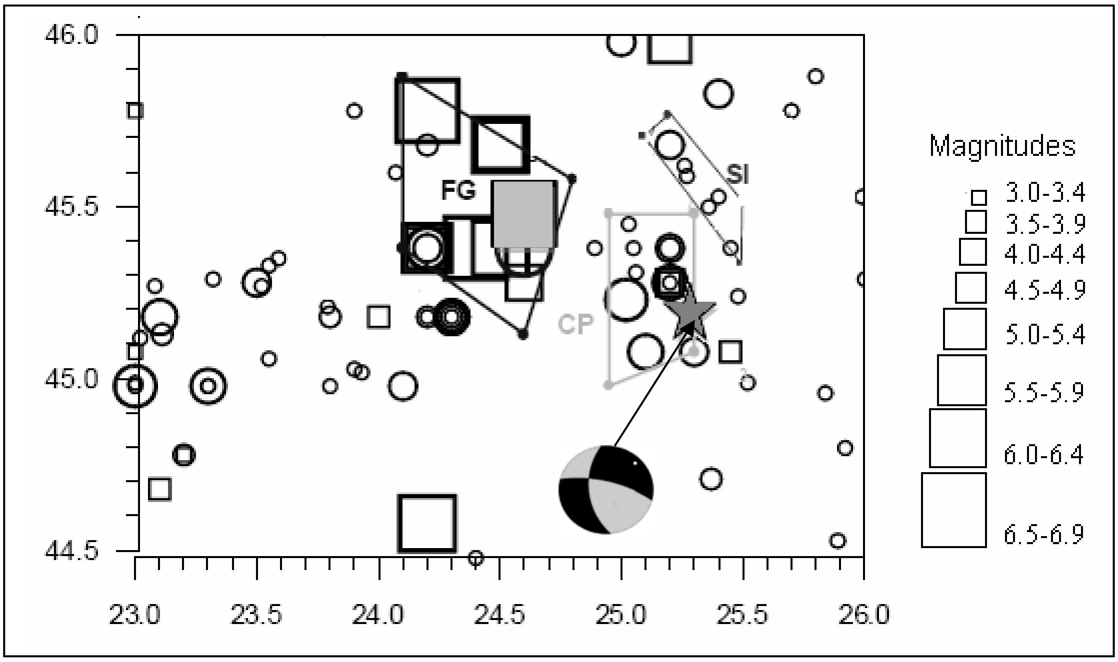

Figure 3. Fagaras Seismogenic Zone: Map of epicenters. Gray star is the new epicenter; gray square-the old epicenter; SI-Sinaia area, CP-Campulung area, FG-Fagaras area; magnitude symbols: squares-earthquakes occurred before 1900; circles-earthquakes occurred after 1901

We can observe that the magnitudes obtained in this paper are identically with those previously published by Oncescu et al. (1999) and Shebalin et al. (1998), but the new location and focal depth are quite different (Table 1, Figure 3) changing somehow the space pattern of the local seismicity. Fagaras Seismogenic Zone (FSZ) has three active areas with the

epicenters clustered on faults almost well known. These areas with high level of seismicity are known as Fagaras-Lovistea Depression, Campulung area and Sinaia area, respectively (Figure 3). The previously location of the studied event belongs to Fagaras-Lovistea Depression area, our new epicenter being shifted towards southeast, within Campulung seismic active area of FSZ.
It is worth to also mention that the two strong aftershocks (Mw=5.0 and Mw=5.2) catalogued by the other authors mentioned above in this paper were not identified on the historical seismograms.

The results obtained in this paper and the results obtained by Oros (2008) for the western part of Romania sustain the necessity of a new and detailed interpretation of all historical strong earthquakes to review the seismicity patterns on instrumental basis. For this aim the database of the EuroSeismos 2002-2006 Project which offer a huge number of historical seismograms and bulletins (the first author is full-partner in the project).

Acknowledgements

This paper could be accomplished only by the contribution of all the partners of EuroSeismos 2002-2006 Project and by the work of the INGV Rome/Sismos team.

References

Atanasiu I (1961). Romanian Earthquakes. *Romanian Academy Press, Bucharest.*

Caciagli M. & Oros E (2006). On the XXth Century strongest western Romanian earthquakes: preliminary results from EuroSeismos Project. *Abstracts, "First European Conference on Earthquake Engineering and Seismology", 3-8 septembrie 2006 Geneva, Switzerland (Joint ESC/EAEE Conference)*

Enescu D., Popescu E. & Radulian M (1996). Source characteristics of the Sinaia sequence of May-June 1993, *Tectonophysics, 261, 39-49.*

Karnik V. (1968). Seismicity of the European Area. Part 1. Catalogue of earthquakes (1901-1955). *Publishing House of the Czechoslocak Academy of Sciences, Praga.*

Kondorskuya N.V. & Kopnichev Yu.F (1988). Historical Seismograms and Interpretation of Strong Earthquakes. *in Historical Seismograms and Earthquakes of the World (Lee W, H. Meyers H., Shimazaki K, eds.), Acad. Press, INC. Harcourt Brace Jovanovich, Publishers*

Havskov J., & Ottemoller L., (eds.) (2004). Seisan: Earthquake analysis software. Version 7.2 şi 8.0. *Inst. Of Solid Earth Physics, Univ. of Bergen, Norway (www.ifif.uib.no).*

Oncescu M.C., Marza V., Rizescu M. & Popa M (1999). The Romanian earthquakes catalogue between 984-1997. *In Vrancea Earthquakes: Tectonics, Hazard and Risk Mitigation; F, Wenzel, D. Lungu (eds.), pp 43-47, Kluwer Academic Publishers.*

Oros E., Popa M. & Moldovan I.A (2008). Seismological DataBase for Banat Seismic Region (Romania)-Part 1: The Parametric Earthquake Catalogue. (2007). *Romanian Journal of Physics (vol. 53, no. 7-8) (in print)*

Oros E (2008). Review of Historical Seismicity in the western and south-western territory of Romania (Banat Seismic Region). *Acta Geodaetica et Geofisica Hungarica, 43, 2-3, pp.153-161.*

Pintore S., Quintiliani M. & Franceschi D (2005). Teseo: a vectorizer of historical seismograms. *Computers & Geosciences, Volume 31, Issue 10, December 2005, Pages 1277-1285. (http://dx.doi.org/10.1016/j.cageo.2005.04.001)*

Radulian M., Popescu E., Bala A. & Utale A. (2002). Catalog of fault plane solutions for the earthquakes occurred on the Romanian territory, *Romanian. Journal of Physics,47, 5–6, 663 –685.*

ROMPLUS. The Romanian Earthquake Catalogue; updated version (www.infp.ro)

Shebalin N. V., Leydecker G., Mokrushina N.G., Tatevossian R.E., Erteleva O.O., & Vassiliev Yu. (1998). Earthquake Catalogue for Central and Southeastern Europe 342 BC - 1990 AD, *European Commission, Report No. ETNU CT 93 - 0087, Brussels.*

Morpho-Tectonic Features of the Golbasi-Turkoglu Segment of East Anatolian Fault Zone Derived From Geographic Information System Analysis, Remote Sensing Analysis and Field Observations

Ozsarac V (1), Tekin B M (1), Kuterdem N K (1), Erkmen C (1), Nurlu M (1)

(1)Turkish Republic Ministry of Public Works ans Settlement General Directorate of Disaster Affairs Earthquake Research Department, Eskisehir Yolu 10.km, 06530, Ankara, Turkey.
ozsarac@deprem.gov.tr, bmtekin@deprem.gov.tr, kuterdem@deprem.gov.tr

Keywords: East Anatolian Fault Zone, geographic information system, morpho-tectonic, remote sensing, satellite images

Introduction

The East Anatolian Fault Zone(EAFZ) is a left-lateral strike-slip fault trending NE-SW between Karlıova and Antakya in Eastern Turkey. The width of the zone is approximately 30km, and it is about 580km long. Six different fault segments with lengths varying between 50km to 145km constitutes the EAFZ. The EAFZ intersects the right-lateral strike-slip North Anatolian Fault Zone(NAFZ) to the east of Karlıova. These two active faults play an important role in the neotectonic regime of Turkey. As the result of motion on them the Anatolian block (McKenzie 1972; Dewey et al. 1986) is escaping westward direction with average 2cm/year speed (fig.1).

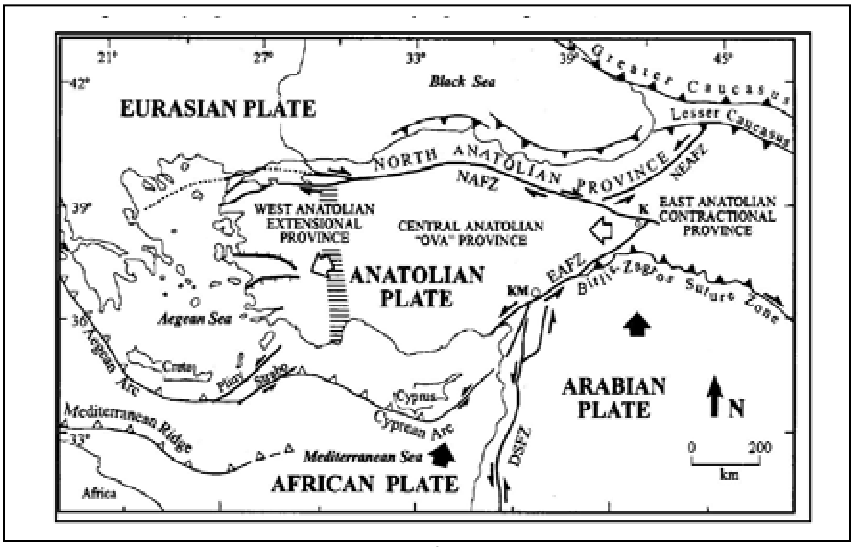

Figure 1. Neotectonics of Turkey (Bozkurt 2001)

On the basis of geological evidence, activity on the EAFZ has began in the Late Pliocene. The principal evidence for strike-slip motion is the offset of lithological contacts, morphologic features such as offset and shutter ridges, fault valleys, sag ponds, elongate and offset ridges and seismic activity (Saroglu et al. 1992). Golbasi-Turkoglu segment of EAFZ is highly popular amongst other segments for being a seismic gap.

Structural Characteristics of Golbasi-Turkoglu Segment of East Anatolian Fault

Golbasi-Turkoglu segment of EAFZ starts nearby Pervari (NE of Golbasi District). The main azimuth of the fault is N55E. From Pervari EAFZ has a zonal characteristics followed almost 20-30 km. There are different models proposed for the formation of Golbasi basin but the structural features reveal that releasing wedge type tectonics caused the Golbasi basin to form. In Golbasi Basin there are three sequent lakes called Golbasi Lake, Azapli Lake and Inekli Lake in the same direction of The fault system. Recent swamp deposits, alluvial fans and other lacustrine deposits constitute the Golbasi Basin. The main active fault crosses from the southern margin of Golbasi Lake and causes a left lateral slip on the plio-quaternary Aktepe and Segin tepe hills and continues through Kisik Dere region where main fault is observed as a single line in the Valley. The fault crosses Cretaceous Ophiolits and Paleocene limestones. Along this valley active fault caused almost 4 km. left lateral slip on the Kisik river. From Sakarkaya Village to Kartal village Golbasi-Turkoglu segment observed mainly as a fault zone consisting of several faults. Between this area Golalani depression is occurred as a small scaled pull-apart basin with left step-over of main fault. From this point, main fault continue to Turkoglu (SW) as a fault zone with approximate average of N60E.

Morpho-Tectonic Features of the Golbasi-Turkoglu Segment of East Anatolian Fault

Golbasi – Turkoglu segment of EAFZ is 90km. in length with average trends of N55E. Historical and instrumental earthquake data reveals that, Golbasi-Turkoglu segment of EAFZ is seismically dormant since last 500 years and also this segment is accepted as a seismic gap on EAFZ which has a potential to pose a seismic risk on nearby settlement areas. This study aims to determine the main active faults and fault associated land surfaces by using geographic information system tools (GIS), remote sensing analysis and field observations in the study area

The study is conducted in two phases. The initial phase can be defined as office work where morphological analysis and data preparation were performed by using GIS software. The second and the last phase of the study consisted of extensive field surveys, data verification. In the first part of the study a 1/25.000 scaled digital elevation models(DEMs) and derived morphological maps and Landsat ETM and SPOT 5 PAN images were analyzed for the study area. Dems, slope, aspect and hillshade maps were produced by using GIS software and tectonic features of the study area were determined before field study (fig. 2).

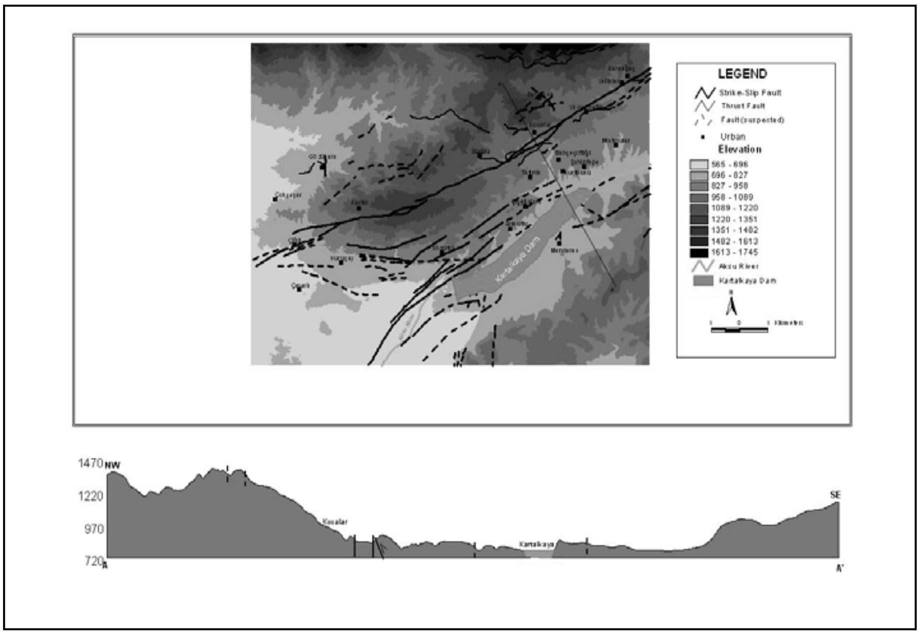

Figure 2. Tectonic structure of the study area.

Lineaments were also extracted from DEMs and satellite images and analyzed. Those analysis were correlated with field observations and Analgyph satellite images of the study area. Main strike slip fault related landforms like alluvial fans, river offsets and landslides were determined from morphological analysis. Lineaments maps and rose diagram of the study area were prepeared by using 1/25.000 scaled DEMs were produced from hillshade (fig. 3). The main azimuth of lineaments are dominated in N50-60E direction which can easily be delineated in Figure 3.

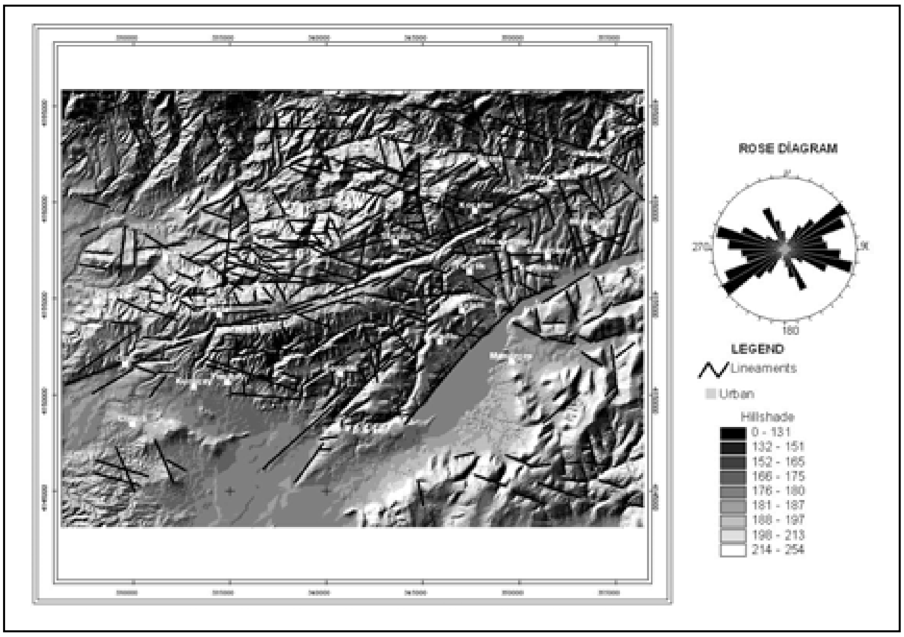

Figure 3. Lineaments analysis and rose diagram derived from hillshade image of south western part of the study area.

Results and Discussion

As the result of this study the active faults of the study area were mapped. This data is also used in the site selection of trenches for paleoseismological studies. Further steps will be the paleoseismological studies which will put definite outcomes for the seismic hazard evaluation of this segment and nearby region. It is noteworthy that GIS and remote sensing applications in geology, especially in tectonics and geomorphology, proposes practical and valuable solutions in determining the structural features of any area before applying extensive field studies.

References

Bozkurt E. (2001). Neotectonics of Turkey – a Synthesis, *Geodinamica Acta, 14, 3-30.*

Dewey J.F., Hempton M.R., Kidd W.S.F., Şaroglu F. & Sengor A.M.C.(1986). Shortening of continental lithosphere: The neotectonics of eastern Anatolia-a young collision zone, in Collision Tectonics, *Spec. Publ. 19, edited by M.P. Coward and A.C. Ries, Geological Society of London, 36p.*

McKenzie D.P. (1972). Active tectonics of the Mediterranean Region,Geophys, *J. R. Astron. Soc., 30, 109-185.*

Saroglu F., Emre E.& Kuscu İ.(1992). The east Anatolian fault Zone of Turkey, *Annal. Tecn., 6, 99-125.*

Space manifestation of the seismic energy time variation and seismic hazard assessment in the Ionian Sea region

Papadopoulos G A (1), Baskoutas I. (2)

(1) Earthquake Planning and Protection Organization, Seismotect. Div., Xanthou32, 15451 Athens, gpapadopoulos@oasp.gr
(2) Geodynamic Institute, National Observatory of Athens, P.O. Box 20048 118 10 Athens, i.basko@.gein.noa.gr

Keywords: Seismic parameters, time variation, spatial variation, seismic hazard assessment

Introduction

Earthquake prediction is a very difficult and tricky problem so several attempts proposed have been disputed hardly, nonetheless for many geoscientists still remains a very attractive and challenging research field (Keilis Borock & Soloviev 2003). Time variation study of the seismicity, expressed in term of some seismic parameters, is a very common approach (Hebermann & Wyss, 1984; Papadopoulos & Voidomatis 1987, Wiemer, 2001; Papadopoulos et al., 2003), which can be used for seismic hazard assessment (Fedotov & Riznitchenko 1984; Sobolev et al 1991; Zavyalov 2002). Previous studies on these seismic parameters , in several areas of the world, show significant temporal changes (Wiemer & Wyss 2002; Enescu & Ito, 2003; Baskoutas et al., 2007). In many cases the observable sharp temporal changes can be considered as anomalies. The coincidence in many cases of strong earthquake occurrence with previously mentioned anomalies may signalise indicators (precursors) of fore-coming strong earthquakes (Wyss & Baer 1981; Gao & Gao, 2002; Papadopoulos & Baskoutas 2006). Generally it is believed that studies in this field are of special interest and they may contribute to toward to intermediate term earthquake prediction.

In this study the detailed time series for the seismic energy released, in the form $logE^{2/3}$ were obtained by the means of new proposed FastBEE tools, proposed (Papadopoulos et al., 2003). Moreover, the statistical reliability of the “internal” estimations (Steyerberg et al., 2003) were examined in respect to data samples from independent neighbour seismogenic local zones, being in common the processing method, definition of analysis parameters and properties of the earthquake catalog used. Finally, the seismic energy released time variations were examined in order to reveal the regularity of its spatial manifestation in the front of the subduction zone of the north-western part of the Hellenic Arc. This area is characterized by the frequent occurrence of strong earthquakes and hence permits the close examination for correlation of the calculated temporal changes of energy released with respect observed strong earthquake occurrence.

Method and data

To reveal the spatiotemporal temporal variation of the seismic energy released first six independent and adjacent local zones (hereafter LZ) were defined. These local zones have a rectangular shape with sizes of about 200x60 km. Their main axis is perpendicular to the front of the subduction zone of the Hellenic Arc (figure 1). Second, estimates were obtained by the means of FastBEE tools proposed by the authors (Papadopoulos et al., 2003). In this approach the release seismic energy is expressed in the form $logE^{2/3}$ proposed by Keilis-Borok (1959). Seismic energy, in erg, is obtained by the means of the relationship (1):

$$\log E = 1.5M + 4.7 \quad (1)$$

proposed for the Greek territory by Papazachos and Papazachou, (2000). In these estimates standard error is calculated by relationship (2):

$$\sigma_{\log E} = 0{,}4343/\sigma_E \quad (2)$$

Time series of the considered parameter were obtained for each local zone by averaging the seismic data within 13 months (in this work) time interval, with one-month step. To distinguish more essential fluctuations of energy released time series a triangular form filter of the same width (13 months window) were applied. The filter allows passing periods equal or greater of the half filter width (Jenkins & Watts, 1968) and thus fluctuations, with wave periods more than 6 months, are evident. Filtered time series are displayed superposed to the smoothed estimates as bolder curves. Moreover the strong earthquakes origin time within the examined time period have been also marked by chronologically numbered arrows perpendicular to the time axis.

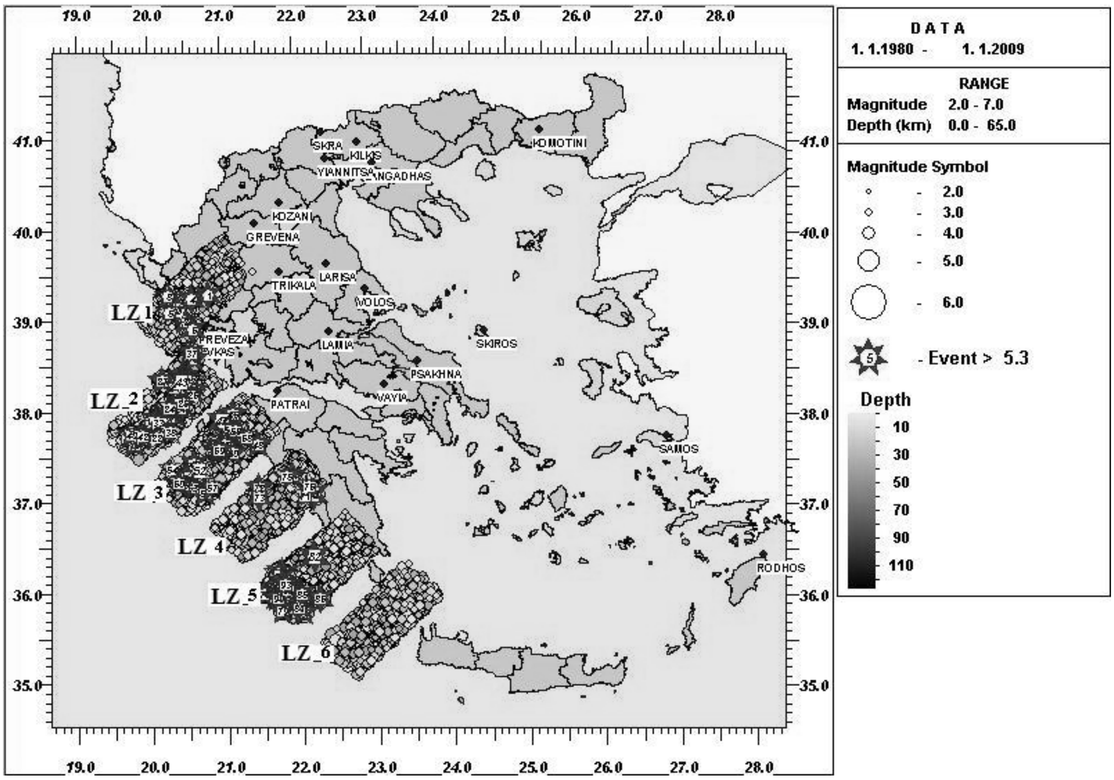

Figure 1. Seismic epicenters maps of the local zones used in the analysis.

Detailed time analysis was performed on separate earthquake data set for each local zone mentioned previously. Seismic data used have been taken from the Bulletin of the Geodynamic Institute of National Observatory of Athens in the time period 1980 up today. Table 1 show the total number of earthquakes, for each local zone, with Ms > 3.5, which were used in the present study.

Table 1. Number of earthquakes used in this study for each local zone.

Local Zones	Number of Earthquakes
LZ_1	1627
LZ_2	2731
LZ_3	4707
LZ_4	1195
LZ_5	1954
LZ_6	620

Table 2 shows the list of all strong earthquakes with M > 5.7 which occurred in each localzone (LZ) and displayed in the respective time series plot.

Table 2. List of the strong earthquakes for each local zone, which appear on figure 2.

Date	Origin time	Lat N°	LonE°	Depth	Magn
LZ_1					
1981 MAR 10	15 16 18.0	39.30	20.80	0	5.8
1990 JUN 16	02 16 20.4	39.13	20.38	38	6.0
1993 JUN 13	23 26 40.0	39.25	20.57	5	5.9
2000 MAY 26	01 28 22.0	38.91	20.58	5	5.8
2007 JUN 29	18 09 11.2	39.25	20.26	19	5.7
LZ_2					
1981 JUN 24	18 41 26.0	37.80	20.00	0	5.7
1981 JUN 28	17 20 21.0	37.90	20.10	0	6.0
1983 JAN 17	12 41 30.9	37.97	20.25	9	6.7
1983 JAN 19	00 02 15.5	38.05	20.41	6	6.0
1983 JAN 31	15 27 .6	38.05	20.41	2	5.8
1983 MAR 23	23 51 7.6	38.19	20.40	10	6.2
1987 FEB 27	23 34 54.1	38.37	20.42	1	5.9
1988 MAY 18	05 17 42.7	38.35	20.47	1	5.8
1989 AUG 24	02 13 13.4	37.89	20.11	1	5.7
1996 FEB 1	17 57 56.5	37.72	19.85	1	5.7
1998 OCT 8	03 50 17.1	37.79	20.27	5	5.7
2007 MAR 25	13 57 58.2	38.34	20.42	15	6.0
LZ_3					
1988 OCT 16	12 34 5.4	37.90	20.96	4	6.0
1994 APR 16	23 09 36.4	37.43	20.58	30	5.8
1997 NOV 18	13 07 36.9	37.26	20.49	5	6.6
1997 NOV 18	13 13 48.3	37.36	20.65	5	6.1
1998 JAN 10	19 21 54.3	37.12	20.73	5	5.7
2002 DEC 2	04 58 56.4	37.80	21.15	17	5.8
2005 OCT 18	15 25 59.5	37.58	20.86	22	6.1
2006 APR 4	22 05 3.3	37.58	20.93	18	5.7
2006 APR 11	00 02 41.5	37.64	20.92	18	5.7
2006 APR 11	17 29 28.4	37.68	20.91	18	5.9
2006 APR 12	16 52 1.2	37.61	20.95	19	5.9
LZ_4					
1986 SEP 13	17 24 33.8	37.10	22.19	1	6.0
1993 MAR 5	06 55 6.4	37.07	21.46	1	5.8

2001 SEP 16	02 00 48.5	37.29	21.83	5	5.7
LZ_5					
1983 JUL 14	02 54 21.6	35.80	22.03	18	5.7
1994 JAN 11	07 22 53.3	35.84	21.95	40	5.9
1997 OCT 13	13 39 39.2	36.41	22.18	6	6.1
1998 APR 29	03 30 37.1	35.99	21.98	5	6.0
2000 MAY 24	05 40 37.5	36.00	22.01	5	5.9
2003 OCT 17	12 57 8.7	35.96	22.25	37	5.8
2008 FEB 14	12 08 55.2	36.22	21.75	38	6.6
2008 FEB 20	18 27 4.9	36.18	21.72	25	6.5
2008 FEB 26	10 46 5.1	35.96	21.70	5	5.7
LZ_6					
1992 NOV 21	05 07 19.0	35.51	22.38	93	6.3
2006 JAN 8	11 34 54.0	36.21	23.41	69	6.9

Results

Time series of $\log E^{2/3}$ plots of six independent adjacent local zones across the front of the subduction zone of the Hellenic arc system, were obtained and plotted together (Figure 2).

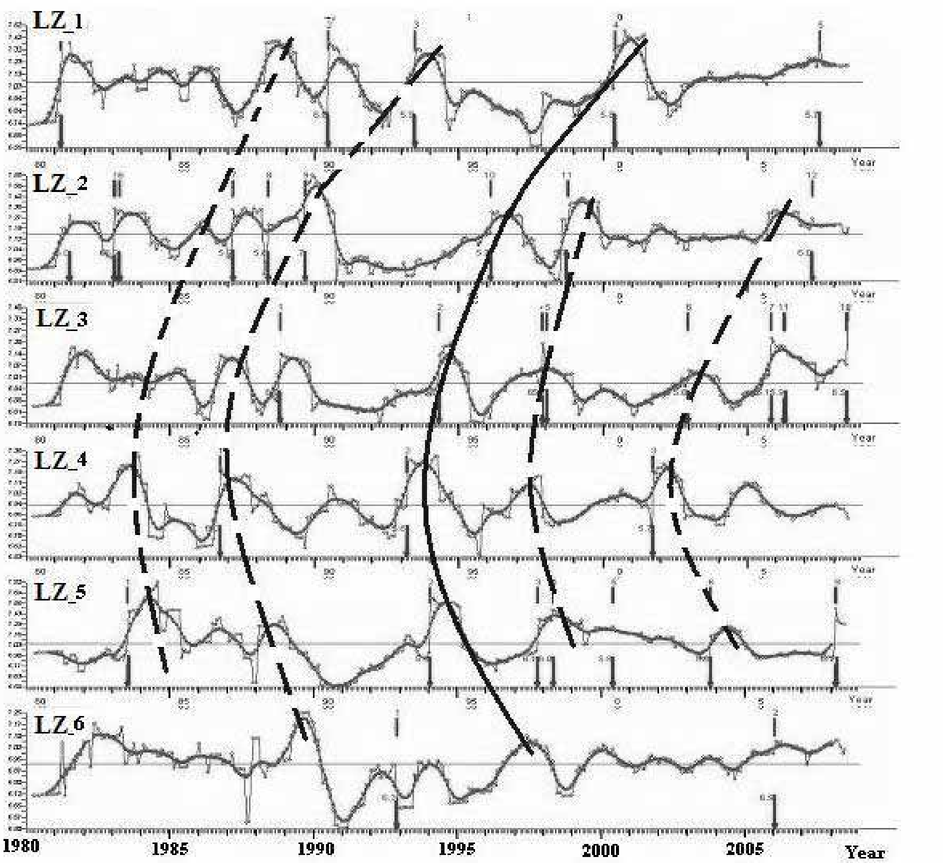

Figure 2. Temporal variation plots of seismic energy released in adjacent seismogenic local zones in the front of the Hellenic arc. Solid and dashed lines connect the picks of the anomalies in the seismic energy time series (discussed in detailed in the text). Numbered arrows perpendicular to the time axis shows the origin time of strong earthquakes in each local zone.

In all examined individual plots, significant deviations of the temporal variation fluctuations of the seismic energy released from their mean values can be considered as anomalies. Precisely fluctuations anomalies forms relative maxima (like deficit of the energy released) increasing then to reach a consecutive relative maxima, forming picks. The careful visual inspection of figure 2 shows a clear sifting of the anomalies (solid and dashed lines, connecting picks of consecutive neighbour local zones), in either side of the local zone 4, toward to north and south. At the same time, in most of the cases, time energy variations anomalies are associated to strong earthquake (M> 5.7) precisely before the energy relative maxima (picks).
As an example the foresaid solid line connecting the picks of the greater estimated anomalies in all adjacent local zone plots (figure 2) shows a clear spatial and time sifting in respect to central local zone LZ_4, toward to north and to south. Thus temporal variation of local zone 3 (LZ_3) shows a clear negative anomaly from 1990 to 1994. The end of this anomaly is associated with the M = 5.8 strong earthquake of April 16, 1994 occurred in this local zone. Similar anomaly from 1991 to 1995, can be observed in the plot of LZ_2 but with a small time sifting, which also is associated with a M=5.7 strong earthquake of Jan 1, 1996 in this local zone. The same form anomaly from 1995 to 2000 can also be observed in LZ_1 with small time sifting, which also is associated with the Ms = 5.8, strong earthquake of May 26 , 2000 in this local zone. In the same way similar anomalies can be identified to the south on plots of consecutive local zones LZ_5, LZ_5, LZ_6 respectively. These anomalies again are sifted toward to the time axis and again strong earthquake occurrence is presented at the end phase of the anomalies. Precisely energy anomaly, even not so clear shaped in the LZ_4 is associated with M=5.8, March 5, 1993 earthquake. Again strong earthquake, M=5.8, of Jan 11, 1994 is associated with anomaly of LZ_5 curve. Nonetheless greater anomaly of LZ_6 is not correlated to any strong earthquake as could be expected. Instead it seams to be truncated by smaller size energy anomalies and the strong earthquake M= 6.3 of Nov 21, 1992 is observed. On the basis of previously mentioned observations it is possible to talk about a propagation of the anomalies, which shows a clear time sifting and space migration in either side of the middle local zone 3, toward to north and south. Similar behaviour of the temporal variation anomalies, in the previous or later times, even smaller and not so clear are marked by dashed lines, figure 2.

From this observation we may conclude that strong earthquakes occurrence can be expected with 1 or 2 years delay, in the neighbour adjacent local zones, next to LZ_4 (being a reference point), toward north and south. As an example we can report the case of the strong earthquake of 1993 in local zone 4 which is followed, to the north, from Ms = 5.8, of April 16 , 1994 (LZ3), Ms = 5.7, of Jan 1 , 1996 (LZ2) and the Ms = 5.8, of May 26 , 2000 (LZ1), earthquakes respectively. Knowing the distances of the geometrical centers of consecutive zones, the energy anomalies propagation velocity can be estimated to be 100 to 150 km/year.

The study of the correlation of the calculated anomalies in respect to the strong earthquake occurrence permit the validation of the successful intermediate term earthquake predictions and to confirm or not the possibility to use the results for seismic hazard assessment in the area. Table 3 shows the number of the strong earthquakes, the respective successful correlation with seismic energy anomalies and failed cases in each local zone. Probability then is calculated as:

$$P= 24*100/34 =70.5\%$$

Table 3. Number of the successful and failed cases in each local zone

Local zone	Number of EQs	Successful cases	EQ with no anomaly	Anomaly With no EQ
LZ_1	5	4	1	1
LZ_2	9	6	2	1
LZ_3	8	5	2	1
LZ_4	3	3	-	3
LZ_5	7	5	3	0
LZ_6	2	1	1	2

Sum	34	24	9	8

Discussion conclusions

In this work we examine the temporal variation of the seismicity focusing on the seismic energy released (in the form $\log E^{2/3}$) analysis, under the assumption that its temporal changes are closely related to the acting geodynamic process. Obtained time series of seismic energy, shows significant fluctuations that can be considered in most of the cases as anomalies. Under the foresaid assumption these anomalies reflect the influence of the geodynamic regime dominated the area on the spatio temporal manifestation of the seismic activity. It is observed that in many cases strong earthquake seismic activity occurrence can be associated with seismic energy anomaly phases. Precisely it is observed that, the strong earthquake occurrence coincide with the increasing phase of the energy after passing a relative minimum. Nonetheless the size and the duration of the anomalies observed are not proportional to the size of the associated strong earthquake. In some cases the presence of energy anomaly is not associated to any strong earthquake but to a cluster of smaller size earthquakes and so correlation is unclear. From the physical point of view it is possible to consider such temporal behaviour as a result of the deformation regime, which causes accumulation or redistribution of the energy for future seismic activity in the same or neighbour areas. This may constitute a plausible explanation for the absence of strong earthquake although the presence of the foresaid anomalies. The statistical reliability of the “internal” estimations (Steyerberg et al., 2003) in computing temporal variation estimates was tested positively, against independent seismic data sets from neighbour local zones, being in common the processing method, analysis parameters, and properties of seismic catalog.

There are several attempts presented on deformation dynamics, kinematics and stress acting in the margins of the convergence of tectonic plates, like a typical subduction zones (Bott and Dean, 1973; Turcotte, 1983; Kreemer et al., 2004; Schenk et 2007). Within this frame evidences for tectonic waves or creep waves, have been reported (Ovcharenko et al., 2002, 2005; Gao and Crampin, 2004, 2006). Observed, spatio temporal anomalies propagation, in either side of the middle local zones 3 and 4, of figures 1 and 2, toward to north and south across the front of the subduction zone, can be considered as “energy wave”. Assuming that propagating anomalies can be related to the acting stress then we can infer that observed sifting can be an evidence of tectonic wave. The presents of the transform faulting in the Ionian Sea area (Scordilis et al., 1985; Sachpazi et. al., 2000) may be rule the observed temporal sifting, in respect to the central Ionian Sea area.

As a conclusion we may state that the seismic energy released propagation, like “energy wave” can be an evidence of tectonic wave. Estimates temporal anomalies can be associated with observed strong earthquake occurrence. The high probability of successful intermediate term earthquake prediction was proved. These results may help seismologist to add information for the seismic hazard assessment in a given area. Moreover we believe that the proposed approach can also help to draw new hypothesis on spatio temporal variation of seismicity.

References

Baskoutas I., Papadopoulos G. A. ,Karakostas V. & Papdimitriou E (2007). Recent 2005-2006 strong seismic activity in Greece under the aspect of seismicity parameters temporal variation. Bulletin of Geological Society of Greece, *XXX/3, 1055-1062.*

Bott M.H.P & Dean D.S (1973). Stress diffusion from plate boundaries, *Nature, 243, 339-341.*

Carter J.A. & Berg E. (1981). Relative stress variations as determined by b-values from earthquakes in Circum-Pacific subduction zones, *Tectonophysics, 76, 257– 271.*

Enescu B. & Ito K (2003). Values of b and p: their Variations and Relation to Physical Processes for Earthquakes in Japan, *Annuals of Disas. Prev. Res. Inst., Kyoto Univ., No.46 B.*

Fedotov S.A & Riznitchenko Y.V (1984). Long- and short-term prediction of strong earthquakes, *In earthquake prediction. Unesco. Terra. Sci. Publ. Co. Tokyo. 477-485p.*

Fedotov S. A., Sobolev, G.A. & Boldyrev S.A (1977). Long- and short-term earthquake prediction in Kamchatka. *Tectonophysics, 37, 305-321.*

Gao Y. & Crampin S (2004). Observations of stress relaxation before earthquakes. *Geophys. J. Int., 157, 578-582.*

Gao Y. & Crampin S (2006). A stress-forecast earthquake (with hindsight), where migration source earthquakes causes anomalies in shear-wave polarisation, *Tectonophysics, 426, 253-262.*

Gao A. & Gao S.S. (2002).Temporal variation of seismic b-values beneath NE Japan island arc, *Geoph. Res. Letters, 29, 9.*

Hebermann and Wyss (1984). Background Seismicity Rates and Precursory Seismic Quiescence: Imperial Valley, California, *Bull. Seismol. Soc. Am., 74, 1743-1755.*

Jenkins G.M & Watts D.G (1968). Spectral Analysis and its Applications*, Holden–Day Publishing Co., New York.*

Keilis-Borok V.I & Soloviev A.A (2003). Nonlinear dynamics of the Lithosphere and Earthquake Prediction, *Springer, 330p.*

Keilis-Borok V.I.(1959). On the estimation of the displacement in an earthquake source and of source dimensions, *Annali di Geofisica, 12, 205 -214.*

Kreemer C, Chamont-Rooke N. & Le Pichon X (2004). Insights into the evolution and the vertical coherency of deformation in the northern Aegean from a comparison of geodetic and other strain indicators, *Geoph. Res. Abstracts, 6, 02653.*

Ovcharenko A., Sokolov V., Loch C.H. & Wen K.L (2005). Modelling of dynamic deformation of the Earth crust: A tool for evaluation of future earthquake parameters, *EGS XXVII General Assembly, Nice, 21-26 April 2002, abstract #18.*

Papadopoulos G.A & Voidomatis Ph (1987). Evidence of periodic seismicity in the inner Aegean seismic zone, *Pageoph, 125 (4), 613-628.*

Papadopoulos G.A. & Baskoutas I (2006).Prognostic character of FastBEE analysis for seismic hazard assessment in Greece, *2nd International Workshop on Earthquake Prediction, Rion Patras June 26, 2006.*

Papazachos C.B. and Papazachos B.C (2000). Accelerated preshock deformation of broad regions in the Aegean area, *Pure and Appl. Geophys. 157, 163-168.*

Papazachos B.C. (1990). Seismicity of the Aegean and surrounding area, *Tectonophysics, 178, 287308.*

Sachpazi M., Hirn A., Clement C., Haslinger F., Kissling E. & Charvis P (2000). Western Hellenic Subduction and Cephalonia Transform: Local Earthquakes and Plate Transport Strain, *Tectonophysics, 319, 301-319*.

Scordilis E.M., Karakaisis G.F., Karakostas B.G., Panagiotopoulos D.G., Comninakis P.E. & Papazachos B.C (1985). Evidence for transform faulting in the Ionian Sea. The Cephalonia island earthquake sequence of 1983, *Pure Appl. Geophys., 123, 388-397.*

Sobolev G.A., Chelidze T.L., Zavyalov A.D., Slavina L.B. & Nikoladze V.E (1991).The maps of expected earthquakes based on a combination of parameters, *Tectonophysics, 193, 255-265.*

Schenk V., Schenková Z. & Jechumtálova Z (2006). Geodynamic hazard and risk assessments for sites close or in tectonic zones with shear movements, *Environmental Geology, 51, 7.*

Steyerberg E.W, Bleeker S. E., Moll H.A. & Grobbee D.E. & Moons K.G (2003). Internal and external validation of predictive models: a simulation study of bias and precision in small samples, *J. Clin. Epid. , 56(5), 441-448.*

Sykes L R. & Jaume S.C (1990). Seismic activity on neighboring faults as a long-term precursor to large earthquakes in the San Francisco Bay area, *Nature, 348, 595-599.*

Turcotte D L (1983). Mechanisms of crustal deformation, *J. Geolog. Soc., 140, 5, 701-724.*

Wiemer S (2001). A software package to analyse seismicity: ZMAP, *Seism. Research Letters, 72, 373-382.*

Wiemer S. & Wyss M (2002). Spatial and temporal variability of the b-value in seismogenic volumes: An overview, *Advances in Geophysics, 45, 259-302.*

Wyss M. & Baer M (1981). Seismic quiescence in the western Hellenic arc may foreshadow large earthquakes, *Nature, 289, 785-787.*

Zavyalov A. D (2002). Testing the MEE prediction algorithm in various seismically active regions in the 1985-2000 period: results and analysis, *Izvestiya, Physics of the solid Earth, 38, JVs 4, 262-275.*

Geo-engineering Mapping with Respect to Liquefaction Susceptibility of the Region of Thrace, North-Eastern Greece

Papathanassiou G (1), Valkaniotis S (2), Pavlides Sp (3)

(1) Department of Geology, Aristotle University of Thessaloniki, gpapatha@auth.gr
(2) Department of Geology, Aristotle University of Thessaloniki, svalkan@geo.auth.gr
(3) Department of Geology, Aristotle University of Thessaloniki, pavlides@geo.auth.gr

Keywords: Liquefaction susceptibility, Thrace, Greece, engineering geology

Introduction

The region of Thrace is located at the north-eastern part of Greece; an area that plays a significant role regarding the status of energy in Greece due to the fact that two of the major pipelines, of natural gas and oil, will pass through this area. Consequently, the avoidance of an earthquake-induced damage to these lifelines is a major task for the country.
The region of Thrace is characterized as low seismicity area due to the limited information regarding historical and instrumental seismicity. However, the fact that large tectonic structures that were mapped during geological surveys are classified as active indicates that the occurrence of a big earthquake must not be excluded. In addition, the fact that two of the largest rivers in Greece traverse the region and deposit material susceptible to liquefaction increases the possibility of a liquefaction-induced ground failure.
Liquefaction is the transformation of saturated, unconsolidated granular material from a solid state to a liquid state as a consequence of increased pore pressures that reduce the effective strength of the material (Youd, 1973). The liquefaction of a subsoil layer may induced ground failures such as ground settlements, sand boils and lateral spreading and lead to structural damages at buildings, pipelines, bridges etc.
In order to prevent and/or to minimize the effectiveness of soil liquefaction, investigations regarding the susceptibility and the potential of liquefaction are taken place. Areas susceptible to liquefaction can be identified through detailed geologic, geomorphic and hydrologic mapping (Witter et al. 2006) while the liquefaction potential is evaluated based on data regarding the susceptibility to liquefaction of the soil layer and the expected value of ground motion triggered by the earthquake.
Liquefaction susceptibility maps have been compiled for several regions and countries including USA, Japan, Iran, Turkey etc. In particular, maps were developed for the San Francisco Bay region (Youd and Perkins, 1987; Knudsen and others, 1997; Sowers et al., 1998; Knudsen et al., 2000; Holzer et al., 2002), for Los Angeles urban area (Tinsley et al. 1985). These maps do not predict liquefaction-related ground failures, although ground failures may accompany liquefaction and are more likely to occur in areas with higher liquefaction susceptibility (Tinsley et al., 1985)
The main goal of this paper is to present a preliminary map of liquefaction-prone zones in the region of Thrace, North-Eastern Greece. The susceptibility map was developed based on the 1:50,000 scale geological maps of the region and the existing correlation of geological units with the susceptibility to liquefaction.

Materials and Methods

The criteria proposed by Wakamatsu (1992) and the guidelines published by the California Department of Conservation, Division of Mines and Geology (CDMG, 1999) were used in order to evaluate the liquefaction susceptibility of deposits in the area of Thrace.

Wakamatsu (1992) classified sedimentary deposits using geomorphological criteria in 3 categories of liquefaction susceptibility under the ground motion at the MMS intensity VIII (Table 1): likely, possible and not likely. Areas classified as “not likely” liquefaction susceptibility define zones where liquefaction-induced failures are not expected. On the contrary, zones where geomorphological units such as natural levee, former river channel, sandy dry river channel and artificial fill were classified as the highest level of liquefaction potential, i.e. liquefaction likely (TC4, 1999). At these areas, further investigation using in-situ test and quantitative parameters of subsoil layers must be performed.

Table 1. Susceptibility of detailed geomorphological units to liquefaction subjected to ground motion of the MMS intensity VIII (Wakamatsu, 1992)

Geomorphological conditions		Liquefaction potential
Classification	**Specific conditions**	
Valley plain	Valley plain consisting of gravel or cobble	Not likely
	Valley plain consisting of sandy soil	Possible
Alluvial fan	Vertical gradient of more than 0.5%	Not likely
	Vertical gradient of less than 0.5%	Possible
Natural levee	Top of natural levee	Possible
	Edge of natural levee	Likely
Back marsh		Possible
Abandoned river channel		Likely
Former pond		Likely
Marsh and swamp		Possible
Dry river bed	Dry river bed consisting of gravel	Not likely
	Dry river bed consisting of sandy soil	Likely
Delta		Possible
Bar	Sand bar	Possible
	Gravel bar	Not likely
Sand dune	Top of dune	Not likely
	Lower slope of dune	Likely
Beach	Beach	Not likely
	Artificial beach	Likely
Interlevee lowland		Likely
Reclaimed land by drainage		Possible
Reclaimed land		Likely
Spring		Likely
Fill	Fill on boundary zone between sand and lowland	Likely
	Fill adjoining cliff	Likely
	Fill on marsh or swamp	Likely
	Fill on reclaimed land by drainage	Likely
	Other type fill	possible

According to the criteria listed in Table 1, the susceptibility to liquefaction of a geological unit can be evaluated based on its depositional environment; the depositional process affect the liquefaction susceptibility of sediments since fine and coarse grained soils sorted by fluvial or wave actions are more susceptible than unsorted sediments (Youd, 1998).
Moreover, the geological units of Thrace were correlated to liquefaction susceptibility based on their age; it is well established that the susceptibility of a soil layer reduces with its age since cementation and density increase with age. In order to compile a liquefaction susceptibility map based on aging, the guidelines of CDMG (1999) were employed.
According to CDMG (1999) an area is characterized as Liquefaction zone when meeting one or more of the following criteria:

- evidence of historical liquefaction occurrences

- data from in-situ tests and analyses indicate that the soils are likely to liquefy

in case of lacking of the above data, a site is considered as susceptible to liquefaction when:

- area containing soils of late Holocene age, the groundwater is less 13 meters deep and the peak ground acceleration (PGA) having a 10% probability of being exceeded in 50 years is greater than 0.1g
- soils of Holocene age where the depth of groundwater table is less than 10 meters and the PGA (10% in 50 years) is greater than 0.2g

Though, these factors are reliable for the evaluation of susceptibility, they may not be themselves uniquely define liquefaction potential at a site.

Geological Mapping and Characterization

In order to evaluate the liquefaction susceptibility based on the above recommendations, we used data provided mainly by geologic maps published by IGME as a base layer. Afterwards, the geological units were classified into two categories based on their ages, pre-quaternary and quaternary (figure 1). This separation was made in order to further analyze and evaluate the liquefaction susceptibility of the deposits of Quaternary sediments since pre-Pleistocene deposits are classified as very low susceptibility units (Youd, 1998).
Evaluation of geological units was made using mainly geologic maps in 1:50.000 scale by IGME (Geological Survey of Greece). Supplementary data and coverage of areas with unpublished map sheets were collected using topographic maps, satellite (Landsat 7 ETM+) and aerial images, and digital elevation model from SRTM data, along with field surveys. Low-land saturated coastal and fluvial sediments, wetlands and river flood-plains usually depicted as undivided Quaternary/Holocene sediments in geological maps were traced using the above combination of data: candidate areas were identified using digital elevation and geology raster data, and manually checked in Landsat 7 images and/or aerial images (if provided).

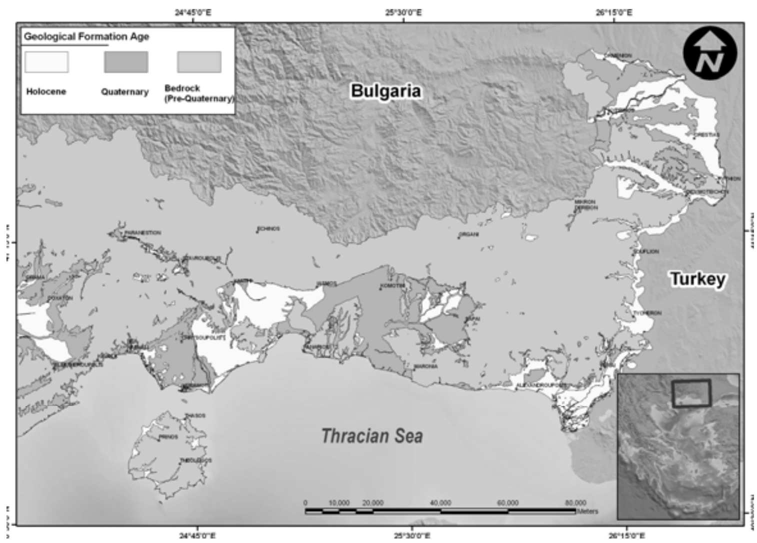

Figure 1. Map showing the distribution of the quaternary and pre-quaternary geological formations.

Seismotectonics Characteristics

The region of Thrace is considered as a low seismicity area according to the historical seismicity and the instrumental seismicity data in Greece for the years after 1911 (Kiratzi et al. 2005). According to Papazachos et al. (2007) only three earthquakes with magnitude M>5.5, the 1752, 1756 and 1784 events, occurred at the area that is examined in this study. In particular, the earthquake of 1752 (M 7.4) caused damages to Edirne (Ambraseys and Finkel, 1987) while the houses at the towns of Havsa and Haskoy and the villages of Zerna, Kozkoy, Ferecik were totally destroyed (Kiratzi et al. 2005). The event of 1784 (M 6.7) induced the collapse of 500 buildings in the area of Komotini. Though, the limited number of earthquakes in the region of Thrace, the occurrence of similar events could trigger soil liquefaction, since the lowest bound of an earthquake-induced liquefaction magnitude is smaller than the above ones (Papadopoulos and Lefkopoulos, 1993; Papathanassiou et al., 2005). In what concerns the expected value of PGA in Thrace, the Greek Seismic Code defines that the designed peak ground acceleration (PGA) is equal to 0.16g, having a 10% probability of being exceeded in 50 years (EAK, 2000).

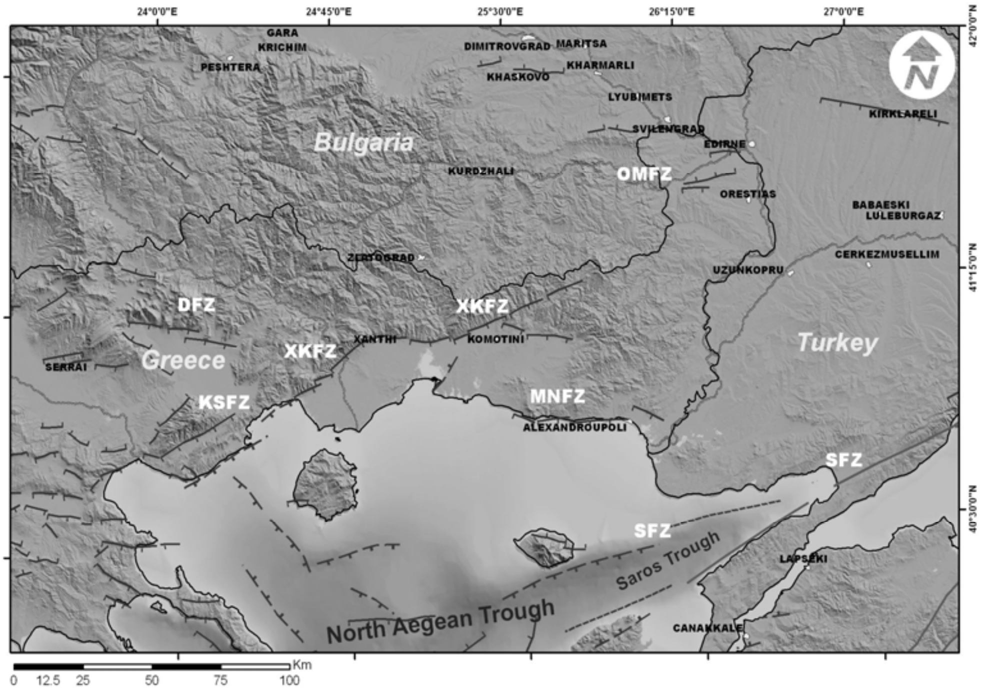

Figure 2. Main active and possible active faults (shown in red line) in the broad area of Thrace. Fault data from Pavlides et al. (2007). OMFZ – Orestias-Mikri Doxipara Fault Zone, XKFZ – Xanthi-Komotini FZ, DFZ – Drama FZ, KSFZ – Kavala-Strimonas FZ, MNFZ – Maronia-Makri FZ, SFZ – Saros FZ.

Additionally, tectonic structures capable to trigger big events are present in the broad area and active faults have been mapped and documented during field surveys. Active faults in the area have a general W-E orientation according to the present N-S extensional stress regime (Koukouvelas I.K., Aydin, A., 2002; Pavlides et al 2006). They are mostly normal-oblique faults in the mainland, with strike-slip faulting off-shore along the North Aegean Trough. As it is shown in figure 2, the major faults are the large Kavala-Strymonas (KSFZ) and Xanthi-Komotini (XKFZ) Fault Zones. Those two fault zones seem to connect, creating an impressive active fault zone reaching 200 km in length. Known active fault zones are also the Drama Fault Zone (DFZ), the Maronia-Makri Fault Zone (MNFZ) and the Orestias-Mikri Doxipara Fault Zone (OMFZ). Another important tectonic structure is the Saros Fault Zone (SFZ), the westernmost extension of the North Anatolia Fault, which can produce significantly large earthquake although it is situated outside the area of Thrace.

Evidence of past liquefaction phenomena indicates a possible high liquefaction hazard because liquefaction tends to recur at the same site, providing site conditions have not changed (Youd, 1984). Historical occurrences of earthquake-induced liquefaction have been reported in many places in Greece (Papathanassiou et al. 2005). However, at the region of Thrace only once an historical liquefaction occurrence was reported; liquefaction manifestations in the city of Dedeagac (today known as Alexandroupolis) were triggered by the event of 1912 Murefte, Turkey (Ambraseys and Finkle, 1987). Though, the fact that the existence of a description of liquefaction-induced ground failure triggered by past earthquake indicates a possibility of future liquefaction, the lack of evidence does not provide a proof for classifying a site as non liquefiable (Youd, 1998).

Evaluation of the Depth of the Groundwater Table

The evaluation of the depth of the groundwater is a crucial issue for the estimation of liquefaction potential since soil layer can be liquefied only when it is saturated. In this study, we assumed that the groundwater table depth is less than 6 meters thus; the degree of liquefaction susceptibility is characterized as high according to Youd and Perkins (1978). This assumption was based on the fact that the groundwater level at many sites fluctuates seasonally and consequently; unsaturated deposits during one season can become saturated the next one and capable for liquefaction. Therefore, it was decided to be conservative regarding the groundwater table at this scale liquefaction susceptibility map. Areas that are characterized as liquefiable should be further investigated in detail using groundwater measurements.

Liquefaction Susceptibility Maps

Liquefaction is the transformation of saturated, unconsolidated granular material from a solid state to a liquid state as a consequence of increased pore pressures that reduce the effective strength of the material (Youd, 1973). The process of liquefaction may or may not lead to ground deformation or related surface manifestations, including lateral spreading, ground settlement, bearing capacity failure, sand boils, and ground cracking.

Liquefaction susceptibility map can be developed using information provided by geologic, geomorphologic and hydrologic investigations. Liquefaction hazard maps have been compiled based on this approach at many region in the world and especially the western part of USA; for the Monterey-Santa Cruz area (Dupré and Tinsley, 1980; and Dupré, 1990), the greater Los Angeles urban area (Tinsley et al., 1985), and the San Francisco Bay region (Youd and Perkins, 1987; Knudsen et al., 1997; Sowers et al., 1998; Knudsen and others, 2000; Holzer et al., 2002). The liquefaction susceptibility map does not predict liquefaction-related ground failures, although ground failures may accompany liquefaction and are more likely to occur in areas with higher liquefaction susceptibility (Tinsley et al., 1985). Hence, the information provided by a liquefaction susceptibility map should be used only as a screening guide for planning purposes since for site-specific conditions a detailed geotechnical investigation must be performed for the evaluation of liquefaction potential of a soil element.

In this study, liquefaction susceptibility maps for the region of Thrace were developed using the recommendations for delineating seismic hazard zones of the California Division of Mines and Geology (CDMG, 1999) and the geomorphological criteria that are listed in Table 1, proposed by Wakamatsu (1992).

For the application of CDMG (1999) criteria, the Holocene sediments were classified in one group due to the fact that the separation into late Holocene age and Holocene deposits, respectively could not be establish in this scale. Therefore, taking into account the guidelines of CDMG (1999) and the fact that the value of PGA at the region of Thrace is expected to be 0.16g (EAK, 2000) we concluded that the zones where Holocene sediments were mapped (figure 1), are considered as liquefaction-prone areas.

Furthermore, the geomorphological characteristics of the surface materials that were mapped in the same area were identified and classified according to the criteria published by Wakamatasu (1992). In figure 3, is shown the liquefaction susceptibility map that was compiled using these depositional criteria that are listed in Table 1. From the 4138.63 Km^2 of the area covered by Quaternary sediments, 277.16Km^2 are delineated as likely to liquefaction zone; 3561.38Km^2 are bounded as possible to liquefaction zone while the rest of the area (300.09Km^2) as non likely to liquefaction.

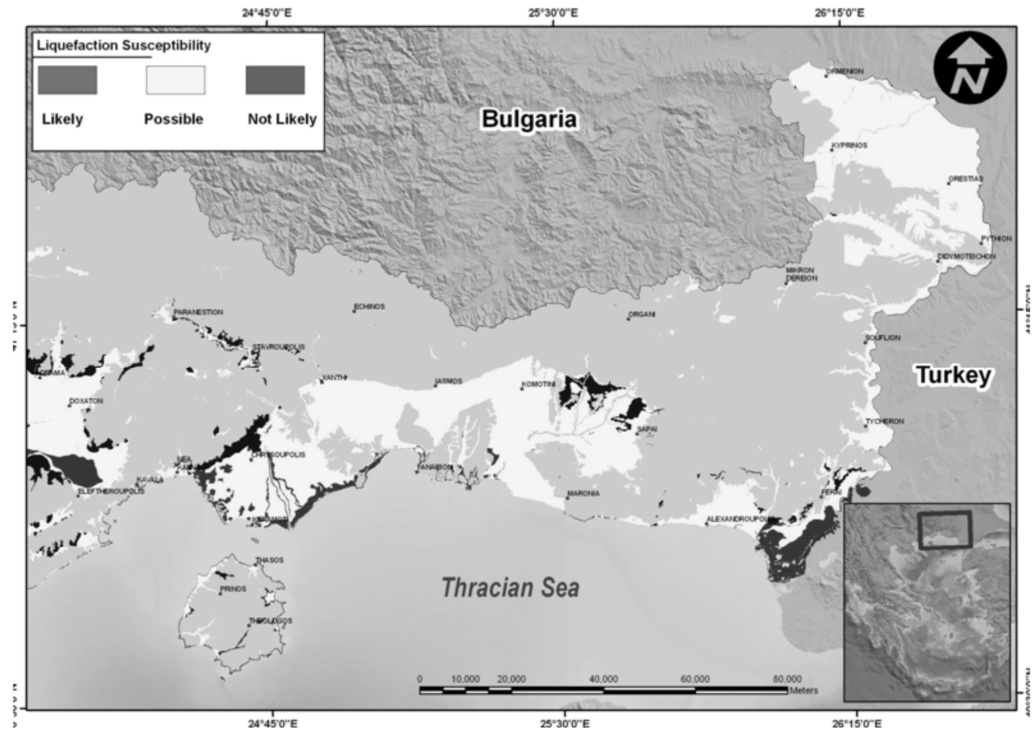

Figure 3. Liquefaction susceptibility map of the region of Thrace based on the criteria published by Wakamatsu (1992).

The areas defined as likely to liquefaction are mapped close to the delta of the two major rivers, Nestos and Evros, which traverse the region of Thrace, including the coastal area of Keramoti. Furthermore, two of the urban areas of the region, the cities of Komotini and Alexandroupolis are located in areas characterized as possible to liquefaction. Thus, it is necessary for the evaluation of liquefaction potential and the quantification of the liquefaction hazard to analyzed data from in-situ tests performed in these two cities.

Results and Discussion

The goal of this study was the identification of areas where liquefiable units exist at the region of Thrace using geological and geomorphological data. This map can be used as a screening guide of liquefaction hazard for planning purposes since areas where liquefaction occurrences pose a substantial hazard are delineated.
The liquefaction susceptibility maps were compiled using geological maps with reference to criteria published by Wakamatsu (1992) and CDMG (1999). In these maps, zones where geological units susceptible to liquefaction during earthquakes exist are delineated. The geological units that were mapped by previous field surveys were classified into three categories of liquefaction susceptibility regarding their depositional environment (Wakamatsu, 1992) while the areas where Holocene sediments are mapped, are classified as liquefaction-prone areas (CDMG, 1999).
This study resulted that a total of 277.168 Km^2 at the region of Thrace are bounded as likely to liquefaction while 3561.38 Km^2 are considered as possible to liquefaction. The rest of the area covered by Quaternary sediments, 300.09 Km^2, is considered as not likely to liquefaction-induced ground failures. Particularly, two cities of the region, Komotini and Alexandroupoli are situated at possible to liquefaction areas while the port of Keramoti is located at a likely to liquefaction zone. However, in order to evaluate the severity of liquefaction-induced failures is necessary to collect and process data regarding the geotechnical characteristics of the liquefiable soil layers.

References

Ambraseys N.N. & Finkel C.F. (1987). The Saros-Marmara earthquake of 9 August 1912. Earthq, *Engine. Struct. Dyn. 15,189-211.*

Ambraseys N.N. & Jackson J.A. (1998). Faulting associated with historical and recent earthquakes in the Eastern Mediterranean region, *Geophys. J. Int., 133, 390-406.*

CDMG, (1999). Guidelines for analyzing and mitigating liquefaction hazards in California. *California Dept Conservation, Division of Mines and Geology, Special Publication,117, 63p.*

Dupré W.R. (1990). Maps showing geology and liquefaction susceptibility of Quaternary deposits in the Monterey, Seaside, Spreckels, and Carmel Valley quadrangles, Monterey, California, *U.S. Geological Survey, Map MF-2096.*

Dupré W.R. & Tinsley J.C. (1980). Maps showing geology and liquefaction potential of northern Monterey and southern Santa Cruz counties, California*, U.S. Geological Survey Miscellaneous Field Studies MF-1199.*

EAK (2000). Greek seismic code, *Earthquake planning & Protection Organization, Athens-Greece, 72p. and 7 Appendixes (in Greek).*

Holzer T.L., Bennett M.J., Noce T.E., Padovani A.C. & Tinsley J.C., III (2002). Liquefaction hazard and shaking amplification maps of Alameda, Berkeley, Emeryville, Oakland, and Piedmont, California, a digital database, *US Geological Survey Open-File Report 2002-296.*

Kiratzi An., Benetatos Ch. & Roumelioti Z. (2005). Seismicity and seismotectonic characteristics of NE Aegean Sea and its surrounding lands, *Bulletin of Geological Society of Greece, XXXVII, 9-18.*

Knudsen K.L.& Lettis W.R. (1997). Preliminary maps showing Quaternary geology of twenty 7.5-minute quadrangles, eastern Stockton, California, 1:100,000 quadrangle, *National Earthquake Hazards Reduction Program, U.S. Geological Survey, Final Technical Report , Award #1434-94-G-2499.*

Knudsen K.L., Sowers J.M., Witter R.C., Wentworth C.M.& Helley E.J. (2000). Preliminary Maps of Quaternary Deposits and Liquefaction Susceptibility, Nine-County San Francisco Bay Region, California, A Digital Database, *U.S. Geological Survey Open-File Report 00-444, Digital Database by Wentworth, C.M., Nicholson, R.S., Wright, H.M., and Brown, K.H. Online Version 1.0.*

Koukouvelas I.K.& Aydin A., (2002). Fault structure and related basins of the North Aegean Sea and its surroundings, *Tectonics, 21, 1-27.*

Papadopoulos A.G.& Lefkopoulos G. (1993). Magnitude – distance relation for liquefaction in soil from earthquakes, *Bull. Seism. Soc. Am. 83, (3), 925-938.*

Papathanassiou G., Pavlides S., Christaras B. & Pitilakis K., (2005). Liquefaction case histories and empirical relations of earthquake magnitude versus distance from the broader Aegean Region, *Journal of Geodynamics, 40, 257-278.*

Papazachos B.C, Comninakis P.E, Scordilis E.M, Karakaisis G.F & Papazachos C.B (2007). A catalogue of earthquakes in the Mediterranean and surrounding area for the period 1901 - 2006, *Publ. Geophys. Laboratory, University of Thessaloniki.*

Pavlides S., Caputo R. (2004). Magnitude versus faults' surface parameters: quantitative relationships from the Aegean Region, *Tectonophysics, 380, 159-188.*

Pavlides S., Chatzipetros A., Zervopoulou A., Kürçer A. & Triantafyllos D. (2006). Post-Roman seismic activity in Mikri Doxipara – Zoni archaeological excavation (NE Greece), *European Geosciences Union General Assembly, Vienna, Austria, 2-7 April 2006, Geophysical Research Abstracts, 8, 06483.*

Şaroğlu F., Emre Ö., Kuşçu I. (1992). Active Fault Map of Turkey (scale 1:1,000,000), *General Direct. Mineral Res. Explor. (MTA),Ankara, Turkey.*

Sowers J.M., Noller J.S., Lettis W.R. (1998). Quaternary geology and liquefaction susceptibility, Napa, California 1:100,000 quadrangle: a digital database, *U.S. Geological Survey Open-File Report 98-46.*

TC4, (1999). Manual for zonation on seismic geotechnical hazards (revised version), *Technical Committee of Earthquake geotechnical engineering ISSMGE, 219p.*

Tinsley J.C., Youd T.L., Perkins D.M. & Chen A.T.F (1985). Evaluating Liquefaction Potential, in Ziony, J.I., ed., Evaluating earthquake hazards in the Los Angeles Region - an earth-science perspective, *U.S. Geological Survey Professional Paper 1360, 263-316.*

Wakamatsu, K., 1992. Evaluation of liquefaction susceptibility based on detailed geomorphological classification, Proc. Technical Papers of Annual Meeting Architectural Institute of Japan, Vol. B, pp. 1443-1444 (in Japanese)

Witter C.R., Knudsen L.K., Sowers M.J., Wentworth M.C., Koehler D.R. & Randolph C.E. (2006). Maps of Quaternary Deposits and liquefaction susceptibility in the Central San Francisco Bay Regio, California, *Open file report 2006-1037, USGS, 43p.*

Youd T.L. (1973). Liquefaction, flow and associated ground failure, *U.S. Geological Survey Circular 688, 12p.*

Youd T.L. (1984). Recurrence of liquefaction at the same site, *Proc. 8th world conf. on Earthquake Engineering, San Francisco, Calif. 3, 231-238.*

Youd T.L. (1998). Screening guide for rapid assessment of liquefaction hazard at highway bridge site. T*echnical report, MCEER-98-005, 58p.*

Youd T.L. & Perkins J.B. (1987). Map showing liquefaction susceptibility of San Mateo County, California, *U.S.G.S, Map I-1257-G.*

Zagorchev I.S. (1995). Structure and tectonic evolution of Pirin–Pangaion structure zone, *Geol. J. 29, 241– 268.*

Liquefaction-Induced Ground Disruption Triggered by the Earthquake of June 8, 2008 in NW Peloponnesus, Greece

Papathanassiou G (1), Valkaniotis S (1), Chatzipetros Al (1), Neofotistos P (1), Sboras S (1), Pavlides Sp (1)

(1) Department of Geology, Aristotle University of Thessaloniki, gpapatha@auth.gr

Keywords: Liquefaction, Peloponnesus, Greece, sand volcanoes

Introduction

A strong earthquake occurred on the NW Peloponnesus on June 8, 2008 inducing several surface effects and structural damages in the broader epicentral area. The Ms 6.5 NW Peloponnesus earthquake, caused by a N20E to N30E (according to the available focal mechanisms) dextral strike slip fault, affected a large area from Kato Achaia to the north to Amaliada to the south. According to the National Observatory of Athens, Institute of Geodynamics (NOA), its focus was located at 37.98^{o}N 21.51^{o}E at depth 25 km while the event was located by the Seismological station of the Aristotle University of Thessaloniki at 37.944^{o}N 21.544^{o}E and 3 km depth.

The secondary effects triggered by the event were spread over a wide area at the NW Peloponnesus, though the most severe ones were reported in the direction of the fault. In particular, landslides were observed close to the epicenter at the village of Valmi while rock falls were observed at the villages of Santomeri and Portes, respectively, causing damages at roads and houses. Moreover, ground ruptures with local normal character and slight strike-slip component up to 20cm vertical and 15cm horizontal movement was observed close to the village of Nisi, causing damage to a bridge.

In this paper, the earthquake-induced liquefaction phenomena are presented while a map of the area was compiled showing their distribution. Moreover, published criteria regarding the occurrence of liquefaction manifestations such as historical seismicity of the area and the epicentral distances of the sites are examined. Finally, the grading characteristics of the sandy material that was ejected from ground fissures are presented and compared to the boundary curves proposed by Tsuchida (1971) regarding the possibility of liquefaction.

Geology of the area

Most part of the NW Peloponessus is covered by a thick (>1km) sequence of Neogene – Quaternary sediments. These formations of Pliocene – Pleistocene age, consist of sands, shales, clays, marls, limestones and conglomerates, deposited in shallow marine/littoral and lacustrine conditions (Hageman, 1976; Tsoflias, 1977,1980, Fleury et al., 1981). The area around Lake Pinias is covered by sediments of Valmi Formation, consisting of intercalations of brown and green clays, white to yellow sands and silts, and conglomerates (Fleury et al., 1981; Stamatopoulos & Kontopoulos 1994). Valmi Formation is inderdigitated laterally with Vounargos and Olympia Formations (Hageman, 1976; Kamberis, 1987). The Alpine basement of the NW Peloponessus comprises Mesozoic-Early Cenozoic formations that belong to three different isotopic units (from west to east): Ionian Zone, Tripoli-Gavrovo and Pindos-Olonos. Outcrops of these formations in the studied area, include flysch sediments (intercalations of sandstones, shales, conglomerates and limestones), marine limestones, schists, cherts and evaporates (Decourt, 1964; Kamberis, 1987).

Historical seismicity

The existence of descriptions regarding historical liquefaction occurrence in an area is one of the criteria that can be used in order to characterize the area as liquefaction prone zone. Thus, the historical seismicity of an area can help to the delineation of such zones. In our case, at the North-Western part of Peloponnesus, at least two earthquakes induced liquefaction surface manifestations; the 1988 Bartholomio event and the 1993 Pyrgos one.

In particular, the earthquake of October 16, 1988 triggered liquefaction phenomena such as ground fissures with ejection of sand-water mixture and sand volcanoes. According to Lekkas (1991) and Papadopoulos & Profis (1990), liquefaction-induced ground disruption was observed at the western bank of the river Pinios, about 400m from the sea shore and to the east of the area of Kastro. Moreover, at the area of Bartholomio, according to eye-witnesses water and sand was ejected from fissures at the fields creating sand craters with diameter up to 60cm. The 1993 Pyrgos earthquake, caused liquefaction phenomena in the area of Spiantza, close to the river Alfios (Lekkas, 1994). Mixture of sand and water was ejected form ground fissures with length up to 30m and created sand craters with diameter up to 50cm.

However, though these two events occurred in the vicinity of the studied area, no liquefaction surface evidences were observed at the sites where ground failures triggered by the last event.

Liquefaction-induced ground disruption

The most characteristic secondary effects triggered by the event of June 8, 2008 were the liquefaction manifestations. Impressive sand volcanoes and vent fractures were observed in many places, both at the areas located to the north (Kato Achaia, Alikes, and Nisi) and to the south from the epicentre at the banks of the river Pinios and at the shore of Lake Pinios. These liquefaction-induced ground failures appeared to be concentrated in areas formed by alluvial deposits.

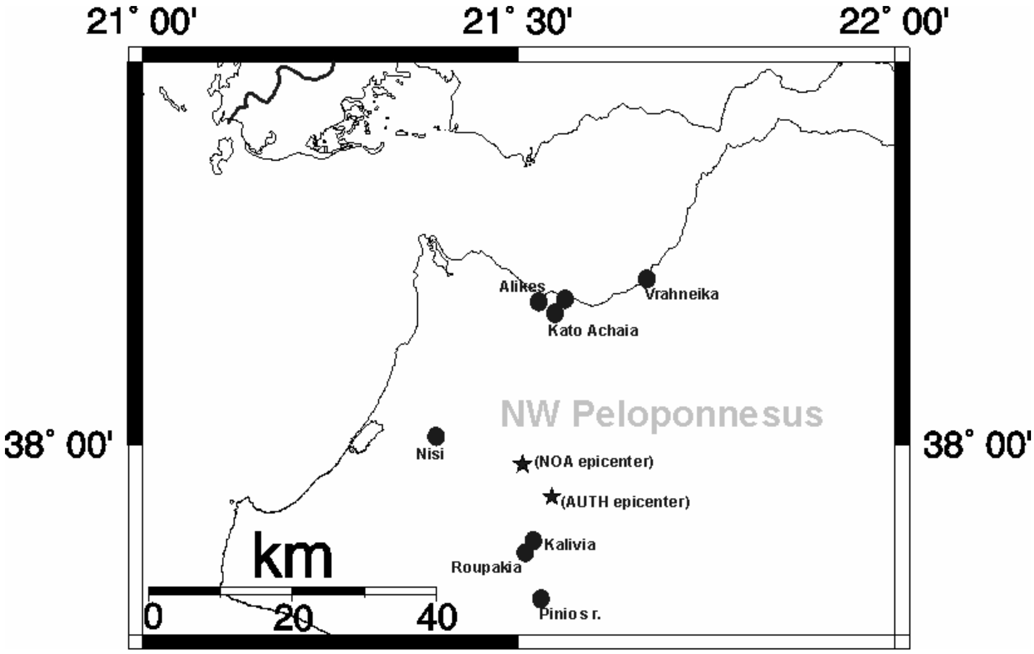

Figure 1. Map showing the distribution of the liquefied sites and the epicenters provided by NOA and AUTH

Particularly, the most characteristic liquefaction phenomena were reported at the shore of the Lake Pinios, close to the village Roupakia, about 9 Km from the epicentre as it was defined by NOA. At this site we observed typical examples of liquefaction surface evidences; 2 sand-mud boils with diameter up to 85cm and 3 smaller ones with diameter up to 70cm each, vent fractures with length more than 5 meters and width up to 15 cm and sand volcanoes with diameter up to 17 cm (figure 2). Moreover, a lateral spreading at the banks of the river was observed.

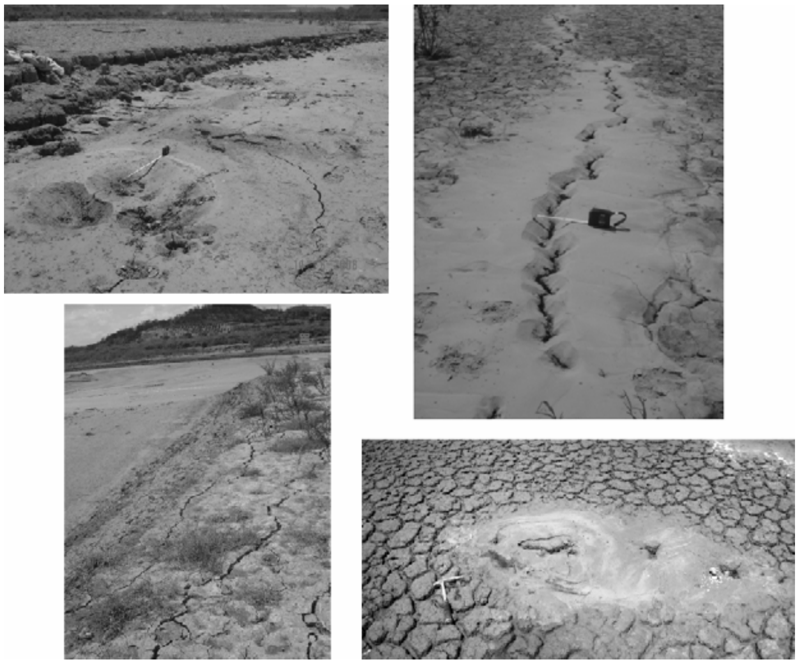

Figure 2. Liquefaction surface evidences at the site Roupakia. Sand boils with diameter up to 85cm (up left); Vent fractures 85cm (up right**);** lateral spreading towards the river (down left); Sand volcanoes (down right)

Close to this site and approximately at the same epicentral distance, is located the site of Kalivia. At this area, fine grained material was ejected from ground fissures as it is shown in figure 3.

Few kilometres to the south, at the banks of the river Pinios, small ground cracks were observed from which coarse grained material was ejected. At the same place, a horizontal displacement of 1-2 cm towards the river was observed (figure 3).

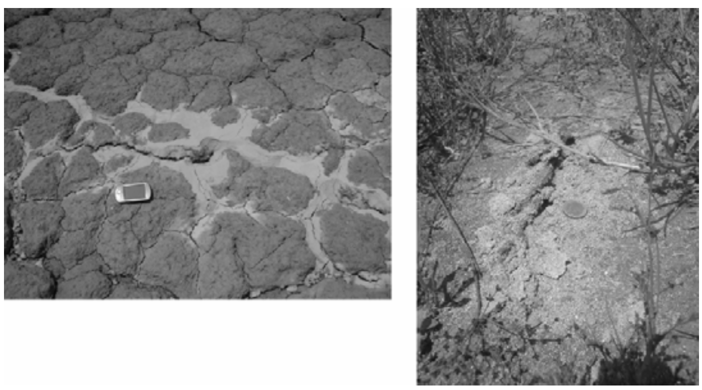

Figure 3. Liquefaction surface evidences at the site Kalivia and at the banks of the river Pinios. Ejection of sand-water mixture at the shore of Lake Pinios (site kalivia); Ejection of sand-water mixture at the banks of Pinios river.

The other sites where liquefaction phenomena were observed are located northern to the epicenter. The most impressive ones were mapped at the sea shore of the village Kato

Achaia (figure 4) where ejected sandy grey material formed vent fractures with length from 50cm to 4 meters and width up to 22cm and sand volcanoes with diameter up to 8 cm. From this area, samples from the ejected material were collected in order to perform laboratory tests regarding its grading characteristics. Moreover, at the same site two ground cracks with horizontal displacement of 4cm toward the sea and vertical subsidence of 2cm were mapped. The mean direction of these cracks was parallel to the coastline. Furthermore, at a distance of 600 meters, towards the mainland, ejection of grey sand was observed.

Figure 4. Formation of vent fractures of 4 meters long (left) and vent fractures with 12cm width (right) at the sae shore of Kato Achaia

Sand volcanoes and lateral spreading were observed at the river mouth of a torrent at a site called Alikes (figure 5), located 2 km western from the village of Kato Achaia. The diameter of the volcanoes ranged from 4 to 12 cm while from small scale cracks on the pavement, sandy material was ejected. Few meters distance from this site, an opening on the asphalt pavement with 3m length and 8cm width was triggered by the event.

Finally, close to the village Nisi, where surface rupture of 20cm vertical and 18 cm horizontal displacement were mapped, a small sand volcano was observed (figure 5).

Figure 5. Liquefaction manifestations at the site Alikes (left) and Nisi (right)

Structural damages that could be induced by the liquefaction of the subsoil layers were observed at the waterfront area of the village Vrahneika, at an epicentral distance of 25 km. In this area, the pavement was cracked and the lifelines were damaged. The mean direction of the cracks was parallel to the coastline while their length was measured up to 500 meter. The horizontal displacement ranged from 3cm to 7cm while in some places a vertical displacement of 3cm was reported (figure 6). However, no clear evidence of liquefaction such as ejection of material from the cracks or/and creation of sand volcanoes was observed at this area.

Figure 6. Structural damages at the waterfront area of Vrahneika. Subsidence (left) and crack on the pavement (right)

Performing back-analyses for the evaluation of liquefaction susceptibility

In order to assess the liquefaction susceptibility in an area, several criteria must be examined. According to Kramer (1996), historical, geologic and compositional data should be tested regarding the liquefaction susceptibility and potential of an area. In this study, we examined the susceptibility of the sites where liquefaction phenomena were observed by the application of the above criteria.

Empirical relationship of earthquake magnitude versus epicentral distance

The maximum epicentral distance of a liquefied site that can be triggered by an earthquake magnitude M can be estimated using empirical relationships. Three studies have been performed, regarding this issue, concerning the Aegean region and specifically Greece and relatively correlations were proposed by Ambraseys (1988), Papadopoulos and Lefkopoulos (1993) and Papathanassiou et al. (2005). In this study, we took into consideration the upper bound curves (for Greece and for the Aegean region) that were proposed by Papathanassiou et al. (2005) for the assessment of the liquefaction susceptibility of an area.

The estimation of the epicentral distances, of the sites where liquefaction phenomena were observed, was performed using the focal parameters of the event as they were published by the NOA (National Observatory of Athens, Institute of Geodynamics) and the AUTH (Aristotle University of Thessaloniki, Seismological Station). The epicentral distances range from 8 to 25 km based on NOA parameters and from 4 to 27 km based on AUTH data and they are listed in Table 1. Afterwards, the values of the distance of the liquefied sites were correlated to the M of the earthquake and they were plotted in the diagram (figure 7) for examine the susceptibility to liquefaction.

Table 1. Estimated epicentral distances of liquefied sites

	NOA focal parameters	AUTH focal parameters
Site	Epicentral distance	Epicentral distance
Pinios river	15	11
Roupakia	9	6
Augi	13	11
Alikes	19	24
Kato Achaia	19	23
Vrahneika	25	27
Kalivia	9	4
Nisi	10	12

As it is shown in figure 7, the sites where liquefaction phenomena triggered by the event of June 8, 2008 are plotted within the area that is defined as liquefiable zone by Papathanassiou et al. (2005). Thus, based on this back-analysis we concluded that the earthquake-induced liquefaction at these sites could be predicted based on the proposed diagram.

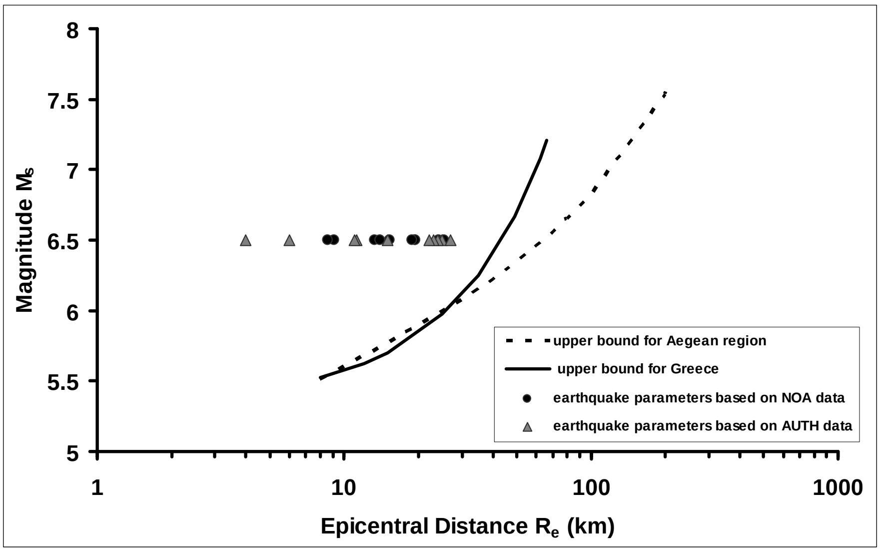

Figure 7. Distribution of the liquefied sites based on their epicentral distance and comparison to the upper bound curves proposed by Papathanassiou et al. (2005) for the assessment of liquefaction susceptibility.

Laboratory results

Few days after the earthquake, field investigations were taken place. During these investigations ejected samples were collected from sand craters and vent fractures in the areas of Kato Achaia and Roupakia, with a view to examine their compositional characteristics that include grain size distribution, liquid limit and Plasticity index (Kramer, 1996). The laboratory testing of the collected material was performed at the Laboratory of Engineering Geology and Hydrogeology of the Department of Geology at the Aristotle University of Thessaloniki.

The three collected samples Rou1, Rou2, Rou3 from the shore of lake Pinios are classified as silty sand (SM). The fines content of these soils are 24%, 30% and 21%, respectively. The material that was collected from vent fractures and sand boils in Kato Achaia, (Kac1, Kac2) is classified as fine grained sand (SP); the content of clay and silt is 8% and 5%, respectively.

The results of grain size analysis of the samples are plotted to diagrams and compared to the proposed curves by Tsuchida (1971) for well graded soils and for soils at uniform grading. As it is shown in figure 8 and figure 9, the grain sizes distribution curves of the materials plotted within the suggested range of possibility of liquefaction, concluding that these diagrams can still be used for the prediction of the occurrence of liquefaction-induced ground disruption at one site.

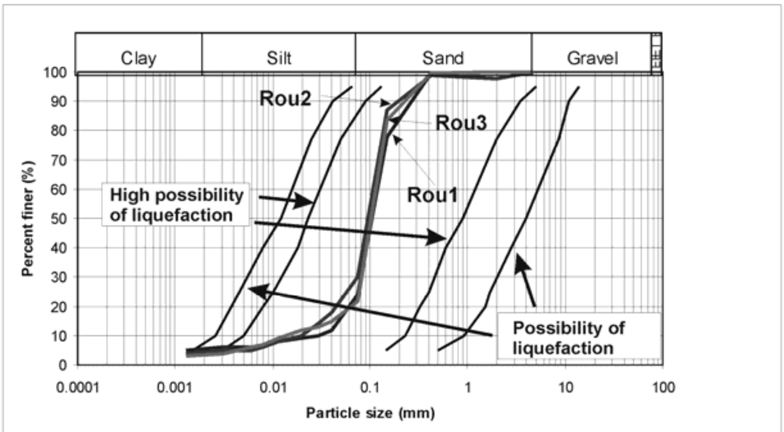

Figure 8. Comparison among the grain size distribution curves of the collected samples Rou1, Rou2 and Rou3 and boundaries curves for most liquefiable soils suggested by Tsuchida (1971)

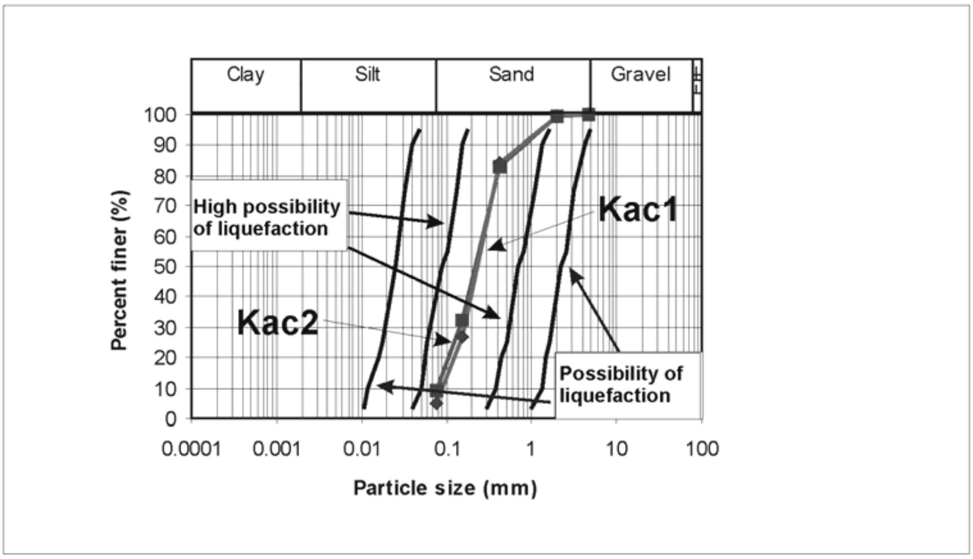

Figure 9. Comparison among the grain size distribution curves of the collected samples kac1, Kac2 and and boundaries curves for most liquefiable soils suggested by Tsuchida (1971)

Results and Discussion

The earthquake of June 8, 2008 triggered secondary effects that were spread in a wide area. The most characteristic of them were liquefaction-induced ground failures, appeared to be concentrated in areas formed by alluvial deposits.

Large scale liquefaction surface evidences as sand boils, vent fractures, sand volcanoes and ejection of sand-water mixture were observed at the waterfront area of village Kato Achaia, Alikes to the north of the epicenter and to the shore of the lake Pinios (close to the village Roupakia) to the south of the epicenter. Smaller scale liquefaction phenomena were reported at the site Nisi and at the banks of the river Pinios.

In order to examine liquefaction susceptibility, at the sites where liquefaction phenomena were observed, back-analyses were performed. Initially, the susceptibility was evaluated using published empirical relationships correlating their epicentral distances with the earthquake magnitude M. The distribution of the liquefied sites, on the published diagram, is in agreement with the delineated liquefaction-prone zone, indicating the usefulness of this method to the preliminary evaluation of the liquefaction susceptibility.

Afterwards, ejected samples from the sites Roupakia and Kato Acahia were collected in order to examine the liquefaction susceptibility of the soil layers. The distribution curves, outcome from the grain size analyses, of the ejected material plot within the area defined as high possibility to liquefaction by Tsuchida (1971), concluding that these soils are susceptible to liquefaction regarding their grain size.

References

Ambraseys N.N. (1988). Engineering seismology*, Int. J. Earthq. Eng. Struct. Dyn, 17, 1-105*

Decourt J. (1964). Contribution a l'etude géologique d'un secteur du Péloponnèse septentrional, *Ann. Geol. Pays. Hellen., XV, 1-418.*

Fleury J.J., De Wever P., Izart A. & Dercourt J. (1981). Goumero Sheet. Gelogical Map of Greece in scale of 1:50.000, *Institute of Geology and Mineral Exploration, Athens.*

Hageman J. (1976). Stratigraphy and sedimentary history of the Upper Cenozoic of the Pyrgos area (Western-Peloponnesus), Greece, *Ann. Geol. Pays Hellen., XXVIII, 299-333.*

Kamberis E. (1987). Geology and Petroleum geology of NW Peloponnesus, *PhD Thesis, National Technical University, Athens.*

Kamperis E., Alexiadis Ch. & Phillipe G. (1979). Amalias Sheet. Gelogical Map of Greece in scale of 1:50.000, *Institute of Geology and Mineral Exploration, Athens.*

Kramer S.V. (1996). Geotechnical Earthquake Engineering, *Publ. Of Practice may, New Cork, 653p*

Lekkas E. (1991). Macroseismic observations alter the earthquake of October 16th 1988 in Killini peninsula (NW Peloponnesus), *Bul. Geol. Soc. Greece, 313-328*

Lekkas E. (1994). Liquefaction risk zonation and urban development at western peloponnesus, *Proc. 7th Int. IAEG Cong*.

Papadopoulos A.G. & Profis Th. (1990). Macroseismic observations related with the strong shock of October 16th, 1988, in NW Peloponnesus Greece: the important role of the microzonation conditions, *J. Geodyn*, *12, 217-231*

Papadopoulos A.G.& Lefkopoulos G. (1993). Magnitude – distance relation for liquefaction in soil from earthquakes, *Bull. Seism. Soc. Am., 83, 925-938.*

Papathanassiou G., Pavlides S., Christaras B. & Pitilakis K. (2005). Liquefaction case histories and empirical relations of earthquake magnitude versus distance from the broader Aegean Region, *J. Geodyn.*, *40, 257-278.*

Stamatopoulos L. & Kontopoulos N. (1994). Geomorphology and evolution of the region between Lapa and Eleotopos, Northwestern Peloponnesus (Greece), *Il Quaternario, 7, 537-544.*

Tsoflias P. (1970) Geological structure of the northern part of Peloponnese (Achaia County). *Ann. Geol. Pays Hellen.*, *XXI, 1-554.*

Tsoflias P. (1977). Nea Manolas Sheet. Gelogical Map of Greece in scale of 1:50.000, *Institute of Geology and Mineral Exploration, Athens.*

Tsoflias P. (1980). Patra Sheet, Gelogical Map of Greece in scale of 1:50.000, *Institute of Geology and Mineral Exploration, Athens.*

Tsuchida H. (1971). Estimation of liquefaction potential of sandy soils*, Proc. 3rd Joint Meeting, US-Japan, UNJR.*

Seismo-Gravitational Oscillations of the Earth and a Solvable Model of a Tectonic Plate Under a Localized Boundary Stress

Pavlov B(1), Petrova L. (1)

(1) V.A. Fock Institute of the Physics, St. Petersburg University, St.Petersburg, Petrodvorets, Ul'yanovskaya , 1, Russia, 198504, pavlov@math.auckland.ac.nz, gull@LP1722.spb.edu

Keywords: oscillations, deformation, thin plate, zero-range potential, operator extension

Introduction

Characteristics and basic properties of background oscillations of the surface of Earth were not studied systematically as an independent object of study. We guess that these data, concerning various parts of spectrum, contain weak, but stable oscillations of different blocs of the planet. The backgroung seismical process is clearly observed by modern geophysical devices on Geoscope and Iris stations. The corresponding systematic observations of the processes with periods 1-5 hours is organized over 30 years in Sankt-Petersburg State University (SPbGU). Reliable observations in such a long-period domain if the spectrum became possible due to high level protection against temperature and atmospheric fluctuations due to specially formed characteristics of the devices in the corresponding interval of the spectrum (Linkov et all, 1996). The oscillations in that interval of frequencies were called seismo-gravitational oscillations of Earth (SGO), because the vertical seismographs used in the series of observations write down the inertial and gravitational components of the corresponding acceleration. Analysis of the data enabled us to establish basic and specific properties of the seismic process with periods 1-5 hours (Petrova, 2000). These oscillations were observed by seismographs of various types, by Geoscope stations and SPbGU, on one continent (Petrova, 2002) or on few continents simultaneously (Petrova, Ljubimtsev, 2006). Eventually the planetary character of SGO and the stability of their frequencies was confirmed. On these frequencies the Earth is excited most frequently.

We guess that the processes inside the tectonic plate and on the boundary are reflected by the tension of the medium. In particular, the local stress applied on the boundary may be revealed by observation in remote zones. By the moment we already have an analytic machinery allowing us, in principle, to reveal changes of frequencies and shapes of SGO, in remote zone, depending on the localized stress in an active zone on the boundary (Berezin, Faddeev,1961; Pavlov, 1987; 2007 and Petrova, Pavlov,2008). In this paper we describe experimental data which can be used in course of mathematical modeling aimed to defining of coordinates of the active zone from the data collected in remote zone.

Materials and Methods

Observation Material

In this section we represent the data on vertical displacements of the surface of Earth observed simultaneously on few Geoscope stations in 1999 and in St. Petersburg in 2004. Characteristics of the instruments. In the interval of periods 1-6 hours the magnification of the amplitude of oscillations of the Z-component in St-Petersburg is 10 times higher than in Geoscope network for the period 1 hour, and 20 times higher than in Geoscope for the period

6 hours. For the the period 55 minutes the magnifications are equivalent. Coordinates of stations are given in the table 1. SGO Main peculiarities of SGO during this period are represented by Fig.1(*1*) are the following: beginning from the moment f during 16-18 September the seismic process is registered by all three vertical channels of devices on all three stations.

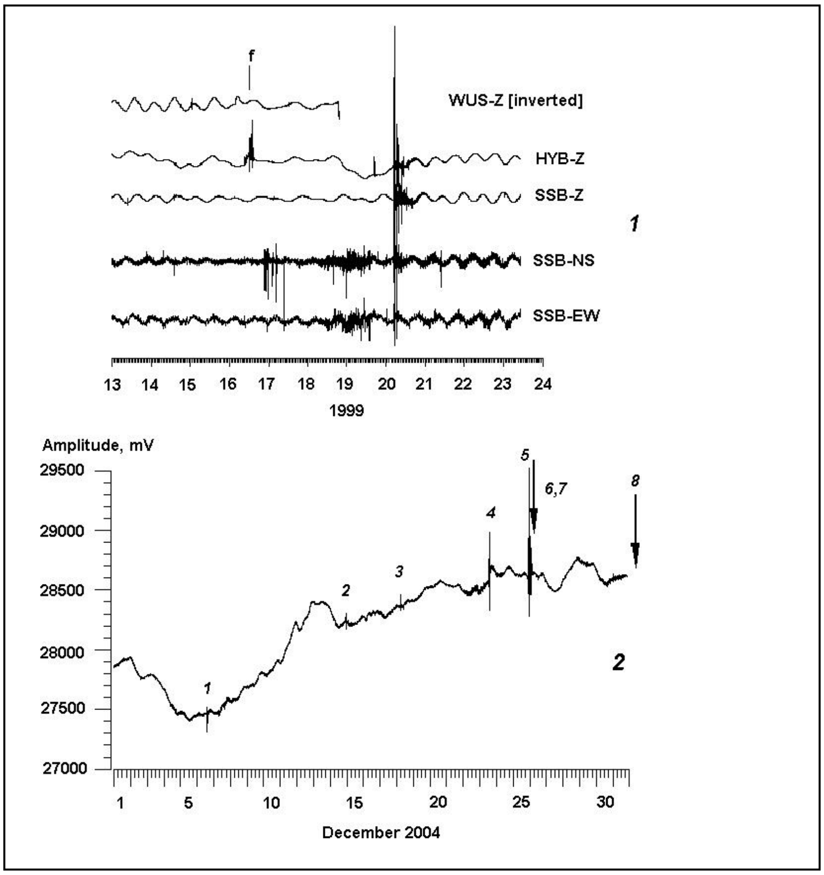

Figure 1. Examples of large-scale deformation in September 1999 (*1*) observed Geoscope stations before Earthquake in Taiwan (M =7.7) and record of seismogravimeter before filtration in Sankt-Petersburg, December 2004 (*2*). Informations of the Earthquake 1-8 see tabl.2

The stretch/contraction deformation is found in the records of the stations HYB and WUS (the records were interrupted after 5 days series of observations). It has length 1,5 day. During the same period the horizontal channels in France recorded impulses and growth of the intensity of the background oscillations with more short periods before the earthquake.

Table 1:Coordinates of the stations

Station	φ	λ
SpbU (Russia)	59,46	30,19
SSB (France)	45,28	4,54
WUS (China)	41,20	79,22
HYB (India)	17.42	78,55

One should say that standard or equivalent positioning of devices in all Geoscope stations is an important condition of monitoring of SGO. The signs of displacements on the WUS stations are opposite, so that we invert them to compare the records. Besides the stations

WUS and HYB are situated on different tectonic plates (on the Euro-Asia plate and on the Indian plate respectively). The growth of the intensity of the background oscillations (SGO) is observed also in St-Petersburg record 2004, see Fig.1 (*2*). This is connected with long-lasing deformations. They last for the periods 2 to 12 days. The numbers on the top mark the earthquakes listed in the table 2.

Table 2 :Earthquakes in the December 2004 (magnitude more 6.0)

No	Day	Time	Coordinates	M	Location
1	06	14-15- 11.8	42.900; 145.228	6.8	Hokkaido, Japan
2	14	23-20- 13.3	18.958; -81.409	6.8	Cayman Islands
3	18	06-45-23.2	49.070; 156.150	6.5	Kuril Islands
4	23	14-59-04.4	-49.312; 161.345	8.1	Macquarie Island
5	26	00-58-53.4	3.295; 95.982	9.0	Northern Sumatra
6	26	04-21-29.8	6.910; 92.958	7.1	Nicobar Islands
7	26	09-20-01.6	8.879; 92.375	6.6	Nicobar Islands
8	01/01	06 25 44.8	5.099; 92.304	6.7	Northern Sumatra

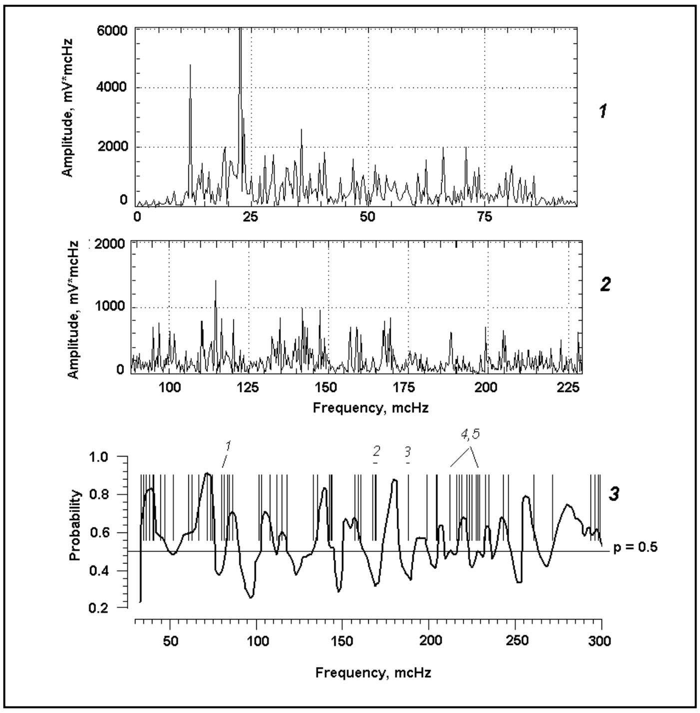

Fig.2 Grouping of frequencies and concentration of the spectral power for the frequencies greater that 50 mcHz (*1,2*) and the correspondence of the central frequencies of the groups with thew statistical spectrum most often excited oscillations of the Earth (*3*)

The curve on Fig.1(*2*) shows the perturbations acting straight on the base of the vertical seismograph. It is taken from the photo-electrical transformer before the analog filtration in the measurement channel. After separation of the long-period component from the curve, with

by means of method slitherring average, the spectral analysis was done on the remaining high-frequency part. Spectrum is presented by Fig.2(*1,2*) before frequency 225 mcHz.
Characteristic properties of the SGO are clearly seen in the resulting Fig.2. For frequencies more than 50 mcHZ (period ~ 6 hours) we can see grouping the power of the spectrum along frequency axes, noticed earlier (Petrova,2000) in statistical spectra. It is represented on Fig.2 which shows the probability of finding frequencys of SGO in the spectrum. The part of the area which is situated under the curve, but higher than the line p=0.5, indicates the SGO observed most often. The vertical lines mark the positions of the central frequencies from observed grouping of the power of the spectrum from the interval 50- 300 mcHZ, with periods 333-55 minutes. Numerals overhand mark a difference in the correspondence of frequencies. The components marked by the underlined 2,3 stay aside from the statistical spectrum, the components marked by 1 are shifted a little. The components 4,5 are accepted, since probability of their excitement p=0,5.

The Method

The stability of the frequencies of SGO, observed during the active periods, is obviously connected with the oscillation properties of certain blocks of the Earth. For large periods these blocs are just tectonic plates, with the corresponding eigen-modes excited by the stress. In this paper we assume that the viscose contact with underlying layers of the astenosphere is present. Based on dimensionality we conclude that the viscosity is small for long-period processes. Denoting by D the "the bending stiffness", connected with Young modulus E, the thickness h of the plate and the Poisson coefficient σ by the formula $D = Eh^2[12(1-\sigma^2)]^{-1}$, we represent, following (Landau,1991), the corresponding dynamical equation for the normal displacement u as

$$\rho \frac{\partial^2 u}{\partial \tau^2} = D\Delta^2 u,$$

where ρ – density, τ - time. We consider time-periodic solutions $u(\omega\tau, x)$ of the equation and separate the time, thereby reducing the dynamical problem to the spectral problem $\lambda u = \Delta^2 u \equiv Au$ with the spectral parameter

$$\lambda = \rho D^{-1}\omega^2$$

We choose some natural conditions on the boundary of the plates and take into account the contact with the underlying layers of the astenosphere, see (Kuleshov, 2005) and references therein. The small size of the active zone, compared with the wavelengths of the process and the size of the plates allows us to use the corresponding zero-range model for description of changes of the characteristics of SGO caused by the localized stress.

The zero-range model based on operator extensions A_M of the bi-harmonic operator A, for relatively thin plates, with appropriate boundary conditions on the boundary. Contrary to the Fermi zero-range model in quantum mechanics, see (Berezin,1964), the zero-range model for the tectonic plate is constructed via inclusion into the domain of the extended operator not one, but three singular functions: the Green function $g_0(x,a,i)$ with the pole a at the center of the active zone and its tangential derivatives g_1, g_2 of the first and second order. In (Petrova, Pavlov, 2008) we suggested a zero-range solvable model of a thin tectonic plate under a boundary stress, which is modeled by a 3X3 real hermitian matrix M attached to the stressed point *a* of the boundary. We interpret the elements of the matrix as Saint Venant parameters of the corresponding seismic process. The solvable model gives approximate explicit formulae for the variations $\delta\Lambda_0$ of the eigenfrequencies and the shapes of the eigenfunctions $\delta\varphi_0$

$$\delta\varphi_0 \approx (1+\lambda_0^2)\langle P\varphi_0 MK(\lambda_0)\varphi_0\rangle, \qquad \delta\varphi_0 \approx -(\lambda_0 - i)K_{-i}M\varphi_0$$

caused by the localized stress. Here $\lambda_{0,}\varphi_0$ is the eigenpair of the unperturbed bi-harmonic problem, and K, K_i are non-polar parts of the corresponding spectral expressions framed by projections P onto the linear hull of singular functions g_0, g_1, g_2 (deficiency elements):

$$P\frac{I+\lambda A}{A-\lambda I}P = (1+\lambda_0^2)\frac{P\varphi_0\rangle\langle P\varphi_0}{\lambda_0-\lambda} + \mathrm{K}(\lambda),\ \ \frac{\mathrm{A}+\mathrm{iI}}{\mathrm{A}-\lambda\mathrm{I}} = (\lambda+\mathrm{iI})\frac{\varphi_0\rangle\langle\varphi_0}{\lambda_0-\lambda} + \mathrm{K}_{-\mathrm{i}}(\lambda).$$

where I is identiti operator. Fitting of the model can be based on the data collected from the parallel monitoring of variations of SGO on different stations during calm periods. Comparing the data computed based on the fitted model with the experimental observations can help to localize the active zone and to estimate the power of the expected earthquake.

Results and Discussion

To use the above zero-range model it is impotant to fit the model properly, establishing the connection between the matrix parameter of the model and the characteristics of the seismo-gravitational process: typical frequencies, polarization, phase-characteristics of the components. The Saint Venant principle affirms that all these characteristics in the remote zone are functions of a small numbers of essential parameters. We guess that the role of the Saint Venant parameters may be played by the elementys of the matrix parametrizing the extension of the bi-harmonic operator under the localized boundary stress, and the experimantal data report on the changes of tension in the tectonic plate, under the boundary stress. Find below an example where the connection between the experimental data and the tension of the tectonic plate was observed . This example is not unique.

Dynamics of seismo-gravitational oscillations observed in St.Petersburg 22–29 March 2000 is varying with time (see Fig.3, intervals 0,1 and 2). A typical phenomenon of intense seismo-gravitational pulsation (SGP) was registered on the vertical component Z on the initial interval marked by 0. This phenomenon was also noted in the earlier paper (Linkov et al., 1992). See more about SGP in the further text, after figure 3.

Variation of the character of SGO is seen from comparison of the graphs of the amplitudes of SGO on 48 h intervals of time separated by the vertical dotted lines. The graphs on these intervals show the reaction of the device on the oscillations of the ground. The components *Z*, EW and NS are obtained after filtration. The graph on the interval 1 shows the reaction of the filter on the maximal phase of the earthquake 28 March 2000 in Japan. The non-filtered graph *Z* represents the reaction of the base of the vertical seismograph on the flexural oscillations of the ground. Spectral-time cards, see below figure 3 represents the effect of growing of frequencies of SGO in visual form. The data of the observations were filtered by the band filter with the band strip (60–300 min). We used the gliding time window length 700 min, and step-wise shifts with the 5 min steps. The interval of frequencies, measured in micro-Hertz, was chosen as [70 mcHz, 250 mcHz] =: [$F_{\min}$, $F_{\max}$]. For resolution 0.034 mcHz the steps were halved to guarantee better smoothness of the spectral function. Effect of growing of the frequency of SGO was detected only on spectral-time cards (ST-cards) of the vertical component of SGO, see below figure 3(*2*). The frequencies are marked on the horizontal axes, time in hours—on the vertical axes, for the intervals 0,1,2, respectively. The level of spectral amplitudes is represented by the variation of the color.

Oscillations with large spectral amplitudes, higher than the average level on the spectrum, are marked by gray color. The maximal amplitudes are marked by white color. The values of these amplitudes on the interval 0 are 3.5 times greater that the average amplitude, (frequency aboutbr 200 mcHz). On the interval 1 they exceed the average amplitude in 1.8 times (the frequency about 200 mcHz). On the interval 2 they exceed the average amplitude in 3 times (the frequency about 160 mcHz). For SGO with frequencies 90–110 mcHz and 170–190 mcHz the amplitudes are 1.75 and 2.75 is times larger than the average amplitude. All three parts 0,1,2 of figure 3 reveal two patterns of inclined gray domains (left-down to right-up and left-up to rightdown) which correspond to SGO with growing and decreasing frequencies, correspondingly.

This patterns provide an evidence of increment of the stored elastic energy in the system and discharging the stored elastic energy, respectively in form of oscillation modes with certain frequencies.

Growing of the frequency on the interval 2:
(1) The frequency is growing from *f*min = 80 mcHz to 123 mcHz during the period of 15 h.
(2) The frequency is growing from *f*min = 130 mcHz to 185 mcHz during the period of 28.5 h.
(3) The frequency is growing from *f*min = 170 mcHz to 200 mcHz during the period of 8 h.

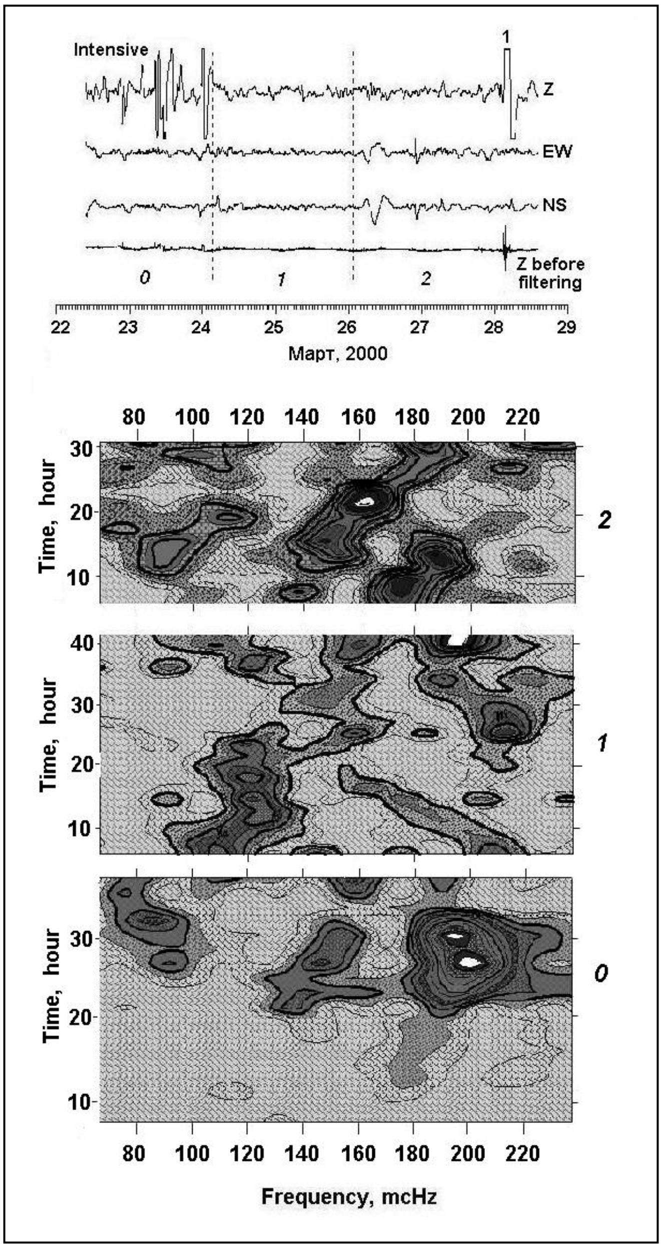

Figure 3. Dynamics of seismo-gravitational oscillations observed in St Petersburg, 22–29 March 2000 and time–frequency analysis of the vertical component of SGO, see the text below.

Growing of the frequency on the interval 0:
(1) The frequency is growing from F_{min} = 165 mcHz to 205 mcHz during the period of 33 h.
(2) The frequency is growing from F_{min} = 125 mcHz to 165 mcHz during the period of 15 h.
Growing and decreasing of frequencies of SGO are easily noticeable also on the interval 1.

Growing of the frequency is characterized by the ratio $\Delta\nu / \Delta\tau$, where $\Delta\nu$ is the increment of the frequency and $\Delta\tau$ is the corresponding time interval, when the growing was observed. Other domains, where the frequency of the modes decrease with time growing, may be interpreted as an evidence of local relaxation of the stress, probably caused by local destruction of the plate (forming cracks).
We conjecture that the extended growth of frequencies of the SGO may be considered as a precursor of strong earthquakes. Our ability to extract useful information from the observations of frequencies and the shape of SGO is limited by our understanding of the mechanism of the variation of the frequency and the shape of SGO modes arising from the boundary stress on the tectonic plates.

There were also other observations of the shift of frequencies of selected modes of SGO. This phenomenon was noted first in (Linkov et al., 1992) and was given the name of "seismo-gravitational pulsations", SGP. Statistical analysis was done based on the data of the 6 months monitoring of SGO in St Petersburg. This analysis confirmed that the connection between SGP and the subsequent strong earthquake is not random, with probability 95%.
Note, that in numerous observations on SGO in Leningrad (St Petersburg) intense short pulses were also recorded. They are constituted by several sinusoidal harmonics with periods from 30 min to 1 h, and the total duration of the process 6–10 h. In several cases they were also followed by powerful earthquakes—in 2–4 days.

Conclusions

Seismological observations reveal the statistical spectrum of oscillation of the Earth with periods 0.5-5 hours. The oscillations with periods from this spectrum are most stable and most frequently observed. They were called seismogravitational oscillations (SGO) of the Earth. These oscillations were observed by seismographs of different types on one continent, or on few continents simultaneously. The tectonic plates composing the Earth are seismically isolated from each other by disperse materials which can't store an essential amount of elastic energy and from the underlying layers. For slow dynamical processes, viscosity is relatively small. Thus permitting independent transversal oscillation of the tectonic plates, with periods 30 min.- 1 hour. Collisions of the tectonic plates at active zones cause the the point-wise stress, because the size of the active zones is small compared to the linear size of the plates. Based on bi-harmonic model of the thin elastic tectonic plate in form of a compact 2-d domain with boundary relatively smooth "in average with" respect to the wavelength of SGO, we introduced a zero-range model of the point-wise stress on the boundary of the plate. The corresponding wave-process in remote zone is defined, in full agreement with the prominent Saint-Venant principle, by a boundary condition at the active zone, parametrized by a 3 × 3 real hermitian matrix M. Based on Krein formula for the Green function of the perturbed problem we succeeded to find an explicit formula for the perturbed eigenfunctions and eigenvalues of the plate under a boundary stress. Analysis of the instrumental observation of changes of frequencies and shapes of SGO with the theoretical results obtained based on the fitted model can help to localize the active zones involved into the changes, to estimate the accumulated elastic energy, and, eventually, to predict powerful earthquakes.

Acknowledgements

The authors are grateful to Doctor Colin Fox for an inspiring discussion of the Saint-Venant principle. L Petrova acknowledges support from the RFFI grant 01-05-64753, B Pavlov acknowledges support from the grant of the Russian Academy of Sciences, RFFI 97-01-01149.

References

Berezin F.A.& Faddev L.D. (1961). A remark on Schr¨odinger equation with a singular potential , *Sov. Math.Dokl., 2 372–376.*
Kuleshov A.A. (2005). O chislennom metode reshenija zadachi poperechnyh kolebanij tonkih uprugih plastin, Matematicheskoe modelirovanie, 17,4,10-26.(in Russian).

Landau L.D. & Lifschitz E.M. (1991). Textbook of theoretical physics (‘Landau-Lifschitz’), vol VII) Elastizit¨attheorie (Elasticity Theory), 7th edn (translated from the Russian by B. Kozik and W. G¨ohler), *Berlin: Akademie-Verlag, 223 p.*

Lin’kov E.M., Petrova L.N. & Osipov K.S. (1992). Seismogravitational Pulsations of the Earth and Atmospheric Perturbations as Possible Precursors to Strong Earthquakes, *Doklady the USSR Academy Sciences, Earth Sci. Section, 306, 76–79 (translations).* Linkov E.M., Orlov E.G., Petrova L.N.& Karpinsky V.V. (1996). Seismogravitational complex, *Razvitie metodov i sredstv eksperimentalnoj geofiziki, vyp.2, Moskov,252-259. (in Russian)*,Transl.: Development of metods and tools of experimental geophysics.

Pavlov B. (1987). The theory of extensions and explicitly-solvable models, *Russ. Math. Surv. 42, 127–168.*

Pavlov B. (2007). A star-graph model via operator extension, *Mathematical Proc. of the Cambridge Philosophical Society, March, 142,365–384.*

Petrova L.N. (2000). The seismic process in the frequency range 0.05-0.5 mHz: Patterns and Peculiarities, *Volc. Seis., 21, 573-585.*

Petrova L. N. (2002). Seismogravitational oscillations of the earth from observations by paced vertical pendulums in Eurasia, *Izvestiya, Phys. the Solid Earth*, *38, 325–336.*

Petrova L.N., Lyubimtsev D.V (2006). Global Nature of the Seismogravitational Oscillations of the Earth, *Izvestiya Physics of the Solid Earth, 42, 2, 114-123*.

Petrova L.N., Orlov E.G., Karpinskii V.V. (2007). On the Dynamics and Structure of Earth's Oscillations in December 2004 from Seismic Gravimeter Observations in St. etersburg,Izvestiya, *Physics of the Solid Earth,43, 2, 111-118*.

Petrova L., Pavlov B. (2008). Tectonic plate under a localized boundary stress: fitting of a zero-range solvable model*, J. Phys. A: Math. Theor. 41, 085206, 15p.*

MMI and ShakeMap® Intensities, Plus a New Back-Predicted Scenario of the Loma Prieta, 1989 Earthquake

Pettenati F (1), Sirovich L (1), Sandron D (1)

(1) Istituto Nazionale di Oceanografia e di Geofisica Sperimentale OGS. Borgo Grotta Gigante 42/c Sgonico, Trieste, sirovich@ogs.trieste.it

Keywords: ShakeMap, Loma Prieta, macroseismic intensity, scenario

Introduction

Following the suggestion of an anonymous Associate Editor of the BSSA, in the present paper we compare the MMI intensities observed in the field after the Ms 7.1, 1989 Loma Prieta earthquake, with: i) the instrumental intensities obtained by the USGS using the ShakeMap® algorithm; ii) the new scenario intensities that we produced with our *KF*-Montecarlo parametric procedure (back-predicted in 1988; see later).

We recall that: i) the MMI intensities (one value in each town, also known as "felt reports" in the U.S.) were obtained by the US Geological Survey (USGS) according to the original definition by Wood and Neumann (1931) and are the official intensity map of the U.S. government (J. W. Dewey, written communication, 2008); ii) according to the ShakeMap® procedure (Wald et al., 2006), instrumental intensities are calculated as real numbers in a finely sampled grid; iii) our scenario is calculated in a semi-empirical way with the *KF* kinematic model for S body waves (Sirovich, 1996, 1997), using a Montecarlo parametric procedure for the 11 source parametres of the *KF* formula (see two preliminary presentations of this kind of scenario in Pettenati and Sirovich, 2006, and Sirovich and Pettenati, 2007; a more thorough presentation is underway). It should be also remembered that i) the aim of ShakeMap® is to produce a fast, a-posteriori picture of what happened; ii) whereas, our scenario must be thought of as an a-priori forecast, because it uses pre-1988 information. Thus, one can observe that: i) ShakeMap® should match post-earthquake observations; ii) but, a scenario with a preventive objective is probably cautious. Therefore, a direct comparison between the two maps is ill-posed. We basically agree with this criticism. We also note, however, that both a-priori and a-posteriori attempts should be validated taking experimental evidence as a reference (the MMI intensities by the USGS). So, we followed the aforementioned suggestion also because it came out that the comparison is interesting anyway.

Very recently, we also attempted to calculate parametric scenarios in Italy, in terms of maximum ground displacements, still with our *KF* scenario technique. This work was done in the framework of Project S5 of the Italian Civil Defence and the Istituto Nazionale di Geofisica e Vulcanologia (coordinated by E. Faccioli and A. Rovelli). Our displacements agreed with hazard results on a national scale for recurrence times of the order of 10^3 years (Faccioli and Rovelli, 2007; Faccioli and Villani, 2007; see: http://progettos5.stru.polimi.it/ ask permission for the latter report).

Finally, let us remind the reader that *KF* uses the nucleation coordinates, the fault-plane solution, the seismic moment, the rupture velocities and the along-strike and anti-strike rupture lengths, and the shear wave velocity in the half-space. To back-predict (1988 reference date) the regional intensity scenario of a destructive earthquake south east of San Francisco, we had to consider the uncertainties of the sources hypothesized at that time (see later). This was done by parametrically treating the aforementioned 11 source parametres by Montecarlo.

Materials and Methods

For the present back-prediction, we used only the sources hypothesized before 1988 by the following authors: Lindh, 1983; Sykes and Nishenko, 1984; Wesnousky, 1986; the Working Group on California Earthquake Probabilities, 1988. All these studies pointed to the Santa Cruz Mountains area, with uncertainties about the locations of the future event, about the approximate extent of its source and its mechanism. As said, these uncertainties were considered by treating the 11 source parametres of *KF* in a parametric way. As an example of the ranges adopted for the parametric calculations, we chose a +/-15° strike variation (with 5° step) to take into account the uncertainty of the strike angles of the various sources which were suggested before 1988. Thus, by combining all the uncertainties, 59,049 sources were used to calculate the mean intensities (and standard deviations) in the sparse sites surveyed by the USGS after the earthquake of 1989.

The reference intensities of the study earthquake are in Fig. 1 (MMI scale, in Roman numbers). The black dots are the towns surveyed by the US Geological Survey after the earthquake (so-called "felt reports"; courtesy of J. W. Dewey, written communication, 2003). Intensities were contoured by an evolution of our natural-neighbour bivariate interpolation scheme (Sirovich et al. 2002). Let us underline that our isoseismals are determined uniquely, and strictly honor the data. In other words, everybody obtains the same isoseismals with the same data also because no contouring parametres are needed.

The ShakeMap® intensities of the Loma Prieta, 1989 earthquake are in Fig. 2 (since they were calculated as real numbers, here we used Arabic numbers). The graphical look of the figure looks different from that of the original ShakeMap®. This is due to the grey scale; but we assure the reader that the original data, provided by the USGS (file «Text X, Y, Z Values (480 kB)» from http://earthquake.usgs), were used. Note that we drew also the isolines corresponding to 9.0, to 8.0 and so on. These isolines help the reader understand the structure of the instrumentally-derived values. In particular, one can pick out the areas with no strong-motion data, where the shape of the field was conditioned by the use of an attenuation law. Then, in Fig. 2 one is also able to guess the effects of the amplification factors applied by ShakeMap® according to the VS30 approach (at the Fig. 2 scale, this is hardly visible; refer to the grey soft shades, and note that they follow rifts, valleys and loose deposits). The rectangle marks the dimension of Figs. 1 and 5 for reference (unfortunately, different geographical projections were used).

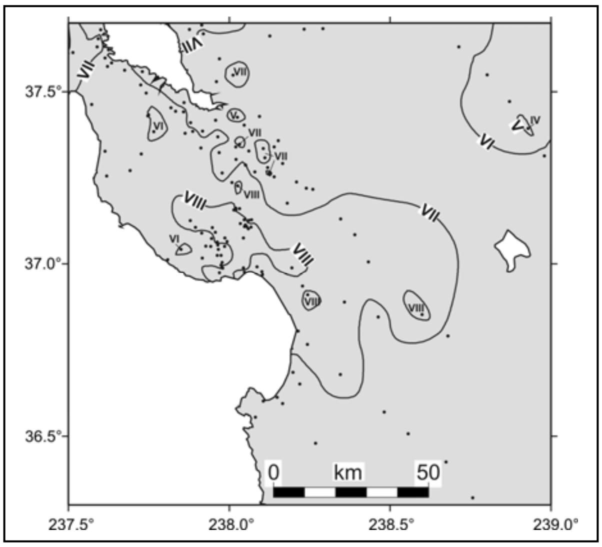

Figure 1. MMI intensities (in Roman numbers) observed by the US Geological Survey in theblack dots (so-called "felt reports"; courtesy of J. W. Dewey, written communication, 2003); intensities were interpolated by an evolution of our natural-neighbour algorithm (Sirovich et al. 2002).

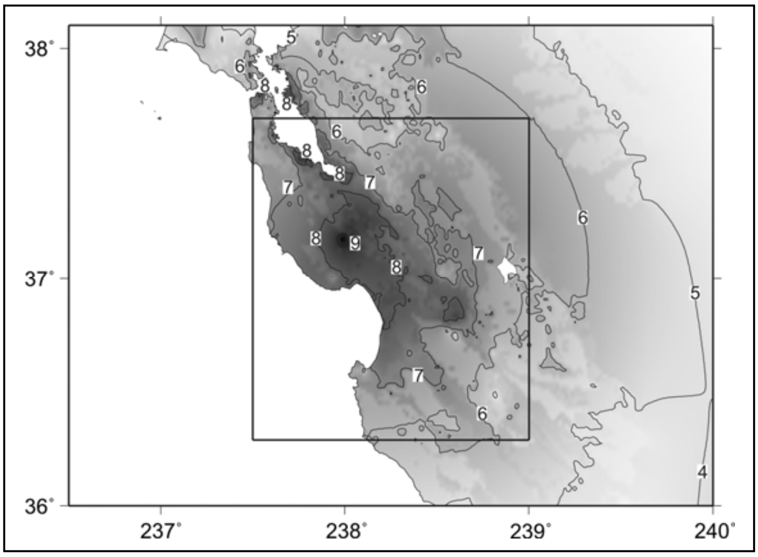

Figure 2. ShakeMap® intensities of the Loma Prieta, 1989 earthquake (redrawn; Arabic numbers). The file «Text X, Y, Z Values (480 kB)» from http://earthquake.usgs was used. Note that we also plotted the isolines that mark the full degrees.

Results and Discussion

The intensities of Fig. 1 (MMI degrees in the surveyed towns) were compared with the ShakeMap® intensities of Fig. 2 (which are real numbers in a dense grid). This was done picking the ShakeMap® values nearest to the black dots in Fig. 1 and taking the MMI degrees as integer numbers.

The comparison is in Fig. 3. As can be seen, the instrumental intensities overestimate the MMI ones, mainly for the degrees lower than 7; overestimation is close to 1-1.5 degrees. Fig. 4 shows the geographical distribution of the residuals (Fig. 1-minus-Fig. 2). Voronoi polygons were used. Negative residuals mean overestimation by ShakeMap®. Note the widespread negative areas, with some positive values (even +2 and +3) in San Francisco and Oakland. This means that Fig. 2 was not able to reproduce the high damage caused there in 1989, likely because no strong motion data were available and the attenuation used could not take local effects into account.

Coming back to the overestimations in Fig. 3, it is worth remembering, however, that Faccioli and Cauzzi found that ShakeMap® understimated the MCS intensities observed in many European towns (they used a case history from Italy, Greece, Turkey and Algeria). Since the differences between the MMI and the MCS scales do not explain these different results, one can tentatively conclude that instrumental intensities need to be calibrated locally.

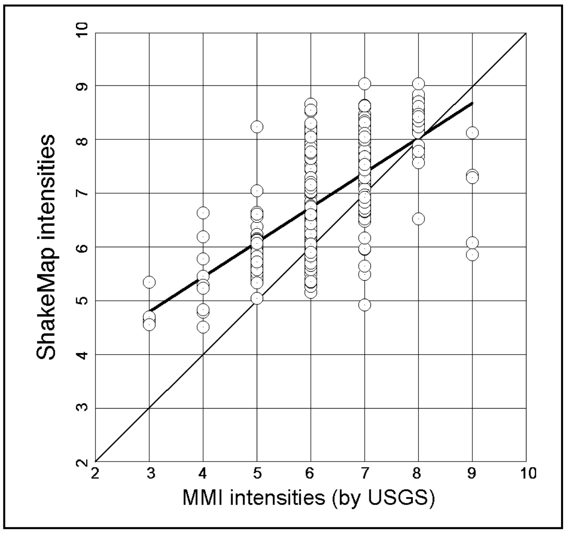

Figure 3. Comparison between the ShakeMap® intensities (real numbers) and the MMI intensities observed by the US Geological Survey.

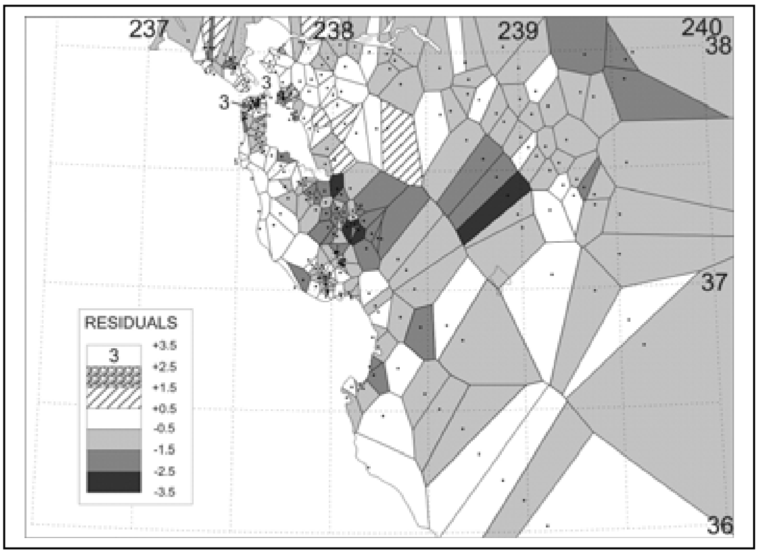

Figure 4. Comparison between the ShakeMap® intensities (real numbers) and the MMI intensities observed by the US Geological Survey.

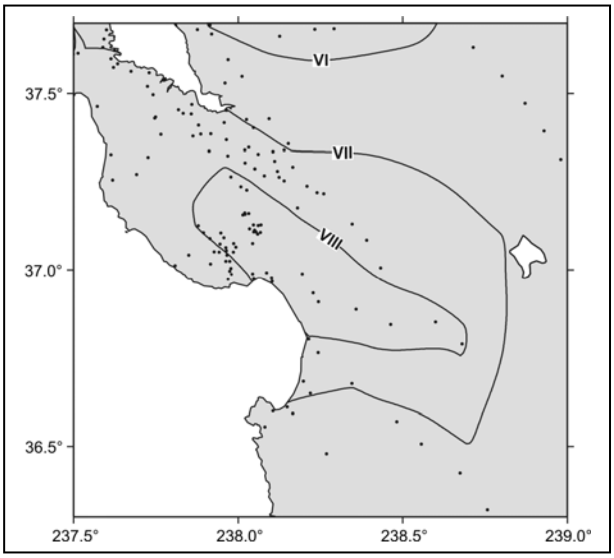

Figure 5. Back-prediction (1988 reference date) of an intensity scenario SE of San Francisco, CA; mean values are shown. Parametric Montecarlo calculation using the *KF* approach and the pre-1988 seismotectonic knowledge. 59,049 sources were used.

Fig. 5 shows our new KF scenario for the study earthquake. As said, it is back-predicted to 1988, and we show mean values from 59,049 sources. Obviously, no recording or field observation of the 1989 earthquake was used. The result shown is predictive, because it starts only from the pre-1988 seismotectonic knowledge and from the *KF* procedure. In other words, the goal of a preventive scenario like this is not to match the empirical evidence of 1989 at best, which would be an impossible task but, rather, to forecast the intensity field of 1989 with some caution.

At this point, we wanted to measure the ability of ShakeMap® in best fitting the data of Fig. 1, and that of KF in back-predicting them. We started from the reasonable assumption that a one degree uncertainty in the estimate of the intensity is common in the field, and an error of two degrees is unlikely. Thus, we computed the residuals calculated-minus-observed in the reference sites and summed up their squared values; this emphasizes the relevant misfits. Given the premise, in theory, one could espect zero residuals from an ideal post-earthquake interpolator. On the other hand, a predictive scenario necessarily gives residuals greater than zero, and they should all be positive and almost uniformly distributed throughout the territory. This condition ensures that the algorithm was able to catch the physics of the phenomenon; instead, many negative and positive residuals and/or those concentrated in some areas, would mean that the algorithm produced a result which is intrinsically alien to the experimental evidence.

The value of the squared residuals of Fig. 2 minus Fig. 1 (inside the rectangle) is 139. That of Fig. 5 minus Fig. 1 is 73. In our opinion, the former is not a good result. Regarding the latter (73), a general criterion of judgment is not available, but the reader can check the shape of the scenario intensity of Fig. 5. Doing so, he sees that: i) it retains the aspect of the intensity field of Fig. 1, and ii) it is cautious almost everywhere. In fact, note in Fig. 5 that the areas enclosed by the isoseismals are larger than the corresponding ones in Fig. 1; then, the geographical distribution of the residuals (not shown) is quite uniform. Regarding the standard deviations (not shown), they reach a value of 1.2 SSE of the sources. One small area of 1.2 is also found to the NNW. The scenario intensities are well constrained close to the sources, as well as in the NE corner of Fig. 5, where the standard deviation is approximately 0.6 (not shown). Our scenario intensities are sensitive to the orientations of the source planes; in fact, the standard deviations reach their maximum values in the direction of the fault sources (129°±180°) ± 15°.

Going back to Fig. 2, keeping in mind that in the areas with few recordings the intensities are controlled by an attenation law (e. g. NE of the source), the paths of the isoseismals show that: i) they go far from the source where no recorded data are available, and ii) they go closer to it (with complicated shapes) to obey the strong-motion evidence in the instrumented areas. This suggests that some of the high residuals could come from an unsatisfactory calibration of the instrumental intensity. Then, there is the problem of the use of VS30 for the convolution and the deconvolution of the data, but this is completely beyond the present subject matter.

Conclusion

The strategic target of our works on intensity is twofold: i) to increase the knowledge of the pre-instrumental sources, which is a key question for the understanding of the seismic hazard for example in most Mediterranean regions; ii) to optimize the treatment and the use of this 'poor' information, which is precious, however, for applications in engineering seismology as well as for public information.

In this short paper we cannot go into the many details of the use of the traditional intensities and, on the other hand, on the development and treatment of instrumental intensities and of the applications of the intensity output of ShakeMap®. In general, we think that any forecasts, scenarios or synthetic results should be validated, whenever possible, with reference to the experimental evidence expressed in terms of certificated intensities according to the known macroseismic scales.

Regarding our new *KF* scenarios, as said Fig. 5 was obtained using many hypothetic sources. We know that one rupture plane close to them (see figure 6 and table 5 in Pettenati and Sirovich, 2007) is able to fit the MMI intensities of 1989 well, the SW protuberance of degree VIII included (see Fig. 1 here). This rupture plane was not used here, but the mean values of Fig. 5 still resemble Fig. 1. This encourages us to try to validate our scenarios with more earthquakes.

The aforementioned satisfactory results obtained with our model in terms of maximum ground displacements (and other evidence) could suggest that the regional pattern of intensity (read: damage) of a destructive shock are controlled mainly by the low frequency content of strong motion.

Then, Molchan et al. (2004) noticed that our *KF* formula can also be thought of as an attenuation law for body-waves, which includes the source finiteness, the directivity and the radiation patterns of the horizontal components of S body-waves. We think that we can try to follow this implicit suggestion and perhaps we can try to include our formula inside ShakeMap® for distances compatible with the prevalence of body-waves. *KF* is freeware, however.

The Subprogram S3 2008-2009 of the National Civil Defense of Italy and of the Istituto Nazionale di Geofisica e Vulcanologia (INGV) supported this research. We thank the U.S. Geological Survey for its data.

References

Faccioli E. & Rovelli A. (2007). Determination of the seismic input in Italy for displacement based design; final scientific report (in Italian) *(Jul. 31, 2007). INGV-DPC S5 report,* pp. 52 http://progettos5.stru.polimi.it.

Faccioli E. & Cauzzi C. (2006). Macroseismic intensities for seismic scenarios, estimated from instrumentally based correlations. *First European Conference on Earthquake Engineering and Seismology, 3-8 September, 2006, Geneva, Switzerland*

Faccioli E. & Villani M. (2007). Seismic hazard maps for Italy in terms of Displacement Response Spectra for different return periods*. INGV-DPC S5 Deliverable D23* http://progettos5.stru.polimi.it/Deliverables.html (permission requested).

Lindh, A.G. (1983). Preliminary assessment of long-term probabilities for large earthquakes along selected fault segments of the San Andreas fault system in California. *U.S. Geol. Surv. Open-File Rep. 83-63, 14 p.*

Molchan G.M., Kronrod T.L. & Panza G.F. (2004). Shape of Empirical and Synthetic Isoseismals: Comparison for Italian Earthquakes. *Pageoph, 161, 1725-1247.*

Pettenati F. & Sirovich L. (2006). Two validations of a kinematic approach to calculate seismic hazard scenarios, in *Proc. 1st European Conf. Earthquake Engineering and Seismology*, *Sept. 3-8, 2006, Geneva, Switzerland (abstract).*

Pettenati F. & Sirovich L. (2007). Intensity-Based Source Inversion of Three Destructive California Earthquakes, *Bull. Seism. Soc. Am.*, *BSSA, 97, 5, 1587-1606*.

Sirovich L. (1996). A simple algorithm for tracing out synthetic isoseismals, *Bull. Seism. Soc. Am. 86, 1019-1027.*

Sirovich L. (1997). Synthetic isoseismals of three earthquakes in California-Nevada, *Soil Dyn. and Earthq. Engng. 16, 353-362.*

Sirovich L. & Pettenati F. (2007). A new Kinematic Approach to Calculate Seismic Hazard Scenarios (Intensity and Peak Ground Displacement); an Example in SE Sicily, in *Proc. Joint Ass. AGU2007, May 22-25*, *Acapulco, ref. n. S51A-01.*

Sirovich L., Pettenati F., Cavallini F. & Bobbio M. (2002). Natural-Neighbor Isoseismals, *Bull. Seism. Soc. Am. 92, 5, 1933-1940.*

Sykes, L. R., and S. P. Nishenko (1984). Probability of occurrence of large plate rupturing earthquakes for the San Andreas, San Jacinto, and Imperial faults, California, 1983-2003, *J. Geophys. Res., 89, B7, 5905-5927.*

Wald D.J., Worden B.C., Quitoriano V. & Pankow K.L. (2006). ShakeMap® Manual; technical manual, users guide, and software guide, Version 1.0 6/19/06, 1-156.

Wesnousky, S. G. (1986). Earthquakes, Quaternary faults, and seismic hazard in California, *J. Geophys. Res., 91, 12,587-12,631.*

Wood H. O. & Neumann F. (1931). Modified Mercalli intensity scale of 1931, *Bull. Seism. Soc. Am., 21, 277-283.*

Working Group on California Earthquake Probabilities (1988). Probabilities of large earthquakes occurring in California on the San Andreas Fault, *U.S. Geol. Surv. Open-File Rep. 88-398,* Menlo Park, California 1-64.

Enhanced Earthquake Location Using Robust Algorithms and Automatically Determined Arrival Time Picks. Application to Swiss Seismic Network Data

Pinsky V (1), Husen S (2), Lomax A. (3)

(1) Geophysical Institute of Israel, vlad@seis.mni.gov.il
(2) Swiss Seismological Service, ETH Zurich, Schafmattstr. 30, CH 8093 Zurich, Switzerland, husen@sed.ethz.ch
(3) Anthony Lomax Scientific Software, 161 Allee du Micocoulier 06370 Mouans-Sartoux, France

Keywords: automatic arrival picking, robust earthquake location, network beamforming, equal differential time likelihood function

Introduction

The problem of reliable and accurate real-time seismic event location is a key issue in seismic event monitoring for automatic bulletin production and early warning systems. This issue is determined by how we can deal with various detrimental factors such as sporadic seismic noise, poor network configuration, heterogeneity of the Earth, incorrect phase association or simultaneous, multiple events with a minimum given number of phase readings. The goal of this paper was testing and comparison of two new location techniques, Network beamforming (NB) and probabilistic, non-linear, global-search earthquake location using the equal differential time likelihood function (NonLinLoc-EDT), as applied to the Swiss Network data with the target to achieve the best performance in hypocenter location in the presence of large errors in arrival time picks.

Materials and methods

The Data

The Swiss Seismological Service (SED) at ETH Zurich operates the Swiss Digital Seismic Network (SDSnet) consiting of 32 permantly installed broadband instruments. It represents the most homogeneous and dense regional broad-band network in the European-Mediterrean region. P-wave arrival times are determined automatically and manually and archived in the SED data base.
From the data base we have chosen 127 well located events of magnitude $M_L > 2.0$ in the period between 2004-2007 (Figure 1). The data was presented by P-wave arrival time estimations of the three types: 1) "MANUPICK" - manually determined by a qualified analyst, 2) "AUTOPICK - automatically determined by the Baer-Kradolfer picker (Baer-Kradolfer, 1987), 3) "TRIGGER" - simple STA/LTA trigger times delivered by the NAQS acquisition system. The MANUPICK's are supposed to be most accurate, while the TRIGGER's are the most rough and uncertain estimates of the first arriving P-wave arrival time.

The Methods

The most severe automatic pick and trigger time errors leading to large hypocenter deviations occur due to missing or misinterpretation of seismic phases or triggering at noise or spikes causing data outliers. The maximum likelihood approach based on the Gaussian probability density function (pdf) (defined as L_2 method or least-squares) (Tarantola and Valette, 1982)

$$pdf(x,t_0) = \propto \exp(-\frac{1}{2}\sum_j [T_{obsj} - TT_j(x) - t_0]^2 / \sigma^2) \qquad (1)$$

provides at the maximum of the $pdf(x,t_0)$ under the assumption that all arrival time observations T_{obsj} have Gaussian distribution with average $TT_j(x)+t_0$ and variance σ^2. However, this solution is not the best in the cases when this assumption is violated. On contrary large mistakes in parameter estimation are possible, due to large sensitivity of the function to the outliers in the vicinity of the true (x,t_0) parameter point. Hence, when the data includes outliers robust aproaches should be considered (Huber, 1972), such as removing or automatically reduced the weight of data with large deviations. The latter is done in the equal differential time NLL-EDT pdf of (Lomax, 2005), based on the sum of exponents, and applied to differential time data.

$$pdf(x) \propto \sum_{k,j} \exp(-\{(T_{obsj} - T_{obsk}) - [TT_j(x) - TT_k(x)]\}^N / \sigma^2) \qquad (2)$$

The sum in (2) is taken for all station pairs "k" and "j" at which phase arrivals are observed.

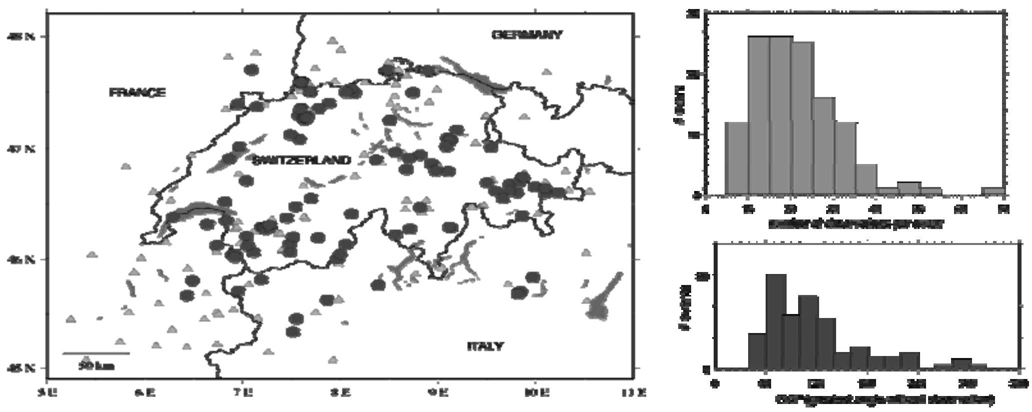

Figure 1. Data set of 127 SED network (triangles) events (circles) m >2, collected for comparison of the location algorithms.Histograms show distribution of the number of manual P phase picks (top) and of the azimuth gap (bottom), showing quality of the data for location.

Figure 2 depicts the NLL-EDT $pdf(x)$ in the case when a number of true correct observations and one outlier observation are present, producing a local maximum at a false location. However, the global maximum position remains at the true event location stability of the EDT alogorithm and the predimuance of the correct observations.

The second method, network beamforming (NB) (Pinsky, 2006), considered in this study is based on the system of the travel time equations:

$$t_{0k} = T_{obsk} - TT_k(x)\,, \qquad (3)$$

expressed with the help of complex exponents:

$$\exp(it_{0k}/\sigma) = \exp\{[iT_{obsk} - TT_k(x)]/\sigma\} \qquad (4)$$

The least-squares optimal solution for the system of equations (4) is achieved by maximizing

$$pdf(x) = |\sum_k \exp\{[iT_{obsk} - TT_k(x)]/\sigma\}/K| \qquad (5)$$

where the sum is taken over all the stations. Figure 3 illustrates the principle of the algorithm. Each complex exponent is the radius vector in the complex values plain C^2 with a variable rotation angle equal to its argument depending on unknown $\boldsymbol{x}$. According (5) the best solution is obtained at a point $\boldsymbol{x}$ where the average radius vector is the longest. The algorithm is not sensitive to outliers when number of "true" observations is relatively large. Both algorithms

(NB and NLL-EDT) can use grid-search or the Oct-tree grid-search (Lomax et al., 2000) of the $pdf(x)$ maximum for the parameter estimation. We used the Oct-Tree search since it gives similiar results as a grid-search but computationally is much faster.

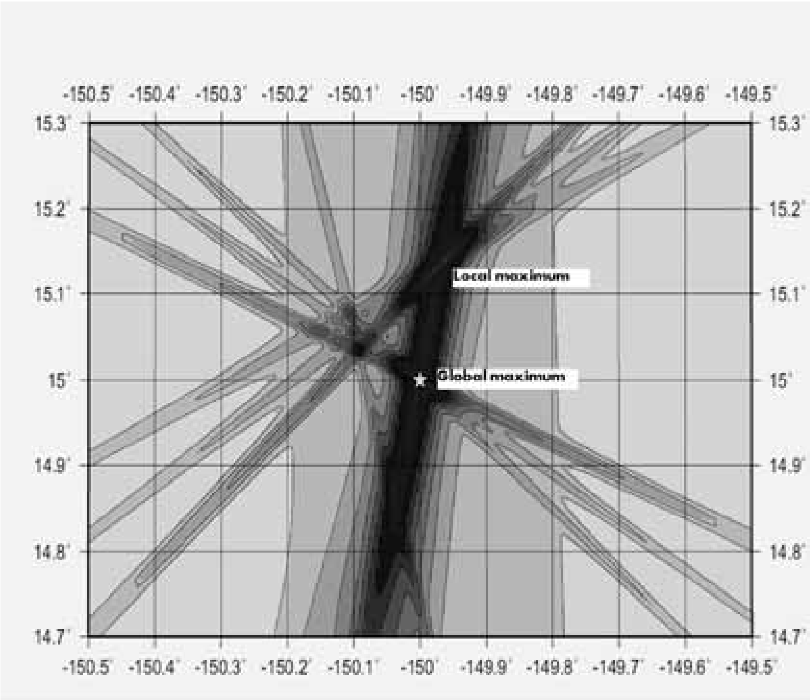

Figure 2. Synthetic example of the $pdf(x)$ for the NLL-EDT in the presence of several picks with large deviations, providing local maximum.

Testing procedure

Our testing procedure included the following steps:

- Relocate 127 events from the accumulated data base using two sets of arrival times (AUTOPICKs & TRIGGERs) by each locator (NLL-EDT & NB)
- Compare locations (epicenter mislocations) against reference locations computed using MANUPICKs and NLL-EDT

In all the relocations the minimum 1D velocity model was used (Husen et al, 2003), upgraded using the events of this study (2004-2007). This model was used for the travel-time $TT_k(x)$ calculations.

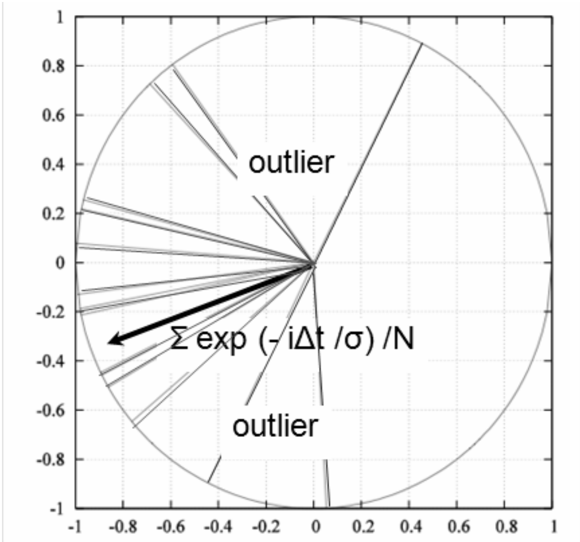

Figure 3. The best NB solution is obtained at a point $\boldsymbol{x}$,where the average radius vector is the longest.

Results and Discussion

Relocations using AUTOPICKs

The results of the computations using AUTOPICKs are summarized in the Figures 4 and 5 where the mislocation vectors (auto - manual) = (dx,dy) are shown as filled circles of different grey scale scattered over the plane. Different scales of grey are used to distinguish NLL-EDT, NB and L2 methods. The histogram embedded in the Figures show the percent of events within mislocation distance bins of 2 km length.

The histograms show that both NLL-EDT and NB have approximately equal behavior, essentially outperforming the L2 method. For example, 83% of epicenters estimated by NLL-EDT and 82% of the NB estimates locate within 4 km radius circle relative the reference epicenters as compared to 38% for L2.
Several outliers exceeding 10 km bin constitute 7% for NLL-EDT 6% for NB and 14% for the L2. The large deviations in event epicenter estimates correspond to the cases when false automatic picks prevent correct event location, while true automatic picks form poor sub-network configuration.

Relocations using TRIGGERs.

The results of the computations using TRIGGERs are summarized in the Figure 6.
Only 61% of the epicenters hit the 4 km target circle for both NLL-EDT and NB. Worse performance of the algorithms using TRIGGERs is evident due to the poorer quality of the picks for small events.

Discussion

It is easy to show that NB (5) is equivalent to the sum of cosine functions over Equal Differential Times (EDT) $\sum_{k,j}\cos\{(T_{obsj}-T_{obsk})-[TT_j(x)-TT_k(x)]/\sigma\}$ for all pairs of stations. So NB differs from the NLL-EDT only by using cosine instead of Gaussians exp(-x^2/2) in expression for the *pdf(x)*. According to (Andrews et al, 1972), who were doing computer experiments with various robust statistics the cosine target function (sine loss function) was qualified as the best M-estimator, but there is yet no explicit theory to prove it. Computationally NB (5) is more efficient than NLL-EDT since it computes a sum over 2n pairs of observations instead of n(n-1)/2 in NLL-EDT, thus requires ~ n/4 times less computations. Comparison of the NB and EDT locations using Autopicks of the 127 events show that EDT provides slighly improved accuracy for “good events” but perhaps some more outliers in difficult cases.

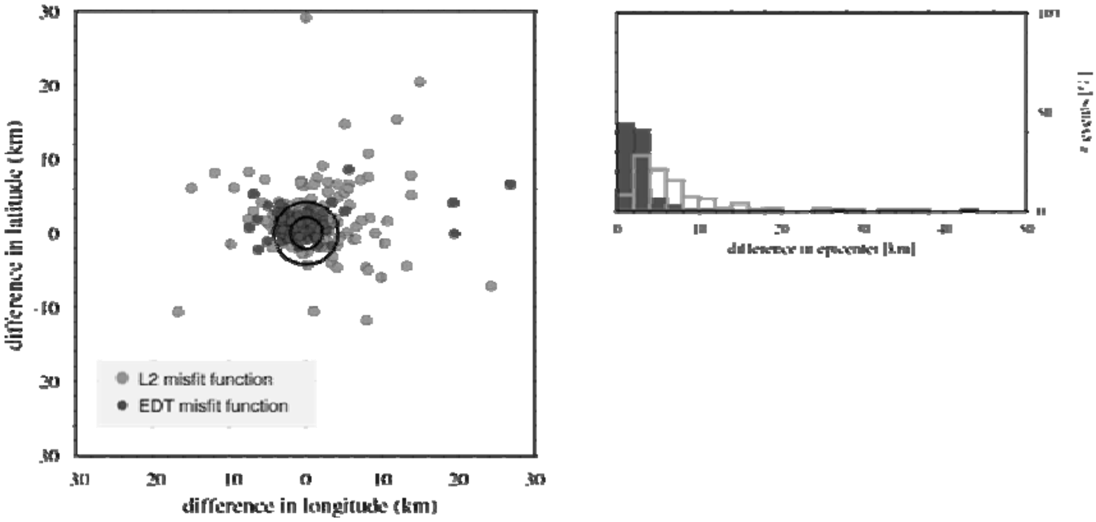

Figure 4.(dx,dy) epicenter mislocations of NLL-EDT and L_2 using Autopick data and the corresponding distribution of the mislocation distances (histograms).

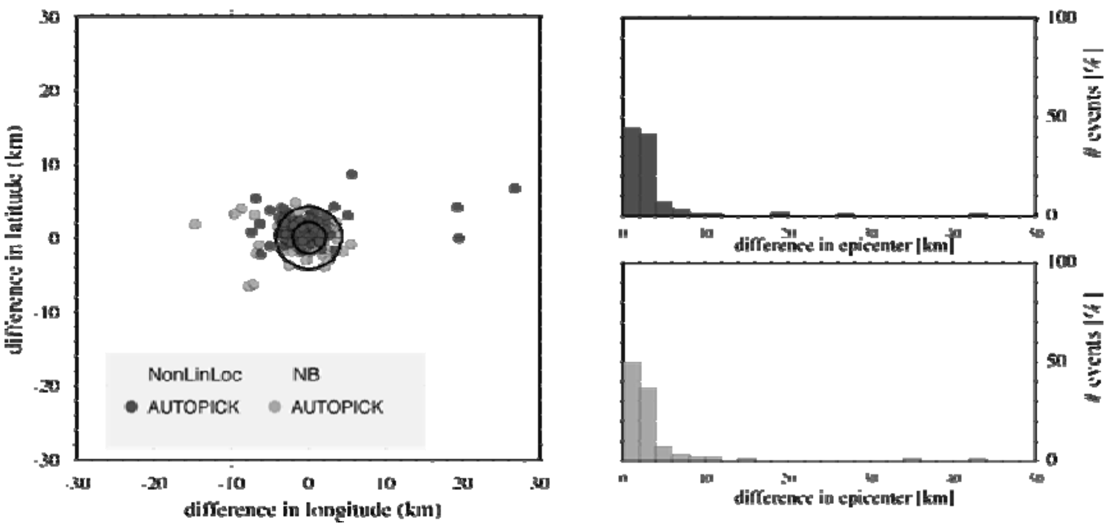

Figure 5. (dx,dy) epicenter mislocations of NLL-EDT and NB using Autopick data and the corresponding distribution of the mislocation distances (histograms)) NonLinloc (up) and NB (bottom).

.

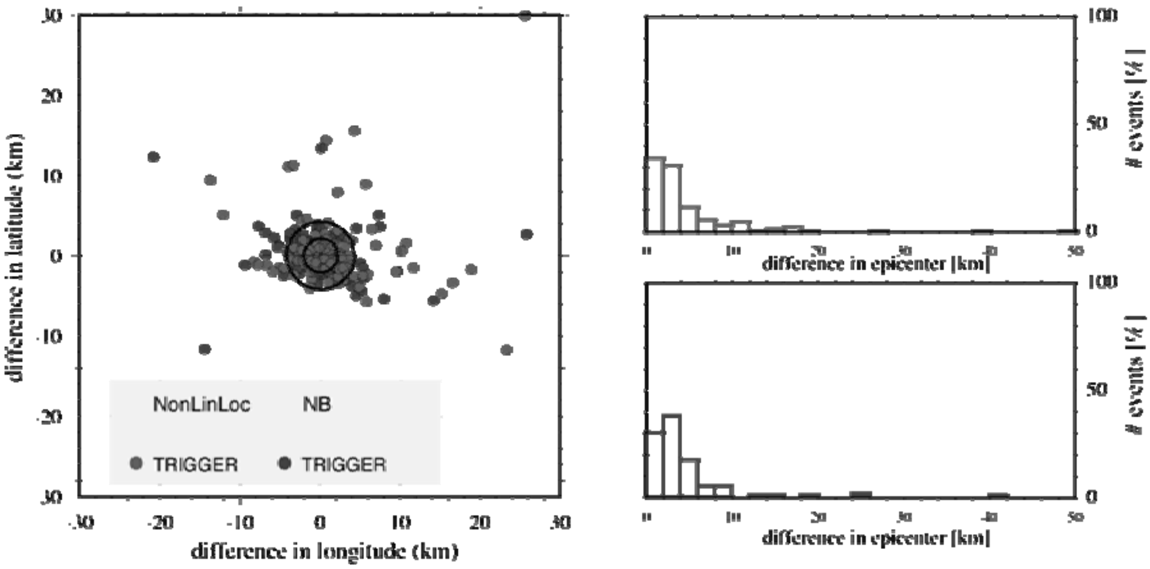

Figure 6. (dx,dy) epicenter mislocations of NLL-EDT and NB using Trigger time data and the corresponding distribution of the mislocation distances (histograms) NonLinloc (up) and NB (bottom).

Examples of difficult cases.

1. Both the NB and the EDT NonlinLoc algorithms failed to locate an Ml=2.5 event which occurred on 2004/12/06 01:52:17.1, Lat=47.43˚ Long=7.89˚, Z=11 km. The analyses showed that majority of the automatic picks (ten of thirteen) belonged to a previous small event, which occurred a minute before the event listed in the MANUPICs list, but were associated with it. The presence of a preceding event is a common cause for the severe outlier picks.
2. For an earthquake of Ml=2.1 which occurred on 2006/12/08 15:30:36.5 Lat=47.58˚ Long=7.60˚, Z=4.6 km the NB failed because only 5 of 10 AUTOPICs were correct (and very accurate:RMS=0.12 sec) . The remaining five observations deviated from the true P wave arrival time by as much as 5 to 22 seconds and by chance in such a manner that the pdf value (5) of NB in the true point was equal to only 0.16; this value is much less than the maximum possible value of 0.48 for this case, reached far away. In contrast NLL-EDT provided the correct location of the event due to the strong, exponential suppression of the contribution of the outlier picks at points around the true location. In fact the problem of outlier picks with large deviations can be partially solved by preliminary testing of travel times between the stations and removing outstanding picks with travel times outside of thresholds given by admitted velocity range.
3. There are two events of Ml=3.7 and Ml=2.7, which occurred in France, close to Grenoble, and were manually located accurately and reliably (Gap=43˚) due to the additional French stations (see Figure 1), which were not included in the AUTOPICK's. Despite the availability from the Swiss network of N=35 AUTOPICK's for the first event and N=27 for the second one, the solution of the NLL-EDT deviates by 32 km for the first and by 22 km for the second epicenter. It happens because of poor network configuration (GAP=250˚) and difference in travel times. The solution of NB is unstable either for the case: 19 km away from the first epicenter and 16 km from the other. However, with reduced number of AUTOPICKS (N=18) both algorithms manage to get solution which deviates less than by 4 km from the true epicenter.

Conclusions

Automatic epicenter location of the SED events with magnitude Ml > 2 and station gap < 180 using Autopics is shown to be as accurate as 4 km in approximately 83% of the cases and 10 km for more than 93% of the cases by both NB and NLL-EDT locators. Using rougher TRIGGERs time data yields in 61% of epicenter solutions within 4 km range for both of the algorithms. Hence, with improving quality of arrival time data hypocenter locations become more reliable, i.e. have less deviations from the reference locations as was expected. For further improvement of the location results we shall have better tuning the algorithm's parameters (scatter parameter, number of stations to use, distant depending weighting etc) the given network conditions. For this purpose we shall analyze the large error cases and try to reduce the error. We plan providing a broader data selection including neighbor networks and using boot-strap for better performance demonstration. Various scenario of large earthquakes including double events will be considered using real and synthetic data.

References

Andrews D.F., Bickel P.J., Hampel F.R., Huber,P.J., Rogers W.H. & Tukey J.W. (1972). Robust Estimates of Location, *Princeton: Princeton University Press.*

Baer M. & Kradolfer U. (1987) An automatic phase picker for local and teleseismic events, *Bul. Seis. Soc. Am., 77, 1437-1445.*

Bondar I, Myers S.C., Engdahl E.R. & Bergman E.A. (2004). Epicenter accuracy based on seismic network criteria, *Geophys. J. Int., 156, 483-496.*

Kissling E., Ellsworth W.L., Eberhart-Phillips D. & Kradolfer U. (1994). Initial reference models in local earthquake tomography, *J. Geophys. Res., 99, 19635-19646.*

Lomax A., Virieux J., Volant P. & Berge C. (2000). Probabilistic earthquake location in 3D and layered models: Introduction of a Metropolis-Gibbs method and comparison with linear locations, in Advances in Seismic Event Location Thurber, C.H, and N. Rabinowitz (eds.), *Kluwer, Amsterdam, 101-134.*

Lomax A (2005). A reanalysis of the Hypocentral Location and Related Observations for the Great 1906 California Earthquake, *Bull. Seism. Soc. Am., 95, 861-877.*

Husen S., Kissling E., Deichmann N., Wiemer S., Giardini D. & Baer M. (2003). Probabilistic earthquake location in complex three-dimensional velocity models: Application to Switzerland, *J. Geophys. Res., 108(B2), doi: 10.1029/2002JB001778.*

Pinsky V. (2006). Using beamforming for the global network location, *Physics of the Earth and Planetary Interiors, 158, 1, 75-83.*

Tarantola A. & Valette B. (1982). Inverse Problems = Quest for Information, *J. Geophys., 50, 159-170.*

Multihazard Risk Mapping Methodology and Application – A Scenario to the Bulgarian North Black Sea Coast

Ranguelov B K (1)

(1) Geophysical Institute – BAS, Acad. G. Boncev str., bl.3, Sofia 1113, Bulgaria, branguelov@gmail.com

Keywords: Black Sea, multirisk, earthquakes, tsunamis

Introduction

The different methodologies developed and used about the mulirisk assessment usually resulted in different values, scenarios, decision and management solutions, etc. according Vetere et al., 2003, Bethke et al,1997, ESPON Project, 2003. Each methodology has its own specifics which makes incompatible the results and issues. Always similar approaches are preferable in use Blaikie et al,1994, ESPON Proj.2004, etc. to compare and assess the results. The main task is to cover larger number of elements and parameters influencing the final outcome – most frequently – the multirisk maps according IADB,2005. The results obtained, the sensitivity of the methodology and the influence of the different parameters and indicators always resulted on the maps – the most visible product of such approach.

Materials and Methods

The main methods of the suggested and applied methodology are incorporated in the last version on the multirisk assessment - IADB, 2005 - of the Inter-American Development Bank (IADB). The modifications done by us are targeted to adapt the differences in the different parameters, and the data and information necessary for their assessment. The existence (or lack) of the basic parameters due to different economic conditions in Bulgaria and the USA has been used for the changes introduced for the adaptation about the different European economic environment
Four main factors are considered in use for the multirisk assessment:

- natural hazards
- exposure
- vulnerability
- coping capacity

To each factor the indicators are attributed for the quantitative assessment:

a) *natural hazards* include the behavior of the respective hazards in the past and possible expected effects (the indexes used consider the observed maximum magnitudes and intensities and the extrapolated future expected possibilities. The indicators are H1-H4 and the values are extracted by the recurrences in time (4 indicators – 8% of the total numbers used).

b) *exposure* – the indicators consider economical and infrastructure elements: buildings and facilities, roads, ports, total population and local GDP. The values of the indexes are mainly based on the statistics. (7 indicators – E1-E7 – 14% of the total number).

c) *vulnerability* - the indicators V1-V15 consider economic and social vulnerability unemployment/employed density of population, social security etc. The indexes are due to the statistics. (15 indicators - 30%),

d) *coping capacity* – the indicators C1-C24 indicate reinforcement and codes applications, economical and management elements – (24 indicators - 48%)

It is visible that from each factor to another the number of indicators increased approximately by factor of two. – fig. 1.

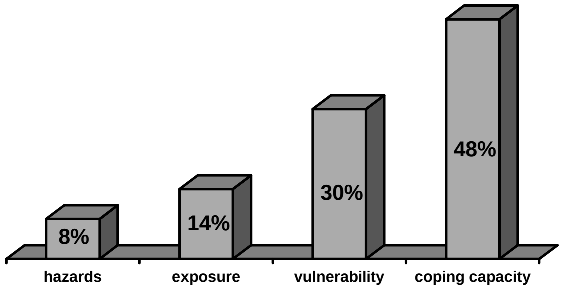

Figure1. Percentage of the number of indicators according the main risk factors

The general algorithm for the multirisk assessment is a set of consecutive operations:

1. The general and priority hazards assessment of the selected region. Usually 2-3-4 hazards are of most importance (there are no any limitations on their number, but for the better visualization 3-4 are enough). The prioritization is essential to cover the most important cases and threats.
2. The assessment of the main indicators. Usually this is done on the basis of available data and information.
3. Assessment of the weighting coefficients for the different factors of the complex risk. Formally they are equal to 0.25. This is an important operation because this is one of the most influencing values to the results of the 4 factors.
4. Assessment of the Scaled indicators values. Usually there are three levels – low (1), medium (2) and high (3).
5. Fill the risk tables – one of the most important operations – needs expert judgment and careful assessment of the indexes
6. Calculations of the factor scores – by multiplications of the weighting coefficients and the Scaled indicator values
7. Calculations of the “risk” values R by the formulae (1) according IADB, 2003:

$$R=0,25.H + 0,25.E + 0,25.V - 0,25.C \qquad (1)$$

where,

H are the values about the hazards indicators
E – values about the exposure of the different elements to the natural hazards
V – vulnerability values
C – coping capacity values.

8. Sensitivity assessment of the methodology to the different factors influence.
9. Risk profile construction.
10. Multirisk mapping

Sensitivity analysis and errors estimations

The sensitivity analysis to the suggested methodology is developed to many of the influencing factors and their influence to the analysis output. The weighting coefficients are equal to all elements of the risk.

The “scaled indicator values” are strongly influencing the “factor scores” – main risk quantity values. In our case these values are changing from 1 – low, trough 2- medium up to 3 – high. Several combinations of these values are presented on fig. 2. and fig. 3. Both graphs have the similar combinations, but different weighting coefficients visible in table 1 and table 2. The behavior is almost linear, but some fluctuations could be observed.

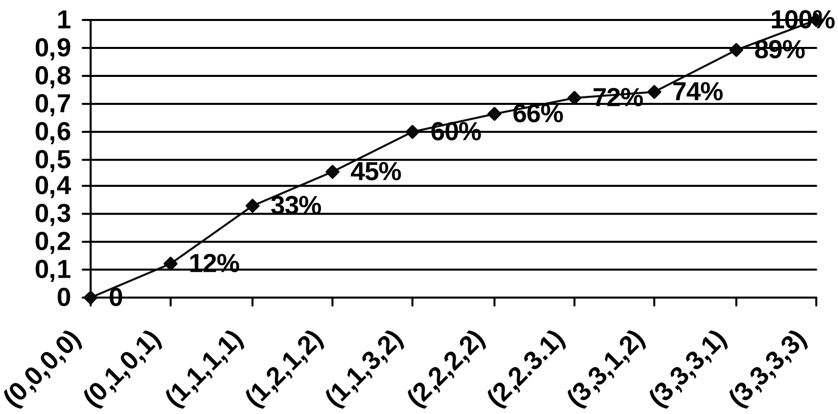

Figure 2. Influence of the scaled values combinations (fixed weighting coefficients) according table 1.

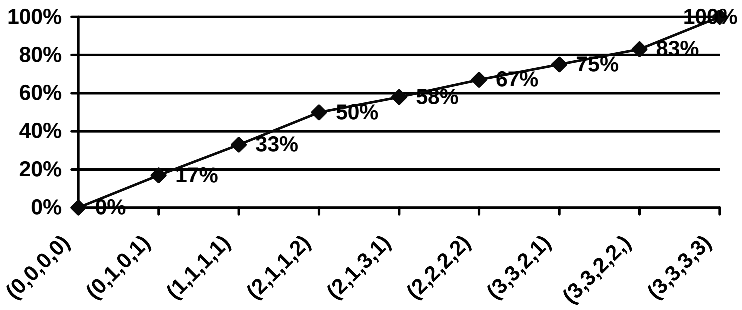

Figure 3. Influence of the scaled values combinations (fixed and equal weighting coefficients) according table 2.

Table 1. Values due to the combinations of the scale values (weighting coefficients fixed, different values and sum - equal to 25)

Weighting coefficient	Scaled values combinations	Influencing values due to the scaled coefficients
	0,0,0,0	0%
	0,1,0,1	12%
	1,1,1,1	33%
8	1,2,1,2	45%
5	1,1,3,2	60%
8	2,2,2,2	66%
4	2,2,3,1	72%
(sum 25)	3,3,1,2	73%
	3,3,3,1	89%
	3,3,3,3	100%

Table 2. Values due to the combinations of the scale values (weighting coefficients fixed, equal values and sum - equal to 25)

Weighting coefficient	Scaled values combinations	Influencing values due to the scaled coefficients
	0,0,0,0	0%
	0,1,0,1	17%
6,25	1,1,1,1	33%
6,25	2,1,1,2	50%
6,25	1,3,1,2	58%
6,25	2,2,2,2	66%
(sum 25)	3,3,2,1	75%
	3,3,2,2	83%
	3,3,3,3	100%

The increase of the indicators number by factor of two, decrease their influence approximately twice. The indicators number and their influence to the final results are presented on fig.4.

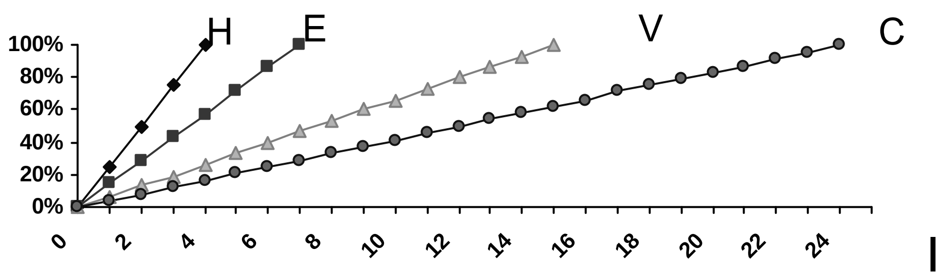

Figure 4. The percentage distribution of the number of indicators I: H (hazards), E (exposure), V (vulnerability), C (coping capacity).

The linear influence is clearly expressed, but the combination of indicators gives sometimes light nonlinear effects, due to their combined action (if some of the indicators are missing, the combined effects could be balanced by others or vice versa)
It is important to mention also that the weighting coefficients have the strongest influence and needs the expert judgement for the correct practical applications - Frantzove et al, 2005.
The calculated risk values are in the diapason scale from 10 to 50. This shows the stability of the methodology. To assess quantitatively the influence of the different parameters numerical experiments have been performed.
An ideal variant has been investigated considering maximum, medium and low values. It is clear if some hazard is missing, no more calculations have to be performed. The most influencing are the Scale indicator values – they can change the results up to 3 times (if the scale has three levels, as in our case). The variations of the different indicators are smaller, because of their larger number. The weighting coefficients have the ‘inside” influence in each of the investigated elements of the risk – hazard, exposure, coping capacity, vulnerability. The influence have different directions (increase and decrease), which could bring the effect of the “compensation” “inside” each element.
The analysis of these results shows that the larger influence could be expected from the hazards and vulnerability. The coping capacity and exposure are less influencing. This means that the assessment of the hazards and the vulnerability need special attention and research for the estimation of they values. This means – more correct and exact results. That’s why these elements must be assessed more carefully to obtain more exact results. Neglecting these values could be confusing and can lead to wrong results. The “season’s factor” is about 10-15% which in general means serious influence. The same values could be expected as well as for the “day-night” effects especially during the “high (active) season” time.

Results and Discussion

The area selection is based on the multi factor analysis considering many and different elements and factors. The region is treated by many natural hazards with a large diapason of power (earthquakes, landslides, tsunami, erosion, abrasion, storms, floods, etc. [6, 7, 8]. The high probability of interaction between different hazards exists. The chains of consequences could be expected. The region has complicated infrastructure and different economic activities – tourism, agriculture, industry, larger and small inhabited areas, cultural heritage. The data and information availability is also an influencing factor for the risk table fulfillment. An important element is the changing population density. There is not another region in the country with so variable parameter. Due to the tourist industry the changes could be twice and more. After the multifactor analysis the following natural hazards have been selected (earthquakes, tsunamis, landslide and stonefalls). These hazards could be interacting during the same time or consequently.
Better classification is presented on the next table 3:

Table 3. Main parameters classification for the natural hazards in the selected region.

Natural hazards/ Main parameters	Destructive potential	Area coverage [м^2]	Frequency	Trigerring possibilities	Duration of the process [s]
Earthquakes	L-M-H	10^3-10^5	Low	No	10^1-10^2
Landslieds	L-H	10^1-10^3	High	No/Yes	10^3-10^{5-6}
Tsunami	M-H	10^2-10^4	Low	Yes	10^2-10^4

The destructive potential is defined as incorporated masses (or energy) and the velocity of the processes. L - low; M - middle, H – high. The different events have different diapason of the power expression.
The area coverage is in м^2 and shows the natural limitations of the area affected by the different hazards.
The frequency shows the number of events of the selected time interval. It depends of the time interval and the power of the natural disaster.
The triggering possibilities show if one or several hazards can trigger each other. In our case – the earthquakes can not be triggered by landslides or tsunami. The landslides can be or could be not triggered by earthquakes and tsunamis can be triggered by earthquakes and landslides and or rockfalls.
The fastest are earthquakes, tsunamis are longer lasted and the longest time development and duration have landslides. This classification is important from point of view of the future consequences scenarios development.
Appling the described methodology, several mulirisk maps have been created covering the coastal zone of the North East Bulgarian Black Sea Coast according Ranguelov B. & Jelinek R. 2007. The region has been separated to three sub regions covering the north part: from cape Kaliakra up to the Bulgarian-Romanian boundary (region 1), from Kranevo to Cape Kaliakra (2) and from Varna city to the village of Kranevo (3). The possible dangerous zones due to the tsunamis, earthquakes and landslides have been outlined – fig. 5-6-7 and mapped.
The risk profiles for each zone (region 1, region 2 and region 3) as well as for the high (active summer) season time and the rest time of the year have been calculated. – fig.8, 9 and 10.

Conclusions

The modifications and improved methodology of the Inter American Development Bank for the multirisk assessment is successfully adapted to the European conditions. The sensitivity analysis and the results obtained show that the influence of the main parameters is essential. The lack of data and information for some not very important indicators show they could be skipping without significant influence.

Figure 5. Multirisk map for Region 1. Hatched areas are seismic prone, lunar symbols – landslide prone and white line – tsunami prone areas.

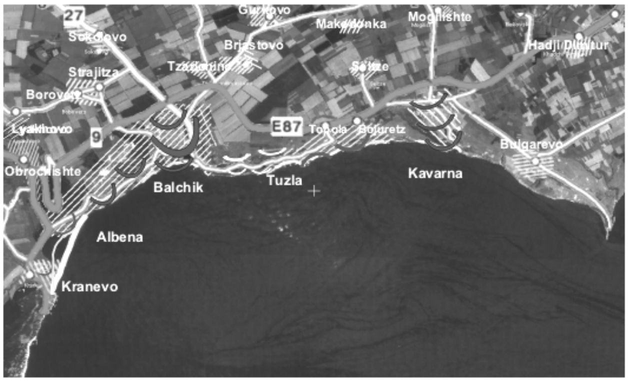

Figure 6. Multirisk map for Region 2. Hatched areas are seismic prone, lunar symbols – landslide prone and white line – tsunami prone areas.

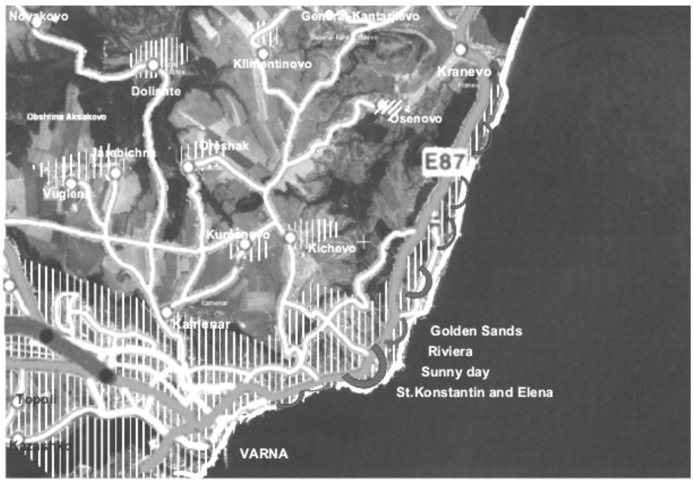

Fig.7. Multirisk map for Region 3. Hatched areas are seismic prone, lunar symbols – landslide prone and white line – tsunami prone areas.

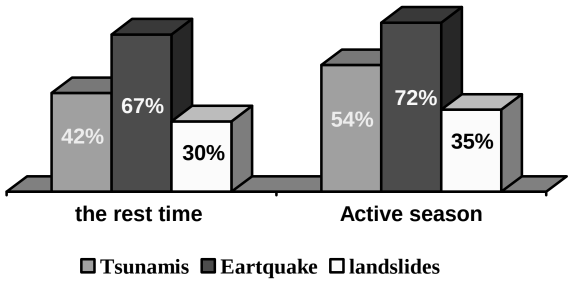

Figure 8. Risk profile – Region 1.

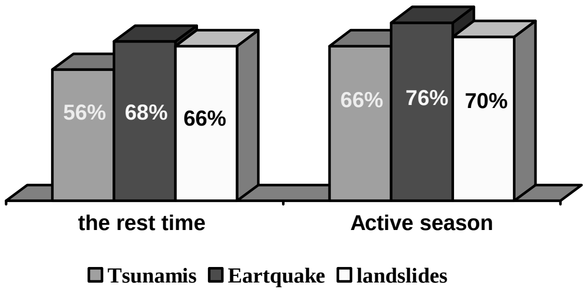

Figure 9. Risk profile – Region 2.

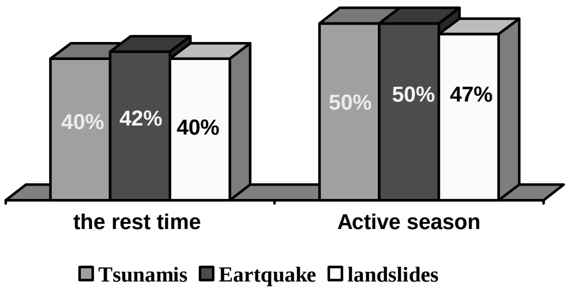

Figure 10. Risk profile – Region 3.

But there is a “sanitary” minimum which could not be eliminated. The assessment show that the methodology works reliable up to about 50% of the total number of indicators. After that the obtained results could be not correct even confusing. The application to the North Bulgarian Black Sea coast shows that the obtained results are reliable and stable for the multirisk assessment and mapping. The “risk profiles” can help the risk management institutions to take fast and reliable solutions to decrease the risk factors.

Acknowledgments

This paper was partially supported by the SCHEMA EU Project

References

Vetere Arellano A.L., Nordvik J.P.& Ranguelov B.K. (2003). In search of a common methodology on damage estimations: from an EU perspective. *Proc. Workshop: "In search of a Common Methodology on Damage Estimation.", Delft, 23-24 May,195 – 206.*

Blaikie P., Cannon T., Davis I. & Wisner B. (1994). At risk. Natural hazards, people's vulnerability and disasters, *Routledge, London,362 p.*

Bethke L., Good J.&Thompson P. (1997). Building Capacities for Risk Reduction, *232 p.*

Cannon T. (2000). Vulnerability Analysis and Disasters. *In Parker Publishing, D. (Ed.) Floods, London: Routledge, 43-55*

ESPON 1.3.1 Hazards Project (2003). The spatial effects and management of natural and technological hazards in general and in relation to climate change, *1st Interim Report, March 2003. 100 p.*

ESPON 1.3.1 Hazards Project (2003). The spatial effects and management of natural and technological hazards in general and in relation to climate change, *2nd Interim Report, August 2003. 168 p. + 1 annex (123 p).*

ESPON 1.3.1 Hazards Project (2004). The spatial effects and management of natural and technological hazards in general and in relation to climate change. *3rth Interim Report, March 2003, 100 p.*

Frantzova A., Ranguelov B. & Mardirossian G. *(2005).* Multirisk analysis for the South Bulgarian Black Sea Coast. *Processing of Scientific Conference "SES'2005", Varna, June, 2005,Book II, 251-256.*

IADB/GTZ (2003). Comprehensive Risk management by Communities and Local Governments. Component III; Indicator and other disaster risk management instrument for communities and local governments. Inter-American Development bank for the Regional Policy Dialogue: *Natural Disaster network – III meeting. Preliminary Draft. Deutsche Gesellschaft für Technische Zusammenarbeit (GTZ) GmbH.. Washington, D.C., 2003, www.iadb.org*

IADB (2005). Indicators of Disaster Risk and Risk Management. Main Technical report. Program for Latin America and Caribbean. *National University of Columbia– Manizales (Columbia), Institute of Environmental Studies. Washington D.C., 2005., 224 p.*

Heitzmann K., Sudharshan R., Canagarajah P. & Siegel B. (2002). Guidelines for Assessing the Sources of Risk and Vulnerability. *Social Protection discussion paper N0218, Social Protection Unit, Human Development Network, The World Bank, available on www.worldbank.org*

Kreimer A., Arnold M. & Carlin A. (2003). Building Safer Cities: The Future of Disaster Risk. Disaster Risk Management Series. *The World Bank, Disaster Management Facility, Washington, D.C. 299 p.*

Reed S. (1997). Introduction to Hazards. *Disaster Management Training Programme*, *3 th.edition, United Nation Development Programme (UNDP), Bureau for Crisis Prevention and Recovery (BCPR). Available on http://www.undmtp.org/*

Smith K (2001).Environmental Hazards. Assessing Risk and Reducing Disaster, *Third edition. Routledge, London,. 392 p.*

UNISDR (2002). Living with risk. A global Review of disaster reduction initiatives, *With special support from the Government of Japan, World Meteorological Organization and Asian Disaster Reduction Centre (Kobe, Japan), Printed by United Nation, Geneva, Switzerland, 148p.*

UNDP/DMTP (1992).An Overview of Disaster Management, *2nd Edition, UNDRO, 133 p.*

Wisner B. (1993).Disaster Vulnerability: Scale, Power and Daily Life, *Geojournal, 30(2):1, 27-40*

Ranguelov B. & Jelinek R. (2007). Methodology and multirisk mapping for the Northeast Bulgarian Black Sea coast., *Proc. Intl. Conf., 'Protection of the natural disasters disturbed regions'., Strbske pleso, 18-22 November, Slovakia. 23-33.*

The archeoseismology in Bulgaria – Present and Expectations

Ranguelov B K (1)

(1) Geophysical Institute – BAS, Acad. G. Boncev str., bl.3, Sofia 1113, Bulgaria, branguelov@gmail.com

Keywords: Archeoseismology, Bulgaria, examples

Introduction

Introduction of the new methods of investigations and interpretation leads to new, more effective and sophisticated approaches used by the interdisciplinary compound of methodologies and by different disciplines. The new one and fast developing during the last years is the symbiosis between seismology and the archaeology. The new born discipline is archeoseismology and its first steps and developments in Bulgaria are discussed.

The archeology with its methods and ways of data and information collection is a discipline which increase the knowledge about the objects covered by the soil layers and preserved the archeological objects. Frequently the preserved artifacts keep information about the destructive hazardous events – like volcanic eruptions, meteoritic impacts, earthquakes, landslides, tsunamis, floods, epidemics, etc., occurred to the inhabitants of the ancient world (cities, villages, singe or multiple temples and castles, etc.). The important methodological issue is to separate and reliable explain the observations, keeping their original and not disturbed facieses. Frequently it leads to the contradictions – sometimes to display the preserved artifacts in their original environment, needs to remove other (very frequently) important parts, preserved the influences of the negative factors. Some of them are responsible to the most powerful forces responsible for the inhabited and prosperous society death. The Pompeii city is one of the most famous examples of the disappearance of an ancient town due to the disaster (volcanic eruption - Vesuvius) occurred during 73 AD.

The seismology is a discipline, with its recent accurate methods of measurements. It is a combination of the descriptive methods and approaches (the historical seismology) combined with the new and sensitive equipment registrations (the recent seismology). Due to many circumstances the history of seismology shows a development from descriptive to the measurements phase. From another side the old and not so reliable and accurate data make important evidence - the possibility to collect and interpret from recent scientific point of view, the descriptions of the natural phenomena – earthquakes into measurable units and recent scientific language. It is well known by the history of the seismology that the longest world catalogue – the Chinese one – consists of the period of about 3000 years. Only about 100 of them are covered by the instrumental measurements. The rest part is based on the descriptions, chronics and other historical documentation due to which the seismologists can extract the essential and important information about past earthquakes and other natural disasters. During the last years so called paleoseismology has been developed based mainly on the geological evidences writhen by the recent and ancient geological events and phenomena and their influence to the surface geological layers and other geology studied objects – active faults and cracks, seismic dislocations and other phenomena all of them recorded and preserved the seismic influence on the investigated objects. On the third side – the historical documents prepared during the written history of the mankind provide also many descriptions and other evidences in writhen form (texts, pictures, chronics, etc.) giving information of primary importance to the seismologists about huge cataclysms (very often earthquakes). There is a time interval, between the writhen histories (when the information about the strong regional or local earthquakes could be extracted only from the written

documents) and the mankind history before letters were invented. These are certain time periods when great historical events occurred (like the “Great movement of the peoples”) and during which a lot of information have been lost (due to the destructions, invasions religious and “human”-like behavior, when a lot of written texts have been lost.
Due to these important events another alternative way of data and information retrieval is invented and these are the archeological excavations. They can provide the missing information. The time interval when these data could be extracted is located at a very important period – between the paleoseismology studies and the written documentation. This time interval is not always complete about the seismic events. The traces left to the different archeological objects could be retrieved by the methods of archeoseismology.

Methodology notes

What could be the main methodological aspects of the archeoseismology development in Bulgaria? Up to now, not so much attempts have been applied to discover the links between the seismology and the archeology in the country (Christoskov L. et al (1995).
According our view and the world archeology practices several directions of future investigations could be outlined (there are enough seismological and archeological data and information to use them together effectively about):

- seismic events data and information about the known ancient and historical evidences, which happened on the territory of Bulgaria
- outside sources which could affect some archeological sites during the ancient times
- main archeological sites, which had been possibly affected by the local or regional seismic events
- overlap of the known seismic zones with the main archeological sites for searching possible seismic effects on them. The effects could be produced as result of the seimogenesis (like faults scarps, etc.) and/or by the macrosiesmic influence and or secondary generated natural events
- possible interpretation of the observed phenomena and their relations with earthquakes or similar geodynamic phenomena
- search of a complex effects proving this or that natural disaster affected some archeological sites, because frequently the seismic events triggered secondary effects like landslides, tsunamis, boiled and liquefied soils, etc.

The archeological sites on the territory of Bulgaria, have been selected on the base of geography localization and time of existence and development. Several time intervals have been investigated – most ancient one – up to the VI-V century BC, Thracian itself – V-IV BC, Hellenistic Thracian VI-II BC - Roman Thracian – I-IVAD. The comparison with the seismic activity known now, shows the possible influence on the ancient sites – Figure 1.
Up to the VI-V BC there are not so much evidences, which could support the investigations about seismic effects on the archeological sites. Then V-IV century time period could be exploited about search of seismic effects on the Thracian tombs, temples and other ancient buildings. For example prospective objects located near on Expected Seismic Source Zones (ESSZ) with the respective Mmax given are: Pistiros-M7.5-8.0; Philipopolis-M7-7.5; Alexandrovo - M6.5-7.0 (PSZ); Kabile (JMB) – M5.6-6.0, Sevtopolis, Shipka, Kazanluk – M6.5-7.0, Starosel, Sveshtari – M5.0-6.0. The most prospective looks the interval of the Hellenistic epoch – VI-II BC with possible effects to be investigated at: Babiak, Belovo, Dobrashtica (KKZ), Pistiros (PSZ), Bisone, Durankulak (SKZ) – M7.5-8.0, Philipopolis, Halka Bunar, Malko Trunovo, Iabalkovo, Brezovo (PSZ) –M6.5-7.0, Alexandrovo, Cepina, Dragoina (PSZ) -M6.5-7.0, Sevtopolis, Shipka, Kazanluk, Krun (GOZ) 6.5-7.0 , Resilovo, Dolna Koznica – M6.5-7.0, Starosel, Sveshtari, Rozovets – M5.0-6.0. The next is the time interval I-IVAD for which the sites which may give some additional information are: Nikopolis ad Istrum (GOZ), M6-7, Phylipopolis M7-7,5(PZS), Pautalia (Kustendil Zone), Serdika (SZ), M6.5-7. From the historical data and information there are only few examples of strong earthquakes during this time period – (VIth BC-IVth AD). The most famous one is the seismic event from Ist (III?) century BC described by Strabo as a major catastrophe due to which the ancient Greek colony Bisone “sank in the sea waters” and have been moved from the sea shore to the upper hills around (see below).

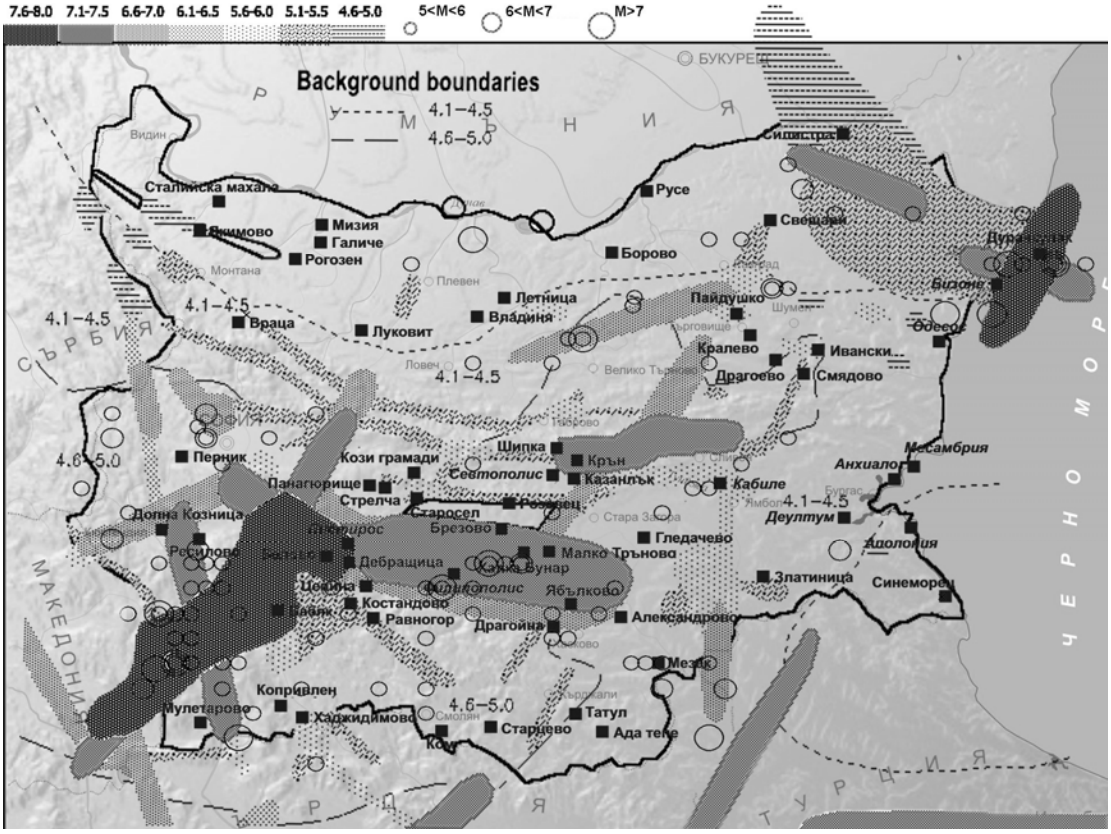

Figure 1. Locations of the seismic source zones (expected Mmax: 4 - 8) and the main archeological objects of the country.

It is important to mention that most major archeological sites (more than 50 %) are located outside the well known seismic sources of the Bulgarian territory. So, there only macroseismic influence and some secondary effects could be expected. Nevertheless the rest part could be a useful source of knowledge about the possible primary and/or secondary seismic effects on the ancient structures and artifacts. Such approach is dominated by the idea that many and not discovered up to know old prints to the different archeological objects could be dialed with the increased attention as important source of information about ancient disasters (not only earthquakes and tsunamis)-Ranguelov B. & Bojkova A (2008)

Data and Examples

The Seismological Data

The seismicity data and information is extracted mainly from the Historical Catalogue of earthquakes. More than 150 seismic events with magnitude greater than 5 have been documented on the territory of Bulgaria. The time distribution of these events are presented on figure 2 .The figure 3 – presents the seismic events with magnitude greater than 5 occurred during the XX century – their number is more than 60.

This information means at least 2 important facts :

- the seismicity in Bulgaria appears non randomly in space, but following the main seismogenic zones – Figure 2.
- the seismicity in Bulgaria appears like episodes with different duration – Figure 3 and Figure 4.
- there are several intervals (mainly at the beginning of the Ist millennium (from Christ birthday to the end of 999) when a lot of seismic events are missing. Two explanations are possible: no stronger earthquakes occur (less probable) and no earthquakes documented (i.e. they occurred, but have not been documented in some way). The second hypothesis looks more probable.

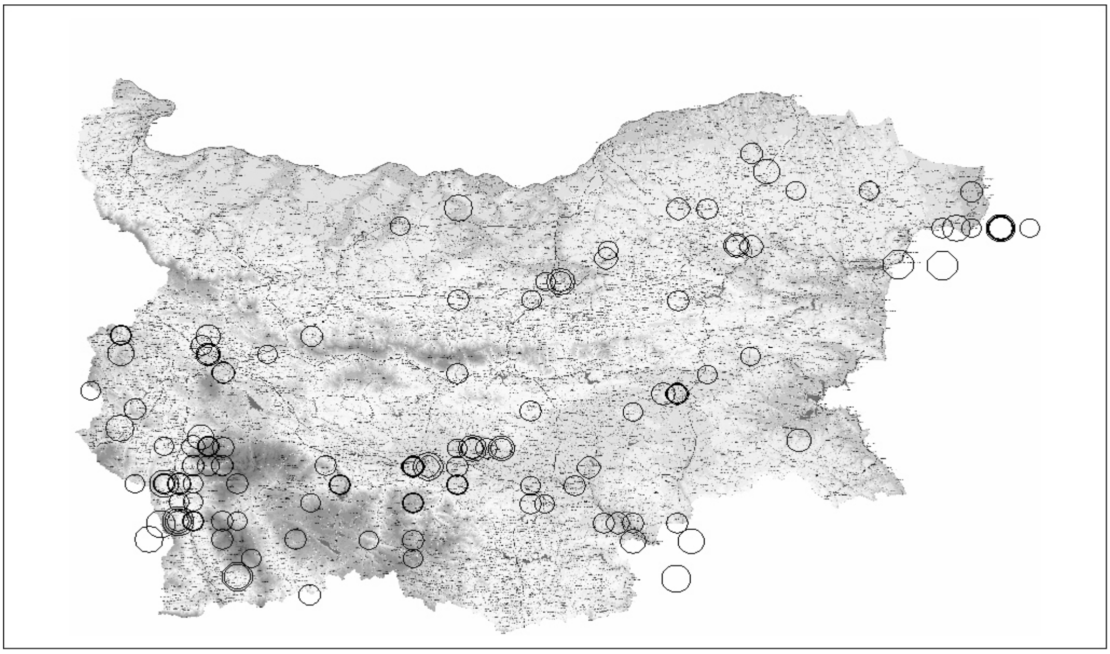

Figure 2. All known earthquake epicenters in Bulgaria and near surroundings with magnitude M>5.0

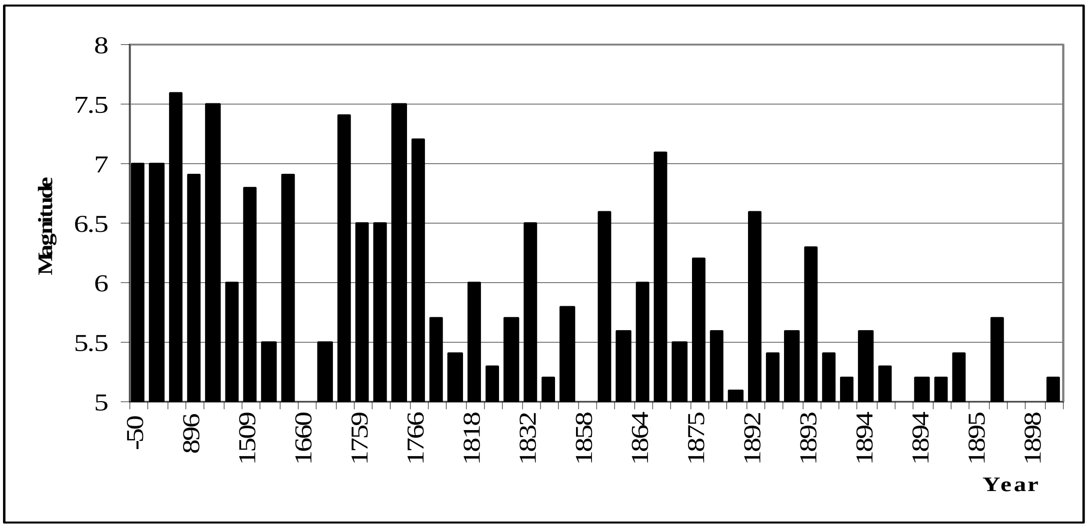

Figure 3. Magnitude-time plot of the earthquakes of Bulgaria with M>5.0 up to XX century

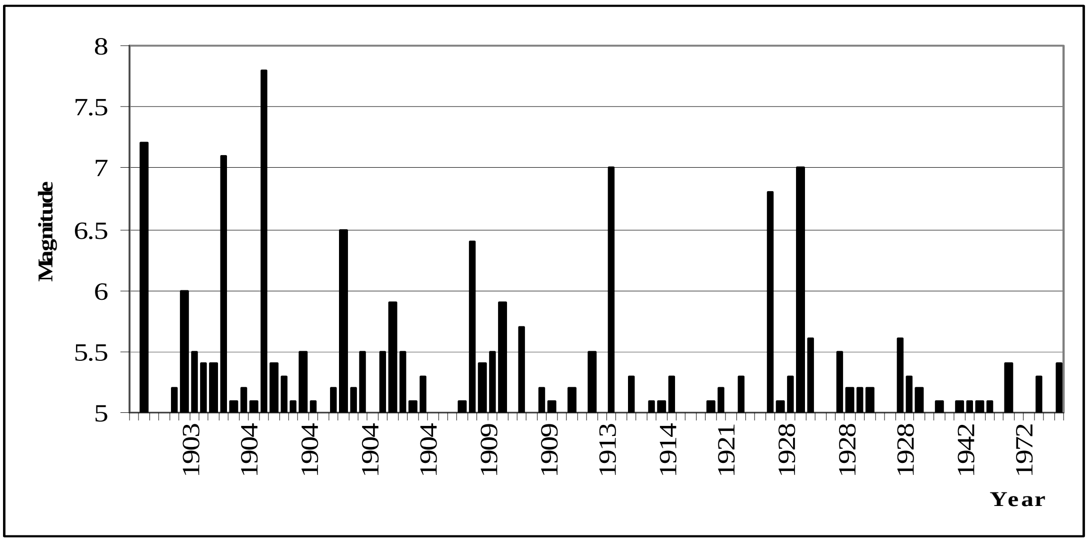

Figure 4. Magnitude-time plot of the earthquakes of Bulgaria with M>5.0 during the XX c.

If such a hypothesis looks more probable, it could be exploited about the search of more seismic events by the archeoseismology methods. Most of the well known and mapped archeological objects cover just this time interval. In this way they could provide clear and more reliable information about the past seismic events. Something more – despite the earthquakes occurred in the different seismogenic zones, most of the archeological findings are located near or on such zones.

Some Examples

Not systematic research in Bulgaria has been applied to the different archeological objects to discover the respective earthquake evidences proved that this or that archeological object had been affected by the seismic influence of any kind. The combination of the methods of archeology relatively reliable dating different objects and the seismology (when to stick an archeological object to the ancient seismic (or other natural disaster), which frequently have some descriptions, but no other evidences about an earthquake, could give much more information about the correct assessment – what happen – and to translate this in the recent scientific measurable units – intensity, magnitude, size of the affected area, etc.
Just few – up to now – cases of the combined approach using archeological data and seismological evidences have been investigated. The most impressive of them are:

Starosel Thracian temple
Excavated in 2000, there are several clear evidences supporting the idea that the temple had been affected by earthquake (or several seismic events):

- The cracked and moved horizontally thick about 10 cm marble plate at the roof of the entrance
- The temple is located near the Plovdiv seismic zone, and all model calculations show that such effects could be produces by a strong enough earthquake.
- The sheet like cracks and destructed parts of the heavy stones building the entrance walls of the temple.

The plaleoseismological excavations established high amplitude vertical movements printed on the seismic dislocations due to the 1928 and some earlier historical events buried under the surface soil layers just a few kilometers to the south.

Cybele temple in Balchik
Starting diggings in April 2007 (and continuing even now) the Cybele temple presents an extreme example of the relatively well documented complex disaster event influence consisting probably(?) by effects of earthquake(s), tsunami and landslides influencing simultaneously (and/or consecutively), destructing and preserving the remains of the temple. The 543 earthquake (the most probable reason of the temple's destruction), was mentioned

by E.Guidoboni in the book – "The Mediterranean earthquakes" - as a possible generator of a local tsunami. The diggings process discovered a low (down to the floor of the temple) small layer of burned material mixed with the sand and sea shell mollusks. In this layer as well as up, a lot of marble artifacts have been indicated. They are mixed and broken, together with the stable preserved parts of the marble chairs, fixed on the floor. A broken marble plate with written names of the sponsors of the ancient temple was discovered. After the reconstruction all parts of this plate have been puzzled, which shows that the plate was broken on the floor and no parts extracted afterwards. This means that the broken process occurred due to the falling down of the plate parts during the earthquake. Then the parts have been mixed most probably due to the sliding inside masses. The preservation of the walls to the certain height means that these walls have been buries by the surrounding masses.
The total reconstruction of the processes printed in the ruins could be the follow – Figure 5:
Burned roof followed by the collapse (due to, or not the earthquake (or separately of it); earthquake, which destroyed the bigger part of the temple (cracks and slightly moved visible elements on the walls and the floor) and the inside located marble elements – plates, statues, etc. – some of them broken due to the fall down process; tsunami which brought sand and mollusks shells; landslides (at once or several times) which filled the space into the destructed temple, mixed some artifacts and buried the remains of the temple. This can explain the observed fact, why the rest of the walls are untouched up to a certain level.
This very clear interpretation shows how much information could be retrieved by ruins in case of well preserved archeological sites.
The ancient chronics by Strabo outlined that strong earthquake accompanied by huge soil masses slides and possible generated tsunami flooded the ancient Greece colony Bisone in Ist (III?) century BC. This leads to the movement of the port-city, located near shore to the up hills position and a new development of the town. Probably the same occurred with Dionisopolis (Balchik) after the destructive 543 seismic event. This heavy disasters influence sometimes leaded to the movements of relatively large colonies (town and villages with their inhabitants), had heavy and huge consequences to the ancient people, changing their stile of everyday life and work.

Discussion

Following the observations, the known and newly discovered sites many new and not discovered findings could be expected in the future.
The prospective areas of increased interest to the archeoseismological research could be:

- Region of Plovdiv (Plovdiv sesimogenic zone - PSZ)
- Region of Varna (related to the Shabla-Kaliakra zone - SKZ)
- Region of SW Bulgaria (due to the influences of the Kresna -Kroupnik zone - KKZ)
- Area of the Central North Bulgaria (to the Gorna Oriahovitza zone - GOZ)
- Area of Sofia and surroundings (SZ)

From the seismic sources located outside the territorial boundaries of Bulgaria:

- Vrancea zone (with possible effects to the North and North east Bulgaria)
- Marmara Sea and Odrin (Edirne) zones (with possible influence to the south and South East Bulgaria)
- Morava zone (to the West peripheries)

It must be mention that these are mainly the regional zones. The local influences can be expected everywhere when earthquake greater than M>5 have occurred and could create visible consequences. For example one prospective site appears to be Nikopolis ad Mestum area – near the Mesta seismic zone. The recent observed facts on some local archeological sites show that an influence can be expected even from small shocks (for example the Kurdzali earthquake with M4.3 and its influence on Perperikon archeological site (fallen big stones).
Similar effects (some more clear, some – not so) have been discovered near the boundaries of Bulgaria. For example, near Adrianopoulis the excavations of an ancient tomb discovered buried walls which show clear evidences of fault movements printed on the moved walls of the ancient tomb - Pavlides S. et al., (2008). Several examples exist of the destruction of the ancient structures on Crete, Jordan, Greece, Syria, Algeria, etc. Some more evidenced could be extracted by detailed studies of the ancient sites like Sveshtary tomb, the Perperikon site, the Antonovo site as well as others like St.George and St. Sofia churches in Sofia, etc. May

be more focused investigations in the areas with well known seismic activity such as PSZ, GOZ, SZ, SKZ and KKZ can improve our knowledge about the seismic effects on the ancient people inhabited areas. From another side – new discovered archeological sites, can help the seismologist to clarify many parameters (even to discover new events) of the ancient earthquakes – local or regional.

Conclusions

The comparison between the active seismogenic zones and the main archeological sites in Bulgaria is performed, showing a lot of coincidences of the locations. This could be used for the focused search of archeoseismiligical evidences for the past earthquakes and possible estimations about their parameters in recent scientific terms. Several remarkable examples of new discovered sites, influenced by ancient earthquakes are explained, supported by the recent interpretations. The symbiosis between seismology and archeology could be perspective and prospective tool for better knowledge and improved cultural environment of Bulgaria.
The main aim of this work is to focus the attention of the specialists – seismologists and archeologists to keep attention during their working process and to expect to find more and useful information supporting the professional activity of both sides.

Acknowledgements: This paper was partially supported by the EU SCHEMA Project.

References

Christoskov L. et al (1995). Traces of seismic effects on archaeological sites in Bulgaria. *Anali di Geofisica, 38, No 5-6, 907-918.*

Gergova D. Iliev I. Rizzo V. (1995). Evidence of seismic event on Thracian tombs dated to the Hellenistic period (Sveshtari, Northeastern Bulgaria), *Anali di Geofisica, 38, No 5-6*, 919-925.

Pavlides S. et al., (2008). Post-Roman seismic activity in Mikri Doxipara – Zoni archaeological excavation (NE Greece), *Abstracts AGU*, Viena.

Ranguelov B. & Bojkova A (2008). The Archeoseismology in Bulgaria. *Proc. Intl. Symp. Geoarcheology*, Sofia, 28-29 Oct. (submitted)

Comprehensive Seismic Site Effect Analysis: Results from the URban Seismology and Drilling Projects in Bucharest, Romania

Ritter, J R R (1), Bala, A (2), Balan, S F (2), Hannich D (1), Huber G (1)

(1) Universität Karlsruhe (TH), Germany, joachim.ritter@gpi.uni-karlsruhe.de
(2) National Institute for Earth Physics, Bucharest, Romania, bala@infp.ro

Keywords: site effects, seismic amplitudes, seismic hazard

Introduction

Bucharest, the capital of Romania, is at a very high seismic risk (Dilley *et al*., 2005). In the nearby Vrancea zone (Figure 1), at the bend of the Carpathian Mountains, the Tisia Dacia block overthrusted the Moesian plate which was delaminated and pushed into the mantle. This steeply hanging lithospheric slab generates up to 3-4 earthquakes per century with moment magnitudes (Mw) exceeding 7 (Radu, 1974, Oncescu *et al*., 1999). The seismic moment release rate in this small volume is comparable to southern California (Wenzel *et al.* 2002). The foreland of the Carpathian Mountains is made up of deep sedimentary troughs, including thick layers of only partly consolidated sediments. During earthquakes this special situation causes large seismic amplitudes in Bucharest, which is about 120-150 km SW from Vrancea, and other major towns in the region (for a summary see Wenzel *et al.,* 1999a,b). During the March 1977 event (Mw=7.4) more than 1500 people were killed, mostly in Bucharest, and extensive damage occurred.

The damage pattern across the city area of Bucharest is quite variable as a result of variable subsurface conditions (Mandrescu et al., 2004, 2007; Bala *et al.,* 2006). Peak ground acceleration varies by a factor of up to 4 (Wirth *et al*., 2003), and there is possibly a time varying component due to changes in the depth to the water table (Hötzl *et al.,* 2004). Such very localised influences on the ground motion are called seismic site effects. The main contributing factors are loose soils and sediments. Thus it is necessary to characterise the geotechnical properties of the involved geological layers, to model the expected spectral acceleration function and to compare it with measured seismic waveforms. Such an approach is an important contribution to seismic hazard assessment and direct benefit for the public, provided civil engineers use this information. In the case of Bucharest, numerous studies in site effects were conducted in the past (e.g. Aldea *et al*., 2002, Cioflan *et al*., 2004, Lungu *et al*., 1999, Mandrescu *et al*., 2007, Moldoveanu *et al*., 2004, Sokolov *et al*., 2004). However, most studies lack modern geotechnical parameter estimations combined with *in situ* seismic down-hole measurements (check shot velocity survey), a reasonable spatial coverage across the city and the possibility for a direct comparison with seismic recordings of Vrancea events.

In this contribution we report on two recent experimental studies to quantify the seismic site effects in Bucharest. In 2003/2004 thirty-two broadband stations were deployed in the city and its surroundings. This URban Seismology project (URS) continuously recorded the ground motion (Ritter *et al*., 2005, Balan *et al*., 2007), and the waveforms could be used for a wide range of studies, including structural and site effect analyses. Following in 2006/2007, ten 50 m deep boreholes were drilled at carefully selected sites and used for core recovery including a geotechnical analysis and seismic measurements. The interdisciplinary projects involve seismologists, applied geologists and civil engineers from Romania and Germany. The results from both studies are combined to achieve a comprehensive model of the site effects in Bucharest including an updated microzonation map.

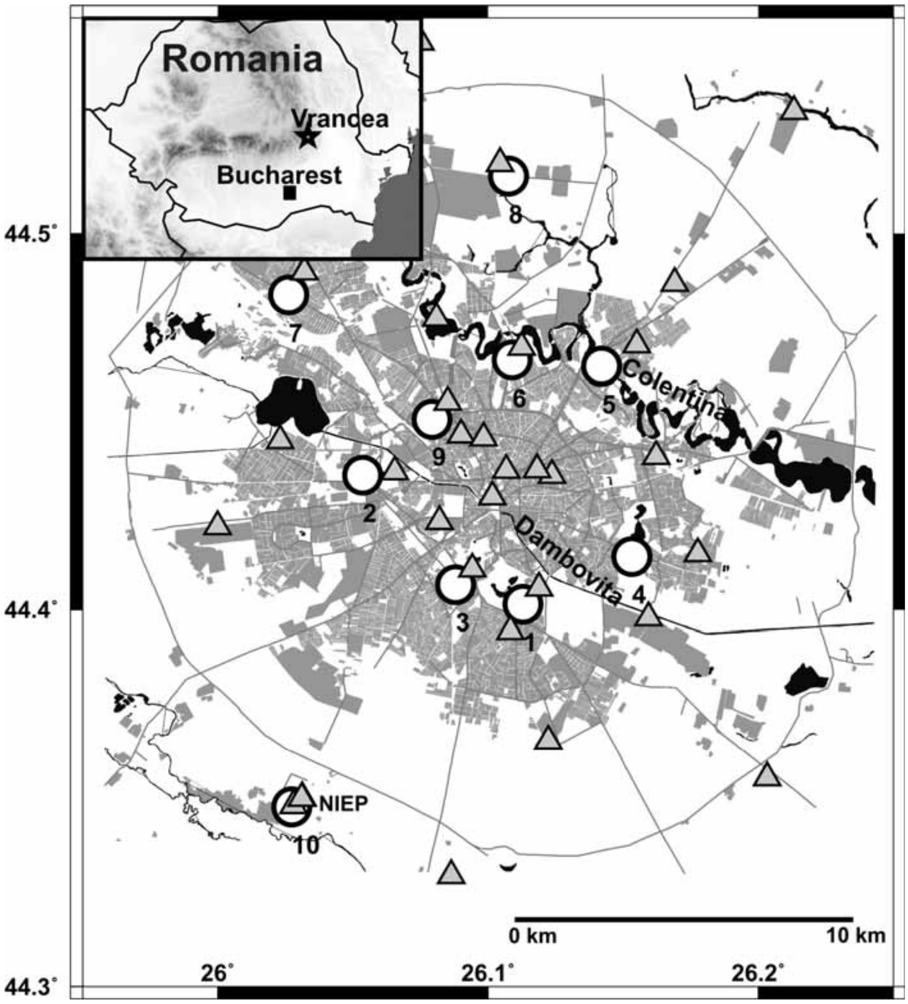

Figure 1. Map with area under investigation and measurement sites of the URS anddrilling projects. The metropolitan region of Bucharest, Romania is mainly inside the characteristic ring road with a diameter of about 20 km. Residential and industrial areas are indicated in grey; lakes, rivers and channels in indicated in black. Sites with broadband instruments during the URS experiment (Ritter *et al.*, 2005) are shown as triangles. The ten sites, where drilling, core recovery and seismic measurements were done, are indicated as circles and numbers. The inset shows the geographical context with the Vrancea earthquake zone at the bend of the Carpathian Mountains.

Background Geology

As site effects are dominated by the mechanical properties of the local near-surface soil and rock material, it is necessary to assess and to understand the geological conditions. Bucharest is built on the foreland basin of the Carpathian mountains. The roughly known crustal structure consists from top to bottom of loose loess-like and recent fluvial sediments (~0-50 m), Quaternary and Tertiary sediments (~600 m in the south and ~2000 m in the north), more competent Mesozoic and Palaeozoic sediments, the crystalline crust (starting at 6-8 km depth) and the Moho (~38 km depth). The sedimentary and crustal thicknesses increase from south to north, for further details see Mândrescu *et al*. (2004) and Martin & Ritter (2005).

The near-surface geology below Bucharest, which is relevant for seismic site effects, is characterised by a laterally quite variably layering of Quaternary deposits (Table 1). These partly unconsolidated and partly consolidated sediments were deposited mainly under fluvial and lacustrine conditions, at the top there is also man-made debris (backfill) and loess. The

fluvial deposits are due to the Dambovita and Colentina rivers with cross the city (Figure 1). Most layers are thicker in the north of the city compared to the south. This dipping layering of the Quaternary sediments is responsible in frequency sensitive seismic amplification pattern (Cioflan *et al*., 2004). The reason is positive amplitude interference with layer thickness equal to a fourth of the wavelength (λ/4).
The complete Cenozoic sediments also vary considerably with about 700 m thickness in the south and nearly 2000 m north of the city (Figure 2; Mandrescu *et al*., 2004). This variable thickness causes amplification pattern in the low-frequency seismic wavefield (see below).

Table 1. Quaternary layers below Bucharest that are relevant for seismic site assessment. The data are taken from Mandrescu et al. (2004, 2007) and Ciugudean-Toma & Stefanescu (2006). Layers 1-5 were found in the new boreholes (see text).

no.	name / description	approximate thickness / m	lithology
1	backfill, soil	< 15	backfill, soil, clayey sediments
2	Upper Sandy-Clayey Complex	< 16	loess, loam
3	Colentia Gravel	< 20	gravel, sand
4	Intermediate Clay Complex	< 23	clays
5	Mostistea Sand Complex	10-15	sand
6	Lacrustine Complex	10-60	clays, silty clays
7	Fratesti Sands Complex	100-180	sand, gravel

URban Seismology Experiment – Main Results

During the URS project (Ritter *et al*., 2005) 32 seismological broadband stations were deployed in Bucharest city and its surroundings (Figure 1). The network consisted of 32 Earthdata 24-bit data loggers with 3 and 6 input channels, GPS time synchronisation and removable 6.4 GByte harddisks. As sensors we used 22 Streckeisen STS-2 seismometers (120 s free period), 5 Geotech KS2000 (100 s), 3 Güralp 40T and ESP (30 s) and 2 Lennartz LE-3D (5 s). The stations covered 34 different sites. Installation started at the end of October 2003, and station dismounting was done at the beginning of August 2004. The recording was performed in continuous mode with a sampling rate of 100 Hz. Additionally we can make use of the data from the permanent K2 strong-motion network of 40 stations which is run by the Universität Karlsruhe (TH) and the National Institute for Earth Physics (NIEP) at Bucharest-Măgurele.
The URS dataset is used to improve models of the elastic structure underneath the city. Using teleseismic P-wave receiver functions (RF) at periods of 0.5-12 s, Diehl & Ritter (2008) find major interfaces from the converted P-to-S phases. Synthetic waveform modelling combined with a Monte Carlo approach for the starting models results in the following main shear wave velocity (*vs*) discontinuities in the crust: At ~3 km depth there is a *vs* jump from ~1.4 km/s to ~3 km/s (possibly low unconsolidated - consolidated sediment interface), at ~9 km depth *vs* jumps to ~3.9 km/s (sediment-basement) and at 37-40 km depth (Moho) *vs* reaches ~4.5 km/s in the uppermost mantle. The sedimentary layer dips from south to north. These results are confirmed by high-resolution P-wave RF from Vrancea earthquake waveforms at shorter periods of 0.2-2.0 s. The Vrancea RF reveal much more structural elements, e.g. another interface is found (Figure 2) that dips from ~0.7 km depth in the south of the URS network to ~1.6 km depth in the north (Neogene-Cretaceous boundary).
Sèbe et al. (2008) studied Love waves from eight East European earthquakes. Using a frequency-wavenumber analysis, they find that the Love wave dispersion varies distinctly from north to south. At the base of the Tertiary higher phase velocities are found in the north compared to the south (Figure 2).
Site effect and seismic amplitude amplification pattern are also studied with the URS dataset. At low frequencies (0.14-0.43 Hz) larger amplitudes are found in the NW of the network compared to the SE (Sudhaus & Ritter, 2008). This trend reverses at 0.71 Hz and 0.86 Hz with larger amplitudes in the SE. The amplification pattern can be explained with a λ/4 resonance in the dipping Tertiary sediments (Figure 2).

The variation of ground motion was also studied with the ratio between signal power of horizontal components and vertical components (*H/V* ratio). Ziehm (2006) determined two peaks in the *H/V* ratio observed at all stations. One maximum in *H/V* ratio is observed at ~0.7 Hz across the whole URS network and has a complex shape with partly two peaks. The other maximum appears at lower frequencies between 0.09 Hz and 0.26 Hz and varies with latitude from high frequencies in the south to low frequencies in the north. Again the dependency of the lower frequency peak on latitude is attributed to the dipping of the Neogene-Cretaceous boundary from 800 m in the south to 2000 m in the north (Balan *et al*., 2007).
Bartlakowski *et al*. (2006) used the URS recordings to improve the rapid shakemap compilation after future earthquakes. By calculating calibration functions for ground motion at the sites of the URS and K2 stations, they show that more detailed shakemaps can be constructed if only few actual recordings are available.

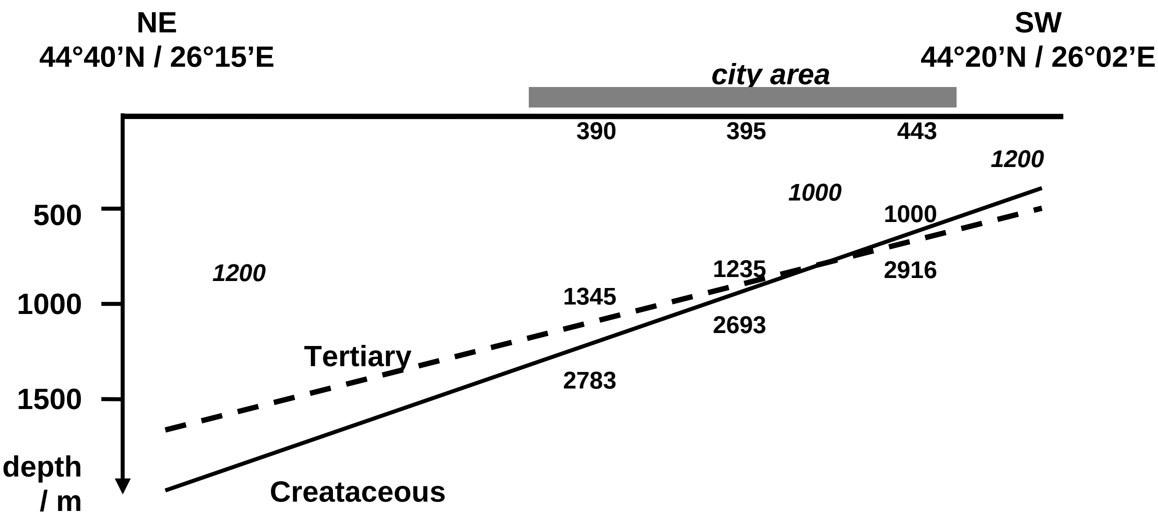

Figure 2. Sketch summarising the structural findings of the URS project along a NE-SW profile. The solid line indicates the Tertiary-Cretaceous boundary after Mandrescu et al. (2004), the dashed line corresponds to a seismic discontinuity found with receiver function modelling (Diehl & Ritter, 2008). The numbers are shear wave velocities in m/s after Sèbe *et al*. (2008) using surface waves; the values from the receiver function study are given in italics. The near-surface values are presumably average values for the complete Quaternary layer (see also Bala *et al*., this volume).

Drilling Project – Overview and First Results

To better understand the shallow site effects across the city of Bucharest, drilling combined with geotechnical studies at core material and geophysical investigations are required. Such combined studies were done at very few places across the city, and these studies were not done in the same way for each site. Also the spatial distribution of the previous studies left uncovered areas across the city. Results from previous drilling or geophysical borehole programmes can be found in Bala *et al*. (2005, 2006, 2007) or Ciugudean-Toma & Stefanescu (2006). In order to fill these gaps we conducted a new programme that was financed by a NATO Science for Peace project (SfP 981882). Ten 50 m deep boreholes were drilled across the city in 2006 and 2007 (Figure 1 and Table 2). At each site sampling of the cores was done and seismic down-hole measurements (check shot velocity survey) were performed to obtain *in situ* seismic *vp* and *vs* values at high resolution. Together with the results from geotechnical measurements at the core samples (see Balan *et al*., this volume), these values will be used for linear (see Bala et *al*., this volume) and non-linear (Grandas *et al*., 2007) modelling of spectral amplitudes.

Table 2. Locations of the ten new boreholes for geotechnical and geophysical studies which are drilled in Bucharest in 2006 and 2007; see also Figure 1.

No	Location	Latitude	Longitude	Date
1	Tineretului Park	44^0 24’ 05.4”	26^0 06’ 46.3”	May 2006
2	Ecologic University	44^0 26’ 09.0”	26^0 03’ 13.4”	May 2006
3	Astronomic Institute	44^0 24’ 24.2”	26^0 05’ 17.0”	May 2006
4	Titan 2 Park	44^0 24’ 51.2”	26^0 09’ 11.8”	June 2006
5	Motodrom Park	44^0 27’ 52.8”	26^0 08’ 31.1”	May 2007
6	Tei Park	44^0 27’ 59.1”	26^0 06’ 32.1”	May 2007
7	Bazilescu Park	44^0 29’ 01.0”	26^0 01’ 34.4”	May 2007
8	Rom. Sport Shooting Fed.	44^0 30’ 54.7”	26^0 06’ 27.2”	June 2007
9	Geological Museum	44^0 27’ 02.6”	26^0 04’ 45.6”	Sept. 2007
10	NIEP, Magurele	44^0 20’ 51.5”	26^0 01’ 38.5”	Oct. 2007

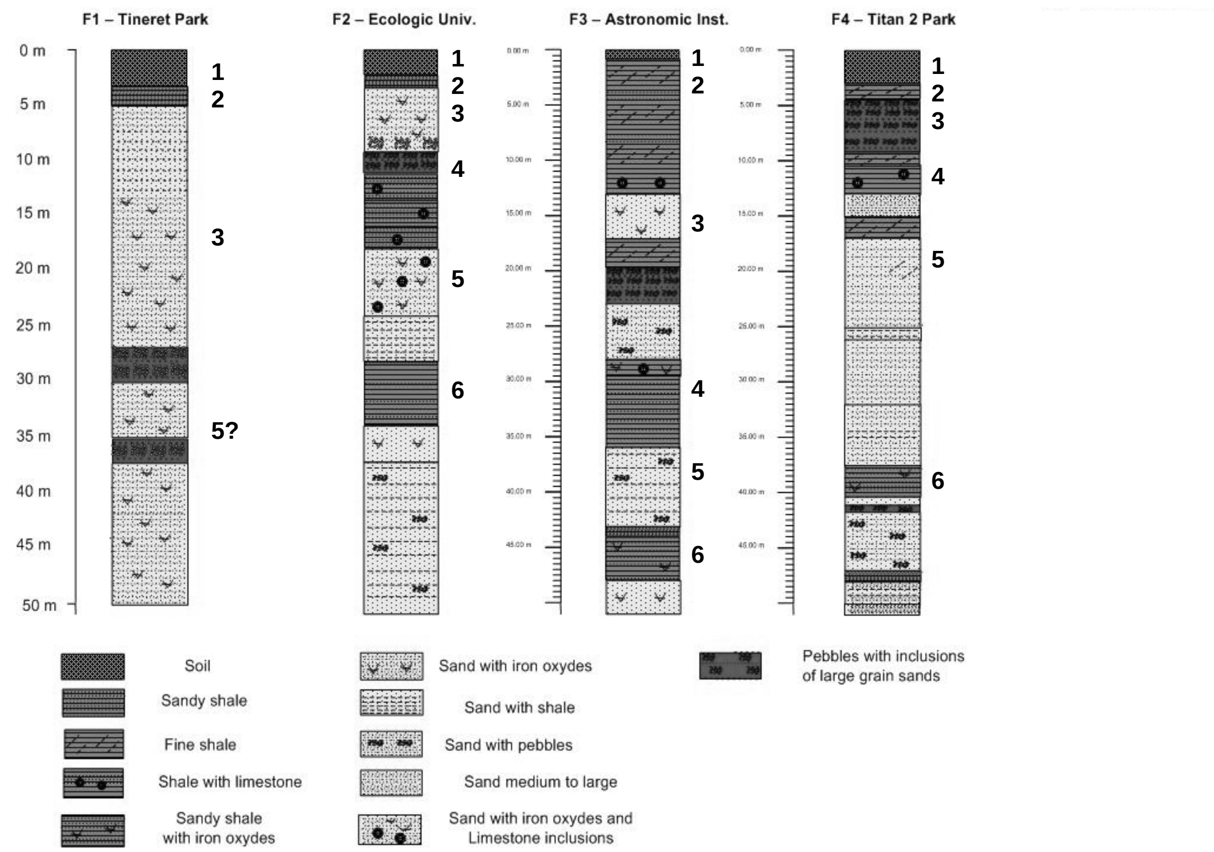

Figure 3. Geological profiles from 4 selected boreholes (for location see Figure 1 and Table 2). The profiles indicate that the lithology varies significantly across the city of Bucharest and that poorly consolidated soils / rocks prevail. The numbers refer to the main Quaternary layers in the city area (see Table 1).

In Figure 3 the geological profiles of four boreholes are shown. They demonstrate that the soils and rocks below the city are poorly consolidated, because the sedimentary material is composed of backfill, pebbles, sands and shales in the upper 50 m depth. The variation of layer thicknesses shows the complex layering across the city that results in varying amplitude amplification effects. Representative core samples were collected for each layer at the different sites for geotechnical tests (resonant colunm, compression settling, plastic limit etc.) (see Balan *et al*., this volume). The seismic down-hole measurements provided *vp* and *vs* for each layer as well as average *vs* values for the upper 30 m and 50 m depth. These vs_{30m} and vs_{50m} values are very low across the city area mainly between 300 m/s and 360 m/s (Bala *et al*., this volume). Together with the varying depth to the ground water table this situation can cause large seismic amplitudes and even liquifaction (Hannich *et al.*, 2006) during strong Vrancea earthquakes.

Acknowledgements

The URS project was financed by the Deutsche Forschungsgemeinschaft, the National Institute for Earth Physics (Bucharest-Magurele), the Universität Karlsruhe (TH) and the State of Baden-Württemberg. The drilling project and core analysis was financed by NATO through SfP project 981882. Cristian Arion, Klaus-Peter Bonjer, Tobias Diehl, Dominik Ehret, Thomas Forbriger, Carlos Grandasa, Joachim Rohn and Henriette Sudhaus provided important assistance for the URS and drilling projects.

References

Aldea A., Lungu D. & Arion C. (2004). GIS mapping of seismic microzonation and site effects in Bucharest based on existing seismic and geophysical evidence, in: *Lungu D, Wenzel F, Mouroux P, Tojo I (eds) Earthquake Loss Estimation and Risk Reduction 1, Independent Film, Bucharest, 1, 237-249.*

Bala A., Raileanu V., Mandrescu N., Zihan I. & Dananau E. (2005). Physical properties of the Quaternary sedimentary rocks in the eastern Bucharest area, *Rom. Rep. in Phys. 57, 151-163.*

Bala A., Raileanu V., Zihan I., Ciugudean V. & Grecu B. (2006). Physical and dynamic properties of the shallow sedimentary rocks in the Bucharest Metropolitan Area, *Romanian Reports in Physics, 58, 2, 221-250.*

Bala A., Zihan I., Ciugudean V., Raileanu V. & Grecu B. (2007). Physical and dynamic properties of the Quaternary sedimentary layers in and around Bucharest City, *Proceedings of the International symposium on Seismic Risk Reduction, ISSRR-2007*, *paper 7, 359-366, Bucharest.*

Bala, A., Balan, S.F., Ritter, J.R.R, Hannich, D. & Rohn, J. (2008). Seismic site effect modelling based on in situ borehole measurements in Bucharest, Romania, *this volume*.

Balan, S.F., Bartlakowski, J., Diehl, T., Forbriger, T., Groos, J., Jaskolla, B., Rehor, L., Ritter, J.R.R., Sebe, O., Sudhaus, H., Wenzel F. & Ziehm, J. (2007). Results from the URban Seismology (URS) project in Bucharest, Romania, in: *International Symposium on Strong Vrancea Earthquakes and Risk Mitigation, Proceedings, Matrix Rom, Bucharest, 277-283.*

Balan, S.F., Ritter, J.R.R., Bala, A. & Huber, G. (2008). Geotechnical investigations at core samples from the Bucharest metropolitan area, *this volume*.

Bartlakowski J., Wenzel F., Radulian M., Ritter J.R.R. & Wirth, W. (2006). Urban shakemap methodology for Bucharest, *Geophys. Res. Lett. 33:L14310, doi:10.1029/2006GL026283.*

Cioflan, C.O., Apostol B.F., Moldoveanu C.L., Panza G.F. & Marmureanu Gh. (2004). Deterministic approach for the seismic microzonation of Bucharest, *Pure appl. Geophys. 161, 1149-1164, DOI 10.1007/s00024-003-2496-8.*

Ciugudean-Toma, V., Stefanescu, I.(2006), Engineering geology of the Bucharest city area, Romania, *paper no. 235, IAEG -2006 Proceedings, Engineering Geology for Tomorrow's Cities*.

Diehl T. & Ritter J.R.R. (2008). High-resolution receiver functions across the Bucharest metropolitan area, *in prep.*

Dilley, M., Chen, R.S., Deichmann, U., Lerner-Lam, A.L. & Arnold, M. with Agwe, J., Buys, P., Kjekstad, O., Bradfield Lyon, B. & Gregory Yerman, G. (2005). Natural disaster hotspots: A global risk analysis, *synthesis report*.

Grandas, C., Huber, G., Hannich, D., Ehret, D., Hötzl, H. & Ritter, J.R.R. (2007). Field investigations and site response analysis for Bucharest, *International Symposium on Strong Vrancea Earthquakes and Risk Mitigation, Bucharest, Proceedings, 253-258.*

Hannich D., Huber G., Ehret D., Hoetzl H., Balan S., Bala A., Bretotean M., Ciugudean V. (2006). SCPTU Tecniques Used for shallow geologic/hydrogeologic Site Characterization in Bucharest, Romania, *3-rd International Symposium on the Effects of Surface Geology on Seismic Motion, Grenoble, France, 30 Aug. - 1 Sept. 2006, paper 71*.

Hötzl, H., Hannich, D., Bretotean, M., Ciugudean, V., Zamfirescu, F. & Danchiv, A. (2004). Influence of hydrogeology on site effects, in *Lungu, D., Wenzel, F., Mouroux, P. & Tojo, I. (eds.), Earthquake Loss Estimation and Risk Reduction, Independent Film, Bucharest, 261-270.*

Lungu D., Cornea T. & Nedelcu C. (1999). Hazard assessment and site-dependent response for Vrancea earthquakes, in: *Wenzel F, Lungu D, Novak O (eds) Vrancea Earthquakes: Tectonics, Hazard and Risk Mitigation, Kluwer Academic Publishers, Dordrecht, 251-267.*

Mândrescu N. & Radulian M. (1999). Macroseismic field of the Romanian intermediate-depth earthquakes, in: *Wenzel F, Lungu D, Novak O (eds) Vrancea Earthquakes: Tectonics, Hazard and Risk Mitigation, Kluver Academic Publishers, Dordrecht, 163-174.*

Mândrescu N., Radulian M. & Marmureanu Gh. (2004). Site conditions and predominant period on seismic motion in the Bucharest urban area, *Revue Roumaine de Geophysique 48, 37–48.*

Mândrescu N., Radulian M. & Marmureanu Gh. (2007). Geological, geophysical and seismological criteria for local response evaluation in Bucharest urban area, *Soil Dyn. Earthq. Engng. 27, 367-393.*

Martin, M., Ritter, J.R.R. & the CALIXTO working group, (2005). 3D Crustal seismic velocity model of SE Romania: Implications for 3D vs. 1D crustal correction strategies for high-resolution teleseismic tomography, *Geophys. J. Int., 162, 448-460, doi: 10.1111/j.1365-246X.2005.02661.x .*

Moldoveanu C.L., Radulian M., Marmureanu Gh. & Panza G.F. (2004). Microzonation of Bucharest: state-of-the-art, *Pure appl. geophys., 161, 1125-1147, DOI 10.1007/s00024-003-2499-5.*

Oncescu M.C., Marza V.I., Rizescu M. & Popa M. (1999). The Romanian earthquake catalogue between 984-1997, in: *Wenzel F, Lungu D, Novak O (eds) Vrancea Earthquakes: Tectonics, Hazard and Risk Mitigation, Kluver Academic Publishers, Dordrecht, pp 43-47.*

Radu C. (1974). Contribution a l'etude de la seismicite de la Roumanie et comparaison avec la seismicite de sud-est de la France. *PhD Thesis, Universite de Strasbourg, 404p.*

Ritter J.R.R., Balan S.F., Bonjer K.-P., Diehl T., Forbriger T., Marmureanu G., Wenzel F. & Wirth W. (2005). Broadband urban seismology in the Bucharest metropolitan area, Seism. Res. Lett., 76, 574–580.

Sèbe O., Forbriger T. & Ritter J.R.R. (2008). The shear wave velocity underneath Bucharest city,Romania, from the analysis of Love waves, *Geophys. J. Int., submitted.*

Sokolov V., Bonjer K.-.P. & Wenzel F. (2004). Accounting for site effect in probabilistic assessment of seismic hazard for Romania and Bucharest: a case of deep seismicity in Vrancea zone, *Soil Dyn. Earthq. Engng., 24, 929-947*.

Sudhaus H. & Ritter J.R.R. (2008). Broadband frequency-dependent amplification of seismic waves across Bucharest, Romania, *J. Seism., revised.*

Wenzel F., Lungu D. & Novak O. (1999a). Vrancea Earthquakes: Tectonics, Hazard and Risk Mitigation. *Kluwer Akademic Publishers, Dordrecht.*

Wenzel F., Lorenz F.P., Sperner B. & Oncescu M.C. (1999b). Seismotectonics of the Romanian Vrancea area, in: *Wenzel F, Lungu D, Novak O (eds.) Vrancea Earthquakes: Tectonics, Hazard and Risk Mitigation, Kluver Academic Publishers, Dordrecht 15-25.*

Wenzel F., Sperner B., Lorenz F. & Mocanu V. (2002). Geodynamics, tomographic images and seismicity of the Vrancea region (SE-Carpathians, Romania), *EGU S. Mueller Spec. Publ. Ser. 3, 95-104.*

Wirth W., Wenzel F., Sokolov V.Y. & Bonjer K.-P. (2003). A uniform approach to seismic site effect analysis in Bucharest, Romania, *Soil Dyn. Earthq. Engng. 23, 737–758.*

Ziehm J. (2006). Seismisches Monitoring einer Großstadt, Analyse von H/V-Spektralverhältnissen, *Diploma Thesis, Geophysikalisches Institut, Universität Karlsruhe (TH), 89 pp (in German).*

Damage Detection without Baseline Modal Parameters Utilizing the Baseline Stiffness Method and Independent Component Analysis for Modal Parameter Extraction

Rodríguez-Rocha R. (1), Rivero-Angeles F.J. (2), Gomez-Ramírez E. (3)

(1) Escuela Superior de Ingeniería y Arquitectura, IPN. Avenida Juan de Dios Batiz. Edificio 12, Col. Zacatenco, CP 07738, México DF, México, rrodriguezr@ipn.mx
(2) Universidad Justo Sierra, Escuela de Arquitectura, Eje Central Lázaro Cárdenas 1150, Col. Nueva Industrial Vallejo, CP 07700, México DF, México, frivero@alumni.neu.edu
(3) LIDETEA. Posgrado e Investigación, Universidad La Salle. Benjamín Franklin 47, Col. Condesa, CP 06140, México DF, México, egr@ci.ulsa.mx

Introduction

Seismic instrumentation acquires multivariate data, which in turn, a suitable representation of this data is a common problem encountered in many disciplines such as structural dynamics, statistics, data analysis, signal processing and artificial neural networks.

System identification has gained much interest by researchers for quite a few years now including a wide range of approaches (Kalouptsidis & Theodoridis, 1993); these methods include linear regressions, Wiener and Kalman filters, state-space predictors, adaptive and tracking methods, nonlinear regressions, least mean squares, recursive and non-recursive deterministic or stochastic approaches, adaptive filters, deconvolutions, spectral analysis, equalization, echo cancellation, neural networks and artificial intelligence, among others.

In the damage detection area several methods to compute a reference state of structures without baseline modal information have been developed. Stubbs & Kim (1996) proposed the Sesitivity Method to compute baseline modal parameters from a structure iteratively. However, the algorithm may not converge depending on initial conditions. Kharrazi et al. (2000) applied sensitivity techniques to fit the analytical model and structure using experimental measurements. The Stiffness-Mass Ratios Method (Barroso & Rodríguez, 2004) determines the undamaged state of only shear beam buildings with regular mass distribution per floor using damaged information. This method does not identify damage per structural element, solely per story, which is a limitation.

A recently developed linear method is Independent Component Analysis (ICA) (Hyvärinen, 1999), in which the output representation minimizes the statistical dependence of the components of the original representation and captures the essential structure of the data.

In this paper, the Baseline Stiffness Method (BSM) is presented to assess damage in buildings without baseline modal parameters. The proposed method utilizes output responses from damaged structures and the approximate undamaged lateral stiffness of the first story to determine a pre-damage state. In order to extract modal parameters the ICA is applied to acceleration signals from instrumented structures. These identified parameters are used to adjust and compare stiffness quantities with the BSM in order to detect loss of stiffness on each element of the structure. The authors use ICA to develop a representation of the acceleration output acquired by a seismic instrumentation. Fourier transform of this new representation yields clearer spectral analysis to select the structural frequencies. Moreover, the recovered signals show one large peak associated to a particular frequency, avoiding pain staking peak selection in normal Frequency Response Functions. Finally, mode shapes are obtained by conventional spectral analysis with transfer functions and phase angles of the original acceleration output.

The structure of the paper is the following; first, the ICA and BSM methods are presented to extract modal parameters and detect damage without baseline modal information respectively. Then, two study cases from the literature are studied. The effect of limited modal information is also investigated. Results are discussed which demonstrate the feasibility of the methods. Finally, conclusions are stated showing advantages and limitations of the proposed methodology.

Independent Component Analysis Method

An important problem in structural engineering is to find a suitable transformation of the data to facilitate the analysis for subsequent processes, such as pattern recognition, visualization, system identification or damage detection. Consider the case of a building structure: the acceleration output at each story x corresponds to a realization of an m-dimensional discrete-time signal $x(t), t=1,2,\ldots$. Then the components $s_i(t)$ are called source signals, which are usually original, uncorrupted signals or noise sources. Such sources are often statistically independent from each other, and thus, the signals could be considered as linear mixtures x_i of a transformed signal (Hyvärinen, 1999).

The previous paragraph hints to a very important issue: the acceleration output at each level could be considered as a linear mixture of independent sources (independent signals originated from the frequencies and mode shapes of the structure).

Independent Component Analysis (ICA) is a recently developed linear transformation method which separates the sources from the acquired data. The observed m-dimensional random vector is denoted by $x=(x_1,\ldots,x_m)^T$. ICA of the random vector x consists of finding a linear transform $s=Wx$ so that the components s_i are as independent as possible, in the sense of maximizing some function $F=(s_1,\ldots,s_m)$ that measures independence. In that sense, ICA of a random vector x consists of estimating the following generative model for the data $x=As$, where A is a constant $m\times n$ mixing matrix, and the latent components s_i in the vector $s=(s_1,\ldots,s_n)^T$ are assumed independent (Jutten & Herault, 1991).

In the previous model, the noise has been omitted since acceleration output usually contains noise during acquisition. The choice of the model is a tractable approximation of the more realistic noisy model, yet the results justify the use of the simpler model because it seems to work for certain kinds of real data. The model is asymptotically equivalent to the natural relation $W=A^{-1}$ with $n=m$.

A very simple MATLAB (The MathWorks, 2007) code is given in Parra (2007), though this method is not robust, with poor statistical and numerical performance; nonetheless, it could be a good start for tutorial purposes. The reader is referred to the works of Parra & Sajda (2003) and Cardoso & Souloumiac (1993) for better results and improved performance.

Adaptive algorithms based on stochastic gradient descent may be problematic where no adaptation is needed. Convergence is often slow and depends of the learning rate sequence. A fixed-point algorithm, named FastICA was introduced using kurtosis or general contrast functions. The expectations are estimated using sample averages over a sufficiently large sample of the input data (Hyvärinen & Oja, 1997; Hyvärinen, 1999b). This algorithm is parallel and distributed, but is not adaptive. FastICA uses sample averages computed over larger samples of data. Hyvärinen (1999c) also showed that when FastICA is used with symmetric decorrelation, it is essentially equivalent to a Newton method for maximum likelihood estimation, that is, FastICA is a general algorithm that can be used to optimize contrast functions.

Baseline Stiffness Method

The Baseline Stiffness Method (BSM) is presented to detect damage in buildings without baseline modal parameters (undamaged state). This method utilizes stiffness-mass ratios to determine a reference state (baseline) from the structure based on modal parameters from the damaged system and the approximated lateral stiffness from the first story. This identified reference state is compared to the damaged one.

For a damaged plane frame of s number of floors and i mode shapes and performing signal processing techniques, natural frequencies ϖ and their corresponding mode shapes $[\phi]$ can be computed. Lateral stiffness and mass matrix, $[\overline{K}]$ and $[\overline{M}]$ respectively, are unknown and of dimensions $s \times s$. On the other hand, it is possible to compute a vector $\{u\}$ of ratios k_i/m_i (Barroso & Rodríguez, 2004) with dimensions $2s-1\times 1$:

$$\{u\} = \left\{ \left(\frac{k_1}{m_1}\right) \left(\frac{k_2}{m_1}\right) \left(\frac{k_2}{m_2}\right) \cdots \left(\frac{k_i}{m_i}\right) \left(\frac{k_{i+1}}{m_i}\right) \cdots \left(\frac{k_s}{m_s}\right) \right\}^T \tag{1}$$

This vector $\{u\}$ is computed utilizing modal parameters from the damaged structure and the first story approximated lateral stiffness k_1 assuming a shear beam behavior. It is well known this assumption is valid for limited real cases, however, this is proposed just as an initial condition and the flexural effect will be included later on. In this sense, k_1 can be determined as:

$$k_1 = \sum \frac{12EI_1}{h_1^3} \tag{2}$$

Substituting k_1 into equation (1), some parameters p_i are obtained using back substitution as:

$$\begin{aligned} p_1 &= k_1 \\ p_{i-j} &= \frac{p_{i-(j+1)}u_{(j+4)}}{u_{(j+5)}} \\ &\vdots \\ p_{i-1} &= \frac{p_{i-2}u_4}{u_5} \qquad \text{for } j = 2,3,\ldots,(i-2) \\ &\vdots \\ k_i &= \frac{p_{i-1}u_2}{u_3} \end{aligned} \tag{3}$$

Once all k_i are known, the lateral stiffness matrix of the structure without damage $[\overline{K}]$ can be determined. In order to calculate m_i, m_1 is utilized in equation (3) instead of using k_1. These m_i are used to obtain the mass matrix of the structure $[\overline{M}]$. The former approach was applied to buildings without shear beam behavior and it was observed that an approximated mass matrix $[\overline{Ma}]$ is obtained, which differs in magnitude to $[\overline{M}]$. The difference is null if k_1 is k_1/c, where c is a coefficient that adjusts shear to flexural behavior and it was found to correspond to the greatest eigenvalue of $[\overline{M}][\overline{Ma}]^{-1}$. Thus, when the adjustment by k_1/c, for structures without shear beam behavior is performed, the BSM provides its undamaged state $[\overline{K}]$. Simultaneously, a mathematical model of the structure is created considering connectivity and geometry of its structural elements and a unit elasticity modulus. Thus, approximated stiffness matrices $[ka_i]$ for each element are obtained. The global approximated stiffness matrix of the structure is

$$[Ka] = \sum [ka_i] \tag{4}$$

According to Escobar et al. (2005), $[Ka]$ can be condensed to obtain $[\overline{Ka}]$ using the transformation matrix $[T]$ as:

$$[\overline{Ka}] = [T]^T [Ka][T] \tag{5}$$

where

$$[T] = \begin{bmatrix} [I] \\ -[Ka_{22}]^{-1}[Ka_{21}] \end{bmatrix}; [Ka] = \begin{bmatrix} [Ka_{11}] & [Ka_{12}] \\ [Ka_{21}] & [Ka_{22}] \end{bmatrix} \tag{6}$$

For a shear beam building, $[\overline{K}]$ and equation (5) just differ on material properties, specifically, on the magnitude of the elasticity modulus that can be represented using the matrix $[P]$ as $[\overline{K}] = [P][\overline{Ka}]$. Solving $[P]$ from last equation yields:

$$[P] = [\overline{K}][\overline{Ka}]^{-1} \tag{7}$$

On the other hand, stiffness matrices for each structural element of the undamaged state of the structure are calculated as:

$$[k_i] = P[ka_i] \tag{8}$$

Where P is a scalar that adjusts the material properties of the structure from the proposed model. This scalar is obtained as the average of the eigenvalues of matrix $[P]$, given in equation (7). Eigenvalue computations are performed because are useful to obtain characteristic scalar values of a matrix, in this case $[P]$. It was found that the average of these eigenvalues is precisely P. Once the undamaged state of the structure, represented by $[k_i]$, is identified and condensed, it is compared against the stiffness matrix of the damaged structure $[\overline{Kd}]$ using the Damage Submatrices Method (DSM, Rodríguez & Escobar, 2005). This method is applied to locate and determine magnitude of damage, in terms of loss of stiffness, in percentage, at every structural element. According to Baruch & Bar Itzhack (1978), $[\overline{Kd}]$ can be computed from measured modal information. Thus, the condensed stiffness matrix of the damaged system can be reconstructed as:

$$[\overline{Kd}] = \left[[\overline{K}] - [M][Z] \right][H] + [M][q][\Omega]^2[q]^T[M] \tag{9}$$

where $[H]=[I]-[Y]$; $[Y]=[q][q]^T[M]$; $[Z]=[q][q]^T[\overline{K}]$; $[q]=[\phi]\left[[\phi]^T[M][\phi]\right]^{-\frac{1}{2}}$; $[\phi]$ is the modal matrix of the structure and $[\Omega]^2$ is a diagonal matrix containing the eigenvalues of the system.

Numerical Examples

Modal parameter extraction of a four-story shear frame utilizing ICA

In order to extract modal parameters, the ICA method was applied to a four-story shear building studied by Bernal & Gunes (2000), Figure 1. Mass and lateral stiffness values are k=7.5x10^7 N/m. m_1=3600 kg, m_2=m_3=2850 kg, m_4=1800 kg.

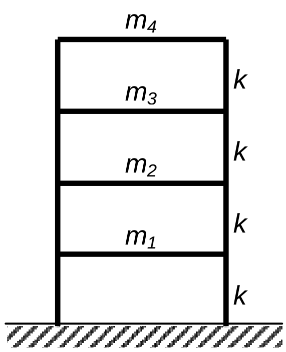

Figure 1. Four-story shear building (Bernal & Gunes, 2000)

This model was excited with random normal-distributed noise at a sampling rate of 0.02 seconds. Figure 2 shows the Fourier spectra of the acceleration output signals. Note that the peak selection below 0.04 seconds becomes quite difficult to extract. Figure 3 shows the Fourier spectra of the extracted sources from ICA.

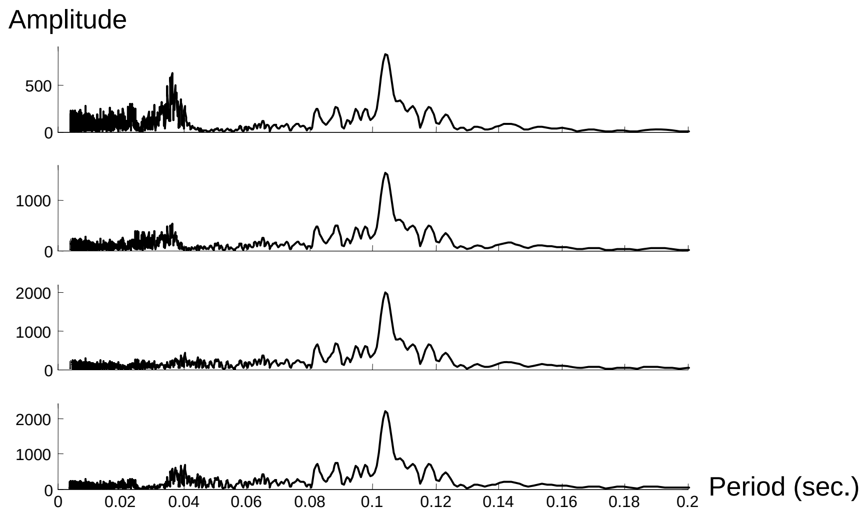

Figure 2. Fourier spectra of the acceleration output at each floor.

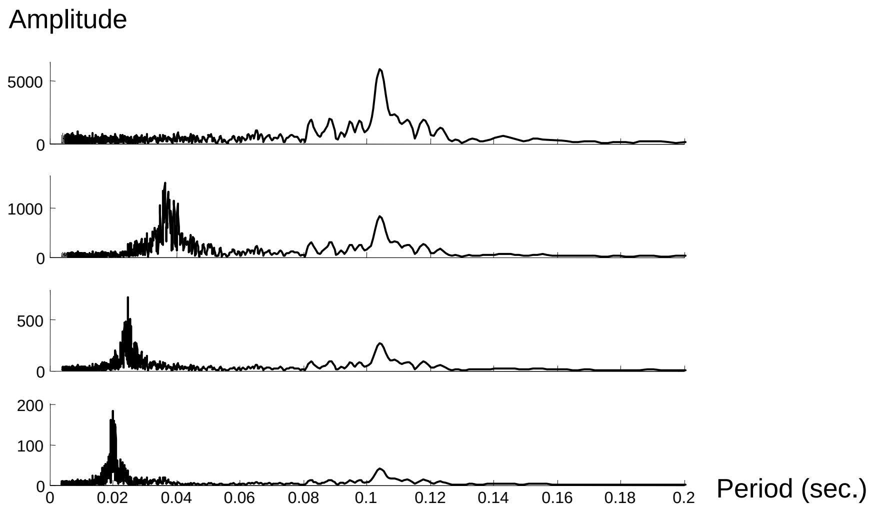

Figure 3. Fourier spectra of the unmixed sources, extracted with ICA.

There is no physical interpretation as to which level does it correspond, instead, they are the unmixed original sources for each frequency. Note here that each signal contains only one large peak, quite easy to select, even for periods below 0.04 seconds. The extracted periods from Figure 3 are shown in Table 1. A comparison of these results and the ones from Bernal & Gunes (2000) is also presented.

Table 1. Periods (sec.) using ICA applied to the four-story shear building

Theoretical	Computed by ICA	Error (%)
0.103	0.104	-1.0
0.038	0.036	5.3
0.025	0.025	0.0
0.020	0.020	0.0

It can be noted from Table 1 that errors are less than 10%, acceptable in engineering.

<u>Damage detection of a three-story frame utilizing BSM</u>

Figure 4 shows the frame building model proposed by Biggs (1964). According to Biggs, the flexural stiffness of the columns from story 1 is 2,688,218.5 N/m, stories 2 and 3 is 3'887,846.3 N/m. The weights for floors 1 to 3 are 241,537.7 N, 226,857.2 N, and 113,433.5 N, respectively.

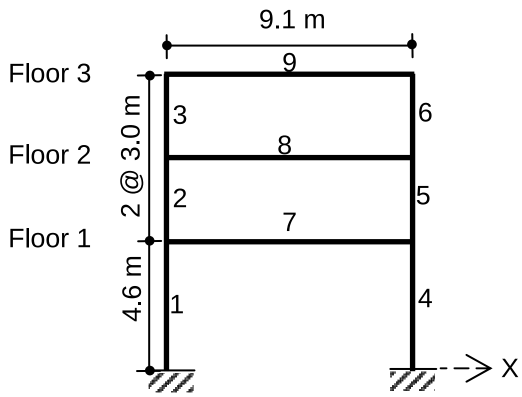

Figure 4. Three-story frame (Biggs, 1964)

Two damage cases, D1 and D2, were simulated. D1 consists of a 10% loss of stiffness on element 8. For D2, elements 2 and 4 were damaged 20% and 30% respectively.

Again, ICA was used to extract the periods of the structure as shown in the previous section. To obtain mode shapes the conventional spectral analysis (Bendat & Piersol, 1986) was used. The transfer function of the power spectral density function (PSD) of each level to the ground PSD was calculated. Then, for each frequency obtained with ICA, the amplitude of the transfer function was calculated and divided by the amplitude of the transfer function of the ground. This method gives the amplitude of the mode shape. The polarity of the mode shape was computed with the phase angle of the cross PSD functions. If the angle is between 0 and 90º, a (+) sign is given, if it is between 90 and 180º, a (-) sign is assigned; thus, obtaining the complete mode shape. Modal parameters computed using ICA and the simulated ones are presented in Table 2.

Table 2. Modal parameters for the three-story frame

	Undamaged case			Damage case D1			Damage case D2		
Mode	1	2	3	1	2	3	1	2	3
T (sec.) ICA	0.743	0.260	0.179	0.745	0.260	0.179	0.802	0.274	0.183
Mode shape. ICA	1.000	-1.000	1.000	1.000	-1.000	1.000	1.000	-1.000	1.000
	0.893	-0.117	-0.699	0.893	-0.117	-0.703	0.907	-0.222	-0.948
	0.597	0.993	0.390	0.598	0.993	0.390	0.618	1.00	0.298
T (sec.) Simulated	0.744	0.260	0.179	0.744	0.260	0.179	0.803	0.274	0.183
Error (%)	0.2	0.0	0.0	-0.1	0.0	0.0	0.1	0.0	0.0

In Table 2, the period values (T) and mode shapes for the undamaged case calculated with ICA are very similar to those reported by Biggs (1964). Note that error values are 0.2% or smaller. The period T, and the related mode shape values for damage cases D1 and D2, computed using ICA, were utilized by the BSM to detect structural damage for both scenarios, knowing and not knowing the undamaged case (baseline modal parameters).

Figure 5 presents degradation of damage in percentage computed by the BSM. It can be observed from Figure 5 that the proposed damage identification method localized damaged elements for both cases. Note for D1, that when baseline modal parameters are not known the method determined a higher value of degradation of stiffness. For D2 some false damaged elements were identified, however, degradation values were smaller than the real ones.

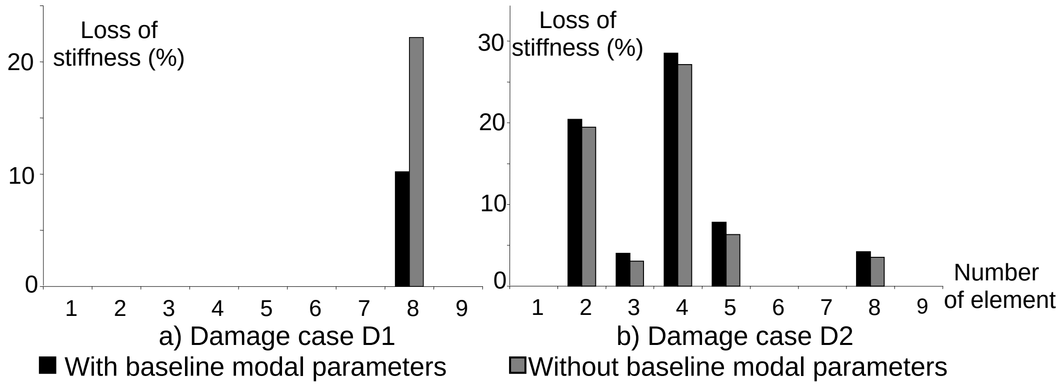

Figure 5. Degradation of stiffness using the BSM applied to the three-story frame, with and without baseline modal parameters.

The effect of limited modal information was also studied when baseline modal parameters are unknown. The number of identified mode shapes from the damaged structure computed was varied from 3 to 1. Figure 6 presents these results for damage case D2.

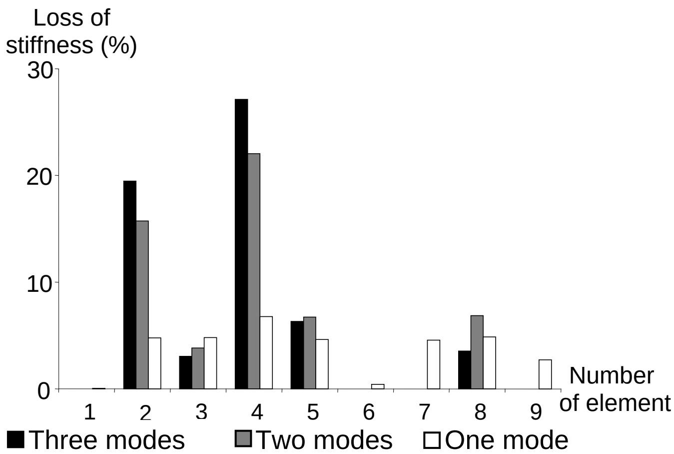

Figure 6. Degradation of stiffness for Damage case D2 using the BSM applied to the three-story frame, without baseline modal parameters.

As it was expected, the fewer the number of modes used to determine the damaged stiffness matrix, the less precise the method is. When all modes were utilized, error values were 2.6% and 9.6% for elements 2 and 4 respectively. Note also that when 2 modes were utilized, the BSM localized adequately the damaged elements. This is an advantage of the method since in practice only some modes can be extracted from dynamic measurements, not all of them. For the one mode case the BSM identified the most damaged element along with several false locations.

Conclusions

It has been proven that ICA is a powerful tool to obtain the structural periods and mode shapes. Also, for these particular study cases, the BSM with a sufficient number of mode shapes determined location and severity of damage in terms of loss of stiffness from a structure, without baseline references. When only a limited number of modes (1 or 2) were used to fit the damaged stiffness from dynamic measurements, the BSM was capable to determine the location of damage.

Acknowledgement

The authors would like to gratefully acknowledge the *Instituto Politécnico Nacional* for supporting this research project, No. 20080145.

References

Barroso L. & Rodríguez R. (2004). Damage detection of a benchmark structure without baseline information, *ASCE Journal of Engineering Mechanics*, *130(2), 142-151.*

Baruch M. & Bar Itzhack IY. (1978). Optimal weighted orthogonalization of measured modes, *American Institute of Aeronautics and Astronautics*, *16(4), 346-351.*

Bendat J.S. & Piersol A.G. (1986). *Random data. Analysis and measurement procedures,* John Wiley & Sons.

Bernal D. & Gunes B. (2000). Performance of an observer state-space identification in the presence of mild nonlinearities, *2000 American Control Conference*, *Chicago, Illinois, 2, 986-990.*

Biggs J.M. (1964). Introduction to structural dynamics, *McGraw-Hill.*

Cardoso J.F. & Souloumiac A. (1993). Blind beamforming for non Gaussian signals, *IEE Proceedings-F*, *140(6), 362-370.*

Hyvärinen A. (1999). Survey on Independent Component Analysis, *Neural Computing Surveys*, *2, 94-128.*

Hyvärinen A. (1999b). Fast and robust fixed-point algorithms for independent component analysis, *IEEE Transactions on Neural Networks*, *10(3), 626–634.*

Hyvärinen A. (1999c). The fixed-point algorithm and maximum likelihood estimation for independent component analysis, *Neural Processing Letters*, *10(1), 1–5.*

Hyvärinen A. & Oja E. (1997). A fast fixed-point algorithm for independent component analysis, *Neural Computation*, *9(7), 1483-1492.*

Jutten C. & Herault J. (1991). Blind Separation Sources, Part I: An adaptive algorithm based on neuromimetic architecture, *Signal Processing*, *24, 1-10.*

Kalouptsidis N. & Theodoridis S. (1993). Adaptive System Identification and Signal Processing Algorithms, *Prentice Hall International Series in Acoustics, Speech and Signal Processing.*

Kharrazi M.H.K., Ventura C.E., Brincker R. & Dascotte E. (2000). A study on damage detection using output-only modal data, *20th International Modal Analysis Conference*, *Los Angeles, California.*

Parra L. & Sajda P. (2003). Blind Source Separation via Generalized Eigenvalue Decomposition, *Journal of Machine Learning Research, 4, 1261-1269.*

Parra L. (2007). Quickie Blind Source Separation. Revised on-line on 2007/02/11, *http://newton.bme.columbia.edu/~lparra/publish/quickiebss.html*

Rodríguez R., Escobar J.A. & Gómez R. (2005). Detección de daño en edificios utilizando submatrices de daño, *XV Congreso Nacional de Ingeniería Sísmica*, *Mexico City, 15,1-7.*

Stubbs N. & Kim J. (1996). Damage localization in structures without baseline modal parameters, *American Institute of Aeronautics and Astronautics Journal*, *34(8).*

The MathWorks, Inc. (2007). Matlab ® The Language of Technical Computing, R2007a.

Analysis of the Aftershock Sequences of the Most Recent Strong Events Generated in the Vrancea Area

Rogozea M (1), Popa M.(1), Radulian M. (1)

(1) National Institute for Earth Physics, 12 Calugareni St., 077125, PO Box MG-2 Magurele, Romania, mrogozea@infp.ro

Keywords: Vrancea, aftershock, frequency-magnitude

Introduction

The Vrancea seismic region is located at the sharp bend of the Eastern Carpathians Arc, in Romania, where frequent strong earthquakes (M > 7) occur at intermediate depths (60 - 180 km). The extreme geometrical lateral limitation of the seismogenic body controls the possible rupture extension for the largest shocks and the area of the associated aftershock sequences. Three significant events occurred in the last 30 years, relatively well constrained by instrumental data: March 4, 1977 (M_w=7.4), August 30, 1986 (M_w=7.1) and May 30, 1990 (M_w=6.9). The scope of this paper is to analyze the properties of the aftershock sequences following these events and to interpret them in terms of specific rupture process properties.

Distribution in space and time

Aftershock sequences of the main shocks of March 4, 1977, August 30, 1986 and May 30, 1990 are mostly clustered along a NE – SW oriented vertical plane (Bojer et. al. 1979, Radu 1992, Radu and Oncescu 1989, Trifu and Oncescu 1987, Trifu et. al. 1992). In the first two months after the main shock, the catalog contains 108 aftershocks in 1977, 226 aftershocks in 1986, 298 aftershocks in May 1990.

The seismic moment release distribution during the last 30 years (1977 – 2007) in the Vrancea region, given in Fig. 1, outlines the three important stages of seismic energy release in 1977, 1986 and 1990.

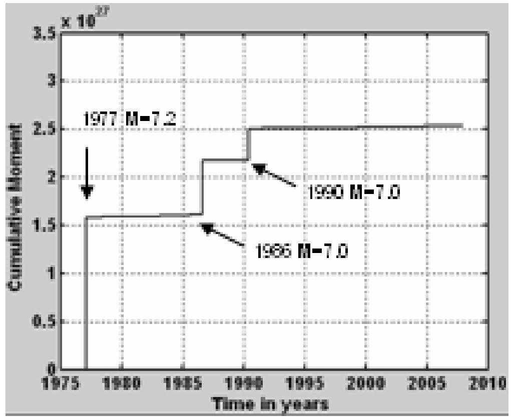

Figure 1. Cumulative moment curve of earthquakes with M>1.5 that occurred between 1977 and the 2007 in Vrancea zone. Arrows mark the events with M>6.5.

The depth-time distributions of the aftershocks associated with the 1977, 1986 and 1990 events are plotted in Fig. 2. Except the case of event of 1977 for which the depth errors are large, the aftershock activity reproduces well the depth extension observed in the main shock (Oncescu and Bonjer 1997), 130-150 km in 1986 and 80-100 km in 1990.

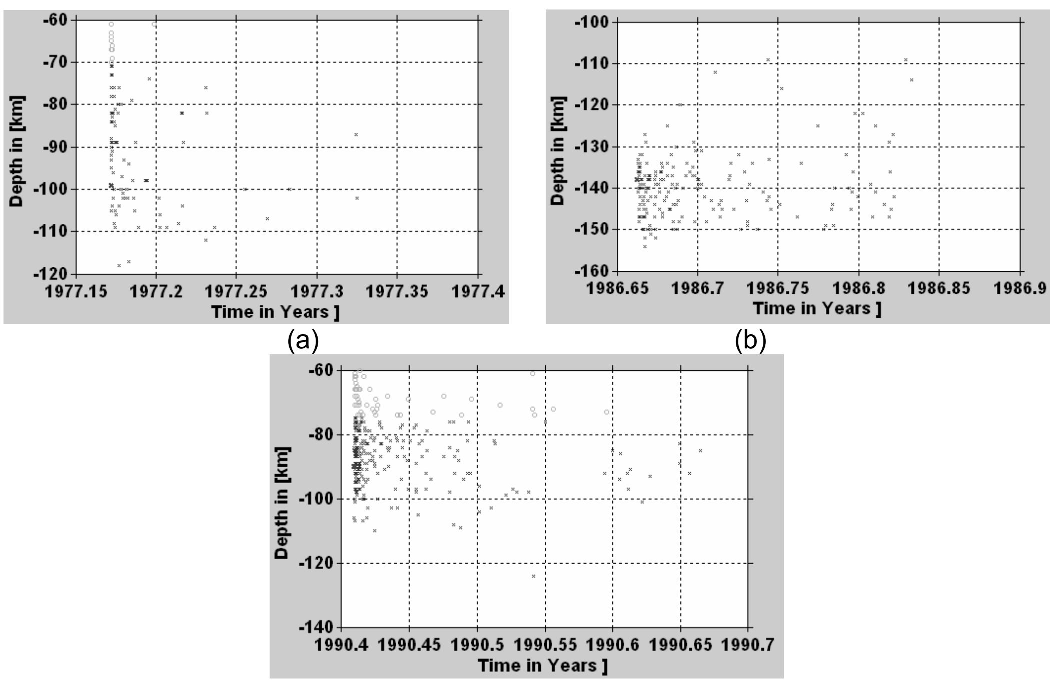

(a) (b) (c)

Figure 2. Depth-time evolution of the aftershocks for the 1977, 1986, 1990 events.

The evolution in time of the seismic moment release during the aftershock activity is represented in Fig. 3. A strong decay is noticed in all cases after 5 – 15 days which suggests a very efficient stress release process during the main shock. This efficiency explains also the large gap between the main shock magnitude and the largest aftershock magnitude: 3.2 units for 1977, 2.9 units for 1986 and 2.7 units for 1990, significantly larger than the gap predicted by the Bath law for shallow earthquakes.

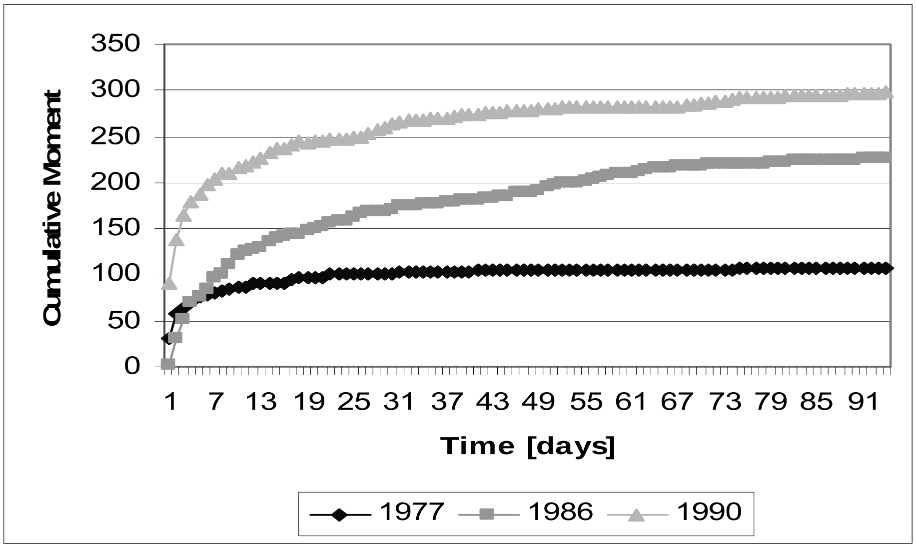

Figure 3. Cumulative moment release during the aftershock activity.

Frequency-magnitude distribution and Omori law

Two important distributions which characterize the aftershock activity are the frequency-magnitude distribution and Omori law. The frequency of earthquake occurrence as a function of magnitude is in many cases described by a linear relation (Gutenberg-Richter, 1944):

$$\log N = a - bM$$

where N is the number of events with magnitudes above or equal to M and a and b are constants that in general, are different for different regions. The b value has often been used as a means to characterize the tectonic setting of a region. Changes in b value with respect to time have been proposed to have a possible correlation with changes in the pre-mainshock stress state (Smith, 1986). Wiemer and Katsumata (1999) showed that the b coefficient varies mostly from 0.6 to 1.4. Also, it is summarized by Utsu (1971) that b-values change roughly in the range 0.3 to 2.0, depending on the different region.

The temporal distribution of aftershocks can be described using the modified Omori law (e.g., Utsu et al., 1995) which can be expressed by the following equation:

$$n(t) = \frac{k}{(t+c)^p}$$

where n(t) is the frequency of aftershocks, K, c, p are constants. p is a decay parameter, ranging from 0.5 to 1.8 (Wiemer and Katsumata 1999; Olsson, 1999). *K* depends on the total number of events in the sequence, *c* on the rate of activity in the earliest part of the sequences. The constant *c* is a controversial quantity (Utsu *et al.*, 1995) and strongly influenced by incomplete detection of small aftershocks in the early stage of sequence (Kisslinger and Jones, 1991). This variability may be related to the tectonic condition of the region such as structural heterogeneity, stress, and temperature or the crustal heat flow in the source volume (Kisslinger and Jones, 1991; Utsu *et al.*, 1995).

Fig. 4 shows the frequency-magnitude distribution for Vrancea aftershock events. The magnitude of completeness is Mc=2.2 for 1977, Mc=2.7 for 1986 and Mc=2.2 for 1990. The parameters a and b are determined using maximum likelihood method. The b values are at the lowest limit in all cases: 0.427±0.03 for1977, 0,681±0.06 for 1986 and 0.56±0.03 for 1977 indicating a relative poor production of small aftershocks.

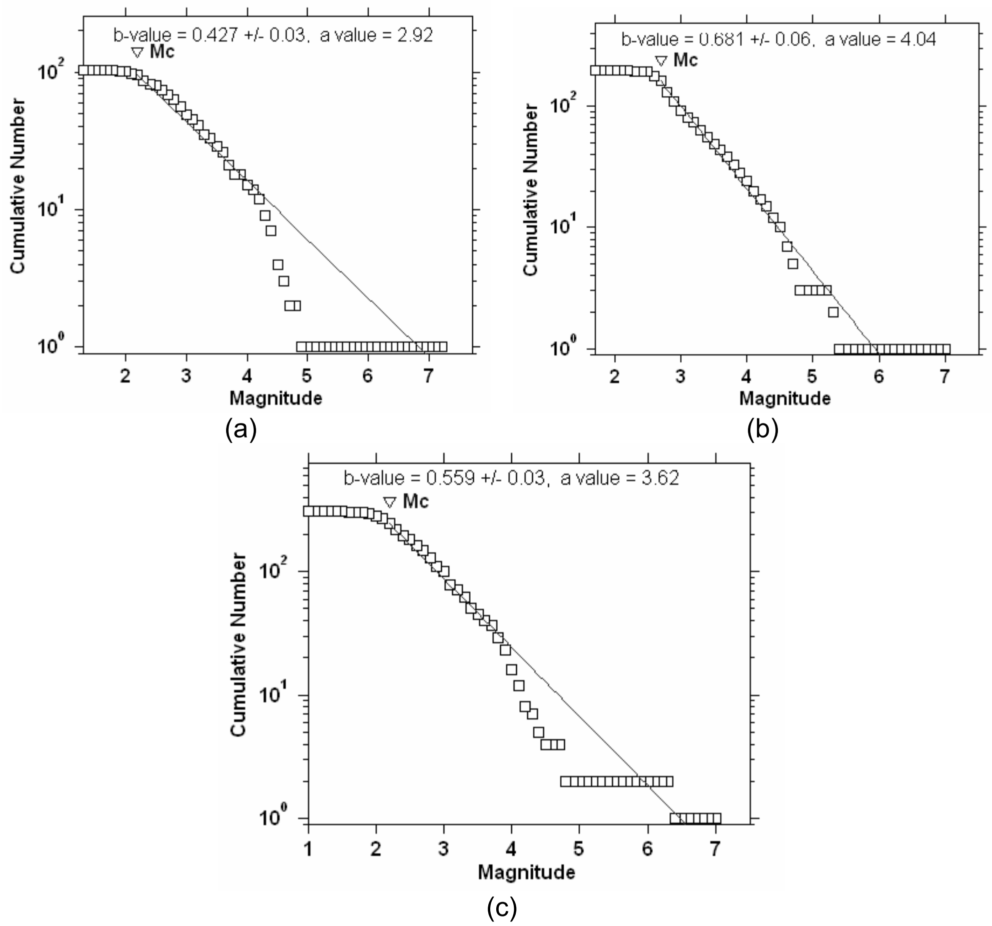

Figure 4. Frequency-magnitude distribution for (a) 1977 event (Mc=2.2), (b) 1986 event (Mc=2.7) and (c) 1990 event (Mc=2.2). The b value and its standard deviation and a value are given in each case. Mc is the magnitude of completeness.

The temporal decay rates of aftershocks for the three sequences are shown in Fig. 5. The p, c and k parameters are obtained using the maximum likelihood procedure and the occurrence rate is modeled by the modified Omori law: p =1.11±0.008 for 1977, p=0.98±0.13 for 1986 and p=1.09±0.06 for 1990.

The relatively small p values characterize regions with lower temperature (Mogi, 1962) or that did not experience significant recent ruptures (e.g., Wiemer and Katsumata, 1999; Yagi and Kikuchi, 2000; Sekiguchi and Iwata, 2000). Higher temperatures imply faster stress relaxation, while the frictional heating created during the main shock causes a faster decay of aftershocks (since the regions where the slip was large during the main shock probably also experienced such an increased frictional heating). For the Vrancea intermediate-depth earthquakes, it looks like the healing process is fast and the influence of the previous large slip events is less important as compared with the earthquakes in the crust. Therefore, the p values are rather small and they tend to be smaller when depth increases.

This is compatible with the low b-values, which are probably characteristic for regions under higher applied shear stress after the main shock. Fast healing leads to faster recovering of the stress strength. However, future studies are needed in order to understand better the underlying physical mechanism of the *b* and *p* value variation patterns.

The c values are c = 0.037 ± 0.03 for 1977, c = 0.945 ± 0.644 for 1986 and c = 0.117 ± 0.043 for 1990. Some seismologists consider that the number of aftershocks can not be counted completely in the beginning of a sequence when smaller shocks are often obscured by larger ones due to overlapping, thus too large value of c is obtained. The value of c might be zero if all shocks should be counted (Utsu, 1971).

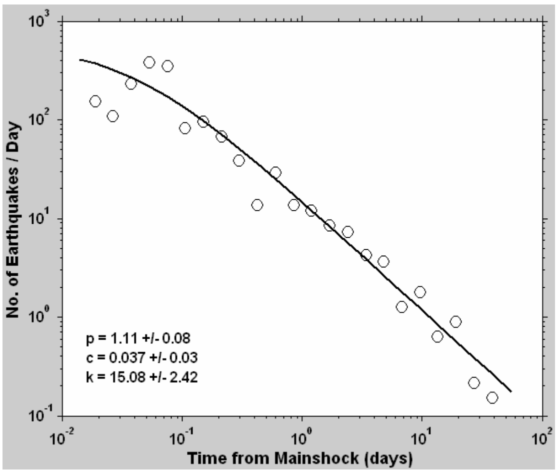

(a)

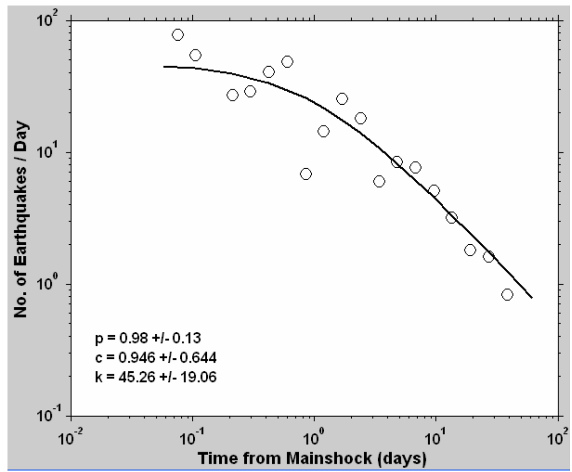

(b)

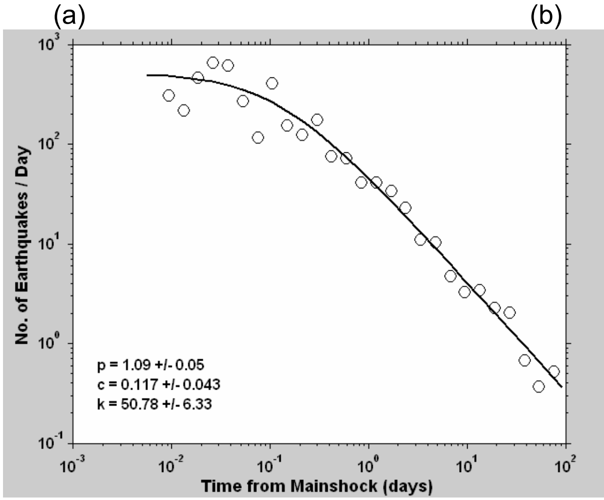

(c)

Figure 5. Temporal change of the number of aftershocks per day (a), 1977, (b), 1986, (c), 1990. The p, c and k values in the modified Omori formula are also given.

Conclusions

Different studies on Vrancea intermediate-depth seismicity outlined the presence of two characteristic seismic active segments in the lithospheric body pulled down below crust. One is hypothetically related to the nucleation of strong events around 100 km depth (events of March 4, 1977 and May 30, 1990), the other to the nucleation in the deeper part, around 140 km depth (events of November 10, 1940 and August 30, 1986). The differences in seismic process pointed out between the two segments let some authors to consider different physical processes that are responsible for earthquake generation in the two segments.

In the present paper we check if such differences can be detected in the aftershock activity as well. For example, the linearity breaking off around magnitude 4 in the frequency-magnitude distribution for 1977 and 1990 events (Fig. 4) which is not obvious for 1986 event. Also, the decay parameter of the aftershock activity has very close values for 1977 and 1990 sequences ($p = 1.11$ and $p = 1.09$), slightly different from the value of 1986 sequence ($p = 0.98$). In all cases, the rather small p values correlate with the low b values and are interpreted in terms of a fast healing process in Vrancea intermediate-depth domain. The rapid recover of the shear stress strength explains the relative poor production of small events and the slower decay rates in the aftershock activity.

Acknowledgements

For all our computations, we used the computer program ZMAP (Wiemer and Zuniga, 1994; Wiemer, 2001).

References

Bonjer K.P., Bock G.& Enescu D. (1979). The Romanian earthquake of March, 1977 and its aftershocks, *Newsletter, 14, EGS, London.*

Gutenberg R. & Richter C.F. (1944). Frequency of earthquakes in California, *Bull. Seismol. Soc. Am., 34, 185-188.*

Kisslinger C. & Jones L.M. (1991). Properties of aftershock sequences in Southern California, *J. Geophys. Res.*, *96(B7), 11,947–11,958.*

Mogi K. (1962). Study of the elastic shocks caused by the fracture of heterogeneous materials and its relation to earthquake phenomena, *Bull. Earthq. Res. Inst., Univ. Tokyo*, *40, 125–173.*

Olsson R. (1999). An estimation of the maximum b-value in the Gutenberg-Richter relation, *Geodynamics, 27, 547–552.*

Oncescu M.C. & Bonjer K.P (1997). A note on the depth recurrence and strain release of large Vrancea earthquakes, *Tectonophysics, 272, 291 – 302*.

Radu C. (1992). The aftershocks of Vrancea (Romania) large intermediate earthquakes, *Proc. and Activity report of 22 nd Gen. Assem. ESC., Barcelona, 17-22 September, 1990, II, 685-690, Servei Geologic de Catalunya, Barcelona.*

Radu C. & Oancea V. (1989). The earthquake of August 30, 1986: Temporal analysis of the aftershock sequence, *Ferlands Beitr. Geophysik 98, 138-145, Leipzig, 1989.*

Sekiguchi H. & Iwata T (2000). Rupture process of the 2000 Tottori-Ken Seibu earthquake using strong ground motion data, *Web page: http://sms.dpri.kyoto-u.ac.jp/iwata/ttr e.html.*

Trifu C.I. & Oncescu M.C. (1987). Fault geometry of August 30, 1986 Vrancea earthquake, *Ann. Geophys. 5B, 727-730.*

Trifu C.I., Deschamps A., Radulian M. & Lyon-Caen H. (1992). The Vrancea earthquake of May 30, 1990: An estimate of the source parameters, *Proc. of the XXIInd ESC Gen.Ass., Barcelona, 1990, 1, 449-454.*

Utsu T. (1971). Aftershock and earthquake statistic (III): Analyses of the distribution of earthquakes in magnitude, time an space with special consideration to clustering characteristics of earthquake occurrence (1), *J. Faculty Sci., Hokkaido University, Ser. VII (Geophys.), 3, 379-441.*

Utsu T., Ogata Y. & Matsu'ura R.S. (1995). The centenary of the Omori formula for decay law of aftershock activity, *J. Phys. Earth, 43, 1-33.*

Wiemer S., (2001). A software package to analyze seismicity: ZMAP, *Seis. Res. Lett.*, *72(2), 374–383.*

Wiemer S. & Katsumata K. (1999). Spatial variability of seismicity parameters in aftershock zones, *J. Geophys. Res., 104(B6), 13,135-13,151.*

Wiemer S. and Zuniga R.F. (1994). ZMAP—A software package to analyze seismicity (abstract), *EOS Trans. AGU, 75(43), Fall Meet. Suppl., 456.*

Wyss M., Wiemer St. & Zúňiga R.(2001). ZMAP - A tool for analyses of seismicity patterns, *1-57.*

Yagi Y. & Kikuchi M. (2000). Source Rupture Process of the Tottori-ken Seibu earthquake of Oct. 6, 2000,*Web page: http://wwweic.eri.u-tokyo.ac.jp/yuji/tottori/*.

Some Main Aspects and Features of Seismic Activity 2007

Ormeni R (1)

(1)Institute of Geosciences, Polytechnic University, Tirana, “Don Bosko”street, Nr.60
rrapo55@yahoo.com

Keywords: Earthquakes, Seismicity, epicentre, faull, focal mechanism

Introduction

Albania is situated in Alpine-Mediterranean seismic belt comprising the zone of contact between lithosphere plates of Africa and Eurasia. Here African and Eurasian plates collide, giving origin to some seismically active belas. In particular Albania is at the junction between the Adriatic micro plate and Eurasian plate as it is known, Albania is a country of high seismic activity. It is characterized by intense micro seismic activity and small and medium-size earthquakes and only seldom by large event. The earthquake foci are concentrated mostly along the active faults[1].

We present here the results of the analysis in parameters of events and some features of Seismicity that have occurred in the Albania and surrounding area during 2007. On that territory, 441of total number of earthquakes was located and 35 of them were felt by population of Albania.

The strongest earthquake occurred on the16th of April at 07:38 local time, with Richter magnitude of 4.5. According to ASN data occurred on the vicinity of Elbasani town, Central Albania, The seismic activity reached an intensity of VI degrees on MSC-98 scale. The presence of different faulting mechanisms, evidenced by earthquakes occurring around Elbasani, indicates the complexity of faulting environment in this area[1],[3].

On September 5, 2007, an earthquake of ML=4.5 according to ASN data occurred on the vicinity of Durresi town, Western Albania, causing damages of V-VI degree of EMS-98 scale on epicenter area. This earthquake was generated by a thrust faulting environment according to the neotectonic zonation map of Albania

Materials and Methods

Data

Routinely, seismic signals recorded by Institute of Geosciences, Polytechnic University of Tirana are visually inspected to recognize seismic events. Earthquakes with an epicentral distance from the closest station of less than 100 km, recorded by least 3 dtations are located.

During year 2007, Institute of Geosciences, Polytechnic University of Tirana using seismic network consist of 13 stations, has recorded a moderate seismic activity at the Albania territory

and a slight increase of activity in its surroundings in southern part. On that territory, between 39°00'- 43°00' N and 18°50'-21°50'E, 1271 earthquakes were recorded totally, and 441of total number of earthquakes was located.
Albanian bulletins have location errors, which are negligible for civil protection purposes and large scale seismotectonic analyses, more accurate hypocentral determinations are necessary for detailed seismotectonic and geodynamic studies[5]. Seismic phases recorded by the Albanian network, integrated with data of Montenegro, Thessalonicy (Greece) and Macedonia networks, are used to prepare the database for this study. Figure 1 shows the Seismicity relocated for the period of time 2007.

Method

P-wave arrivals from 441 located earthquakes which occurred during 2007 within Albania and surrounding area have been accurately re-picked to obtain a high quality data set and are formatted in New eve program of Seisan. We relocated the earthquakes, which occurred in the Albania in the last year, achieving constrained hypocentral determinations for the events in the Albania[2].

The standard procedure uses the program HYPO71 [4](Haskov,et.al.2001) of the SEISAN packet, and velocity model Vel-Albanid [6](Ormeni Rr.2007) for earthquake locations, while the local magnitude of near earthquakes is estimated according to Richter scale. Some formula for determination of the magnitude according to the time duration of the seismic signal are also used.

For felt earthquakes of M_L > 3.5, questionnaires are distributed in the affected areas, in order to estimate the macro seismic intensity.

Results and Discussion

Results

In the vicinity of Peshkopia, on the 10th of February the first earthquake occurred at 21:20 local time, with Richter magnitude of 3.2 and for a period of some months was registered a small series of earthquakes. In that series, the strongest earthquake occurred on the 11th of March at 22:14 local time, with Richter magnitude of 3.6 and maximum intensity of IV-V degrees MSC scale. The earthquake felt with intensity of IV degrees on the MSC-98 scale on Peshkopia area.

Moderate seismic activity was recorded at the Lushnje-Elbasan-Dibra transversal fault zones, especially during April. The strongest earthquake occurred on the16th of April at 07:38 local time, with Richter magnitude of 4.5. This earthquake has been felt by the population of central Albania and has induced panic. The seismic activity reached an intensity of VI degrees on MSC scale. On the south of Montenegro this earthquake felt with intensity of III degrees on the Marcella Scale. In the series of about 49 earthquakes were located in this fault. The earthquakes on the fault Lushnje-Elbasan-Dibra during 2007 have occurred mainly in the Elbasani area. From the Seismotectonic point of view, the area belongs to a complex faulting environment, and according to the actual map of neotectonic zonation of Albania (Fig. 2), it is located in the boundary between the two main tectonic zones characterized by compressional and extensional movements[1],[3].

Some increasing of seismic activity was registered at the Durresi region where the strongest earthquake occurred on the 5th of September at 07:08 local time, with Richter magnitude of 4.5. This earthquake has been felt by the population of Central Albania and has induced panic. The earthquake felt with intensity of V-VI degrees MCS scale at the towns of Durresi, Tirana and Kruja, with intensity of V degrees MCS scale on Kavaj, Laci, area, with intensity of IV-V degrees MCS scale on Lezha area, with intensity of III-IV degrees MCS scale on Shkoder, Burrel, Elbasan, Lushnje, Fier areas. In the series of about 49 aftershock were occurred and 5 earthquakes were located. The epicenter position of this event is presented in the Figure 2 together with an excerpt of the neotectonic map of Albania. The hypocentral depth determinations are of the order of 13km by a thrust faulting environment according to the neotectonic zonation map of Albania (Aliaj et al.1996) and this explains the wide area where the shaking generated by this event was felt[7]. The Durres area is included in the Ionian-Adriatic seismogenic zone. This is a large and long segment of the Adriatic and Ionian coastal frontal thrust fault zone, which continues along the western coasts of Montenegro, Albania and Greece. Its length is around 250 km and it varies in width from 70 to 80 km in Albania. By and large, the Seismicity across this seismogenic zone to the south of Shkodra-Peja transversal decreases gradually from the folded front eastwards. It is necessary to underline that Durres town is located near the Albanian Orogene front, in convergence with Adria micro plate, concretely with Albanian basin (South Adriatik basin) and for this reason compress ional movements here are strongest ones. This tectonic position and the active tectonic faults are the source of strong earthquakes that have stricken Durres and the surrounding areas during the centuries.

Two main events occurred on 16the April and 5the of September was recorded by both short period and broad-band stations managed by the ASN, and were immediately located by the Hypoinvers and Hypo71 programs , which provided civil protection authorities with the first hand hypo central and magnitude estimates.

On the northern part of Albania, in the fault zone of Thethi a small increase of seismic activity was recorded about 19 earthquakes. The strongest earthquake occurred on the 18th of April at 04:16 local time, with Richter magnitude of 2.8.

Increased seismic activity was registered on the Greece territory, especially in its northern part.

The strongest earthquake occurred on the 29th of June at 20:09 local time, with Richter magnitude of 5.3. The seismic activity reached an intensity of VII degrees on the MSC scale. On the south of Albania this earthquake felt with intensity of IV-V degrees on the MSC Scale. In the series of earthquakes recorded at Greece region the strongest aftershock occurred on the 12th of August 14:20 local time, with Richter magnitude of 4.4 and maximum intensity of V-VI degrees MCS scale.

During the previous year, in the south Montenegro, an increased Seismicity was registered. In that series, the strongest earthquake occurred august 2 at 14:45 local time, with Richter magnitude of 3.2. On that territory was Regis rated 45 earthquakes.
During this year the Seismicity is mainly concentrated in the predominant belt in Lushnje-Elbasan-Diber, with extensions in north of its.

On the epicentral maps showed below, the earthquake activity was presented for the Albanian territory and its surroundings. The epicenters are presented in different colors depending on the hypocentral depth. The frequency of earthquake occurrence in the region can be perceived from the attached diagrams, through the cumulative number of earthquakes per month.

Figure 3 shows the number of earthquakes recorded and located each month in Albania.

In January there were 37 located earthquakes. From July to September there were 12 to 14 located earthquakes. In April the number of located earthquakes largely increases (57) due to the Elbasan seismic sequence, while in October the number of located earthquakes stabilizes to less than 35 earthquakes.

The local earthquakes are distributed in depth between 0 and 25 km, with maximum concentration between 4 and 8 km.

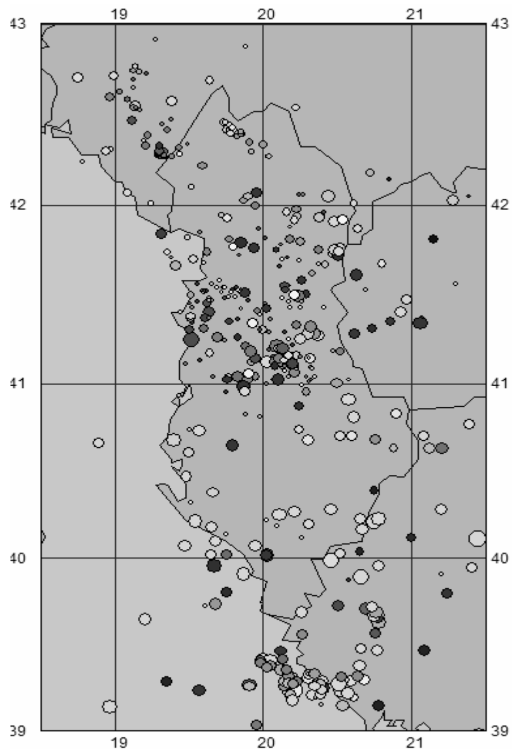

Figure 1. Epicentral map of earthquakes occurrence during 2007, for the Albanian territory and surrounding area.

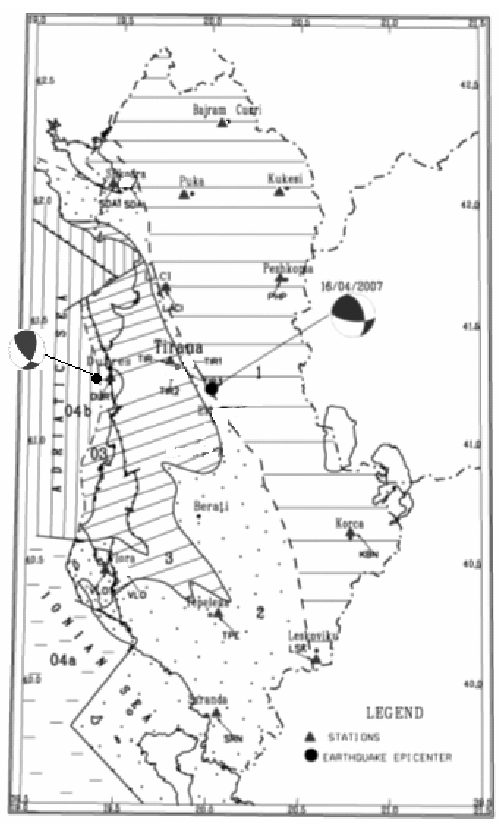

Figure 2. Map of Neotectonic Zonation of Albania (Aliaj et al. 1996). The country is subdivided in 4 large neotectonic units: i) Internal area of Alpine folding affected by extensional tectonics; ii) External area of Alpine folding strongly affected by pre-Pliocene compression movements (02-offshore sectors); iii) Peri-Adriatic Foredeep strongly affected by post-Pliocene compression movements (03-offshore sectors); iv) Pliocene-Quaternary Foreland in Adriatic and Ionian offshore (04a-Apulian platform; 04b-Albanian basin). Presented are also the earthquake locations, occurrence date of the events analyzed, fault plane solution for two of them and seismological stations of the ASN.

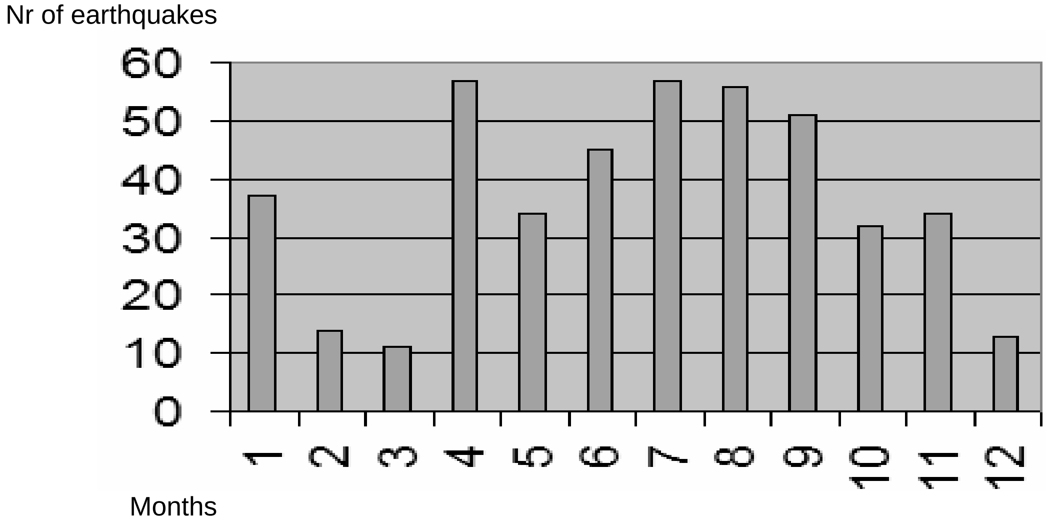

Figure 3. The diagram of earthquake frequency occurrence per month during 2007 for the Albania territory and surrounding

Discussion

The to main earthquakes inside the Albanian territory, analyzed in this paper have been generated in an area with complex features from the neotectonic point of view. According to the Neotectonic Zonation Map of Albania (Aliaj et al. 1996), both normal and thrust faults could be encountered in Central Albania, and Elbasani area in particular The earthquake of Durresi was generated by a thrust faulting environment according to the neotectonic zonation map of Albania (Aliaj et al. 1996).

The local earthquakes are distributed in depth between 0 and 25 km, with maximum concentracion between 4 and 8 km.

In the vicinity of Peshkopia was registered a small series of earthquakes.

Increased seismic activity was registered abroad of Albania on the Greece territory, especially in its northern part and the strongest ones are felt in Albania.

Reference

Aliaj Sh., Sulstarova E., Muco B. & Kociu S. (2000). Seismotectonic map of Albania, schale 1:500.000, *Seismological Institute Tirane.*

Claudio C. & Alberto F. (1997). Minimum 1D velocity models in Central and Southern Italy: a contribution to better constrain hypocentral determinations, *Anali Di Geophysics, XL, N.4.*

Koçiaj S. (1988). The risk of the Albanian's earth crust and its specification for the ground of Construtsion*, PhD thesis, Tirana.*

Haskov J. & Ottemoller L. (2001). Seisan: The earthquake analysis software, *University of Bergen, Norway.*

Manfred K. & Jody K. (1992). Simultaneous Determination of Hypocenter Location and Crustal Structure in Virginia Seismic Region. Florida State University, Thelasenicy, J*ournal Geophysical Research, 97.*

Ormeni Rr. (2007). The general model of construction of the Albanian earth crust and its seismoactive feature according to the seismological data, *PhD thesis, Tirana.*

Bianko P., Lavecchia G., Milana G. & Rozzi B. Seismogenesis in Central Apenines, Italy: An integral analysis of minor earthquake sequences and structural data in the Amatrice-Campotosto area.

Analysis of Ambient Seismic Noise in Turkey and Surrounding Regions

Samut Cambaz M D (1), Karabulut H (1)

(1) Bogazici University, Kandilli Observatory and Earthquake Research Institute, Istanbul, Turkey didem.samut@boun.edu.tr , kara@boun.edu.tr

Keywords: ambient noise, cross-correlations, surface waves, tomography

Introduction

Seismic velocities in the Earth can be determined from the recordings of active or passive sources using body and surface waves with appropriate arrays. Although active sources are the most traditional ones, the cost and poor S/N ratio in urban areas, limits applicability in the crustal investigations. Seismic waves from earthquakes are also widely used in seismology in order to constitute the images of the subsurface. However the poor path coverage of earthquakes usually provides insufficient resolution. In order to overcome some of the shortcomings of conventional techniques, a new method that is called *Passive Imaging Technique*, has been proposed (Weaver & Lobkis 2001, Derode *et al.* 2003, Snieder 2004, Larose et al. 2004). The method was first tested in ultrasonic and acoustics (Weaver & Lobkis, 2001), then applied in a number of disciplines. Nowadays, surface wave tomography, based on cross-correlations of ambient seismic noise has been applied successfully at local and regional scales (Shapiro & Campillo, 2004, Campillo & Paul 2005)

In this study we used ambient seismic noise to determine the group velocity variations in Turkey and surrounding regions. A waveform database has been formed by using both temporary and permanent broadband stations in the region. A comprehensive noise analysis has been performed in the region in order to understand the spatial and temporal variations of noise. Power spectral densities (PSD) were computed in the frequency range of 0.01 – 10 Hz. Probability density functions (PDFs) as a function of noise power for each of the octave bands have been analyzed for the stations and components. Noise maps have been constructed via the power spectral density estimates of selected stations in order to see the temporal and geographical variations in the region.

Cross correlations of the ambient noise have been calculated to determine the Green's function of station pairs. Group velocity maps were obtained from the calculated Green's function using multiple filter analysis.

Data

In order to study the group wave velocity variations in the region, a waveform catalog has been formed by using three component broadband data from the permanent and temporary stations in and around the region (Figure 1). A temporary broadband network was operated between 1999-2001, with 29 broadband stations during the Eastern Turkey Seismic Experiment (ETSE) (Sandvol et al. 2003). The average station separation was approximately 50 km for the network. Western Anatolia Seismic Recording Experiment (WASRE) operated from November 2002 to October 2003 with 45 short period and 5 broadband stations (Akyol et al, 2006). In this study, only the broadband stations of WASRE network have been used.

TUBITAK operates 7 of the broadband stations in this study. These stations are operating temporarily in the Marmara Region with CMG 40T and CMG 3T sensors. Kandilli Observatory and Earthquake Research Institute (KOERI) have 75 stations operating continuously with different types of sensors. The stations of GEOFON and IRIS/USGS, operating continuously in the region have STS-1 and STS-2 sensors. CHOS station belongs to Aristotle University of Thessaloniki (AUTH) operating continuously in the region with a CMG-3ESP (100sec - 50Hz) sensor.

Figure 1. Permanent and temporary seismic stations used in the study. Permanent stations were operated by KOERI, TUBITAK, GEOFON, IRIS/USGS and AUTH. Temporary network of The Eastern Turkey Seismic Experiment (ETSE) stations were operated from October 1999 to August 2001. Western Anatolia Seismic Recording Experiment temporary stations were operated from November 2002 to October 2003.

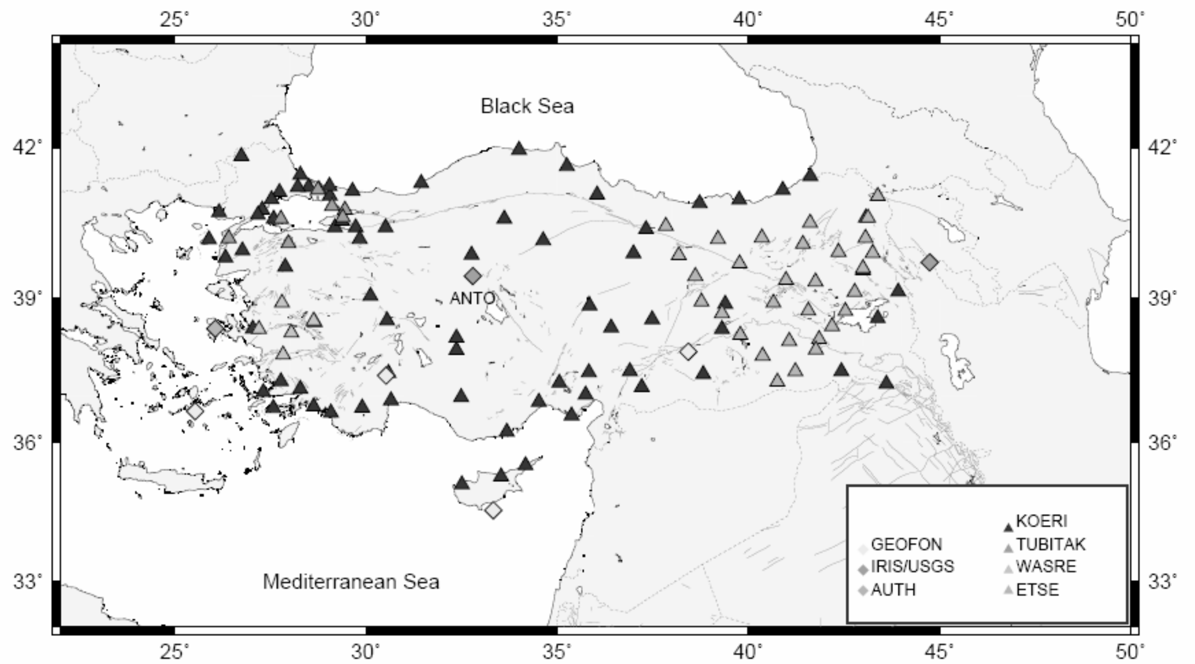

Power Spectral Density (PSD) Method

The station distribution which was used in this study is shown in Figure 1. A waveform database containing 125 broadband stations were formed. The stations consisted of different types of sensors and sampling rates. During the pre-processing, the data were down sampled to 20sps for the stations in order to remove the diversities and one hour-long data segments have been constructed. In the data processing step, a method was used as described by McNamara & Buland (2003) and McNamara & Boaz (2005). Neither the earthquakes nor the system transients and data glitches were removed in the processing.

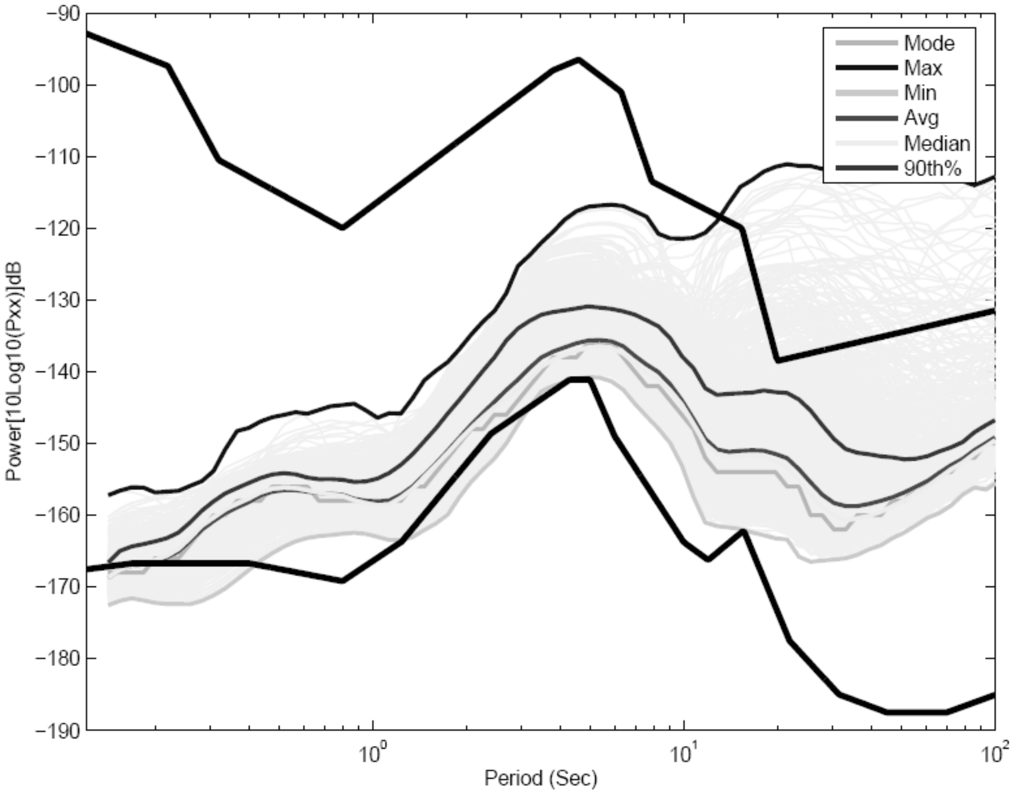

Figure 2. Power spectral densities for ANTO station BHZ component for day time hours. Green curves indicate individual PSD function for each hour. Thick black lines show high and low noise levels of Peterson. Different colors indicate the statistical variations such as Mode, Maximum, Minimum, Average, Median and %90th percentile.

The first step in the processing was to remove instrument response, mean and long period trends, which was followed by computing the power spectral densities. The power spectral density estimate for each hour recording has been computed by using the Welch technique (Welch, 1967). The Welch technique estimates the power spectral density of the input signal using Welch's averaged modified periodogram. In this technique, the time series data has been segmented into sections of equal length, with a definite overlap. Each segment has been windowed with a window that is the same length as the segment. The power spectral density curves plotted for each station as a function of period (sec) to decibel (dB) with respect to acceleration $(m/s^2)^2$/Hz. The lowest and the highest noise levels of Peterson (Peterson, 1993), has been also plotted for the noise levels comparison. After all, segments were averaged to provide a PSD for each one-hour time series. Raw frequency distributions were constructed by gathering individual power spectral densities by binning periods in 1\8 octave intervals and binning the power in 1dB intervals. Each raw frequency distribution bin was normalized by the total number of PSDs for constructing a Probability Density Function (PDF). The probability of occurrence of a given power at a particular period was plotted as a comparison to the high and low noise models of Peterson. Statistical properties were also calculated and plotted for a wealthy seismic noise characterization. These properties are the minimum, median, mode, average, maximum and the %90th percentile. A detailed description of the data processing procedure can be found in McNamara & Buland (2003) and McNamara & Boaz (2005).

Spectral densities were calculated for the stations shown in Figure 1 for the year 2007 in the frequency range 0.01 – 10 Hz. Differences in noise spectra due to different installation properties and diurnal, seasonal and geographic variations were investigated. In order to discriminate between the variations of day and night, day-time calculations were performed in

the time period from 10:00 to 18:00 and night-time calculations include time period 22:00 to 06:00. Seasonal variations of seismic noise were computed by averaging power spectral density over quarters for the year of 2007. The PSD calculated from 1 years of data was stacked and statistical properties such as median, mode, average, minimum, maximum and the %90th have been obtained for 3 component recordings.
In Figure 2 the power spectral density estimates of the seismic noise for the vertical component of ANTO station over a period of 1 year for day time hours. The lowest and the highest noise levels of Peterson (Peterson, 1993) were also presented on the figure. Average PSD estimates lie within the highest and lowest noise levels of Peterson.

Geographic variations have been mapped by using average power spectral density estimates for selected period ranges. A kriging algorithm has been used to obtain the maps. In Figure 3, geographical variations of noise were presented for 1s, 4s, and 15s periods. At 1 sec period strong correlation with coastal and populated areas were observed. Seismic noise levels are lower at continental stations. Coastal stations have a higher noise level than continental stations. Variations on 4 sec and 15 sec maps do not show significant perturbations.

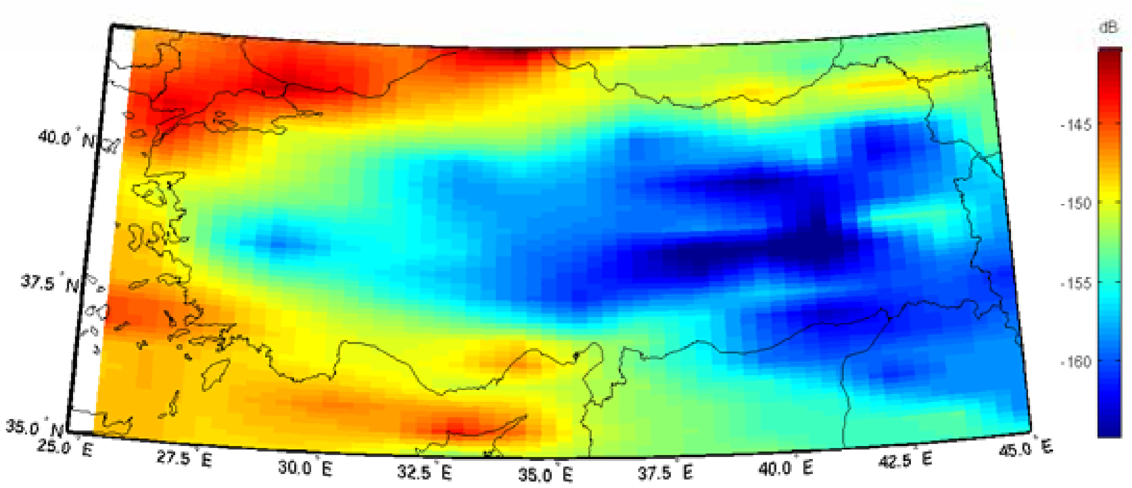

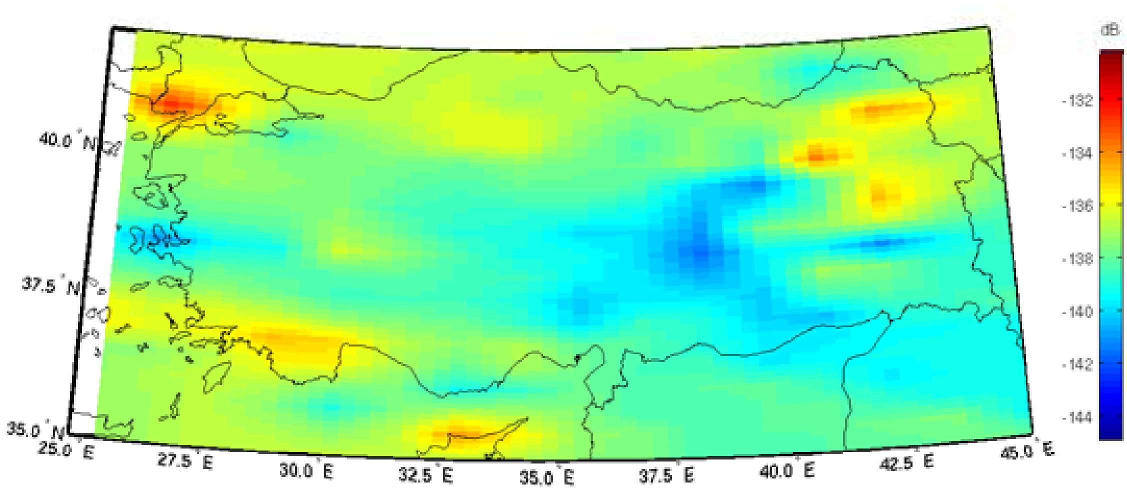

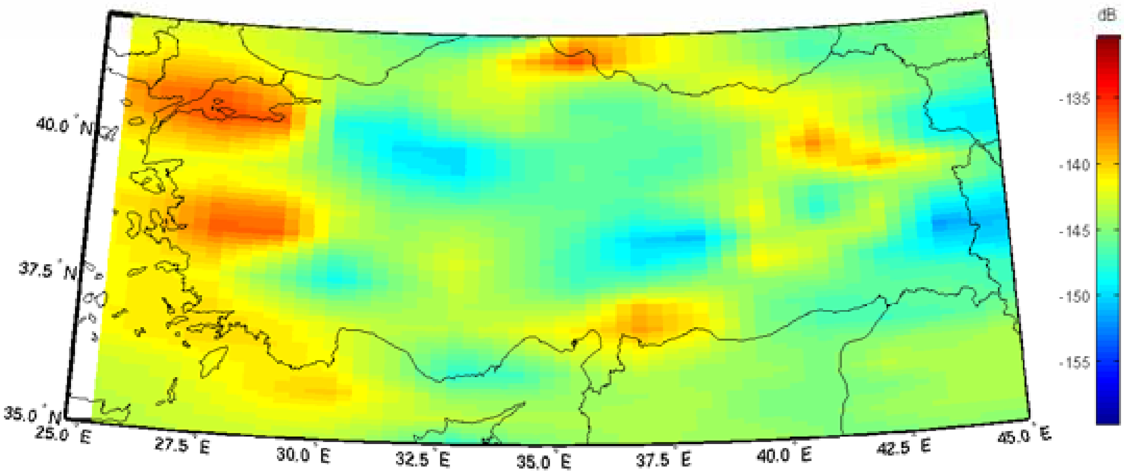

Figure 3. Noise maps created from the power spectral density estimates for 1s, 4s, and 15s periods.

Correlation of Ambient Seismic Noise

The correlation of ambient seismic noise has been studied by a database which has been formed by using 125 stations recording in the region (Figure 1). Data from all the stations in the region has been collected and 12 hour long data segments have been formed for each station. The data processing procedure applied here was similar to the one described at *Bensen et al*. (2007). Raw seismic data have been re-sampled to 10sps and filtered in the period range of 18s to 22s after the mean and trends were removed. Filtered data were then normalized in time, in order to remove the unwanted events such as earthquakes, instrumental irregularities and non-stationary noise sources near to stations (Bensen et al, 2007). In temporal normalization, an automated event detection and removal has been applied. Spectral whitening applied after the temporal normalization. After this single station process completed, cross correlations were computed and stacked to produce 12 months of time series for each station pairs. The resulting cross-correlations contain surface wave signals coming from opposite directions along the path linking the stations that can be related with the energy flux of the waves traveling between these stations (Paul et al, 2005). Figure 4 shows an example of a 1 year stack of vertical component broadband cross correlations plotted with respect to ANTO station. Clear signals can be seen for both positive and negative correlation lags. Group velocity as a function of period can be obtained by applying multiple filter analysis. In this study, however in order to compute group velocities, we calculated envelopes of the signal, and group velocities are simply estimated from the maximum value of the envelope of the signal and distance. More than 3500 station pairs were used to estimate Green's functions.

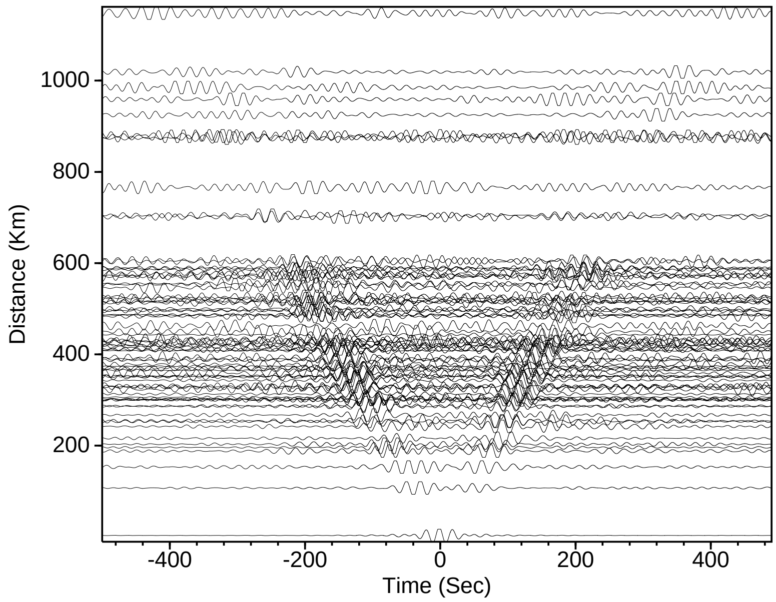

Figure 4. A record section centered at the station ANTO. Cross-correlations are ordered by station distances. Both positive ('causal') and negative ('acausal') lags are shown. Two-sided Green's Functions filtered between 18 and 22 seconds period.

The Rayleigh wave dispersion measurements from one year cross-correlations were used to map at 20 sec period using a method as described in Pasyanos (2005). Grid spacing was 50 km and we used a smoothing parameter of 250. The result at 20 sec period is shown in Figure 5. Rayleigh wave velocities are typically slower at the Mediterranean coast part and in the inner parts of the Anatolia than the other regions such as the Aegean and Black Sea coasts. Higher velocities (>3.5km/s) were found beneath the entire north and west and east parts of the region at 20sec period. Rayleigh waves of this period sample the crust.

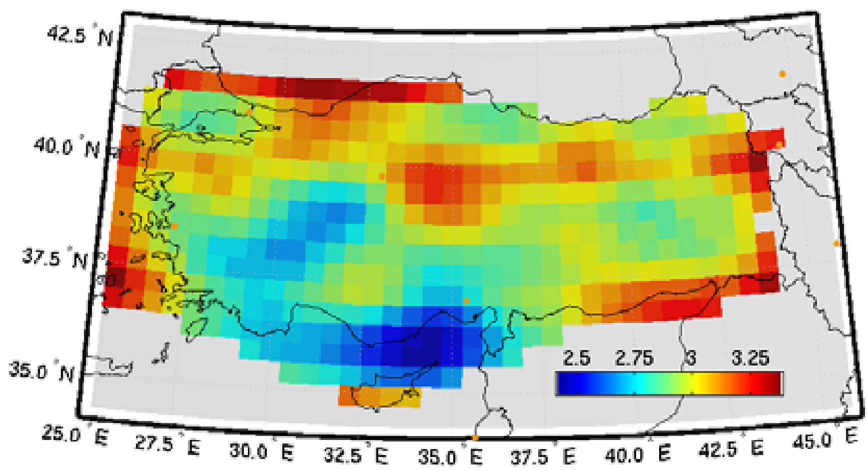

Figure 5. Rayleigh wave group velocity map for 20 sec.

Results and Discussion

A comprehensive noise analysis has been performed for the broadband stations operating in Turkey and surrounding regions. Power spectral densities were computed to determine diurnal, seasonal and spatial variations of noise. Noise maps have been created in the region for having a detailed understanding of the noise characteristics variations. Seismic noise level is lower at continental stations than the coastal stations. This variation is more visible at especially 1 sec noise maps. There are weak variations at 4 and 15 sec maps in the range of a few dB.

Correlation of ambient noise has been studied in order to determine Green's function between station pairs. Continuous data from both permanent and temporary stations recorded in the region has been used for the analysis. One year cross-correlations are used to invert for group velocity maps at different period ranges using the conjugate gradient method. Variations in group velocity maps can be associated with known geological structures.

Acknowledgements

I would like to thank to Bogazici University Kandilli Observatory and Earthquake Research Institute and also to TUBITAK for providing me the data for this study. Data of the temporary broadband stations used in this research were downloaded from the continuous ftp database of the IRIS Data Management Center. Data of the permanent broadband stations used in this research were downloaded from Orfeus Data Management Center.

References

Akyol N., Zhu L., Mitchell B.J., Sozbilir H. & Kekovali K (2006). Crustal Structure and Local Seismicity in Western Anatolia*, Geophys. J. Int., 166/3, 1259-1269*

Bensen G.D., Ritzwoller M.H., Barmin M.P., Levshin A.L., Lin F., Moschetti M.P., Shapiro N. M. &Yang Y. (2007). Processing seismic ambient noise data to obtain reliable broadband surface wave dispersion measurements, *Geophys. J. Int., 169, 1239-1260*

Campillo M. & Paul A. (2003). Long range correlations in the seismic coda. *Science, 299, 547-549*

Derode A.E., Tanter L.M., J de Rosny, Tourin A., Campillo M. & Fink M. (2003). Recovering the Green's function from field-field correlations in an open scattering medium. *J. Acoust. Soc. Am*., *113.*

Larose E., Derode A., Campillo M. & Fink M. (2004). Imaging from one-bit correlations of wideband diffuse wave fields, *J. Appl. Phys. 95, 12.*

Lees M.J. & Crosson S.R. (1989). *Tomographic Inversion for Three-Dimensional Velocity Structure at Mount St. Helens Using Earthquake Data, J. Geophys.Res., 94, 5716-5728*

Lin F.C., Ritzwoller M.H., Townend J. & Bannister S. (2007). Ambient Noise Rayleigh wave tomography of New Zealand, *Geophys.J.Int.*

McNamara D. & Buland R.P. (2003). Ambient Noise Levels in the Continental United States, *Bull.Seism.Soc.Am*.

McNamara D. & Boaz R.I (2005). Seismic Noise Analysis System: A Stand-Alone Software Package, *Preprint for a USGS Open File Report*, *ver2.0*

Pasyanos M.E. (2005). Avariable resolution surface wave dispersion study of Eurasia, North Africa, and surrounding regions, *J.Geophys.Res. Vol.110.*

Paul A., Campillo L., Larose M.E. & Derode A. (2005). Empirical synthesis of time-asymmetrical Green functions from the correlation of coda waves, *J. Geophys. Res*., 110

Peterson (1993). Observation and modeling of seismic background noise, *U.S. Geol. Surv. Tech. Rept., 93-322, 1-95.*

Sandvol E., Turkelli N., Barazangi M. (2003). The Eastern Turkey Seismic Experiment: The study of a young continent – continent collision, *Geophys. Res. Lett.*

Shapiro N.M.& Campillo M. (2004). Emergence of broadband Rayleigh waves from correlations of the ambient seismic noise, *Geophys. Res. Letters, 31, L07614.*

Sneider R. (2004) Extracting the Green's function from the correlation of coda waves:A derivation based on stationary phase, *Physical Review*, 69.

Weaver R.L. and Lobkis O.I. (2001). Ultrasonics without a source: thermal fluctuation correlations at MHz frequencies, *Phys. Rev. Lett. 87, 134301.*

Welch P.D. (1967). A direct digital method of power spectrum estimation, *IBM J. Res. Develop. 5, 141.*

Yang Y. & Ritzwoller M.H. (2008). The characteristics of ambient seismic noise as a source for surface wave tomography., *Geochemistry Geophysics Geosystems, 9.*

Yang Y., Ritzwoller M.H., Levshin A.L. & Shapiro N.M. (2007). Ambient noise Rayleigh wave tomography across Europe, *Geophys. J. Int., 168, 259-274.*

Small aperture array MIKHNEVO as part of seismological observations on the East-European Platform

Sanina I A (1), Gabsatarova I P (2), Chernykh O A (1), Riznichenko O Yu (3), Volosov S G (3), Nesterkina M A (1), Konstantinovskaya N L (1)

1) Institute of geospheres dynamics RAS, Leninsky prosp., 38/1, Moscow 119334, Russia, irina@idg.chph.ras.ru
(2) Geophysical Survey RAS, Lenina 189, Obninsk, Kaluzhskaya reg.,Russia, ira@gsras.ru
(3) Institute of Physics of the Earth RAS, B.Gruzinskaya 10, Moscow 123995, Russia, riznichenko@ifz.ru

Keywords: seismicity, East-European platform, small aperture array

Introduction

Seismic monitoring of the territory of the East-European Platform is part of the complex study of dynamics of tectonic processes, man-made influence and geo-ecological effects [Malovichko et.al., 2007]. Observation of weak seismicity allows accumulating large amount of statistically reliable data in comparatively short time period. Together with different other geophysical data and geological background knowledge it can be used for the purposes of detailed seismic zoning.

Modern seismological monitoring of the EEP is carried out by Geophysical Survey of Russian Academy of Sciences (GS RAS) in close contact with different regional organizations, including academic and university research units. Digital stations SDAS [Digital seismic station, 2004], provided by GS, make the basis of this observational system and are operated by regional staff. Local networks and processing centers are set up near the Russian cities of Voronezh, Perm, Saint-Petersburg, and Arkhangelsk.

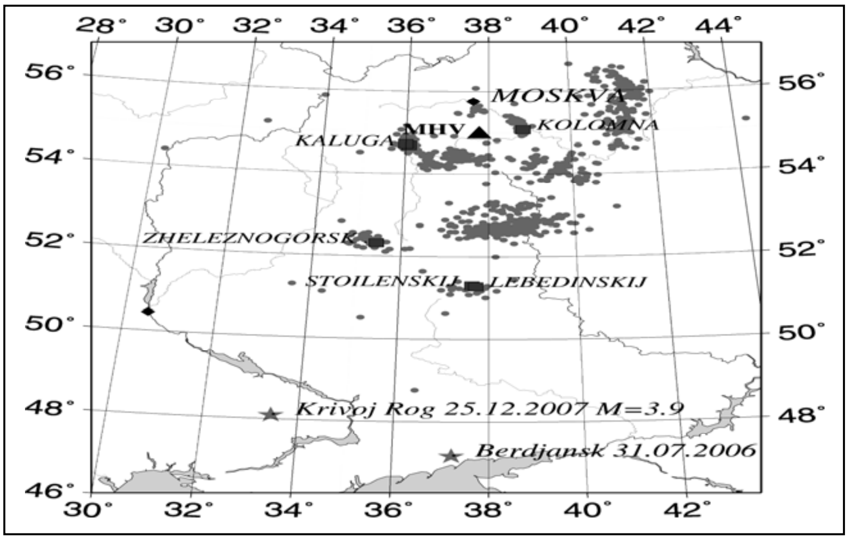

Figure 1. Position of MIKHNEVO array in the central part of the East-European platform, together with the main quarry sites (dots) and recently recorded earthquakes (stars).

Seismic events are indicators of geodynamic activity of the territory. The experience of seismic observations on the East-European platform proves that the magnitude of most events does not exceed M=2.5 – 3. Recording of these events requires sensitive instruments and dense networks in the studied area.

The resolution property of the observational network with separated 3-component stations in the urban area is usually rather low, especially in the central part of the East-European platform. It can be enhanced by integration with a local small aperture array in order to suppress industrial noise in highly populated area. In 2004 Institute of Geospheres Dynamics RAS (IDG RAS) installed a small aperture array of a NORESS type MIKHNEVO (MHV) near Moscow [Adushkin et al., 2004, 2005]. The two existing stations in the central part of the EEP are Moscow (MSC) and Obninsk (OBN). They are situated within the cities with growing population and industrial activity and have restricted capability in recording low magnitude events contaminated by high level ambient noise.

Preliminary results of integration of small aperture array MIKHNEVO into EEP monitoring system are presented.

Materials and Methods

MIKHNEVO is situated in the quiet area of the Moscow region, 80 km to the south of Moscow (Figure 1). Traditionally seismic arrays of this type are installed on rock massifs with little thickness of sediments (less than 10 m). The main feature of MIKHNEVO is that the constantly operating small aperture array is installed in the region with the presence of sedimentary cover 1.5 -2 km thick. Nevertheless systematic measurements of the short period noise spectra were carried out during the year period at MHV and showed comparatively low level. The average value of microseism noise spectral density for displacements is equal to 2 nm^2/Hz at 1 Hz, which is comparable to array conditions at other sites.

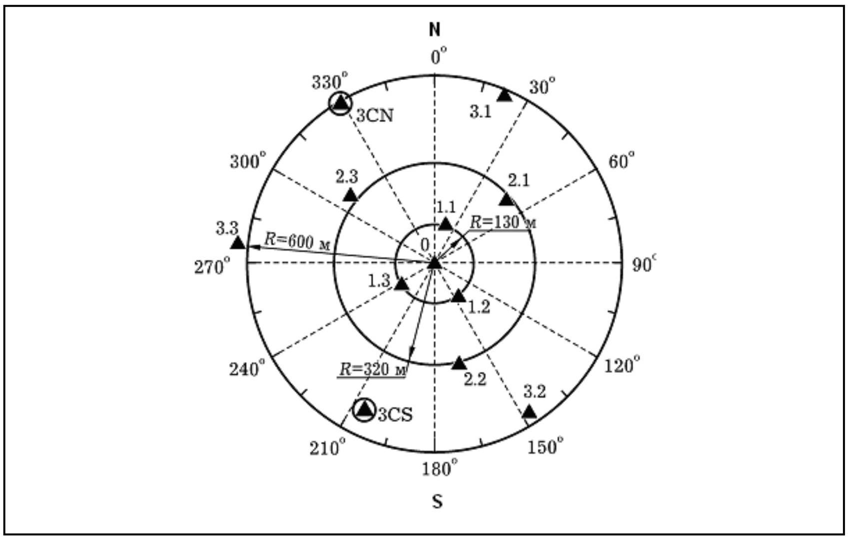

Figure 2. Array configuration. Small triangles denote vertical components. Triangles in circles refer to 3-component stations.

The frequency band of recording is 0.5-40 Hz. Analog-to-digital converter is 24-level. Sampling is 200 Hz. Dynamic range is about 96 dB.

Characteristics of co-array and energy characteristics of array directivity (Figure 3) provide the uniform azimuth coverage of recorded signals [Sanina et al., 2007].

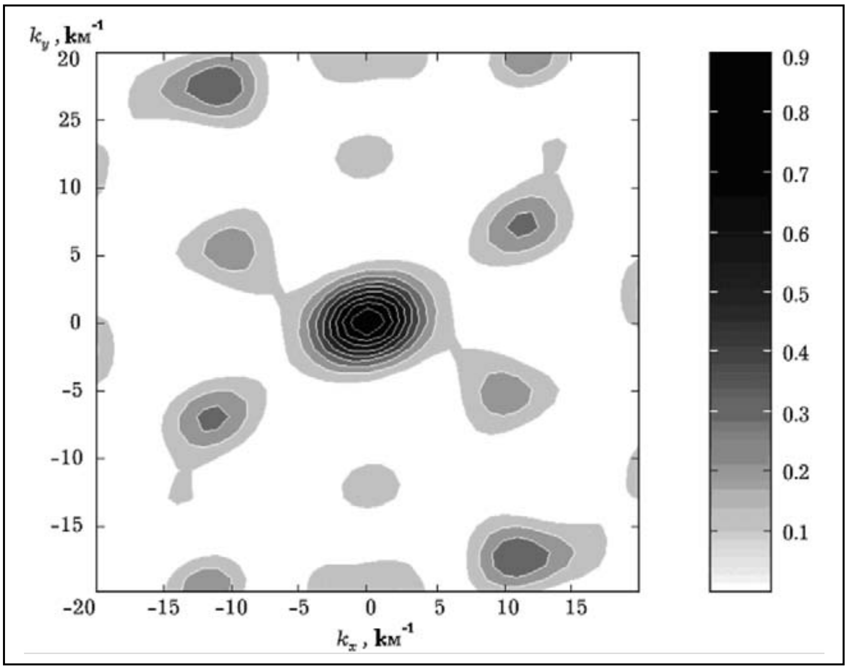

Figure 3. Energy characteristics of array directivity.

MHV performs location of the regional events according to the P-S time difference and azimuth of the recorded signal. Figure 4 shows very high coherency of waveforms of teleseismic events recorded by vertical channels of the array. Dynamic properties of the signal are used for the estimate of local event magnitude.

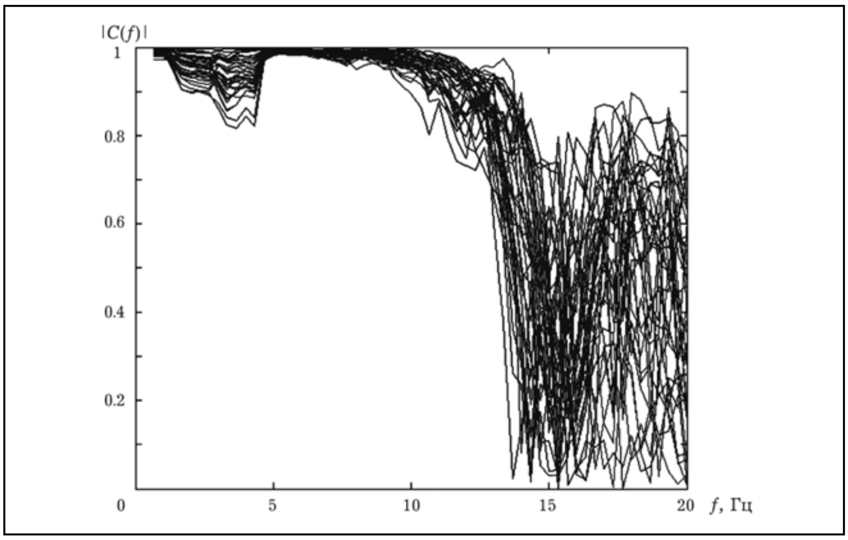

Figure 4. Coherency plot of Sumatera, 2004 earthquake records.

Magnitude Estimates

One of the most important aspects of seismic monitoring is estimation of magnitude level for events of different origin. Magnitude evaluation techniques were previously worked out in GS RAS for the seismic active regions of Northern Eurasia, and are not applicable to EEP conditions. At present regional seismic research groups are working on local magnitude scales taking into consideration the attenuation law at small distances from the epicenter [Malovichko & Ivanova, 2006]. At MIKHNEVO we applied the method, conventionally used by CTBT IDC, which is based on array data analysis. We used the formula for calculation of local magnitude for the events at regional and local distances from the epicenter ($\Delta<15^o$). First Pg or Pn arrivals are used for M_L estimations. Large explosions at Kursk mining area and seismic events in Crimea and Caucasus at epicentral distances up to 12 degrees were processed to construct local magnitude scale. Local magnitude in MIKHNEVO is therefore calculated through the formula: $M_L = \lg A + 1{,}96 \cdot \lg\Delta + 0{,}18$, where lgA equals $0{,}5 \lg (A_{STA}^2 - A_{LTA}^2)$; A_{LTA}^2 is the mean square amplitude in a long window before the first arrival (its length is not less than 10 s), the mean square amplitude of microseism noise, respectively. A_{STA}^2 - is the mean square amplitude in a short window before the first arrival. The length of short window is selected as 2.5 s. Amplitudes are measured in nm/s [Chernykh & Sanina, 2007].

Results and Discussion

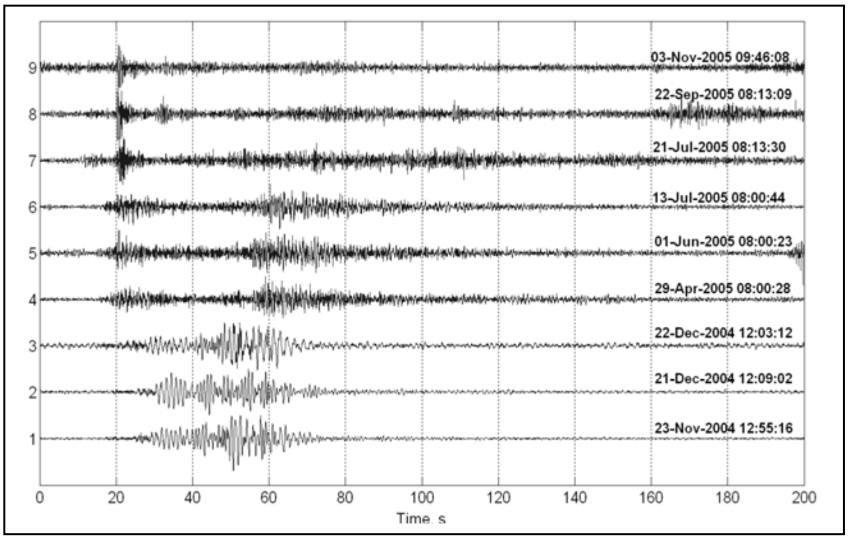

Figure 5. Characteristic waveforms for three quarries: 1-3 - Kolomna1; 4-6 – Kolomna2; 7-9 - Lebedinsky (see Figure 1).

Identification Problem

More than two thousand regional seismic events besides the teleseismic ones have been recorded since the installation of small aperture array in 2004. Different available criteria have been applied to seismic records to identify natural tectonic events and industrial explosions. Previously these criteria have been worked out for identification of chemical explosions and earthquakes in Kirgizia (criteria K) for the epicentral distances 40-400 km, and for classifying of nuclear explosions in Semipalatinsk for the epicentral distances 180-2000 km (Criteria S) [Gamburtseva et al., 2006]. Criteria K uses the S/P amplitude ratio, while criteria S includes parameters Tp and Ts (P- and S-wave predominant periods) and S/P amplitude ratio, corrected for the epicentral distances. Additional analysis of spectral content, day-time distribution, recurrence and clustering of events has been carried out. It was concluded that major part of the recorded events belong to the industrial explosions (quarry blasts). Despite large differences in waveforms, caused by the influence in explosion techniques, explosive positioning in space and depth, we were able to identify eight quarries with regular repeated waveforms of explosions, located at distances 15 to 450 km from array site. The waveform portraits of these explosions are best recognized in 5-minute time window record, thus making possible visual identification of the most characteristic man-made seismic signals. Figure 5 shows characteristic waveforms for three quarries located at distances 110 km, 119 km, and 120 km, which can be immediately identified by the operator.

Tectonic Seismic Events on EEP

According to paleo-seismic data and historical records earthquakes of medium magnitude were not seldom on EEP. Natural seismicity on EEP exists, and it is proved by more than 40 seismic events of tectonic origin in the area with magnitude 1.5≤M≤4.5 recorded by GS RAS during the period 2004-2007. The geography is varying from Rostov region, Salsk ,2001 to Kaliningrad region,2004, where the biggest events observed on EEP during this period happened. Moderate earthquakes occurred in 2004 in Donbass, in Kirovsk region in 2000 and 2005, also in Voronezh crystalline massif and Azov Sea area. More weak events were recorded near Arkhangelsk, on the Baltic Shield and on the Kola Peninsula [Earthquakes in Russia, 2003-2005]. All the recorded earthquakes have been carefully analyzed by GS RAS using additional data from international seismic networks. The recorded signal is processed with the help of modern methods and techniques, enhancing the quality of records [Malovichko et.al., 2007]. The complexity of the record and hence the non-adequate estimation of source parameters of weak local events is hidden in the complex structure of the uppermost lithosphere and in the high level of industrial noise inevitably present in densely populated area of the European part of Russia [Sanina et.al., 2006].

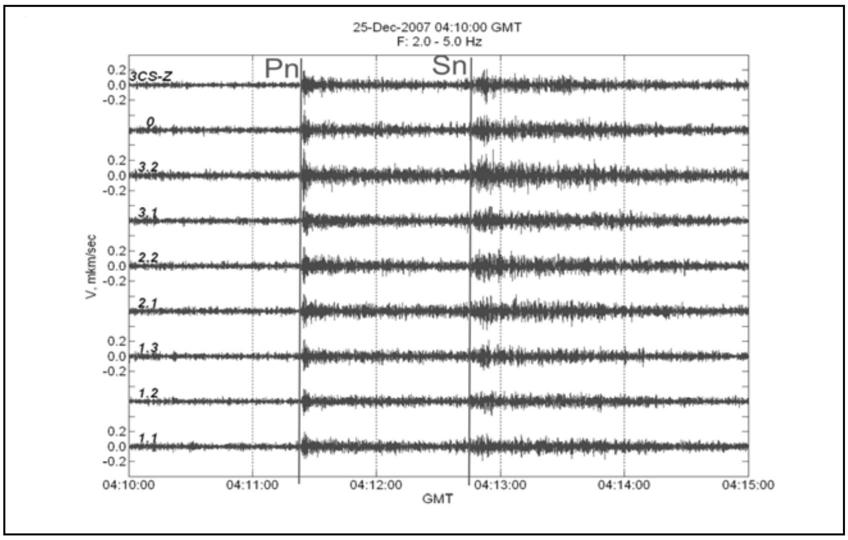

Figure 6. Krivoy Rog earthquake as recorded by vertical short-period channels at MIKHNEVO

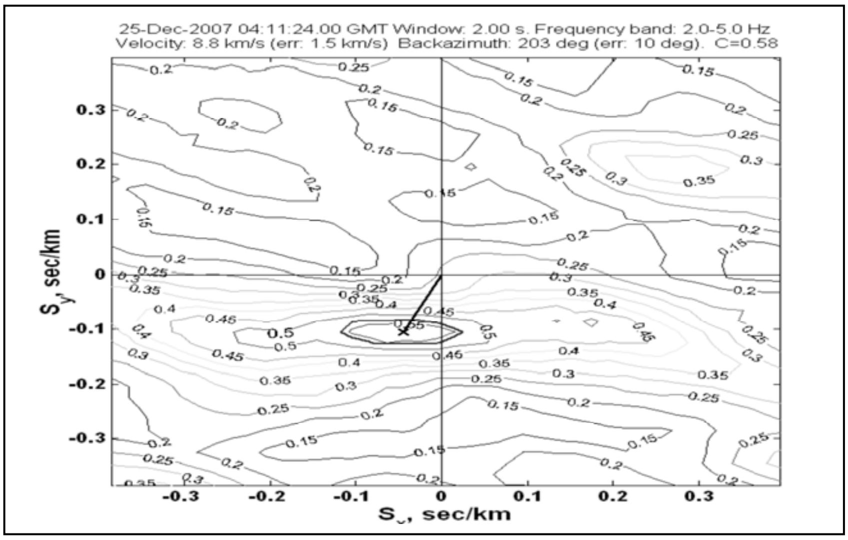

Figure 7. F-K analysis of Krivoy Rog earthquake waveforms, 25.12.2007.

The first efforts to integrate results of small aperture array observations into the regular EEP seismic monitoring have been made. MIKHNEVO array provides high quality coherent data on seismic events in EEP up to the distances 600-900 km. The most recent event in Krivoy Rog, Ukraine on 25.12.2007, M=3.9, is shown in Figure 6 as recorded by all vertical channels of MHV. Direction to the epicenter is obtained from MIKHNEVO waveforms with the help of F-K analysis with the accuracy 10 degrees (Figure 7). Another identified earthquake occurred in Berdyansk region (M=3.9). These supplementary data are very essential for reliable evaluation of seismic situation on EEP.

Only during the last three months of 2008 two earthquakes with magnitude about ML=4 occured in the territory of EEP: on April 26th, 2008 at 13h 14m in the Western Kazakhstan near lake Shalkar and on May, 29th at 11h 03m, in Republic Tatarija , close to Almetyevsk city. The named areas are near to the largest oil deposits, where operation has been conducted for a long time, and it is still continuing. Therefore the earthquakes can have actually tectonic, as well as induced nature. Huge quantity of the main oil pipelines and gas mains pass through the territory of Republic Tatarija, and such earthquakes can threaten with ecological accident for these places. These facts once again confirm the urgency of research in natural and technogenic seismicity on EEP.

References

Adushkin V.V., Zetzer Yu.I., Sanina I.A.,Ushakov A.L. & Chernykh O.A. (2004). Multifunctional small aperture array MIKHNEVO. In: Geophysical processes in lower and upper spheres of the Earth, *Publ. of IDG RAS, M., 389-392 (in Russian).*

Adushkin V.V., Zetzer Yu.I., Sanina I.A., Nevsky M.V., Riznichenko O.Yu., Ushakov A.L. & Chernykh O.A. (2006). Small aperture seismic array MIKHNEVO in: Geophysics of XXI century, 2005. *Proceeding of 7 Geophysical hearings in the memory of V.V.Fedynsky, Moscow, Nauchny mir, 257-262 (in Russian).*

Chernykh O.A. & Sanina I.A. (2007). Determination of magnitudes of seismic events on the Russian platform. In: Changing geological environment: time-space interacting of endogenous and exogenous processes. *Proceeding of international conference. Kazan, 309-312 (in Russian).*

Digital seismic station SDAS. Description and instructions (2004). *Publ.COME GS RAS, Obninsk, 94 p (in Russian).*

Earthquakes in Russia in 2003 (2006). *GS RAS, Obninsk, p.112*.

Earthquakes in Russia in 2004 (2007). *GS RAS, Obninsk, p.140.*

Earthquakes in Russia in 2005 (2007). *GS RAS, Obninsk, p.180.*

Gamburtseva N.G., Nesterkina M.A. & Chernykh O.A. (2006). Possibility of identification of seismic events recorded by seismic array MIKHNEVO on the Russian platform. In: Dynamic processes in interacting geospheres, *Moscow, IDG RAS, 34-40 (in Russian).*

Malovichko A.A., Gabsatarova I.P., Chepkunas L.S. & Starovoit O.E. (2007).Instrumental seismological observations in the East-European Platform. In: Earthquakes and microseismicity in the problems of modern geodynamics of the East-European Platform. Part.1 Earthquakes (Sharov, Malovichko, Shyukin, Eds.), *Publ. of Karelian Sci.Centre RAS, 14-66 (in Russian).*

Malovichko D.A. & Ivanova Yu.V. (2006). Calibration of the local magnitude scale M_L for the West-Urals region. In: Modern methods of processing and interpretation of seismological data. Proceeding of international seismological school. *GS RAS, Obninsk, 103-107 (in Russian).*

Sanina I.A., Chernykh O.A., Ushakov A.L., Nesterkina M.A., Pylaeva T.S. & Volosov S.G. (2006). Seismic events on the Russian platform from small aperture array MIKHNEVO data. In: Active geological and geophysical processes in lithosphere. *Proceeding of XII international conference.Voronezh (in Russian).*

Sanina I.A., Volosov S.G., Chernykh O.A., Asming V.E., Soldatenkov A.M. & Riznichenko O.Yu. (2007). Synthesis and experimental application of two-dimensional small aperture seismic array MIKHNEVO, *Seismic instruments, 44, 3-16 (in Russian).*

A Review of the Greek Strong Motion Database: Needs, Improvements and Future Development

Segou M(1), Voulgaris N(2), Makropoulos K(3), Stavrakakis G(4)

(1) Department of Geophysics-Geothermics, Faculty of Geology and Geoenvironment, National and Kapodistrian University of Athens, msegou@geol.uoa.gr
(2) Department of Geophysics-Geothermics, Faculty of Geology and Geoenvironment, National and Kapodistrian University of Athens, voulgaris@geol.uoa.gr
(3) Department of Geophysics-Geothermics, Faculty of Geology and Geoenvironment, National and Kapodistrian University of Athens, kmacrop@geol.uoa.gr
(4) Institute of Geodynamics, National Observatory of Athens, g.stavr@gein.noa.gr

Keywords: database, strong motion, Greece, processing scheme.

Introduction

During last decades the rapid progress of strong motion seismology and earthquake engineering practice lead to an increasing number of seismic hazard studies. The multi-parametric nature of these studies implies that the development observed so far is related to a number of components; technical ones such as modern strong motion instruments operation and personal computer's increased processing power, or analytical ones, related with the overall evaluation of the strong ground motion, the advances in processing techniques applied at a the significant number of strong motion recordings and new insights related with seismic rupture propagation.

In this paper we will focus on the importance of the strong motion database itself since it provides the basic seismological data for any seismic hazard study. The paradigm of the Greek strong motion database is a difficult one since it is quite inhomogenous and only few decades long. Since the early 70's strong motion seismology made important steps; mainly analogue recordings provide strong motion data from destructive earthquakes until late 90's when digital instruments replace a number of analogue accelerographs. However the population of the digital instruments is far from being adequate for a country of high seismic risk as Greece.

Concerning digital instruments, some deficiencies observed to certain types of instruments are pointed out and the role of good quality strong motion records, in terms of earthquake and engineering seismology practice, is discussed through the paper.

A secondary purpose of the paper is to introduce the future user of any strong motion database to criteria, for choosing between existing databases and among strong motion records of a unique database, depending on the researcher's needs.

Materials and Methods

The Greek Reprocessed Strong Motion Database (GReD) is a part of the Reprocessed Strong Motion Database (ReD), since the latter contains reprocessed data from around the world.

At the first stages of the GReD' s development a number of 410 analogue strong motion records, provided by Greek institutions, were peer reviewed through the visual inspection of their uncorrected time series in order to make an initial assessment of their quality.
The number of analogue records included finally in GReD corresponds, to 35% of the total number of analogue records primarily inspected, with instrument operator for the selected records being the National Observatory of Athens.

GReD consists of 151 three component analogue (Stavrakakis et al. 1992, Kalogeras & Stavrakakis, 1995, Kalogeras & Stavrakakis, 1998) and 70 digital records (Kalogeras & Stavrakakis, 1999, Kalogeras & Stavrakakis, 2007) of major earthquakes of Greece from 1973 until 2006. Processing techniques have been developed, following standards from institutions and organizations of Strong Motion Seismology, after performing extensive tests, leading to a Matlab-based software under the name Proschema (Segou et al, 2008, under publication).

Spacing errors were found to be quite common in Volume 1 format files as well as misplaced values providing critical earthquake metadata. Through computer code utilization useful parameters have been stored in the form of metadata tables and a more flexible format has been chosen.

To address the inhomogeneity of the database each component was processed individually since digital and analogue recordings suffer from different sources of error. It is noted that, in order to maintain internal consistency, the horizontal components have been processed with the same specifications.

The first step of processing involved the derivation of a quality factor assigned to each record. The identification of rectangular pulses and clipping problems in the majority of analogue recordings refrain us from using further the records above in seismic hazard studies, due to their deficiency to produce credible spectral ordinates or even, in some cases, peak parameter values (Fig.1). Although the Fourier Amplitude Spectrum provides an excellent representation of the frequency content of a record, similar errors, as the aforementioned, can be detected only through the visual inspection of the uncorrected waveform. The evaluation of the quality of analogue records and their meticulous processing made possible to retain a great number of old but useful, recordings in the current database in an improved condition.

Secondly there has been a trivial need of generating equally sampled time series in a significant number of analogue recordings, in order to solve this problem new strong motion records equally sampled were created with step equal to the minimum digitization time interval of the original time series of the V1 format, as disseminated by the provider.

A common sampling rate at 200 samples per second was set from the beginning of the database's development which equals the sampling rate of the digital recordings whereas in analogue recordings the above rate was met after performing oversampling and decimation techniques, improving the overall quality of the latter. In order to prevent pseudo-aliasing phenomena a low pass filter was used when decimation is performed (Karl, 1989, Sherbaum 1996).

Instrument correction has been performed for analogue recordings, since the digital ones have flat response over a wide frequency range, by a second order differential equation which can adjust for the instrument response for frequencies reaching up to ¼ of the Nyquist frequency (Boore and Bommer, 2005); a frequency which is close to the nominal natural frequency of most operating analogue instruments.

The most critical step of any processing scheme lies in filtering of the time series in order to identify and remove the noise contamination and reproduce the actual ground motion.

Filter specifications correspond to a band pass 2p4p (2 pass 4 pole) infinite impulse response filter of Butterworth type implemented in the frequency domain. Acausal implementation is directly connected with bi-directional filtering after padding the original time series. Following comments found in Boore (2005) padding with appropriate number of samples (zero samples in our case) preceded acausal implementation to make allowance for the filter's impulse response.

Especially for the digital A-800 accelerometer of Teledyne-Geotech caution is advised when choosing the low cut off frequency, since its datalogger already includes a 0.1 Hz low cut filter. For the reason above when processing these records either no additional low cut filtering should be performed or the chosen cut off frequency should provide a usable data bandwidth inside the one defined from the previous hardware filtering. In any case, the hardware filtering didn't provide good quality velocity and displacement time series, and the need for choosing a higher frequency was pronounced. It is our belief that in most cases this hardware filtering deteriorates rather than improves the original time series.

Especially for choosing the suitable low cut off frequency, an additional step of visual inspection of acceleration, velocity and displacement time series corresponding to an acausal implementation of five filters with different user-defined cut off's, has been added.

It should be noted that the zero pads are retained throughout the integration for the velocity and displacement time series as well as for calculating Fourier Amplitude spectrum of the corrected acceleration time series and response spectra.

In any processing stage the authors refrain from performing further baseline adjustments since there is no real evidence of the affected frequency band after applying this correction. It is the authors' belief that no additional action, except filtering, for removing long period noise should be performed because this would represent the implementation of a second filter of unknown cut off frequency (Boore & Bommer, 2005).

The final major processing step involves the computation of the response spectra of the corrected acceleration time series with final products being the pseudo acceleration, the pseudo velocity and pseudo displacement for 0, 2, 5, 10 and 20 percent value of the critical damping and for a set of 159 period estimators ranging between 0.01s and 10s.

Since commonly used response measures in strong ground motion prediction equations, depend on the orientation of the sensors as installed in the field, the calculation of the two new measures of geometrical mean GMRotDpp and GMRotIpp, independent of the sensor orientations, as defined in Boore et al. (2006), can be helpful for seismic hazard studies and engineering practice. The calculation of these orientation independent measures is based on a set of geometric means computed from the as-recorded orthogonal horizontal motions rotated through all possible non-redundant rotation angles.

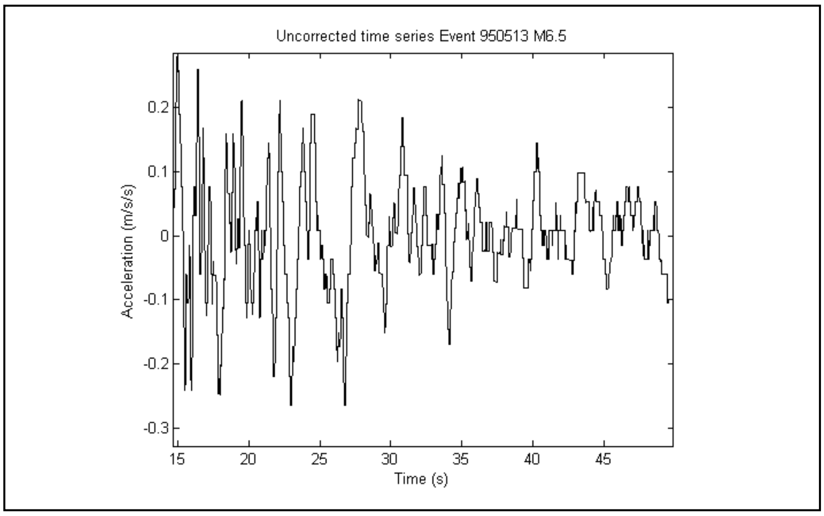

Figure 1. Poor quality strong motion record, not included in the GReD.

Results and Discussion

It is the authors' belief that the processing scheme described previously incorporates basic needs together with advanced techniques, combining principles of digital signal processing and main seismological practice.

The design of stable infinite impulse response filters, now available through the Matlab platform, contributes in preserving the actual frequency content of each recording and provides a well defined usable data bandwidth. It should be also noted that performing major corrections, as instrument and baseline adjustment, is within Proschema capabilities, but a detailed appreciation of the effects of each one on the frequency content of the recording preceded their final implementation.

The GReD consists of more than 250 carefully selected three-component strong motion records according to Volume 1, Volume 2 and Volume 3 format specifications. An additional Volume has been created to incorporate the new spectral measure GMRotI50 (Fig.2) in terms of pseudo acceleration, pseudo velocity and pseudo displacement for 5 percent value of the critical damping. The maximum response spectral ordinate in a single direction (Watson-Lamprey & Boore, 2007), which is found to be useful in some engineering applications, is also available. Although earthquake engineers are often provided with already processed data by engineering seismologists, the first should be able to understand that there is no such thing as corrected values and that spectral ordinates can be subjective, within limits, whereas the second should be able to understand the reason for this subjectivity as well as the influence of their processing approach on the disseminated data. The last two spectral ground measures are proposed for further use in both, seismic hazard studies and engineering practice, so that their contribution would be assessed and lead to a development of common ground between engineering seismologists and engineers.

The secondary purpose of this paper is to draw attention to the importance of choosing the appropriate processing scheme, bearing in mind the needs of the individual researcher, and to point out the sensitivity of spectral ordinates to different processing schemes. For this reason the GReD is provided diversified; the first version corresponds to an database of educational use after processing with pre-specified parameters affecting all strong motion recordings whereas the second version supports elaborate component-by-component processing which addresses each recording's needs and deficiencies. In both cases a suggested usable data bandwidth is clearly stated according to the filter's specifications.

Each strong motion recording is found in a number of formats; either as a binary file, as both a joint couple of binary .mat files containing strong motion data and a processing log for further Matlab use and in SAC format or as an ascii file according to smc format specifications or the format specifications of European Strong Motion Database. It should be also noted that Proschema supports the visualization of the time series in terms on waveforms or Fourrier and response spectra. It is also possible to convert between the aforementioned formats through the utilities of the software.

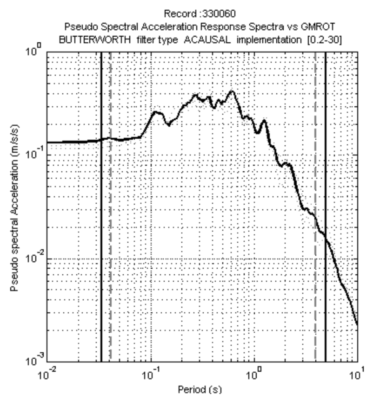

Figure 2. Orientation independent spectral acceleration response spectrum versus standard acceleration response spectra of the horizontal components for 5 percent value of the critical damping.

In the future the growing number of digital recordings is expected to improve the quality of the Greek database, but it is the authors' belief that the combination of both, better quality records and changes in standard processing of the existing strong motion records are necessary for further development of the database. For deriving credible spectral ordinates for period estimators greater than 3s digital recordings are necessary. A significant number of such operating instruments located near well known seismic sources could facilitate the study of hanging wall and directivity effects; improving seismic hazard assessment in the near field.

References

Boore D. & Bommer J. (2005). Processing of strong-motion accelerograms: needs, options and consequences, *Soil Dynamics and Earthquake Engineering, 25, 93-115.*

Boore D. (2005). On Pads and Filters: Processing Strong-Motion Data, *Bull. Seis. Soc. Am., 95, 2 ,745-750*.

Boore D., Watson-Lamprey J. & Abrahamson N. (2006). Orientation-Independent Measures of Ground Motion, *Bull. Seis. Soc. Am., 96, 4A ,1502-1511*.

Kalogeras I.S. & Stavrakakis G.N (1995). Analysis of Greek accelerograms recorded at stations of NOA' s network. Time Period: 1990-1994. *National Obs. Athens, Geodyn. Inst., Publ. No 5, 404p.*

Kalogeras I.S. & Stavrakakis G.N (1998). Analysis of greek accelerograms recorded at stations of NOA's network. Time period: 1994 - 1996. *National Obs. Athens, Geodyn. Instit., Publ. No 7, 152p .*

Kalogeras I.S. & Stavrakakis G.N (1999). Processing of the strong motion data from the September 7th, 1999 Athens earthquake, *National Observatory of Athens, Geodynamic Institute, Publ. No 10 (CD-ROM).*

Kalogeras I.S. & Stavrakakis G.N (2007). Analysis of greek accelerograms recorded at stations of NOA's network. Time period: 2000 - 2006. *National Obs. Athens, Geodyn. Instit., Publ. No 17, 245p.*

Karl, J.H. (1989). An introduction to digital signal processing, *Academic Press, Inc, pp 341.*

Scherbaum, F. (1996). Of poles and zeros, Fundamentals of digital Seismology, *Kluwer Academic Publishers, 256p.*

Segou M., Voulgaris N. & Makropoulos K. (2008). PROSCHEMA: A Matlab based environment for processing strong-motion records, *submitted for publication in the Proceedings of the 3rd PCEEES, 5-7 November 2008, Athens.*

Stavrakakis G. N., Kalogeras I. S., & Drakopoulos J. C. (1992). Preliminary analysis of Greek accelerograms recorded at stations of NOA's network: Time period 1973–1990. *National Observatory of Athens, Geodynamic Institute, Publ. No 4, 430p.*

Watson-Lamprey J.A. & Boore D. (2007).Beyond Sa_{GMROTI} : Conversion to Sa_{Arb}, Sa_{SN}, and Sa_{MaxRot}.*Bull. Seis. Soc. Am., 97, 5, 1511-1524*.

Site Response Studies in Kochi City, Kerala, India

Shanker D (1), Singh H N (2), Neelakandan V N (3), Shravan Kumar V (3), Paudyal H (2), Banerjee M (2), Singh V P (2)

(1) Department of Earthquake Engineering, Indian Institute of Technology Roorkee, Roorkee –247667 Uttaranchal, INDIA, tel: +91-1332-285128; fax: +91-1332-276899/273560, dayasfeq@iitr.ernet.in
(2) Department of Geophysics, Banaras Hindu University, Varanasi 221 005, INDIA, hridaynarain.singh@gmail.com (HNS)
(3) Centre for Earth Science Studies, P.B. No. 7250, Akkulam Trivandrum-695 031, INDIA

Keywords: ambient noise, CityShark seismic recorder, hinterlands

Introduction

It is generally accepted that chances of predicting location, time and magnitude of an impending earthquake is remote, the main emphasis is now shifting to predict the hazard at a particular site. Hence, understanding of the site-specific behaviour is important for the prediction of seismic hazard due to local and/or distant earthquakes. The concept of seismic Microzonation is to identify individual critical areas based on their potential for hazardous earthquake effects. The earthquake generated ground motion is very much dependent on local surficial site conditions. The site response involves the effects of shallow near-surface sedimentary layers on the propagation of seismic waves. Under certain conditions, the character of upper one hundred meters or less of rock and soil beneath any site has more conspicuous effect on the level of earthquake shaking than the magnitude of the earthquake itself. When seismic waves encounter a low-velocity near surface sedimentary layer, three phenomena i.e. increase in amplitude, bending of wave path towards vertical, and the trapping of the waves in the near surface layer take place. These phenomena increase the shaking of the ground locally resulting in increased damage to the man made structures. In view of this, the damage pattern in any particular locality can be forecast with the help of site response data derived through various techniques. The three effects; amplification, resonance and attenuation all depend on the depths and the properties of the sediments (Gibson, 1990). The Nakamura method estimates experimentally the combined effects of these three parameters compared with bedrock motion.

In the present work, we have selected Kochi city of Indian subcontinent for site response studies through measurement of microtremor data and preparation of seismic microzonation map. The city is one among the largest harbour cities in the country and is the main commercial and industrial city of Kerala state with an area of about 100 km^2 (Fig. 1). The city and its surroundings are situated mostly on loose sediments of alluvium, clay, loamy sands, silt, laterites etc. and have vast area of intermittent water bodies. Most of the waterlogged low-lying area has been reclaimed for various developmental activities such as residential, commercial and industrial. This is a fast growing city with high-density population where many high rising buildings have come up during the past few years- the trend is on the increase, which exert tremendous pressure on the limited land resources. Under the circumstances, damage due to an earthquake (local and/or distant large earthquake) could be alarming since such land systems are generally susceptible for amplification of seismic waves. This map would be useful to take precautionary steps in future construction and developmental activities.

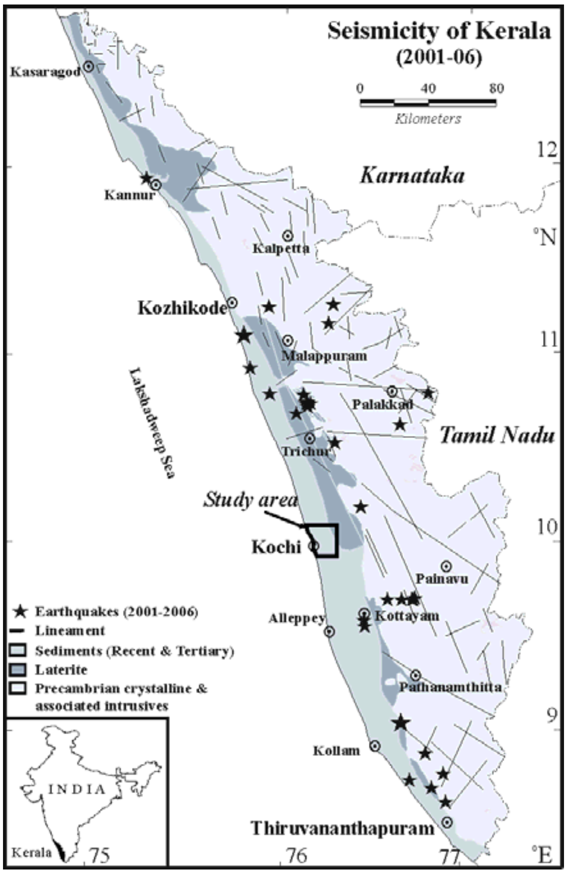

Figure 1. Map of the Kerala state, southwest Peninsular India showing general geology, lineament patterns and seismicity from 2001-06 and the study area in Kochi city in which microtremor data were collected for estimation of site responses for the preparation of seismic Microzonation.

Resonance and amplification in low velocity unconsolidated sediments

Near surface soils modify the spectral response and transmission of energy waves released from a seismic rupture plane. These effects are usually unique to a specific site. Typically rock or stiff soil sites have greater short period response (i.e. greatest energy within the 0-0.4 second range), but experience more rapid decay and lower long period response (Fig. 2). Conversely soft soils may filter (attenuate) some short period response, resonate and therefore amplify excitation when the basement excitation is sympathetic with their own natural period, and have little effect on longer period response (King, 1996). S waves are most destructive in near field (10s of a km) from the hypocenter, whereas surface waves cause most of the damage from far field (> 100s of km) earthquakes. To assess local site effects, the following methods are generally used as response analysis of soil surface in earthquake damage assessment. (1) Multiple reflection theory of elastic response; (2) equivalent linear approach of non-linear response; and (3) other methods (e.g. Matsuoka and Midorikawa, 1994).

Multiple reflection theory of elastic response is the basic method in response analysis (e.g. Haskell, 1960) which explains that ground motion tends to be amplified at soft-soil site. However if incident wave has large amplitude, ground motion at soft-soil site is actually weaker than at stiff site. This phenomenon is called non-linear behaviour of soil and observed when large earthquake occurred, but multiple reflection theory of elastic response cannot explain this phenomenon. In order to take non-linear behaviour into consideration, equivalent linear approach of non-linear response was developed. In earthquake damage assessment, SHAKE (Schnabel et al., 1972) has often been used as equivalent linear approach of nonlinear response, but recently the method which can consider frequency-dependent effect of shear modulus and damping factor, e.g. FDEL (Sugito et al., 1994), is being used widely.

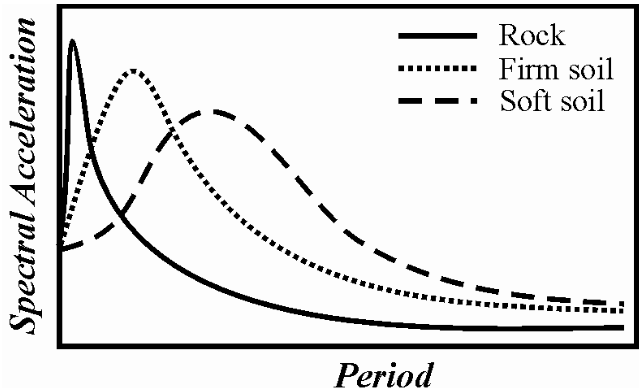

Figure 2. Site influence on spectral response (King, 1996).

On the other hand there are simple methods for evaluating site amplification factor. For example, Matsuoka and Midorikawa (1994) can calculate site amplification factor from geomorphologic unit or geology, altitude and the shortest distance from a river. The advantage of this method is that it does not need detailed parameters about soil, which is derived through field investigation such as drilling. On the other hand, the disadvantage is that it cannot explain non-linear behaviour of soil.

Records of ambient noise (microtremor) have been used widely for site response studies (Nakamura, 1989; Lermo et al, 1988; Brady, 1999; Gamal, 2001; Mukhopadhyay et al, 2002, Mukhopadhyay and Bormann, 2004; Singh et al., 2007). In seismic microzonation one has to estimate the variation in seismic response of the subsurface and subsequently delineate the zones where the soil induced amplification exceeds to certain level that may damage the buildings or other structures at that location. Frequently peak ground acceleration is used to determine the maximum horizontal forces that can be expected at a site. However, merely determining the spatial variation of peak ground acceleration is not adequate, because peak acceleration often correspond to high frequencies, which are out of range of the natural frequencies of most structures. Therefore, large values of peak ground acceleration alone can seldom initiate either resonance in the elastic range or be responsible for large scale damage in the inelastic range (Singh, 1995). In this paper, we have used resonance frequency and site amplification data in Kochi City and delineated the zones with appreciable ground motion amplification that may result damage to the engineering structures (Table 1).

Field surveys and instruments used

Microtremor recording in Kerala was carried out by employing a CityShark II 3-component Seismic Recorder, a Lennartz LE-3Dlite triaxial active geophone with 1 Hz natural frequency, and a handheld Garmin GPSMAP 76S (for station location). About 1000 sites were occupied in 100 days period spread over 7 months from February-August 2005 in Kerala state. In Kochi city (76.18°-76.43° E; 9.82°-10.08° N), 988 sites were occupied which are distributed in an area 28 km x 29 km. Finally, 924 microtremor data were found suitable for the site response studies and the preparation of seismic microzomation map. The microtremor records were obtained from varied geological setup such as beach sectors, islands, backwater zones, laterites and charnocknites formations.

Estimation of site response parameters

H/V technique developed by Nakamura (1989) was used for estimating site response parameters for seismic microzonation for Kochi city. The data processing and estimation of site response parameters were carried out using J-SESAME software (version 1.08) developed under European Project SESAME 2000-2004 (SESAME European project 2003, 2004) for microtremor data processing. H/V (Fig. 3) is computed by merging the horizontal (NS and EW) components with a geometric mean option.

Table1: Estimated site response data used for the seismic microzonation map for the Kochi city with five classes of resonance frequency.

Delineated Seismic zones	Total area of Microzones (km^2)	Resonance frequency (Hz)	Site amplification
Microzone III	**175.8**	**<1.1**	**<5.1, 5-10, >10**
Microzone II	**155.7**	**1.1-3.0, 3.1-5.0**	**<5.1, 5-10, >10**
Microzone I	**188.6**	**5.1-10.0, >10.0**	**<5.1, 5-10, >10**

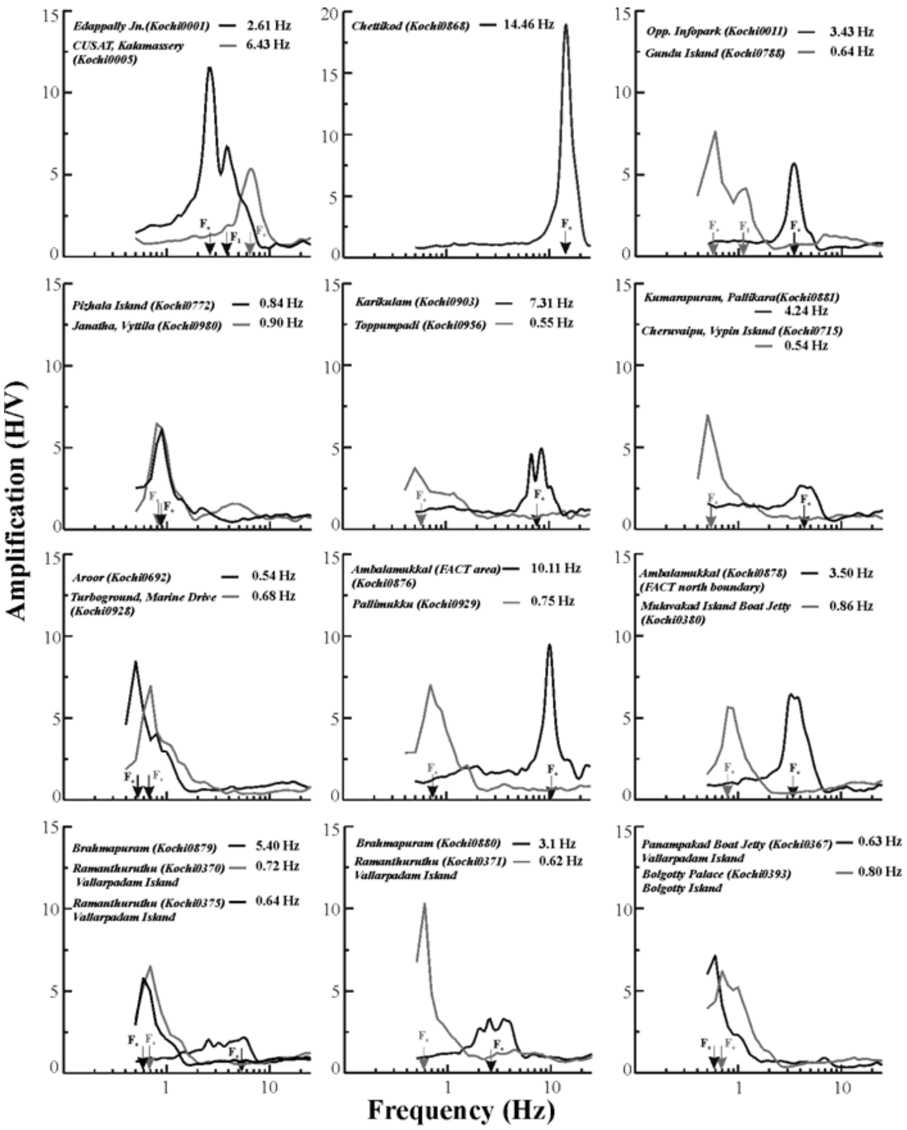

Figure 3: H/V spectral ratio for the merged horizontal components observed at 24 sites in the Kochi city. Fo is the resonance frequency pertaining to first peak at which maximum site

amplification is observed whereas F_1 is the frequency associated with second peak (in certain cases only) in H/V curve.

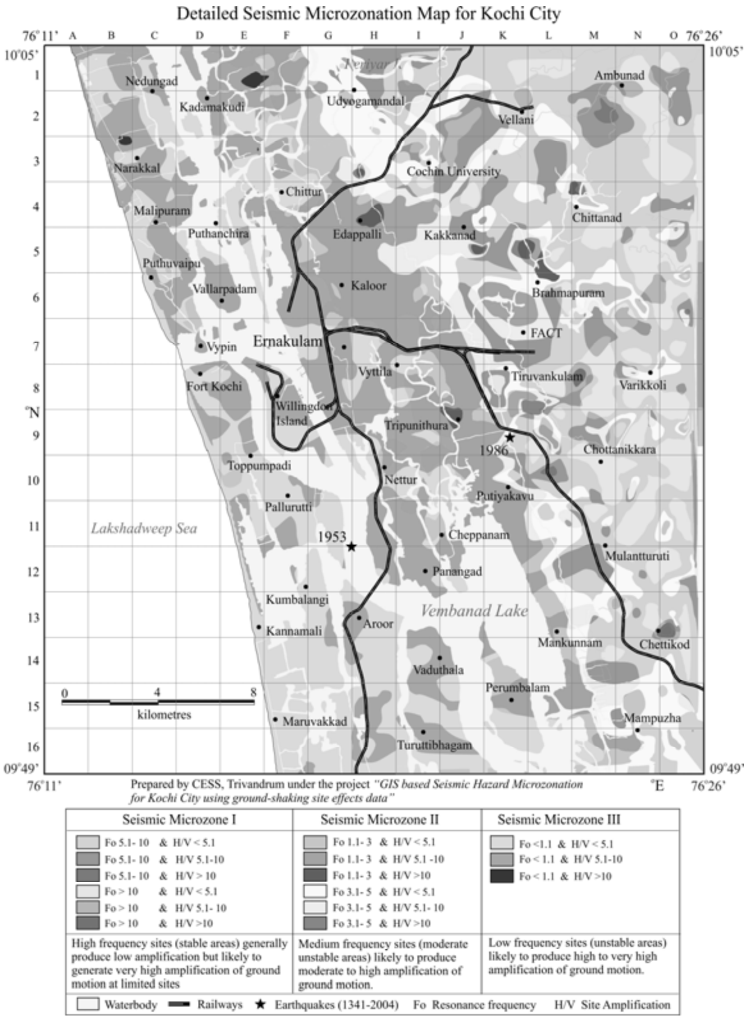

Figure 4. Seismic microzonation map for Kochi city prepared using five classes of resonance frequency (Fo <1.1; 1.1-3.0; 3.1-5.0, 5.1-10.0 & >10.0 Hz) and three classes of site amplification (H/V <5.1; 5.1-10.0 & >10.0). Major portion of the study area (western portion) falls in Seismic Mocrozone II & III which are liable to deliver high level of ground amplification in an earthquake.

Seismic microzonation

Seismic microzoning is the usual procedure to have the local effects taken into account for engineering design and land-use planning, and it is an useful tool for earthquake risk mitigation. Site response parameters (resonance frequency and amplification) estimated in the present work is used for the preparation of seismic microzonation map for the Kochi city. The details such as class intervals of resonance frequency and site amplification used for preparing microzonation map and the area of individual identified microzones are furnished in Table 1. Microzones I and III (Fig. 4) occupy the easternmost and westernmost part of the study area whereas Microzone II is sandwiched between them. These three microzones are distinct in their site response characteristics and are elongated in NW-SE direction parallel to the west coast.

Microzone III is characterized by low resonance frequency (≤ 1.0 Hz), Microzone II with medium level of resonance frequency (1.1-5.0 Hz) and Microzone I has highest level of resonance frequency more than 5 Hz. Though the average level of site amplification (H/V) is more in Microzone III, there are certain scattered pockets of similar nature in Microzones I and II. Longest characteristic site periods more than 6.3 sec. for Microzones III, medium period 1.2-6.3 sec. for Microzone II and minimum of less than 1.2 sec. for Microzone I were estimated. This information suggests that buildings and structures in Microzone III have highest probability to achieve resonance as compared to Microzones II and I when the natural frequency of ground motion resulting due to an earthquake matches with that of the natural frequency of structures. This investigation indicates that the entire Microzone I and the adjoining portion of Microzone II are comparatively safer as compared to the remaining areas comprising of Microzones III and II.

Discussion and conclusion

The whole effort of collecting microtremor data, in the present case, showed that the use of CityShark for microzoning saves a considerable amount of time and provides quick and reliable estimates of resonance frequency and site amplification. It is inferred that the resonance frequency estimated through closely spaced interval microtremor data are very useful to identify boundaries of different geological formations that play a vital role in amplifying ground motion. Hence, understanding of site-specific behaviour is important for the prediction of seismic hazard (Singh et al., 2004) due to local and/or distant earthquakes. The distribution pattern of resonance frequency and site amplification show that soft soils with thick sedimentary columns (tidal, fluvial and palaeo beach deposits) in and around the coastal belt and backwater zones are invariably associated with low resonance frequency and are likely to amplify ground motion greatly that may result in relatively more damage. On the other hand, the eastern portion of the study region covered with charnockite and laterite exhibit high resonance frequency and may not amplify ground motion much. In such areas, damage will be limited. But strong amplification may occur in scattered sites having undulating topography and basement

Seismic Microzones I, II and III identified from the microzonation map have different Characteristics. Seismic Microzone I indicates High frequency sites (stable areas) generally produce low level site amplification but likely to generate very high amplification of ground motion at limited sites; Seismic Microzone II Medium frequency sites (moderately unstable) likely to produce moderate to high amplification of ground motion while Seismic Microzone III: Low frequency sites (unstable areas) likely to produce high to very high amplification of ground motion.

Aknowledgements

First author is thankful to head department of earthquake engineering for providing necessary facilities for the computational works. Second, third and fourth authors are grateful to the Kerala State Council for Science, Technology & Environment for providing financial support to carry out the project work. These authors are also indebted to the Director, CESS for extending necessary support to carry out this work.

References

Bard P.Y (1999). Microtremor measurements: a tool for site effect estimation ?, State-of-the-art paper, Second International Symposium on the Effects of Surface Geology on seismic motion, Yokohama, December 1-3, 1998, Irikura, Okada & Sasatani (eds.), *Balkema, 1999, 3, 1251-1279.*

Gamal M.A (2001). Seismic hazard analysis of Egypt and seismic microzonation of the Greater Cario based on empirical and theoretical models, PhD. *Faculty of Acience, Geophysics Dept. Cario University Egypt.*

Gibson G. (1990). An Introduction to seismology, in conference on the Newcastle Earthquake, Newcastle, *15-17 Feb. 1990*

Haskell N. A (1960). Crustal reflection of plane SH waves, *J. Geophys. Res., 65, 4147-4150*

King A. (1996).The fundamentals of an earthquake standard *in proceedings of a seminar held by the Australian Earthquake Engineering Society, Adelaid, S.A., 8-15.*

Lermo J., Rodriguez M. & Singh S.K (1988). Natural periods of sites in the valley of Mexico from microtremor measurements and strong motion data, *Earthquake Spectra, 4, 805-814.*

Matsuoka M. & Midorikawa S. (1994).The digital national land information and seismic microzoning, 22nd symposium of earthquake ground motion*, 23-34 (in Japanese with English abstract).*

Midorikawa S., Matsuoka M. & Sakugawa K. (1994). Site Effects on Strong-Motion Records Observed during the 1987-Chiba-ken-toho-oki, Japan Earthquake, *Proc. Ninth Japan Earthq. Engnrg. Sympo., E085-E090.*

Mukhopadhay S., Pandey Y., Dharamraju R., Chauhan P.K.S., Singh P. & Dev A. (2002). Seismic Microzonation of Delhi for ground shaking site effects, *Current Science, 82 (7), 877-881.*

Mukhopadhyay S. & Bormann P. (2004). Low cost seismic microzonation using microtremor data: an example from Delhi, India, *Jour. of Asian Earth Sciences*, *24, 271-280*.

Nakamura Y. (1989). A method for dynamic characteristic estimation of surface using microtremor on the ground surface, *Q. Rep. Railw. Tech. Res. Inst. (Tokyo), 30, 25-33.*

Schnabel P.B. Lysmer J. & Seed H.B. (1972). SHAKE a computer program for earthquake response analysis of horizontally layered sites, *EERC, 72-12.*

SESAME European project (2004): J-SESAME *User Manual, Version 1.08.*

Singh J.P (1995). Lecture notes for "Seismic Loading: Code Versus Site Specific" presented at a "*Portland Regional Seminar on Seismic Engineering Issues" in September, 1995*.

Singh H.N, Neelakandan V.N. & Shravan Kumar V. (2007). GIS based seismic microzonation of Kochi, *Proc. Vol. of XXVII INCA Congress (Nov. 2007), 292-299*.

Singh H.N., Mathai J., Neelakandan V.N., Shanker D. & Singh V.P (2004). A database on occurrence patterns of unusual geological incidents in Southwest Peninsular India and its implication on future seismic activity, *Acta Geod. Geoph. Hung., 40(1), 69-88*.

Sugito M., Goda, G. & Masuda T. (1994). Frequency dependent equi-linearized technique for seismic response analysis of multi-layered ground, *Proceedings of JSCE, 493, 49-58 (in Japanese with abstract).*

Analysis of Taipei Basin Response on Earthquakes of Various Depth and Location using Empirical Data

Sokolov V (1), Wen K-L (2), Miksat J. (1), Wenzel F (1), Chen C-T (2)

(1) Geophysical Institute, Karlsruhe University, Hertzstr. 16, Karlsruhe 76187, Germany, Vladimir.Sokolov@gpi.uni-karlsruhe.de
(2) Institute of Geophysics, National Central University, Jungli City, Taiwan, R.O.C.

Keywords: Site effect, Taipei basin, deep and shallow earthquakes

Introduction

The seismicity in the Taiwan area is very high, and many large earthquakes (M > 6.5) occurred in the region since 1900. Some of these earthquakes, among which the recent Chi-Chi earthquake of 21 September 1999 should be mentioned, caused severe damages. Taipei City is the capital of Taiwan and it is located on a sediment-filled basin in the northern part of the island. The area experienced several damaging earthquakes, the most recent of which occurred on March 31, 2002. The results of the previous researches on earthquake ground motion peculiarities in the Taipei basin (e.g. Loh et al. 1998; Wen and Peng 1998; Sokolov and Jean 2002; Fletcher and Wen 2005) showed that the basin reveals a large variation in ground-motion characteristics (peak ground acceleration, response spectra, dominant frequencies, etc.).

Recent needs of earthquake engineering require consideration of site effect in seismic hazard analysis. When applying probabilistic approach for seismic hazard estimation for urban territories, it is necessary to take into account the following. 1. Extended areas covered by large cities are characterized by variety of local geological and geotechnical conditions. 2. Different engineering structures (buildings, bridges, lifelines, etc.) require consideration of different parameters of ground motion within relatively broad frequency range of the motion; 3. Optimization of engineering decisions demands estimation of ground motion parameters for different return periods (probabilities of being exceeded) concerning structures of different importance factors. 4. Consideration of various recurrence intervals and a broad frequency range of ground motion cause the necessity to cover the influence of different earthquakes that may occur in different seismogenic zones.

In this study we analyzed frequency-dependent response of the Taipei basin using records of recent earthquakes. The strong-motion database, which includes records obtained at 32 stations of the Taipei network during 83 deep and 142 shallow earthquakes (M > 4.0) occurred in 1992-2004 (Figure 1). The most of the selected stations cover evenly the territory of the basin; in addition we consider two stations located outside the basin (TAP053 and TAP071).

The Method

For estimation of the site response from earthquake records it is necessary to remove the source and propagation path effects. Various techniques for the site-response estimation, which use the S-wave window, have been already developed and studied. The most common procedure for estimation the site response from earthquake data is to determine the sediment-to-bedrock ratio by dividing the Fourier spectrum of a site by that of a nearby reference (rock) site using earthquake records. However, in many cases, including the Taipei basin, it is not possible to find the station, which is suitable to be accepted as a “hard-rock reference” station.

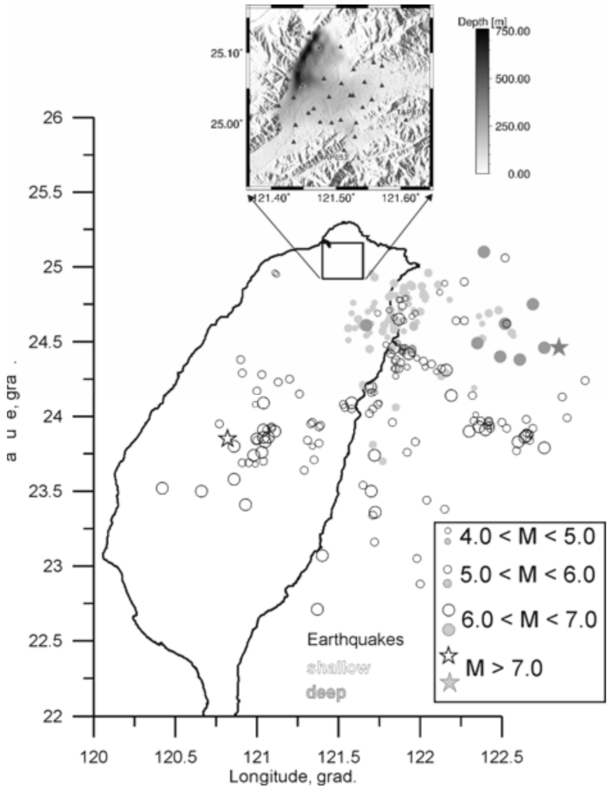

Figure 1. Distribution of epicentres of earthquakes used in this study (open circles – shallow events, grey circles – deep events) and location of the considered stations (triangles) within the Taipei basin. The depth of Quaternary sediments is also shown in gradations of grey colour.

Alternative methods not requiring a reference site have been developed recently. One of them involves dividing the horizontal-component shear-wave spectra at each site by the vertical component spectra observed simultaneously at that site (Lermo and Chavez-Garcia 1993). The H/V technique, as has been shown recently by many authors provides results that are consistent with the general geological conditions of the recording sites. The results of the application of the H/V technique, however, are affected by local and subsurface factors influencing the vertical component of ground motion. Such effects may be minimized by using data only from rock stations (e.g. Chen and Atkinson 2002; Sokolov et al. 2007).

It was proposed recently (Sokolov et al. 2000) to use so-called “very hard rock” (VHR) spectral model for the estimation of site response characteristics in terms of frequency-dependent amplification (spectral ratios). The approach consisted in calculating spectral ratios between the spectra of actual earthquake records (horizontal components) and those modelled for a hypothetical VHR condition. Besides local site response, the spectral ratios may include effects of source rupture peculiarities and inhomogeneous propagation path. When using a large enough number of events varied by magnitude, depth and azimuth, the effects of faulting and directivity are expected to be averaged out. The approach was applied for evaluation of characteristics of amplification for particular sites in Taipei basin (Sokolov and Jean 2002; Sokolov et al. 2000) and for generalised site conditions in Taiwan (Sokolov et al. 2007).

The specification of the “very hard rock” spectrum is of particular significance in the approach. The ground motion database collected in Taiwan provides an opportunity to study both regional source scaling and attenuation models for the region, as well as local site response on earthquake ground motion. The FAS models for typical site conditions in Taiwan were recently re-evaluated by Sokolov et al. (2006) using a large number of acceleration records obtained during earthquakes occurred during 1992-2004. These models were used in this work.

The Data and Processing

The data were obtained during implementation of the Taiwan Strong Motion Instrumentation Program. The program is conducted by the Seismological Observation Center of the Central Weather Bureau (CWB), Taiwan, R.O.C. The program installed more than 650 digital free field strong-motion instruments. These instruments are capable to record high-resolution ground motion within ± 2 g and with a pre-event and post-event memory.

Fourier amplitude spectra were calculated, using 10% cosine window, for selected parts (the strongest shaking) of the acceleration records (Figure 2). The strongest part of the shaking contains the S-wave portion and, in some cases, surface waves from large distant earthquakes and additional waves generated by the basin. However, to avoid the predominant influence of the additional waves, we did not use the signal window longer than 30 seconds. The calculated Fourier spectra were smoothed twice within 0.2 Hz running window.

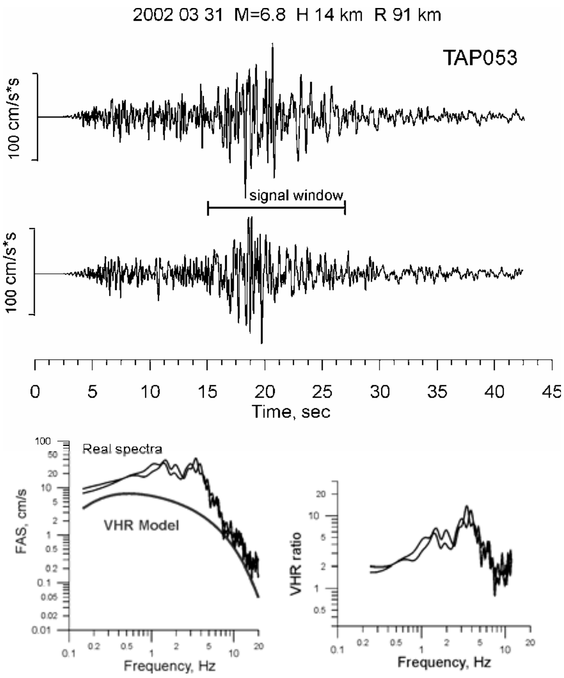

Figure 2. Calculation of the VHR spectral ratio.

For the low-frequency range, besides the noise level, it is necessary to consider the effect of truncation in the time domain. The truncation leads incorrectly to a flat spectrum for long periods. It is recommended to use a time-domain-window length at least equal to twice the lowest analyzed wave period. The truncation effect is especially important for spectral analysis of records from small earthquakes, for which the signal duration does not increase 2 - 3 seconds.

Reference VHR spectra were calculated using the recently proposed regional models (Sokolov et al. 2006). Estimations of seismic moment (M_0) and stress parameter ($\Delta\sigma$) are not available for almost all of the considered earthquakes. When using the empirical relationship between seismic moment and local magnitude, it is necessary to bear in mind the possible scatter of the M_0 values. Ideally, the observed and theoretical spectra should fit each other at low frequencies where the influence of local geology is believed to be negligible. The influence may be very small for the case of rock sites or sites with a thin layer over rigid bedrock. Such case may be considered as a reference site when selecting the proper values of the earthquake source parameters. It has been found in our previous study (Sokolov et al. 2000), that station TAP053 satisfies the requirements for such reference site; the station is characterized by narrow band amplification at frequencies around 4 Hz. At the same time, the station, as well as station TAP071, is located outside the basin that minimizes possible influence of relatively long-period waves trapped within the basin.

Results and Discussion

The site amplification functions or the ratios between the observed and the modelled spectra should not depend on earthquake magnitude for the case of linear soil response on earthquake motion. If the proper spectral models are used for various magnitudes, the characteristics (averaged amplitudes and shape) of the ratios between observed and modelled spectra should be approximately the same for different earthquakes, at least for those of similar distance and azimuth. The characteristics of the VHR ratio evaluated for stations located outside the basin (TAP073 and TAP071) are shown in Figure 3. In general, the ratios obtained using records from the deep (*VHRD*) and shallow (*VHRS*) earthquakes exhibit the similar nature. The *VHRS* ratios are characterized by slightly higher amplitudes at frequencies less than 2-3 Hz than the *VHRD* ratios, which may be explained by the presence of surface waves generated by shallow and distant earthquakes, which do not considered in our simple spectral models.

Let us analyse the VHR ratios calculated for stations located within the basin. The stations near the basin edge (Figure 3) at relatively shallow deposits (e.g. TAP002 and TAP027) reveal the same character of the ratios, as the stations located outside the basin, namely: the *VHRD* and the *VHRD* ratios show approximately the same amplitudes in the whole considered frequency range. For the central part of the basin (e.g. TAP004, RAP010, TAP014, TAP017, TAP020, TAP037), the difference between the *VHRS* and *VHRD* ratios at low frequencies becomes much larger than that for the basin edge. We can suggest that the difference reflects the influence of additional waves generated within the basin. However, to check the suggestion we have to answer the following question - in what extent do the VHR curves reflect the real site response? We used a simple 1-D technique that allowed us calculating theoretical spectral amplification of a multi-layered soil column overlying a rigid half-space for SH- and SV-waves approaching the bottom of the soil with arbitrary angles of incidence.

The subsurface geology of the Taipei basin has been established by boring, electrical and seismic prospecting. The geological structure inside the basin consists of Quaternary layers above tertiary base rock. The geotechnical properties of the Quaternary deposits in the Taipei basin have still not been studied in detail. A very low *Q* value is expected for high crack density and fluid-saturated soil in the Taiwan region (Shieh 1992). Amplitudes of ground motion amplification are very sensitive to the degree of damping (quality factor). Therefore, for comparison we used two variants of the *Q*-model. In the first one (*Q*1-model), the quality factors were taken as those provided by Wen and Peng (1998). The higher, gradually increasing with depth, values of the quality factor were accepted in the second model (*Q*2-model) (see also Sokolov et al. 2007).

We calculated the theoretical spectral amplification assuming the bottom of the basin as the rigid half-space. Despite of the approximate character of the 1D model, the results of the modelling show that in almost all considered cases the theoretical spectral ratios reveal a good agreement with the VHR data obtained from records of deep earthquakes (Figure 4). In general the site amplification characteristics for the areas located near the basin edge (e.g. TAP027) reveal one or two separate peaks within relatively narrow frequency bands reflecting influence of particular layers. The areas with thick sediments are characterized by broadband amplification. The comparison of empirical and theoretical data may also allow a proper selection of geotechnical properties for further, more detailed, modelling.

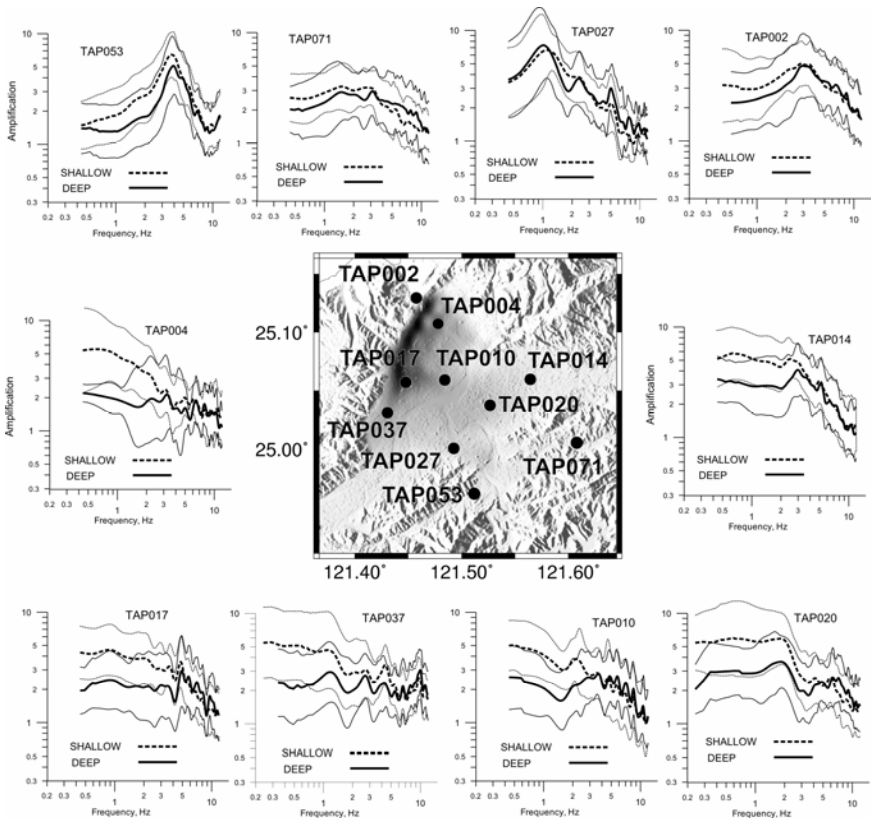

Figure 3. Characteristics of the VHR spectral ratios (mean amplitude values and 1 standard deviation limits) for particular stations. The depth of Quaternary sediments is shown in gradations of grey colour.

To analyse site amplification characteristics obtained from records of shallow earthquakes we applied the following scheme. The FAS amplitudes for the records obtained outside the basin during deep [$A_{OUTD}(f)$] or shallow [$A_{OUTS}(f)$] earthquakes may be expressed as follows

$$A_{OUTD}(f) = A_{VHR}(f) \times AMPL_D(f), \text{ or } A_{OUTS}(f) = A_{VHR}(f) \times AMPL_S(f), \tag{1a}$$

$$AMPL_D(f) = SG(f), \; AMPL_S(f) = SP(f) \times SG(f) \tag{1b}$$

where f is the frequency, Hz; $A_{VHR}(f)$ is the spectrum at rock basement; $AMPL(f)$ is the overall spectral amplification; $SP(f)$ reflects influence of propagation path (surface waves) and $SG(f)$ is the amplification caused by site geology. The FAS amplitudes for the records from shallow earthquakes obtained inside the basin $A_{INBS}(f)$, besides the influence of propagation path and local geology, may reflect influence of the additional waves generated within the basin (basin factor) $SB(f)$ and the expression may be written as

$$A_{INBS}(f) = A_{VHR}(f) \times SP(f) \times SG(f) \times SB(f). \tag{2}$$

Let us, for example, consider a pair of stations that are located outside (e.g. TAP053) and within (e.g. TAP020) the basin (see Figures 4 and 5), which recorded the large numbers of earthquakes (Table 2). The VHR ratio averaged from available set of deep earthquakes (VHRD) can be accepted as description of influence of local geology, or the $SG(f)$ term, for both stations, i.e. $VHR_D(f) = AMPL_D(f) = SG\,(f)$. The ratio $SDR(f)$ between the averaged VHR ratio for shallow earthquakes (*VHRS*) and the averaged VHR ratio for deep earthquakes (*VHRD*) for station TAP053 (reference station located outside the basin) may be considered as description of the influence of propagation path, or the $SP\,(f)$ term, i.e.

$$SDR_{TAP053}(f) = \frac{VHR_S(f)}{VHR_D(f)} = \frac{AMPL_S(f)}{AMPL_D(f)} = SP\,(f) \qquad (3)$$

The ratio for station, which is located inside the basin, e.g. TAP020, may be considered as a description of the joint influence of propagation path and the basin, or $SDR_{TAP020}(f) = SP(f) \times SB_{TAP020}(f)$. Of course, in this case the function $SDR_{TAP020}(f)$ reflects only the generalized characteristics obtained from many earthquakes occurred at different locations. However, when comparing the data, which were obtained at both stations from the same set of shallow earthquakes, we can assume that generalized characteristics of the additional waves generated in the basin, or the $SB_{TAP020}(f)$ term, may be evaluated as

$$SB_{TAP020}(f) = SDR_{TAP020}(f) / SDR_{TAP053}(f) \qquad (4)$$

However, station TAP053 is characterized by high-amplitude amplification at frequencies between 2 - 5 Hz. The high variability of the VHR ratios within this frequency range could cause unstable values of the SDR-factor evaluated form different sets of earthquakes. Therefore, for analysis of the influence of propagation path (the *SP*-term) and the basin effect (the *SB*-term), we also used the data from station TAP071.

The average-amplitude frequency-dependent basin effect ($SB(f)$ term) evaluated for particular stations, which are located within the basin, is shown in Figure 5. It seems that it is possible to divide the basin into, at least, three zones showing (a) almost negligible amplification due the basin effect (near the basin edge); (b) relatively high-amplitude low-frequency amplification (deepest part of the basin); (c) transition zone.

The characteristics of the propagation path (the *SP*-term) and the basin (the *SB*-term) effect may be evaluated for various sets of shallow earthquakes (large and small, nearby and distant, etc.). Together with regional source scaling and attenuation models, characteristics of propagation path effect and site amplification due to local geology (1D effect), they may be used for probabilistic seismic microzonation of the basin when considering many possible earthquakes located at different distances and azimuths. Particular events, however, may reveal some peculiarities in frequency content of ground motion. It seems that the 2D and 3D simulation is necessary to model the seismic shaking in the Taipei basin when considering the particular large events, which may be chosen as the scenario (e.g. the worst-case or the dominant earthquakes).

Conclusion

Application of the recently developed regional spectral models (Sokolov et al. 2006) together with available ground-motion database for analysis of site amplification of the Taipei basin allow concluding the following. (1) The characteristics of frequency-dependent site response for particular points (stations of the TSMIP network) in the Taipei basin, which were obtained using records of deep earthquakes (depth > 35 km), exhibit a good agreement with the theoretical ratios calculated using the 1D-models based on available geological and geotechnical data. (2) The data from shallow earthquakes show influence of (a) surface waves generated when travelling from distant sources to the basin and (b) relatively low-frequency (< 1 - 2 Hz) waves generated within the basin. (3) Some shallow earthquakes produce extremely high amplification at frequencies 0.3 – 1 Hz within the basin that may be dangerous for high-rise buildings and highway bridges.

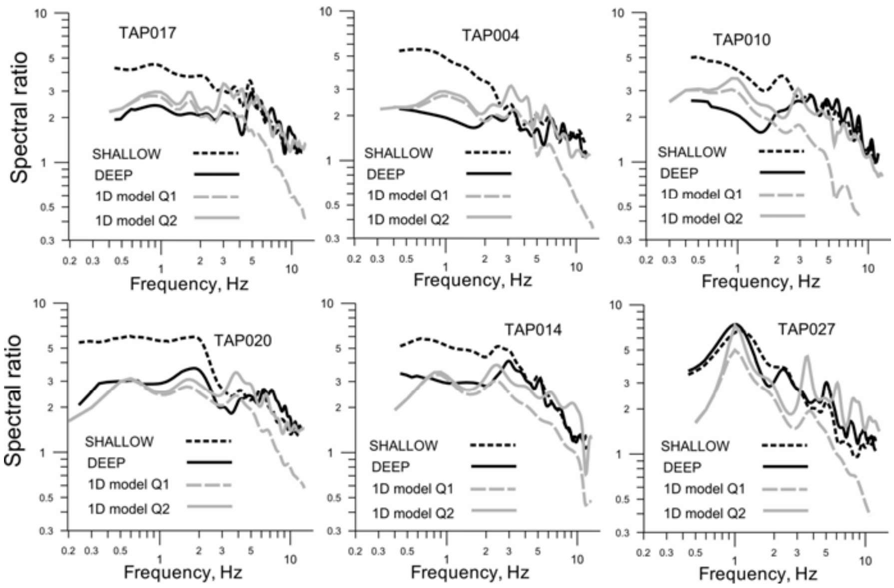

Figure 4. Comparison of the VHR spectral ratios (average values) calculated using the data from deep and shallow earthquakes and the results of 1D modeling (the Q1- and Q2-models).

The results may be used in probabilistic seismic microzonation of the basin when considering many earthquakes located at various distances (Sokolov et al. 2001). We have to note that the frequency-dependent amplification functions were obtained in this study within a limited frequency range from 0.3 Hz to 12 Hz. The ground-motion characteristics for the lower frequencies may be studied using numerical 2D and 3D modeling. For the prediction of seismic influence from particular large earthquakes, a special procedure that combines the long-period (modelling) and the high-frequency (stochastic simulation) waveforms should be used.

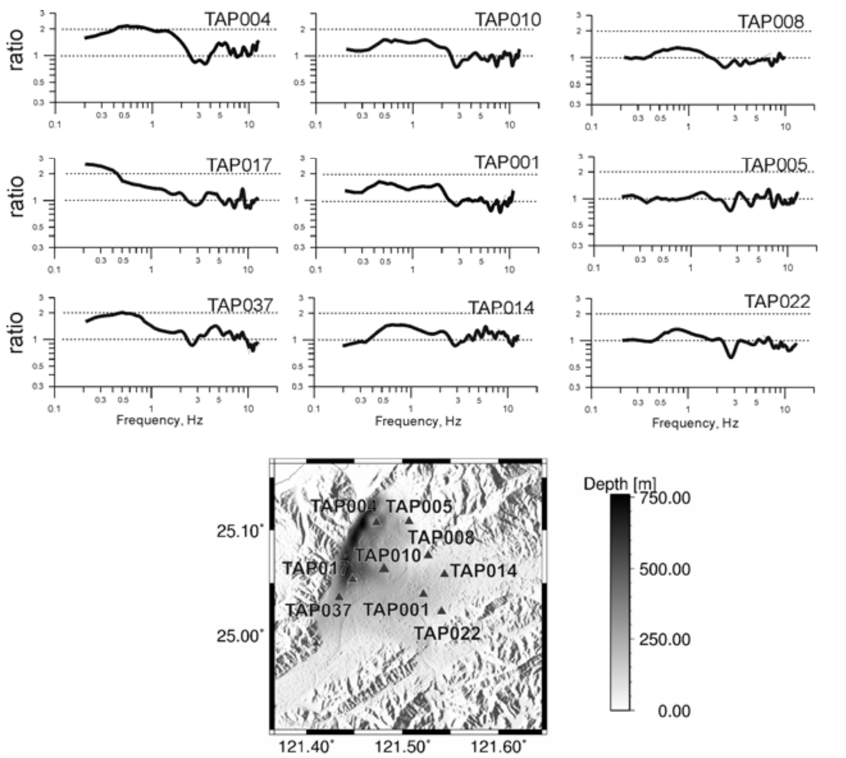

Figure 5. Characteristics of the basin effect for particular stations (mean amplitude amplification), which were obtained using the data from all earthquakes recorded at every station.

Acknowledgements

This work was sponsored by National Science Council, R.O.C. (grant NSC 96-2119-M-008-007) and Deutsche Forschungsgemeinschaft (DFG), Germany, (project WE 1394/13-1).

References

Chen S.Z. & Atkinson G.M. (2002). Global comparisons of earthquake source spectra, *Bull.* Seis. Soc. Am., 92, 885-895.

Fletcher J.B. & Wen K.L. (2005). Strong ground motion in the Taipei basin from the 1999 Chi-Chi, Taiwan Earthquake, *Bull. Seis. Soc. Am., 95, 1428-1446.*

Lermo J. & Chavez-Garcia F.J. (1993). Site effect evaluation using spectral ratios with only one station, *Bull. Seis. Soc. Am., 83, 1574-1594.*

Loh C.H. & Hwang J.Y. & Shin T.C. (1998). Observed variation of earthquake motion across a basin – Taipei city, *Earthquake Spectra, 14, 115-133.*

Shieh C.F. (1992). Estimation of Q value by SP/S spectral ratio, Terrestial*, Atmospheric and Oceanic Sciences, 3, 469-482.*

Sokolov, V.Yu. & Loh C.H. & Wen K.L. (2000). Empirical study of sediment-filled basin response: a case of Taipei city, *Earthquake Spectra, 16, 681-707.*

Sokolov V.Yu. & Loh C.H. & Wen K.L. (2001). Site-dependent input ground motion estimations for the Taipei area: a probabilistic approach, *Probabilistic Engineering Mechanics, 16 (2), 177-191.*

Sokolov V.Y. & Jean W.Y. (2002). Ground motion characteristics in the Taipei basin from earthquakes of various locations, *Struct. Engin., 17(3), 18-30 (in Chinese).*

Sokolov V.Yu. & Loh C.H. & Jean W.Y, (2006). Strong ground motion source scaling and attenuation models for earthquakes located in different source zones in Taiwan. *Proc. of the 4th International Conference on Earthquake Engineering*, *12-13 October 2006, Taipei, Taiwan, CD-ROM, paper 03.*

Sokolov V.Yu. & Loh C.H. & Jean W.Y. (2007). Application of horizontal-to-vertical (H/V) Fourier spectral ratio for analysis of site effect on rock (NEHRP-class B), Soil Dynamics and Earthquake Engineering, 27, 314-323.

Wen K.L. & Peng H.Y. (1998). Strong ground motion observations in the Taipei basin. K. Irikura, K. Kudo, H. Okada, and T. Sasatani (Editors), *Proc. of the Second Int. Symp. on the Effects of Surface Geology on Seismic Motion*, *Yokogama, Japan, 1-3 December 1998, Balkema, Rotterdam, 263-270.*

Geological Grounds of Seismic Hazard Assessment in Syria

Trifonov V G (1), Karakhanian A S (2), Ivanova T P (3), Dodonov A E (1), Bachmanov D M (1), Ammar O (4), Rukieh M (4), Minini H (4), Al-Kafri A-M (4), Ali O (4)

(1) Geological Institute of RAS, 7 Pyzhevsky, Moscow 119017 Russia; trifonov@ginras.ru
(2) Institute of Geosciences of NAS, 24a Marshal Bagramyan Ave., Yerevan, Armenia, georisk@sci.am
(3) Institute of Dynamics of Geospheres of RAS, B. 6, 38 Leninsky Ave., Moscow 117334 Russia, trifonov@ginras.ru
(4) General Organization of Remote Sensing, P.O. Box 12586, Damascus, Syria, gors@mail.sy

Keywords: neotectonics, active faults, seismic zones

Introduction

The goal of this paper is to demonstrate geological grounds of seismic hazard assessment in Syria. The Neotectonic map and data on the Late Cenozoic tectonics and the Map and parameters of active and possibly active faults are represented and discussed in the paper. The maps were compiled in scale 1:1000000 for all studied region and 1:500000 for Western Syria. The region occupies the territories of Syria and 100–150 km surrounding it and includes the northern part of the Arabian plate and the border structures: the Dead Sea Transform zone (DSTZ) and the southwestern termination of the East Anatolian fault zone (EAFZ), as well as adjacent parts of the Levantine basin of the Mediterranean and the transition zone between the EAFZ and Cyprus arc. The northern Arabian plate is differentiated to: the Marginal folded zone; the Aleppo block; the folded and thrusted belt of the Palmyrides; the Jebel Arab (Harrat Ash Shaam) volcanic highland; the northwestern termination of the Mesopotamian foredeep; and the main part of the plate (Rutbah block).

Neotectonic evolution

The southern part of the DSTZ (between the Aqaba and Hula pull-apart basins) is characterized by inherited sinistral motion since the Early Miocene (Quennell, 1959; Freund et al., 1968; Walley, 1988). It was originated between ~20 and 18–17 Ma, because the DSTZ offset the belt of dykes, small volcanoes and extrusions along the northeastern side of the Red Sea rift. The belt was the most active 24–21 Ma and continued to develop till ~20 Ma (Camp, Roobol, 1992; Segev, 2005). The oldest sediments in the Dead Sea and Sea of Galilee are dated by 18–17 Ma (Garfunkel, Ben-Abraham, 2001; Hurwitz et al., 2002).
Unlike the southern part of the DSTZ, its northern (Lebanon-Syrian) part as well as the northern convergent plate boundary zone changed for the Neogene–Quaternary. During the Early Miocene, the Roum fault and its continuation in the continental slope of the Mediterranean were the most active strand of the DSTZ and joined in the N with the Latakia oblique (sinistral-thrust) fault zone (Barazangi et al., 1993; Rukieh et al., 2005) (Fig. 1). The Leban and Coastal anticlines were originated in the “Arabian” side of the Miocene DST. The Latakia zone continued by the Cyprus arc in the W and by the Taurus (Bitlis) thrust in the E and further by the Main Thrust of Zagros. During the Middle Miocene and the beginning of the Late Miocene (the Helvetian and Tortonian), the tectonic activity weakened in the northwestern boundaries of the Arabian plate. Only in the Yizre’el depression between the Galilee Sea and the Lower Jordan valley segment of the DSTZ in the E and the NW-trending associated Haifa fault zone in the SW, subsidence and basaltic eruptions continued up to 10 Ma (Garfunkel, 1989; Segev, 2005). The activity was high in that time in the northeastern plate boundary, where the Main Thrust of Zagros and the Mesopotamian foredeep developed

intensively. Subsidence of the foredeep continued later, but the motion on the Main Thrust of Zagros reduced in some segments and transformed to the dextral slip on the Main Recent Fault of Zagros and thrusting and folding in the outer Zagros, i.e. in the northwestern side of the foredeep (Bachmanov, 2001; Bachmanov et al., 2004). The same asymmetric folds were formed between the Taurus thrust and the Mesopotamian foredeep in the southeastern Turkey and adjacent parts of Syria and Iraq.

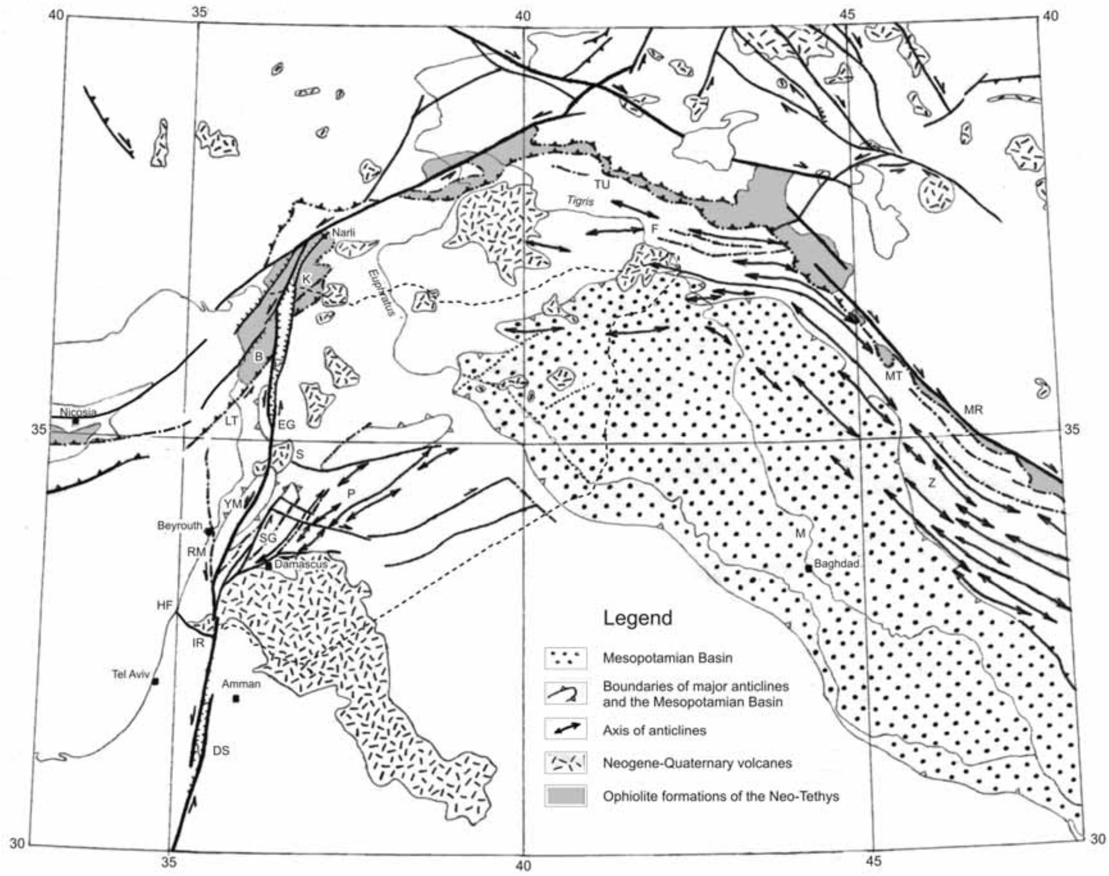

Figure 1. Schematic neotectonic map of Syria and adjacent territories. Segments of the DSTZ: DS, Dead Sea; JR, Jordan River; RM, Roum and its offshore continuation; YM, Yammuneh; EG, El Ghab. Other faults: HF, Haifa; LT, Latakia; MR, Main Recent fault of Zagros; MT, Main Thrust of Zagros; SG, Serghaya; TU, Taurus (Bitlis) thrust. Structural elements: B, Bassit, F, Marginal Folds of Turkey; K, Kurd Dagh; P, Palmyrides; S, Shin Plateau; Z, Folded Belt of Zagros; M, Mesotopamian Basin.

In the Messinian and Early Pliocene, activity of the Roum fault and its offshore continuation was renewed, but was accompanied by intensive folding and thrusting in the Anti-Leban–Palmyride belt that separated the Aleppo block from the main part of the plate (Ponikarov et al., 1967; Chaimov et al., 1990). The Messinian–Early Pliocene volcanic activity in the Shin plateau and adjacent coastal territory demonstrated changes of the lithosphere of this part of the DSTZ that created conditions for principal rebuilding of all its northern part. New strand of the DST was formed in the Shin area and progradated both to the S (the Yammuneh segment) and to the N (the El Ghab segment), where the latter joined with the new-formed EAFZ (Zanchi et al., 2002; Rukieh et al., 2005). The rebuilding took place between 4.3 ± 0.2 Ma (age of the youngest Shin basalts, offset by the El Ghab strand (Leonov, 2000)) and ~3.5 Ma (age of the oldest sediments within the El Ghab zone near the town of Myssiaf (Trifonov et al., 1991)). The data of Devyatkin and Dodonov (Leonov, 2000) on the Pliocene age of mollusks in the lower layers of the El Ghab pull-apart basin conforms this conclusion.
The new-formed segments of the DST are accompanied by the smaller NE-trending faults. The Rachaya and Serghaya faults represent the fault zone which branches out the Hula basin and the Saint Simeon fault branches out the northeastern side of the El Ghab basin. The W-trending Ein-Qita and Tripoli faults with uplifted southern sides create the stepped longitudinal

profile of the Coastal–Leban anticline system. The E-trending convex to the south faults (Jhar, Olab, Akfan and several smaller ones) cross the Palmyrides and the northern part of the Rutbah block. The largest Olab fault offsets dextrally the Palmyride folds and big tributaries of the Euphrates River to 2.5–3 km.
All faults, formed or renewed in the Pliocene continued to develop in Pleistocene and partly Holocene, i.e. they can be classified as active or possibly active faults.

Active faulting

The active faults are those with manifestations of the Holocene and Late Pleistocene movements. The faults, demonstrating the older Pleistocene offsets and signs of the Late Quaternary activity on some segments are estimated as possibly active faults. All active faults are concentrated in the DSTZ and the southwestern termination of the EAFZ (Fig. 2). First of all, these are the Yammuneh and El Ghab segments of the DSTZ. The NE-trending Yammuneh fault demonstrates young sinistral offsets with reverse component. According to the GPS data (McClusky et al., 2003), the motion on the fault is portioned between 6±1 mm/a left-lateral component parallel to the fault and 4±1 mm/a fault-normal shortening. The N-trending El Ghab fault demonstrates young sinistral offsets. They are often accompanied by normal component, particularly in both sides of the El Ghab pull-apart basin. To the south of it, the fault is composed by several en echelon strands. The total Holocene offset on them is estimated as 60±5 m. The aqueduct of the first century A.D. is offset on the main fault strand to ~12 m near the village of Al Harif (Meghraoui et al., 2003; fig. 10 in Rukieh et al., 2005). This gives the average rate of the Holocene motion ~6 mm/a. The GPS measurements were started on the El Ghab fault in 2005–2006 by Sh. Al-Yesef and S. Al-Daud from the General Organization of Remote Sensing in Syria. The preliminary results give the sinistral slip along the fault to ~2–3 mm/a. On some lines, strike slip is accompanied by fault-normal lengthening.
The Serghaya and Rachaya faults seem to be linked to each other: the Late Quaternary motion on the Rachaya fault reduces to the NE and is transformed into motion on the Serghaya fault that increases in the same direction. The sinistral offsets of the Late Quaternary drainage features to 100–200 m were found near the village of Serghaya and to the N of the town of Baalbek. Gomez et al. (2003) reported about the 10.2±0.5 m sinistral offsets on the fault to the S of the town of Zebadaneh during last 6,000 years that gave the average rate of strike slip ~1.4 mm/a; ratio of lateral and vertical components of motion was estimated as 4:1 ÷ 5:1. A lot of evidence of sinistral motion with small reverse component were found on the Saint Simeon fault (Karakhanian et al., 2008). The largest offsets of drainage features reach 1.2 km. The valley near the village of Burj Abdalo curves to the left by 550 m. The dense calcified pebble-stone Middle Pleistocene (?) alluvium have preserved on the slopes of the valley segment that strikes along the fault. It shows that curving of the valley began probably in the Middle Pleistocene and average rate of motion is not more than ~2 mm/a. Some smaller offset and deformed features looks to be formed in the historical time.
The offshore NNW-trending Tartus fault zone strikes on the shallow shelf along the Mediterranean coast and represents probably the renewed segment of the northern continuation of the Roum strand of the DSTZ that was originated and was particularly active in the Miocene. Near and southward the city of Tartus, the zone is manifested by the left en echelon row of small gentle anticlines, separated from the coast by a system of small basins up to 20–30 m in depth. En echelon location of the anticlines demonstrates presence of the sinistral component of motion along the zone. These structural features have been formed by the offshore continuation of the Late Pleistocene (Tyrrhenian) marine terrace that is exposed in some anticlines (the Arwad and El Abbas islands) and in the Syrian coast. The shells within the limestone and sandstone terrace cover give the U-Th age from 83.4+4.6/-4.4 Ka to 128.5+10.4/-9.2 Ka (99.9+7.4/-6.8 Ka in the Arwad Island) (Dodonov et al., 2008). Recent activity of the Tartus zone as well as offshore parts of the Roum, Tripoli and Latakia faults is increased by accelerated subsidence of the Levantine basin of the Mediterranean.
The total rate of sinistral slip in the northern DSTZ, including the associated faults reaches ~8 mm/a, i.e. it is approximately coincide with the Late Quaternary slip rate on the Dead Sea–Jordan River segments of the zone. The rate can decrease in the northern DSTZ to the N because of activity of the W–E-trending faults in both its sides. The Late Quaternary activity of the Tripoli fault is manifested by steep scarps on the young geomorphologic surfaces, including the shallow shelf near Tripoli. The Ein-Qita fault offsets the Tyrrhenian marine terrace to the N of town of Banyas.

Figure 2. Active tectonics of Western Syria and adjacent territories. (1) Active faults; (2) Possibly active faults; (3) Quaternary extension faults with volcanoes; (4) High uplifted anticlines; (5) Small anticlines; (6) Foredeep and intermountain basins; (7) Pull-apart basins; (8) Weakly subsided coastal areas; (9) Areas of subsidence in the Mediterranean; (10) Areas of intense subsidence with the sub-oceanic crust; (11) Quaternary basalts. Segments of the DSTZ and associated faults: EQ, Ein-Qita; EG, El Ghab; HF, Haifa; JR, Jordan River; RA, Rachaya; RM, Roum and its offshore continuation; SG, Serghaya; SM, St. Simeon; TA, Tartus; TR, Tripoli; YM, Yammuneh. Segments of the EAFZ: AF, Aafrin; AM, Amanos; AN, Antioch; KR, Karasu; LT, Latakia; YG, Yakapinar-Görsun. Other possibly active faults: AK, Akfan; DM, Damascus; JH, Jhar; OL, Olab

According to the Westaway's (2004) modeling, the Pliocene–Quaternary sinistral slip rate on the southwestern termination of the EAFZ is estimated as ~8 mm/a, portioned between ~2 mm/a on the Yakapinar-Göksun fault onshore of Iskenderun Bay, 1–1.7 mm/a on the Amanos fault and 2.5–4.3 mm/a on the East Hatay fault. The slip had reverse component (Adiyaman & Chorowicz, 2002). All these faults demonstrate the Late Quaternary activity. The Latakia and Aafrin faults represent a single fault zone which was active mainly in the Miocene and Early Pliocene and was offset later on the El Ghab segment of the DST. Different elevation of the Late Pleistocene marine terraces on the Latakia fault sides gives evidence of the Late

Quaternary activity. In the southeastern fault side, there are two accumulative terraces: 27–34 m (it is attributed to the discussed above Tyrrhenian transgression) and 17–20 m (it demonstrates, probably, a fall of the sea level at the end of the transgression). They correlate with two terraces in the northwestern fault side: 41 m (it has been found only in one site) and ~20 m. Those are abrasion terraces with very thin and fragmental cover of scattered marine pebbles. The section across the Aafrin fault zone near the village of Kara-Bash demonstrates several parallel faults in the Lower Miocene limestones with tectonic breccias and small block of the steeply dipped Paleogene limestones. Some faults are complicated by carst cavities filled by the Quaternary deposits. One of them demonstrates vertical (reverse) offset of the Late Quaternary colluvium to 0.4 m.
In the Palmyrides and the Arabian plate to the E of the DST, only few possibly active faults are identified. The most evident signs of the fragmental Late Quaternary activity have been found on the W–E-trending Jhar fault. Scarps, deformation of terraces and oblique striation on the fault plains prove reverse offsets with big strike-slip component. Sense of strike slip is under discussion. Kopp (Leonov, 2000) reported about dextral bending of small intersected streams up to several tens of meters. But the fault is accompanied by several NE-trending grabens in its northern side. The grabens are filled by the Pliocene–Quaternary sediments and normal fault on the graben sides demonstrate very fresh (Holocene?) displacements. These normal faulting can manifest sinistral slip on the Jhar fault. The faults in the Syrian desert (the southeastern Palmyrides and adjacent part of the Rutbah block) are represented in topography by gentle scarps or weak linear depressions which are masked by intensive eolan sedimentation. The Middle–Late Quaternary vertical offsets are not more than 10 m.

Seismic zones

Active faults of the DSTZ can be qualified as the main zones of strong crustal earthquakes in the region. Preliminary estimates of their Mmax, grounded on the lengths of fault segments (Wells, Coppersmith, 1994) are represented in Table 1. The zones are 70–240 km long and their Mmax are estimated as 7.3–7.8. Although some possibly active faults in the DSTZ (Roum, Ein-Qita and Damascus faults), EAFZ (Latakia and Aafrin faults) and outside them (Akfan, Olab and Jhar faults) are long, their segments with proved Late Quaternary activity are short and their seismic potential is much smaller. Nevertheless, the latter exists that is demonstrated by several moderate earthquakes in the offshore part of the Latakia fault in the XX century. Relatively long active segments are characteristic for the Jhar fault. Probably, just its activity caused the Medieval earthquake, whose archaeoseismological manifestations have been found in ruins of Palmyra.

Table 1. Characteristics of main linear seismogenic zones of Western Syria

Name & code of the zone	***Kinematics of the zone***	***Length of the zone, km***	***Estimate of Mmax (SRL) by (Wells, Coppersmith,1994)***
Yakapinar-Görsun, F1	Reverse-sinistral	280 ?	7.9 ?
Amanos, F2	Sinictral	200	7.7
Antioch, F3	Sinictral	160	7.6
Karasu, F4	Sinictral	220	7.8
St. Simeon, F5	Sinictral	80	7.3
West El Ghab, F6	Sinictral	130	7.5
East El Ghab, F7	Sinictral	120	7.5
Tartus, F8	Sinictral	75	7.3
Tripoli, F9	All	75	7.2
Roum, F10	All	210 ?	7.7 ?
Yammuneh, F11	Sinictral	170	7.7
Serghaya, F12	Sinictral	170	7.7
Hula-Rachaya, F13	Sinictral	110	7.4
Haifa, F14	Normal	200 ?	7.7 ?
Jordan, F15	Sinictral	240	7.8

? means that the fault demonstrates only fragmental activity and Mmax can be less.

References

Adiyaman Ö & Chorowicz J. (2002). Late Cenozoic tectonics and volcanism in the northwestern corner of the Arabian plate: a consequence of the strike-slip Dead Sea fault zone and the lateral escape of Anatolia, *J. of Volcan. and Geothermal Res., 117, 327-345*.

Bachmanov D.M. (2001). Age zoning of course molassa in the outer Zagros and migration of recent orogeny, *Geotectonics, 35, 505-509*.

Bachmanov D.M., Trifonov V.G., Hessami Kh.T., Kozhurin A.I., Ivanova T.P., Rogozhin E.A., Hademi M.C. & Jamali F.H. (2004). Active faults in the Zagros and central Iran, *Tectonophysics, 380, 221-241*.

Barazangi M., Seber D., Chaimov T., Best J., Litak R.D. & Sawaf T. (1993). Tectonic evolution of the northern Arabian plate in western Syria, *Boschi E., Mantovani E. & Morelli A. (Eds.), Recent evolution and seismicity of the Mediterranean region, Kluwer Acad. Publ., Dordrecht, 117-140*.

Camp V.E. & Roobol M.J. (1992). Upwelling asthenosphere beneath western Arabia and its regional implication, *J. Geophys. Res., 97, 15255-15271*.

Chaimov T.A., Barazangi M., Al-Saad D., Sawaf T. & Gebran A. (1990). Crustal shortening in the Palmyride fold belt, Syria, and implications for movements along the Dead Sea fault system, *Tectonics, 9, 1369-1386*.

Dodonov A.E., Trifonov V.G., Ivanova T.P., Kuznetsov V.Yu., Bachmanov D.M., Minini H., Ali O. & Al-Kafri A.-M. (2008). The Late Quaternary marine terraces in the Mediterranean coastal area of Syria, *Quaternary Intern., in press*.

Freund R., Zak I. & Garfunkel Z. (1968). Age and rate of the sinistral movement along the Dead Sea rift, *Nature, 220, 253-255*.

Garfunkel Z. (1989). Tectonic setting of Phenerozoic magmatism in Israel, *Isr. J. Earth Sci., 38, 51-74*.

Garfunkel Z. & Ben-Abraham Z. (2001). Basins along the Dead Sea Transform, *Ziegler P.A., Cavazza W., Robertson A.H.F. & Crasquin-Soleau S. (Eds.), Peri-Tethys Memoir 6: Peri-Tethyan Rift/Wrench Basins and Passive Margins, Memoires du Museum National d'Histoire naturelle, 186, 607-627*.

Gomez F., Meghraoui M., Darkal A.N., Hijazi F., Mouty M., Suleiman Y., Sbeinati R., Darawcheh R., Al-Ghazzi R. & Barazangi M. (2003). Holocene faulting and earthquake recurrence along the Serghaya branch of the Dead Sea fault system in Syria and Lebanon, *Geophys. J. Intern., 153, 658-674*.

Hurwitz S., Garfunkel Z., Ben-Gai Y., Reznikov M., Rotstein Y. & Gvirtzman H. (2002). The tectonic framework of a complex pull-apart basin: seismic reflection observations in the Sea of Galilee, Dead Sea transform, *Tectonophysics, 359, 289-306*.

Karakhanian A.S., Trifonov V.G., Ivanova T.P., Avagyan A., Rukieh M., Minini H., Dodonov A.E. & Bachmanov D.M. (2008). Seismic deformation in the St. Simeon Monastery (Cala'at Sim'an), Northwestern Syria, *Tectonophysics, in press*.

Leonov Yu.G. (Ed.), (2000). Outline of Geology of Syria, *Nauka, Moscow, 204 p. (in Russian)*.

McClusky S., Reilinger R., Mahmoud S., Ben Sari D. & Tealeb A. (2003). GPS constraints on Africa (Nubia) and Arabia plate motions, *Geophys. Jour. Intern., 155, No.1, 126-138*.

Meghraoui M., Gomez F., Sbeinati R., Van der Woerd J., Mouty M., Darkal A.N., Radwan Y., Layyous I., Al Najjar H., Darawcheh R., Hijazi F., Al-Ghazzi R. & Barazangi M. (2003). Evidence for 830 years of seismic quiescence from palaeoseismology, archaeoseismology and historical seismicity along the Dead Sea fault in Syria, *Earth and Planet. Sci. Let., 210, 35-52*.

Ponikarov V.P., Kazmin V.G., Mikhailov I.A., Razvalyaev A.V., Krasheninnikov V.A., Kozlov V.V., Soulidi-Kondratyev E.D., Mikhailov K.Ya., Kulakov V.V., Faradjev V.A. & Mirzayev K.M. (1967). Geological Map of Syria, scale 1:500,000, Explanatory Notes, Part I, *Ministry of Industry, Damascus, 230 p*.

Quennell A.M. (1959). Tectonics of the Dead Sea rift, *Assoc. de Servecios Geolocos Africanos, Actas y Trabajos de las Reuniones Celebradas en Mexico en 1956, Mexico, 385-405*.

Rukieh M., Trifonov V.G., Dodonov A.E., Minini H., Ammar O., Ivanova T.P., Zaza T., Yusef A., Al-Shara M. & Jobaili Y. (2005). Neotectonic Map of Syria and some aspects of Late

Cenozoic evolution of the north-western boundary zone of the Arabian plate, *J. Geodyn., 40, 235-256*.

Segev A. (2005). Magmatic rocks, *Geological framework of the Levant, vol II, part 4, Historical Production-Hall, Jerusalem, 553-576*.

Trifonov V.G., Trubikhin V.M., Adjamian J., Jallad Z., El Hair Yu. & Ayed H. (1991). Levant fault zone in the north-western Syria, *Geotectonics 25, 145-154*.

Walley Ch.D. (1988). A braided strike-slip model for the northern continuation of the Dead Sea Fault and its implications for Levantine tectonics, Tectonophysics, 145, 63-72.

Wells D.L. & Coppersmith K.J. (1994). New Empirical Relationships among Magnitude, Rupture Length, Rupture Width, Rupture Area, and Surface Displacement, *Bull. Seismol. Soc. Amer., 84, 974-1002*.

Westaway R. (2004). Kinematic consistency between the dead Sea Fault Zone and the Neogene and Quaternary left-lateral faulting in SE Turkey, *Tectonophysics 391, 203-237*.

Zanchi A., Crosta G.B. & Darkal A.N. (2002). Paleostress analyses in NW Syria: constraints on the Cenozoic evolution of the northwestern margin of the Arabian plate, *Tectonophysics, 357, 255–278*.

Laboratory Study of Microseismicity Caused by Pore Pressure Change

Turuntaev S B (1), Zenchenko E V (2), Eremeeva E I (3)

(1) Institute of Geosphere Dynamics, Russian Academy of Sciences, turunt@postman.ru
(2) Institute of Geosphere Dynamics, Russian Academy of Sciences, zench@idg.chph.ras.ru
(3) Institute of Geosphere Dynamics, Russian Academy of Sciences, eva_10b@mail.ru

Keywords: microseismicity, induced seismicity, water injection, laboratory experiment

Introduction

In addition to the potential danger of seismic events related with hydrocarbon development for buildings and personnel, seismicity data in hydrocarbon fields holds useful information (see Adushkin et al. (2000)). Seismicity and microseismicity are related with displacements along faults of different scales, with change of stress-strain state of a reservoir and surrounding rock mass, with a flooding front propagation. Passive seismic monitoring is used for detection of size and location of hydraulic fractures. It was shown by Shapiro et al. (2002) a possibility to estimate a reservoir permeability by means of measurement the rate of propagation of front of microseismic events caused by fluid injection.

It is hard (or impossible) to resolve the questions only by theoretical analysis and interpretation of real field data, because natural geophysical objects are very complicated and it is impossible to control all the parameters defining the studied phenomena. That is why it becomes reasonable to make physical laboratory modeling. For correct simulation it is necessary to take account for a scale effect (both spatial and temporal) and to meet a condition of invariance of some dimensionless combinations of defining parameters. At the same time, even in case of strict simulation criteria validity, the direct quantitative application of results of laboratory experiments to natural processes is complicated by simultaneous action of many factors, which were not considered during the experiment. But even a qualitative understanding of real processes, obtained in laboratory experiments, can help in correct interpretation of the field data.

In presented paper, results of laboratory experiments on study of relation between acoustic emission (AE), which corresponds to microseismic emission in real scale, and increase of pore pressure in a model sample under load with different vertical-horizontal stress relations are considered.

Materials and Methods

The study of an acoustic emission (AE), caused by change of pore pressure and stresses in porous medium was carried out using a stress-flow cell shown in Fig.1. The stress-flow cell is a stainless steel box with rectangular cross-section filled by porous modeling material. Time-size-flow rate and stress-strength dimensionless simulation criteria were used to choose modeling medium. Crushed pine rosin with grains from 2.5 to 7 mm was chosen as a modeling material. Initially, the cell was filled by crushed rosin, and then the rosin was pressed up to a porous bound state. The rubber diaphragm separates the porous medium from a cover of the box. To load the reservoir by external pressure, water was injected into the gap between the cover and the diaphragm. To open or close the inlet and outlet of the cell, solenoid valves were used. An adjustable filter was installed after the cell outlet, which allows controlling the pore pressure at outlet.

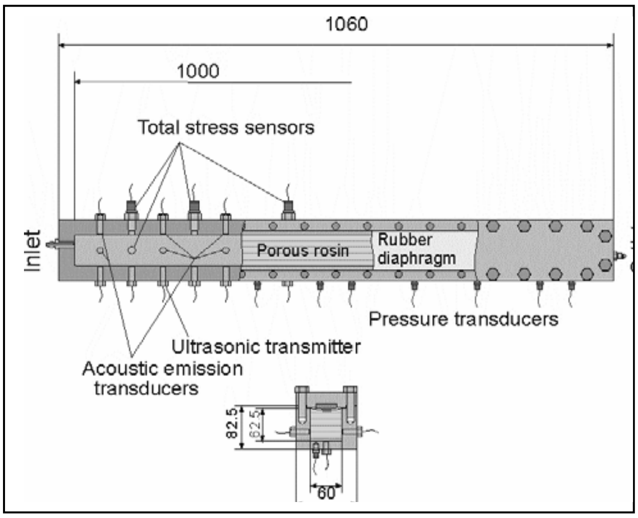

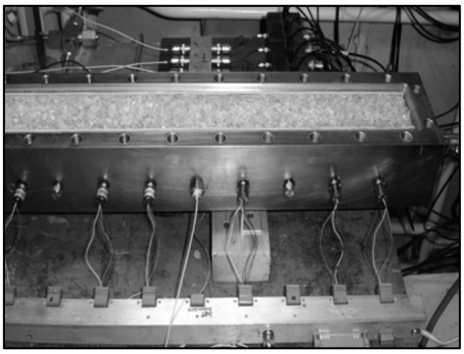

Figure 1. Layout and photous of the stress-flow cell.

The pressure drop at this filter was approximately 0.3 MPa at maximum flow rate 0.35 cm^3/s. Assembled cell was vacuumized and filled by distilled water to prevent air bubbles formation in pores. Registrations were made by means of pressure and force transducers and accelerometers. Both pore pressure and stress sensor readings were registered by PC-based AD converter with sampling frequency 10 Hz and saved to a hard disk. Piezoceramic acoustic emission transducers were placed in the sidewalls of the stress-flow cell and in the bottom. The AE signals were amplified by preamplifiers and then digitized by high speed AD converter with sampling frequency 800 kHz.
Pumping unit injected water into the stress-flow cell with constant flow rate, which was set according to reservoir permeability. External pressure was maintained constant as far as possible by means of mechanical loading machine. Maximum external pressure was about 7 MPa. After starting the water pumping unit, the inlet valve had been opened and the pore pressure began to rise along the stress-flow cell. The record of AE pulses lasted up to 50 seconds. Then, when pressure distribution along the cell became stationary, the flow rate through the reservoir had been measured to calculate average permeability of the reservoir.
Preliminary, the reservoir permeability was estimated by means of sound velocity measurements. The pair of opposite AE transducers was used for this purpose. One of transducers was actuated by applying short high-voltage pulses at rate 50 Hz, whereas the other received ultrasonic oscillations passed trough the reservoir. The similar procedure was used for relative AE sensors calibration. The obtained calibration data were used during AE pulses processing.
Two types of experiments were made. In the first one, elastic layers of rubber were placed between the cell side walls and the model reservoir. In the second experiments, there were no rubber layers. This resulted in change of relation between horizontal and vertical stress components.
Preliminary AE records (samples are shown in Figure 2) processing included discrimination of ADC records into individual channels, separation of individual AE pulses from each channel, their digital filtering, and Burg spectra calculation. The further data reduction included calculation of sums of maximum amplitude of AE pulses within certain period of time (0.1 second) and tracing this value (regarded as AE activity) vs. time. Using data from opposite AE sensors enable us to localize the foci of AE pulses origins across the stress-flow cell.

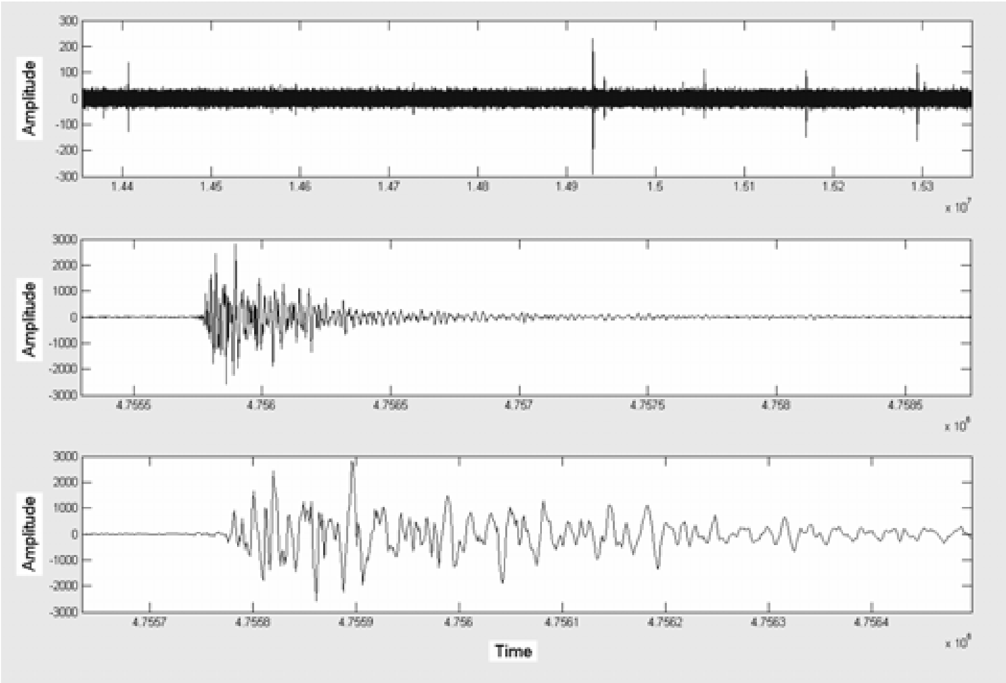

Figure 2. Samples of acoustic emission records in different time scale.

Results and Discussion

Acoustic emission measurements had been held for the permeability from 36 to 1.8 mD. Time-pressure diagrams for permeability 36 mD are presented in figure 3a. Figure 3b demonstrates time dependence for both vertical and horizontal stresses as well as pore pressure and the difference between external and pore pressures at the stress measuring points. Discrepancy between initial external pressure and vertical stress may be caused by different loading "history". The longer is the period of loading, the smaller is the difference.

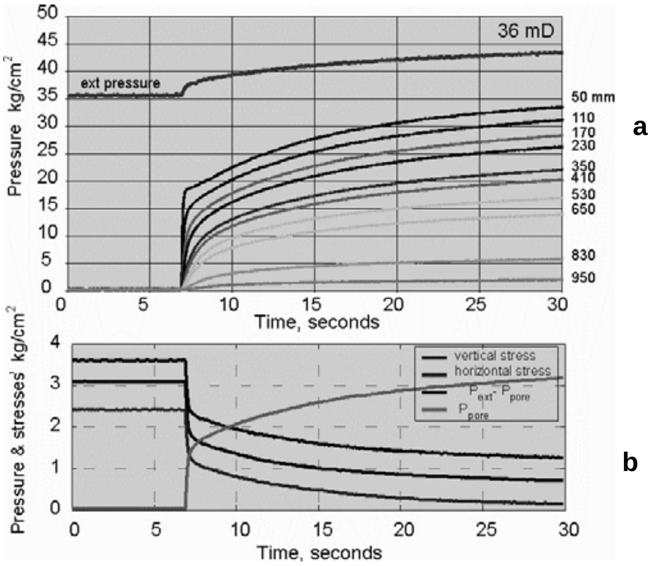

Figure 3. (a) Pressure vs. time at different points along the cell. (b) Effective stresses and pore pressure at point 170 mm vs. time

The difference between the experiments with different cell side wall softness resulted in different relation between horizontal and vertical stress components. In experiments with elastic walls we had (fig.4)

$$\sigma_h = a_1\sigma_v^2 + a_2\sigma_v + a_3$$

with coefficients

$$a_1 = 0.05 \pm 0.01$$
$$a_2 = 0.11 \pm 0.07 .$$
$$a_3 = 0.6 \pm 0.05$$

In experiments with hard walls we got (fig.5)

$$\sigma_h = b_1\sigma_v + b_2$$

with averaged coefficients

$$b_1 = 1,\ b_2 = -0.75 .$$

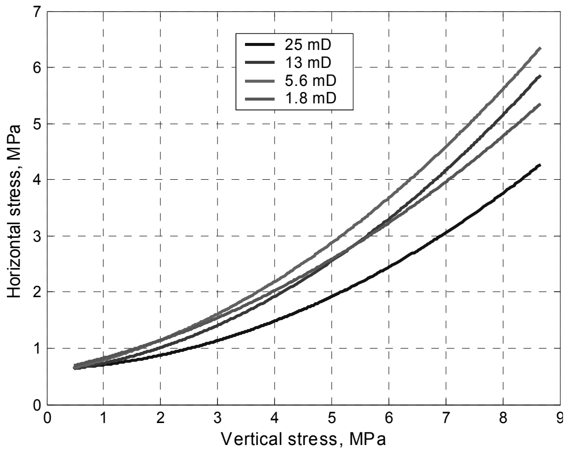

Figure 4. Relation between horizontal and vertical effective stresses in experiments with “soft walls”. Permeability of the samples is shown.

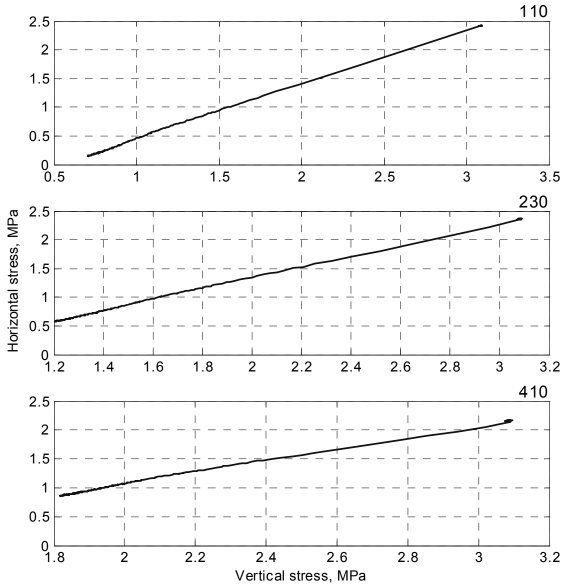

Figure 5. Relation between horizontal and vertical components of effective stresses in experiments with “hard walls” in different sections of the cell (permeability 36 mD).

Localized pulses had been used for temporal-spatial distribution evaluation. It was found, that all events were approximately uniformly distributed across reservoir sections.

Relations between spatial change of pore pressure and locations of AE pulses are shown in Fig.6 and Fig.7. Values of AE activity were averaged in space and time, and then 3D plots were plotted in form of “shaded relief’, which represent change of AE activity both along model reservoir and in time.
In the same plots, isolines of equal pore pressures (normalized by unconfined compression strength of the model material, which was measured experimentally) are shown by thin lines. Bold lines are approximations of AE migration with time from point of injection. It can be clearly seen, that velocity of AE migration changes with change of the model permeability. As it can be seen in Figure 6, in experiments with soft walls AE migration correlates with normalized pore pressure isolines 1±0.5 in different experiments. It means that AE emission migration corresponds to spreading of pore pressure values, equal to compression strength. Meanwhile both vertical and horizontal stresses are not equal to zero at the moments of AE emission start. The main distinction in AE spread in experiments with hard walls is that front of AE propagates significantly faster than in experiments with soft walls (compare fig.6 and fig.7). In these experiments the value of pressure for AE starting is smaller and approximately equal to 0.2 – 0.4 of compression strength.

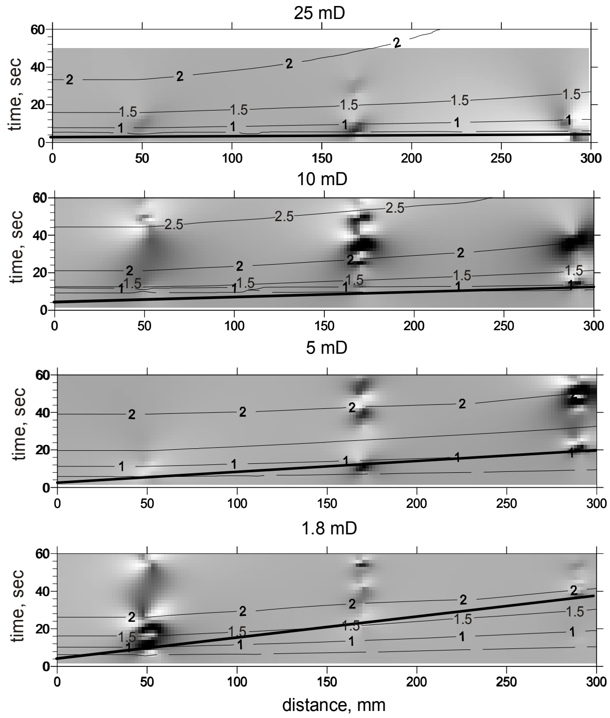

Figure 6. Experiments with “soft walls”. Spatial and temporal change of AE activity (shown by “shaded relief”) in comparison with normalized pore pressure (shown by thin isolines). Bold lines present an approximation of AE spread. Pore pressure is normalized by compression strength of samples.

We suppose that the nature of AE pulses is related with inelastic behavior of the rosin and existence of residual stresses. In papers Zhu et al, (1985), Rodionov et al (1999), the problems of fracturing under action of residual stresses were considered both by analyzing of natural observations (like a core disking) and by laboratory and theoretical modeling. There are a lot of attempts to understand a role of residual stresses in fracturing phenomena, but it continue to be unclear, mainly because of difficulties in estimation of residual stress values.
To make further analysis, we transformed the obtained catalogue of AE pulses into the form of “acoustic activity”. Acoustic activity is defined here as a function of the energies of acoustic events which appeared on a given area at a given time interval. AE pulse energy was estimated as squared amplitude of the pulse, so AE activity was calculated as an approximation:

$$A(t) = \sum_{\substack{i\in(t,t+\Delta t)\\ j\in(x,x+\Delta x)}} (A_{i,j})^{2\alpha}$$

where $A(t)$ – AE activity, $A_{i,j}$ – pulse amplitude, α - parameter, suggested by Sadovsky & Pisarenko, 1991 for statistical stabilization of A. It was shown, that to diminish an influence of rare high amplitude events on A, the value of α must be $\alpha < \gamma/2$, where γ is the slope ratio of energy-frequency relationship (an analog of *b*-value for magnitude-frequency relationship). Idescribed experiments $\gamma \approx 0.9$.

Changes of AE activity in several sections of the cell are shown in Figure 8. An approximation of AE activity mean variation (trend) is shown there by red line. The trend was calculated as

$$A_{trend} = at \cdot \exp(-bt) + c$$

where a, b, c – parameters of approximation to best fit the data.
It can be presumed, that AE activity variation in time reflects change of pore pressure. Pore pressure change leads to an increase of effective stresses, which results in fracturing. The simplest model of the fracturing processes can be based on two suggestions:

- a fracture appears when the pore pressure reaches some threshold value;
- the threshold value spatial distribution can be described by Gaussian error function (Shapiro et al. 2002, Del´epine et al., 2004).

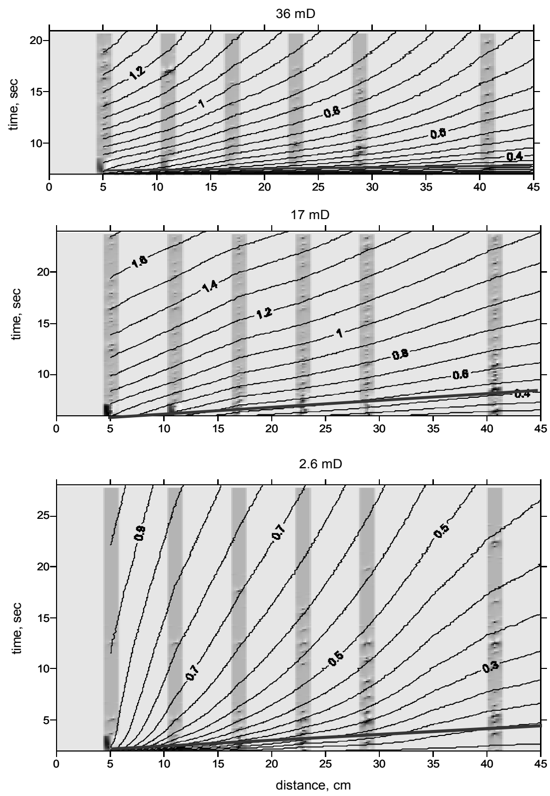

Figure 7. Experiments with “hard walls”. Spatial and temporal change of AE activity in comparison with normalized pore pressure. Bold lines present an approximation of AE spread. Pore pressure is normalized by compression strength of samples

We used experimental pressure data recorded at different sections along the cell to produce synthetic catalogue of AE pulses. For each time interval the pore pressure range was taken from experimental data, and the number of discontinuities for which the threshold values fall in this pore pressure range was calculated. It was assumed that all such discontinuities will gave rise to AE pulses of the same amplitudes during considered time interval. AE activity was calculated as a sum of the pulse amplitudes. Parameters of Gaussian error function were calculated to provide the best correspondence between experimental and synthetic AE variations in section 50 mm; the same parameters were used for sections 230 and 410 mm. The mean value of Gaussian error function was found to be equal to 8 MPa, which is less by 1 – 2 MPa than external vertical load. The standard deviation was found to be 3 MPa. The trend curve was calculated by the same manner as for experimental data to best fit synthetic data. The synthetic AE activity variations are shown in Figure 9.

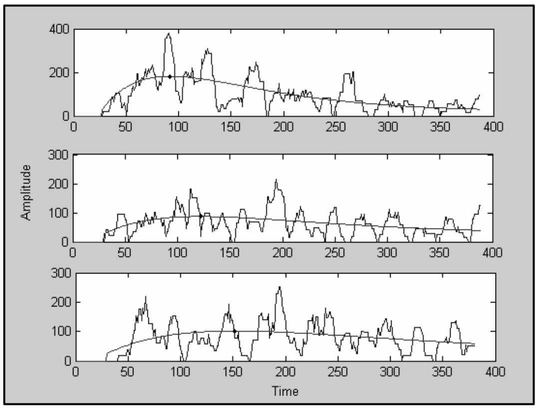

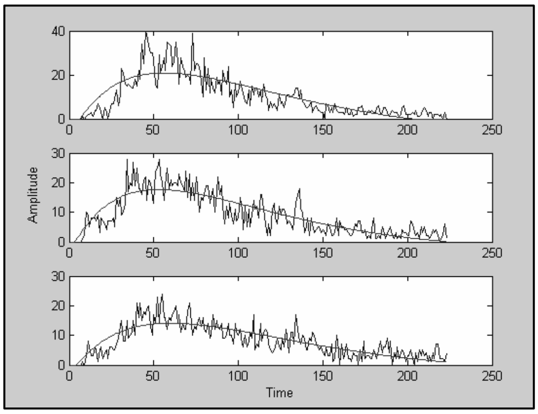

Figure 8 (left). Experimental AE activity variations at points 50, 230 and 410 mm and its trend,
Figure 9 (right). Synthetic AE activity variations at points 50, 230 and 410 mm and its trend.

If one compares Figures 8 and 9, good correspondence between their mean trend curves can be seen, which means, that the proposed model can be used for the AE trend description.
Let's compare experimental data on pore pressure diffusion with one of the simplest model – a piezoelastic one. The piezoelastic equation:

$$\frac{\partial p}{\partial t} = \frac{k}{\mu_0 \beta m_0} \nabla^2 p,$$

where $\beta = a_m + a_p$ is effective compressibility of the porous medium. Initial condition:

$$p(x,0) = p_0$$

A constant fluid rate Q at the inlet end of the cell and constant pressure at the outlet end were taken as boundary conditions:

$$\frac{\partial p(0,t)}{\partial x} = -b, \; b = \frac{Q}{k}$$

$$p(1,t) = p_0$$

The solution can be written as:

$$p(x,t) = p_0 + b(1-x) - 2b \sum_{k=0}^{\infty} \frac{e^{-\mu_k{}^2 a^2 t}}{\mu_k{}^2} \cos \mu_k x$$

where $\mu_k = \frac{\pi}{2} + \pi k$, $k \in \{0\} \cup N$. The solution is plotted in Figure 10 as a variation of the pressure with time at one point in comparison with experimental data. The significant discrepancy between analytical and experimental results can be diminished by taking into account higher compressibility of the saturated porous sample due to presence of small amount of residual gas (not more than 0.1%) and permeability inhomogeneity along the cell.

Finally, let us consider some general characteristics of AE in the experiment. As it was shown by a number of researchers (Sadovsky & Pisarenko, 1991 and references there), a linear type of energy (*E*) – frequency of seismic events occurrence (*N*) relation in logarithm scale is observed for seismic events of any energies, from strong earthquakes (Gutenberg – Richter low

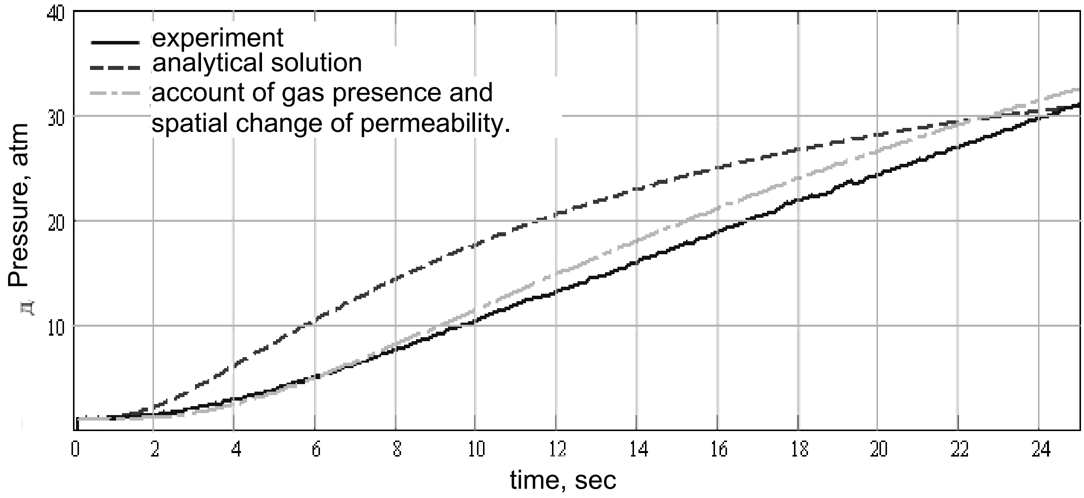

Figure 10. Comparison of pressure diffusion one-dimensional analytical solution, experimental data and corrected solution for pressure variation with time at one point of the cell.

for magnitude – frequency relation) up to laboratory acoustic pulses registering during lab samples fracturing.

$$\lg E = A + \gamma \lg N \qquad (1)$$

A declination from this linear relation in the range of small events is considered as an indication of insufficient sensitivity of recording equipment; the declination in range of strong events is considered as a test of insufficient duration of observations. Value *A* is called sometimes "seismic activity"; it is a characteristic of average level of seismic energy release. Value γ is a slope of energy – frequency relation, it is a characteristic of respective number of small events in comparison with strong events. In case of magnitude – frequency relation instead of γ - value term *b* – value term is used. The relation between *b* –value and γ – value can be estimated as $b \approx 1.5\ \gamma$.

There are a lot of research works dealing with an explanation of physical reasons for (1) law and a study of γ -value dependencies on various parameters. For our study, a research of S.D.Vinogradov, 1983 is of particular interest. He studied in lab experiments a relation between γ-value and samples strength. We calculated γ-values for acoustic pulses registered in experiments on water injection and pore pressure release. The energies of AE pulses were estimated as squared amplitudes of the pulses. It was found that energy – frequency relation obey to linear low (in logarithmic scales). In Fig.11 relation between γ-values and the sample strength are show both obtained in our experiments and in experiments of S.D.Vinogradov, 1983. One can see that our data for porous saturated material are in agreement with the data obtained for solid materials. So, the graph in Fig.11 can be used for estimation of a strength of reservoir zones in which seismic or microseismic events are recorded.

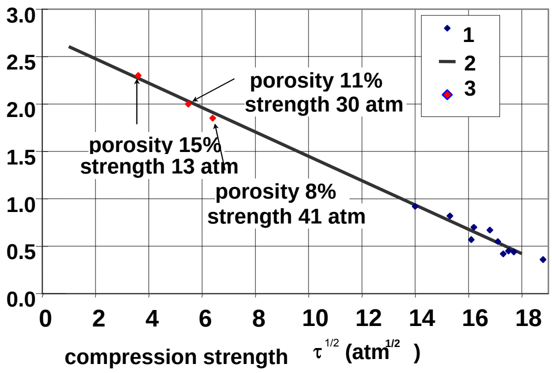

Figure 11. Frequency-energy relationship slope □ dependence on compression strength of rock samples and of laboratory model material: 1 - data of lab experiments of D.S. Vinogradov; 2 – interpolation; 3 – data for porous rozin.

Conclusions

A relation between pore pressure changes and acoustic emission was studied in laboratory experiments. In experiments with “soft” walls the propagation of AE corresponds to pore pressure increase up to values approximately equal to uniaxial unconfined compression strength (which depends on porosity of the sample). In experiments with “hard” walls the value of pressure for AE starting is smaller and approximately equal to 0.2 – 0.4 of compression strength. The relation between pore pressure diffusion and AE front occurred to be dependant not only on the permeability, but on the stress state and stress state change of the sample.

A comparison of experimental AE changes with synthetic catalogue (based on suggestion that pore pressure threshold value for fracturing is distributed in accordance with Gaussian error function) shows good correlation between their mean variations. The pressure diffusion can be calculated by piezo-conductivity equation, if one take into account real value of the porous material compressibility and real permeability distribution. It was shown by Shapiro et al, that it is possible to solve inverse problem: to estimate permeability distribution by analysis of microseismicity diffusion from the point of fluid injection.

The γ–value of energy-frequency relationship for acoustic pulses registered during pore pressure changes is in correspondence with the data on relation between γ–value and the strength of rock samples under uniaxial load. This result can be used for estimation of strength of reservoir zones in which microseismic events are recorded.

Acknowledgements

The authors wish to acknowledge the generous support of Russian Foundation for Basic Research (RFBR project # 07-05-00722).

.

References

Adushkin, V.V., Rodionov, V.N., Turuntaev, S.B., Yudin, A.E. (2000). Seismicity in the Oil Field. *Oilfield Review. 12, 2, 2-17*.

Rodionov V.N., Sizov I.A., Tsvetkov V.M. (1999). A core disking in stressed rocks, *Problems of safety and improvement of mining, 2, 2-10* (in Russian).

Sadovsky M.A., Pisarenko V.F. (1991). Seismic processes in blocky medium, *Moscow, Nauka*, 110p.

Shapiro, S. A., Rothert, E., Rath, V., & Rindschwentner, J. (2002). Characterization of fluid transport properties of reservoirs using induced microseismicity, *Geophysics*, *67, 212–220*

Zhu W., Li G., Wang K. (1985). Analyses of disking phenomenon and stress field in an underground powerhouse, *Rock Mech. and Rock Engineering*, *18, 13. 1-17.*

A Seismotectonic Study for the Broader Area of the Corinthiakos Gulf

Valkaniotis S (1), Koravos G (2), Papadopoulos G (3), Pavlides S (1) and Tsapanos T (2)

(1) Aristotle University of Thessaloniki, School of Geology, Geological Department, 54124 Thessaloniki, svalkan@geo.auth.gr
(2) Aristotle University of Thessaloniki, School of Geology, Geophysical Laboratory, 54124 Thessaloniki, koravos@geo.auth.gr
(3) National Observatory of Athens, Institute of Geodynamics, 11810 Athens, papadop@gein.noa.gr

Keywords: Seismotectonics, Active Faults, Historical Earthquakes, Corinth Gulf, Central Greece

Introduction

The broader area of the Corinthiakos gulf is one of the most active areas in the whole Greek territory. Active tectonics, earthquakes and tsunamis dominate the whole area. Based on the geodynamics of the Aegean, the tectonic forces of the area are horizontally tensional in a N-S direction. The result of this, is the generation of normal faults that have a general direction of E-W. Most of them belong to the Quaternary epoch and their distribution is mainly in the margins of the gulf of Corinth forming this way an intense relief. Field observations show that in many cases there is a re-activation of these faults in the NW-SE and the SSW-NNE directions. Many of the strong earthquakes occurred in the area are in close correlation with these faults. A study on the earthquakes of the broader area of the Corinth Gulf is undertaken. The study is restricted in shallow earthquakes, only. The data used cover the period from 373 B.C up to the first half of 2007. The seismic hazard is expressed through peak ground acceleration, and is estimated for an intermediate type of soil. The faults of the area are, also, taken into account. The obtained results show that there are sites in the area which exceed the seismic acceleration, officially given (0.24g) by the National Seismic Code. Well-defined zones are observed for these values of exceedance, which ranged between 0.28g-0.36g. We interpreted these results in the means of the strong earthquakes and the faults of the area. The 54% of the strong earthquakes with magnitude Mw>6.0 and the 61% of the existed faults are within those high seismic hazard zones.

Materials and Methods

The Gulf of Corinth, located in central Greece, is a tectonically active graben, with a high slip rate of expansion (6-20 mm/yr). Geodetic data (Hollestein et al. 2008), focal mechanisms from earthquakes (Hatzfeld et al. 2000, Kiratzi & Louvari 2003), and fault-slip analysis show an extension of roughly N-S direction. Extensional deformation in the Gulf of Corinth started in Pliocene times (Doutsos and Piper 1990), while uplift of the Corinth graben initiated in the Early Pleistocene for the southern inland part. In the northern inland part, the current faulting regime initiates in the Early – Middle Pleistocene with the formation of the Amfissa-Itea and Delphi-Arahova incised valleys and uplift of Amfissa and Desfina plateaus. The southern side of the Gulf of Corinth is bounded by a series of major north-dipping normal fault zones, while the northern side displays a more complex fault pattern with south- and southwest-dipping normal to oblique fault zones.

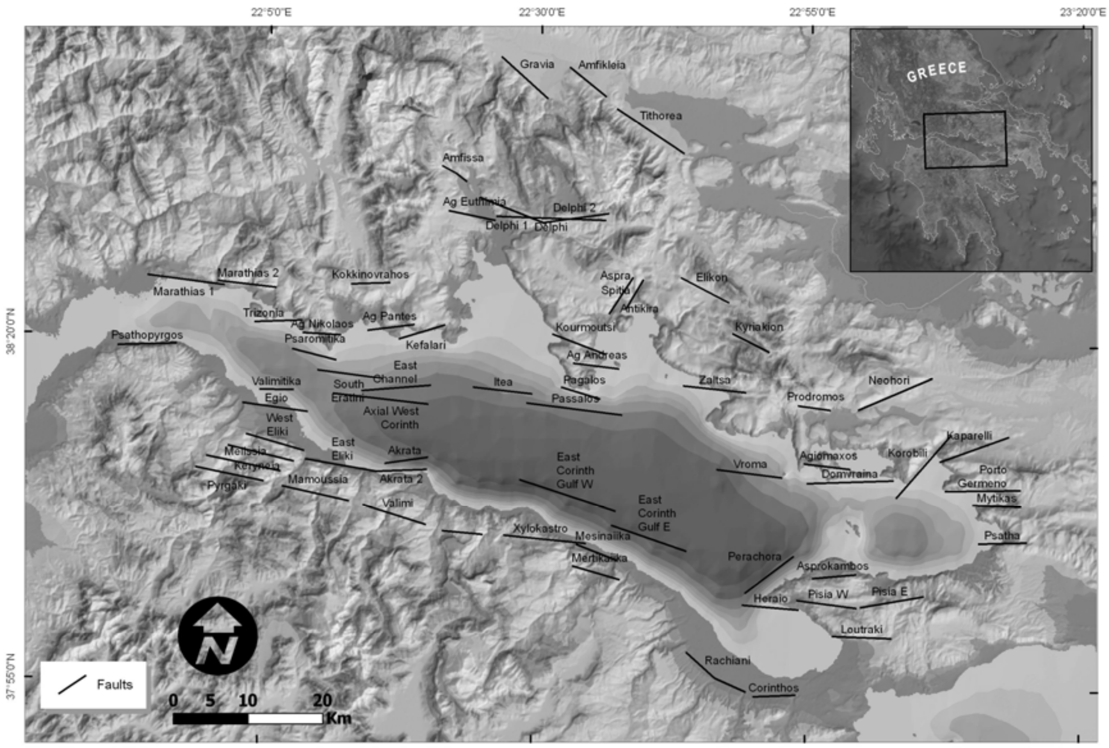

Figure 1. Main active and possible active faults in the broad area of Corinth Gulf used in this study. Faults are simplified and modelled for use in the PGA assessment. Data from Poulimenos (1991), Goldsworthy et al. (2002), Roberts & Koukouvelas (1996), Stefatos (2005), Zygouri et al. (2008) and field work from the first author.

Active faults of Corinth Gulf exhibit a distinct geomorphic imprint, especially in the eastern and northern parts, where impressive fault scarps and deeply-incised valleys are formed. Kinematic and geomorphological characteristics show a dominance of WNW-ESE to W-E striking faults with normal slip, with a number of faults having a significant oblique-normal slip. A significant number of faults seems to reactivate older faults, like Miocene-Pliocene normal faults and Alpine thrust and strike-slip faults. This is mainly observed in the northern part (Viotia and Parnassos areas), where older NW-SE and W-E faults are prone to reactivation by the current extensional stress regime (figure 2).

The most important faults/fault systems of the area studied are the Delphi-Arahova-Amfissa Fault System (with strong historical earthquakes in 279BC, 551AD, 1509 and 1870), the Helike Fault (373BC and 1861AD), Kaparelli, Pisia and Perachora Faults (1981), Xilokastro Fault (1402) and the Egion Fault (1995). Many historical earthquakes are associated with the submarine faults near Galaxidi town (996 AD, 1660, 1794 and 1992), while a sequence of strong events is related to the faults in the Nafpaktos (Lepanto) town (Ambraseys & Jackson 1998, Papadopoulos et al. 2000). A significant number of faults in the northern part of the Corinth Gulf area (like Elikon, Levadia, Psatha, Domvraina, Amfissa, Amygdalea, Eratini faults) exhibit geological and morphological criteria enough to characterize them as active faults, although they are not associated with historical or recent earthquakes. This is something to be expected regarding possible gaps in historical accounts, especially in Middle Ages, and the long recurrence period for faults in the Aegean area (>1000 yrs).

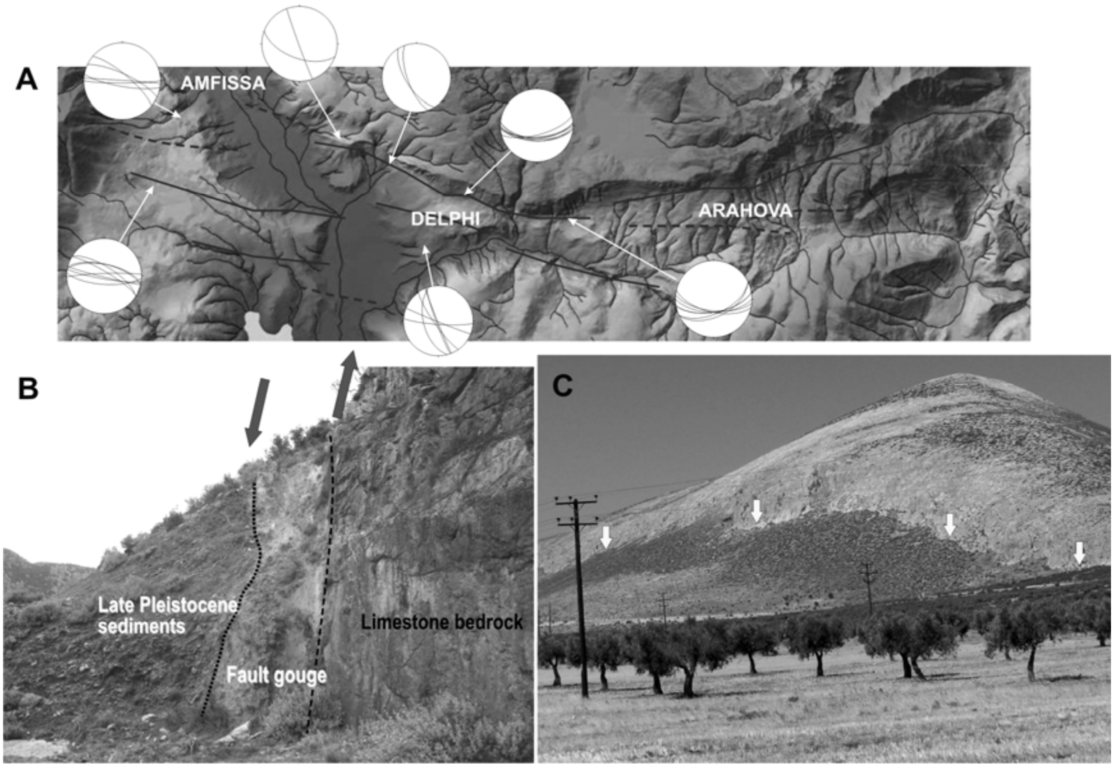

Figure 2. A) The Amfissa-Delphi-Arahova Fault System trace (with red lines) overlaid on digital elevation model. Fault planes measured are shown in stereogpraphic plots. B) The Amfissa Fault, as exposed by an artificial cut northeast of the city of Amfissa. C) The Neohori Fault in Viotia.

Study on the earthquakes of the area

As we aforementioned the area is very seismotectonically active. Earthquakes since the historical era (B.C), as well as recently ones occurred in the area. In figure (3), the spatial distribution of the earthquakes with magnitudes Mw>4.0 in the broader area under investigation is illustrated. A first inspection to this figure reveals that most of the strong (Mw>6.0) events occurred near the coasts (of both sides) of the gulf of Corinthiakos. For reinforcing our observation we draw these strong earthquakes, separately, in figure (4). The completeness of the data is then assessed. This was done by dividing the whole time period into sub-periods and observing the rate of change of the cumulative number of reported earthquakes, above a threshold magnitude, with time (Table 1).

Table 1. The time periods and the corresponding completeness thresholds of the magnitudes

Time periods	Magnitudes
1982 – 2007	M> 4.0
1975 – 2007	M> 4.7
1943 – 2007	M> 5.0
1909 – 2007	M>5.3

The most common and known statistical law of Gutenberg and Richter (1944) is then applied. The parameters found equal to am=7.23 and b= -0.98+0.09. The plot of the magnitude-frequency relationship of the area is illustrated in figure (5).

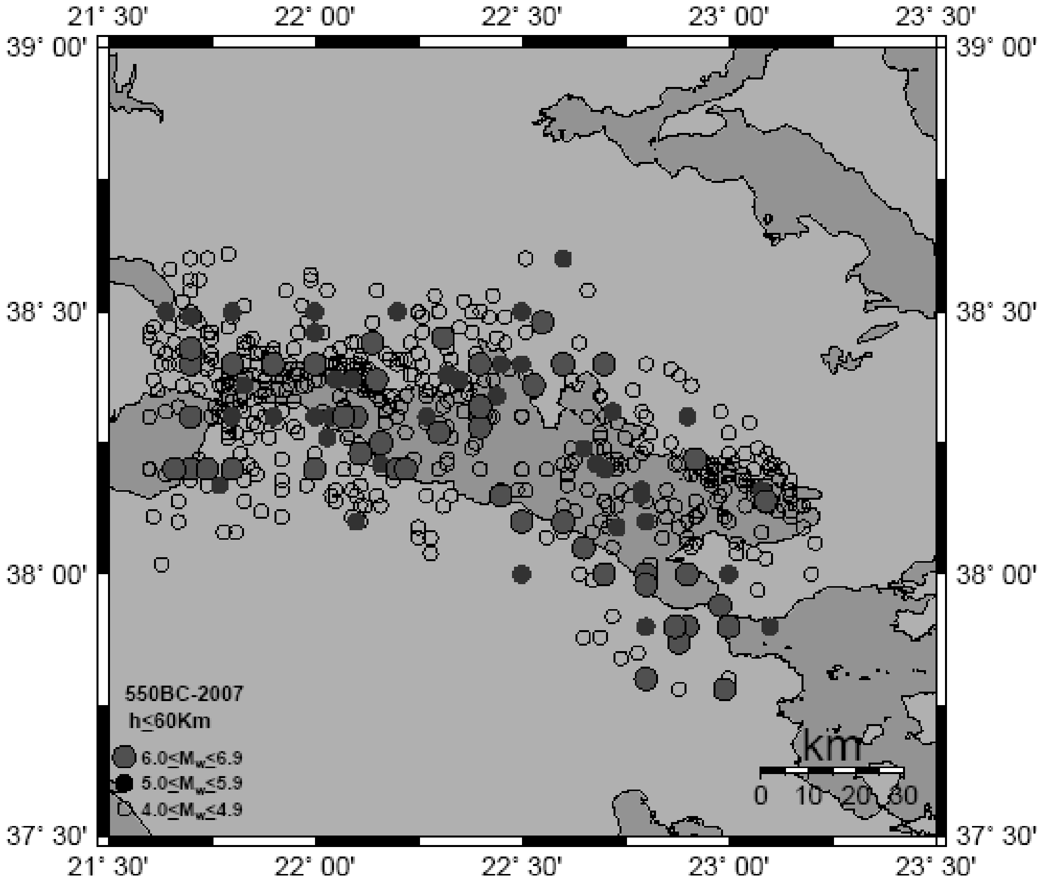

Figure 3. The geographical distribution of the earthquakes with magnitude Mw>4.0 in the broader area.

In order to establish our results the method of Kijko and Graham (1998, 1999) is applied. The procedure involves the area-specific and the site-specific parts. The approach is very flexible allowed the use of earthquake catalogues with incomplete reported historical and complete instrumental data, the consideration of different magnitude thresholds and the incorporation of magnitude uncertainties. The maximum likelihood method is employed to estimate the parameters for area-specific part which are the regional maximum magnitude , the mean seismic activity rate λ, and the b-value of the Gutenberg-Richter law. The results found equal to: b= -0.97+0.03, =6.81+0.20 and λ=14.2+1.6 (for events with Mw>4.0). The results are very compatible comparable with those previously obtained by other authors (Hatzidimitriou, et al., 1985; Papazachos and Papazachou, 1997; Papazachos, 1999).
The site-specific part of the method expressed as probabilities that a given peak ground acceleration (PGA) value will be exceeded at least once during a time interval of t-years. The most important advantage of the method is that it does not require any determination of seismic zones. As an attenuation law we considered adopted the one derived by Skarlatoudis et al. (2003). This law is very comprehensive allowing the use of the faults mechanism and the type of soil. From engineering point of view the maximum peak ground acceleration expected at a given site during a time interval, t, is of special interest. The results of the procedure is demonstrated in figure (6).

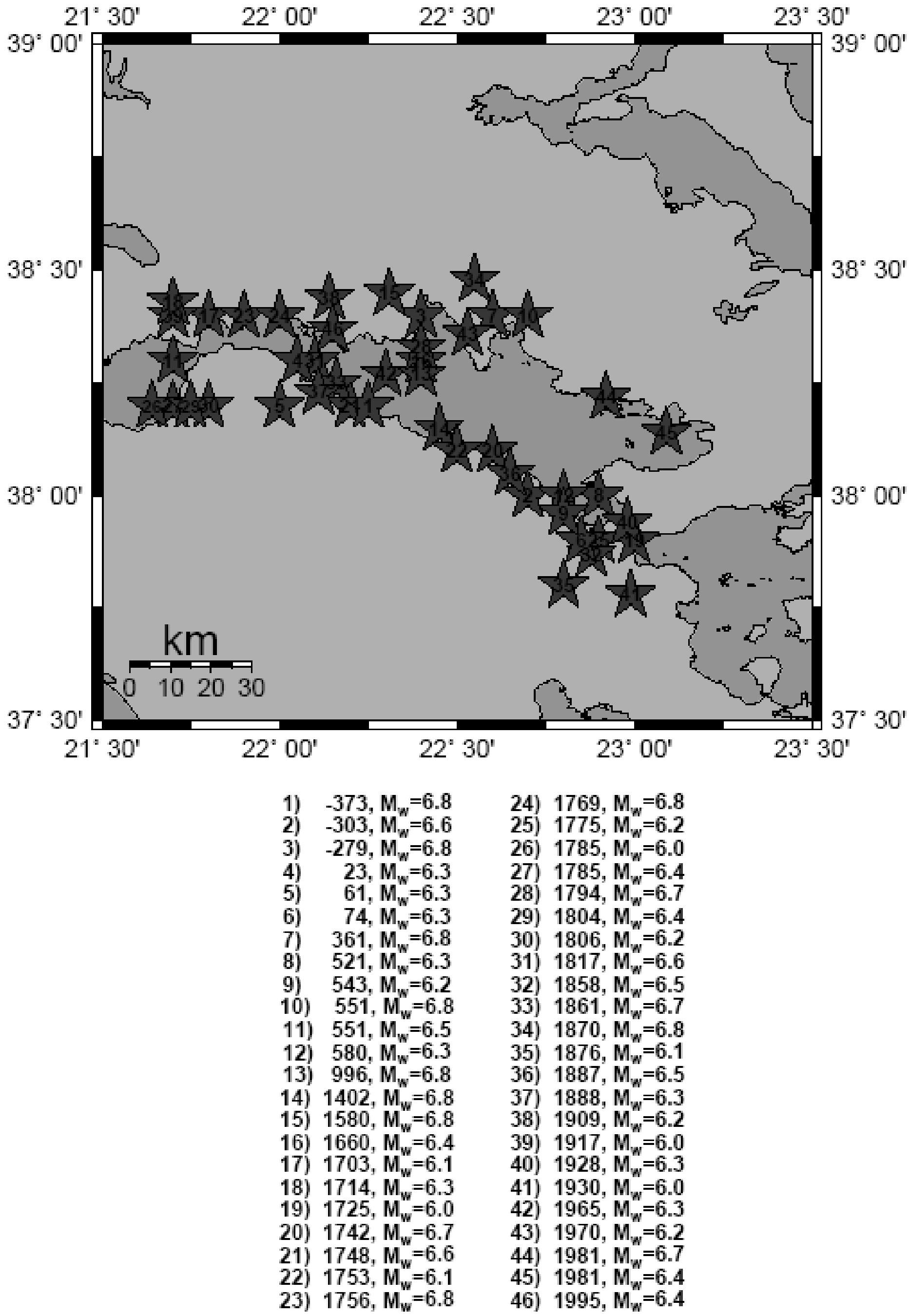

Figure 4. The spatial distribution of the strong (Mw>6.0) earthquakes in the broader area of the Corinthiakos gulf. Each star has a number which is in accord to the number of the corresponding earthquake and its year of occurrence in the bottom part of the figure.

The obtained results show that high PGA values (>0.28g) dominate in the middle part of the Corinthiakos gulf. These values exceed the seismic acceleration, officially given (0.24g), for the area, by the National Seismic Code. Well-defined zones of these high values, which have reached the 0.36g, are observed in this particular place. The highest values are revealed in the small gulf of Itea. An attempt made to interpret these values in the means of seismotectonics. We observed that in the whole area surrounded by PGA values >0.28g, 25 strong (Mw>6.0) earthquake occurs in respect with the 46 shocks generated in the broader area of the Corinthiakos gulf. Moreover 40 of the 65 faults of the whole area of the gulf of

Corinthiakos dominated in this specific area. Given that the applied attenuation law includes the fault type it is easy to understand the obtained high PGA values, in this specific segment of the examined area.

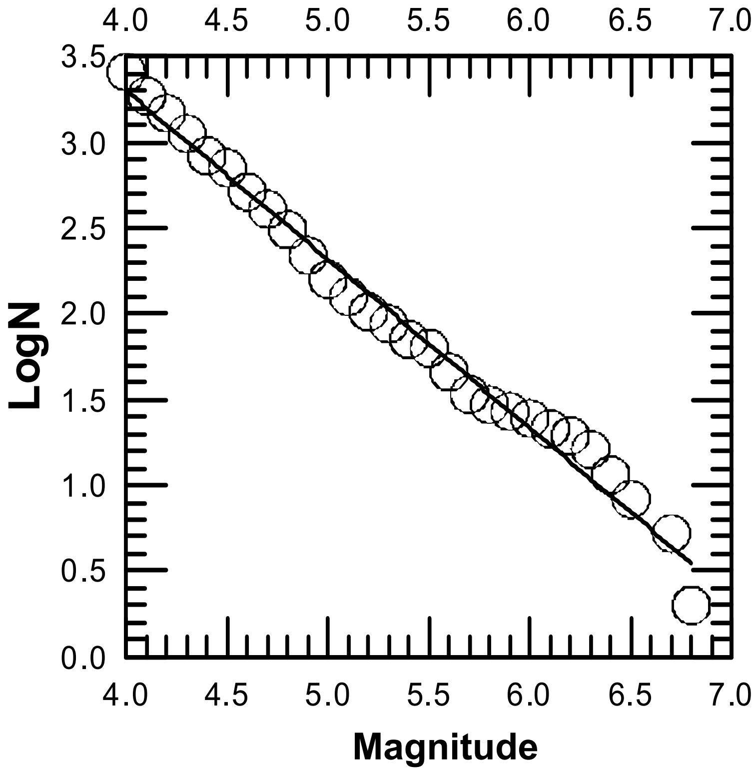

Figure 5. The magnitude-frequency distribution for the broader area of the Corinthiakos gulf.

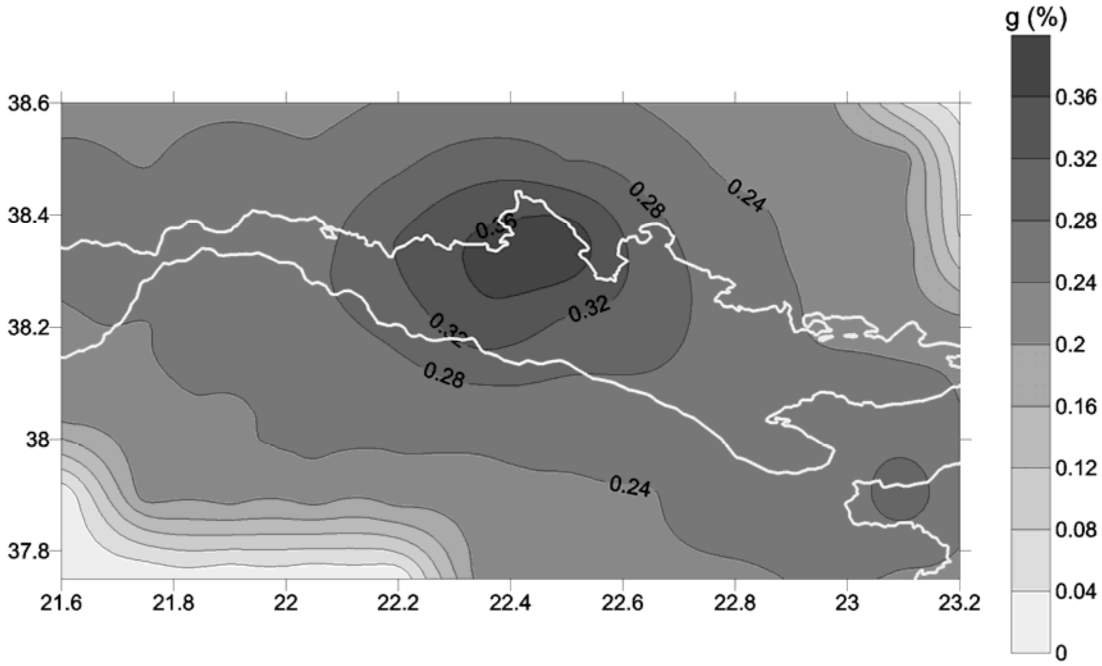

Figure 6. Seismic hazard map of the broader area of the Corinthiakos gulf, as PGA values with 10% probability of being exceeded at least once during a time interval of 50-years. The faults of the area are taken into account as well as the intermediate type of soil.

Results and Discussion

The broader area of the gulf of Corinth is located in central Greece. Kinematic and geomorphological characteristics show a dominance of WNW-ESE to W-E striking faults with normal slip, with a number of faults having a significant oblique-normal slip. In many cases, there is a reactivation of older faults, like Miocene-Pliocene normal faults and Alpine thrust and strike-slip faults. Most of the faults in the area are in close connection with the earthquakes' occurrence. The broader area experienced of 46 large (Mw>6.0) earthquakes since the historical epoch which caused heavy damages and victims. The seismic hazard is estimated, in terms of peak grand acceleration, for the whole area and shows that there are well-defined zones that exceeds the officially given value (0.24g), for the area, by the National Seismic Code. The highest value is observed in gulf if Itea. We conclude that this observation is the consequence of the number of faults dominated in the area, as well as the number large earthquakes occurred there.

References

Ambraseys N. & Jackson J. (1998). Faulting associated with historical and recent earthquakes in the Eastern Mediterranean region, *Geophys. J. Int., 133, 390–406*.

Doutsos T. & Piper D.J.W. (1990). Listric faulting, sedimentation and morphological evolution of the quaternary eastern Corinth rift, Greece: first stages of continental rifting, *Bull. Geol. Soc. Am. 102, 812-829*.

Goldsworthy M. Jackson J. & Haines J. (2002). The continuity of active fault systems in Greece, *Geophys. J. Int., 148, 596–618*.

Gutenberg B. and Richter C.F. (1944). Frequency of earthquakes in California, *Bull. Seism. Soc. Am., 34, 185-188*.

Hatzidimitriou P.M., Papadimitriou E.E., Mountrakis D. M. & Papazachos B.C. (1986). The seismic parameter b of the frequency magnitude relation and its association with the geological zones in the area of Greece, *Tectonophsics, 120, 141-151*.

Hatzfeld D., Karakostas V., Ziazia M., Kassaras I., Papadimitriou E., Makropoulos K., Voulgaris N. & Papaioannou C. (2000). Microseismicity and faulting geometry in the Gulf of Corinth (Greece), *Geophys. J. Int., 141, 438-456*.

Hollenstein Ch., Müller M.D., Geiger A. & Kahle H-G. (2008). Crustal motion and deformation in Greece from a decade of GPS measurements, 1993–2003, *Tectonophysics, 449, 17-40*.

Kiratzi A. & Louvari E. (2003). Focal mechanisms of shallow earthquakes in the Aegean Sea and the surrounding lands determined by waveform modelling: a new database, *J. Geodynamics, 36, 251-274*.

Kijko A. & Graham G. (1998). 'Parametric-historic' procedure for probabilistic seismic hazard analysis. Part I. Estimation of maximum regional magnitude mmax, *Pageoph, 152, 413-442*.

Kijko A. & Graham G. (1999). 'Parametric-historic' procedure for probabilistic seismic hazard analysis. Part II. Assessment of seismicc hazard at specified site, *Pageoph, 154, 1-22*.

Papadopoulos G.A., Plessa A. & Vassilopoulou A. (2000) Historical earthquakes and tsunamis in the Corinth rift, Central Greece, *Institute of Geodynamics, National Observatory of Athens, Publ. No. 12, Athens*.

Papazachos B.C. & Papazachou C. (1997), The earthquakes of Greece, *Ziti Publications, Thessaloniki, 304pp*.

Poulimenos G.A. (1991). Tectonic analysis and sedimentology of the western part of Corinth Rift, *Unpublished PhD thesis, Department of Geology, University of Patras, Greece, 298p*.

Roberts G.P. & I. Koukouvelas (1996). Structural and seismological segmentation of the Gulf of Corinth fault system: implications for models of fault growth, *Ann. Geofisica, 39 (3), 619-646*.

Skarlatoudis A.A., Papazachos C.B., Margaris B.N., Theodulidis N., Papaioannou Ch., Kalogeras I., Scordilis E.M. & Karakostas V. (2003). Empirical peak ground motion predictive relations for shallow earthquakes in Greece, *Bull. Seismol. Soc. Am., 93, 2591-2603*.

Stefatos A. (2005). Study of sedimentological processes and tectonic structures in the Gulf of Corinth using geophysical methods. *Unpublished Phd Thesis, University of Patras, 221p*.

Zygouri V., Verroios S., Kokkalas S., Xypolias P. & Koukouvelas I.K. (2008). Scaling properties within the Gulf of Corinth, Greece; comparison between offshore and onshore active faults, *Tectonophysics, 453, 193-210*.

A HMM Involving Stress Release and Etas Models

Varini E (1), Rotondi R (2)

(1) CNR-IMATI, via Bassini 15 - 20133 Milano (Italy), elisa@mi.imati.cnr.it
(2) CNR-IMATI, via Bassini 15 - 20133 Milano (Italy), reni@mi.imati.cnr.it

Keywords: Hidden Markov Models, doubly stochastic Poisson processes, sequential Monte Carlo methods, Stress Release model, Etas model

Introduction

Self-exciting and self-correcting models are classes of probability models widely used in hazard analysis of seismic catalogues. The former describes the tendency of the earthquakes to occur in clusters; the latter assumes that the tectonic stress builds gradually over time and decreases abruptly when an earthquake occurs. Both the models catch different and important features of seismicity, but they behave contrary in a forecasting perspective: "*the first prescribes that earthquakes make future nearby earthquakes more likely; the other predicts that earthquakes make future nearby events less likely*" (Schoenberg and Bolt, 2000).
Schoenberg and Bolt (2000) proposed a new model obtained as linear combination of a self-exciting and a self-correcting model.

Taking the cue from their work, we consider the Etas model in the self-exciting class (Ogata 1999) and the stress release model (SRM) in the self-correcting class (Vere-Jones 1995) in the framework of the Hidden Markov model (HMM) .

We assume that the ETAS describes the seismicity in the intervals in which the inter-event times are shorter, and the SRM describes the activity in the remaining intervals.

This behaviour is modelled by a two state HMM, that in this particular case it is also called doubly stochastic Poisson process since the observation processes depend on the entire history as well. State 1 and State 2 respectively define the time intervals dominated by the SRM or by the Etas model.

EM algorithm and sequential Monte Carlo methods (or particle filtering) are suitable and powerful statistical tools to study HMM, since they provide the estimates of the unknown model parameters and the approximation of the filtering probabilities (the probabilities that the process is in a state at each time). We study the seismic region of Kresna (Bulgary).

Materials and Methods

The data set

We consider the seismic catalogue of the Bulgarian region of Kresna (Dineva *et al.* 1999).
We study $N = 130$ earthquakes occurred from 1890 to 1995 with magnitude $M_S \geq M_0$, where $M_0 = 4.5$ is a fixed threshold due to the completeness of the catalogue (Figure 1 and 2, bottom reading).
The strongest two earthquakes of the sequence occurred both on April 4, 1904, the former with magnitude $M_S = 7.1$ and the latter, occurred just after 23 minutes, with $M_S = 7.8$. Only two events, in addition to the above mentioned, have magnitude greater than 6.5: the

earthquakes of 1902 and 1931 respectively having $M_S = 6.6$ and $M_S = 6.7$. Figure 1 (bottom reading) represents magnitude versus time of the data.
We denote time and magnitude of the earthquakes by couples (t_i, m_i) for $i = 1,...,N$ and we set $t_0 = 1890$ and $t_{N+1} = 1995$.

The proposed Hidden Markov Model

Point processes are widely used probability models to study sequences of time-magnitude earthquakes. A point process $N(t)$ counts the number of events occurred up to t and is completely defined by its intensity function $\lambda(t)$.
The intensity function $\lambda(t)$ is the instantaneous probability that an event occurs at time t when the seismic history $H_t = \{(t_i, m_i) : t_i < t\}$ up to t is known.
Many point processes have been proposed in the literature and two main classes can be detected: the self-exciting and the self correcting models. We select the models among the most famous and representative ones of these classes, the stress release model (SRM) and the Etas model, whose intensity functions are given respectively by:

$$\lambda_S(t) = e^{\alpha + \beta[\rho t - s(t)]} \qquad\qquad \lambda_E(t) = \sum_{i:t_i<t} \frac{k e^{\gamma(m_i - M_0)}}{(t - t_i + c)^p}$$

where $\alpha, \beta, \rho, k, \gamma, c, p$ are unknown parameters and $s(t) = \sum_{i:t_i<t} 10^{0.75(m_i - M_0)}$ represents the stress release of the earthquakes up to t, as derived from the Benioff formula.
These models catch different seismic behaviours: in the SRM the stress is assumed to cumulate gradually and linearly over time and then decrease abruptly when earthquakes occur; while the Etas model is typically used to describe sequences of aftershocks.
The difference in their physical meaning is well expressed by their intensity functions: $\lambda_S(t)$ is piecewise increasing, while $\lambda_E(t)$ is piecewise decreasing.

These models are usually used on different kinds of data sets: the SRM is applied to medium-strong events and to catalogues covering as long as possible time intervals; the Etas model is applied to aftershocks and relatively short time intervals.
In order to incorporate both aspects of the seismic behaviours, Schoenberg and Bolt (2000) proposed the SELC model, obtained as sum of a self-exciting model and a self-correcting model. Analogous purpose leads us to propose the following Hidden Markov Model (HMM).
A HMM is a probability model composed by two processes: the state process $X(t)$ and the observed process $N(t)$. We define $N(t)$ to be a point process with intensity function $\lambda_{X(t)}(t)$ depending on $X(t)$; the resulting HMM is also known as a doubly stochastic Poisson process.

Each state represents a distinct physical behaviour; the state process jumps from a state to another at random times and is usually unobserved. Let i be the present state in a time interval between consecutive state jumps; the events (here earthquakes) observed during this time interval come from the process $\lambda_i(t)$.

We propose a HMM having two states defined as follows:
state 1 corresponds to the SRM characterized by the intensity function $\lambda_1(t) = \lambda_S(t)$;
state 2 corresponds to the Etas model: $\lambda_2(t) = \lambda_E(t)$.

The latent state process $X(t)$ is chosen to be a continuous-time two-state pure jump Markov process and it is completely defined by its generator matrix $Q = (q_{ij})_{i,j=1,2}$ and its initial state probabilities $\pi = (\pi_1, \pi_2)$. Both Q and π are to be estimated.

The generator Q is such that $q_{11} + q_{12} = 0$, $q_{21} + q_{22} = 0$ and $q_{ij} \geq 0$ for $i \neq j$; the transition probability from state i to state j are given by $-q_{ij} / q_{ii}$ and the holding times in state i have exponential distribution with mean $-1/q_{ii}$.

Let $\tau_1, \tau_2, ..., \tau_K$ be the jump times and $s_1 = X(\tau_1), s_2 = X(\tau_2), ..., s_K = X(\tau_K)$ be the visited states of the latent process; given the parameters $\theta = (\alpha, \beta, \rho, k, \gamma, c, p, q_{12}, q_{21})$ and π, the complete likelihood of the HMM is given by:

$$L^{(C)} = \pi_{s_0} \prod_{k=0}^{K} \left\{ q_{s_k s_{k+1}} \exp\left[-q_{s_k s_k} u_k - \int_{\tau_k}^{\tau_{k+1}} \lambda_{s_k}(s) ds \right] \prod_{j: \tau_k < t_j < \tau_{k+1}} \lambda_{s_k}(t_j) \right\}$$

where $u_k = \tau_{k+1} - \tau_k$ are the holding times in state s_k, for $k = 0, ..., K$, and $\tau_0 = t_0$, $\tau_{K+1} = t_{N+1}$, $s_0 = X(t_0)$ and $s_{K+1} = X(t_{N+1})$.

Particle filtering and EM algorithm

The inference of a doubly stochastic Poisson process focuses on the estimate of the unknown parameter vector θ and of the latent process $X(t)$. Inference on $X(t)$ consists of the approximation of the filtering probabilities, here denoted by $\phi_i(t)$ and defined as the probabilities that the latent process is in state i at time t given the previous observed history H_t:

$$\phi_i(t) = \text{Prob}\left\{ X(t) = i \,\middle|\, \theta, H_t \right\} \qquad \text{for } i = 1,2$$

By assuming θ as known and by exploiting the martingale representation of a point process, it is possible to apply the innovation method (Brémaud 1981) and to obtain the following system of equations, where the unknowns are functions $\varphi_i(t)$ such that $\phi_i(t) = \dfrac{\varphi_i(t)}{\sum_{j=1,2} \varphi_j(t)}$, for all i and t (Varini 2008):

$$\begin{cases} \varphi_i(t_0) = \pi_i \\ \varphi_i(t) = E^{(n)}\left[\delta_i(X(t)) \exp\left(-\int_{t_n}^{t} \sum_{j=1}^{2} \lambda_j(s) \, \delta_j(X(s)) \, ds \right) \right] & \text{for } t_n < t < t_{n+1} \\ \varphi_i(t_{n+1}) = \lambda_i(t_{n+1}) \varphi_i(t_{n+1}^{-}) \end{cases}$$

where $\delta_i(X(t)) = 1$ if $X(t) = i$ and $\delta_i(X(t)) = 0$ otherwise; the expected value in the second equation is to respect the state process by assuming $\{ \phi_i(t_n) : i = 1,2 \}$ as initial probabilities at time t_n. Moreover the marginalised likelihood with respect to the state process (that is the integral of $L^{(C)}$ with respect to the distribution of all possible state histories) can be obtained as follows: $L = \sum_{n=1}^{N+1} \sum_{i=1}^{2} \varphi_i(t_n)$.

The second equation of the system has no analytical solution and we approximate it by exploiting the Monte Carlo method. The initial probabilities $\pi = (\pi_1, \pi_2)$ are chosen to be uniform because of the lack of information. Sequentially in n, we simulate a number H of state histories $x_n^{(1)},\dots,x_n^{(\mathrm{H})}$ in the time interval (t_n, t) from the latent process such that its initial probabilities are given by $\phi_i(t_n)$ for $i = 1,2$. Then the approximated second equation of the system is given by:

$$\tilde{\varphi}_i(t) = \frac{1}{\mathrm{H}}\sum_{h=1}^{\mathrm{H}} \delta_i\left(x^{(h)}(t)\right)\exp\left(-\int_{t_n}^{t}\sum_{j=1}^{2}\lambda_j(s)\,\delta_j\left(x^{(h)}(s)\right)ds\right) \qquad \text{for } t_n < t < t_{n+1}$$

The proposed sequential solution is essentially due to the iterative nature of the system; it is worth to note that it is a computer intensive method equivalent to the particle filtering where the importance distribution is exactly the distribution of the latent process with suitable initial distribution.

By sampling back in time from the filtering probabilities $\tilde{\phi}_i(t)$'s, we reduce the Monte Carlo noise and obtain the following approximated smoothing probabilities:

$$\hat{\phi}_i(t) \approx \mathrm{Prob}\left\{ X(t) = i \,\middle|\, \theta, H_{t_{N+1}} \right\}.$$

It remains to tackle the problem of the parameter estimation.

Rydén (1996) applied the Expectation-Maximization (EM) algorithm to infer on a Markov-modulated Poisson process, where the intensity functions of the observed processes are constant. We modify the Rydén's EM algorithm in order to deal with the time-dependent intensity functions of our HMM.
EM algorithm, due to Dempster *et al.* (1977), iteratively constructs a sequence of parameter vectors $\theta_0, \theta_1, \theta_2, \dots$ starting from a random vector θ_0. It is proved that the sequence converges to the maximum likelihood estimator $\hat{\theta}$.
Given θ_{j-1}, the EM algorithm calculates next vector θ_j by following two steps:

(E) calculate the expectation $\mathrm{Q}(\theta;\theta_{j-1}) = E_{\theta_{j-1}}\left[\ \log L^{(C)}(\theta) \ \middle|\ \{(t_i, m_i)\}_{\mathrm{i}=1,..,\mathrm{N}} \right]$

(M) set $\theta_{\mathrm{j}} = \max_{\theta} \mathrm{Q}(\theta;\theta_{j-1})$

Since step (E) cannot be solved as in Rydén (1996) because our intensity functions are time-dependent, we approximate $\mathrm{Q}(\theta;\theta_{j-1})$ by particle filtering.

Results and Discussion

We run 50 times the described EM algorithm based on particle filtering where the number of particles is set equal to 60. As comparison, SRM and Etas model are separately fitted to the Kresna's data by an usual maximum likelihood methodology.
The results are summarized in the Table 1:

	SRM	***ETAS***	***HMM***
$\hat{\alpha}$	0.2712	-	0.3529
$\hat{\beta}$	10^{-7}	-	0.9956
$\hat{\rho}$	10^{-7}	-	3.7881
$\hat{k}$	-	0.0259	0.0185
$\hat{\gamma}$	-	1.3156	1.5442

$\hat{c}$	-	$0.51 \cdot 10^{-5}$	$0.40 \cdot 10^{-5}$
$\hat{p}$	-	0.8891	0.8680
$\hat{q}_{12}$	-	-	1.3087
$\hat{q}_{21}$	-	-	0.7085
$\log \hat{L}$	-83.6912	133.2181	138.9135
AIC	173.3824	-258.4362	-259.8270

Table 1

We use the Akaike Information Criterion (AIC) to evaluate the goodness of fit for the models in Table 2. By definition AIC $= 2\mathrm{k} - 2\log\mathrm{L}$, where k is the number of the model parameters. Since the preferred model is the one with the lowest AIC value, the proposed HMM has the best fit .

The top reading of Figure 1 represents the average intensity function $\hat{\lambda}(t)$ obtained through the smoothing probabilities $\hat{\phi}_i$ for $i = 1,2$:

$$\hat{\lambda}(t) = \hat{\phi}_1(t)\hat{\lambda}_1(t) + \hat{\phi}_2(t)\hat{\lambda}_2(t) .$$

We associate each time t to state 1 if $\hat{\phi}_1(t) > \hat{\phi}_2(t)$ and to state 2 otherwise and we obtain the most probable sequence of states in the time interval of the data. By observing the variations of the state in this sequence, we estimate the jump times of the state process. Figure 1-bottom reading represents the data of Kresna (magnitude versus time) and the most probable state jumps; the middle reading of Figure 1 represents the intensity function $\hat{\lambda}_{\max}(t)$ obtained through the most probable states:

$$\hat{\lambda}_{\max}(t) = \hat{\lambda}_1(t) \cdot \delta_t(A) + \hat{\lambda}_2(t) \cdot [1 - \delta_t(A)]$$

where $A = \left\{ t : \hat{\phi}_1(t) > \hat{\phi}_2(t) \right\}$ and $\delta_t(A) = 1$ when t belongs to A, $\delta_t(A) = 0$ otherwise.

From the comparison of the AIC values for the Kresna's data, a clear evidence in favour of the ETAS model emerges against SRM. Nevertheless SRM joined with ETAS in a sophisticated model such as HMM leads to a slight significant improvement. From the results of this simple example, the HMM's seem powerful tools to combine the available knowledge from the analysis of seismic sequences; in spite of their complexity, HMM's keep a high goodness of fit and can provide supplementary information, for example, on the possible changes in the seismic activity. Futur researches will be carried out to improve the performance of the HMM's.

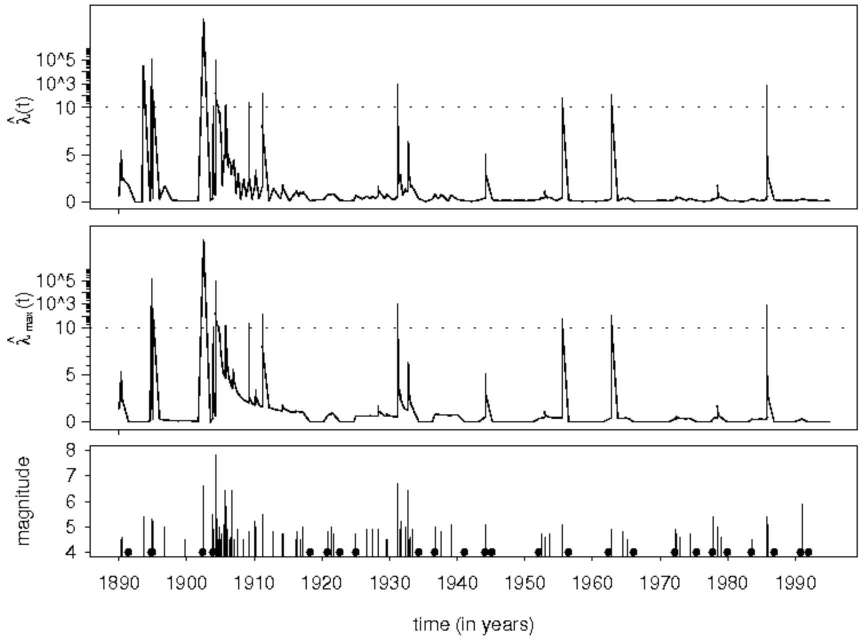

Figure 1. Top : average intensity function $\hat{\lambda}(\cdot)$. Middle: intensity function $\hat{\lambda}_{\max}(\cdot)$ when the state process is composed by the most probable states. Bottom: magnitude versus time of the Krena's earthquakes (vertical bar) and estimated state jumps (dots).

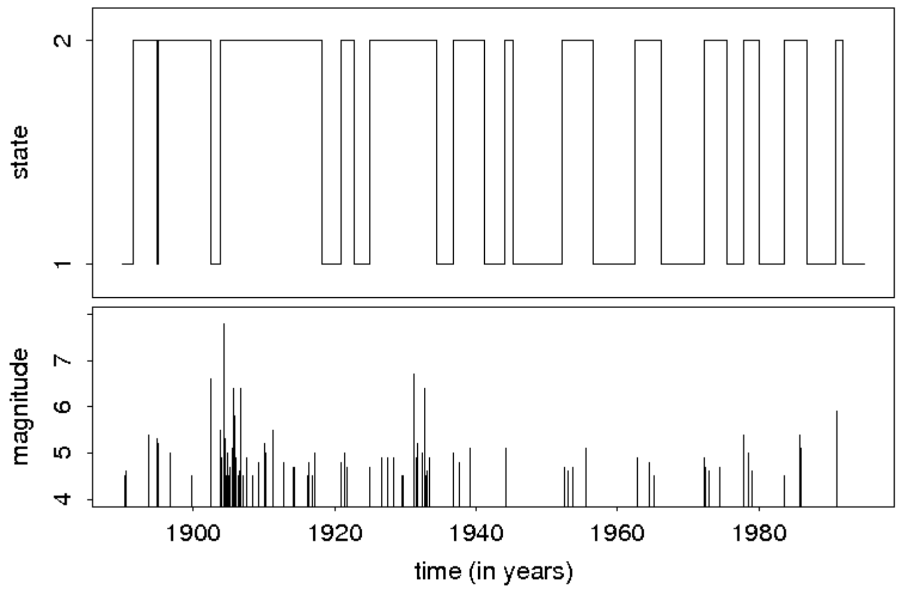

Figure 2. Magnitude versus time of the Kresna's data (bottom) and estimated states (top).

References

Brémaud P. (1981). Point processes and queues. *Springer Verlag, New York*, *354p.*

Dempster A., Laird N. & Rubin D. (1977). Maximum likelihood from incomplete data via the EM algorithm, *Journal of the Royal Statistical Society, B, 39, 1-38.*

Dineva S., Sokerova D. & Mihaylov D. (1999). Catalog of earthquakes in SW Bulgaria and border regions (52 to 1995), *manuscript, Geophysical Institute of Bulgarian Academy of Sciences.*

Doucet A., De Freitas N. & Gordon N. (2001). Sequential Monte Carlo methods in practice, *Springer-Verlag, New York, 581p.*

Ogata Y. (1999). Seismicity analysis through Point-process modeling: A Review, *Pure and Applied Geophysics, 155, 471-507.*

Rydén T. (1996). An EM algorithm for estimation in Markov-modulated Poisson processes, *Computational Statistics & Data Analysis, 21, 431-447.*

Schoenberg F. & Bolt B. (2000). Short-term, long-term correcting models for earthquake catalogs, *Bulletin of the Seismological Society of America, 90, 894-858.*

Varini E. (2008). A Monte Carlo method for filtering a marked doubly stochastic Poisson process, *Statistical Methods & Applications, 17,183-193 (doi:10.1007/s10260-007-0051-y).*

Vere-Jones D. (1995). Forecasting earthquakes and earthquake risk, *Int J. Forecast, 11, 503-538.*

Interdisciplinary Reliable Methodologies for Deterministic Earthquake Prediction

Venkatanathan N. (1)

(1) Faculty of Physics, School of Electrical and Electronic Engineering, SASTRA University, Thanjavur, Tamil Nadu, India. Pin: 613 402, physics16972@gmail.com

Keywords: Resonance effect, Gravitational stress, Thermal Anomaly, Triggering Distance and triggering mechanism

Introduction

Horrible occurrences at Bhuj 2001 Earthquake, Sumatra 2004 Earthquake and recent Sichuan Earthquake are generating a huge amount of fear among all of us. More than physical devastation, natural calamities often leave scars on the collective psyche of an entire community or population. Due to earthquakes, there are some effects like ground shaking, ground displacement, liquefaction, flooding (tsunami), and fire which are hazardous to human beings (Walker, 1982). The hazards mentioned above are avoidable if prediction can be made early, which would enable mitigation of the natural hazard, reduce damage to life and property drastically and facilitate precautionary measures by government and NGOs.

Earthquake prediction, so for considered as “ELUSIVE” due to the complexities involved, but now it is getting importance due to its societal implications and also due to the availability of sophisticated new techniques. Scientists from China (Li et al, 2003), European Countries (Van Genderen, 2004), Russia and Japan have seriously taken up the research encompasses multidisciplinary integrated strategy by using both ground and space borne monitoring systems to understand the earthquake precursors. By incorporating various multidisciplinary integrated methodologies, the initial research have proved the fact, earthquake prediction can be lifted to an unprecedented level of accuracy with regard to location, magnitude and time.

Objectives

In order to explore the possibility of predicting earthquakes more accurately, the following aspects will be considered in detail.

a) Study of tectonic plate movements.
b) Study of nature of fault lines and their relation to tectonic plate movements.
c) Study of paleoseismic events including all small earthquakes have occurred.
d) Analysis of infra red satellite imageries to find thermal anomalies for particular region.
e) Analysis of temperature data NOAA global monitoring programme to cross verify the IR satellite imageries.
f) Observations of the movement of celestial bodies and their resonance effect with earth.
g) Correlating above mentioned observations in order to increase the reliability of earthquake prediction.

The present study aims how the Geo – Astrophysical (GAP) modeling and Thermal Anomaly study can be useful tools to predict the occurrence of devastating earthquakes.

Materials and Methods

From the orbital and spin periods of all the bodies in the solar system, it can be found that many of the periods are commensurable, indicating the existence of a number of resonance effects between mutually coupled resonators. There are resonances between the orbital periods of members of the solar system and there are also resonances between the orbital and spin periods of rotating bodies.

Such resonances seem to be very important features of the solar system. These resonances can be either stable or unstable in nature. The resonance effects among the planets and other celestial bodies with earth, causes gravitational stress to the earth and their gravitational forces acting directions are the triggering mechanism for the release of accumulated stresses at plate boundaries/Intraplate faults and resulting in earthquakes.

Orbital Resonance

Orbital resonance occurs when two orbiting bodies exert a regular, periodic gravitational influence on each other. Mostly these resonances are unstable in nature. Due to this the celestial bodies exchange their momentum and gravitational influences. This in turn causes gravitational stress on earth's surface, which would change the speed of rotation of the Earth in its orbit. When the speed of rotation of the earth changes the tectonic plate motion also gets affected and acts as a triggering mechanism for the accumulated stress at faults and plate boundaries to be released abruptly. Change in planetary gravitational force on or a day before the main shock acts as triggering mechanism. Also the energy released from the after shock sequences maintaining proportionality with resonance force change (http://history.nasa.gov/SP-345/ch8.htm).

Spin Resonance in Earth–Moon System

In the Earth–Moon system (Fig. 1), the moon exerts its gravitational force on Earth and it pulls the Earth towards it. Of the three points on the earth's surface, the point 'A' (Fig. 1) which is, farthest from the moon and experiences least gravitational force due to the gravitational pull of the moon. On the other hand, it also experiences greatest centrifugal force in the direction opposite to that of moon's gravitational force. Therefore, the net force will be solely due to the centrifugal force. The point 'B' on the Earth, which is at the centre of the Earth experiences equal amount of gravitational force (due to the moon's gravitational pull) and centrifugal force, but as they are opposite to each other, they nullify each other. So at point 'B' the net force is zero. The point 'C' (Fig. 1) on the Earth, which is closest to the moon experiences greatest gravitational force due to the moon. At the same time, it also experiences least centrifugal force but in the same direction of gravitational force, which is due to the rotation of the Earth. Therefore, the net force will be addition of these two forces at point 'C', acting away from the centre of the Earth. The poles of the earth would be pulled towards the equator due to the inward pull by the force of gravity, which would tend to squeeze the planet. This inward squeeze causes an outward squish at the "equator" of the earth. The aforesaid forces and the squeezing effect produce two bulges along the circumference of the Earth. Due to this change in circumference of the earth alters the speed of rotation of the Earth, which in turn affects tectonic plate's motion.

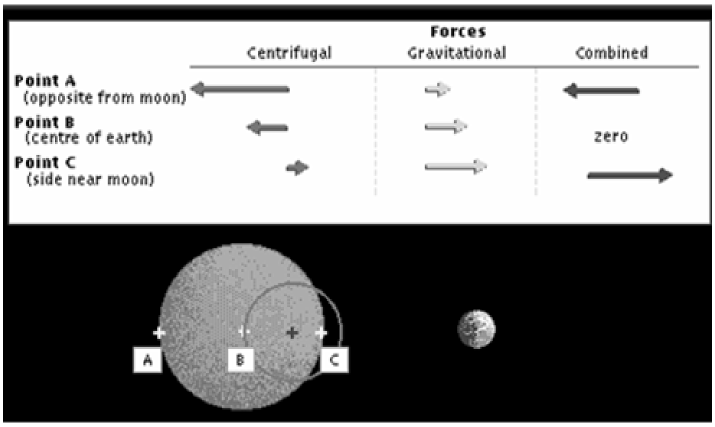

Figure 1. Earth–Moon system (Courtesy: Microsoft Encyclopedia)

Force of Attraction by Planets, Sun and Moon:

$F_{p1} = GMm/r_1^{2}$;
$F_{p2} = GMm/r_2^{2}$;
Total Force = $F_{p1} + F_{p2}$ N;
$L = GMm / v$ kgm^2s^{-1}
Where,

F_{p1} – Force due to the first celestial body (N),
F_{p2} – Force due to the second celestial body (N),
G – Universal Gravitational Constant (6.673 x 10^{-11} Nm^2kg^{-2})
r_1 – Distance between first planet and the Earth (m),
r_2 – Distance between second planet and the Earth (m),
L – Angular momentum of planets, Moon and Sun (kgm^2s^{-1}),
v – Orbital velocity of the planets.

With this total angular momentum, the total force acts at the epicenter in the opposite direction to the rotation of the earth. At the epicenter, the speed of rotation of earth can be calculated with help of software available. This does not, however, mean that earthquakes will occur at all edges of the plate boundaries. In order to trigger an earthquake in one particular place two conditions should be satisfied. They are a) Triggering distance (T.D.) and b) direction of planetary force acting at the possible epicenter.

Thermal Anomaly

Remote sensing satellites with thermal sensors can sense the earth's surface emissivity at regular interval and it is successful in detecting pre-earthquake thermal anomalies prior to impending devastating earthquakes. Thermal anomalies appear 1 day to 2 months in advance, with a change (either increases or decreases) in temperature of about 2-6°C, covering 0.1 square km to 0.7 square km. The anomalies disappeared along with the earthquake events. With the aid of thermal sensors like Advanced Very High Resolution Radiometer (AVHRR) on board National Oceanic and Atmospheric Administration (NOAA), Multi-spectral Visible and Infrared Scan Radiometer (MVISR) on the Feng Yun (FY) Chinese series of satellites, Moderate Resolution Imaging Spectroradiometer (MODIS) on board satellites Terra and Aqua, Advanced Space borne Thermal Emission and Reflection Radiometer (ASTER) on board the satellite Terra, and other thermal Infrared sensors (Arun K. Saraf and Swapnamita Choudhury, 2005) thermal anomaly can be calculated.

Using this methodology the magnitude of the earthquake can be calculated accurately. The magnitude of an impending earthquake based on two criteria.

- The increase in the brightness of thermal anomaly, more the brightness more the magnitude and
- The area in which the thermal anomaly appears, more the area more the magnitude

In this method it is difficult to fix exact location of the epicenter, but magnitude of the earthquake can be found, since it is the direct function of brightness value and area of the thermal anomaly (Ramanamurthy M. V., 2005).

If the correlation is done between GAP modeling (in which location time can be found) and Thermal Anomaly, accurate prediction possible.

Results and Discussion

Bhuj, India 2001 Earthquake

No Indian can forget the 51st Republic Day morning (8.45 am Local Time). Within two minutes, the furious ground shock completely wiped out Bhuj and the life style of Bhuj people was turned upside down. Those who survived in the quake took their dead on vegetable carts to cremation and burial grounds. More than physical devastation, natural calamities often leave scars on the collective psyche of an entire people. A family leading a full life till the actual event is suddenly engulfed in trauma and left in the wilderness out on the street. This catastrophic event catapulted me to do research into the intricacies of the earthquake prediction.

The data sequence of infrared data images from the Moderate Resolution Imaging Spectroradiometer (MODIS) onboard the NASA Terra satellite of the region surrounding Gujarat, India showed a 'thermal anomaly' appearing on January 21, 2001 prior to the January 26th quake (Figures 2,3,& 4). The anomaly disappeared on January 28, 2001 shortly after the quake (NASA, 2004).

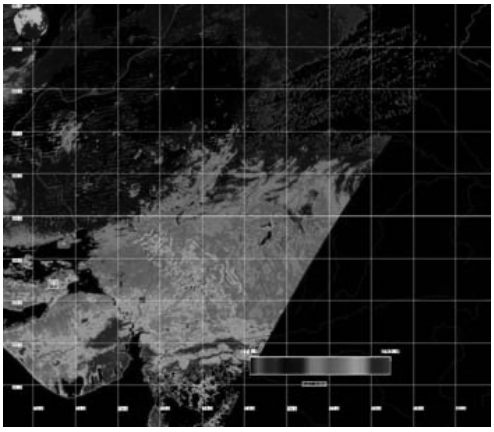

Figure 2. Moderate Resolution Imaging Spectroradiometer (MODIS) onboard the NASA Terra satellite of the region surrounding SW of Gujarat, on January 06, 2001

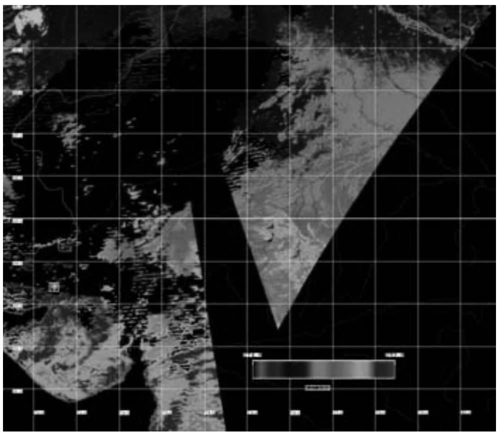

Figure 3. Moderate Resolution Imaging Spectroradiometer (MODIS) onboard the NASA Terra satellite of the region surrounding Gujarat, India shows a ‘thermal anomaly’ appearing on January 21, 2001

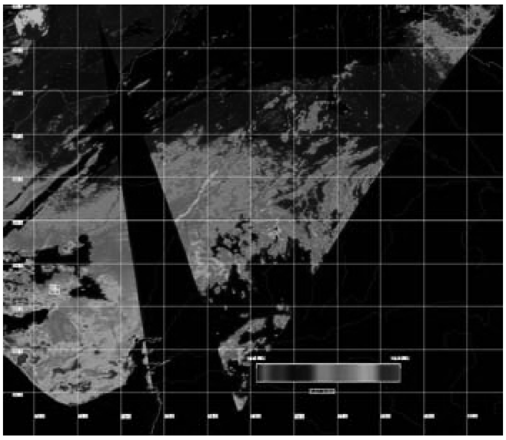

Figure 4. Moderate Resolution Imaging Spectroradiometer (MODIS) onboard the NASA Terra satellite of the region surrounding Gujarat, India shows a disappearance ‘thermal anomaly’ on January 28, 2001

Before the Bhuj earthquake in Gujarat, India, 2001, MODIS imagery was able to detect a land surface temperature anomaly of 4°C five to eight days (January 18, 2001) before the earthquake hit (Figure 5). This thermal anomaly was hypothesized to occur due to high levels of rock stress prior to the earthquake.

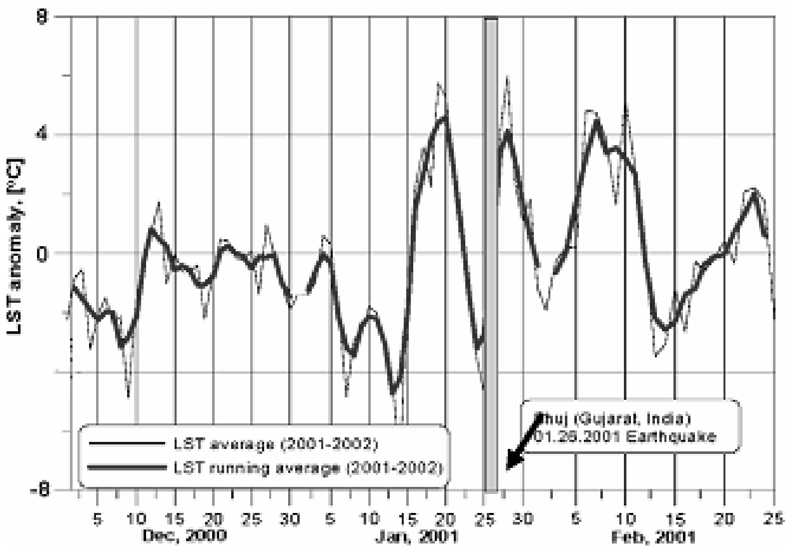

Figure 5. Land surface temperature anomaly of 4°C, 5–6 days before the Bhuj earthquake hit in Gujarat, India 2001 from Ouzounov et al (2006).

From the analysis of resonance effect of celestial bodies (Table 1) at the time of earthquake, it is quite understandable that how gravitational stresses of celestial bodies on Earth induces stress on rocks in that region.

Moderate Resolution Imaging Spectroradiometer (MODIS) onboard the NASA Terra satellite first detected the anomaly in that SW of region (surrounding SW of Gujarat), on January 06, 2001 (Fig. 3). On January 06, 2001 gravitational stress was created on Earth due to the alignment of Jupiter, Saturn and Moon (Table 1). But the resonance was unstable, since the moon was moving away from the alignment in the next day.

On January 18, 2001 again the thermal anomaly appear in the Gujarat region by having temperature 4°C above normal temperature. On this day Moon, Mars and Saturn (Table 1) were aligned and their gravitational stress due to the resonance effect influences earth's rotation speed, which in turn causes stress in the rock. This resonance effect was unstable, due to the movement of moon in its orbit, so that the anomaly was short lived one and the thermal emissivity became normal along the faults as can be seen from Figure 2 on January 22.

Table 1: Planetary position for different dates prior to Bhuj 2001 earthquake, planetary force and T.D. during the time of occurrence of Bhuj 2001 earthquake.

Date	Planets	RA	DEC	Planets	RA	DEC	Planetary Force (N)	T.D. (km)
06/01/01	Jupiter	59.868	19.75	Saturn	52.573	16.756		
	Moon	56.734	15.91					
18/01/01	Moon	224.48	-12.11	Saturn	52.279	19.693		
	Mars	222.64	-15.11					
22/01/01	Moon	274.86	-22.34	Saturn	52.235	16.749		
	Mars	224.88	-15.78					
26/01/01	Mars	227.20	-16.44	Saturn	59.211	19.707	1.38×10^{23} (NE – SW)	3130.625
				Jupiter	52.223	16.767		
	Moon	326.83	-16.77	Venus	326.80	-13.79		

The average apparent ground surface temperature over the ten-hour period of the night of January 25th became more elevated when compared with January 24th (Ouzounov et al 2006). During this period complex resonance effect was acted on Earth due to two different alignments. Due to the alignment of Mars, Jupiter and Saturn on either side of the earth (Table 1) cause a resonance effect. This resonance effect was countered by another resonance effect due to the alignment of Moon and Mercury (Table 1), which is at 90^{o} from first alignment. Since both alignments were perpendicular to each other, complex gravitational stress was exerted on Earth, which affected the rotational speed of Earth. Change rotational speed of earth in combination with the presence of fault at triggering distance (T.D.) of planetary forces from effective planetary position on the earth's surface and direction of planetary force which acted perpendicular to the Bhuj thrust fault causes increased stress in rocks in the Bhuj region and triggered an earthquake by releasing accumulated stress on January 26, 2001 morning 8.45 am IST.

Conclusion

By adopting multidisciplinary comprehensive strategy reliable, deterministic and accurate earthquake prediction can be made which will lead the mankind to understand more about the changes takes place underneath of the earth and behaviour of soil. This will help the civil engineers and architects to construct safe buildings. It will also help planners and governments, before they construct installations like atomic power stations, roads, bridges and river linking tunnels.

The hazards of earthquake are avoidable if prediction can be made early, which would enable mitigation of the natural hazard, reduce damage to life and property drastically and facilitate precautionary measures by government and NGOs. The gas pipe lines and electric power can be cut early, so that fire accidents due to them can be avoided.

References:

Ouzounov D., Bryant N., LoganT., Pulinets S.& Taylor P. (2006). Satellite thermal IR phenomena associated with some of the major earthquakes in 1999–2003, *Physics and Chemistry of the Earth, 31, 154–163.*

Dino J. (Editor) (2004). National Aeronautics and Space Administration (NASA), *http://ww.nasa.gov/centers/ames/news/releases/2002/02images/quakes/earthquakes.html.*

Li J.Z., Bai Z.Q., Chen W.S., Xia Y.Q., Liu Y.R. & Ren Z. (2003). Strong earthquakes can be predicted: a multidisciplinary method for strong earthquake prediction, *Natural Hazards and Earth System Sciences, 3, 703- 712.*

Ramanamurthy M.V. (2005). Global Trends in Earthquake Prediction Research, *Jour.Geol.Soc.India, 66, 504 – 509.*

Saraf Arun K. & Swapnamita C. (2005). Thermal Remote Sensing Technique in the Study of Pre- Earthquake Thermal Anomalies, *J. Ind. Geophys. Union, 9, 3, 197-207.*

SP-345, Evolution of the Solar System, *http://history.nasa.gov/SP-345/ch8.htm*

Gillespie T.W., Chu J., Frankenberg E. &Thomas D. (2007). Assessment and prediction of natural hazards from satellite imagery, *Progress in Physical Geography, 31(5), 459–470.*

Van Genderen, J.L. (2004). An integrated global observing strategy for earthquake prediction. *Paper presented at IGOS International Workshop on "Towards the implementation of an Integrated Global Observing Strategy", 4-6 February 2004, Tokyo, Japan.*

Walker, B. (1982). Earthquake, Alexandria, VA, *Time-Life Books Inc., 176 p.*

Gap Modelling to Predict Main Shock & After Shock Sequences

Venkatanathan N. (1)

(1) Faculty of Physics, School of Electrical and Electronic Engineering, SASTRA University, Thanjavur, Tamil Nadu, India. Pin: 613 402, physics16972@gmail.com

Keywords: Orbital Resonance, Spin Resonance, gravitational stress, Speed of rotation of Earth and Geo – Astrophysical

Introduction

More than physical devastation, natural calamities often leave scars on the collective psyche of an entire community or population. Due to earthquakes, there are some effects like ground shaking, ground displacement, liquefaction, flooding (tsunami), and fire which are hazardous to human beings (Walker, 1982). The hazards of earthquakes are avoidable if prediction can be made early, which would enable mitigation of the natural hazard, reduce damage to life and property drastically and facilitate precautionary measures by government and NGOs. During the past several decades, there have been several attempts at earthquake prediction from different perspectives.

Scientists have attempted to predict earthquakes using the “seismic gap” theory, by observing animal behaviour patterns or studying the changing colour of water in natural springs. Seismologists have used warning signs like a) foreshocks, b) strain in rocks, c) ground water levels, d) chemical changes in ground water, e) radon gas in ground water, f) thermal anomaly, g) ground tilting, and h) P–wave velocity (Ranjit, 2001) for predicting earthquakes and issuing advance warnings to the people in the area likely to be affected. Research efforts in USA, Russia, China, Japan and other countries have not been able to find reliable methods for predicting and forecasting, with adequate forewarning on the occurrence of earthquakes, thereby making people to evacuate dwellings in time and preventing loss of lives. This attempt aims at how establishing resonance effect of celestial bodies influence rotational speed of earth, which in turn acting as a triggering mechanism for the devastating earthquake.

Due to the devastating nature of earthquakes, scientists have shown great interest in predicting the location and time of large earthquakes (Ludwin, 1990). To understand earthquake prediction, three different time frames have been assigned by scientists: long-, intermediate-, and short-term predictions.

- In long-term predictions, the time frame is usually a decade or more, with limited usefulness for public safety (Carayannis, 1989).
- Intermediate-term prediction is with a time span of a few weeks to a few years, with no great practical usefulness (Carayannis, 1989).
- Short-term prediction is useful for the public and evacuation can be done, since it gives specific information on the time and location of an earthquake within days or weeks (Carayannis, 1989).

Objectives

In order to explore the possibility of predicting earthquakes more accurately, the following aspects will be considered in detail.

a) Study of tectonic plate movements.
b) Study of nature of fault lines and their relation to tectonic plate movements.
c) Study of paleoseismic events including all small earthquakes have occurred.
d) Observations of the movement of celestial bodies and their resonance effect with earth.

The present study ascertains how the Geo – Astrophysical (GAP) modeling can be a useful tool to predict main shocks and after shock sequences.

Materials and Methods

From the orbital and spin periods of all the bodies in the solar system, it can be found that many of the periods are commensurable, indicating the existence of a number of resonance effects between mutually coupled resonators. There are resonances between the orbital periods of members of the solar system and there are also resonances between the orbital and spin periods of rotating bodies.

Such resonances seem to be very important features of the solar system. These resonances can be either stable or unstable in nature. The resonance effects among the planets and other celestial bodies with earth, causes gravitational stress to the earth and their gravitational forces acting directions are the triggering mechanism for the release of accumulated stresses at plate boundaries/Intraplate faults and resulting in earthquakes.

Orbital Resonance

Orbital resonance occurs when two orbiting bodies exert a regular, periodic gravitational influence on each other. Mostly these resonances are unstable in nature. Due to this the celestial bodies exchange their momentum and gravitational influences. This in turn causes gravitational stress on earth's surface, which would change the speed of rotation of the Earth in its orbit. When the speed of rotation of the earth changes the tectonic plate motion also gets affected and acts as a triggering mechanism for the accumulated stress at faults and plate boundaries to be released abruptly. Change in planetary gravitational force on or a day before the main shock acts as triggering mechanism. Also the energy released from the after shock sequences maintaining proportionality with resonance force change (http://history.nasa.gov/SP-345/ch8.htm).

Spin Resonance in Earth–Moon System

In the Earth–Moon system (Fig. 1), the moon exerts its gravitational force on Earth and it pulls the Earth towards it. Of the three points on the earth's surface, the point 'A' (Fig. 1) which is, farthest from the moon and experiences least gravitational force due to the gravitational pull of the moon. On the other hand, it also experiences greatest centrifugal force in the direction opposite to that of moon's gravitational force. Therefore, the net force will be solely due to the centrifugal force. The point 'B' on the Earth, which is at the centre of the Earth experiences equal amount of gravitational force (due to the moon's gravitational pull) and centrifugal force, but as they are opposite to each other, they nullify each other. So at point 'B' the net force is zero. The point 'C' (Fig. 1) on the Earth, which is closest to the moon experiences greatest gravitational force due to the moon. At the same time, it also experiences least centrifugal force but in the same direction of gravitational force, which is due to the rotation of the Earth. Therefore, the net force will be addition of these two forces at point 'C', acting away from the centre of the Earth. The poles of the earth would be pulled towards the equator due to the inward pull by the force of gravity, which would tend to squeeze the planet. This inward squeeze causes an outward squish at the "equator" of the earth. The aforesaid forces and the squeezing effect produce two bulges along the circumference of the Earth. Due to this change in circumference of the earth alters the speed of rotation of the Earth, which in turn affects tectonic plate's motion.

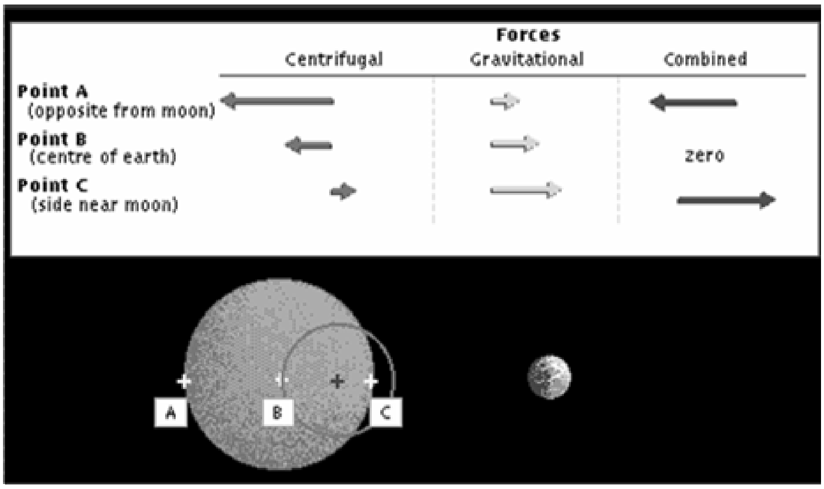

Figure 1. Earth–Moon system (Courtesy: Microsoft Encyclopedia)

Force Of Attraction By Planets, Sun And Moon:

$F_{p1} = GMm/r_1^2$;
$F_{p2} = GMm/r_2^2$;
Total Force = $F_{p1} + F_{p2}$ N;
$L = GMm / v$ kgm^2s^{-1}
Where,

F_{p1} – Force due to the first celestial body (N),
F_{p2} – Force due to the second celestial body (N),
G – Universal Gravitational Constant (6.673×10^{-11} Nm^2kg^{-2})
r_1 – Distance between first planet and the Earth (m),
r_2 – Distance between second planet and the Earth (m),
L – Angular momentum of planets, Moon and Sun (kgm^2s^{-1}),
v – Orbital velocity of the planets.

With this total angular momentum, the total force acts at the epicenter in the opposite direction to the rotation of the earth. At the epicenter, the speed of rotation of earth can be calculated with help of software available. This does not, however, mean that earthquakes will occur at all edges of the plate boundaries. In order to trigger an earthquake in one particular place two conditions should be satisfied. They are a) Triggering distance (T.D.) and b) direction of force acting at the possible epicenter.

Results and Discussion

The Great Sumatra 2004 Earthquake (M 9.0)

The devastating mega thrust earthquake of December 26, 2004, with magnitude 9.0 on Richter scale occurred on the interface of the India and Burma plates and was caused by the release of stresses that develop as the India plate subducts beneath the overriding Burma plate. It was the third largest earthquake recorded in the world and the tsunami was crossed into the Pacific Ocean and was recorded in New Zealand and along the west coast of South and North America (USGS).

Table 1: Table showing Energy released by the earthquakes and Change in Planetary force in the Sumatra Region between December 24, 2004 and December 28, 2004.

	Date	Energy released by earthquake (Joule)	Change in Planetary Force (N)
1	24-Dec-2004	2.70738E+11	-5.71257E+14
2	25-Dec-2004	0	1.81034E+20

3	26-Dec-2004	1.60092E+18	-1.81034E+20
4	27-Dec-2004	8.16704E+14	-5.07973E+14
5	28-Dec-2004	1.8248E+14	-4.79733E+14

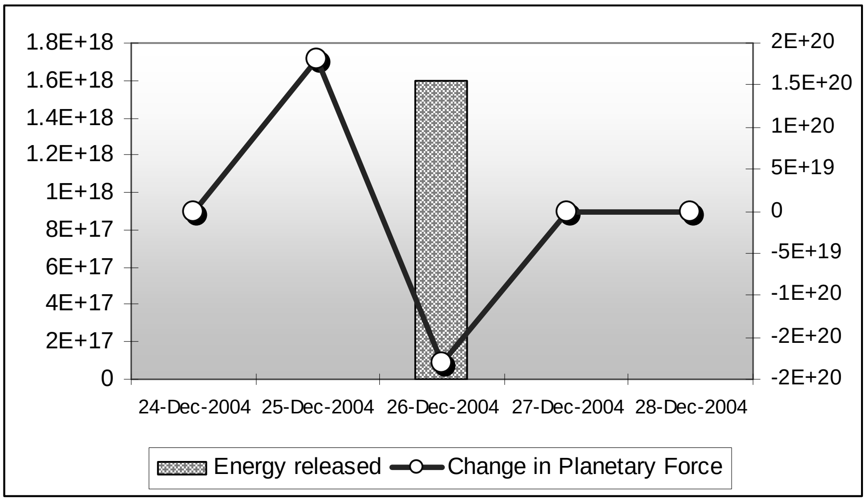

Figure 2. Energy Released Vs Change in Planetary Force Graph for Dec 26, 2004 Earthquake

From the analysis of the Sumatra earthquake it can be inferred from table given below that due to the resonance effect of Venus, Mercury and moon with earth was triggering mechanism for the occurrence of the earthquake. There is abnormal change in planetary gravitational force from negative value to positive value with power of twenty. There was greater gravitational influence on December 25, 2004 due to the resonance created by the alignment of Moon, Venus and Mercury. But gravitational influence got suddenly dropped to negative value due to change in resonance effect, since moon was moving away from the alignment and this causes changes the rotational speed of Earth due to alterations in the radius of the Earth, which changes Indian plate motion and causes the rupture due to the accumulated stress in that region.

In comparison with December 25, 2004, on December 26, 2004 the Earth spin faster due to the reduction in tidal bulge, since moon has moved away from the alignment at the time of earthquake. This view is strengthened by Richard Gross, a geophysicist with NASA's Jet Propulsion Laboratory in California, theorised that a shift of mass towards the Earth's centre during the quake caused the planet to spin faster by three microseconds, or three millionths of a second, and to tilt about 2.5 centimetres on its axis.

Northern Sumatra Earthquake M 8.7 (March 28, 2005)

The earthquake of March 28, 2005 occurred principally on the interface of the Australia plates and Sunda plates. This earthquake was likely triggered by stress changes caused by the December 2004 (M9.0) earthquake. However, it occurred on a segment of the fault 100 miles (160 kilometers) to the southeast of the rupture zone of the M9.0 Sumatra earthquake (USGS).

Table 2: Table showing Energy released by the earthquakes and Change in Planetary force in the Sumatra Region between March 26, 2005 & March 30, 2005.

	Date	**Energy released by earthquake (Joule)**	**Change in Planetary Force (N)**
1	26-Mar-05	0	1.67598E+19
2	27-Mar-05	0	2.17846E+20

3	28-Mar-05	5.87316E+17	2.06815E+19
4	29-Mar-05	1.35287E+14	2.08068E+19
5	30-Mar-05	3.66408E+14	2.09317E+19

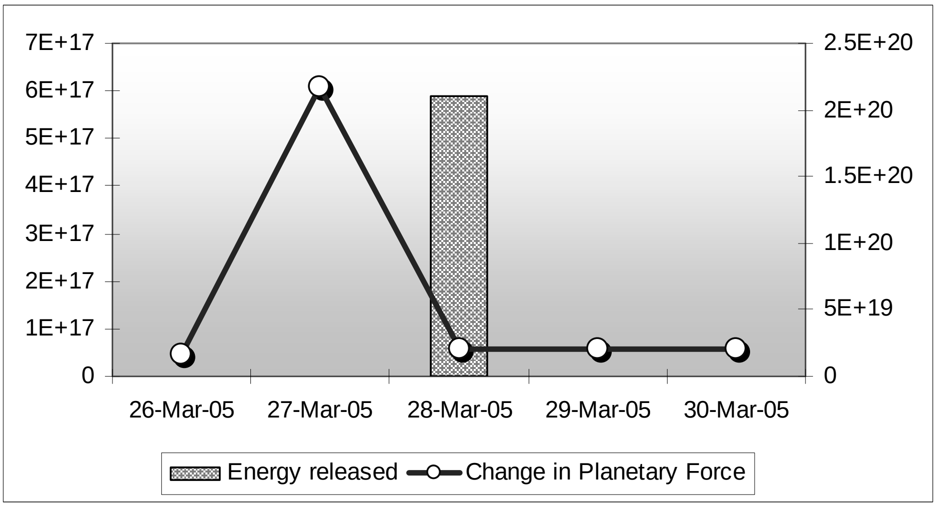

Figure 3. Energy Released Vs Change in Planetary Force Graph for March 28, 2005 Earthquake

In this earthquake, the resonance change was brought by two celestial bodies. One is due to Mercury because of its retrograde motion and forming alignment with Sun, Venus and Jupiter. The other change is due to change in distance between Earth and Sun, which get increased on March 28, 2005. On March 27, 2005 the planetary force was increased and on the next day (March 28, 2005) it gets dropped. Due to this there was sudden drop gravitational force on Earth, the rotation speed of Earth get altered, which effectively affect the motion of plate tectonics.

Kashmir Earthquake 2005 and its After Shocks

Earthquakes and active faults in northern Pakistan and adjacent parts of India and Afghanistan are the direct result of the Indian subcontinent moving northward at a rate of about 40 mm/yr (1.6 inches/yr) and colliding with the Eurasian continent. This collision is causing uplift that produces the highest mountain peaks in the world including the Himalayan, the Karakoram, the Pamir and the Hindu Kush ranges. A major earthquake occurred at 03:50:40 (UTC) on Saturday, October 8, 2005. The magnitude 7.6 event has been located Indo – Pak Border (USGS).

Table 3: Table showing Energy released by the earthquakes and Change in Planetary force in the Sumatra Region between October 08, 2005 & October 12, 2005.

Date	Energy released by earthquake (Joule)	Change in Planetary Force (N)
07/10/2005	0	2.01E+20
08/10/2005	2.21E+16	8.26E+17
09/10/2005	8.87E+13	8.26E+17
10/10/2005	9.44E+12	8.25E+17
11/10/2005	2.57E+12	8.25E+17
12/10/2005	2.08E+13	2.18E+20

From the table it can be inferred that the main event was due to the sudden drop in gravitational force. The energy released by the after shocks in the following days gets decreased and finally on October 12, 2005 it gets increased. It was due to increase in gravitational forces on October 12, 2005.

Conclusion

From the above analyses of specific earthquakes like Sumatra 2004 earthquake, Sumatra 2005 earthquake and Kashmir 2005 earthquake, the influence of resonance effect celestial bodies on Earth are acting as a triggering factor for the occurrence earthquakes and also it establishes that GAP modeling theory are useful tools in predicting earthquakes accurately.

Refrences

Carayannis, G.C. (1989). Earthquake Prediction Some Basic Principles, Second International Tsunami Workshop on the Technical Aspects of Tsunami Warning Systems, Tsunami Analysis, Preparedness, *Observation and Instrumentation, Novosibirsk, USSR.*

Ludwin R. (1990). Earthquake Research at Parkfield, California, for 1993 and Beyond, *U.S.G.S. Circular, 1116, 14p.*

Preliminary Earthquake Report, U.S. Geological Survey, National Earthquake Information Center, World Data Center for Seismology, Denver URL: *http://neic.usgs.gov/neis/bulletin/neic_slav_nr.html*

Ranjit B. (2001), The Quake Manual, *Outlook, 5, 26–27p.*

SP-345. Evolution of the Solar System, *http://history.nasa.gov/SP-345/ch8.htm*

Walker B. (1982). Earthquake, Alexandria, VA, *Time-Life Books Inc., 176 p.*

Reappraisal of Four Betics Earthquakes of the XVI Century

Vidal F (1), Espinar M (2), Navarro M (3,) Vidal L(4)

(1) Andalusian Institute of Geophysics, Granada University,18080 Granada, Spain, fvidal@iag.ugr.es
(2) Dep. Medieval History, Granada University, 18071 Granada, Spain, mespinar@ugr.es
(3) Dep. of Applied Physics, Almeria University, 04120 Almeria, Spain, mnavarro@ual.es
(4) Dep. of Economics, Granada University, 18071 Granada, Spain

Keywords: Historical earthquakes, documentary sources, seismicity, Southern Spain.

Introduction

The Betics region (Southern Spain) presents a low-to-moderate seismic activity (in a world context), associated with the continent-continent collision between Africa and Eurasia plates and distributed over a wide area. Seismic energy is released predominantly through frequent, small seismic events and unusual earthquakes of moderate magnitude, most of them at shallow depth (h < 40 km), a significant number with foci at intermediate depth (40 < h < 150 km) and only a few rare very deep events (≈630km) (Vidal, 1986; Morales et al, 1997; Buforn et al., 2004). This region is acknowledged to be the most seismically active zone in Spain according to historical and instrumental seismic data and is considered the most hazardous seismic zone by the Spanish Building Code (NCSE,2002) (Vidal et al, 2008). For this reason, the most part of the historical seismicity studies have been focused in this region, e.g. those of Sánchez, 1917, 1921; Galbis, 1932, 1940; Vidal, 1986; Espinar, 1994; Oli-vera, 1995, Martinez and Mezcua, 2002, among others.
In relation to availability and quality of historical earthquake data of the last millennium, three time periods belonging to X to XV, XVI to XIX and XX centuries, respectively can be identified in the historical seismicity of the Betics region. During the first period (before XVI century), the historical seismicity is not well known because most of primary historical sources are lost, the documents are incomplete and scarce due to the area changed from muslim to christian dominion. After the XV century the documentary information gradually improves. According to historical sources, during the last 500 years, most part of the largest earthquakes of Spanish region occurred in the Betics. The most important with onshore epicentral location are those of the years 1431, 1522, 1680, 1804, 1829 and 1884 (intensity I ≥ IX EMS scale) and others occurred in 1406, 1504, 1518, 1531, 1645, 1658, 1674, 1748, 1806 (with I_{EMS} ≥ VIII). Another important historical events with epicentre in sea reached in land an intensity VIII: 1494 (South of Malaga), 1357 (Almeria Gulf), 856 and 1722 (Gulf of Cadiz). Furthermore, two relative distant earthquakes of large magnitude (1356 and 1755) located SW of Portugal coast affected with I_{EMS}=VIII Huelva and Cádiz (Southern Spain).
During 106-year instrumental period, the registered Betics earthquakes have low magnitude (Mw ≤ 5.5), exception done of 1910 Adra coast earthquake (Mw 6.2) and the very deep 1954 Durcal earthquake (Mw 7.0) but several strong earthquakes (Mw ≥ 6.5) have taken place in surrounding areas, e.g. those of 1954, 1980 and 2004 in northern Algeria during the last half century. The historical and instrumental seismicity of the region point out the study of the largest historic earthquakes becomes crucial in regional seismic hazard assessment.
The purpose of this paper is to analyse some considerable information available in numerous primary and secondary sources, to the reappraisal of the four important Betics earthquakes of the first half of XVI century imperfectly known but with direct historical records. A careful examination of documents and references joint to geological and archaeological data from recent studies permit a new intensity allocation, and other earthquake parameters estimation.

Materials and Methods

The four damaging Betics earthquakes to be re-evaluated are: the April 5th,1504 Carmona earthquake, that caused heavy damage in the town of Carmona, and other nearby villages of Cantillana, Tocina, Villanueva, and Lora (Espinar et al, 2006)*;* the November 9th, 1518, Vera earthquake that caused heavy damage in Mojacar, Garrucha and Cuevas de Almanzora, and destroyed completely Vera's town (Vidal et al, 2006); the November 9th, 1522 Almeria earthquake, which caused the complete destruction of Almeria city and several small villages and also heavy damage and collapse in the buildings and farmhouse distributed over a wide area of Almeria and Granada provinces (Olivera, 1995); and finally, the September 30th, 1531 Baza earthquake, with epicentre between Baza and Benamaurel (both towns destroyed) (Espinar et al, 2008).

The Data

The historical records of each event analyzed are primary and secondary documents corresponding to official and private historical documents obtained from Municipal Archives (of the main affected cities, towns and villages), regional archives as Provincial Notary Public, The Alhambra, or Ecclesiastical Archives, and national ones as National Historic Archive, Archive of Simancas and the Archive of the National Library of Madrid. The sources contemporary to each event investigated were usually: historical records (royal, noble and municipal chronicles), municipal records (council agreement books, reports, accounting books, letter registers, public announcements…) and miscellaneous records (ecclesiastic records, visitor reports, lawsuit documents, letters, notary public testimonies..) Secondary documents, chronically and historical studies, have been also revised, and a set of seismological references have been consulted. On the other hand, geological, geophysical and archaeological data from recent studies have been also considered. Furthermore, several surveys in each earthquake affected areas have been carried out.

The Methodology

The existing original primary sources contemporary to the events have been compiled and the information analysed; in many cases documents had to be translated by using palaeographic techniques. Damage descriptions contained in available historical records are not always direct, accurate in details or give complete information about main effects in felt areas. Consequently, analysis of many contemporary and direct accounts related to ground effects, to building damage and towns and villages reconstruction are necessary because the information appearing in these documents has to be contrasted one set of data with another (Vidal et al, 2006). Secondary sources or material not directly concerned with the earthquake have been nearly excluded of the analysis, but sometimes information contained in these documents has been necessary to assess adequately primary source data.

The descriptions and other data belonging to contemporary and near-contemporary documents have been the more decisive data in the analysis of seismic effects and consequently, in assessing parameters of each of the earthquakes: epicentral location, epicentral intensity, maximum intensity, locality intensity, tentative depth and macroseismic magnitude. Furthermore, it has been also looked for amplification phenomena due to topographic or ground conditions because ground motion distribution of each of the analysed historic earthquakes could be considered as a natural full-scale laboratory.

The correct assessment of documentary information need a deep and critical historic data processing but a correct final interpretation requires an interdisciplinary work made by seismologists, historians, geologists, engineers, geographers, economists, etc, as here it has performed. In our damage evaluation we took advantage of a recent study carried out by Breton et al. (2008) about construction materials and techniques of constructions of the region in the first half of XVI century. This interdisciplinary analysis has revealed important aspects related to villages and material characteristics and with the construction techniques of city walls, fortress, castles, churches, houses, cisterns, etc. All that information has been useful to analyze seismic damage in buildings. This vulnerability knowledge has been of great importance because macroseismic intensity is mainly measured from the ground motion effects on constructions and consequently its dependence of the weakness of man-made structures must be removed to approximate the level of the ground motion. Furthermore, for

assessing intensity it is important to distinguish between damage caused directly by dynamic earthquake loading and damage generated by secondary, quasi-static after- effects such as foundation spreading, liquefaction, slides, rock-falls and aftershocks (Ambraseys, 2004).
Earthquake location was defined as the centre of the isoseismal lines and/or centred into the area worst affected. On the other hand, seismogenic faults close to stronger damage area have been also taken into account after removing site amplification effects. Focal depths are poorly estimated from intensity distribution and the instrumental focal depth of recent seismicity has been considered. The earthquakes here studied are shallow events.
In order to evaluate M_w magnitude from macroseismic data it has been applied the relations for shallow events proposed by Papazachos & Papaioannou (1997) (for a region with similar attenuation), considering intensity values I at different places situated at hypocentral distances R:

$$M_w = 0.62\ I + 2.035\ \log R + 0.002\ R - 0.96 \qquad (1)$$

and the empirical relation M_w - $I_{máx}$ proposed by Rueda & Mezcua (2001):

$$M_w = 0.575\ I_{\max} + 1.15 \qquad (2),$$

Results and Discussion

The April 5th, 1504 Carmona earthquake

This earthquake affected a very extensive territory of Andalusia: Seville, Cordoba, Malaga and Granada provinces. It was also felt in Castille, Murcia, South of Portugal and North of Morocco areas. The radius of perceptibility was more than 450 km. The city of Carmona was shaken by aftershocks for at least 5 months. Chronicler and historians wrote all about this events and there is an abundant documentation about the effects.
The most important damage took place in the city of Carmona where reached an intensity of VIII (EMS); and could reach a maximum intensity of VIII-IX near the city and also locally in some places of the city. There were important damages in public, privates and religious buildings of the city, some crypts collapsed, like the ones in Los Jeronimos Church and Santiago Church. Salvador Church was destroyed and other temples had to be restored. The Roman aqueduct of Los Caños almost disappeared and the towers of the fortress and four of the five gates of the city were destroyed. The city walls were broken and some of its enormous stone blocks were displaced. All the house roofs fell down and a great number of buildings suffered heavy damage or collapsed. The number of victims in Carmona was 29 fatalities and a great number of injured. Large cracks in ground: 50 m long appearing into the city and 200m long in places 3 km far away. Rock-falls were reported in Carmona city slopes and between Carmona and Alcala de Guadaira. Others reported effects on ground were liquefaction (e.g. in Sevilla city), change in flow of springs (e.g. in Almadén and Cazalla), waves in Guadalquivir river, etc.
According to testimonies, other towns and villages like Cantillana, Tocina, Villanueva and Lora del Rio had an intensity of VIII. In these towns there were amplification phenomena due to soil conditions. The city of Seville and the villages of Alcala del Rio, Palma del Rio and Los Palacios were affected with intensity VII and locally with VII-VIII. In Seville, the roofs of San Francisco and San Pablo Churches collapsed, the cathedral cracked and very important damages occurred in the buildings.
The epicentre was estimated to be close to Carmona (37.47N, 5.66W) following the method explained before and considering other seismic effects like intensity of earthquake noise and the proximity of active faults. Focal depth is approximated to 15±5 km, in accordance with intensity distribution and instrumental depth obtained for recent seismicity in the zone. The estimated M_w has been 6.2±0.2 and 6.0 using formulas 1 (for 6 places) and 2, respectively.

The November 9th, 1518, Vera earthquake

According to new documents two large earthquakes really occurred. The first earthquake devastated the city of Vera that had to be rebuilt in a nearby site, and destroyed a set of towns as Mojacar, Garrucha, Cuevas and small villages of the Almanzora's river. Eyewitness of the shakes testified that second event was almost as large as the first and occurred soon afterwards in the same way that just completed to knock down all that remain upright.

Vera, placed at the upper half of a conical shape hill, it was one of the most affected towns. All the constructions and the 200 houses were heavily damaged and most of them suffered collapse. The fortress and its walls, at the top of the hill, were totally destroyed and the city walls too. Large stones fell down from the top of the hill, and rolled down crushing buildings and the remainder city walls. The city walls fell down entirely. The houses of suburbs, outside of the city walls, collapsed and suffered heavy damage by the shaking and also by the falling down of blocks and pieces of the city walls. A fifth part of Vera's inhabitants (about 150) lost their lives in the catastrophe and almost all the rest were injured (except for 6 or 7 people). The shakes also caused serious damage to bridges, water supplies, fountains, etc. Only one of the three strong cisterns remained upright. A circular masonry tower placed at the Cerro de Vera (between Vera and Cuevas de Almanzora) was also heavy damaged. The city was rebuilt in a new nearby place.

The earthquake completely sank the tower of the Garrucha village, and caused collapse or heavy damage in the remainder constructions. This watchtower was a typical nazarite of strong solid construction of stone masonry located beside the sea. Other five surveillance towers placed along the coast from South of Mojacar to Villaricos village also collapsed. All these towers are close or nearby to Palomares fault, a sinistral strike-slip fault with N20E trends and with a total movement of 14 km according to upper Miocene folding displacement.

Mojacar, a walled town with a strong fortress, was severely affected, although not as much as Vera. A third part of the houses was heavily damaged or collapsed, and the remaining ones so badly affected in such a way that they were in danger of suffering ruin (Olivera, 1995). The fortress was sunken almost completely, their towers collapsed and serious failure in their walls opened up in 46 points. The fortress was reconstructed same as the previous one adding a new tower. In the nearby quarter La Villa, outside of the Mojacar city walls, many of the houses were destroyed or with substantial damage and threatening to knock down. The church of the La Villa was also much damaged. Ten people died inside the fortress and four people in La Villa quarter. Most of the inhabitants of Mojacar were injured.

The villages of the Almanzora valley had a similar damage to that of Vera. In one of them, Cuevas de Almanzora, the damage is referred not less than that of Vera. The testimonies say that neighbours that escaped (of the earthquake) are in the field, they neither determine to reconstruct the houses where they were. The castle of Cuevas de Almanzora, a very strong construction of thick mortar walls, suffered substantial damage included its main tower that still stands up. The former Overa village and its castle were destroyed, only remained upright the lower part of its main tower. The former Huercal village and its castle suffered less damage than Olvera. There are clear archaeological evidences of these damages. It is reported that the village of Antas and other small villages of the Almanzora valley also had serious damage but detailed information is not available.

The intensity of the affected places has been assessed in the EMS-98 scale considering the quantity and degree of damage of the first earthquake from documentary and archaeological data previously mentioned. Consequently, a maximum intensity degree of VIII-IX or IX was locally reached in Vera town, since it caused the collapse of the fortress, break of the sandstone blocks that supported the fortress walls and failure of the city walls. Garrucha village (close to Palomares fault) had an intensity degree of VIII-IX. Mojácar had a degree of VIII (that locally could be VIII-IX at the fortress). According to archaeological data Cuevas de Almanzora, and the former Overa were shaken with an intensity of VIII. Similar intensity values were probably reached in Antas and other villages of the Almanzora valley but damage referred in the documents is not sufficient detailed. It has been detected that hill topography may have influenced the characteristics and level of the shake in Vera, Mojacar and the former villages of Overa and Huercal. The occurrence of two earthquakes close in time could have influenced some contemporary damage descriptions and the resultant damage from both events could have been considered as produced by the first one but some documents are clearly resounding to assign what grade of damage belonged to each shock.

Using all macroseismic data, the epicentre of the first event could be located at 37.20±0.05 N, 1.85±0.05W, near to Vera and Garrucha, because this point is the centre of the highest intensity values, and close to offset of Palomares fault and in accordance with eyewitness descriptions about earthquake noise. Focal depth is approximated to 7±5 km, in accordance with intensity distribution and considering instrumental focal depths in this area are usually smaller than 10 km. The estimation of macroseismic magnitude (equivalent to moment

magnitude Mw) has been 6.1±0.3 and 6.0 using formulas 1 (at 7 places) and 2, respectively. The corresponding magnitude using the general empirical relation of Bäth (1973) is 6.3.
The parameters of the aftershocks cannot be estimated because any direct description related with them it appeared in the collected accounts, exception done of the first one, with a slight smaller epicentral intensity and magnitude and it was close to mainshock epicentre. Nevertheless, some documents indirectly inform about the effects of new shakes saying that affected buildings that increased each day its damage and they were threaten to collapse.

The September 22nd, 1522 Almeria earthquake

This is one of the largest earthquakes of the last five centuries occurred in Southern Spain. The quake devastated almost all the buildings of Almeria city (mainly the Almedina, Juderia and San Cristobal quarters) although their constructions were established on hard rock I=IX). The cathedral (former main mosque), monasteries and churches were nearly totally destroyed, the greater part of the walls and towers of the city-walls felt down and the seaport was also ruined. The towers and walls of the fortress suffered heavy damage included their stronger parts although had been reinforced several years before. This can be checked with archaeological remains. It is said 2500 people died in Almeria, but it is not clear if it is the total number of people died in the earthquake or only those corresponding to the city.
According to a sufficiently detailed documentary information more than 80 towns, villages and farmhouses of Granada and Almeria provinces were devastated, mainly those placed in the Alpujarras and Andarax river zones. For example, all dwelling buildings of Ugijar town were destroyed, only 2 of their 200 houses remained standing up (but they were in danger of collapse); other stronger constructions like the public buildings, the church, its tower and a defending tower felt down too (I≥ VIII-IX). More than 150 people died only there. The Alpujarras territory was still administrative organized in the old Moorish district known as Tahas, with the name of its more important town. The towns and villages destroyed (I≥ VIII) in the following Tahas were: 19 in the Ugijar ones, 12 in the Andarax, 15 in Berja, 8 of 9 in Luchar, 7 of 11 in Marchena (Espinar, 1996). 17 villages of these Tahas reached I= VIII-IX and several of them were deserted. Other heavy damage had the fortress of Tabernas, Marchena, Gergal, Alisan and Haratalgima (that were destroyed) and the towers of Fiñana fortress and defending towers placed on the Tahas of Berja, Andarax, Ugijar and Luchar fell down. With an intensity VI-VII or greater were shaken the cities of Granada, Baza, Guadix, and those towns and villages of Almanzora river as Purchena, Albox, Vera, etc. The quake was felt in an extensive area at the north of Algeria and Morocco (Galbis, 1932), referring tsunami effects there.
The more relevant effects on ground collected on documents were large landslides and rock falls, especially cutting Andarax river, slope failure on main ways, strong changes in flow of springs, some of them were dried. Documents also speak about the occurrence of a tsunami affecting Almeria coast (mainly the city), Oran (Algeria) and Moroccan coast, probably because the epicentre was in Almeria Gulf, in the submarine part of the Carboneras fault (Figure 1), a sinistral strike-slip fault (150 km long) cutting the recent sedimentary materials (Holocene) as it has been proposed by Gracia et al (2006) and Reicherter and Hübscher (2007). In this case, the approximated epicentre coordinates could be 36.83N, 2.50W. Martinez and Mezcua (2002) locate the epicentre at 36.96N, 2.66W and give a magnitude of 6.5. Focal depth is approximated to 15±5 km and magnitude Mw here estimated is 7.3±0.3, for marine epicentre, and 6.9 ±0.3 for inland epicentre (using formula 1).

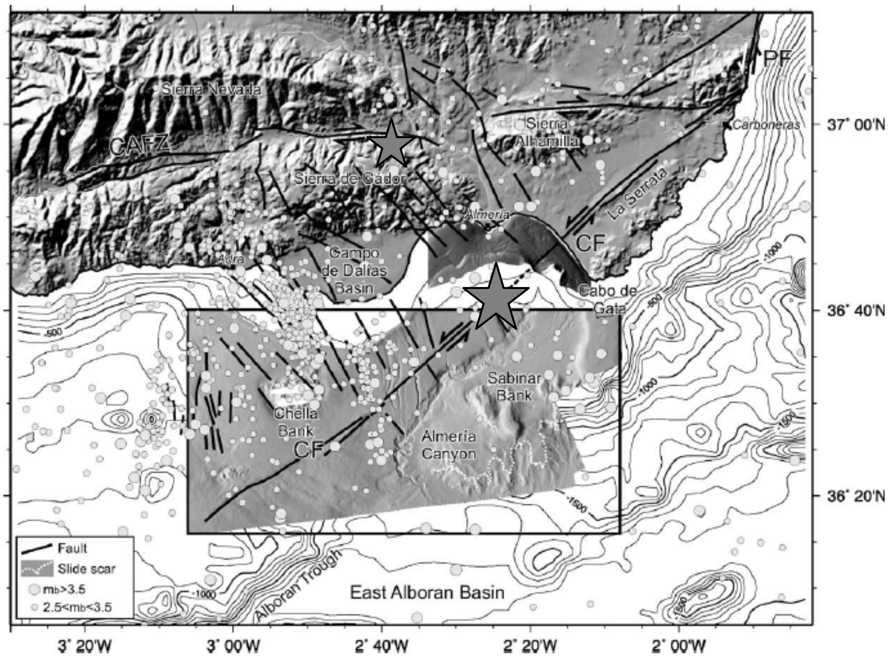

Figure 1. Trace of the Carboneras fault (CF) and the Corridor of the Alpujarras fault zone (CAFZ) and 1970-2000 seismicity (dots) (Gracia et al, 2006). Large star is the marine epicentre here considered and small star that one proposed by Martinez and Mezcua (2002).

The September 30th, 1531 Baza earthquake

The Benamaurel village was completely destroyed (only 6 of the 250 houses remained standing up) and the church and the fortress with very heavy structural damage. This castle was demolished later. According to documents, 100 to 150 people died.

In Baza town, 966 buildings were ruined (61%) (damage grade 4 and 5), and there was serious damage in relevant constructions as the fortress (top of its towers and several walls fell down), the city-walls (damage greater than fortress, nearly destroyed in several parts), and several churches and monasteries suffered damage grade 3 and 4. Primary sources indicate 310 inhabitants perished (Olivera, 1995; Martinez Solares & Olivera, 2007)). Dwelling economic losses in Baza and Benamaurel were estimated in 10.4 millions of "maravedíes" and the royal crown let them off the taxes during ten years and contributed with 2.8 millions for this purpose and 5 millions were destined in the reconstruction of only three main churches.

The buildings of Orce village had heavy damage and also the towers and walls of its fortress. Velez Blanco, a town 70 km distant from epicentre, had damage grade 2 and 3 in its fortress and church, respectively. Others villages as Zújar, Caniles, Cúllar, Benzalema, Cortes de Baza, etc., had to be damaged but data do not appear in the revised documents related to asking for aids to reconstruction because their inhabitants were predominantly Moorish and there were no strategic constructions.

Benamaurel and Baza had an intensity degree of VIII-IX and VIII (EMS-98), respectively, because several relevant churches of recent construction, fortresses and the most part of buildings were heavily damaged or destroyed. Orce fortress damage indicates an intensity ≥VII-VIII and Cullar and Vélez Blanco could reach ≥VII and VI-VII, respectively.

The epicentre was located at 37.53 N, 2.57W, between Baza and Benamaurel (Figure 2), probably associated to the central part of Baza fault, a normal active fault 37 km long and with a total vertical motion between 2 and 3 km (Alfaro et al, 2007). The estimated macroseismic magnitude Mw has been 6.1±0.3 and 6.0 using formulas 1 (at 4 places) and 2, respectively and with the formula of Bäth (1973) is 6.3.

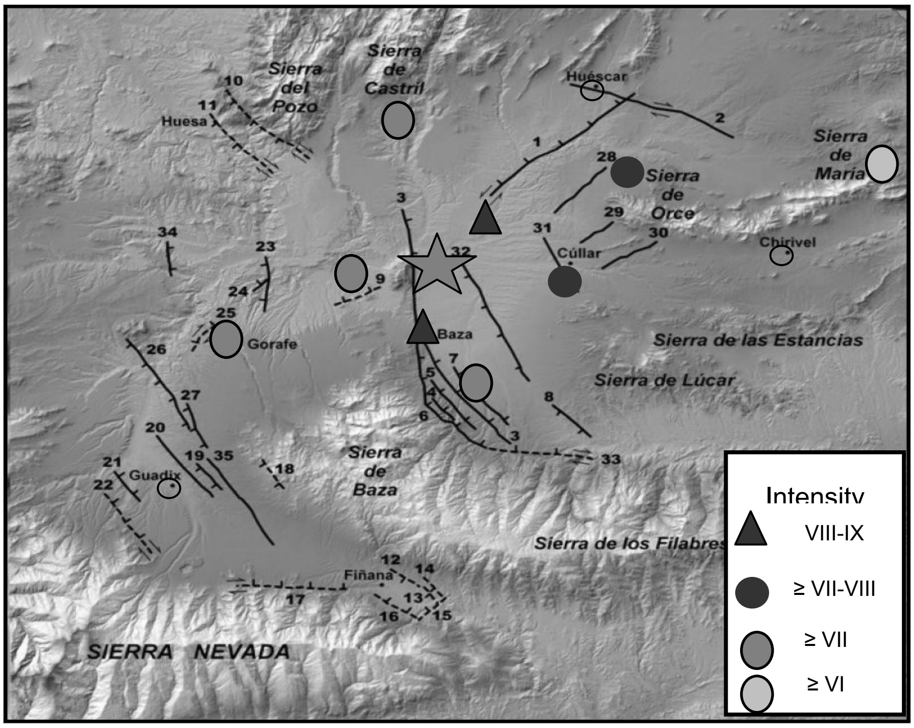

Figure 2. Intensity values of affected towns obtained from documentary data. Fault number 3 could be associated to 1531 earthquake, and with less probability the 32 fault. The active faults (continuous lines) have been drawn by Sanz de Galdeano et al (2007).

Conclusions

During the first part of XVI century four earthquakes with I_o≥VIII-IX and Mw from 6.1 to 7.3 occurred in a short time span in southern Spain, showing spatial-time dependence. This characteristic of the seismicity has been observed more times with historical and instrumental shocks in this low-to-moderate seismicity region, showing a trend to seismic clustering.
The seismic parameters evaluation of these historical earthquakes has been possible due to a reappraisal of relatively well documented information. In spite of the vulnerability influence of damage, its documentary assessment on buildings and stronger constructions has permitted an adequate reappraisal of intensity from historical data, and in many cases archaeological data were also taken into account. Furthermore, the intensity distribution here assigned has been used for the assessment of magnitude and epicentral location, but not those intensity values associated to topographical effects. The contouring intensity drawn here has pointed out the more probable active faults associated to each earthquake.
The instrumental seismicity of the region shows an apparent quiescence that does not reflect the potential hazard. The historical and archaeological data confirm that some zones at present near quiescent could generate damaging earthquakes and taking into account tectonic data some of them could generate relatively large earthquakes, the 1522 Almeria event is a historical example. For this reason, it is recommended that reappraisal of historical earthquakes is essential for assessing seismic hazard in this and others low-to-moderate active regions.

Acknowledgements

The authors would like to thanks to all those who helped us during the study, especially to Drs. J. Grima, D. Ortiz, Cara and P. Murphy, for constructive comments, data and aid during field studies in the epicentral areas. This research was supported by the CICYT project CGL2007-66745-C02-01/BTE .

References

Alfaro P., J. Delgado, C. Sanz de Galdeano, J. Galindo-Zaldívar, F. J. García-Tortosa, A. C. Lopez-Garrido, C. Lopez-Casado, C. Marín-Lechado, A. Gil y M. J. Borque (2007). The Baza Fault: a major active extensional fault in the central Betic Cordillera (south Spain). *Int J Earth Sci (Geol. Rundsch.*), *13 p*.

Ambraseys, N (2004). The state-of-the-art and practice of long term seismicity. *Annals of Geophysics, 47, 2/3, 335-338*.

Bäth, M. (1973). *Introduction to Seismology.* Wiley & Sons. New York.

Espinar, M. &Vidal, F. (1990): "El terremoto de Baza en 1531", *XXII General Assembly of the European Seismological*, Barcelona, 1990.

Espinar, M. (1994): "Los estudios de sismicidad histórica en Andalucía: Los terremotos Históricos de la Provincia de Almería", in *El estudio de los terremotos en Almería*, *16. Instituto de Estudios Almerienses, 115-180*.

Espinar, M (1996). El terremoto de 1522 y sus efectos en algunas zonas de las Alpujarra. *Sismología Aplicada*, *Servicio de publicaciones, Almeria University, 245-266*.

Espinar M., Vidal F., Esquivel J.A., Ocaña E. & Navarro M. (2006). Daños sísmicos del terremoto de Carmona de 1504, *5ª Asamblea Hispano-Portuguesa de Geodesia y Geofísica, 2006*, Sevilla, España.

Espinar M, Vidal F., Navarro M., Vidal L. & Ocaña E. (2008). Documentary study of the 1531 Baza (Spain) earthquake. *6ª Ass. Luso Espanhola de Geodesia e Geofísica.* Tomar. 2p.

Galbis Rodríguez J. (1932). *Catálogo sísmico de la zona comprendida entre los meridianos 5 E y 20 W y paralelos 45 N y 25 N*, Madrid, Instituto Geográfico y Catastral.

Gracia E, Pallas R, Soto JI, Comas M, Moreno X, Masana E, Santanach P, Diez S, Garcıa M, & Dañobeitia J (2006). Active faulting offshore SE Spain (Alboran Sea). Implications for earthquake hazard assessment in the Southern Iberian Margin. *Earth Planet Sci Lett, 241, 734– 749.*

Olivera Serrano, C. (1995). Geografía y poblamiento, *Sismicidad histórica del Reino de Granada (1487-1531),* Instituto Geográfico Nacional, Monografía, *nº 12, 37-283*.

Martínez Solares, J.M. & Mezcua, J. (2002). Catálogo Sísmico de la Península Ibérica (800 a.C.-1900), *Monografía No. 18. Ministerio de Fomento. Inst. Geográfico Nacional. 253 p.*

Martinez Solares, JM & Olivera, C (2007). The 1531 Baza (Granada) earthquake in *La Cuenca de Guadix-Baza, Jaen University, 312-326*.

Morales J, Serrano I., Vidal F. & Torcal F (1997). The depth of the earthquake activity in the Central Betics (Southern Spain). *Geophys. Res. Lett*., *24, 3289- 3292.*

NCSE-02 (2002). Norma de Construcción Sismorresistente: Parte General y Edificación Real Decreto 997/2002, de 27 de Septiembre, *Published in BOE, 244,35898-35967*.

Papazachos B.C. & Papaioannou C.A. (1997). The macroseismic field in the Balkan area. *J Seismology, 1, 181–201.*

Reicherter K. & Hübscher Ch. (2007). Evidence for a seafloor rupture of the Carboneras Fault Zone (southern Spain): Relation to the 1522 Almerıa earthquake?. *J Seismol, 11, 15–26.*

Rueda J. & Mezcua J. (2001). Sismicidad, Sismotectónica y Peligrosidad Sísmica en Galicia, *Publicación Técnica, 35, Instituto Geográfico Nacional, Madrid, 64 p.*

Sánchez Navarro Neumann M. (1921). Lista de los terremotos más notables sentidos en la Península Ibérica desde los tiempos mas remotos, hasta 1917, inclusive, con ensayo de agrupación en regiones y períodos sísmicos, *Estación sismológica y observatorio astronómico y meteorológico de Cartuja (Granada)*,11-65

Sánchez Navarro Neumann M. (1917). Datos referentes a la sismicidad de la porción oriental de la Península Ibérica, *Memorias de la Real Academia de Ciencias y Artes de Barcelona,* 3a. época, *XIII, no. 8, 179-188.*

Vidal Sánchez F. (1986). Sismotectónica de la región Béticas-Mar de Alborán, *Tesis Doctoral, Universidad Granada, 457 p.*

Vidal F., Espinar M., Breton M. & Ocaña E. (2006). The 1518 Vera (Spain) Earthquake, *First European Conference on Earthquake Engineering and Seismology*, *Geneva, Switzerland, 3-9 September 2006.*

Development of the U.S. Geological Survey's Prompt Assessment of Global Earthquakes for Response (PAGER) System

Wald D J (1), Earle P S (1), Allen T I (1), Jaiswal K (1), Porter K (2), and Hearne M (1)

(1) U.S. Geological Survey, Golden, Colorado, 80401, USA, wald@usgs.gov
(2) Dept of Civil Engineering, University of Colorado, Boulder, Colorado, 80309, USA

Keywords: PAGER, earthquake, losses, assessment, intensity

Introduction

The Prompt Assessment of Global Earthquakes for Response (PAGER) System plays a primary alerting role for global earthquake disasters as part of the U.S. Geological Survey's (USGS) response protocol. As World Data Center for Seismology, Denver, the mission of the USGS National Earthquake Information Center (NEIC) has long been to determine rapidly the location and size of all destructive earthquakes worldwide and to immediately disseminate information about earthquake severity to concerned national and international emergency management agencies, scientists, and the general public. The PAGER project is a natural extension of this role, improving global earthquake information and response by rapidly quantifying the impact of all significant events. The NEIC produces automated earthquake solutions. These solutions are human reviewed and disseminated nearly instantaneously by in-house seismic analysts 24x7. In addition, near real-time earthquake source analyses have been rapidly evolving at NEIC, as have technological tools for disseminating new earthquake information and products. These elements, developed on-site, provide essential input and tools that form much of the backbone of the PAGER system. Yet, PAGER requires specific tuning of these earthquake source analysis tools and further development of new elements, mainly pertaining to estimating shaking intensity and losses. Likewise, fundamental to such an alerting system, we are also developing the computational and communications infrastructure necessary for rapid and robust operations and worldwide notifications.

Here we provide an overview of the PAGER system, both its current capabilities and our ongoing research and development. PAGER monitors the USGS's near real-time U.S. and global earthquake origins and automatically identifies events that are of societal importance, well in advance of ground-truth or news accounts. Current PAGER notifications and Web pages estimate the population exposed to each seismic intensity level. In addition to being a useful indicator of potential impact, PAGER provides a new standard in the dissemination of rapid earthquake information.

We are currently developing and testing a more comprehensive alert system that will include casualty estimates. This is motivated by the idea that an estimated range of possible number of deaths will aid in decisions regarding humanitarian response. Underlying the PAGER exposure and loss models are global earthquake ShakeMap shaking estimates, constrained as quickly as possible by finite-fault modeling and observed ground motions and intensities when available.

Loss modelling is being developed comprehensively with a suite of candidate models that range from fully empirical to largely analytical approaches. Which of these models is most appropriate for use in a particular earthquake depends on how much is known about local building stocks and their vulnerabilities. A first-order country-specific, global building inventory has been developed, as have corresponding vulnerability functions. For calibrating PAGER loss models, we have systematically generated an Atlas of 5,000 ShakeMaps for significant global earthquakes during the last 36 years for which loss data exist. For many of these events, auxiliary earthquake source and shaking intensity data are also available. Refinements to the loss models are ongoing.

While the primary purpose of PAGER is rapid dissemination of earthquake impact assessments for decision-making purposes, the intermediate PAGER data, databases, and by-products are also useful tools and sources of earthquake and impact information. For example, in the research and development of PAGER, we have, and will make openly available, databases on earthquake occurrence and their associated population exposures and losses, Vs30 soil site-condition maps for the world, and a suite of other tools and products (discussed below and summarized in Table 1). Despite being a developmental system, a wide range of users has already recognized beneficial by-products from PAGER. For example, they are currently used by government agencies, the re/insurance industry, national and foreign aid organizations, the military, rapid response groups, and by the media.

This report provides a brief overview of the PAGER system, its operations and status, intermediate products and databases, and ongoing developments. Related USGS developments in progress under the auspices of the PAGER project not specifically addressed in this short article include rapid finite-fault modeling, global ShakeMap enhancements, ground motion and loss uncertainty analyses, and more informative ways to portray casualty and loss information (as well as their uncertainties); these projects are addressed in depth in related articles.

The PAGER System

An overview of the conceptual, computational, and developmental framework of the PAGER system is provided in Figure 1. Arrows connecting the four subsystems in Figure 1 indicate the exchange of intermediate products or information that become rapidly, publically available using standard protocols, particularly via Extensible Markup Language (XML) files and Really Simple Syndication (RSS) feeds. The subsystems themselves consist of four basic PAGER elements.

Earthquake Source

Fundamental, rapid earthquake information necessary to inform and trigger the PAGER system is produced at the NEIC within 20 min of significant earthquakes worldwide (within 5 min domestically). Hypocentral and magnitude estimates then trigger secondary systems that produce source mechanisms and seismic-moment estimates using body- and surface-wave moment-tensor inversions. These latter estimates in turn inform finite-fault waveform inversions which currently provide source-rupture models within several hours. In the interim time period, source dimensions are inferred from aftershock distributions, if possible. All available source parameters become constraints for the Global ShakeMap system (GSM).

Shaking Distribution

Once triggered, Global ShakeMap (Allen et al., 2008c; Wald et al., 2006) incorporates all available pertinent information and produces the full suite of ShakeMap products (Wald et al., 2005) within about a minute. While only hypocenter and magnitude parameters are required, shaking uncertainty is significantly reduced by additional constraints, particularly rapid USGS "Did You Feel It?" macroseismic intensity data, seismic station peak-ground motions where available, and fault dimensions (Allen et al., 2008c; Wald et al, 2008).

Loss Modeling

ShakeMap produces (among other products) a grid of shaking parameters, including intensity. PAGER takes these grid values and computes the population exposed to each level of intensity using the global LandScan2006 (e.g., Bhaduri, 2002) database. Currently, these exposure estimates constitute the PAGER summary notifications. However, the primary goal for the PAGER system is to rapidly estimate potential fatalities from any earthquake worldwide. Given the complexity of this challenge, we have adopted a comprehensive three-tiered approach to fatality estimation.

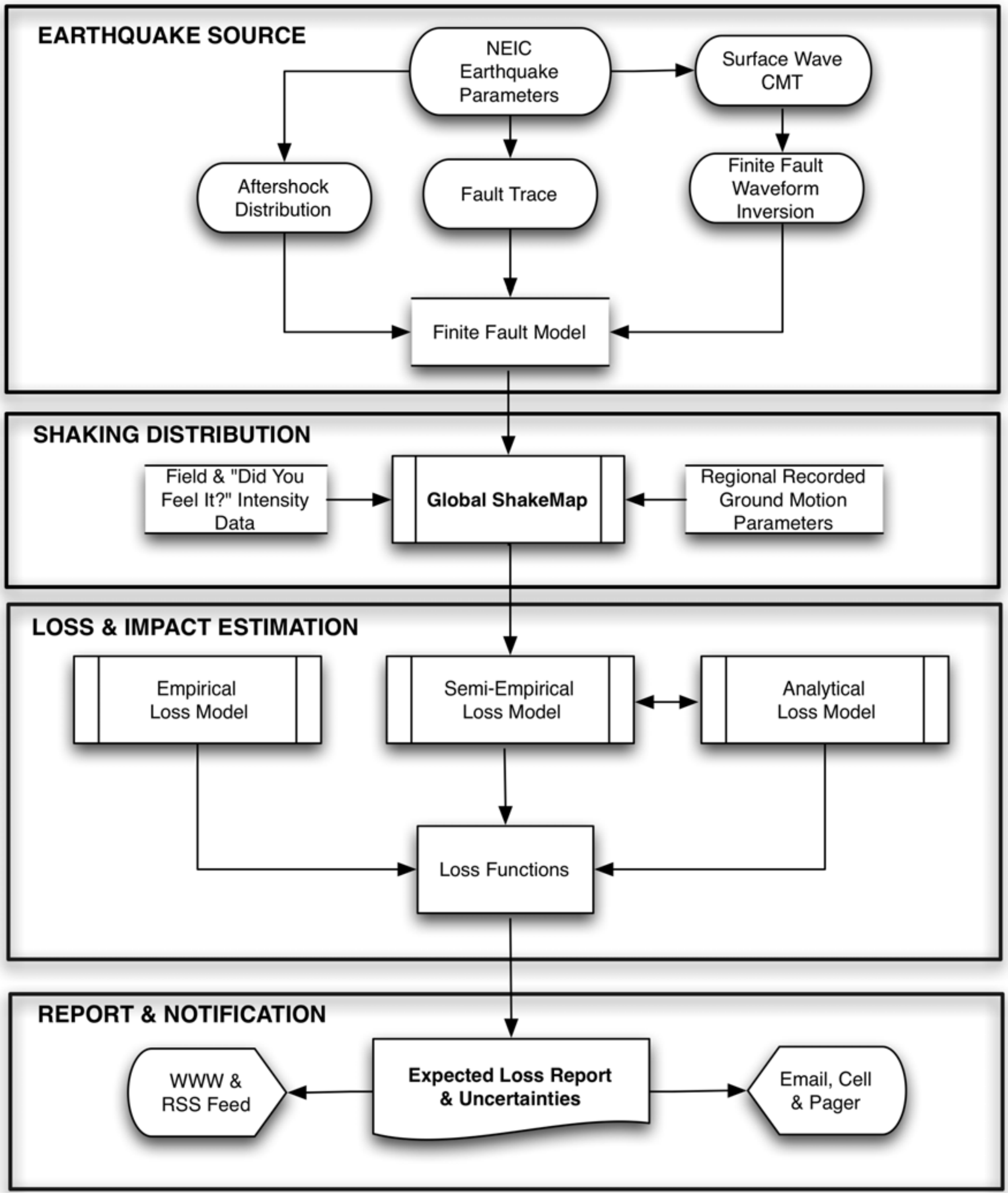

Figure 1. PAGER flowchart for operations, calibration, and loss estimation.

In regions that have experienced numerous earthquakes with high fatalities historically, typically in developing countries with dense populations living in vulnerable structures, enough data exist to calibrate fatalities from the historical earthquake record alone (Jaiswal et al, 2008a). In such regions, building inventories are typically lacking, as are systematic analyses of their vulnerabilities; hence, analytical tools are inadequate for loss estimation. In contrast, in the most highly developed countries, particularly those with substantive building code implementation, structural responses are more easily characterized analytically and their distributions and occupancy are more readily available (e.g., HAZUS; FEMA, 2006). Due to the success of such building codes, for the purpose of fatality loss modeling, this category of country typically has had relatively few fatal earthquakes, making it difficult to use empirical calibration from past events alone. In such cases, fatality estimates are largely informed from analytically-derived collapse rates and inferred fatality ratio given a structural collapse.

Finally, we further consider an intermediate approach, the semi-empirical model, which, for each country, requires a basic description of building inventory and distribution, their occupancy at the time of the earthquake, and their vulnerability (in the form of collapse rates) as a function of shaking intensity (see Jaiswal and Wald, 2008a,b). This approach also requires estimates of fatalities for each structure type given collapse.

As the empirical model does not require knowledge of the building inventory, it cannot be employed directly for impact assessments beyond fatalities—the data used in its calibration. Alternatively, both the semi-empirical and analytical approaches, which require at least basic building inventories and estimates of the number of structural collapses, thus allow for the computation of other losses, including injuries, homelessness, and financial impact. In the following subsections we briefly describe the empirical, semi-empirical, and analytical model approaches for PAGER loss computations using a consistent nomenclature. Jaiswal et al. (2008a), Jaiswal and Wald (2008b), and Porter et al. (2008a,b) provide more comprehensive descriptions of the loss-modeling approaches.

Empirical: In the empirical approach, the building stock distribution and its relative vulnerability are not modeled explicity; the effective fatality rate defined in terms of persons killed per number exposed, at each intensity level (MMI VI-IX), directly incorporates these variations at a country level. For each country *k,* the estimated total number of fatalities can be computed for earthquake *j* by summing the population exposed at each intensity level and then multiplying by the fatality rate for that intensity level:

$$E_j = \sum_{i=1}^{n} v_{i,j} y_k(s_i)\varepsilon_k \tag{1}$$

Here, *v* is the population exposure at grid cell *i*, *s* is the intensity in grid cell *i, y* is the fatality rate for intensity *s,* and ε_k is a residual error obtained for each country by hindcasting their past earthquake losses. For each country, values of *y* are determined by solving for the best mean and standard deviation values (beta, theta) for a lognormal cumulative distribution of fatality rate as a function of Modified Mercalli intensity (Jaiswal et al, 2008a). We minimize a combined L2 and logarithmic norm between the observed and estimated earthquake fatalities. In the forward calculation the fatality rates are given at each ½ intensity unit and are applied to the population exposed to intensity *s* (±1/4 intensity unit) that experiences that intensity range. Countries lacking historical earthquake loss data are assigned fatality rates from an analogous country using expert judgment (for details, see Jaiswal et al., 2008a).

Semi-Empirical: In the semi-empirical approach, building inventories are considered along with each structure type's occupancy (derived from distributing the population per grid cell), intensity-based vulnerability (here, collapse rates), and fatality rate (given a collapse of that type of structure). In a forward sense, for each country *k,* the fatalities can be estimated for each grid cell first, by distributing the grid cell population in different structure types (as a function of local time of the earthquake) using knowledge of building inventory distributions and their occupancy pattern, and by then analyzing the structure-specific vulnerability to compute earthquake fatalities. Vulnerability analysis consists of computing the number of collapsed structures for each structure type exposed to the intensity in that cell, and multiplying by the fatality rate for collapse of that structure type. The estimated total number of fatalities for earthquake *j* in country *k* is then:

$$E_j = \sum_{i=1}^{n}\sum_{t=1}^{m} v_{i,j,t}\, c_t(s_i) f_t\, \varepsilon_k\,, \tag{2}$$

where $v_{i,j,t}$ is the population exposure for earthquake *j* in structure type *t* of grid cell *i*; $c_t(s_i)$ is the collapse rate for structure *t* and for intensity at grid cell *i;* f_t is the fatality rate for each structure given collapse of a particular structure type *t; n* and *m* are the number of cells and structures, respectively. The residual error term ε_k is obtained for each country by hindcasting past earthquake losses using the semi-empirical approach. The building distribution, collapse, and fatality rates are provided from models available in the literature and collected using expert judgment via the USGS PAGER/Earthquake Engineering Research Institute (EERI) World Housing Encyclopedia (WHE, http://www.world-housing.net/) collaborative effort (Porter et al., 2008). For countries with a sufficient number of calibration earthquakes, we can improve the model's predictability by accurately deducing the collapse and fatality rates for the most common building types using past earthquake damage data (Jaiswal and Wald, 2008b). The modified collapse functions are propagated to comparable structures for countries that lack empirical calibration fatality data. Calibration to refine the collapse and fatality rates will be based on losses and associated intensities for events in the ShakeMap Atlas, from data now aggregated in the PAGER earthquake exposure catalog (Allen et al., 2008a).

Analytical: For the analytical method, the building inventory and occupancy databases derived for the semi-empirical approach are used. However, the collapse rates are now determined from basic engineering considerations (i.e., using openly-available versions of the HAZUS capacity-spectrum-based approach; Porter, 2008a,b). Since the only differences from the semi-empirical model are the collapse functions, the forward model for the analytical approach can thus be formulated similarly to the semi-empirical model (Equation 2). In order to calibrate the analytical model against earthquake loss (fatality) data, the inverse problem is analogous to the semi-empirical approach. However, in this case, only the assumed fatality rates are modified since the analytic vulnerability functions were determined from basic principles and laboratory testing.

Proper, relative weighting of the results of the three loss modelling approaches will require further investigation. Hindcasting past losses, and losses for events in recent years not used in the calibration process, will be used in countries for which there are sufficient loss data to do so. For other countries, consideration of the relative quality of constraints for each approach will be made by expert opinion, considering i) the assignment empirical models to neighbouring or analogous countries, ii) the quality of inventory and expert-based vulnerability functions, and iii) the applicability of existing or specially-developed analytical models to the country's building inventory structural types.

Notifications

Currently, the PAGER system alerts select users for any earthquake that has populations exposed to high (MMI>VI) intensities, though the alerting level is customizable. PAGER alerts can be sent to cell/pager or emailed, with information content commensurate with the delivery mechanism. Each summarizes the population exposed to each level of intensity, a good proxy for potential impact. The signature product is called the "OnePAGER" (Earle and Wald, 2007); it provides a comprehensive summary of shaking, population, cities, and exposure to different intensity levels. These same summary files are available online with expanded content in near real time at http://earthquake.usgs.gov/pager/.

Table 1. Databases, Products, Tools, and Services associated with the research, development, and operations of PAGER.

Database/Product	Description	Use	Reference
Earthquake Source			
Fast Finite Faults	Rapid (few hours) slip models for major earthquakes	Constraints for shaking; stress changes	Ji et al (2004); Hayes & Wald (2008)
PAGER-Cat	Quality composite	Source input for	Allen et al (2008a)

	earthquake catalog (1900-2006)_	ShakeMap Atlas; ExposureCat	
Shaking Distribution			
Global Slope Data	Topographic slope	Landslides, Vs30	Verdin et al (2007)
Global Vs30 Server	Vs30 values for the globe	Estimating site amplification	Allen & Wald (2008); Wald & Allen (2008)
Global “Did You Feel It” Intensities	Rapid intensities from Internet users	Constrains Shake-Map & event bias	Wald et al (2006)
ShakeMap Uncertainty	Quantitative & Qual-itative shaking values	Computing loss uncertainty	Wald et al (2008)
ShakeMap Atlas	ShakeMaps for global earthquakes (1970-present)	Scenarios, planning, hazard calculations	Allen et al (2008b)
Rapid Global ShakeMaps (GSM)	Estimated ShakeMaps for earthquakes (M>5.5)	Shaking input for loss estimation, decision making	Wald et al (2006)
Loss & Impact Estimation			
Deadly Earthquake List	Online resource list (1900-2006)	General Reference	On Wikipedia: see “List of Deadly Earthquakes”
Exposure-Cat	Population exposure to intensity for each Atlas ShakeMap	Fatality rates calculations	Allen et al. (2008a)
Global Building Inventory	Country buildings collapse rates	Country-specific loss estimation	Jaiswal & Wald (2008); Porter et al (2008)
Empirical Loss Model	Country-specific fatality rates	Fatality estimates given exposure	Porter et al (2008a) Jaiswal et al (2008)
Semi-Empirical Loss Model	Country building vulnerability	Fatality estimates based on structures	Jaiswal et al (2008)
Analytical Loss Model	HAZUS vulnerability functions	Structure dependent loss computations	Porter (2008b)
Reporting & Notifications			
OnePAGER	Population Exposure Notifications	Post-earthquake decision making	Earle & Wald (2008)

We now produce in-house estimates of fatalities for the empirical and semi-empirical systems, but both are undergoing rigorous calibration and testing prior to public release. We are also trying to quantify uncertainty in hazard as well as loss estimates. The PAGER information products will be modified to provide intuitive descriptions of potential fatalities and their associated uncertainties. At that time, alerts will be available publicly and we will allow them to be selective, with user-customizable regions around the globe as well as by alert levels.

Intermediate and Derivative Products

Table 1 summarizes the current list of databases, products, and tools established in the process of developing PAGER. While the most visible outcome of the PAGER system are the notifications and alerts described above, it is anticipated that significant benefits to other global loss modeling, earthquake response, and mitigation efforts will come out of these intermediate and derivative tools and by-products. Some tools, for instance the Global Vs30 Server (Allen and Wald, 2007) are already in wide use, providing generalized maps of estimated shallow shear-wave velocities for all regions of the globe. Other tools listed in Table 1, including the fast finite-fault inversion system, are ongoing and comprehensive complements to the PAGER system and NEIC efforts, in general. As such, while they are intended to provide immediate benefit in the short term, they will require extensive long-term development and operational capabilities that will take time and effort to fully implement.

The open availability of the tools and products listed in Table 1 is in notable contrast with analogous but proprietary systems developed primarily for commercial use. Such proprietary models tend to be result-oriented, so their databases, intermediate results, and models are not openly available for use or assessment. It is hoped and anticipated that given the open nature of the PAGER data and models, interactive and collaborative efforts will facilitate more rapid hazard estimation updates, further exchange of real-time seismic data and more difficult to access loss data, and improved loss methodologies.

References

Allen T. & Wald D.J. (2007). Topographic-slope as a proxy for seismic site-conditions (V_S^{30}) and amplification around the globe, U.S. Geological Survey, *Open-File Report, 2007-1357, 69p.*

Allen T.I., Earle P.S. & Wald D.J, Lin K. & Hearne M. (2008a). Development of an earthquake exposure catalog for PAGER loss modeling**,** Seism. Res. Lett., in prep.

Allen T.I., Marano K.D., Earle P.S. & Wald D.J (2008b). PAGER-CAT: A composite global earthquake catalogue for casualty estimation**,** *Seism. Res. Lett., in review.*

Allen T.I., Wald D.J., Hotovec A., Lin K. Earle P.S. & Marano K.D. (2008c). An Atlas of Shake-Maps for Selected Global, *U.S. Geological Survey Open File Report 2008-xxxx*.

Bhaduri B., Bright E., Coleman P. & Dobson J. (2002). LandScan – locating people is what matters, *Geoinformatics, 5, 2, 34-37.*

Earle P.S. & Wald D.J. (2007). Helping solve a worldwide problem—rapidly estimating the impact of an earthquake: PAGER (Prompt Assessment of Global Earthquakes for Response), *U. S. Geological Survey, Fact Sheet 2007-3101, 4p..*

FEMA (2006). HAZUS-MH MR2 Technical Manual: *Federal Emergency Management Agency.*

Hayes G.P. & Wald D.J. (2008). Developing framework to constrain the geometry of the seismic rupture plane in subduction zones *a priori* – a probabilistic approach, submitted to *Geophys. J. Int*.

Jaiswal K. & Wald D.J. (2008a). Creating a global building inventory for earthquake loss assessment and risk management, *U.S.G.S. Open File Report 2008-1160, 113 p.*

Jaiswal K. & Wald D.J. (2008b). Estimating casualties for large worldwide earthquakes using a semi-empirical approach, *U.S.G.S. Open File Report (in prep.).*

Jaiswal K., Wald D.J. & Hearne M (2008a). Estimating casualties for large worldwide earthquakes using an empirical approach, *U.S.G.S. Open File Report (in prep.).*

Jaiswal K., Wald D.J., Porter K. & Earle P.S. (2008b), Creating a global building inventory for earthquake loss estimation and risk management, *Earthquake Spectra (in prep.).*

Ji C, Helmberger D.V. & Wald D.J. (2004). A teleseismic study of the 2002, Denali, Alaska, earthquake and implications for rapid strong motion estimation, *Earthquake Spectra*, *20, 617-637.*

Porter K.A. (2008). Cracking an open safe: HAZUS vulnerability functions in terms of structure-independent spectral acceleration, *Earthquake Spectra (submitted)*,

Porter K.A., Greene M., Jaiswal K & Wald D.J. (2008a). WHE-PAGER project: A new initiative in estimating global building inventory and its seismic vulnerability, *14WCEE, Beijing.*

Porter K.A., Wald D.J., Earle P., Allen T.I. & Jaiswal K. (2008b). An empirical fatality model for the U.S. Geological Survey's Prompt Assessment of Global Earthquakes for Response (PAGER) system, *14WCEE*, *Beijing.*

Verdin K.L., Godt J., Funk C., Pedreros D., Worstell B. & Verdin J. (2007). Development of a global slope dataset for estimation of landslide occurrence resulting from earthquakes, U. S. Geological Survey, *Report Series 2007-1188*, *25p.*

Wald D.J., Lin K., Porter K. & Turner L. (2008a). ShakeCast: Automating and Improving the Use of ShakeMap for Post-Earthquake Decision-Making and Response", *Earthquake Spectra, in press.*

Wald D.J., Lin K. & Quitoriano V. (2008b). Quantifying and Qualifying USGS ShakeMap Uncertainty, *USGS Open File Report, 2008-1234.*

Wald D. J. & Allen T.I. (2007). Topographic slope as a proxy for seismic site conditions and amplification, *Bull. Seism. Soc. Am. 97, 1379-1395.*

Wald D.J., Earle P.S., Lin K., Quitoriano V. & Worden B.C. (2006a). Challenges in rapid ground motion estimation for the prompt assessment of global urban earthquakes, *Bull. Earthq. Res. Inst.*, *81, 275-283.*

Wald D.J., Quitoriano V., Dewey J.W. (2006b). USGS “Did You Feel It?” Community Internet Intensity Maps: Macroseismic Data Collection via the Internet, *ISEE Proceedings , Geneva.*

Wald D.J., Worden B.C., Quitoriano V. & Pankow K.L. (2005). ShakeMap manual: technical manual, user's guide, and software guide, U.S. Geological Survey, Techniques and Methods 12–A1, http://pubs.usgs.gov/tm/2005/12A01/, *128 p.*

Seismic Density and its Relationship with Mid-Strong Historical Earthquakes in Austria

Wang J (1), Hammerl Ch (2)

(1) Institute of Geophysics, China Earthquake Administration, No.5 Minzu Daxue Nan Rd., Beijing 100081, China, wangjcsb@hotmail.com
(2) Central Institute for Meteorology and Geodynamics, 1190 Vienna, Hohe Warte 38, Austria, christa.hammerl@zamg.ac.at

Keywords: seismicity, historical earthquakes, earthquake cluster, Eastern Alps, Austria.

Introduction

Since the end of nineteenth century small earthquakes have been recorded worldwide. The accumulation of these data raised a fundamental question: what are the characteristics and the physical nature of small earthquakes? Since the destructive 1966 Xingtai Earthquakes, regional earthquake observation networks have been built in China. Most stations were built in North China (110°-125°E, 30°-43°N), where the earthquake catalogue for magnitudes greater than M_L2 is estimated to be almost complete, from 1970 onwards. On the basis of these instrumental data, seismic patterns were calculated and the spatial-temporal distribution analyzed (Wang, J., 2001). Apart from these instrumental data, abundant information of historical earthquakes in North China is found in the archives (Wang, J., 2004a).
A very interesting phenomenon was noticed with both historical and instrumental data. Small earthquakes still cluster near the epicentres of mid-strong earthquakes, even if those occurred several hundred years ago (Wang, Z.G., 1985; Wang, J., 1999). Therefore the relationship between seismic density and mid-strong earthquakes in North China was analyzed (Wang, J., et al., 2004b; Wang, J., 2007a) and different types of seismic densities were proposed according to the spatial-temporal distribution of small earthquakes.
Is this phenomenon unique for China? Instrumental data have existed in China for about forty years, whereas earthquakes in Austria have been recorded for more than 100 years. The question arises whether the above-mentioned regularity is true also for more comprehensive data files?
A bilateral project between Austria and China gives us a chance to utilize quantitative methods to deal with instrumental seismic data in both countries to compare seismic characteristics.
The results of this paper will verify the validity of data collected about mid-strong earthquakes and, consequently, improve seismic hazard assessment. In a subsequent phase, it may help to improve the prediction of earthquakes over periods of medium-term length.

Materials and Methods

Seismic data

There are 1637 earthquakes listed in the catalogue for Lower Austria, Upper Austria and Styria, most entries are magnitude 2 earthquakes (48%). Table 1 shows that earthquakes with a magnitude of 1 and below can be regarded as negligible. The range of earthquake focal depth is from 0 to 35 km, with most earthquakes belonging to the section of 5-9 km.
From Fig.1 we can notice that epicentre distribution is not homogeneous, but that there are some obvious clusters. From Fig.2a it becomes obvious that before 1800 there were only 7 earthquakes with a magnitude bin within 3.9 and 6. From 1800 to 1899 there were 86

earthquakes with magnitude bin within the range 1.8 to 5.4. According to the catalogue earthquakes with magnitude greater than 2 are almost complete from 1897 on.

Table 1 Magnitude and focal depth distribution

Magnitude	0-.9	1.0-1.9	2.0-2.9	3.0-3.9	4.0-4.9	5.0-5.9	6.0-6.9
Number	65	479	780	257	44	11	1
Ratio	4.0%	29.2%	47.7%	15.7%	2.7%	0.6%	0.06%

Depth (km)	0-4	5-9	10-14	15-19	20-35
Number	256	1276	76	17	12
Ratio	15.6%	78.0%	4.6%	1.0%	0.7%

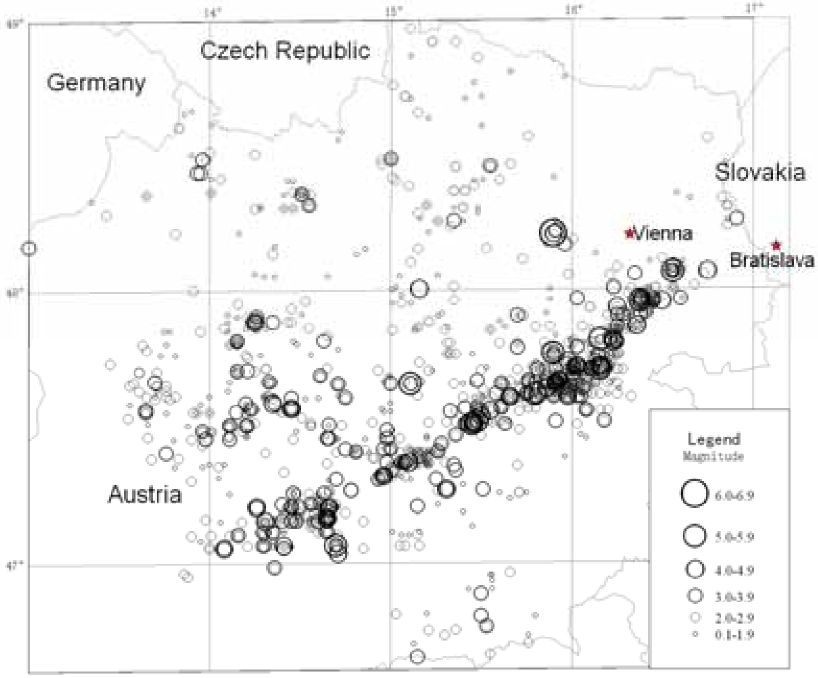

Figure 1 Epicenter distribution of earthquakes in the East of Austria.

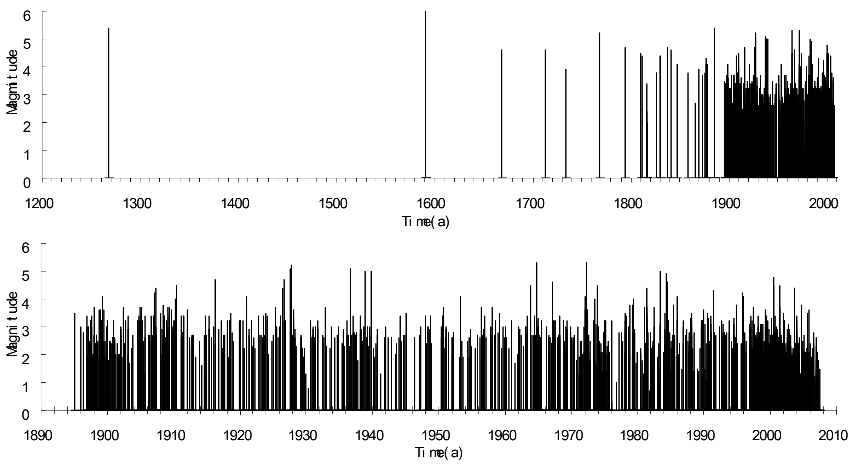

Figure 2a Magnitude vs time distribution of the earthquakes in the East of Austria.

In Fig.2b 544 earthquakes with a magnitude lower than 2 are plotted. Three time periods can be delineated: 1897 to 1969, 1970 to 1997 and 1998 to 2007. It is only in the third period that the earthquakes with a magnitude of 1.5 to 1.9 seem to be complete.

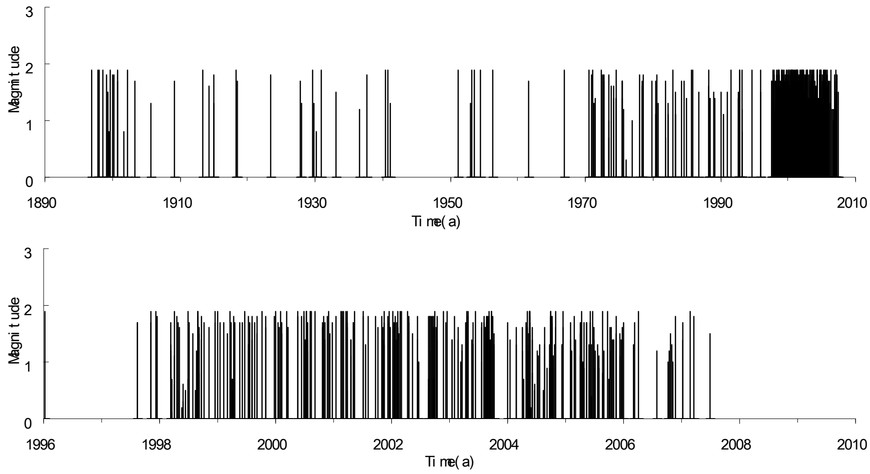

Figure 2b Magnitude vs time distribution of the earthquakes in the East of Austria (M<2).

A quantitative method to depict earthquake clustering

In order to depict earthquake clusters quantitatively, we first delineate grids with interval Δ in longitude and latitude. For each grid node, we specify a circle with the grid node as the centre and R as radius. For the *j*th node, only the earthquakes within the circle will be added to the value, while earthquakes outside circle will be accounted to the neighbouring node. The grid size (Δ) should be related to the accuracy of the epicentre location, and the choice of *R* should refer to the grid size. When calculating the distance between the *j*th grid node and the *i*th earthquake epicentre (r_{ij}), the error of the epicentre location has to be considered, i.e. the error of r_{ij} is equivalent to the error of epicentral location. No correction is made for the focal depth, because in any case this uncertainty is in any case greater than that of the epicentre.
For the *j*th node, the seismic density value is defined by

$$I_j = \sum_{i=1}^{n} \frac{m_i}{M_{Max} Ln(r_{ij})} \qquad R_{min} \le r_{ij} \le R \qquad (1)$$

In formula (1), m_i is the magnitude of *i*th earthquake, M_{Max} is a normalization factor, which is equal to the upper magnitude. The concept of R_{min} depends on the accuracy of epicentre locations. Supposing the *i*th earthquake located on the same site with *j*th node, r_{ij} is zero. Considering the error of the epicentre location, r_{ij} may not be exactly zero; it should be the resolution of accuracy. Seismic density I_j increases with the magnitude m_i and the number of earthquakes *n*, but is inverse to the distances r_{ij}. Once the calculation has been applied to every node, we can construct contours of the seismic density.

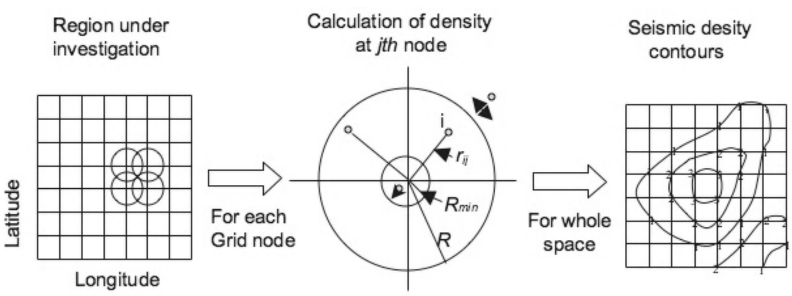

Figure 3 Sketch of seismic density calculation.

The determination of parameters

In our calculation, we take the grid size Δ as 0.05 degree of longitude and latitude, which is approximately equal to 5 km. The R_{min} represents the resolution of epicentre location. We

assume that R_{min} = e (e≈2.71828). The determination of R should be suitable with the selection of grid size Δ . R should not be too large in case that many earthquakes are calculated repeatedly, but it should be large enough in order that no earthquake is missed. R should be larger or at least equal to ($\Delta\times\sqrt{2}$). For example, if Δ is 5 km, R should not be smaller than 7.1. In this paper, we take R = 8 km. The normalization factor M_{Max} is determined by the upper magnitude, here the upper magnitude is 4.
The results of the sensitivity analysis (Wang J., 2001) have proved that the effect of grid size to seismic density ratio is not very great. If the grid size is small, the isolines of seismic density seem denser in some places. The value of R directly determines the seismic density. From this point, we know that the value of seismic density is relative. It corresponds directly to R. For this reason, we should keep parameters uniform throughout the whole research region when calculating seismic density. If there is an error of magnitude, it will also affect the seismic density value. The effect will be almost equal at each node.
We calculate the seismic density of small earthquakes. Here small earthquakes mean the magnitude bin of 2 to 4, which is relatively complete. The earthquakes with magnitude larger than 5 are regarded as mid-strong earthquakes. In Fig.4, we draw the seismic density contours and the epicentre distribution of these small earthquakes. The values of isolines start from 1 and increase with 1. From Fig.4, one can notice that many earthquakes are concentrated in the seismic density zone. With earthquakes scattering, the seismic density value is lower or neglected completely. The density zones can suitably express the characteristics of earthquake clusters.

Results and Discussion

Characteristics of seismic density in Austria

Spatial-distribution of Seismic density

In Fig.5 we can notice that there are more than ten seismic density zones; we delineated the main seismic zones. The principle and method to determine the seismic density zone is mainly based on exterior envelopes of seismic density isolines. Besides squares and rectangles, polygons are used according to the shape of a seismic density zone. In Table 2 we list the seismic density values of the main zones. Seismic zones from 1 to 8 form a seismic belt before the Alps, with the seismic density value greater than 9. The highest value of a seismic density zone is 45 in zone 4.

Table 2 Number of earthquakes M≥2 and relative values in each zone

Zone	1	2	3	4	5	6	7	8	9	10	11	12	13	14
Number	26	47	89	280	45	101	70	87	3	14	12	42	29	42
Seismic density	9	18	22	45	16	21	20	19	3	3	5	9	7	9
b value	.45	.53	.78	.68	.61	.87	.65	.82		.59		.79	.60	.70

Note: there are not enough earthquakes to calculate b values in zone 9 and zone 11.

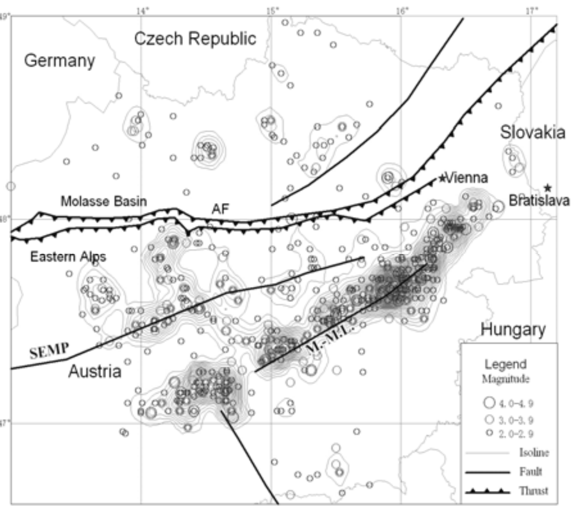

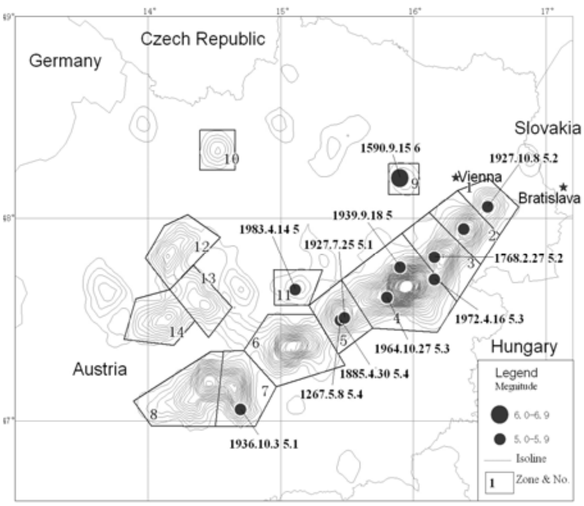

Figure 4 Seismic density and small earthquakes. Figure 5 Seismic density zones and mid-strong earthquakes.

There is a total 12 mid-strong earthquakes with a magnitude greater than 5, including 4 mid-strong earthquakes which occurred before 1897. From Fig.5, all mid-strong earthquakes fall in the seismic density zones. The earliest mid-strong earthquake occurred in 1267 with M5.4 and other two mid-strong earthquakes belong to zone 5. There are also three mid-strong earthquakes in zone 4. There are other six zones with one mid-strong earthquake in each zone. It is obvious that seismic density is consistent with mid-strong earthquakes.

Temporal distribution of earthquakes in the seismic density

In this section, we will display the temporal distribution of the earthquakes in the seismic density zones. We calculate the annual number of earthquakes in each magnitude bin for each density zone. As an example, the temporal distributions of density zone 2, zone 4, zone 5 and zone 11 are shown in Fig.6. Relative parameters such as mean value and variance, which describe statistical characteristics, are listed in Table 3. From the temporal distributions, three types of seismic zones can be determined.

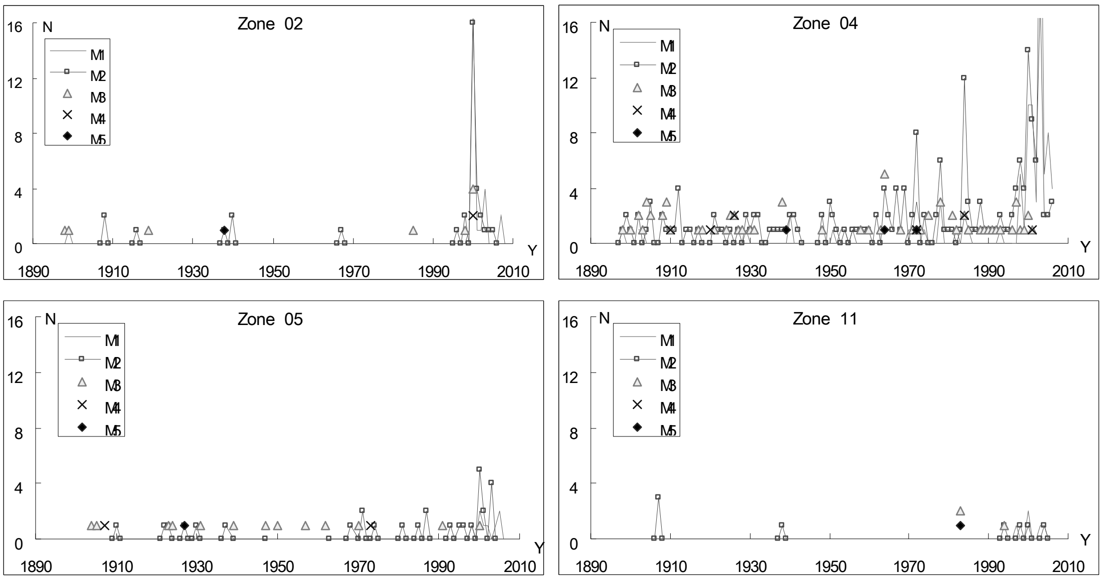

Figure 6 Temporal-distribution in selected seismic density zones.

1. A lot of small earthquakes where the temporal distribution is almost stationary; it seems that there is no gap in the time axis. Zone 3 to zone 8 and zone 12 to zone 14 are of this kind. The mean value of this kind is from 0.198 to 1.809. Although the highest variance (28.62) appeared in zone 4, its normalized variance (variance divided by mean value) is not high (15.8). The statistical characteristics of this kind of seismic density zone are a relatively high mean value and a relatively lower normalized variance (lower than 33). From the temporal distribution, we see that the seismic density zones are not composed by the aftershocks of mid-strong earthquakes. For example, in zone 5, an M5.1 earthquake that occurred in 1927 had no clear aftershocks. The same situation appeared in zone 7. Generally, the b value is larger than 0.6.

2. There are several earthquake clusters in temporal distribution, but there are also long gaps between clusters. Zone 1 and zone 2 are of this kind. In zone 1, there were about four clusters; the most active appeared around 1930. An earthquake M5.2 occurred in 1927 and there were obvious aftershocks in the following two years. In zone 2, there were several clusters, the most active appeared from 1996 to 2006. An earthquake M5 occurred in 1938 and there were obvious aftershocks in the following year. The statistical characteristics of these seismic density zones are a mid mean value (0.171 and 0.315) and high-normalized variances (41.2 and 53.5). The b values are relatively low (lower than 0.55).

3. The temporal distribution of the third type is not as continuous as that of the first kind. There are not very high peaks in the annual numbers. Zones 9 to zone 11 are of this kind. The highest peak of annul number is not higher than 4. The statistical characteristics of this

seismic density zone are a lowest mean value (lower than 0.15). There are not enough data to calculate the b value.

Table 3 Mean value and variance of earthquake temporal distribution in seismic density zone

M	Zone 1		Zone 2		Zone 3		Zone 4		Zone 5		Zone 6		Zone 7	
	Mean	Var	Mean	Var	Mean	Var	Mean	Var	Mean	Var	Mean	Var	Mean	Var
2	.171	7.05	.315	16.85	.694	13.48	1.809	28.62	.261	7.71	.622	20.55	.387	7.09
3	.045	2.19	.081	4.50	.072	3.07	.636	9.67	.117	3.39	.261	5.78	.207	5.31
4			.018	1.99	.036	1.96	.072	3.38	.018	1.40	.036	2.42	.03	1.71
M	Zone 8		Zone 9		Zone 10		Zone 11		Zone 12		Zone 13		Zone 14	
	Mean	Var	Mean	Var	Mean	Var	Mean	Var	Mean	Var	Mean	Var	Mean	Var
2	.505	9.58	.018	1.40	.108	5.17	.072	3.66	.279	7.64	.198	4.86	.261	7.71
3	.252	6.08			.018	1.40	.027	2.22	.090	4.14	.045	2.60	.117	4.18
4	.027	1.71							.009	.99	.018	1.40		

Relationship between seismic density and mid-strong earthquakes

From the viewpoint of fracture mechanics, a strong earthquake occurrence is regarded as the result of crustal medium faulting or displacement. Large amount of aftershocks should add some small-scale cracks or frictions in original cracks. Due to strong earthquakes and the aftershocks, local crustal medium should change gradually. The process of this change cannot be traced back and maybe still continue at least for several hundred years or even longer. The seismic density of present earthquakes around the epicentres of mid-strong earthquakes can be seen as an "exhibition" of this process. To understand this process, regional stress and local crustal medium are two basic elements, which are contradictory. Generally stress plays a dominant role in some cases. Without stress, there should be no fracture. Fracture is more likely to occur in the medium with cracks than in integral one under the same pressure, which has been confirmed in fracture mechanics and rock experiments. The results of rock experiments have shown that acoustic emission exhibits spatial-temporal density. The number of acoustic emission is a function of peak pressure and cyc-pressure number (Haimson, 1974, Sondergeld, et al., 1981). These results show that the earthquake number has a relation not only with stress, but also with the medium. While it is not a reversible process from integrity to fragmentation, once a weakened zone has formed, there should be more events in the next load.

In order to understand the seismicity in Austria, we roughly divide regional stress into two states and local crustal medium into three states. The two states of stress are relatively high and low. Three states of medium are relatively integrity, with few cracks and fragmentation separately. As different combination of stress and medium, there should be a corresponding seismic pattern. If stress and fragmentation of local crustal medium is high, small earthquakes should be frequent. This situation corresponds with the firs type of zones (Zone 3 to zone 8 and zone 12 to zone 14). If high stress with few cracks, there maybe some clusters of medium and small earthquakes, which correspond to the second type of zones (zone 1 and zone 2). If the regional stress is relatively low, the seismicity should be sparse not only in spatial, but also in temporal distribution. Seismic density from zone 9 to zone 11 is of that kind. The characteristic like the value of seismic density is low and the peak of temporal distribution is not obvious. We suppose that the local crustal medium is relative integrity with no seismic density or mid-strong earthquakes. Till now even relative high-level stress does not cause earthquakes in such places. However, a strong earthquake or seismic density may occur only when stress exceeds the level. With the same stress, a mid-strong earthquake or seismic density may easily occur in the local medium with few cracks.

Discussion

Relationship with geological setting

Our research region includes the Vienna basin, the Styrian basin and part of the Eastern Alps and the Pannonian basin. This region is considered to be the result of a two-stage continent–continent collision during the Cretaceous and Tertiary periods. At present, most of the area of the Eastern Alps exposes the Austroalpine upper unit, a nappe complex of African continental affinity, which has been stacked in Cretaceous times and is generally described in terms of three, internally imbricate, tectonostratigraphic thrust sheets named Lower, Middle and Upper Austroalpine nappe complexes. The collision of stable Europe in the north and the Austroalpine/Adriatic microplate in the south led to overriding of the stable European crust by Penninic continental and oceanic units, and by the Austroalpine nappe complex. Postcollisional N–S compression in the central area of the Eastern Alps caused eastward

lateral extrusion of crustal blocks towards the unconstrained and eastward extending margin of the Pannonian realm. Large-scale E–W extension initiated the local rifting of the brittle uppermost crust and the formation of the Styrian basin and the Vienna basin. This process of lateral extrusion, a combination of gravity-driven orogenic collapse and lateral tectonic escape, and the rollback of the remnant oceanic lithosphere in the Carpathian realm were accompanied by subsequent subsidence and extreme E–W extension of the Pannonian realm and of the eastern range of the Eastern Alps. The E–W extension in turn caused eastward crustal thinning and the detachment of the brittle Austroalpine upper unit, which extended by faulting, and the Penninic lower unit, which extended by ductile pure shear. The eastward extruding block was confined by the sinistral Mur-Mürz wrench corridor in the north and the dextral Periadriatic lineament in the south (Reinecker, J., et al., 1999; Graßl, H., et al., 2004; Behm M., et al., 2007).
From Fig.4, it seems that seismic density zone 3 to zone 6 correspond to the Mur-Mürz fault. Zone 1 and zone 2 withstood the Mur-Mürz fault and changed to NNW orientation. Statistical characteristics and b values showed that the two zones are newly formed. It reminds us of the new development of seismicity under the geological setting.

Complex of seismic density
From the examples in China, we know that the factors which influence the seismic density are complex. Besides the magnitude of the mid-strong earthquakes, local crustal medium, fault frames and regional stress level at present days should be considered. Some cases in China showed that the formation of a seismic density belt might have deep dynamics. Reciprocity of mantle convection and the mountain roots maybe an important element (Wang J., et al., 2007b).
This phenomenon illustrated that historical earthquakes in Austria are of high credibility; on the other hand it also suggested that some historical earthquakes maybe missed. For example, seismicity in zone 6 suggested that there maybe at least a mid-strong historical earthquake in this area.
In the last decade (from 1996 to 2006) the peak of temporal distribution in some seismic zones (such as zone 2 to zone 6) suggested that the crustal stress is not stable along the seismic density belt, which may change with time.
The results of this paper let us know more about the complex of seismicity. At least, not every seismic density can be regarded as precursor to predict earthquakes, because some of them have relations to previous strong earthquakes, but the method can be used to judge correctly epicentres of historical earthquakes of poor contemporary information.

Conclusions
(1) Instrumental data in Austria belong to the first recorded worldwide. From about 1897, the records of earthquakes with magnitude greater than 2 seem to be relatively complete. We applied a quantitative method to calculate the seismic density of magnitude bin of M2 to M4. The seismic density depicts earthquake spatial-distribution precisely. There are 14 seismic density zones in the area of interest. Some of them crowd each other to form a seismic density belt just before Eastern Alps.
(2) There are twelve mid-strong earthquakes with M5 or M6, including four historical earthquakes. The epicentres of all these mid-strong earthquakes are located in the seismic density zones. Mid-strong earthquakes and seismic density of small earthquakes are consistent in each case, which reveals the persistent weakness of local crustal medium together.
(3) Temporal distribution of small earthquakes in each seismic density zone is analyzed quantitatively. The b values are calculated. According to statistics, three types of seismic density are distinguished. One type of seismic density corresponded to historical mid-strong earthquakes, where small earthquakes seem to have occurred continuously more than 100 years.
(4) Synthesizing spatial-temporal distribution, causation and geodynamics of different seismic density types are analyzed. These phenomena may help us to understand the earthquake population dynamics and to improve locations of the epicentres of strong historical earthquakes.

Outlook

In a historical research project, funded by the Government of Lower Austria NC 59-2003 and NC 65-2006 the catalogue of Lower Austria will be revised on the basis of original sources. Based on these new data the method described in this paper will be applied anew. This would be another valuable contribution to estimate the influence of historical earthquake research.

Acknowledgements

We thank Wolfgang Lenhardt (ZAMG Austria) for providing the catalogue of Austria and Miss Xuan WU of the Institute of Geophysics, CEA, to draw the figures in this paper. Both Science and Technology Ministry of China and Austria (CN08/2007) supported the work described in this paper.

References

Behm M., Brückl E. & Mitterbaur U. (2007). A new seismic model of the Eastern Alps and its relevance for geodesy and geodynamics. *Vermessung & Geoinformation, 2, 121-133.*

Haimson B C. (1974). Mechanical behavior of rock under cyclic loading. *Advances in Rock Mechanics (Proc. 3rd Congress of the Intl. Soc. for Rock Mechanics), 2,373-378.*

Hammerl Ch. (2007). Historische Erdbebenforschung in Niederösterreich. Die khirchen dermassen zerschmetert und zerlittert, das man nit darein darf … *Studien und Forschungen aus dem NÖ Institut für Landeskunde. Hg. Rosner, Willibald und Gertrude Langer-Ostrawsky, Bd.46, 21-43.*

Graßl H., Neubauer F., Millahn K. & Weber F. (2004). Seismic image of the deep crust at the eastern margin of the Alps (Austria): indications for crustal extension in a convergent orogen. *Tectonophysics, 380(1-2), 105-122.* doi:10.1016/j.tecto.2003.12.003.

Kummerow, J., Kind, R., Oncken, O., Giese, P., Ryberg, T., Wylegalla,. K. & TRANSALP Working Group (2004). A natural and controlled source seismic profile through the Eastern Alps: TRANSALP. *Earth Planet Sci. Lett., 225, 115-129.* doi:10.1016/j.epsl.2004.05.040.

Reinecker, J. & Lenhardt, W. A. (1999). Present-day stress field and deformation in eastern Austria. *International Journal of Earth Sciences, 88(3), 532-550.* doi: 10.1007 /s005310050283

Sondergeld C. H. & Estey L. H. (1981). Acoustic Emission Study of Microfracturing During the Cyclic Loading of Westerly Granite. *J. Geophys. Res., 86, B4, 2915-2924.*

Wang J. (1999). Research on Characteristics and Application of Seismic Magnitude-Number Constitution. *Ph.D. dissertation thesis, Institute of Geophysics, China Seismological Bureau (in Chinese, with English abstract).*

Wang J. (2001). Seismic Pattern treatment method through calculation seismic density at Grid Nodes. *Acta Seismologica Sinica, 14(3), 274-279.*

Wang J. (2004a). Historical Earthquake Investigation and Research in China. *Annals of Geophysics, 47(2/3), 831-838.*

Wang J., Zhang X.D., Wu X. & Wang Su-yun (2004b). Seismic characteristics near the epicenter of Hongtong, Shanxi, M=8 earthquake in 1303 and its implication. *Acta Seismologica Sinica,17(4), 274-279.*

Wang J. (2007a). Historical earthquakes and a tsunami in Bohai Sea. *Acta Seismologica Sinica, 20(5), 584-592.*

Wang J., He X.S. & Li Y.Q. (2007b). Seismic characteristics of strong deep focal earthquakes and associated phenomena in Northeast Asia. *Advances in Geosciences, Vol.9: 23-39.* Solid Earth, Ocean Science & Atmospheric Science (2006). World Scientific Publishing Co.Pte.Ltd., Singapore.

Wang Z.G. (1985). The “long-term” activity of large earthquake areas. *Acta Seismologica Sinica*, *7(3)*, *254-266* (Chinese with English abstract).

Deriving Source Time Function and Moment Tensor from Moment Tensor Rate Functions

Wéber Z (1)

(1) Seismological Observatory of the Hungarian Academy of Sciences, H-1112 Budapest, Meredek u. 18., Hungary, weber@seismology.hu

Keywords: source time function, moment tensor, moment tensor rate functions, earthquake source mechanism, nonlinear inversion

Introduction

Moment tensor rate functions (MTRFs) are the most general description of a seismic point source. The MTRF description of an earthquake allows the moment tensor to vary arbitrarily as a function of time. This variability can represent changes in faulting geometry during the rupture process as well as the simultaneous rupture of two or more different faulting geometries. Since there is a linear connection between seismograms and the MTRFs, the determination of the MTRFs is a linear inverse problem. Several investigators have taken advantage of this desirable characteristic (e.g., Sipkin 1982, Koch 1991, Sileny at al. 1992, Panza & Sarao 2000, Wéber 2006).

After finding the MTRFs, most researchers take the reasonable scientific approach that we should seek to determine the fewest number of earthquake parameters that will still provide an adequate explanation of the data. Thus, we should try to represent an earthquake by just one moment tensor and one source time function (STF), if possible. This approach is particularly justified when dealing with weak local events. However, the quantitative implementation of the above idea is tricky because extraction of a moment tensor and STF from the MTRFs is essentially a nonlinear inverse problem. Furthermore, due to errors and incompatibilities in the observed seismograms, as well as the incomplete knowledge of the velocity distribution and earthquake hypocenter, the inversion for the MTRFs always produces a time-varying moment tensor.

The problem of decomposing the MTRFs into a time-invariant moment tensor and an STF has already been addressed by some authors. Ruff and Tichelaar (1990), for example, determine the STF by averaging the MTRFs with weights related to the errors of the individual MTRFs. Vasco (1989) puts the individual MTRFs into the columns of a matrix and uses principal component analysis to find the appropriate STF. Sileny (1998) solves the nonlinear inverse problem by a genetic algorithm to find the global minimum of the highly irregular objective function.

This paper introduces a new technique to retrieve the best moment tensor and STF from the MTRFs obtained by waveform inversion. In order to allow only forward slip during the rupture process, we impose a positivity constraint on the STF. The method is thoroughly tested by the decomposition of synthetic MTRFs generated for simple point sources as well as for complex mechanisms. Then, it is applied to a local event that occurred in the central part of the Pannonian basin.

Materials and Methods

Using the moment tensor representation for body waves, the *j*th component of the far-field displacement seismogram for a point source approximation may be written as (Aki & Richards 1980, Sipkin 1982)

$$u_j(\mathbf{r},t) = \sum_{k=1}^{6} m_k(t) * g_{jk}(\mathbf{r},\mathbf{h},t) \tag{1}$$

where $m_k(t)$ are the six independent moment tensor rate functions (MTRFs), $g_{jk}(\mathbf{r},\mathbf{h},t)$ the corresponding Green's functions, **r** is the position of the receiver, and **h** the hypocenter. The symbol * denotes temporal convolution. This equation expresses a direct linear connection between the seismograms and the MTRFs, allowing us to use a linear inverse method to estimate both the MTRFs and their model covariance matrix.

However, when the focal mechanism is considered as constant in time during the rupture process, all of the $m_k(t)$ components have the same time dependence $s(t)$:

$$m_k(t) = M_k \cdot s(t) \tag{2}$$

where M_k are the six independent, time-invariant elements of the moment tensor and $s(t)$ is the STF.

The aim of this paper is to present a method for retrieving the moment tensor and STF from the MTRFs estimated earlier by waveform inversion. Unfortunately, the reparameterization of the source description from $m_k(t)$ to $M_k \cdot s(t)$ makes the simultaneous estimation of M_k and $s(t)$ a nonlinear inverse problem. Furthermore, the problem becomes even more complicated if we impose a positivity constraint on the STF. The positivity constraint is necessary to guarantee a physical sense of the STF, because it allows only forward slips.

In order to find the optimum moment tensor and STF to the nonlinear problem (2), we search for the solution to the following minimization problem:

Minimize $E = \sum_{k=1}^{6} \sum_{i=1}^{N} \left| w_{ki} \left(m_{ki} - M_k s_i \right) \right|^p$

subject to the constraints (3)

$$s_i \geq 0$$

$$\tau \sum_{i=1}^{N} s_i = 1$$

where *i* denotes the time index, *N* is the length of the MTRFs and STF in number of samples, τ the sampling interval, and w_{ki} represent the positive weights (usually the inverse of the standard deviation of the MTRFs). The second constraint imposed on the STF ensures that the decomposition of the MTRFs is unique and the resultant moment tensor correctly defines both the geometry and the seismic moment of the inspected earthquake.

If *p* is chosen to be 1, Eq. (3) involves a linear programming problem. On the other hand, if *p=2*, then a non-negative least squares problem has to be solved. Throughout this paper we employ the L_1 norm minimization technique (*p=1*).

By the inspection of Eq. (2), one can easily recognize that the inversion problem is linear in the moment tensor elements M_k, keeping $s(t)$ fixed, and it is also linear in $s(t)$, keeping

M_k fixed. This simple relationship suggests the following iteration procedure to estimate the moment tensor and STF from the MTRFs by minimizing the error function defined in Eq. (3):

Step 1: Define the initial guess, $\mathbf{M}^0$, for the moment tensor.
Step 2: Estimate the STF, keeping M_k fixed, by solving Eq. (3).
Step 3: Estimate the moment tensor, keeping $s(t)$ fixed, by solving Eq. (3).
Step 4: Calculate the value of *E* for the moment tensor and STF just estimated.
Step 5: If *E* has not changed significantly relative to the previous iteration step (ΔE is less than a predefined threshold value), the iteration is stopped. Otherwise, go to Step 2.

As for any nonlinear inverse problem, the initial guess of the model parameters should be in the vicinity of the global minimum of the error function in order to not get trapped in a local minimum during the minimization procedure. According to our experience, the initial moment tensor can be reliably estimated from the MTRFs: if the elements of $\mathbf{M}^0$ are set equal to the corresponding MTRF values at the time instant when the greatest amplitude appears in the MTRFs, the proposed inversion method converges in a few iteration steps.

Estimating uncertainties in the retrieved model parameters is a must for all inversion procedure. The problem of error estimation in the case of the original MTRF inversion problem (Eq. (1)) is easily solved, since the equations are linear. Therefore, we can readily assume that both the MTRFs and their variances are available for further analysis. We then generate a set of 1000 trial MTRFs, by assuming a Gaussian random distribution, based on the previously calculated MTRFs and their variances. Then each generated time-dependent source mechanism is decomposed into a time-invariant moment tensor and the corresponding STF. The distribution of the resulting set of 1000 moment tensors and STFs approximates well the posterior probability distribution of the focal mechanism. Once the moment tensors are retrieved, their principal axes are deduced. Then each moment tensor is decomposed into an isotropic part, representing an explosive or implosive component, and into a deviatoric part, containing both the double-couple (DC) and the compensated linear vector dipole (CLVD) components. Finally, the resulting 1000 mechanisms are displayed on the focal sphere as a scatter plot representing the uncertainty of the moment tensor.

In this study, the method of Riedesel & Jordan (1989) is employed to display the scatter plot of the moment tensor solution. The principal vectors of a moment tensor define the tension (T), neutral (N) and compression (P) axes, while the principal values give their magnitudes. In the principal axis system, various unit vectors can be constructed using various linear combinations of the principal vectors. The vector that describes a general source mechanism is MT, a DC source mechanism has the vector representation DC, the vector corresponding to a purely isotropic source is the vector ISO, and two possible CLVD vectors can also be defined (Jost & Herrmann 1989). The scatter plot for the MT vector, together with the DC, ISO and CLVD vectors corresponding to the best moment tensor solution are then plotted on the surface of the focal sphere. The great circle that connects the DC and CLVD vectors on the unit sphere defines the subspace on which MT must lie for a deviatoric source. The distribution of the MT scatter plot with respect to the DC, ISO, and CLVD vectors informs us on the significance of the DC, ISO and CLVD parts of the solution: if the vector DC lies within the MT scatter plot, the mechanism is a DC; for a reliable CLVD solution, the MT scatter plot lies on top of one of the CLVD vectors; and when the MT scatter plot lies off the deviatoric great circle, the isotropic portion is reliable.

Results and Discussion

A set of tests with synthetic MTRFs have been performed with the intention of showing the capability of the proposed inversion method to retrieve the moment tensor and STF.

In the course of the tests, synthetic MTRFs are computed for an assumed STF and fault geometry. These MTRFs are considered as input data for the proposed inversion method, and the fault geometry and STF used in the computation are the 'correct' source parameters to be estimated. Then the MTRFs are decomposed into an STF and moment tensor as described in the previous section.

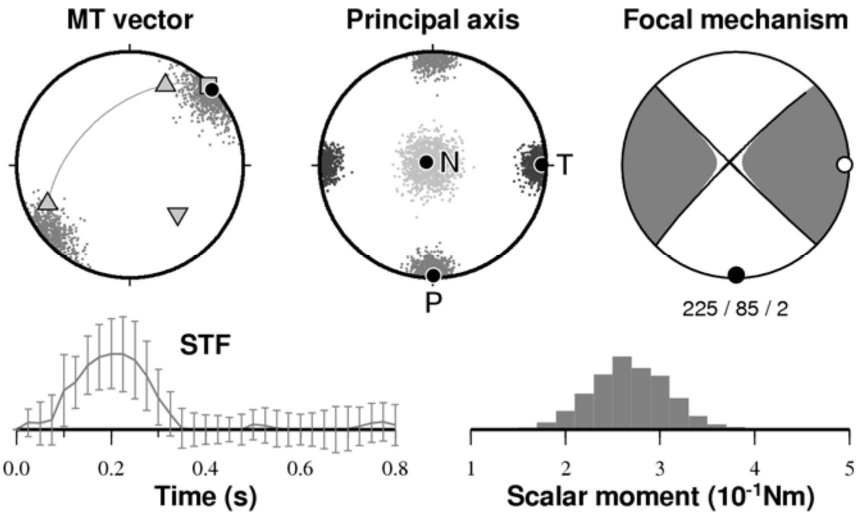

Figure 1. Decomposition of the noisy synthetic MTRFs generated for a vertical strike-slip mechanism. The error bars shown on the plot of the source time function (STF) are constructed for the 95 per cent confidence level. The histogram illustrates the uncertainties in the scalar seismic moment. For displaying the scatter plot of the moment tensor (MT), the method of Riedesel & Jordan (1989) is employed (symbols: solid circle: MT vector; square: DC vector; triangles: CLVD vectors; inverse triangle: ISO vector). Below the beach ball representation of the deviatoric part of the mechanism, the focal plane parameters are shown (strike/dip/rake, in degrees). Equal area projection of lower hemisphere is used.

For the generation of the synthetic MTRFs, we use a 0.3 s long trapezoidal STF with 0.05 s rise time representing a seismic source with $M_0 = 0.2$ Nm scalar moment. White noise with variance reaching 20 per cent of the peak amplitude of the MTRFs is then generated, filtered by a bandpass filter from 1 to 5 Hz, and superimposed on the synthetic data.

The first source used for generating the synthetic MTRFs is a vertical strike-slip with strike 45º, dip 90º and rake 0º. Fig. 1 illustrates the results of the proposed inversion method. The error bars shown on the STF plot are constructed for the 95 per cent confidence level. The variance of the STF has been estimated from the 1000 trial solutions as described in the previous section. The only peak of the STF closely resembles the trapezoidal STF used to generate the MTRFs. According to the scatter plots of the source parameters, the retrieved mechanism is also in good agreement with the strike-slip mechanism to be reconstructed. The MT scatter plot is concentrated around the DC vector and the best MT vector practically coincides with the pure DC solution. The principal axes are also well defined, while the scalar moment is slightly overestimated. We can conclude that the reparameterization of the MTRFs has been able to successfully reconstruct the correct source mechanism.

To model the effects of extended sources, two subevents are considered with the same seismic moment and STF. The first subevent has a vertical strike-slip mechanism with strike 45º, dip 90º and rake 0º, while the mechanism of the second subevent is defined by strike 20º, dip 60º and rake 30º. We assume that the second subevent is triggered by the first one with a time offset of 0.1s.

Since the STF has a time duration of 0.3 s, the MTRFs cannot resolve the complex nature of the above described event. In this case the result of the reparameterization algorithm should be a combination of the two subevents. This composite mechanism can be approximated by a

DC component with strike 33º, dip 69º and rake 13º in addition to an about 30 per cent CLVD part.

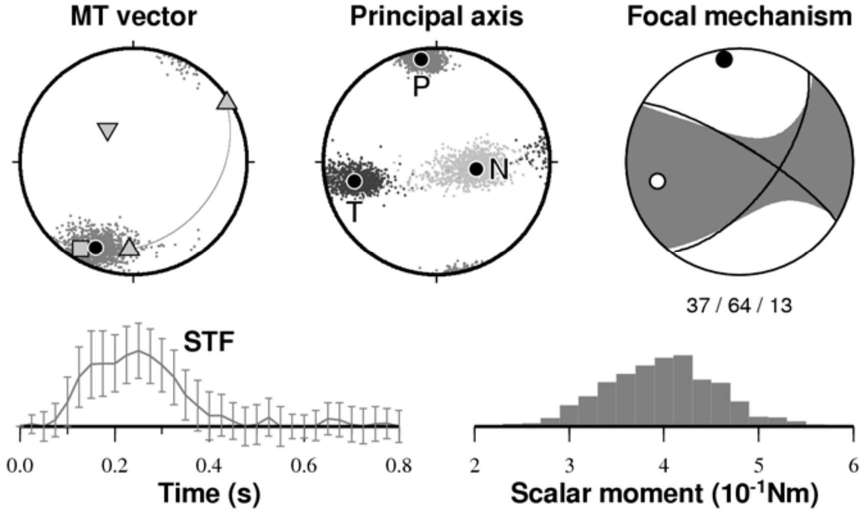

Figure 2. Decomposition of the noisy synthetic MTRFs generated for a seismic source composed of two overlapping DC mechanisms. For details see the caption of Fig.1.

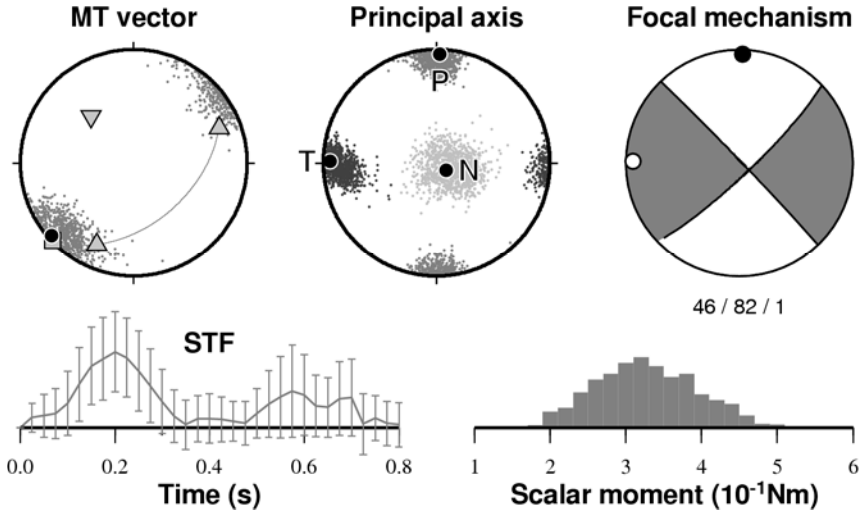

Figure 3. Decomposition of the noisy synthetic MTRFs generated for a seismic source composed of two well separated DC mechanisms. For details see the caption of Fig.1.

The solution of the proposed inversion technique approximates well the composite mechanism of the two subevents (Fig. 2). Because the first subevent has just the same strike-slip mechanism as the one investigated earlier, it is worth comparing the two results (cf. Figs 2 and 1). The uncertainties of the MT vector and the principal axes for the complex event are larger than those for the pure strike-slip mechanism: the scatter plots of the N and T axes are stretched in such a way that a rotation of the mechanism around the P axis is possible. According to our expectations, the STF has been broadened, but the two subevents cannot be resolved. The obtained CLVD percentage is fairly close to the theoretical one (35 vs. 30 %). Similarly, the composite scalar moment is also well determined.

If the second subevent is delayed by 0.4 s with respect to the first one, the two subevents are clearly resolved by the MTRFs. The MTRF reparameterization algorithm, however, can resolve only the first subevent (Fig. 3). The retrieved STF has two lobes, but the second lobe is statistically not significant at the 95 per cent confidence level. Moreover, the second part of the MTRFs is not fitted at all (not shown here). The retrieved moment tensor corresponds to that of the first vertical strike-slip subevent, but its uncertainty is larger than that for the single vertical strike-slip event (cf. Figs 3 and 1). The derived scalar moment is significantly underestimated: its most probable value is well below the theoretical moment (0.4 Nm).

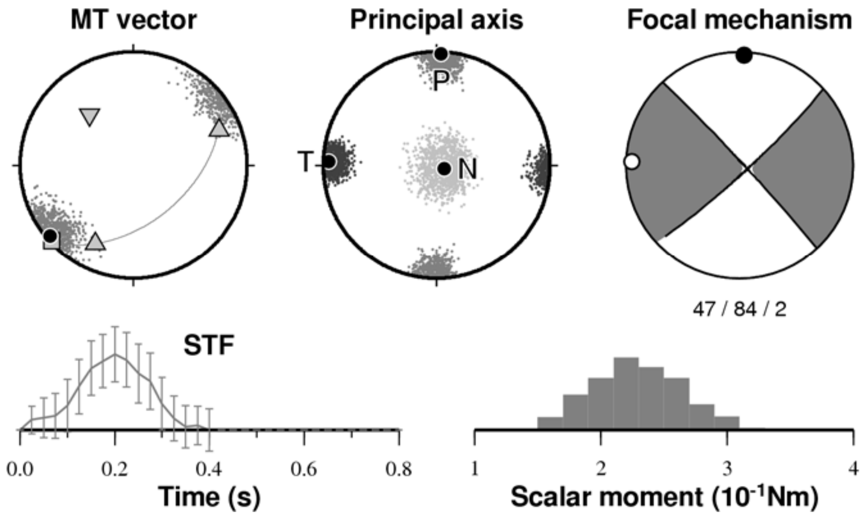

Figure 4. Decomposition of the first half of the noisy synthetic MTRFs generated for a seismic source composed of two well separated DC mechanisms. For details see the caption of Fig.1.

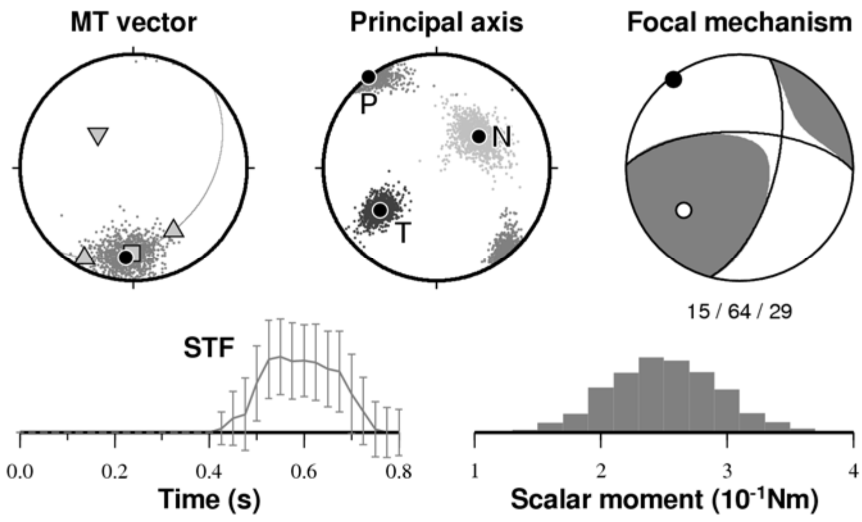

Figure 5. Decomposition of the second half of the noisy synthetic MTRFs generated for a seismic source composed of two well separated DC mechanisms. For details see the caption of Fig.1.

Then, a natural step is splitting the MTRFs into subintervals and allowing a different mechanism in each of them. Now, if we split the MTRFs into two subintervals with equal duration and perform the MTRF decomposition in these subintervals separately, we arrive at the solutions shown in Figs 4 and 5.

The reparameterization of the first subinterval also results in the vertical strike-slip mechanism, but the uncertainties of both the STF and moment tensor are much less than when decomposing the whole MTRFs (cf. Figs 4 and 3). Indeed, the uncertainty of the solution is practically the same as that for the single vertical strike-slip event (cf. Figs 4 and 1). When decomposing the second subinterval of the MTRFs, the retrieved moment tensor approximates well the mechanism of the second subevent (Fig. 5). Since the signal-to-noise ratio is lower in the second subinterval than in the first one, the uncertainties are greater than for the first subevent.

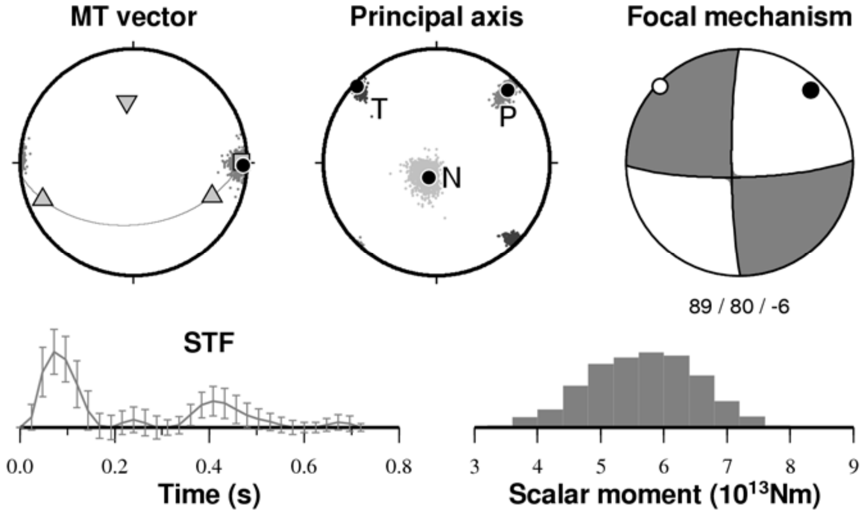

Figure 6. Decomposition of the MTRFs obtained for a local earthquake that occurred in the Hungarian part of the Pannonian basin. For details see the caption of Fig.1.

Finally, we illustrate the proposed method through the MTRF decomposition for a local earthquake that occurred in the Hungarian part of the Pannonian basin. The MTRFs were estimated from the observed seismograms by the method described in Wéber (2006) and then decomposed using the algorithm discussed in this paper.

The retrieved STF has two peaks significant at the 95 per cent confidence level (Fig. 6). The main energy release lasts about 0.15 s, while the second one is concentrated around 0.4 s. The reliability of the second peak is, however, much less than that of the main one. The MT scatter plot is fairly small in dimension, that is the source parameters are determined with high reliability. It contains the DC vector, thus, a pure DC may be the solution of the inversion. Indeed, the MT vector practically coincides with the DC vector. The tightly confined zones of the principal axes allow only a small variation of the orientation of the mechanism.

Conclusions

Three-component waveform data present us with an opportunity to detail the properties of seismic sources. Linear inversion of body waves for the time-varying MTRFs is a powerful method for studying such data. The method illustrated in this paper is able to retrieve simultaneously the STF and the full seismic moment tensor from the MTRFs obtained earlier. The error analysis, carried out by using a bootstrap approach, allows us to estimate and display the uncertainties of the source parameters. On the basis of the resulting moment tensor uncertainties, the statistical significance of the DC, ISO and CLVD parts of the solution can be readily assessed.

Tests on synthetic data indicate that the presented algorithm gives good results for both simple and complex sources. Confidence zones for the retrieved STFs are usually fairly large. The mechanisms, on the other hand, are mostly well resolved. The scalar seismic moment is also determined successfully: its histogram spreads not more than its most probable value. If the MTRFs cannot resolve the complex nature of a source, the proposed method yields the average source mechanism. If the subevents are well separated in time, their mechanisms can be estimated by appropriately splitting the MTRFs into subintervals.

The method has also been applied to a local earthquake that occurred in the central part of the Pannonian basin. The inversion of the previously determined MTRFs was successful. The isotropic component of the moment tensor solution is insignificant, implying the tectonic nature of the event. The principal axes of the source mechanism agree well with the main stress pattern published for the epicentral region (Bada et al. 1999).

Acknowledgments

The reported investigation was financially supported by the Hungarian Scientific Research Fund (No. K68308).

References

Aki K. & Richards P. (1980). Quantitative Seismology: Theory and Methods, Freeman, San Francisco, California.

Bada G., Horváth F., Gerner P. & Fejes I. (1999). Review of the present-day geodynamics of the Pannonian basin: progress and problems, *J. Geodyn., 27, 501-527.*

Jost M.L. & Herrmann R.B. (1989). A student's guide to and review of moment tensors, *Seism. Res. Lett., 60, 37-57.*

Koch K. (1991). Moment tensor inversion of local earthquake data - I. Investigation of the method and its numerical stability with model calculations, *Geophys. J. Int., 106, 305-319.*

Panza G.F. & Sarao A. (2000). Monitoring volcanic and geothermal areas by full seismic moment tensor inversion: are non-double-couple components always artefacts of modelling?, *Geophys. J. Int., 143, 353-364.*

Riedesel M.A. & Jordan T.H. (1989). Display and assessment of seismic moment tensors, *Bull. Seism. Soc. Am., 79, 85-100.*

Ruff L.J. & Tichelaar B.W. (1990). Moment tensor rate functions for the 1989 Loma Prieta earthquake, *Geophys. Res. Lett., 17, 1187-1190.*

Sileny J. (1998). Earthquake source parameters and their confidence regions by a genetic algorithm with a 'memory', *Geophys. J. Int, 134, 228-242.*

Sileny J., Panza G.F. & Campus P. (1992). Waveform inversion for point source moment tensor retrieval with variable hypocentral depth and structural model, *Geophys. J. Int., 109, 259-274.*

Sipkin S.A. (1982). Estimation of earthquake source parameters by the inversion of waveform data: synthetic waveforms, *Phys. Earth Planet. Inter., 30, 242-259.*

Vasco D.W. (1989). Deriving source-time functions using principal component analysis, *Bull. Seism. Soc. Am., 79, 711-730.*

Wéber Z. (2006). Probabilistic local waveform inversion for moment tensor and hypocentral location, *Geophys. J. Int., 165, 607-621.*

Seismicity of the Guba - Davachi Region of Azerbaijan Republic

Yetirmishli G.J. (1), Farajov V.A. (2)

(1) Republican Seismic Survey Center of Azerbaijan National Academy of Sciences and 9, Nigar Rafibeyli str., AZ1001, Baku, Azerbaijan, science@azeurotel.com
(2) Republican Seismic Survey Center of Azerbaijan National Academy of Sciences and 9, Nigar Rafibeyli str., AZ1001, Baku, Azerbaijan, vugarf@gmail.com

Deep sub-laterals (general-caucasian) and meridional (anti-caucasian) faults dissecting all territory of republic create complex block structure. Caucasus as a whole, the Azerbaijan territory as also the Guba-Davachi region of the Azerbaijan republic are part Alpine of folded system which is characterized by sufficient high seismic activity.And it is connected with discrepant tectonic motions in big depth faults of territory. It is supposed its forming in the Cainozoic according to thick the 3rd and 4th period sediments which have widely spread in the inside of Guba - Davachi depression which located in the northern-east part of the Big Caucasus Megaanticlinorium. In reality this depression is consider south-east part of the depression system of the front Caucasian. Concerning to Shahdagh – Khizi structure going down amplitude of Guba – Davachi structure elements which lie in enough big distances and which have formed in the orogenic development stage of the Big Caucasus, on Siyazan fault which intensive rising and separating diametrical zones is 1300-1600m [1]. It is known that related with this fault epicentres of numerous middle strong earthquake. According to form and measure of the Pleystoseyst areas are shown that depth of earthquakes near to the surface is 5-6 km and middle depths is 20-25km [2], 27.09.1925 with ml=4 , 13.10.1953 with ml=4, 26.03.1962 with ml=4.6 and middle strong earthquakes have happened in the result of tectonic movements in Siyazan fault.

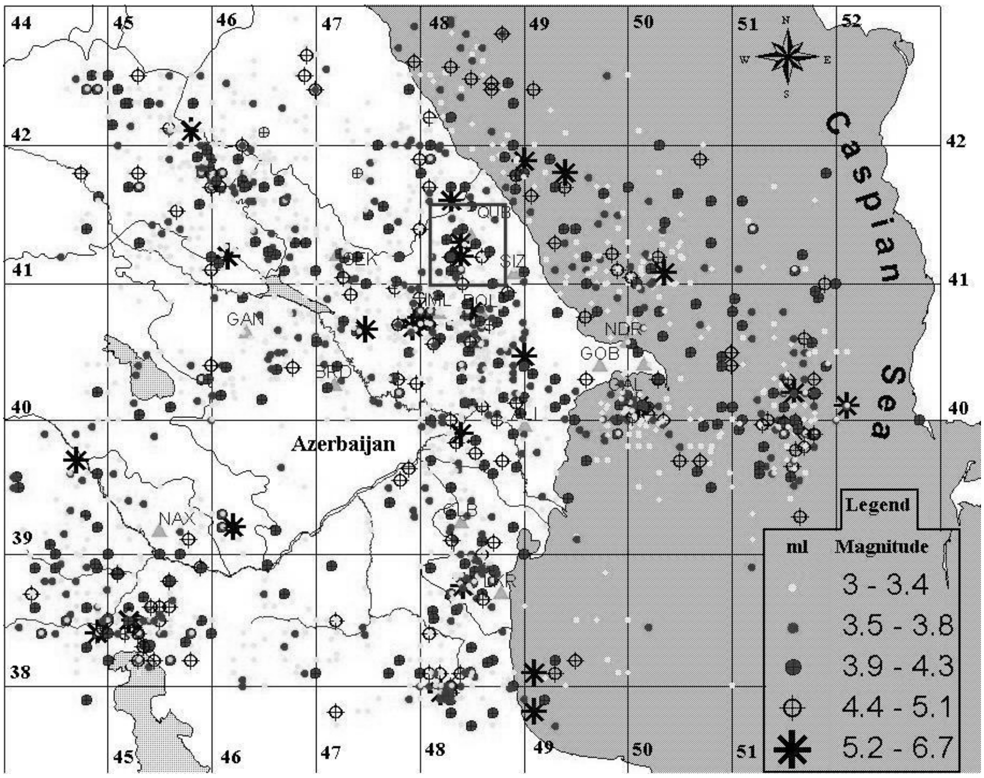

Figure 1: Distribution of epicentres at the Azerbaijan Republic and border regions (Seismicity 1965-2007 ml = > 3). Guba-Davachi region in red square.

Caspian and Khudat - Khachmaz tectonic deformations are another faults which playing important role in forming seismicity of Guba - Davachi depression. In 1966 year in the first fault zones has happened strong earthquake M=5.7 and has been felt in Laka, Vertil, Archuk villages by intensity of 7 point, Hulug, Usore, Khazri etc., villages by intensity of 6 point and center of Guba and Khudat districts by intensity of 5 point. Depth fault named Gurush-Gonagkend [3] located south from Guba town by liying north wing of central rise of the Big Caucasus breaks the system of the wrinkls which organized from sediments of hard carbonate and Yura aged schists. Here have been registered strong earthquakes where magnitude of earthquakes closes to 5. But at present seismic zoning scheme-map of Azerbaijan territory seismicity Fig.1 of Guba-Davachi region is valued 8 points and its parts close to border of Daghistan is valued by intensity of 9 points (by MSK-64 schedule) [4]. Also hundreds of weak seismic shocks are registered in the Azerbaijan territory in the year, definite part of these (we should note that big part of them happening mountainous and foothill areas) happened in the investigation territory [5]. Solution of the mechanisms of center of weak and middle eatrhquakes in the depression zones of Azerbaijan, including Guba-Davachi depression shows that tension of the stretching is directing transverse to lay direction of the zones of fault on horizontal flatness [6].

References

Ахмедбейли Ф.С. Неотектонические движения и их отражение в структуре предгорий Большого Кавказа (в пределах Азербайджана) Азерб. Гос. Изд-во. Баку 1962, 80 с.

Ахмедбейли Ф.С., Гасанов А.Г. Тектонические типы сеймических очагов Азербайджана. Баку, элм 2004, 130с.

Агомирзоев Р.А.Сейсмотектоника Азербайджанской части Большого Кавказа. Баку, Элм, 1987, 124 с.

Ахмедбейли Ф.С., Гасанов А.Г. и др. Новые схемы областей возникновения очагов сильнейших землетрясений и сейсморайонирование территории Азербайджана.

Каталог сейсмопрогностических наблюдений на территории Азербайджана в 1987 году. Элм, Баку, 1991, с.62-68.

AMEA RSXM – nin hesabatları. (1997-2006 – cı illər)

Агаларова Э. Б. Детальное исследование напряженного состояния сейсмических областей Азербайджана. Автореф. дисс. конд. геол. – мин. наук. , М. 1975, 18с.

Non Double Couple Seismic Sources and Stress State Inhomogeneity

Yunga S L (1), Lutikov A I (2)

(1) Institute of physics of the Earth, Russian academy of sciences, B.Gruzinskaya, 10, Moscow, 123995, Russia, syunga@ifz.ru
(2) Geophysical Survey, Russian academy of sciences, B.Gruzinskaya,10, Moscow, 123995, Russia, ail@ifz.ru

Keywords: focal mechanism, stress, seismic sources

Introduction

The use of earthquake focal mechanisms or seismic moment tensors for analysis of seismotectonic deformation is a fundamental part of the modern geodynamics. As such, it has been widely used to evaluate, in a more or less independent manner, the nature of recent crustal deformations on scales ranging from global to regional and local. Tectonic deformations and other geodynamic manifestations may be viewed as a response of the Earth to stresses acting in its upper layers and resulting in such phenomena as seismicity and the modern relief, which is formed mainly during the neotectonic phase. For seismic manifestations we can identify the seismotectonic deformation component caused by manifold slips in earthquake sources (Molnar, 1983). The relationship between seismic and geodynamic processes is of great importance for understanding the nature of the plate tectonics. On the other hand, current seismological observations suggest that the pattern of seismic waves from some earthquakes cannot be produced by slip along a planar fault surface (Frohlich, 1994, 1995; Zhang, 1998; Vavrycuk, 2002). Other physical mechanism is required to explain the observed varieties of these non-double-couple earthquakes (Kuge, Lay, 1994; Nettles, Ekstrom, 1998). We propose that these earthquakes are complex, with the stress released on several nonparallel fault surfaces.

Materials and Methods

Data

The Harvard centroid moment tensor catalog has been analyzed to study NDC sources. Centroid-Moment-Tensor (CMT) solutions are produced on a routine basis for events with moment magnitudes (M_W) greater than about 5.5. The CMT method is described in several key references (Dziewonski, Woodhouse, 1983; Dziewonski, Cho, Woodhouse, 1981). The CMT catalog entries provide thorough and detailed description of earthquakes, including errors in seismic moment tensor components. In rather many cases the large non-DC component were just connected with a poor moment tensor solution. Naturally, such earthquakes have been excluded.

Methods of a regional scale

One of the traditional problems of geodynamics, in which focal mechanism solutions are used, particularly for zones of major strike-slip faults, is to determine the active part of a deep fault responsible for a movement (slip) caused by a catastrophic earthquake (Aki, Richards, 1980). Another approach is based on the generalization of focal mechanisms in the framework of seismotectonic deformations (STD), in case if specific features of the regional deformation field can be analyzed (Yunga, 1996; Lukk, Yunga et al, 1995). STD or seismic strain rate tensor is determined as a normalized sum of local seismic moment tensors (or centroid moment tensors) for a representative number of seismic events. Please note that the analysis of all presently available statistics on focal mechanisms for the entire world provides a comprehensive seismotectonic deformation picture. Uniaxial compression, strike-slip movement as well as extensional environment were clearly revealed.

Methods of a local scale

On the local scale the stress state and deformation process can be investigated using CMT-solutions, especially for the NDC earthquakes (Dziewonski et al, 1981). Non double couple sources are usually considered in a framework of the hypothesis that the process of seismic rupture can be viewed as a result of complicated fault geometry and its segmentation. The present study focuses on the comparison of the deformation modes of the NDC sources with the states of stresses in its vicinity. The states of stresses are determined based on a first approximation summation of seismic moment tensors. A measure of the NDC part of moment tensor or deformation mode is described by the Lode-Nadai coefficient, which corresponds to eigenvalues of characteristic equation of considered tensor. This parameter is of particular interest as it describes a deformation mode.

Coefficient Lode-Nadai μ_{CMT} was used for the specification of NDC-measure, μ_{CMT}=3 $M_2/(M_1-M_3)$, where M_1 M_2, M_3 are principal values of seismic moment tensor Mij ($M_1 \le M_2 \le M_3$), (abs (μ_{CMT})≤1).

Analytical approach is found to reveal reliability of the NDC measure taking into account the values of seismic moment tensor errors (Yunga, Lutikov, Molchanov, 2005).

Results and Discussion

Currently, most authors relate geodynamic features to horizontal movements of lithospheric plates. In collision zones the oceanic lithosphere undergoes subduction, plunging into the mantle, and the continental lithosphere is compressed, with both compensated by the formation of a new oceanic lithosphere in spreading zones (Yunga, 1996). Since spreading is known to be compensated mainly by subduction, the role of the compression within the continental lithosphere needs to be illuminated at both global and regional scales.

For example, it is generally accepted that the actual background longitudinal compression of the Alpine-Himalayan belt formed at the Mesozoic passive margin of the ancient ocean neo-Tethys is consistent with key requirements of plate tectonics and with a pressure induced by largest plates (African, Indian-Australian, and Pacific), which transfers across a buffer mosaic of smaller plates (Arabian, Tibetan, Tarim, Amur, Okhotsk, and others) to the Eurasian Plate.

Deformations of other orientations and types, which are caused by superposition of other factors probably acting under neotectonic and recent conditions, develop in particular zones: at the flanks and in the central regions of the Alpine-Himalayan belt, against the regional seismotectonic background reflecting the plate collision effects in the characteristic latitudinal (at the flanks), or longitudinal orientation of compression (Yunga, 1996; Lukk, Yunga et al, 1995). Such zones of change in the seismotectonic deformation type are noted at the flanks of the Baikal rift and in the Olekma-Stanovoi seismic belt, Russian Far East.

This key circumstance allows us to estimate the intensity of collision processes relative to other geological factors using an effect of superposition of the stress fields of the first and second levels. In particular, in the Olekma-Stanovoi seismic belt, which extends away from the subduction zone of the Pacific Plate to the west, the gradual weakening of the stresses caused by subduction may be determined by the rearrangement of the prevailing orientations and types of seismotectonic deformation. In this area the megaregional stresses transferred to the continental plate through a complex system of microplates and blocks from the Pacific Plate appear to be weakening with distance from the boundaries of the megaplates, so that the regional and local processes are clearly manifested on this background. On the other hand the collision effects of the Pacific Plate on the Kurile-Kamchatka and Aleutian subduction zones is much more stronger.

A tectonophysical interpretation is proposed to highlight the role played by stress factor in the local kinematics of structural discontinuities during the seismic rupture process.

Most of the accumulated seismic strain is released by large earthquakes. So it is most attractive to perform an analysis of large NDC earthquakes, especially with the same type of NDC, and then compare it with the deformation mode. To estimate the later we calculate STD in 1.5 degree vicinity surrounding an epicenter of an initial earthquake. Such NDC earthquakes, their parameters, and the results of STD calculation are presented in tables 1, 2.

Table 1. Parameters of large NDC earthquakes.

N	Year	Month	Day	M_S	φ	λ	H	Region
1	1976	05	05	6.8	-29.93	-177.84	35	KERMADEC ISLANDS
2	1977	04	01	6.0	27.55	56.33	29	SOUTHERN IRAN
3	1977	05	30	6.0	52.43	-169.71	33	FOX ISLANDS, ALEUTIANS
4	1977	11	18	5.9	-4.35	102.02	33	SOUTHERN SUMATERA
5	1981	07	06	7.0	-22.26	171.73	33	LOYALTY ISLANDS
6	1982	09	28	6.1	-24.17	-176.75	40	SOUTH OF FIJI ISLANDS
7	1983	03	23	6.2	-6.62	154.61	41	SOLOMON ISLANDS
8	1984	04	06	6.0	-55.49	147.06	10	MACQUARIE ISLAND
9	1984	07	16	5.9	-55.26	-129.47	10	S PACIFIC CORDILLERA
10	1984	12	30	6.9	-36.73	177.50	33	OFF E CST NORTH IS.,N.Z.
11	1985	09	26	6.9	-34.63	-178.69	33	SOUTH OF KERMADEC IS.
12	1987	02	06	6.0	36.88	141.71	36	NR E COAST HONSHU,
13	1987	09	27	6.6	10.76	-86.40	33	COSTA RICA
14	1990	08	05	6.0	36.30	141.08	42	NR E COAST HONSHU,
15	1991	02	16	5.7	48.22	154.37	44	KURIL ISLANDS
16	1991	03	03	6.1	-21.83	-175.18	43	TONGA ISLANDS
17	1992	05	29	5.7	31.22	141.75	19	SOUTH OF HONSHU
18	1992	11	06	6.0	38.08	26.95	17	AEGEAN SEA
19	1993	06	18	6.7	-28.54	-176.85	20	KERMADEC ISLANDS
20	1995	04	01	5.6	52.28	159.13	47	KAMCHATKA TRENCH
21	1995	06	27	6.3	-17.23	66.83	10	MASCARENE ISLANDS
22	1995	09	17	6.3	-17.25	66.63	10	MASCARENE ISLANDS
23	1995	11	24	6.3	44.54	149.09	33	KURIL ISLANDS
24	1996	01	30	6.7	-32.83	-178.27	33	SOUTH OF KERMADEC
25	1997	12	05	6.5	53.75	161.75	33	KAMCHATKA TRENCH
26	1999	12	10	6.2	-36.21	-97.32	10	WEST CHILE RISE
27	2004	11	28	6.1	-26.52	-113.83	10	EASTER ISLAND REGION
28	2005	01	27	6.0	8.02	94.15	10	NICOBAR ISLANDS, INDIA
29	2005	04	07	5.9	0.63	97.39	30	NIAS REGION, INDONESIA

Table 2. Results of STD calculation and its comparison with parameters of NDC earthquakes.

N	N_{STD}	N_{NDC} total	N_{NDC} same signes	μ_{CMT}	μ_{STD}	Σ	Δ_{CMT}
1	219	50	43	0.23	-0.01	-	0.03
2	41	7	7	0.21	0.08	y	0.13
3	104	14	13	0.21	-0.04	-	0.07
4	105	15	12	0.22	-0.05	-	0.07
5	94	21	18	-0.42	0.15	n	0.03
6	109	15	12	0.47	-0.08	n	0.05
7	195	20	17	0.30	-0.06	-	0.07
8	36	10	10	-0.21	-0.02	-	0.08
9	39	8	8	-0.31	-0.05	-	0.07

10	30	10	10	-0.22	-0.56	y	0.06
11	65	18	14	0.41	-0.05	-	0.03
12	127	16	15	0.23	0.04	-	0.05
13	75	9	9	0.30	0.07	y	0.16
14	141	18	17	0.46	-0.01	-	0.07
15	89	9	8	0.36	-0.03	-	0.07
16	186	35	24	0.25	-0.01	-	0.05
17	69	15	12	0.25	0.08	y	0.09
18	27	9	8	-0.44	-0.51	y	0.05
19	195	46	35	0.24	-0.05	-	0.03
20	122	17	13	0.27	0.03	-	0.03
21	22	7	7	-0.36	-0.03	-	0.10

In the table 2 N_{STD} is the total number of CMT used in the calculation of STD, $N_{NDC\text{-}total}$ is the total number of NDC events in the vicinity of main earthquake, $N_{NDC\text{-}same\ signs}$ is the number of NDC events with the same signes in the vicinity of main earthquake. μ_{STD} gives type of STD; μ_{CMT} is NDC measure of CMT, Σ is the result of comparison μ_{STD} with μ_{CMT} (yes if coincided), Δ_{CMT} is the uncertainty of normalized CMT**.**

This technique, together with the construction of diagrams of principal axes, allows us to analyze the stress-field pattern and to determine the deformation modes of faulting and fracturing, which may take place at a small scale in earthquake focus, as well as at a regional scale within a geological unit.

Based on the results of this analysis we test the validity of the self-similarity assumption. In nine cases these assumption meet definitely positive answer, marked as "yes". Only in two cases answer was definitely "no". In eighteen cases deformation modes were poorly resolved and could not be used to distinguish local and regional deformation regimes.

In some typical examples of large NDC EQs are shown the P-, T-diagrams, as well as nodal line of an average mechanism (fig.1). The STD pattern, as well as individual NDC diagrams, is represented.

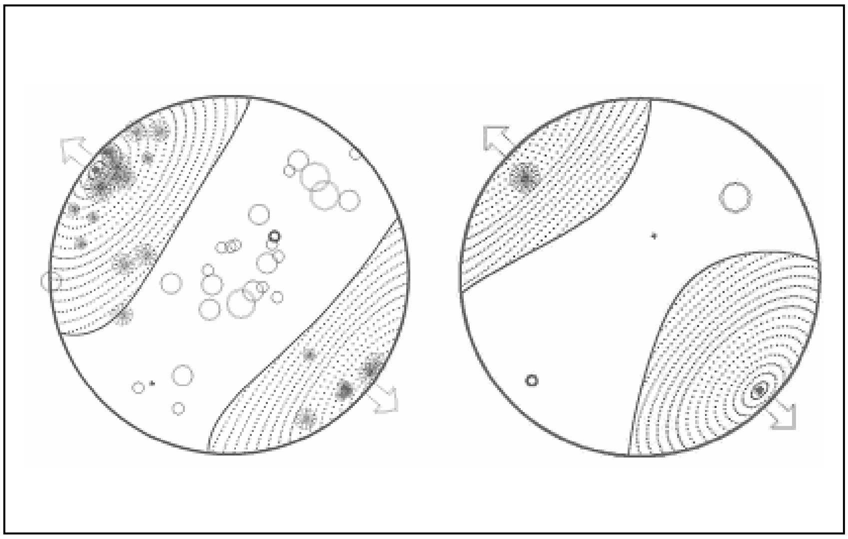

Figure 1. The diagrams of STD (left) and NDC (right) tensors in the vicinity of earthquake 84/12/30 (Tabl. 1). P-axes are shown by filled circles, and T-axes are marked by open circles.

.

Our results indicate that among numerous geodynamic zones only twenty nine are characterized by an uniform NDC deformation mode. The majority of the NDC events have mixed NDC modes in their vicinities. This may be considered as an evidence for the inhomogeneity of a deformation mode as whole. Therefore, for the whole data set, in contradiction with this result, the scaling relations do not verify the self-similarity. This further implies that second order factors, such as hydrothermal or magmatic pore fluids in rocks, likely influence source characteristics and bring new complications in scaling relations.

In accordance to theoretical expectations the complex NDC seismic events occurred mainly in the regions of stress concentrations in this overcomplicated process. Thus, the complex micro-structure may course the stress intensity in the process zone to increase too much, so that the uniform regional plate tectonic stress field has not a significant influence (Yunga, Lutikov, Molchanov, 2005). The last consideration could not be considered as the only. The self-organized criticality (SOC) phenomenon has drawn much attention in connection with the seismic process (Turcotte, 1997, 1999). The system in a state of SOC oscillates about a state of marginal stability with a series of slip events. We propose that observed NDC events should be studied in terms of SOC methodology. Thus, in the terms of SOC these NDC events treated as non-steady deformation may be taken as examples of chaotic flows in nature.

Acknowledgments

The USGS and Harvard University kindly provided access to their centroid-moment tensor data. This work was partly supported by RFBR № 07-05-00436.

References

Aki K. & Richards P. (1980). Quantitative seismology, *Freeman & Co., San Francisco, Cal., V I, 557p., II, 373p.*

Dziewonski A.M., T.-A. Chou & Woodhouse J.H (1981). Determination of earthquake source parameters from waveform data for studies of global and regional seismicity, *J. Geophys. Res., 86, 2825-2852.*

Dziewonski A.M. & Woodhouse J.H. (1983). An experiment in the systematic study of global seismicity: centroid-moment tensor solutions for 201 moderate and large earthquakes of 1981, *J. Geophys. Res., 88, 3247-3271.*

Frohlich C. (1994). Earthquakes with Non-Double-Couple Mechanisms, *Science, 264, Iss 5160, 804-809.*

Frohlich C. (1995). Characteristics of Well-Determined Non-Double-Couple Earthquakes in the Harvard CMT Catalog, *Physics of the Earth and Planetary Interiors. 91, Iss 4, 213-228.*

Kuge K. & Lay T. (1994). Systematic Non-Double-Couple Components of Earthquake Mechanisms - The Role of Fault Zone Irregularity, *Journal of Geophysical Research. Solid Earth , 99, Iss B8, 15457-15467.*

Lukk A.A., S.L. Yunga, V.I. Shevchenko & M.W. Hamburger (1995). Earthquake Focal Mechanisms, Deformation State, and Seismotectonics of the Pamir-Tien Shan region, Central Asia, *Journal of Geophysical Research, 100, 20321-20343.*

Molnar P. (1983). Average regional strain dye to slip on numerous faults of different orientations, *J. Geoph. Res., B58, № 8, 6430-6432.*

Nettles M. & Ekstrom G. (1998). Faulting Mechanism of Anomalous Earthquakes Near Bardarbunga Volcano, Iceland. *Journal of Geophysical Research. Solid Earth., 103, Iss B8, 17973-17983.*

Turcotte D.L. (1999).Seismicity and self-organized criticality, *Phys.Earth Planet. Int., 111, 275–293.*

Turcotte D. L. (1997). Fractals and Chaos in Geology and Geophysics, 2nd ed., *Cambridge Univ. Press, Cambridge, 300p.*

Vavrycuk V. (2002). Non-double-couple earthquakes of 1997 January in West Bohemia, Czech Republic: evidence of tensile faulting, *Geophysical Journal International,149, 2 , 365-374*

Yunga S., Lutikov A. & Molchanov O. (2005). Non double couple seismic sources, faults interaction and hypothesis of self-organized criticality, *Natural Hazards and Earth System Sciences, 5, 11-15.*

Yunga S.L. (1996). Seismotectonic Deformation of the Northern Eurasian Fold Belts in the Neotectonic Phase. Izvestiya, *Physics of the Solid Earth, 32, No. 12. 955-974.*

Zhang J.J. (1998). Inversion of Surface-Wave Spectra for Source Parameters of Large Earthquakes Using Aspherical Earth Models, *Physics of the Earth and Planetary Interiors. V107, Iss 4, 327-350.*